

Peter C. Wille

Sound Images of the Ocean



with CD-ROM

in Research
and
Monitoring



Springer



ATLAS ELEKTRONIK

A BAE SYSTEMS COMPANY

Peter C. Wille

Sound Images of the Ocean
in Research and Monitoring



Peter C. Wille

Sound Images of the Ocean

in Research and Monitoring

With contributions of more than 120 sound image authors
and marine experts of 22 countries

With 452 Images

 Springer

Author

Professor Dr. Peter C. Wille

Kitzeberger Straße 31
24226 Heikendorf
Germany

Cover image: Seafloor relief of the *South Pacific Rise* near the *Wilkes Transform Fault*, a very fast spreading Mid Ocean Ridge (Sect. 5.2.4.1).

Image ©: J. R. Cochran, Lamont-Doherty Geological Observatory of Columbia University, Palisades, USA.

Multibeam system: Atlas Elektronik, type *Hydrosweep DS*, 12 kHz.

Library of Congress Control Number: 2005920699

ISBN-10 3-540-24122-1 Springer Berlin Heidelberg New York
ISBN-13 978-3-540-24122-5 Springer Berlin Heidelberg New York

This work is subject to copyright. All rights are reserved, whether the whole or part of the material is concerned, specifically the rights of translation, reprinting, reuse of illustrations, recitations, broadcasting, reproduction on microfilm or in any other way, and storage in data banks. Duplication of this publication or parts thereof is permitted only under the provisions of the German Copyright Law of September 9, 1965, in its current version, and permission for use must always be obtained from Springer. Violations are liable to prosecution under the German Copyright Law.

Springer is a part of Springer Science+Business Media

springeronline.com

© Springer-Verlag Berlin Heidelberg 2005

Printed in Germany

The use of general descriptive names, registered names, trademarks, etc. in this publication does not imply, even in the absence of a specific statement, that such names are exempt from the relevant protective laws and regulations and therefore free for general use.

Cover design: Erich Kirchner, Heidelberg

Typesetting: Büro Stasch · Bayreuth (stasch@stasch.com)

Production: Luisa Tonarelli

Printing: Stürtz GmbH, Würzburg

Binding: Stürtz GmbH, Würzburg

Printed on acid-free paper 30/2132/LT – 5 4 3 2 1 0



Foreword

A technical invention and its evolution during the last decades of the twentieth century, comparable to the invention of photography and X-ray imaging at the end of the nineteenth century, happened nearly unnoticed by the public. This evolution has created a special art of imaging considered impossible before: the ability to generate images of large areas of the ocean floor nearly as detailed as aerial photographs. These images are three-dimensional and generated by sound. Echo-sounding, invented already in the second decade of the last century, produced depth data along the ship's course but no images of the kind we are familiar with. Imaging requires covering a surface. The breakthrough of imaging the sea floor by three-dimensional sampling of its surface along broad stripes instead of lines became possible only with the concurrence of three fundamental technologies: precise and worldwide *satellite navigation*, high speed *computers* with storage of huge amounts of data and the hard- and software of *multibeam echosounders* of up to a hundred sound beams and more in parallel.

It is a peerless maritime imaging technology in kind, accuracy and resolution, and it deals with a unique documentation. It is the history of the ocean floor, imprinted in its relief, visualized by sound imaging. The deep sea floor has preserved its geodynamic history over many millions of years; on the continents most of such traces have been lost due to erosion. Imaging the ocean floor is exemplary for the role of scientific imaging: *it is the visualisation of the reality that has guided research, brought forth discoveries, and confirmed or refuted theoretical presumptions*. This applies in particular to fields of high complexity like marine geo-science, exploring the specific and significantly different interacting processes of the vast variety of ocean areas. High resolution sound imaging provides also a guide for follow up research applying non acoustic methods such as magnetometry, gravimetry, close-up photography and bottom sampling and -coring. But advanced sound imagery has become itself an indispensable diagnostic tool to identify fundamental processes reshaping the floor of the ocean.

The sound images presented in this book comprehend examples of quite different areas and formations of the world's oceans provided by more than a hundred image authors from institutions of over 20 countries. The amazing progress is evident from the age of the images shown: the majority are a few years old at most. The progress encloses the development of further methods of sound imaging the sea, below, at, and above the sea floor. It has resulted in a broad and ever growing field of scientific, technical, economic, and governmental applications. These applications, their achievements and possibilities are definitely deserving of a sur-

vey. The fascination of the images, revealing widely unknown scenarios of the hidden side of our planet will inspire and raise interest of scientific neighbors and of non-experts. It will be a contribution to an interdisciplinary understanding of the subject of sound imaging the ocean which is in fact a common tool, connecting ocean research, utilization, and protection.

The understanding of the interaction between the hot interior of the Earth and its surface, the lithospheric plates causing volcanism and earthquakes, the rise of new sea floor at the mid ocean ridges and the processes of sea floor subduction at the opposite margins of the tectonic plates, is essentially based on acoustic imagery. This includes the outer relief as well as the internal structure. Comparable time spans of many million years of climate history are documented in the sediment stratification. It is part of the prehistoric diary of the Earth, resolved by advanced high resolution sub-bottom profilers, which also disclose sub-sediment morphologies and discover large deposits of hydrocarbons. Acoustic Doppler current profilers, together with other acoustic facilities and methods give us the features of ocean current systems, the Conveyor Belt of by far the largest amount of mobile heat energy on Earth, determining the climate of continents. It has been disclosed by acoustic means that current systems are guided by the sea floor relief far beyond the ridge crests. Marine acoustics quantifies also other processes of climate relevance like air intrusion into the sea. It has imaged coastal sediment motion like the migration of large dunes and various types of erosion and re-sedimentation up to past coastal slides of thousands of cubic kilometers with disastrous impact.

It is true: imaging the sea by sound has developed to an admirable degree of perfection but it cannot remove the fact that imaging of entire oceans is time consuming to say the least. It is realized with research- and hydrographic survey vessels proceeding not much faster than a bicycle as they cover the sea floor with a carpet of soundings, a few times the width of the water depth at most. Thus, only a minor part of the deep sea floor, in other words, of two thirds of the Earth's surface, is as yet known in as much detail as the surface of the moon.

The book compares the *slow but high resolution* acoustic imaging with another, *indirect* kind of ocean floor imaging: a *rapid but low resolution* method where satellite technology is the key requirement. Scanning the sea surface by satellite radar provides a coarse copy of the floor relief below by utilizing its varying local gravity. Undersea mass concentrations like large mountains attract the water above slightly more than the girdling abyssal plain, and deep valleys with their mass deficit correspondingly less, which causes bulges and dents respectively at the surface. This *gravity anomaly* method has revealed large scale structures of the ocean floor for the first time in their totality and in remote ocean areas. It has become an important guide to select sites of interest for detailed tectonic and geologic research relying on advanced ship-borne sound imagery. The overviews based on gravity anomaly, improved in resolution by blending with soundings are presented as global depictions and in comparison with high resolution acoustic imagery.

Limitation was necessary. Beyond scope are methods of acoustic underwater communication and remote control, in particular for offshore construction activities. Ocean surveillance and reconnaissance by Sonar in the framework of military defense is excluded as well – with the exception of acoustic sea mine hunting – although the navies also deal with acoustic imaging and naval underwater acous-

tic technology has often been the forerunner of ocean research applications. Nevertheless Naval officers, in particular Sonar-operators, need to familiarize themselves with the acoustic features of their environment, its various peculiarities and varying potential of natural camouflage, hiding or simulating targets of interest by acoustic similarities.

Some of the sea floor images of large areas with many details would require a much larger type area than a book can provide. These images are copied in addition for zooming on the CD attached to the book. The CD moreover contains several *Fledermaus*-versions of sea floor reliefs where choosing the preferred direction of view is essential. This is particularly necessary with the *Globe* containing the complete land and sea relief of our planet with a resolution of 5 arc minutes. The *Fledermaus-Globe* can be easily turned around the two axes with the PC-mouse and arbitrarily zoomed. Several virtual flight-animations through undersea landscapes of recent high resolution relief imagery and a quick-motion movie of dune migration from a panorama-echosounder are included as well. Some examples of different sea floor material acquired by the respective acoustic backscatter can be visualized as genuine 3D-depictions with red-green binoculars.

The book, covering a wide variety of special subjects of international sound imaging application in the sea is necessarily a composite product. The main part consists of course of the sound images, many of them unpublished, and scientific information provided by the image authors and their institutions. Most of the section texts and image captions including the introduction to the basic facts are written by the author of the book. The image-related texts are based on the correspondence with the various experts and image authors and have been reviewed by them. The correspondence included thorough discussions as to how to explain complex relationships to non experts and to condense the results to the essence of the investigation, the "message". Two key sections are complete articles specially written for the book by the respective experts. They are indicated by the authors' names, as well as a few others which have been essentially written or rewritten by the respective experts.

The book respects the reader who is interested in key technologies and achievements of ocean research but does not want to be confused with highly specialized terminology or wearied by complicated theory. The book therefore relies heavily on the direct, nearly self-explanatory evidence of the product of ocean acoustics: the authentic, quantitative sound image. There is strong emphasis on practical results in order to outline what we can expect in reality in accordance with the limits set by physics and environment. Mathematics are replaced by verbal explanations. An appendix includes some formal relations and the literature indexes of the subject sections refer to the related textbooks and recent original papers.

Altogether this way of generating an interdisciplinary special book provides much of the authenticity and actuality of congress proceedings and also much of the homogeneity of a normal textbook. The contributors provided their voluntary and generous collegial support because they consider such a book useful, even necessary.

Hans Werner Schenke
Alfred-Wegener-Institut
für Polar- und Meeresforschung



Foreword by the Sponsor

In this book, Peter C. Wille opens the hidden world of seafloor landscapes, which until now were nearly accessible exclusively to specialists. The impressive images presented here were generated during recent years by means of advanced echosounder systems of various techniques. The beauty of these sound images and their almost self-explanatory message will also fascinate other scientists and a wider public. The images have been contributed by 120 experts from 22 countries engaged in geosciences, offshore industry, offshore economy, surveillance and even archaeology.

The comparison of sound images of the sea floor with its coarse copy by the sea surface relief deformed by mass attraction of the seamounts below and recorded by satellite radar is of particular interest. It underlines the peerless role of high resolution acoustics but also the necessity to complete our insufficient knowledge of the deep sea floor world which is disclosed in detail by only a few percent as yet. But the sound images also reveal the necessity for protection because the future of mankind will depend to a great extent on the resources to be taken from the ocean volume and the seafloor.

For many decades now, our company has been one of the major players on the scene of ocean acoustic system development and production. In particular multi-beam systems and non-linear high resolution sediment echosounders facilitated the hydroacoustic examination of the seafloor. These activities encompass the whole range of hydroacoustic surveying equipment: from portable units for the survey of riverbeds and inland waterways to permanently installed systems for oceangoing research vessels. The acoustic data collected by research vessels have been processed in the images which are part of this book.

In the future, however, autonomous underwater vehicles (AUV) will increasingly be used for the research and inspection of the water volume, the seafloor and the structures built upon the seabed. These vessels will take over many of the tasks which until now could only be performed by complex and expensive research vessels. For these tasks, the AUV will have its own intelligence, very precise navigation systems, optical and acoustical sensors, communication and fuel cell energy and propulsion systems. The growing market of AUV will be expanded by products which can be summarized as *robotics*. In the years to come, not only the unmanned and autonomous exploration but also the automatic execution of manual functions will become possible in the “blue waters”. Comparable developments can be

seen in the military naval sector, where this trend is aptly described as *the sonars are leaving the ships*. Both markets are served by ATLAS ELEKTRONIK GmbH with products that are setting new trends as our multibeam echosounders did years ago. The further deployment of AUV will be analogous to the missions of space probes with the distinction that operations in the hydrosphere offer the benefit of repeated use.

Our commitment in the compilation of this book is characterized by our participation in the worldwide gathering of *Sound Images of the Ocean* through the provision of our multibeam- and sediment echosounders. Additionally, we realize that this largely unknown part of our blue planet, presented with this book, is worthy of appreciation by a wider audience.

ATLAS ELEKTRONIK GmbH
Bremen, December 2004

Manfred Meyersieck Manfred Siegel



Preface

The particular fascination evoked by many of the sound images of the sea floor presented in this book has changed its character since the 26th December 2004. Formations of scientific and general interest, where large parts of the sea floor, the tectonic plates, are being subducted under adjacent tectonic plates have now become a frightening subject of another dimension. The mechanisms of destruction of human settlements by tectonic processes were known before: the majority of earthquakes and volcanism happen at or near plate margins. History reports of giant waves, propagating at enormous speed, which devastated coastal areas. The Japanese, overrun by the largest number of this kind of deluge, generated by a sudden uplift of the overriding tectonic plate, named them *Tsunami*. Through the last four centuries nearly two dozen giant Tsunamis have been recorded, each of which killed from more than 2 000 up to 40 000 people. The Sumatra Tsunami of December 2004, when presumably more than 300 000 died and millions became homeless, is unparalleled in history however: an apocalyptic catastrophe. The earthquake magnitude 9.0 is one of the highest ever recorded and corresponds to the energy of 32 000 Megatons TNT. The disaster, unimaginable before, has created an overwhelming response in charity worldwide, but has made us aware again that we are living on the cool but fragile skin of a glowing globe of which we still know only little. The need for a global Tsunami warning system has become strikingly evident. Though earthquakes cannot be predicted, they can be detected, localized and measured in magnitude, and the arrival of resulting Tsunamis, propagating oceanwide, can be made known in advance to save human lives.

The compilation and preparation of this book was completed before the date that shocked the world. However, the publisher has agreed to insert an image of the sea floor relief with the epicenter area in the Indian Ocean. This image, on short notice personally prepared and provided by the Director of the Center for Coastal and Ocean Mapping, L. Mayer, USA, is based on the Sandwell and Smith predicted topography data from NGDC, available prior to the Sumatra Tsunami. Scientific evaluation of actual seismic records in detail and subsequent mapping of the area in near future by high resolution sound imaging will throw light on the origin of this tragedy.

This book is the first attempt to publish a comprehensive overview of the wide variety of acoustic applications in the fields of research, of utilization, surveillance and protection of the ocean. This sound image collection covering a large number of subjects and sites of the world's oceans and coastal waters is both interdisciplinary and international. It has been enabled by the generous support of more than 120 ex-

perts and sound image authors from 22 countries. The images have been selected as representative of the work of the image authors and their subjects. These subjects range from the evidence of plate tectonics and continental shift and from methane-hydrate deposits, containing more than twice the amount of all other carbon hydrates on Earth, to indications of ocean warming imaged by acoustic tomography; from submerged cities to historic ship wrecks; from large submarine canyons to huge landslides; from sea lane surveillance and biomass monitoring to images and sound tracks of whale echosounding and communication; from sub-polar ice imaging to steering of the Gulf stream by undersea topography; and from the Arctic Ocean to Antarctica. Unlike the continents and islands inhabited and shaped by man, the deep sea, much more than the continental shelf, is the exclusive territory of nature with marginal human impact hitherto, apart from relics of ship disasters and wars through the centuries and communication cables in the last few decades.

The book is not a high-resolution sound imaged atlas of the world's sea floor. Two-thirds of the globe is ocean, and only a low percentage of ocean floor has been sound imaged by advanced technology so far. Nevertheless, the book *does* provide a global atlas of the hidden side of the Earth, albeit in less detail. All available echosounder data – the sparse sounding lines in remote areas of the world as well as the denser measurements near coasts and sea lanes – has been merged with satellite radar data of the sea surface relief, providing a coarse copy of the sea floor beneath. The weak bulges and dents are generated by gravity anomalies which attract the sea volume above a submarine mountain slightly more than above a valley. The merger of these two independent data sets, combined to form a complete globe – a pioneering work by leading experts – is the best possible overview at present of the nearly infinite variety of sea floor formations. This overview has become indispensable as a guide for site selection of follow-on high resolution acoustic close-ups of the outer relief and the structure below, to reveal the details of processes for further on-site research. The CD included with the book allows zooming and turning of the relief globe, as well as of very large sound images.

The book demonstrates the capability of the various technologies of sound imaging as *diagnostic tools* – similar to ultrasonics in medicine – but the aesthetic appearance of many of these images evokes appreciation beyond mere information. The book is intentionally written for the non-expert who may be a scientist from a neighboring faculty. All comments and textual documentation accompanying the image collection, as well as the introduction to the basic facts of ocean acoustic imaging, have been reviewed and supplemented by the respective experts. The intention is to raise and maintain interest in those formations and processes of the ocean which are beyond the access of photography – by far the majority.

Peter C. Wille April 2005



Acknowledgments

The generous support of the book project by the subsequent sound image authors and marine experts is cordially and respectfully appreciated. These experts contributed sound images typical of their respective fields of work as original, unabbreviated files, often prior to their own publications and provided the related scientific and technical information together with text reviews, supplements, and literature. The willingness and patience to discuss the formulation of the scientific message for non-expert readers deserves particular respect. The names of researchers who provided supplementary reviews and revisions of image comments in the field of their special expertise for images provided by colleagues are indicated by an asterisk. Book sections and box insets written by image authors and other experts carry the respective names.

<i>Juan Acosta Yepes</i>	Geology and Geophysics Dept., Instituto Español de Oceanografía, Madrid, Spain (<i>Sect. 5.3.5, 5.6.1, 5.6.2</i>)
<i>Dr. Matina Alexandri</i>	Dept. of Marine Geology & Geophysics, Institute of Oceanography, Hellenic Centre for Marine Research, HCMR, Athens, Greece (<i>Sect. 5.6.4</i>)
<i>Tom Avsic</i>	Leibniz Institut für Meereswissenschaften an der Universität Kiel, Germany (<i>Sect. 6.1.3</i>)
<i>Pietro Basciano</i>	RESON MEDITERRANEAN SRL, Casalecchio di Reno, Italy (<i>Sect. 5.2.6, 7.1.3, 7.3.1</i>)
<i>Andrea Bellettini</i>	Nato Undersea Research Centre, La Spezia, Italy (<i>Sect. 7.1.5</i>)
<i>George Bernardel</i>	Law of the Sea Group, Geoscience Australia, Canberra, Commonwealth of Australia (<i>Sect. 5.2.2</i>)
<i>Manfred Bersch</i>	Institut für Meereskunde, Universität Hamburg, Germany (<i>Sect. 6.1.2</i>)
<i>Dr. Eckhard Bethke</i>	Bundesforschungsanstalt für Fischerei, Institut für Fischereitechnik und Fischqualität, Hamburg, Germany (<i>Sect. 6.3.1</i>)
<i>Andreas Beyer</i>	Alfred-Wegener-Institut für Polar- und Meeresforschung AWI, Bremerhaven, Germany (<i>Sect. 5.3.4, 5.3.6</i>)
<i>Dr. Daniel Bideau</i>	Institut français de recherche pour l'exploitation de la mer, Ifremer, Issy-les-Moulineaux Cedex, France (<i>Sect. 5.2.3</i>)

- Dr. Halim Birkan* Turkish Navy Department of Navigation, Hydrography and Oceanography, Istanbul, Turkey (*Sect. 5.6.5*)
- Prof. Dr. Dr. h.c. Leif Bjørnø* DIC, Department of Industrial Acoustics, Technical University of Denmark, Lyngby, Denmark (*Sect. 7.3.5*)
- Prof. Dr. Antje Boetius* Max-Planck-Institute for Marine Microbiology, Bremen, Germany (*Sect. 6.2.2*)
- Edoardo Bovio* Nato Undersea Research Centre, La Spezia, Italy (*Sect. 5.6.3, 7.1.4*)
- Prof. Dr. David L. Bradley** Applied Research Laboratory ARL, PennState University, United States of America (*Sect. 2.11*)
- Thomas Brüggemann* Bundesanstalt für Gewässerkunde, Koblenz, Germany (*Sect. 7.1.1*)
- Dr. Neville Ching* Land Information New Zealand (LINZ), New Zealand (*Sect. 5.5.4*)
- Robert A. Church* Marine Archaeology Section, C & C Technologies, Inc., Lafayette, United States of America (*Sect. 7.4.1*)
- Dr. James R. Cochran* Lamont Doherty Earth Observatory Palisades, United States of America (*Sect. 5.2.4*)
- Dr. Martin Dean* ADU, University of St Andrews, Fife, United Kingdom (*Sect. 7.3.2, 7.3.3*)
- Thomas Dehling* Bundesamt für Seeschifffahrt und Hydrographie BSH, Rostock, Germany (*Sect. 5.7.3, 7.1.1*)
- Kai-Martin Dührkop* RESON Niederlassung Kiel, Germany (*Sect. 7.1.4, 7.3.2*)
- Czesław Dyrzc* Captain, Hydrographic Office of the Polish Navy, Poland (*Sect. 7.1.4*)
- Michael Emmerich* Niederzier, Germany (*Sect. 7.3.3*)
- Dr. Rudolf Eandler* Baltic Sea Research Institute, Rostock-Warnemuende, Germany (*Sect. 5.7.6*)
- Dr. Neville Exon* Marine Regional Geology Group, Geoscience Australia, Canberra, Commonwealth of Australia (*Sect. 5.2.7, 5.3.6*)
- Dr. Gordon B. J. Fader* Geological Survey of Canada (Atlantic), Bedford Institute of Oceanography, Dartmouth, Nova Scotia, Canada (*Sect. 5.3.8, 5.3.9*)
- Prof. Dr. David M. Farmer* Graduate School of Oceanography, University of Rhode Island, United States of America (*Sect. 6.2.3*)
- Dr. Volker Fiekas* Forschungsanstalt der Bundeswehr für Wasserschall und Geophysik FWG, Kiel, Germany (*Sect. 2.9*)
- Dr. Jürgen Fischer* Leibniz-Institut für Meereswissenschaften an der Universität Kiel, Germany (*Sect. 6.1.2*)
- Dr. Jörg Förster* Forschungsanstalt der Bundeswehr für Wasserschall und Geophysik FWG, Kiel, Germany (*Sect. 3.6.3*)
- Prof. Dr. André Freiwald* Institut für Paläontologie, Universität Erlangen, Erlangen, Germany (*Sect. 5.3.4*)
- Dr. Leonard Gajewski* Operational Oceanography Department, Maritime Institute, Gdańsk, Poland (*Sect. 5.7.4*)
- Dr. James V. Gardner* Center for Coastal & Ocean Mapping CCOM, University of New Hampshire, Durham, United States of America (*Sect. 5.1.2, 5.2.5, 5.2.8*)

- Dr. Cem Gazioğlu** Istanbul University, Institute of Marine Sciences and Management, Istanbul, Turkey (*Sect. 5.6.5*)
- Dr. Eberhard Götze* Bundesforschungsanstalt für Fischerei, Institut für Fischereitechnik und Fischqualität, Hamburg, Germany (*Sect. 6.3.1*)
- Dr. Jens Greinert* Leibniz-Institut für Meereswissenschaften an der Universität Kiel, Germany (*Sect. 6.2.1*)
- Prof. Dr. Haflidi Haflidason* Department of Geology, University of Bergen, Norway (*Sect. 5.3.1*)
- Andrew W. Hall* courtesy: The PAST Foundation, Ohio, United States of America (*Sect. 7.4.1.3*)
- Prof. Dr. John K. Hall* Geological Survey of Israel, Jerusalem, Israel; on sabbatical: Center for Coastal and Ocean Mapping /Joint Hydrographic Center CCOM/JHC, University of New Hampshire, Durham, NH, United States of America (*Sect. 5.6, 5.6.7*)
- Dr. Dieter Hartwig** German Naval Association, Kiel, Germany (*Sect. 7.1.4.4*)
- Dr. Jun Hashimoto* Faculty of Fishery, Nagasaki University, Japan (*Sect. 5.2.2*)
- Dr. Jörn Hatzky* Bathymetrie und Geodäsie, Alfred-Wegener-Institut für Polar- und Meeresforschung AWI, Bremerhaven, Germany (*Sect. 5.2.6, 5.4.1, 5.5.2*)
- Prof. Dr. Jean Pierre Henriët* Renard Centre of Marine Geology (RCMG), University of Ghent, Belgium (*Sect. 5.3.4, 5.3.5*)
- Dr. Karl-Heinz Herwig* Forschungsanstalt der Bundeswehr für Wasserschall und Geophysik FWG, Kiel, Germany (*Sect. 6.2.3*)
- Richard Hill* Reson Offshore Ltd. (*Sect. 7.2.3*)
- Prof. Dr. Karl Hinz** Bundesanstalt für Geowissenschaften und Rohstoffe BGR, Hannover, Germany (*Sect. 5.5.1*)
- Constanze Hohmann* Nicola Engineering GmbH, Hamburg, Germany (*Sect. 5.5.3*)
- Egil Ingebretsen* Marine Surveys, Pipelines and Marine Operations, Norsk Hydro ASA, Norway (*Sect. 5.3.7*)
- Prof. Dr. Martin Jakobsson* Center for Coastal and Ocean Mapping CCOM, Joint Hydrographic Center, University of New Hampshire, United States of America (*Sect. 5.1.1, 5.4.1*)
- Dr. Wolfgang Jans* Forschungsanstalt der Bundeswehr für Wasserschall und Geophysik FWG, Kiel, Germany (*Sect. 4.3.5*)
- David Jepsen* Geoscience Australia, Commonwealth of Australia (*Sect. 5.2.2*)
- Dr. Wilfried Jokat** Alfred-Wegener-Institut für Polar- und Meeresforschung AWI, Bremerhaven, Germany (*Sect. 5.5.1*)
- Dr. Kelsey Jordahl* Monterey Bay Aquarium Research Institute, Moss Landing, United States of America (*Sect. 5.2.4*)
- Heiner Josenhans* Geological Survey of Canada (Atlantic), Bedford Institute of Oceanography, Canada (*Sect. 5.3.9*)
- Ingo Junge* Institut für Strömungsmechanik und Elektronisches Rechnen im Bauwesen, ISERB, University of Hannover, Germany (*Sect. 7.1.2*)

- Edward L. King* Geological Survey of Canada (Atlantic), Bedford Institute of Oceanography, Canada (Sect. 5.3.9)
- Dr. Dirk Kläschen* Leibniz-Institut für Meereswissenschaften an der Universität Kiel, Germany (Sect. 6.2.1)
- Dr. Martin Klenke* Alfred-Wegener-Institut für Polar- und Meeresforschung AWI, Bremerhaven, Germany (Sect. 5.4.2)
- Carol Kohl* National Topographic Hydrographic Authority, Land Information New Zealand, National Office, Wellington, New Zealand (Sect. 5.5.4)
- Dr. Peter Kohr** Universitätsklinikum Schleswig-Holstein, Radiologie, Kiel, Germany (Sect. 2.5, 2.6)
- Ralf Krockner* Alfred-Wegener-Institut für Polar- und Meeresforschung AWI, Bremerhaven, Germany (Sect. 2.7, 5.1.2, 5.5.1)
- Fred Kroh* Geoscience Australia, Commonwealth of Australia (Sect. 5.2.2, 5.2.7, 5.3.6)
- Dr. Hermann-Rudolf Kudrass* Bundesanstalt für Geowissenschaften und Rohstoffe BGR, Hannover, Germany (Sect. 5.3.2)
- Dr. Thomas Kuhn** Institut für Mineralogie der TU Bergakademie Freiberg, Germany (Sect. 5.2.6)
- Dr. J. S. Laberg* University of Tromsø, Norway (Sect. 5.3.2)
- Dr. Stefan Ladage* Bundesanstalt für Geowissenschaften und Rohstoffe BGR, Structural Geology, Hannover, Germany (Sect. 5.2.1)
- Dr. Douglas N. Lambert* Naval Research Laboratory, Stennis Space Center, United States of America (Sect. 6.2.2)
- Mark Lawrence* Alcatel, Paris, France (Sect. 7.2.1)
- Richard Lear* RESON Offshore Ltd., Aberdeen, Scotland, United Kingdom (Sect. 7.1.4)
- Dr. Wolfram Lemke** Institut für Ostseeforschung IOW, an der Universität Rostock, Germany (Sect. 5.7.3)
- Dr. Walter Lenz** Institut für Meereskunde, Universität Hamburg, Germany (Sect. 2.11)
- Dr. Michael Z. Li* Geological Survey of Canada (Atlantic), Bedford Institute of Oceanography, Canada (Sect. 5.3.9)
- Prof. Dr. Char-Shine Liu* National Center for Ocean Research, Institute of Oceanography, National Taiwan University, Taipei, Taiwan, Republic of China (Sect. 5.2.9)
- Dr. Benoît Loubrieu* DRO Institut français de recherche pour l'exploitation de la mer, Ifremer, Brest, France (Sect. 5.6.6)
- Dr. Jean Mascle** Geosciences-Azur, Villefranche/Mer, France (Sect. 5.6.6)
- Prof. Dr. Douglas G. Masson* Southampton Oceanography Centre, United Kingdom (Sect. 5.3.1)
- Prof. Dr. Dr. h.c. Larry Mayer* Center for Coastal and Ocean Mapping CCOM/NOAA-UNH Joint Hydrographic Center, University of New Hampshire, Durham, United States of America (Sect. 5.2.1, 5.2.2, 7.3.5)
- Dr. Lev Merklin* P. P. Shirshov Institute of Oceanology, Academy of Sciences of Russia, Moscow, Russian Federation (Sect. 5.4.3, 5.7.7)

- Prof. Dr. Jürgen Mienert* Department of Geology, University of Tromsø, Norway (Sect. 5.3.5)
- Dr. Doris Milkert* Forschungsanstalt der Bundeswehr für Wasserschall und Geophysik FWG, Kiel, Germany (Sect. 5.3.3, 7.2.4, 7.3.4)
- Dr. David C. Mosher* Natural Resources Canada, Geological Survey of Canada (Atlantic) Dartmouth, Nova Scotia, Canada (Sect. 5.3.9)
- Dr. Sergey Muyakshin* IAP, RAS, Nizhny Novgorod, Russian Federation (Sect. 6.3.2)
- Gijs Nieuwenhuijs* EGS Survey Pte Ltd (Sect. 7.2.3)
- Bernd Nützel* Forschungsanstalt der Bundeswehr für Wasserschall und Geophysik FWG, Kiel, Germany (Sect. 6.2.3)
- Dr. Atle Nygård* Department of Earth Science, University of Bergen, Norway (Sect. 5.3.2)
- Walter Offenborn* Marineamt Abt GeoInfoW – Geo 1, Rostock, Germany (Sect. 7.1.1)
- Toshio Ohyagi* Nihon Zitan /Toyo Corporation, Japan (Sect. 7.2.3, 7.1.3.4)
- Prof. Dr. Dimitrios Papanikolaou* Department of Marine Geology, University of Athens, Greece (Sect. 5.6.4)
- Russell Parrott* Geological Survey of Canada, Natural Resources Canada, Dartmouth, Nova Scotia, Canada (Sect. 5.3.9)
- Gianni Pavan* Centro Interdisciplinare di Bioacustica e Ricerche Ambientali Università degli Studi di Pavia, Pavia, Italy (Sect. 6.3.3)
- Dr. Harald Peine* Forschungsanstalt der Bundeswehr für Wasserschall und Geophysik FWG, Kiel, Germany (Sect. 7.1.5)
- Herman Peters* Rijkswaterstaat, The Netherlands (Sect. 7.1.1, 7.2.2, 7.3.2)
- Hartmut Pietrek* Bundesamt für Seeschifffahrt und Hydrographie BSH, Hamburg, Germany (Sect. 5.7.3)
- Fernando Maia Pimentel* *Commander*, Hydrography Division, Instituto Hidrográfico, Portugal (Sect. 5.3.6)
- Marc Pinto* Nato Undersea Research Centre, La Spezia, Italy (Sect. 7.1.5)
- Dr. Katrin Premke* Alfred-Wegener-Institut für Polar- und Meeresforschung AWI, Bremerhaven, Germany (Sect. 6.3.2)
- Dr. Cesar Ranero* Leibniz-Institut für Meereswissenschaften an der Universität Kiel, Germany (Sect. 5.1.2, 5.2.1, 5.2.3, 5.2.6)
- Dr. Michael D. Richardson* Seafloor Sciences Branch, Marine Geosciences Division, Naval Research Laboratory, Stennis Space Center, United States of America (Sect. 5.7.2, 6.2.2)
- Claudia Roedle* Wasser- und Schifffahrtsamt WSA, Hamburg-Wedel, Germany (Sect. 7.1.2)
- Cris A. Sabo* RESON Inc., Goleta, United States of America (Sect. 7.1.4, 7.2.2)
- Dr. Eberhard Sauter* Alfred-Wegener-Institut für Polar- und Meeresforschung AWI, Bremerhaven, Germany (Sect. 6.2.2)

- Dr. Hans Werner Schenke* Alfred-Wegener-Institut für Polar- und Meeresforschung AWI, Bremerhaven, Germany (Sect. 5.2.6, 5.3.4, 5.3.6, 5.4.1, 5.4.2, 5.5.1, 5.5.2, 5.5.3)
- Dr. Thomas Scholz* Forschungsanstalt der Bundeswehr für Wasserschall und Geophysik FWG, Kiel, Germany (Sect. 2.1)
- Dieter Seefeldt* Strom- und Hafenanbau, Hamburg, Germany (Sect. 7.1.3)
- Dr. Torsten Seifert* Institut für Ostseeforschung IOW, an der Universität Rostock, Germany (Sect. 5.7.1, 5.7.2)
- Prof. Dr. Uwe Send* Leibniz-Institut für Meereswissenschaften an der Universität Kiel, Germany (Sect. 6.1.3)
- Prof. Manfred Siegel** Atlas Elektronik and Hochschule Bremen, Germany (Sect. 2.11)
- Jonathan S. Smith* Geomatics, EP Technology, Shell International Exploration and Production Inc., Ashford, Houston, United States of America (Sect. 7.4.1.2)
- Dr. Deborah K. Smith* Woods Hole Oceanographic Institution, Woods Hole, United States of America (Sect. 5.2.3)
- Dr. Per Söderberg* FOI, Stockholm, Sweden (Sect. 5.7.5)
- Prof. Dr. Volkhard Spiess* Marine Technology/Environmental Research, Department of Earth Science, University of Bremen, Germany (Sect. 5.3.2)
- Prof. Dr. Rüdiger Stein* Alfred-Wegener-Institute for Polar- and Marine Research, Bremerhaven, Germany (Sect. 5.4.3)
- Prof. Dr. Peter Stoffers* Institut für Geowissenschaften GPI, Universität Kiel, Germany (Sect. 5.2.4)
- Dr. Siegfried Stolte* Lüneburg, Germany (Sect. 2.9)
- Federico De Strobel** Nato Undersea Research Centre, La Spezia, Italy (Sect. 2.11)
- Prof. Dr. Erwin Suess** Leibniz-Institut für Meereswissenschaften an der Universität Kiel, Germany (Sect. 6.2.1)
- Dr. Franz Tauber* Institut für Ostseeforschung Warnemünde IOW an der Universität Rostock, Germany (Sect. 5.7.1, 5.7.2)
- Dr. Jaroslaw Tegowski* Institute of Oceanology, Polish Academy of Science, Sopot, Poland (Sect. 5.7.2)
- Alex Trangeled* Nato Undersea Research Centre, La Spezia, Italy (Sect. 6.3.4)
- Juliusz Tuszyński** Hydrographic Office Polish Navy HOPN, Poland (Sect. 7.1.4.4)
- Michael Unger* Forschungsanstalt der Bundeswehr für Wasserschall und Geophysik FWG, Kiel, Germany (Sect. 3.2.2)
- Heinz G. Urban** Atlas Elektronik Bremen, Germany (Sect. 4.4.1–4.4.8)
- Nat Usher* EPT GeoDrilling; technical guidance to GeoHazards, GeoPressure, Geodetics, BP America Inc, Houston, United States of America (Sect. 7.4.1)
- Prof. Dr. Tore O. Vorren* Dpt. of Geology, University of Tromsø, Norway (Sect. 5.3.7)
- Prof. Dr. Peter Wadhams* Department of Applied Mathematics and Theoretical Physics, University of Cambridge, United Kingdom (Sect. 5.4.4)

<i>Donald J. Walter</i>	Naval Research Laboratory, Stennis Space Center, United States of America (Sect. 6.2.2)
<i>Daniel J Warren</i>	Marine Archaeology Section, C & C Technologies, Inc., Lafayette, United States of America (Sect. 7.4.1)
<i>Dr. Tjeerd C. E. van Weering</i>	Netherlands Institute for Sea Research (NIOZ), Texel, The Netherlands (Sect. 5.3.4)
<i>Dr. Wilhelm Weinrebe</i>	Leibniz-Institut für Meereswissenschaften an der Universität Kiel, Germany (Sect. 5.1.2, 5.2.1, 5.2.3, 5.2.6)
<i>Stein Wendel</i>	Norsk Hydro ASA, Ormen Lange Project, Aker Kværner, Lysaker, Oslo, Norway (Sect. 5.3.1, 7.4.2)
<i>Prof. Dr. Gert Wendt</i>	Institut für E-Technik der Universität Rostock, Germany (Chap. 1–4, Sect. 6.2.2, 7.2.2)
<i>Dr. Friedrich Werner</i>	Kiel, Germany (Sect. 5.3.3)
<i>Dr. Thomas Wever</i>	Forschungsanstalt der Bundeswehr für Wasserschall und Geophysik FWG, Kiel, Germany (Sect. 6.2.2)
<i>Roger Wiik</i>	Fugro Survey AS, Oslo, Norway (Sect. 5.3.7)
<i>Nico van Woerkom</i>	NeSA B.V./ Thales GeoSolutions, The Netherlands (Sect. 7.1.3)
<i>Dr. Tim J. Worthington*</i>	Institut für Geowissenschaften GPI, Universität Kiel, Germany (Sect. 5.2.2, 5.2.4)
<i>Dr. Sébastien Zaragosi</i>	Département de Géologie et Océanographie, Université de Bordeaux I, France. (Sect. 5.3.2)
<i>Dr. Manfred Zeiler</i>	Bundesanstalt für Seeschifffahrt und Hydrographie BSH, Hamburg, Germany (Sect. 5.3.3, 7.1.1, 7.2.2)
<i>Dr. Walter Zenk</i>	Leibniz-Institut für Meereswissenschaften an der Universität Kiel, Germany (Sect. 6.1.1)
<i>Prof. Dr. Günter Ziehm*</i>	Passau, Germany (Sect. 2.11)

ATLAS ELEKTRONIK, Bremen, the company with the longest echosounder tradition and pioneering developments has kindly sponsored color prints throughout the book to enable the presentation of the original image versions. This generous support is particularly appreciated.

Particular Acknowledgments

I am indebted to *Prof. Dr. Lorenz Magaard*, School of Ocean and Earth Science and Technology, University of Hawaii at Manoa, USA, and *Mr. Chris Miller*, Ocean Acoustics Laboratory/Ocean Acoustic Observatory Point Sur, USA, for convincing friends to support the book project with rare, unpublished sound images.

Mrs. Heather Barrett-Pironti, former Directorate Secretary of the NATO Undersea Research Centre, deserves my most cordial and respectful gratitude for conducting the native speaker's review of the book texts with professional care and incessant patience. My sincere thanks go to *Dr. Jens Greinert*, Geomar, Kiel, who generously provided his professional assistance in image processing matters, and to *Dr. Ivor Nissen*, Forschungsanstalt der Bundeswehr, FWG, Kiel who designed and realised the appendix. *Mrs. Susanne Lau*, FWG, Kiel supported the project with graphics and image formatting work which is gratefully appreciated. Cordial thanks are also due to *Mr. Kai Martin Dührkop* and *Mrs. Kelly Scott* of Reson Germany and

USA, as well as to *Mr. Karstein Vestgård*, Kongsberg Simrad, Norway, for outstanding help in providing information and user contacts. Further I wish to thank Mrs. Claudia Jew, The Mariners' Museum, USA, Mr. Martin Morgan, The National D-Day Museum, USA, and Mr. Robert Shindle, The Steamship Historical Society of America for their kind provision of image copyrights. *Dr. Heinz A. Gorges*, Melbourne, was a source of great encouragement, supporting the manuscript production with substantial comments and suggestions. Mrs. *Luisa Tonarelli*, Springer-Verlag, Geosciences, Germany has been exemplary in her sympathetic, encouraging and always immediate support on behalf of the publisher, which is particularly appreciated. *Mr. Armin Stasch* deserves grateful respect for his layout work.



Contents

Part I	
The Basic Facts of Imaging the Ocean 1	
1	Preliminary Remarks 3
2	Alternatives to Imaging the Sea by Sound and First Acoustic Trials 7
2.1	Visible Light 8
2.2	Infrared 9
2.3	Microwaves 9
2.4	Ultra-Long Radio Waves 9
2.5	X-Rays 10
2.6	Gamma Radiation 10
2.7	Gravity Anomalies 10
2.8	Magnetic Anomalies 11
2.9	Hydrodynamic Effects 13
2.10	The Acoustic Solution 14
2.11	First Acoustic Trials 14
2.12	Four Lines of Evolution of Ocean Echosounding 18
2.13	Conclusion of Chapter 2 19
3	Acoustic Features of the Sea 21
3.1	The Speed of Sound, Determining Quantities 22
3.1.1	Dependence on the Static Pressure 22
3.1.2	Dependence on the Salinity 22
3.1.3	Dependence on the Temperature 23
3.2	Sound Refraction in the Sea 23
3.2.1	Snell's Law 23
3.2.2	Sound Refraction and Ducted Propagation; "Acoustic Superconductivity" 23
3.3	Sound Attenuation 27
3.3.1	Absorption 27
3.3.2	Spreading Loss 28
3.3.3	Above and below the Ocean Volume; a Comparison 28
3.3.4	The Wavelength Handicap 28
3.3.5	The Optimum Compromise 29

3.4	Echo Formation	29
3.4.1	Acoustic Impedance	29
3.4.2	Impedance Steps	30
3.4.3	Colorless Sound Images	30
3.4.4	The Minimum Object Size	30
3.4.5	Echosounding under Slant Angles	31
3.4.6	Restriction to Compressional Waves	31
3.5	Reverberation	31
3.6	Noise	32
3.6.1	Sources of Noise: The Ship Traffic	32
3.6.2	Wind-Driven Noise	33
3.6.3	Rain Noise	33
3.6.4	Noise Fighting	34
3.6.5	The Spatial Filter	34
3.6.6	The Frequency Filter	35
3.6.7	Tailoring the Filter	35
3.6.8	Further Sources of Noise and Very Large Acoustic Events	36
3.6.9	Marine Mammals and Noise	38
3.6.10	Self Noise	38
3.7	Sonar Equation	39
3.8	Conclusion of Chapter 3	39
4	Technical and Physical Characteristics of High Resolution Echosounders	41
4.1	Conversion of Electrical and Acoustical Energy	42
4.1.1	The Piezoelectric Effect	42
4.1.2	Quartz: The Prototype of Piezoelectricity	42
4.1.3	Polarization of LZT	42
4.1.4	LZT-Ceramics as Sound Source	42
4.1.5	Transducers at Resonance	43
4.1.6	The Cavitation Limit	43
4.1.7	Conclusion	44
4.2	The First Type of Sound Imaging: The Fan- or Multibeam Echosounder	44
4.2.1	Satellite Navigation	45
4.2.2	Predecessors of Navigation	45
4.2.3	The Fan Echosounder, Requirement for Motion Compensation ...	46
4.2.4	Phased Array Beam- Forming; The Radar Solution	46
4.2.5	The Fan Echosounder Solution	46
4.2.6	Sampling of Lines and Rows	47
4.2.7	Time Parallel Sampling	47
4.2.8	Two Line Arrays Instead of a Matrix	47
4.2.9	Motion Compensation	48
4.2.10	Conclusion	48
4.3	The Second Type of Sound Imaging: The Sidescan Echosounder	48
4.3.1	Line by Line Sampling	49
4.3.2	Throwing Shadows	49
4.3.3	The Towed Fish for Rail-like Motion	49
4.3.4	Acoustic Astigmatism	50

4.3.5	Focusing	50
4.3.6	Limits of Focusing Advantages	51
4.3.7	Multi-Aspect Sounding	52
4.3.8	Long-Range Versions	52
4.3.9	Conclusion	52
4.4	The Third Type of Sound Imaging: The Sediment-Penetrating Echosounder	52
4.4.1	The Resolution Dilemma	53
4.4.2	The Parametric Echosounder	53
4.4.3	Non-Linear Mixing	53
4.4.4	Advantage of Depth Resolution	54
4.4.5	Advantage of Beamwidth	54
4.4.6	End-Fire Array	54
4.4.7	Array Length and Beamwidth Relations	54
4.4.8	The Receiving Mode	55
4.4.9	Conventional Sediment Echosounders	55
4.4.10	Seismic Sounding	55
4.4.11	The Source	55
4.4.12	The Receiver	55
4.4.13	Conclusion	56
4.5	The Fourth Type of Sound Imaging: The Acoustic Doppler Current Profiler (ADCP)	56
4.5.1	The Principle of Acoustic Current Measurement	56
4.5.2	The ADCP-Concept	56
4.5.3	Speed Components and Doppler Shift	57
4.5.4	The Determination of the Current Vector	57
4.5.5	Slow Speeds	58
4.5.6	Speed Resolution	58
4.5.7	The First Dilemma: The Sampling Problem in a Varying Field	59
4.5.8	The Second Dilemma: Echosounders Cannot Measure Temperature	59
4.5.9	The Need for Combined Concepts	59
4.5.10	Acoustic Tracking	60
4.5.11	Conclusion	60
	Part II	
	Applications of Acoustic Imaging the Ocean	61
5	The Sea Floor – Natural Formations	63
5.1	Merger of Satellite Altimetry and Acoustic Bathymetry	64
5.1.1	Globes of the Sea Floor Relief	66
5.1.1.1	The Globe, Atlantic Ocean	69
5.1.1.2	The Globe, Pacific Central	71
5.1.1.3	The Globe, Pacific Australia	73
5.1.1.4	The Globe, Indian Ocean	75
5.1.1.5	The Globe, Arctic Ocean	77
5.1.1.6	The Globe, Antarctica	79

5.1.2	High Resolution Bathymetry Versus Satellite Altimetry	80
5.1.2.1	Daikakuji, a Seamount on the Hawaiian Emperor Chain Bend	80
5.1.2.2	Freeden Seamount and Eltanin Impact Area	82
5.1.2.3	The Sea Floor near the Volcano Island Kauai, Hawaii ..	84
5.2	Geodynamics of Tectonic Plates	85
5.2.1	Chile-Type Margins of Convergent Tectonic Plates	85
5.2.2	Marianas-Type Convergent Plate Margins	106
5.2.2.1	The Mariana Trench and the Philippine Plate	107
5.2.2.2	The Challenger Deep in the Marianas Trench: The Deepest Place on the Earth's Surface	109
5.2.2.3	Philippine Trench	110
5.2.2.4	Java Trench Area	112
5.2.2.5	Macquarie Ridge Complex (MRC)	115
5.2.3	Mid-Oceanic Ridges, Slow Spreading Type	117
5.2.3.1	Mid-Atlantic Ridge, Northern Hemisphere; Cut-out Sections of a Slow Spreading Mid-Ocean Ridge; Feature Comparison of Relief and Backscattering	119
5.2.3.2	Mid-Atlantic Ridge, Southern Hemisphere; Relief Details of a Fracture Zone	121
5.2.3.3	Mid-Atlantic Ridge, Northern Hemisphere; Combined Multibeam and Sidescan Image of a Central Valley Segment with a Volcano	122
5.2.4	Mid-Oceanic Ridges, Fast Spreading Type	123
5.2.4.1	A Very Fast Spreading Mid-Ocean Ridge: The South Pacific Rise near the Wilkes Transform Fault	123
5.2.4.2	The Southern East Pacific Rise (EPR)	125
5.2.4.3	Marquesas Fracture Zone, One of the Large Pacific Fracture Zones, Relics of a Reorganized Mid-Ocean Ridge	127
5.2.5	Strike Slip Fault Plate Margin	129
5.2.6	Volcanic Formations	131
5.2.6.1	Ampère Seamount	131
5.2.6.2	Unnamed Volcano near Juan De Fuca Ridge	133
5.2.6.3	The Sea Floor around the Volcano Stromboli, Italy	133
5.2.7	Prominent Seamounts: The Tasmanian Seamounts, Marine Reserve	137
5.2.8	Hot Spots Islands: The Hawaii Region	138
5.2.9	Taiwan and the Tectonic Activities at the Western Philippine Plate	140
5.3	Passive Continental Margins: Examples of the Prevailing Formations and Processes on the Shelf	145
5.3.1	Submarine Escarpment Slides	146
5.3.1.1	Storegga Slide	148
5.3.1.2	Trænadjupet Slide	151
5.3.1.3	Landslide on Atlantic Islands; Canary Islands	153
5.3.2	Sediment Fans; Flow and Strata	155

5.3.2.1	Morphology of the Celtic Fan, Gulf of Biscay	155
5.3.2.2	Glacigenic and Non-Glacigenic Debris Flows on the Upper North Sea Fan	156
5.3.2.3	Bear Island Trough Mouth Fan (TMF) and Glacigenic Debris Flows, Western Barents Sea	159
5.3.2.4	The Largest Sediment Fan in the World Fed by a Giant Shelf Canyon in the Bay of Bengal	161
5.3.2.5	Sediments off Callao/Peru	166
5.3.3	Sediment Bedforms	167
5.3.4	Carbonate Mounds and Cold Water Corals on the West European Margin	171
5.3.4.1	Carbonate Mounds in the Porcupine Bight and Rockall Trough Margin	171
5.3.4.2	Cold Water Corals on the West European Margin	176
5.3.5	Mud Volcanoes and Diapirs	178
5.3.5.1	Mud Volcanoes	178
5.3.5.2	Diapirs	183
5.3.6	Submarine Canyons, Channels	184
5.3.7	Norwegian Fjords	188
5.3.8	Bedrock Structures	190
5.3.9	Canadian Formations	192
5.3.9.1	Scotian Shelf, Canada	192
5.3.9.2	West Coast of Canada, Giant Underwater Dunes	198
5.3.9.3	Queen Charlotte Islands off British Columbia, Canada	200
5.4	Arctic Ocean	202
5.4.1	Arctic Ocean and Its Constituent Seas; Bathymetry and Physiography	202
5.4.2	The Fram Strait with the Deepest Depression in the Arctic	206
5.4.3	Arctic Sediments	208
5.4.4	Under Ice Sound Imaging in the Fram Strait	212
5.5	Antarctic Features	216
5.5.1	Features of the Weddell Sea, Antarctica	217
5.5.2	The Orca Seamount Region, Antarctica	222
5.5.3	Antarctic Iceberg Plough Scars	224
5.5.4	Features of the Ross Sea, Antarctica	228
5.6	Mediterranean Sea Formations, the Overview	232
5.6.1	Chella Bank, Western Mediterranean Sea	235
5.6.2	Balearic Islands	236
5.6.3	Tyrrhenian Sea Floor Features	237
5.6.4	Features of the Aegean Sea	238
5.6.5	The Marmara Sea Trough	242
5.6.6	The Deep Eastern Mediterranean Sea and Its Tectonic Convergence	245
5.6.7	Shelf Formations off Israel	248
5.7	Baltic Sea Formations	251
5.7.1	Relief Image of the Baltic Sea; Overview	252

5.7.2	The Western Baltic Sea	255
5.7.3	Kadetrinne, Baltic Sea	256
5.7.4	Gulf of Gdańsk, Baltic Sea	258
5.7.5	Stockholm Archipelago, Bedrock Area	260
5.7.6	Sedimentation in the Baltic Sea; Examples of the Bight of Mecklenburg	261
5.7.7	Gulf of Finland, Gaseous Sediment and Gas Plume	263
6	The Ocean Volume	265
6.1	Ocean Water Mass Transport and Heat Content	266
6.1.1	Mid-Depth Circulation in the North Atlantic. Large Scale Drifter Field Experiment	266
6.1.2	Acoustic Measurements of Ocean Currents by Doppler Profiling	269
6.1.3	Acoustic Tomography	274
6.1.3.1	Acoustic Measurements of Heat Content across the Mediterranean Sea	277
6.1.3.2	Acoustic Measurements of Heat Content of the Central Labrador Sea	279
6.1.3.3	Monitoring the Outflow through the Strait of Gibraltar by Acoustic Tomography	281
6.2	Gas in the Sea	282
6.2.1	Methane Hydrate Deposits	282
6.2.2	Methane in Shallow Sediments; Acoustic Sea-Floor Classification	291
6.2.2.1	Examples of Acoustic Features of Methane in Shallow Sediments	293
6.2.2.2	Application of the Acoustic Sea Floor Classification System (ASCS) for Shallow Sediments ..	296
6.2.3	Air Intrusion by Breaking Sea Waves	299
6.3	Submarine Fauna	306
6.3.1	Estimation of Fish Stocks by Echosounding	307
6.3.1.1	Monitoring of Fish Stocks, South Eastern North Sea	309
6.3.1.2	Monitoring of Fish Stocks, Baltic Sea	310
6.3.1.3	Monitoring of Fish Stocks in Shallow Waters, Western Baltic Sea	311
6.3.1.4	Monitoring of Fish Stocks, North Atlantic, Irmingier Basin	312
6.3.2	Finding Food in the Deep Sea	314
6.3.3	Voice Sonograms of Marine Mammals	316
6.3.4	Example of Marine Flora Sound Imaging	322
7	Man-made Matter	325
7.1	Surveillance and Maintenance of Coastal Sea Lanes	326
7.1.1	Surveillance of Sea Lanes and Fairways	326
7.1.2	Estuary Surveillance	335

	7.1.2.1	Floor Features of the Elbe Estuary	336
	7.1.2.2	Relief Changes of the Sea Floor in the Bight of Meldorf	339
7.1.3		Harbor Surveillance and Maintenance	340
	7.1.3.1	Hydroacoustic Spotlights of the Port of Hamburg	340
	7.1.3.2	Inspection of Canale Grande, Venice	343
	7.1.3.3	The Dock of London: A Dumping Area of Scrap Iron	344
	7.1.3.4	Seabed Surveys in the Hong Kong Area	346
7.1.4		Survey of Wrecks in Coastal Waters	348
	7.1.4.1	Freighter Sunk in the Persian Gulf	348
	7.1.4.2	Two Shipwrecks on Plain Sandy Bottom off Cinque Terre, Northern Italy	349
	7.1.4.3	Intact Wreck of a Sailing Ship	350
	7.1.4.4	The Wrecks of the German Refugee Ships Wilhelm Gustloff, Goya, and General von Steuben, Sunk in the Baltic Sea at the End of WW II	351
	7.1.4.5	Wreck of an Aircraft Sunk in a Lake at 50 m Depth	355
7.1.5		Acoustic Search for Buried Objects and Sea Mines	355
7.2		Submarine Constructions	362
	7.2.1	Submarine Cables	362
	7.2.2	Submarine Pipelines	366
	7.2.3	Protection of Shores and Harbors	370
	7.2.4	Basement of the Off-Shore Research Platform Nordsee	372
7.3		Underwater Archaeology	374
	7.3.1	Sunken Roman City Complex	374
	7.3.1.1	City of Baia, Italy. Imaging of Urban Architecture	374
	7.3.1.2	The Submerged Porto Giulio, Italy. Imaging of Port Architecture	378
	7.3.2	Historic Ship Wrecks and Wreck Sites	381
	7.3.3	Battleship Archaeology at Scapa Flow. German War-Ship Wrecks of WW I	390
	7.3.4	Submerged Viking Dike Built around AD 740	396
	7.3.5	D-Day: Documentation of the Relics	397
7.4		Close-Up Deep Water Imagery by Autonomous and Remotely Operated Underwater Vehicles (AUV and ROV)	402
	7.4.1	Deep-Water Sound Imaging of Shipwrecks – Wrecks of Two US-Cargo Freighters and a German Submarine Sunk in the Gulf of Mexico during WW II	403
	7.4.1.1	The Sinking of the Passenger Freighter Robert E. Lee	404
	7.4.1.2	Wreck of the Cargo Freighter SS Alcoa Puritan Sunk in the Gulf of Mexico during WW II	405
	7.4.1.3	Wreck of the Only German Submarine Sunk in the Gulf of Mexico in WW II	409
	7.4.2	The Ormen Lange Gas Field inside the Storegga Slide Area. A Sea-Floor Relief Exploration for Pipeline Route Planning. Imaging by Surface Vessels and Deep Diving AUV	414

Final Remarks	421
Literature Index	423
A Appendix	443
A.3.1 The Speed of Sound, Determining Quantities	443
A.3.2 Sound Refraction in the Sea	443
A.3.2.1 Snell's Law	443
A.3.2.2 Sound Refraction and Ducted Propagation	444
A.3.3 Sound Attenuation	444
A.3.3.1 Absorption	444
A.3.4.1 Acoustic Impedance	446
A.3.5 Reverberation/Scattering Strength of the Sea Floor and Sea Volume ...	446
A.3.5.1 Sea Floor	446
A.3.5.2 Sea Volume	447
A.3.6 Noise	447
A.3.6.5 The Spatial Filter	447
A.3.6.6 The Frequency Filter	448
A.3.7 Sonar Equation	448
A.4.5 The Acoustic Doppler Current Profiler (ADCP)	450
A.4.5.3 Speed Components and Doppler Shift	450
CD Attachment Index	451
Subject Index	453



List of Images

Image 1-1.	M. F. Maury, bathygraphic map of the North Atlantic, Italian edition of 1877	5
Image 2.1-1.	Shallow area in the Baltic Sea with algae. Laser-bathymetry	8
Image 2.1-2.	Penetration depths of electromagnetic waves and sound waves in the sea ..	9
Image 2.7-1.	Relief of the Eltanin Massif; acoustic multibeam bathymetry and satellite radar altimetry	11
Image 2.9-1.	Sea floor imaging by an hydrodynamic effect. Acoustics and radar	12
Image 2.9-2.	Weak internal waves also influence the sea surface. Acoustic current meter image	12
Image 2.9-3.	Scylla and Charybdis in the Strait of Messina. Large internal wave package and its copy on a radar screen	13
Image 2.11-1.	Reginald Fessenden	14
Image 2.11-2.	Alexander Behm	15
Image 2.11-3.	Hugo Lichte	15
Image 2.11-4.	Fessenden Oscillator	16
Image 2.11-5.	The Meteor crossings of the South Atlantic of 1925–1927	17
Image 2.11-6.	The depth contours of the Meteor Expedition of 1925–1927	17
Image 2.11-7.	The depth chart derived from the Meteor data	18
Image 3.2.2-1.	Scheme of the Sofar-Channel sound speed profile with corresponding undulating sound rays	24
Image 3.2.2-2.	The global Sofar-Channel: the depth of the channel axis	25
Image 3.2.2-3.	The global Sofar-Channel: the speed of sound at the channel axis	26
Image 3.2.2-4.	Acoustic surveillance of the Comprehensive Test-Ban Treaty (CTBT) of the United Nations of nuclear weapons; global network of seismic- and hydroacoustic monitoring stations	27
Image 3.6.3-1.	Underwater noise by raindrop impact. Laboratory experiment	34
Image 3.6.8-1.	Sonogram of a submarine earthquake	36
Image 3.6.8-2.	Sonogram of a submarine volcano eruption	36
Image 3.6.8-3.	Sonogram of a submarine nuclear test	37
Image 4.2.8-1.	Multibeam echosounder transducer head	48
Image 4.3.1-1.	Scheme of sound irradiation by a hull mounted sidescan echosounder	49
Image 4.3.3-1.	Example of a tow fish with the pair of sidescan echosounder transducers	50
Image 4.3.5-1.	Scheme of focusing	50
Image 4.3.5-2.	Effect of focusing; sidescan image of sand ripples	51
Image 4.5.2-1.	Schematic depiction of an acoustic Doppler current profiler (ADCP) ..	57

Image 5.1.1.1-1.	The Globe, Atlantic Ocean	69
Image 5.1.1.2-1.	The Globe, Pacific Central	71
Image 5.1.1.3-1.	The Globe, Pacific Australia	73
Image 5.1.1.4-1.	The Globe, Indian Ocean	75
Image 5.1.1.5-1.	The Globe, Arctic Ocean	77
Image 5.1.1.6-1.	The Globe, Antarctica	79
Image 5.1.2.1-1.	Schematic map of the Hawaiian Chain and the Emperor Chain with Daikakuji at the bend	80
Image 5.1.2.1-2.	Altimetric relief of the seamount chain bend around Daikakuji	80
Image 5.1.2.1-3.	The Daikakuji Seamount. Multibeam relief image	81
Image 5.1.2.2-1.	The Eltanin Massif. Multi beam image and derived from satellite altimetry/gravity anomaly	82
Image 5.1.2.2-2.	The central massif cut out of the Eltanin. Multibeam image and altimetric counterpart	83
Image 5.1.2.3-1.	High resolution multibeam echo sounding from a surface vessel	84
Image 5.2-1.	Schematic world map of the plates and their margins	86
Image 5.2.1-1a,b.	Color coded bathymetry and elevation map along 600 km of the Central American Trench along Costa Rica and Nicaragua. Multibeam image	88–90
Image 5.2.1-2.	Perspective view of the bathymetry offshore from Central Costa Rica. Multibeam image	91
Image 5.2.1-3.	Area of Image 5.2.1-2. Seismic profiles mounted on the perspective relief	93
Image 5.2.1-4.	Perspective view of the sea-floor morphology offshore from central Chile. Multibeam image	95
Image 5.2.1-4a.	Same as Image 5.2.1-4, but as slant view looking north. Multibeam image	96
Image 5.2.1-4b.	Bathymetric and altimetric comparison of features. Relief image derived from satellite altimetry	97
Image 5.2.1-4c.	Bathymetry of the Southern Chilean Margin. Multibeam image	99
Image 5.2.1-4d.	Oceanic Nazca Plate Margin. Multibeam image	99
Image 5.2.1-4e.	Chilean Margin with the Mocha Fracture Zone. Multibeam image ...	100
Image 5.2.1-4f.	Chilean continental slope and trench horizon. Close up multibeam image	101
Image 5.2.1-5.	Perspective view of the sea-floor morphology offshore a segment of the Alaska continental slope. Multibeam image	103
Image 5.2.1-6.	Perspective view with a close-up of the central area of Image 5.2.1-5	104
Image 5.2.2.1-1.	Overview of the Philippine Plate. Image derived from the combined satellite altimetry- and acoustic bathymetry data set (ETOPO2)	107–108
Image 5.2.2.2-1.	Challenger Deep looking downward at 25°. Multibeam relief image	109
Image 5.2.2.2-2.	Same as Image 5.2.2.2-1, but looking downwards at 40°	109
Image 5.2.2.2-3.	Same as Image 5.2.2.2-1, but looking downwards at 60°	110
Image 5.2.2.2-4.	Ground track of the research vessel RV Kairei during the Kaiko survey along the Mariana Trench	110
Image 5.2.2.3-1.	The trench area as a Fledermaus visualization. ETOPO2 data	110
Image 5.2.2.4-1.	The Java Trench. ETOPO2 data	112
Image 5.2.2.4-2.	The area of the Giant Tsunami of December, 2004. ETOPO2 data	114
Image 5.2.2.5-1.	The Macquarie Ridge and Hjort Trench. Overview of the relief, various data sources	115
Image 5.2.2.5-2.	The Hjort Trench and Ridge. Multibeam image	116
Image 5.2.3.1-1.	Northern segment with part of the Oceanographer Transform Fault. 3D-multi-beam, shaded relief image	118

Image 5.2.3.1-2.	Same segment as of Image 5.2.3.1-1 but depiction of echo strength of the sea floor	119
Image 5.2.3.1-3.	Southern segment with part of the Hayes Ridge Transform Intersection. 3D-multibeam, shaded relief image	120
Image 5.2.3.1-4.	Same segment as of Image 5.2.3.1-3 but depiction of echo strength of the sea floor	120
Image 5.2.3.2-1.	Cut out north of the Ascension Fracture Zone. Multibeam Image	121
Image 5.2.3.3-1.	The central valley of the Mid-Atlantic Ridge at 29° N. 3D-multibeam image draped with the sidescan image	122
Image 5.2.3.3-2.	Close ups of the southern volcano	123
Image 5.2.4.1-1.	A section of the South Pacific Rise near 9 degrees south. Multibeam image	124
Image 5.2.4.2-1.	This southern EPR segment is about 250 km long	125
Image 5.2.4.2-2.	This section is a 3D-close up of the southern part of the preceding image	126
Image 5.2.4.2-3.	The northern segment of the EPR	126
Image 5.2.4.2-4.	A close up of the preceding image	127
Image 5.2.4.3-1, 1a.	Section of the locked fault and close up. Overlay of the bathymetric and altimetric relief	129
Image 5.2.5-1.	Cut out of the strike slip fault margin, Los Angeles area off California. 3D-multibeam sound image	130
Image 5.2.6.1-1.	Ampère Seamount, Horseshoe Seamount Chain off Gibraltar. Multibeam echosounder image in red-green anaglyphic stereo-depiction	131
Image 5.2.6.1-2.	Ampère Seamount. Multibeam echosounder image in color coded 3D-depiction	132
Image 5.2.6.2-1.	Demonstration of coverage and resolution by a single multibeam run	133
Image 5.2.6.3-1.	View of the volcano area with Stromboli on the left. Multibeam image	134
Image 5.2.6.3-2.	View over the lower part of the volcano flank. Multibeam image	134
Image 5.2.6.3-3.	Gas ascending in the Eolian Volcanic Arc. Multibeam image	134
Image 5.2.6.3-4.	Lava on the sea floor near the island of Panarea. Multibeam image ..	135
Image 5.2.6.3-5.	Rock impact on the sea floor near the island of Panarea. Multibeam image	136
Image 5.2.6.3-6.	Plume of steam from a lava clod impact near the island of Panarea. Photograph	136
Image 5.2.7-1.	Cut-out of the field of the Tasmanian Seamounts. Multibeam image ..	137
Image 5.2.8-1.	Kahoolawe area; coral reef area between Hawaiian Islands. Multibeam image	138
Image 5.2.8-2.	Close-up cut-out of the coral reef between three Hawaiian Islands, Kahoolawe area. Multibeam image	139
Image 5.2.9-1.	Overview of Taiwan and its offshore region. Multibeam image	140
Image 5.2.9-2.	In combination with Image 5.2.9-1: The Penghu Canyon in the south-west. Multibeam image	142
Image 5.2.9-3.	The canyon system east of Taiwan. Multibeam image	143
Image 5.2.9-4.	A ridge enters a subduction trench. Multibeam image	144
Image 5.3.1.1-1.	Overview of the northern Storegga Slide escarpment. Sidescan mosaic image	148
Image 5.3.1.1-2.	Close-up of the northern Storegga Slide escarpment. Sidescan mosaic image	149
Image 5.3.1.1-3.	Close-up of the northern Storegga Slide escarpment. Western cut-out of the sidescan mosaic image	150

Image 5.3.1.2-1.	Overview of Trænadjupet Slide and Storegga Slide. Composite relief image	151
Image 5.3.1.2-2.	Close up of the southern Trænadjupet Slide escarpment. Mid range sidescan mosaic image	152
Image 5.3.1.3-1.	Slant view from northwest onto the western Canary Islands. Multibeam sound image	153
Image 5.3.1.3-2.	The El Golfo-landslide of El Hierro. Multibeam image	154
Image 5.3.1.3-3.	North flank of Tenerife	154
Image 5.3.2.1-1.	Celtic deep-sea Fan relief. Multibeam image	155
Image 5.3.2.1-2.	Celtic Deep-sea Fan. Backscatter image	156
Image 5.3.2.2-1.	Glacigenic debris flow surface morphology. Sidescan mosaic image ..	157
Image 5.3.2.2-2.	Non-glacigenic debris flow, inner morphology. Horizontal slice through a 3D-seismic record	158
Image 5.3.2.3-1.	Trough Mouth Fan (TMF) and debris flows. High resolution seismic cross sections	161
Image 5.3.2.4-1.	The outer relief of the feeder canyon. Multibeam image	162
Image 5.3.2.4-2.	Sediment structure along the axis of the canyon. Parametric sediment echosounder image	163
Image 5.3.2.4-3.	The transport channel in the middle Bengal Fan. Multibeam image ..	164
Image 5.3.2.4-4.	Sediment structure of the Bengal Fan across the transport channel. High resolution parametric sediment echosounder image	165
Image 5.3.2.5-1.	Bifurcation of sediment strata. Parametric echosounder image	166
Image 5.3.2.5-2.	Submarine channels. Parametric echosounder image	167
Image 5.3.3-1.	Boundary between sediment bed-forms. Sidescan image	168
Image 5.3.3-1a.	Example of several closely adjacent bedforms. Sidescan image	168
Image 5.3.3-2.	Sand dunes, superimposed by small scale ripples. Sidescan image ...	168
Image 5.3.3-3.	Large sand dunes superimposed by ripple fields. Sidescan image	169
Image 5.3.3-4.	Comet marks behind stones at high speed of flow. Sidescan image ...	169
Image 5.3.3-5.	Sickle-shaped dunes (barchans). Sidescan image	170
Image 5.3.3-6.	Sand ribbons. Sidescan image	170
Image 5.3.3-7.	Erosional furrows. Sidescan image	171
Image 5.3.3-8.	Erosional furrows. Sidescan image	171
Image 5.3.4.1-1.	Ensemble of carbonate mounds, Porcupine Bight. High resolution multibeam image	172
Image 5.3.4.1-2.	Cross section of carbonate mounds, northern Porcupine Bight. High resolution seismic image	173
Image 5.3.4.1-3.	Cross section of buried carbonate mounds, northern Porcupine Bight. High resolution seismic image	173
Image 5.3.4.1-4.	Internal relief of buried carbonate mounds, northern Porcupine Bight. High resolution 3D-seismic image	174
Image 5.3.4.1-5.	Giant carbonate mounds along the Rockall Trough margin. Seismic section	175
Image 5.3.4.2-1.	Deep cold water corals off Norway. Sidescan sonar image	176
Image 5.3.4.2-2.	Deep cold water corals of the main reef B, Sula Reef Complex, off Norway. Sidescan sonar image	177
Image 5.3.5.1-1.	The Al Idrisi mud volcano. Multibeam image	179
Image 5.3.5.1-2.	Interfingering of the mud volcano outflows. High resolution seismic profile	180
Image 5.3.5.1-3.	The Håkon Mosby Mud Volcano (HMMV). Low resolution sidescan images of the morphology	181
Image 5.3.5.1-3a.	The Håkon Mosby Mud Volcano HMMV. Mid range sidescan image ..	181
Image 5.3.5.1-4.	The Håkon Mosby Mud Volcano HMMV. High resolution seismic profile	182

Image 5.3.5.2-1.	Canary Islands diapirs sea floor outcrops. Multibeam image	183
Image 5.3.6-1.	Section of the Gollum Channel System, Porcupine Bight. Multibeam image	184
Image 5.3.6-2.	Same section of the Gollum Channel System, but backscattering as anaglyphic red-green stereo version of a black and white depiction .	185
Image 5.3.6-3.	Nazaré Canyon, north of Lisboa, Portugal. Multibeam image	186
Image 5.3.6-4.	Murray Canyons, South Australia. Multibeam image	187
Image 5.3.7-1.	Bjørnsundet Fjord. Multibeam image	188
Image 5.3.7-2.	Balsfjorden close to Tromsø, northern Norway. High-resolution seismic profile across the fjord	189
Image 5.3.7-3.	Hardanger Fjord, Hordaland. Multibeam image	189
Image 5.3.7-4.	Sandsfjorden, Rogaland. Multibeam image	190
Image 5.3.8-1.	Halifax Harbor and the adjacent inner Scotian Shelf. Multibeam sound image	190
Image 5.3.9.1-1.	Bedford Basin. Multibeam sound image	192
Image 5.3.9.1-2.	The Gully. Multibeam sound image	194
Image 5.3.9.1-3.	Sand ridges off Sable Island	195
Image 5.3.9.1-4.	Moraines on the inner Scotian Shelf of Canada. Multibeam relief image	197
Image 5.3.9.1-4a.	Backscatter intensity image of the preceding moraine field. Same data set; gray tone coded echo intensity	197
Image 5.3.9.2-1.	The place of giant underwater dunes. Bathymetric overview of the area, Eastern Juan de Fuca Strait, British Columbia, Canada	198
Image 5.3.9.2-2.	The Giant sand dunes; perspective view of the bedrock trough. Multibeam image	199
Image 5.3.9.2-3.	The giant sand dunes as sub-bottom profiles	199
Image 5.3.9.2-4.	The giant sand dunes and their small scale morphology. Sidescan sonar image	200
Image 5.3.9.3-1a, b.	Werner Bay, map of area and multibeam image	200–201
Image 5.4.1-1.	Bird's eye view over the shaded, color coded relief of the Arctic Ocean area as a plain	203
Image 5.4.1-1a.	Slant view of a cut-out of Image 5.4.1-1 with the axis cross through the North Pole	204
Image 5.4.1-2.	The names of the major formations, attached to the spherical depiction	204
Image 5.4.1-3.	Spherical depiction of the shaded, color coded relief of the Arctic Ocean area	205
Image 5.4.2-1.	View upon the deepest part of the Fram Strait. Multibeam 3D-image	207
Image 5.4.3-1.	Siberian river run-off in the Kara Sea, Arctic Ocean: Map of the study area	208
Image 5.4.3-2.	The Yenisei Estuary. High resolution seismic imaging	208
Image 5.4.3-3.	Crossing the eastern Barents-Kara Sea margin. High resolution seismic image	209
Image 5.4.3-4.	Thick well stratified mud, Kara Sea. High resolution seismic image ..	210
Image 5.4.3-5.	South Barents Basin, Arctic Shelf; cross section of Quaternary sediments, part one. High resolution parametric sediment echosounding	210
Image 5.4.3-6.	South Barents Basin, Arctic Shelf; cross section of Quaternary sediments, part two. High resolution parametric sediment echosounding	211
Image 5.4.3-7.	Gas-Charged Sediments (GCS) in the Arctic; South Barents Basin, Barents Sea	211

Image 5.4.4-1.	AUV-tracks Under Ice	212
Image 5.4.4-2.	The Autonomous Underwater Vehicle (AUV)	212
Image 5.4.4-3.	Recovery of the AUV by the starboard side crane. Photograph	213
Image 5.4.4-4.	Sidescan image of ice floes from below	214
Image 5.4.4-5.	Example of a thick floe	214
Image 5.4.4-6.	Examples of floe shapes	215
Image 5.4.4-7.	Statistics of ice floe draught	215
Image 5.5.1-1.	Overview of the Weddell Sea. Composite and multibeam image	216
Image 5.5.1-2.	The Weddell Sea; continental margin in the south-east. Multibeam image	217
Image 5.5.1-3.	The Weddell Sea; close-up of the preceding image, left part. Multibeam image	218
Images 5.5.1-4a, b.	The Weddell Sea; Herringbone Relief. Comparison of high resolution multibeam bathymetry and satellite altimetry	219–220
Image 5.5.2-1.	Orca Seamount, Antarctica. Close up multibeam echosounder image	222
Image 5.5.2-2.	Environment of the Orca Seamount. Multibeam echosounder Image (overview)	223
Image 5.5.2-3.	Environment of the Orca Seamount. Multibeam echosounder Image (semi close up)	223
Image 5.5.3-1.	Overview of the Antarctic Continent, cut out of Image 5.1.1.6-1	224
Image 5.5.3-2.	The migration paths of the main iceberg drift	224
Image 5.5.3-3.	Iceberg plough scars, Weddell Sea, Antarctica. Multibeam echosounder image	225
Image 5.5.3-4.	Longest iceberg plough scars measured, Weddell Sea, Antarctica. Multibeam echosounder image	226
Image 5.5.3-5.	Deep and old iceberg plough scars. Multibeam echosounder image	227
Image 5.5.4-1.	Balleny Islands flank area, Antarctica. Multibeam image	228
Image 5.5.4-2.	Cape Hallett, Ross Sea, Antarctica. Multibeam image	230
Image 5.5.4-3.	Possession Islands surroundings, Ross Sea, Antarctica. Multibeam image	231
Image 5.6-1.	The Mediterranean sea floor	233
Image 5.6.1-1.	A flat-top former volcano in the Alboran Sea. Multibeam image	235
Image 5.6.2-1.	The sea floor around the Balearic Islands. Multibeam image	236
Image 5.6.3-1.	Calcareous bedrock near marble deposit areas on the north-west coast of Italy. Sidescan image	237
Image 5.6.3-2.	Tripod field on plane sand bottom off Cinque Terre, Italy. Sidescan image	238
Image 5.6.4-1.	The North Aegean Trough system. Multi-beam image	238
Image 5.6.4-2.	Schematic map of tectonic plate motion including the Aegean Sea ...	240
Image 5.6.4-3.	A slump in the North Aegean Basin – the largest single failure event ever observed in the Aegean. Relief image	240
Image 5.6.5-1.	Marmara Sea	242
Image 5.6.5-2.	Entrance of North Anatolian Fault into Marmara Sea (Çınarcık Basin) from Izmit Bay	242
Image 5.6.5-3.	Çınarcık Basin and Eastern Ridge	243
Image 5.6.5-4.	Central Basin	244
Image 5.6.5-5.	Western Ridge and Tekirdağ Basin	244
Image 5.6.6-1a, b.	The Deep Eastern Mediterranean Sea formations. Multibeam bathymetric relief	245–247
Image 5.6.7-1.	Shelf break off Northern Israel. Multibeam image	248
Image 5.6.7-2.	Kurkar bedforms off Jaffa Port. Multibeam image	249

Image 5.6.7-3.	Pockmarks indicating gas deposits off Ashdod, southern Israel. Multibeam Image (collage)	251
Image 5.7.1-1.	Relief image of the Baltic Sea	252
Image 5.7.2-1.	Relief image. Relief of the shallow western side of the Baltic	255
Image 5.7.2-2.	Sea floor backscattering	255
Image 5.7.2-3.	Trans-sediment section through the Bight of Kiel, western Baltic Sea, imaged by the Acoustic Sea Floor Classification System ASCS	256
Image 5.7.3-1.	A bottle neck of the Baltic Sea. Multibeam image	257
Image 5.7.4-1.	Morphology of the sea floor near Sopot, Gulf of Gdańsk. 3D-multibeam image	258
Image 5.7.4-2.	Sand dunes and ridges on the sea floor near Sopot. Sidescan sonar mosaic image	259
Image 5.7.4-3.	Close up of the preceding sidescan sonar image of dunes and ripples on the sea floor near Sopot	259
Image 5.7.5-1.	Bedrock area off Stockholm, Baltic Sea. Seismic profile	260
Image 5.7.5-2.	Cut out of the cliff profile	260
Image 5.7.6-1.	Post glacial sediments. Parametric sediment echosounder image	261
Image 5.7.6-2.	Contour-following post glacial sediment. Parametric sediment echosounder image	262
Image 5.7.6-3.	Post glacial sediment with gas enclosure. Parametric sediment echosounder image	262
Image 5.7.7-1.	Gaseous sediment and gas plume. High resolution seismic image	263
Image 5.7.7-2.	High resolution seismic image. Cut out of Image 5.7.7-1	264
Image 6.1.1-1.	Mid-ocean current in the northeastern North Atlantic; field of float trajectories	267
Image 6.1.1-2.	Mid-ocean mean current drifter field; upper level	268
Image 6.1.2-1.	Scheme of an autonomous acoustic Doppler current profiler system (ADCP), mounted on a semi-submerged buoy	269
Image 6.1.2-2.	Lowered acoustic Doppler current profiler (LADCP)	270
Image 6.1.2-3.	Comparison of three echosounder current profiler systems. 75 kHz Ocean Surveyor: zonal velocity along 35° W	271, 272
Image 6.1.2-4.	Comparison of three echosounder current profiler systems. 38 kHz Ocean Surveyor: zonal velocity along 35° W	271, 272
Image 6.1.2-5.	Comparison of three echosounder current profiler systems. Lowered ADCP: zonal velocity along 35° W	271, 272
Image 6.1.2-6.	Subpolar current section	272
Image 6.1.2-7.	Deep water cross-section of the northern North Atlantic current field. Acoustic Doppler current profiler (ADCP) measurements combined with current computations from measured water density profiles	273
Image 6.1.3.1-1.	Tomographic network, project Thetis II	277
Image 6.1.3.1-2.	Sound rays along the main acoustic connection	278
Image 6.1.3.1-3.	Seasonal cycle of heat content across the Mediterranean Sea. Tomographic data compared to local samples and long term statistics	278
Image 6.1.3.2-1.	The tomographic network	279
Image 6.1.3.2-2.	The sound ray paths between the stations K1 and K2	280
Image 6.1.3.2-3.	The results of the five years experiment	280
Image 6.1.3.3-1.	The transceiver range	281
Image 6.1.3.3-2.	Ray tracing through the Strait of Gibraltar	281
Image 6.1.3.3-3.	Tidal periodicity of the Gibraltar outflow. Tomographic monitoring ...	282
Image 6.2.1-1.	The Hydrate Ridge, overview seen from southwest. 3D-multibeam image	283

Image 6.2.1-2.	The Hydrate Ridge with methane flares; close up seen from southwest. 3D-multibeam image with gas bubble flares	284
Image 6.2.1-3.	The Hydrate Ridge with inserted seismic cross section; close up seen from southwest. 3D-multibeam image with seismic data	285
Image 6.2.1-4.	The Hydrate Ridge, northern summit seen from southwest. 3D-multibeam image with sidescan image overlay and inserted methane flares	286
Image 6.2.1-5.	Acoustic evidence of a methane hydrate deposit: Seismic profile crossing the northern Hydrate Ridge off Oregon	287
Image 6.2.1-5a.	Zoomed cut outs of different resolution of the preceding seismic profile	288
Image 6.2.1-6.	Southern summit of the Hydrate Ridge; Seismic profile of a Pinnacle Area	290
Image 6.2.1-7.	Southern summit of the Hydrate Ridge; Seismic profile, crossing the preceding one	291
Image 6.2.2.1-1.	Sediment cross section of a pockmark, Eckernförde Bay, Baltic Sea. Sediment echosounder image	292
Image 6.2.2.1-2.	Pockmark of methane generating mud, Bight of Eckernförde. 3D-multibeam image from an autonomous underwater vehicle (AUV)	293
Image 6.2.2.1-3.	Gas layers in soft sediments of the western Baltic Sea; trans-sediment section by the Acoustic Sea Floor Classification System ASCS	293
Image 6.2.2.1-4.	Seasonal variability of the methane gas horizon of the Bight of Eckernförde. Time series of a local depth profile of a methane layer	295
Image 6.2.2.1-5.	Methane plumes in the North Sea; Parametric echosounder image ..	295
Image 6.2.2.2-1.	Acoustic mapping of carbonate sediments. Track plot of echo strength	296
Image 6.2.2.2-2.	Contour Map of carbonate sediment types, based on echosounder data	297
Image 6.2.2.2-3.	Sediment pond in the western Baltic Sea. Trans-sediment section by the Acoustic Sea Floor Classification System (ASCS)	298
Image 6.2.2.2-4.	Trans-sediment section through the carbonate sand wave Rebecca Shoal west of Key West, Florida. Imaged by the Acoustic Sea Floor Classification System (ASCS)	298
Image 6.2.3-1.	Upward looking echosounder for monitoring air intrusion by breaking waves in shallow water of 30 m depth. Schematic depiction ..	299
Image 6.2.3-2.	Air intrusion by bubble clouds, the sound image of a cloud	300
Image 6.2.3-2a.	Panorama of bubble clouds scanned by a submerged buoy	300
Image 6.2.3-3.	Air intrusion by bubble clouds; wind speed effect	302
Image 6.2.3-4.	Effect of strong gale	302
Image 6.2.3-5.	Frequency effect	303
Image 6.2.3-6.	Half the frequency	303
Image 6.2.3-7.	Effect of strongly different frequencies	303
Image 6.2.3-8.	10 kHz instead of 50 kHz	303
Image 6.2.3-9.	Sound absorption inside the bubble clouds	304
Image 6.2.3-10.	General results of sound absorption inside of air bubble clouds	304
Images 6.2.3-11, 12.	Radar and sonar backscatter from the sea surface	305
Image 6.3.1.1-1.	The depiction of herring swarms is – as usual – strongly compressed in the horizontal for quick inspection of long runs	309
Image 6.3.1.1-2.	Though the size of sprat swarms is much smaller, typically a few meters only, there are also herring swarms of similar size	309
Image 6.3.1.2-1.	Sprat likes to stay in layers at 60 to 80 m depth	310

Image 6.3.1.2-2.	Due to the notorious deficiency of oxygen near the bottom the fish stay away from it	310
Image 6.3.1.2-3.	Since the salinity of the Baltic Sea decreases with the distance from the western entrance to the North Sea, the sprat behaves different in the Gotland Basin	311
Image 6.3.1.3-1.	Part of the fish stays at a preferred depth of 8 m above the sea floor .	311
Image 6.3.1.3-2.	The record reveals no other preference of spatial distribution than the vicinity to the floor	312
Image 6.3.1.4-1.	The most obvious echo formations, looking like dense clouds between 300 and 500 m depth	312
Image 6.3.1.4-2.	The echo record shows compact schools of herring and sprat	313
Image 6.3.1.4-3.	This record taken near Bodø is typical of echograms of the Blue Whiting off the coast of northern Norway	313
Images 6.3.2-1-5.	Time series of 5 images: Groups of carcass eating scavengers approach a bait in the Arctic. Panorama scanning echosounder images	315
Images 6.3.3-1-2b.	The Sperm Whale, famous as Moby Dick in Melville's novel, is the largest toothed whale (Odontocetes)	316
Images 6.3.3-3-3b.	The Striped Dolphin	319
Images 6.3.3-4, 4a.	The Pilot Whale	320
Images 6.3.3-5-5b.	The Bottlenose Dolphin	321
Image 6.3.4-1.	Posidonia meadow. Multibeam image	323
Image 7.1.1-1.	Wreck residues of the German passenger ship Gneisenau in the Baltic Sea. Sidescan image	326
Image 7.1.1-1a.	The wreck of the ferry Jan Hevelius. Sidescan sonar image	327
Image 7.1.1-2.	Wreck of a tjalk-type ship in the Baltic Sea. Sidescan image	328
Image 7.1.1-3.	Wreck of the Condul in the Baltic Sea. Sidescan image	328
Image 7.1.1-4.	Wreck of a submarine in the North Sea. Sidescan image	329
Image 7.1.1-5.	Misfired sunken torpedo found in the Baltic Sea. Sidescan image	329
Image 7.1.1-6.	Misfired water-bomb found in the Baltic Sea. Sidescan image	329
Image 7.1.1-7.	Wreck of an offshore tower, German Bight, North Sea. Sidescan image ..	330
Image 7.1.1-8.	Lost load of stones, Dutch Continental Shelf. Multibeam 3-D-relief image	331
Image 7.1.1-9.	The same lost load of stones. Sidescan image of the sea floor structure	331
Image 7.1.1-10.	Maas-Channel. Multibeam image	332
Image 7.1.1-11.	Maas-Channel. Multibeam 3-D image, depicted as low angle view ...	332
Image 7.1.1-12.	Dumping location. Multibeam image	333
Image 7.1.1-12a.	Quality control of pump dredging a channel section. Autofocus multibeam image	333
Image 7.1.1-13.	Elbe River near Dessau, Sachsen-Anhalt, Germany. Multichannel sound image inset	334
Image 7.1.2.1-1.	Dune field in the Elbe-Estuary, sea lane of Hamburg Harbor. Multibeam image	336
Image 7.1.2.1-2.	Flow induced deep erosion of the river Elbe Estuary. Multibeam image	337
Image 7.1.2.1-3.	Traces of dredging work for sand mining off the fairway; Elbe Estuary. Multibeam image	337
Image 7.1.2.1-4.	Deposit of dredged material. Multibeam image	338
Image 7.1.2.1-5.	Sperrwerk Este (locking device), river Elbe. Multibeam image	338
Image 7.1.2.1-6.	Deposit basin of dredged material. Multibeam image	338
Images 7.1.2.2-1, 2.	Reliefs of the Bight of Meldorf. Composite images	339

Image 7.1.3.1-1.	Overview of the fairway near the Port of Hamburg, 2002. 3D-standard grid image derived from multibeam echosounder data	340
Image 7.1.3.1-2.	The fairway profile of the Hamburg Harbor entrance. 3-D multibeam image	341
Image 7.1.3.1-3.	Map of the city side of the harbor entrance	342
Image 7.1.3.1-4.	Row of steel poles of a quay construction	342
Image 7.1.3.1-5.	Ship accident inside the Port of Hamburg, mid fairway. 3D-standard grid image computed from Multibeam echosounder data	343
Image 7.1.3.2-1.	A floor section of Canale Grande. 3D-multibeam image	344
Image 7.1.3.3-1.	Passenger car wreck. High resolution multibeam image	344
Image 7.1.3.3-2.	Capsized car wreck. High resolution multibeam image	345
Image 7.1.3.3-3.	Car and container of a truck trailer; imaged by a forward scanning multibeam system	345
Image 7.1.3.4-1.	Sewage outfall diffusers in Hong Kong. Bathymetric map derived from high resolution multibeam surveying	346
Image 7.1.3.4-2.	Seabed exploration off Hong Kong for tunnel drilling. Bathymetric map derived from high resolution multibeam surveying	347
Image 7.1.4.1-1.	Bird's eye view of the wreck. Multibeam image	348
Image 7.1.4.1-2.	Side view of the wreck. Multibeam image	349
Image 7.1.4.2-1.	Sunken torpedo-boat destroyer. Side-scan image	349
Image 7.1.4.2-2.	Wreck of the tug boat Vittoria. Sidescan image	350
Image 7.1.4.3-1.	Photograph of the Cleona under sail	351
Image 7.1.4.3-2.	Wreck of the Cleona. Multibeam image	351
Image 7.1.4.4-1.	Wilhelm Gustloff. Sidescan image	352
Image 7.1.4.4-2.	Goya. Sidescan image	353
Image 7.1.4.4-3.	General von Steuben. Composite sidescan image	354
Image 7.1.4.5-1.	A PB4Y-2 Privateer Aircraft wreck on the bottom of Lake Washington, Seattle region, USA. Forward looking 2D-sonar image	354
Image 7.1.5-1.	Finding of buried objects and sea mines; the conventional approach. Multibeam sediment-penetrating image, enhanced contours	356
Image 7.1.5-2.	Finding of buried objects and sea mines; conventional multibeam image, depiction of the original data	357
Image 7.1.5-3.	Detection of a buried relic of Viking times; the parametric alternative. Imaged by a tilted, narrow beam sediment echosounder	358
Image 7.1.5-4.	Proud rock and mines; the synthetic aperture sonar alternative. Synthetic sidescan sonar image	359
Image 7.1.5-5.	Buried mines in very shallow water. Synthetic aperture sonar image with an 8–15 kHz sidescan sonar	360
Image 7.1.5-6.	Deeply buried mine detection in shallow water. Synthetic aperture sonar image with a low frequency sonar looking vertically down from an autonomous underwater vehicle AUV	361
Image 7.2.1-1.	Map of North Atlantic fiber-optic submarine cables	362
Image 7.2.1-2.	Map of North Pacific fibre-optic submarine cables	362
Image 7.2.1-3.	Section of a projected transatlantic cable route. 3D-multibeam strip mosaic image	363
Image 7.2.1-4.	Section of a projected transatlantic cable route. 3D-multibeam strip mosaic image, slant direction of view	364
Image 7.2.1-5.	Section of a projected transatlantic cable route; map of escarpment slopes. The slopes are derived from the 3D-multibeam strip mosaic map	365
Image 7.2.1-6.	Jetting tool – equipment for submarine cable burial	365

Image 7.2.2-1.	Pipeline crossings; sidescan sonar image of the external structure ...	367
Image 7.2.2-2.	Pipeline crossings; sub-bottom profiler image	367
Image 7.2.2-3.	Proud and buried pipe. Parametric sediment echosounder image ...	368
Image 7.2.2-4.	Protection of a pipeline- and cable-crossing by stone coverage, German Bight. Sidescan image	369
Image 7.2.2-5.	Pipeline diffusers, off Santa Barbara, California. Multibeam image ...	369
Image 7.2.2-6.	Close-up of a diffuser; multibeam image	370
Image 7.2.3-1.	Tetrapods protecting a breakwater, Bay of Hibikinada, Kyushu, Japan. Multibeam image	370
Image 7.2.3-2.	Tetrapods protecting a breakwater, Bay of Hibikinada, Kyushu, Japan. Multibeam image, unconnected image pixels	371
Image 7.2.3-3.	Wedge of concrete cubes protecting a breakwater in Bilbao Harbor, Spain. Multibeam image, unconnected image pixels	371
Image 7.2.3-4.	The same wedge of concrete cubes as in the preceding image of a breakwater in Bilbao Harbor	372
Image 7.2.4-1.	Polygonal concrete basement. Sidescan image	373
Image 7.2.4-2.	Submarine cable, research platform Nordsee. Sidescan image	373
Image 7.3.1.1-1.	Submerged environment of the sunken Baia with the city complex outline	375
Image 7.3.1.1-2.	Baia, overview of city complex, birds view	376
Image 7.3.1.1-3.	Slant view upon Baia with the protecting poles in the foreground	376
Image 7.3.1.1-4.	Details of the caldarium	377
Image 7.3.1.1-5.	Another detailed section with the survey vessel scanning along circle course, showing only irregular fragments	377
Image 7.3.1.2-1.	Porto Giulio, relief of the port outline with the access canal in bird's view depiction	378
Image 7.3.1.2-2.	Same as Image 7.3.1.2-1, but coded by shaded gray scale to enhance contours	379
Image 7.3.1.2-3.	Same, but slant view, underlining the optical relief impression	379
Image 7.3.1.2-4.	Close up with contour enhancement processing showing the geometrical structure of details	380
Image 7.3.1.2-5.	Aerial photograph of Porto Giulio	380
Image 7.3.2-1.	Wreck of the WW II battle cruiser Blücher. Multibeam image	381
Image 7.3.2-2.	Overview of the wreck and its environment. Multibeam image	383
Image 7.3.2-2a.	Close up of the bow part of SS Richard Montgomery	384
Image 7.3.2-2b.	Further close up of a mid-ship section. The multibeam sound image is impressive by its high resolution, reminiscent of a photograph	384
Image 7.3.2-2c.	Further close up of the bow section	385
Image 7.3.2-3.	Wreck of the historic submarine HMS A1, Multibeam image	385
Image 7.3.2-3a.	Wreck of a historic warship. Sidescan sonar image	386
Image 7.3.2-4.	The wreck site; multibeam image	387
Image 7.3.2-4a.	The central area; multibeam image	387
Image 7.3.2-5.	Place of excavation of the historic ship wreck HMS Mary Rose. Multibeam image	388
Image 7.3.2-6.	The Salcombe area, overview. Multibeam image	389
Image 7.3.2-6a.	Close up of the Salcombe wreck site	390
Image 7.3.3-1.	Battle cruiser SMS König. Schematic drawing	391
Image 7.3.3-1a.	The SMS König, built in Wilhelmshaven and launched in March 1913	391
Image 7.3.3-2.	The SMS Kronprinz Wilhelm, built in Kiel and launched in February 1914	391
Image 7.3.3-3.	The SMS Markgraf, built in Bremen and launched in June 1913	392
Image 7.3.3-4.	Light cruiser SMS Dresden II. Schematic drawing	392

Image 7.3.3-4a.	The SMS Dresden II, built in Kiel and launched in April 1917	392
Image 7.3.3-5.	The SMS Cöln II, built in Hamburg and launched in October 1916	393
Image 7.3.3-5a.	The SMS Cöln II	393
Image 7.3.3-6a.	The SMS Brummer, built in Stettin and launched in March 1916	394
Image 7.3.3-6.	Light cruiser SMS Brummer. Schematic drawing	394
Image 7.3.3-7.	Light cruiser SMS Karlsruhe. Schematic drawing	395
Image 7.3.3-7a.	The SMS Karlsruhe built in Wilhelmshaven and launched in January 1916	395
Image 7.3.3-8.	Battle cruiser SMS Bayern. Schematic drawing	395
Image 7.3.3-8a.	The SMS Bayern, built in Kiel, launched in February 1914	396
Image 7.3.4-1.	The place of the semi-buried ancient wooden pole- and stone construction on the bottom of the fjord Schlei is located on the German Baltic coast near the former Haitabu	397
Image 7.3.5-1.	The multibeam image reveals a well-preserved example of caisson units in the middle of the Omaha Beach harbor area	398
Image 7.3.5-2.	These strongly damaged caissons of the former Omaha Beach harbor belong to the western edge of the caisson-line parallel to the shore	399
Image 7.3.5-3.	This image appears to document a major ship disaster	400
Image 7.3.5-4.	These remnants were the former concrete pontoons or Beetles, which supported a section of bridge running from the Mulberry Artificial Harbor complex to the shore	401
Image 7.3.5-5.	The object in the center is one of three wrecks of a special Sherman duplex drive (DD) tank found 4 km off Omaha Beach	401
Image 7.3.5-6.	Aerial photograph of Mulberry Harbor	402
Image 7.4.1.1-1.	The passenger freighter Robert E. Lee. Photograph	404
Image 7.4.1.1-2.	Wreck of the Robert E. Lee. Sidescan sonar image of a deep tow array	405
Image 7.4.1.2-1.	The SS Alcoa Puritan. Photograph	406
Image 7.4.1.2-2.	The wreck of SS Alcoa Puritan. Multibeam 3D-image generated from multibeam bathymetry data acquired by a deep tow system	406
Image 7.4.1.2-3.	Seismic cross section of the wreck of SS Alcoa Puritan. Subbottom profiler image made by a deep tow system	407
Image 7.4.1.2-4.	The wreck of SS Alcoa Puritan. Low frequency (120 kHz) version of a sidescan image made by a deep diving autonomous underwater vehicle (AUV)	408
Image 7.4.1.2-5.	The wreck of SS Alcoa Puritan. High frequency (410 kHz) sidescan-image made by a deep diving autonomous underwater vehicle (AUV)	408
Image 7.4.1.3-1.	Mid scale survey of the two wreck area with the passenger freighter Robert E. Lee and the German submarine U166. Overlay of search track pattern with sidescan image made by a deep-sea AUV	409
Image 7.4.1.3-2.	Close up of the wreck of the passenger freighter Robert E. Lee. Sidescan image made by a deep-sea AUV	409
Image 7.4.1.3-3.	Close up of two units of the wreck of the U166. Sidescan image made by a deep-sea AUV	410
Image 7.4.1.3-4.	Analyzed close up of the main units of the wreck of the U166. Sidescan image made by a deep-sea AUV	410
Image 7.4.1.3-5.	Site Specific close up pattern of U166	411
Image 7.4.1.3-6.	Two parts of the wreck of the German submarine U166 inside of impact craters; 3D-multibeam image made by a deep-sea AUV	411
Image 7.4.1.3-7.	Main part of the wreck of the German submarine U166. Sidescan image made by a deep-sea AUV	412

Image 7.4.1.3-8.	Two parts of the wreck of the German submarine U166; images combined. Sidescan images made by a deep-sea AUV	413
Images 7.4.1.3-9, 9a.	Schematic plan and side view of the class drawing with superstructure	413
Image 7.4.2-1.	Large area overview of the Storegga Slide. Composite image	415
Image 7.4.2-2.	Cut out map containing the upper part of the Storegga Slide area	415
Image 7.4.2-2a.	Overview of the major part of the Storegga-Slide area. Composite data image	416
Image 7.4.2-3.	First composite close up image of a Storegga Slide area taken by the prototype AUV	417
Image 7.4.2-4.	Cut out of the preceding area	418
Image 7.4.2-5.	Close up image taken by an essentially improved AUV	419
Image 7.4.2-6.	Close up near the site of Image 7.4.2-5, seen in downward direction .	420
Image A.1.	Sound speed in the ocean	443
Image A.2.	Sound refraction in the sea	443
Image A.3.	Sound refraction and ducted propagation	444
Image A.4.	Absorption of sound waves and electromagnetic waves in the sea ...	445
Image A.5.	Temperature effect in the absorption; cut out of Image A.4	446
Image A.6.	Bottom backscattering strength	446
Image A.7.	Volume backscattering strength	447
Image A.8.	The graphic scheme provides the beamwidth of a transducer of the indicated size and the frequency by connecting the quantities by a straight line as indicated	447
Image A.9.	Directivity index DI and beamwidth	448
Image A.10.	Source level and acoustic power	449
Image A.11.	Transmission loss with absorption and geometrical spreading combined	449
Image A.12.	Noise spectrum level of wind- and sea traffic noise	449

Part I

The Basic Facts of Imaging the Ocean

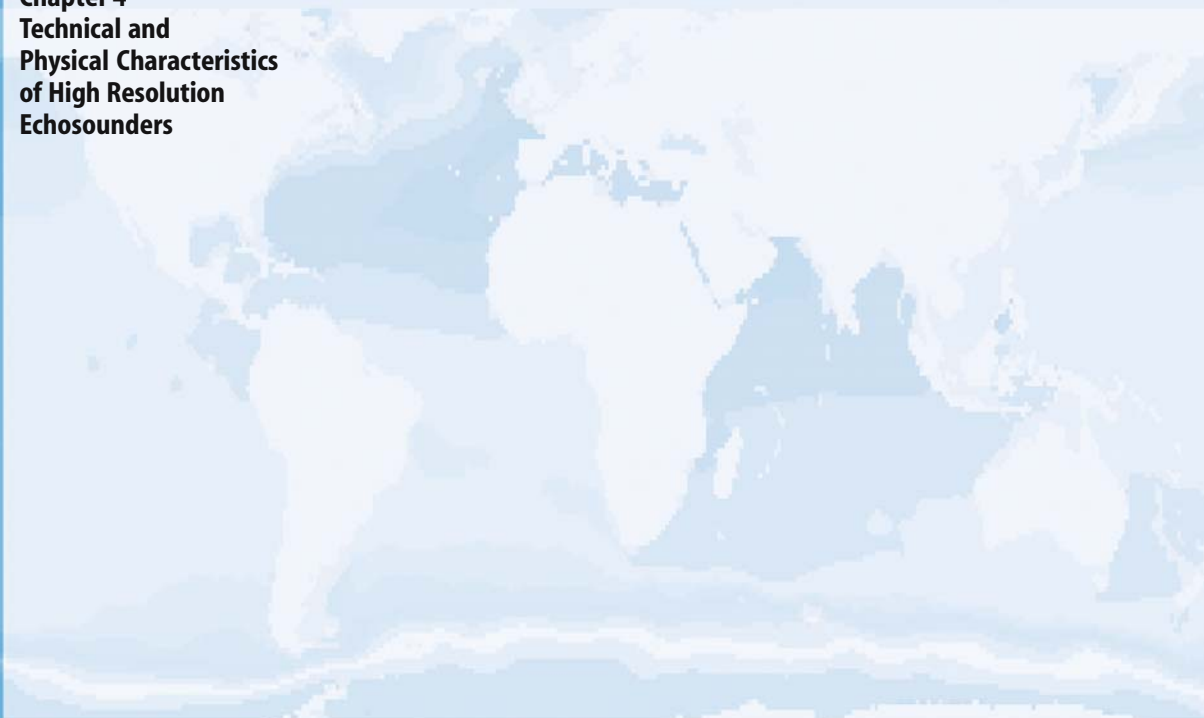
Chapter 1 **Preliminary Remarks**

Chapter 2 **Alternatives to Imaging the Sea by Sound and First Acoustic Trials**

Chapter 3 **Acoustic Features of the Sea**

Chapter 4 **Technical and Physical Characteristics of High Resolution Echosounders**

The book is subdivided into two main parts: the first 4 chapters deal with the basic facts of ocean imaging by treating the environmental characteristics and the technical requirements of echosounding. Chapters 5–7 present the various types of application. Their fascination has been the motivation for this book.



Preliminary Remarks

Young couples expecting their first child are enthusiastic and happy when they see the most fascinating image they can imagine: the prenatal *sound image* of the foetus, their baby, long before it is born. Diagnostic imaging by ultrasonics in medicine works in principle like a modern multibeam echosounder by which the ocean floor is being imaged. Both techniques apply a fan of many narrow sound beams and their echo patterns are combined on the computer to form the image. Both are indispensable diagnostic tools to reveal facts and processes hidden from sight. But only sound imaging in medicine is well known; people are fascinated that they can personally experience *to seeing the invisible* by means of sound.

Ocean imaging by sound is still widely unknown though with more and more exceptions. The fascination evoked by the sea and the growing interest in the ocean world has been nearly exclusively the merit of photography. The visible beauty of fauna and flora make us forget that we can see only the environment nearby; the short range of light in the sea hides everything from sight at a distance beyond a few tens of meters even in clear tropical waters. The domain of sound imaging the sea consists of formations of another dimension. The revolutionary discovery of the dramatic tectonic processes which permanently reshape the deep-sea floor and which have generated undersea formations of tens to hundreds, even thousands of kilometers in size has been decisively based on the diagnostic capability of ocean echosounding. Nevertheless and despite its fundamental role, the products of this technique remained a matter for experts for a long time apart from echosounders and bathymetric charts for seafarers and other users like fishery.

One should admit however that sound images of the sea floor have achieved the technical quality and resolution of aerial photographs only since recently. Since sound images can be depicted as landscapes as they are also presented in this book they can be understood by many more than the experts without complicated explanations. These images show another world to the one we are familiar with and though some might look like science fiction, the images are authentic and provide insight into reality of the two thirds of our planet beyond the reach of photography.

It is true that echosounding the ocean was invented long before any application in medicine was even thought of. But the generation of real ocean images was impossible for a long time simply because the ocean is not a cooperative patient at all. Ocean imaging has to cope with weak echoes partly buried in noise and with distorting sound refraction. And even more it has to cope with complex motions of the ship caused by sea waves and wind blurring the image without complicated corrections and precise positioning, which were impossible and unavailable before the recent past.

Many of the facts dealing with the ocean are well known meanwhile, even common place. We know, the oceans are the cradle of life on our planet, we know well, that they cover more than two thirds of the Earth's surface. It is also known that the ocean current systems, the conveyor-belts of heat, actively determine the climate of continents. Coastal areas are the homeland of the majority of mankind. The world economy relies on the sea as a resource of food and fossil energy and even more on the sea lanes, the highways of world trade. Though we know all this, our state of knowledge of fundamental processes in the ocean is the result of the research of only the last few decades. High resolution imaging of the sea floor is still in a comparatively early phase: only a minor part is as yet known in as much detail as the surface of the moon and even of the planet Mars.

Our present state of understanding of the most dramatic changes of the solid skin of the globe, the *Earth's crust* and its fundament, termed *lithosphere*, was developed only in the sixties and seventies of the twentieth century when the technical development of high resolution sound imaging, one of the decisive tools of ocean research, made a quantum leap: the multibeam echosounder became available. The scientific breakthrough has been the *tectonic plate theory*, the later and modified verification of Alfred Wegener's visionary hypothesis of the continental drift as suggested in the early twentieth century. The slow but permanent motions of the tectonic plates, their rise, shift and final set, proceeding by centimetres per year occur nearly exclusively in the oceans. They cause the great majority of all earthquakes and volcanic activities, most of them located along plate margins. The sound images of the characteristic deformations of diverging and converging margins are the subject of Sect. 5.2 of this book.

The sea floor is also a record of the *climate history*. The stratification of the sediments, similar to annual rings on trees (Sect. 5.3.2, 5.4.3), contains information on climatic events and changes over similar time scales as the geodynamic processes and contributes to verify or to refute concepts of modeling the future climate development.

The oceans are full of superlatives and extremes: They are the habitat of the greatest diversity of species, including the largest animals brought forth by

evolution (Sect. 6.3.3). They represent the largest storage of mobile thermal energy, thus dominating climate processes (Sect. 6.1). There are deep-sea trenches, the result of tectonic plate collisions, which are incised three times deeper than the Grand Canyon (Sect. 5.2.2), and mid-ocean ridge formations, the product of magmatic sea-floor spreading, which are larger and longer by far than the largest mountain chains on the continents (Sect. 5.2.3, 5.2.4). Methane-hydrate deposits in the ocean, according to recent estimates, contain more than twice the amount of all other previously known carbon-hydrates (Sect. 6.2.1).

Over the last decades global changes in the oceans, the marginal seas, and coastal areas have become the subject of international, interdisciplinary cooperation in maritime research. This is perhaps the most important and certainly the most extensive contribution of the nations to the investigation and the protection of the environment, the living conditions of man and nature of today and the future. It is a new and rational view of the sea, different from the past, where romantic emotions, and even legendary fantasies together with robust interests were the driving forces.

Man and the Sea – this has been a unique relationship over a long period of history: attraction and fear, full of myths, of battles and heroes, of violence and passion, bringing to light human virtues and failings. But the sea was a technical challenge as well. The development of ships, the largest mobile constructions ever, enabled discoveries which have changed the world. With merchant ships the sea was the source of wealth through trade between orient and occident; with warships the sea became the symbol of world power through sea sovereignty of powerful nations over the centuries. And the sea, at all times was experienced by seafarers as an arena of raging, devastating forces of nature as well as a world of silence and peace. A unique relationship indeed – and an image of countless aspects and facets. This image of the sea, however, created during the history of man was in its essence *an image of the surface of the sea*. Far off the coast its depth was the abyss: unknown and unimaginable.

It was only during the 19th century that the sea became the subject of systematic research. "Physical Geography of the Sea" published in the fifties by

M. F. Maury was a pioneering textbook which presented collected data on weather and climate and even current systems of the world's oceans. Maury's charts on winds and currents and the sailing directions revolutionized the navigation of all nations, reducing sailing time between ports by designating new ocean routes. The deep-sea work has been fundamental to ocean science. It visualized already in some detail the origins of the *Gulf Stream* and most remarkably gave the contemporary state of a depth chart of the *North Atlantic* up to 50° latitude (Image 1-1;

for zooming s. attached CD), based on the presumably very first bathymetric chart of the Atlantic of 1853. The data bases were manual measurements gained by wearisome wire-soundings from ships which had to stop for hours during this very lengthy procedure. This small data collection was grouped into five depth classes, down to more than 7 000 m, from which corresponding sea areas were derived. These early sea trials enabled a first, though very rough impression of the shape of the entire North-Atlantic sea floor. The map indicated already the submarine continental

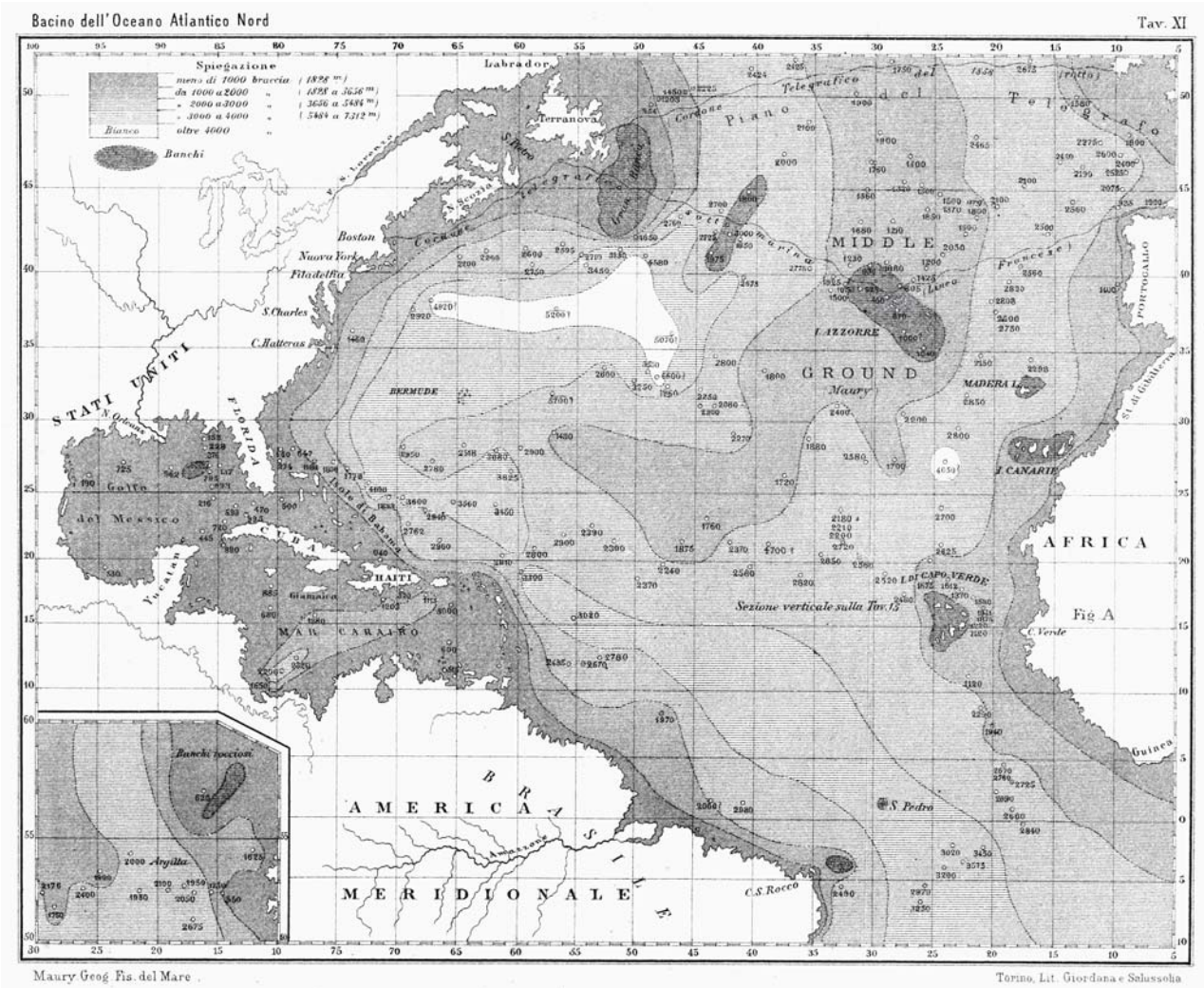


Image 1-1. M. F. Maury, bathymetric map of the *North Atlantic*, Italian edition of 1877. The map content is identical with the original American edition of 1855 ■

margins and a shallower area between broad deep basins, later known as the *Mid-Atlantic Ridge*. Should we say:

A first image of the deep-sea floor?

In fact, the number of wire soundings, the basis of this bathymetric chart was just of the order of a hundred with a few accumulations and very large gaps in between. In other words: just one to two samples per

area of the size of France or Germany. In respectful hindsight, this mechanical approach reminds us more of a blind man groping the floor with his stick than of a method to substitute the direct *visual image*. This kind of imaging is in its essence *sensing from a distance*, without a physical contact, or expressed by its technical term: *remote sensing*. The substitute to imaging the ocean interior by light is its *imaging by sound*, the subject of this book. But is this substitute really necessary? What do we know about alternatives to sound imaging?

Alternatives to Imaging the Sea by Sound and First Acoustic Trials

2.1 Visible Light

2.2 Infrared

2.3 Microwaves

2.4 Ultra-Long Radio Waves

2.5 X-Rays

2.6 Gamma Radiation

2.7 Gravity Anomalies

2.8 Magnetic Anomalies

2.9 Hydrodynamic Effects

2.10 The Acoustic Solution

2.11 First Acoustic Trials

2.12 Four Lines of Evolution of Ocean Echosounding

2.13 Conclusion

To obtain an image of the interior of the sea such as the shape of the sea floor, we need to *illuminate* or *irradiate* the scenario with an appropriate radiation. To get sufficient radiation back, its *absorption* by the environment needs to be small. A practical and simple definition to compare the various types of radiation regarding their individual absorption by sea water is the so called *penetration depth*. At this depth of reference, 9/10 of the initial irradiation energy is absorbed and only 1/10 remains for further penetration. At twice this depth, 9/10 of the *remaining energy* is absorbed and so forth. A larger penetration depth thus means a better irradiation of the undersea scenario.

However, the physics of the sea offers also other possibilities of imaging than by radiation. The most capable of them is treated in the book as an important supplement to imaging by sound.



2.1

2.1
Visible Light

What about the absorption of *visible light* in the sea? All of us have certainly seen movies of beautiful underwater habitats with fabulous vegetation, populated by exotic fish of brilliant, opalescent colors, brightly illuminated by sunlight. As mentioned, we tend to forget that such scenarios are usually found in tropical waters, very clear and very close to the surface. If the photographer could be protected against the water pressure to go deeper, say 100 m, he would find that the light *intensity* is merely 1/10 of the condition he had at the surface. According to definition, he arrived at the *penetration depth* of visible light in very clear sea water, which is only about 100 m. Another 100 m, and the intensity has decreased to 1/100. This is just the depth regime of the plateau surrounding the continents, the *continental shelves*.

Since the light intensity decreases by a fraction of 1/10 for every 100 m descended the decrease towards absolute darkness is dramatic, following an *exponential law*. At 1 000 m depth, the regime of the upper *continental slope*, the photographer, who would now be protected by a capsule resistant against the water pressure of 100 bar, would see nothing at all. The rest of the daylight is now merely one tenth of a billionth. Switching on his battery-searchlight of say 100 W, he would see even less far than with his car headlights. To just replace this poor illumination by stronger daylight at the sea surface would require several million times the light energy of the sun. This is an absurd consideration, of course. But it may demonstrate what absolute darkness means. However, the average depth of the deep oceans is about 4 000 m, moving the decimal point of the daylight fraction by another 30 places, one per every 100 m, not to speak of the deep-sea trenches down to 10 000 m and more.

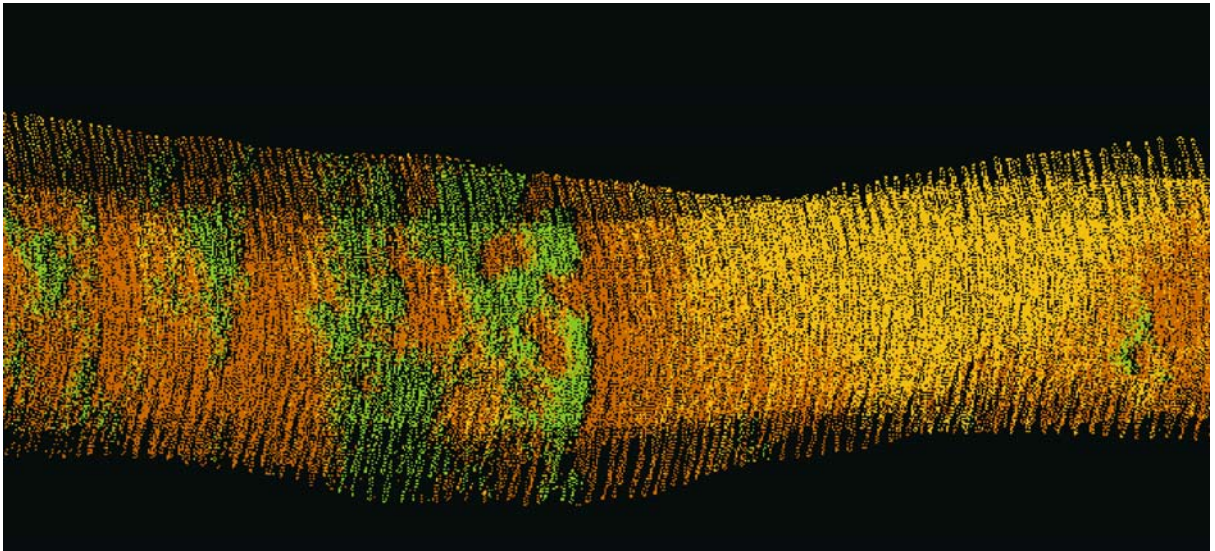


Image 2.1-1. Shallow area in the Baltic Sea with algae. Laser-bathymetry. The image shows the raw data of a Laser-borne depth chart stripe of a very shallow test area, less than 10 m deep, in the western Baltic Sea. Each of the color coded pixels corresponds to one Laser-pulse, transmitted downwards by a high intensity blue-green Laser, carried by a helicopter 200 m above the water. The widened Laser beam had a footprint of 1.5 m when entering the water column. The swivel range of the beam axis scanned a sea floor width of 50 m. The nanosecond pulse-length provided a depth resolution of 20 cm on the echoreceiver located in the aircraft. The yellow field is 8–9 m deep; brown means 9–10 m depth. For accuracy control the cross-flight was repeated three times with incomplete overlapping. The clouds of green pixels are attributed to algae above the sea floor, which are opaque to laser-light but wouldn't have screened the sound signals of a sonar device. The measurements were conducted under benign conditions of low sea state and low turbidity.

Swedish-German Cooperation, 1999

Image ©: Thomas Scholz, Forschungsanstalt der Bundeswehr, FWG, Kiel, Germany ■

The reality is a bit more complex than this simple consideration. There are deep water fish, crustaceans, and other animals which produce some light by bioluminescence known from glow-worms to attract partners or prey. Some produce even a kind of impulse flash light but the effect of illumination of the dark environment is much less than by starlight at midnight in a desert and no moon shining.

All this is the optimum clear water case where mapping the depth of very shallow sites from aircraft by strong Lasers is in fact possible (Image 2.1-1). At least, when the sea surface is calm and the Laser-beam has only to deal with the strong reflection loss when entering and again when leaving the water and, of course, with the extra loss in the water on its way back.

European shallow waters are different. Their normal state is turbid. The fine particles of the sediment are stirred up by tidal currents or by storms, often producing an extremely dense fog effect. In addition, marine life, such as algae bloom, adds considerably to the optical reality of European shelf waters and estuaries which may then remind us of a snow storm. Divers report that sometimes they can hardly recognize the end of their own arm stretched out.

However, visible light, a small fraction of the entire spectrum of electromagnetic waves, is the only window through which there is illumination of the interior of the sea at all as pointed out in the following. Moreover, it is only the *blue-green light* of the famous aquamarine color where the absorption is smallest. This is where the evolution of the only sensor of animals that provides images, the eye, has optimized its sensitivity. The simplified scheme of Image 2.1-2; (complete diagram: s. Appendix, A.3.3.1) underlines this exceptional status of visible light within the regime of electromagnetic waves. The review of all the other candidates of electromagnetic radiation can thus be very brief.

2.2 Infrared

Somewhat surprising to those who enjoy swimming in comfortably warm water may be the other extreme to visible light regarding penetration depth: the *infrared* or heat radiation. An extremely thin water film of some microns absorbs already 9/10 of the incoming heat radiation from the sun. The distribution of this heat energy down into the water column happens essentially by wind- and current-induced turbulent mixing. The

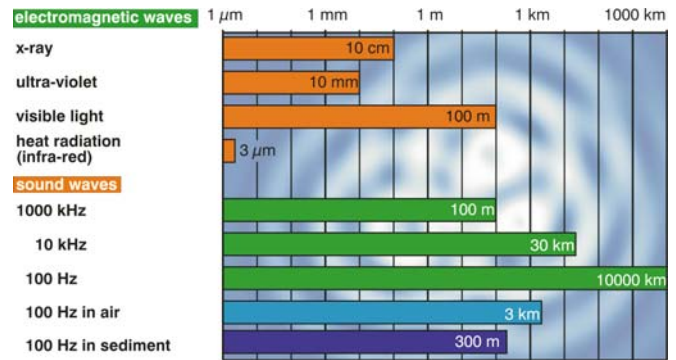


Image 2.1-2. Penetration depths of electromagnetic waves and sound waves in the sea. X-ray- and UV-ranges vary by decades. ■

comparatively poor thermal conductivity of water contributes slightly when the weather is dead calm. In fact, what we see on satellite images in the weather forecast is the water temperature at the sea surface, indicating the temperature of the mixed layer just beneath. Its depth and often complex structure is governed by how and where turbulent mixing by counter-rotating vortex structures have done their work (Sect. 6.2.3).

2.3 Microwaves

Electromagnetic waves of a few centimeters wavelength, labeled microwaves but often called radar waves, penetrate clouds though not normally rain showers and the water not more than a fraction of their wavelength. (This fact is experienced often with the microwave oven at home: a substance consisting mainly of water is less hot towards the center of the volume.) However, radar satellites are a most capable means to *indirectly* acquire the relief of large scale formations of the sea floor by their gravity anomalies deforming the sea surface (Sect. 2.7). This fundamental method became the basis of global sea floor mapping in connection and merging with acoustic bathymetry (Sect. 5.1).

2.4 Ultra-Long Radio Waves

Much longer wavelengths like those of ultra-long radio waves seem to enter the sea deeper but this still remains a fraction of a wavelength, thus being no al-

ternative to gain images of the ocean floor. This extreme wavelength regime has achieved only some importance for slow communication with submerged submarines.

2.5 X-Rays

X-Ray radiation applied in medical diagnosis reach just to 6–10 cm reference range at 9/10 loss in water – and tissue. The maximum of about 120 cm reference range is only achieved far beyond medical application. *Ultraviolet radiation* between visible light and X-rays varies strongly in penetration depth: within UVA, the regime near to visible light, the reference range is between 30 m and 7 m. But near the lower X-Ray regime the UV-range shrinks to less than the infrared penetration.

2.6 Gamma Radiation

The wavelength regime between X-Ray and *cosmic radiation*, named *Gamma radiation* does not offer more than the 120 cm range of 9/10 loss. The interval of cosmic irradiation of highest energy *does* provide penetration of the water column of the deep ocean but only by secondary sub-nuclear particles by which echo imaging would be science fiction, moreover with energies far beyond technical possibilities.

This concludes the review of the entire electromagnetic spectrum but does not necessarily yield an exhaustive exclusion of other options than sound to image the ocean. We shall therefore inspect potential alternatives provided by physics without wave propagation.

2.7 Gravity Anomalies

The mass of a seamount enhances the local gravity a little which attracts the water above slightly more than the abyssal plain around and a trench a little less, forming weak bulges and dents in the sea surface respectively. The discovery that these deformations can be acquired from space enabled the utilization of the gravity anomaly as the only effect physics can offer to map the sea floor relief nearly worldwide within a short time and without touching the sea surface at all, though only resolving structures beyond several kilometers in the horizontal.

The method became possible with the technology of Satellites operating radar-altimeters. Scanning the local heights of the sea surface by a downward looking, narrow beam radar along the satellite orbit while the globe rotates beneath acquires a relief that appears like a weak and coarse copy of the sea floor (Sect. 5.1). The main hurdles to cope with have been the ever present sea surface deformations of other origin, most of them comparable in amplitude or even exceeding the gravity effect, such as waves, tides, currents, varying air pressure, different densities of warmer and colder ocean water and of course the geoid, deviating from a sphere by 40 km oblateness as the only invariant reference.

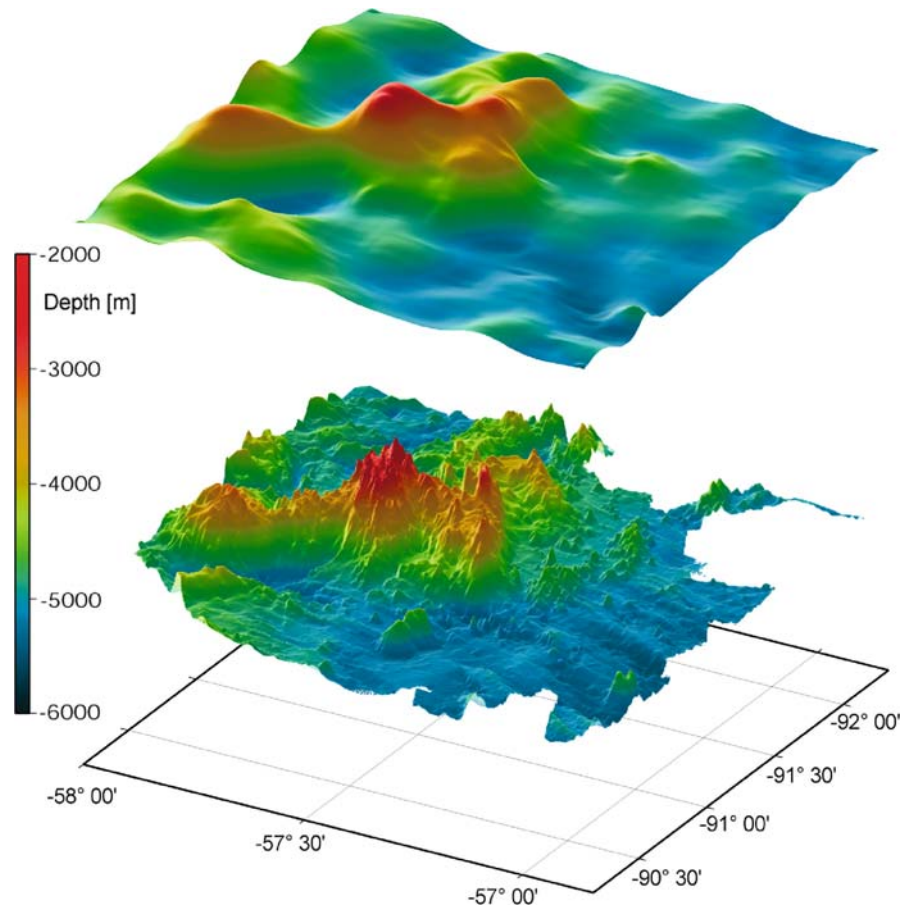
The successful strategy was threefold: first to correct for, or average out, as much as possible of the superimposed disturbances; second to invert the model which provides the sea surface deformations generated by the gravity field of the mass distribution beneath and third, particularly important, to merge the resulting relief data set with all available bathymetric data from echosounding worldwide. The product is the global relief as shown in Sect. 5.1.1 with a horizontal resolution of 2 arc minutes or about 3 km. This fundamental innovation enabled the perception of large scale formations of the sea floor also in remote areas of the ocean without any or with nearly no bathymetric data from echosounding.

There is a fundamental limitation however, to derive the bathymetric relief from satellite altimetry: *the gravity relief is only a measure of the mass distribution*. Therefore it does not necessarily follow the actual sea floor relief because the Earth's crust and the lithosphere are more or less inhomogeneous in their density. Particularly evident is the effect of sediment coverage. A seamount, when completely hidden by thick sediments of lower density may still stand out in the gravity relief without any indication in the bathymetry. The Image pair 5.2.1-4a and 5.2.1-4b demonstrate this effect as well as the difference in resolution between multibeam echosounding and satellite altimetry. The direct comparison of high resolution acoustic bathymetry and satellite altimetry is shown as the area of the *Eltanin Massif* of about 100 km square in the *South Pacific* (Image 2.7-1), also shown in the context of Sect. 5.1.2.2. It reveals both the difference in resolution and significant deviations of the average relief. (The attached CD permits turning and zooming the scene for closer inspection).

Further examples of systematic deviations between both methods are discussed in other contexts (Sect. 5.5.1).

Image 2.7-1.

Relief of the *Eltanin Massif*; acoustic multibeam bathymetry (*bottom*) and satellite radar altimetry (*top*) ■



They make evident that they supplement each other because gravity anomalies which do not appear in the sound image may indicate major geological dislocations and faults. Systematic deviations between gravimetry and bathymetry are guides for investigating the geodynamic processes involved and support the interpretation of seismic soundings of the internal sea floor structure.

2.8 Magnetic Anomalies

The other static field which is not screened by the sea volume either is the *magnetic field*, which cannot contribute anything to acquire the shape of the sea floor but has become a unique indicator of geological date assignment. The discovery of magnetic *zebra stripes* on the sea floor during the sixties of the twentieth century revealed a long term calendar of the age of the ocean bottom. In fact, ferromagnetic minerals of the sea floor

are being magnetized during the hot phase of their genesis through extruding magma at the mid-oceanic ridges (Sect. 5.2.3, 5.2.4) by the contemporary magnetic field of the Earth. The actual direction of the magnetization is preserved after cooling and remains permanent even after reversion of the polarity of the Earth's magnetic field. Since this happens in time periods of some hundred thousands to some millions of years, the speed and the direction of the sea floor spread can be read from its frozen magnetic history.

However, the signature of local *magnetic anomalies* is even more severely averaged out than that of anomalies of the *unipolar gravity field* when measured at a distance. This is already true for mapping such anomalies by aircraft, another type of rapid and therefore economic data acquisition covering large sea areas. Therefore satellites are much too far away for such magnetic measurements which essentially have to rely on slow ship-borne data acquisition.

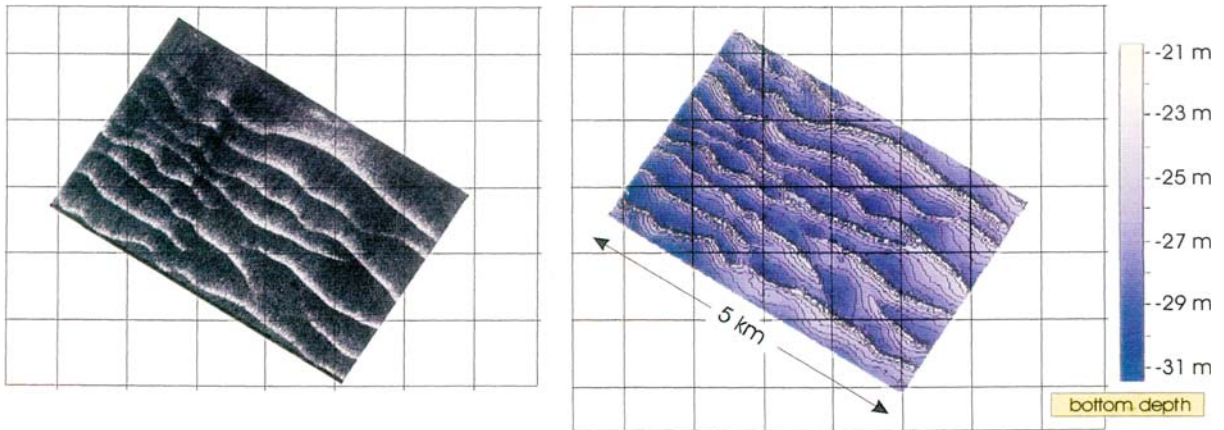


Image 2.9-1. Sea floor imaging by an hydrodynamic effect. Acoustics and radar. The radar image (left) of the disturbed sea surface reveals the contours of the dune crests below though with little information on the shape of the relief in between. Thus the most hazardous part affecting fairway clearance is clearly indicated. The water depth at the site of measurement near Hoek van Holland is 22 m with dune crests of 4 m height. The speeds of wind and current were 0.6 m s^{-1} and 1.0 m s^{-1} respectively. The acoustic bathymetry (right) shows the complete relief with the shape of troughs and crests independent of their relative depths. However, both entirely different principles of imaging provide essentially identical maps of the highest crest ridges.

Project: EU C-Star
 Synthetic Aperture radar; P-band, 50 cm wavelength
 Aircraft: DLR, Oberpfaffenhofen
 Research vessel: *RV Belgica*

Single beam-echosounder: STN-ATLAS, type: DESO 20;
 frequency: 210 kHz, beamwidth: 9°
 Radar image ©: DLR, Oberpfaffenhofen, Germany
 Sound image ©: C. Vernemmen, Univ. of Gent, Belgium ■

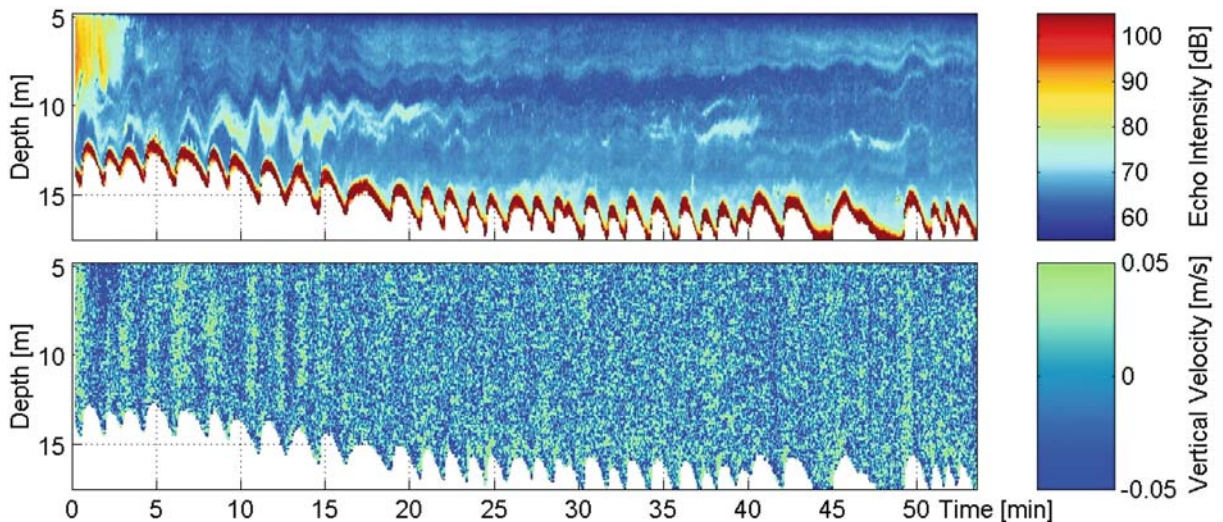


Image 2.9-2. Weak internal waves also influence the sea surface. Acoustic current meter image. The wavy sound scattering layer above the dune shaped shallow site in the Baltic Sea (north of Fehmarn) looks like an ascending copy of the washboard below. But it is the snapshot of an independent internal wave, called *lee wave*, because it is excited by a sea current on the lee side of the highest crests. The lower image shows the instantaneous pattern of the local up and down components of the same wave motion, which obviously reach up towards the surface. The motion pattern was measured by an acoustic Doppler current profiler (Sect. 4.5.2) which also recorded the wave by its undulating scattering strength.

Image ©: Volker Fiekas, Forschungsanstalt der Bundeswehr FWG, Kiel, Germany ■

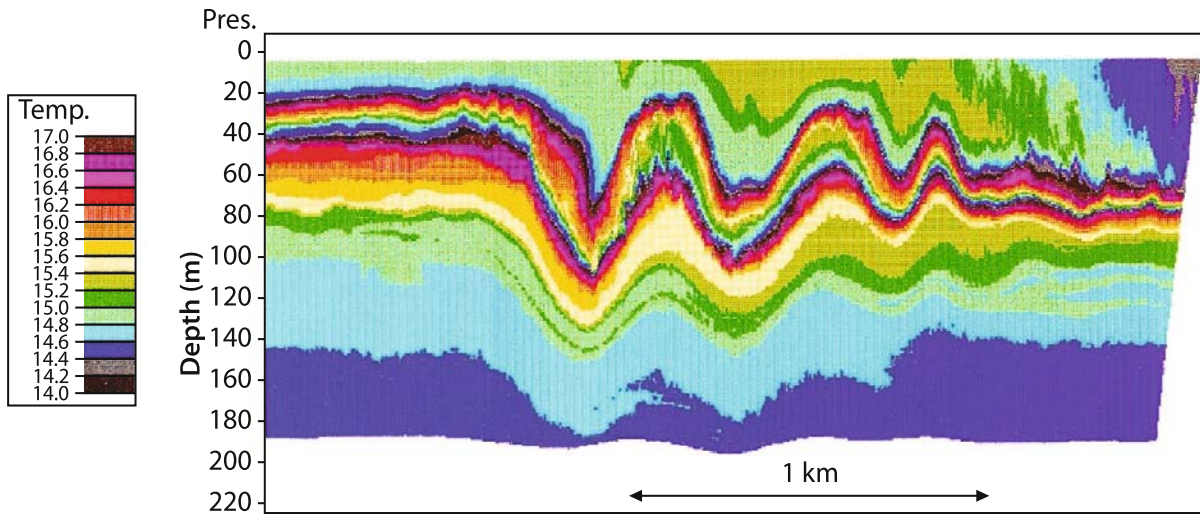
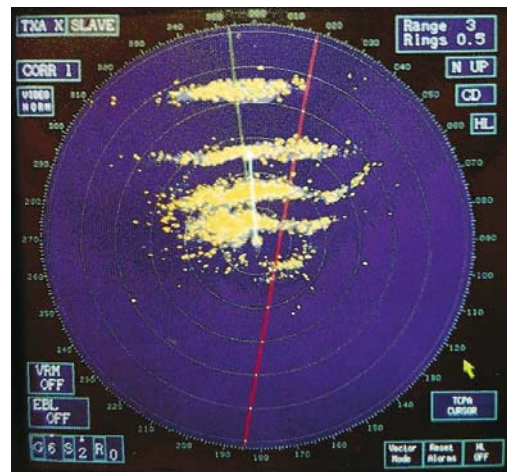


Image 2.9-3. Scylla and Charybdis in the Strait of Messina. Large internal wave package and its copy on a radar screen. The internal wave package shown in the *upper* image as a cross section through the temperature field is typical of the oceanic conditions in the Strait of Messina between Sicily and Italy. Its treacherous currents were attributed in antiquity to the legendary characters of Scylla and Charybdis. The strong current through the Strait and the warm water layers on top of colder ones with the corresponding water densities are ideal ingredients for the excitation of such internal waves which can reach amplitudes of many meters. The internal wave generates a current pattern at the sea surface which varies the shape of the short surface waves visible on the *lower* image of a radar-screen. The cross section through the wave deformed temperature field was acquired by a chain of temperature sensors, towed at a steep angle.

Image ©: Volker Fiekas, Forschungsanstalt der Bundeswehr FWG, Kiel, Germany ■



2.9 Hydrodynamic Effects

Trying to be complete with non-acoustic alternatives, we mention a particular *hydrodynamic effect* which, under special conditions, can provide another kind of sea floor image. However, this “special effect” will at most reveal features of the floor profile rather than quantitative depth information. The effect became somewhat popular through satellite radar images of the English Channel with clearly visible underwater dunes despite the sea water being totally opaque for radar. What is the explanation? The strong tidal current, when crossing the dunes, accelerates its speed because the free cross-section of the water column is reduced on

top of the crests. Higher speed of flow however changes the shape of the short waves at the sea surface. Higher and steeper sea wave crests generate stronger radar-echoes within the same wavelength regime, which produce bright spots above the underwater dune formations. Despite the difficulties in quantifying this imaging process, it will inform rapidly on dune origin and migration, hazardous to ship traffic. Since the hydrodynamic effect is most pronounced in very shallow waters, this indirect imaging is particularly advantageous for timely shoal warning (Image 2.9-1). It may appear like a lucky irony of hydrodynamics that shallow tidal areas which are especially hazardous through frequent shoal formation reveal these places just by the tidal current, the originator of the danger.

Another flow-induced surface effect which can visualize internal hydrodynamics, interesting for oceanographers is also observable from satellites or aircraft. Periodic stripes of the sea surface roughness reveal the presence of so called *internal gravity waves*. They may occur when sun and wind or other processes of air-sea interaction have generated a stratification of the water density. The most simple case is a warm mixed surface layer on top of colder water below. This internal “surface” between warm and cold which means lower and higher density can propagate waves similar to the sea surface (Image 2.9-2) but often with much longer wavelengths and impressive wave-heights of tens of meters. Their horizontal flow components at the internal wave crests are again visible from space due to changes in the pattern of the short sea surface waves (Image 2.9-3).

By the way: a strong spatial change of the speed of flow in the sea can be observed by looking at the wake behind a ship when maneuvering before leaving port: the short sea waves look smoothed or may be nearly removed within sharp boundaries.

2.10 The Acoustic Solution

Echosounding is no invention of man. Bats in the air and dolphins in the sea are unequaled artists in recognition of prey and their way of signal processing is still a kind of mystery (Sect. 6.3.3). Perhaps one day our technical approach might be able to acoustically discriminate such tiny differences of matter as practised by these protagonists of acoustic remote sensing. However, the independent technical evolution of imaging by sound has brought forth capable tools of high sophistication which have been successfully tailored meanwhile to a wide variety of tasks quite different from those in which bats and dolphins are specialized.

The impressive progress of technical sound imaging the ocean during recent years is the result of three independent developments, the *godfathers of success*, so to speak. All three have been decisive requirements:

- *the precise global positioning satellite navigation (GPS),*
- *the advanced computer and data storage capability, and*
- *the high-tech echosounder hardware.*

Being aware of the comprehensive technical convenience of the present time we owe a respectful view back on the very beginnings of the art of imaging the ocean by sound, in other words: the cradle of the echosounder.

2.11 First Acoustic Trials

None of the three technical godfathers was standing at the cradle of the ocean echosounder which soon turned out to induce a kind of revolution in ocean exploration. At that time, the early twenties, not even electronic amplifiers were available. As far as we know, the key invention happened independently at two places, which were the two first centers of underwater acoustics worldwide: *Boston in the United States of America* with the Canadian engineer *Reginald A. Fessenden* (Image 2.11-1) as the inventor and first successful applicator of the ocean echosounder and *Kiel in Germany* with the German physicist *Alexander Behm* (Image 2.11-2) as an independent close second.

Though the fundamental idea was nearly as commonplace as listening to the echo of a call in the mountains and though even the application of echosounding the sea floor had been suggested by several authors before, there were several difficult technical problems to overcome together. Some of the earlier patents did not even identify the major hurdles and, in hindsight with our present knowledge, had no chance of success. The most critical problem to be solved before the era of electronics must have been the precise and automatic measurement of the travel time of the returning signal.

Behm’s invention was stimulated by a disaster and – irony of history – was a failure in respect of his primary intention. The stimulation was the most infamous but

Image 2.11-1.
Reginald Fessenden
1866–1932 ■

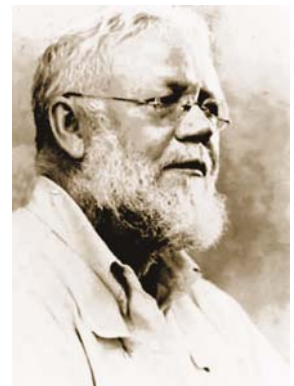


Image 2.11-2.
Alexander Behm
1880–1952 ■



Image 2.11-3.
Hugo Lichte
1891–1963 ■



meanwhile glorified sinking of a huge ocean liner on her maiden voyage, after collision with an iceberg in 1912: the *Titanic*. Behm devised a method for protecting ships against such collisions in the future by early warning. He thought that ships could be equipped with an echosounder to detect icebergs. In fact, this proposed method of detection with horizontal sound propagation did not work during his test trials. Very probably the weather caused severe downward refraction of the sound signals (Sect. 3.2) which Behm could not be aware of. The governing sound propagation conditions in the sea, in particular the varying refraction by sea water of different temperatures and salinities, were not yet understood.

However, the other application which Behm tested at sea, on the 13th February 1916, was a pioneering success. It was the echosounding of the sea floor. Due to his expertise in measuring precisely very short time intervals down to a fraction of a second which he practised years before in a small test tank at his laboratory in Vienna, he was able to measure the depth of only some 10 m of the shallow *Kiel Fjord*, using small explosives as sound source. At that time there were still strong doubts, whether the muddy sea floor would generate sufficient echoes at all to be detected.

Fortunately, the most important property of sea water for depth echosounding had been known for a long time: the *speed of sound*. Probably the first scientific hydro-acoustic experiment, conducted in the *Lake of Geneva* in 1826 with an underwater bell as sound source and a dipped ear-trumpet for listening yielded a sound speed of 1 435 meters per second (m s^{-1}). The scientists were the Swiss physicist *J. Daniel Colladon* and the French mathematician *J. K. F. Sturm*. The dependence of that occasional value on temperature, salinity and static pressure was determined theoretically

only in 1917 by the German physicist *Hugo Lichte* in Kiel (Image 2.11-3). He is acknowledged to be the founder of *ocean acoustic physics*, having been ahead of his contemporaries by decades. Lichte was the first to understand and quantify the refractive sound propagation by the sound speed stratification of the ocean, forming ocean-wide sound ducts (Sect. 3.2.2).

At the time of Behm's invention Kiel was already well-known for setting up a large network of underwater sound sources along the *English Channel* and the coasts of the *North Sea* and *Baltic* to guide ships through fog, since airborne fog horns could not compete in range. The first installations were again underwater bells with mechanical or electrical clappers based on patent licenses of the *Boston Centre*. But in the early twenties most of the lightships were retrofitted by electromagnetic transducers developed by the German engineer *Heinrich Hecht* in Kiel through enlarging and modifying the principle of a telephone headset. Accordingly, the underwater acoustic receivers of that time, installed on both sides of the ship's hull were carbon grain microphones, similar to those of the well proven telephone technology. Though the *electromagnetic* transducer constituted progress as compared to a bell, its basic features were closer to the first and simple headphones with their steel membranes than to an underwater version of a modern *electrodynamical* loudspeaker, providing unimpaired sound quality up to high amplitudes.

Such an advanced high powered underwater sound transducer was developed by Fessenden (Image 2.11-4). His ingenious invention, one among many others of his, is considered to have been earlier by one year than Hecht's electromagnetic concept. The moving element of the *Fessenden Oscillator* can oscillate freely, not lim-

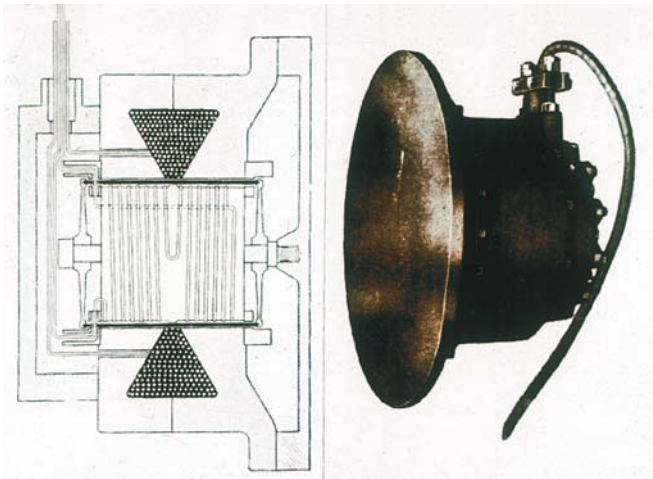


Image 2.11-4.

Fessenden Oscillator. *Cross section:* the membrane on the right is driven by a copper cylinder moving in the circular slit of an electromagnet. The wire coil does not move like the driving coil of a loudspeaker but is fixed on the central iron core. The wire coil and the driving cylinder work as the primary and secondary windings of an electric transformer with the cylinder as a one-turn coil. Thus the solid moving element can cope with the high alternating forces needed to radiate high power underwater sound whereas the fragile primary winding is protected by fixing. Note that the circular electromagnet activated by the direct current coil has both its poles on the slit side which requires opposite turns of the two halves of the fixed coil. The construction is as simple and robust as it is ingenious. The drawing is part of the patent ■

ited in motion like a *steel* membrane in front of and attracted by an electromagnet. Fessenden's membrane was driven instead by a copper tube conductor moving in the magnetic field inside a circular slit, corresponding to the freely moving coil of a modern loudspeaker. Fessenden emphasized as an important advantage of his *Oscillator* as against mechanical sound sources like bells that it worked also inverse. We would say: it is then nothing other than an enlarged – and reinforced – underwater version of the dynamic microphone, now perhaps the most widespread receiver of airborne sound. This particular feature of source-receiver inversion would have functioned also with the electromagnetic concept of Hecht's echosounders but the separate carbon grain microphones were given preference. It was Fessenden who applied the same transducer to transmit and thereafter to receive the sound signal, the concept of most echosounders until today.

In hindsight it is noticeable that the preferred frequency of echosounding of that time was around 1 000 Hz, independent of the transducer technology applied. We will see later that this frequency regime is far below those of the high resolution systems of today which provide three-dimensional underwater landscape imaging. The early echosounders were not acoustic searchlights with a radiation direction of preference. Neither the sound source nor the receiver had any directionality sufficient to scan the sea floor. Therefore the arrival time of the echo onset had to be taken to indicate the shortest distance from the ship to the sea floor, in other words: the local water depth. An echo coming in earlier under slant angles from a sloping bottom nearby thus inevitably indicates a shallower sea floor beneath than is actually the case.

Fessenden, not Behm, was the first to successfully detect an iceberg by an echosounder even from a distance of 2 nautical miles. Perhaps he was occasionally supported by benign though unknown sound propagation conditions. He conducted this famous experiment in April 1914, already two years after the Titanic disaster. Occasionally, as it were, Fessenden also received echoes from the sea floor of 2 km depth.

The real breakthrough however in the application of the ocean echosounder was the result of an epoch-making cooperation at sea: the very first systematic survey of a world ocean with echosounding bathymetry, which took place from 1925–1927. The name of this famous survey was “*Grosse Atlantische Expedition*” (Large Atlantic Expedition), conducted with the German research vessel *Meteor*, a converted warship. Three hydro-acoustic companies, *Behm* and *Signal-Gesellschaft* in Kiel and *ATLAS Werke AG* in Bremen, operated their own echosounder developments in parallel, checked by selected wire measurements. The expedition was initiated by *A. Merz* also acting as scientist in charge, representing the ocean research community.

Over two years the ship crossed the Atlantic 13 times, from 20° north to 55° south. The crossings were nearly equidistant and about 600 km apart (Image 2.11-5). The bulk of the data of more than 60 000 soundings was provided by the systems of *ATLAS* and *SIGNAL* which both “worked excellently without major breakdowns during the 2¼ year-long expedition”, according to the cruise report which explicitly mentions the engineers in charge *Kunze* (*ATLAS*) and *Settegast* (*SIGNAL*). Though the intense survey was still a sampling along

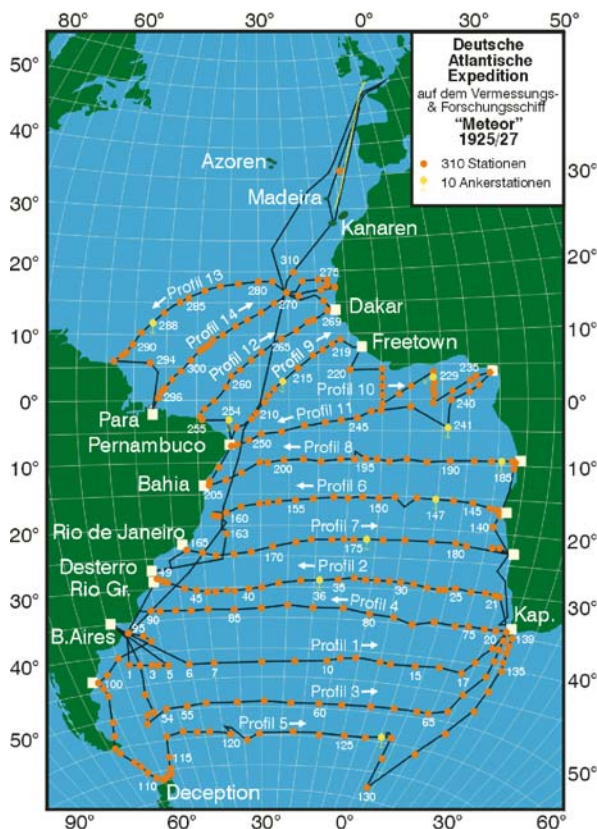


Image 2.11-5.
The *Meteor* crossings of the South Atlantic of 1925–1927 ■

lines, about 600 km apart from each other, thus leaving large uncovered gaps in between, the expedition discovered the dimensions of the famous *Mid-Atlantic Ridge*, now known as being by far the largest geological formation on Earth, the origin of the Atlantic sea floor. (Image 2.11-6).

The depth chart derived from the *Meteor* data is depicted as a facsimile of the original in Image 2.11-7. It is interesting to see the very modest progress achieved since until the large format map of 1940 (s. attached CD) which is still essentially based on the *Meteor* data set. There is no information at all of the kind of structure of the Mid-Atlantic Ridge. What a difference, compared to the actual relief globe presenting the Atlantic Ocean, a product of the turn of the 20th Century shown in Sect. 5.1.1.1! (also on the CD) This quantum leap in resolution is a convincing demonstration to what amount the concept of plate tectonics is based on advanced sea floor imaging.

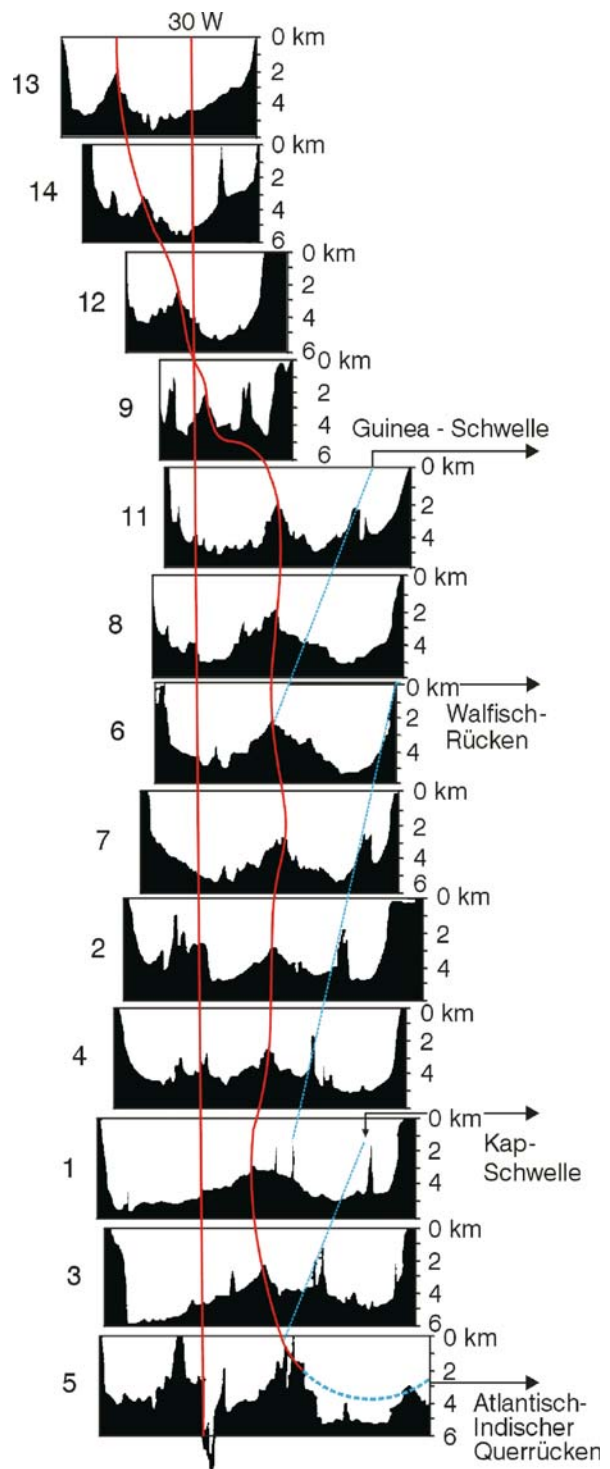
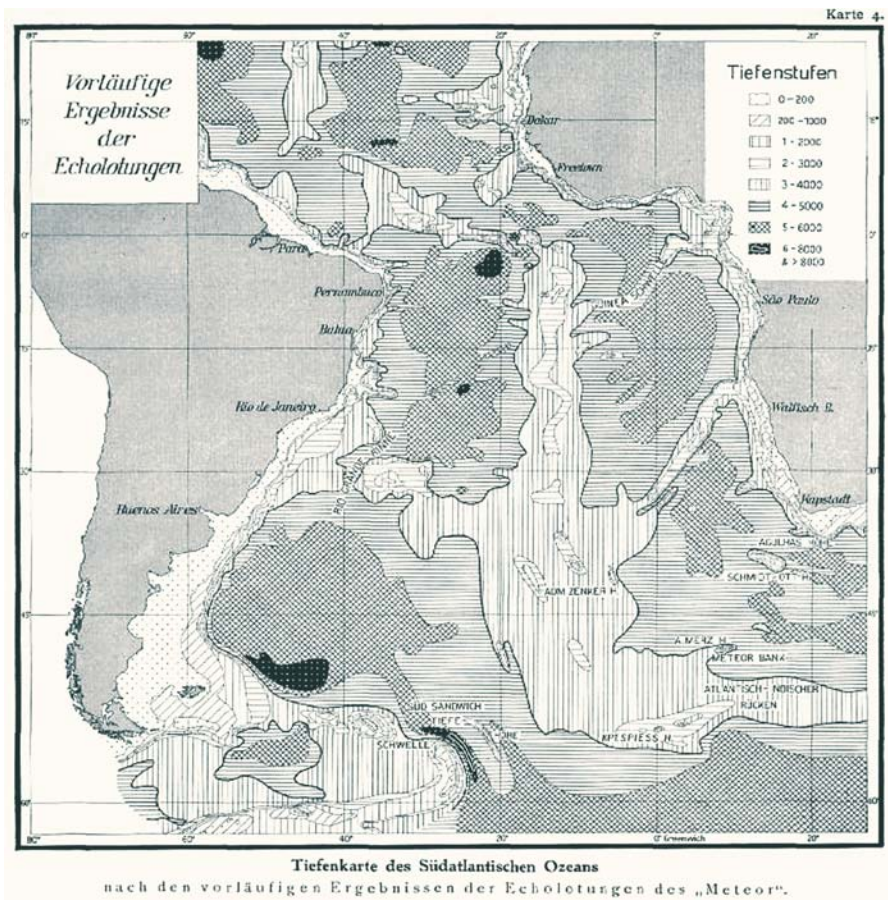


Image 2.11-6.
The depth contours of the *Meteor* Expedition of 1925–1927 ■

Image 2.11-7.
The depth chart derived from the *Meteor* data ■



Acoustic sounding along lines, though with high data density, remained the state of art during four decades after the *Meteor* survey. The inherent limits of line sounding were regarded dispassionately by the contemporary professionals, reviewing the potential profit from the steep increase in the sheer amount of data. Instead of providing a genuine three-dimensional relief of the sea floor with significantly higher resolution than by wire-soundings, the main progress was primarily two-dimensional. The new technology revealed bottom contours of smaller scales and contributed considerably to a more solid knowledge of large-scale features. Already in the thirties it was pointed out however, that only a substantial increase in the profile density would surpass the existing results significantly. *In hindsight this anticipates already the demand for multibeam technology which appeared on the scene only in the sixties.*

2.12

The improved along-track resolution however, was of particular interest for telephone companies. A more detailed reconnaissance of the bottom contour helped to avoid breakage of the expensive and vulnerable trans-Atlantic submarine cables by their hanging unintentionally between outcropping sharp-edged rocks. The majority of the contemporary trans-ocean depth profile surveys were thus devoted to such economic rather than to scientific purposes.

2.12 Four Lines of Evolution of Ocean Echosounding

During the following decades of the twentieth century the development of underwater acoustic techniques has brought forth essentially *four lines of echosounder evolution*, stimulated by the various emerging applications. They all share the attempt to achieve the best resolu-

tion of acoustic imaging under the prevailing conditions at sea and the specific purpose of the imagery.

- *The Multibeam or Fan Echosounder* for imaging the sea floor relief and other objects; the successor to the classical echosounder,
- *The Sidescan Echosounder*, for imaging the small-scale morphology of the sea floor and the shape of structures,
- *The Sediment Penetrating Echosounder* for imaging the internal structure of layers and to detect buried objects,
- *The acoustic Doppler current profiler* for monitoring ocean currents.

Instead of tracking these lines as a kind of history of underwater acoustics, which would require another book, we intend to jump across the seven decades from the milestone of the historic Meteor Survey of the Atlantic Ocean up to the present.

In the framework of this introduction into the basic facts we will deal next with the most important *acoustic features of the sea*, that are decisive for sound imaging. Thereafter the *technical and physical characteristics of high resolution echosounding* will be considered, in order to become familiar with the requirements and features of the four main sound imaging technologies applied today.

The main part of the book however, dealing with the various applications has to follow the respective purposes of sound imagery rather than the imaging technologies for a simple reason: The reality of the exploration, utilization, and surveillance of the sea and their concept of success is the optimized *combination of various tools*, acoustic and non-acoustic, remote and local or on-site.

Thus, the appropriate structure of the main part of the book with the Chap. 5–7 is the *application, the purpose of acoustic imaging*, demonstrated by typical image examples. This approach may be considered a kind of educational sound image collection which provides evidence of the individual capabilities of the methods applied under the real – and limiting – conditions at sea. Some special tasks require special methods such as *one way signal transmission for ocean surveillance*, for *tracking current drifters*, and for *acoustic tomography*. They will be treated together with the image series of the application concerned.

When discussing the advanced methods of acoustic imaging we should keep in mind that by far the most numerous echosounders in use today are being operated by all kinds of sea going vessels to monitor safety clearance from the sea floor and to support fishery. Many of them are low price standard technology without particular sophistication and of course without the intention of scientific imaging. They are based on the same technical concept as the fan echosounders restricted to a single beam and don't need separate treatment here.

The present state of imaging the ocean by sound is all the more remarkable as ocean acoustics has to cope with severe handicaps which are unknown to remote sensing in air by light or radar. Part of these problems and inherent limitations, as well as the exploitation of various, even unparalleled advantages will be discussed hereafter and in some more special detail in the context of the respective sound imaging applications.

2.13 Conclusion of Chapter 2

The sea is an impermeable screen of any signals of the entire electromagnetic spectrum with visible light as the only exception. Altogether, three fundamental solutions of imaging the sea floor remain for reasons of physics; hydrodynamics is not among them. It is only of exceptional help under very special shallow water conditions. The first solution is the *extremely "short sighted"* one we are all familiar with: the underwater photography. It does not reach farther than some tens of meters in the sea at most, but is indispensable for close ups of highest resolution, in particular of biology. Second: the *extremely "long sighted"* solution by satellite radar echo imaging the sea surface which provides a coarse copy of the sea floor beneath through its gravity anomalies. Third: the *echo-imaging solution by sound*. This method, the subject of this book, will be pointed out in the following sections. The gravity anomaly method and the acoustic method are complementary supplements to each other with their different strengths and limitations. However, as we will see, there is neither a substitute in kind nor a competitor in range and resolution to the *direct, quantitative echosounding imagery*.

Acoustic Features of the Sea

3.1 The Speed of Sound, Determining Quantities

3.2 Sound Refraction in the Sea

3.3 Sound Attenuation

3.4 Echo Formation

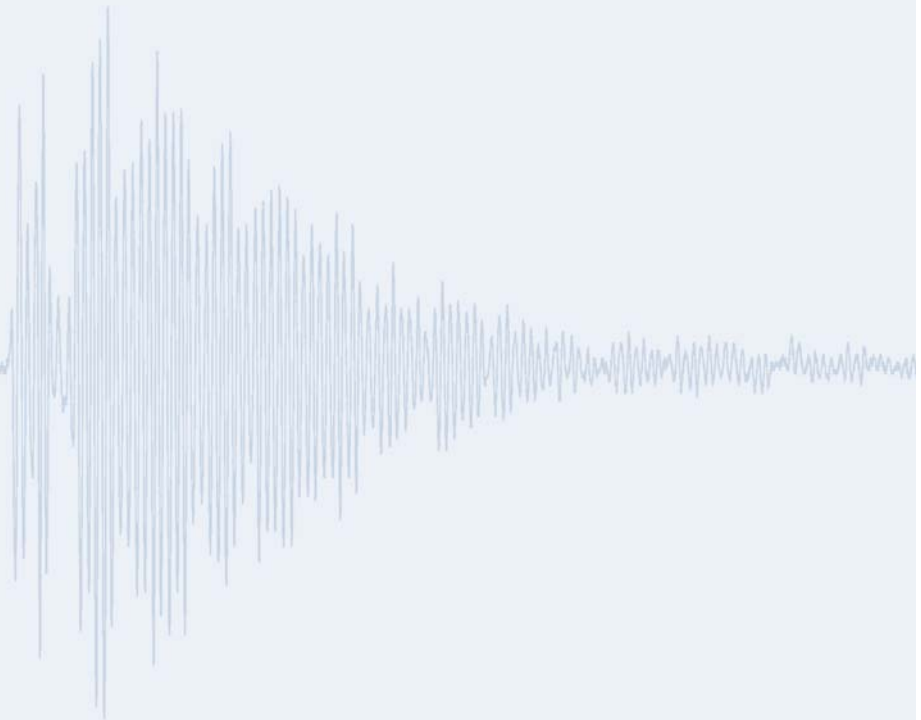
3.5 Reverberation

3.6 Noise

3.7 Sonar Equation

3.8 Conclusion of Chapter 3

Sound propagation in the ocean differs fundamentally from sound in other media. Due to the famous water anomaly, low frequency sound can propagate ocean-wide with the least absorption of all mechanical waves on earth. The characteristics of ocean acoustics, the features of the varying sound speed, and the increase of sound absorption towards higher frequencies, necessary for high resolution imaging, are considered in this chapter. Typical features of echo formation and limits of imaging caused by noise of natural and man-made origin are treated as well.



3.1

3.1 The Speed of Sound, Determining Quantities

The principle of echosounding is almost commonplace: the distance between sounder and object is merely the sound speed times half the elapsed time at the echo arrival. It is *half* the time simply because the signal is passing the distance twice: to and fro. However, the devil is in the details.

1 500 m s⁻¹ is used as a kind of standard speed of sound in sea water. This is about 4.5 times the value of sound speed in the atmosphere. But underwater sound is slow by a similar factor compared to the deep interior of the Earth. About 5 000 m s⁻¹ are also typical for some places where rock like granite or limestone crop out on the sea floor. Young marine sediments like sand however are closer to the sound speed in water and are even slightly below that value in fresh mud.

Basically the sound speed of any kind of fluid depends on only two *physical quantities*: The *density* and the so termed *compressibility*. *Higher density as well as higher compressibility mean lower speed of sound.*

According to extensive empirical investigations there are three easily accessible parameters which together determine the density and the compressibility of sea water and thus the speed of sound:

- the *static pressure* or the *water depth*,
- the *salinity*, and
- the *temperature*.

Simplifying the complicated empirical formula given in the Appendix we provide only rule of thumb numbers hereafter for a rough estimate. The variability of the measured sound speed in the open sea in all climate regions and nearly all existing water depths amounts to less than 10%. Only on the floor of the deepest trenches of 11 km, does the increase slightly exceed 12%. This variability is far below those of the interior of the Earth. Otherwise the sound speed in sea water is independent of frequency, when it is free of non-dissolved air and other gases. A very weak increase at high frequencies is negligible against the changes due to other environmental reasons.

3.1.1 Dependence on the Static Pressure

Increasing the pressure will evidently raise the density and lower the compressibility. But the non-linear change of the latter is stronger than the nearly linear change of the former: the result is *increasing speed by increasing pressure*. Raising the static pressure by 6 bar or going deeper by 60 m means approximately 1 m s⁻¹ higher speed of sound.

3.1.2 Dependence on the Salinity

Increasing salinity, surprisingly without a more detailed specification of the chemical contents works similarly to increasing external pressure. This is due to the stronger atomic electric forces which the increasing number of ions of the salt solution exert upon each other. We certainly recall that the electrical conductivity of salt water is due to partial ionization of the molecules. Raising the salinity by 0.1% will raise the sound speed by about 1 m s⁻¹.

The average salinity of the open oceans is nearly 3.5% with very little variability. In nearly closed basins like the *Mediterranean Sea* with more evaporation than river inflow the salinity increases up to 4%, but it may decrease down to 1% and less when the fresh water inflow prevails as in the *Baltic Sea*. Salinity is mainly sodium chloride, the normal table salt. There are a number of further components, in particular sulfate of magnesia, also known as *Epsom Salts*, which make sea water bitter and undrinkable and are partly responsible for the higher sound absorption compared to fresh water. Altogether there are 11 major chemical constituents which contribute at least 1 mg per liter each to the salt content of sea water. Chemical analysis has shown that this composition is nearly independent of the local salinity and is essentially constant within the so called "*Neptunian waters*", which are interconnected and exchange water, though over very long periods of time in numerous cases. This may explain why the simple percentage of the salinity can be used to characterize the sound speed together with the two physical quantities, pressure and temperature.

3.1.3 Dependence on the Temperature

The reason for the higher sound speed of warmer water is less easy to understand. In fact, water behaves in a different way to other fluids. The thermal expansion of a *normal fluid* leads to a lower density and a higher compressibility. Both quantities don't compensate each other completely because the compressibility effect is stronger. Thus the resulting sound speed shows a net decrease.

The famous *water anomaly*, being responsible for the nearly unique increase of sound speed by increasing temperature is the result of a particular triangle shape of the water molecule. This feature is of extraordinary importance (Sect. 6.2.1) in many fields of organic chemistry and is in fact decisive even for the existence of life on our planet.

The *water anomaly* refers to a special open structure of the water molecules beyond the melting point. This structure appears similar to the ice-crystalline lattice of low density and disappears only gradually when the water is warmed up. In other words: the so called "densest package of spheres" with the highest density possible is established gradually as well, together with the lowering of compressibility. Again, the decrease of compressibility overcompensates the initial increase in the density similar to the effect of static pressure. This is the physical reason for the unusual increase in sound speed by temperature. Just 1° centigrade will raise the sound speed roughly by 3 m s⁻¹ at 20° centigrade, about 4 m s⁻¹ at 10° and about 5 m s⁻¹ near 0°. Of course, the normal thermal expansion will finally win but that happens only beyond 70° centigrade.

Dependence on the temperature is by far the dominating contribution to the regional variability of the sound speed in the world's oceans. This fact enables ocean-wide acoustic thermometry by one way tomographic sound transmission as we will demonstrate later (Sect. 6.1.3).

Regarding the regime of ocean temperatures, we should exclude in this context temperature anomalies, such as found in so termed *hot spot* areas, a particular type of volcanism (Sect. 5.2.8). This type is found on tectonic plates in the deep ocean, far away from plate margins. At some places water is heated up even far beyond 100° but kept in its fluid state due to the static pressure of several hundred atmospheres on the deep-sea bed. This is a more local phenomenon however which does not impair sound imaging at a distance.

3.2 Sound Refraction in the Sea

3.2

3.2.1 Snell's Law

The predominantly horizontal layering of sound speed in the ocean waters with the temperature normally decreasing and the pressure always increasing downwards affects sound propagation by refraction in two ways: one of them enables ducted sound propagation in the *horizontal* along ocean-wide ranges (Sect. 6.1.1, 6.1.3); the other one limits the swath width of sound imaging the sea floor under *slant angles* of view (Sect. 4.2, 5.2–5.7).

We recall the basic facts of refraction needed to understand what happens when sound propagates in a stratified ocean, starting with sound refraction at a boundary between volumes of different sound speeds. As pointed out in the Appendix, sound refraction at a boundary is governed simply by *Snell's Law*, known from school physics: *sound is always refracted towards the region of higher refraction index which means lower sound speed.*

Snell's law is derived from an elementary requirement of physics: *there can be only one and the same pressure at the same point and the same time.* That means in particular: the alternating sound pressure of the incoming and refracted sound waves will always have the same phase along the common boundary which is essentially horizontal in the ocean. Accordingly, the *horizontal components of the speed of phase propagation* are necessarily the same for the incoming and the refracted wave. *These equal horizontal components are therefore the sound speeds in the adjacent volumes divided by the sines of the respective angles.* This equation is already Snell's law: *the ratio of the sound speeds called refraction index equals the ratio of the sines of the angles.* Thus a slant angle of the incident wave will become steeper when entering the layer of lower speed and vice versa. In other words: *sound is refracted towards the region of higher refraction index. A vertical sound beam is thus not refracted when propagating through the horizontal layering of the ocean.*

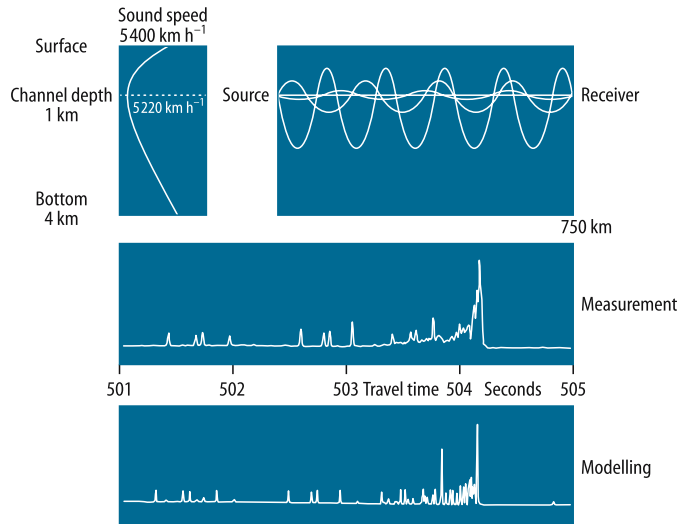
3.2.2 Sound Refraction and Ducted Propagation; "Acoustic Superconductivity"

The sound speed in the ocean volume does not change in steps with sharp boundaries however, but continu-

Image 3.2.2-1. ▶

Scheme of the Sofar-Channel sound speed profile with corresponding undulating sound rays. The earliest signal arrivals belong to the steepest rays; the latest are propagating near the Sofar axis where the sound speed is lowest.

Archive FWG, Kiel, Germany ■



ously. Typical deep-sea profiles look like the example shown (Image 3.2.2-1): The sound speed is high at the warm sea surface due to the water anomaly and high again near the sea floor where the static pressure is highest. To compute the sound propagation in such a stratified environment, the curved sound speed profile is segmented into short *linear sections*, a kind of polygon track representing the sequence of layering. This is a more realistic approximation than a sequence of steps.

Inside such a layer the sound speed is not constant but changes slightly at a *constant rate*. Then, the sound propagates inside such a layer along an arc of an exact circle (s. Appendix), bent towards the side of lower speed, until it enters the next layer to continue along a circle again but with another curvature: The higher the rate of sound speed change inside a layer, the smaller the circle radius. The connected sections of circle arcs represent a sound ray. A layer of nearly constant speed means a very large radius or nearly straight propagation. When a ray passes through the broad minimum of the sound speed profile shown in the Image 3.2.2-1, where the rate of speed change is decreasing to zero, the ray thus becomes straight until it enters the other side of the curved profile. Then the ray is bent back again towards the horizon of lowest sound speed – or highest refraction index – and so forth, undulating through the ocean like garlands, thereby touching neither surface nor bottom.

The sound speed profile of the deep ocean with a minimum of sound speed between higher sound speeds near bottom and surface forms a so called sound duct or sound

channel. This ocean acoustic phenomenon which we owe to the water anomaly has been known at least since the second world war and was called Sofar-Channel, “*sound fixing and ranging*”. The utilization of the Sofar-Channel was suggested for seafarers or aircraft pilots for SOS-emergency calls, which could be located by three triangulating coastal stations. However, the idea of passive ocean-wide Sofar-location has been adopted technically only now, more than half a century later. Acoustic long distance calls using the sound channel effect are not applied first by man however. Most famous is certainly the long distance communication of the world’s largest animals, the *Blue Whales*.

The oceanic sound duct which connects the three oceans, the Pacific, the Atlantic, and the Indian Ocean is of fundamental importance for any ocean-wide signal transmission. It represents first of all the foundation of the ocean surveillance concept as part of the United Nations Comprehensive Test Ban Treaty (CTBT) of nuclear weapons. The network of monitoring stations is shown in Image 3.2.2-4. At present the oceanic sound duct is being applied also for tracking drifting submerged buoys deployed to monitoring ocean current systems (Sect. 6.1.1) and for ocean acoustic tomography, monitoring the heat content of currents and their net mass transport over time spans of climate relevance (Sect. 6.1.3).

A similar profile of the *optical index of refraction* is being applied for low loss propagation of light signals in fiber-glass cables for broad-band telecommunication (Sect. 7.2.1).

The Sofar-Channel enables the lowest by far absorption of all mechanical waves propagating on Earth. So far one of the two prerequisites, the duct formation caused by the water anomaly is understood. The other decisive requirement is *the extremely low intrinsic sound absorption of water*. There is no plausible explanation however why low frequency sound in the sea is absorbed by three orders of magnitude less than in the air (Sect. 3.3.1). The unique phenomenon of global low loss propagation in the ocean deserves to be called “acoustic superconductivity”. Of course the technical term *superconductivity* is restricted to an entirely different phenomenon of quantum physics: the abrupt and complete disappearance of electric resistance at very low temperatures. This term is intentionally misused here to attract attention to an extraordinary feature of ocean acoustics.

The data base utilized for the global Sofar maps is the merit of a century of oceanographic research. It comprehends the geographical distribution of the monthly averages of temperature and salinity in the oceans. The data, resolved at 30 depth intervals and mesh widths of a geographical degree square are meanwhile public domain under the label *Levitus*. Though the weather dependent variability of these oceanic quantities of the uppermost few hundred meters cannot be derived from these historical, or *climatological* data, they are of inestimable value for world wide surveillance tasks and also very important for deep-sea research. The depth of the sound speed minimum, named channel axis, is depicted as a global map as well as the sound speed at channel axis (Images 3.2.2-2, 3.2.2-3).

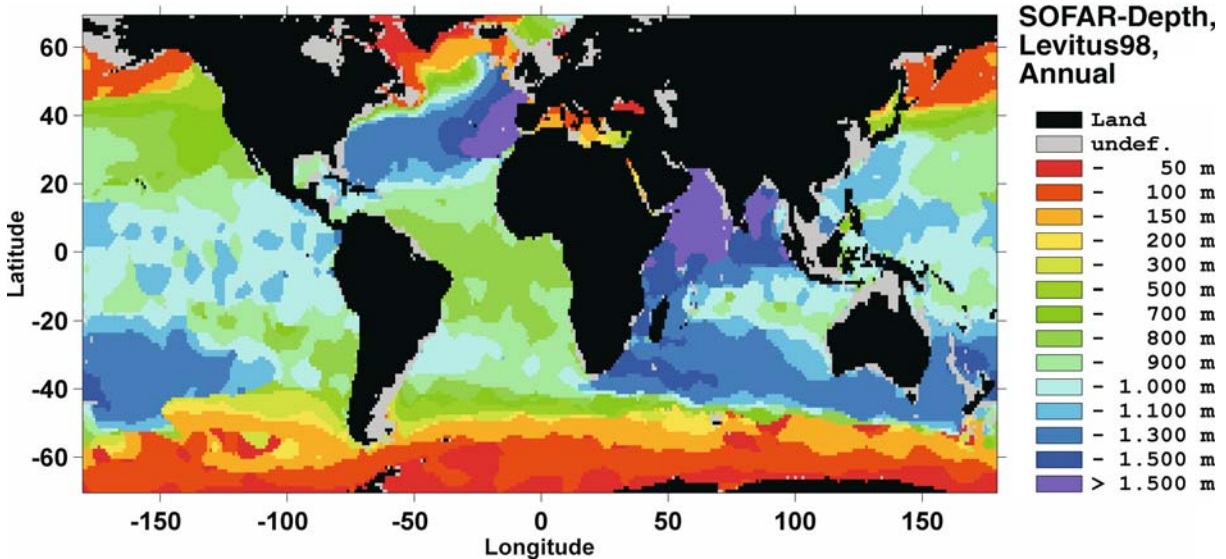


Image 3.2.2-2. The global Sofar-Channel: the depth of the channel axis. The depictions are derived from the global *Levitus Atlas of Oceanography* (WOA 98). It provides fundamental data of the ocean volume, such as the monthly average of the ocean temperature and salinity at a grid of one degree longitude and latitude and at up to thirty-three depths each. The data are the achievement of more than a century of ocean expeditions by a large number of countries and ships. The global distribution of the local minimum of the speed of sound, computed from temperature, salinity, and water pressure, represents the *Sofar-Channel* axis. The shelves and other areas which prohibit the Sofar-Channel by insufficient water pressure are indicated in gray.

The yearly average of *the axis depth* repeats the essential features of the sound speed in a sense: the deepest areas of 1300 m and more are found where the speed at axis is highest: the Mediterranean outflow and the Indian Ocean where the variability is most pronounced. The shallower tongue west of *Australia* comes from inflowing water of less salinity through the *Indonesian passage*. The broad, deep band south of Australia goes around the globe at that latitude except for the *South Atlantic*. A kind of standard axis depth at equatorial waters is 1000 m with at most 20% up and down at large scales. The axis ascends nearly or completely to the surface towards polar waters for the same reason as the speed of sound.

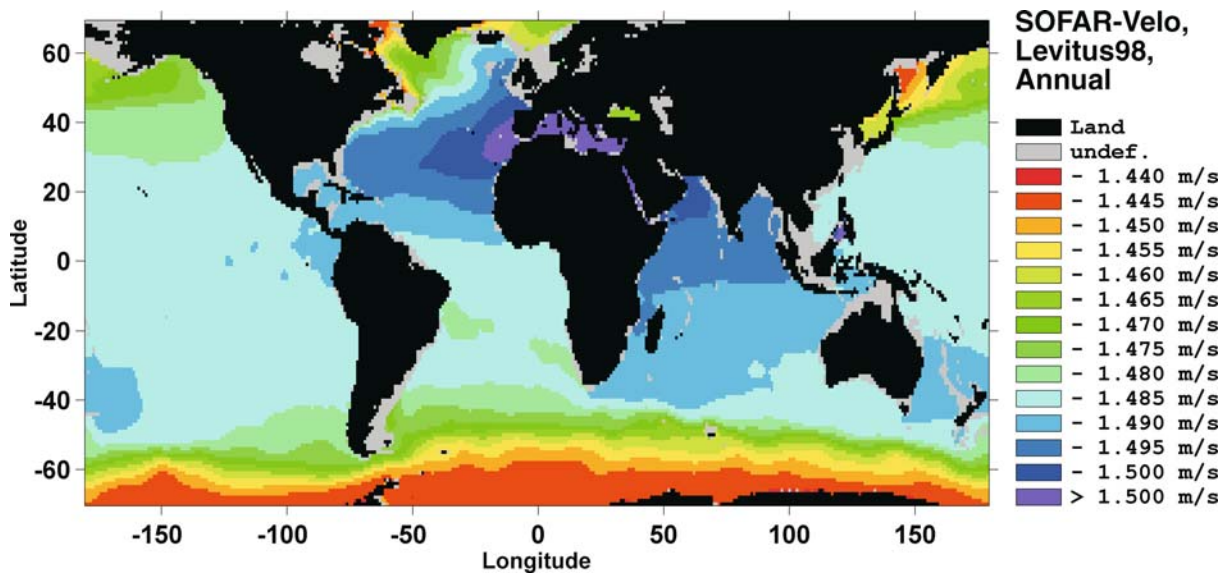


Image 3.2.2-3. The global *Sofar-Channel*: the speed of sound at the channel axis. The yearly average of the sound speed at axis depth varies only little and on a large scale. The *Pacific*, confirming its name even in this respect, appears most benign. The color code visualizes 1485 m s^{-1} as the sound speed of by far the majority of its area. The speed decreases smoothly to 1440 m s^{-1} towards the colder waters at high latitudes. The *Atlantic* in contrast shows a surprising feature: the outflow of the *Mediterranean* with its higher salinity increases the sound speed at Sofar-axis depth to 1495 m s^{-1} , crossing the Atlantic in a broad tongue larger than the African continent. The *Indian Ocean* appears to behave similarly, as if the *Red Sea* outflow of high temperature and salinity into the Indian Ocean increases the at-axis sound speed ocean-wide. The main reason is different however: in the north of the Indian Ocean the enclosed warm surface water reaches unusually deep to more than 1300 m, which shifts both the axis down and the sound speed at axis up. Deep warm water is also the reason for the broad belt of higher sound speed in the south of the Indian and Pacific Oceans. This is considered the result of the interaction between the *circumpolar current* and the *trade winds*.

Image ©: Michael Unger, FWG, Kiel ■

The other effect of sound refraction limits the extension of the range of sound. When the sound source is at or near the surface but beyond channel trapping as with ships (Sect. 3.6.1), the radiated sound is refracted downwards but touches the bottom which normally causes a major loss (s. Appendix, A.3.4.1). This is particularly true in shallow water.

In this context we shall deal with intentional downward sound radiation for sea floor imaging in the deep sea. Then the upward refraction due to the increase of sound speed with static pressure restricts the swath width of wide angle multibeam fan echosounders (Sect. 4.2 and A.3.2.2) and impedes further improvement in economic imaging surveys. The outer beams of the fan are inevitably refracted away from straight

propagation. Though this seemingly widens the width of the irradiated “sound carpet” it eventually generates grazing contacts with poorly defined depth information. Beams which leave the echosounder at even more oblique angles don’t arrive at the sea floor at all but turn back, refracted around a circle arc, similar to the lowest ray of duct propagation. This upward refraction is the stronger, the shallower the angle of incidence chosen. The extreme in shallow irradiation is the side-scan echosounder (Sect. 4.3). It is mostly towed near the bottom to achieve long sound shadows of the sea floor morphology by nearly grazing incidence. Sound refraction in the ocean thus affects the application of two of the four main types of echosounder technology treated in this book.

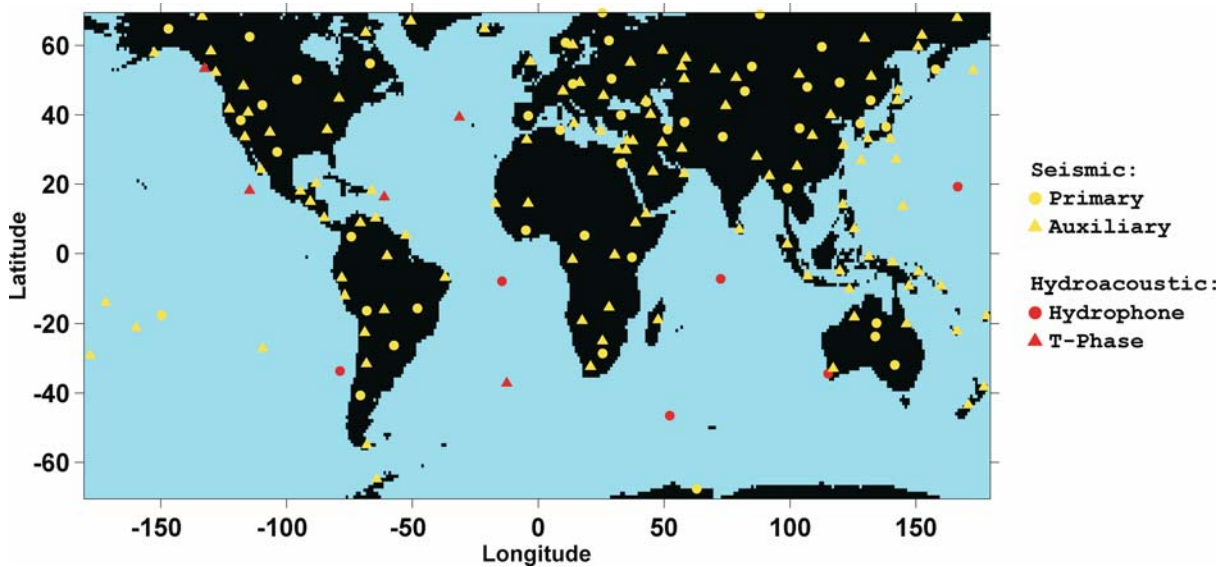


Image 3.2.2-4. Acoustic surveillance of the *Comprehensive Test-Ban Treaty (CTBT)* of the United Nations of nuclear weapons; global network of seismic- and hydroacoustic monitoring stations. The global surveillance of the land masses is achieved by 130 seismic stations but by only 11 hydroacoustic receiving units to cover the much larger area of the world oceans. Three stations are the minimum for locating major explosion events by triangulation within an ocean basin. The ocean-wide acoustic transparency for low frequencies, which we owe to the global *Sofar-Channel*, enables detection and location of nuclear explosions down to 1 kt TNT-equivalent within an uncertainty circle of 35 km diameter, the treaty requirement world wide. Only 6 of the ocean stations indicated in red are genuine hydroacoustic; the other 5 are so called T-wave stations to save funds, which are seismometers for receiving hydroacoustic signals after conversion into seismic signals at the coast or on islands. Differing from seismics, the hydroacoustic signal contains the unmistakable signature of an explosion (Sect. 3.6.8).

Image ©: Michael Unger, FWG, Kiel; based on maps of CTBTO, Vienna ■

3.3 Sound Attenuation

3.3.1 Absorption

The *long-range monopoly of remote sensing by sound in the ocean* has been established by its unrivaled record of low absorption. Returning to the scheme of penetration depths (Image 2.1-2) where we discussed the electromagnetic wave regime, we now inspect the sound wave branch. The superiority of range against electromagnetic waves is in fact striking and the technical term “penetration depth” appears somewhat misplaced. At about 100 Hz, where the *sound absorption* in the sea is minimum, the sound signal will propagate 10 000 km, a quarter of the circumference of the globe, until 9/10 of the initial acoustic energy has been absorbed. At the

average sound speed of $1\,500\text{ m s}^{-1}$ this will last nearly two hours. It is in fact like dealing with a kind of “hydro-acoustic superconductor”. Very long uninterrupted propagation paths are found not only in the Pacific, by far the largest of the world’s oceans but in all deep water areas. It has been pointed out why this low frequency sound follows the Earth’s curvature trapped in a channel, thereby touching neither the surface nor the floor of the ocean, where it would lose most of its energy after just a few reflections.

The 10 000 km transmission path of reference is no merit of salinity. On the contrary: Two ingredients of the salt in the sea, magnesium sulfate and boron acid together enlarge the low frequency sound absorption by a factor of about 300. Imaginary freshwater oceans would permit the sound of 100 Hz to circulate the globe even 70 times to lose 90% of the initial sound energy – a nearly genuine “acoustic superconductivity” indeed!

At a first glance the problem of irradiating the ocean by sound for long-range imaging might appear solved in principle. However, the extreme ranges are achieved at very low frequencies only. Ocean-wide *one-way sound transmission* for surveillance and monitoring deals with *non-directional sources* and is not applicable for sound imaging. Scanning a scene requires narrow sound beams. Anticipating the scale relationship between the size of the echosounder and the wavelength (Sect. 4.2.5), a typical beamwidth of 2° as realized for deep-sea imaging with a 3 m array at 15 kHz and 10 cm wavelength would require a monstrous echosounder of about 500 m when going down to 100 Hz, corresponding to 15 m wavelength which is simply the ratio of sound speed and signal frequency. Even if such a monster were realized, it could not scan an ocean-wide panorama of the sea floor from a fixed station. The reason is simple: the channel formation which enables the ultra-long-ranges screens the sea floor beyond a very moderate range (Sect. 3.2.2). This coverage is easily achievable by sidescan echosounders working at high frequencies and with sharp beamwidths of 1/10 of the fictitious monster.

3.3.2 Spreading Loss

Discussing loss by absorption, we should not forget the so called *spreading loss*, which adds to the decrease of intensity by distance from the source. This is nothing other than the distribution of wave energy on an increasing spherical surface during propagation, well known from school lessons. Doubling the distance means *four times* the surface that has to share the outgoing energy. This *spherical spreading loss* holds of course for light and radar as well.

However, along very large propagation ranges, such as trans-ocean sound propagation trapped within the Sofar-Channel, the spreading loss is different because of a different geometry. In such cases where even the 4 km average depth of the deep-sea floor is small against a range of, say 4 000 km, there is no longer any room for spherical spread. The *three dimensional distribution of sound energy, after a range of transition, becomes two dimensional*. It is then a kind of propagation within a skin. Considering a model of the globe of 1 m diameter, the deep ocean would in fact be a thin skin of merely 1/3 mm. In other words: doubling the distance then means only *twice* the surface, that has to

share the outgoing energy. Long-distance sound propagation in the ocean thus saves energy. This amounts to a factor of 1 000 at the distance of the 4 000 km example, whereby the range of transition, saving less, has been taken into account already.

3.3.3 Above and below the Ocean Volume; a Comparison

The mentioned high sound absorption in air is a well known phenomenon. When we estimate the distance of lightning during a thunderstorm by the elapsed time before the following thunder, we hear merely a strongly damped dull rumble after 9 s which means the 3 km range of 90% loss at 100 Hz, according to the sound speed in air of 330 m s^{-1} .

However, the sound absorption in the sea floor which is of particular interest for ocean imaging is even stronger than in the atmosphere. Some of the sea floor sediments, including those we know from the beach, need only 300 m to absorb 9/10 of the initial sound energy at 100 Hz. It is quite obvious from this simple comparison that the exploration of the interior of the Earth has to cope with problems of another dimension than that of imaging the ocean volume and the surface of its floor. The implications and achieved solutions are discussed in Sect. 4.4.

3.3.4 The Wavelength Handicap

Regarding the monopoly of sound for long ranges in the sea, physicists may however argue that this kind of comparison between sound and light is somewhat misleading. In fact, the result would be just the opposite if the *numbers of wavelengths along the path of the penetration depth* were counted. They represent the cycles through which the absorption process happens. Blue-green light with its typical wavelength of only $0.5 \mu\text{m}$, when passing a distance of 100 m in water, achieves about 300 times the number of cycles of the 100-Hz sound along 10 000 km with its wavelength of 15 m. *This is an important fact:*

The monopoly of sound for long ranges in the sea is penalized by the severe disadvantage of long wavelengths, many orders of magnitude larger than those of light.

This handicap seriously limits the resolution of structures we can see by sound even if we go to much higher frequencies to reduce the wavelengths correspondingly. Since the acoustic penetration depth in water as in all viscous fluids lessens almost proportionally to the square of the frequency, it decreases to about 100 m at 1 Megahertz (Image 2.1-2). Here, sound is no longer superior in range to visible light in ideally clear water. But even then the sound wavelength is not smaller than 1.5 mm. Thus, acoustic imaging is inevitably a compromise between range and resolution. Fortunately, the notorious, nearly opaque turbidity of European shallow waters and estuaries doesn't affect the sound propagation seriously in most cases. In those optically turbid waters we often need the best image resolution possible, mainly for reasons of safe shipping. Thus, acoustic imaging in the high frequency regime is indispensable, simply because there is no other choice.

Ultrasonic imaging in medicine applies frequencies up to more than 10 MHz where the actual sounding depth is merely a few centimeters, just sufficient to image subcutaneous blood vessels but with wavelengths less than 0.15 mm.

3.3.5 The Optimum Compromise

The *optimum compromise* between range and resolution depends on the kind of application and is decisive for the frequency band of choice. Imaging the deep ocean down to the depth of trenches of more than 10 km is being conducted preferably at about 15 kHz with 10 cm wave-length as mentioned (Sect. 5.2). The continental shelf waters with their typical depth of 200 m are imaged best within the regime of very few 100 kHz (Sect. 5.3). Finally, the surveillance of coastal sea lanes with the highest safety demands requires frequency bands nearer to 1 MHz (Sect. 7.1).

To study the internal structure of sediments only down to a few tens of meters requires compromising to much lower frequencies of about 3 kHz, where both a narrow beam and a high vertical resolution are difficult to achieve (Sect. 4.4, 5.3.2, 5.4.3). Reducing the frequency to increase the penetration depth in sediments achieves less than in water. The reason is the different frequency dependence of loss in both media. Sound absorption by friction loss in granular substances varies only proportionally to the frequency instead of by the

square of the frequency as in viscous fluids like water (s. Appendix, A.3.3.1). Correspondingly, the exploration of the sea floor down to the lithosphere and even deeper, which is beyond the scope of this book, requires frequencies which have to be decades lower than the kilohertz regime.

3.4 Echo Formation

The next fundamental feature of ocean acoustics we address in the context of basic facts is *echo formation* which provides another decisive quantity of successful sound imaging. Any sudden inhomogeneity within the medium where a sound wave propagates is a source of so called secondary waves. A short wave package will thus release an echo as we know it from a loud call in the mountains. If the inhomogeneity is a nearly plane surface typical of many areas of deep-sea sediments, it will act like a mirror, reflecting the incoming wave package. This echo formation is called *specular reflection*. Rough or fissured *surfaces* of the sea floor, as well as irregular, inhomogeneous *volumes* like fish shoals, reradiate the sound in all directions which is called *scattering*. A rough sea floor scattering sound is similar to an unpolished wall scattering light: it is visible from all sides. Sound scattering is the origin of all echo formation induced by echosounders operating off specular reflection. In other words: sound images of undersea landscapes visualize scattered sound.

3.4.1 Acoustic Impedance

What kind of feature is being recognized as an echo generating inhomogeneity by the sound wave propagating in the sea? Underwater sound, in contrast to complicated effects of light, simply discriminates any object from the surrounding water only when it differs by its so called *acoustic impedance*. This is nothing other than the *product of the density and the speed of sound* inside (s. Appendix). This means: a change of only one of both quantities is sufficient to produce an echo. On the other hand, a density increase can be compensated by a corresponding decrease in sound speed to avoid a reflection, thus achieving perfect camouflage. Fortunately for sound imaging this is very unlikely in the real seabed. On the contrary: a higher density of sediments

normally occurs together with a higher speed of sound. Even tiny differences in this sound impedance inside the sediment appear as clearly recognizable layering. Here, acoustic remote sensing can be more sensitive than the laboratory analysis of sediment core samples brought up from the sea floor.

3.4.2 Impedance Steps

Imaging sediment layers will demonstrate that an “*impedance step*” is required to generate an echo. Continuous transitions which happen along a path of a wavelength and more are invisible to the echosounder. It will be shown that the seabed may have no echo producing layers during even thousands of years of continuous sedimentation. On the other hand the presence of a clearly discernible layer is an indication of an event of sedimentation, disrupting continuity. A difference of only one percent and even less in the impedance of adjacent layers may appear as a visible horizon.

The temperature stratification of the water volume (Sect. 3.2) is not directly visible in the sound image for two reasons: the transition between the water masses is hardly ever sufficiently abrupt and the decrease in sound speed with lower temperature downwards due to the water anomaly is partly compensated by the increase in density. Looking at echo records of the sea volume taken to monitor biomass inventories (Sect. 6.3.1) we nevertheless see such internal boundaries quite often. What we see however are the echoes of plankton which appear to rest at such horizons, carried by the higher density below.

3.4.3 Colorless Sound Images

Since the sound speed in water as well as in the sediments is essentially independent of frequency, the acoustic impedance which determines the echo intensity also does not depend on the frequency. This means: *there is no genuine acoustic color of nearly all sound images of the ocean.* The only exceptions are air- or gas bubbles. Their echo is maximum at their individual, sharp, and single resonance (Sect. 6.2.3). This corresponds to a pure, monochromatic optical color. Due

to the absence of other natural resonators in the sea in the frequency regime of echosounders, the typical sound image is a *kind of black and white picture*, however with a *large dynamic range of the gray scale.*

We should admit however, that the *frequency dependence of sound absorption* will reduce the bandwidth of a short echosounder signal, taking the higher frequencies away. In optical terminology we could say: finally only the “red” components of a “white” signal will return (Sect. 3.6.6).

In order to achieve sound images with easily accessible quantitative information the gray scale is often converted to a false color scale, similar to the practice with radar images. Bathymetric depictions, in particular the landscape images are color coded to easily visualize the corresponding depth intervals.

3.4.4 The Minimum Object Size

To cause an echo, the impedance step of an inhomogeneity by contrast with the surrounding water is a necessary condition. But it is not yet sufficient. The additional requirement is the *minimum size* of an object to contribute to a sound image. The echo of nearly any object smaller than a wavelength will become much weaker than we would expect from its real cross-section. The only exception as mentioned are air bubbles which appear balloon-like “blown up” regarding their echo when insonified at their resonance (Sect. 6.2.3). The “acoustic size” of the other objects will shrink by the second or even third power, depending on their impedance, when we reduce the frequency of the echosounder and thus enlarge the wavelength correspondingly.

This effect, called *diffraction* is well known from the optical counterpart where it limits the resolution of a microscope for instance. We have to cope with this problem in particular when imaging nearly plane areas of the deep-sea floor of fine grain sediments. Being forced to apply wavelengths much larger than the grain size means acoustic smoothing of the sea floor. This is advantageous at vertical incidence, the “classical” way of sounding the water depth. The single-beam echosounder, when looking downwards, is facing a smooth, nearly horizontal mirror reflecting directly upwards: the optimum case of *specular reflection.*

3.4.5 Echosounding under Slant Angles

This is quite different with modern *fan echosounders* (Sect. 4.2). In order to achieve a large number of parallel soundings simultaneously from a single ship, a multibeam fan transverse to the ship's course samples the sea floor under different grazing angles, ranging from vertical to 45 degrees and less. Nearly plane sediment areas, smoothed in addition by the necessary decimeter wavelength reflect the slant beams away by the same angle. What is then left over to produce echo-intensity is expected to be the fine sediment grains acting as *sound scatterers*. They should be even less "visible" than dust particles on an optical mirror because these are not small compared to the light wavelength.

Fortunately again, the slant echoes are considerably stronger in many cases than expected from this simple assumption. Though the reason for this echo formation is not yet quite clear, there are for sure further – and presumably larger – *backscattering inhomogeneities* buried within the uppermost few centimeters of the sediment. They will be reached by the decimeter wavelength under all inclination angles of the sound beam. Apparently there are nearly plane bottom types as well which are both fine grained and homogeneous at least a wavelength deep. In such cases, the echo intensity coming back in a slanting direction may be only 1/10 000 of the specular echo from below. Such strong contrasts feign a non existing lateral sediment variability. To remove them from the sound image is a challenge to signal processing.

3.4.6 Restriction to Compressional Waves

It may be surprising that the sea floor sediments in terms of underwater sound are characterized only by the product of their density and sound speed in the same way as the water above. We have to admit that this is a simplification. Whenever there is a solid body, it differs from a fluid by its rigidity, its stiffness against external forces. In water, as in all fluids and gases, only the so called *compressional waves*, usually known as *sound waves* can propagate.

The situation in solid matter is much more complex. There are other types of waves in addition to the sound

wave with its alternating pressure, called *sound pressure*. In particular so called *shear waves* with horizontal motion, known from disastrous earthquakes, are superimposed on the compressional waves which propagate at the highest speed. The different wave types interact with mutual conversion at internal inhomogeneities. The analysis of this complex conglomerate of waves is the scientific tool of *seismology*. It is the prerequisite for investigating the structure of the interior of the Earth, utilizing very low, infrasonic frequencies to overcome the high absorption. The application of major economic importance in this field of research is prospecting for mineral oil and gas deposits.

Fortunately for imaging the sediment structure by sound waves, shear waves are only weakly excited in the sediments by echosounding at or near vertical incidence, which is the classical sounding direction of a surveying ship. Anticipating a conclusion to be discussed later we clarify therefore:

The sound images of the ocean interior including the upper sea floor presented in this book are generated by compressional waves or sound waves. This is considered the criterion for selecting the examples of the various fields of application, independently of the frequency regime applied.

The physics governing this simplification means that we treat the sediments acoustically as quasi-fluids, which is justified in practice as a realistic approximation.

3.5 Reverberation

Strong backscattering by the sea floor may mask weak echoes of interest. This is a problem of major concern for the navies when conducting underwater surveillance and reconnaissance of the surrounding panorama. A submarine for instance may be too far away to be recognized by shape clues and discriminated from random or similar sea floor formations. If the random backscatter from the sea floor exceeds the imbedded echo of interest, it is said that the detection range is *reverberation limited* instead of being *noise limited* which is the most frequent situation of imaging the sea floor by the various kinds of echosounders.

The only naval reconnaissance task treated in the framework of this book is the detection of buried sea mines (Sect. 7.1.5) which is perhaps the most difficult challenge of sound imaging so far. Though the objects which cause a natural camouflage of the buried mine are stones distributed at random, they are not normally a problem of random backscatter from an unstructured background. Instead, the more frequent problem is the acoustic similarity of mines and stones of comparable size. This situation is named a false target background or -environment. Such situations occur also when searching for a shipwreck (Sect. 7.1.4). As soon as the object of interest can be recognized and discriminated from false targets by shape clues through high resolution, the masking effect is removed and the situation is no longer *reverberation limited*. Since the subject of this book is *imaging by sound* which implies clue discriminating resolution, it is noise, not reverberation that has to be treated here as the limiting background of imaging. Random backscatter from the sea floor is not the limiting factor in this context but it is on the contrary the signal by which the relief of interest is visualized (Sect. 3.4.5). The Appendix provides a set of empirical sea floor- and sea volume backscattering curves for the estimation of imaging ranges by means of the sonar equation.

3.6

3.6 Noise

The last fundamental quantity of the acoustic environment we have to consider in the context of sound imaging is the *noise in the sea*. Noise, together with the loss of signal intensity in both directions, decides whether sound imaging of a particular scenario is possible by a given echosounder system radiating a defined level of sound energy. Of course, we may easily amplify a weak signal to any wanted level. However, the omnipresent noise, inevitably and inseparably received together with the echoes we want to image, is then amplified by the same amount. A signal that is buried by noise in the same frequency regime is irretrievable.

The quantity that decides whether or not sound imaging is possible under given conditions is the so called signal to noise ratio S/N .

To discriminate between echosignal and noise is a matter of probability because noise is a random pro-

cess. According to a simplified rule one can say: if the signal intensity is ten times the average noise intensity then the probability of receiving a real signal instead of a random noise peak is more than 90%. In reality we have to consider this value sufficient for sound imaging under normal environmental conditions. But particularly in the deep ocean where the echoes are often very weak, several handicaps may accumulate and the quality of the sound images may then look nearly like the “snow” on a TV-screen when the antenna is defective. *Fighting noise* is therefore essential.

Environmental noise in the sea, man-made noise above all, has become a subject of particular concern of biologists investigating the behavior of marine mammals (Sect. 3.6.9). The reasons are similar and may be even more severe than the impact of airborne noise deteriorating the quality of human life and state of health. We restrict the consideration of noise in the sea in this context essentially and intentionally to its role as a limiting factor of ocean imaging.

3.6.1

Sources of Noise: The Ship Traffic

It is the *sea surface* which brings forth the ever present background noise. One of the two main sources is man-made: the *ship traffic*. Its noise usually dominates at frequencies up to a few 100 Hz. Sea lanes emit underwater noise similar to highways on land. But the resulting noise intensity appears modest at first sight, in view of the excellent sound conductivity of the sea, in comparison to the atmosphere. Expressed in the standard A-scale of airborne noise referring to the *human* hearing threshold and the equivalent sound intensity, the sea traffic noise, at a distance from individual ships, sea lanes, and harbors hardly exceeds the sound of leaves in a wood when moved by wind. This seemingly low noise level is misleading however. A single ship with a defect machinery or defect sound insulation can stand out with its noise far beyond the average, similar to a car with a defect muffler. Moreover, propagation conditions in the sea with a surface duct (Sect. 3.2.2) typical of high latitudes and calm sea can aggravate the noise irradiation at a distance.

However, the ship traffic density is orders of magnitude smaller than highway traffic. Less than 30 000 ships of over 1 000 tons are registered worldwide, one third of engine driven vessels registered as of 2001. Another reason for the relatively modest noise contribution of

an individual ship is its low speed. Jet aircraft with engines of similar power generate noise of tens of kilowatts because of the steep increase in flow noise with increasing speed of flow. Most sea-going vessels emit noise only up to a few watts with their piston engines as the main source and propeller cavitation (Sect. 4.1.6) as another one but with comparatively negligible contribution of radiated flow noise. Research vessels especially equipped for silencing radiate only up to a small fraction of a watt of noise power within the entire frequency regime. Such silent ships are exceptional up to now, however. As long as there are no legal limits of noise emission by ships into the sea, an increase of the average noise level at least in the vicinity of sea lanes, caused by the increase in number and power of ships following the global trade expansion, appears inevitable.

There is a third important reason for the still relatively moderate traffic noise intensity in the sea. The statement of excellent sound conductivity is in fact oversimplified. Horizontal sound propagation is severely affected by refraction caused by temperature stratification within the water volume, in particular close to the sea surface at lower latitudes. This effect is a notorious problem for navies when conducting reconnaissance and surveillance tasks using sonar. Due to the frequent downward refraction of sound generated at or near the sea surface the detection ranges may decrease dramatically. Most of the sound arrives at the sea floor which is very often a poor reflector.

A corresponding refraction effect towards the environment of lower sound speed is well known from *sound propagation in air*: We cannot hear as well when the sound comes against the wind rather than with it. Here, the reason is *upward refraction*, away from the listener. This is because the local speeds of sound and wind are subtracted or added depending on their relative direction of propagation. Sound facing headwinds encounters low sound speed at greater heights where the wind always blows stronger, thus reducing the sound speed more than down below. If the direction of sound and wind is the same, the sound is *refracted down*, towards the listener who then receives even the sound that would have gone up in calm weather.

3.6.2 Wind-Driven Noise

The other dominating source of surface noise is also a process of climate relevance by air-sea interaction

(Sect. 6.2.3). Sea waves break at higher wind speeds and cause impact noise. However, the main contribution of wave induced or *wind-driven noise* is more complicated. The wave collapse intrudes air into the water and clouds of billions of tiny bubbles are generated. The impact energy forces strong oscillations at resonance of the individual bubbles, and the entire clouds at the moment of their genesis. Depending on their size all of them radiate short tones of different pitch. The superposition of all the tones merges into a nearly uniform noise.

According to empirical laws the wind-driven noise intensity *increases* approximately by the square of the wind speed within the entire frequency regime of infrasonics up to ultrasonics. Further, the intensity of this noise type *decreases* nearly by the square of the frequency beyond the broad maximum of the noise spectrum at some hundred Hertz.

Later, after consumption of the impact energy, these bubbles, to the extent that their air content has not been dissolved, climb up to the surface again. During this state they are highly effective sound absorbers as well as sound scatterers at their resonance frequency. This effect is even strong enough to screen the high frequencies of the surface noise at very high wind speeds down to the noise of a breeze. We will point out later that air bubbles are the only existing natural resonators in the sea at sound frequencies. This is a feature which enables the acoustic determination of the size distribution of the bubbles and therefore the total quantity of air intrusion. The process of air bubble cloud formation is of climatic relevance because the greenhouse gas, carbon dioxide, coming in from the atmosphere is highly soluble in water.

3.6.3 Rain Noise

There is another source of noise at the sea surface which is also of natural origin: the rain noise. A strong rain shower is the strongest natural source of noise in the ocean at higher frequencies of several kHz up into the ultrasonic regime. A raindrop impacting on the sea surface generates splash noise followed by an air cavity as generated by the impact of a bullet, though much shorter and smaller, more similar to a tiny cup. This unstable depression closes rapidly at the sea surface where the kinetic energy of the convergent flow causes small jets, both upward and downward. The downward jet, when penetrating the bottom of the void, can trap a

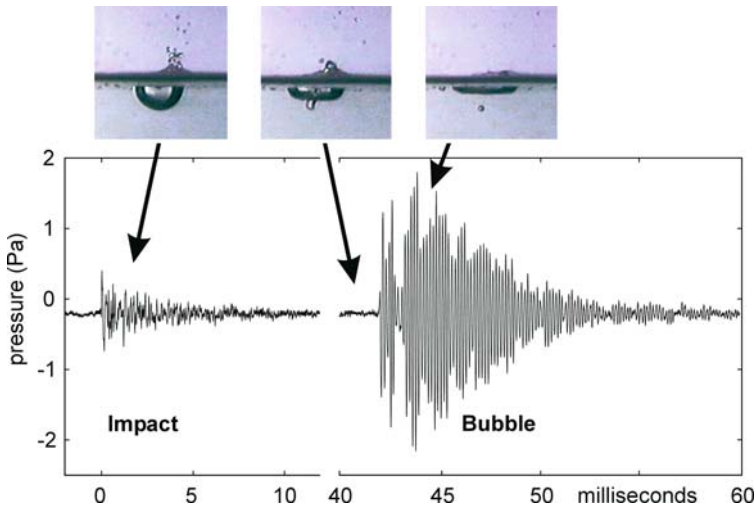


Image 3.6.3-1.

Underwater noise by raindrop impact. Laboratory experiment. A laboratory experiment with freefalling water drops revealed the hydrodynamic and acoustic side of the rain noise generation which is also a simplified model of the ever present natural ambient noise in the sea. A high speed camera observed the impact process through a window from the side while a hydrophone received the acoustic signal inside the basin. The drop diameter was 2.8 mm, the impact speed of 7.7 m s^{-1} corresponds to the final free fall velocity.

The first of three phases shows the instant of drop impact with the formation of a small, bowl-like cavity in coincidence with the signature of the short splash, lasting a few milliseconds. The splash signature depicted below looks irregular with no periodicity. The next phase is the tiny double jet into the air and the water resulting from the collapsing bowl cavity. This phase is obviously a silent pause of noise, lasting about six times longer than the preceding splash noise. The third and final phase is the most amazing one. A tiny bubble, much smaller than the initial bowl separates from the lower jet whereas the shallow rest of the bowl flattens out towards the surface.

It is the tiny bubble that wins the noise production contest by far. The initial energy of the high speed bubble, driven by the mini jet of several meters per second is partially converted into forced oscillations. The bubble, pulsating at its resonance frequency radiates a sinusoidal tone with much higher amplitude and longer duration than the random splash. The pitch of this short tone depends on the size and speed of the drop. The bubble shown rings at more than 6 kHz which means a bubble diameter of 1 mm. Though it is a loud tone, only one per mille of the kinetic energy of the rain drop is converted into sound.

Laboratory experiment and image ©: Jörg Förster, Forschungsanstalt der Bundeswehr, FWG, Kiel, Germany ■

tiny bubble underwater which oscillates due to its kinetic energy, and thus radiates a tone (Image 3.6.3-1).

This mechanism of sound generation is evidently similar to the generation of noise by bubble oscillations induced by the collapse of sea waves, and it is much more effective than splash noise. However, since the rain induced bubbles remain close to the sea surface and therefore don't form deep going clouds, which oscillate also in total at lower frequencies, the resulting rain noise is essentially of a high frequency type. Unlike the wind-driven noise, the noise intensity of rain showers cannot be quantified by simple laws. Like the rain itself, it is often a local rather than a regional event and as such hardly predictable. The problem

is that the effect of this kind of noise has the greatest influence on the frequency regimes of most echosounders.

3.6.4 Noise Fighting

All these surface noise components, including the man-made ship traffic noise, are of course unavoidable. A research vessel can neither wait until the weather is dead calm to start sound imaging the sea floor nor is it realistic to restrict the research to sea areas free of traffic. There remain *three technical options* which are requirements in reality for improving the signal to noise ratio within the limits of physics. We shall discuss these options in the following paragraphs. All of them are essential when sound imaging has to be conducted under unfavorable environmental conditions, thus with weak echoes and strong noise. We anticipate some of the features of an echosounder here. These will be discussed more fully later in the context of high resolution imaging (Chap. 4).

3.6.5 The Spatial Filter

The *first option* is primarily decisive for high resolution imaging. It is the requirement that the acoustic receiver should cut off as much as possible from the incoming noise. The echosounder therefore needs narrow or "pencil" beams (Sect.4.2.3). Then only the noise

coming in from the same direction and within the narrow receiving cone will be received together with the echo signal, thus cutting off the noise from all other directions. Following this option the acoustician will kill two birds with the same stone – as it were – because the high angular resolution provided by the narrow beam is a requirement of image quality anyway: All that is needed to resolve a scenario are a sufficient number of pixels.

3.6.6

The Frequency Filter

The *second option* to cut off part of the noise accompanying the echosounder signal is to filter in the frequency regime. This is much less expensive than noise fighting by directionality because it is only software, not hardware effort, as we will see later. But, whereas the pencil-beam noise cutter *improves the lateral image resolution* by reducing the pixel size, the simple and cheap method for cutting the noise off more and more by a narrower frequency filter would finally *cause deterioration in the resolution, in the dimension of range or depth* respectively, as we will see right now.

The depth is the classical echosounder information. The echoes of two small objects within the same beam of the echosounder will merge into only one when their distance is shorter than the spatial length of the signal pulse passing by at a sound speed of 1500 m s^{-1} . For example: the spatial length of a signal pulse of one millisecond (0.001 s) duration is 1.5 m. The echosounder will discriminate the two objects only if they are at least 0.75 m apart in range. Why not 1.5 m? Well, the distance traveled by the pulse between the two small objects, when returning to the echosounder, is the *to and fro path*, which is twice the 0.75 m.

If we need more depth resolution, for instance when a shipwreck needs to be identified by its sound image, then one tenth of a millisecond pulse duration may be required to provide a 7.5 cm range discrimination capability. What does this mean however in the context of *signal to noise ratio*? Anticipating and simplifying the comment on this matter in the Appendix, we can say: the longer and the shorter signal differ also by the width of their frequency spectrum. However, it is by the *inverse* of the same factor: the shorter the sound signal, the broader its spectrum.

To give an extreme and plausible example: the spectrum of a *very long* tone is just a *very narrow* line, in other words: a “monochromatic” signal. If this tone is buried by so called *broadband noise*, reaching from low to high frequencies, there is no problem in eliminating the noise. We just need to apply a *very narrow filter* through which only the tone can pass, together with the same narrow part of the noise spectrum. This unavoidable remainder of the noise will be the less the longer the tone is made, and therefore the narrower the filter.

Increasing the width of the filter works in exactly the opposite way. If the noise intensity were independent of the frequency, then doubling the filter window would transmit exactly twice the noise power. A factor of even ten times the width of the spectrum opens the noise power window by the same factor and the signal to noise ratio S/N is then only $1/10$, if nothing happens to the echo signal.

3.6.7

Tailoring the Filter

Returning to the example of a 7.5 cm resolution instead of 75 cm, we see that it requires widening the filter by a factor of 10 and accepting that the S/N decreases correspondingly. Of course we could think of enhancing the echo signal intensity by increasing the radiated power of the echosounder correspondingly, to compensate for the loss of S/N , but this would perhaps already exceed the technical limits.

It may happen that the environmental noise is too high to work with such short signals, with the filter necessarily wide open. However, enlarging the pulse duration and closing the noise window correspondingly would gain S/N only when the signal power is maintained. Otherwise we would only lose resolution and gain nothing. In any case the width of the noise cutting filter should be exactly tailored to the necessary width of the signal spectrum.

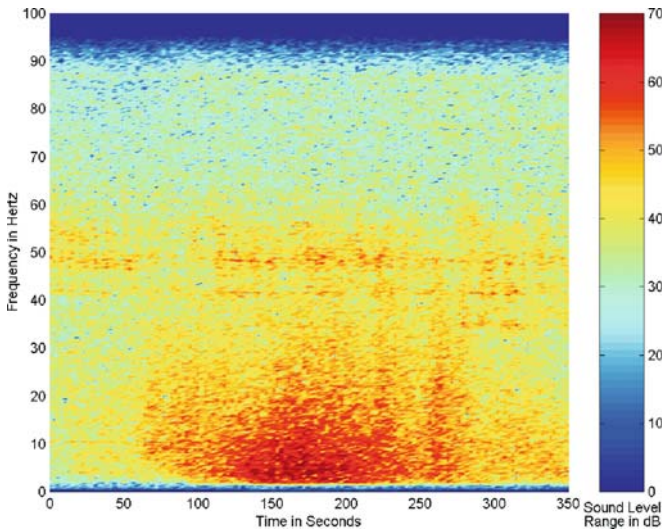
We can see that we have to optimize – and compromise – again when we reach the limits of physics, as we already had to regarding frequency and range. The procedure of optimization can be rather complicated when several quantities have to be taken into account. This is the reason why the sonar equation (Sect. 3.7) is such an important tool for achieving the best possible results of sound imaging the sea.

3.6.8 Further Sources of Noise and Very Large Acoustic Events

There are several other natural sources of noise in the sea which have not yet been mentioned. The most important of these occur spontaneously as single events and radiate enormous amounts of sound energy, though at very low frequencies. We are talking about large geodynamic events: oceanic earthquakes and volcanic eruptions. Though these events are accompanied by thunder-like noise outbreaks, not less than a submarine nuclear explosion of several kilotons TNT-equivalent, they seldom disturb the sound

imaging activities because of their very low frequency signals. These large event signals which travel ocean-wide are on the other hand a means of locating their origin.

The three very large acoustic events shown are: a *submarine earthquake*, a *volcanic eruption*, and a *test of a nuclear explosion*, all of them in the *Pacific Ocean*. The three depictions (Images 3.6.8-1 to 3.6.8-3) reveal characteristic features of the main types of extraordinarily large underwater sound events in the ocean received from a long distance. The receiver was a deep submerged hydrophone near *Pt. Sur*, 30 km South of *Monterey, California*.

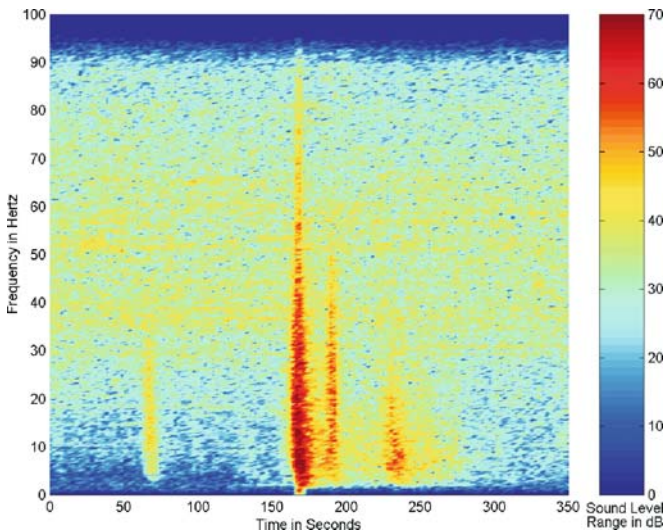


◀ Image 3.6.8-1.

Sonogram of a submarine earthquake. The epicenter of the earthquake in the Japanese Sea was 8 000 km away from the receiver in Pt. Sur, corresponding to a signal travel time along the Sofar-Channel of about 1½ h. The seismic event depicted over the time scale lasted about 300 s and its sound energy reached up to about 40 Hz on the frequency scale. Three features are characteristic: *First*: the onset of the single signal as well as its decay show a continuous transition. *Second*: the event duration is of the order of minutes. *Third and particularly important*: the maximum frequencies are significantly below the cut-off frequency of the Sofar-duct of about 100 Hz which means that the earthquake was a low frequency event since its origin.

Image ©: Lothar Ginzkey, FWG, Kiel, Germany; based on archive data of the US-Navy receiving station Pt. Sur, Monterey, USA

Data ©: Chief of Naval Operations, Undersea Surveillance, United States of America ■



◀ Image 3.6.8-2.

Sonogram of a submarine volcano eruption. The eruption in the Hawaiian area was 4 000 km away from the receiver in Pt. Sur, corresponding to a signal travel time along the Sofar-Channel of about 45 min. Four features are characteristic: *First*: there is a sequence of several similar signals. In other words: several partial eruptions are typical. *Second*: the signals show abrupt onsets and short decays of the signal. *Third*: the duration of the partial events is of the order of seconds. *Fourth and particularly important*: the maximum frequencies reach up or come near to the cut-off frequency of the Sofar duct of about 100 Hz.

Image documentation: same as for Image 3.6.8-1 ■

The international task of monitoring violations of the *United Nations Comprehensive Test Ban Treaty* (CTBT) of nuclear weapons (Sect. 3.2.2) is to reliably *detect, localize, and recognize* potential nuclear explosions worldwide. This is realized by a global network of receiving stations on land and in the sea, with transmission of the signals via satellites to the international CTBT-Centre in Vienna. The nature of long range underwater sound propagation by the oceanic Sofar duct enables the discrimination of large man-made explosions from acoustic events of natural origin by their characteristic acoustic clues. The main natural events comparable in radiated sound energy are the frequent submarine earthquakes and the relatively rare volcanic eruptions. The typical acoustic signatures of all three event types are shown in the respective images.

The radiated acoustic power of the events is comparable and is of the order of Megawatts. The result of the special spectrum analysis of the signals shown is named *sonogram*. The method is essentially the same as applied for voice recognition in the field of forensic investigations and also used in marine bioacoustics (sonograms of whale signals are shown in the Sect. 6.3.3): A sound signal which varies its pitch-composition and level, in other words: a non stationary signal is analysed by subdividing the long signal into a sequence of short fractions. These fractions are considered approximately stationary and taken for spectrum analysis. The resulting short-time spectra are then depicted along the time axis. They show the colour coded sound intensity at each frequency interval and at any instant of time: warm colours indicate higher intensities. The colour bar reveals the spectrum level indicated red to be larger by about 30 dB than the light blue-green background noise. 30 dB means: the signal intensity received at the site of the hydrophone exceeds the noise intensity by 1 000 times for the examples shown. The corresponding sound tracks are available on the CD attached to the book. The records are speeded up by 10 and 15 times the original duration to shift also the infrasonic parts of the signals into the audible frequency regime.

Very small man-made detonations are used for seismic exploration of marine mineral oil deposits by special vessels. The so called *air guns* work with a sudden release of compressed air whereby their energy corresponds from only some grams up to mostly much less than a kilogram TNT equivalent (Sect. 4.4.11). However, these signals cause more disturbance to echo-

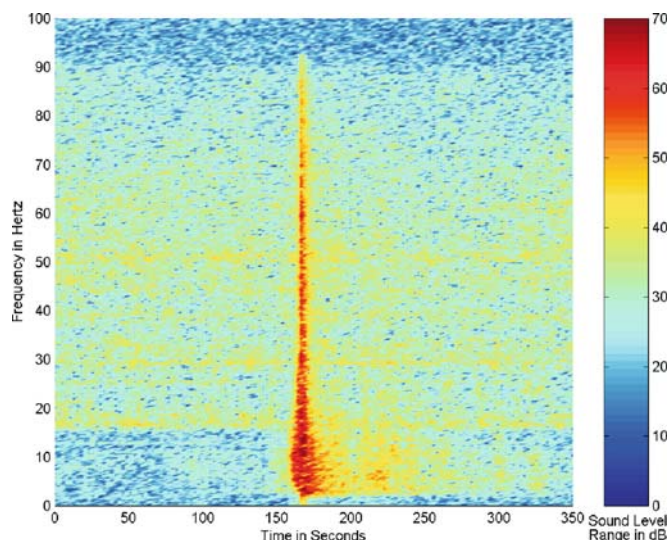


Image 3.6.8-3.

Sonogram of a submarine nuclear test. The test was conducted on the Mururoa Atoll on 21. October 1992 as an underground explosion, 6 600 km away from the receiver in Pt. Sur. The shock wave generated a short underwater sound signal containing very high frequencies. Three features of the received signal are characteristic: *First:* the single signal shows an abrupt onset and a short decay similar to a partial volcanic eruption. *Second:* the duration of the signal is of the order of seconds, again similar to the partial eruptions. *Third and most evident:* the maximum frequencies reach up to the cut-off frequency of the Sofar duct of about 100 Hz.

However, the features of the received signal from a nuclear explosion are only indirectly determined by the signal origin. The signal duration is neither caused nor governed by the explosion itself, which is only a tiny fraction of the sound signal duration after its long propagation through the Sofar-Channel. The actual travel-time spread is entirely due to the different sound ray paths which are undulating through different horizons of the water column and thus through layers of different sound speed (Sect. 3.2.2). The frequency regime of 100 Hz is also without any relationship to the much higher frequencies produced by the shock front of the nuclear explosion. The cut-off frequency is only the result of the sound absorption in the ocean, which increases steeply beyond 100 Hz (Sect. 3.3.1).

The recognition criteria based on the received signal are simplified. The individual, suspicious event requires the judgment of experienced geophysicists. Nevertheless: the general problem of surveillance is overcharging the human observer due to the number of decisions required per day. Mechanised pre-decisions based on reliable criteria of exclusion are indispensable to reduce the number of expert judgments to a minimum.

Image documentation: same as for Image 3.6.8-1 ■

sounders when they are released nearby than those of a distant earthquake and they disturb more frequently, two to three times a minute, which is a typical repetition rate of airguns.

The drilling noise caused by offshore platforms underwater is sometimes overestimated. Within a short distance it usually drops below the noise background generated by natural sources. Noise of the drilling head has to pass thick sediment layers of high sound absorption before it reaches the water volume above. The conditions of underwater sound radiation by wind driven offshore power plants are different. The shaft tube in direct contact with the water transmits the gear noise of the propeller effectively if the gear lacks sound insulation. The steel construction of offshore platforms can perform similarly, regarding noise of the Diesel power plant.

3.6.9

Marine Mammals and Noise

Marine mammals also generate sound signals, the large baleen whales to communicate at low frequencies near or within the infrasonic regime, the smaller toothed-whales (*Odontocetes*) both to echolocate their prey and to communicate with their partners (Sect. 6.3.3). In particular their ultrasonic detection-clicks may sometimes interfere with their technical ship-borne competitors and vice versa. These bioacoustic signals are the subject of scientific investigations of motion, migration and social behavior and also indicators of potential hazards caused by a noisy environment or acoustic events rather than being a problem for sound imaging.

The question has been raised as to whether signals of reconnaissance sonars radiating in horizontal directions might be hazardous to marine mammals by affecting their threshold of hearing or even by panicking them. Systematic investigations, in particular of the temporary shift of the hearing threshold of dolphins, have provided quantitative data of sound levels below threshold shift. However, several whale strandings have been observed where sonar signals as a potential cause could neither be excluded nor unquestionably confirmed. One mass stranding event in the region of the *Bahamas* has been attributed for the time being to mid frequency sonar signals in combination with other more or less essential adverse circumstances.

As a consequence of potential sound induced risks there are recommendations for precaution regarding

maximum sound source levels and even dimming of acoustic devices in cases of doubt. Nevertheless, whales are endangered by orders of magnitude more through many kinds of accidents, including unintentional and intentional fishing. Moreover, we should be aware of the omnipresent and highly variable natural and traffic-induced noise background, together with the rumbling of about 7 000 outstanding, dramatic geodynamic earthquake events per year worldwide, each of a thousand tons TNT-equivalent and more. If evolution has achieved inurement of marine mammals against such terrifying noise events is speculative though probable. The facts may help however to appreciate the comparatively marginal contribution to danger by technical echosounders in the context of reality. Nevertheless: instead of accepting the lesser of two evils, marine biologists rightly endeavor to minimize man-made hazards to endangered species *in general*.

3.6.10

Self Noise

The *third mandatory noise-fighting option* is of a different kind. The more successful we have been in fighting the ambient noise, the more dominating the toughest enemy on the noise front becomes. It is literally self made: the so called *self noise* of the sounding ship. This kind of noise has various origins; it may follow different paths and enter the echosounder through several doors, as it were. Apart from the radiated noise of the ship which enters the echosounder from the waterside there are many types of hull vibrations, excited by the machinery and auxiliary units but also by the propeller and related hydrodynamic forces. Because the hull vibrations enter the echosounder from the rear side, “through the rear door” so to speak, a narrow receiving cone cutting “front door sound”, cannot therefore help us. Further, other on-board echosounders, when operated at the same time, may cause acoustic interference in spite of their different frequencies. Moreover it may happen that the echosounder signal is being screened completely because air bubble clouds generated by the ship’s movement and enforced by its pitch motions are drawn under the acoustic window.

To fight all this successfully is a science and a technology in itself and has for long been a prerequisite in research vessel construction requirements. These measures require no less effort than the entire echosound-

ing systems on board and will be all the more expensive when part of the problems become evident only after commissioning of the ship. However, ship silencing is doubtless the most effective, though technically complicated contribution, to fully exploit the possibilities of imaging the sea by sound within the limits of the physics of the sea.

Recent developments in fuel-cell power plants for propulsion and power supply of submarines and research vessels open completely new perspectives for engine driven ship propulsion systems, which are free of emission both of combustion gases and of noise. This might appear like the fairy tale of the *Flying Dutchman* but the first vessels of this new generation are already operational.

3.7 Sonar Equation

The *sonar equation* is an almost universal formal tool of underwater acoustics. The formula provides simple but realistic estimates as to whether sound imaging will be successful under given conditions. The sonar equation is famous within the community of underwater acousticians because of its versatility in dealing with nearly all applications of underwater acoustics. The

equation is based on the *signal to noise ratio*, resulting from the contributions of all respective quantities under control as well as those imposed by nature and by non-removable facts. The basic idea supporting this will be outlined in the Appendix. The sonar equation can treat simple as well as complicated problems with the least effort because of its dimensionless quantities and reduction in terms of the Decibel scale, which only have to be added or subtracted.

3.8 Conclusion of Chapter 3

The basic quantities of underwater acoustics as discussed in this chapter should have provided more than a mere overview of the main acoustic properties of the sea, that hydro-acousticians have to cope with. It is the first step in judging on the strengths and weaknesses of imaging the ocean with sound. Together with the information in Chap. 4 and the Appendix it will be possible to conduct some interesting and surprising estimations of echosounder capability by means of the sonar equation and to get a feeling for the effect of working the adjustment handles for optimization of a complex system.

Technical and Physical Characteristics of High Resolution Echosounders

4.1 Conversion of Electrical and Acoustical Energy

4.2 The First Type of Sound Imaging: The Fan- or Multibeam Echosounder

4.3 The Second Type of Sound Imaging: The Sidescan Echosounder

4.4 The Third Type of Sound Imaging: The Sediment-Penetrating Echosounder

4.5 The Fourth Type of Sound Imaging: The Acoustic Doppler Current Profiler (ADCP)

Similar to diagnostic imaging in medicine by ultrasonics, the technical goal of echosounding the ocean is resolution and range. However, the surface of the seafloor requires other imaging techniques than the structures below and above. This chapter deals with the types of imaging and the tailoring of the options under the different requirements and natural limits. Special methods, in particular acoustic tomography by one-way sound propagation are treated mainly in Chap. 6.

4.1 Conversion of Electrical and Acoustical Energy

We should now inspect the present state of the art of the progress in echosounder evolution. All of them have in common that the conversion of electrical energy into sound energy and vice-versa is realized by a particular *piezo-ceramic* material also used for very prosaic daily applications such as cigarette lighters. Mechanical deformations of this material cause a direct electric response, only due to special crystal properties and without any moving coils, magnets, and membranes. This effect of piezoelectricity is reversible: An applied voltage causes a mechanical deformation.

The ceramic material, called *Lead-Zirconate-Titanate (LZT)*, has meanwhile replaced essentially all other *transducer*-materials for at sea applications. It is mechanically robust with a high degree of conversion efficiency of up to 80%. This efficiency is much better by the way than that obtained from electric motors and generators. One of the most important advantages of LZT is a typical feature of all ceramic materials: the possibility of cheap production of nearly any wanted shape. Thus the material can be tailored to the mechanical vibration of preference.

4.1.1 The Piezoelectric Effect

The piezoelectric effect is based on a particular structure of the crystal lattice atoms. They represent electric dipole elements which become slightly longer or shorter, which means stronger or weaker, when the lattice bond is deformed mechanically. Altogether the dipoles then generate an electric field between opposite surfaces of the crystal. When these surfaces are plated by a metal film, like an electric capacitor, they provide an electric voltage.

4.1.2 Quartz: The Prototype of Piezoelectricity

The most well known material in which the piezoelectric effect was discovered is quartz, also known as rock crystal. Because of its extremely low mechanical loss and therefore sharp resonance, quartz vibrators became the “heart” of essentially every cheap precision wrist-watch of today. The reason for the movement precision

however is also the extremely low thermal expansion of this crystalline material. Since its piezo-effect is lost when trying to make polycrystalline ceramics of quartz and also because its electromechanical conversion efficiency is only low, quartz cannot compete with LZT for underwater-acoustic applications. Moreover, the feature of providing sharp resonances is not a virtue for hydro-acoustic transducers, as we will see.

4.1.3 Polarization of LZT

To avoid oversimplification, we should admit that LZT ceramics are polycrystalline without a regular lattice but have irregular, random dipole directions instead. However, when a very strong electric field is applied at sufficiently high temperatures, the dipoles, forming so called *domains* switch into the direction forced by the external field. This forced orientation of the dipole domains remains when cooled down to environmental temperatures again and the “polarization field” is removed afterwards. There is obvious similarity to the behavior of ferromagnetic materials like iron, where similar domains are oriented by strong magnetic fields, thus generating a permanent magnetism. When this effect accompanies mechanical deformations, the ferromagnetic material such as nickel is called *magnetostrictive*. Because of this similarity, LZT is called more precisely an “*electrostrictive*” material.

4.1.4 LZT-Ceramics As Sound Source

As mentioned, the piezo-effect works in the reverse when cause and effect are inverted. Applying an alternating voltage deforms the crystal correspondingly: the principle of a “loudspeaker” or underwater *acoustic transmitter*. A silver-plated disc of LZT ceramics, excited to thickness vibrations by a driving voltage to radiate sound in water in fact appears similar to a loudspeaker. However, there are two main points which differ from usual loudspeakers. First, air is much more compressible than water, by a factor of about 20 000. That means: the forces necessary to compress – and dilate – the water during the cycles of vibration are correspondingly much larger. On the other hand, the amplitudes of vibration are much smaller in water than in air when compared with the same acoustic power.

The second essential difference as compared to loudspeakers is the requirement for high sound intensities beyond audible frequencies up to the ultrasonic regime. Any light, fragile membrane, appropriate for radiating sound in air would neither act as a stiff piston at those frequencies nor would it be able to generate the necessary forces at all. A large “membrane”, both strong and stiff enough at ultrasonic frequencies has to be a solid body, producing the vibrational forces without any mechanical links, just by intrinsic deformations of the material itself. This is the main reason for the peerless advance of LZT-transducers in underwater-acoustics.

4.1.5 Transducers at Resonance

The best efficiency in the conversion of electric and acoustic energy is achieved when the “body” is excited at *resonance*. The so called thickness resonance of an LZT-plate, 20 mm thick occurs at 100 kHz. According to a rule of thumb: doubling the plate thickness bisects the frequency of resonance. There are problems again when a thin plate is made too large because the vibrations occurring will be other than those of pure thickness and will therefore be counterproductive.

Transducer resonance is also subject to compromising and optimizing. A sharp resonance means the response will decrease rapidly when the exciting frequency deviates only a small fraction from the “*eigen*”-frequency. This is advantageous when a *long signal* of a single frequency is transmitted because the efficiency is best. However, to transmit a *short signal* pulse in order to achieve a high range resolution of an echosounder requires the corresponding width of the spectrum, also called *bandwidth* (Sect. 3.6.6).

LZT-transducers normally offer a bandwidth of about 10% of the resonance frequency (Sect. 4.4.1). Within this frequency interval the efficiency by definition will not decrease by more than a half. We may easily prove whether this is sufficient for the example of the deep-sea fan echosounder of 15 kHz mentioned earlier. Here, the 10%-bandwidth of 1.5 kHz corresponds to a minimum signal duration of 2/3 of a millisecond. As explained already, the spatial length is then 1 m which means a range resolution of 1/2 m because of the to and fro path of the pulse between the two objects to be discriminated. Fortunately this resolution is more than adequate in many cases.

The situation is problematic however when we want to penetrate the sea floor sediments with their high sound absorption to resolve the layers of stratification which contain the climate diary. The compromise frequency of a sediment echosounder, belonging to the third type of sound imaging mentioned, is typically 3 kHz (Sect. 4.4.1). 10% means 300 Hz and therefore 2.5 m depth resolution. We simply get this result by scaling the already treated example of 1.5 kHz and recalling that bandwidth and signal duration are inverse to each other. The 2.5 m range discrimination is by far too large. Significant sediment layers are at most a few decimeters apart and often much less when sedimentation rates are of the order of centimeters per millennium. There is a way out of this dilemma between the necessary low frequency for sufficient penetration and the requirement for sufficient resolution, which we will consider in the context of the third type of sound imaging, the sediment echosounder. Special constructions to extend the bandwidth have achieved far more than the 10% mentioned. About 100% bandwidth is available, compromising though with reduced efficiency.

To construct a large transducer array with a large number of LZT-elements to achieve nearly ideal narrow sound beams at the frequency regime and beam orientations wanted is an art of high tech sophistication and specialization. We don't intend – and don't need – to go into details of transducer technology when we only want to convey the prerequisites in kind of high resolution sound images of the sea.

4.1.6 The Cavitation Limit

We should mention however, that there are limits to the radiated acoustic power of transducers which are not primarily set by a mechanical or electrical overload. It is the environment, setting a critical threshold by the so called *cavitation*. This destructive effect is perhaps more known from ship propellers which can become dangerously eroded when operated at too high rotational speeds. Here the *hydrodynamic forces causing negative pressure* at the blade surface are sufficient to disrupt or cavitate the water volume. The response is the generation of cavitation bubbles which are unstable and implode due to the low pressure inside. The resulting micro-flows reach extremely high speeds of more than a hundred meters per second and erode the metal surface like micro-mills. The implosion is accompanied by a hissing noise, the prevailing contribution

to the radiated noise of a fast going vessel when the propeller does not prevent cavitation by an appropriate blade shape.

When cavitation happens in front of a high power underwater acoustic transducer during the periodic phases of *negative sound pressure*, the bubbles screen the transducer window, produce strong noise as one kind of self-noise, and erode the transducer surface. Again, as a rule of thumb, more than a few watts of acoustic power per cm^2 are already beyond the cavitation threshold at a usual keel depth or draught of the echosounding vessel.

4.1.7

Conclusion

LZT-ceramics has achieved a kind of monopoly for converting electric power into acoustic power at ocean echosounder frequencies because of its high versatility, efficiency and resistance against high static pressure and aging. Further development deals primarily with long life resin-ceramic watertight compounds under strongly varying sea water pressure rather than with alternatives to ceramics.

4.2

4.2

The First Type of Sound Imaging: The Fan- or Multibeam Echosounder

Optimizing an echosounder system for a particular purpose involves both *physical* and *technical* facts. To become familiar with the decisive options we should briefly deal with those relations of physics which govern the *resolution of the systems* and thus the image quality.

Resolution of a normal, two dimensional image simply means discrimination of adjacent elements of the scene. The usual measure is the size of the image elements, called pixels. The *necessary* resolution of course depends on the scale of the structure we want to see. The *possible* resolution of a sound image is primarily limited by the minimum wavelength we can afford. This concerns again the compromise between range and resolution: the longer the range required, the lower the frequency needed to cope with the frequency-dependent sound absorption. This is the compromise dealing with *physics*. The *technical* compromise is essentially the size of the array we can afford or can match to the size of the ship.

Before discussing the relationship between array size and pixel size, we recall the decisive difference between a two-dimensional photo and a fan-echosounder image which contains and quantifies the third dimension. Of course, we normally depict the sound image in the same, two-dimensional manner as a photo. But, since the data set of the fan-sounder image contains the complete relief information, it is possible, just by computer data handling, to turn the direction of view as we want (the attached CD presents several examples for turning and zooming). We may apply the classical *bathymetric depiction*, the so called *depth chart* used for nautical purposes with lines of constant depth or *isobaths*. Or we might prefer the “*landscape depiction*” from a frog’s perspective up to a bird’s eye view. We may rise and turn a virtual sun to illuminate and shade the scenario and we can, if we wish to, change the type of projection into a central perspective (Sect. 5.4.2). We may go even further and project upon a spherical surface when the Earth’s curvature becomes essential (Image 5.4.1-3). When looking for peculiarities of geodynamic processes for instance, the landscape depictions similar to aerial photographs are usually most helpful because that is how we normally see our own environment. They also need the least training and the least explanations for the non-expert. Therefore most of the fan-images will be presented like that, either as bird’s eye or slant view (Sect. 5.2). Some images with highly complex sea floor structures are moreover shown as 3D-depictions or even as animated flights (s. attached CD) to come as close as possible to reality.

We should not forget to mention that there is also genuine 3D-airborne photography, called *holography*. It requires the light of a laser to illuminate the scene, a so called *coherent radiator*. A source of coherent light became available only several decades later than the echosounder, which was the first coherent radiator of all, also earlier than radar. Within narrow limits the optical hologram can be turned for other aspects of view. But quantitative information on the third dimension is only indirectly available whereas the echoacoustic relief provides the real, quantitative geometry.

In the context of noise fighting we have already mentioned the two components for achieving three dimensional resolution, which are typical for echosounding. The *lateral* and the *radial* resolution are different in kind because *lateral* means *angular* resolution by the

sound beam whereas *radial* means travel-time resolution of the echo. Having discussed the inverse relationship of signal duration and signal spectrum width or bandwidth already, regarding the radial or range resolution (Sect. 3.6.6), we still need to know the corresponding relations of beam-forming.

Anticipating and simplifying the relations depicted in the Appendix we can say: the size of the echosounder, i.e. the diameter of the radiating surface and the width of the acoustic beam, are also inverse to each other, similar to signal duration and signal spectrum width. In other words: the larger the transducer size, the narrower the beamwidth. For example: taking a size of 3 m and a sounder frequency of 15 kHz, typical for deep-sea multibeam echosounding, the beamwidth will be about 2°. The physical relationship refers to the number of wavelengths as the relevant measure, and can be arbitrarily scaled up and down. Therefore: at 150 kHz the transducer size needs to be only 30 cm in diameter to achieve the same beamwidth. Or, the opposite way: if 3° beamwidth is considered sufficient, the deep-sea fan-echosounder needs only be 2 m in size.

The narrowest beamwidth of about 0.2° has been realized so far with sidescan echosounders (Sect. 4.3). This beamwidth requires a transducer size of 50 cm at 500 kHz. We will see that such a narrow beam needs an extremely stable platform as a carrier. But even 1–2° cannot normally be held by a ship underway. The problem of motion compensation has therefore to be addressed as well. But, any progress of resolution cannot be realized in the sea when the decisive requirement would be missing. That is exact positioning. Since this is true for all four types of echosounding we should deal with this indispensable achievement before we specialize further into the four kinds of sound imaging techniques.

4.2.1 Satellite Navigation

A sound image of high resolution is achievable only when each acoustic pixel is positioned correctly. Modern multibeam echosounders of more than a hundred individual “pencil beams”, of a degree beamwidth each, produce a corresponding pixel size of about 50 to 100 m at a deep-sea floor of 4 000 m. Going shallow, for instance to a coastal region of only 40 m depth the pixel

size, according to simple triangle geometry, will shrink to 0.5 m when the same beamwidth is applied. In reality, in shallow water much narrower beamwidths are achieved. This illustrates the required precision in location. But in reality it happened vice-versa.

It was in fact the high precision *satellite navigation* GPS that initiated the development of the echosounders of today and became the first of the three *godfathers of success* of advanced sound imaging of the ocean. GPS in its present day precision became operational step by step in the *nineties*. Location accuracies of an order of meters and less worldwide must have been a dream of mariners before, and have doubtless been a quantum leap in the long tradition of navigation at sea. GPS has rapidly, like an avalanche, superseded and replaced essentially all former methods of navigation at sea, as well as on the continents.

4.2.2 Predecessors of Navigation

The art of *astronomical navigation*, highly renowned for centuries with its precision chronometers and nautical sextants, represented the contemporary high tech of their time. It disappeared in a niche after having survived even the succeeding *radio navigation*, despite its location tolerances of a nautical mile and more. The radio navigation technology which held the lead during most of the 20th century provided great progress in precision – and therefore ship safety – within coastal areas endangered by high traffic densities. The principle of this navigation method is triangulation. The radio signals of at least three fixed land stations were received by the ship, which then determined lines of constant differences of distance from each two stations known as hyperbolas. The crossing point of two of such curves was the ship’s position. The more dense the station network, the better the crossings, which provided good accuracies, at least ten times better than astronomical, but limited however to sea areas of at most a few hundred kilometers away from the coast. There were also more long-range versions, important for high sea radio navigation named Omega and Loran. But apart from land stations to support GPS for extreme precisions of the order of centimeters the radio navigation networks are being removed and the remaining receivers are meanwhile a kind of decoration on the ship’s bridge.

4.2.3

The Fan Echosounder, Requirement for Motion Compensation

GPS has doubtless been revolutionary for imaging the ocean by sound. Nevertheless, removing the key problem on top of the list usually puts the next one in its place. The second and in the meantime first enemy of high resolution sound imaging is doubtless that kind of ship motion, which is notorious for causing seasickness. As soon as the pitch or roll angle of the ship exceeds the narrow beamwidth of the echosounder system the image will look like a blurred photo, taken by a moving camera. Particularly obvious is a typical stripe texture (Sect. 7.3.3) athwart of the ship's track, caused by pitch. This effect does not require high sea states. One to two degrees up and down of the bow, much less than the seasickness threshold of sensitive passengers, is already beyond tolerance. Of course: to image only in dead calm weather is impossible, not only because of the expensive ship time.

There are two possibilities for coping with the inevitable ship motions. The first one is not aimed at steering the echosounder electronically to keep the vertical axis, but limits the effort to correct positioning of the pixel rows according to GPS and gyro reference. This avoids blurring but generates converging and diverging pixel rows, forming the stripes mentioned. The second, comprehensive solution by instantaneous electronic steering the echosounder to compensate pitch and roll as well as heave has turned out to become one of the most demanding high-tech components of the entire sound imaging business.

However, aside from the sensors for monitoring the instantaneous components of motion, the principle of motion compensation is part of the beam forming and beam steering necessary anyway for advanced fan echosounders. First of all a precise gyro has to provide the vertical reference as steering signal. It is, via computer, the input to move the *acoustic array axis* to the real vertical direction, slanting to the instantaneous position of the *ship's vertical axis*. In fact, the large, heavy-weight high resolution deep-sea echosounders cannot be tilted mechanically, simply to keep the additional hydrodynamic drag forces low. This requires by itself a streamlined integration into the ship's hull or into a streamlined body.

4.2.4

Phased Array Beam-Forming; The Radar Solution

The electronic solution to the problem is perhaps known better from large airborne radar-arrays which look like a "mattress" of many small elements. These arrays cannot be steered mechanically, also because of weight and size. Referring to this more familiar technique helps also to understand the substantial difference between imaging by sonar and radar. The method of electronic steering is called *phased array beam-forming*: When the radar antenna radiates straight forward, all the small antenna elements which together represent the large plane matrix array get their electric signal input exactly at the same time, which means: at the same signal *phase*. Altogether they form the *phase front* which is itself a plane, parallel to the plane surface of the antenna array. The axis of the antenna thus coincides with the axis of the phase front, which is the *direction of radiation*.

When the matrix antenna radiates in slanting directions *off axis*, the elements receive their individual signal with a small incremental delay from neighbor to neighbor, as provided by the beam-forming computer. This means that there is still a plane phase front but it is inclined against the array plane. Now, since *the axis of radiation is always the axis of the phase front* according to the physics of wave propagation, the array will radiate correspondingly as if it had been turned by that angle. When the antenna is switched over to receive the echo coming in from that direction, the element signals are of course phase shifted in the same way. To provide the complete radar image of such a stationary array, the direction of radiation of the radar signal, in other words the line of sight, is scanned by lines and rows similar to scanning a TV-screen.

Instead of defining incremental *phase delays*, the method can be understood easier when working with corresponding *time delays* of the signals. Then it is evident that a short signal with its broad spectrum of frequency components keeps its shape when delayed.

4.2.5

The Fan Echosounder Solution

A high resolution acoustic array for deep-sea imaging, called *fan- or multibeam echosounder*, is steered also by

the *phased array method* into the typically one hundred different directions to generate the same number of pixels. Each beam provides the echo of its respective slant angle and range to the sea floor and thus the depth at that spot. But there are two substantial differences, typical of hydro-acoustic imaging as compared to airborne radar.

4.2.6

Sampling of Lines and Rows

First: the fan echosounder scans the sea floor line by line whilst the ship proceeds, each line consisting of the hundred pixels athwart the ship's course. The speed of the ship thus has to be adjusted to the scanning speed to achieve seamless lines of pixels adjacent to each other, forming a three dimensional image "carpet" of lines and slowly but continuously growing rows. These pixel lines and rows are thus generated similar to a television image but of continuously growing length. The width of the image carpet depends on both the fan angle and the water depth according to simple triangle geometry. The pixel lines are demonstrated best by looking at real multibeam images as shown in Sect. 7.1.4, where the pixels are not connected to form a closed surface.

4.2.7

Time Parallel Sampling

The reason for the second difference is the slow sound speed. Whereas the radar signals propagate by the speed of light, amounting to 200 000 times the speed of sound in the sea, the radar echoes return fast enough from each line of sight of the antenna to scan the scenario *sequentially in time*. The fan echosounder however can't wait for the echo returning from the deep-sea floor of a particular beam before switching over to the next one, simply because the hundred beams would then need more than 13 min just to sample one complete pixel line. Since a typical pixel size at the deep-sea floor of 4 km depth is about 50 to 100 m, depending on the beamwidth, the sounding ship could not proceed at more than 0.25 or 0.5 km h⁻¹ because the pixel lines need to follow in an adjacent and seamless mode. The only way out of such a snail's pace speed is to scan the beams *parallel in time*. Then the ship may go ahead by 25 km h⁻¹ or 13.5 knots, the speed of a bicycle though, which doesn't sound much but is the typical speed of research vessels even today.

4.2.8

Two Line Arrays Instead of a Matrix

In order to achieve the *simultaneous sampling* of a pixel line, the fan echosounder could certainly consist of a matrix array like the radar example. However, this option is not an adequate solution for deep-sea operations and would be much more voluminous, heavy, and expensive than the elegant concept which has been realized instead. The idea was to separate the sound source array from the receiver array and to replace the matrix by only two line arrays, which are positioned like a windmill cross, flush to the keel region of the ship's hull. Both arrays have no directionality around their line but have the direction of their narrow maximum of the source intensity, as well as their respective maximum receiving sensitivity athwart. That means: The source array will irradiate a narrow stripe instead of a small pixel and the receiving array will receive the sound from a narrow stripe instead of from a small pixel. Since both stripes cross each other, they overlap only at the size of a pixel. Irradiation and reception only coincide there.

To fulfill the requirement of simultaneous scanning of the complete line of pixels, the irradiated stripe has of course to be oriented athwart the ship's course, whereas the phased array steering needs to be applied only to the receiving array. But differing from the radar version, *all predetermined sets of phase shifts are applied at the same time to each of the receiving array elements*. In other words: the output of each receiver element is subdivided into a hundred channels with stepwise increasing phase shifts. The high resolution receiving line array thus "looks" into all the preformed beam directions at the same time. This ability could remind us of an insect's faceted eye.

The mill cross array mounted flush into the ships hull widens the slant beams, which deteriorates their resolution because the apparent (effective) length necessary for beamforming shrinks with the sine of the inclination angle. To provide beamforming which is less dependent of inclination, the array is formed like a roof or a bow, which is easier to realize at higher frequencies and correspondingly smaller arrays. The photo (Image 4.2.8-1) shows such a "roof" solution (ATLAS Elektronik).



Image 4.2.8-1.

Multibeam echosounder transducer head. The array units of transmitter (horizontal) and receiver (“slant vertical”) are mounted flush and symmetrically on the streamlined body with the roof-shaped keel. The length of the units in number of wavelengths determines the beamwidth and thus the width of the stripes of irradiation and reception respectively on the sea floor, increasing with depth. The width of the units determines the length of the stripes of irradiation and reception. (Note the inverse relationship of beamwidth and array length/width.) The width of the transducer units, dimensioned to yield the wide angle stripe length, provides also the necessary size of the transducer surface to avoid cavitation. This size is made about the same also for the receiving array, to enable a switch-over of transmitter and receiver function for calibration of refraction-induced errors, a specialty of this type series. The size of the transducer head, tailored to the frequency of 30 kHz, permits the roof-shape to optimize the average beamwidth in slant angles. Transducer units of lower frequencies, sufficient to image even the deepest trenches on Earth, are not appropriate for exposed nacelles any more but are mounted flush into the keel area of the hull of the research vessel. Multibeam units of higher frequencies can be mounted on ascent shaft nacelles.

MultiBeam Echo Sounder: STN-ATLAS, type: Hydrosweep MD2; frequency: 30 kHz

Image ©: ATLAS Elektronik ■

4.2.9 Motion Compensation

Moreover, the instantaneous compensation of the pitch and roll motion of the ship monitored by precision gyros requires permanent correction of all the phase shifts. It is quite obvious that the hundred and more

different phase shifts per receiver element times the number of elements forming the receiving array requires an enormous endeavor of signal processing and data management. It is by orders of magnitude larger than for the classic single beam echosounder, and was out of reach prior to the development of high speed computers with large, fast access memories, the *second “godfather of success”* of imaging the ocean by sound.

4.2.10 Conclusion

Multibeam echosounders are successfully utilized for various depth and corresponding frequency regimes and essentially all scientific and surveillance applications of the outer relief. They are considered at present to be the peerless concept for high resolution 3D-imaging, reaching from the exploration of deep-sea trenches to the identification of shipwrecks endangering sea lanes through coastal shallow water areas.

However, the echo data contain more than the travel time which provides the *shape or the relief* of the sea floor scenario. The *echo intensity* comprehends additional information of scattering properties and thus of the type of the imaged matter. The Sect. 5.2.3, 5.3.6 or 5.3.9 present examples of utilizing the scattering strength for analysis. Above all, scattering strength imaging is the domain of sidescan echosounders, the second type of sound imaging, which acquires this feature as the only one depicted.

4.3 The Second Type of Sound Imaging: The Sidescan Echosounder

The sidescan echosounder came on the market in the seventies at about the same time as the first multibeam system became operational. But the less complex sidescan technology was the first to provide high resolution imaging, though restricted to two dimensions instead of three. From the first trials up until today this technology is indispensable for imaging *small scale morphology*, in particular to identify the types of sediment and sediment erosion (Sect. 5.3) and also objects such as wrecks in coastal areas (Sect. 7.1.1) by their specific features. Sidescan systems of lower frequencies image also features of *larger scales* in deeper water (Sect. 5.3.5) where a *primary, overview survey of broad*

swath width is useful before the full display of echosounders such as multibeam, short-range sidescan, and sediment-echosounders are operated in the identified area of interest. The economic strategy of surveying in steps tailored to the specific task is particularly important for off-shore industries (Sect. 7.4.2).

4.3.1 Line by Line Sampling

The basic concept of sampling the sea floor line by line or more correctly stripe by stripe is the same as performed by the fan sounder. But instead of sampling the stripe by a large number of narrow beams which provide the *depth profile*, the sidescan echosounder yields merely the backscattered *echo intensity* along the stripe. A line array similar to the line source of the fan echosounder irradiates a narrow stripe of the sea floor athwart of the line and the vessel course respectively. The simplified scheme of Image 4.3.3-1 depicts only the starboard side of the narrow irradiation slice generated by a hull mounted version of a sidescan echosounder.

Different from the multibeam sounding method, the line source acts also as the receiver array after having transmitted the short signal. This is nothing other than the normal echosounder function known from mono-beam systems: the electroacoustic transducer is alternately switched between the source and receiver function. Both functions have the same narrow directionality.

In principle the sidescan echosounder is a mono-beam echosounder that looks at the bottom nearly horizontally sideways from the vessel underway. Each signal pulse generates a new stripe, adjacent to the previous one in the same way a TV image is generated. The narrow beamwidth is restricted to provide high resolution in the horizontal; in the vertical, the system is intentionally broad beam. The transducer unit is therefore long but slim (Image 4.3.3-1). The proceeding ship with the sidescan echosounder thus generates a sounding carpet like the multibeam sounder. The difference between both concepts however is not only the two dimensions instead of three. The width of the “carpet”, called *swath width* of the sidescan sounder is usually and intentionally larger. It is limited only by the local sound refraction conditions (Sect. 3.2.2) or by the sound absorption at higher frequencies (Sect. 3.3), not by a fan angle.

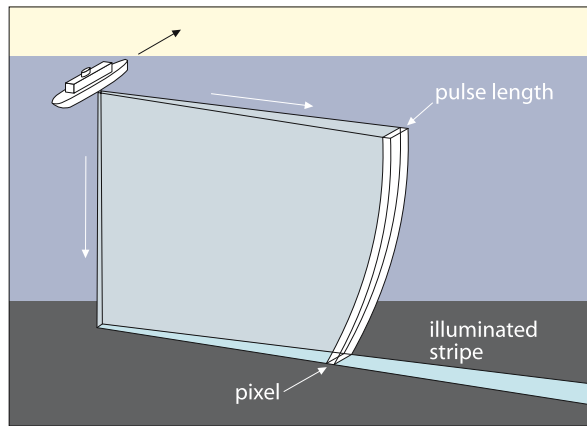


Image 4.3.1-1.
Scheme of sound irradiation by a hull mounted sidescan echosounder; the starboard side is depicted ■

4.3.2 Throwing Shadows

The long irradiated stripe generates a chain of stronger or weaker echoes depending on the individual scatterers or the type of sediment on the sea floor along the stripe. According to experience, the sidescan echosounder provides the most informative images of the kind of sea floor structure when the individual objects like stones, boulders, or sand ripples for instance throw long shadows. These enhance the contrast and enlarge or reveal otherwise nearly invisible features. Moreover, some height information may also be estimated from the shadow length. To achieve this grazing irradiation, the sounding equipment is usually towed close to the sea floor, by a streamlined body, a so called towed fish.

4.3.3 The Towed Fish for Rail-like Motion

An example of a towed fish sidescan device is depicted in Image 4.3.3-1. Note that the transducer is a twin unit, symmetrical to the towed-fish axis to optimize the athwart irradiation, similar to the multibeam configuration. To separate the echosounder from the research vessel by integration into a streamlined carrier towed behind the ship is necessary also for a second reason: the extremely narrow beamwidth. High frequency sidescan echosounders achieve about 0.2° , the best angu-

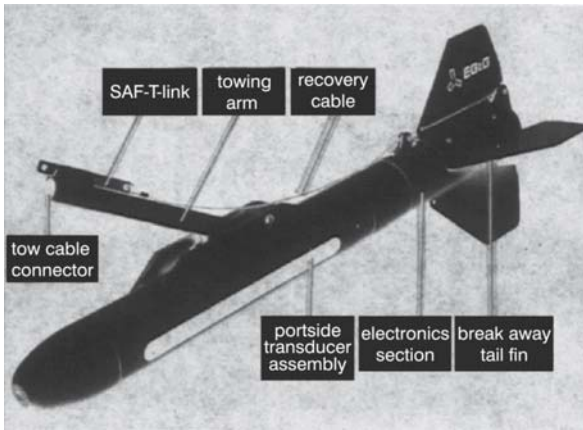


Image 4.3.3-1.
Example of a tow fish with the pair of sidescan echosounder transducers; the portside element is visible ■

lar resolution of all sound imaging systems. Trying to stabilize such a narrow angle would overcharge the pitch and roll compensation of a surface vessel. These two requirements, the nearness to the bottom and the avoidance of pitch and roll by the towed fish outweigh the problem of deviations from the precise GPS-navigation of the tow ship due to tow cable dynamics. Such extremely narrow beamwidths of 0.2° , five to ten times narrower than those of deep-sea multibeam echosounders, are obtained with the highest frequencies used in underwater acoustics and thus the strongest absorption. Typical ranges at 500 kHz and beyond hardly exceed 100 m. Since the small scale resolution of sidescan systems can exceed the lateral resolution capability of multibeam sounders, a direct combination of both images by draping the 2D-sidescan image like an overlay on the 3D-relief sums the strengths of both (Sect. 5.2.3.3, 6.2.1).

4.3.4 Acoustic Astigmatism

A high *lateral resolution* of some tenths of a degree should correspond, when possible, to a similarly high *radial resolution*. In fact, the ideal sound image should consist of pixels which are no longer than they are broad. Otherwise we have a kind of acoustic “astigmatism”, also known as a special defect of sight. If the bandwidth of the transducer allows, the range resolution can be easily adjusted by the appropriate signal

pulse duration. Recalling the typical bandwidth of 10% of high efficiency transducers, which means 50 kHz in the case of the 500 kHz-example, the signal of 0.02 ms could resolve 1.5 cm. There is no ocean echosounder beam however, which can be made that narrow.

4.3.5 Focusing

For an objective comparison, we need to look at what the beamwidth really means in terms of stripe width at the sea floor. At 100 m distance the 0.2° -beam opens already to 35 cm. In relation to a pulse length of only 1.5 cm this would be a very strong astigmatism indeed. But even that is still oversimplified. The reality is worse, if we just think in terms of simple geometry. We should not forget that the size of the line array source, i.e. its length required for the 0.2° beamwidth at 500 kHz, is already 50 cm, which must be added to the 35 cm, according to the beam angle. This demonstrates convincingly that the simple searchlight geometry would give away what is known from optics as *focusing*. In fact, it is possible – and necessary – to simulate a zoom lens to achieve a convergent beam: a variable *gliding focus* (Image 4.3.5-1).

Fortunately this is possible by treating the line array as a *phased array* by electronically steering the phase of all individual transducer elements of the array. In the same way as steering the directions of the multibeam echosounder beams, the *phase front* has to be shaped. By appropriately shaped delays of the central element signals vis-à-vis the outer ones, a good approximation of a circle arc phase front can be

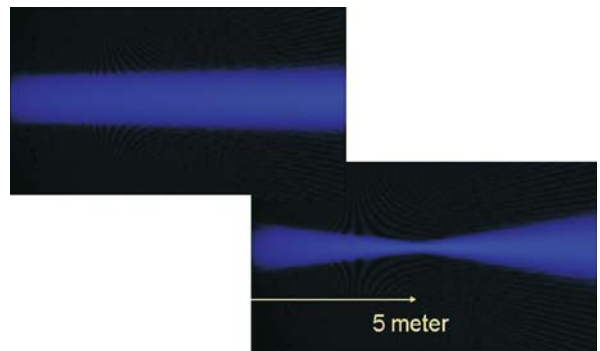


Image 4.3.5-1.
Scheme of focusing ■

formed. The center of the circle is the focus we want to achieve. Rapid tuning of the radius of the circle by pre-formed sets of phase delays forces the focus to move towards the transducer with the speed of sound, time parallel to the incoming echoes. Then every range unit, called bin, will be focused best. To do that, the computer is challenged hardly less than with the multi-beam-forming of the fan echosounder. The difference between a focused and unfocussed image is demonstrated with a 200-kHz experimental system (Image 4.3.5-2). Since recently the autofocus beamforming has also been achieved for high frequency multi-beam systems of nearly 500 kHz (Sect. 7.3). Multi-autofocus beamforming requires as many times the real-time computing effort as the number of beams compared to a monobeam sidescan system. Computer controlled focusing is considered the most significant progress in achieving real high resolution echosounder imaging in general.

Image 4.3.5-2. ►

Effect of focusing; sidescan image of sand ripples. The sound image visualizes a coastal seabed of 25 times 43 m. Sand ripple fields are surrounded by distributed single stones on fine sand. The ripple flanks produce stronger sound scattering than the plane sand surface which appears darker due to weaker scattering when irradiated under low grazing angles.

Upper image: unfocussed. The stones appear stretched according to the length of the sound transmitter of 2 m; the ripple structure is smeared to an average gray tone.

Lower image: focused. Two ripple fields are clearly recognizable. The small stones appear with much less “astigmatism”.

Experimental sidescan sonar EXMASS of FWG; frequency: 206 kHz, beamwidth: 0.2°, pulse length 125 μ s or 10 cm
Image ©: Wolfgang Jans, FWG, Kiel, Germany ■

4.3.6 Limits of Focusing Advantages

There are two essential ‘however’s’ we should mention. First: the quality of the focus which is in reality a constriction called *caustic*, depends on the size of the transducer array expressed in wavelengths, the larger the better. Second: the focussing is range limited. It works only as long as the phase differences between outer and inner transducer element signals are sufficient for the necessary cancellation by interference of echoes coming in off axis. In the optical analogy this range regime is known as *Fresnel near field*. The regime beyond that range is called *Fraunhofer far field*. The highest resolution achieved by multibeam focussing of 450 kHz-arrays (Sect. 7.3) resolves structure details of centimetres. These examples were taken from distances of hardly more than a few tens of meters, well inside the Fresnel range. Beyond, the astigmatism increases continuously



and inevitably. Deep sea sound imaging of the highest resolution within the limits of physics thus requires deep diving vehicles, remotely controlled or autonomous (Sect. 7.4).

Enlarging the focusing array more and more will eventually cease to improve the angular resolution. Random and patchy inhomogeneities of the water temperature due to incomplete turbulent mixing simulate slight bulges in the array which widens oblique sound beams slightly. The patchiness of the index of refraction is most pronounced in shallow waters within the upper tens of meters. However, the widening effect hardly amounts to more than a few tenths of a degree. Other environmental causes of distortion like incomplete compensation of random motion of the carrier vessel are usually stronger. Sound imaging of the highest, unimpaired resolution is thus to be expected from arrays mounted on deep diving autonomous vehicles, remote from the acoustical and mechanical impact of the sea surface.

4.3.7 Multi-Aspect Sounding

There are situations where a particular object on the sea floor can hardly be identified from an unfavorable direction of view of the sidescan sounder passing by. A typical example is a sea mine of cylindrical shape. When looking nearly in axial direction of the cylinder, the mine image may not differ conspicuously from a big stone, in particular if the mine had been laid in a stony field, a typical and frequent relic of glacial times. Instead of imaging the same scene again from another direction the visual aspect or line of sight may be turned – within certain limits – also by turning the phase front off axis, in the same way as the multibeam sounder beams are being tilted electronically. In other words: the irradiated stripe is then no longer oriented athwart the towed fish. It is also possible to look athwart tilted in several angles during one and the same course, thereby applying the glide focus from all aspects of view.

4.3.8 Long-Range Versions

Whereas the high frequency version of the towed sidescan sounder is optimum for shallow water areas of the continental shelf with an average depth of about 200 m,

the long-range exploration of the deep sea needs lower frequencies, which requires compromising the resolution. Perhaps the most famous of the deep-sea sidescan sounders called *Gloria* (Sect. 5.3.5) achieved a swath width of several tens of kilometers on both sides of the ship at 6.5 kHz, though with a modest range resolution of 50 m and the unavoidable lateral astigmatism. We will see examples of such surveys which permit decisions for selecting features for fan sounder close-ups and finally for taking bottom samples under TV-guidance. There are requirements for surveying regions of intermediate depths, in particular the continental slope. The mid frequency version of 30 kHz named *Tobi* with 0.5° beamwidth has been applied by several scientific institutions and contributed to the discovery of geodynamic features which occur predominantly in such steep slope areas (Sect. 5.3.1).

4.3.9 Conclusion

The sidescan echosounder is complementary to the multibeam echosounder, with the former being the tool of choice for imaging small scale morphology and sea floor texture and the latter for providing high resolution 3D-reliefs with the option of landscape depiction. Both supplement each other in various applications. They are often operated together during scientific expeditions and off-shore industry exploration and also for surveillance of sea lanes and off-shore constructions. Direct overlay superposition of both independent images combines highest small scale resolution and best relief documentation. Long range, low-frequency sidescan versions provide overviews for guiding the imagery of details. However, both methods visualize the *features of the surface of the sea floor* in shape and in kind. To reveal the *internal structure* requires the bottom penetrating imagery, the third type of the four sound imaging methods.

4.4 The Third Type of Sound Imaging: The Sediment-Penetrating Echosounder

Sediment echosounding, also named sub-bottom profiling, means paying a high price for penetration depth. The deeper we need to go, the lower the resolution of imaging. The reason is quite simple: The sound absorp-

tion in sediments is 3 000 times stronger than in sea water at 15 kHz, typical for deep-sea echosounding. This fact enforces much lower frequencies and thus longer wavelengths to penetrate the sediment. But: even if we turn the frequency drastically down to the frequently used 3 kHz, the achievable depth range will hardly exceed 100 m. Beyond that depth, the ever present background noise will win the battle against the echoes coming from the internal sediment layers. To reduce the penetration even further to the benefit of resolution is no acceptable option. It would sacrifice the possibility to reveal the key processes of sediment-formation and reshaping in many areas. These structures indicate causal relationships to local and remote changes of environmental conditions during the climate history of the oceans.

4.4.1

The Resolution Dilemma

The dilemma of imaging the *internal sediment structure* is thus the contradiction between the need for *high resolution* and *deep penetration*. The former requires short signals and therefore large frequency bandwidths. These are available with conventional transducers of high efficiency only at *high frequencies*. The latter requires *low frequencies* for low absorption. Moreover, the analysis of sediment stratification, representing the document of its history, requires both: *high vertical resolution* to discriminate the layers and *high horizontal resolution* to visualize significant, even dramatic lateral variations of the sediment structure. The necessary narrow beams are again the privilege of high frequency transducers, as long as we rely on conventional technology. In other words: the dilemma cannot be solved by conventional means.

4.4.2

The Parametric Echosounder

Surprisingly, there is indeed a non-conventional possibility to maintain the two decisive benefits of high frequency transducers, *large bandwidth* and *narrow beamwidth* when going to the indispensable low frequencies. It is a most unusual method for generating low frequencies, and it takes into account that the efficiency of the conversion of electric into acoustic energy is only one tenth of a percent and less. However,

the lower sound absorption at the lower frequencies outweighs by far the very poor acoustic output. The idea is to exploit the slightly *non-linear compressibility* of water to generate the ideal broad band, low frequency pencil beam without any otherwise necessary large size transducers.

4.4.3

Non-Linear Mixing

We know the non-linear compressibility from the slight increase of sound speed by high *static pressure* (Sect. 3.1.2). This increase is also effective at high *sound pressure*. It means that a very loud, pure tone, represented by an ideal sine function, will change its form towards a more saw-tooth-like shape during propagation. The reason is simply the higher sound speed towards the maxima of the sine function of the sound pressure: those high pressure parts gradually overtake those with lower pressure, which deforms the original sine curve correspondingly.

A saw-tooth curve does not represent a pure tone anymore but a composition of further frequency components. Though this effect is only weak it can be utilized technically by radiating *two* tones of different pitch and high intensity with the same high frequency transducer. Both tones are then superimposed within essentially the same beam. The most pronounced new frequencies that are generated within the water volume of high sound intensity are the *sum* of and the *difference* in the two tones. If for instance 30 and 33 kHz are applied as the primary frequencies, both of which cannot penetrate the bottom more than marginally, and their sum of 63 kHz even much less than that, their difference of 3 kHz is the frequency of choice for sediment penetration. But this low efficiency generation of low frequencies alone would be of little interest.

It is the fundamental advantage of the non-linear mixing that the generation of the difference frequency also applies for all the other frequencies within the bandwidth of the primary transducer, transmitting a short signal.

In other words: the 10% bandwidth at 30 kHz remains 3 kHz as the bandwidth of the secondary signal, then reaching from 1.5 to 4.5 kHz. This means 100% instead of 10% before!

This kind of non-linearity is not restricted to underwater sound. On the contrary: the effect is much stronger in the air. More familiar is a quite different example of drastic non-linearity which is not of acoustic origin: the croaking sound distortion by an over-saturated amplifier. The electric signal distorted within the electronic device contains frequencies which are not present in the original sound but come from non-linear mixing of the original components. The result depends on the characteristics of the non-linearity as the decisive *parameter*. Therefore the sediment echosounder working with the non-linearity parameter of water is named *parametric echosounder*.

4.4.4 Advantage of Depth Resolution

The improvement in depth resolution by this frequency mixing procedure is impressive: The “secondary bandwidth” of 3 kHz enables a resolution of 25 cm instead of 2.5 m. The latter is the reality of depth resolution when radiating the 3 kHz signal *directly* by a conventional transducer with 10% bandwidth or 300 Hz. We will see image examples where conventional low frequency transducers have been carefully tuned to provide considerably more bandwidth than 10%, even comparable to the parametric bandwidth (Sect. 5.7.7), but the parametric concept remains superior because of the other inherent advantage, the narrow beam.

4.4.5 Advantage of Beamwidth

This second fundamental advantage of the parametric echosounder, its *narrow beam*, is comparable to the beamwidth of the primary source. Beamforming like this would require a conventional transducer ten times larger in the case of the example above. The parametric beam-forming principle is completely different. In fact, the process of generating the difference frequency takes place within the volume of high primary sound intensities, which is a narrow cone in front of the transducer around its axis. The volume elements along that cone radiate their difference frequency signals of course synchronously to the originating primary signals. That means: the secondary signals propagate along the transducer axis at sound speed as well.

4.4.6 End-Fire Array

Radiating elements along a straight line remind us of a line array such as applied for the multibeam echosounder or the sidescan echosounder. We recall the beam steering method of these line arrays by incremental phase shifts from element to element: the beam axis is then accordingly inclined (Sect. 4.2.5). Of course it is possible in the same way to steer the beam axis eventually into the direction of the line array itself, which is then named *end-fire array*. The instantaneous phase along the array necessarily propagates with the speed of sound. This is essentially what happens with the volume elements along the cone of non-linear mixing when radiating the low difference frequency: together they behave like a conventional end-fire array. Consequently the same relations regarding the beamwidth apply. The longer the mixing cone, the narrower the beam.

4.4.7 Array Length and Beamwidth Relations

The relation between array length and beamwidth differs from a line array which radiates athwart. To bisect its beamwidth the array length has to be *doubled*. In contrast, the end-fire array needs *four times* the length to achieve the same. However, there is no abrupt change from one beamforming relationship to the other but a smooth transition. The effective array length relevant for the width of a tilted beam of a conventional array is only the *sine of the tilt angle*, in other words, the *apparent length*, visible from the respective slant direction. We should keep that fact also in mind when comparing fan angles of fan echosounders: the width of a beam tilted 45° off axis is already widened by 30%. To avoid this drastic increase in beamwidth, the transducer units of conventional multibeam echosounders are inclined, forming a roof (Sect. 4.2.8).

Since the effective length of the mixing cone theoretically depends on the power of the primary radiator, the beamwidth of the parametric array will follow correspondingly. Practically, the parametric sounder will always be operated at maximum load, close to the cavitation threshold (Sect. 4.1.6) because the efficiency of the non-linear mixing is so small. This virtual end-fire beam should not be cut by the sea floor. The effective length of the mixing cone of the example mentioned is about 10 m which means 20 wavelengths or a beamwidth of about 5°.

4.4.8

The Receiving Mode

The non-linear mixing of course works only during the radiation mode because the high intensity of both components is necessary. The reception mode is therefore conventional: the transducer is operated far below its resonance with much less sensitivity and a wider beam. That means: the high angular resolution is the merit of the parametric transmission mode only.

4.4.9

Conventional Sediment Echosounders

There are tasks of sediment sounding where neither a high lateral nor a high radial resolution is indispensable. For instance discrimination between soft mud and the underlying hard substrate within a broad and shallow basin of the sea floor is such a task. Then the classical record of the echo onset will be sufficient. Profiling the depth of sediments covering sloping substrates is even easier with a poorer beam resolution. Here, the narrow beam of a parametric system would provide the best results only when appropriately inclined towards the slant floor. The low resolution sounder, receiving the echo onset would automatically record the slant distance of closest approach. Moreover the conventional sediment echosounder neither needs the high electric power of several kilowatts of the parametric sounder nor its sophisticated pitch and roll compensation, nor is the minimum distance to the sea floor as critical. The small, conventional low power “boomers” are therefore typically appropriate for small boats and very shallow, coastal waters and estuaries where young, rapid sedimentation needs monitoring. Accordingly, the parametric advantages can be partially maintained when the penetration depth and thus the low frequency requirements are less stringent. Then this unconventional sediment profiler can be more light-weight and also operated on small vessels (Sect. 7.2.2).

4.4.10

Seismic Sounding

Parametric echosounders normally don't reach deeper than a hundred meters. The depth regime below is considered the domain of seismics which is beyond the scope of this book. However, the recently discovered

huge methane-hydrate deposits on continental margins (Sect. 6.2.1) are often found about five hundred meters below the sediment surface where seismic imaging is indispensable. We should therefore briefly deal with the *sound wave* or *compressional wave* version of this method. As defined earlier shear waves will not be considered in this context.

4.4.11

The Source

In fact, within this framework, seismic sounding differs from mono-beam echosounding essentially by the much lower frequency regime of a hundred Hertz at most. This requires very high amplitudes of the sound source beyond the regime which can be covered by fragile LZT-ceramics. The typical omni-directional seismic sound source is a so-named *airgun* which works by sudden release of compressed air contained in a metal chamber of a few liters. The explosion-like expansion of the air volume causes a short shock and subsequent bubble oscillations. These produce the necessary low frequency sound signal pulse of high intensity, depending on the volume and pressure of the chamber which is filled again, several times a minute.

4.4.12

The Receiver

The receiving unit is a linear array of several hundred meters length, called *streamer*, which has thus to be towed behind the survey vessel. The average beam-width of this array of 10 to 20 wavelengths at 100 Hz is about 4°. As with all one dimensional linear arrays the system has its maximum sensitivity athwart the line but cannot discriminate whether the echo comes from directly below or from any slant direction. The elegant fan-sounder solution of crossing stripes of irradiation and echo reception is not possible for simple reasons of geometry: The ship width is of the order of one wavelength only. The sound source is therefore essentially non-directional and irradiates a large undefined area of the sea floor. However, it is possible to focus the long streamer to reduce the stripe width of echo reception. This is advantageous and even necessary since the methane deposits are found where the water depth is of the same order as the length of the streamer.

This sound image at seismic frequencies does not look very different from a conventional monobeam sediment echosounder image (Sect. 6.2.1). The lack of resolution of the former in lateral direction and the poor resolution of the latter in general require coping with the echo onset in lieu of dealing with well defined image pixels. However, sophisticated signal processing supports the interpretation of the seismic image, as we will see when dealing with the examples.

4.4.13 Conclusion

Nearly everything we know about the deep interior of the Earth and its structure we owe to the evaluation of very low frequency mechanical waves below 100 Hz and much less, far into infrasonics, called seismic waves. However, the depth regime of many sea sediments behaves benignly and permits the application of compressional waves or sound waves and thus those methods of acoustic exploration which are developed for frequencies within the lower kHz-regime with good spatial resolution. Sediment acoustics needs verification by coring and probing regarding mineralogy, chemistry, and fossils. But it can reveal on its own even very weak reflecting horizons and is peerless in verifying whether a core stratification is only a local peculiarity or a symptomatic regularity over an extended ocean region. Any lateral structure formation, which provides information on sedimentation and sediment motion and migration processes is the exclusive domain of sediment acoustics. The combination with high resolution multibeam echosounders for the acquisition of the outer morphology enables a kind of differential diagnosis (Sect. 5.3.2). This combined method is unique indeed in verifying or refuting hypotheses of processes which have shaped the sea floor by non-tectonic incidents or in superposition of them.

4.5

4.5 The Fourth Type of Sound Imaging: The Acoustic Doppler Current Profiler (ADCP)

The *acoustic Doppler current profiler (ADCP)* is the only remote sensing current meter based on echo sounding. We therefore need to discuss the basic facts

of resolution and range as we have done with the other three types of sound imaging, in the context of this introduction.

Due to the impossibility of genuine simultaneous acquisition of an ocean current field varying in time by an acoustic Doppler current profiler on a ship underway, the alternative *drifter concept* is discussed in the context of the ADCP-method, though the approach is fundamentally different. Both concepts are complementary to each other in some ways. The third acoustic method, based on the *tomographic* concept is outlined separately (Sect. 6.1.3).

4.5.1 The Principle of Acoustic Current Measurement

A well known special application of the Doppler effect is more feared than popular: the traffic speed control. Apart from working with sound instead of radar the principle of measuring ocean currents from a distance is the same. The cars traveling along a street when passing a radar beam are replaced by small particles in the sea, so to speak, plankton for instance, traveling together with the flow at the same speed when passing the echosounder beam. The oceanic application is more sophisticated however. The goal is not just the determination of the speed of encounter of a single target. The research vessel underway should record the *vertical profile* of the ocean current with its *speed and direction* as far as possible at any depth from the sea surface to the sea floor, the so called *current vector profile*.

4.5.2 The ADCP-Concept

Technically the ship-borne ADCP consists of at least three high frequency narrow beam echosounders which radiate downwards in different directions, transmitting at the same time and receiving their echo sequence coming in from the range sections of the irradiated cone of each beam (Image 4.5.2-1). The echo signal of each range or depth section is processed separately regarding the frequency, or the arrival time of the short pulse respectively, to determine the Doppler shift. What is the procedure for acquiring the *current vector profile* from such data?

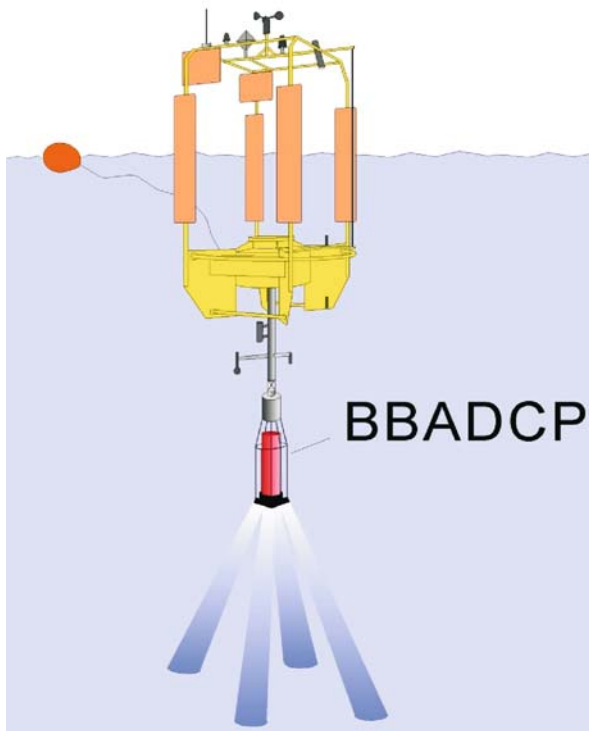


Image 4.5.2-1.

Schematic depiction of an acoustic Doppler current profiler (ADCP). When installed on a ship instead of on an autonomous, drifting buoy as shown, the transducer head with the four divergent looking high-frequency units is mounted flush near the ship's keel. BB means broad band; the Doppler shift is measured as arrival time offset of a very short pulse instead of by a frequency shift.

Image documentation: s. Sect. 6.1.2 ■

4.5.3 Speed Components and Doppler Shift

Anticipating the result of the formal relationship outlined in the Appendix we state:

The frequency shift of the echo generated by a scatterer moving towards the echosounder is twice the ratio of the speed of this motion and the speed of sound, times the frequency of the transmitted signal.

In fact, an observer moving together with the scatterer would measure only the *single* ratio of the two

speeds. This is just the situation when listening to an approaching police car with a siren. However, when the sound is radiated back to the echosounder by the moving scatterer, the same frequency shift happens again. The to and fro together therefore cause the duplication.

It is only the speed of encounter that determines the Doppler shift, independent of whether the echosounder were moved instead of the scatterer, or whether both moved against each other. More precisely, *the speed of encounter in this context means the component of the motion, which is either decreasing or increasing the net distance between sounder and scatterer.* Decreasing the distance increases the frequency and vice versa. We know that from the police car siren passing by: the pitch is high until the closest point of approach and low afterwards.

4.5.4 The Determination of the Current Vector

The most frequent configuration in the sea is a *nearly horizontal flow*, marked by scatterers, such as plankton for instance, and the ship traveling with the ADCP beams looking obliquely downward. Then the speed component of a particular scatterer pointing towards one of the sounders is the *horizontal speed reduced by the cosine of the inclination angle.* However, to measure the *vector of the current* requires the components in *all three dimensions.* For this purpose the complete ADCP consists of three beams and a fourth one for evaluation whether the assumption of horizontal current homogeneity is reasonable or not. They look into four different slant directions towards the sea floor, similar to the four edges of a pyramid (Sect. 6.1.2). Then the normal rectangular components can be easily computed applying sine and cosine. There is an obvious simplification involved: The vector components are not determined at the same place but the more they are apart from each other, the deeper the measurement goes at the diverging edges of the pyramid. According to experience, the horizontal variation of the prevailing ocean currents is not dramatic and the assumption of stationarity within the distance of the corresponding pyramid sections at the same depth is justified.

4.5.5 Slow Speeds

Ocean currents are comparatively slow, down to a few centimeters, up to one or two meters per second. This is much less than the speed of the ship and often also less than the speed of the orbiting flow under the sea waves. In other words: a very small “disturbance” of a large quantity has to be determined as the quantity of interest. We will see that compromising and optimizing is even more difficult than with the other three types of sound imaging, all of which deal with characteristics of shape and of related properties derived from the echo intensity.

4.5.6 Speed Resolution

Speed resolution by a Doppler profiler means *frequency resolution* of the backscattered signal. (The alternative of measuring the shift of arrival time of short signals is not discussed here.) We recall: a nearly infinitely long signal of a single tone has a spectrum of a single, nearly infinitely narrow line; the frequency and thus the speed are precisely defined. The reality is different. Neither is there a constant flow independent of time nor independent of depth. According to experience the *spatial* variability over the depth of an instantaneous vertical current profile is more critical than the *temporal* variability at the same place. The resolution requirements are therefore governed by the profile features. High resolution of frequency, requiring *long* signals and high resolution of depth requiring *short* signals are once more contradictory requirements.

To understand the necessity to compromise, we assume a sounding depth of 200 m, typical for continental shelf waters, and wish to acquire the current profile at 10 vertical sections. Then the sound signal needs 0.027 s to run 20 m to and fro, as we know from the depth resolution of an echosounder. This short time window is also the time interval for measuring the average of the current speed within the 20 m-section of the irradiated cone by analyzing the frequency shift of the backscattered sound. Since signal duration and width of the signal spectrum are inverse to each other, which we have also pointed out in the context of depth resolution (Sect. 3.6.6), we obtain 37 Hz. A frequency shift less than that cannot be recognized because this

represents the resolution unit in the dimension of frequency for this example. Doubling the section length by defining the current profile at only 5 sections would therefore permit discriminating a Doppler shift of only 18.5 Hz. To find out what minimum speed difference we then resolve we look again at the Doppler frequency-speed relation.

The quantity of this relation which we have not yet mentioned is the frequency of the sounder. In fact, the Doppler-shift increases proportionally to the echosounder frequency. The higher the frequency, the lower the speed of the current that can be measured. If we take for instance a frequency of 500 kHz as applied for high resolution sidescan echosounders we get a minimum current speed of 5.5 cm s^{-1} from the Doppler-relation outlined in Sect. 4.5.3, when we want 10 profile sections over a depth of 200 m. We should not forget however, that this minimum speed refers to the *speed of encounter*. The real horizontal minimum speed is larger, according to the slant angle of the sounder beam. Moreover, a profile resolution of 20 m may be insufficient already, as we will see when discussing the image examples (Sect. 6.1.2). On the other hand, a further increase in the frequency means higher sound absorption and is only possible when we reduce the depth range to be covered.

In other words: oceanic depths are not the regime of measuring very low speeds by ADCP. To reach 1 000 m for instance, which is only the depth of the continental slope, not of the deep sea of 4 000 m average, we can hardly take higher frequencies than 100 kHz. Sampling a current profile of that 1 000 m length by sections of 50 m we get a minimum speed of about 11 cm s^{-1} which is still a reasonable sensitivity. Again: high sensitivity for measuring low current speeds by a ship underway is penalized by coarse spatial sampling. We should admit that some improvement is possible by sophisticated signal processing but this requires a very good signal to noise ratio. This condition is, however, seldom encountered in the sea. The comments on the examples of ADCP-measurements presented in Sect. 6.1.2 deal in particular with the noise problem.

Beyond the conflict of range and resolution requirements, typical of all types of echosounders, there are additional and fundamental dilemmas when measuring the ocean current field. They are the result of a permanently moving scenario.

4.5.7

The First Dilemma: The Sampling Problem in a Varying Field

Imaging the three-dimensional current field of an ocean area is more problematic than compromising the dilemma between high sensitivity to measure very *slow motions* and sufficiently *high spatial resolution* to reveal the structure of the flow as deep as possible. In fact, it is *the fundamental dilemma of sampling a field of motion by a sounding vessel of finite speed*. This problem is literally of another dimension than imaging the “frozen” structures of the seabed, where the duration of the acquisition does not cause deterioration in the results.

A sensor moving at the speed of sound in the sea to achieve nearly simultaneous sampling over a long distance is a sound signal in itself. At sufficiently low frequencies large, even ocean-wide, distances can be covered by one way sound propagation ranges. Then the shift of the signal travel time is usually applied instead of the frequency shift. This is the principle of *ocean acoustic tomography*, pointed out in Sect. 6.1.3 in the context of results.

4.5.8

The Second Dilemma: Echosounders Cannot Measure Temperature

There is another fundamental problem regarding the underlying scientific question. Acoustic remote sensing of motion by echosounding can at most acquire the *transport and distribution of water masses*. The field of main interest however regarding processes of climate relevance is the *transport and distribution of heat energy* by the system of ocean currents. They are considered the conveyor belt of by far the largest amount of mobile thermal energy on Earth, and determine the climate of continents.

Unfortunately acoustic remote sensing of the temperature profile is not possible by echosounding. We recall the requirements of echoformation which are not fulfilled by the temperature stratification of the ocean (Sect. 3.4.2): Varying temperature does not produce echoes. However, it changes the signal travel time between separated and fixed source-receiver stations. Again, it is acoustic tomography that offers a solution of simultaneous acquisition of a large ocean section

and in this context it deals with the transport of heat (Sect. 6.1.3).

In principle, a large number of fixed vertical thermistor chains distributed over an ocean area could sample a three dimensional temperature field and its spatial variability. But it is unrealistic because of tremendous costs and logistic effort. Therefore the concept of mobile temperature profilers, towed by a ship, has been developed, which is of course restricted to two dimensional cross-sections and cannot overcome the variability with time. A string of many sensor packages containing *thermistors* together with *salinity sensors* is towed at a steep angle to sample a sufficient section of depth. This non-acoustic, direct way of acquiring a kind of thermal cross-section through an entire ocean is also a method of high resolution, both in vertical and horizontal direction, and in the dimension of temperature and salinity, though restricted to cover the upper few hundred meters. Together with an acoustic Doppler current profiler operated by the same ship, the cross-sections of flow and heat permit conclusions regarding the two dimensional structure of the net heat flow, though with substantial restrictions.

4.5.9

The Need for Combined Concepts

Apart from the restriction to two-dimensional data sets of a three-dimensional process of flow, the state of the flow field *changes* during a long survey cruise of the research vessel. Complicated gyros of various scales and water masses of different origin are superimposed on a net flow which may be described as a conveyor belt of heat, highly simplifying the complex oceanic reality (Sect. 6.1.1).

Altogether, there is neither a simple nor a single solution to cope with this multi-handicap. Actually the approach for acquiring at least the dominating processes of the complex reality is a combination of measuring concepts, consisting of ship-borne (Sect. 6.1.2), stationary tomographic (Sect. 6.1.3), and drifting multifunction sensor packages with data transmission, as well as location and tracking of the drifters by satellites or by acoustic triangulation (Sect. 6.1.1). The requirement for multi-tool and multi-concept approaches is true also for other fields of ocean research but nowhere else is the need so indisputable as for the research of heat flow within oceanic dimensions.

4.5.10 Acoustic Tracking

The acoustic contribution to ocean current acquisition deals with two fundamentally different concepts of current measurement. The first has already been discussed: the *local vector profile* is acquired by the Doppler shift of the backscattered sound coming in from the respective depth horizons. The technical term of the entirety of these *local speed measurements* is the *Eulerian* description of flow. The second concept is a field of submerged drifter buoys which go along with the current, providing the *space-time history of their track*. This description of flow by track history is called *Lagrangian*.

Technically the underwater tracking of the drifters happens by acoustic signals (Sect. 6.1.1). The method is inverse to the already mentioned triangulation with at least three remote receiving stations of an acoustic event occurring at an unspecified instant of time (Sect. 3.2.2). Here, only two stations with exactly known positions need to transmit signals at precise times and the drifters receive them, thus determining their actual distance from the stations by the time elapsed from transmission according to their internal clock. These two time intervals provide the lengths of the two sides of the determining triangle, with the third known as the transmitter distance from each other.

The drifter buoys are adjusted by buoyancy to a chosen set of depths or water density. Depending on the drifter concept they either store their data package, in particular temperature, salinity, and pressure for depth control on board until their recovery, or they transmit the data back to the stations by sound, or they climb up to the sea surface to transmit their data to satellites by ra-

dio-link. The result of this three-dimensional *Lagrangian* flow record is an image of complicated curls indicating the accompanying temperature as the most important quantity, together with the flow itself (Sect. 6.1.1).

4.5.11 Conclusion

The peerless advantage of the ADCP-concept is its nearly continuous acquisition of current vector profiles by a ship underway. Since the ship speed can be measured sufficiently accurately by satellite navigation, the determination of the much lower current speed is no longer handicapped by a large systematic error. The main short-coming of ADCP operated by ships is the restriction to two dimensions and less good resolution in deep water. Short range, high resolution ADCPs are essentially the only way to measure current induced small scale processes in turbid waters, for instance turbulent mixing. The resolution of ADCPs in depth, range and speed is usually higher than by drifters, which are indispensable for acquiring the current system of a large ocean area synoptically in all three dimensions. The drifter concept is the method of choice to study the influence of large scale sea floor formations on current fields regarding stability of heat flow against factors of other origin. Anticipating the results of acoustic ocean tomography (Sect. 6.1.3), this synoptic method is superior to a field of sensors and shipborne methods because it integrates over the given cross-section and thus acquires the net flow of current and heat but does not resolve horizontal variability and is two-dimensional. It is considered to be the method of choice for long term monitoring of changes of climate relevance at key cross-sections.

Part II

Applications of Acoustic Imaging the Ocean

Chapter 5 The Sea Floor – Natural Formations

Chapter 6 The Ocean Volume

Chapter 7 Man-Made Matter

The three subsequent Chap. 5–7 – the focus of the book – deal with the sea floor, the ocean volume and man-made matter. The structure of the chapters is inevitably a composite of feature-related subjects and geographic regions. The sections of 5.2, dealing with tectonics and of 5.3, dealing with passive continental margins, are mainly structured in the kind of features; Sections 5.4 to 5.7 are mainly regional. Chapter 6, the ocean volume, contains also the sections dealing with gas in the sea, which could of course belong to Chap. 5 as well. But the acoustic relations and similarities suggest the sea volume context. The man-made matter of Chap. 7 is certainly the most inhomogeneous with many overlaps and cross links. Human activities, their products and relics are – up to now – concentrated on shallow water areas of the continental shelves, though there is already deep water trawling and exploitation of hydrocarbon resources. High resolution deep water imaging, even more than shallow water imaging, needs autonomous underwater vehicles (AUV), a technology of major future potential. This is where the offshore industry has been the driving force of development. There are several sections throughout the chapters dealing with AUV but the last section of the book deals with this subject in particular.

The majority of the sound images are shown in perspective view depiction with simulated sunlight, shadows and color coding to quantify the depth scale. Vertical relief enhancement is usual to visualize topographic characteristics. This enhancement factor is indicated in the image caption when essential. There is no internationally accepted standard color code; the image authors have their individual preference for coding and image projection. For authenticity this has not been changed. The large variety of sea floor formations shown together with the individual treatment of the depiction is intentional. Both together visualize the state of the art of sound imaging. The technical image documentation is attached to the image caption which describes the features and mentions imaging peculiarities to demonstrate sound imaging as a diagnostic tool. The acoustic device is identified by manufacturer and type, with frequency and beamwidth which are the main characteristics for lateral resolution. Sediment echosounders are characterized in their vertical resolution mostly by the signal bandwidth, the inverse of the pulse duration. Due to the easy and actual internet access to all other kinds of technical features of echosounders and survey vessels mentioned, as well as to the institutions and companies involved, voluminous lists have been relinquished. For easy reading, references to literature have not been inserted in the texts, only the cross references. Instead, the entire literature index, structured into the corresponding sections has been placed at the end of the book; *off-shore industries do not normally publish their survey results.*

The Sea Floor – Natural Formations

5.1 Merger of Satellite Altimetry and Acoustic Bathymetry

5.2 Geodynamics of Tectonic Plates

5.3 Passive Continental Margins: Examples of the Prevailing Formations and Processes on the Shelf and of Utilization and Protection of Coastal Waters

5.4 Arctic Ocean

5.5 Antarctic Features

5.6 Mediterranean Sea Formations

5.7 Baltic Sea Formations

The sea floor is the classical subject of ocean acoustics and the sound images presented are among the most spectacular ones. The six globe images shown as the first series, a comprehensive blend of acoustic bathymetry and satellite altimetry, provide an overview of the large-scale environment of the areas for which high resolution sound images are shown as close-ups in the subsequent sections. They present major tectonic features of the deep ocean and also typical sediment formations of the continental shelves.

The six globe reliefs of 2 arc minutes resolution are available in addition on the attached CD for zooming. The CD provides also the complete, rotating globe of 5 arc minute resolution, instead of 2 min, to avoid slow downloading and the requirement for a large RAM capacity. Several particularly large and detailed sound images are also accessible on the CD, which further provides sound tracks, animations and 3D-reliefs that can be turned.



5.1 Merger of Satellite Altimetry and Acoustic Bathymetry

Multibeam sound images of the deep-sea floor taken from surface vessels guided by satellite navigation resolve structures of 100 m and less (Sect. 4.2.3). Their quality appears similar to aerial photographs taken with a clear sky and they provide moreover the third dimension: the real relief. However, only a few percent of the sea floor are covered like that as yet. Most of the formations of the two thirds of the globe under water have been explored primarily by monobeam sounding lines along the tracks of ships, acquired through decades, denser near coasts and harbors, less dense in the open ocean and sparse to nearly non-existent in many remote areas of the world. Sea-floor maps relying exclusively on these inhomogeneous bathymetric data would vary correspondingly in their resolution or they would give much of the information away when the same standard grid is applied to map the world's oceans.

With this premise invaluable progress was made towards a more uniform globe coverage when the idea of imaging the ocean floor from space by radar was realized. Though microwaves penetrate the ocean only a few centimeters (Sect. 2.3), they can however acquire the relief of the sea surface, which is a kind of weak and coarse copy of the sea floor relief beneath (Sect. 2.7), revealing itself by slightly varying gravity. The ingenious idea was to utilize the gravity deformed sea surface and blend the very modest resolution of the sea floor relief, derived from the gravity anomaly relief, with genuine acoustic sounding where available. By improving both entirely independent imaging methods the resulting resolution is meanwhile 2 arc minutes or about 3 km worldwide, except for polar regions beyond reach of the satellite orbits. Here, the sea floor relief has been acquired purely by acoustics and in parts resolved even better. The globes seen from six sides shown hereafter are the result of the strategic merger named *ETOPO2*. They are at least sound images in part and, though the resolution of advanced multibeam sound images compared to their resolution corresponds to a modern digital camera of 5 000 000 pixels compared to only 5 000 pixels, our present knowledge of the large scale formations of the ocean floor is essentially based on this unique radar-sonar marriage. The fundamental facts of the non-acoustic part of sea floor imaging are therefore briefly outlined since both types of imagery are used also in this book to supplement each other.

The basic idea appears quite plausible: large elevations and valleys change the local gravity field which can be used to indicate the presence of such features from a distance. A seamount, for example, exerts a small but measurable gravitational pull on the water around it, creating a bump on the sea surface from decimeters up to meters in height. Such elevations are detectable by a satellite radar-altimeter, provided that the superimposed sea waves are averaged out and corrections for other spatial and temporal influences are made. Tides, currents, temperature and even air pressure also deform the sea surface. Finally, the large scale deviations of the real geoid from an exact sphere are taken as reference.

The resulting pattern of ocean surface topography, scanned by the orbiting altimeter thus provides insight into the shape of the sea floor. However, there are several factors that limit the resolution and the sensitivity of imaging the sea floor structure by satellite altimetry, which in fact is – and will remain – far behind the resolution of genuine acoustic bathymetry by present day multibeam technique. The first and dominant reason at present is the resolution of the orbiting radar. The satellite cannot discriminate deep-sea features smaller than the effective footprint size of the radar beam on the sea surface. In practice the accuracy of the travel time measurement corresponds to an uncertainty area of a few kilometers diameter at the surface. That helps to average out the small-scale sea-surface roughness due to wind and waves. However, the sea surface roughness produces travel time data scatter around the average values. The signal is thus superimposed by noise which hides small features. Noise limits the actual sensitivity of the altimetric method in the same way as with all detection methods, including acoustic echosounding (Sect. 3.6). In addition, the water column itself also limits the resolution. The deeper the water, the more the details of the sea floor relief are averaged out at the sea surface, deformed by the gravity anomaly. Moreover, there is no general conversion model between altimetry and bathymetry. Local variations in the density of the sea floor can produce gravity anomalies mimicking those produced by seamounts for instance. Sediments pose a special problem for satellite-“bathymetry”. Because the basalt of the ocean crust is denser than typical sediments, a buried seamount or the floor of a sediment filled trench will still show up in the gravitational field.

The final global *ETOPO2*-maps of the sea floor are a weighted blending of satellite radar altimetry and ship-borne acoustic bathymetry. The merger permits com-

binning the strengths of the two independent concepts. Satellite altimetry enables the coverage of remote areas with sparse or no bathymetric data and the present bathymetric data volume improves the spatial resolution from about 10 km of pure altimetry to the mentioned grid of about 3 km. And this is only the present state of global mapping. In some areas such as the Mediterranean (Sect. 5.6), deep water acoustic bathymetry with a possible resolution of 3 arc seconds or a grid of 100 m will eventually replace the present 1-km grid of the complete Mediterranean relief, based essentially on comparatively dense conventional echosounding.

To sum up: Satellite mapping with its uniform global coverage has provided the first view of the ocean floor structures in many remote areas of the Earth. Unknown sea floor features discovered and localized by rapid, though coarse satellite mapping are a way of

guiding the slow but precise ship-borne bathymetry, which is becoming more and more indispensable. The sections to follow on various applications of sound imaging will demonstrate that only multibeam technology can provide images of aerial photographic quality of the real sea floor relief. Detailed bathymetry is essential for understanding the fundamental tectonic processes of the Earth's lithosphere with rise of new sea floor, its subduction and resulting continental shift. High resolution bathymetry reveals the submarine transport routes and deposits of sediment masses and the role of the sea floor relief regarding the transport of water masses in the ocean: currents and tides are controlled by the overall shapes of the ocean basins as well as by ocean ridges, plateaus, margin profiles, troughs and seamount clusters, all of which are also habitats of marine life of a still widely unknown variety and distribution.

Box 5.1-1. Satellite altimetry

According to the laws of physics, the surface of the ocean is an *equipotential surface* of the Earth's gravity field. Basically this means that if one could place balls everywhere on the surface of the ocean, none of the balls would roll downhill because they are all on the same "level". To a first approximation, this equipotential surface of the Earth would be a sphere when waves, winds, tides and currents are ignored for the moment. However, because the Earth is rotating, the equipotential ocean surface is more nearly matched by an ellipsoid of revolution where the polar diameter is 43 km less than the equatorial diameter. While this ellipsoidal shape fits the Earth remarkably well, the actual ocean surface deviates by up to 100 m from this ideal ellipsoid. These bumps and dips in the ocean surface are caused by minute variations in the Earth's gravitational field. For example the extra gravitational attraction due to a massive mountain on the ocean floor attracts water toward it causing a local bump in the ocean surface; a typical undersea volcano is 2 000 m tall and has a radius of about 20 km. This bump cannot be seen with the naked eye because the slope of the ocean surface is very low. The tiny bumps and dips in the geoid height can be measured using a very accurate radar mounted on a satellite.

For example, the *Geosat* satellite was launched by the US Navy in 1985 to map the geoid height at a horizontal resolution of 10–15 km and a vertical accuracy of 3 cm. *Geosat* was placed in a nearly polar orbit to obtain high latitude coverage up to 72° latitude north and south. The satellite orbits the Earth 14.3 times per day, resulting in an ocean track speed of about 7 km per second. The Earth rotates beneath the fixed plane of the satellite orbit, so over a period of

1.5 years, the satellite maps the topography of the surface of the Earth with a ground track spacing of about 6 km.

Two very precise distance measurements must be made in order to establish the topography of the ocean surface to an accuracy of 3 cm. First, the height of the satellite above the ellipsoid h^* is measured by tracking the satellite from a globally-distributed network of lasers and/or Doppler stations. The trajectory and height of the satellite are further refined by using orbit dynamic calculations. Second, the height of the satellite above the closest ocean surface h is measured with a downward looking microwave radar on board the satellite, operating in a pulse-limited mode on a carrier frequency of 13 GHz where the ocean surface is a good reflector. The radar illuminates a rather large spot on the ocean surface about 45 km in diameter. A smaller effective footprint of a few km in diameter is achieved by forming a sharp radar pulse and accurately recording its two-way travel time. The footprint of the pulse must be large enough to average out the local irregularities in the surface due to ocean waves. The spherical wavefront of the pulse ensures that the altitude is measured to the closest ocean surface. A high repetition rate of 1 000 pulses per second is used to improve the signal to noise ratio, especially when the ocean surface is rough. Corrections to the travel time of the pulse are made for ionospheric and atmospheric delays and known tidal corrections are applied as well. The difference between the height above the ellipsoid and the local altitude above the ocean surface is approximately equal to the geoid height $N = h^* - h$.

Larry Mayer • Center of Coastal and Ocean Mapping, USA

Box 5.1-2. The General Bathymetric Chart of the Oceans (GEBCO)

As a result of the Seventh International Geographic Congress 1899 in Berlin, a “Commission on Sub-Oceanic Nomenclature and Preparation and Publication of a Bathymetric Map of the Oceans” was formed. The members of this commission, international highly respected oceanographers and geographers from seven countries worldwide, compiled and developed under the leadership and sponsoring of Prince Albert I from Monaco, based on approx. 20 000 soundings, the first edition of GEBCO, which was presented to the Eighth International Geographic Congress 1904 in Washington DC.

Driven by the rapid development of the sonar technique after the First World War and the distinct inquisitiveness about the sea-floor topography for scientific, hydrographic and maritime technical uses, sounding data were collected worldwide, and this led to four subsequent editions of GEBCO.

The fifth edition of GEBCO, published in 1984, was developed under the umbrella of the International Hydrographic Organization (IHO) and the International Oceanographic Commission (IOC). The compilation was performed by marine scientists and hydrographers, using all available soundings collected and archived by international research institutions and Hydrographic Offices. In areas with sparse data, the contouring was based on the compiler’s knowledge about morphotectonic processes on the sea floor.

Between 1988 and 1994 the contour lines, tracks and spot soundings of the fifth edition were digitized, and published in 1994 as the GEBCO Digital Atlas (GDA) in order to meet the needs of present day users in the digital world. The GDA was developed and is maintained by the British Oceanographic Data Center (BODC) under the monitoring of GEBCO’s Sub-Committee on Digital Bathymetry. The latest version of the GDA, the Centenary Edition (GDA CE), presented in 2003 at the celebration of GEBCO’s

centenary, comprises large regions with new bathymetric information, for example from multibeam surveys in the Indian and Arctic Oceans, and in the northern and southern Atlantic. The GDA CE comprises a one-arc-minute grid of global coverage, which was derived from contour lines, new multibeam data and soundings using GIS-based state-of-the-art modeling techniques.

GEBCO rules under the aegis of the IHO/IOC also the definition of the nomenclature and the terminology of undersea features of the world’s oceans. GEBCO’s standing Sub-Committee on Undersea Feature Names (SCUFN) is the international recognized authority for reviewing and approving names for submarine features, which were proposed by individuals. Today nearly 3 500 names of undersea features are documented in the SCUFN Gazetteer of Undersea Feature Names, which is serviced by the International Hydrographic Bureau in Monaco.

Bathymetry provides basic information for marine research and development. Thus it is indispensable for the future of our Earth to survey the world’s oceans with maximum resolution and accuracy. Considering that it would take more than 200 years ships time to complete a full-coverage survey of the world’s oceans with multibeam, a near-term development for GEBCO should focus on a meaningful combination of the GEBCO one-arc-min grid with existing “bathymetry from space” estimates, derived from satellite altimetry observations. This combination of remote sensing data and modern acoustic measurements will improve the knowledge about the invisible sea-floor morphology and topography, and consequently improve the image from the ocean floor.

Hans Werner Schenke · Alfred-Wegener-Institut für Polar- und Meeresforschung (AWI)

Imaging the ocean floor is exemplary for the role of scientific imaging in general: it is the improved visualization of the reality that has guided research, brought forth discoveries, and confirmed or refuted theoretical presumptions. This applies in particular to fields of high complexity like marine geo-science, exploring the specific and significantly different interacting processes of the vast variety of ocean areas.

5.1.1**5.1.1
Globes of the Sea Floor Relief**

The globe depictions of the sea floor relief are the most comprehensive demonstrators of the large scale features

of geodynamic processes with the tectonic plate margins as witnesses of their activities. The six globe images appear as if the ocean floor were laid bare with its large and conspicuous undersea formations. The globes are the spherical depictions by Jakobsson of a global data set named ETOPO2, derived from the merger of satellite altimetry data with acoustic bathymetry. The data set includes the famous map compiled by Smith and Sandwell between 72° S and 72° N, the maximum latitude of the satellite orbits. The authors incorporated all available bathymetry, that is all public, unclassified, digital sounding data in public national or international data centers, or provided privately by investigators. Even so, this is only about 3% of the world that is covered by

such data, and the coverage is moreover biased toward coastal areas, favorite harbors, and contains a modest selection of seamount and a few hundreds of kilometers of tectonic plate margins. The great majority of all open ocean areas are still unexplored.

The horizontal resolution achieved by the combination of the altimetric and bathymetric data has enabled a *global map of a grid of 2 arc minutes or about 3 km*. The vertical accuracy depends on the sea floor topography because the inevitable structure averaging clips narrow peaks and it is limited by the uncertainty about the density anomalies. It is thus important, even decisive, whether and where the modeled bathymetric relief is corrected by genuine echosounder data. The examples selected for comparison of sea floor cut-outs derived from gravity anomaly vis-à-vis high resolution acoustic multibeam bathymetry respectively (Sect. 5.1.2) are already adjusted for reference depths and show mainly the drastic difference in resolution.

In the North, beyond reach of the satellite orbits, the relief of the *Arctic Ocean* region up to the *North Pole* has been acquired solely by genuine bathymetric measurements, achieved despite the ice coverage handicap. The data of many contributors (Sect. 5.4.1), enabled a grid width of 2.5 km, a slightly better resolution than by ETOPO2. However, this does not mean that the Arctic Ocean is fully covered by echo sounding measurements. The reality is that this ocean is very heterogeneously sampled and in many areas depths for the grid with 2.5 km resolution had to be interpolated from nearby measurements.

In the south, beyond 72° southern latitude towards the *South Pole* the sea floor consists only of parts of the shelves of the *Weddell Sea* and the *Ross Sea* adjacent to the *Antarctic Continent*. Here the bathymetry has been provided also by echosounding and in parts by multibeam technology. But this high resolution coverage is more sporadic as yet and mainly concentrated on the Weddell Sea.

However, to expect global sea floor maps of high resolution by multibeam echosounding – supplemented by sediment penetrating acoustic imagery – in the near future appears more than optimistic based on the fleet of survey and research vessels owned by the nations. It would require an endeavor of the order of 250 ship years, even if the ships were working in coordinated international cooperation for such a mapping program exclusively and continuously around the clock. The transfer time as well as maintenance and other unavoidable interruptions are not even included. In

other words: the reality of sea floor reconnaissance and exploration is restricted at present to the acquisition of large scale formations by rapid but coarse satellite altimetry on one hand and of small to intermediate scale formations by slow but high resolution acoustic imaging on the other. In this context, the large scale features are the main guidance for selecting the sea areas where high resolution close-up imagery is necessary for revealing the processes in detail. Both fundamentally different ways are indispensable and mutual supplements to each other as diagnostic tools.

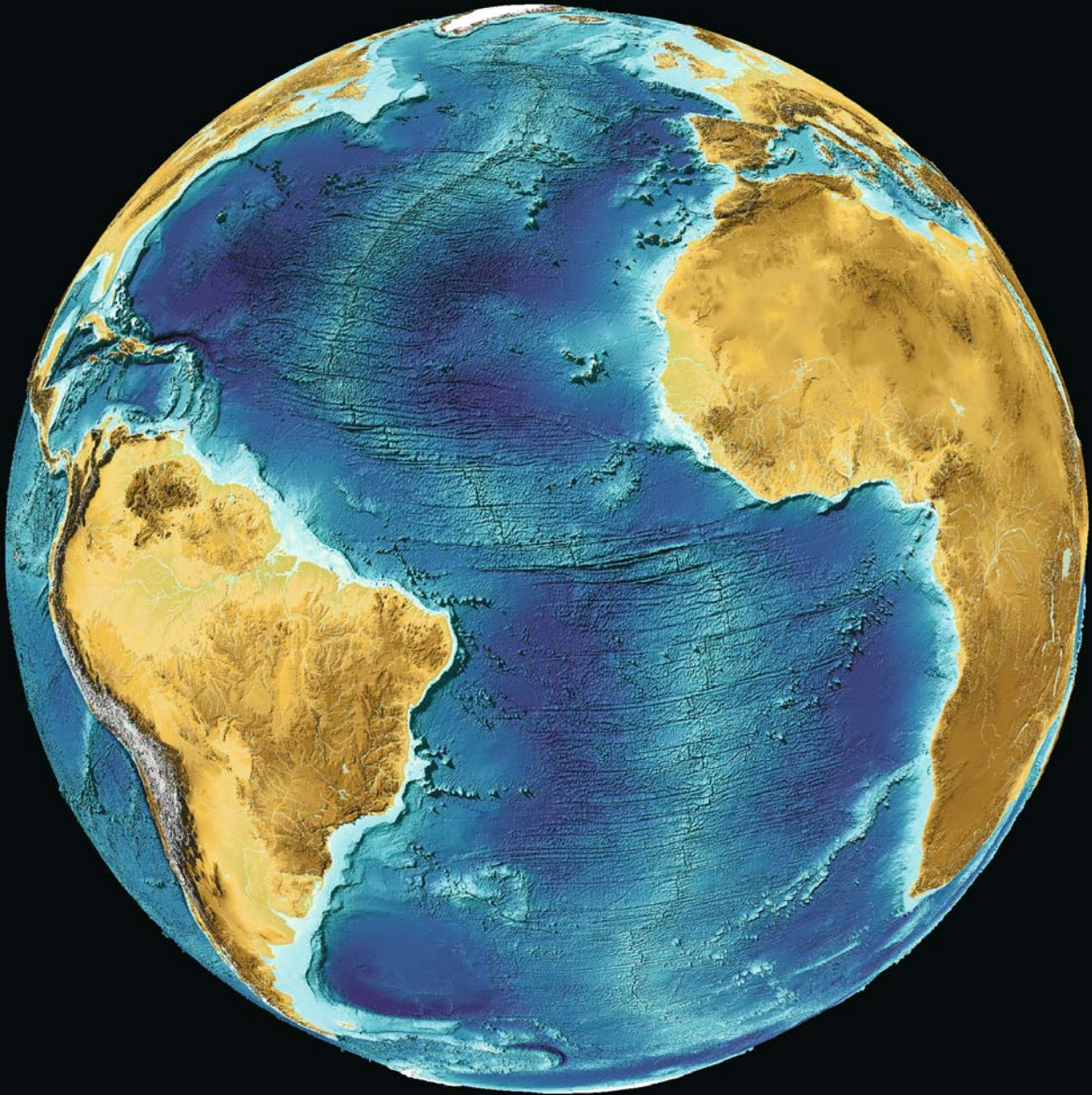
It should be mentioned however, that the technology for significantly more economic solutions to acoustic high resolution sea floor mapping is already available: Autonomous underwater vehicles (AUV) meandering in close distance to the sea floor (Sect. 7.4) have successfully proven to yield multibeam 3D-relief images of peerless quality and resolution. Once onboard power supply such as fuel cell technology has achieved operational maturity, a new era of exploring the hidden side of our planet may become reality.

The depiction of the sea floor and the continents of the six globes as *shaded, color coded relief* instead of *isobaths*, the frequently used lines of constant depth or height, is applied throughout the book. Thus the characteristic features of shape and texture are visualized in the way we are accustomed to see without losing information compared to isobath depictions. The relief is enhanced to make less spectacular formations also recognizable. This enhancement is optimized for the respective relief images shown in the book but is chosen constant as a factor of 5 for all the globe depictions of this series. The globe images need zooming to show details of the large scale textures and structures which cannot be resolved even by full page reproduction. *To provide such close-ups, these 6 images are stored on the CD attached to the book for zooming by the PC*. In addition, there is a less resolved globe of 5 arc minutes resolution on the CD that can be both zoomed and turned by the PC for choosing the optimum direction of view. The data-set of this turnable GEBCO5 globe is not the result of a merger of bathymetry and satellite altimetry as of the ETOPO2 images but is derived from digitized contour lines of depth charts, sound tracks, and spot soundings which are based on directly measured bathymetry (see Box 5.1-2).

The six images presented as globe projections contain an immense number of sea floor features which would

require a separate book to be explained. However, the spherical depictions are particularly suited to show the largest formations of the ocean floor up to global scales: the margins of the tectonic plates. They embody the fascinating and also terrifying processes which connect the

hot interior of the Earth with the biosphere of our planet. The image captions will thus concentrate on these large scale formations since the high resolution sound images dealing with these tectonic processes (Sect. 5.2) represent close-ups which reveal the processes in detail.



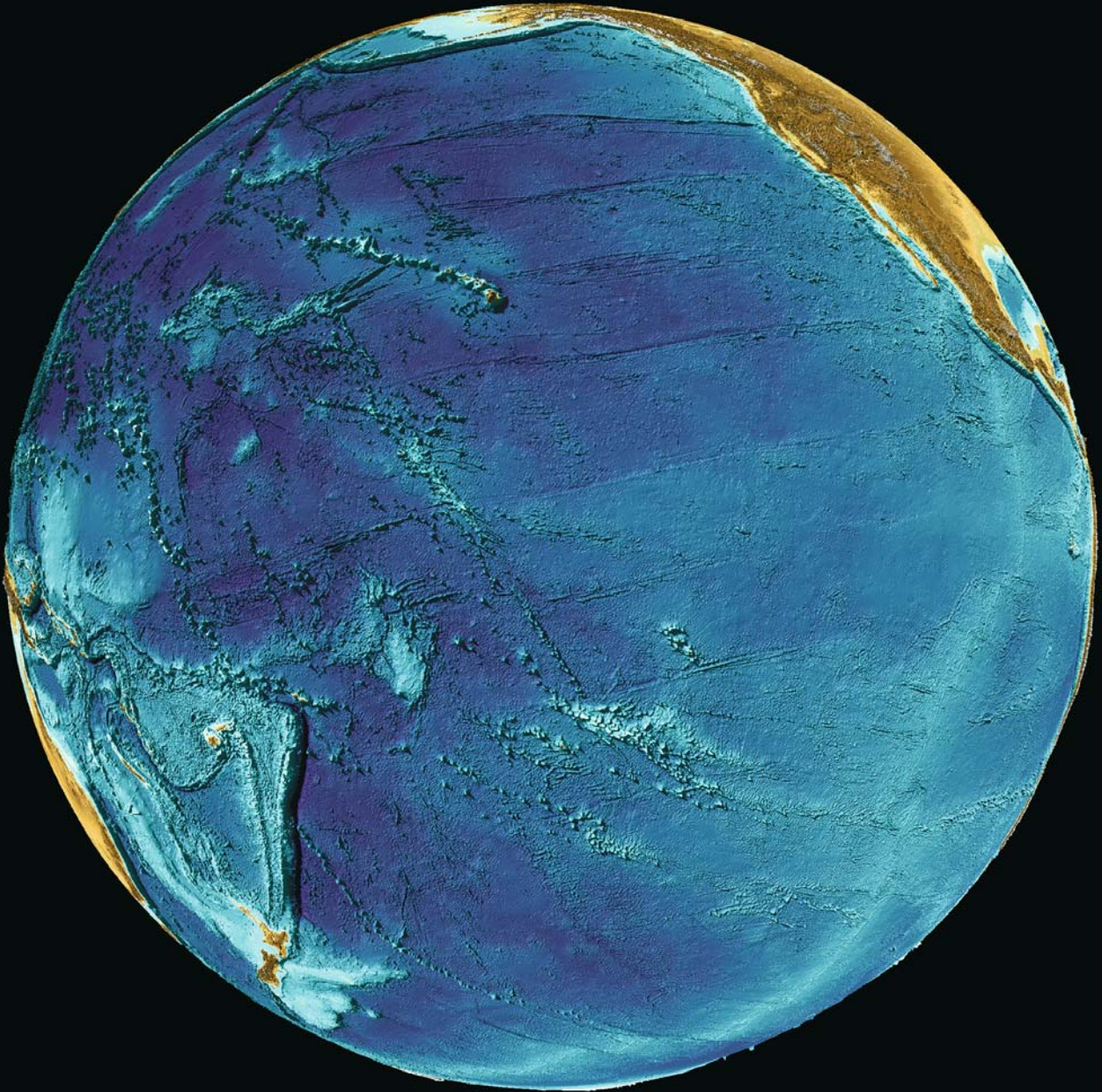
5.1.1.1 The Globe, Atlantic Ocean

◀ Image 5.1.1.1-1.

The Globe, Atlantic Ocean. The most conspicuous feature of the *Atlantic Ocean* is the *Mid-Atlantic Ridge (MAR)* formation (Sect. 5.2.3) of about half the circumference of the globe. It is the spreading zone of new sea floor of this ocean with the texture of dense and extremely long transform faults and large ridge axis offsets parallel to latitudes. The southern extension of the MAR was already discovered during the first acoustic survey of an ocean of 1925–1927 (Sect. 2.11). The S-form follows nearly the center line between the coasts of the *Americas* in the west and of *Africa* and *Europe* in the east indicating their continental break up which proceeds at the present speed of about a centimeter per year, one of the slowest among the spreading zones. The Mid-Atlantic Ridge is the only visible tectonic plate margin

of the entire Atlantic except two comparatively short trench arcs indicated dark blue. These are the subduction zones (Sect. 5.2.1, 5.2.2) of two small tectonic plates named *Caribbean* and *Scotia* which are adjacent to the South American Plate in the north and south respectively. (The tectonic plates of the globe are depicted in the map of Sect. 5.2.) The trench of the Scotia Plate is visible in the middle of the lower rim of the globe. The well known island groups of volcanic origin, in particular Cape Verde, Canaries, and Azores are shown together with their submarine seamounts.

Image ©: Martin Jakobsson, Center for Coastal and Ocean Mapping/Joint Hydrographic Center, University of New Hampshire ■



Box 5.1.1.2-1. Large Pacific Fracture Zones

Some 120 million years ago, the *Pacific Plate* was much smaller than it is today, separated by a spreading ridge to its east from the then largest tectonic plate on Earth, the *Farallon Plate*. The great Pacific fracture zones formed at transform faults, offsetting this spreading ridge. The Farallon Plate was being consumed along subduction zones on the west coast of North and South America at a rate faster than it was being produced at the Pacific-Farallon spreading ridge, gradually diminishing in size as it migrated eastwards. Around 35 million years ago the ridge arrived at the subduction zone near present-day California, forming the infamous strike-slip plate boundary we call the *San Andreas Fault* and breaking the Farallon Plate into two pieces. This breakup continued, the spreading centers underwent a period of reorganization, and the fragments related to the old Farallon Plate became the present-day *Juan de Fuca*, *Cocos* and *Nazca* Plates. Remains of the Farallon Plate, subducted tens of millions of years ago, are still detectable with seismic methods under North America.

The present-day fast spreading ridge of the Pacific, the *East Pacific Rise* (Sect. 5.2.4) is much younger. Its fracture zones go back only 10–20 million years.

Plate tectonics has had great explanatory power in the Earth sciences but it is still primarily a kinematic model. That is, it can tell us a great deal about how plates are moving, including the fact that fracture zones are the traces of transform faults that accommodate offsets in spreading ridges, but in itself the theory has little to say about the physical causes of these phenomena. Fracture zones sometimes seem to accommodate the shape of a rift that grew to become an ocean basin, as in the Atlantic where the Mid-Atlantic Ridge still mirrors the coastlines on either side of the basin. It is less clear in the Pacific, which has a more complex history of spreading ridges. One physical argument for the regular spacing of the Pacific fracture zones is that transform faults may relieve thermal stresses in the lithosphere, while others have argued that the origin of ridge segmentation lies in instabilities in the buoyant upwelling of the mantle.

Kelsey Jordahl • Monterey Bay Aquarium Research Institute

5.1.1.2 The Globe, *Pacific Central*

◀ Image 5.1.1.2-1.

The Globe, Pacific Central. This central view over the *Pacific* shows the “water side” of the globe framed by the contours of *East Asia* and the *Americas*. Here the *Hawaiian Island Chain* in the upper middle part is the most pronounced feature. It includes the much longer and older group of submarine seamounts along the chain towards the northwest and the adjacent *Emperor Seamount Chain* in the north in a different direction, indicating a change of the Pacific Plate shift (Sect. 5.2.4). Obviously most of the Pacific islands are grouped in chains, an indicator of hot spot processes (Sect. 5.2.8).

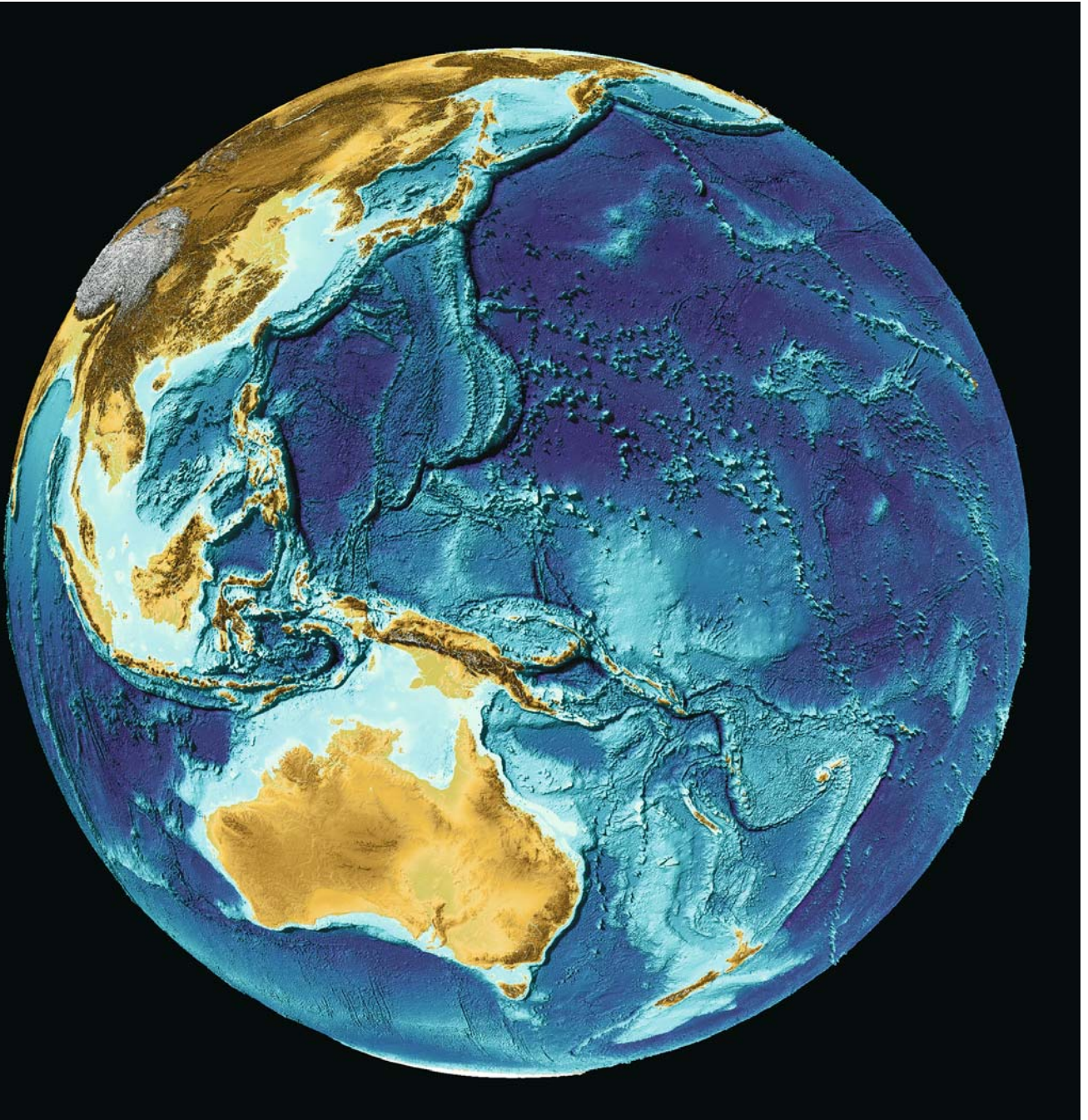
Nearly as conspicuous are the series of eight parallel and nearly equidistant fracture zones crossing most of the eastern Pacific, followed by the subduction trench of the Aleutians in Alaska on the upper rim of the image. These fracture zones have their origin from sea floor spreading and they are visible due to the thin sediment cover on the sea floor of the Pacific (Box 5.1.1.2).

The Aleutian Trench belongs to the northern part of the *Pacific Ring of Fire* (Sect. 5.2.1, 5.2.2) where most of the earthquakes and volcanism of the world originate. On the eastern side of this belt of active tectonic margins around the Pacific only the *Nicaragua Trench* is visible on the right hand side of the globe image. The long *Chile Trench* is already beyond the image rim but visible on the preceding image. The most pronounced trench feature to the lower left of this globe aspect is the *Kermadec Trench* indicated in dark blue. It is about

9 000 m deep and ends north of *New Zealand*. This trench is also the end of the Pacific ring of fire on the west side.

Surprisingly unspectacular is the relief of one of the most productive sources of new sea floor worldwide: the *East Pacific Rise* (EPR, Sect. 5.2.4). Starting inside the *Gulf of California* at the upper right side of the image, the EPR proceeds southward and then, near Antarctica, to the west as a broad light blue band without clear contours. The two branches of the EPR towards *Central-* and *South America* (map of Sect. 5.2) are hardly recognizable at all. The narrow line of the central ridge is only visible when zooming the image on the attached CD. However, the obvious difference in fabric and texture between the Atlantic and Pacific, such as the shape of the spreading ridges, the number of fracture zones, and the roughness of the sea floor, is real. It is not simulated by density anomalies recorded by the satellite altimetry, which is the main source of data of the globe images. Acoustic soundings from ships confirm this and it has been known since the late 1950s. The large area high resolution sound image of a section of the fast spreading *South Pacific Rise* reveals a multi-ridged texture indicating the periodic spreading process with many volcanic seamounts which are not resolved by the grid of this globe of about 3 km.

Image ©: Martin Jakobsson, Center for Coastal and Ocean Mapping/Joint Hydrographic Center, University of New Hampshire ■



◀ 5.1.1.3

The Globe, *Pacific Australia*

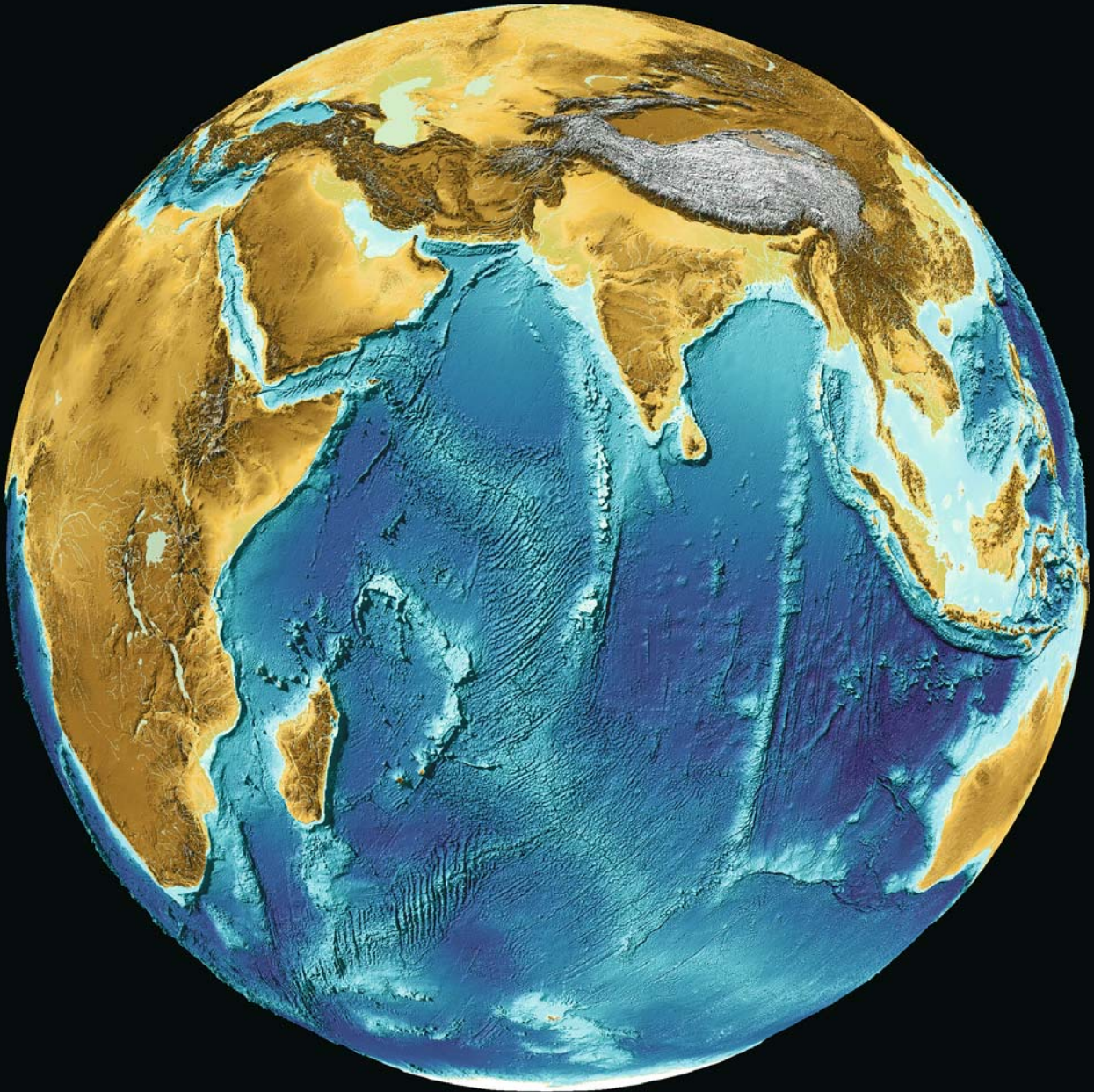
Image 5.1.1.3-1.

The Globe, *Pacific Australia*. This is doubtless the most dramatic view over the *Pacific Ring of Fire* with four tectonic plates in touch with each other at the north-western end of the mountain ridge of *New Guinea*. These are the *Pacific Plate*, the *Philippine Plate*, the *Eurasian Plate* and the *Indo-Australian Plate*. The conspicuous plate margins look like a complex agglomeration of deep trenches, easily identifiable by their dark blue color. It is a sequence of subduction zones (Sect. 5.2) which is visible on this globe view up to Alaska and is infamous with its concentration of earthquakes and volcanism. Slightly above the middle of the image is the *Marianas Trench* (Sect. 5.2.2) with the *Challenger Deep*, the deepest place on Earth at 11 000 m. The *Marianas Trench* is the prototype as it were, of the subduction of an oceanic plate under another oceanic plate. Obviously the overriding plate to the west is torn apart by the trench,

migrating out into the ocean, and has left several *back arc basins*. The *Marianas Trench* is the eastern margin of the *Philippine Plate*. Its western margin is among the “close seconds” in depth: the *Philippine Trench* at 10 500 m.

The island arc of *Melanesia* forms a nearly uninterrupted chain forming the *Salomon Islands*, the west *Fiji Islands* and *Tonga*. The *Tonga Trench*, with its 10 800 m is nearly as deep as the *Marianas*. Except the Arctic Ocean area, the continental shelves of East- and South-East Asia and North Australia together are largest on Earth with further large areas of shallow water surrounding the many hundreds of islands.

Image ©: Martin Jakobsson, Center for Coastal and Ocean Mapping/Joint Hydrographic Center, University of New Hampshire ■



5.1.1.4 The Globe, Indian Ocean

◀ Image 5.1.1.4-1.

The Globe, Indian Ocean. The *Indian Ocean*, much smaller in size than the *Pacific*, has a different tectonic plate structure (map of Sect. 5.2). Instead of the subduction trenches prevailing in the Pacific there is a pronounced sea floor spreading ridge system as the dominating plate margin pattern. The two most obvious ridges however are not the spreading ridges but the long and straight seamount chains *Chagos-Laccadive Ridge* in the middle and the *Ninety East Ridge* (which follows nearly exactly the name giving longitude) in the east of the Indian Ocean, comparable in length with the *Hawaiian Chain*. The genuine spreading ridge system has its origin in the *Red Sea*, passes the *Gulf of Aden* and then turns southward forming a long arc. This *mid-ocean ridge* (Sect. 5.2.3, 5.2.4) is similar in texture to the *Mid-Atlantic Ridge* with its large number of transform faults, but it subdivides into two branches of different character at the latitude of southern *Madagascar*. Only the western branch continues with its strong fault structure towards the *Atlantic* between the *African Plate* and the *Antarctic Plate*. The eastern branch, in contrast, is reminiscent of the *East Pacific Rise* in its inconspicuous fabric. It remains the plate margin of the *Indo-Australian Plate* but is now adjacent to the Antarctic Plate.

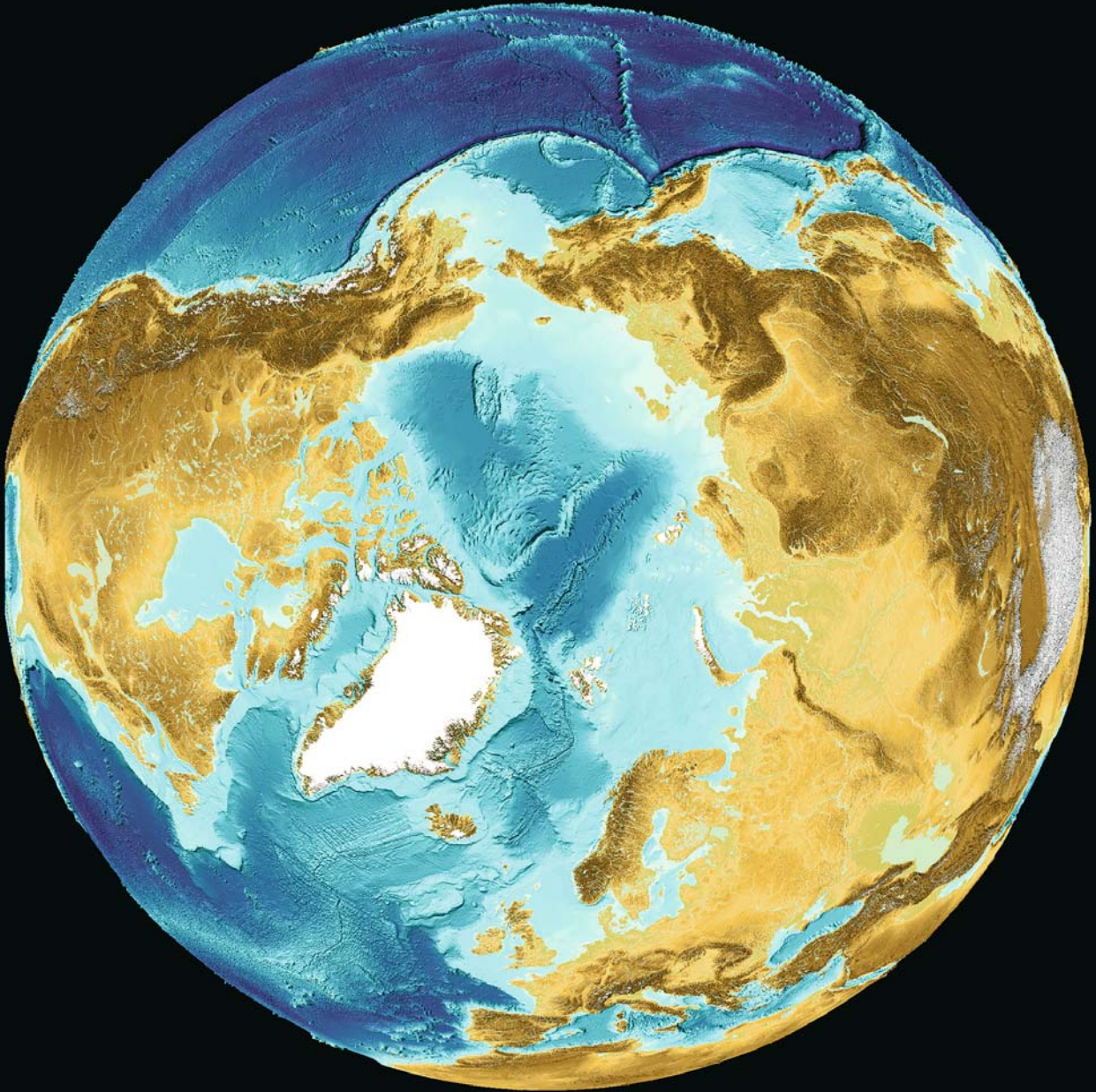
Though less conspicuous, there are also plate margins of the subduction type, acting as a sink of the sea floor (Sect. 5.2.1, 5.2.2). In this respect the Indian Ocean is strongly asymmetrical. Only the eastern side has a subduction zone, the margin between the *Indo-Australian Plate* and the *Eurasian Plate*. The deepest trench of this subduction zone is named *Java Trench* (Sect. 5.2.2.4), the long dark blue arc south-west and south of the Islands of *Sumatra*, *Java*, *Flores* and *Timor*. Its seemingly benign looking, also arc-shaped, continuation west of the tip of *Sumatra*, named *Sunda Trench* neighbors the arena of the origin of the most devastating Tsunami in history, having killed

presumably more than 300 000 people on coastal regions of the Indian Ocean on the 26th December 2004. The epicenter of the earthquake (Image 5.2.2.4-2) that released the sudden rise of a fault area comparable in size with the island of *Java* was in the trough adjacent to the Island of *Sumatra*.

The subduction zone, after having reached the east coast of the *Gulf of Bengal* (Sect. 5.3.2.4), proceeds on land (map of Sect. 5.2), along the southern margin of the *Himalayas* and ends near the region of the *Nanga Parbat* massif. The plate margin then changes its direction and type: the connection between the Himalayan subduction zone and the spreading zone curve in the *Gulf of Aden* is a transform fault margin type, also named strike slip fault (Sect. 5.2.5). On land it proceeds inconspicuously southward along the mountain contours between the Eurasian- and Indo-Australian Plate as before. On the sea floor however, the transform fault which is named *Owen Fracture Zone (OFZ)* is obvious by its relief, reminiscent of a chain of ridges, and it has changed its western plate neighbor: it is the small *Arabian Plate* now.

The most dramatic non-geodynamic process which covers an area larger than the Indian subcontinent is the *Ganges Delta* in the *Gulf of Bengal*. It is presumably the largest, extremely fast growing and most extended river delta worldwide (Sect. 5.3.2.4), far greater than the *Indus Delta* on the western side. The huge Bengal sediment deposit is the final station of the transport system from the *Himalayas*, and is a highly productive source area of sediment material through erosion and weathering.

Image ©: Martin Jakobsson, Center for Coastal and Ocean Mapping/Joint Hydrographic Center, University of New Hampshire ■



5.1.1.5

The Globe, Arctic Ocean

◀ Image 5.1.1.5-1.

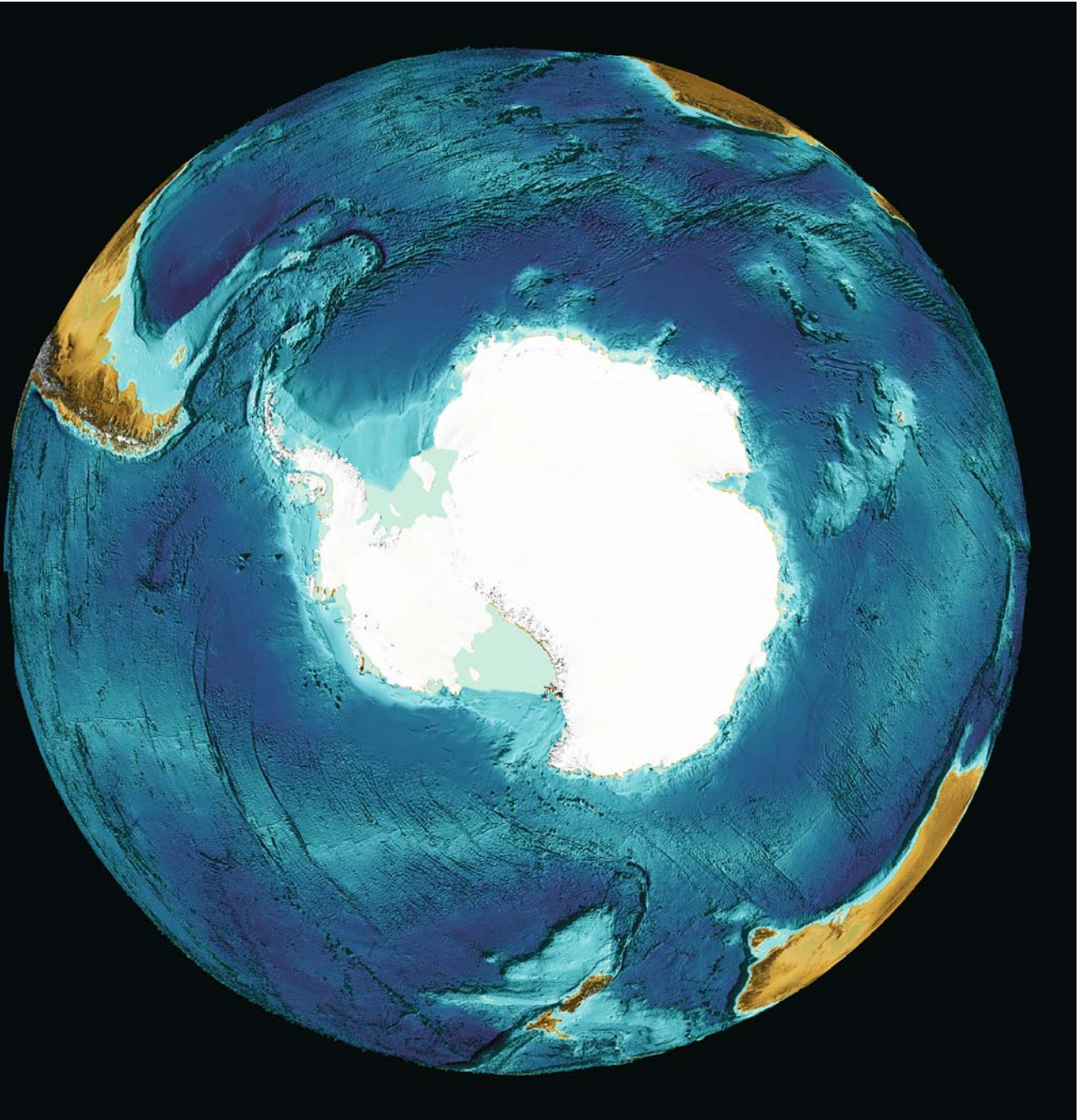
The Globe, Arctic Ocean. The *Arctic Ocean* floor of this *North Pole* centered view is laid bare in a double sense: both the ocean water volume is removed and also the nearly permanent ice cover. The sea ice of several meters thickness has prevented a comprehensive exploration for many decades and has made echosounding a challenging venture with icebreakers until today. The structure of the sea floor and the method of the relief map generation from a large variety of international bathymetric data sources are discussed in detail in the special Sect. 5.4.1.

Dealing with the margins of the tectonic plates – the main subject of comments of the globe depictions – the polar view reveals the essentials of this region more clearly than the usual map projection with the Equator as the center line can provide (Sect. 5.2). Right in the middle, there is perhaps the most remarkable phenomenon of the boundary between two large tectonic plates. The exploration of the basin structure of the *Atlantic Ocean* has confirmed on the one hand the earlier assumption of the existence of the *Mid-Atlantic Ridge (MAR)* up to the North pole area, but on the other hand that the spreading ridge appears to end there. There is no morphological evidence of a continuation of this feature that connects to the Pacific. The *North American Plate* and the *Eurasian Plate* thus appear interconnected without any visible fraction along several thousand kilometers. The polar section of the MAR passes the Arctic Ocean between the *Amundsen-* and *Nansen Basin*, about three degrees below the

North Pole and ends before the shelf break which delimits these basins. This northernmost MAR section is named *Gakkel Ridge*. Towards the *Atlantic* the ridge proceeds through the *Fram Strait* (Sect. 5.4.2) and approaches *Iceland* which is part of the MAR, the only section that towers above the sea surface. Iceland is one of the most active volcanic regions of our Planet with about two hundred active volcanoes. The transition between the furrowed northern MAR and Iceland is not clearly evident from the relief because the island is surrounded by a kind of shelf. The southern connection is remarkable due to the long *Reykjanes Ridge* without a central valley which reappears only at the latitude of *South Greenland*. The structure of the sea floor relief in these northern regions, in particular the ridges, was found to be decisive for the distribution of the current system, which plays a major role for the climate of Europe (Sect. 6.1.1).

The Pacific side of this globe view shows the complete sequence of the subduction zone arc trenches indicated dark blue at the *Alaska Peninsula* and the *Aleutian Islands* – the northern part of the *Pacific Ring of Fire* (Sect. 5.2.1). Also evident is the extension of the *Hawaiian Chain* (Sect. 5.2.8) to the north and the *Emperor Seamount Chain* which ends in the corner formed by the *Aleutian Trench* and the *Kamchatka Trench*.

Image ©: Martin Jakobsson, Center for Coastal and Ocean Mapping/Joint Hydrographic Center, University of New Hampshire ■



5.1.1.6

The Globe, Antarctica

◀ Image 5.1.1.6-1.

The Globe, Antarctica. This unusual view over the globe shows the *South Pole* at the center and the *Antarctic Continent* with its entire topography covered by ice. The view shows the seas around the sixth continent with the *Davis Sea* and the *Amundsen Sea* among them, and also the *Bellinghousen Sea* with the impact area of *Eltanin*, the largest meteorite collision on Earth known (Sect. 5.1.2). The two southernmost sea-floor areas are the shelves of the *Weddell Sea* (Sect. 5.5.1) framed in the west by the *Antarctic Peninsula* south of *Cape Horn* and the *Ross Sea* (Sect. 5.5.4) south of *New Zealand*. The Arctic waters, in particular the *Weddell Sea* are considered the most important origin of cold water which propagate along the bottom of the oceans.

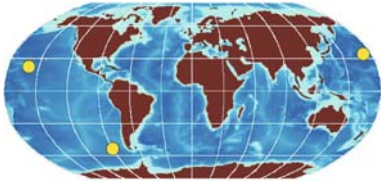
The Antarctic Continent is the center of the *Antarctic Plate* (Sect. 5.2), one of the seven large tectonic plates of the Earth's lithosphere. This globe depiction includes the margins of the *Antarctic Plate* completely. Nearly all of them are of the sea floor spreading ridge type which are discussed in Sect. 5.2.3, 5.2.4. We see the light blue band with its narrow ridge-line passing halfway between the *New Zealand Plateau* near the bottom of the globe image and the Antarctic margin. When following the ridge anticlockwise further, it proceeds south of *Australia* as the eastern branch of the spreading ridge of the *Indic Ocean*. Then it continues north of the lobster claw shaped *Kerguelen Plateau* where it now becomes the western branch of the *Indic Ocean's* spreading ridge. This ridge section which then passes halfway between South Africa and Antarctica is similar in texture to the *Mid-Atlantic Ridge*,

MAR which is the next point of ridge encounter. The southern end of the MAR is easily recognizable by its very extended transform faults. After this long tour we have passed only about half of the margins around the Antarctic Plate.

The next passage meets two exceptions from the spreading type margin: we see the dark blue arc halfway between the *Weddell Sea* and the globe horizon. This is one of the two – and short – subduction zones of the entire Atlantic (map of Sect. 5.2, Sect. 5.5.1), named *South Sandwich Trench*. A short section of its southern end is part of the margin ring around the Antarctic Plate. However, the connection between the merger with the MAR and this subduction zone is the second exception: it is a transform fault, also named strike slip fault where the plates are forced to slip against each other (Sect. 5.2.5). This type of margin which is usually the least conspicuous of the three types continues between the *Antarctic Peninsula* and *Cape Horn* of South America until it meets the southern side arm of the *East Pacific Rise* EPR west of southern Chile. With the long southern extension of the EPR the ring of margins around the Antarctic Plate is now full circle. It should be mentioned that the ocean around Antarctica which is essentially the sea area defined by its plate margins is named *Southern Ocean*. The official definition is the latitude of 60° south.

Image ©: Martin Jakobsson, Center for Coastal and Ocean Mapping/Joint Hydrographic Center, University of New Hampshire ■

5.1.2 High Resolution Bathymetry Versus Satellite Altimetry



The three examples selected for this demonstration are especially generated by the image authors

for this book. One example is from the *Eltanin Massif* considered to be part of the impact area of an asteroid in the *South Pacific*. The bathymetric relief of the massif and its central part are both compared with the altimetric ETOPO2 relief. The two other examples are from the *Hawaiian Chain*: the volcano island *Kauai* where the bathymetric relief is compared with the ETOPO2 relief and the *Daikakuji Seamount* at the corner between the *Hawaiian* and *Emperor Chains* compared with the ETOPO5 relief with 5 arc minutes resolution, the predecessor to ETOPO2 with only 2 arc minutes. It may be interesting for the reader to find out where systematic deviations between both independent methods of imaging occur, apart from the drastic difference in resolution.

5.1.2.1 *Daikakuji*, a Seamount on the *Hawaiian Emperor Chain Bend*

This seamount is a kind of cornerstone indicating the sharp bend of the hotspot chain in the *Pacific*: the

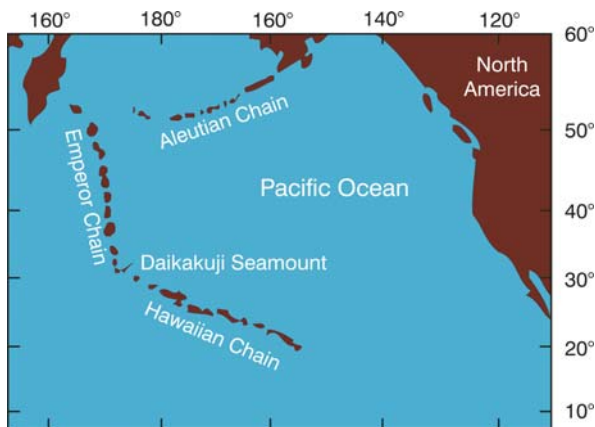


Image 5.1.2.1-1. Schematic map of the *Hawaiian Chain* and the *Emperor Chain* with *Daikakuji* at the bend

Image ©: FWG, Kiel ■

younger *Hawaiian Chain* and the older *Emperor Chain*. *Daikakuji* is a volcanic feature, as well as the other seamounts and islands of these chains, interconnected by the same hotspot origin (Sect. 5.2.8). The age of this seamount is a crucial indicator of the time of reorganization of Pacific Plate motion. According to the dating of dredged samples from *Daikakuji* this turn of motion occurred 43 million years ago. Since this change, the Pacific Plate has been moving to the northwest by 8–9 cm per year. The multibeam relief is compared with the older ETOPO5 altimetry relief of 5 arc minutes resolution.

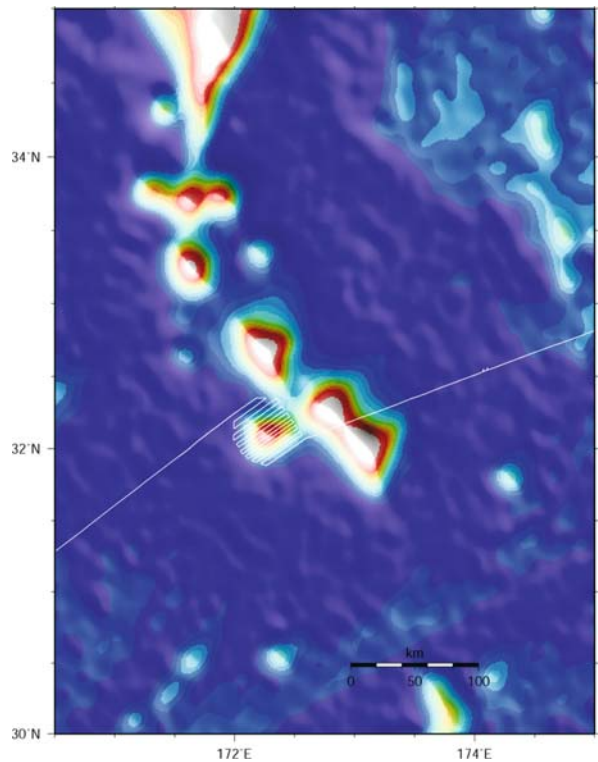


Image 5.1.2.1-2. Altimetric relief of the seamount chain bend around *Daikakuji*. The color-coded large scale relief of the bend area around *Daikakuji* is derived from the Smith and Sandwell global data set based on satellite altimetry (Sect. 5.1), the older ETOPO-version of a grid of 5 arc minutes or about 8 km. No features of the volcano cone are visualized. The meandering track of the fan-echosounding research vessel is indicated on the *Daikakuji*.

Image ©: Wilhelm Weinrebe, Geomar, Kiel, Germany; based on ETOPO5, CCOM, USA ■

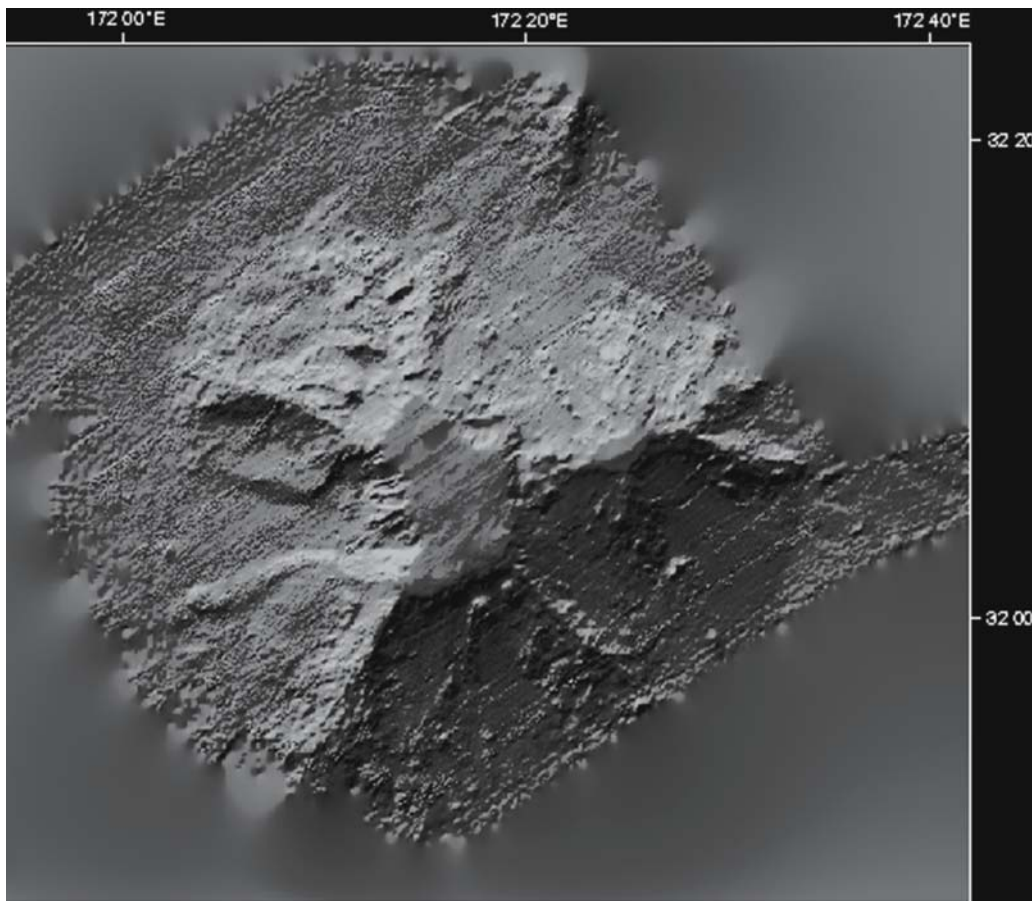


Image 5.1.2.1-3. The Daikakuji Seamount. Multibeam relief image. The shaded relief with the *Daikakuji* is a multibeam sound image of 100 m resolution at 5 000 m distance, the depth of the surrounding sea floor at this place. The steep seamount with approximately 30 km in diameter at the base emerges 4 000 m from the abyssal plane. The summit area at 1 000 m is resolved correspondingly better.

Due to the flat top of Daikakuji Seamount this formation is of a guyot-type, exposed above the sea level in the past which caused erosion and abrasion of the summit. The current depth is due to progressive subsidence of the oceanic plate as it cools with age. The cooling causes thickening of the plate that sinks deeper in the underlying asthenospheric mantle. In relation to the sea level the oceanic plate with Daikakuji subsided more than 1 000 m.

The edifice of Daikakuji Seamount deviates strongly from a cone shape and is more reminiscent to a pyramid with edge ribs and more or less plane flanks indicating heavy abrasion by sliding and massive slumping, possibly released by earthquakes in the tectonically active area. Regarding the steep slope of up to 27% of the seamount flank, earthquake-induced slides are not unusual.

The seemingly granulated small scale texture of the deep seafloor along the multibeam strips is mainly due to noise, superimposed on the weak echo signals. For demonstration, the noise induced roughness is not averaged out in this image. The effect is less pronounced on the flanks and upper parts of the seamount where the echo intensity and thus the signal to noise ratio S/N is correspondingly higher. The visible strip contours are produced by incomplete calibration of individual beams. The morphology of Daikakuji with its characteristic flank features is real and obvious, despite the perturbations.

Project: Research Cruise SO112

Research vessel: *RV Sonne*, Bremen, Germany

Multibeam system: ATLAS Elektronik, type: Hydrosweep; frequency: 15.5 kHz, beamwidth: 2.3°, 59 beams

Image ©: Wilhelm Weinrebe, IfM-Geomar, Kiel, Germany ■

5.1.2.2 Freeden Seamount and Eltanin Impact Area

The area in the southern Pacific was named after the American research vessel *Eltanin* which brought up sediment cores in the sixties from this site, indicating an anomaly of the Platinum metal Iridium, according to chemical analysis many years later. This anomaly is considered stringent circumstantial evidence of an *asteroid impact*, the only deep ocean event of this kind

known. Estimations speak of a size of several kilometers and date the event to two million years ago, much younger than the submarine mountain massif of this impact area. The location of the impact is still unknown since a crater is hardly to be expected; very probably the asteroid was vaporized before reaching the sea floor at 5 km depth. Perhaps a survey of the extension of the Iridium anomaly will bring light to the enigma and a comprehensive acoustic survey of the sea floor morphology may even retrieve some debris of the asteroid.

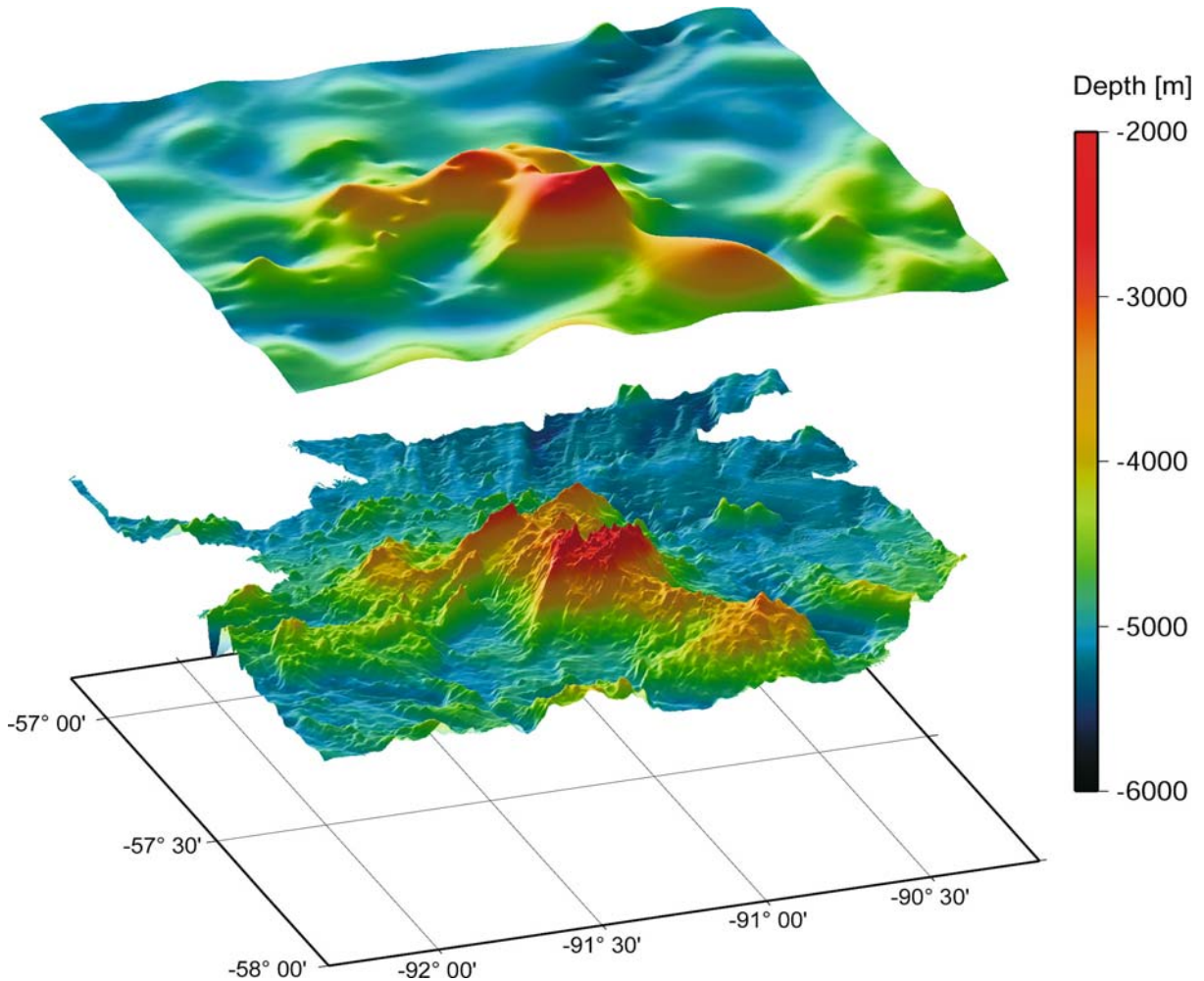


Image 5.1.2.2-1. Bottom: The Eltanin Massif. Multi beam image. The Eltanin massif, a singularity within a large abyssal plane, first surveyed in 1995 is itself of interest. The highest peak named *Freedan Seamount* at 57°35'40" S and 91°17'30" W, stands out 2 240 m below sea level and is surrounded by many further peaks of the central massif. Freedan towers nearly 3 000 m above the abyssal plane which is severely broken up by the massif ridges and various small basins in between. The Freedan Seamount, together with the many other less pronounced mounts around it, is of volcanic origin. The entire relief, although it is apparently irregular in shape and structure has nevertheless an overall orientation of the slopes in the direc-

tion south-west to north-east, which is the direction of the nearest sea floor spreading and fracture zone between the *Pacific* and the *Antarctic Plate*. In the north the *Freedden Seamount* shows an abrupt boundary, formed by a steep ridge, again in south-west to north-east orientation, visualizing the influence of tectonic plate reorganization.

The name *Freedden Seamount*, proposed by H. W. Schenke was appointed by the IOC-IHO/GEBCO Sub Committee on Undersea Feature Names (SCUFN). The oceanographer *Wilhelm von Freedden* (1822–1894) was the founder of the *Norddeutsche Seewarte* (predecessor to the *German Hydrographic Office*).

Project: Eltanin. First survey: 1995
 Research vessel: *RV Polarstern*, Germany
 Multibeam echosounder: ATLAS Hydrographics, type: DS-2; frequency: 15.5 kHz, beamwidth: 2.3°, number of beams: 59, fan width: 90°
 Height exaggeration factor: 10, simulated sunlight from northwest. See also attached CD
 Image ©: Ralf Krockner, Hans-Werner Schenke, AWI, Bremerhaven, Germany

Image 5.1.2.2-2.

Bottom: The central massif cut out of the *Eltanin*. Multibeam image. Here, the shape and orientation of the ridge leading to the summit area as well as the area adjacent to it with many smaller seamounts strewn over the large mountain formation are quite characteristic.

Image documentation:
 same as for Image 5.1.2.2-1,
 multibeam

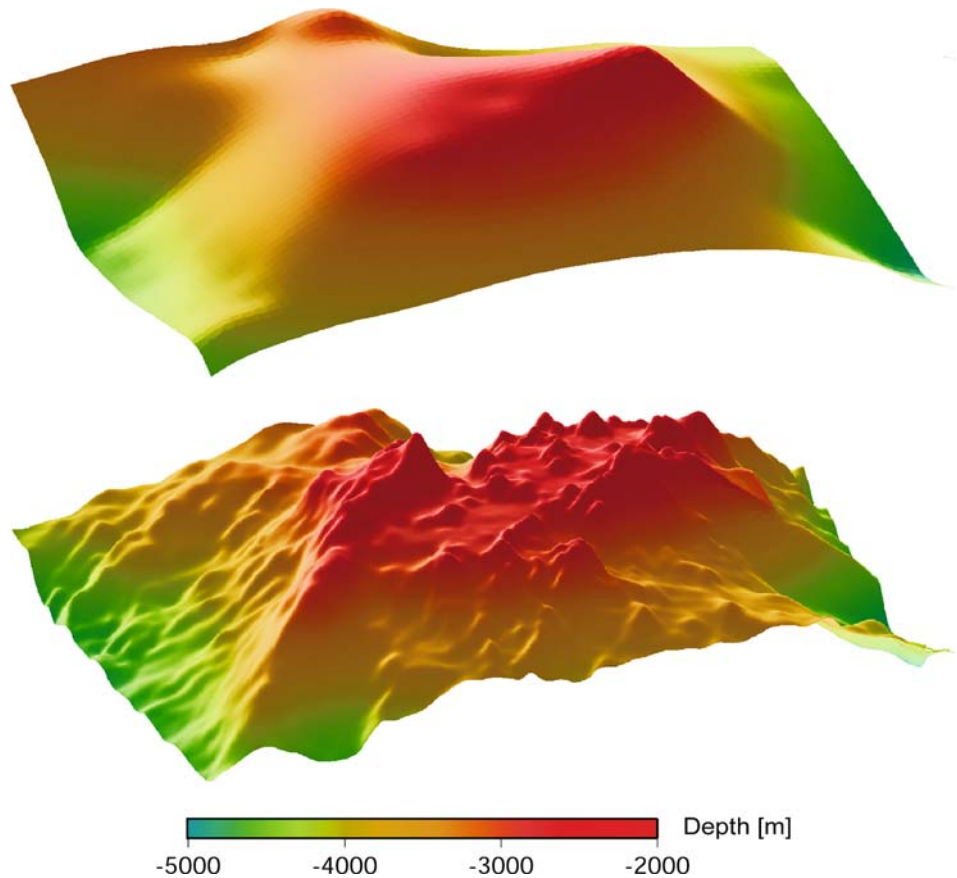
Top: Altimetric counterpart. The altimetric image is only seemingly similar. The top of the conspicuous bathymetric ridge is cut off here and the mountain chain branching off the main ridge in the bathymetry is taken as the leading formation by the altimetry. This deviation is not simply explainable by sediment coverage and demonstrates that one should be cautious with plausibility.

Image documentation:
 same as for Image 5.1.2.2-1,
 altimetry ■

Top: Same relief area as below but derived from satellite altimetry/gravity anomaly. The ETOPO2-data set of satellite altimetry merged with monobeam bathymetry where available (Sect. 5.1) shows more similarities with the corresponding acoustic relief than the other two examples for two main reasons: The relief is of a larger scale in the horizontal and thus more matched to the low altimetric resolution. Further: the relief is also larger in the vertical which means a more pronounced distribution of masses and thus a gravity relief that the altimetry can see. However, there are significant deviations beyond the different resolution: The complex bathymetric ridge structure is not only smoothed in the altimetry but deformed and the altimetry shows mounds in the right corner which don't show up at all in the bathymetry to mention only the obvious deviations.

The most conspicuous deviations between both imaging results shown in this book are found in the *Weddell Sea* of the *Antarctica* (Image pair 5.5.1-4) where low density sediment layers of several kilometer thickness hide the rugged structure below in the bathymetry but not in the altimetry.

Image ©: Ralf Krockner, AWI, Bremerhaven, Germany; from ETOPO2 data, CCOM, USA ■



5.1.2.3

The Sea Floor near the Volcano Island *Kauai, Hawaii*. Imaged by Gravimetric Anomaly from Satellite Altimetry and by Multibeam Bathymetry

The pair of images demonstrates the capability of advanced acoustic and non acoustic technologies for

imaging sea floor features. Both depict the same area off the south flank of the *Island of Kauai* in the *Hawaiian Islands*. The volcano of *Kauai* is the largest of the Hawaii Archipelago. The images are oblique views looking north. The water depths range from 31 to 3 120 m. The vertical exaggeration of the relief is factor 5.

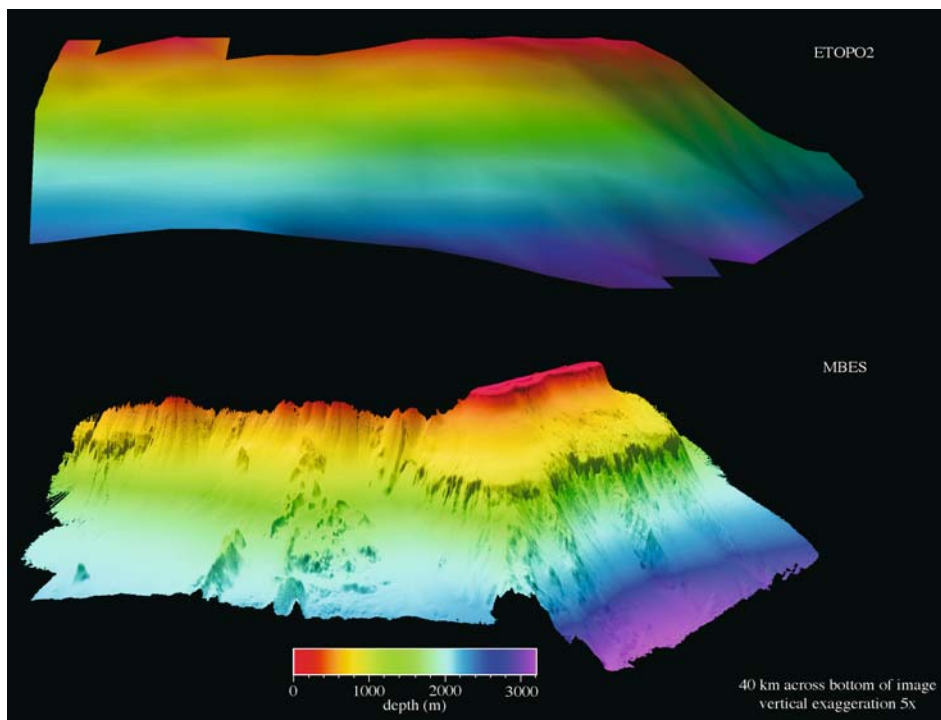


Image 5.1.2.3-1. Bottom: High resolution multibeam echo sounding from a surface vessel. The bottom image is from a multibeam echosounder of 20 m average resolution. This sound image provides about the highest resolution possible from a surface vessel. It shows the insular slope of the island of *Kauai* in the *Hawaiian Islands*. The modern reef complex is shown in red colors on the eastern side in water depths of less than 20 m. This reef complex sits upon an older one that is found at about the 800 m depth horizon indicated in yellow. The entire southern side of the insular slope depicted in the image has collapsed in a giant landslide called the *South Kauai Debris Avalanche*, leaving behind huge blocks that are scattered downslope. The landslide apparently carried away both the older and younger reef complexes on the south side.

Top: Corresponding cut out of the global map ETOPO2. The smooth relief with 2 arc minutes or about 3 km grid resolution (Image series 5.1.1) is derived from Satellite altimetry, merged with mono-beam bathymetric data where available (Sect. 5.1). It is of the same size as the multibeam image below and is obviously insufficient to reveal geodynamic processes of the dimensions shown. There is no hint at all in the image of the large avalanche, only a benign, unstructured slope area.

Center coordinates: 21°49' N, 159°27' W

Research vessel: *RV Ocean Alert*, USA, 1998

Multibeam echosounder: Kongsberg Simrad EM300;

30 kHz, beamwidth 1° and 2°, 135 beams, ship yaw compensation using subdivision of the receiving fan

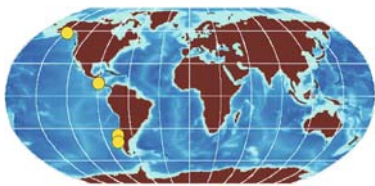
ETOPO2 mapping: NOAA, 2001, USA

Image ©: James V. Gardner, U.S. Geological Survey, Menlo Park, USA ■

5.2 Geodynamics of Tectonic Plates

Literally the deepest understanding of the processes that permanently change the outer shell of our planet is the theory of *plate tectonics*. This fundamental theory, based on measured and imaged facts of the last decades confirms the essentials of Alfred Wegener's visionary hypothesis of continental drift half a century later. It is certainly the most remarkable achievement of sound imaging the ocean in general to have been able to provide the necessary diagnostic tools to verify the theoretical statements. This chapter demonstrates the main processes of plate tectonics by means of high resolution multibeam sound images of the sea floor, which yield circumstantial evidence of these processes of unimaginable forces caused by the hot interior of the Earth. The schematic world map of the plates and their margins (s. next page) summarizes and simplifies the present status of plate tectonics.

5.2.1 Chile-Type Margins of Convergent Tectonic Plates



The margins around the Pacific Ocean are also named *Pacific Ring of Fire*, the infamous belt of dramatic tectonic activities with the majority of earthquakes and volcanism on Earth.

This belt with its tectonic subduction zones represents the major sink of ocean floor and drives most of the continental drift. The two sides of the Pacific differ in the type of plate subduction. In the west, the oceanic plate is subducted under another oceanic plate; in the east, the overriding plate is continental. Though the reality described hereafter and in the next Sect. 5.2.2 is less simple, it is obvious that the subduction trenches along the Americas are shallower with sediment fill from continental erosion and the western trenches are steeper and deeper.

The images shown visualize the characteristic formations and illustrate fundamental results of tectonic research. The subduction processes in the east are more complex and are discussed first. The trench off *Chile* gives the name to this type; in the west, it is the *Mariana Trench*, the deepest worldwide. The subsequent article

dealing with the Chile type of subduction is written for this book by experts of tectonic processes and ocean acoustic imagery, who investigated and documented the areas shown. The sea floor off the *Americas* and *Alaska* imaged by high resolution multibeam echosounders with a 100-m grid amounts to about 100 000 km², the largest tectonic scenario scanned and mapped by this grid spacing so far. The relief depictions in bird's eye view images, together with slant view close-ups are shaded by simulated sunlight to achieve the familiar landscape impression and color coded to provide the depth information. The image stripes produced by the multibeam wide angle fan are broad in deep water (violet: 5 000 m) but shrink accordingly when covering the shallow shelf edge (light blue: 200 m). The image pixel density of the high resolution sound images exceeds the land relief depiction by a factor of a hundred.

The high resolution sound image of the *Central Chile Trench* is compared with the corresponding cut out of the satellite altimetry data set ETOPO2 to demonstrate the difference of feature reconnaissance and resolution, supplementing the Sect. 5.1.2. The images of the southern, less deep Chile Trench complement features explained in the subsequent article.

Tectonic Processes at Subduction Zones

César R. Ranero · Wilhelm Weinrebe

GEOMAR Forschungszentrum für Marine Geowissenschaften und SFB 574, Christian-Albrechts-Universität zu Kiel, Wischhofstrasse 1–3, 24148 Kiel, Germany

Introduction

The outer rigid layer of the Earth that can support long-term stresses is the lithosphere. The lithosphere is about 200–250 km thick under continents and 60–80 km underneath much of the oceans (Gung et al. 2003). The lithosphere “floats” and moves over the hotter underlying asthenospheric mantle that deforms more readily to stresses. The Earth's lithosphere is segmented into a series of plates that move with respect to each other along plate boundaries where most of the world seismicity and volcanism takes place (Sect. 5.2). Convergence between lithospheric plates currently occurs along about 60 000 km of plate boundaries (Parsons 1981). About 40 000 km of the convergent plate boundaries are along

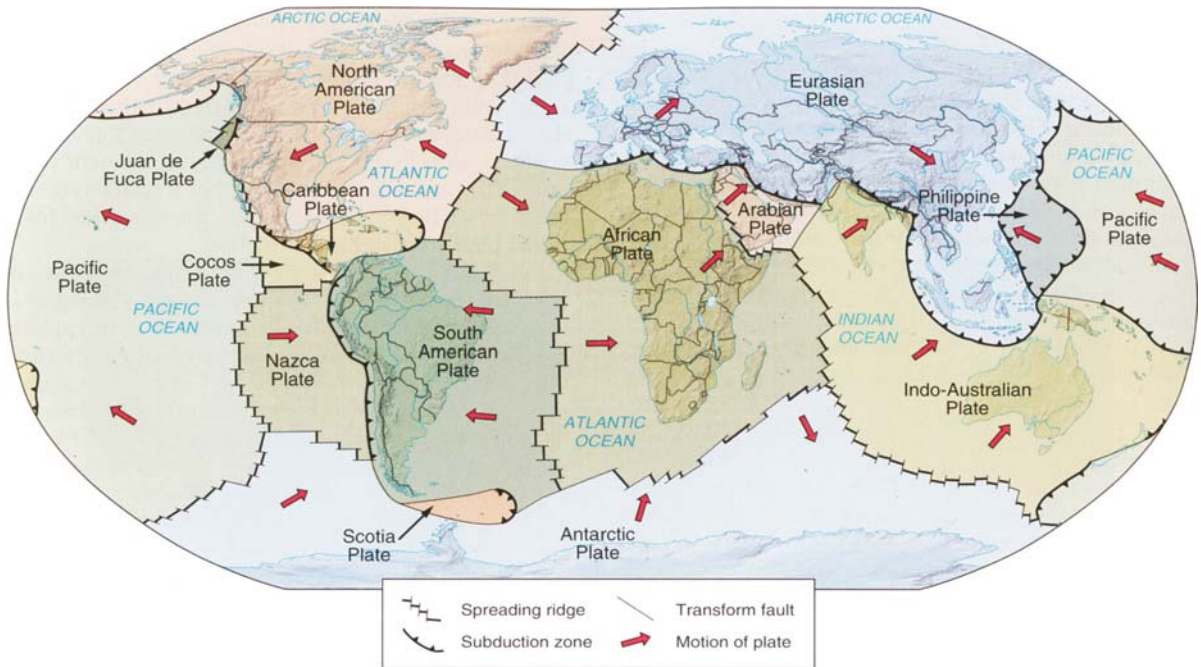


Image 5.2-1. Schematic world map of the plates and their margins. The map visualizes three types of margins between seven very large areas and seven areas of different size in between. These fourteen areas, subdividing the entire surface of our planet represent the famous *tectonic plates*, the strong outer shell of the Earth, called lithosphere, at most 250 km thick or 2% of the diameter of the globe. The plates move slowly relative to each other, at different speeds between less than a centimeter per year up to more than a decimeter, enforced by large scale thermodynamic convection processes of the Earth's mantle. During the motion, new oceanic sea floor is created by ascending magma at the *oceanic spreading ridges* – one of the three types of plate margins – whereas older sea floor is gradually removed from the solid Earth's surface. This takes place in the second type of plate margins, the *subduction zones*, most of these being continental- or island arc margins. There are also segments of plate margins which are neither divergence nor convergence zones. This third category is labeled *transform faults* or, more descriptively: *strike slip faults* where plates move along each other, exerting shear forces often with abrupt release of the accumulated tensions. The plate motions generate specific deformations of the sea floor in the margin zones, accompanied by the majority of all earthquakes and volcanism on Earth. The reconnaissance of these deformations, their analysis and attribution to the complex processes of plate tectonics was essentially enabled by advanced acoustic imaging.

The large plates enclose the six continents and adjacent oceans except one, which covers most of the Pacific Ocean. The smaller plates are oceanic except one, which covers the Arabian peninsula. There are fundamental differences however between the world's oceans and the nature of their plate margins. Most of the plate margins of the *Pacific* are either continental (Sect. 5.2.1) or island arc subduction zones (Sect. 5.2.2), or they are sea floor spreading ridges (Sect. 5.2.4). The *Atlantic* has the longest and nearly symmetrical mid-oceanic ridge (Sect. 5.2.3), extending around almost half of the globe but this ocean has no subduction zone of its own except two short arcs near the Caribbean and near Antarctica. The *Indian Ocean* has a mid-oceanic ridge nearly as symmetrical as the Atlantic but the ridge subdivides into two branches in the south at a point where three large continental plates spread away from each other. The Indian Ocean is bounded by a subduction zone only on the eastern side. Strike slip fault margins (Sect. 5.2.5) are found in all of these oceans. They are mostly shorter than the margins of convergence and divergence.

Simplifying drastically, one could say the subduction margins around the Pacific Ocean are the major sink of oceanic lithosphere. Since the Atlantic, the Southern Ocean around the Antarctica and the western Indian Ocean lack subduction zones of their own, the spreading of their sea floor must be compensated through a shift of entire continental blocks towards the Pacific. This continental drift as part of global plate tectonics is the confirmation of Wegener's visionary hypothesis.

Map ©: Exploring Earth; Davidson Reed Davis, Prentice Hall, Inc., 1997. Plate Tectonic Figure 6.1 (a)

Two errors of the map should be mentioned: The Philippine Plate is subducted under the Eurasian Plate at both depicted western subduction zones and with inverted subduction at the Manila Trench in between which is not depicted (Sect. 5.2.2, 5.2.9) ■

ocean margins where an oceanic plate underthrusts and subducts beneath continental or island arc lithosphere. Currently about 3 km² of oceanic lithosphere are subducted each year (Le Pichon et al. 1993) and eventually will be recycled into the sub-lithospheric mantle.

After the oceanic lithosphere is formed at a mid-ocean ridge (Sect. 5.2.2, 5.2.3) and drifts away it continuously loses heat, cools and thickens. The oceanic lithosphere is just a few km thick at the mid-ocean ridge, but the continuous heat loss implies that material from the weaker underlying asthenospheric mantle cools, becomes stronger and is attached to the base of the moving plate. As the oceanic plate moves towards a subduction zone, the heat loss normally causes the plate to become denser than continental or island-arc lithosphere. Due to its lower buoyancy the oceanic plate dives into the subduction zone underneath lighter continental or island-arc lithosphere. During convergence and subduction, the plates become greatly deformed and different processes lead to material and fluids being transferred at different depths along the plate boundary. When an oceanic plate approaches the subduction zone it bends forming a trench and breaking along great faults that cut tens of km into the crust and upper mantle.

During that bend-related faulting, large amounts of sea water percolate into the oceanic lithosphere leading to profound changes in the chemical composition and mechanical properties, the *rheology* of the oceanic plate. Other tectonic processes may cause transfer of material from the subducting oceanic plate to the upper overriding plate and vice versa. Material transfer from the oceanic plate to the upper plate leads to the growth of the continental crust through several processes. During underthrusting of the oceanic plate, the shallow portion of the sediment accumulated at a trench is stripped off and added to the frontal area of the overriding plate forming *accretionary prisms* (von Huene and Scholl 1991; Moore and Vrolijk 1992). As an oceanic plate subducts into the mantle whereby pressure and temperature increase, the lithosphere undergoes metamorphic changes and releases fluids into the overriding mantle triggering partial melt that leads to arc volcanism (Reymer and Schubert 1984). In addition, subduction processes may also involve the removal of material from the upper plate and transfer to the subducting plate, leading to *tectonic erosion* and thinning of the overriding plate (von Huene and Scholl 1991; Ranero and von Huene 2000). When a subduct-

ing oceanic plate contains anomalously thick crust formed by the magmatism of a hot spot (Sect. 5.2.8), it produces a great deformation of the upper plate.

The multibeam bathymetric data sets presented in this chapter illustrate those tectonic processes at several representative subduction zones. The high resolution bathymetry shows a detailed morphological map of active tectonic and erosional structures related to current subduction processes. The subduction zone of *Central America* has a highly faulted oceanic plate and a continental plate shaped by *tectonic erosion* processes. The subduction zone of *Central Chile* displays the rapid change from an active *accretionary prism* to *tectonic erosion* processes. These two areas also display the tectonic effect of the active subduction of an anomalously thick oceanic crust. The third example from the subduction zone off *Alaska* shows a large *accretionary prism* and also displays the tectonic effects caused by the recent subduction of a large block of thick oceanic crust.

Central America

The bathymetric map of offshore *Costa Rica* and *Nicaragua* (Image 5.2.1-1) displays a well defined narrow trench axis striking northwest-southeast changing in depth from about 1 500 m in the SE to about 5 500 m in the northwest. The oceanic plate exhibits a remarkable variability in morphology along the subduction zone. The lateral variability in oceanic plate morphology and depth are the result of the combination of magmatic and tectonic processes. The shallow oceanic plate in the SE is a portion of the *Cocos Ridge* that was formed about 14 million years ago by the interaction of magmatic processes at the mid-ocean ridge with the activity of the *Galapagos* hot spot creating a thick crust that causes the plate to be anomalously buoyant. The magmatism of the *Galapagos* hot spot formed the large volcanic constructions spotted through areas of the oceanic plate similar to the *Hawaiian Island* chain (Sect. 5.2.8). The volcanic constructions include conical seamounts and the *Quepos Plateau*, a large guyot that was exposed above sea level and currently has a flat top due to wave-surf erosion (Werner et al. 1999). Where the thick crust of *Cocos Ridge* is subducting (Segment 1 in Image 5.2.1-1), the plate bends only little due to the buoyancy of the lithosphere and the trench is shallow. However, to the northwest the plate bends more and flexure is partially relieved by faulting across the ocean trench slope.

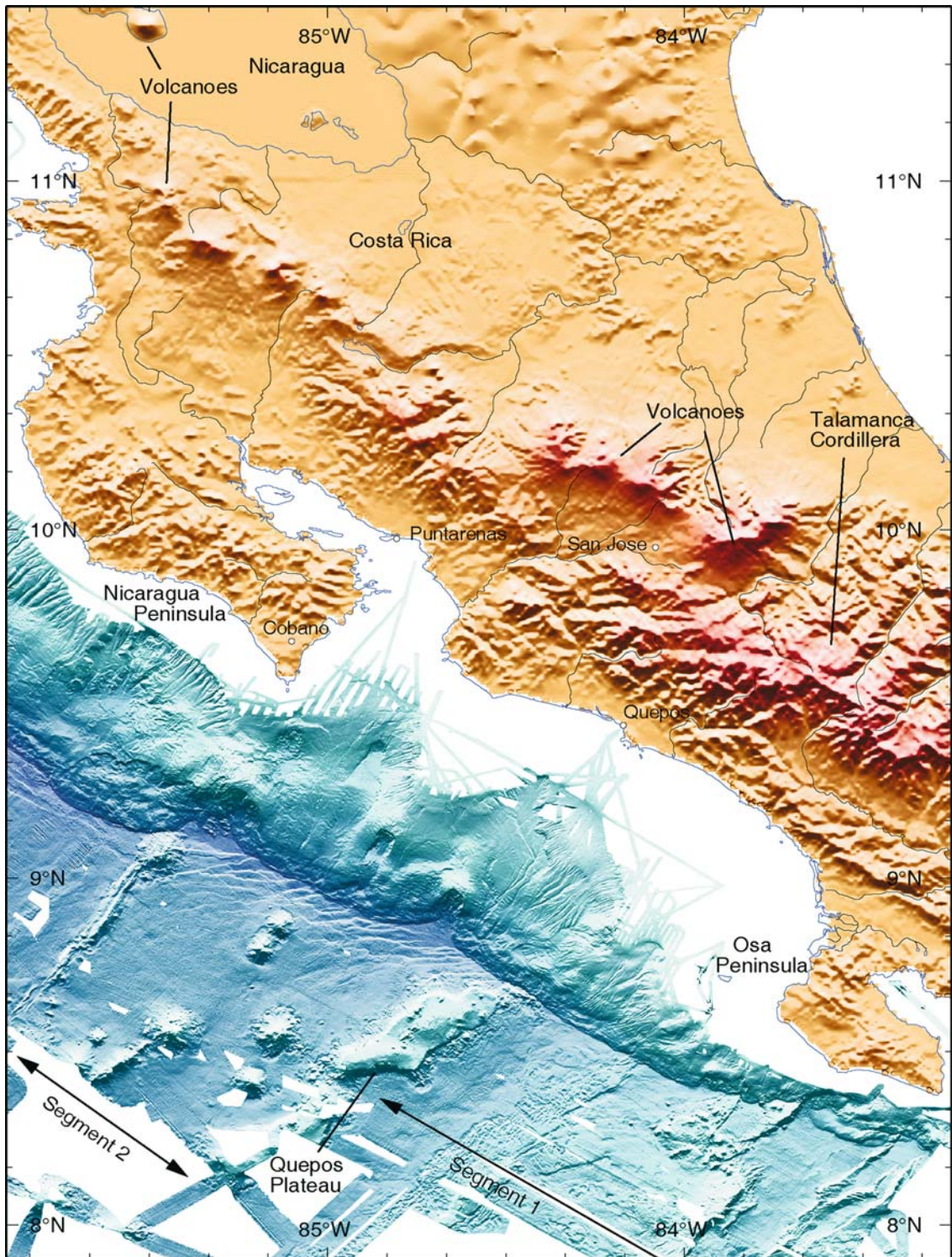


Image 5.2.1-1a. (see page 90)

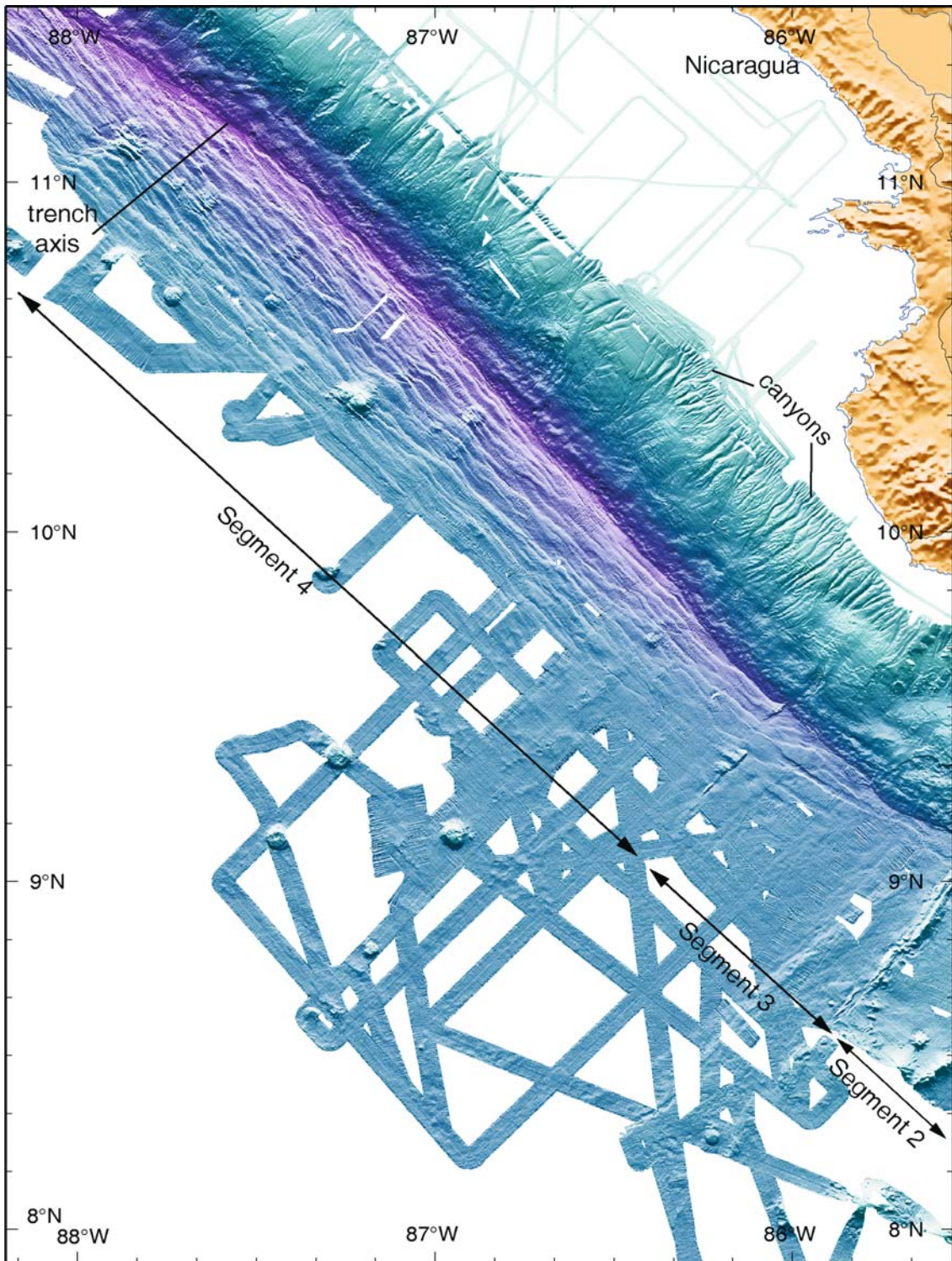


Image 5.2.1-1b. (see page 90)

◀ **Image 5.2.1-1a,b.** Color coded bathymetry and elevation map along 600 km of the Central American Trench along Costa Rica and Nicaragua. **Multibeam image.** Bathymetric soundings have been devoided of spurious values prior to gridding into a 100 m grid spacing. The bathymetric measurements were converted into depth using water velocity profiles collected during different cruises. Land topography is from a 30-arc-second data base from a US geological survey. The bathymetric data display the deformation of the oceanic plate due to the bending just prior to subduction. Fairly abrupt morphological boundaries separate four distinct segments of the oceanic plate (black arrows mark segments). The 1st segment is off southern Costa Rica, where the thick crust of the Cocos Ridge bends little, and no faulting develops near the trench. The 2nd segment shows pervasive faulting with a strike oblique to the trench axis. The 3rd segment has the smoothest morphology with a few small-offset faults developing roughly parallel to the trench. Here the plate bends less than at contiguous segments and little deepening occurs toward the trench axis. A small trench-perpendicular linear scarp in the ocean plate separates the 3rd and 4th segments. Lithosphere to the SE (1st to 3rd segments) formed at the Galapagos mid-ocean ridge, whereas lithosphere to the NW (4th segment) formed at the East Pacific Rise mid-ocean ridge. The 4th segment has the most pervasive normal faulting along the margin. The continental slope shows a similar segmentation. Opposite the Cocos Ridge is a steep continental slope, a broad shelf and the uplifted *Osa Peninsula*. In front of the seamounts of segment 2 is a rugged continental slope. Opposite the smooth sea floor of segment 3 is the most stable continental slope with canyons reaching the middle slope. Where the faulted ocean floor of segment 4 subducts, the continental margin has numerous small slump scars, a complex lower slope morphology and a steep middle slope. Onshore, the active volcanic arc runs parallel to the trench at about 150 km distance. In the southeast, the Talamanca Cordillera is an extinct volcanic arc that has been uplifted by the shallow angle subduction of the Cocos Ridge. For zooming these images: see attached CD.

Project: Compilation of data from projects: SO-101 CONDOR, SO-161 SPOC; cruises SO-101/SO-161, years of data acquisition: 1995/2001

Research vessel: *RV Sonne*, Germany; Multibeam system: SO-101: ATLAS Hydrosweep DS; frequency: 15.5 kHz, beamwidth: 2.3°, 59 beams, 90° fan width; SO-161: Simrad EM-120; frequency: 12 kHz, beamwidth: 2°, 191 beams, 150° fan width

Image ©: César R. Ranero · Wilhelm Weinrebe, GEOMAR Forschungszentrum für Marine Geowissenschaften and SFB 574, Christian-Albrechts-Universität zu Kiel ■

Bending-related faults strike roughly parallel to the trench and generally reactivate and enlarge faults that were formed at the mid-ocean ridge during crustal construction. These faults remain active across the trench slope and facilitate the infiltration of sea water into the oceanic crust and upper mantle, where it reacts with minerals and produces widespread alteration and the formation of new minerals that bind chemically large quantities of water along the faults. As the ocean plate undergoes metamorphism during subduction these minerals become unstable and release great amounts of water along the faults formed at the trench. The release of water facilitates the reactivation of the faults producing earthquakes up to several hundred kilometer deep into the subduction zones. When that water reaches the asthenosphere of the upper plate it lowers the temperature necessary for melting mantle rock, triggering partial melt. The melt will rise across the lithosphere intruding into the crust of the overriding plate and extruding to the surface to form volcanic arcs.

In Central America, as in most subduction zones around the world, a volcanic arc occurs parallel to the plate boundary, about 150 km away from the trench axis (Image 5.2.1-1). However, in southeast Costa Rica, the

volcanic arc has been extinct for about 3–4 million years. This is the region of the *Talamanca Cordillera*, with the highest peak summits in central America of up to 3600 meter high (Image 5.2.1-1). In the *Talamanca Cordillera* a drainage river system has deeply incised the topography. In contrast, the active volcanoes have a smoother morphology, indicative of recent lava flows that even the volcanoes slope morphology. The *Talamanca Cordillera* has been created by the subduction of the buoyant Cocos Ridge that descends at an anomalous shallow angle and uplifts the continental plate in a broad area. In addition, the Cocos Ridge does not subduct deep enough into the mantle to promote large scale partial melting.

The morphology of the continental slope and the shelf vary along the margin, paralleling in a remarkable manner the changes in crustal structure and relief of the oceanic plate. These variations occur in regional and also local scales along the margin. On a regional scale, the Cocos Ridge and oceanic plate with numerous seamounts correspond to a continental margin with a rugged morphology (Segments 1 and 2 in Image 5.2.1-1). The more subdued relief of the oceanic plate to the northwest faces a continental margin, off-

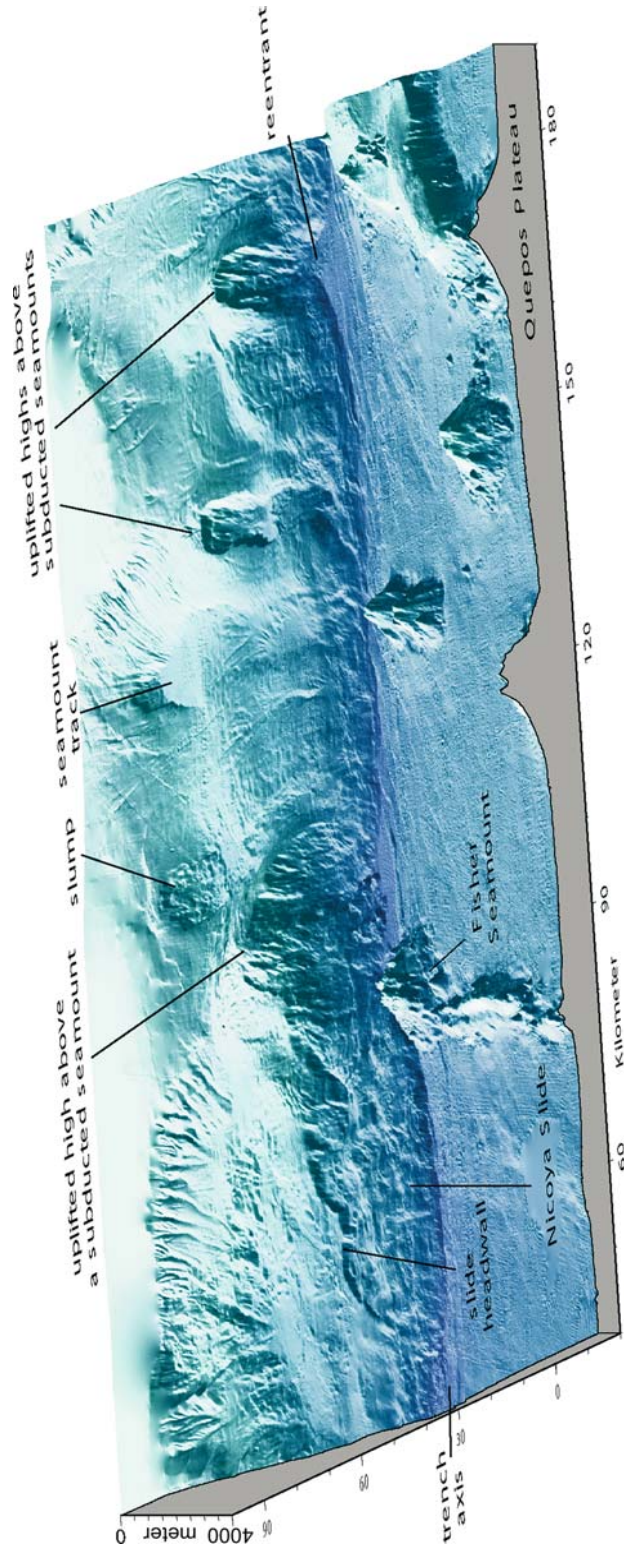
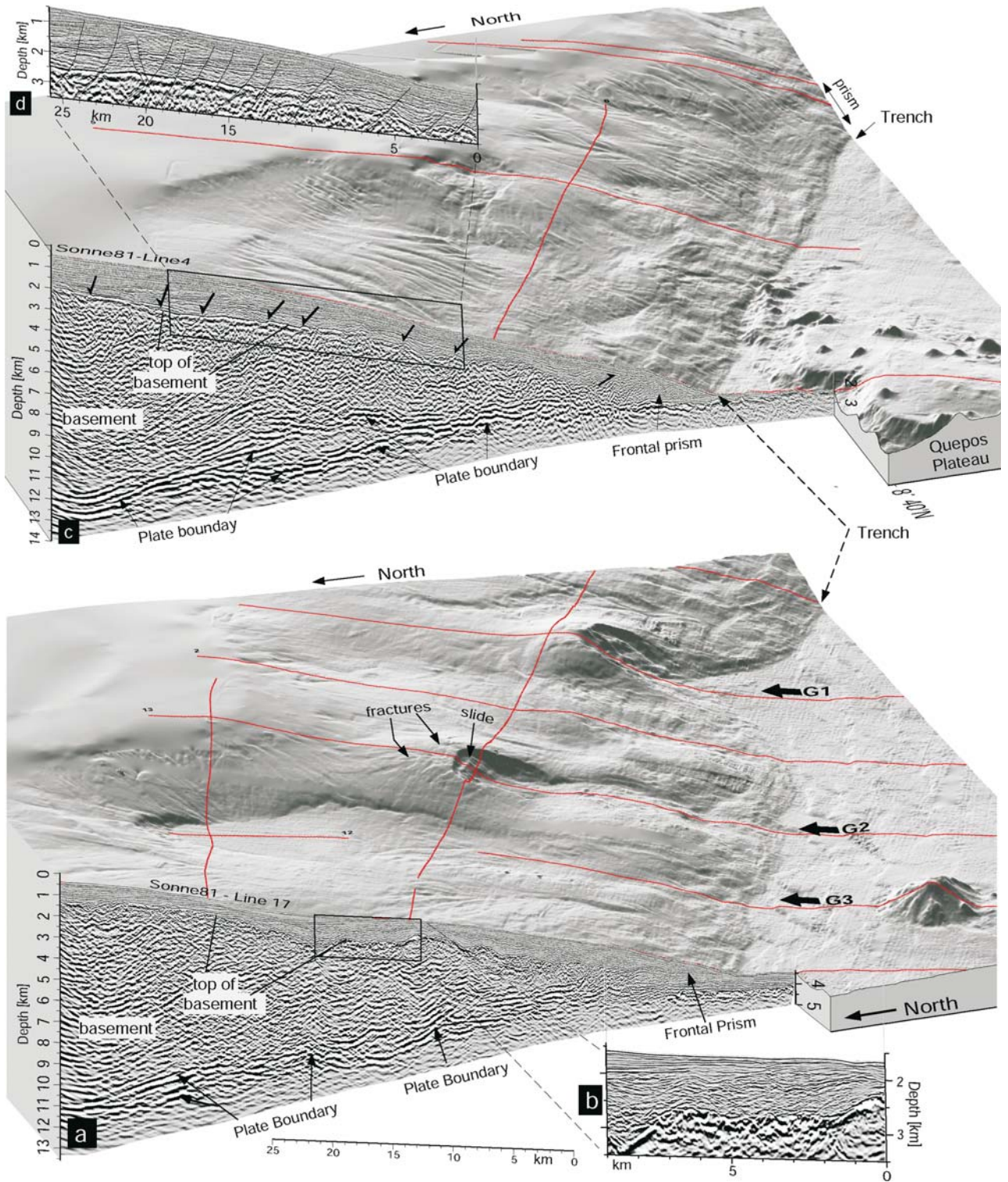


Image 5.2.1-2. Perspective view of the bathymetry offshore from *Central Costa Rica*. Multibeam image. Subducting seamounts produce a spectacular deformation across the continental slope. Seamounts tunnel beneath the slope and leave behind a groove of deformed material parallel to the convergence vector and marking the trail of the subducting seamounts. The uplifted areas of the continental slope indicate the location of currently subducting seamounts. As seamounts move deeper into the subduction zone the material that has been uplifted above them collapses catastrophically, producing slumps and slides. The collapsed Nicoya slide involves more than 50 km of material along the margin, and could have caused a large tsunami wave.

Cut out of the data set of the large Image 5.2.1-1a ■



◀ Image 5.2.1-3.

Area of Image 5.2.1-2. Seismic profiles mounted on the perspective relief. SONNE-81 lines 17 and 4 projected on bathymetry perspective, showing the structure of the continental margin and plate boundary. Resolution of the data near the sea floor is a few tens of meters and decreases with depth to about 0.5 km at 10 km. (A) Line 17 is 55 km long from the slope toe to the upper continental slope. The line is located in the area where oceanic seamounts are subducting. Note the small sediment frontal prism, the continuity of plate boundary reflections and the distinct top of the continental basement. The ~40 frontal km of the slope have a rough basement topography (inset B) produced by the underthrusting of seamounts like those shown in the bathymetry. Arrows in the bathymetry point to grooves in the slope (G1–G3) produced by subducting seamounts and uplift of the slope sea floor indicates the location of two of those seamounts. (C) Line 4 is 58 km long from the toe to the upper continental slope. The top of the continental basement is smooth beneath the upper slope, cut by many small offset normal faults (inset D). The canyon system in the upper and middle slopes indicates a relatively stable environment where no seamount has recently underthrust. Thrust faulting occurs only at the small frontal sediment prism. In the bathymetry the frontal sediment prism is also a distinct morphological unit, tectonically active as indicated by the termination of the slope canyon system. ■

shore *Nicoya Peninsula* and *Nicaragua*, with a less irregular morphology and a well developed canyon system in the middle-upper slope (Segments 3 and 4 in Image 5.2.1-1). On a local scale, the continental margin facing the oceanic seamounts displays large embayments, narrow grooves and topographic highs (Images 5.2.1-1 and 5.2.1-2). The highs occur at the end of linear grooves in the continental slope topography and are aligned with the chains of seamounts on the oceanic plate (Images 5.2.1-1 and 5.2.1-2). The highs mark the locations of seamounts that have been subducted and are currently underneath the continental plate. The grooves are parallel to the direction of the incoming plate, the *convergence vector* and indicate the subduction trail of the seamounts. Three of these grooves are shown in Image 5.2.1-3 (G1–G3) and two of them (G1 and G2) end in highs of the slope, corresponding to uplifted areas above subducted seamounts. The subducted seamount that formed groove G3 has traversed underneath the entire continental slope and it is deep into the subduction zone.

Two different *tectonic erosion* processes occur during seamount subduction: Frontal erosion at the slope toe and basal erosion along the underside of the upper plate. Seamount impact breaches locally the slope toe producing re-entrants at the base of the continental slope (Images 5.2.1-2 and 5.2.1-3, G2). However, gaps in the slope toe, where seamounts transit through it, appear to heal rapidly by accretion. At the front of G2, where the groove and a domal uplift in the middle slope denote the current location of a subducted seamount, the slope toe is completely restored indicating that the process is achieved in less than 140 thousand years assuming current convergence rates (Image 5.2.1-2). The grooves indicate that each subducting seamount removes material from the overriding plate producing *tectonic erosion* and carrying it deep into the subduction zone (Ranero and von Huene 2000). The long-term repeated subduction of the seamounts through time has produced the large embayments along the continental margin and a landward retreat of the slope in central-southern Costa Rica, compared to the structure of the margin offshore from the *Nicoya Peninsula* and *Nicaragua*. The disrupted continental slope in the area where the large seamounts and *Cocos Ridge* are subducting indicates that repeated seamount subduction is an effective agent of upper plate erosion. Evidence from long-term *tectonic erosion* has also been observed in seismic sections. Seismic images show a prominent boundary separating the slope sediment from the underlying margin basement (Image 5.2.1-3). This boundary corresponds to an unconformity formed by wave-surf erosion at sea level in a beach environment. However, the unconformity is currently several kilometers deep below sea level and covered by a thick section of sediment indicating a prolonged margin-wide subsidence of the continent related to long-term thinning of the overriding plate. This unconformity, and thus the evidence of widespread subsidence, has been observed along the entire continental margin. The dramatic thinning of the overriding plate has been caused by removal of material along the plate boundary due to basal *tectonic erosion*. Therefore *tectonic erosion* occurs along the entire margin, but where a rough oceanic plate partially covered by seamounts like milling teeth is subducting, *tectonic erosion* processes are accelerated. The eroded material is carried

by the subducting plate as a conveyor belt and recycled into the Earth's mantle. In Central America, and many convergent margins around the world, the formation and geometry of the current continental slope is the result of millions of years of activity of *tectonic erosion* processes.

Seamount subduction, in addition to *tectonic erosion*, also produces large-scale mass wasting of the slope sediment. As seamounts tunnel underneath the continent they uplift the slope and as they continue moving deeper into the subduction zone, the uplifted sediment collapses in slumps into the grooves in the wake of subducting seamounts. Most slumps are about 5 km wide and involve a pile of sediment a few hundreds of meters thick. However, large seamounts can produce much larger mass wasting events. The so-called *Nicoya slide* has a sharp head-wall fault that runs more than 50 km along the margin (Image 5.2.1-2) and involves up to 1 km thick slope material. The slide toe has run up the oceanic trench slope about 5 km (Image 5.2.1-1). If the Nicoya slide failure were catastrophic, i.e. instantaneous instead of slow creeping, it could have generated a tsunami wave 30 m high in open sea.

Central Chile

The multibeam bathymetric data along central Chile shows the dramatic effects that the subduction of the *Juan Fernández Ridge* has on the sediment distribution along the trench, the development of bending-related faulting and continental margin tectonics. The Juan Fernández Ridge was formed by hot spot magmatism that modified the *Nazca Plate*, and is currently subducting underneath Central Chile offshore from the town of *Valparaíso* (Image 5.2.1-4). In the area affected by the hot spot, the crust was modified by magmatism and extrusive volcanism. The volcanic chain forms a topographic ridge more than 100 km wide and crested with a few large seamounts. Hundreds of small conical seamounts span the ridge and indicate the area of influence of the hotspot volcanism that intruded and modified about 38 million years old ocean lithosphere 8–9 million years ago. (von Huene et al. 1997). The elongated low-relief NW-SE trending ridges are features formed at the mid-ocean ridge dur-

ing crustal formation and indicate the area where the original structure has not been modified by the hotspot magmatism.

The Juan Fernández Ridge strikes NE-SW at an angle oblique to the subduction zone and, due to the plates' convergence vector perpendicular to the trench, the area where the volcanic ridge collides with the continent progressively moves along the subduction zone from north to south sliding along the subduction zone at 20 mm yr⁻¹ (Yáñez et al. 2001). This implies that the deformation of the continental margin and the control on sediment distribution in the trench associated with the volcanic ridge subduction has affected and will affect progressively to hundreds of kilometers of the Chile subduction zone in the course of time. As we explain in the following, the subduction of the ridge is a first order tectonic process that shapes the structure and evolution of the continental margin.

When the ocean plate plunges into the subduction zone it bends with laterally changing dip angles. The changes in bending behavior correspond to changes in the development of bend-related normal faults. At most subduction zones, ocean plates usually break roughly parallel to the trench during bending (Image 5.2.1-1). However, near Juan Fernández Ridge only a few faults develop subparallel to the trench. In contrast, most faults develop striking at high angles to the trench and parallel to the volcanic ridge. The faults have small offsets at their western end but the offsets increase to about 1 000 m near the trench, indicating that some faults form at about 100 km from the trench and continue breaking as bending increases (Image 5.2.1-4d).

The combined effect of the volcanic ridge and the parallel faulting creates a local topographic high at the trench that controls the distribution of the turbiditic sediment along the Chile-Peru Trench. The turbiditic sediment filling the trench dominantly comes from the denudation of the southern *Andes* and is transported to the north for hundreds of km along the trench. The Juan Fernández Ridge forms a barrier in the trench axis that restricts sediment transport. South of the area where the crest of the ridge is subducting, the trench is flooded with turbidites that spread towards the oceanic plate and form a broad and flat trench axis (Images 5.2.1-4, 5.2.1-4c). In this area

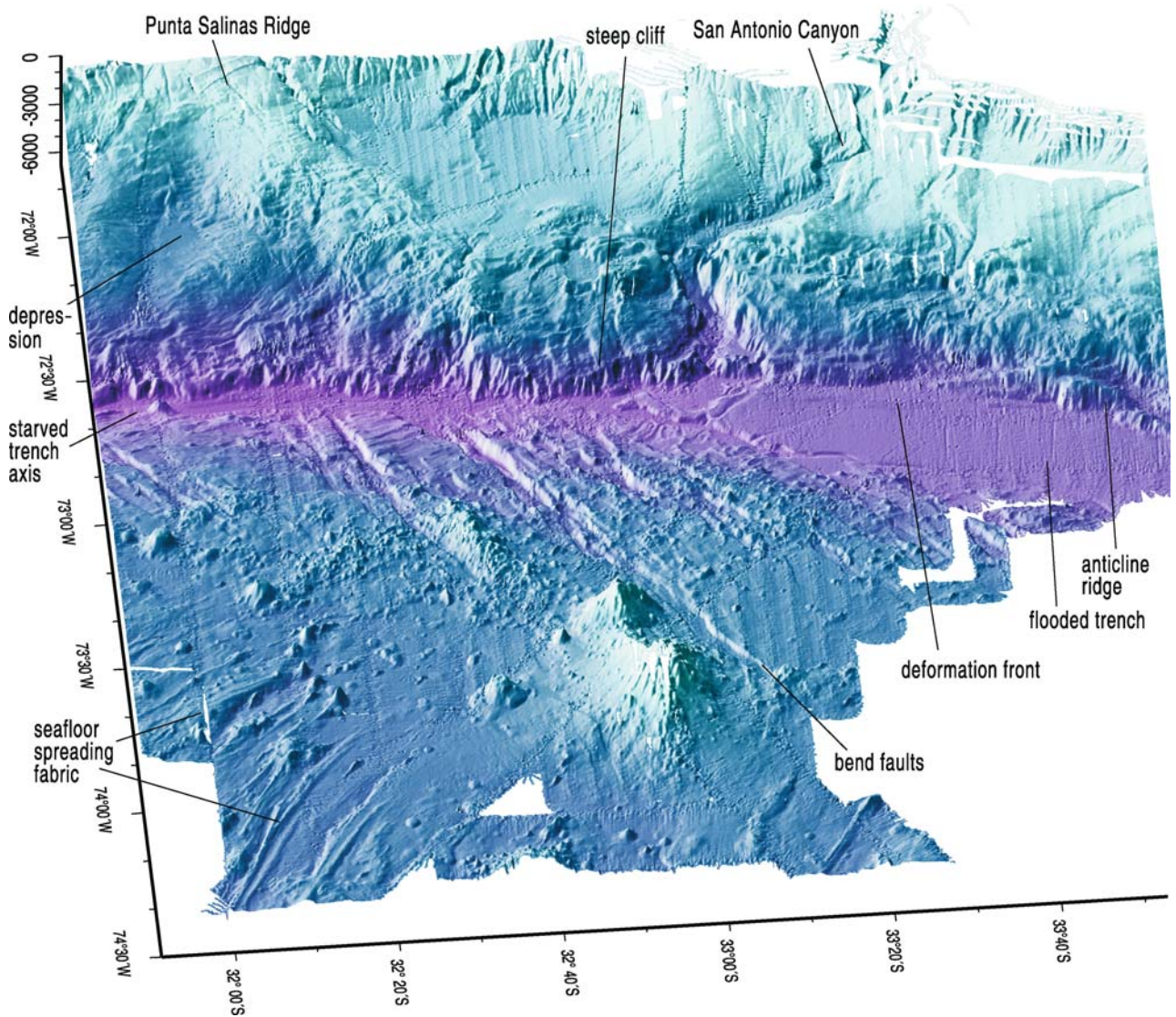


Image 5.2.1-4. Perspective view of the sea-floor morphology offshore from central Chile. Multibeam image. The oceanic plate contains hundreds of seamounts formed by the magmatic activity of a hotspot. The sea-floor spreading fabric formed at the mid-ocean ridge has been obliterated across much of the area by the younger volcanic constructions, but it is still locally visible. Where the seamount chain collides with the continental plate there is a dramatic change in the continental slope morphology and in the amount of sediment in the trench. The morphological high of the volcanic chain in the oceanic plate prevents the sediment coming from southern latitudes to spread to the north causing a trench flooded with turbidites to the south and starved of sediment to the north.

Cut out of the data set of the large Image pair 5.2.1-1a,b ■

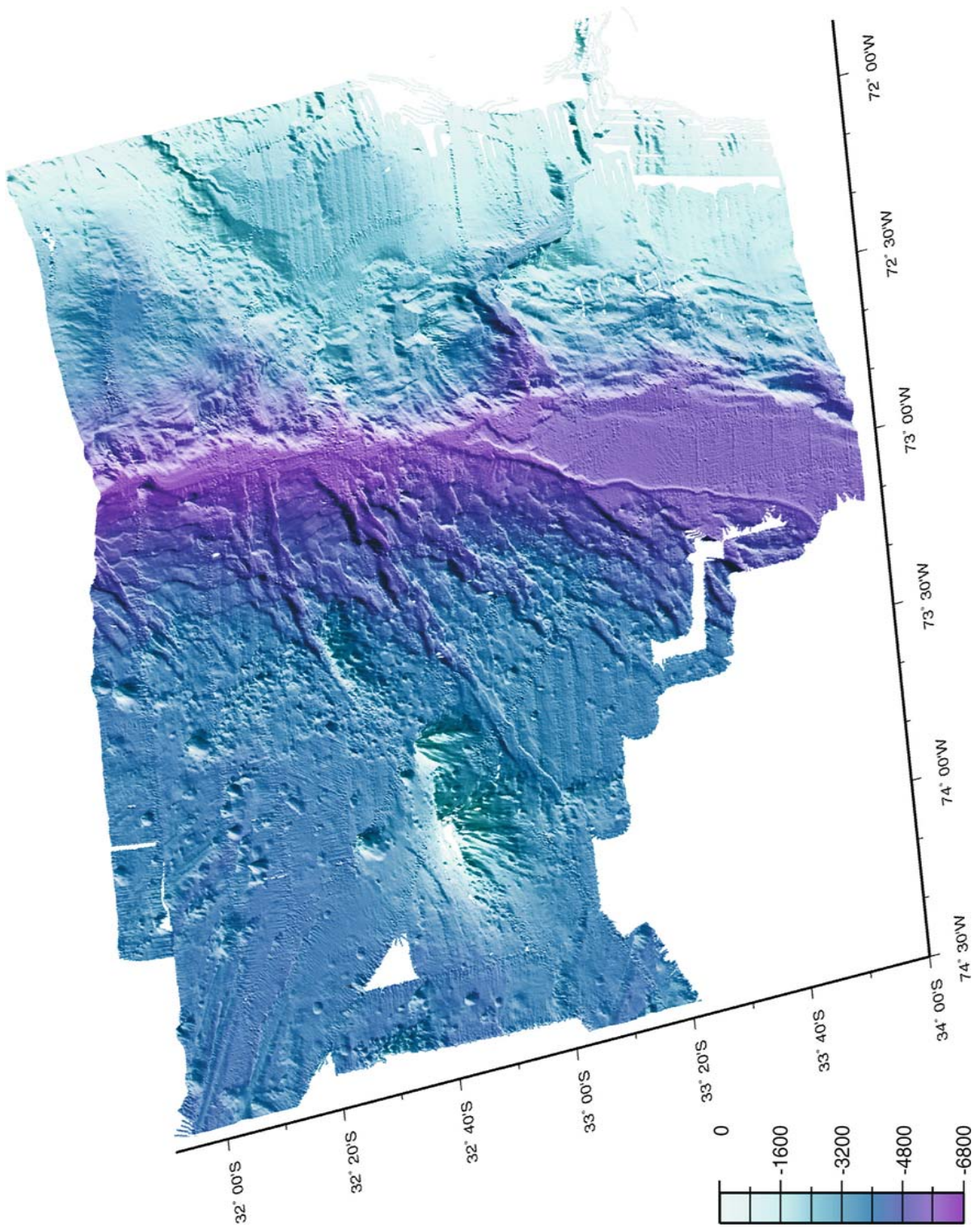


Image 5.2.1-4a. Same as Image 5.2.1-4, but as slant view looking north. Multibeam image. The version shows the surface of the sediment fill in the foreground with the turbidity flow “river bed” and is made for better comparison with the corresponding altimetric Image 5.2.1-4b. ■

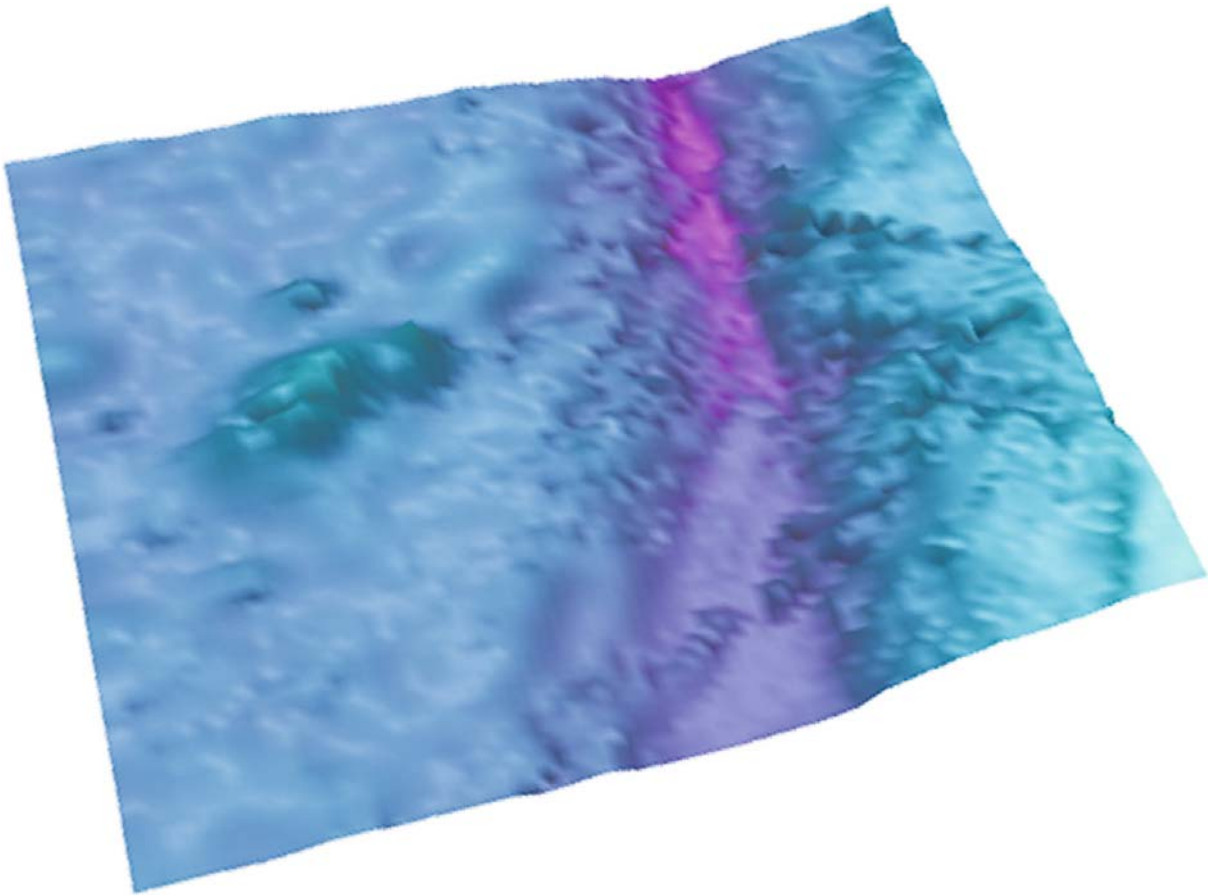


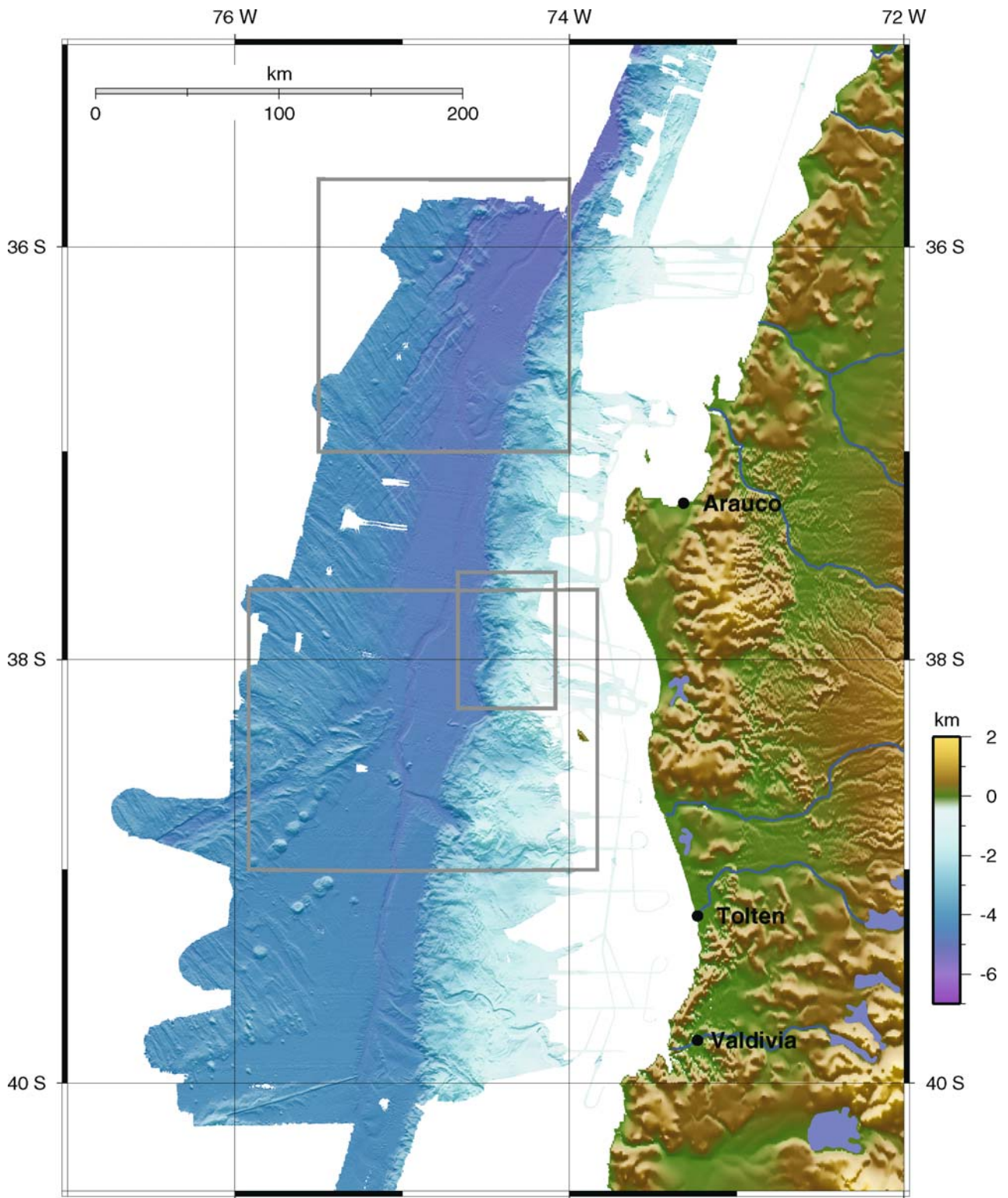
Image 5.2.1-4b. Bathymetric and altimetric comparison of features. Relief image derived from satellite altimetry. The subduction zone off *Central Chile* is a prime example of the complementary differences between acoustic and gravimetric imaging as discussed in Sect. 5.1.2. The acoustic multibeam-scanner “sees” the real sea floor – the nearly plane surface of the sediment fill incised only by a submarine gravity flow channel (Image 5.2.1-4a). The satellite radar however recognizes the gravimetric anomaly caused by the mass defect of the trench, which is not completely compensated by the sediment fill: its density is lower than the magmatic basalt of the subducted oceanic *Nazca Plate* below. As a result, the gravimetric image derived from the ETOPO2-data set looks through the sediment – as it were – and reveals trench floor structures. Despite the much lower gravimetric resolution this is quite obvious in the foreground of the trench: two large peninsula-like ridges are protruding against each other into the valley floor which thus appears not at all plane.

Though both image types concur on the east with the deep *San Antonio Canyon* (Image 5.2.1-4) and on the west with an outstanding double summit volcanic massif which belongs to the *Juan Fernandez Ridge* and a seamount behind, the ETOPO-version shows molds where the sound bathymetry reveals seamounts in the background. The entire mid-scale fabric has no recognizable similarities, apart from the bathymetric texture of erosion and faulting on the oceanic plate margin in the west, which cannot be resolved by ETOPO-imaging. The geodynamic analysis dealing with the convergence zone off *Central Chile* presented here would have been evidently impossible without high resolution multibeam imagery.

The partial structural concurrence of the two fundamentally different methods of sea floor relief imaging applied to this example cannot be generalized. The sea floor density can vary even more strongly than the large bathymetric formations can contribute to the local gravity. This is particularly evident in the *Weddell Sea* of the *Antarctica* (Sect. 5.5.1).

Data set: ETOPO2, CCOM

Image ©: Larry Mayer, CCOM, USA ■



◀ **Image 5.2.1-4c. Bathymetry of the Southern Chilean Margin. Multibeam image.** The overview relief map covers the subduction zone between the latitudes of Concepcion and Valdivia with a maximum depth of more than 5 000 m. The bird's eye view depiction reveals the morphology of the descending oceanic plate and a southward widening sediment trench fill incised by a well developed axial submarine channel (1) with 400 km length shown. Large canyons (2) dissect the shelf and narrow slope of the continental margin. The oceanic Nazca Plate, where not covered by sediments, reveals a crest and furrow texture, obliquely crossed by the Mocha Fracture Zone (3) and seamount chains (4). The frames indicate the subsequent detail cut-outs.

Project: Study of the Subduction Processes Off Chile (SPOC); cruise SO 161, 2001

Research vessel: *RV Sonne*, Germany

Multibeam echosounder: SIMRAD EM120; 12 kHz, beamwidth: $2 \times 2^\circ$, fan width: 90° or 20 km at 4 km depth

Horizontal resolution: 100 m at trench depth, simulated sunlight from north-west

Land topography: GTOPO30, resolution 30 arc seconds or ~ 1 km; Land Processes Distributed Active Archive Center (LP DAAC), U.S. Geological Survey EROS Data Center

Image ©: BGR with Stephan Ladage, Hannover, Germany ■

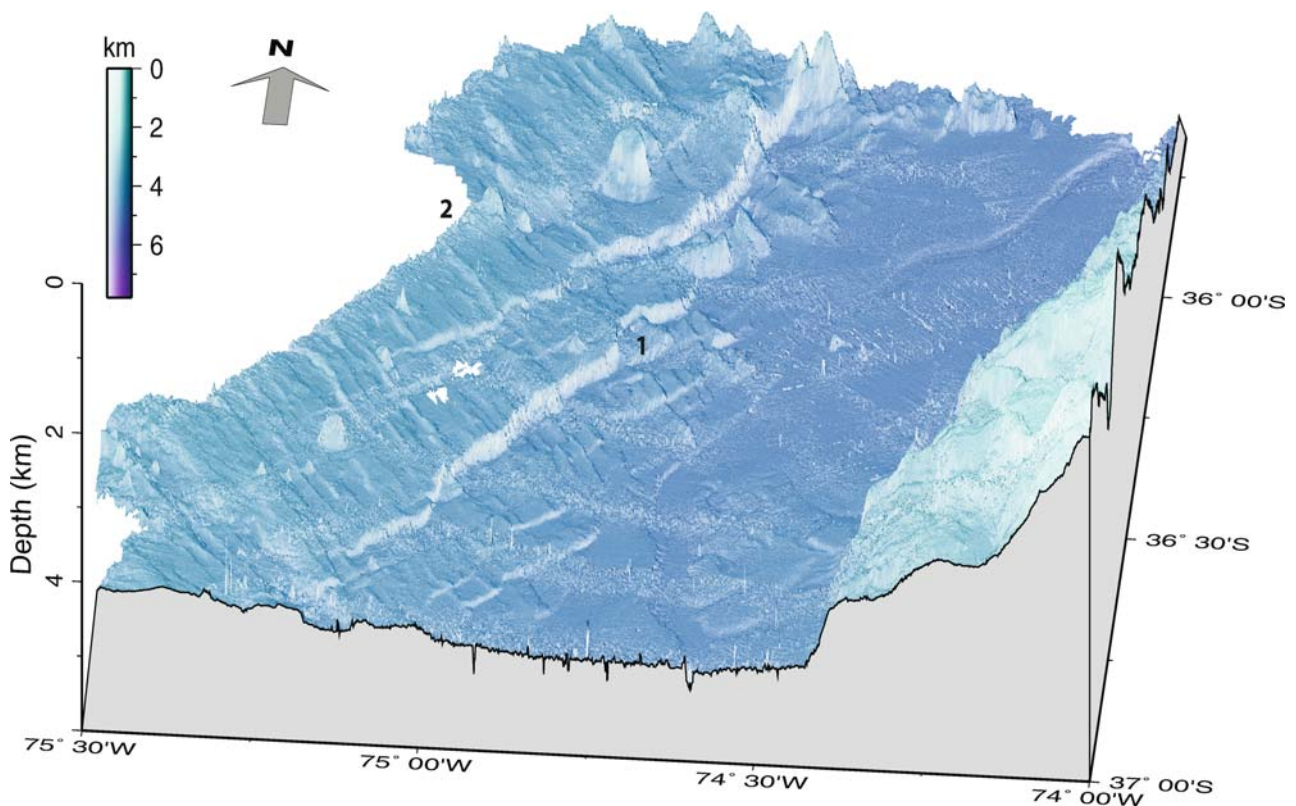


Image 5.2.1-4d. Oceanic Nazca Plate Margin. Multibeam image. Large faults (1) with steep flanks disrupt the oceanic plate due to bending forces, as it descends beneath the South American continent. The faults crosscut a pre-existing fabric (2) of the plate, which is interpreted to be the remnant of the spreading processes during the origin of the Nazca Plate (northern cut-out A).

Project: Study of the Subduction Process Off Chile (SPOC); cruise SO 161, 2001

Research vessel: *RV Sonne*, Germany

Multibeam echosounder: SIMRAD EM120; 12 kHz, beamwidth: $2 \times 2^\circ$, fan width: 90° or 20 km at 4 km depth

Horizontal resolution: 100 m at trench depth, height exaggeration factor: 10, simulated sunlight from south-east

Image ©: BGR with Stephan Ladage, Hannover, Germany ■

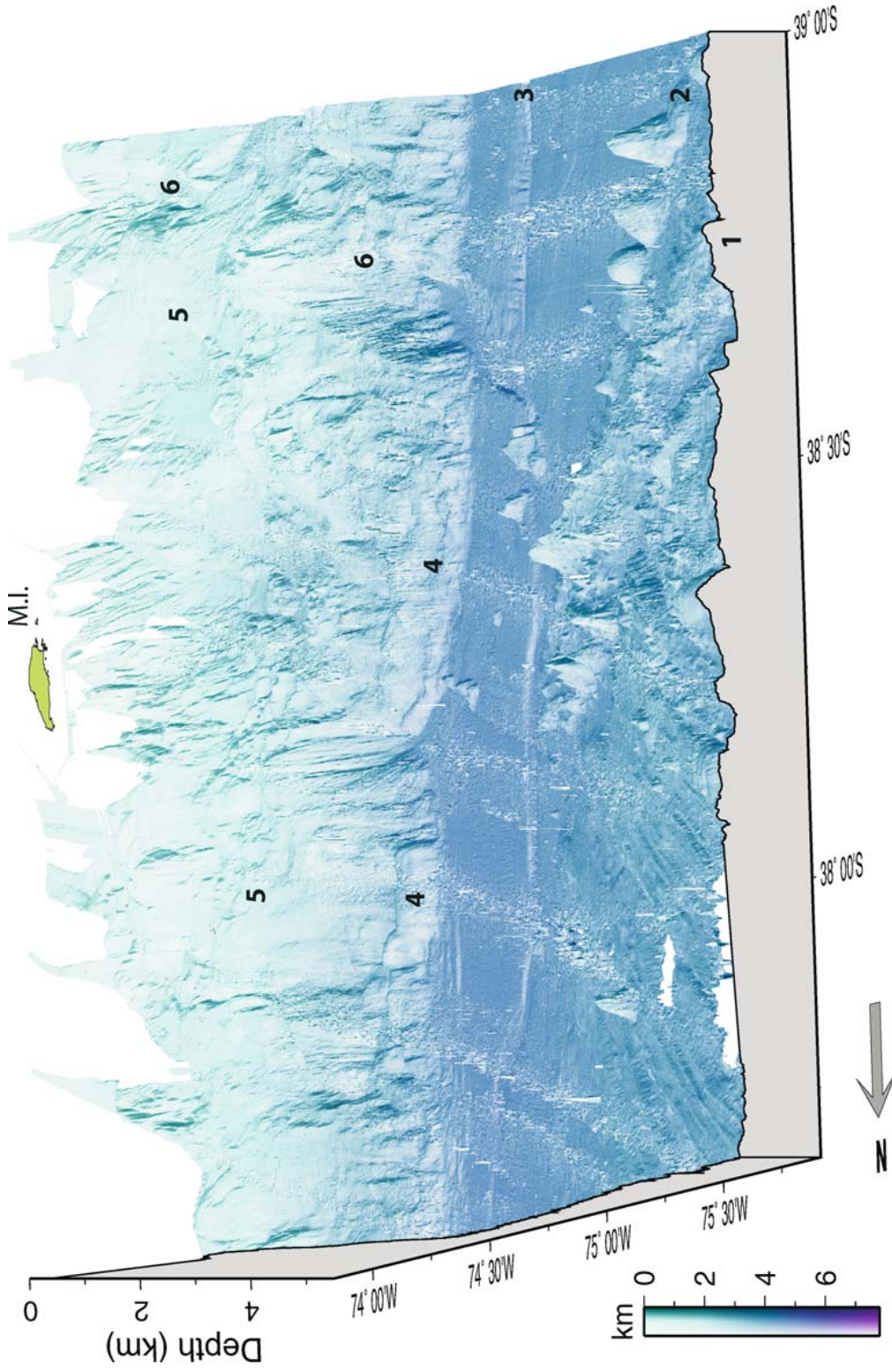


Image 5.2.1-4e. Chilean Margin with the Mocha Fracture Zone. Multibeam image. The perspective eastbound view of the trench system (southern cut-out B) shows the Mocha Fracture Zone (1) in the foreground. The MFZ enters obliquely from SE into the trench, accompanied by a chain of seamounts (2). These are partly buried by the trench fill. A submarine channel (3) up to 200 m deep is incised into the trench sediments. The continental slope depicts a steep frontal part inclined up to 12°. At the base of the slope, folds of deformed trench fill have developed (4). At the midlevel slope several so-called piggy-back basins can be observed (5). Trapped sediments in these basins lead to a local smoother relief. A several hundred meter deep canyon cross-cuts the shelf and slope (6). (M.I. is Mocha Island).

Image documentation: same as for Image 5.2.1-4d

Height exaggeration factor: 10, simulated sunlight from north-west. Several stripes of roughness crossing the image are artifacts of the multibeam sampling ■

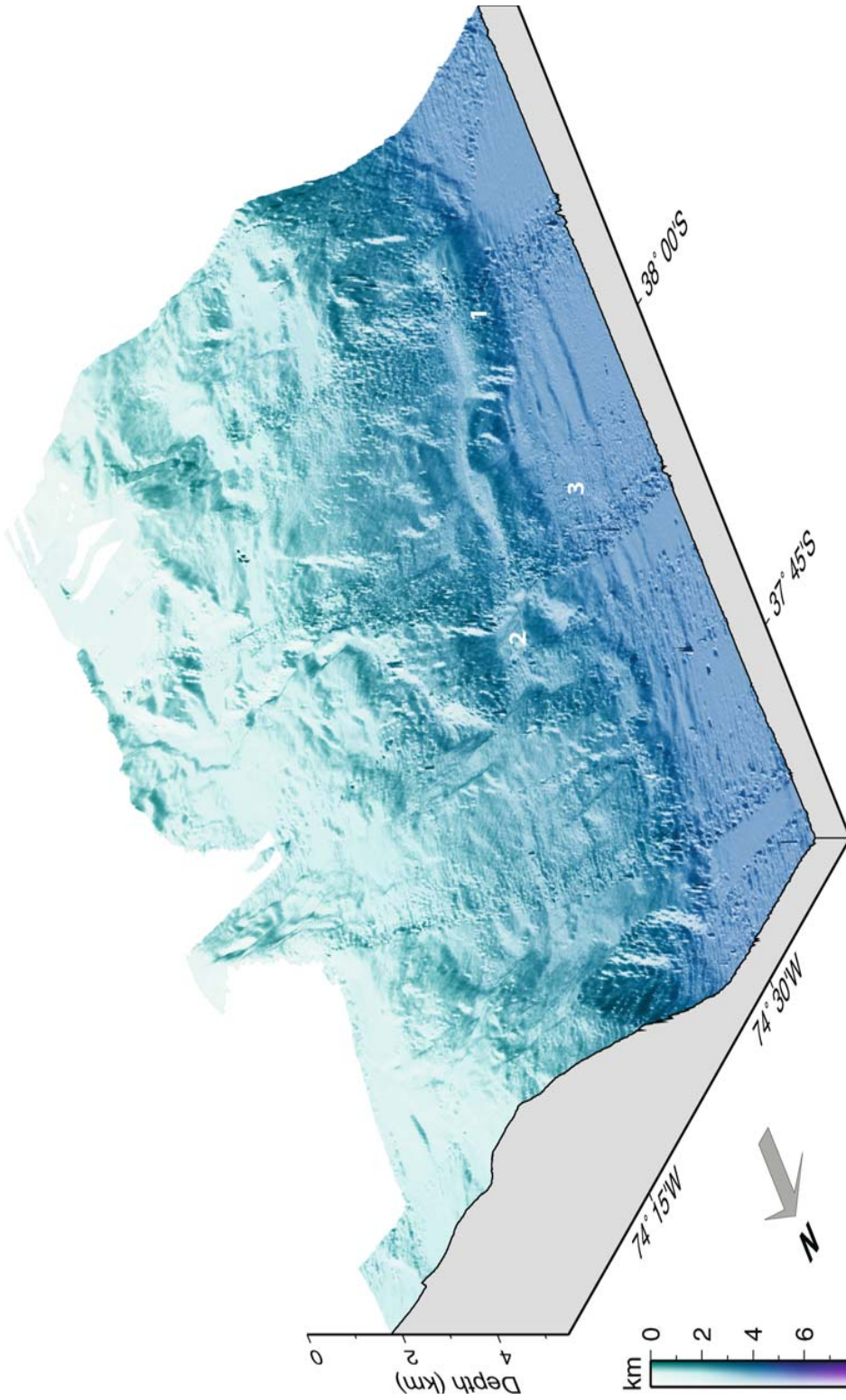


Image 5.2.1-4f. Chilean continental slope and trench horizon. Close up multibeam image. The base of the slope is built up of young, large folds some hundred meters high (1). These document the ongoing deformation of the trench fill due to the subduction of the Nazca Plate. The folds partially block the tributaries into the trench of the large canyons incising the slope (2). Sediments from up-slope, which would otherwise be deposited in the trench, are now trapped by these folds. In front of the embayment in the lower slope a set of three gently curved, incipient faults – clearly identifiable as reverse faults in reflection seismic profiles – are observed (3). These show a rearrangement of the deformation front in this area. Note also the steep escarpment of the lower slope in the north of the Image (4). The origin of this scarp is not yet clear. (Close-up C in overview.)

Image documentation: same as for Image 5.2.1-4d

Height exaggeration factor: 10, simulated sunlight from north. Several stripes of roughness crossing the image are artifacts of the multibeam sampling ■

turbidite trench infill may reach 2 500 m thick, but the sediment infill rapidly thins towards the north. The channel distributing the turbidites is observed as a clear incision on the smooth morphology of the trench axis (Images 5.2.1-4a, 5.2.1-4b, 5.2.1-4c, 5.2.1-4e) but disappears close to the ridge crest. Over the crest and to the north little turbidite transport occurs and the trench infill is only 500 m thick (von Huene et al. 1997). Further north sediment infill further decreases and all of the trench along northern Chile is a starved sediment trench (von Huene and Ranero 2003). Therefore, sediment distribution along much of the Chile Trench, from about latitude 45° S to 20° S, is fundamentally controlled by the Juan Fernández Ridge topography.

Where the volcanic chain of seamounts enters the subduction zone, the continental margin north and south of the ridge displays different structures. The ridge subduction provokes the uplift and deformation of the frontal part of the continent. The subducted extension of the Juan Fernández Ridge beneath the continental plate is marked by the Punta Salinas Ridge. Beneath the continental slope the volcanic ridge pushes up the continental plate above the oceanic plate topography. The Punta Salinas Ridge relief increases upslope from the trench in spite of the increasing depth of the subducting oceanic plate beneath the continental plate. Surprisingly, Punta Salinas Ridge is a prominent feature in the upper slope where the subducting oceanic plate underneath is about 30 km deep. It is unlikely that the subducting seamounts, only 2–3 km high and 30 km deep into the subduction zone, can produce such a prominent uplift. The Punta Salinas Ridge rather indicates that the relief of the ocean plate increases deeper into the subduction zone. A feasible explanation is that the faults parallel to Juan Fernández Ridge and with offsets of about 1 km at the trench continue growing as the plate subducts beneath the continental plate enhancing the dimensions of the subducted oceanic plate topography.

South of the area where the crest of the ridge is subducting, the trench is flooded with turbidites that create a broad trench with smooth morphology. Turbidites are rapidly deposited and in spite of the 85 mm yr⁻¹ convergence between the plates, they appear little deformed (Image 5.2.1-4c). However, near the slope toe, low relief ridges parallel to the margin indicate the beginning of the deformation of the trench infill (deformation

front in Images 5.2.1-4, 5.2.1-4f). These ridges indicate the position of thrust faults that are cutting up from the base of the sediment pile and starting to uplift it. The ridges are the surface expression of anticlines (concave-up folds of sediment strata) formed above the thrust faults that are detaching the sediment from the subducting oceanic plate. This process is the initiation of the accretion of sediment to the continental margin. A series of margin-parallel higher relief ridges occur along the lower continental slope indicating sediment that has already been accreted to the continent (Image 5.2.1-4e).

North of the *San Antonio Canyon* the margin morphology has been strongly modified by the subduction of the volcanic chain. It can be assumed that before the arrival of the ridge at this region of the margin, the morphology was similar to that observed in the south. The current position of the crest of the subducting volcanic ridge, where most deformation is presently occurring is clearly displayed by the uplifted Punta Salinas Ridge in the continental slope. Where the crest of the Juan Fernández Ridge underthrusts the margin, the base of the continental slope is cut by a 1 km high steep cliff with many slump scars. North of the subducting ridge crest, there is no morphological evidence of an accretionary prism. There, the continental slope is characterized by a depression left behind after the passage of the subducting volcanic ridge sweeping along the margin and indicating that a large mass of the overriding plate has been removed by *tectonic erosion*. The sediment starved trench has too little turbidite infill to facilitate the formation of a large accretionary prism destroyed by the subducting ridge. Thus the drifting of the Juan Fernández Ridge along the Chile Trench causes brief climax of major local deformation at the locus of collision and controls the long-term development of the continental margin.

Alaska

The bathymetric map from offshore Alaska displays a continental slope structure remarkably different from Central America and central Chile, documenting how changes in tectonic processes produce a great variability of circum-pacific convergent margin structure (Image 5.2.1-5). Furthermore, the morphology of the continental slope of Alaska also changes dramatically along its strike. The seg-



Image 5.2.1-5. Perspective view of the sea-floor morphology offshore a segment of the Alaska continental slope. Multibeam image. The segment of the margin striking southwest-northeast shows a well developed accretionary prism about 40 km wide constructed by the addition of slices of turbidites on the oceanic plate to the continental plate as the plates converge. The sediment comes from the continent and is transported to the ocean plate along large canyons. The segment of the margin striking roughly east-west shows a different morphology, lacking a well developed accretionary prism, a narrower and steeper slope and possible scars

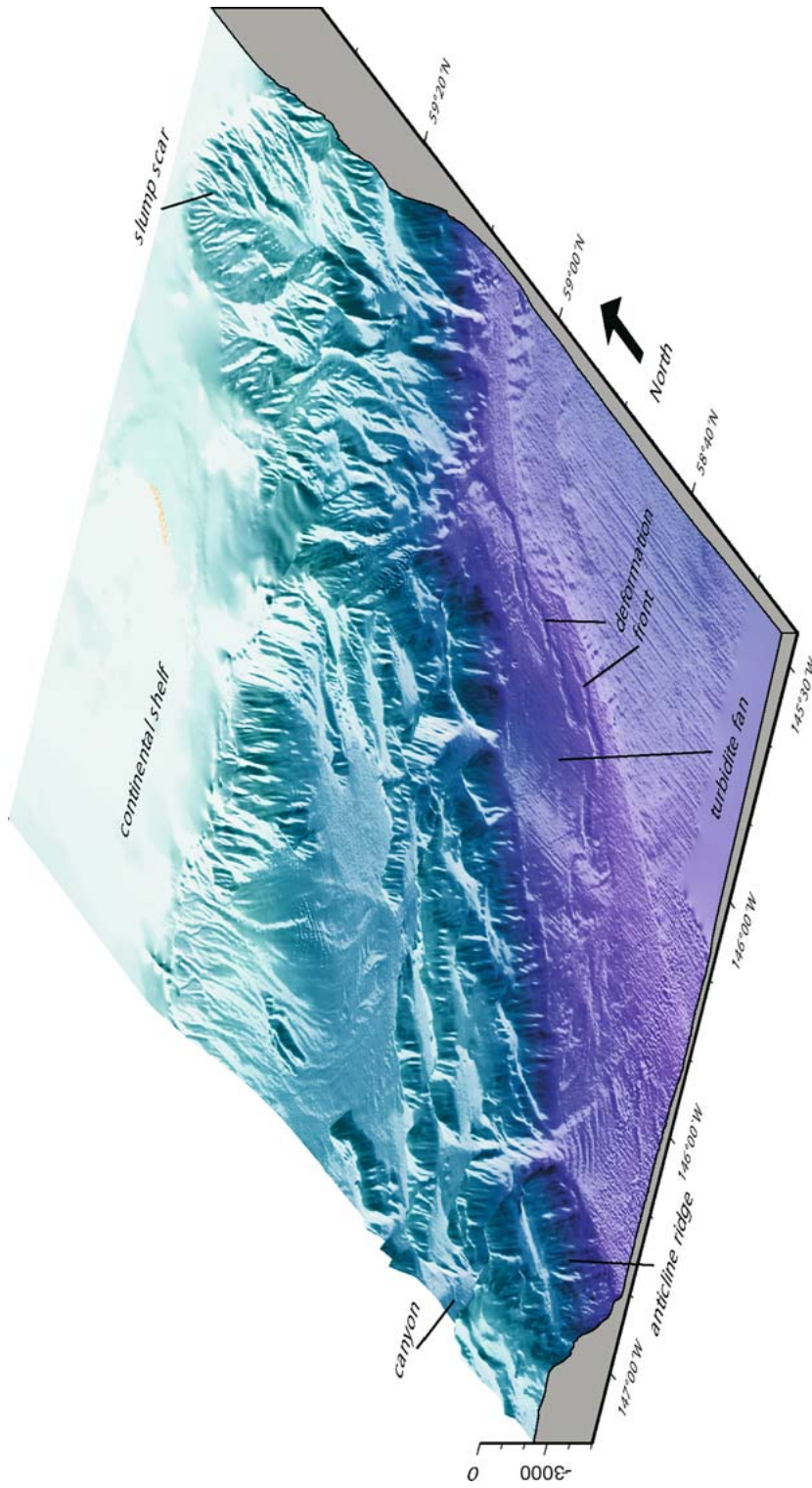


Image 5.2.1-6. Perspective view with a close-up of the central area of Image 5.2.1-5. The bathymetry shows the details of the interaction between sediment deposition at the ocean plate and contractional deformation due to the collision between the oceanic and continental plates. The segment of the margin lacking anticline ridges has a steeper slope and a large slump scar.

Technical data: see Images 5.2.1-1a,b ■

ment of the margin striking SW-NE is characterized by a large *accretionary prism*. The accretionary prism is morphologically defined by a series of trench-subparallel long anticline ridges that become larger and wider towards the continent. These ridges are created by thrusting of slices of the sediment filling the trench as the oceanic and continental plates converge (von Huene et al. 1998). The plate's convergence vector is roughly perpendicular to this segment of the margin and the anticline ridges develop above thrust faults up to 100 km long, that account for the great tectonic contractional deformation occurring where the two plates collide. The thrust faults first become active at the trench (deformation front in Image 5.2.1-5). There, thrust faults cut much of the 2–2.5 km of the trench turbidites coming from the rapid erosion of the continent onshore. As plate convergence continues the thrust faults lift up trench-sediment slices and accrete them to the continental slope. This is clearly displayed in the morphology by the increase in the relief of the anticline ridges, implying that thrust faults continue to grow even as new faults form seawards at the trench.

The high erosional rates on the North American continent at this latitude provide a greater sediment supply to the trench than in many other subduction zones. Sediment provided by rivers passes by the broad continental shelf and is transported to the trench along large canyons that meander and cut across the anticline ridges (Image 5.2.1-5). The sediment channeled along the canyons is delivered to a flooded trench and spreads over the incoming oceanic plate producing a fairly smooth morphology over large distances, where a trench axis proper is poorly defined (Image 5.2.1-5). At the mouth of the canyons, turbidites accumulate locally forming large submarine fans where the deformation front seems to step outward (Image 5.2.1-6).

The segment of the margin striking roughly east-west displays a rather different morphology pointing to a variation in tectonic processes. In spite of the fact that sediment also fills the trench in this region, no trench parallel ridges occur and thus no accretionary structure seems to develop. Sediment is transported across the continental shelf and spilled over a narrow continental slope into the trench along a broad network of small steep canyons. Convergence between the

oceanic and continental plate is very oblique in this region, with the convergence vector almost parallel to the strike of the margin. The change in convergence direction between plates may be responsible for the almost entire subduction of the trench sediment (Fruehn et al. 1999). This segment of the margin, with a narrower and steeper continental slope, exhibits some large spoon-shaped morphological features in the upper slope. These structures may represent the scars of slumps that have removed a large portion of the slope sediment. The structures are relatively old because a drainage system of canyons has sculptured the slump detachment surfaces (Images 5.2.1-5 and 5.2.1-6).

Thus, the Alaskan continental margin exemplifies a classical accretionary margin in the area of normal convergence between continental and ocean plates, whereas an almost complete sediment subduction occurs where subduction is strongly oblique. These two types of tectonic processes lead to the development of fundamentally different margin structures.

Acknowledgments

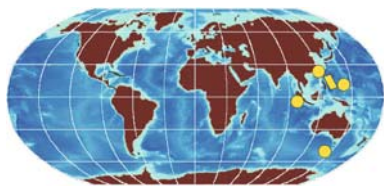
The multibeam bathymetry of Central America was collected during RV Sonne cruises 76, 81, 107, 144, 150 and 163, RV METEOR cruise 54 and RV M. EWING cruises 0005 (Chief Scientist Kirk McIntosh, University of Texas) and 0104 (Chief Scientist Andy Fisher, Santa Cruz Univ.). The multibeam bathymetry of central Chile was collected during RV Sonne cruises 101 and 161. The multibeam bathymetry of Alaska was collected during RV Sonne cruise 96 and also includes data provided by NOAA, USA. Multibeam bathymetry was cleaned using the MBsystem (Caress and Chase 1996). All figures have been produced with the GMT software (Wessel and Smith 1998). We thank all participants and crews from all these cruises who have, through excellent work, permitted the acquisition of this unprecedented compilation of high quality bathymetric data. RV Sonne cruises were funded by Deutsche BMBF, RV METEOR cruise by DFG and RV M. EWING by NSF-USA.

References

See Sect. L.5.2.1.

5.2.2

5.2.2

Marianas-Type Convergent Plate Margins

Most high energy earthquakes and active subaerial volcanoes on Earth are concentrated around the Pacific

Ocean. They occur within a narrow belt whose width is several hundred km, less than that of Chile. This belt proceeds along the west coast of both Americas northwards to Alaska, then west and south along the island arcs of Alaska and East Asia before terminating in New Zealand. The belt has a length comparable to the circumference of the Earth, and was christened the *Pacific Ring of Fire* with respectful awe long before the origin of the terrifying earthquakes and eruptions were recognized as a fundamental part of plate tectonics. The revolutionary theory of plate tectonics was established and gradually verified only in the sixties and seventies of the twentieth century. Much of the conclusive evidence for plate tectonics came from acoustic and seismic imagery of the deep-sea floor

and underlying structures. Such imagery has become one of the key technologies and diagnostic tools of geology.

The Pacific Ring of Fire features two distinct types of convergent margin, both involving the subduction of the ocean floor and lithosphere of one plate beneath another tectonic plate. The *Chile-type* is predominant along the Pacific coast of the Americas (Sect. 5.2.1), where oceanic plates are subducting beneath an adjacent *continental margin*. The *Marianas-type* prevails on the opposite side of the Pacific, where oceanic plates are subducting beneath another *oceanic plate*. These two types of subduction generate different trench characteristics.

The primary characteristic of *Marianas-type* convergent margins is a conspicuously deep and steep-sided trench adjacent to a strongly bent incoming plate. Trenches of this type are typically more than twice as deep as those of *Chile-type* convergent margins, where the subducting plate is less strongly bent and reaches the trench at a shallower angle. One reason for the steeper incidence angle of the incoming plate at *Marianas-type* margins may be the greater age of the subducting Pacific Plate in the western Pacific, often around 170 million years. Oceanic plates become thicker and colder as they age, and thick cold

Box 5.2.2-1. Key features of the *Marianas-type* of plate subduction

In the *Marianas-type* of plate subduction, the incoming oceanic plate is usually sinking faster than the rate at which the two plates are converging by their horizontal motion. Because there cannot be a gap in the Earth's surface, or at least not one deeper than the *Challenger Deep* Trench, the overriding plate has to move out into the ocean towards the incoming plate. In a simple sense, it fills the empty space. This process causes the trench to migrate out into the ocean, and is called *trench roll-back*. It extends the overriding oceanic plate and even tears it apart. That is how *back-arc basins* form. Such basins are behind almost all of the *Marianas-type* margins in the western *Pacific*.

The decisive difference between *Marianas-type* and *Chile-type* margins is the overriding plate in kind: the *oceanic* plate for the *Marianas-type* and the *continental* plate for the *Chile-type* (Sect. 5.2.1). The continental crust is usually forming high mountains; their weathering and erosion are a source of much sediment, transported coastwards by turbidite flow. It builds accretionary wedges and floods the trench with sediment. This is why *Chile-type* trenches are shallower. The sediment wedges are easily deformed when seamounts are subducted. In contrast, in *Marianas-type* trenches there is very little sediment.

Seamounts subduct also at these trenches, but they have less effect and cause less deformation of the hard igneous rocks on the trench walls than they do on soft sediments of the *Chile-type*.

The subducting oceanic plate at both types of margins is essentially the same and contains the same amount of water. Thus, when it is subducted back into the Earth it releases the same amount of energy or generates the same amount of volcanic activity. It happens that at the present-day most of the subducting plates at *Marianas-type* margins are older than those at *Chile-type* margins, but the difference is not very much and there are exceptions from the rule.

It is still under debate how and why subduction has started originally. When an oceanic plate becomes too old and thus too heavy to stay at the surface it should start to submerge at the edge where the instability by overweight is most pronounced. Or the touch with a neighboring plate might force the subduction of the unstable plate at this edge of encounter. Perhaps both mechanisms occurred; no-one knows at the moment.

Tim J. Worthington · Institut für Geowissenschaften,
Kiel University

plates are less buoyant and sink more readily at a trench. Subducting plates steepen as they sink further into the Earth and may become vertical. Some have been traced by seismic methods to depths of 1 200 km in the Earth's mantle, a fifth of the radius of the globe.

The famous *Challenger Deep* is part of the Marianas Trench. It reaches a depth of nearly 11 000 m and is the deepest part of the Earth's surface. A 3D-acoustic image of the *Challenger Deep*, acquired in 1998 by the Japanese research vessel *RV Kairei* with multibeam technology, is shown hereafter. It represents an idealized example of this type of subduction. The Japanese remotely operated deep-diving submersible *Kaiko* landed inside the *Challenger Deep* in March 1995 and recorded the depth as 10 911 m. This confirmed the depth indirectly estimated by J. Piccard in 1960, and was slightly shallower than the first estimate of 11 022 m made by the Russian research vessel *Witjas* in 1949.

Subduction at *Marianas-type* margins is less complicated than that at *Chile-type* margins. There is often little evidence for the complex variety of interaction and deformation processes between the overriding and subducting plates that characterize *Chile-type* margins, and some of these processes do not occur at all (Sect. 5.2.1). In part this reflects the fact that the plates do not actually collide at such margins, but rather the subducting plate sinks into the Earth while the other plate moves into the empty space left above it. Thus, under normal circumstances neither abrasion nor transfer of material occur between the plates at the trench.

However, at both types of convergent margin the subducting oceanic plate is bent and deep fractures develop to a depth of several km, allowing water to penetrate the plate and react with the rocks. This adds to the hydration that occurred firstly when the oceanic plate formed at a mid-ocean spreading center and secondly in the millions of years that the plate has existed in contact with sea water. As the subducting plate descends to greater depths in the Earth's mantle, the temperature and pressure progressively increase until the hydrated minerals in the plate are no longer stable and release their water. This water, or silicate-rich fluid, leaves the subducting plate and rises into the overlying mantle where it triggers melting and the generation of magma. Some of this magma may reach the surface, building arcuate chains of volcanoes on the overriding plate at a distance of 200–300 km from the trench. Unlike *Chile-type* margins, where the volcanoes are almost

entirely on land, volcanoes associated with *Marianas-type* margins commonly form seamounts and only the highest reach sea level. Despite this, volcanoes associated with *Marianas-type* margins are commonly referred to as *island arcs*, and these are a characteristic feature of the East Asian side of the Pacific.

Text supplement: *Tim J. Worthington* · Institut für Geowissenschaften, Kiel University

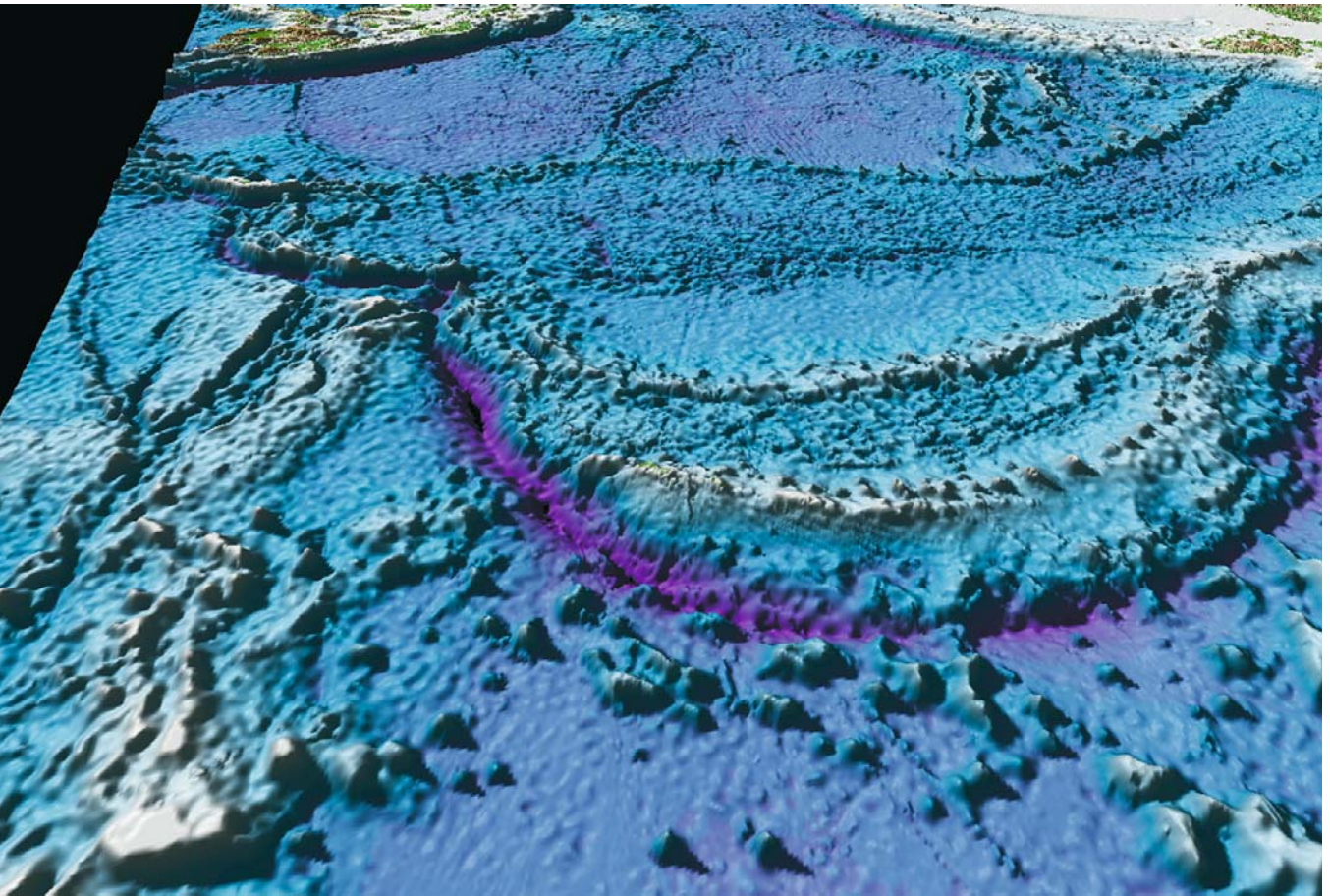
5.2.2.1

The Mariana Trench and the Philippine Plate

Image 5.2.2.1-1. (see next page)

Overview of the Philippine Plate. Image derived from the combined satellite altimetry- and acoustic bathymetry data set (ETOPO2). The sea floor depicted with 3 km (2 arc minutes) grid resolution (Sect. 5.1) shows a deep purple arc of 2 300 km length in the foreground. It is the deepest trench on Earth: the *Mariana Trench*, forming the eastern margin of the *Philippine* tectonic plate depicted behind. The deepest point of all, the *Challenger Deep* of 11 000 m, is the dark chasm near the left end of the purple arc where the curvature is slightly concave. The *Challenger Deep* is also shown as multibeam close-ups (Sect. 5.2.2.2). The *Philippine Plate* is nearly completely depicted and easy to recognize: it is essentially framed by trenches and troughs. Adjacent to the Mariana Trench on the left in clockwise sequence we see the hook-shaped *Yap Trench* followed by the shorter *Palau Trench* and the long conspicuous *Philippine Trench* (Sect. 5.2.2.3) at the left upper edge. On the upper right there is the *Nansei Syoto Trench*. The successor to the Mariana Trench in the north outside the image is the *Izu Ogasawara Trench*, which completes the trench frame around the Philippine Plate. The globe image containing the Philippine Plate is shown in Sect. 5.1.1.3.

The dramatic tectonic history is evident from the sequence of ridges and troughs behind the trench arcs, typical of subduction of an oceanic plate in front of another oceanic plate (Sect. 5.2.2). This opposite plate is torn instead of being pushed up, as happens when the opposite plate is continental (Sect. 5.2.1). The most pronounced sequence of ridge- and trough back-arcs known worldwide is revealed in the center of the image behind the Mariana Trench. The first ridge arc, the *East and Middle Marianas Ridge* with the *Isle of Guam* on the left is both a ridge and an overlapping chain of volcanic islands and subaqueous seamounts. It is followed by the *West Mariana Ridge* and separated by the *Mariana Trough*, which appears partly structured by small, nearly parallel ridges and furrows. The next ridge feature is the longest and narrowest of all: the S-curved *Kyusyu-Palau Ridge*. With its northern end it points at *Kyusyu*, the southernmost island of *Japan* (visible in the upper right corner). Finally its southern end runs parallel to the *Palau Trench* to its west. ▶



- ◀ The two large basins on both sides of the *Kyusyu-Palau Ridge* look entirely different: the large *deep* basin in the background, the *Philippine Basin* (which appears shortened due to the perspective depiction) is crossed by its *Central Fracture Zone* and by compact ridges like the *Daito Ridge* and the *Oki-Daito Ridge* in the northern basin triangle. But the shallower *Parece Vela Basin* on the eastern side of the *Kyusyu-Palau Ridge* is subdivided into different halves: an agglomeration of small ridge- and fault-like structures covers the western half vis-à-vis a nearly unstructured smooth part in the eastern foreground. These morphologically different areas which are themselves more or less homogeneous in kind and together make up the *Philippine Plate* are substantially different from the appearance of the sea floor in the foreground east of the *Mariana Trench*. This is the adjacent *Pacific Plate* with the *East Mariana Basin*, irregularly scattered in the south with the *Caroline Seamounts* and in the middle with the *Magellan Seamounts*.

Altogether this relief is like a demonstrator of the peerless capability of the combined gravimetry and bathymetry to reveal large scale features with their specific characteristics. This is decisively supported by the perspective 3D-relief depiction which provides the familiar landscape impression, in contrast to the frequently applied depth contour mapping. The relief image is particularly appropriate to recognize similarities in kind as well as to discriminate even tiny but significant differences. In other words: these large scale depictions, together with high resolution acoustic imagery, are ideal diagnostic tools to study the still unknown variety of interacting geodynamic processes of a permanently changing Earth. The reality revealed by the imaging techniques forces and enables the research to develop and to modify model assumptions, which attempt to interpret processes of nearly infinite complexity.

5.2.2.2

The Challenger Deep in the Marianas Trench: The Deepest Place on the Earth's Surface

The Challenger Deep, in the Marianas Trench, is the bathtub-like dent in the middle of the incision. It is the deepest place on the Earth's surface, reaching a maximum depth of about 11 000 m. Depths greater than 10 000 m characterize many *Marianas-type* trenches, where one

oceanic plate is subducting beneath another oceanic plate. Compared to *Chile-type* trenches, formed where an oceanic plate subducts beneath a continental plate (Sect. 5.2.1), the *Marianas-type* trenches are deeper and their walls are both steeper and more symmetrical. Also in contrast to *Chile-type* trenches, there are no valleys filled with sediment from turbidite flows or accretionary wedges composed of sediment. Scars in the inner trench wall formed by subducting seamounts are comparatively rare, and not

Image 5.2.2.2-1.

Challenger Deep looking downward at 25°. Multibeam relief image. Direction of view: 250°. The trench axis is hidden from view by the subducting oceanic plate on the right hand side.

Project: Kaiko survey along Mariana Trench; cruise KR 98-05
Research vessel: *RV Kairei*, Japan
Multibeam system: *L3 Communications* SeaBeam Instruments Inc., type: SeaBeam 2112; frequency: 12 kHz; beamwidth: 2°; 151 beams, fan width used: 140° at 1 500 m, 90° at 11 000 m depth; artificial illumination from the NE, vertical exaggeration: 7
Image ©: Japan Marine Science and Technology Center (JAMSTEC) and Jun Hashimoto, Faculty of Fisheries, Nagasaki University, Japan ■

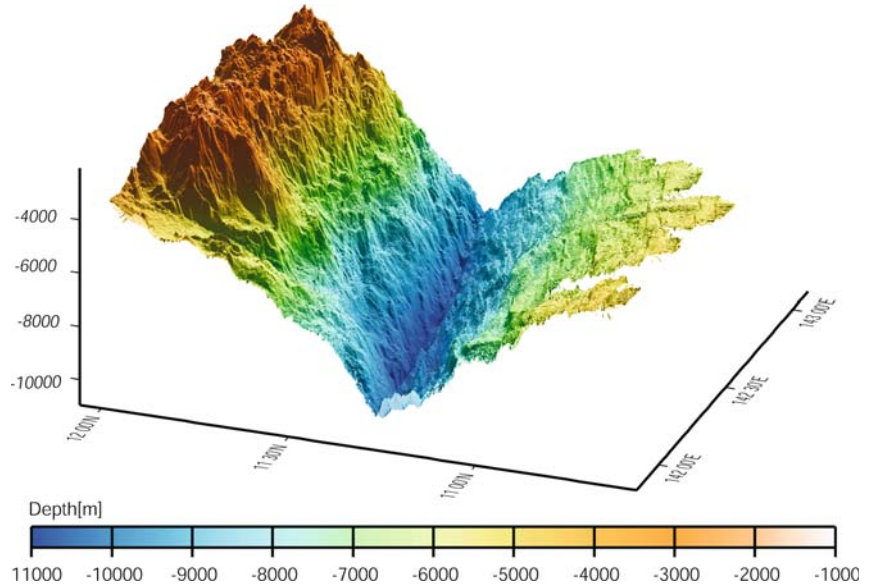


Image 5.2.2.2-2.

Same as Image 5.2.2.2-1, but looking downwards at 40°. The trench axis is now visible with the features described above.

Image documentation: same as for Image 5.2.2.2-1
Depth scale see Image 5.2.2.2-1
Image ©: Japan Marine Science and Technology Center (JAMSTEC) and Jun Hashimoto, Faculty of Fisheries, Nagasaki University, Japan ■

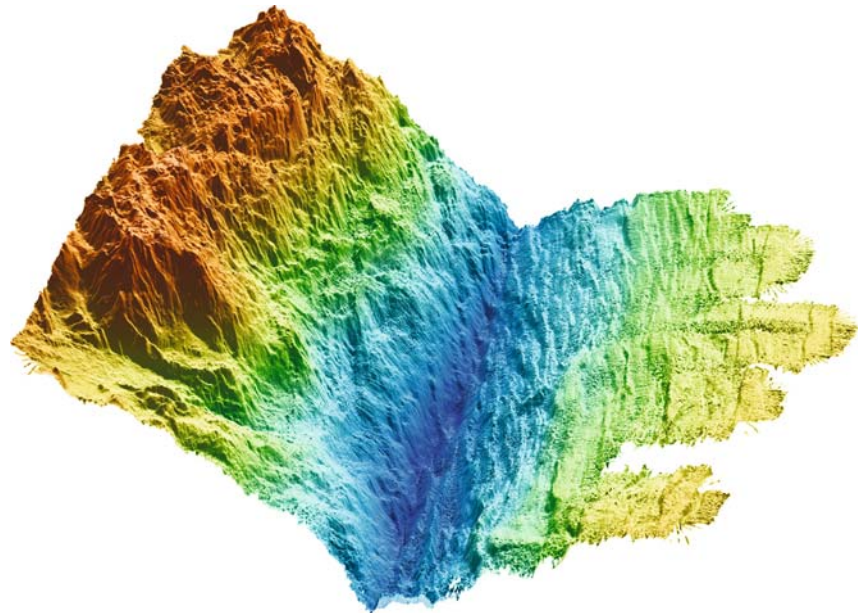


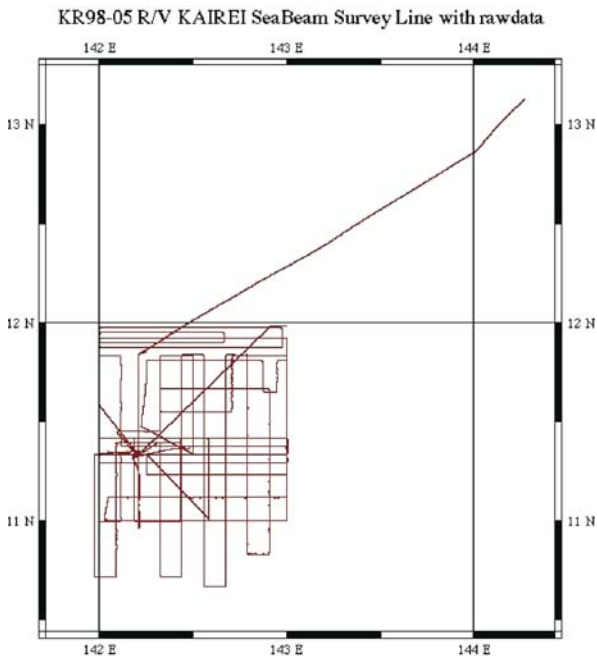
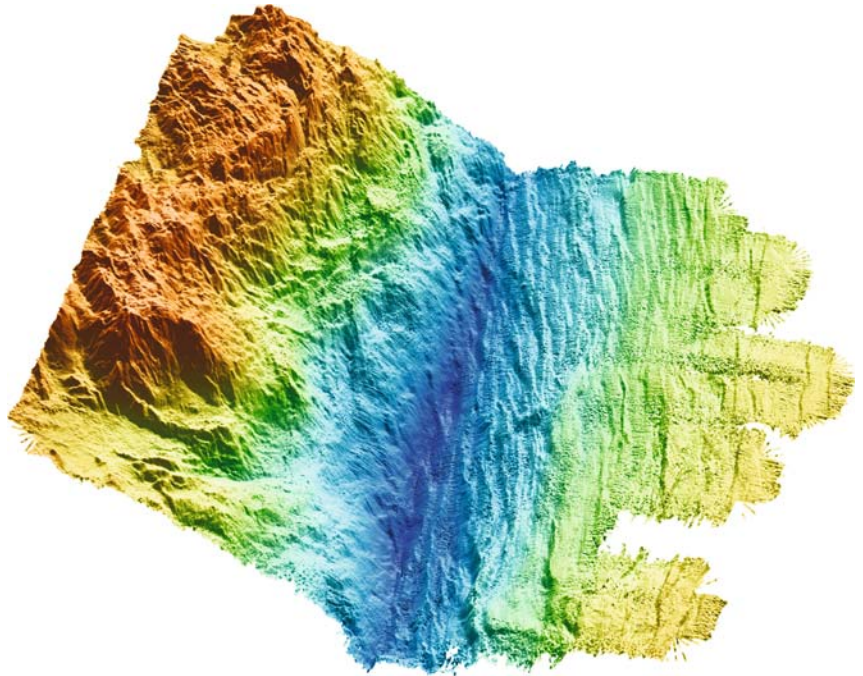
Image 5.2.2.2-3.

Same as Image 5.2.2.2-1, but looking downwards at 60°. The upper plate has a strongly corrugated surface texture that appears to be related to the parallel faults on the lower plate, particular near the trench axis.

Image documentation: same as for Image 5.2.2.2-1

Depth scale see Image 5.2.2.2-1

Image ©: Japan Marine Science and Technology Center (JAMSTEC) and Jun Hashimoto, Faculty of Fisheries, Nagasaki University, Japan ■

**Image 5.2.2.2-4.**

Ground track of the research vessel RV Kairei during the Kaiko survey along the Mariana Trench; KR 98-05 Cruise, 1998

Image ©: Japan Marine Science and Technology Center (JAMSTEC), Japan ■

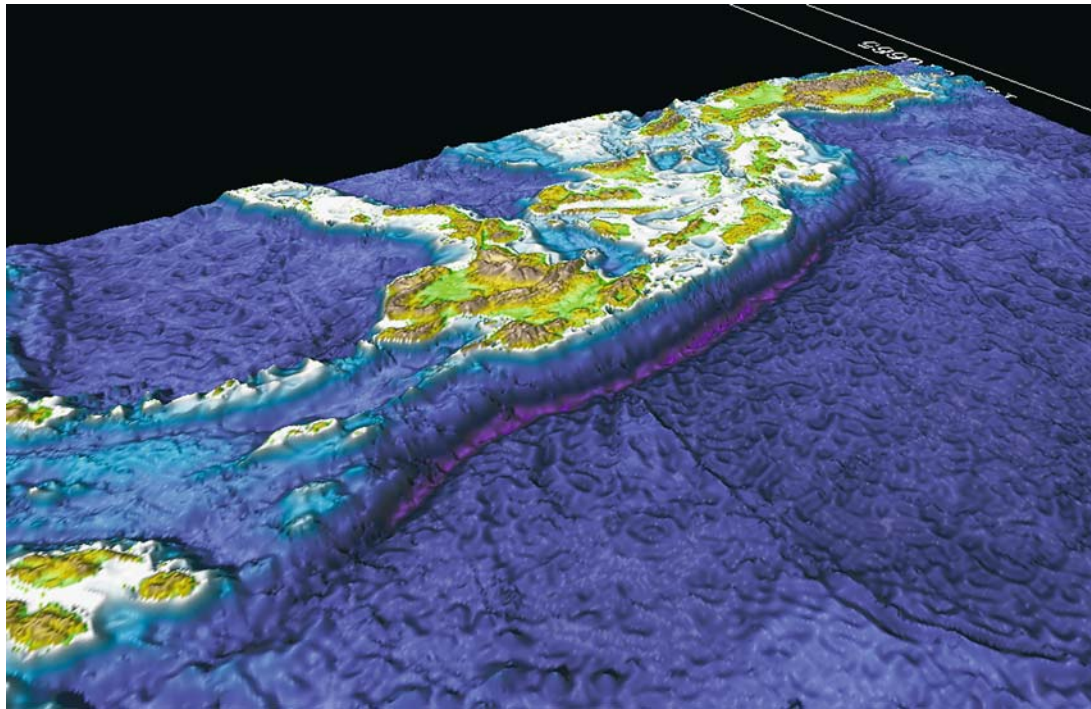
seen in this section. The main feature of the incoming, subducting oceanic plate is a series of faults aligned nearly parallel to the trench axis. There are indications on those images with steeper angles of view that these faults continue into the upper plate towards the north-east. Above 5000 m the surface resembles a sub-merged chain of rocky mountains. The most conspicuous feature is a 40 km long slump on the upper plate in the foreground, with suggestions of possible outflow into the trench.

5.2.2.3***Philippine Trench*****Image 5.2.2.3-1. ▶**

The trench area as a Fledermaus visualization. ETOPO2 data. The image depicts the *Philippine Trench* in total. With its maximum depth of 10 500 m – indicated in brilliant violet – it is one of the three deepest trenches on Earth. This is where the small oceanic *Philippine Plate* which is surrounded entirely by oceanic trenches is subducted under the southernmost part of the large *Eurasian Plate* (Sect. 5.2). This hosts the most extended area of island arcs and archipelagos worldwide. The *Philippines* and *Indonesia* together count about 20 000 islands.

The image covers a panorama of about 2 000 km from the equator on the left side to 18° north on the right side of the relief. Up to now such a large area has not been completely imaged by high resolution multibeam technique. Instead,

the relief presented is a small cut-out derived from the nearly global ETOPO2-data set (Sect. 5.1.1). These gravimetric data, based on satellite altimetry and blended with a minor part of acoustic bathymetry can resolve sea floor structures only larger than 3 km or 2 arc minutes. Despite the limited resolution, the characteristic features of this large trench are clearly visualized: nearly 1 500 km long and conspicuously narrow with a nearly abrupt break of the sea floor and rift-like steep flanks. The trench is not filled in by sediments. Behind the trench the relief of the Philippine



Islands on the right as well as the *Halmahera Islands of Maluku*, Indonesia on the left have been directly imaged by satellite radar and resolved 4 times better, 30 arc seconds. The two basins in the background are the *Sulawesi- (Celebes-)* and the *Sulu Basin*.

The *Philippine Plate* with the *Philippine Basin* in the west – part of it fills the foreground of the Image – is one of the seven smaller plates of the Earth's lithosphere (Sect. 5.2). This plate is the only one surrounded exclusively by subduction zone margins which embody the most dramatic tectonic activities. On its eastern side there is the deepest incision into the surface of our planet: the *Marianas Trench* with 11 000 m depth (Sect. 5.2.2) where the *Pacific Plate* is subducted under the *Philippine Plate*. On its western side the *Philippine Plate* is itself subducted under the *Eurasian Plate*. The globe depiction (Sect. 5.1.1.3) reveals these relief features in their true geospatial relationship. Both sides of subduction zone margins of the *Philippine Plate* are thus part of the infamous *Pacific Ring of Fire* with its concentrated volcanism and earthquakes along the chain of trenches. Simplifying, one could say: the *Philippine Plate* subdivides the western side of the *Pacific Ring of Fire* and combines both ring sections at its south again. The *Pacific Ring of Fire* then leads over to a western side arm which is the *Java Trench*, south of the island arcs of Indonesia and continues with interruptions along the northern and eastern margin of the *Australian Plate*.

Image ©: Larry Mayer, CCOM, USA ■

Box 5.2.2.3-1. Orange peel texture

Those who are familiar with sea floor morphology based on satellite altimetry recognize the so-called *orange peel texture*, which is considered partially an artifact, possibly induced by the pattern of satellite orbits (Sect. 5.1) superimposed by real mid-scale gravity anomaly structure caused by density variability. The globe depiction (Sect. 5.1.1.3) reveals also large areas free of orange peel texture, which supports the presumption of density variability. A unequivocal explanation of this structure is still pending.

Box 5.2.2.3-2. Subduction trenches surrounding the *Philippine Plate*

The subduction trenches surrounding the *Philippine Plate* in the west are not exactly of the same type as those in the east. The *Philippine Trench* looks similar to the *Marianas Trench* in the east, which represents the prototype of *subduction of an oceanic plate under another oceanic plate*. But the plate adjacent to the *Philippine Trench* in the west is continental, though with its island chains less abrupt than the West American continental margin, where the coastal mountain chains provide sediment fill of the adjacent subduction zones, the so-called Chile-type trenches (Sect. 5.2.1).

5.2.2.4 Java Trench Area

The *Java-Sunda Trench* area is the main part of the only zone of tectonic plate convergence and subduction in the *Indian Ocean*. This subduction zone, where the *Indo-Australian Plate* is subducted under the *Eurasian Plate* (map of Sect. 5.2; globe of Sect. 5.1.1.4) caused the most devastating tsunami in history on December 26, 2004. It killed presumably over 300 000 people in more than ten countries of the eastern Indian Ocean and beyond. The epicenter area of the earthquake that released the catastrophe is shown in Image 5.2.2.4-2. Its magnitude of 9.0 is one of the highest ever recorded (table). This giant tsunami had several, though less far reaching predecessors of lower magnitude along the subduction zone of the Indian Ocean; the last was released by an earthquake of magnitude 7.8 east of the island of *Flores* in December 1992 when about 1 700 people lost their lives. *Flores* is the most eastern island visible in the *Indonesian Island Arc* on the right edge of Image 5.2.2.4-1, north of the Java Trench.

Only eight earthquakes worldwide are known which have caused more victims than the Tsunami off Sumatra in 2004. Table 5.2.2.4-1 does not distinguish between the victims of earthquakes and tsunamis of the earlier catastrophes. The published numbers of death toll vary according to the historic source.

The magnitude is marked according to the state of seismic technology. Best magnitude values are available since the sixties of the 20th century. Earthquake magnitude varies *logarithmically* with the wave amplitude recorded by seismographs and corrected for decrease with range. Each whole number step in magnitude represents an increase of 10 times in the amplitude of the recorded seismic waves. The energy release per integer increases by a factor of about 30 times. The magnitude 9.0 corresponds to about 32 000 Megatons TNT energy equivalent. The earthquake of the greatest magnitude ever recorded was off Chile in 1960 with a magnitude of 9.6. The resulting tsunami caused a death toll of 2 000 in Chile and of 200 in Japan. The other three of altogether only 5 earthquakes of 9.0 and more recorded were:

- Alaska 1964: 9.2
- Alaska 1957: 9.1
- Kamchatka 1952: 9.0

Table 5.2.2.4-1. Earthquakes worldwide which have caused more victims than the Tsunami off Sumatra in 2004

Year	Magnitude	Victims	Area
2004	9.0	160 000 ^a	West coast off northern Sumatra
1976	6.3	255 000	Tangshan, China
1927	8.3	200 000	Qinghai, China
1920	8.6	200 000	Gansu and Shaanxi, China
1780		200 000	Iran
1737		300 000	Calcutta, India
1556		830 000	Shansi Province, China
1183		230 000	Aleppo, Syria
856		200 000	Damghan, Iran

Source: BGR, Hannover and Bergen University.

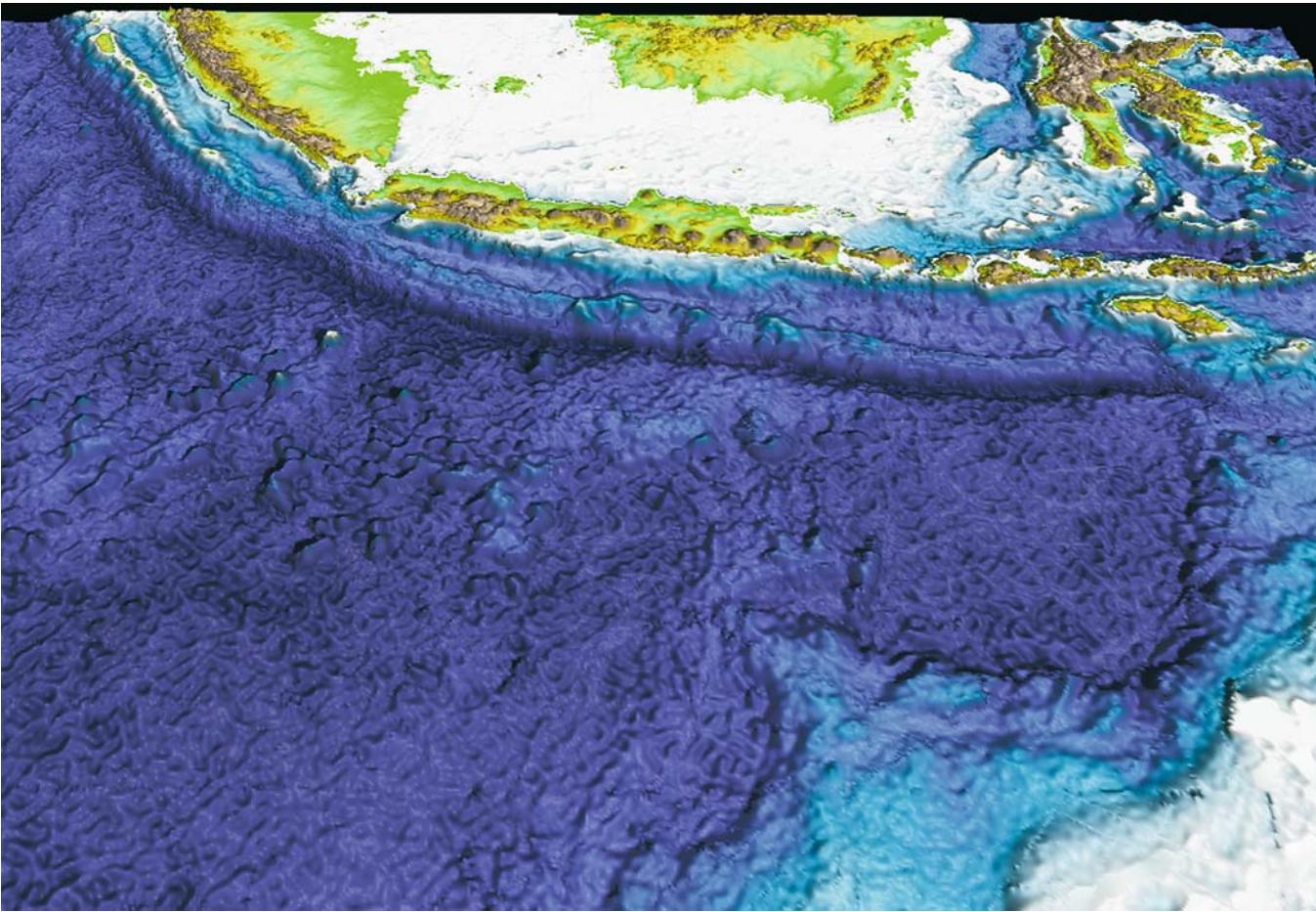
^aState of knowledge: January 2005.

Image 5.2.2.4-1. ►

The Java Trench. ETOPO2 data. The sea floor relief covered by the image is about 2 200 km wide and is derived from the global data set of blended satellite altimetry and acoustic bathymetry named ETOPO2 (Sect. 5.1). The relief shows the Java Trench south of the *Indonesian Island Arc* with the east of the Indian Ocean in the foreground. There is no high resolution multibeam bathymetry data available, covering this region; the image shown is resolved by the 3-km grid of ETOPO2. The view over the globe centered on the Indian Ocean is presented in Sect. 5.1.1.4.

With its maximum depth of 7 550 m the *Java Trench* is considerably shallower than the main subduction trenches of 10 000 m and more of the western *Pacific* around the *Philippine Plate* (Sect. 5.2.2.1). But there is a seeming similarity in the topographic features between the Java Trench area and the famous *Mariana Trench*, the name-giving prototype of *subduction of an oceanic plate under another oceanic plate* (Sect. 5.2.2.1). The similarity concerns the arc shaped formation of island chains, ridges and troughs: Between the *Java Trench* and the main island arc behind, with *Sumatra*, *Java*, *Flores*, and *Timor* as the most well known islands, there is a long trough system with the Sunda trough in the middle followed by a parallel ridge chain. This is the *Mentawai Ridge* with its small islands in the west followed by the *Java Ridge* towards the east.

This outward similarity in the arc-shaped topography could suggest a similarity in the type of subduction. We recall: such back arc formations are formed when the oceanic plate sinks faster into the trench at a *steep angle* than new sea floor can be produced by the mid-ocean ridge on the



opposite side of the plate. Thus the trench is forced to migrate out into the ocean. This tears the overriding plate and even tears it apart, which forms back-arc basins and ridges, typical of the Mariana-type margins in the western Pacific. However, similar ridge- and trough formations can occur also, when accretionary wedges are formed by stripped-off sediments during plate subduction at the trench (Sect. 5.2.9). Accretionary wedges occur in particular at subduction trenches of the Chile type with an *oceanic plate subducting under a continental plate* (Sect. 5.2.1).

The present preoccupying question however, concerns plate margin features regarding *the potential of tsunami generating earthquakes* which are particularly feared because of their far-reaching impact. Unlike earthquakes on land, tsunamis undergo only little propagation loss in the deep ocean and can destroy coastal areas far away from the epicenter of the generating earthquake. According to the epicenter distribution of 299 tsunamis worldwide since 1900, these devastating events occur nearly exclusively in

zones of plate subduction and are concentrated along the *Pacific Ring of Fire* (Sect. 5.1.1.2) with *Japan* as a focal area. Remarkably, almost none have been recorded so far near the deepest trench on Earth, the Mariana Trench, but several were recorded along the subduction zone in the Indian Ocean, even in the north, where the giant tsunami occurred and where the Sunda Trench appears inconspicuous compared to the adjacent Java Trench. The presumably decisive feature or indicator of the tsunami generating potential of a subduction zone is much less obvious than the depth of a trench and unfortunately it is not an exclusive criterion. The next image with the epicenter area of the December 2004 catastrophe illustrates this problem of topographic evidence.

Color scale: same as for the Mariana Trench (Sect. 5.2.2.1)
Image ©: Larry Mayer, CCOM, USA; based on the data set of the Sandwell and Smith predicted topography data from NGDC ■

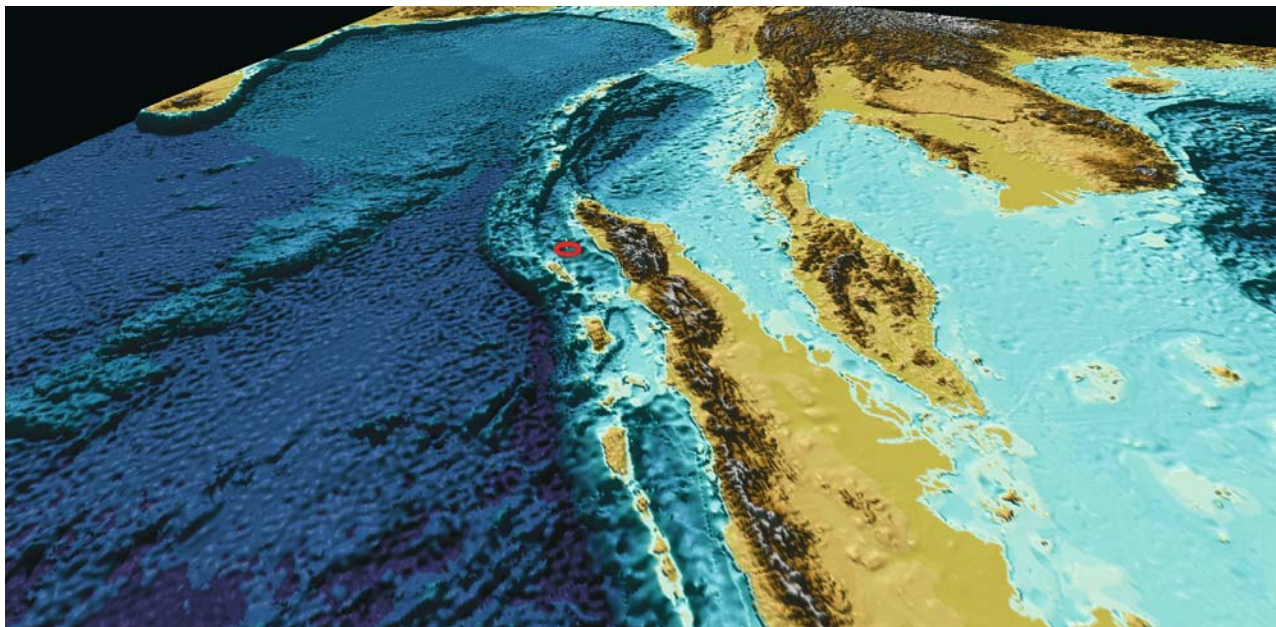


Image 5.2.2.4-2. The area of the *Giant Tsunami of December, 2004*. ETOPO2 data. The epicenter of the earthquake of the exceptionally high magnitude of 9.0 is situated inside the trough as indicated between the northern edge of *Sumatra* and the small island of *Simeulue*, one member of the chain of islands next to the trench. Neither this trough relief reveals anything unusual nor does the comparatively moderate depth of the *Sunda Trench* of less than 5 000 m, the shallower sister of the conspicuous, adjacent *Java-Trench* southeast of it. The existing records of earthquakes of more than magnitude 5.5 in the *Sumatra* area since 1970 have clearly shown that their great majority, including the epicenter of the *Giant Tsunami*, occurred within the shallow strip between the coastline of *Sumatra* and the adjacent subduction trench rim; in other words: *they occurred on the edge of the overriding plate!*

Earthquakes below magnitude 7 don't normally release tsunamis of destruction potential because the energy turnover is not sufficient. To generate a giant wave, the magnitude of the earthquake is only a necessary prerequisite, however. The additional criterion is the size of the displaced net volume and its direction and speed of motion. A shallow epicenter such as that of the *Sumatra* event of about 7 km depth causes a less damped sea surface displacement than a deeper one. A mere horizontal dislocation of the sea floor, such as a pure *strike slip fault* motion (Sect. 5.2.5) without a component of elevation would not generate a wave of the tsunami type. However, if a nearly horizontal motion moves a large volume like a major slide of sediments as happened off the coast of *Norway* (Sect. 5.3.1), a giant wave will be generated. The most efficient mechanism of *Tsunami* generation is certainly the sudden elevation of a large area of the sea floor. It is this fast uplift that produces the volume displacement which cannot be compensated rapidly by an induced flow of the surrounding water. The water column above is elevated as an entity and represents the energy which is transformed into the tsunami.

The physics of such an uplift is understood as the sudden release of tension in the overriding plate, built up by having been bent downward by the subducting plate: Both plates with their irregular surfaces stick together for a long time while the lower plate is slowly drawn into the subduction zone in this area at a shallow angle of about 10° and by about 6 cm per year. The driving force of motion as explained in Sect. 5.2.1 and 5.2.2 is the weight of the subducting plate with its higher density than the hot interior of the Earth's mantle. Once the tension has grown to the local critical value, the edge of the upper plate slips forward and snaps upward. In reaction, the subducting plate will also move, much more than its annual rate. But: it is the vertical component of the motion of perhaps a few meters in this case that causes the tsunami, even if it is usually much less than the horizontal shift.

The provisional reconstruction by seismologists of the sea floor dynamics generating the *Giant Tsunami of Sumatra* was based mainly on the data from remote seismic monitoring stations. Surprisingly, the tsunami did not propagate from the epicenter in concentric wavefronts as from a point source. Instead, the tsunami origin is considered to have acted more like a line source with directionality in an east-west direction, devastating the coastal area of *Sri Lanka* more than that of *Bangladesh*. In fact, the epicenter of the earthquake caused sudden internal fractures in a northward direction along the *Nicobar* and *Andaman* Island chain. Altogether about four such fractures with a total length of over 1 000 km were gener-

ated within a short time. The speed of propagation of such fractures is typically about 3 km s^{-1} . It is about the speed of a propagating rupture inside a rock. The main fracture containing the bulk of energy is estimated to be some 400 km in length. The width of the fracture zone involved is estimated to be about 100 km. Regarding the tsunami wave period of several hours, the displacement caused by all fractures happened nearly simultaneously which means: the Giant Tsunami acted as an energy integrator.

Color scale: same as for the globe in Sect. 5.1.1.4; depth exaggeration: same as for the preceding image
Seismic information: personal communication, Manfred Henger, BGR; Dirk Kläschen, IfM-Geomar, Germany; USGS, BGR, NOAA, and Bergen University internet publications
Image ©: Larry Mayer, CCOM, USA; based on the data set of the Sandwell and Smith predicted topography data from NGDC ■

5.2.2.5

Macquarie Ridge Complex (MRC)

The *Macquarie Ridge Complex (MRC)* is the conspicuous sea-floor formation of more than 1 500 km length in the south polar globe Image 5.1.1.6-1, adjacent to *New Zealand* in the south-west. The MRC is one of the most complex tectonic plate margins of the globe with essentially all three types of margin present in transition. The only elevation exposed above sea level is the small *Macquarie Island*, the southernmost island of *Australia*, just 34 km long and 5 km wide, approximately halfway between Australia and the Antarctic continent, classified as a *World Heritage Site*: The island hosts about three million Royal Penguins, virtually the entire world population and the world's

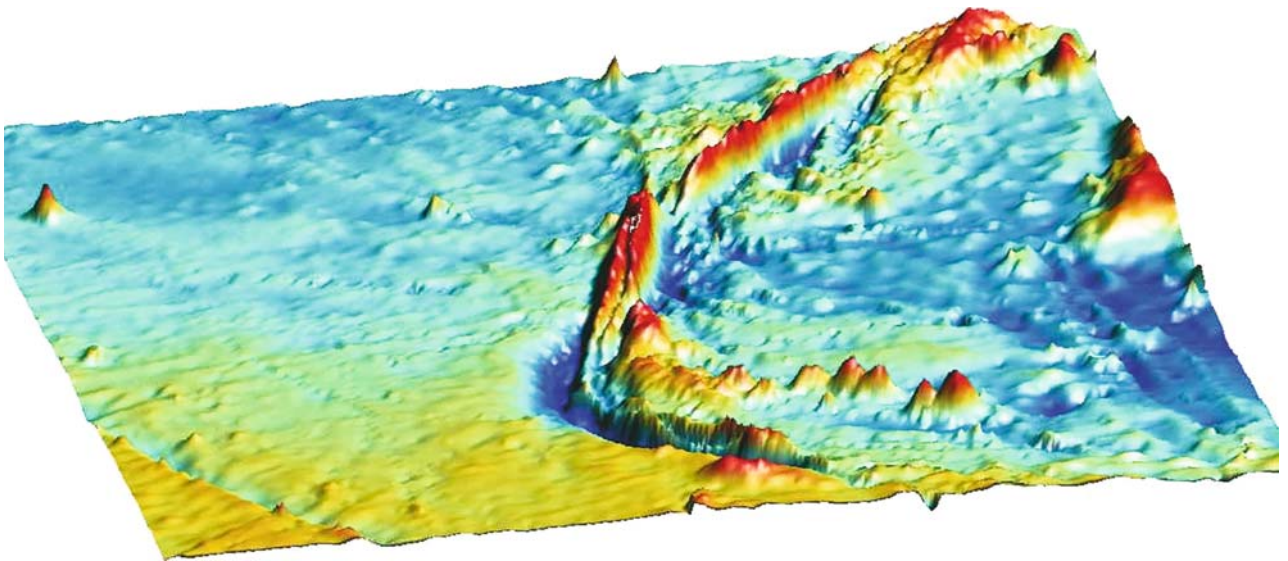


Image 5.2.2.5-1. The Macquarie Ridge and Hjord Trench. Overview of the relief, various data sources. The trench of 6 700 m maximum depth with its arched shape and the southern Macquarie Ridge, looking like a back arc with its central valley are reminiscent of a *Marianas*-type plate convergence (Sect. 5.2.2). Going north beyond the end of the *Hjord Trench* the Macquarie Ridge which rises about 4 000 m above the abyssal plain surprisingly still has an axial valley such as known from the Mid-Atlantic Ridge, where it indicates a slow spreading zone (Sect. 5.2.3). Here, north of Hjord, the tectonic regime of the MRC is considered instead to be dominantly of the *strike slip type* (Sect. 5.2.5), with differential motion *along* the margin rather than a *diverging* or *converging* motion.

However, geodynamic interpretation has to take more features into account than the obvious clues of the outer relief. Combined high resolution multibeam bathymetry, seismic profiling, gravimetry, and magnetometry together indicate that the crest of the southern MRC along the Hjord region is characterized by *sea-floor spreading*.

Project: Australia Environment Survey 2 (AUSTREA 2); responsible: Geoscience Australia; purpose: Geoscientific exploration and Australian marine jurisdiction regarding claims on Exclusive Economic Zones (EEZ) and Extended Continental Shelf (ECS); year of survey: 2000

Survey vessel: *RV L'Atalante*, Ifremer, France; Multibeam system: Simrad EM12D; 11/12 kHz, 150° total beamwidth, 162 beams
Image ©: Geoscience Australia, Canberra ■

fourth largest colony of King Penguins of some 100 000 birds.

There are several remarkable tectonic peculiarities of the Macquarie Ridge Complex, The MRC is the southernmost portion of the active tectonic plate boundary between the *Indo-Australian Plate* and the *Pacific Plate* (mapped in Sect. 5.2). It ends with the *Hjort Trench and Ridge* pair at the triple plate-junction with the *Antarctic Plate* at about 60° S, the latitude defining the *Southern*

Ocean southwards. This Hjort region is also the southernmost plate convergence zone on Earth – apart from the *South Sandwich Trench* of the small *Scotia Plate* (Sect. 5.5.1), on the opposite side of Antarctica as shown in the polar globe Image 5.1.1.6-1. The Hjort Trench is moreover an unusual tectonic scenario: it is the younger Indo-Australian Plate that is subducted under the older Pacific Plate. Typically the older plate of higher density is subducted under the lighter, younger one (Sect. 5.2.2).

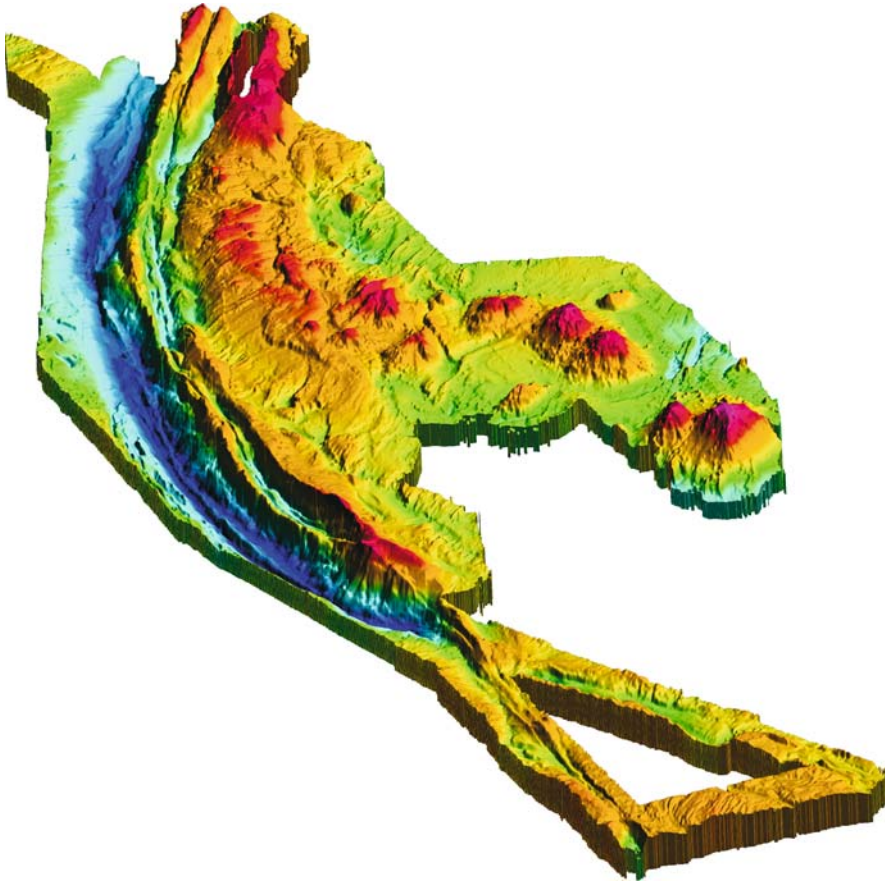


Image 5.2.2.5-2.

The Hjort Trench and Ridge. Multi-beam image. Seamounts and volcanic edifices visible within the spreading fabric east of the trench highlight subduction-related volcanism. Altogether, the tectonic clues in the south appear to support the interpretation that this is the plate convergence type known from the eastern Philippine Plate with the Marianas Trench, which is also combined with spreading of the overriding plate. But here the process is complicated by the neighborhood of the *northern* Macquarie Ridge Complex. For instance: the axial valley dividing the Hjort Ridge is probably the southerly extension of active strike-slip faulting from the north. Thus, in the Hjort region, strain may be partitioned between major thrust and strike slip faults. It is a complex superposition of deformation forces indeed and possibly an ongoing fundamental process of transition of tectonic margin type.

A pronounced sea-floor relief in key areas of ocean currents can exert a steering function directing the flow. Similar to the ridge complex in

the North Atlantic which controls flow features of the Gulf Stream (Sect. 6.1.1), the Macquarie Ridge Complex with its crest of less than 400 m below sea level strongly influences the intensity and circulation pattern of ocean currents south of New Zealand. Above all, it represents a major barrier to the *Antarctic Circumpolar Current*, the Earth's largest ocean current, and thus to north-flowing Antarctic Bottom Water. Evidence of the Macquarie Ridge influence on the transport of water masses was provided mainly by various acoustic survey techniques, revealing the traces of flow-induced sediment erosion and re-sedimentation.

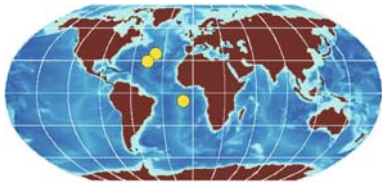
Project: AUSTREA-2; responsible: Geoscience Australia; purpose: Geoscientific exploration and Australian marine jurisdiction regarding claims on Exclusive Economic Zone (EEZ) and Extended Continental Shelf (ECS); year of survey: 2000

Survey vessel: *RV L'Atalante*, Ifremer, France

Multibeam system: Simrad EM12D; 11/12 kHz, 150° total beamwidth, 162 beams

Image ©: Geoscience Australia, Canberra ■

5.2.3 Mid-Oceanic Ridges, Slow Spreading Type



More than 65% of the Earth's crust is less than 3% the age of the Earth. Most of this crust is hidden from view

in the deep oceans, and is quite different in structure and composition to the more familiar high-standing continental land masses. This oceanic crust is continually being generated – and destroyed – on the sea floor at a rate of several cm per year. Generation occurs by the cooling and crystallization of ascending magma along a 70 000 km long system of 2–3 km high ridges that subdivide the oceans. The first ridge to be discovered was the *Mid-Atlantic Ridge (MAR)*, which passes nearly through the middle of the Atlantic Ocean. In consequence such ridges became known as *mid-ocean ridges*, and although the term *mid-ocean ridge* remains in common use, only the MAR actually passes through the middle of an ocean. The network of mid-ocean ridges is shown completely on the globe depiction series of Sect. 5.1.1.1 to 5.1.1.6 and is indicated in the overview map of Sect. 5.2. In the largest ocean, the Pacific, the *East Pacific Rise (EPR)* proceeds south from the Gulf of California past central and South America, where it proceeds to the southwest and eventually turns west as the Pacific–Antarctic Ridge. Passing south of Australia, it then turns northwest into the Indian Ocean as the Southeast Indian Ridge. The ridge splits in the center of the Indian Ocean, with one arm continuing northwest into the Red Sea where it terminates, while the other heads southwest and eventually joins the MAR to the south of Africa. The *mid-ocean ridges*, the *spreading centers* of the sea floor where new crust is created, are thus interconnected like the world's oceans.

Many milestones in ocean research have featured the *Mid-Atlantic Ridge*. The first known map of a major ocean, the *Maury Map* of the North Atlantic, was published in the mid-19th century and already includes part of the most significant contours (Chap. 1). The last bathymetric map of the Atlantic before the modern era of echo sounding is admirable for its details, and was published in 1912. Later, the Atlantic was the subject of the first echographic mapping across an entire ocean, with a major highlight being 13 cross-

ings of the MAR (Sect. 2.11). More recently, high resolution 3D-acoustic images of the MAR achieve grid widths of 3 arc seconds or less. This is the standard resolution for modern multibeam imaging (Sect. 4.2.3) of the deep ocean floor by surface vessels, and can be further improved by using deep towed arrays or autonomous deep diving devices (Sect. 7.4).

The *mid-ocean ridges* are functional elements of the global plate tectonic system (Sect. 5.2) and represent one type of active plate margin. The other main types are subduction zones where sea floor descends into the Earth's interior (Sect. 5.2.1, 5.2.2), and strike slip faults where one plate slides past another (Sect. 5.2.5). The *mid-ocean ridges* are sites of earthquake activity and volcanism, but the earthquakes are weaker and the eruptions less dramatic – although more common – than those associated with subduction zones. When they were first recognized in the fifties and sixties, it was assumed that *mid-ocean ridges* were the driving force behind plate tectonics and pushed the plates along. However, advanced acoustic imagery of the ocean floor and its structure combined with detailed geophysical studies now suggest the ridges play a passive role. Instead, the tectonic plates are drawn into subduction zones as the oceanic crust becomes older, colder and thicker, and eventually subsides back into the Earth. This causes tension in the plates, which sometimes split or tear apart. New magma erupts along the tear, and if the plate continues to separate then a *mid-ocean ridge* can form.

The cross-section of a *mid-ocean ridge* varies, mainly depending upon the spreading rate. Slow spreading rates of 1–5 cm per year – the slow MAR spreads about 1 cm per year – lead to deep axial valleys that run along the center of the ridge and can descend almost to the level of the surrounding sea floor. At medium spreading rates, the axial valley is shallower. Finally, at fast spreading rates of more than 10 cm per year – the fast EPR spreads at that speed – the axial valley is replaced by a central plateau or broad dome. Furthermore, the slope of the outer ridge flanks is more gentle at faster spreading rates and the saw tooth-like flank faults are less pronounced.

One reason for the slow spreading of the MAR could be that only two relatively short subduction zones exist on the margins of the Atlantic (Sect. 5.2). In this model, spreading in the Atlantic would depend in part upon the continued motion of the neighboring plates in response to subduction zones on their far sides. It is important to note that sea-floor spreading at *mid-ocean ridges* is not a continuous process on human timescales.

For example, deep fractures and crevices can develop along the axial valleys of the MAR and may persist for several hundreds of years before being buried by the next lava eruption.

When looking at the relief of the MAR on the globe (Sect. 5.1.1.1), the most dramatic feature is not the nar-

row axial valley along the center of the ridge but rather the large number of transform faults extending from hundreds to more than 1 000 km in length along lines of nearly constant latitude. The ridge axis is displaced at each of these faults, which are mostly less than 100 km apart, and the maximum offsets of 1 000 km and more occur at

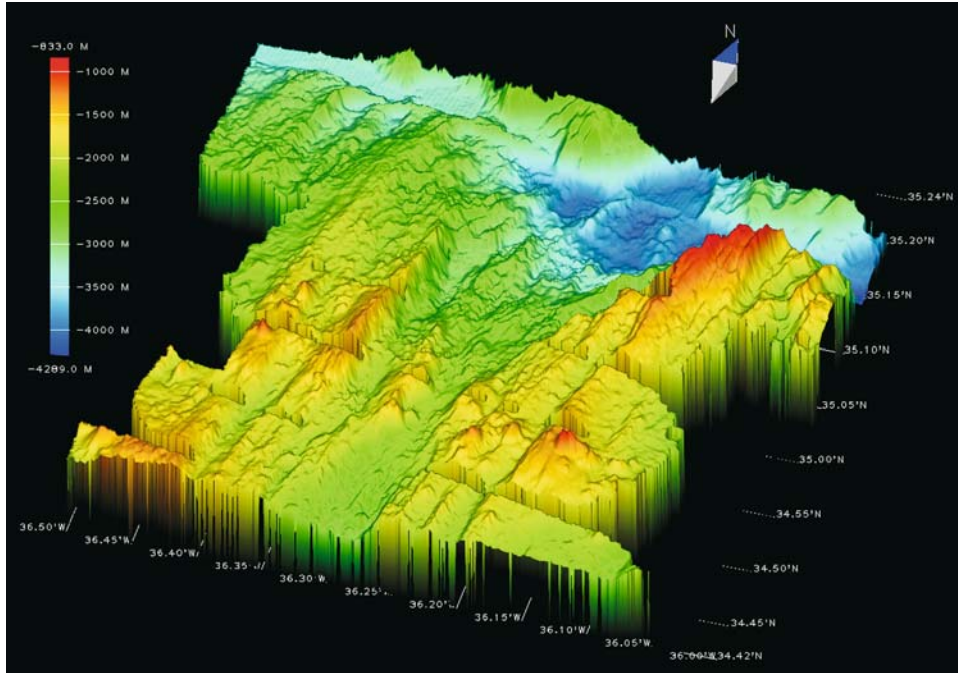


Image 5.2.3.1-1. Northern segment with part of the *Oceanographer Transform Fault*. 3D-multi-beam, shaded relief image. The northern segment contains part of the *Oceanographer Transform Fault* and *Fracture Zone* at the top of the image. Here, the sea floor ascends from 4 000 m depth to only 1 000 m of the eastern ridge crest within about 10 km distance. The adjacent shallower formation south of the depression branches directly athwart from the transform fault and shows the typical central trench of a slowly spreading oceanic ridge but with a median ridge at the axis. This ridge of nearly 1 000 m relief height is considered part of the youngest formation of this segment of the *Mid-Atlantic Ridge*.

The origin of the axial ridge is attributed to the last one million years. The bulges of extruded magma and the formation of summit volcanoes superimposed on the axial ridge appear like an isolated irregular mountain formation, though on a regional scale. But a description of the central part of the MAR as a trench with steep inner flanks and one young axial ridge, with subsequent volcano formation, would be oversimplifying regarding this segment. In reality one can count several “satellite” ridges off axis and in parallel, presumably also former fissures, closed and built over by overflowing magma. These sub-ridges are crossed athwart by a chain of volcanoes at about 34°53' N, where the image has occasional data gaps on the left. (These strips of data gaps occur nearly every 5 minutes latitude in this image.) Four of the volcano cones reaching up to 1 000 m below sea surface have got names: *Fara* on the west side of the ridge axis and *Claire*, *Christelle* and *Eulalla* on the east. According to magnetic signatures and other indicators these volcanoes were originally built at or near the ridge axis.

Project: FARA-Sigma Cruise, 1991. Second part: OCEANAUT, 1995

Research vessel: *RV Atalante*, France, 1991; *RV Nadir*, France, 1995

Multibeam echosounder: *Simrad*, ERM 12 dual; frequency: 13 kHz, beamwidth: 1.8°, fan width: 150°, overlapping beams spaced at 1°, pitch/roll compensation; Data processing for bathymetry and backscattering intensity, height enhancement: 5 times; Equipment of the deep submersible *Nautile* for bottom sampling, magnetic- and gravity surveying

Image ©: Daniel Bideau, Département Geosciences Marines, IFREMER, Centre de Brest, France ■

low latitudes. Both the number of faults and their displacements are greater north of the equator than to the south. The MAR transform fault pattern is reminiscent of an inelastic tissue torn by regional tensions and shear forces, generating a multiplicity of ruptures. In contrast, the fast spreading EPR is far from conspicuous in the global depiction (Sect. 5.1.1.2) on account of its gentle and smoothly sloping flanks. A key difference is the absence of numerous transform faults offsetting the ridge crest. Transform fault patterns similar to those on the MAR develop on the EPR only where the spreading rate is slower. An example is its northern end. The *mid-ocean ridge* acoustic images shown hereafter are small cut-outs or close-ups either of the very slow spreading MAR (Sect. 5.2.3) or the very fast spreading EPR (Sect. 5.2.4).

Tim J. Worthington, Institut für Geowissenschaften,
Kiel University

5.2.3.1

Mid-Atlantic Ridge, Northern Hemisphere; Cut-out Sections of a Slow Spreading Mid-Ocean Ridge; Feature Comparison of Relief and Backscattering

The *Mid-Atlantic Ridge (MAR)*, known as the most extended and most disrupted ridge formation on Earth (Sect. 5.1.1.1) shows the features of transform faults, of fissures and subsequently emerging magma in various forms, in particular on a small scale and as ongoing processes. The two ridge sections, both about 30° west of *Gibraltar* are only 65 km apart but the 3D-sound images appear to differ in nearly all morphological symptoms visualized. These areas between the *Oceanographer Fracture Zone* and the *Hayes Fracture Zone* were imaged in 1991, both for bathymetry and sea floor reflectivity. This acoustic survey was the morphological guidance for subsequent bottom sam-

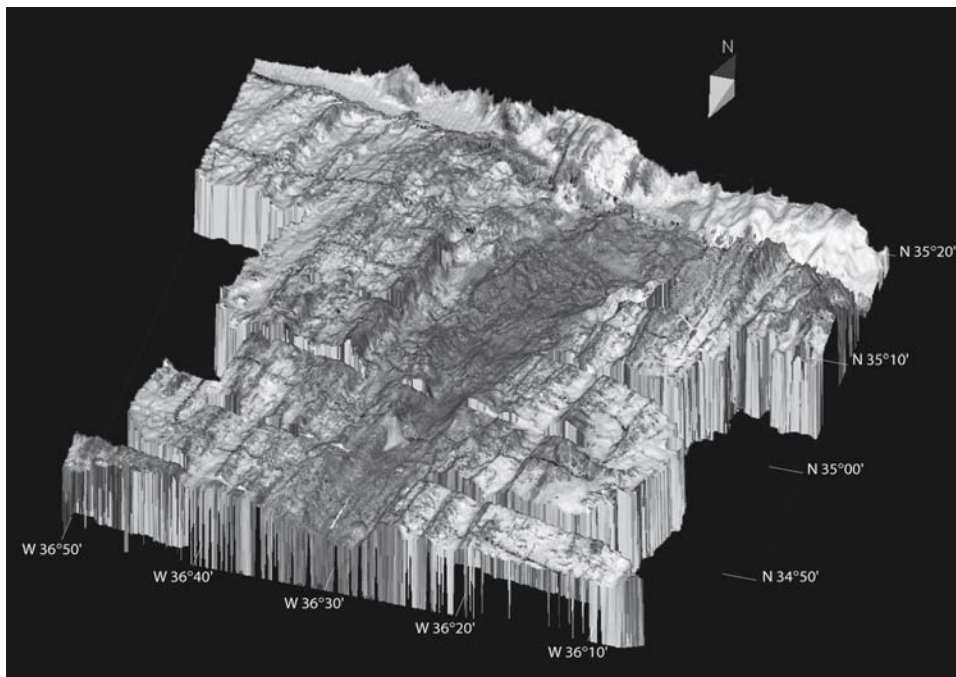


Image 5.2.3.1-2. Same segment as of Image 5.2.3.1-1 but depiction of echo strength of the sea floor. The image visualizes the local echo amplitude superimposed on the shaded bathymetric relief. Here, the dark areas represent *high* reflectivity, or more correctly high backscattering strength, typical of the young basaltic center terrain. The older terrains, in particular north of the *Oceanographer Fracture Zone* at the upper rim of the image, are covered with thick, soft sediment layers of low backscattering strength. The acoustically bright and dark areas are displayed only qualitatively here since the simulated shading of the relief as in Image 5.2.3.1-1 is not removed. The original data set provides quantitative information however.

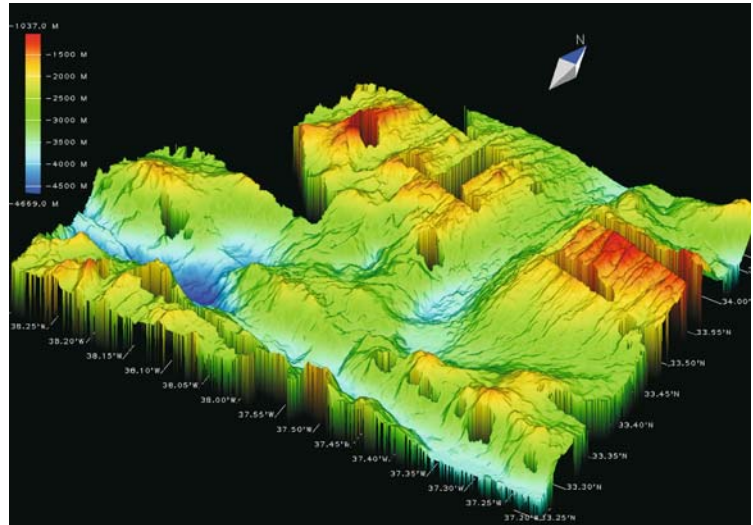
Image documentation: same as for Image 5.2.3.1-1 ■

pling and video close-ups by a deep submersible in 1995 to analyze the mineralogical composition and the tectonic and volcanic processes in kind and age. The comprehensive investigation which included gravity anomaly- and magnetic sensors (Sect. 2.8) onboard the surface vessel for the reconnaissance and dating of fea-

tures demonstrates the effectiveness and research economy of combined acoustic and non acoustic tools. Two further sections demonstrate both the variety of the MAR as well as the options to visualize features of near ridge axis formations by multibeam and sidescan imaging.

Image 5.2.3.1-3.

Southern segment with part of the Hayes Ridge Transform Intersection. 3D-multibeam, shaded relief image. The predominant feature of this image is the *Hayes Ridge Transform Intersection* in the foreground. It has a maximum depth of 4500 m with a 700 m less deep valley athwart of but not directly connected with the incoming ridge valley. This central trench or rift valley differs conspicuously from the previous image taken only 65 km further north. The trench is significantly narrower without any noticeable secondary ridges or volcano edifices. However, the northern part of the 3000–3500 m deep valley floor and its flanks are structured by a texture of faults parallel to the ridge axis. According to later close-up photography taken by a deep submersible, the deep valley floor is in fact dominated by fissures and faults. Altogether, magma supply on this segment was much less than on the northern segment and the tectonic stretching is obviously predominant, indicated by the trench axis offset of the MAR near the Hayes Ridge Transform Intersection. (Data gaps are obvious without description.)



When looking only at these quite different segments, each of about 500 km² size, one could not imagine the entire large scale structure of the Mid-Atlantic Ridge, as shown in the globe image of Sect. 5.1.1.1. This comparison illustrates once more the importance of combining large scale imaging of the gross features of plate tectonics with high resolution acoustic imaging to investigate the geodynamic processes in detail.

Image documentation: same as for Image 5.2.3.1-1 ■

Image 5.2.3.1-4.

Same segment as of Image 5.2.3.1-3 but depiction of echo strength of the sea floor. Similar to Image 5.2.3.1-2, only the trace of the younger, basaltic floor of the ridge trench shows the strongest backscattering, depicted dark. The *Hayes Ridge Transform Intersection* in the foreground is definitely a weak scatterer, which means it is partially filled with thick, soft sediment. The high elevation depicted dark at the upper corner of this image could possibly be due to flank reflection.

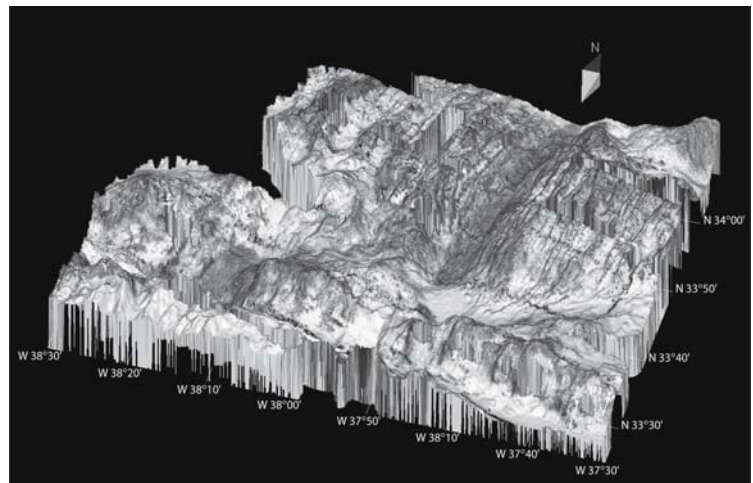


Image documentation: same as for Image 5.2.3.1-1 ■

5.2.3.2

Mid-Atlantic Ridge, Southern Hemisphere; Relief Details of a Fracture Zone

Image 5.2.3.2-1.

Cut out north of the Ascension Fracture Zone. Multibeam Image. The size of the cut out is about the same as of the preceding image series. Most spectacular is the sharp and strait cut of the fracture at the opposite side of the junction with the valley of the *Mid-Atlantic Ridge (MAR)*. The fracture shown is not a major one with a given name like the Ascension Fracture Zone in the south-west and it is already part of the less extended MAR fault pattern of the southern hemisphere. Nevertheless: the short cut-out of the strait fracture side, reminiscent of a steeply shelving coast, is about 70 km long. The central valley with its typical broadening at the nearly athwart junction with the fracture lacks an axial ridge of younger lava extrusion. This secondary ridge formation appears to begin only where the valley shrinks to its normal width in the south.

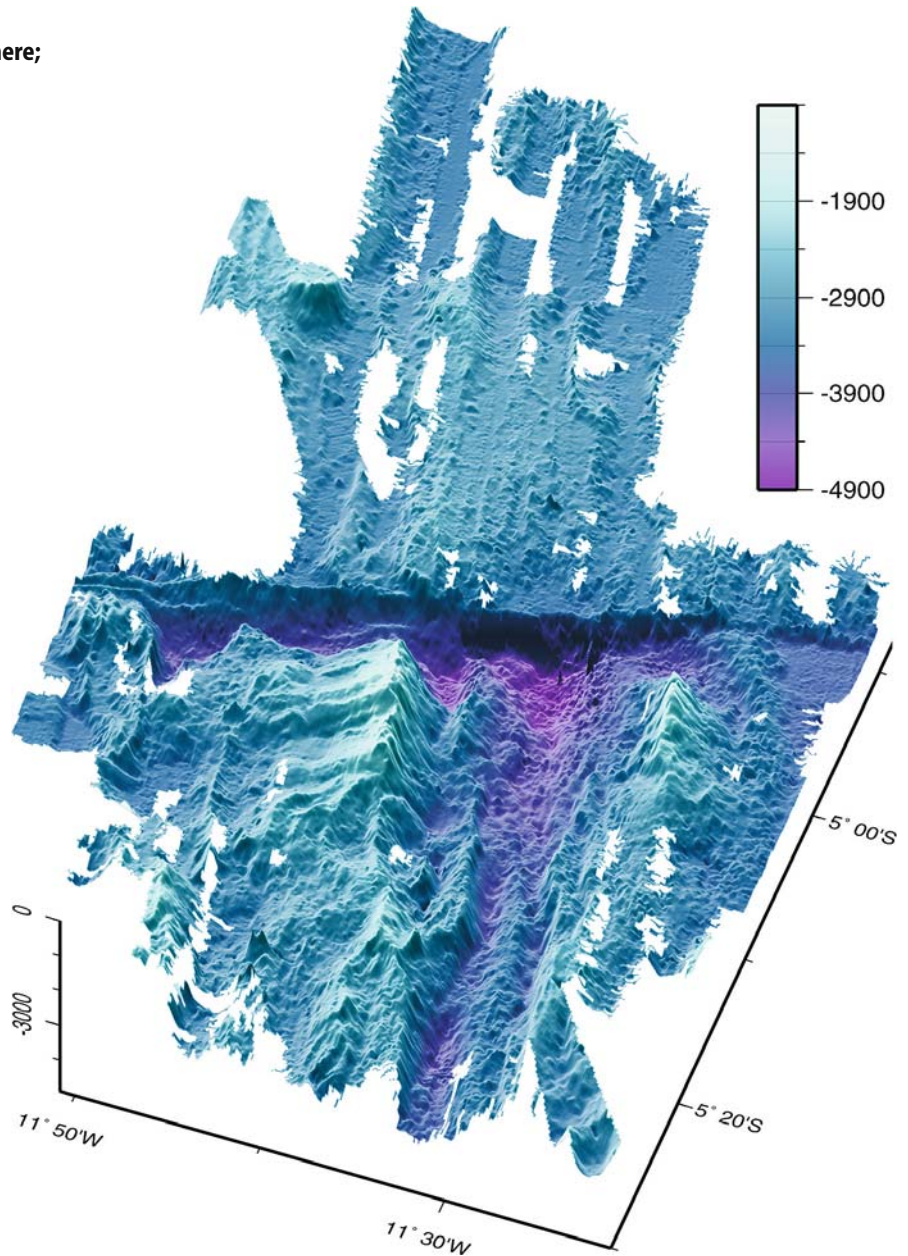
The image shows the asymmetry of the inner and outer flank slopes of both ridge sides particularly clearly near the junction. The valley is framed by the steep walls. The less steep outer flanks don't have any sawtooth-like tension faults, but wrinkles as if compressed along the ridge crest at this area. The southern, irregular rim of the fracture valley shows the strongest depth variations and the steepest slopes. North of the fracture which has offset the former ridge axis by more than a hundred kilometers there is an inconspicuous relief feature which looks like a couple of small ridges, as if continuing the old ridge across the fracture. Moreover, there is a volcano cone topped by a crater on the west side, at the "thumb" of the multibeam scanning pattern, reminiscent of a hand. Such volcanoes are often found where spreading zones are active. The predominating impression of this ridge detail and of the other cut-outs along the MAR is the diversity of structures resulting from enforced sea floor spread. They appear to violate drastically the rules of simplifying models and demonstrate the limits of our present understanding.

Research vessel: *RV Sonne*, Germany; year of survey: 2000

Multibeam echosounder: SIMRAD EM120; 12 kHz, beamwidth: $2 \times 2^\circ$, fan width: 90° or 20 km at 4 km depth

Horizontal resolution/grid width: 100 m, height exaggeration factor: 6, simulated sunlight from north

Image ©: Wilhelm Weinrebe, Geomar, Kiel, Germany ■



5.2.3.3

**Mid-Atlantic Ridge, Northern Hemisphere;
Combined Multibeam and Sidescan Image of a Central
Valley Segment with a Volcano**

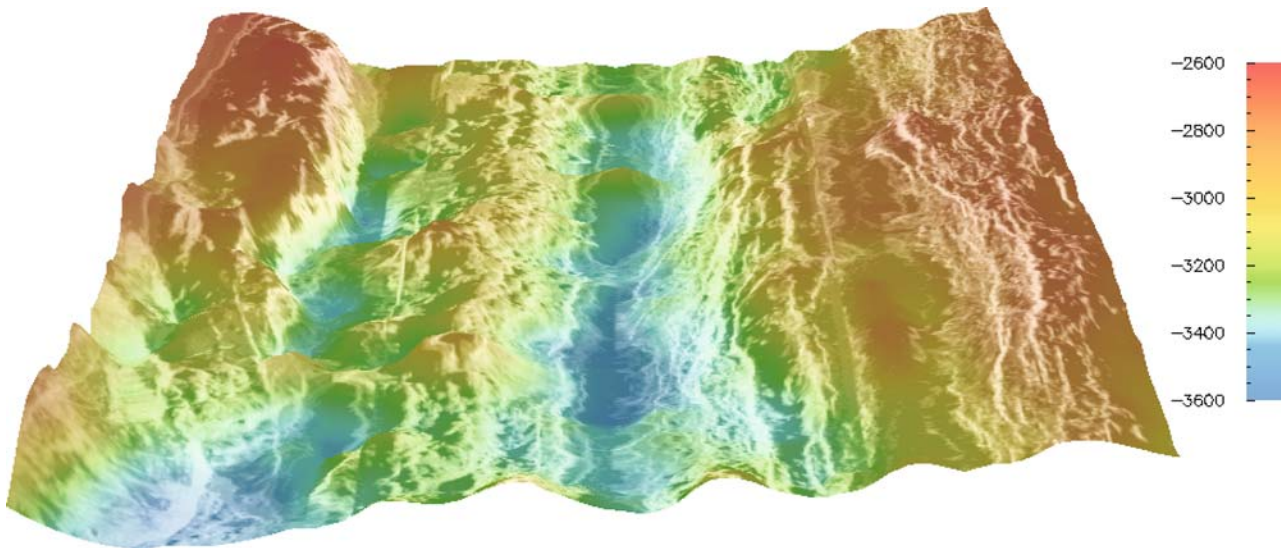


Image 5.2.3.3-1.

The central valley of the *Mid-Atlantic Ridge* at 29° N. 3D-multibeam image draped with the sidescan image. The cut-out image shows both the bathymetry and the texture of the median valley of the *Mid-Atlantic Ridge*. The MAR is one of the slowest sea floor spreading zones on Earth with a spreading rate of 1–5 cm per year. Its spreading processes are only partially understood as yet. One of the necessary steps to reveal the mechanisms and features of magma extrusion at the MAR is a systematic acquisition of the morphologic types of the youngest part of the MAR-formation. This is the nearly omnipresent *axial ridge* of the MAR, subdividing the median valley into two troughs. It is considered evident that the axial ridge is the result of magma overflow at fissures caused by the tensions that force the tectonic plates to diverge (Sect. 5.2.1, 5.2.2). It is unclear however whether the magma extrudes from separate or interconnected sources and how the fissures are filled.

From earlier bathymetric surveys it was known that the axial ridge is superimposed by seamounts which were thought to be volcanoes. But the multibeam bathymetry was insufficient to resolve the morphologic features necessary to classify the types of magma extrusion. The solution was to combine shipborne multibeam 3D-imaging of 100 m grid width with deep towed sidescan 2D-imaging of 10 m pixel size by draping the latter upon the former (Sect. 6.2.1). The color scale identifies the bathymetry and the shadow structure characterizes the morphology. Bright areas indicate strong backscattering; dark ar-

reas indicate an acoustic shadow or attenuated return from sediment-covered terrain (Images 5.2.3.1-2, 5.2.3.1-4). This depiction method is fundamentally different from shadowing the bathymetric relief by simulated sunlight to achieve the aerial photograph appearance. In reality both partial images were not generated during the same survey and each is a mosaic of stripes according to the individual swath width. Thus the superposition was a challenge to scale- and feature adjustment. The result is demonstrated by the cut-out of 13 × 15 km² with two volcanoes on the axial ridge.

Some significant results derived from this combined acoustic visualization should be mentioned: the multitude of the seamounts of 0.5 to 3 km in diameter and 50 to 300 m height identified in the inner valley from previously collected multibeam bathymetry have volcanic constructions. The average volcano density found along the valley between 25° and 29° N is about one per 10 km². 83% of the volcanoes have a hummocky surface reminiscent of mini craters known from the moon. In addition to near circular seamounts small volcanic ridges are abundant in the area which are not seen in the bathymetry. In the less frequent areas without an axial volcanic ridge seamounts are scattered across the valley floor. The inventory of the magmatic features leads to the conclusion that the MAR seamounts are fed by small ephemeral magma pockets rather than by single long lived magma chambers as assumed for the fast spreading East Pacific Ridge (Sect. 5.2.4).

Image documentation: same as for Image 5.2.3.3-2 ■

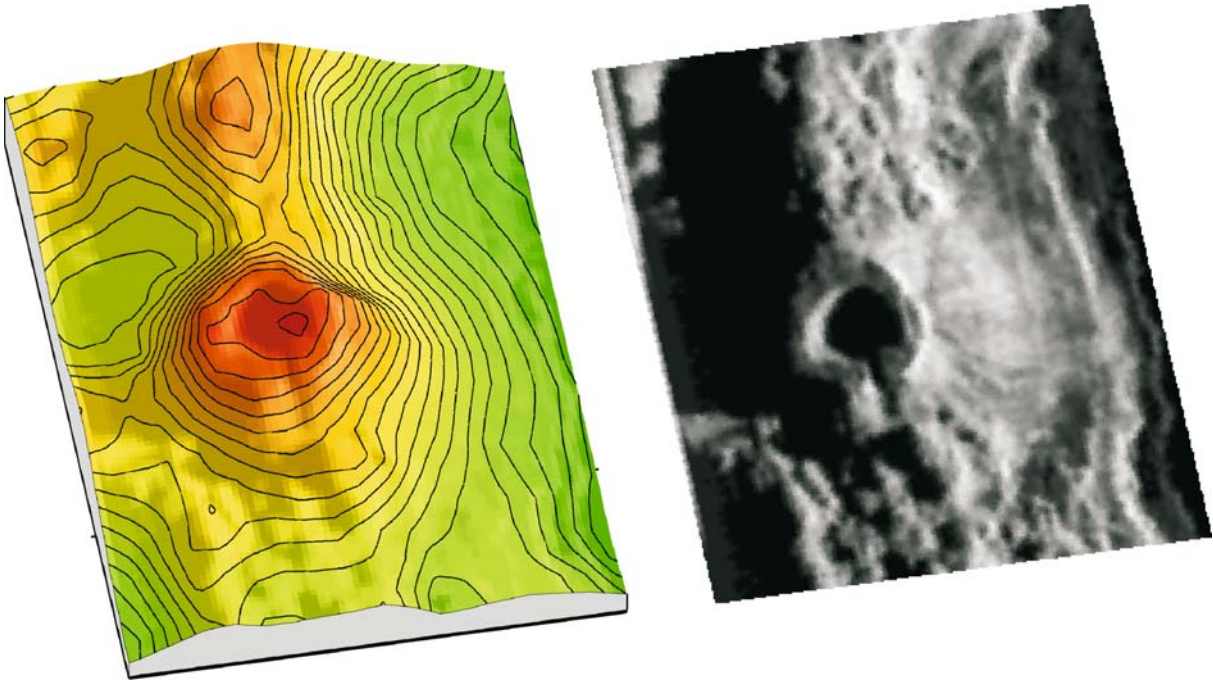


Image 5.2.3.3-2. Close ups of the southern volcano. This volcano edifice with a conspicuous incision of the crater rim is shown as two separate close-ups: the bathymetric relief with 20 m contour intervals and the sidescan image. It is quite obvious that neither the features of the summit crater with its diameter of 600 m nor the hummocky surface of the volcano cone are resolved by the bathymetry.

Project name: Charles Darwin Cruise CD65, 1990 and 1995

Research vessel: *RRS Charles Darwin*

Multibeam system (1990): SeaBeam Instruments; frequency: 12 kHz, beamwidth: 2°, 16 beams

Sidescan sonar (1995): Institute of Oceanographic Sciences, Deacon Laboratory: Towed Ocean bottom Instrument TOBI, towed 500 m above the sea floor; frequency: 30–32 kHz, swath width: 6 km

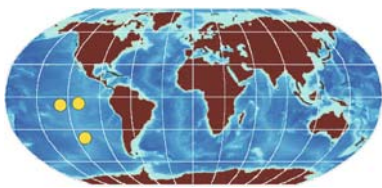
Pixel size: 10 m along track

Further instrumentation of TOBI: subbottom profiler; 7.5 kHz and 3D-magnetometer

Shipborne: Gravity anomaly sensor; dredging of bottom samples

Image ©: Deborah K. Smith, Department of Geology and Geophysics, Woods Hole Oceanographic Institution, Woods Hole, USA ■

5.2.4 Mid-Oceanic Ridges, Fast Spreading Type



The images of this spreading ridge type deal with the *South-* and *East Pacific Rise*, the prototypes of fast sea floor spreading. In addition, an image of a conspicuous relic of a former Pacific spreading ridge is presented in this context. It is the southernmost of the large *Pacific Fracture Zones* (Sect. 5.1.1.2).

5.2.4.1 A Very Fast Spreading Mid-Ocean Ridge: The *South Pacific Rise* near the *Wilkes Transform Fault*

The relief is a high resolution sound image of a 250 km long section of the *South Pacific Rise* (SPR), an extreme among the spreading margins between two tectonic ocean plates: it is the most productive origin of new sea floor on Earth. The spreading rate of 14½ cm per year is about ten times the average annual spread of the Mid-Atlantic Ridge (MAR, Sect. 5.1.1.1, 5.2.3), known as one of the slowest spreading zones.

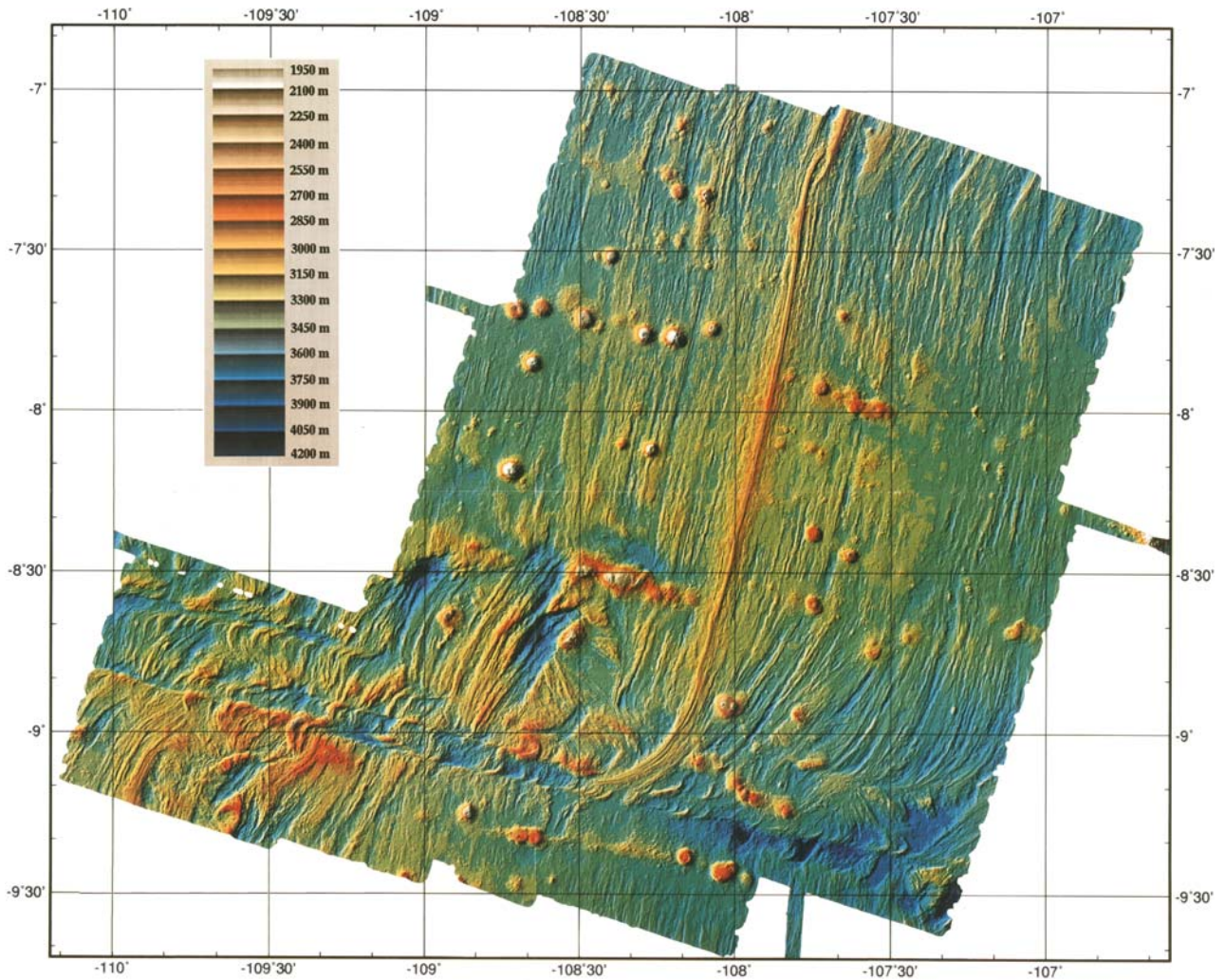


Image 5.2.4.1-1.

A section of the South Pacific Rise near 9 degrees south. Multibeam image. This color-coded 3D-sound image is the first wide swath multibeam record of a Pacific sea floor spreading zone. It shows the details of conspicuous features visualized in totality for the first time: the pronounced ridge, 400 m above its surrounding flanks, broad in the middle of the image, with no central valley, indicating the fast spreading type, the discontinuity at the upper rim, the thinning ridge crest ending here but being continued by an overlapping successor. Then: the multi-ridged structure of the sea floor on both sides of the central ridge, populated by seamounts partially grouped in chains and, above all, the Wilkes Fracture Zone in the southern part where the ridge bends by about 90 degrees and sinks into the fracture trench.

Perhaps the most striking feature of this ridge zone is the multi-ridged texture on both flanks of the ridge crest.

This fine structure is revealed only by multibeam deep ocean sound imagery with a resolution of 3 arc seconds or a grid of 100 m. The best available global sea floor relief map with 2 arc minutes resolution corresponding to a grid of about 3 km (Sect. 5.1.1.2) cannot recognize such textures. Instead, the global relief shows fast spreading ridges conspicuously smooth, quite different from the slow and extremely fissured MAR. This global relief, sufficient to depict the route of the central ridge, major fracture zones and larger seamounts cannot replace the diagnostic capability of high resolution sound imaging to analyze tectonic processes.

The ridged texture of the central ridge flanks hints at the dynamics of the spreading process. It appears like the documentation of past periodic and nearly simultaneous magma eruptions along the ridge crest of this section. According to the periodicity of the ridged floor, the linear eruptions are about 35 000 years apart. The oldest, outward

parts of the spreading process depicted are round about 1.5 million years of age.

Another striking feature which is obvious also to non experts directly from the image is the particular distribution of the seamounts on both sides of the ridge axis. Some look like irregular chains of pearls. These volcanic cones, drifting away from the ridge, together with the sea floor at spreading rate, are the product of major sporadic magma eruptions at or near the ridge axis, superimposed on the nearly periodic and less dramatic line eruptions. Possibly the volcanic eruptions occur at particular spots on the ridge where the magma supply differs in time and amount from most parts of the periodically healed ridge axis. These sporadic eruptions are evidently more infrequent than the line eruptions: roughly 150 000 years elapsed between two seamounts within a chain. This example of deep-sea multibeam imagery visualizes the cradle of the presumably hundreds of thousands of seamounts populating the entire ocean floor. Their actual number worldwide is unknown and the estimations diverge because only a few percent of the sea floor is covered by sufficiently high resolving acoustic bathymetry. A small seamount of only a few kilometers diameter at its base falls through the grid of the global sea-floor map mentioned above.

The most spectacular formation is of course the *Wilkes Fracture Zone* (WFZ) or transform fault at the lower rim of the image. Transform faults of this size are rare along the SPR. The next is several hundred km away, whereas the typical distance of these formations at the MAR is only 50 km. Above all, this South Pacific Rise transform fault is not an abrupt ridge axis offset like those at the MAR, but the central ridge

together with the ridged floor, and thus the entire sea floor bends like a highly viscous fluid. The bent ridge disappears westwards in a fault trench 1 000 m deeper in parts than the height of the straight ridge crest. On the western side the trench appears partially filled by a less regular ridged texture of former line eruptions. In the east, the fault trench is deeper and widens like a funnel. The entire offset of the WFZ is 150 km long, a major dimension of such features in the Pacific but a modest one in the Atlantic. All this is a further example of the multiplicity of realizations of one and the same fundamental mechanism of plate tectonics: the origin and migration of new sea floor.

Project: Survey and study of the South Pacific Rise near the Wilkes Transform Fault; year of survey: 1991
 Research vessel: *RV Maurice Ewing*, USA
 Multibeam system: *ATLAS Elektronik*, type: Hydrosweep DS; frequency: 12 kHz, beamwidth: 2.2°, fan width: 90° with 59 beams, lateral positioning accuracy by correcting for sound refraction: 5 m
 Relief exaggeration: 5 times
 Image ©: J. R. Cochran, Lamont-Doherty Geological Observatory of Columbia University, Palisades, USA ■

5.2.4.2

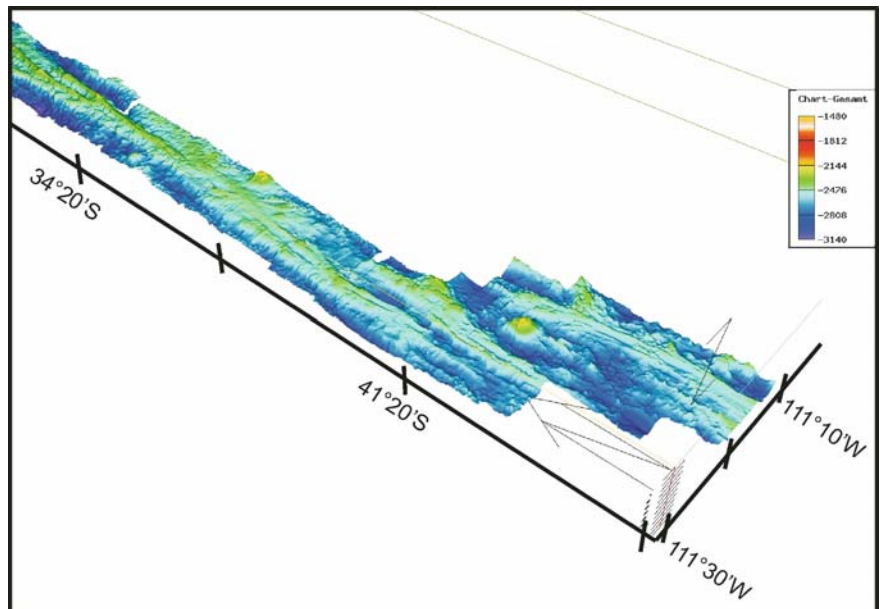
The Southern East Pacific Rise (EPR)

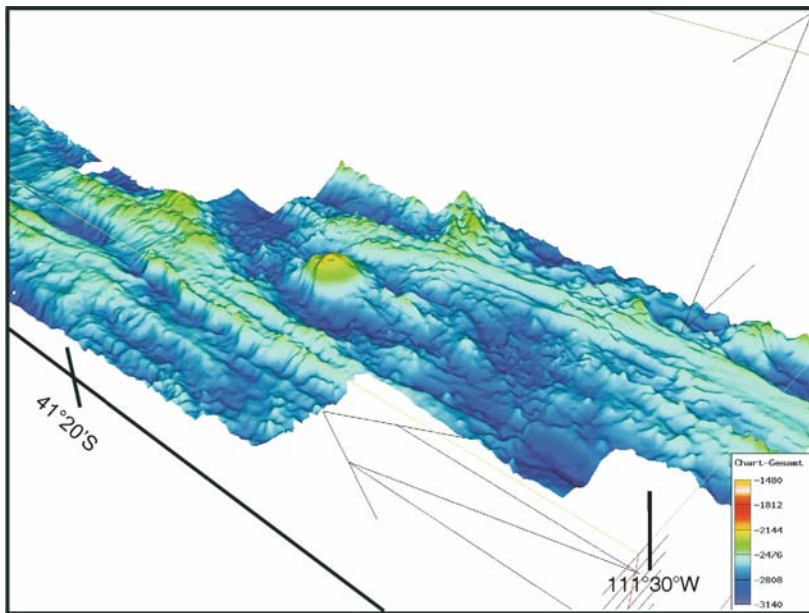
The two segments shown as multibeam 3D-images are part of the southern *East Pacific Rise* (EPR), which separates the *Pacific Plate* from the *Antarctic Plate* (Sect. 5.2).

Image 5.2.4.2-1.

This southern EPR segment is about 250 km long. The axial ridge is best developed on the northern, left side. The EPR becomes more irregular towards the fracture zone marked by the large volcano, where it rises little more than 500 m above the local sea floor. (The thin white line is a processing artifact).

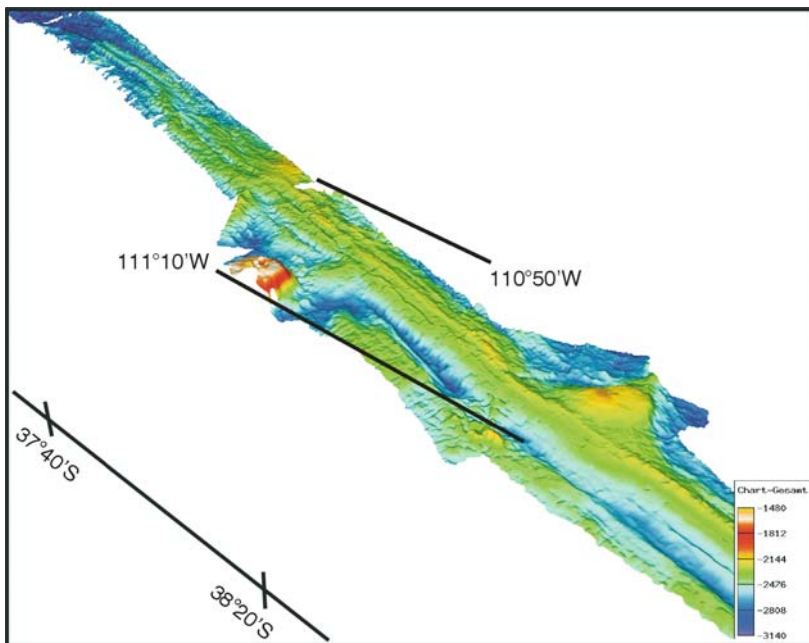
Project: Foundation 3 (East Pacific Rise), SO 157, June–July 2001
 Research vessel: *RV Sonne*, Germany
 Multibeam echosounder: Simrad, EM 120; 12 kHz, bandwidth 1.5 kHz, beamwidth: 2°, 191 beams, fan width 150°, accuracy of DGPS-navigation: better than 50 m
 Image ©: Peter Stoffers, GPI, Universität Kiel, Germany ■



**Image 5.2.4.2-2.**

This section is a 3D-close up of the southern part of the preceding image. The offset axial ridge south of the fracture zone appears as a narrow line at nearly constant crest height with seamounts to its east. Deep furrows occur around and through the volcanic edifice, which rises 150 m above the axial ridge crest.

Image documentation: same as for Image 5.2.4.2-1 ■

**Image 5.2.4.2-3.**

The northern segment of the EPR is textbook-like, devoid of fracture zones, and features an undisturbed prominent axial ridge in the south. However, towards the north the axial ridge is accompanied by low-relief flanking ridges, and at the top of the image the axial ridge appears to branch into two less conspicuous ridges. The most prominent feature of this area is a volcano capped by a broad crater that rises 1000 m above the surrounding sea floor. No crater is apparent on a second volcano, 80 km to the south.

Image documentation: same as for Image 5.2.4.2-1 ■

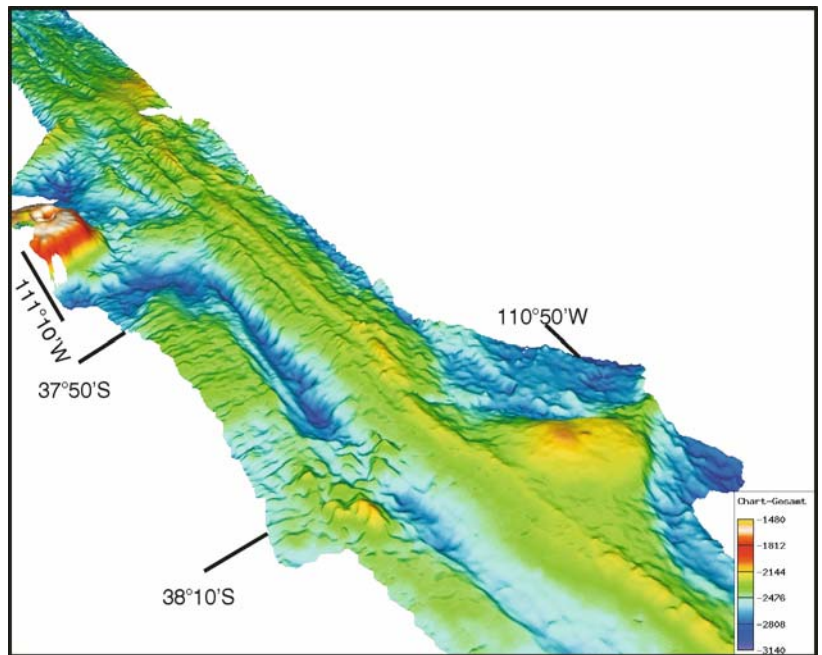
The EPR is the principal source of new sea floor on the Earth's surface at present, but the main force driving this process is the westward pull of the Pacific Plate as it subducts beneath the volcanic arcs of the western Pacific and not actively upwelling mantle magma. Spreading rates here are 90–100 mm per year. This speed of sea floor pro-

duction is slower than the 150–160 mm per year that occurs in the central EPR at the *Pacific–Nazca Plate* boundary west of *Chile* but comparable to the northern EPR at the *Pacific–Cocos Plate* boundary west of central America (Sect. 5.2). Typical of fast spreading *mid-ocean ridges*, the southern EPR has an axial ridge rather than an axial

Image 5.2.4.2-4.

A close up of the preceding image demonstrates that the EPR at 38–41° S is a narrow rise, less than 10 km wide and hardly 1 km high, quite different from the spectacular appearance of the *slowly* spreading MAR. The inconspicuous relief of these segments on the *fast* spreading EPR corresponds to the large scale characteristics shown on the global depiction of mid-ocean ridges (Image 5.1.1). These examples demonstrate that there is no generic behavior of the main mid-ocean ridges. The variability within each ridge type, and of intermediate types, is far from being understood.

Image documentation: same as for Image 5.2.4.2-1 ■



valley. Fracture zones, which offset segments of the ridge axis, are spaced further apart on the EPR than they are on the slow *Mid-Atlantic Ridge (MAR)*. For example, the southern segment (Image 5.2.4.2-1) is crossed obliquely by a weak fracture zone where the axis offset, marked by a volcano at the fracture, is barely 15 km. The next major fracture to the south is 1 000 km distant and involves an axis offset of more than 250 km. Dating of the sea floor by paleo-magnetic inversion stripes (Sect. 2.8) reveals that the area shown is less than 1 million years old. That is about the age of the youngest part of the MAR which is the narrow axial ridge with volcanoes as shown in Image 5.2.3.1-1.

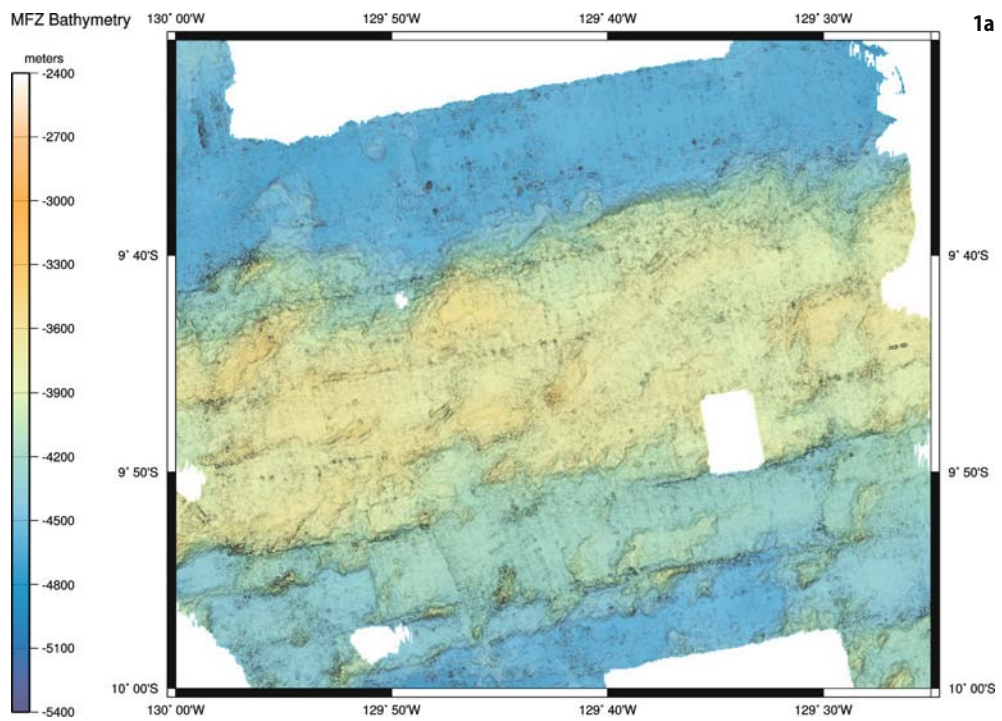
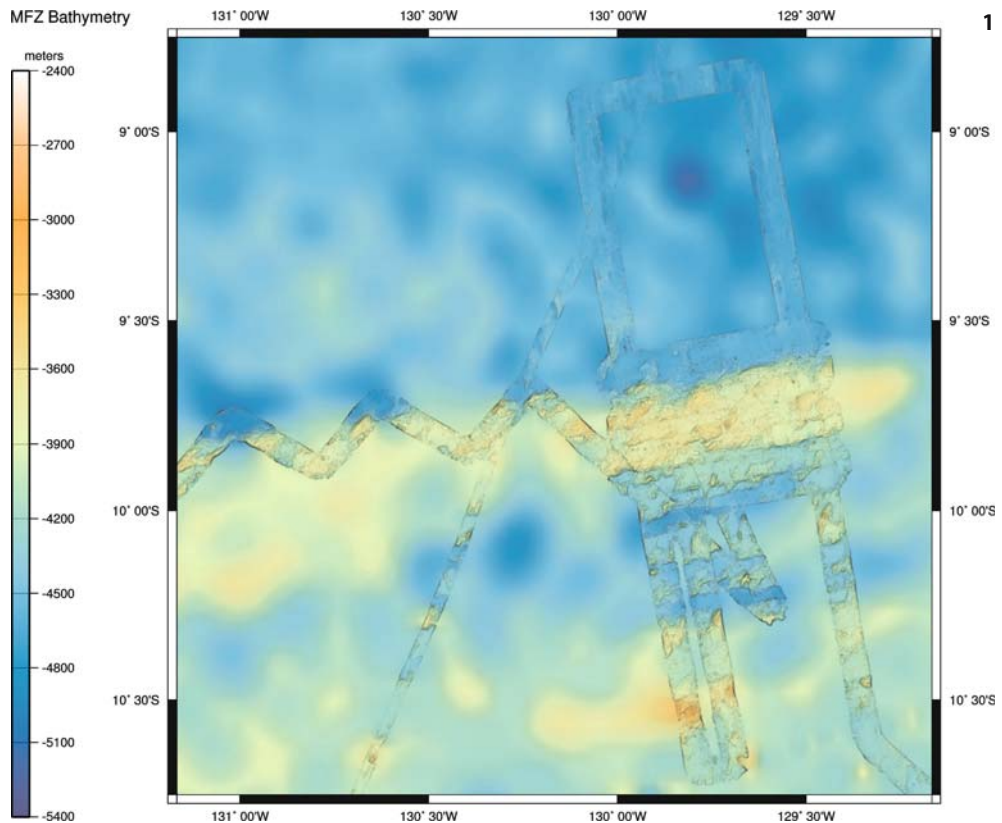
5.2.4.3**Marquesas Fracture Zone, One of the Large Pacific Fracture Zones, Relics of a Reorganized Mid-Ocean Ridge**

On the globe depiction of the *Central Pacific* (Sect. 5.1.1.2) the largest and most conspicuous features of the ocean floor – next to the long island chains – are eight fracture-like lines stretching across the Pacific basin nearly equidistant and nearly parallel between the *Aleutians* and the equator. They are longer than the longest fracture zones associated with the *Mid-Atlantic Ridge* (Sect. 5.2.3). If the large central Pacific faults are also

fracture zones of a *mid-ocean ridge*, where then is their ridge? In fact, these fracture zones are relics of a mid-ocean ridge that was reorganized some 35 million years ago. The ridge was active during an epoch of the Earth's history when the tectonic plates were quite different in shape and configuration. The process of fundamental reshaping is outlined in Box 5.1.1.2-1.

The southernmost of the eight relic trans-Pacific fracture zones visualized in the Central Pacific globe depiction of Sect. 5.1.1.2 was selected to investigate the reason for the notable lack of seismic activity of these fracture zones, in other words: the absence of earthquakes. This fact appeared unusual because the difference in age between opposing sides of a fracture zone is expected to cause vertical motions due to the more rapidly subsiding younger sea floor.

An earlier model to interpret this contradictory behavior as flexure across a locked fault, generating a ridge on the young side of the fracture and a trough on the old side, associated with large gravity anomalies, was refuted recently, underlining the role of comparative imaging. Like an irony of geophysics, the only earthquake to rupture the *Marquesas Fracture Zone (MFZ)* in the last 35 years was located in such a “locked region”. Elsewhere, where the old model predicts a vertical slip, the fault is nevertheless aseismic.



◀ **Image 5.2.4.3-1, 1a.** Section of the locked fault and close up. Overlay of the bathymetric and altimetric relief. The comparative imaging of the sea floor clarifying the enigmatic phenomenon of the MFZ applied two entirely independent, complementary methods: Satellite gravity anomaly imaging through mapping the altimetry relief (Sect. 5.1.1.2) was compared with ship-borne 3D-sound imaging the real bathymetric relief. The combination of both is shown as a 220 km section of the MFZ with the high resolution multibeam image overlaid upon the lower resolved altimetric image. Supplemented by seismic profiling the image analysis has not provided any evidence for vertical slip along the fault. Accordingly, shear stresses caused by differential thermal subsidence do not exceed the strength of this fault, which is considered to be locked against vertical motion by indentation of the opposing sides.

This serrated margin structure reminiscent of mortise and tenon in a carpentry joint is clearly visible in the image, in particular where the multibeam swath meandered across the ridge. Even the altimetric underlay recognizes some of the indentation. The shape and amplitude of this gravimetric anomaly image does not support the early, simple model either. According to the recent results, the margin structure appears capable of sustaining at least 20 MPa of shear stress and remains locked along the entire length of the fault. The origin of this high strength joint is presumed to reach back into the Cretaceous period, later continued in the Tertiary when the predecessor to the present *Juan de Fuca*-, *Nazca*- and *Cocos* Plates (map of Sect. 5.2), the *Farallon* Plate (Box 5.1.1.2-1) turned anticlockwise and then clockwise, causing the serrated rupture with magmatic ascent, the glue as it were, of the carpentry joint. The main strengthening effect however is attributed to the thickening of the lithosphere from below as is cooled, essentially “healing” under the fault.

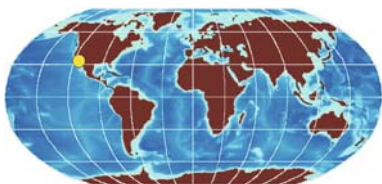
Project: EW9106; year of acoustic survey: 1991

Research vessel: *RV Maurice Ewing*, USA

Multibeam system: ATLAS Elektronik, Hydrosweep; frequency: 12 kHz, beamwidth: 2°, 59 beams; Altimetric data conversion into the sea floor relief: Smith & Sandwell

Image ©: Kelsey Jordahl, Monterey Bay Aquarium Research Institute, USA ■

5.2.5 Strike Slip Fault Plate Margin



Two of the three main types of tectonic plate margins (Sect. 5.2) are mostly and indubitably identifiable by their characteristic relief features of the sea floor. High resolution 3D-sound imaging visualize the con-

Box 5.2.5-1. Plate boundary between the *Pacific Plate* and the *North American Plate*

The actual tectonic plate boundary between the *Pacific Plate* and the *North American Plate* evolves south of the head of the *Gulf of California* from a spreading ridge to a strike-slip transform fault, the *San Andreas Fault*, that is 100 km east of the Los Angeles basin. All of the *Los Angeles Basin* belongs to the *Pacific Plate*. The actual faults in the Los Angeles Basin and immediately adjacent offshore are part of the larger fault system that parallels the plate boundary. The *continental margin*, the transition from the continent to the deep ocean floor (Sect. 5.3) occurs along the *Patton Escarpment*, far to the west of Los Angeles.

The tectonic faulting in the Los Angeles area is a complex composition of deformation processes. Along the northern section it can be summarized as a convergent, thrust faulting margin where the small *Juan de Fuca Plate* (Sect. 5.2), a fragment of the large Pacific Plate, is colliding with the *North American Plate* to form the high mountain range. The collision zone is a result of an “S”-shaped bend in the infamous *San Andreas Fault* in this area. South of the convergence zone, a complex of motions is occurring. These motions are a result of the northward movement of the Pacific Plate relative to the North American Plate causing strike-slip faults with variable amounts of compression with thrust faults and extension with normal faults.

James V. Gardner · Center for Coastal and Ocean Mapping, University of New Hampshire, Durham, NH, USA

vergent margins by their various trench formations in the *subduction zones* (Sect. 5.2.1, 5.2.2) and the divergent margins by their more or less prominent ridge formations in the *mid-ocean ridges* (Sect. 5.2.3, 5.2.4). The third margin type where adjacent plates neither converge nor diverge but exert shear forces by different shifting of the plates along their common margin is often less apparent in the sea floor structure. This margin type is named *transform fault* or *strike-slip fault* which directly describes the geodynamic process (Sect. 5.2). It is infamous and feared for its devastating earthquakes caused by sudden release of accumulated tensions which may also cause uplifts of plate margin segments. The surface expressions of these faults can be traced acoustically by applying multibeam 3D-imaging of the sea floor relief and analyzed together with seismic profiling of the underlying structure.

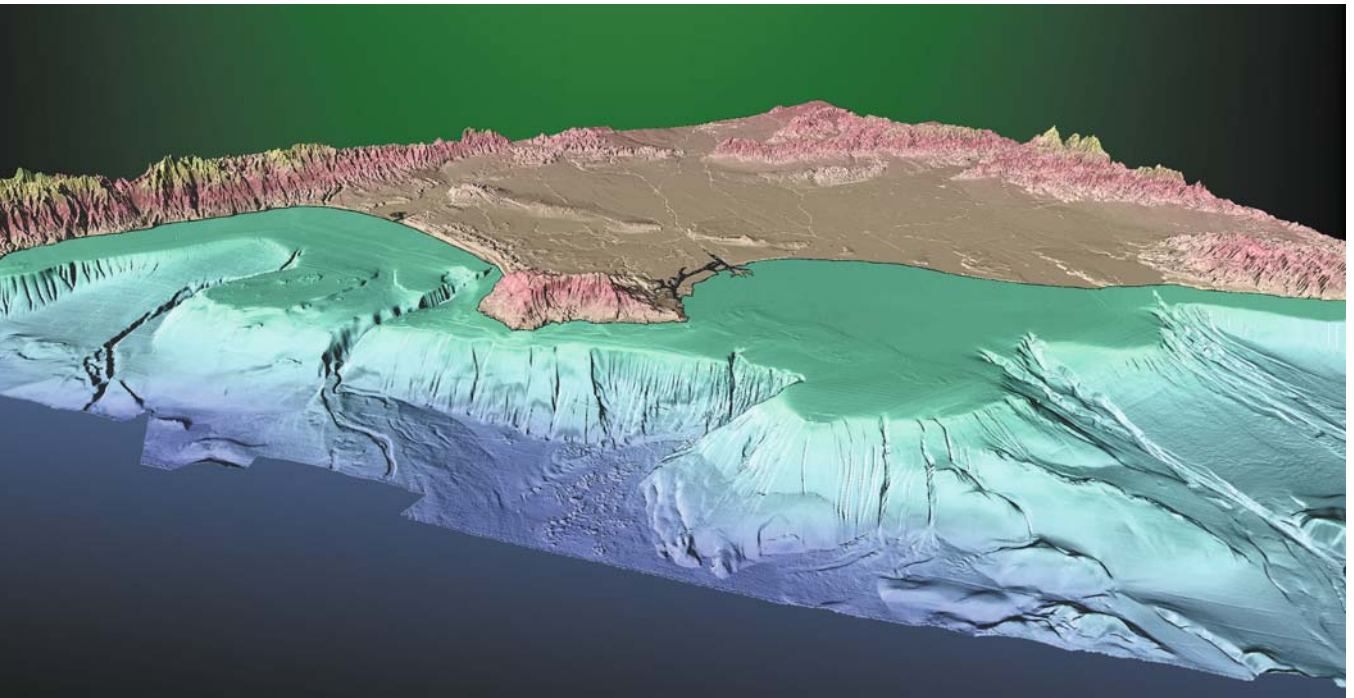


Image 5.2.5-1. Cut out of the strike slip fault margin, *Los Angeles Area off California*. 3D-multibeam sound image. The shaded-relief image of the Los Angeles margin shown is a 130-km section of the southern *California* margin. This section is crossed by a zone of active faults that roughly parallel the main plate boundary, the *San Andreas Fault* to the east. The main plate boundary evolves from the northern-most section of the *East Pacific Rise* (EPR, Sect. 5.2.4.2) that traverses the north-south length of the *Gulf of California*, and comes onshore at the head of the Gulf. This major transform fault slices through southern California with the densely settled Los Angeles basin and emerges back into the ocean south of *San Francisco*. These strike-slip transform faults differ in sense of motion from those transform faults that are pronounced relief features in spreading zones, such as the example at the *Mid-Atlantic Ridge*. (MAR, Sect. 5.2.3.1). Such transform faults occur along fracture zones between two spreading-ridge segments and are evident by ridge axis offsets.

A pronounced bend in the plate boundary in the vicinity of Los Angeles has produced a zone of major faulting throughout the Los Angeles area. One of these faults can be seen south of the *Palos Verdes Peninsula* in the middle of the image. The fault appears to have incised the edge of the continental shelf and upper slope as a multifold rupture of the sea floor.

It is the high resolution imaging that reveals the characteristic features of this rupture named Southern *Palos Verdes Fault* (PVF) in contrast to the two major canyons north of the peninsula which are obviously the result of erosion by sediment flow. However, the strike-slip transform fault type of plate margins is not normally a simple and singular rupture. It can be a complex aggregate of fissures or ruptures more or less aligned in parallel to each other and of finite length and different age, reflecting the history of local processes of tension release.

A newly discovered and investigated fault with the informal name *Avalon Knoll Fault* (AKF) is visible in the foreground of the relief image, about 10 km to the west of the PVE, extending for at least 14 km between the shelf edge and the base of the continental slope. Interpretations of seismic profiles through the sediment layers across the two faults (not shown here), suggest the AKF developed in the Holocene and must be younger than 10 000 years old. The geometry of such faults allows quantitative estimates of the minimum magnitude generated by seismic events along the faults. For the AKF the magnitude would be 6.5. This corresponds to the equivalent of 5 million tonnes TNT or a large nuclear explosion.

Project: Tectonic strike slip fault margin of the *Los Angeles* area; 1998

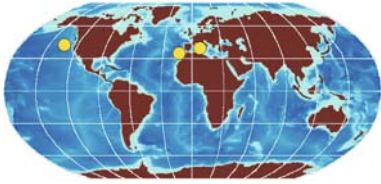
Research vessel: *RV Ocean Alert*, USA

Multibeam echosounder: Kongsberg Simrad EM300; 30 kHz, beamwidth 1° and 2°; 135 beams

Land topography: USGS DEM; resolution: 30 m; Color code of sea floor depths: light green: 50 m; light blue: 800 m

Image ©: James V. Gardner, Center for Coastal & Ocean Mapping, University of New Hampshire, Durham, NH, USA ■

5.2.6 Volcanic Formations



A distinction of volcanic formations and seamounts (Sect. 5.2.7) may appear questionable since the near-

ly innumerable number of seamounts strewn over the sea floor are also of eruptive origin. They were created at the *mid-ocean ridges*, the origin and spreading zones of new sea floor (Sect. 5.2.3, 5.2.4) and migrated away as inactive formations, riding on the new sea floor towards the *subduction zones* (Sect. 5.2.1, 5.2.2). However, many of the still active volcanoes owe their origin to tectonic processes at and near subduction zones and *hot spots* (Sect. 5.2.8). The examples of volcano images shown in this context are not taken in far remote sites like the *Orca Seamount* of the *Antarctica* (Sect. 5.5.2) but they deal with active volcanism in the *Mediterranean*, and with two former active volcanoes, one with an exemplary, textbook-like crater, an unnamed volcano near *Juan de Fuca Ridge* and the other one in the *Atlantic* near the *Strait of Gibraltar* at the transition between the only subduction zone in *Europe* and the adjacent strike slip fault extending to the *Mid-Atlantic Ridge* (map of Sect. 5.2). This is the large *Ampère Seamount*, typical of a *guyot* type with its conspicuously flat summit from erosion during former times of exposure above sea level.

5.2.6.1 *Ampère Seamount*

The *Ampère Seamount*, 600 km west of *Gibraltar*, is one of nine inactive volcanoes along a bent chain, the so called *Horseshoe Seamounts*. All of them ascend from an abyssal plain of 4 000 to 4 800 m depth up to a few hundred meters below the sea surface, except two, which nearly reach the surface: the *Ampère Massif* on the southern flank of the group and the summit of the *Gorringe Bank* in the north. The horseshoe, serrated like a crown, opens towards *Gibraltar* and stands in the way of its outflow. These seamounts are part of the *Azores-Gibraltar* structure, which marks the boundary between two major tectonic plates: the *Eurasian-* and the *African Plate*.

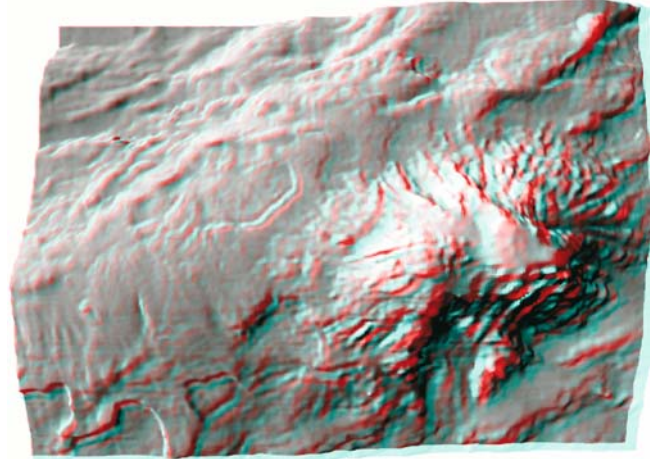


Image 5.2.6.1-1.

Ampère Seamount, Horseshoe Seamount Chain off Gibraltar. Multi-beam echosounder image in red-green anaglyphic stereo-depiction. The bird's view which is most appropriate for stereo depiction reveals the two level abrasive flattening of the Ampère summit more clearly than the slant view. This typical summit shape called *guyot* of a fully submerged seamount indicates its past with wind induced erosion when emerged above sea level. The simulated illumination from north shows deep going landslides in the foreground and traces of volcanic outflow in the west, covering the south west part of the declivity with sharply marked boundaries.

Project: Scientific Expeditions to Antarctica; cruise:
ANT IX/4 (1991)
Research vessel: *RV Polarstern*, Germany
Multibeam echosounder: HYDROSWEEP DS-2; 15.5 kHz,
beamwidth: $2.3 \times 2.3^\circ$, fan width: $90^\circ/8$ km at 4 km depth
Height exaggeration factor: 6
Image ©: Jörn Hatzky, AWI, Germany ■

The submarine volcanism which formed the Horseshoe Seamounts belongs to the sea floor spread area of the *Mid-Atlantic Ridge*. The maximum activity was between 17 and 10 million years ago and terminated thereafter. The volcanoes consist of basalts and tuffs. Most of their flanks and the abyssal plain around are covered by sediments of micro-organic origin.

These sediments, in particular their partial absence on the upper flanks are a circumstantial proof and a kind of diary of the initial rise and subsequent subsidence of about 600 m of these seamounts. The horizons of erosion where the basalt substrate is laid bare indicate the rise above sea level in the past. Since

the Ampère summit is 60 m deep today, this volcano must have been an island 500 m high. The stratification of the sediments covering the surrounding abyssal plain reveals discrete events of downslope suspension flows, called turbidites, separated by tens of thousands of years and perhaps induced by changes in climate conditions.

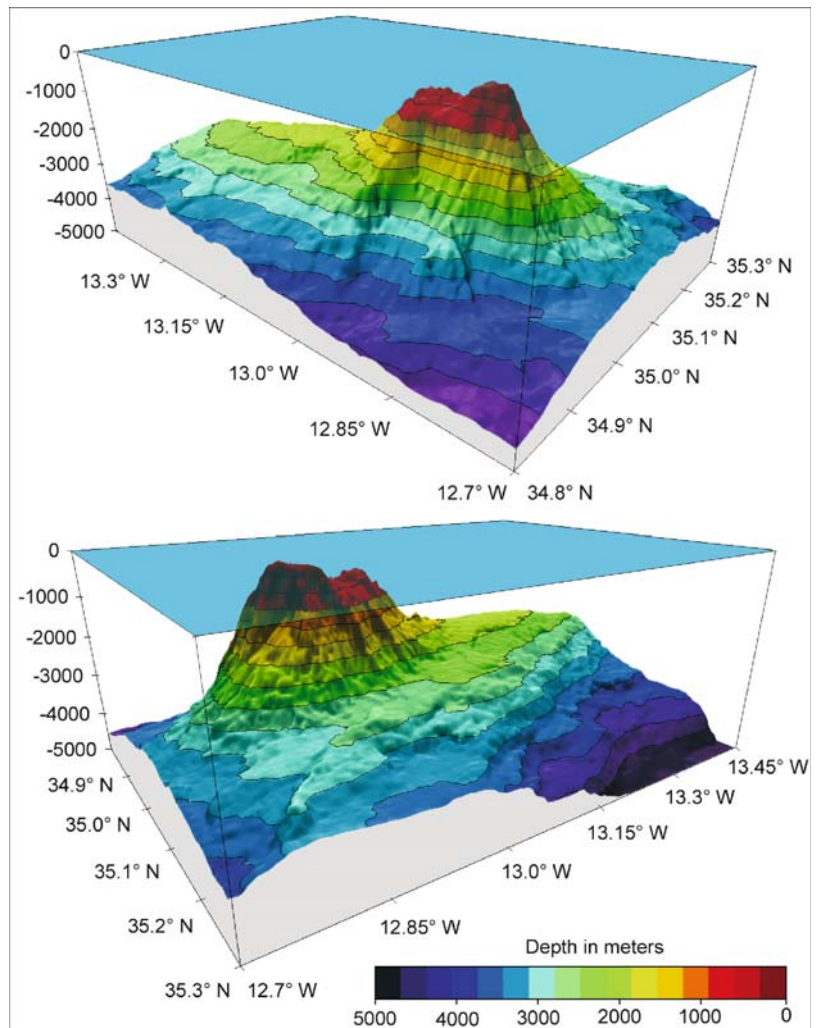
The Ampère Seamount of 4 800 m height and a base diameter of 50 km exceeds the size of the *Mont Blanc Massif*. Its southern and eastern flanks are steep with basalts cropping out, in parts with nearly vertical walls of some hundred meters. The west and north sides consist of terraces and plateaus covered with sediments at 140 m, 400 m, 2 000 m, and 3 500 m.

Image 5.2.6.1-2.

Ampère Seamount. Multibeam echosounder image in color coded 3D-depiction. The pair images showing the Ampère Massif from two opposite sides quantifies the depth regime of more than 4 000 m, as well as the varying slope structure of the flanks ascending from a broad, inclined fundament.

Image documentation:
same as for Image 5.2.6.1-1 ■

The Horseshoe Seamount area is also remarkable as a disturbed crossing of three major oceanic flow systems at different depths and directions with forced upwelling and partial mixing of the water masses. Most prominent is the *Mediterranean Outflow Water (MOW)* with its higher temperature and salinity between 900 and 1 500 m depth. It enters the horseshoe unimpaired from the open eastern side but penetrates the seamount chain through its valleys on the west, thereafter diverging and crossing the entire Atlantic Ocean. Below the MOW is the *North Atlantic Deep Water (NADW)* between 2 000 m and 3 000 m depth flowing *southward* and finally there is the *Antarctic Bottom Water (AABW)* flowing *northward* below the two other systems.



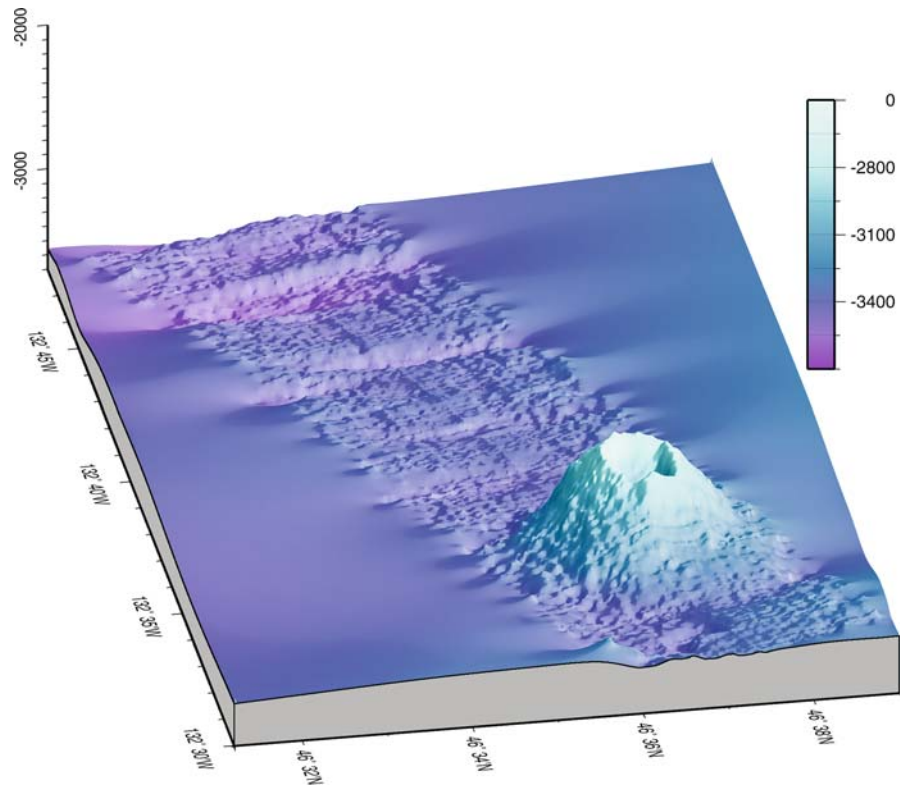
5.2.6.2

Unnamed Volcano near Juan De Fuca Ridge

Image 5.2.6.2-1.

Demonstration of coverage and resolution by a single multibeam run. This textbook-like example of an under-sea volcano was found fortuitously by a single run of the sounding vessel when imaging the sea floor of the northern Pacific tectonic plate near the margin of the small *Juan de Fuca Plate* (Sect. 5.2). The “sounding carpet” covered by the traces of 59 beams had exactly the width of the diameter of the base of the volcano cone – about 5 km – and revealed details of the crater of about 1.5 km diameter. The image processing program has simulated sunlight from northeast with the resulting shadow, and extrapolated the relief slightly beyond the rim of the sounding stripe into the surrounding sea floor of coarser chart resolution.

The image demonstrates the capability to resolve the hummocky surface of the sea floor up to the top of the cone (Sect. 5.2.3.3), despite a typical multibeam artifact. This is the stripe structure along the sounding carpet due to incomplete adjustment of threshold setting of the beams. This artifact can be discriminated easily in this case from the genuine sea-floor features by visual evidence. The small scale tectonic faults crossed by the ship’s track are acquired in three dimensions, as well as several small crater-like dents of the floor in the foreground.



Project: SO-112 “HiResBat”; year of data acquisition: 1996

Research vessel: *RV Sonne*, Germany

Multibeam system: ATLAS Hydrosweep DS; frequency: 15.5 kHz, beamwidth: 2.3°, 59 beams, fan width: 90°

Image ©: Wilhelm Weinrebe, Geomar, Kiel, Germany ■

5.2.6.3

The Sea Floor around the Volcano *Stromboli*, Italy

Stromboli, a volcano island 220 km southwest of *Naples* is one of the few volcanoes on Earth displaying persistent eruptive activity. In the past it was therefore called “Lighthouse of the Mediterranean”. Volcanologists call volcanoes with activity similar to that of *Stromboli* “*strombolian*”. Most of the activity of *Stromboli* is of very moderate size, consisting of brief and small bursts

of gas and glowing lava fragments to heights of rarely more than 100 m above the vents. Occasionally there are periods of stronger, more continuous activities with fountaining, lasting several hours with violent ejection of blocks.

Stromboli produced numerous lava flows during the 20th century but only a very few in the past four decades. At the end of 2002, a quarter of a year after one of the most explosive eruptions on *Etna* for centuries, *Stromboli* followed with a series of strong explosions

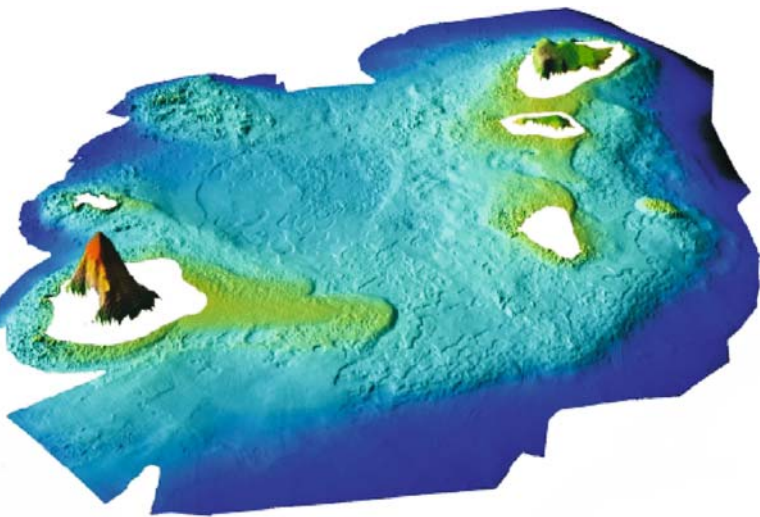


Image 5.2.6.3-1.

View of the volcano area with *Stromboli* on the left. Multibeam image. The width of the depicted area is about 100 km. The shape and thickness of the lava tongues from different eruption events are clearly recognizable. The “white collars” around the islands with extremely shallow water are without acoustic data. The relief images of the islands are taken from the global GTOPO30-map with 1-km grid.

Project: Sea floor survey of the *Stromboli* area; year: 2003
Survey vessel: *CP 875*, Italy

Multibeam systems: RESON, type: SeaBat 8125; frequency: 440 kHz, beamwidth: 0.5°, zoom autofocus, fan of 240 beams; RESON, type: 8160; frequency: 50 kHz, beamwidth: 1.25°, fan width/stripe widths: 750 m at 100 m depth, zoom auto-focus; PDS2000 Hydrographic navigation software

Image ©: Pietro Basciano, NeSA Med. Srl. and RESON MEDITERRANEAN SRL, Italy ■

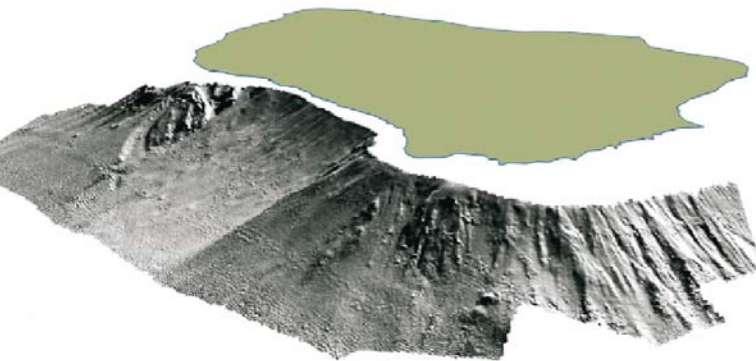


Image 5.2.6.3-2.

View over the lower part of the volcano flank. Multibeam image. The main result of this part of the survey is quite obvious: The slide has removed the scree completely from the broad area on the left. The “lighter” backscattering of the floor indicates a smoother surface. The simulated sunlight comes from above, superimposed to the depiction of the scattering intensity instead of the color coded depth scale (Sect. 5.2.3.1). The image is an example of a very effective and rapid diagnosis, matched to the requirements.

Image documentation: same as for Image 5.2.6.3-1 ■

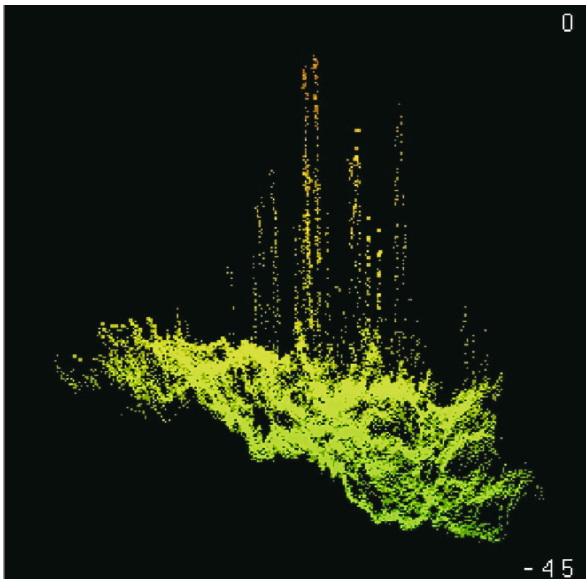


Image 5.2.6.3-3.

Gas ascending in the *Eolian Volcanic Arc*. Multibeam image. *Panarea Island*, 20 km southwest of the famous volcano *Stromboli* in the southern *Tyrrhenian Sea* belongs to the volcanic arc of the *Eolian Islands*. This formation of major tectonic activity is part of the subduction zone crossing the Mediterranean from the *Strait of Gibraltar* to the southern coast of *Turkey*. This is where two of the seven large tectonic plates of the globe converge: the African Plate is subducted under the Eurasian Plate (Map of Sect. 5.2, Sect. 5.6.6).

In November 2002 fishermen of *Panarea* reported the phenomenon of “boiling sea”, with widespread dead fish and a strong smell of sulfur. Although earlier occurrence of gas emission from the sea floor in the region was documented, the reported phenomena denoted a strong and abrupt intensification of gas discharge. Subsequent marine and airborne reconnaissance conducted by several research institutions confirmed the anomalous increase of gas emitted near *Panarea* from the shallow south-eastern plateau of the island.

Under commission of the *Italian National Institute of Geophysics and Volcanology* a research survey of the Panarea sea floor was subsequently conducted. The survey was based on high resolution acoustic imaging to obtain the sea-floor bathymetry and morphology to locate geological features like cracks or faults related to the degassing activity. The sound image shows flares of gas ascending from an area of extremely strong echoformation indicating further gas before release from the ground. Due to the maximum acoustic mismatch between gas and water (Sect. 3.4.1) echosounding is a very sensitive method to detect and localize even small amounts of unsolved gas in the sea. The survey identified several tens of gas emission sites in the area and the respective volcanic sea-floor features down to less than 2 m size.

Project: Gas emission from the sea floor of Panarea

Survey vessel: small motor launch

Multibeam system: RESON, SeaBat 8125; frequency: 455 kHz, beamwidth: $0.5 \times 1^\circ$, 240 beams, fan width: 120° , zoom autofocus; positioning and motion control: RTK GPS, PDS2000, RESON navigation Software, TSS motion sensor, SG Brown Gyro compass, waterdepths: 4–32 m, height of the flares: 8 m, width of the cut out: 10 m
Image ©: Pietro Basciano, RESON MEDITERRANEAN ■

and consequent lava outflow. The glowing flow descended rapidly the *Sciara del Fuoco*, a huge scree formed by earlier lava flow and pyroclastics and entered into the *Tyrrhenian Sea*. It soon became clear that this was not just a repetition of the previous events. Portions of unstable scree collapsed into the sea which caused a *tsunami*, destroying man-made structures on the coast of the island.

The need to perform further research on the way this volcano works initiated also an acoustic imaging survey to investigate the sea floor around the volcano. The requirements stated that the multibeam fan-echosounder should fit on a small vessel, be installed quickly and provide quantitative high resolution images on board for immediate decisions on the survey strategy. The system produced a detailed 3D-relief of the sea floor including the ascending flanks of Stromboli. The survey had to cover the depth regime between very shallow and 2 500 m and thus required the combination of two sounder systems of different

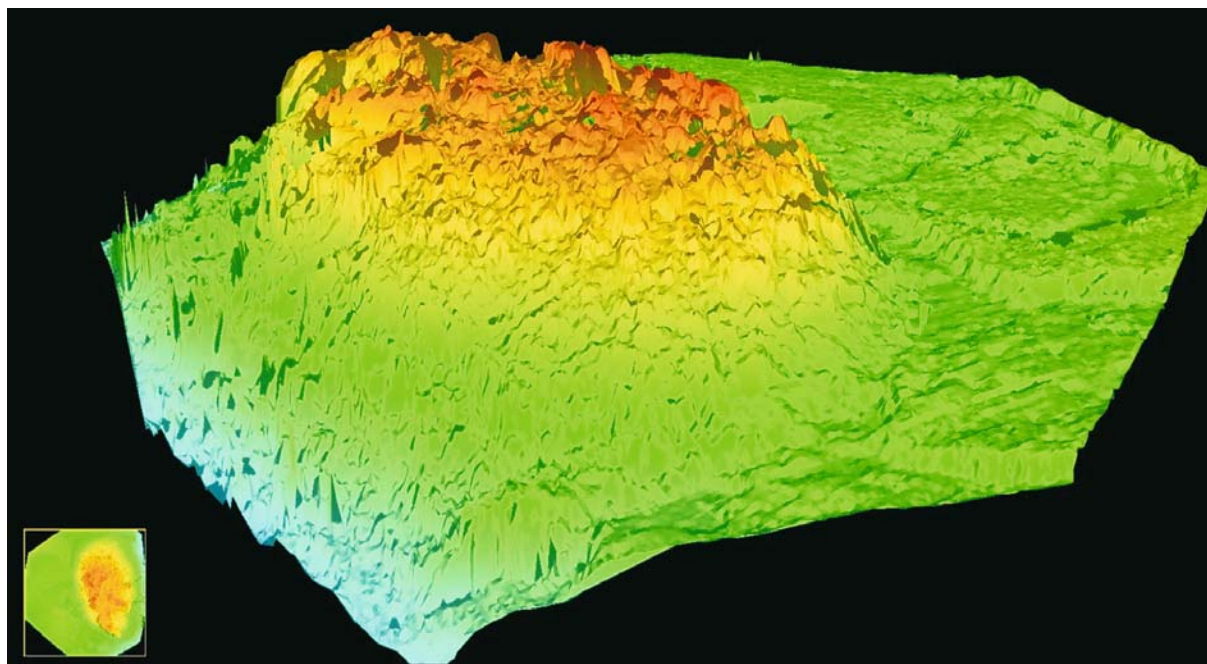


Image 5.2.6.3-4. Lava on the sea floor near the island of *Panarea*. Multibeam image. This corrugated mound looks different from congealed lava flow. It was a large clod of erupted lava abruptly cooled down when passing the water column. The irregular surface is due to rapid cooling. The perspective 3D-image is enhanced 3 times in the vertical to reveal the structure. The height above the surrounding plane is 4 m; the diameter of the hill is 12 m.

Image documentation: same as for Image 5.2.6.3-3, except water depth: 30 m

Image ©: Pietro Basciano, RESON MEDITERRANEAN ■

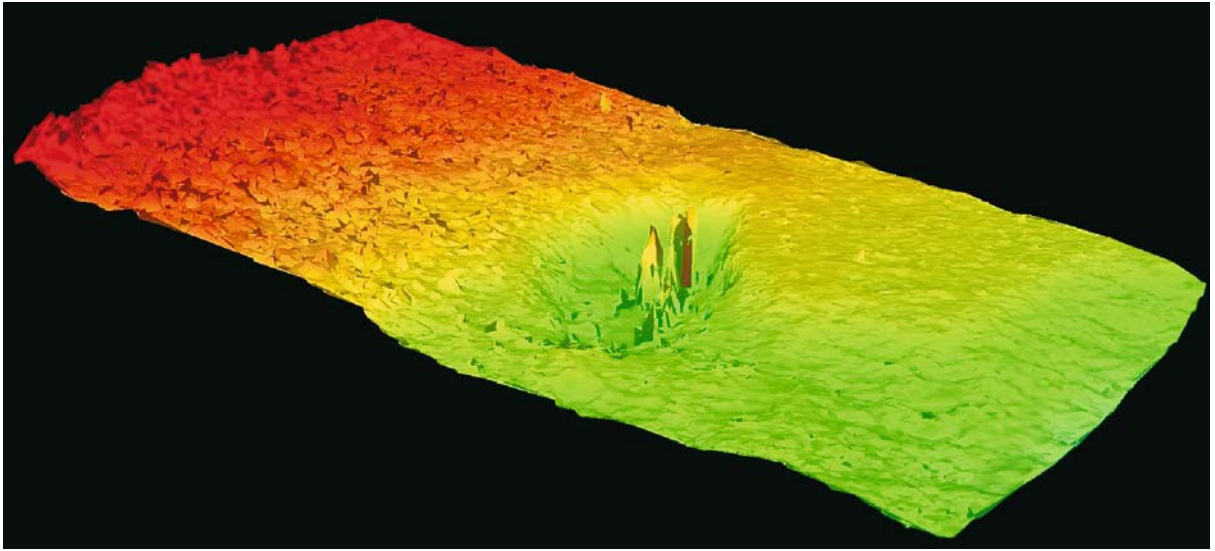


Image 5.2.6.3-5. Rock impact on the sea floor near the island of *Panarea*. Multibeam image. The strongly enhanced relief shows the impact crater with a compact clod thrown out by an eruption. Due to the shallow water depth and the solid state of the clod, the impact speed was high enough to dig the crater, different from the soft clod depicted in the preceding image. The size of the clod is about 2 m, similar to the depth of the crater.

Image documentation: same as for Image 5.2.6.3-3; image enhancement: 10 times

Image ©: Pietro Basciano, RESON MEDITERRANEAN ■

Image 5.2.6.3-6.

Plume of steam from a lava clod impact near the island of *Panarea*. Photograph. The photo as well as the preceding multibeam sound images were taken under hazardous conditions during a phase of volcanic eruption.

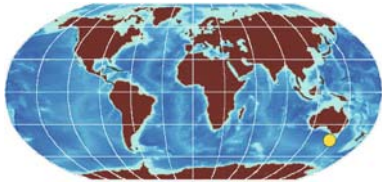
Image ©: Pietro Basciano, RESON MEDITERRANEAN ■



depth range. This program initiated at very short notice confirmed that the technology applied was the appropriate tool for continuous monitoring and quantification of the shape and volume of the submarine

lava flow and submerged scree. This investigation is moreover considered generic and expected to be applicable to other volcanoes which are partially or fully submerged.

5.2.7

Prominent Seamounts:**The Tasmanian Seamounts, Marine Reserve**

The sea floor of the oceans is strewn with an estimated number of 30 000 seamounts, all of them former volcanoes and most of them originally ascended from the mid-ocean ridges, the cradle of new sea floor by ascending magma. Nowhere else however, are so many seamounts accumulated in a close neighborhood than off southern Tasmania. Here, the continental slope is of rough and varied terrain. Some large E-W trending ridges lie near its base, and a number of canyons incise its western half, but more than a hundred volcanic

cones, typically 300 m up to 600 m high and several km across are a most spectacular and unique geologic formation. Due to their agglomeration and large distance from the nearest tectonic spreading zone, a particular origin such as a hot spot activity is under consideration. The area is also of economic interest: The shallower cones are deep-sea trawl fishing grounds for Orange Roughy; this area forms an important component of the south-east fishery.

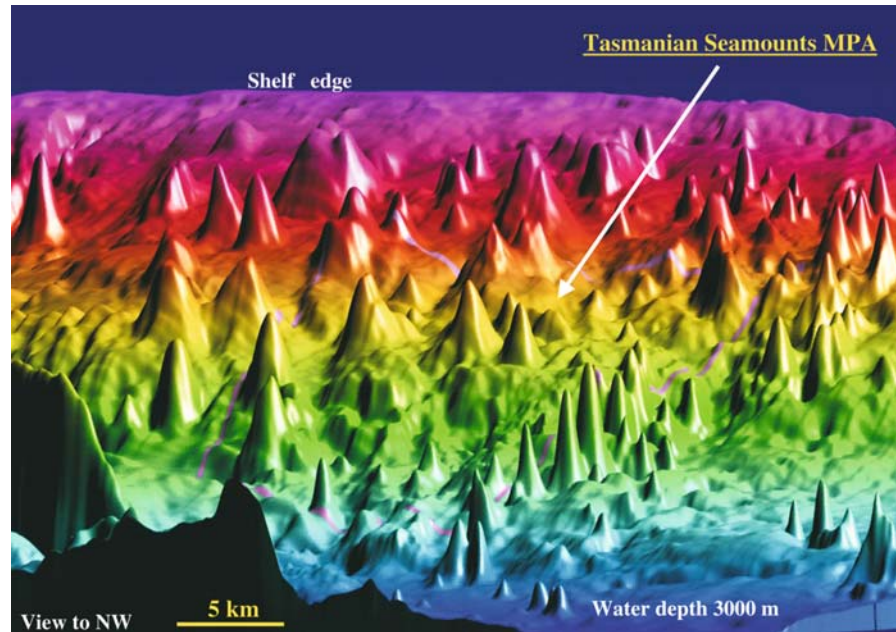
Orange Roughy, a fish with reddish body and fins, large bony head and large eyes is a remarkable deep-sea fish species – apart from its renowned taste. It becomes mature only at 20 years, does not grow larger than 50 cm and is thought to live up to 150 years at a depth of 800–1500 m.

Orange Roughy is found around the world, including the North Atlantic, where the species was first discovered in 1889.

5.2.7

Image 5.2.7-1.

Cut-out of the field of the Tasmanian Seamounts. Multibeam image. The MPA was declared in 1999. The area with 20 of the extinct volcanoes lies on the mid slope 170 kilometers south of *Hobart* with the center coordinates 46° S, 146° E. The Reserve indicated by the pink ribbon in the image covers about 370 square kilometers. Bottom trawling as well as Petroleum and mineral exploration are banned. On very high resolution images the fish become susceptible to overfishing because fishermen use the information to find their hiding places. The details of these data types will continue to introduce environmental and other issue on how Geoscience Australia distributes these images and to what resolution.



Project: Tasmante Swath Mapping and Reflection Seismic Cruise, 1994. The cruise mapped almost all the area covered by the MPA, except a very narrow section along its eastern boundary. This and an adjacent area to the east was fully mapped by AUSTREA-1 in 2000

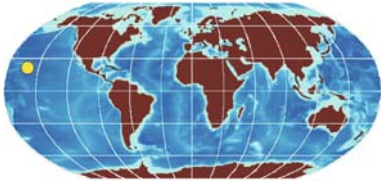
Survey vessel: *RV L'Atalante*

Multibeam system: Simrad EM12D; 11/12 kHz, 150 degree total beamwidth; footprint of the beams at the sea floor: 30–50 m

Potential craters of the seamounts are either not existent or less than 200–300 meters wide, height exaggeration: 10 times

Image ©: Geoscience Australia, Canberra ■

5.2.8 Hot Spots Islands: The *Hawaii* Region



The great majority of volcanic structures worldwide were originally formed at the tectonic plate boundaries (Sect. 5.2). Sub-aqueous structures of volcanic origin, those which originated at the *mid-ocean ridges* (Sect. 5.2.3, 5.2.4) have since migrated with the plate far away from their origin and thus reside all over the oceanic plates, an innumerable number of mostly benign seamounts at present. The most pronounced representatives of active volcanic edifices in the ocean are found at the *island arcs* of the western Pacific (Sect. 5.2.2). But there are prominent ensembles of active volcanic islands far off the oceanic plate margins such as the *Hawaiian Ar-*

chipelago. This ensemble of islands is one of those in the *Pacific Ocean* that are grouped like a straight string of pearls. The well known *Hawaiian Islands* are only the visible part and a small fraction of a chain of submarine mountains 3 000 km long, towering from an abyssal plain, deeper than 5 000 m. The total height of the large Hawaiian Islands exceeds the *Himalayas*.

The key to explain this enigmatic phenomenon was the discovery of the increasing age of the volcanic islands and seamounts with increasing distance from the last, youngest, and most exposed of the islands. This corresponds to the increasing summit erosion along the line. These consistent features led to a fundamental hypothesis suggested in the sixties by Wilson, which became known as the *hot-spot hypothesis*. The postulated process fits into the model of plate tectonics, which was also developed in the sixties, postulating the shift of oceanic plates, mainly forced by their subduction rather than driven by emerging magma at the mid-ocean ridges

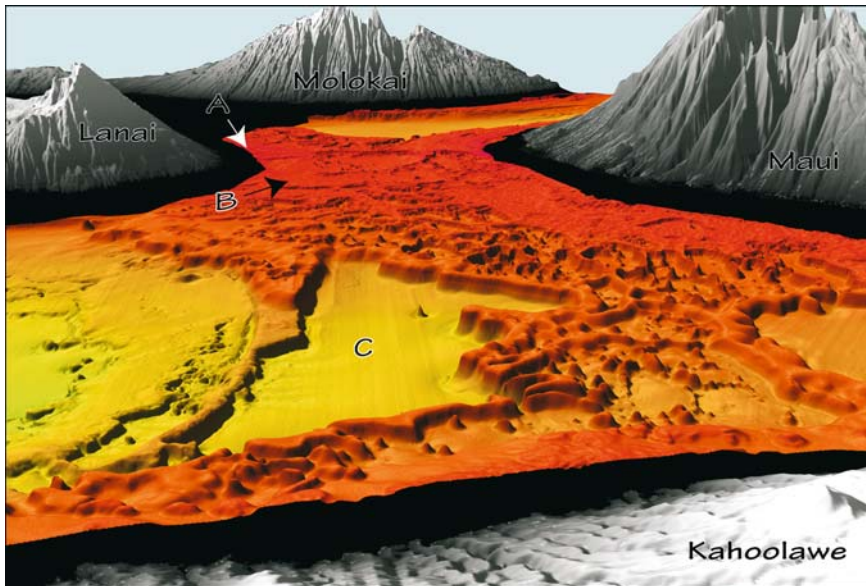


Image 5.2.8-1.

Kahoolawe area; coral reef area between Hawaiian Islands. Multibeam image. The oblique overview shows the sea floor between the islands Kahoolawe in the foreground, Molokai in the background, Lanai on the left, and Maui on the right. The distance between Lanai and Maui is about 20 km; the scale across the image in the foreground is 10 km. The sparse regions indicated in red between Lanai and Maui A are the present living reefs in water depth of less than 40 m. Dark orange areas B are drowned reef platforms and pinnacles in water depths between 50 and 85 m. The black areas of very shallow water are unmapped. The large basin in the middle C is shown in more detail from the opposite side in the subsequent image.

2 mm yr⁻¹ under the load of the volcano, a rate that must have slowed down with time. In addition, long-term sea level rises and falls are about 2 mm yr⁻¹. The area between Lanai and Maui has filled with lava flows as the islands subsided but vertical growth of coral reefs kept pace with sea level fluctuations and island subsidence. However, the coral growth in the area between Lanai, Kahoolawe, and Maui could not keep up with these level variations and lava-flow build-up, and has now been submerged.

Project: Hawaiian Coral Reefs; 1998

Research vessel: *RV Ocean Alert*, USA

Multibeam echosounder: Kongsberg Simrad EM300; 30 kHz, beamwidth 1° and 2°, 135 beams; Resolution: 30 m, vertical exaggeration factor: 5; Land topography: USGS DEM, resolution: 30 m

Image ©: James V. Gardner, U.S. Geological Survey, Menlo Park, USA ■

Image 5.2.8-2.

Close-up cut-out of the coral reef between three Hawaiian Islands, Kahoolawe area. Multibeam image. The image shows an oblique view to the east across the sea floor towards the island of *Kahoolawe* between *Lanai* and *Maui*. The region indicated A is the modern reef platform. The relief is exaggerated 5 times but the escarpment slope in the foreground is in fact 50° steep. The reef platform escarpment consists of layer upon layer of reef material. The slump at the base of the escarpment indicated B shows two large blocks, 5 m high, that have been transported 700 m away from the escarpment. This slump is one of the few occurrences of collapse of the escarpment found in this area. The width of the foreground of the perspective image is 2.7 km. The black area of very shallow water around the islands in the background is unmapped.

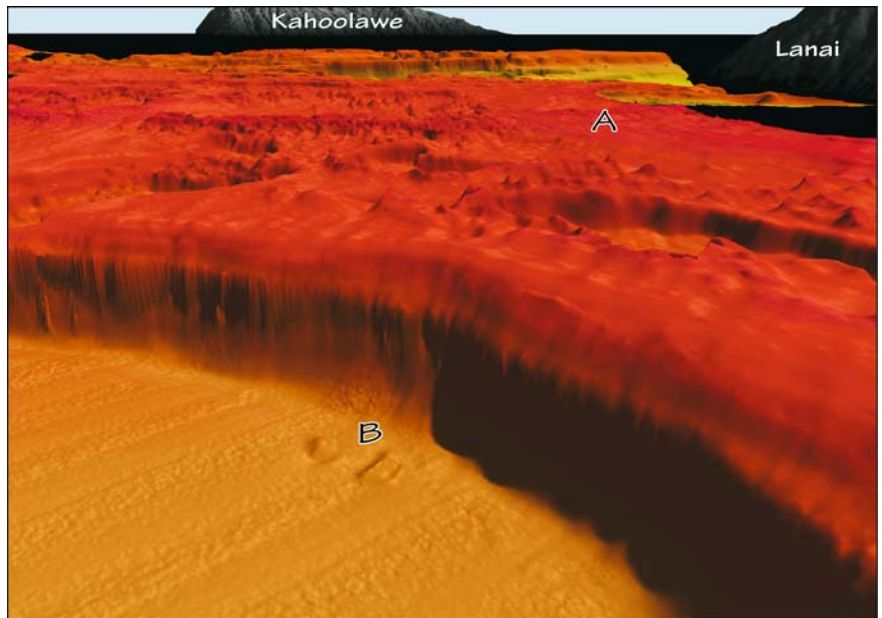


Image documentation: same as for Image 5.2.8-1 ■

(Sect. 5.2). Oceanic lithosphere, with the deep-sea floor as its crust, migrates across a “spot” of hot, melted magma upwelling from the Earth’s mantle below, which is considered more or less fixed. The upwelling magma will push up and disrupt the lithosphere and the crust by its buoyancy, thus giving birth to huge seamounts and even new islands. The upwelling of magma is certainly discontinuous, similar to volcanic eruptions of other origin. Thus, the next island formation will only happen after further migration of the lithospheric “lid” on top of the hot spot. Recent discoveries during the *Ocean Drilling Program (ODP)* confirmed however that the Hawaiian Hot Spot is *not* fixed but has migrated considerable distances through time. The entire paradigm of a fixed hot spot is now open to question.

The depth of the plumes of upwelling basaltic magma was estimated recently by *seismic tomography*, based on the same principle as the oceanographic tomography (Sect. 6.1.3), utilizing one way sound propagation instead of echo sounding. The result, indicating more than 500 km depth of the roots of the *ascending* hot plumes is comparable with the depth reached by the colder and denser *descending* tectonic plates in the oceanic subduction zones.

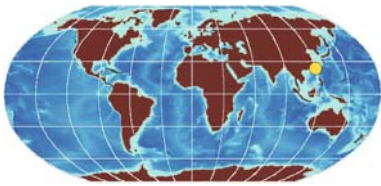
The sequence of hot spot islands indicates not only the time scale of their history but also the history of

the path of the lithospheric shift. This is particularly obvious in the chain of the Hawaiian Islands: The global depiction of the Pacific sea floor (Sect. 5.1.1.2) shows an abrupt change of direction of the Hawaiian chain from north-west to north reaching up to the subduction zone of *Alaska* (Sect. 5.2.1). This second part is named the *Emperor Seamount Chain*. Both chains together are more than 6 000 km long and of a maximum age of 85 million years, reaching back to the time of the saurians.

There are two other major island and seamount chains in the Pacific, farther to the south of the Hawaiian-Emperor chain, which show a similar rate of volcanic migration of about 10 cm per year and all of them changed their direction at about the same time, 42 million years ago. This suggest a change of the direction of motion of large parts of the Pacific Plate. Nevertheless, the research on the presumably frequent occurrence of hot spot volcanism in particular on the continents is still in a primary phase. The two sound images selected to demonstrate features of such “intra-plate” volcanic islands are from the Hawaii group, one of the most active hot spot areas on Earth. A third image near *Kauai* is shown in the context of imaging by bathymetry and altimetry in comparison (Sect. 5.1.2).

5.2.9

5.2.9 Taiwan and the Tectonic Activities at the Western Philippine Plate Depicted by Multibeam Imagery



Taiwan and its offshore region are a focal area of complex tectonic processes. The mountainous island at the north-western edge of the *Philippine Sea Plate* is situated north of a *tectonic exception* from the west-

ward motion of this oceanic plate and its subduction under the *Eurasian Plate* (Sect. 5.2). This exception is the *Manila Trench*, the westernmost margin of the *Philippine Sea Plate*. At this trench, it is the *Eurasian Plate* with the *South China Sea* that is subducted under the *Philippine Sea Plate*. This inversion of plate behavior at the *Manila Trench*, in contrast to the *Philippine Trench* in the south-west, as well as at the *Ryukyu Trench* in the north-west of the *Philippine Sea Plate*, may be seen as compensation for the diverging subduction at these two trenches adjacent to the *Manila Trench*.

▶ p. 145

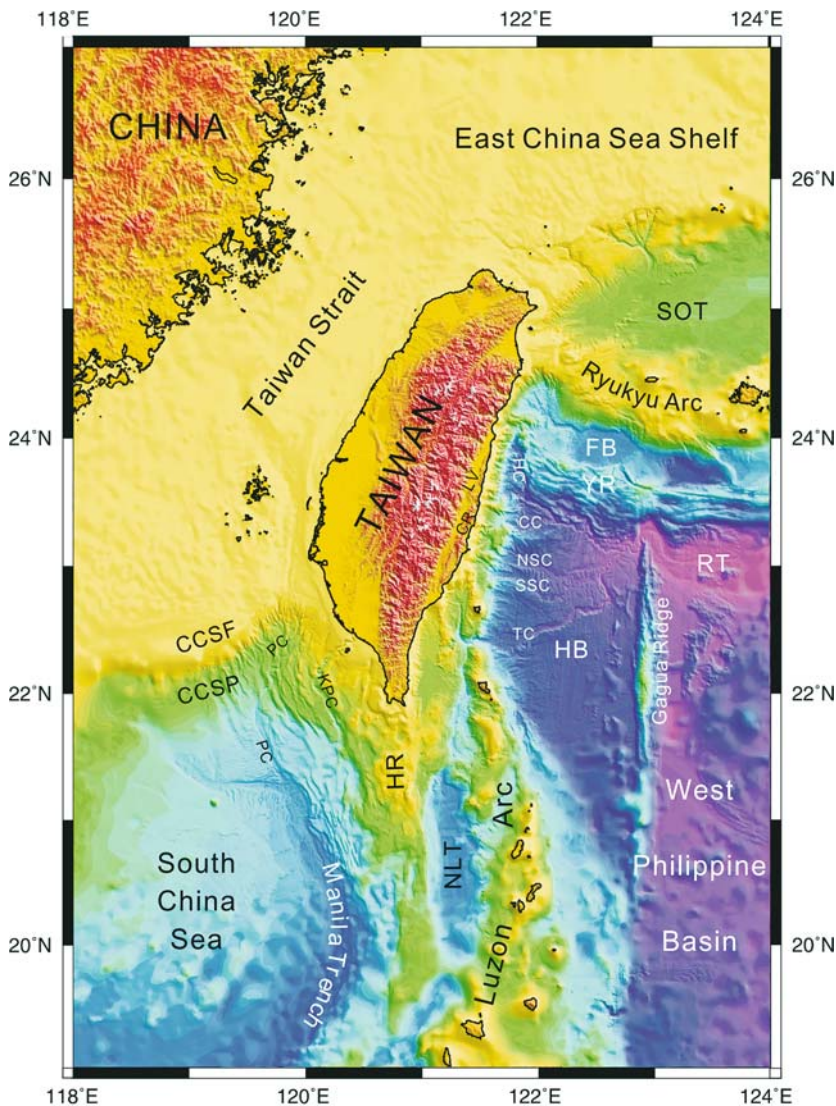
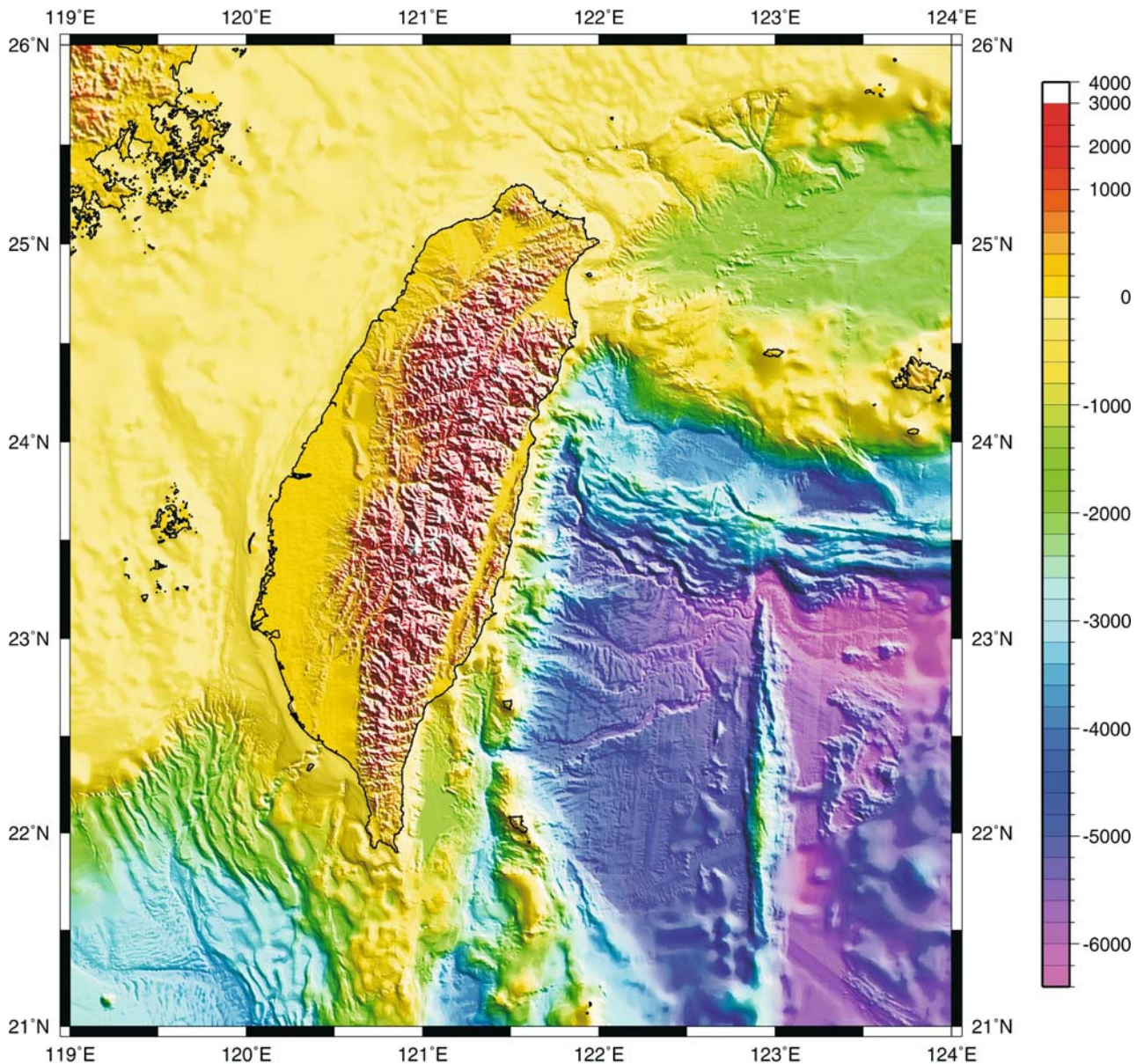


Image 5.2.9-1.

Overview of Taiwan and its offshore region.

Multibeam image. In the north and west of Taiwan the overview shows the continental shelf and slope of the passive Chinese continental margin. Offshore of southern Taiwan the major morphological features are N-S trending ridges and troughs, reminiscent of other subduction zone formations of the *Philippine Sea Plate*. From west to east, these are the *Manila Trench*, which governs the orientation of the subsequent topography, followed by the *Hengchun Ridge* which is an accretionary wedge (Sect. 5.2.1), then followed by the *North Luzon Trough*, which is a forearc basin (Sect. 5.2.2), and the *Luzon Island Arc*. East of the *Luzon Arc* we see the *Huatung Basin* with its canyon systems, separated from the *West Philippine Basin* by the nearly exactly N-S trending *Gagua Ridge* along 123° E.

This N-S trend of the topographic features changes abruptly east of northern Taiwan. Here the sea floor is characterized instead by E-W trending features following the local course of the western end of the dominating *Ryukyu Trench*. From north to south, these formations are the *Southern Okinawa Trough* and the *Ryukyu Island Arc*, followed by a chain of forearc basins, separated from the *Ryukyu Trench* by the *Yaeyama Ridge*. This ridge formation with its multiple folded relief indicates the accretionary wedge type (Sect. 5.2.1) consisting of stripped-off sediments during plate subduction at the *Ryukyu Trench*.



Annotations in Image 5.2.9-1 (left figure): CC: Chi-Mei Canyon; CCSF: Chinese Continental Shelf; CCSP: Chinese Continental Slope; CR: Coastal Range; FB: Forearc basin; HB: Huatung Basin; HC: Hualien Canyon; HR: Hengchun Ridge; KPC: Kaoping Canyon; LV: Longitudinal Valley; NLT: North Luzon Trough; NSC: North San-Hsian Canyon; PC: Penghu Canyon; RT: Ryukyu Trench; SOT: Okinawa Trough; SSC: South San-Hsian Canyon; TC: Taitung Canyon; YR: Yaeyama Ridge
 Project: ACT cruise, funded by CNRS of France, as part of the Taiwan-France Cooperation in the Earth Sciences Program; 1996 Survey Vessel: Atalante, France

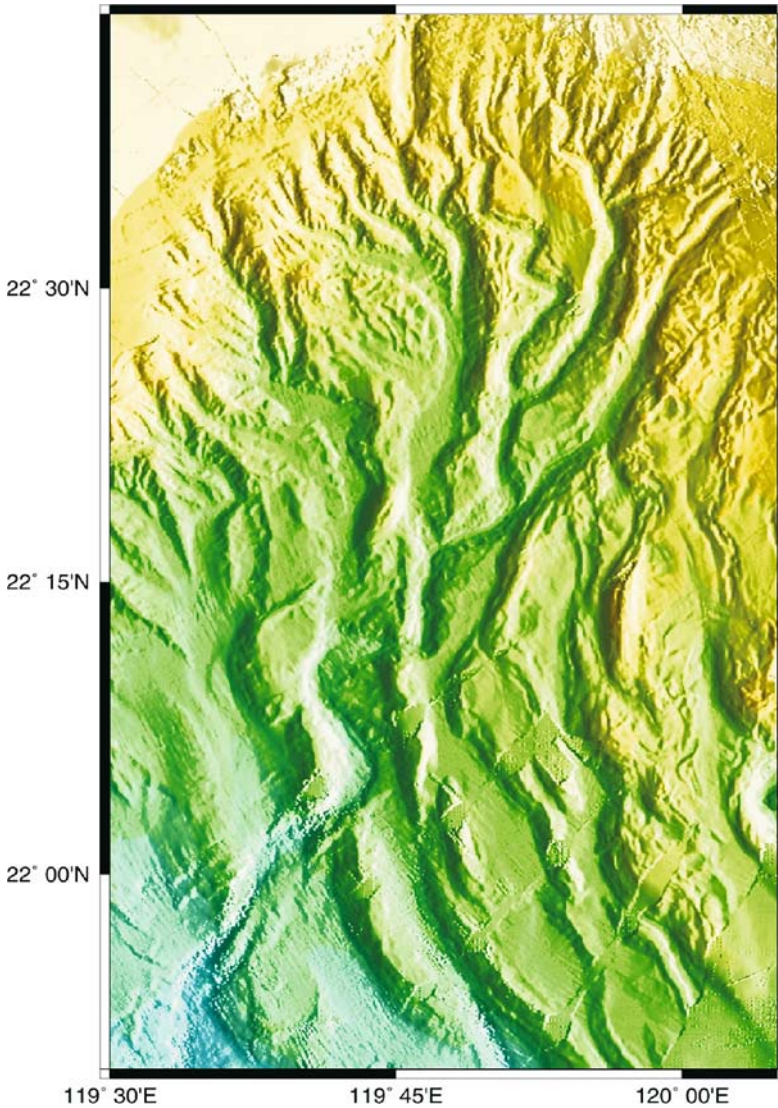
Multibeam echosounder: SIMRAD, EM12-dual, hull-mounted; frequency: 13 kHz, beamwidth: 1.8°/3.5°, 162 beams; fan width: 150°

Image ©: Char-Shine Liu^{1,2}, Serge Lallemand³ and Shao-Yung Liu²

¹ Institute of Oceanography, National Taiwan University, Taipei, Taiwan

² National Center for Ocean Research, Taipei, Taiwan

³ Laboratoire Dynamique de la Lithosphere, CNRS-Universite Montpellier 2, Montpellier, France ■

**Image 5.2.9-2.**

In combination with Image 5.2.9-1: The Penghu Canyon in the south-west. Multibeam image. Offshore south-western Taiwan is the exceptional place where the *South China Sea*, as part of the Eurasian Plate, is subducted under the Philippine Sea Plate instead of vice versa. This “trench of exception”, the Manila Trench, is visible with its northernmost part in Image 5.2.9-1, south of 21° N. The high resolution multibeam image provides evidence of which is subducting what: East of the Manila Trench we see the *Hengchun Ridge* a “ridge of ridges”, similar to the *Yaeyama Ridge* behind the *Ryukyu Trench* east of Taiwan. Such accretionary wedges of sediment ridges are stripped off during tectonic plate subduction. Thus the Manila Trench with its accretionary wedge “head-wall” indicates the exceptional eastward subduction of the South China Sea *under* the Philippine Sea Plate, whereas the *Ryukyu Trench* east of Taiwan with the *Yaeyama Ridge* as its accretionary head-wall is evidence of the “regular” subduction of the Philippine Sea Plate under the South China Sea of the Eurasian Plate.

However, at first sight these ridge formations can look similar in kind to ridge agglomerations of an entirely different origin. Directly north of this tectonic arena of subduction at the Manila Trench we see a conspicuous *non-tectonic* process on the Chinese continental slope: It is the *erosional Penghu submarine canyon complex* which fills the Image 5.2.9-2 with its large number of tributary branches. The Penghu Canyon combines the western tributaries and finally transits into the Manila Trench – the only bracket as it were – of both fundamentally different scenarios.

This close-up of Image 5.2.9-2 reveals the difference in kind between both types of ridges: the valleys of the Penghu tributaries are flat with sand

fill and subdivided by ridges, which are again covered by a network of smaller channels and furrows, indicating complex processes of *erosion*. In contrast, the *subduction*-induced ridges of an accretional wedge are not interconnected like spreading branches but are more or less parallel and their valleys are neither broad nor flat but are sharp incisions, as a result of being pushed together. South of 21°20' N the high resolution of multibeam imaging ends and is replaced by the coarser altimetric image with its typical orange peel surface (Sect. 5.1.1), superimposed on the real sea floor relief. Here, south of the letter M of Manila, the specific character of the ridges is no longer resolved. They are not even recognizable as ridges.

The conspicuous contrast between tectonic-induced accretionary multifolded ridges and erosional ridge-valley formations is slightly overemphasized and simplified here. In reality, the structure of tectonic origin reaches further north and includes both faults and accretionary ridges, but both are indeed superimposed by younger erosional formations with sediment fill and erosive furrows downslope of ridge flanks. The detailed analysis of these primary and secondary processes is also based on high resolution imagery.

Image documentation and ©: same as in Image 5.2.9-1

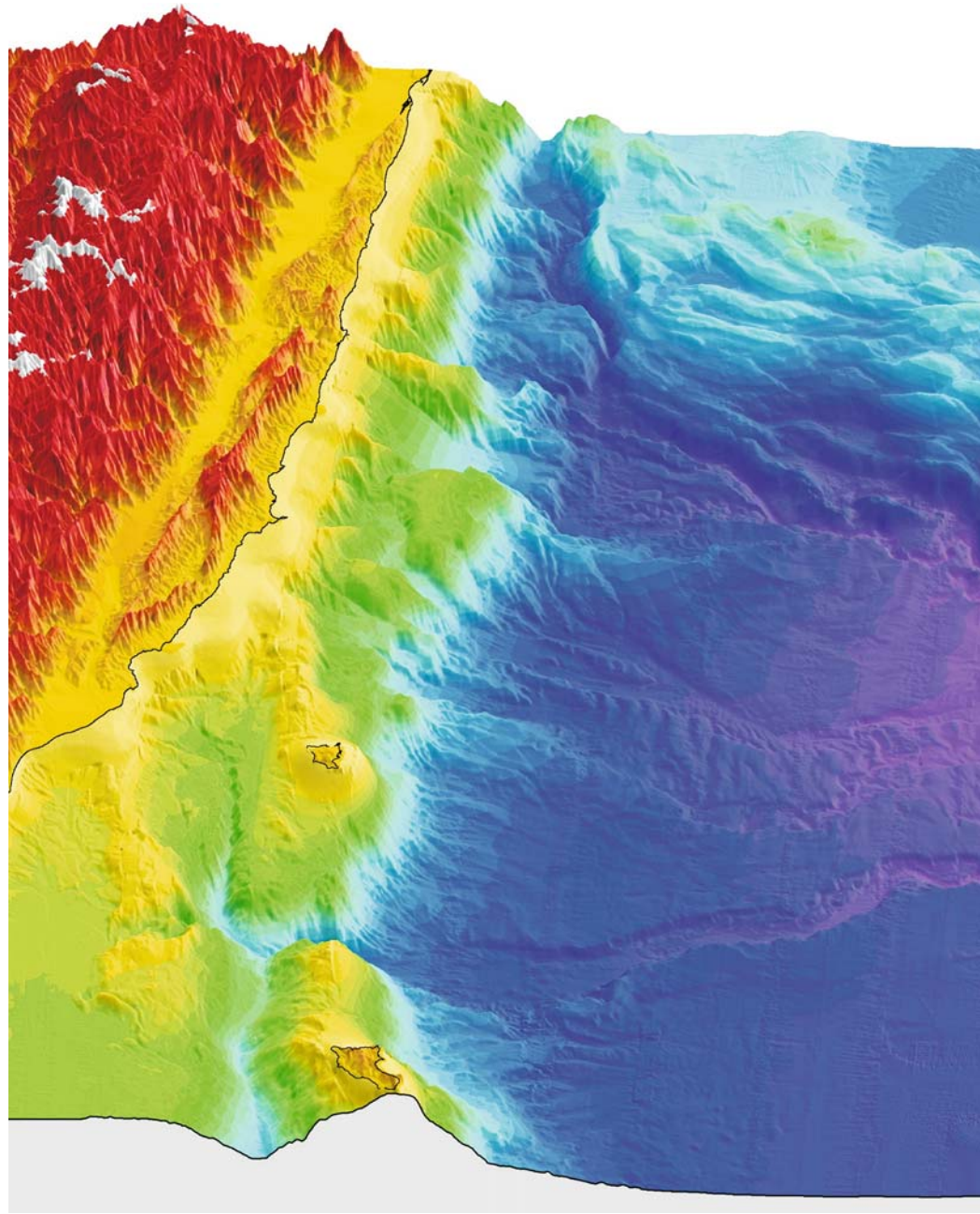
Stripes of data gaps in the southern right-hand part of the image where the multibeam swaths do not completely come together are bridged by altimetric data of lower resolution ■

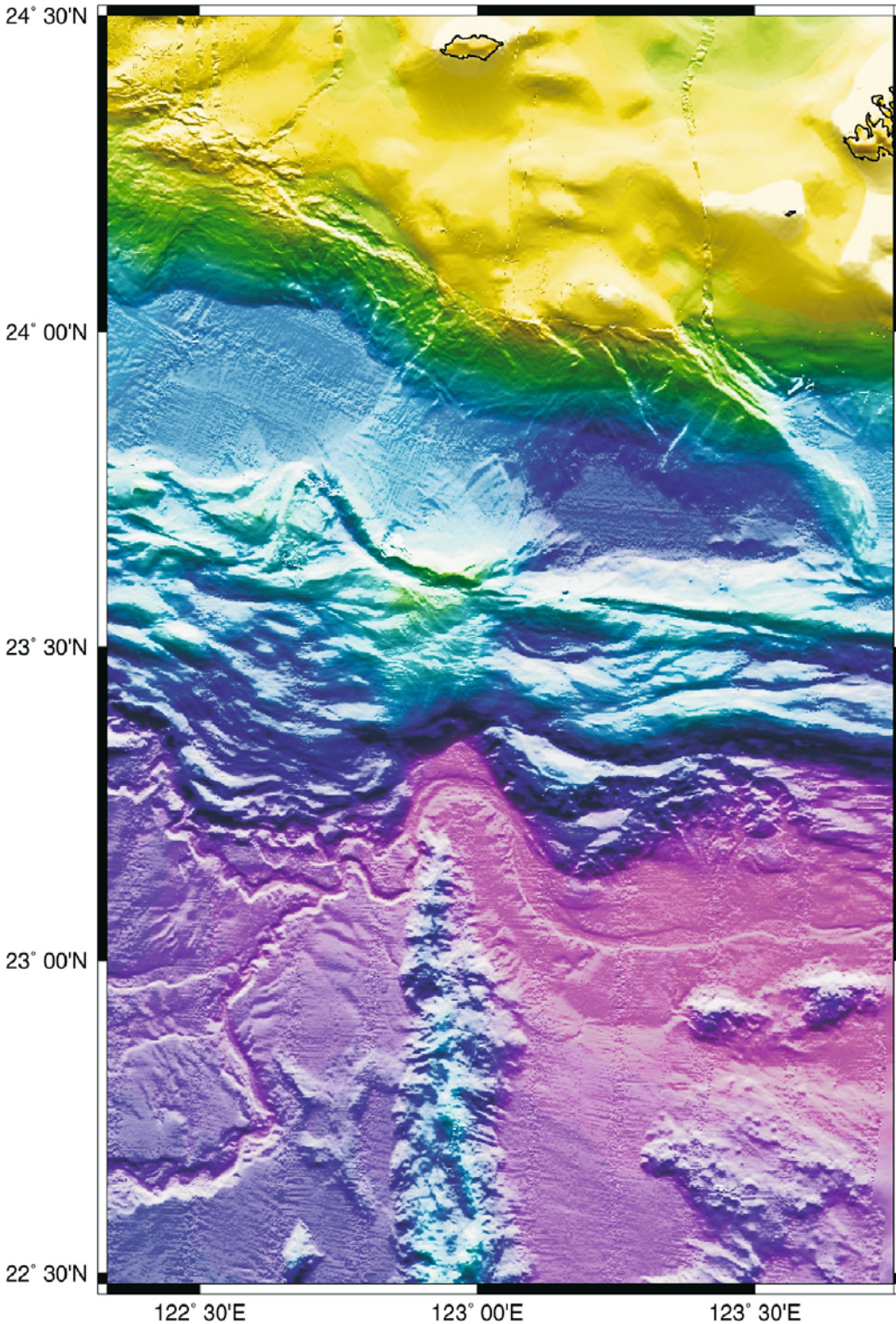
Image 5.2.9-3.

The canyon system east of Taiwan. The multibeam image shows the detailed morphology of the steep eastern slope of Taiwan with the submarine canyon systems in the Huatung Basin. The four canyons which transport sediment in the form of turbidity flow of a higher density than water (Sect. 5.3.2, 5.3.6) show conspicuous similarities with river systems on land.

From south to north, the *first* of the four is the *Taitung Canyon* which originates at the southern tip of the Coastal Range in eastern Taiwan. Starting southward along the axis of the *Taitung Trough* it turns eastward across the Luzon Arc into the Huatung Basin. It then flows north-eastward for about 170 km before entering the Ryukyu Trench at the northern tip of the Gagua Ridge. The *second* is the *San-Hsian Canyon* system. It consists of two submarine canyons, the *South San-Hsian Canyon* and the *North San-Hsian Canyon*. Both originate from the steep slope of east Taiwan. The South San-Hsian Canyon merges into the North San-Hsian Canyon downstream, which then combines with the Taitung Canyon further east. North of the San-Hsian Canyon system we can see the *Chi-Mei Canyon*, the *third* of the series. The Chi-Mei Canyon originates from the *Hsiukuluwan-chi River* on land. The huge amount of sediment carried in by this river, which is the only one that cuts through the Coastal Range, widens and flattens the Chi-Mei Canyon floor downstream. Number *four*, the *Hualien Canyon* originates from the northern end of the *Longitudinal Valley* and flows along the southern edge of the Yaeyama Ridge, where it also merges into the Ryukyu Trench.

Other sedimentary features, such as numerous submarine slumps along the eastern slope and N-S trending fault scarps, revealed by the high-resolution image in the central part of the Huatung Basin, were formed due to eastward slide of the sea floor sediment.



**Image 5.2.9-4.**

A ridge enters a subduction trench. Multibeam image. Another remarkable sea floor morphology is the meridional Gagua Ridge entering the Ryukyu Trench off eastern Taiwan, where it indents the Yaeyama Ridge behind. It is a classic subduction feature of obstacle entrance. The incision process may be reminiscent of seamounts entering the overriding plate during subduction, leaving a kind of gateway behind (Sect. 5.2.1). However, the conspicuous incision into the multiple folded Yaeyama Ridge is certainly of different origin. The opening around the northern tip of the Gagua Ridge must have been forced and maintained by sediment turbidity flow coming down from the mountain chain of Taiwan. The merger of four major canyons west of the Gagua Ridge, the curved path of the resulting single channel incised around the northern tip of the Gagua Ridge, and its eastern extension into the Ryukyu Trench are all clearly evident. Another tectonic process is superimposed however: The prominent E-W trending linear feature observed along the northern edge of the Yaeyama Ridge is a strike-slip fault (Sect. 5.2.5), formed due to the oblique convergence of the Philippine Plate with the southern part of the Ryukyu Trench-arc system.

Image documentation and ©: same as for Image 5.2.9-1 ■

The overview relief image and the three high resolution cut-out close-ups show further processes of complicated tectonics and also of dramatic sediment transport off eastern and southern Taiwan. Its mountain belt was formed by the collision of the *Luzon Volcanic Arc*, extending along the western edge of the Philippine Sea Plate, vis-à-vis the passive *Chinese Continental Margin* of the Eurasian Plate. This arc-continent collision reaches back about 5 million years and is still on-going. Rapid erosion of the Taiwan Mountain belt provides a huge influx of sediment to the sea floor east of the island. Most of this sediment finds its way from near-shore to the deep-sea floor through four main submarine canyons that cross the floor of the *Huatung-Basin* like meandering river beds of turbidity flow. Moreover, there are converging branches of submarine canyon systems off southwestern and eastern Taiwan and along the northern slope of the Southern Okinawa Trough.

The high resolution multibeam image of the region east and south of Taiwan is based on the joint French-Taiwanese ACT cruise in 1996. The image was calculated with the digital elevation model (DEM) by Liu. The obviously less resolved adjacent areas are filled by single-beam depth sounding data and Satellite altimetry (Sect. 5.1.1) from the Smith and Sandwell data base of 1997. The land relief is derived from satellite radar data set ETOPO30.

5.3 Passive Continental Margins: Examples of the Prevailing Formations and Processes on the Shelf and of Utilization and Protection of Coastal Waters

Passive margins means: the formations are not part of or near a tectonic plate margin but represent features of the *continental shelf* down to the adjacent deep-sea floor. The examples presented in this chapter deal primarily with sediment dynamics of the *European Continental Margin* and many of these images are published in the book of Mienert-Weaver (ed.). This complex continental margin contains a textbook-like variety of processes and formations. But there are extreme and unique formations on passive margins of other continents, a collection of which is presented for comparison.

Europe is part of the *Eurasian Plate*, one of the seven large tectonic plates carrying the continents of the globe (map of Sect. 5.2). The nearest active plate margin in the west, the *divergent Mid-Atlantic Ridge* (Sect. 5.2.3) is hundreds to thousands of kilometers away from the coastline. The south of Europe however is divided sharply like a politically defined border from the *African Plate* by a geological line going through the *Strait of Gibraltar* and passing the *Mediterranean* south of *Italy* and *Greece*. This line is a *convergent* plate margin with subduction activities (Sect. 5.6). North of this area, the European Continental Margin is different in kind from active continental margins such as the west coasts of the Americas with their deep trenches generated by the adjacent oceanic plates which are continuously subducted under the large *North* and *South American Plates* (Sect. 5.2.1).

Despite the absence of such dramatic plate tectonic subduction forces with induced volcanism and earthquakes, the west and northwest European continental margin is not at all invariable and benign. In fact, the sea floor is also subject to permanent and abrupt, more or less dramatic reshaping of various origin and within various time scales. But here it is mainly the sediment, not the Earth's crust, that is forced to change its relief and structure. Unlike the young deep-sea floor where the sediment coverage is comparatively thin, the European Shelf has been draped by thick layers since the formation of the western and north-western margin, which happened through rifted break-up of the continent between 120 and 50 million years ago.

The profile of the continental margin of this north-west European type can be described in principle like this: *the margin is the transition zone between the land and the floor of the deep sea, the abyssal plain*. The shallow part of the margin, adjacent to the coast, called *continental shelf* slopes gently down to typically 200 m water depth until it comes to a sudden break into a steep flank. The first, steepest part of it is called *continental slope*. About halfway down the inclination changes and gradually flattens out eventually into the horizontal of the *abyssal plain* of several thousand meters depth.

This last, external zone of the margin, called *continental rise* is less clearly defined because there are often less simple forms of transition to the deep-sea floor with troughs, seabights, ridges, banks, and terraces in

between, representing some of the predominant large scale formations of the *North Atlantic* west of the *United Kingdom*. There are broad shelves measuring hundreds of kilometers, like the *Celtic Shelf* south of *Ireland*, and very narrow ones just nearby at the rim of the *Bay of Biscay* where the continental slope is also very narrow and extremely steep, descending to more than 4 000 m within a few tens of kilometers distance. Altogether, this European Continental Margin varies strongly in origin and shape.

The continental margins, the European one in particular, are the regions of accessible and exploitable marine resources. The mineral oil and gas industry is implementing and exposing platforms and pipelines on the shelf (Sect. 7.2.2). It is the shelf as well, where the main European fishing activities take place (Sect. 6.3.1). The shelves are focal areas of shipping lanes (Sect. 7.1.1) and of the most extended offshore constructions, the intercontinental submarine telecommunication cables (Sect. 7.2.1). From recent times, widespread parks of huge wind-driven power plants are in the planning phase of being erected on the European shelf. Their propellers and carrier towers will be much larger than those operated ashore. Even tidal current power plants are under consideration.

However, the continental margins are also the origin of major hazards for the adjacent coastal lowlands with their high densities of human population. They are often the scenario of severe inundations which may even increase in violence and frequency depending on the development of climate. Fortunately the most disastrous and irreversible inundation of lowland areas is very rare but has occurred within historical times. This is the rise of the water level due to geologic subsidence, with which entire cities were submerged (Sect. 7.3.1). Among major, though rare hazards, are submarine landslides of unstable sediment layers which can cause devastating *tsunamis* (Sect. 5.3.1) and indirectly influence the global climate.

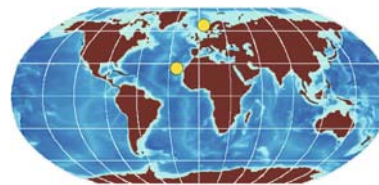
Much more frequent however, than all the other lowland perils are major sediment motions due to storm-induced currents. They erode coastal areas (Sect. 7.1.2) and cause shoals endangering shipping fairways (Sect. 7.1.1) with migrating and increasing dunes. No

less hazardous is the current-induced under-scouring at offshore installations (Sect. 7.2.2). Free span sections of pipelines may then break and contaminate the sea with mineral oil.

From the ocean research point of view these margin sediments are considered a kind of natural laboratory of highly complex, interacting processes of micro- and macro-biology with chemistry of gases, fluids and solid state. These interactions depend on the prevailing and changing conditions of the oceanic environment over various scales of time. Products of these interactions are major carbonate deposits, most obvious as wide spread clusters of mounds with enigmatic inhomogeneity of compounds and consistency (Sect. 5.3.4). Even more spectacular are the enormous deposits of gaseous and solid methane found at continental margins (Sect. 6.2.1). The conditions and mechanisms of their origin, stability and instability are of particular scientific interest, also because of their presumably generic character. The research results derived from selected, exemplary sites may thus apply to continental margins worldwide.

The discoveries of such deposits and the exploration of their external and internal structure have been decisively brought forward by advanced sound imagery. Some series of typical image examples are presented in this context which also includes the *special sections* mentioned. These however deal also with sound images of the utilization of the European Margin and the surveillance and protection of offshore constructions and implementations.

5.3.1 Submarine Escarpment Slides



An avalanche covering an area of the size of Germany with a 10 m thick layer of debris is hardly imaginable.

But such a volume of sediment moved as a submarine slide off the coast of the North European Continental Margin, west of what is now Norway, about 7 000 years ago. The famous *Storegga Slide* is one of the largest exposed submarine slides known. It reached a run out

distance of 800 km and has affected an area of 95 000 km². A sediment volume of about 3 000 km³ has been displaced whereby 250 km³ arrived at the Norway Basin as sediment suspension. The Storegga Slide was discovered, quantified in its size and investigated in respect of its external and internal structure and potential causes of the motion by various methods of ocean acoustic imaging. Storegga Slide, with a total of more than sixty lobe phases developed within a geologically instantaneous time frame as one retrogressive slide event.

A comparison with an avalanche in the mountains is misleading however. On land, an escarpment becomes unstable only at steep slope angles. At the submarine regime of continental margins there are sediment layers which are so loosely connected that an earthquake may suffice to initialize a major slide over hundreds of kilometers at only a few degrees and even less of slope. What is the reason that huge sediment masses can glide more easily than a ship on soft soap at her christening ceremony?

The investigations up to now appear to indicate the accumulation of two possible mechanisms of instability: Instability is created by rapid loading of fine grained hemipelagic deposits and ooze at peak glaciations during the last hundreds of thousand years. Such high sedimentation rates of various origin with a build up of excess pore water pressure are considered one of the potential causes. If this first mechanism is enhanced by methane gas pressure from deposits below (Sect. 6.2.1), it may lead to a kind of liquefaction and/or a weakened layer at a critical sediment horizon. At the “liquefied” layer the stabilizing friction forces between the sediment grains are more or less removed and replaced by the relatively low viscosity of a dense suspension. This quasi fluid acts as a very effective lubricant. The mechanical vibration of an earthquake can then initialize the slide motion even when the escarpment slope is small.

Technical liquefaction of sand sediments is applied as a cheaper substitute for drilling or piling for the insertion of fundament poles in sandy soil for offshore and also inshore constructions needing deep going fundaments for stability. The excess pore water pressure is generated by water injection to make the pole sink into the sediment as if this were a swamp.

The size and structure of layers of instability at continental margins, together with the slope profile, will presumably determine the volume and the run out area of the landslide. It does not appear probable that such landslides occur as a single event. After interruptions the pressure induced liquefaction may start again and the slide process may continue. Methane hydrate deposits which are clearly indicated in high resolution seismograms by the so called Bottom Simulating Reflector (BSR, Sect. 6.2.1), are considered suspicious slide candidates in particular when other environmental conditions are enhancing the probability of slide release.

One of the potential major effects of a sudden slide can be a kind of internal bow wave resulting in an instantaneous depression of the sea surface level above the event. This is the origin of an ultra-long surface wave, propagating with the corresponding high speed. Depending on the energy involved and the slope profile of the opposite coast the high-speed wave called *Tsunami*, approaching the shallow coastal water develops a high crest with a steep flank similar to a shock wave in a rush, resulting in disastrous devastations of coastal settlements. The catastrophic Storegga Slide event corresponds in age to the traces of devastation by a tsunami found along the western coast.

The other potential effect is of climate relevance. This is the emission of large amounts of methane because of the sudden removal of the tight lid of methane hydrate on top of the methane deposit. This extensive surplus cannot be dissolved anymore by the sea water and will thus ascend to the surface. Methane in the atmosphere is considered many times as effective as carbon dioxide in its role as greenhouse gas (Sect. 6.2.1).

This section presents overview- and close-up sound images of the largest and the smallest slide off the Norwegian shelf: the *Storegga Slide* and the *Trænadjupet Slide*. Recent multibeam reliefs of different scales of the Storegga Slide area are presented in the context of deep water imagery by Autonomous Underwater Vehicles (AUV, Sect. 7.4.2). In contrast, landslides on *Atlantic Islands (Canary Islands)* are also shown in this framework of submarine slides.

5.3.1.1 Storegga Slide

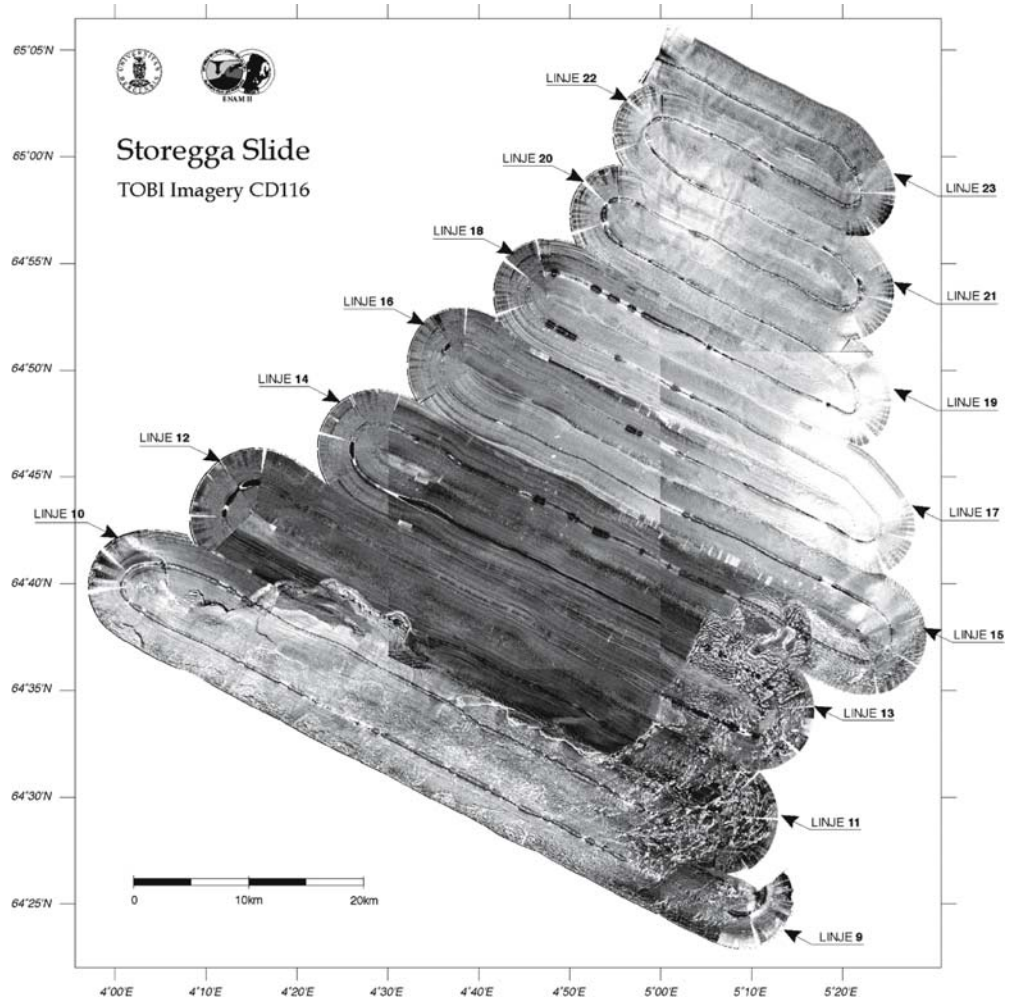


Image 5.3.1.1-1. Overview of the northern Storegga Slide escarpment. Sidescan mosaic image. The meander mosaic of 1997 covers 3 000 km² of sea floor off the Norwegian slope or margin and reveals two extremely different morphologies: The major part in the north has little if any remarkable structure. It shows the southern flank of the *Vøring Plateau*, slightly sloping to the west with undisturbed, smooth sediments. The other type is a northern cut out of the giant *Storegga Slide* depression, obvious through a rough and bright backscattering surface appearing abruptly at the lower margin of the mosaic image and in sharp contrast to the adjacent darker, weakly scattering smooth sediments. The area of investigation is about 3% of the area affected by the Storegga Slide, the largest exposed submarine landslide ever found on the European margin. The total slide area is shown in Sect. 5.3.1.2.

The meander mosaic image was made by the towed sidescan sonar TOBI with a signal frequency of 30 kHz. It is a mid range system of 3 km coverage on both sides with sufficient signal to noise ratio for high quality images. According to beamwidth and signal length, the resolution unit or the size of the seabed footprint varies from 4 × 7 m² at 0.3 km off track to 40 × 2 m² at the 3 km maximum range. The meander with slightly overlapping loops indicates the typical “blind” line of nearly vertical sound incidence below the ship track where the horizontal resolution is undefined (Sect. 4.3.1). In the hair pin bends of the ship track the narrow beam of TOBI naturally leaves fans of blind sectors uncovered. Selected close-ups of the slide morphology in comparison to another large slide are shown hereafter.

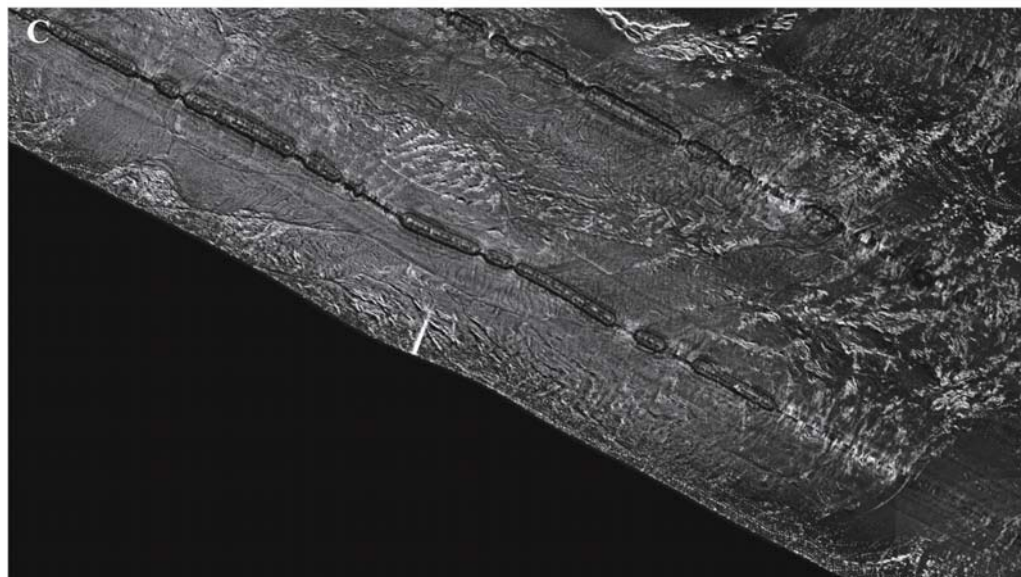
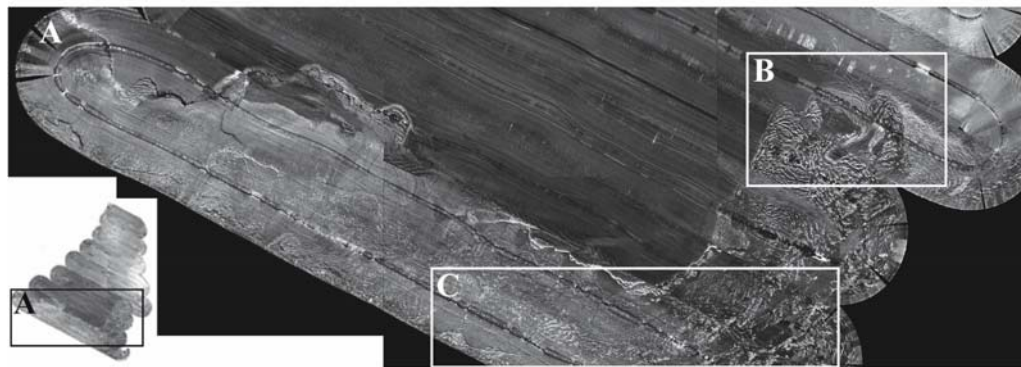
Project/program: Funding of the TOBI operation by the EU Commission under TMR (Southampton Oceanographic Centre), ENAM II and the Seabed Deep Water Industry Project; 1997

Survey vessel: *RRV Charles Darwin*; Sidescan sonar: TOBI; 30 kHz

Image ©: Hafliði Hafliðason, Department of Earth Science, University of Bergen, Norway ■

Image 5.3.1.1-2.

Close-up of the northern *Storegga Slide* escarpment. Sidescan mosaic image. Section A contains the major surveyed part of the *Storegga Slide* area with the frames B and C indicating the two close-ups shown. The close-up of B in the east with its spectacular ridge-furrow patterns belongs to the steep shelf break side where broad sediment transport channels are developed and the relief features, reminiscent of frozen eddies still appear preserved. Down-slope, as shown in the close-up of C, the structures look broken up into block-like units of rafting sediments. Here the deeply corrugated upslope relief of B with crest heights up to 100 m and more is disintegrated and smoothed to smaller scales. The light and shadow structures of the 2D-image are apparently more pronounced in the upslope area; the reason is the stronger backscattering from steeper flanks and larger irradiated flanks and the deeper shadows behind.



Project/program: Funding of the TOBI operation by the EU Commission under TMR Southamton Oceanographic Centre), ENAM II and the Seabed Deep Water Industry Project
 Survey vessel: *RRV Charles Darwin*
 Sidescan sonar: TOBI; 30 kHz, 0.5° horizontal beamwidth, tow depth: 300–400 m above seabed
 Image ©: Hafliði Hafliðason, Department of Geology, University of Bergen, Norway ■

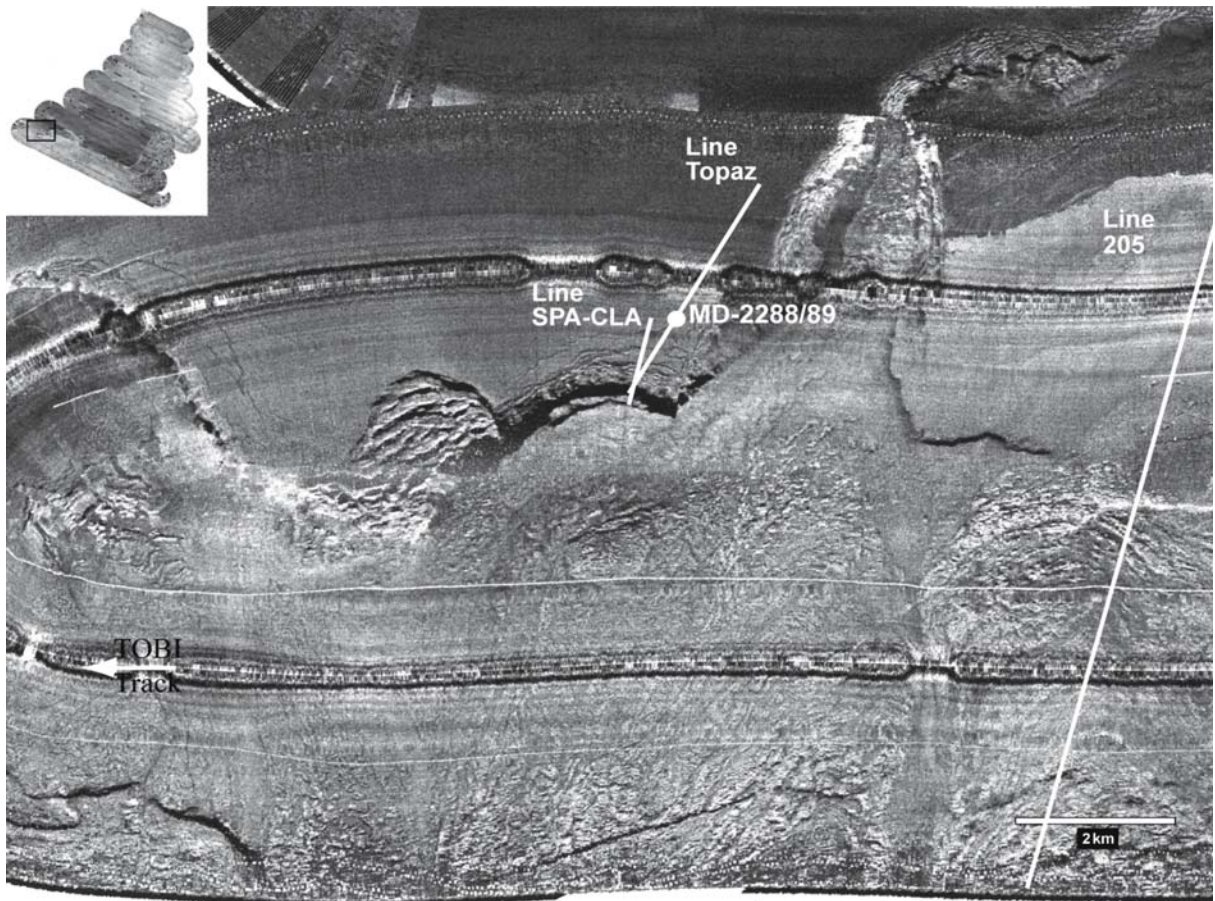


Image 5.3.1.1-3. Close-up of the northern Storegga Slide escarpment. Western cut-out of the sidescan mosaic image. The small insert of the complete mosaic image indicates the cut-out shown to explain major *secondary effects* of the huge Storegga Slide. The boundary between the undisturbed area of the *Vøring Plateau* in the upper left part and the northern rim of the slide below is marked by a conspicuous deep arced fracture in the middle with many smaller fractures disrupting the adjacent plateau outside the Storegga surface. Immediately west of this area of fractures there is another secondary feature of the Storegga Slide depression. Inside of an arced slide scar the sediments of the plateau started to move downslope onto the deeper Storegga surface, forming a system of ridges about 100 m apart, looking like dune crests athwart the sediment motion. This type of fault structures at the plateau rim indicates consolidated sediments up to the shelf break, due to high shelf ice pressure.

At some distance from the shelf break the sediments disintegrated easily by the slide which is obvious in the entire lower part of the mosaic image cut-out. This field is covered by low relief structures where the mobilized sediments created a secondary cross flow pattern onto the surface of Storegga, including a turbidite flow bed of several hundred meters width, visible near the range scale.

This close-up is chosen to demonstrate that the enormous weight of the Storegga Slide masses caused a severe large area depression, which steepened the plateau slope, instead of forming an overlying tongue. Therefore Storegga did not primarily thin out towards its northern side margins, but on the contrary drew uncovered sediment areas of the neighborhood onto the slide. The close-up illustrates also a peculiarity of sidescan imagery: the track of the sidescan towed behind the survey vessel clearly reveals the broad stripes of poor resolution at nearly vertical incidence directly adjacent to the center line, where the necessary grazing sound irradiation has not yet been achieved (Sect. 4.3.1).

Project/program: Funding of the TOBI operation by the EU Commission under TMR Southampton Oceanographic Centre, ENAM II and the Seabed Deep Water Industry Project

Survey vessel: *RRV Charles Darwin*; Sidescan sonar: TOBI; 30 kHz, 0.5° horizontal beamwidth, towed depth: 300–400 m above seabed
Image ©: Hafliði Hafliðason, Department of Geology, University of Bergen, Norway ■

5.3.1.2

Trænadjupet Slide

The *Trænadjupet Slide* is the smallest and perhaps the youngest of three slide complexes on the Norwegian Barents sea margin with high sediment supply. This is considered one of the two decisive reasons of potentially unstable continental margin slopes, the other one being the presence of shallow gas deposits. The slide triggering may have taken place by tectonic earthquake activities as a result of postglacial continental uplift. The *Trænadjupet Slide* happened on the north-eastern side of the *Vøring Plateau* just opposite to the giant *Storegga Slide* on the south-west side of this plateau. The slide scar can be traced 200 km downslope to 2 400 m depth. The area of about 5 000 km² covered by the slide is less than 5% of the *Storegga* coverage.

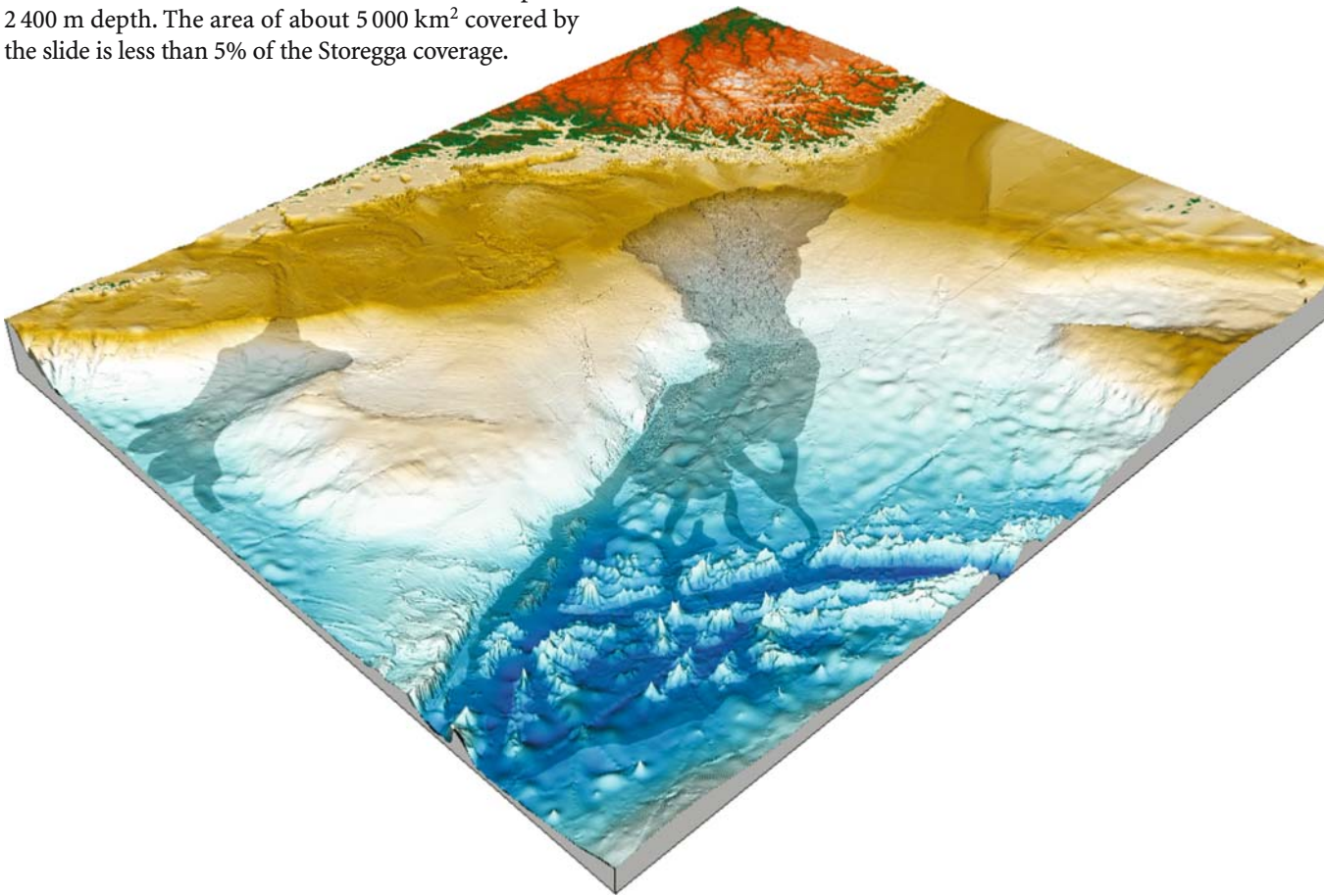


Image 5.3.1.2-1. Overview of *Trænadjupet Slide* and *Storegga Slide*. Composite relief image. The two slide areas are indicated gray with *Trænadjupet* on the left (north) and *Storegga* on the right.

Image documentation: same as Image 7.4.2-2

Image ©: Stein Wendel, Egil Ingebretsen, Norsk Hydro ASA ■

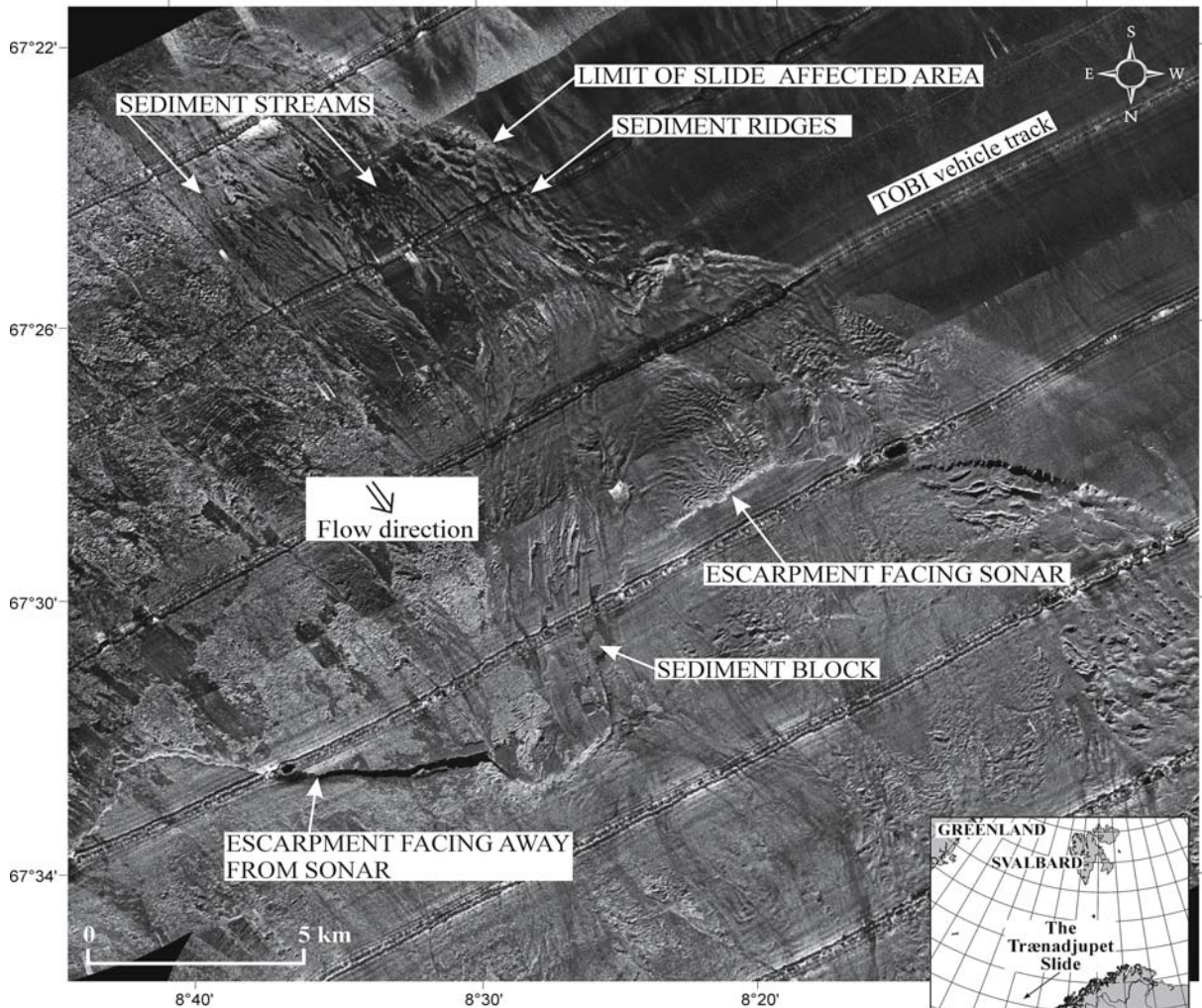


Image 5.3.1.2-2. Close up of the southern *Trænadjupet Slide* escarpment. Mid range sidescan mosaic image. The TOBI-mosaic sidescan image depicts a cut out of the southern rim of *Trænadjupet*. The image demonstrates the capability of the mid range sidescan system TOBI to resolve the morphologic features of a slide surface with its rather shallow but characteristic relief. The bathymetric Image 5.3.1.2-1 does not suffice to supplement the third dimension of the shallow relief and to compete with the structure resolution of the sidescan technology in this case which thus appears optimum for this purpose. Sediment penetrating echosounder imagery (not shown) is of course necessary to acquire the thickness and internal structure of the slide masses.

The relief features indicating the pattern of sediment flow directions – similar to a lava stream – are nearly self explanatory. Since the sound irradiates away from the track line and athwart to it, surface elements which are facing the grazing sound signal appear bright or dark respectively when they are on the shadow side. The direction of irradiation changes just in the middle between the track lines. Particularly remarkable is the bright rim section in the middle adjacent to the Vøring Plateau. This means the slide caused a depression of the plateau, not an overlay.

Project/program: Funding of the TOBI operation by the EU Commission under TMR, ENAM II and the Sea Bed Deep Water Industry Project

Sidescan sonar: TOBI; frequency: 30 kHz, horizontal beamwidth: 0.5°

Image ©: Jan Sverre Laberg, Dpt. of Geology, University of Tromsø, Norway ■

5.3.1.3

Landslide on Atlantic Islands; Canary Islands

The character of landslides on oceanic volcanic islands differs fundamentally from sediment slides on the *European Continental Margin* such as found off the Norwegian coast that occur even at extremely shallow glide angles. The slides that eroded several of the *Canary Islands* are in fact huge avalanches of basaltic debris containing blocks up to a kilometer each in size. The typical Canary Island debris avalanche has a tongue shape extending from a subaerial headwall scarp through a narrow chute to a blocky debris deposit in 3 000–4 000 m depth. Individual

avalanche deposits are up to a few hundred meters thick with a maximum volume of 500 km³. They cover the sea floor up to 4 500 km² and run out to more than 100 km. The most obvious failure scar called *El Golfo* happened to *El Hierro*. Its north-west side appears like a crater which lost nearly half of its rim with a steep avalanche scarp filling the open flank.

The multibeam sound images of the underwater foundations of the islands are merged with onshore land topography leaving a belt of the upper meters of the water without data where the depth is insufficient for echo sounding. The apparent “terraces” are thus artifacts.

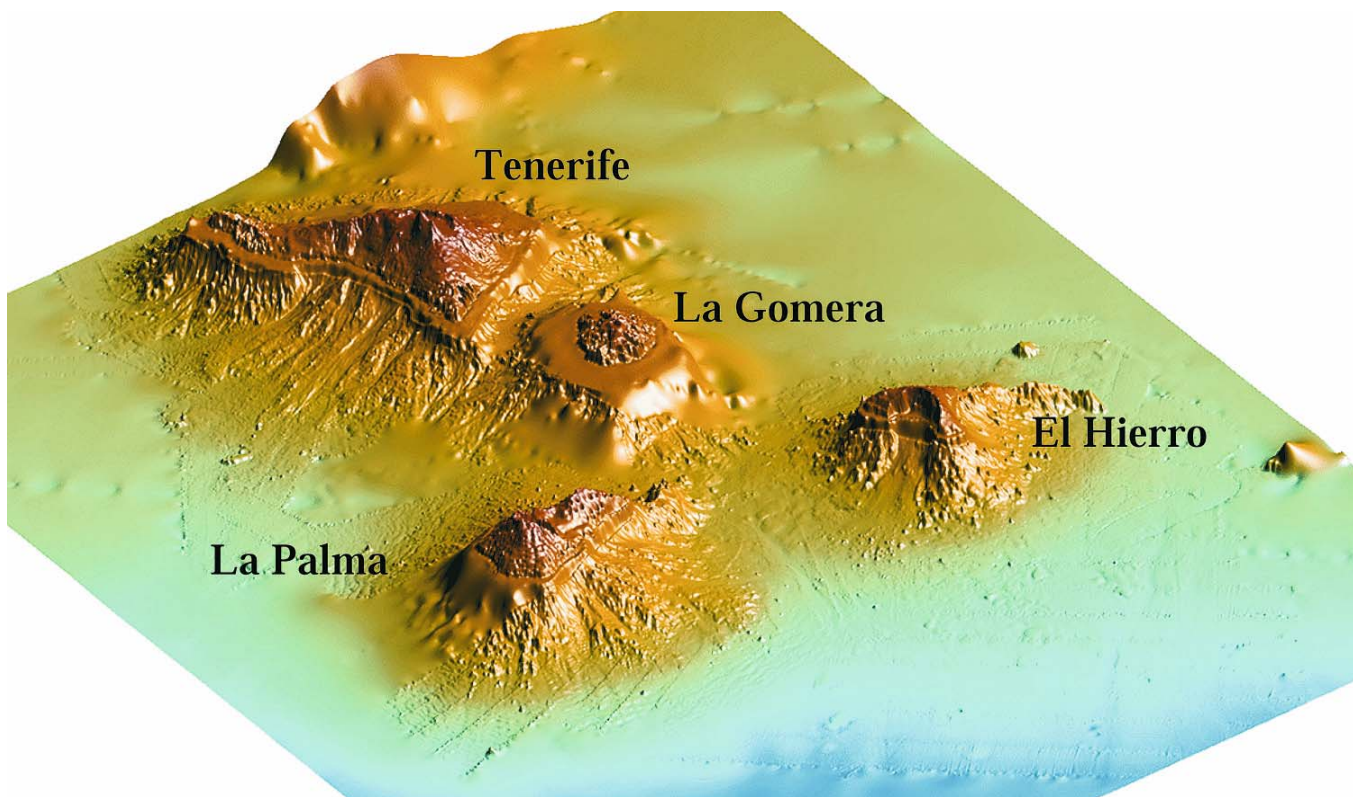


Image 5.3.1.3-1. Slant view from northwest onto the western *Canary Islands*. Multibeam sound image. *Tenerife* and *El Hierro* Avalanche expose major landslides on the view side. The color scale of the 3D-multibeam sound image ranges from 4 500 m below sea level (dark blue) to 3 000 m above (orange). Simulated sunlight from west.

Survey vessel: *RRS Charles Darwin*; cruise 108, 1997

Multibeam echosounder: Simrad, type: EM12; frequency: 12 kHz, beamwidth: 2°, fan width: 140°, but variable depending on water depth, ship speed and survey conditions

Image ©: D. G. Masson, Southampton Oceanography Centre, UK ■

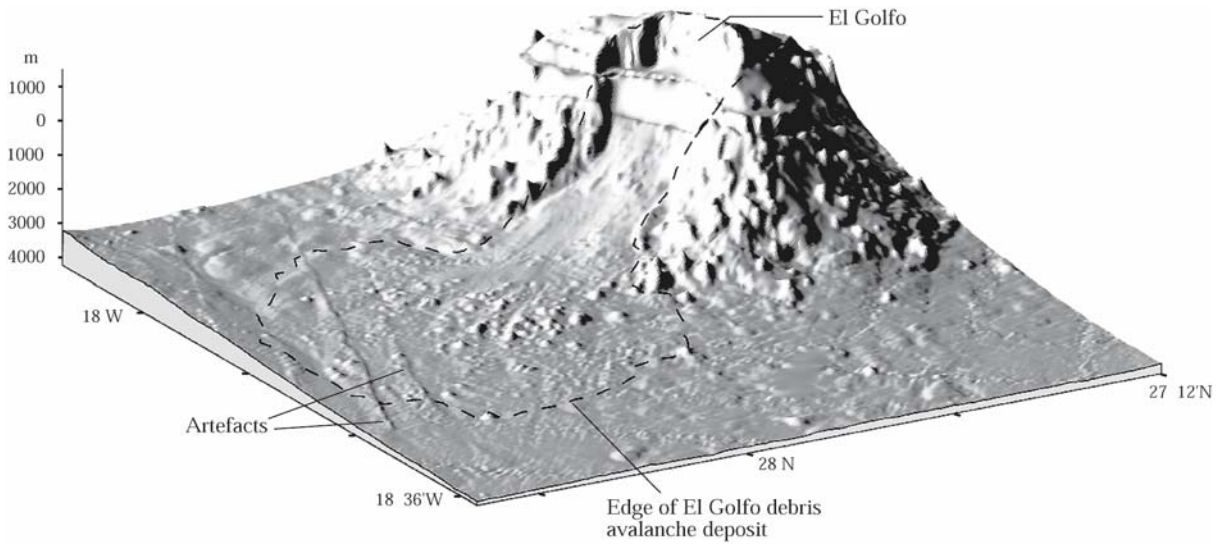


Image 5.3.1.3-2. The *El Golfo*-landslide of *El Hierro*. The multibeam image with geographical scales indicates the slide edges by contours.

Image documentation: same as Image 5.3.1.3-1

Image ©: D. G. Masson, Southampton Oceanography Centre, UK ■

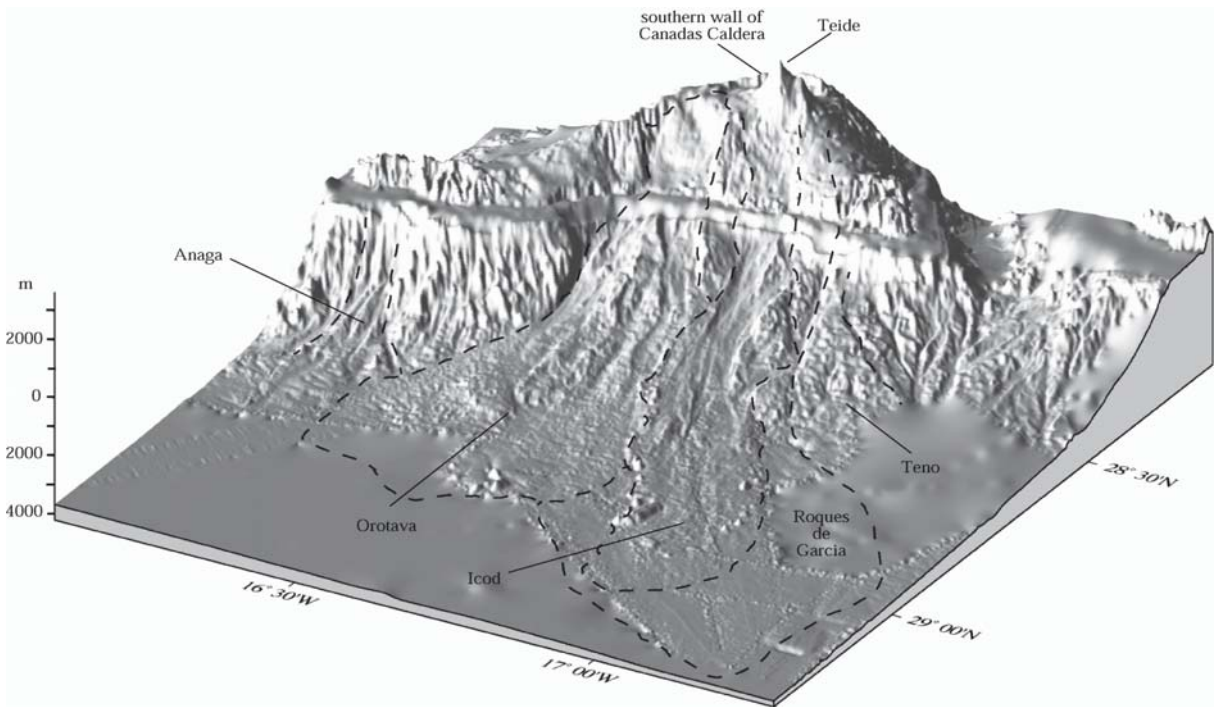
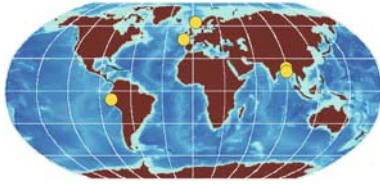


Image 5.3.1.3-3. North flank of *Tenerife*. The morphological contrast between the stable slope in the east and the multiple landslides in the west is clearly visible. The contours drawn indicate slide edges.

Image documentation: same as Image 5.3.1.3-1

Image ©: D. G. Masson, Southampton Oceanography Centre, UK ■

5.3.2 Sediment Fans; Flow and Strata



This section deals with the build up of sediment fans: the imaging of the outer morphology and the inner structure. Major formations fed by the European Continental Shelf are set in comparison with the largest sediment fan known: the Bengal Fan in the Gulf of Bengal.

5.3.2.1 Morphology of the *Celtic Fan*, *Gulf of Biscay*

The European continental margin has been the arena of sediment transfer from the European continent to the ocean by various natural transport systems, mainly during glacial periods. The *Celtic Margin* of the northern *Gulf of Biscay* may be considered a kind of non-glaciated end member of the series, and the mechanism of sediment transport is essentially different from the northern neighbors.

Though the pioneering research on the Celtic margin reaches back to the early fifties of the twentieth cen-

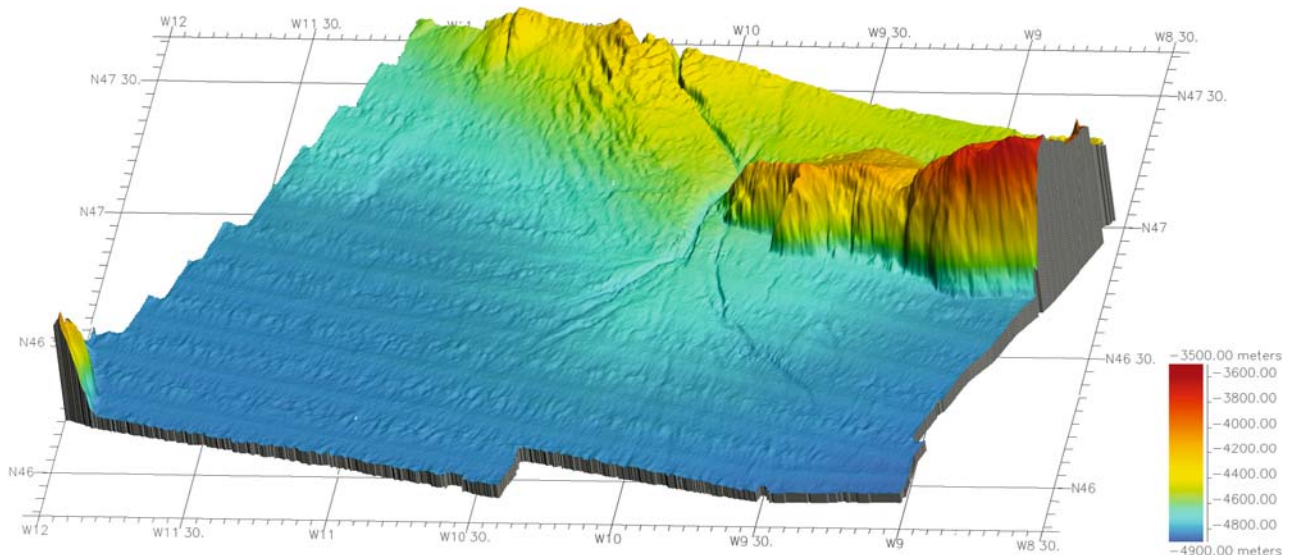


Image 5.3.2.1-1. Celtic deep-sea Fan relief. Multibeam image. This 3D-relief and the 2D-backscattering image (Image 5.3.2.1-2) were taken by the same system at the same time. The echoes were evaluated both for the signal travel time and for the echo amplitude. The backscattering image reveals the texture of the sea floor with the morphology, also indicating sediment features. Both images are composed strip mosaics. The swath width corresponds to the athwart range covered by the multibeam system.

The Celtic Fan is a middle size fan of sediments in the north western part of the *Gulf of Biscay* and covers about 30 000 km². It lies at the foot of the Celtic continental margin between 4 200 and 4 900 m depth. The fan is connected with the Celtic margin slope by two major deep water channels which are linked to and finally supplied by the *Irish Sea* and the *English Channel* respectively. Since both primary sources merge into one channel, the Celtic Fan eventually becomes a single source fan as shown in the 3D-image: The prominent sinuous canyon named *Whittard Channel* and the less pronounced *Shamrock Channel* merge at the valley between the *Whittard Ridge* on the left and the *Trevelyan Escarpment* on the right of the margin formation.

The fan activity began in the Miocene, more than 15 million years ago. Unlike the sudden slide and debris flow phases of glacial fans off Norway, the Celtic fan is mainly fed by benign low density turbidity currents. Simplifying, one could say: the fan build up has happened more or less continuously with the fall out of fine grained suspensions, not by unsorted sediments as found on the Norwegian margin. Despite its higher sedimentation rates, the Celtic Fan is reminiscent of deep-sea sediments with their slow, continuous fine grain sedimentation fed by turbidity currents and oceanic fall out. However, the very recent sandy layers of less than 1 200 years of age located on the uppermost lobe of the Celtic Fan (marker A) indicate also *episodic high density turbidity currents*.

Image documentation: same as Image 5.3.2.1-2 ■

ture, the present view of the submarine bathymetry has only been possible through the high resolution acoustic devices and the high precision of satellite navigation since the eighties. A series of comprehensive joint research programs of European institutions have established a 100% coverage of the bathymetry and a resolution better than 100 m, an achievement that deep-sea research can only dream of.

5.3.2.2 Glacigenic and Non-Glacigenic Debris Flows on the Upper North Sea Fan

During the mid and late *Pleistocene*, several hundreds of thousand years ago, ice streams draining through the *Norwegian Channel*, a major trough feature in the northern North Sea off the southwest coast of Norway ▶ p.159

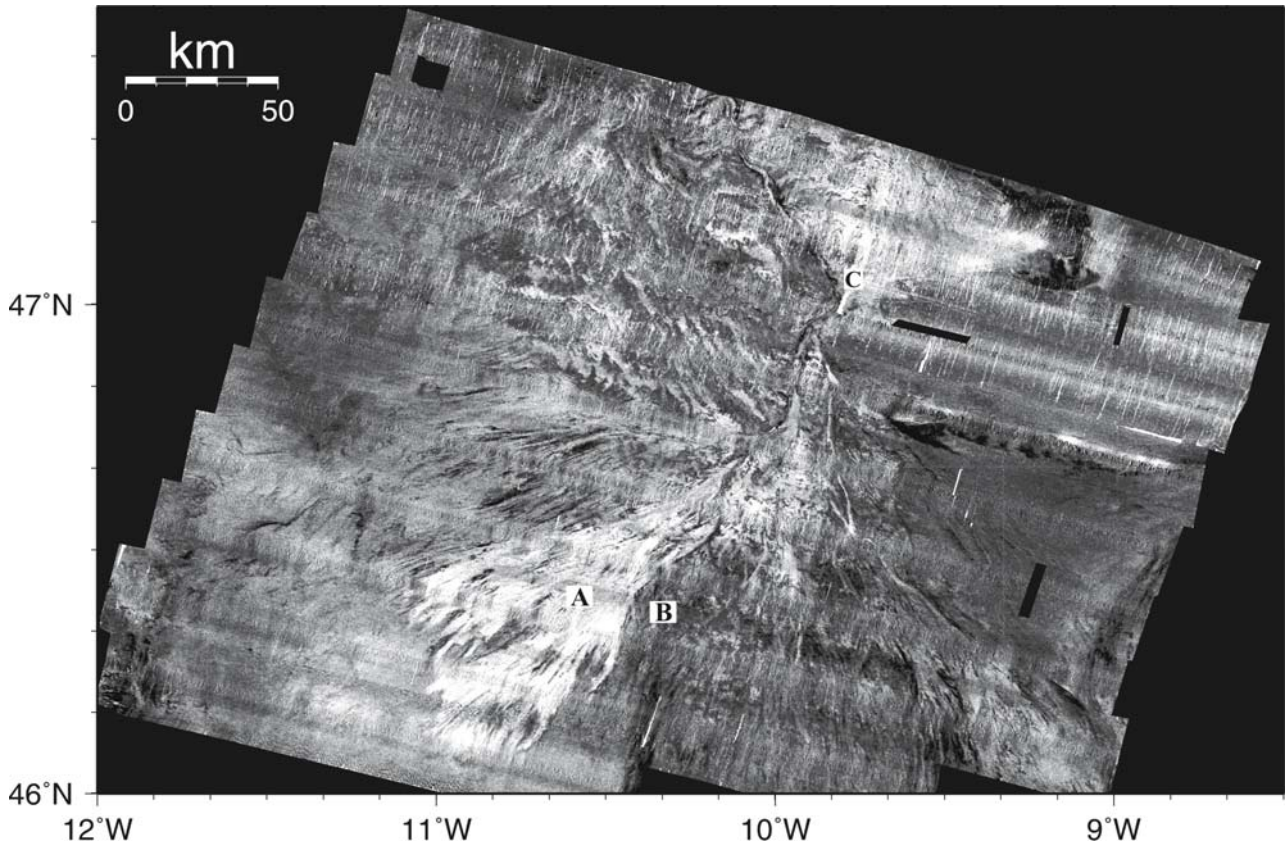


Image 5.3.2.1-2. Celtic Deep-sea Fan. Backscatter image. The gray tone depiction of the relief image reveals backscattering features of newer and older fan lobes. In this image, stronger backscatter is indicated by darker tones. The recent coarse grained but thin sub-fan layer A with a mud layer below is superimposed on the older lobe system B with more intense backscattering. This may be surprising, because coarse material usually causes stronger backscatter. However, the much longer wavelength of the multibeam system as compared to usual sidescan systems provides only weak backscattering from the sand grains and other acoustically prevailing sediment properties such as the lower density of young mud vis à vis the higher density of older, more consolidated sediments can mask the grain size effect.

Project: ENAM II, funded by the EU Commission under IFREMER Institute; 1997

Survey vessel: *Atalante*, France

Multibeam echosounder: SIMRAD, EM12, hull-mounted; dual mode (depth and echo intensity), frequency: 13 kHz, beam-width: 1.8°/3.5°, 162 beams, fan width: 150°

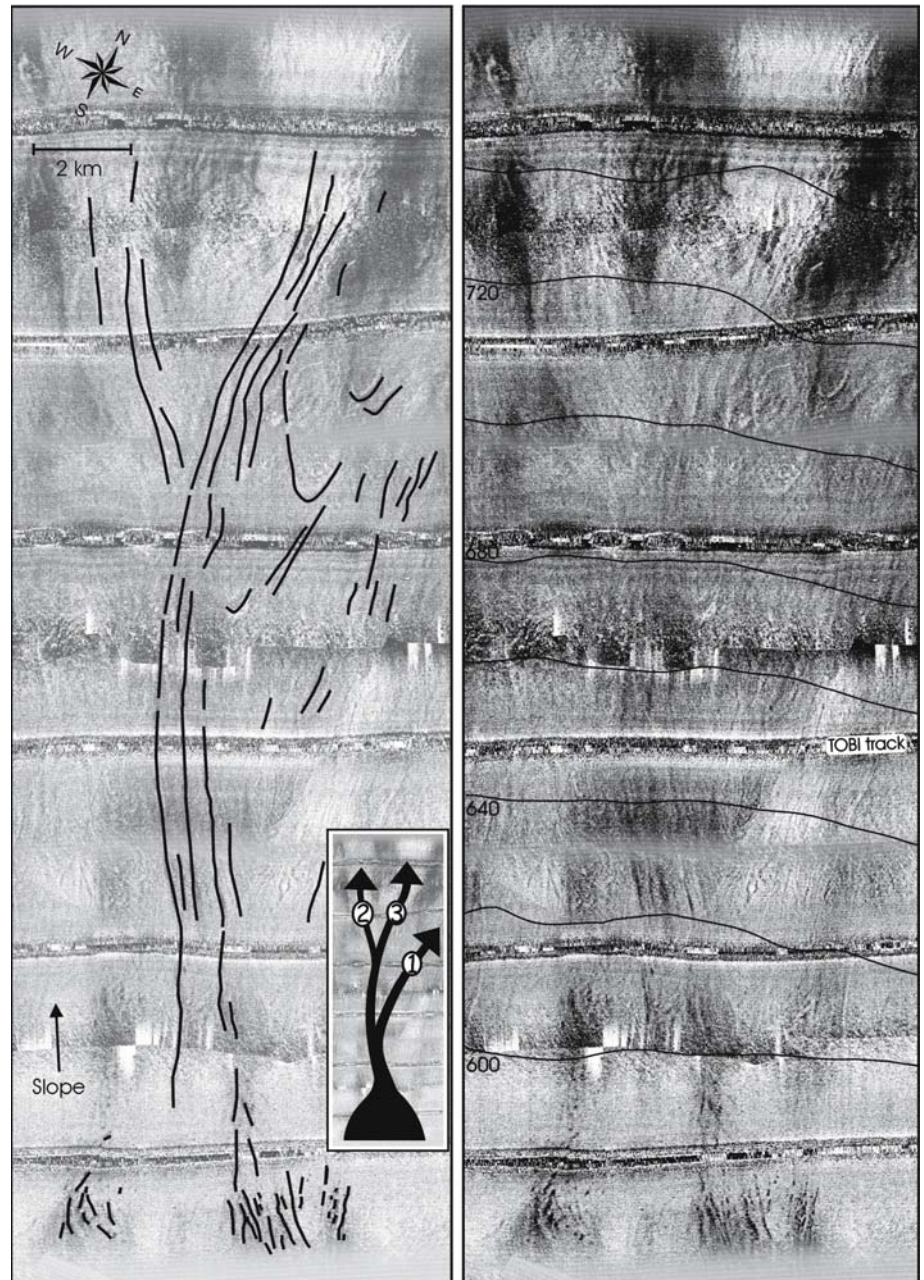
Image ©: S. Zaragosi, Département de Géologie et Océanographie, Université de Bordeaux I, France ■

Image 5.3.2.2-1.**Glacigenic debris flow surface morphology. Sidescan mosaic image.**

The sidescan image composed of the stripes of adjacent runs shows a large and prominent flow complex on the upper part of the fan. In the deeper part of the flow broad bands of strong (bright) and weak (dark) backscatter alternate, being attributed to differences of the post sediment cover in thickness and texture. The sound image, being sensitive to grain size reveals the result of winnowing by bottom currents: The finer fractions with low backscatter are left in the lows.

The insert shows an interpretation where the lineations have been attributed to three fan branches. The conspicuous lineations are interpreted to have developed as a result of shear zones between flowing sediment and sediment that had ceased to flow. Remarkable is the very shallow fan slope of less than 0.7° . Comparable slopes are typical also of other fans as well as of submarine slides. The mechanisms of extremely low friction that enable sediment and debris flows similar to fluids or separated from the basement by quasi fluids is still subject of investigation (Sect. 5.3.1).

The sound irradiation athwart the sidescan tracks meets at the middle between the track lines and shows bright spots or dark parts depending on the inclination of a flank element towards or away from the irradiation.



Project/program: Joint “Deep Marine Sedimentation Process Project” between the University of Bergen and Enterprise Oil Norge Ltd. The TOBI vehicle was operated through funds from Norsk Hydro ASA on behalf of the SEABED project and a grant from the EC TMR-LSF (Contract: ERBFMGECT 950030 with Southampton Oceanography Centre)

Survey vessel: RRV *Charles Darwin*

Sidescan sonar: TOBI, owned by Southampton Oceanography Centre; 30 kHz, 0.5° horizontal beamwidth, towed depth: 300–400 m above seabed

Image ©: A. Nygård, Department of Geology, University of Bergen, Norway ■



Image 5.3.2.2-2. Non-glacigenic debris flow, inner morphology. Horizontal slice through a 3D-seismic record. The image example of exception shown here depicts a relatively small debris flow lobe north-east of the huge – and glaciogenic – *North Sea Fan*. It covers only about 230 km², has a volume of about 15 km³ and differs in all three features from its large neighbor. The most appropriate way of imaging the characteristic features is a horizontal slice through a 3D-seismic record because this reveals both the question of internal structure and transverse flow. This depiction of high sophistication of data acquisition and signal processing is selected for demonstration of advanced acoustic imaging of internal sea floor structures. (The usual vertical 2D-seismic section revealing the destroyed base surface of the flow lens is not shown.) The time slice through the 3D-data set at 1 300 m below sea level is remarkable in two aspects: there is indeed a pronounced internal structure and the pattern is reminiscent of an eddy flow with clear consistency instead of an *unidirectional flow*. The reason for the visible structure is assumed to be due to the heterogeneity of the material, which varies according to the acoustic impedance of the elements (Sect. 3.4.1). Such features have been recognized in “conventional” debris flows on terrestrial and marine environments.

The method of 3D-Seismik is described in the literature cited. Different from multibeam imaging a sea floor surface under slant beam angles, seismic imaging the internal structure of a sediment volume requires a set of vertical slices from which various cuts can be derived. The horizontal cut shown is composed of the slice data at the same signal travel time.

Project: SEABED, SH9602, Consortium Norsk Hydro, Conoco, Mobil, Statoil, Shell, Esso, BP
 Survey vessel: commercial
 3-D seismic system: frequency: 3–100 Hz, vertical resolution 3–4 m
 Horizontal distance of scanning lines: 25 m
 Seismic data provided by the SEABED-Consortium
 Image ©: Atle Nygård, Department of Geology, University of Bergen, Norway ■

(Image 7.4.2-1), have transported thousands of cubic kilometers of sediment to the shelf edge. The result is a fan shaped structure on the slope contrasting strongly with the irregular *Storegga Slide* complex to the north east (Sect. 5.3.1). The fan is characterized by alternating intense deposition of glaciogenic debris flows (GDFs) when an ice stream developed in the Norwegian Channel, and periods without shelf edge glaciation. After losing contact with the ice stream at the grounding line, the material moved hundreds of kilometers down the continental slope forming elongate bodies. These are lense shaped in cross section, similar to those of the *Bear Island Fan*, tens of kilometers wide and up to 60 m thick, filling in the lows between previous GDFs.

The predominance of glaciogenic debris flow features on the Norwegian shelf raises the question as to whether there have been also other debris flows on this part of the European continental margin. In retrospect: a fully developed glaciogenic flow lens is characterized by three conspicuous clues: *first*, the interior of an individual lens appears acoustically homogeneous without any apparent internal structure; *secondly*, the underlying base of the lens indicated by a thin layer of oceanic sediments appears unimpaired by the flow and *thirdly*, there are no obvious transverse flow elements. The example of glaciogenic debris flow is shown in Image 5.3.2.2-1. Image 5.3.2.2-2 demonstrates a – smaller – example of *non*-glaciogenic debris flow, adjacent to the predominating major version.

5.3.2.3

Bear Island Trough Mouth Fan (TMF) and Glaciogenic Debris Flows, Western Barents Sea

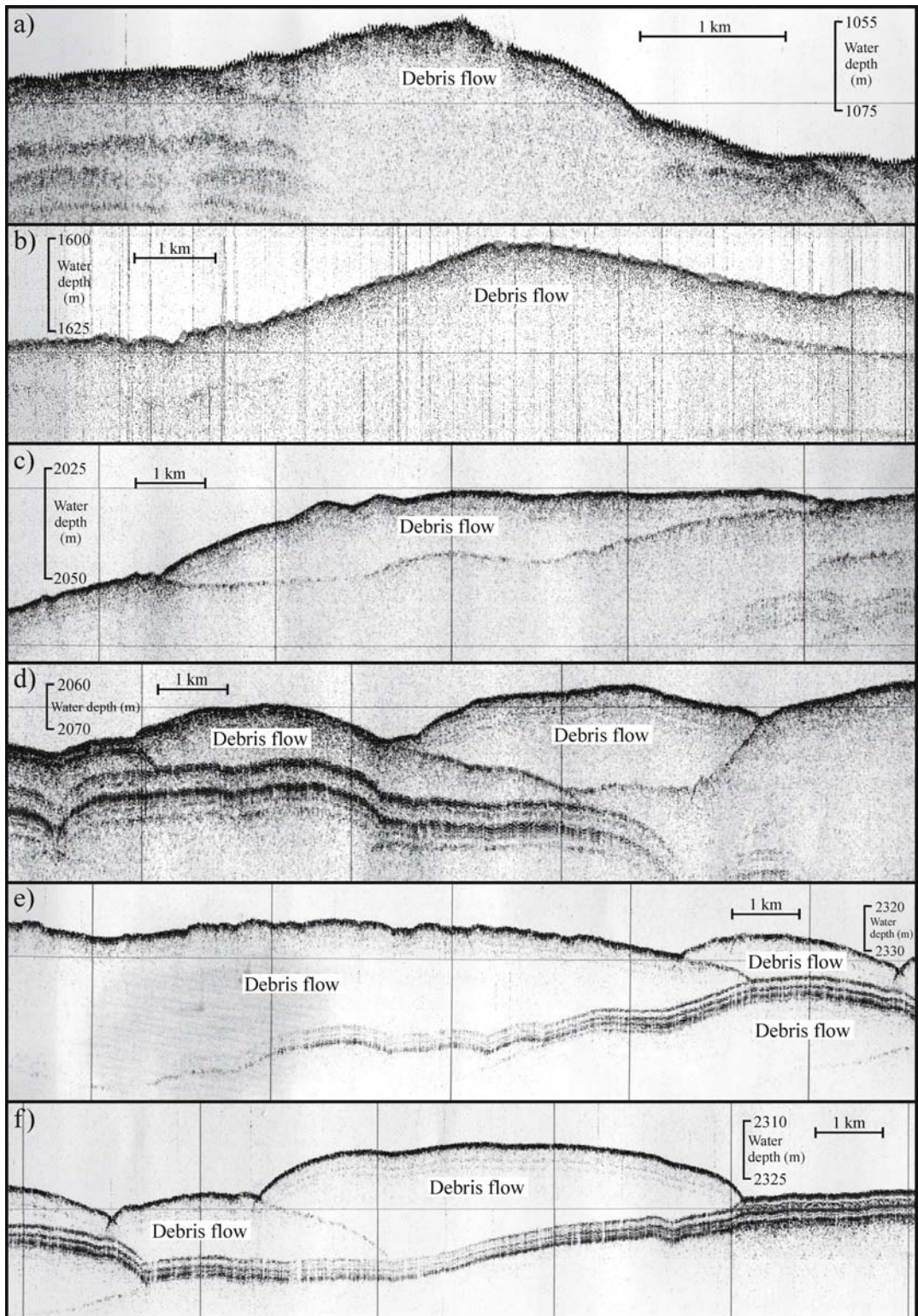
The Norwegian continental margin is a demonstrator of the largest events and processes of sediment and debris transport across the European continental shelf and slope and it is considered a diary of glacial periods. Up to about 70° latitude the major *landslides* of the post glacial, Holocene times appear to predominate in number. They transported hundreds and thousands of km³ sediment mass at high speeds and over surprisingly shallow slopes as though gliding on a fluid. (Sect. 5.3.1). These slides were more or less single events; they were not confined to channels or troughs incised into the shelf and their front ends reached depths of more than two thousand meters.

Beyond that latitude landslides of smaller size are still found. But the prevailing large scale, trans-shelf transport of sediment and debris at higher latitudes followed existing glacial troughs and channels which end at the shelf break. These trough mouths on the Norwegian continental margin are often the origin of protrusions, shaped like multi-fingered fans or deltas, named *trough mouth fans (TMF)* which continued the trans-shelf transport also into more than 2 000 m depth. The resulting deposits consist of a wide variety of unsorted grain size ranging from clay and fine sand up to gravel and single blocks of tens of meters.

In the late eighties of the twentieth century high resolution seismic cross sections have shown that the debris flows are bundled in sets of apparently homogeneous “lenses”, separated by strongly reflecting horizons. The lenses are attributed to debris flows originating on the upper slope, emplaced when the glacier grounding line was near the shelf break. The very high sediment input during those times presumably caused instability and mass movement. The high amplitude reflectors between the lenses are considered to represent periods of low sediment input during inter-glacial times and the entire stratigraphy is expected to permit the interpretation as paleo-climatologic recorders. Therefore, it is suggested that the debris flows which constitute these *trough mouth fans (TMF)* be named *glaciogenic debris flows (GDF)*.

The only major TMF on the Norwegian margin south of 70° N is the *North Sea TMF* north west of the *Storegga slide* area with some overlap of both and with the *Faeroe Islands* in the south west (Sect. 5.3.2.2). This North Sea TMF is the second in size of the altogether four major TMF-areas found off Norway. Though less famous than the largest of the exposed slides, the *Storegga*, its deposit volume is at least three times larger. According to estimations, about 60% of these 15 000 km³ were deposited as glaciogenic debris flow GDF lenses and the “rest” by mega-slides or oceanic sedimentation. The cross sections of GDF-lenses shown hereafter belong to the largest TMF, the *Bear Island TMT*.

Comparing the features of major *slides* with major *trough mouth fans*, there is perhaps more similarity than clearly discriminating clues. Even the very shallow slope at the outer end of the TMF’s of a degree and less is comparable with the astonishing data of the *Storegga slide* for example. Also the “all in one” of the



◀ Image 5.3.2.3-1.

Trough Mouth Fan (TMF) and debris flows. High resolution seismic cross sections. The sections cut through four of the fifteen debris flow branches of the *Bear Island TMF* with section *a* at 1 000 m depth to *e* and *f* at 2 300 m. At *a*, the debris flows are identified by their surface relief. The reflection below, defining the base, disappears beneath the main flow deposit (arrows), indicating erosion. The entire cross section of the debris flow lacks any internal structure as if the flow were a matter of a short period of time. Essentially the same features with eroded base contour are visible at section *b*, 600 m downslope. Section *c*, at 2 000 m depth, 400 m further down than *b* of the neighboring branch has now an uninterrupted basal reflector and the contour of the single debris flow appears to follow to some extent the highs of the base. Should the hydroplaning interpretation reflect the reality, then the accelerated flow at this depth was fast enough to leave the base surface unimpaired. This appears to hold also for the other deeper sections.

Section *d* was cut at the same depth as *c* but belongs to the nearest neighboring flow branch, only 20 km further north. However, it looks surprisingly different from the preceding sections. Its latest deposit with a convex relief did not affect the underlying older one lying on a basal double reflector. At the left of section *d* a further shallow horizon appears, which indicates an even older, though smaller debris flow upon which the next flow has placed a thin overlay of a few meters.

The sections *e* and *f* cut through adjacent fan branches at a depth of 2 300 m with *e* belonging to the same branch as *b* but 700 m deeper. At this depth the debris flow cross-section *e* appears considerably thicker on the left side than at *b* and there is at least one later flow visible on the right. The older flow has a less smooth surface now with small elevations of a meter, indicated by *H*. Section *f* appears to reveal three separate flows partially sitting with a convex contour on the preceding one but all three touch the base which now has a pronounced stratification. The sequence of the sections demonstrates that the cross-over of fan branches at different phases of debris flow is probable and the entire TMF build up is not at all a straightforward sequence of flow processes.

Project: Bear Island Trough Mouth Fan (TMF)
Acoustic device: high resolution seismic echosounder
ORE 137; center frequency 3.5 kHz, 16 elements
Image ©: Jan Sverre Laberg, University of Tromsø, Norway ■

slides instead of separate phases of the TMF-build up is somewhat violated since Storegga is supposed to have a three phase past. The remaining and perhaps decisive difference is the second ingredient which is considered necessary to release a major slide. This is the

gas pressure from methane deposits below, which adds to the pore-water pressure of thick sediment layers built up within short time periods. The two contributors are assumed to produce a *liquefied sediment layer*, a kind of dense suspension with low viscosity (Sect. 5.3.1) on which the thick sediment package can glide at nearly zero slope.

However, TMFs need a similar mechanism to transport sediments at such shallow slope angles. Pure suspension flows are known indeed, even on deep-sea trenches where they proceed as submarine rivers along hundreds of kilometers (Sect. 5.2.1). Such so called *turbidite flows* consist of relatively stable suspensions like sewage in a pipe at sufficiently high speeds of flow which prevents the suspension load from fall out. Another mechanism, a kind of *hydroplaning* has also been suggested to explain the enigmatic TMF-phenomenon. But interpretations are still hypothetical, even speculative and acoustic imaging cannot reveal the secret of gliding, only the fait accompli of the result.

5.3.2.4

The Largest Sediment Fan in the World Fed by a Giant Shelf Canyon in the Bay of Bengal

This system of feeder canyon and sediment fan has been investigated as an interconnected entirety and is therefore treated together in this sequence and in the context of sediment fans. The fact that the routes of sediment transport from the *Himalayas* to the coast are crossed by the active tectonic margin between the converging *Indo-Australian-* and the *Eurasian Plates* (Sect. 5.2) in contrast to the passive continental margin of the European examples of sediment fans is not essential regarding the sediment dynamics considered. The plate subduction which caused the uplift of the Himalayan Mountain range and the Tibetan Plateau is the reason however for the gigantic dimensions of the *Bengal Fan*.

The Giant Shelf Canyon in the Bay of Bengal

The *Ganges-Brahmaputra-Meghna Rivers* are among the largest drainage systems in the world with respect to water run-off and sediment transport. They erode the *Himalayan Mountain* region and the *Tibetan Plateau*, which receive up to 10 000 mm of rainfall per year during monsoonal seasons. Huge sediment deposits are found in the flood plains of *Bangladesh* and *Northeast-*

ern India as well as in the river delta, which is rapidly prograding southwards. Suspended matter from the river outflow and sandy bedload is remobilized by passing hurricanes and transported coast-parallel from the river mouth southwestwards by strong currents. It is trapped only by one deep shelf incision, a canyon named the *Swatch of No Ground*. The gigantic sedimentary fan in the *Bay of Bengal* is exclusively fed by this

canyon. The extreme material throughput finds its imprint in extraordinary sedimentary structure images taken by a *parametric sediment echosounder*.

This unconventional low frequency sediment echosounder (Sect. 4.4.2) combines very narrow sound beams with high resolution of sediment strata and achieves deep penetration to a hundred meters and more. This unparalleled advantage is particularly appropriate to

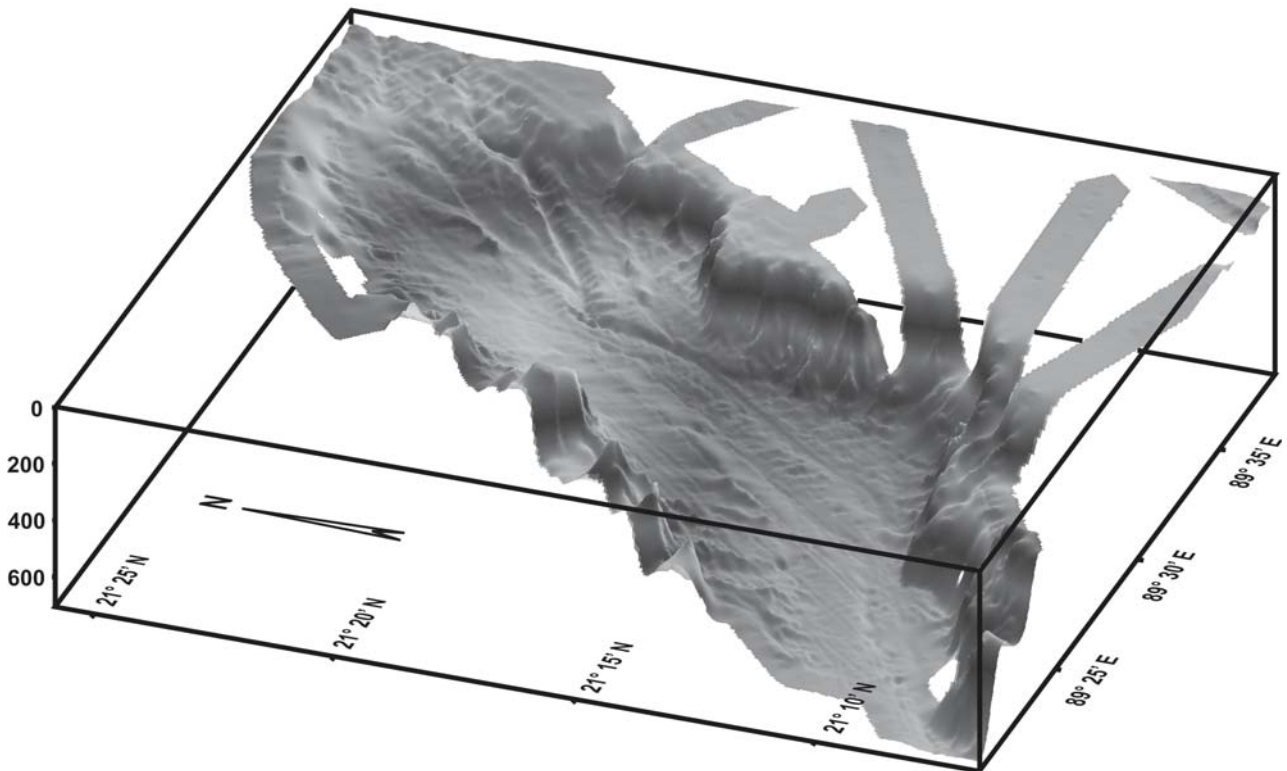


Image 5.3.2.4-1. The outer relief of the feeder canyon. Multibeam image. This trough-shaped, isolated canyon is the only feeder of the largest sediment deposit known: the *Bengal Fan*. The canyon of hardly 15 km distance of the flanks is the throughput of the enormous amount of all fine grained products of erosion and weathering coming down from the *Himalayan Mountain* region and the *Tibetan Plateau* as sediment load of rivers and sandy bedload remobilized by passing hurricanes. Similarly dramatic is the transfer role of this canyon in opposite direction: Tides in *Bangladesh* coast originate in the *Indian Ocean*. They enter the *Bay of Bengal* through two submarine canyons: the *Swatch of no Ground* and the *Burma Trench*. The endangered coastal areas of Bangladesh undergo a permanent change of shape through floods and storms. This concerns also the safe shipping clearance. Sound imaging of coastal areas in this region is thus of major interest beyond research.

The gray-scale depiction reveals the internal channel structure along the canyon more clearly than a color code can provide. Three valleys of the western bank and the single one on the eastern bank enter the canyon. Their contribution to the inflow is indicated by the gully morphology on the canyon floor.

Project: Bay of Bengal

Research vessel: *RV Sonne*, Germany

Multibeam echosounder: ATLAS Elektronik, HYDROSWEEP; frequency: 15.5 kHz, beamwidth: 2°

Image ©: Volkhard Spiess, Tilmann Schwenk, Fachbereich Geowissenschaften, Universität Bremen, Germany ■

reveal the features of complex sediment stratifications with strong lateral variations. The combination of this high resolution sediment echosounder with high resolution multibeam imaging of the outer relief provides an ideal set of diagnostic tools to analyze extreme processes on the sea floor.

Two surveys were carried out by the research vessel *RV Sonne* in 1994 and 1997 to understand the processes

of sediment trapping, transport and remobilization down to water depths of 700 m. Different sound reflection patterns indicate the extreme spatial variability of sedimentation as well as the mobility of the sea floor on decadal and centennial time scales. The sedimentation rates of 10 to 80 cm per year demonstrate how efficiently the canyon works as a trap. The depression would be rapidly filled, if frequent slumping, sliding

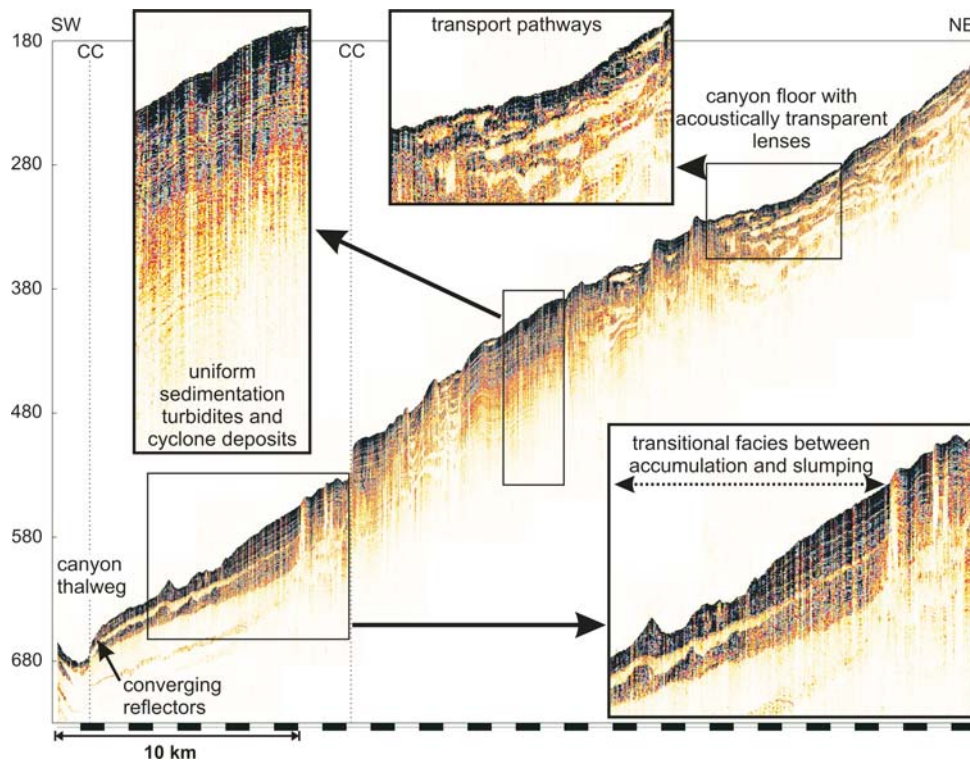


Image 5.3.2.4-2. Sediment structure along the axis of the canyon. Parametric sediment echosounder image. The high resolution image resolves the fine structure of different types of sediment accumulation and slumping. The image of the profile section which is inclined only by 1.3% while descending 500 m is enhanced by a factor of 50 to show the structure more clearly. Three sections are depicted as close ups. Evidently, features showing uniform sedimentation are less frequent than those with acoustically transparent lenses inside indicating creeping sediment slabs and others with transition between accumulation and slumping. Mapping the types of sediment behavior, named *facies* (not shown) is a tool to analyze the varying transport processes which are far more complex than a turbidite flow. The fact of highly efficient throughput of the canyon despite its weak slope is not yet completely understood.

Project: Bay of Bengal

Research vessel: *RV Sonne*, Germany

Sediment echosounder: ATLAS Elektronik, PARASOUND; bandwidth: 1–10 kHz, beamwidth 4°

Processing: ParaDigMA

The echo intensity is color coded by a white-yellow-brown-black scale. The pattern of bright vertical stripes of weak echoes is presumably caused by locally inclined surface “facets” reflecting part of the signal into slant directions

Image ©: Volkhard Spiess, Fachbereich Geowissenschaften, Universität Bremen, Germany ■

and generation of turbiditic currents did not occur to remove material downslope. Transparent lenses indicate such creeping sediment slabs, and erosive truncations of layers and furrows follow the maximum slope.

The Bengal Fan: The World's Largest Sediment Fan with Its Channel-Levee Complex

Sedimentary fans are found worldwide, where large amounts of sediments are brought to shelf areas by rivers, glaciers, or currents. Suspended matter is being transformed into turbidity currents where the flow is acceler-

ated at a shelf slope break and focused in submarine canyons. Turbidity currents erode the bottom of depressions and channels but concurrently build up flank deposits, so-called levees. The flow, which is then constrained by these levees, enhances the vertical grain sorting in the water column, resulting in efficient bedload transport of sand as well as in fine grained overspill deposits. While large sandy depositional lobes can develop at the mouth of such channels, levees can grow up to the height of the suspension clouds, which can easily reach more than a hundred meters and cover an area of some tens of kilometers from an active transport channel in very short time periods.

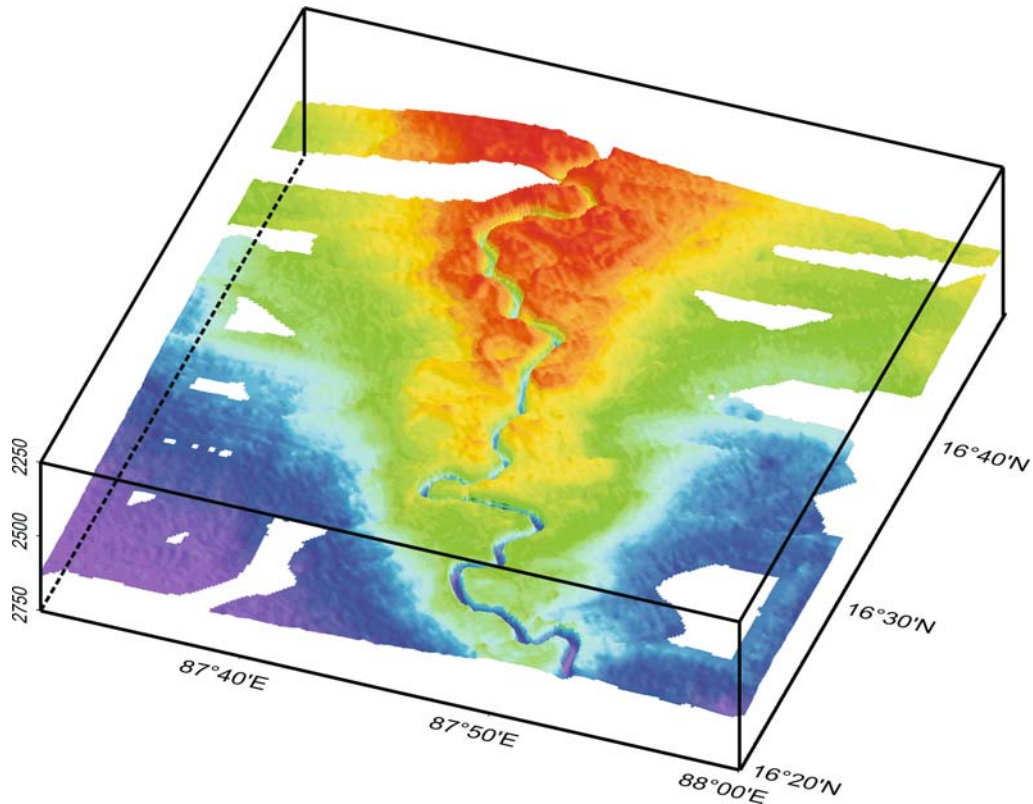


Image 5.3.2.4-3. The transport channel in the middle Bengal Fan. Multibeam image. The 3D-relief reveals two conspicuous features of this channel of about 1 km width and some 50 m depth. First: part of the pronounced meanders form nearly closed loops, indicating an unstable channel route similar to a river on low gradient land. Here, the slope of the Bengal Fan hardly exceeds 0.2° . Second: the flanks of the channel are constructed by a broad and thick sediment wedge. This package of up to 100 m thickness is the *channel-levee* complex built up by dust-fine suspension clouds ascending from the turbidity current of the channel and spreading out tens of kilometers.

Project: Bengal Fan

Research vessel: *RV Sonne*, Germany

Multibeam echosounder: *ATLAS Elektronik*, HYDROSWEEP; frequency: 15.5 kHz, beamwidth: 2° , Relief enhancement factor: 110

Image ©: Volkhard Spiess, Tilmann Schwenk, Fachbereich Geowissenschaften, Universität Bremen, Germany ■

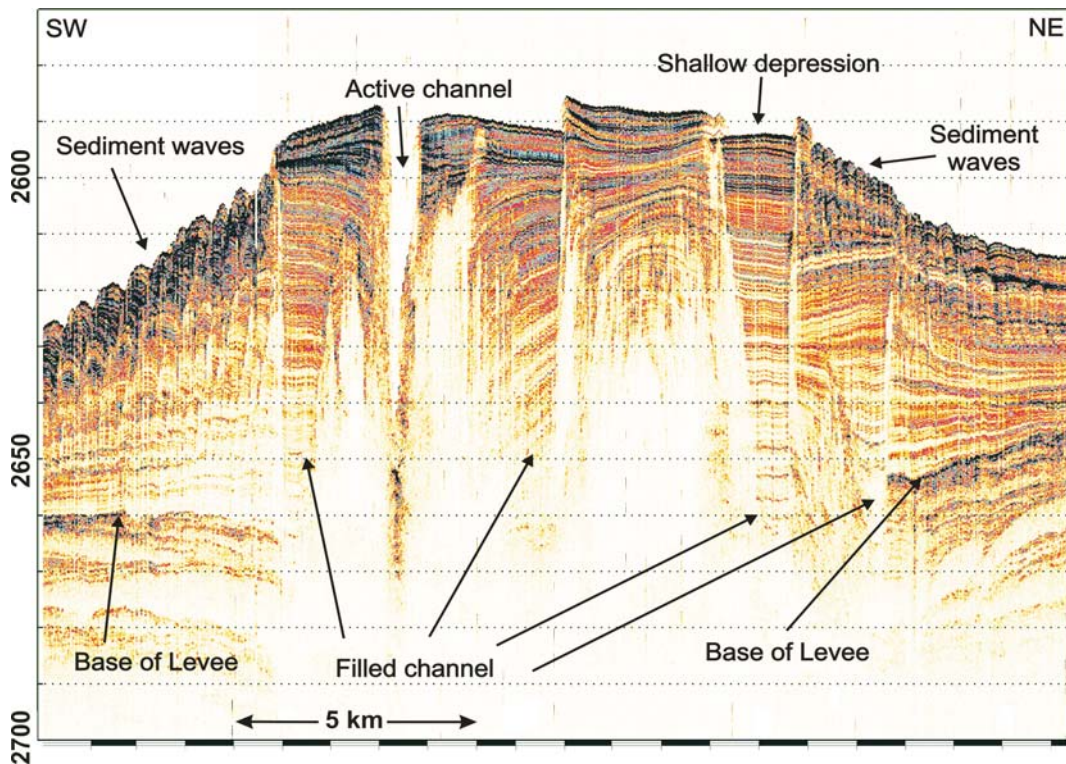


Image 5.3.2.4-4. Sediment structure of the Bengal Fan across the transport channel. High resolution parametric sediment echosounder image. The profile section penetrating more than 80 m reveals the center part of the channel levee build-up down to the base. The depiction is enlarged 125 times in height to demonstrate the complex lateral and vertical structure. The profile shows the presently active channel of 50 m depth with steep flanks inclined 10°. The channel bottom of this section proceeds already 20 m above the base of the levee, in other words: the surface of the continental margin. The seemingly smooth outer flanks of the levee area shown in the preceding multibeam image are in reality the relief of mud waves of different scales which show thin coherent, superimposed layers down to tens of meters, like an invariant pattern over long time periods.

This profile section chosen for demonstration cuts through several older, cut-off meander loops indicated “filled channel”. The abrupt offsets of several meters depth visible on the upper contour are external indicators of sharp lateral segmentations reaching perhaps deeper than the penetration depth of the parametric echosounder. The complex levee build-up and rebuild could be imaged exactly only by the narrow sounding beam and the short signal of the parametric sound generation at low frequencies. The sequence of the channel levee build-up processes are explained in the preceding text.

Project: Bengal Fan

Research vessel: *RV Sonne*, Germany

Sediment echosounder: *ATLAS Elektronik*, PARASOUND; frequency bandwidth: 1–10 kHz, beamwidth 4°

Processing: ParaDigMA; The echo intensity is color coded by a white-yellow-brown-black scale

Image ©: Volkhard Spiess, Tilmann Schwenk, Fachbereich Geowissenschaften, Universität Bremen, Germany ■

The *Bengal Fan* has developed to be by far the largest fan system in the world. It is considered the result of the collision of the Indo-Australian tectonic plate with its Eurasian Plate neighbor. The subduction of the Indo-Australian Plate caused the uplift of the Himalayan Mountain range and the Tibetan Plateau, and its rapid denudation and weathering. Due to the

huge amount of sediment production, the Bengal Fan extends more than 3 000 km southward, even across the equator. In the middle Bengal Fan, the transport channel has developed on this low-gradient continental margin like a river with meanders, cut-off loops and dead arms, as shown clearly by the bathymetric relief.

In the middle Bengal Fan, such channel-levee complexes occur over widths of some 40 km and heights up to 100 m. From sediment coring it was found that these structures grew within only 3 000–4 000 years, while the sea level was rapidly rising in the early Holocene. The sediment echosounder images reveal three distinct features of the fan structure: a pronounced lateral segmentation within the central part, fine scale mud waves on both undisturbed flanks, and clearly separated sedimentary units with the levees.

5.3.2.5 Sediments off Callao/Peru

The sediment images shown were generated as part of a research project on the climate history of coastal areas of *Peru*, in particular due to the *El Niño*-variability. High radial and lateral resolution of sediment stratification imaging was required for similar reasons as for the *Bengal Fan* research (Sect. 5.3.2.4): deep and steep incisions into a sediment fan by canyons and channels and strong lateral variability of the stratification.

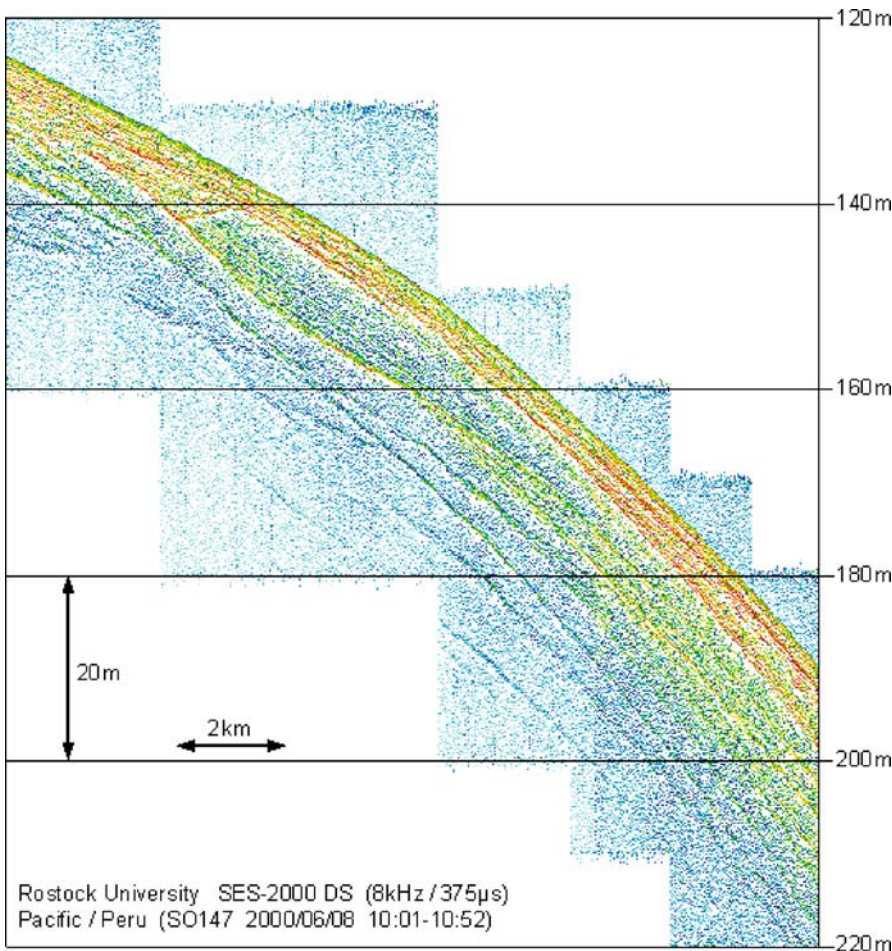


Image 5.3.2.5-1.

Bifurcation of sediment strata. Parametric echosounder image. The most pronounced feature of the sediment penetrating image is the bifurcation of the upper sediment strata. The youngest, post glacial layering on top has a nearly constant thickness with no significant variability along the slope shown. However, the lower band of the bifurcation visible at the left edge of the image behaves strangely: the strong, nearly single reflector branches out at a depth of about 170 m into several more or less smeared layers. Probably this variability of the stratification along only a few tens of meters depth range is the result of sea level changes during the last glacial period. Further, there are well separated deeper scattering layers with no recognisable structure in between. Presumably these discrete streaks are climate induced turbidite events. These precipitations of high density suspension loads are acoustically marked by a different grain size of the sediment flow between long periods of continuous sedimentation which don't cause echoes (Sect. 3.4.1).

Project: Climate history of coastal areas of Peru; year of survey: 2000

Survey vessel: *RV Sonne*, Germany

Parametric echosounder: SES-2000DS, developed by the University of Rostock; center frequency: 6 and 8 kHz, beamwidth: 1–2°

Image ©: Hermann-Rudolf Kudrass, BGR, Hannover, Germany; Gert Wendt, Institute of Telecommunications and Information Electronics, Rostock University, Germany ■

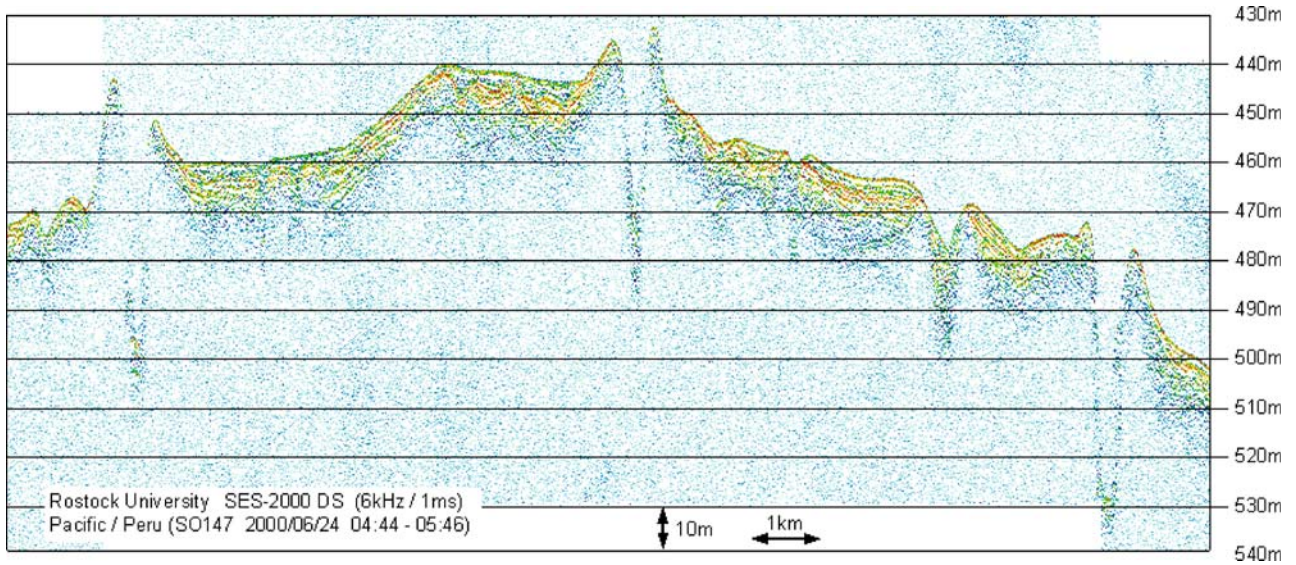


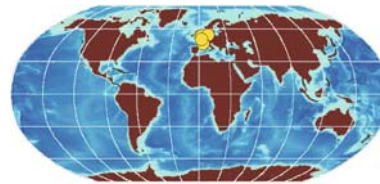
Image 5.3.2.5-2.

Submarine channels. Parametric echosounder image. At the upper continental slope off the coast of Peru there are regions where the sediments are deeply incised by a system of narrow submarine channels of nearly 50 m depth. Their flanks are apparently too steep for the post glacial sedimentation which is found instead between the embankment-like rims of the channels. Such channels which dissect many continental margin areas function like submarine rivers (Sect. 5.3.2.4), transporting turbidite suspensions over long distances up to hundreds of kilometers due to their density which is higher than water.

Image documentation: same as for Image 5.3.2.5-1 ■

Sediment layers indicate phases of high production as well as increased precipitation of turbid flow coming in from river mouths, spatially distributed by a varying near bottom current. The concept was to take bottom samples for laboratory analysis of layer features as the key document of climate events. High-resolution acoustic imaging of the sediment structure was used to define the sampling sites of the various bottom coring equipments. The choice of the exact position was as important as the determination of the optimum length of the corer. The steep slopes of some sea-floor structure of interest required very narrow echosounder beams as well as a high-resolution of the sediment stratification and a penetration depth of several tens of meters. Therefore a parametric system (Sect. 4.4.2) was considered optimum to cope with the three demands.

5.3.3 Sediment Bedforms



Most sea floors are covered by sediments of various origin, layer depth, and age, internal structure, material, grain sizes, fossil enclosures, and other features and parameters. The bulk of the material-related parameters can be discriminated at best indirectly by acoustic imaging. The peerless strength of sound imaging however, is the direct and quantitative acquisition of the sediment shape and structure of areas of many square kilometers within a short period of time, which is in fact the most important information when dealing with hazards by sediment motion in coastal regions.

The driving force to move and reshape the sediments is the friction of flow at the sediment surface. There are *two types of flow* which, under favorable weather conditions, may both be restricted to cause harmless, small scale modeling of the sediment relief by local erosion and re-sedimentation. The first type is the flow orbiting with the sea waves. This periodic flow declines rapidly – in technical terms exponentially – towards the sea floor, but in shallow, coastal areas it is often sufficient to generate ripples at the sandy bottom. We can

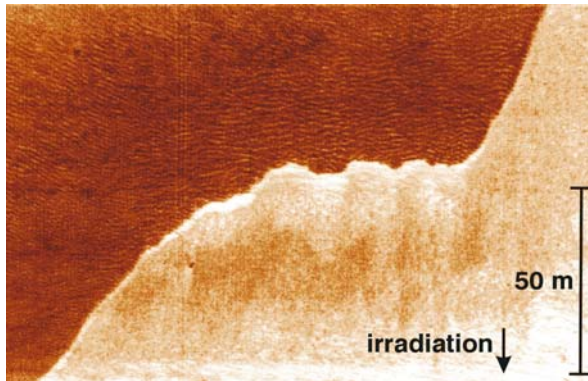


Image 5.3.3-1.

Boundary between sediment bed-forms. Sidescan image. The sharp boundary between coarse sand with small scale wave induced ripples and silty fine sand is caused by the cohesive properties, with silt preventing erosion and ripple formation at the same current velocity. Such sediment patterns are typical of the shallow, tidal areas of German *North Sea*.

Project: Investigation of soil features for monitoring potential basement erosion of the off-shore research platform Nordsee; year of survey: 1986
 Location: North Sea, 74 km west of the island of Sylt; water depth: 30 m
 Research vessel: *WFS Planet*, FWG, Kiel
 Sidescan system: Klein 520; frequency: 100 kHz, beam-width: 1°
 Unfocussed, uncorrected image, image section: 100 m
 Image ©: Doris Milkert, FWG, Kiel Germany ■

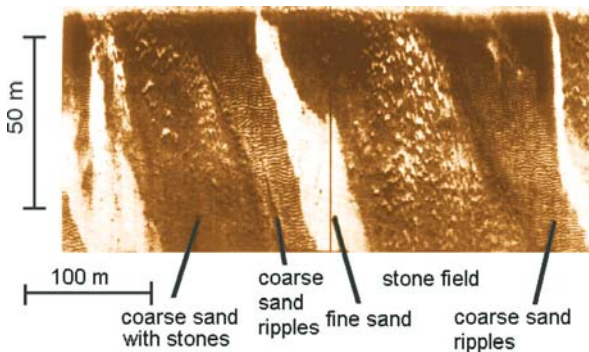


Image 5.3.3-1a.

Example of several closely adjacent bedforms. Sidescan image. The image was taken in the southern North Sea with stone fields of glacial times, coarse and fine sand. The reason for the absence of fine sand ripples is presumably the same as for Image 5.3.3-1.

Technical documentation: similar to Image 5.3.3-1
 Image ©: FWG, Kiel Germany ■

see such a washboard-like relief when they are fallen dry during low tides. The second type are the various forms of ocean currents which may produce similar sand bottom profiles.

But, both types of flow can be of terrifying impact in coastal areas when non benign conditions of the atmosphere and the sea come together. At a shallow coast or a harbor entrance, extreme storm-waves and surf cause devastating erosions of the coastline, destroy coastal constructions and form huge underwater dunes, acting as hazardous shoals for ship traffic (Sect. 7.1). Similarly dramatic is the permanent impact of a strong *tidal flow* which moves the entire water volume, reaching the sea floor at nearly full speed. Well known is the tidal current passing the English Channel, which works like an accelerating funnel. Due to these major forces the scales of the sediment relief can be by orders of magnitude larger than the innocuous, wave induced, coastal effects: there would be dunes, up to tens of

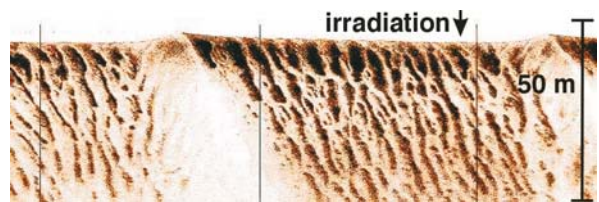


Image 5.3.3-2.

Sand dunes, superimposed by small scale ripples. Sidescan image. The seabed surrounding the Netherlands is covered by extended fields of sand dunes with small ripples riding on the luff-side flanks of the large dunes. The formation conditions of such double structure bed-forms are high tidal current velocities, dominating the sea wave induced alternating currents and non cohesive fine grain sands for the small scale ripples together with coarse sand for the sand dunes or mega-ripples. The image indicates the crests of the dunes by broad, light stripes of more cohesive silty sands without ripples and low backscatter. The crests are oriented athwart the tidal flow and reshape the fine structure every time following the tidal phase. Net sand transport depends on storm events.

Project: Features of mine burial; year of survey: 1996
 Location: Middeldiep, North Sea; water depth: 15 m average
 Research vessel: *WFS Planet*, FWG, Kiel
 Sidescan system: Klein 595; frequency: 100 kHz, beam-width: 1°
 Unfocussed, image section: 100 m
 Image ©: Doris Milkert, FWG ■



◀ **Image 5.3.3-3.**

Large sand dunes superimposed by ripple fields. Sidescan image.

The dune formation was monitored in the German Bight in 1996 off the fairway of the river *Weser*. The crest height of the dunes is 4–5 m; the crests are 50–80 m apart. The superimposed ripples migrate at higher speeds than the large dunes. The environmental impact assessment was necessary for planning the deepening of the Outer Weser by WSA down to a safe shipping clearance of 12 m. The imaged area is 80 m wide and 330 m along track.

Project: Official support of WSA by BSH, 1996
 Survey vessel: *VWFS Atair*, BSH, Hamburg
 Sidescan sonar: EG&G, Model 270, hull mounted; frequency: 390 kHz, beamwidth: 0.5°
 Image ©: Manfred Zeiler, BSH, Hamburg, Germany ■

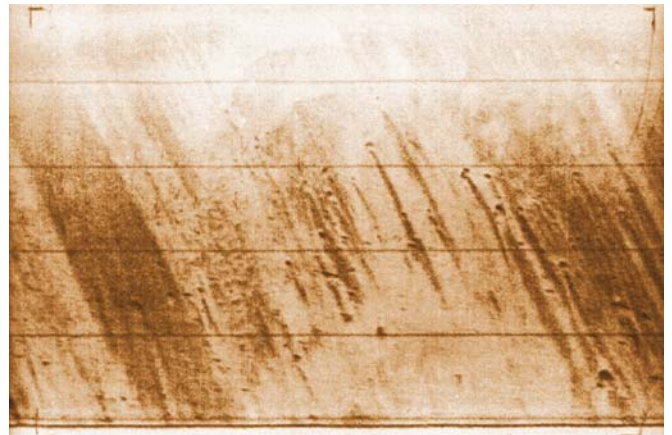


Image 5.3.3-4.

Comet marks behind stones at high speed of flow. Sidescan image.

Storm induced flow can cause abrasive erosion which differs behind an obstacle as against the free sediment surface. Comet marks are thus also named obstacle marks. Note that the sound propagates towards the upper rim of the image; strong scattering is indicated dark. The current induced stream of fine grain sediment is not replaced behind the obstacles and causes stronger backscattering by coarser grains, reminiscent of comet tails.

Site: Baltic Sea
 Sidescan system: EG&G, Mark II Dual Channel System, Towfish 272 TD; frequency: 105 kHz, beamwidth: 1.5°, towing depth: 15–20 m above sea floor
 Paper record; line distance: 10 m
 Image ©: Friedrich Werner, Kiel ■

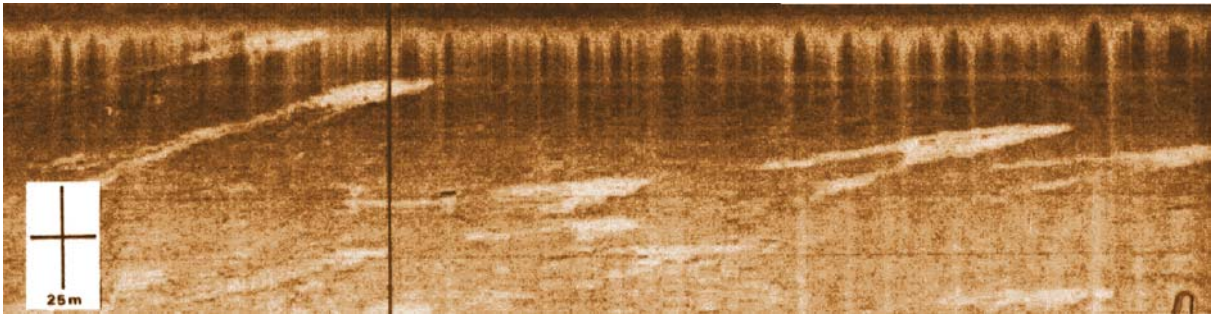


Image 5.3.3-5. Sickleshaped dunes (barchans). Sidescan image. This dune form is also known from migrating dunes on land in deserts of central Asia and elsewhere. The asymmetry of shallow luff-side- and steep lee flanks is similar to the long crested relatives called transverse dunes (Sect. 5.3.9.2 and preceding Images 5.3.3-2, 5.3.3-3 and 5.3.3-3a). The horns of the sickles form always on the lee side known as the *slip face*. The form of the barchans seems to suggest higher speed of the unidirectional (wind induced) flow than of the transverse dunes. However, the barchan shape is due to limited sand supply. As the supply increases, barchan dunes begin to connect with others forming barchanoid ridges. If the ridges become fairly straight, scientists call them transverse dunes. (Note the compression of the horizontal axis.)

Image documentation: same as for Image 5.3.3-4 ■

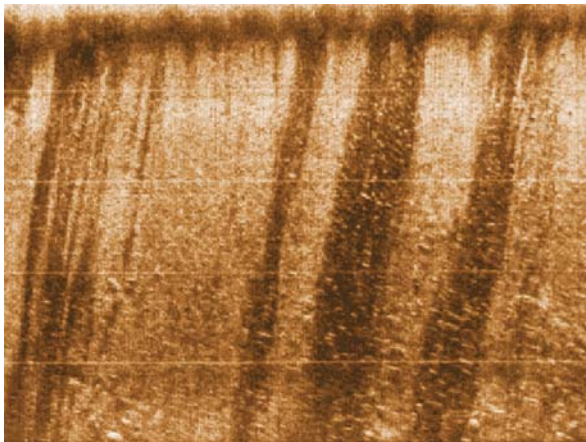


Image 5.3.3-6. Sand ribbons. Sidescan image. The sea floor section is irradiated from the upper image rim. The flow speed causes random stripes of more or less removed fine sand and thus stronger or weaker backscattering respectively. Such phenomena may be an intermediate state and occur when the fine grain particles are not replaced from upstream.

Image documentation: same as for Image 5.3.3-4 ■

meters in height (Sect. 5.3.9) instead of sand ripples, just a few centimeters high. Most dangerous and infamous is the combined action of very heavy storms and high tides.

What can be said about the predictability of sediment erosion, in particular the critical speed of flow to start sediment motion? Of course, fine grained sand and newly-formed, nearly fluid mud are definitely much easier to move than coarse gravel. But compact, consolidated clay sticks together and is nearly immune to erosion up to a considerable speed of flow despite its very fine grain. There are usually several constituents present in a volume of sediment which may vary substantially from place to place. Moreover the static pressure of the water column which supports the consolidation, together with the time elapsed since the last forced motion interrupting the consolidation process, are influential to what happens next. Further, the superposition of waves and currents also contribute to the onset of sediment motion. Altogether, any prediction of the impact of meteorological or oceanological conditions on sediment motion features is even more difficult than the prediction of the agents.

Thus the regular surveillance of endangered coastal areas is considered mandatory and usually conducted by governmental institutions. For this purpose a single acoustic tool such as a sidescan echosounder will not always suffice to provide the authorities with the quantities required for taking protective measures. The sidescan sounder is restricted to yielding only two-dimensional images of the sound scattered by the

sea floor relief though with the highest resolution (Sect. 4.3). To determine the individual heights of the elevations, in other words to reveal the 3rd dimension of the sea floor morphology, requires at least a vertical mono-beam or, better, a multibeam sounding device (Sect. 4.2). However, even the best fan-sounder on principle cannot compete with the lateral resolution of the best sidescan sounder (Sect. 5.3.9.2). Fan sounders scan the sea floor only with the resolution of their beamwidth; thus the pixel size increases with the water depth. The short pulse width of the sidescan sounder with its grazing sound propagation however provides high lateral resolution independent of range (Sect. 4.3.4). Thus both methods of sounding the sediment relief are complementary and supplement each other with their possibilities.

The various *types* of sediment motion and erosion can be discriminated by their sidescan images, a collection of which is shown here. Such records visualize the progress of the processes in different types of sediment, in particular of stripping the fine grains from the structure of the remaining larger particles. Though even the high resolution of the sidescan method cannot resolve individual gravel elements, their presence is revealed by the stronger backscatter of the area which they cover, contrasting with others of finer sediments.

The interpretation of sidescan images requires much geological and mineralogical experience because different types of sediment may cause the same scattering intensity. Regarding the kind of matter in general, remote sensing by sound can only provide circumstantial evidence by the features of shape, structure, reflectivity and backscatter (Sect. 3.4). Verification by analysis of samples, brought up from the sea floor, called “ground truthing” is therefore essential in the frequent cases of doubt.

The Images 5.3.3-1 to 5.3.3-3 demonstrate ripple and dune formations which occur at moderate to higher speeds of flow. The bedforms shown in the Images 5.3.3-4, 5.3.3-6, 5.3.3-7, 5.3.3-8 are caused by unidirectional flow at erosive flow speeds in shelf areas and are also taken with sidescan sonar. Unlike the ripple structures formed at moderate speeds with crests athwart the direction of flow, the abrasive textures trend in flow direction. (The Images 5.3.3-5, 5.3.3-7, and 5.3.3-8 are reproductions of limited quality from Landolt Börnstein.)



Image 5.3.3-7.

Erosional furrows. Sidescan image. The asymmetric furrows are the erosive result of storm induced sediment flow, in a sense small versions of channels such as found at shelf breaks. The oblique irradiation is causing bright and dark sides, not the difference in grain size as of the preceding image. Direction of irradiation: same as of preceding image.

Image documentation: same as for Image 5.3.3-4, except site: off *West Africa* ■

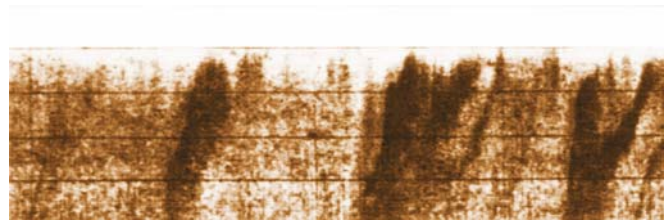


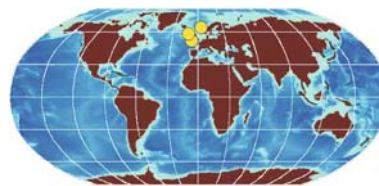
Image 5.3.3-8.

Erosional furrows. Sidescan image. These furrows generated by a storm are more similar to channels with tributaries eroded by sediment flow than depicted in the preceding image. Direction of irradiation: same as of preceding image.

Image documentation: same as for Image 5.3.3-4 ■

5.3.4

Carbonate Mounds and Cold Water Corals on the West European Margin



5.3.4.1

Carbonate Mounds in the Porcupine Bight and Rockall Trough Margin

The largest seabight of the West European Margin named *Porcupine Bight*, deeply incised into the *Celtic*

Shelf southwest of Ireland was and still is subject of major international and interdisciplinary research projects. The bight with its large ensembles of carbonate mounds is considered a key to understand the complex processes of biochemical and environmental interaction.

At the shelf edge the bight is sloping from a water depth of 300 m down to 3 500 m at the mouth of the bight. The place is important due to its hydrocarbon resources in different types of deposits which are preferably found at continental slope areas. The high resolution multibeam echosounder bathymetry of the eastern slope of the bight conducted with the German icebreaking research flagship *Polarstern* in 2000 has

revealed details of *two different types of the sea floor*, showing characteristic clues which indicate processes of their origin.

The *first type*, typical of the north of the eastern slope of the *Porcupine Bight* is a smooth declivity, covered by many similar looking mounds aligned at depths between 700 to 1 000 m. Most of them are of the order of 100 m high with a foot diameter of about 1 km. These mounds, mostly of elliptic cross section differ fundamentally in their origin from the nearly innumerable seamounts along the mid-oceanic ridge areas. Whereas the seamounts are of volcanic origin – in fact all of them have been active volcanoes – the comparatively smaller mounds are the product of biology: they appear to con-

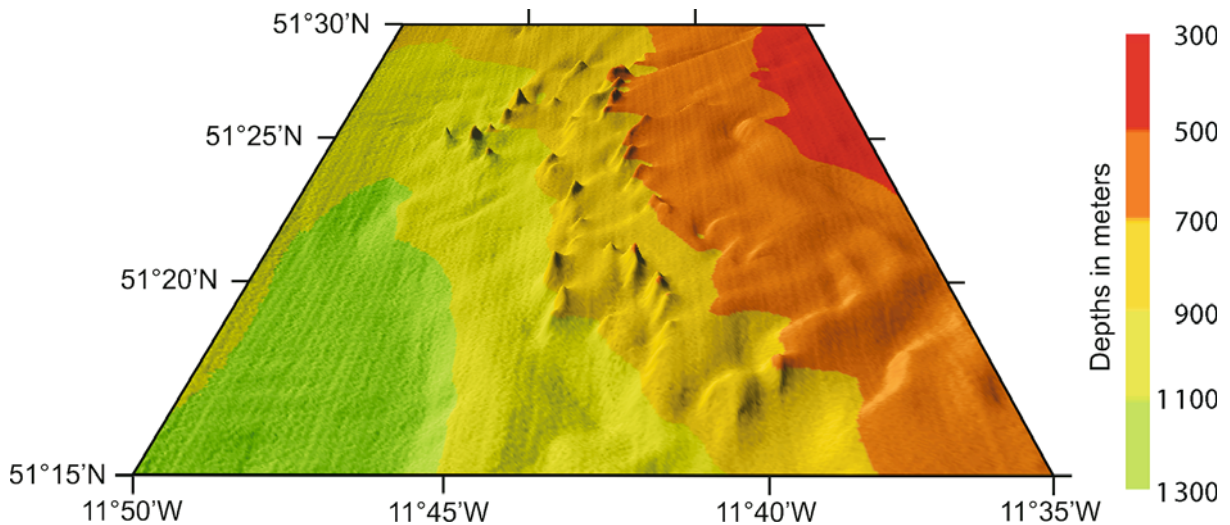


Image 5.3.4.1-1. Ensemble of carbonate mounds, *Porcupine Bight*. High resolution multibeam image. The mounds of about 100 m height form a random cluster of mostly individual, disconnected, non circular cones confined to a limited depth regime. The longer cone axis of a kilometer and more at the bottom is predominantly oriented along isobaths. No mounds were found above 700 m, being almost a sharp boundary and very few below 900 m. The mounds at greater depths are mostly higher and partly surrounded by shallow depressions, possibly from flow induced erosion.

The predominating visual impression is a strong sediment coverage of the escarpment, forming a slightly hilly sea floor above the mound ensemble with some broad irregular furrows, though much less pronounced than the channel system shown in the Images 5.3.4.1-2 and 5.3.4.1-3. The bedspread-like sediment layer broadens the cones at their foot and appears to bury some of them completely. Obviously the bathymetric relief showing the present state of the mounds needs supplementary, sediment penetrating images to reveal the internal structure with hints on their origin. The mound ensemble shown is one of several found at the upper slope of the northern *Porcupine Bight* (see attached CD).

Project: Geomond of the European Union, 2000

Research vessel: *RV Polarstern*, Germany

Multibeam system: ATLAS Elektronik, Hydrosweep DS2; frequency: 15.5 kHz, beamwidth: 2°, 59 beams, fan width: 90°

Landscape depiction with central perspective and artificial sunlight from the north, direction of view: northbound, height exaggeration: 6 times, horizontal resolution (average scanning footprint at the mounds): 30 m

Image ©: Andreas Beyer, Alfred-Wegener-Institut für Polar- und Meeresforschung, AWI, Bremerhaven, Germany ■

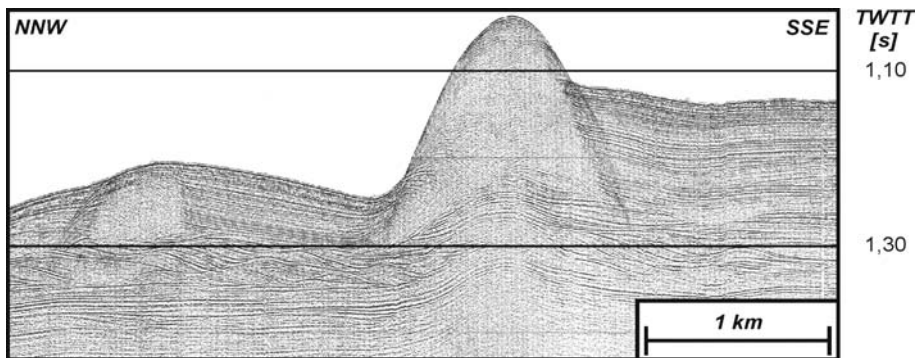


Image 5.3.4.1-2. Cross section of carbonate mounds, northern Porcupine Bight. High resolution seismic image. Presumably the most detailed section image of a large carbonate mound interior shows the symmetrical sugar-loaf form of the mound with the pronounced asymmetry of the surrounding sediments. The height is exaggerated by a factor of 5 in the depiction. The mound stands out about 200 m and appears nearly free of any identifiable internal structure. According to core samples, cold water corals play a significant role in carbonate mound build up. The asymmetry of the sediment profile is current induced with the typical moat on the luff side of the flow and a high lee side shoulder of fine sediment layers. The apparent superposition of the mound contour on the right and a stripe of the sediment strata is an artifact caused by the limited lateral resolution of the seismic sounder in comparison to the higher depth resolution of about 2 m.

Project: GEOMOUND (EU Framework Programme 5)

Coordinates of the section: 51°23' N, 11°43' W

Research vessel: *RV Belgica*, Belgium

SIG surface sparker, 500 J; mid frequency: 600 Hz, frequency band: 250–2000 Hz

Depth resolution: 1–2 m. Sediment penetration at site: 200 m. TWTT: two-way transmission time

Image © and text contribution: Jean-Pierre Henriët, Renard Centre of Marine Geology, Ghent University, Belgium ■

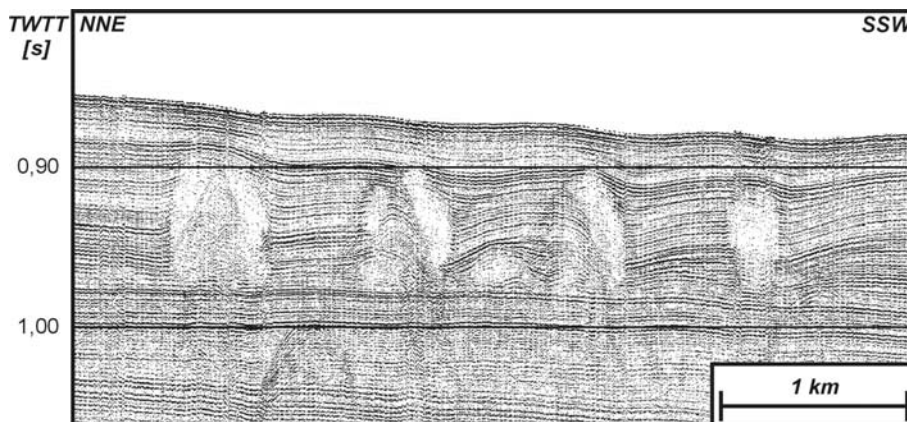


Image 5.3.4.1-3. Cross section of buried carbonate mounds, northern Porcupine Bight. High resolution seismic image. The series of four completely buried carbonate mounds of about 80 m height is part of a prolific cluster of small mounds in the upper Porcupine Bight. They all root from a single horizon as if a sudden and nearly simultaneous growth has taken place which also ceased at about the same time. This argues for decisive and episodic environmental conditions that enabled the complex and still enigmatic biochemical and sedimentological processes of carbonate mound formation. The sediment coverage of tens of meters is a perfect camouflage but the investigation of its stratification will permit the dating of the growth phase and perhaps indicate the kind of change or the local displacement of their decisive conditions.

Image documentation: same as Image 5.3.4.1-2, but coordinates of the section: 52°19.52' N, 13°00.38' W ■

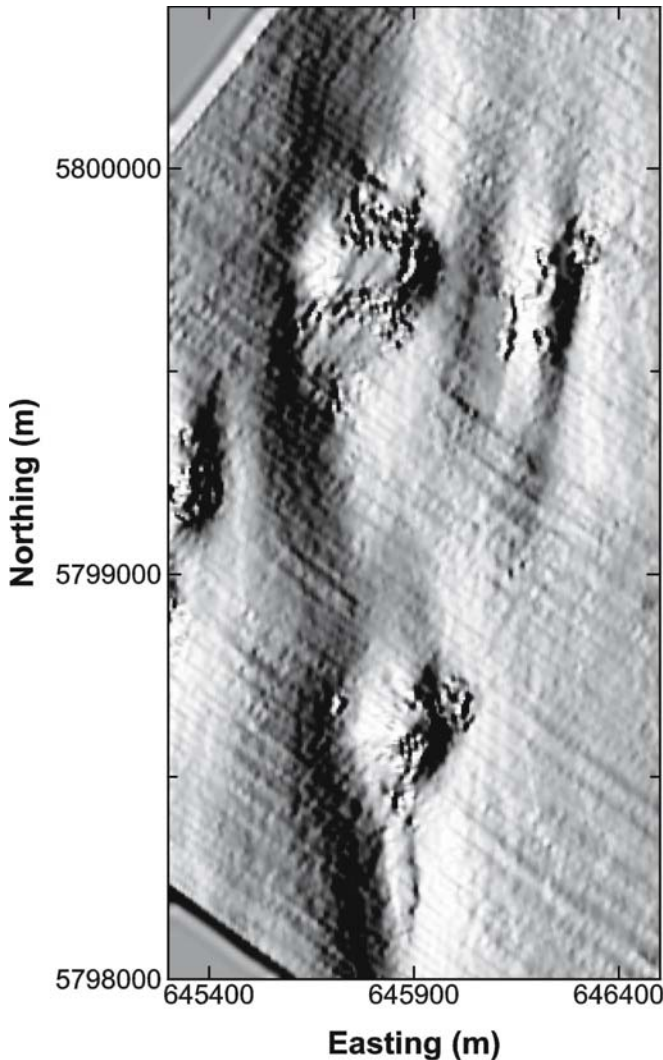


Image 5.3.4.1-4.

Internal relief of buried carbonate mounds, northern Porcupine Bight. High resolution 3D-seismic image. The principle of 3D-sampling of the sea floor *surface* by multibeam echosounder technology has been extended to the sea floor *volume* by advanced multi-seismic sections in narrow, parallel sequence. The 3D-image of the shape of two buried carbonate mounds is a much more complicated product of data acquisition and processing than known from multibeam imaging. Whereas the latter can rely on the mostly well defined though often weak single echo of the outer boundary of the sea floor to construct the connected surface of the relief, the former needs three-dimensional contour-following algorithms of internal layers to be treated as surfaces. The preceding two dimensional seismic section illustrates that the data processing will become the more complicated, the more the selected layer horizon is disturbed or interrupted. The visualization of the upper parts of the mounds and the complete 3D-depiction of the stretched moats by simulated sunlight from the left is essentially the same as applied by the high frequency multibeam technology. The stripe texture shows the sampling pattern in the horizontal and indicates the effort which is necessary to produce data sets which finally provide series of internal surfaces like series of shells. The technical endeavor to such an extent has been invested to improve the precision of exploration of hydrocarbon deposits.

Project: GEOMOUND (EU Framework Programme 5)
 Provision of image by courtesy of *Statoil Exploration (Ireland) Ltd.*, its partners *Conoco (UK) Ltd.*, *Enterprise Energy Ireland LTD.*, *Dana Petroleum Plc.*, and *Chevron UK Ltd.*
 Survey company: PGS
 Seismic sources: 2 sleeve airgun clusters, 144 bar, 41 liters, signal frequency: 100 Hz
 Streamers: 8, vertical resolution: 4 m, horizontal resolution: 12.5 × 12.5 m
 Image ©: Veerle Huvenne and Jean-Pierre Henriët, Renard Centre of Marine Geology, Ghent University, Belgium ■

sist essentially of carbonate and seem to be built up, at least in parts by corals. It is assumed that the corals are linked to currents along the slope with nutrients or possibly to subsurface hydrocarbon reservoirs, partly converted to carbonate as a substrate for follow on coral reefs.

Many of the mounds are surrounded by a shallow furrow, probably due to flow induced erosion of the sediment which has buried some of the mounds completely. Though these don't stand out in the bathymetric relief, they are clearly recognizable in the sediment penetrating sound images which reach down to the roots of the mounds. Other mounds are still growing by active coral population. The increasing scientific

interest in carbonate mounds is guided by the complex interrelationship between marine life and marine biochemistry with the genesis of methane and methane hydrate (Sect. 6.2.1, 6.2.2) as important aspects.

The carbonate mounds of the Porcupine Basin resemble mud mounds in terms of their dimension, geometry, faunal communities and environmental setting. The Porcupine Basin displays – within the North Atlantic realm and perhaps in a global perspective – a unique association and diversity of carbonate mound provinces, which may yield the key to address the question of mound genesis and its significance in a global oceanic plot, from a process-oriented point of view. The

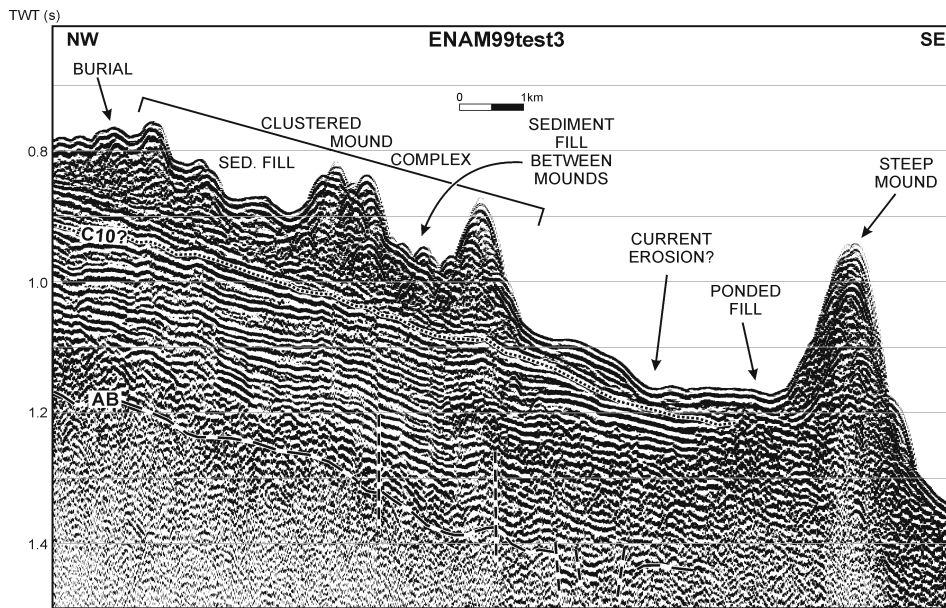


Image 5.3.4.1-5. Giant carbonate mounds along the Rockall Trough margin. Seismic section. The Rockall Trough is a major deep water basin along the western continental margin of Ireland and Britain. Along the upper slope of its southern margin giant carbonate mounds, partially covered with cold water corals were discovered in the late eighties and nineties by echo sounding. These mounds which occur down to 1200 m are mostly larger and more variable in size and shape compared to those found in the adjacent Porcupine areas in the south. The single large pinnacle at the right hand side of the seismic section rising more than 300 m above the seabed stands in close neighborhood of a clustered mound complex. The real slope of the steepest mound flanks can reach 25° or more; the horizontal axis of the depiction is compressed by a factor of 14. The narrowest layers resolved are about 7 m apart. Upslope the sediment fill between the mounds increases whereas the size of the mounds decreases. The valley on the right with horizontal fill partly results from current activities. The upper seismic reflector labeled C10 is a kind of root horizon of the clustered mounds of this image. There are other mounds considered to be much older since they are rooted on or slightly above the horizon labeled AB, like the single steep pinnacle of this image. The dating of the onset of these mound formations is uncertain and may reach back to Early Tertiary age, 60 million years ago whereas the youngest mounds, rooted on the C10-horizon may have started to form during the late Early Pliocene, about 4.5 million years before present.

Project: ENAM II, ENAM99Test3 by NIOZ

Survey vessel: *Pelagia*

Seismic equipment: airgun (10, 20 and 2 × 40 cubic inch, 6 channel streamer) frequency range: 50–400 Hz, resolution vertical: ±7 m, horizontal: ±18 m corresponding to the shot distance

Image ©: Tjeerd C. E. van Weering, Netherlands Institute for Sea Research (NIOZ), Texel, The Netherlands ■

giant mounds on the present seabed surface southwest of Ireland, 200 to 250 m high, the extensive cluster of over a thousand buried reefs embedded in drift sediments, the whole range of mounds towering from a deeply ravine-forming unconformity on the eastern slope of the Porcupine Basin are not mere curiosities, but significant build-ups, which may put Man on the track of hitherto unknown Biosphere processes thriving at the confluence of fluxes from both internal – geological – and external – oceanic – origin. In many as-

pects and *mutatis mutandis*, carbonate mounds might be for the Margins what sulfide mounds are on the Ridges: the product of biologically controlled geological processes, of global significance. The “Porcupine Drilling Project” is driven by four major research projects funded under the 5th Framework Programme of the European Union (GEOMOUND, ECOMOUND, DEEP-BUG and ACES) and hence it mobilizes a multi-disciplinary consortium of 22 institutes and research centers. A range of provoking hypotheses will be tested:

the role of gas seeps as a prime trigger for mound genesis, the role of bacteria as main mound builders, the role of reef-forming corals as a major part of the mound community and their environmental record potential, the significance of mound “events” in a palaeo-environmental plot, the identification of prominent erosional surfaces as products of global oceanic turnovers, the potential of mounds as high-resolution palaeo-environmental recorders, the value of the Porcupine-Rockall mounds as present-day analogs for Phanerozoic reef mounds and carbonate mud mounds, and the potential role of fluid flow as a common source of both slope failures and mound growth. Finally, a virtual link to biological processes is provided by the widespread existence of cold and deep-water coral and sponge reef ecosystems which colonize the flanks of the mounds. However, their nutritional mode, either through benthic-pelagic coupling processes, or through fueling by deep hydrocarbon reservoirs and thus the role of such processes in the evolution of mounds, remains unresolved.

5.3.4.2 Cold Water Corals on the *West European Margin*

“Coral reefs are confined to shallow and warm tropical and subtropical regions”. This was the state of knowledge until increasingly sophisticated facilities for exploring deep-water environments became available in the nineties of the last century. High resolution seabed sound imaging, which enabled insight into fundamental tectonic processes that permanently reorganize the deep-sea floor (Sect. 5.2), have also revealed unexpected habitats of highly organized life in dark and cold waters up to high latitudes. Backed up by manned and robotic submersibles, scientists discovered and explored a variety of coral ecosystems thriving in such seemingly hostile regions. Some of these cold-water corals construct banks or reefs as complex as their tropical cousins. Cold-water coral systems can be found in almost all of the world’s oceans and seas: in fjords, along the edge of the continental shelf and round offshore submarine banks and seamounts.

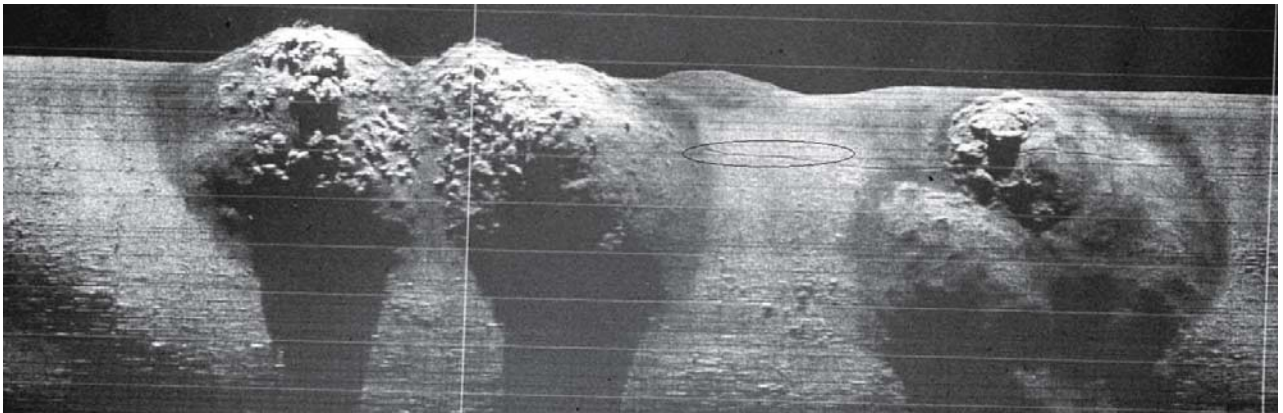


Image 5.3.4.2-1. Deep cold water corals off Norway. Sidescan sonar image. This site of 240–280 m water depth is a small cut-out of the *Sula Reef Complex* between the Norwegian coast and the shelf break of the famous Storegga-Slide area (Sect. 5.3.1, 7.4.2). The mounds of about 50 m in diameter are live and dead *Lophelia* corals respectively. The cauliflower features of strong backscatter represent live coral colonies of the scleractinian *Lophelia pertusa*. Mounds of smooth backscatter are buried by sediments. A trawl mark indicated by an ellipse crosses the mound at the right side, visible as the thin line scar nearly coinciding with a marker line. The sound shadows of this image are set dark. The image pixels appear stretched athwart; a typical feature of the anisotropy of lateral and radial resolution (Sect. 3.3.4).

Project: German Research Foundation DFG He 1671/5 “Cold-water reefs”; center coordinates, imaged area of the *Sula Reef Complex*: 64°00' N and 08°00' E; cooperating institutions: Fachbereich Geowissenschaften, Universität Bremen; year of survey: 1995
Research vessel: *FFS Victor Hensen*, Bremen

Sidescan sonar system: Klein, Model 595; frequency: 500 kHz, horizontal beamwidth 0.2°, no autofocus, towing depth: about 10 m above the floor

Only the portside channel of the sidescan image is shown

Image ©: André Freiwald, Institute of Paleontology, Erlangen University, Germany ■

Without light, and in relatively nutrient-rich sea water, cold-water coral ecosystems function in a substantially different way to shallow-water coral systems. Unlike their warm water relatives cold-water corals living at depth in the dark have no light-dependent symbiotic marine plants and therefore depend on the supply of downward sinking, current-transported particulate organic matter and zooplankton for their food. Such cold-water reefs are constructed by only a few stone coral species such as *Lophelia pertusa* and *Madrepora oculata*. The most abundant reef builders of these cold water specialists are to be found in the North Atlantic, the Mediterranean Sea and the Gulf of Mexico.

The recent discoveries of cold-water reefs are changing our knowledge regarding reef-forming processes and where they occur. Researchers are beginning to realize

that cold-water reefs are members of evolutionary adaptability up to the extremes where, at one end, the evolution of light-dependent symbiosis has allowed corals to survive under low nutritional regimes in the shallow tropics, and at the other end, a sufficient supply of food allows them to thrive as carnivorous organisms in the deep and cold waters of the high latitudes. In this respect there are parallels to crustaceans, like the scavenging, carcass eating amphipods on the sea floor of deep arctic waters (Sect. 6.3.2). However, cold-water coral ecosystems have been seen to be very vulnerable to disturbance regardless of depth. Evidence of human impact is a feature of almost every survey. Of all human activities occurring in deep marine environments, benthic fishery operating with mobile gear, such as trawls, always stands out as the major threat to cold-water corals.

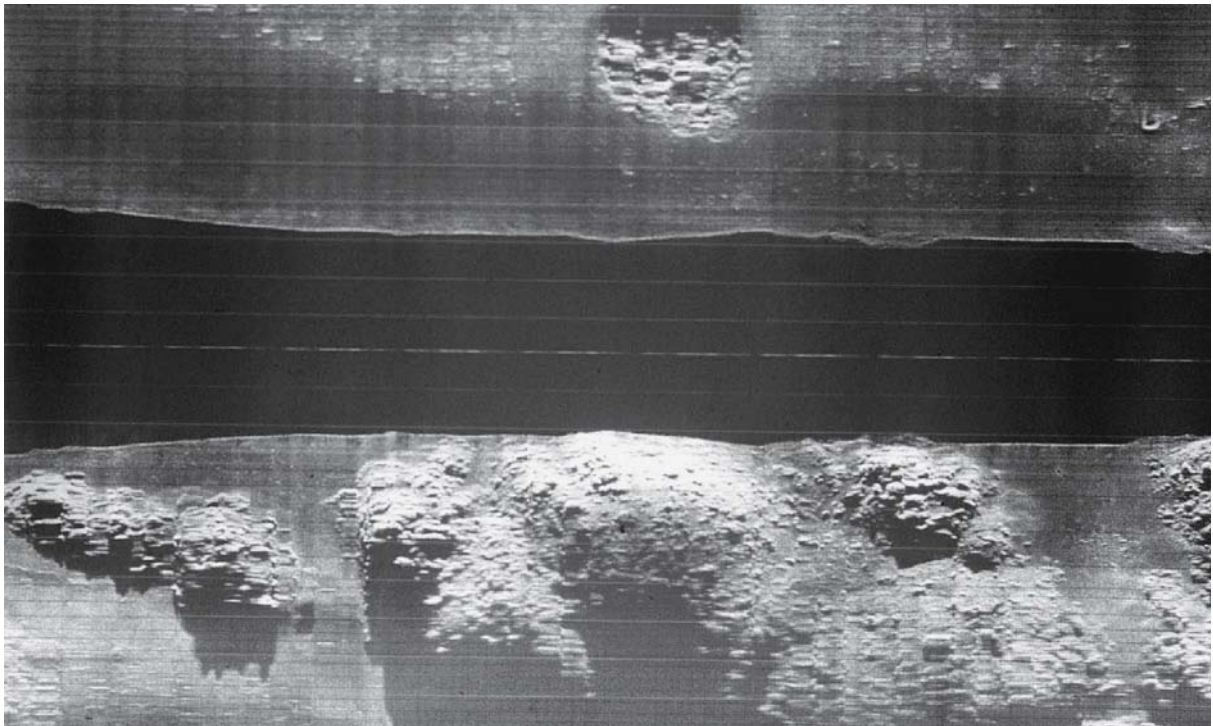


Image 5.3.4.2-2. Deep cold water corals of the main reef B, *Sula Reef Complex*, off Norway. Sidescan sonar image. Another detail of the main coral reef complex at 250 m depth. Again, the cauliflower features represent live coral colonies. To resolve such fine structures requires a deep towed sidescan system. An autonomous Underwater Vehicle (AUV, Sect. 7.4.1) could survey also in close object distance and moreover with systematic meandering search courses, but the cable control of a towed array enables real time confirmation of success. The contours framing the black band correspond to the echo onset.

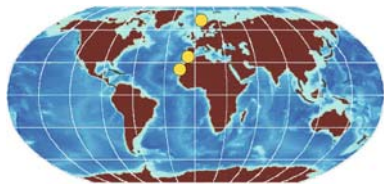
Image documentation: same as for Image 5.3.4.2-1; both sidescan channels are shown

Image © and text contribution: André Freiwald, Institute of Paleontology, Erlangen University, Germany ■

5.3.5

5.3.5

Mud Volcanoes and Diapirs



5.3.5.1

Mud Volcanoes

Mud volcanoes have been discovered on the sea floor along many *active* continental margins and some were found also on *passive* continental margins. They may appear like “cool relatives” of the prototype of a volcano with its rare but spectacular magmatic eruptions. Instead, mud volcano eruptions convey gas, water and sediments up to the surface of the sea floor, where the outflow can reach many kilometers into the surroundings. Their fluid and gas escape features presumably represent the most important source of methane emission into the sea next to methane hydrate deposits. The high concentrations of methane at such sites feed specialized bacteria which can synthesize non gaseous products, preventing part of the greenhouse gas from being dissolved into the sea water. The mud volcanoes with their geo-chemical and bio-chemical interaction processes are thus considered one of the controlling elements of climate relevance.

In May 2002, the *Research Vessel Belgica* unveiled a cluster of shallow, giant mud volcanoes on the *active Atlantic Margin* of Morocco, some 35 km off Larache. Some of the volcanoes reach over 5 km in diameter and tower more than 200 m above the seabed, outclassing in size most of their deeper counterparts in the Gulf of Cadiz or the Mediterranean. Two elongated, NW trending ridges supporting mud volcanoes of various size converge towards a majestic mud volcanic structure: the *Al Idrissi* mud volcano, which rises high above the upper slope, its crater at less than 200 m below sea surface (Image 5.3.5.1-1). The volcanic cones are girdled in oceanward direction by a deep horseshoe-shaped moat. Their flanks are plastered with recent mud flows, protruding in thick convex lobes into the moat. The craters systematically feature a well-shaped outer ring or

circular terrace, and an inner dome. Very-high resolution deep-towed seismic profiles reveal a core with higher acoustic reflectivity, protruding in the central dome and possibly composed of freshly upwelled, gas-charged mud.

A most exciting observation made from high-resolution seismic profiles is the marked episodic character of the outflow (Image 5.3.5.1-2), which moreover appears to be synchronous in distant volcanoes. The buried mudflow lobes in the periphery of the cones dovetail with current-controlled sediments, documenting at least three major eruption stages within the top 200 m of the embedding sediments. Such basin-wide episodicity in the activity of mud volcanoes seated on an accretionary wedge calls for a tectonic tuning, pulsed by the tremors of the converging plates.

One of the rare mud volcanoes located on a *passive margin* has been visited by research surveys several times since its discovery in 1991. It is the *Håkon Mosby Mud Volcano (HMMV)*, found on the Norwegian side of the *Barents Sea* at about 1 250 m water depth. The HMMV has a foot diameter of about 2 km with a “caldera” of 500 m across (Images 5.3.5.1-3, 5.3.5.1-4). Like other mud volcanoes, HMMV is surrounded by a moat but less regular and less deep. However, the outcropping shape of this volcano is quite different from the spectacular cone of an active margin type mud volcano like *Al Idrissi*. The height of HMMV is very modest indeed: just 10–20 m above the surrounding sea floor. Eruptive mud outflows of unknown age have apparently disrupted the outer rim with tongue-shaped coverage.

Since the volcano is located in the youngest part of a major slide which happened about 200 000 years ago in the Pleistocene, HMMV might be even younger. According to seismic profiling, the main part of this mud volcano is a subsurface structure (Image 5.3.5.1-5), reaching several hundred meters down. Remarkable is a “pull down” of the reflecting layers surrounding the root cone of the volcano. This pseudo depression is an indicator of lower sound speeds, feigning deeper horizons. The only possible reason is free gas (Sect. 6.2.2), presumably accompanied by fluids which can both be considered to escape towards the sea floor. HMMV is not part of an ensemble of further mud volcanoes but a single structure. Its origin is still under debate (Henriet).

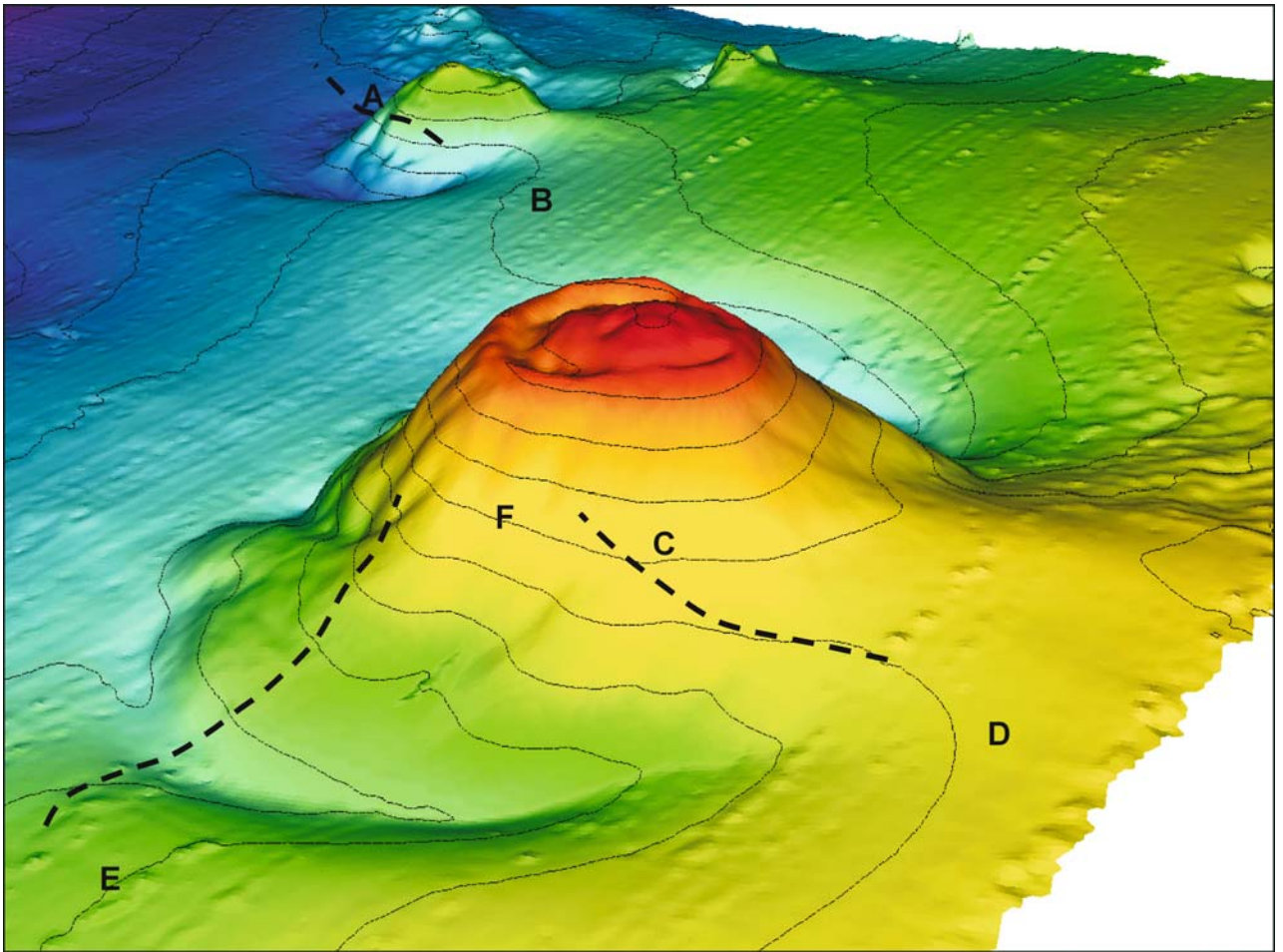


Image 5.3.5.1-1. The Al Idrisi mud volcano. Multibeam image. The Al Idrisi mud volcano in the foreground of the image is situated at 35.25° N, 6.60° W and has a base diameter of about 5 km. Its top is at a depth of less than 200 m, the base at about 450 m. The broken lines indicate the seismic sections over Al Idrisi and the smaller mud volcano nearby. The typical dome inside the crater is clearly revealed by the high resolution multibeam image.

Project: CADIPOR 2002

Research vessel: *Belgica*, Belgium

Multibeam echosounder: SIMRAD, type: 1002; frequency: 95 kHz, beamwidth: 2°, number of beams: 111

Image ©: Jean-Pierre Henriët and Geert Moerkerke, Renard Centre of Marine Geology, Ghent University, Belgium ■

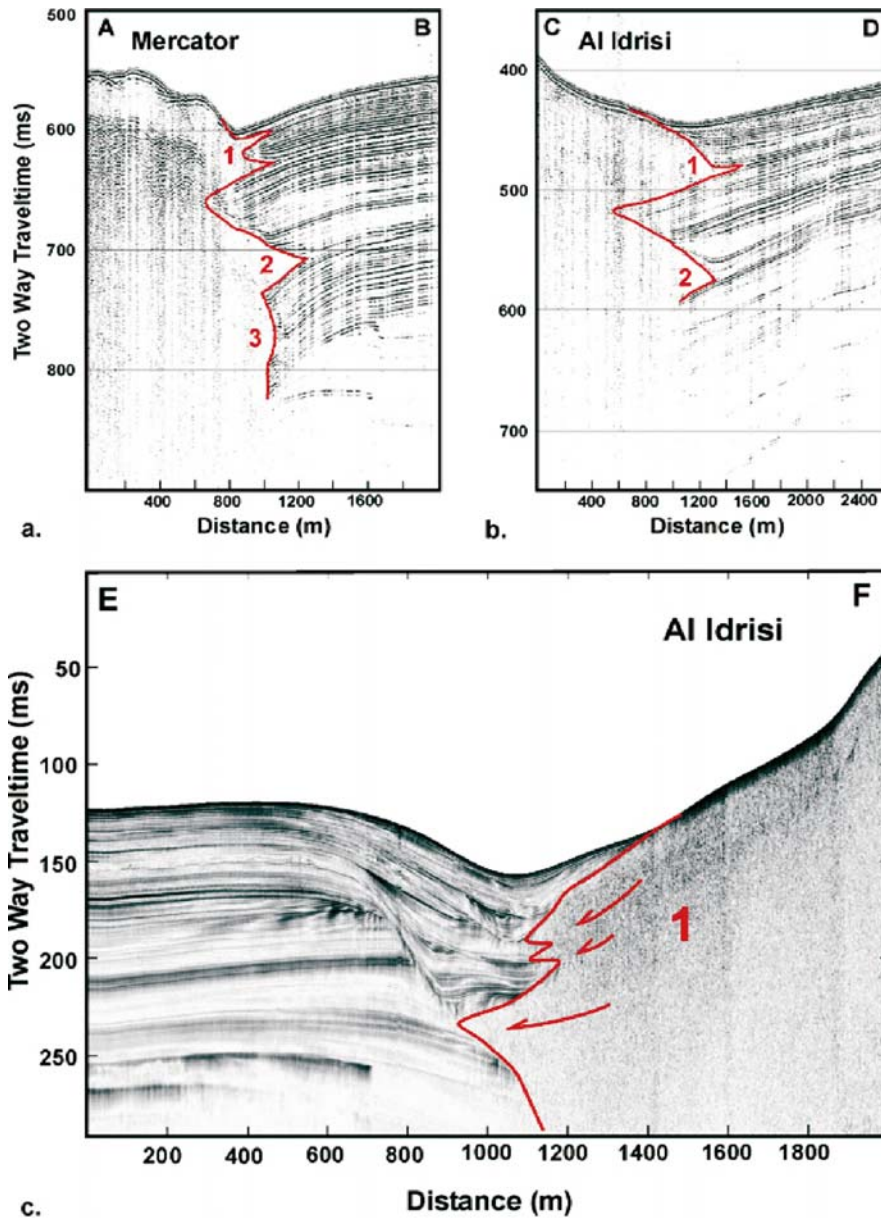


Image 5.3.5.1-2. Interfingering of the mud volcano outflows. High resolution seismic profile. The high resolution seismic sections show the buried mudflow lobes, interfingering with the sediments at the surrounding moat of the cones. They document at least three major eruption stages within the top 200 m of the embedding sediments. The seismic data reveal the fine structure of the sedimentary setting of the Al Idrisi mud volcano.

Project: CADIPOR 2002

Research vessel: *Belgica*, Belgium

Deep-tow seismic profiler. *Ifremer* chirp seismic source; mid frequency: 1200 Hz, frequency band: 650–2000 Hz

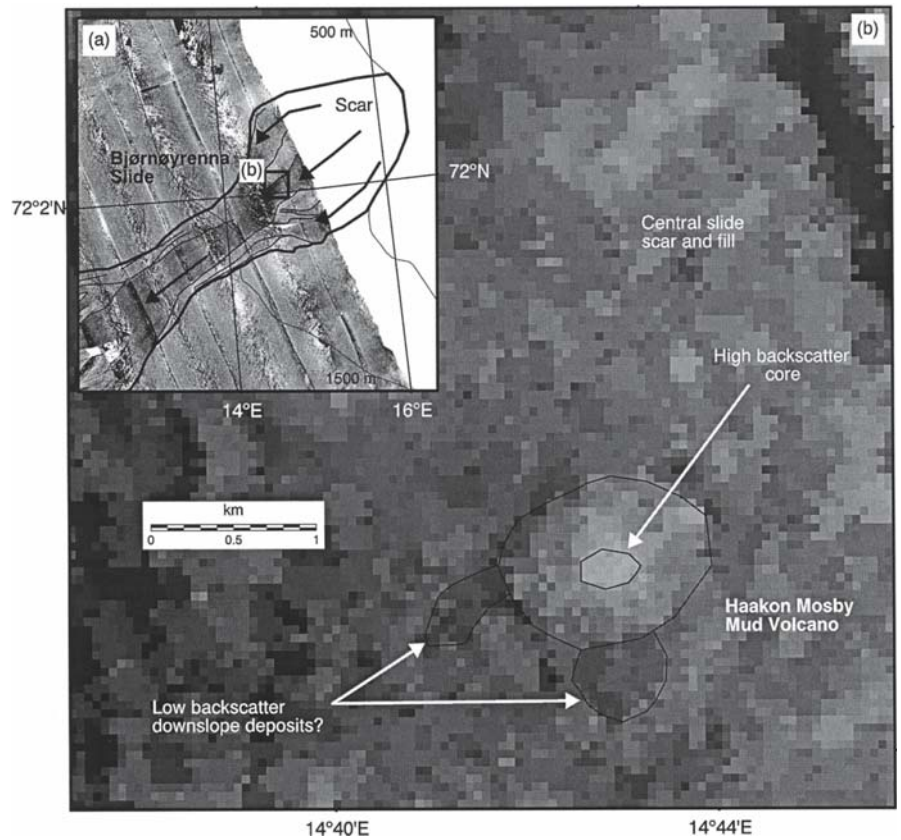
Depth resolution: 1–2 m. Sediment penetration at site: 200 m

Image ©: Jean-Pierre Henriët, Renard Centre of Marine Geology, Ghent University, Belgium and Bruno Marsset, IFREMER ■

Image 5.3.5.1-3.

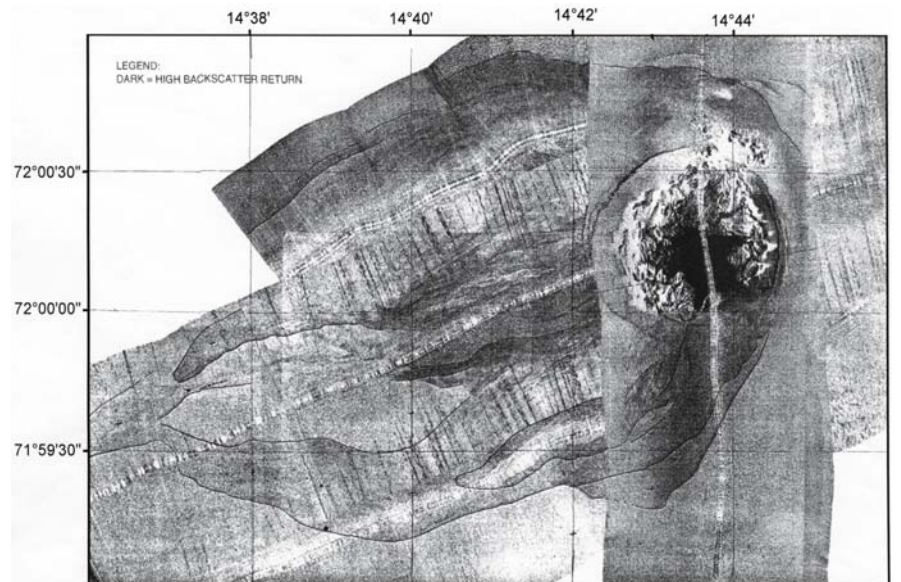
The Håkon Mosby Mud Volcano (HMMV). Low resolution sidescan images of the morphology. The image on top is made with the classical wide range Gloria system of 6.4 kHz, towed at the sea surface. The structure resolution or pixel size is about 80 m (main image) at a swath width of 46 km on each side (insert overview).

Project: Large scale sedimentation on the glacier-influenced Polar North Atlantic margins, 1996.
Barents Sea continental margin.
Water depth: 1 250 m
Research vessel:
RRS James Clark Ross
Longe range sidescan sonar:
Gloria; frequency 6.4 kHz
Image ©: Jürgen Mienert, Department of Geology, University of Tromsø, Norway ■

**Image 5.3.5.1-3a.**

The Håkon Mosby Mud Volcano HMMV. Mid range sidescan image. The image below was recorded by a 30-kHz sidescan system type ORE with 900 m swath width, towed 40 m above the sea floor. The horizontal resolution is several meters depending upon the height above the seabed. The structure of the central part of HMMV is clearly recognizable. A separate run on top of HMMV is mounted into the image of the environment with two outflow tongues.

Image documentation: same as for Image 5.3.5.1-3, except the 30-kHz sidescan system
Image ©: Jürgen Mienert, Department of Geology, University of Tromsø, Norway ■



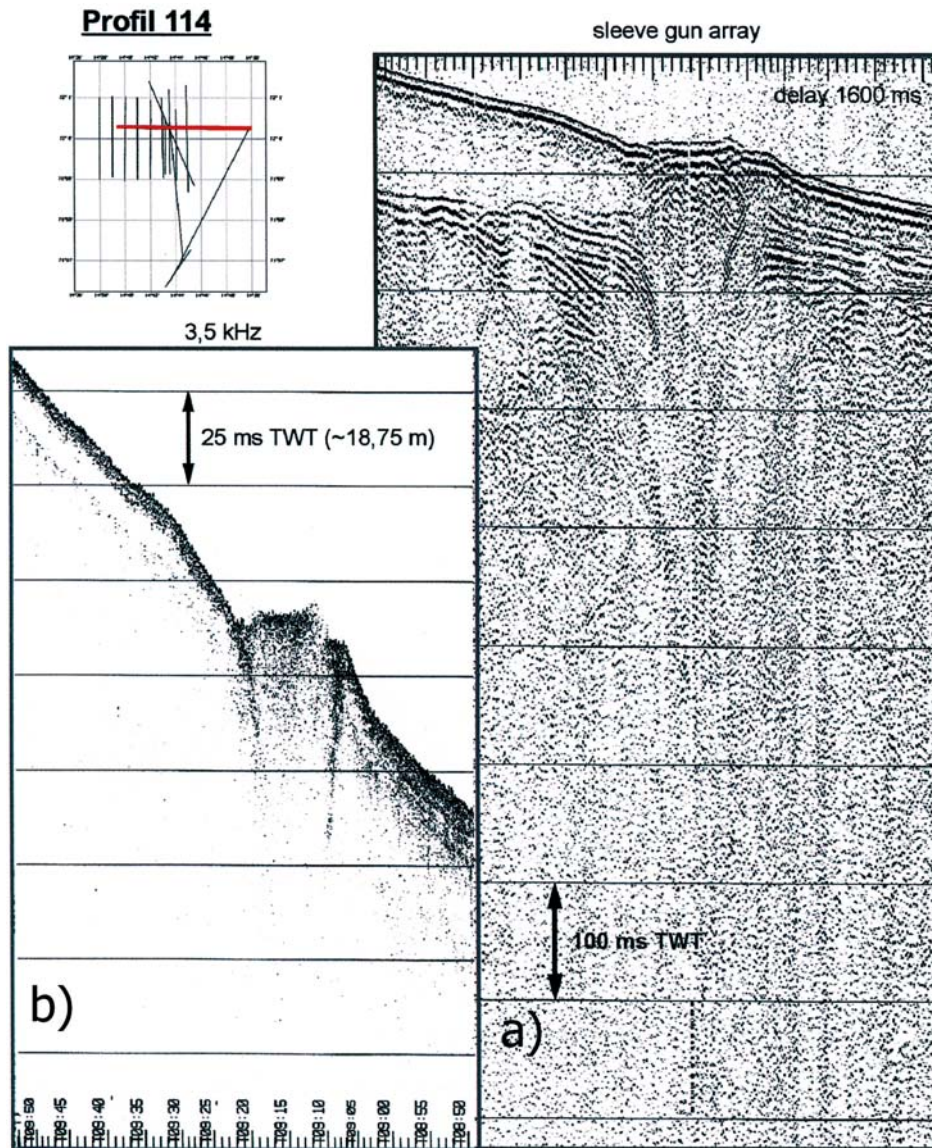


Image 5.3.5.1-4. The Håkon Mosby Mud Volcano HMMV. High resolution seismic profile. The sediment echosounder of 3.5 kHz was steered across the center of HMMV, showing the bottleneck-like inner flanks of the mud volcano down to about 40 m and the rough surface morphology of the crater (left). The seismic profile on the right reveals the plume like structure in the topmost 200 m of the sub-sea floor.

Project: Large scale sedimentation on the glacier-influenced Polar North Atlantic margins, 1996; Barents Sea continental margin. Water depth: 1 250 m
 Research vessel: *RV Jan Mayen*
 Echosounder: Simrad, type: Geopulse 5430A; depth resolution: 0.10 m
 Seismic profiler: Sleeve gun; frequency range: 30–450 Hz; depth resolution: 4 m
 Image ©: Jürgen Mienert, Department of Geology, University of Tromsø, Norway ■

5.3.5.2 Diapirs

Large cavities in rock salt diapirs on land have been subject to comprehensive scientific investigations and also to major public interest in the last decades. Many salt diapirs, such as those in Germany and the Nether-

lands, are targeted as long-term repositories for disposal of high-level radioactive and chemical wastes. The *Gorleben* salt diapir in Germany is one of the most extensively investigated diapirs in the world. Due to the low permeability and high ductility of rock salt the cavities are considered safe against tension induced fissures and thus tectonically inactive.

Image 5.3.5.2-1.

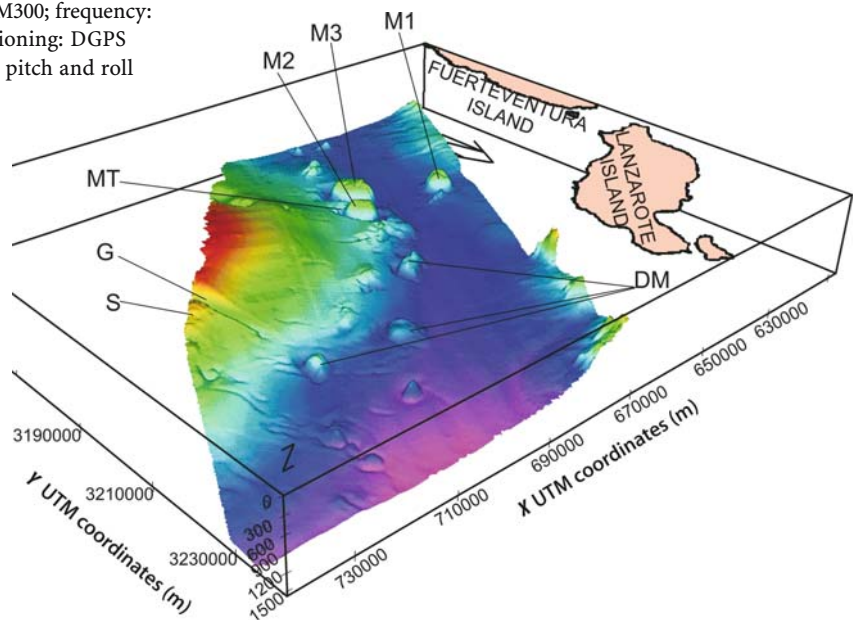
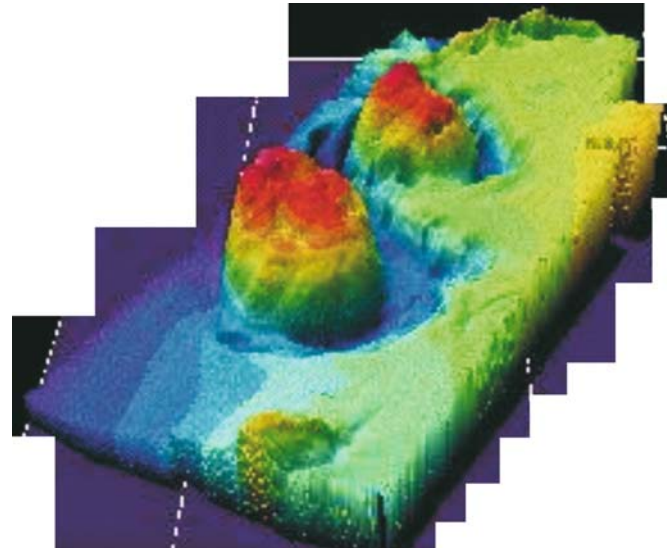
Canary Islands diapirs sea floor outcrops. Multibeam image. In the *Canary Channel* between *Fuerteventura-Lanzarote* and *Africa* a particular local crop out of non-magmatic material on the sea floor was recently discovered by multibeam echosounding. The feature is of conical shape with a typical diameter of thousand meters and a height of hundred meters in this area. The objects are looking similar to the stumps of broken columns but with surrounding circular furrows due to current induced erosion at an object with steep flanks. Such formations are being attributed to intrusive, plastic bodies that may well up through faults under pressure and heat and pierce through the sediment strata above. In this case it is assumed that the material is a kind of salt and gypsum which is known to produce such *evaporitic diapirs*. The limited image resolution is due to the water depth of more than thousand meters.

Project: Spanish Exclusive Economic Zone; years of survey: 2001 and 2002

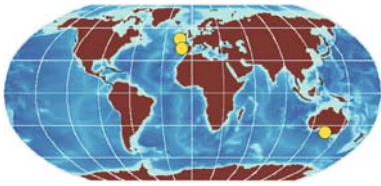
Research vessel: *RV Vizconde de Eza*, SGPM

Multibeam echosounder: Simrad, type: EM300; frequency: 30 kHz, beamwidth 1°, 135 beams, positioning: DGPS with IMU Seapath 200, active electronic pitch and roll compensation

Image ©: Juan Acosta Yepes, Geology and Geophysics Dept., Instituto Español de Oceanografía; Araceli Muñoz, EEZ, Scientific department, Madrid, Spain ■



5.3.6 Submarine Canyons, Channels



These submarine formations are or have been pathways of sediment transport similar to riverbeds on land. Though sediment flow or more correctly sedi-

ment suspension flow along a sloping bottom will erode strongest where already existing grooves focus the flow and increase the speed, thus causing stronger abrasion, very large canyon formations are rare. Glacial times with maximums of sediment flow are typical originators of larger canyon systems. Their shape with often steep flanks can look similar to tectonic faults however, which sometimes serve also as sediment transport routes (Sect. 5.2.9). Erosion and re-sedimentation which increases

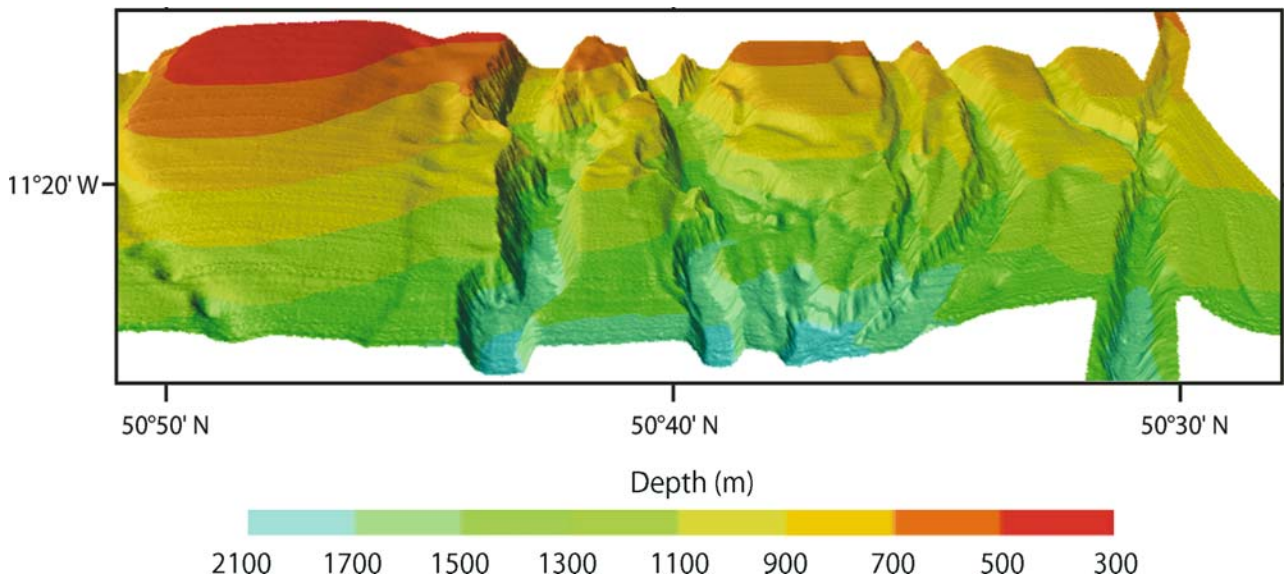


Image 5.3.6-1. Section of the *Gollum Channel System, Porcupine Bight*. Multibeam image. This channel system in the south of the eastern slope of the Porcupine Bight at a water depth of 1 000 m is one of only a few of its kind existing on the *West European Continental Margin*. The sea floor appears corrugated by deep furrows or canyons of 200 down to 400 m depth, building half a dozen slightly meandering and branching channels with steep flanks inclined up to 25°. The system was presumably formed during glacial stages but has been considered inactive for about 10 000 years. Nowadays the channels appear to serve only for sediment transport, driven by tidal currents. (Simulated flight see attached CD.)

The color coded depth scale shows an inclined plateau incised deeply by several channels which are reminiscent of canyons. The steep channel flanks are as obvious as the channel depths of more than half a kilometer. The remarkable phenomenon is the origin of an obviously flow induced canyon system, which was totally submerged from the beginning. A quasi separate flow below a water column of hundreds to thousands of meters along several hundred kilometers means that its effective density must have been significantly higher than that of sea water. Such high densities exist as sediment suspensions of corresponding concentrations. Submerged, channel like erosion is a frequent phenomenon also in other ocean areas.

Project: *Geomond of the European Union*, 2000

Research vessel: *RV Polarstern*, Germany

Multibeam system: ATLAS Elektronik Hydrosweep, DS2; frequency: 15.5 kHz; beamwidth: 2°, fanwidth: 90°, 59 beams

Slant view landscape depiction with artificial sunlight from north

Image ©: Andreas Beyer, AWI; ©: Springer-Verlag ■

the height of the walls as a *channel levee* process (Sect. 5.3.2.4) can occur on the same channel and at the same time. The few examples shown in this section are shelf break incisions which differ strongly

in their features corresponding to different origin. The images are also demonstrators of high resolution multibeam imaging as diagnostic tool of sea floor processes.

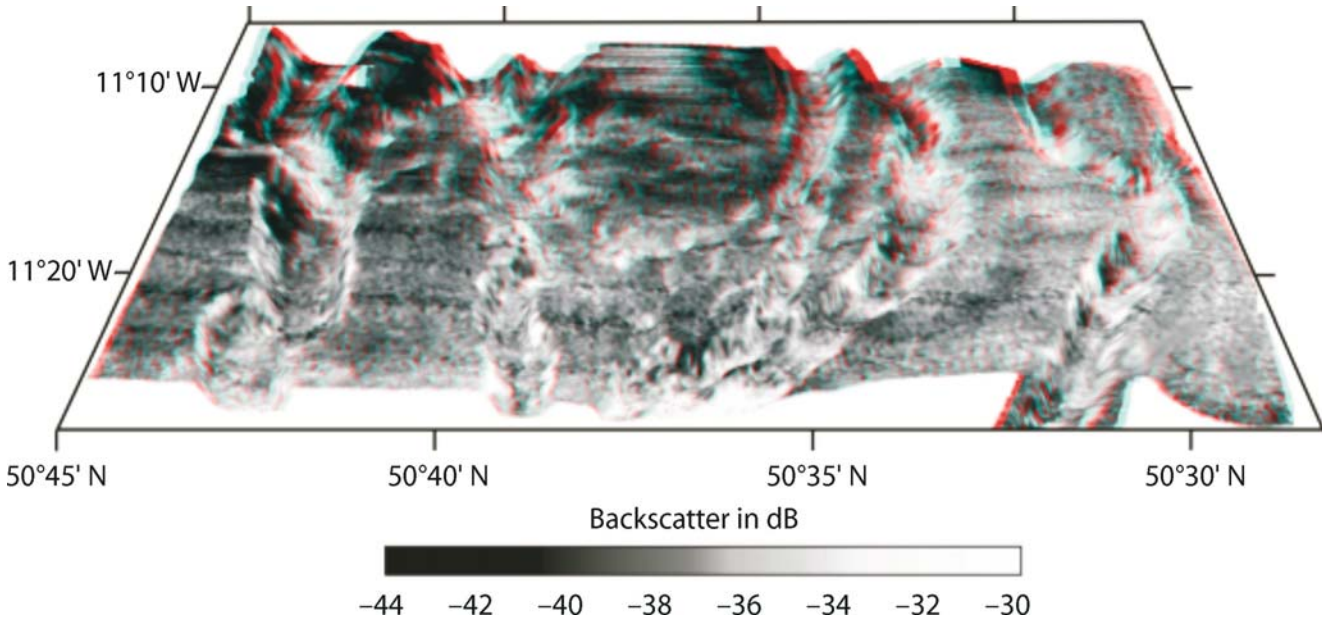


Image 5.3.6-2. Same section of the *Gollum Channel System*, but backscattering as anaglyphic red-green stereo version of a black and white depiction. Dealing with acoustic imagery, it may be interesting to note that traces of sediment motion in such canyons can be visualized by modified multibeam echo sounding. The flow enforced sediment transport separates the grain size along the curves of the channels with fine sand where the flow is slow. This indicator of flow drag forces is not recognizable in the bathymetric relief but can be visualized through the stronger backscattering intensity from the coarser material (Sect. 3.4.4). The anaglyphic red-green stereo version demonstrates the varying brightness of the backscatter, corresponding to the different sea floor material. It is an example of the add-on application of multibeam echosounders to provide bottom type information. This was usually considered the privilege, even the monopoly of the sidescan echosounder (Sect. 4.3), but the grazing incidence needed for this sounding principle is less practical when deeply corrugated structures have to be irradiated by sound without screening shadows.

The bottom of the left channel shows high backscatter in the foreground appearing lighter with alternating higher and lower backscattering towards the background, indicating more or less rough sections respectively of the floor surface. The channel flanks scattering strongly appears to be particularly rough or washed out. Accordingly, the dark plateau-like areas deeply incised by the canyon-like channels are presumably covered by fine grain or muddy sediments. The channel at 50°35' N with a pronounced curvature exhibits lower backscatter at the inner surface of the curve, and thus finer sediments than on the opposite side. The angular dependence of the backscatter has been corrected to achieve comparability of the sediment features.

Project: *Geomond of the European Union*, 2000

Research vessel: *RV Polarstern*, Germany

Multibeam system: ATLAS Elektronik Hydrosweep, DS2; frequency: 15.5 kHz; beamwidth: 2°, fanwidth: 90°, 59 beams

Evaluation of echointensity (red-green binoculars needed to visualize the 3D-depiction), direction of view: eastward

Image ©: Andreas Beyer, AWI, Bremerhaven, Germany ■

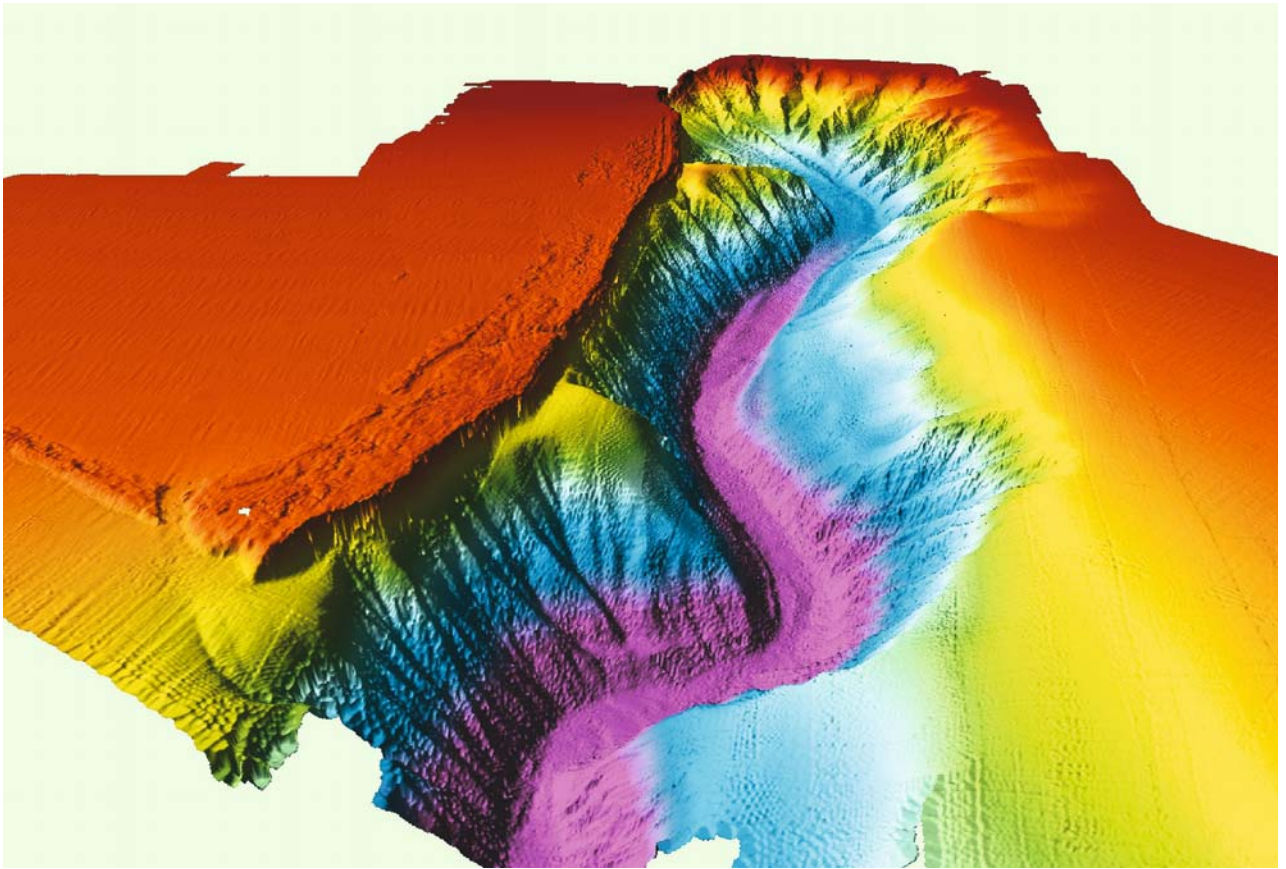


Image 5.3.6-3. Nazaré Canyon, north of Lisboa, Portugal. Multibeam image. This formation, deeply incised into the *Iberian shelf* 100 km north of Lisboa is the head of one of the largest canyons in the *Atlantic Ocean*. The multibeam survey of the Nazaré Canyon was made to obtain a detailed morphology of the canyon head covering the first 5 km down to a depth of 330 m. The Nazaré Canyon has a main axis and a number of tributary axes with very pronounced sand dunes like the *Canadian Gully* (Sect. 5.3.9), but with sheer walls of hard substrate. The area covered is approximately 15 square kilometers in size. The color code corresponds to the depth range from 0 m to 330 m with a grid resolution of 3 m, and is enlarged 3 times vertically.

The origin of Nazaré Canyon is essentially different from other major submarine canyons which are the result of erosion processes of glacial times of the Holocene such as the huge *Gully* at the Canadian *Nova Scotia* shelf break. The Nazaré Canyon which is associated with the activity of a tectonic fault structure was probably formed 5 million years ago during late Miocene to Pliocene times. The entire shelf break off the Iberian Peninsula is deeply fissured, in contrast to the corresponding areas of *Nova Scotia* and the Celtic Shelf southwest of England, both with abrupt shelf break contours without major furrows.

The tectonic fissure of the Nazaré Canyon extends from the beach down to the abyssal plane at 5 000 m depth at a distance of 150 km, thereby incising nearly 1 000 m deep into the continental slope. Similar to other submarine canyons the floor of the Nazaré is an effective transport path of sediment suspension. However, the transport is not simply continuous here: The ooze accumulates locally for a time but finally becomes unstable and is released as a sudden slide. This intermittent process of ooze accumulation and subsequent slide is periodic from decades to centuries, highlighted in seismic profiles not shown here.

Project: Morphodynamic study of Nazaré Canyon Head (SECNA); conducted by: Instituto Hidrográfico, Lisboa, Portugal, for SECNA, 2001

Survey vessel: launch *Coral* of 15 m

Multibeam system: SIMRAD, EM 950; frequency: 95 kHz; beamwidth: 3.3°, number of beams: 60, fan width: 130°

Image ©: Instituto Hidrográfico, Lisboa, Portugal ■

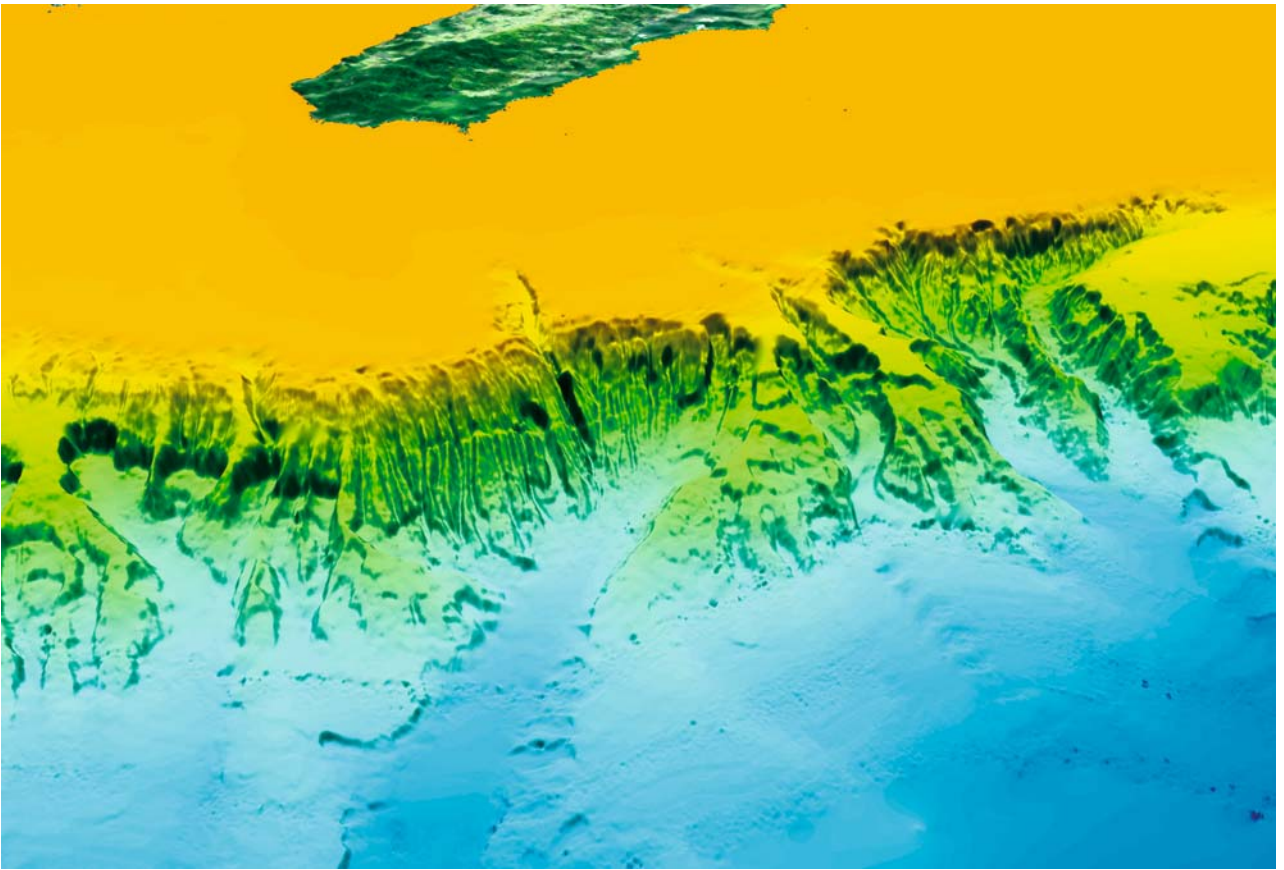


Image 5.3.6-4. Murray Canyons, South Australia. Multibeam image. The Murray submarine canyons are among the largest canyons worldwide, deeply incised into the broad *Australian Shelf* southwest of *Adelaide*. The abrupt but irregular shelf break and steep, corrugated slope shown in the relief image represents a segment of the Australian counterpart of the continental break-up contour of the Supercontinent *Gondwana* (Sect. 5.5.1) though strongly modified by later erosion. The last phase of this continental break up 70 million years ago divided *Antarctica* on its southern side from the Australian block that moved north by continental drift. The spectacular Murray Canyons are no relic scars indicating this continental break up but are incised by abrasive sediment flow down the shelf slope, typical of all submarine canyons. Here, the “feeder” of the Murray Canyons is the *Murray-Darling River*, exporting sediment from inland. Since the continental slope is a direct and steep connection to the abyssal plane of 4.5 km depth in this area, the floor of the deepest canyons is at about the same level – twice as deep as the Grand Canyon.

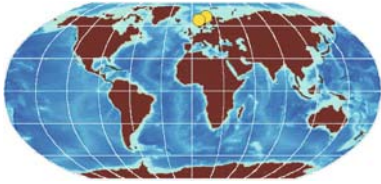
The Murray canyons are a further example of the diversity of canyon formations despite the similarity of erosional origin and beyond the difference of size. The image reveals that the original shelf break was far in front of most of the canyon incisions which have left only several tongues of shelf residues and broad valleys in between which cut through sediment coverage at the sea floor reminiscent of a river bed. Characteristic of this unusual formation are in fact the broad fronts of abrasion instead of the frequent branching of a main canyon combining several tributaries which add their separate sediment flow contribution finally to the mainstream. Here the wall of a canyon shows a peculiar structure of many parallel steep erosional furrows separated by individual sidewalls as if generated by sediment overflow known as *channel-levee effect* (Sect. 5.3.2.4). Further, the erosion relief varies strongly in character along the series of canyons with sudden deep breaks of single or groups of furrows. These are hints on an inhomogeneous shelf rather than on inflow variability.

Project: AUSTREA-1 multibeam survey; conducted by Geoscience Australia and commissioned by the National Oceans Office and Environment Australia

Multibeam system: Simrad EM12D; frequency: 11/12 kHz, fan width: 150°, 162 beams

Image ©: Fred Kroh, Geoscience Australia, Canberra ■

5.3.7 Norwegian Fjords



The extraordinarily long, steep, and rocky coast of Norway is famous for its beauty with its many deeply incised, multiple ramified bights, the fjords. The fjord formations, similar to the firths of Scotland are trough-like valleys eroded and deepened during glacial periods. Though they are partly filled with sediment most of them provide safe fairways even for deep draught ocean liners. The *Bjørnsundet* depicted as the multibeam Image 5.3.7-1 is one of the smaller, less typical fjord formations. It is

located west of *Molde* and south of *Kristiansund* where the irregular rock formation known from the emerged landscape in the west coast of Norway continues underwater. The seismic cross-section through the *Balsfjord* (Image 5.3.7-2) shows the internal structure of the sediment-fill with a non-horizontal surface.

Two typical examples of the submerged part of the steep flanked, narrow trough type of fjords are shown as multibeam images. The former is a section of the large *Hardangerfjord* (Image 5.3.7-3) of *Horlaland*, famous for its landscape; the latter is the smaller *Sandsfjord* (Image 5.3.7-4) of *Rogaland*, the southernmost part of Norway. Note that the 3D-relief of *Sandsfjord* is enhanced by only factor 1.5 and the *Hardangerfjord* relief is not enhanced at all. The purpose of these surveys was to map potential corridors for future power cables instead of large power lines over land.

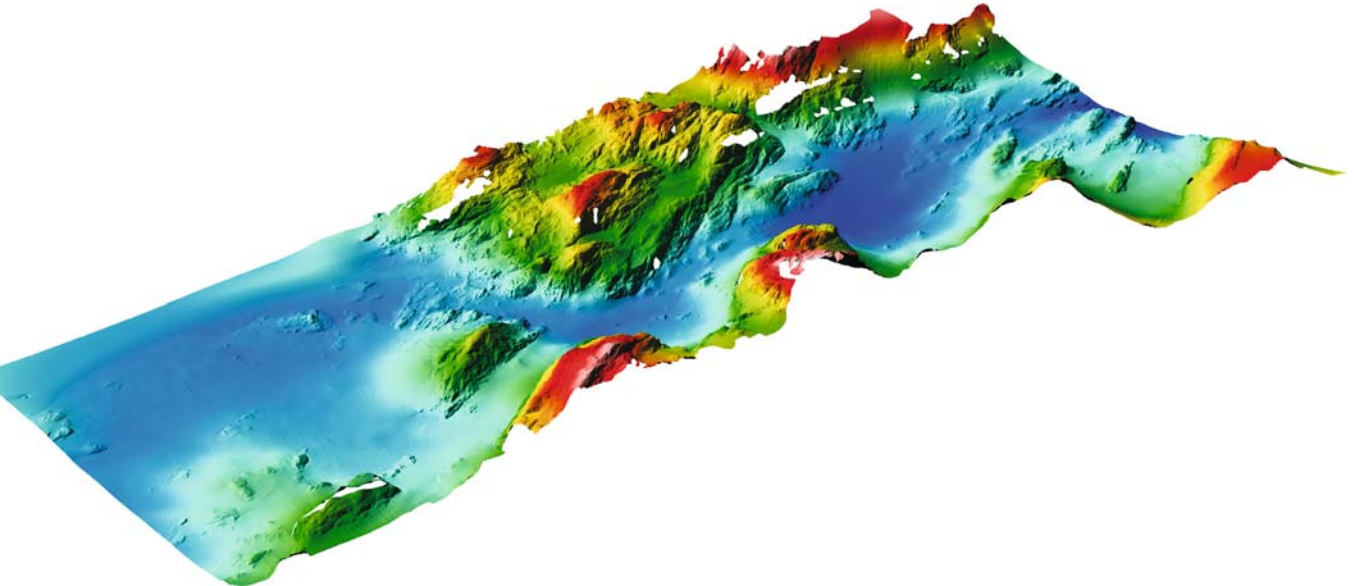


Image 5.3.7-1. Bjørnsundet Fjord. Multibeam image. The section shown is about 4.5 km². Instead of having a nearly plane sediment filled floor such as the *Balsfjord* or the *Oslo Fjord* (Sect. 7.1.4), the deeper areas down to 220 m, indicated blue, appear like smooth troughs with several rock formations standing out from the sediment cover. Obviously the customary imagination of a typical fjord as a sharply incised channel with nearly vertical flanks is oversimplified. The impression from the real high resolution image is more similar to an alpine landscape with an alluvial valley squeezed in between rocky mountains and then completely inundated. Nearly all of the bedrock structures show a seaward, ridged orientation and texture, presumably from glacial scars. Though the slopes of the rock flanks don't appear unfamiliar, they are depicted enhanced by a factor of three.

Project: Ormen Lange; year of survey: 2001

Survey vessel: Remotely operated vehicle (ROV)

Multibeam system: RESON 8125 Dual Head; frequency: 455 kHz, beamwidth: 1°/0.5°, number of beams: 480

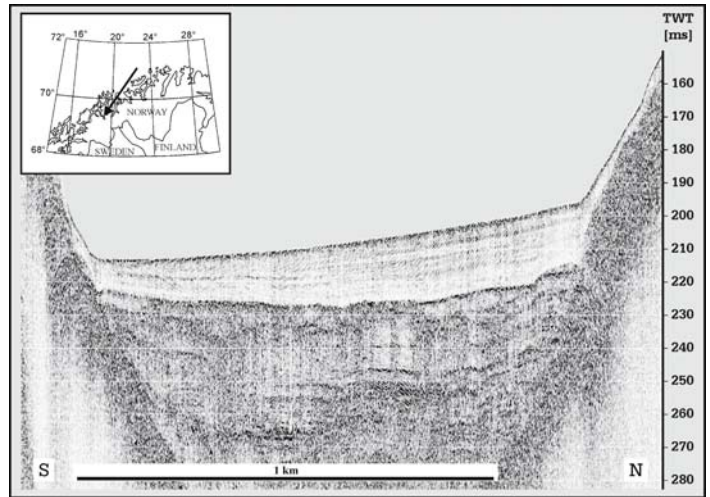
Color code: red 50 m; blue 220 m

Image ©: Egil Ingebretsen, Marine Surveys, Pipelines and Marine Operations, Norsk Hydro ASA, Norway ■

Image 5.3.7-2.

Balsfjorden close to Tromsø, northern Norway. High-resolution seismic profile across the fjord. The acoustic characters of the sediments in Balsfjorden allow a division into two units: one relatively transparent upper unit including some more or less continuous reflections, and one less transparent lower unit comprising irregular reflections. The semi-transparent character and stratification of the lower unit indicate frequent changes of the sediment composition during the deposition. The more transparent character and weak stratification of the upper unit indicate more constant sediment composition.

Based on comparison of the high-resolution seismic data with sediment cores, it is inferred that the less transparent lower part of the profile reflects both glacial marine sediments and gravity-flow deposits. The more transparent character of the upper unit is the result of continuous postglacial sedimentation. The upper unit has an asymmetric shape, thinning from north to south. This is the result of the deflecting *Coriolis force* from the rotating Earth on the bottom current, causing an unsymmetrical sediment transport under enforcing conditions of the local fjord relief geometry.



Project: SPINOF (Sedimentary Processes and Paleoenvironment in Northern Fjords); year of survey: 1998

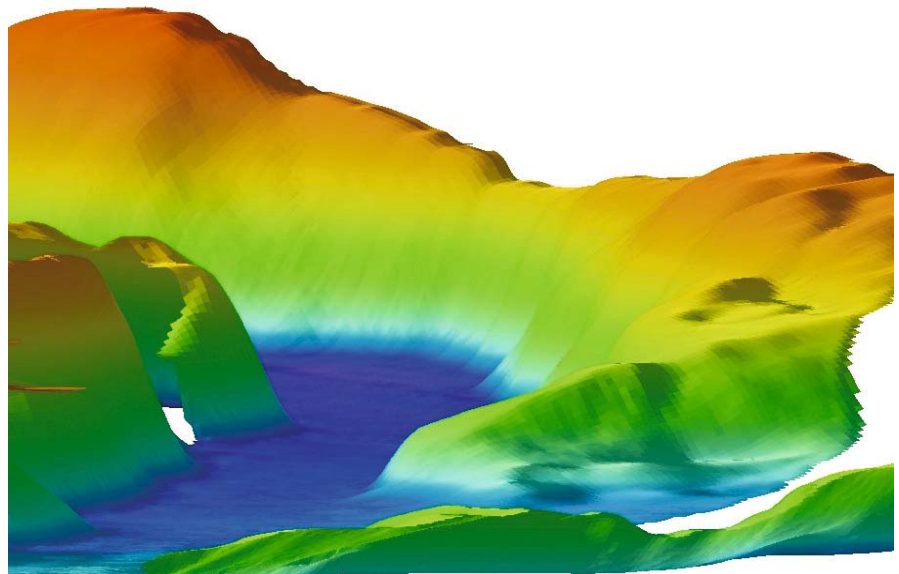
Survey vessel: *RV Jan Mayen*

Seismic profiler: Geoaoustic/Ferranti O.R.E. hull mounted 3.5 kHz sediment penetration echosounder; frequency regime: 3.5 kHz, towed depth: 6 m; Vertical enhancement factor: 8, depth scale: two-way travel time (TWT) ca. 160 m maximum water depth

Image ©: Tore O. Vorren & Matthias Forwick, Dpt. of Geology, University of Tromsø, Norway ■

Image 5.3.7-3.

Hardanger Fjord, Hordaland. Multi-beam image. Such extremely steep slopes of the sea floor of up to 70 degrees and more are rare elsewhere but a typical peculiarity of Norwegian fjords. The color code of the Hardanger Fjord in the neighborhood of the city of *Bergen* ranges from 20 m (brown) to 600 m (dark blue/violet). The sediment fill as the deepest plain which is about 300 m wide slopes only slightly and reveals a sidearm to the right. The flank in the background shows weak vertical furrows from sediment flow. The wide-angle multibeam track has scanned the trough in two to three runs. The image resolution of 10×10 -m grid of the *digital terrain model (DTM)* is evident from the pixel squares visible on the shaded left flank. White spots are data gaps.



Project: Mapping potential corridors for future power cables; year of survey: 1998

Survey vessel: *MV Geo Scanner*; Multibeam system: Simrad Em1000; frequency: 95 kHz, beamwidth: $2.3 \times 3.3^\circ$, 48 beams

No vertical exaggeration; perspective depiction with simulated sunlight and shade

Image ©: Fugro Survey AS, Norway ■

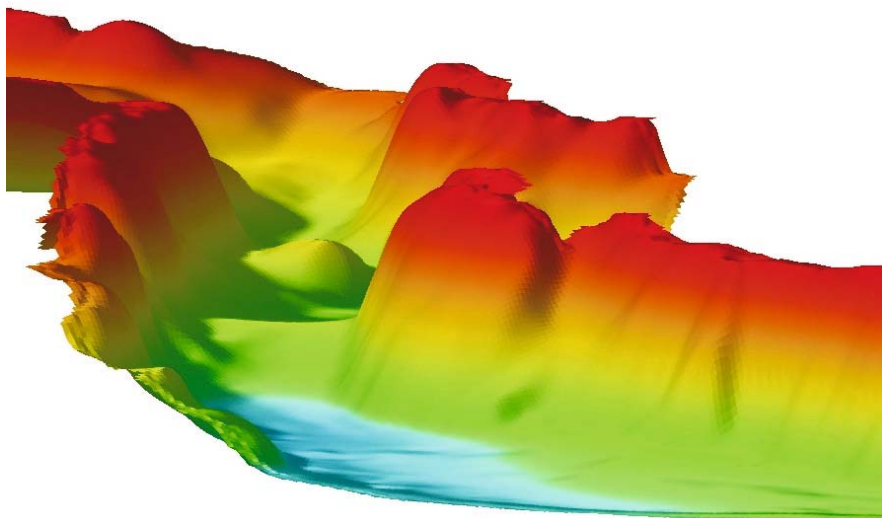


Image 5.3.7-4. Sandsfjorden, Rogaland. Multibeam image. The fjord section shown is the narrowest passage of the Sandsfjorden which itself falls into the huge Boknafjorden near Stavanger and branches off into the Hylsfjorden in the northeast. The depths depicted range from 30 m (dark red) to 400 m (light blue). The S-curved section of the trough ground with ridges, mounds and steeper slope differs strongly from the plain sediment fill of the Hardanger Fjord section show before. The smooth, more plain bottom type is developed only in the foreground of the Sandsfjorden section and is about 150 m wide. Another conspicuous feature is the onset of a terrace-like flattening off on the upper part of the flanks (coded red) which are still 30 m below sea level and appear to be furrowed, reminiscent of sediment flow tributaries. This flattening off below the water line is nearly as evident in the Hardanger Fjord image. The Sandsfjorden survey was difficult due to the narrow and deep profile with thresholds resulting in steep slopes and abrupt variations of water depth. The survey had also to cope with trawling activities in these fjords.

Project: Mapping potential corridors for future power cables; year of survey: 2000

Survey vessel: *MV Geo Scanner*

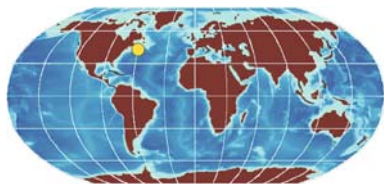
Multibeam system: Simrad Em1002; frequency: 98 kHz, beamwidth: 2°, 111 beams

Vertical exaggeration factor: 1.5, perspective depiction with simulated sunlight and shade, pixel size/digital terrain model: 5 × 5-m grid. The fjord was scanned by two overlapping runs

Image ©: Fugro Survey AS, Norway ■

5.3.8

5.3.8 Bedrock Structures



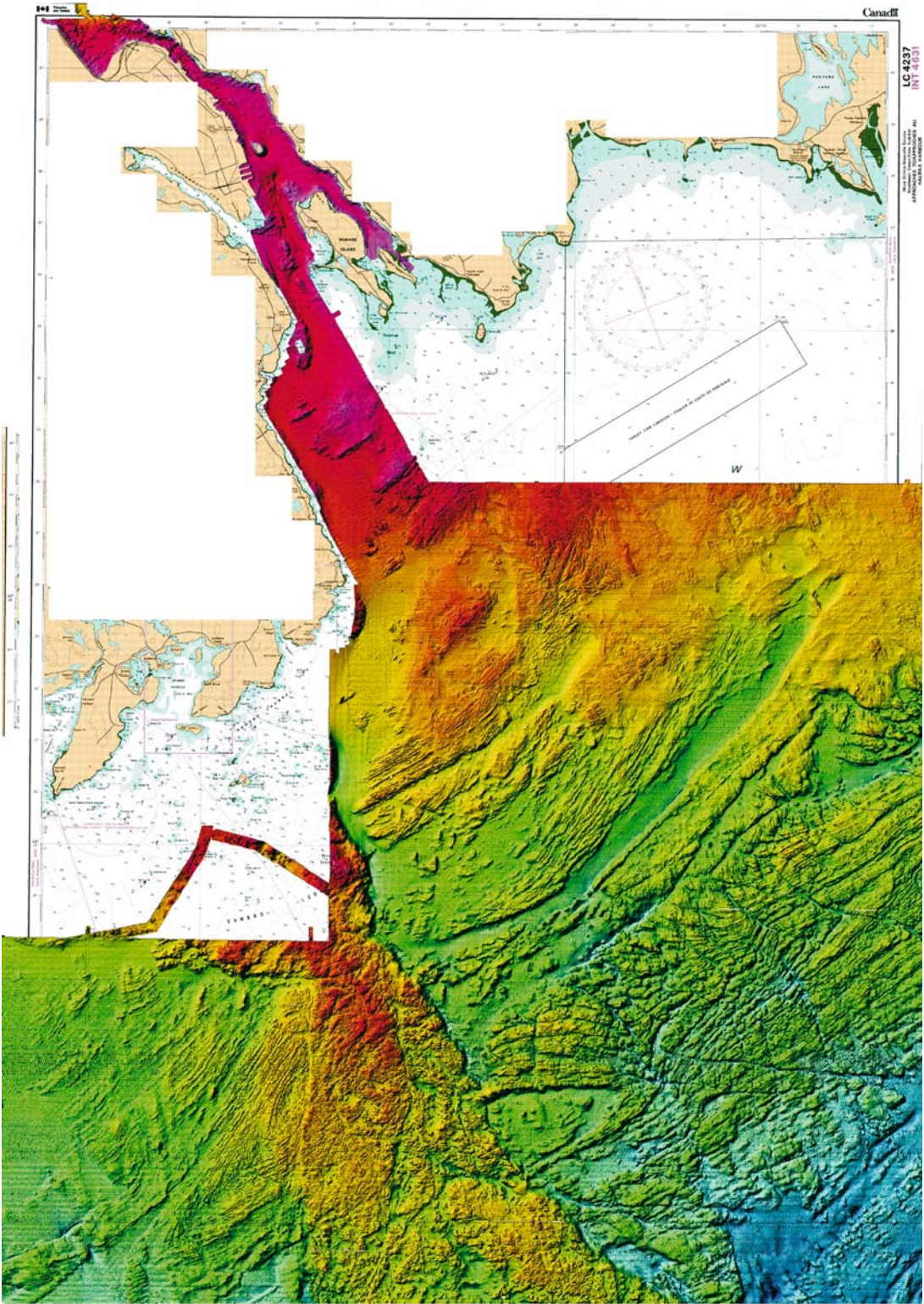
Sound images of exposed bedrock, nearly uncovered by sediment shown in this book were taken at three places: the Salcombe area of southern England, the southern coast of Sweden in the Baltic Sea and the inner Scotian Shelf off Halifax, Canada. Whilst the former two examples are shown in other contexts (Sect. 7.3.2, 5.7.5), the section of the inner Scotian Shelf is presented here as an exceptional area: it is the only site of the Paleozoic Cambrian-Devonian period on the eastern side of the North

American Continent north of 40° latitude whereby the Canadian geologic inventory reaches up to 85° N. It is presumably the oldest shelf area shown in the book visualized by sound imaging.

Image 5.3.8-1. ►

Halifax Harbor and the adjacent inner Scotian Shelf. Multibeam sound image. The systematic high resolution sea floor study of the continental margins of Canada is being conducted by the Geological Survey of Canada (Atlantic), Bedford Institute of Oceanography and the Canadian Hydrographic Service. The detailed 3D-imagery is part of the inventory work to be applied under the Oceans Act which became law in 1997 and includes a national system of marine protected areas.

Halifax, the capital of Nova Scotia, Canada has one of the largest and deepest natural harbors in the world with a minimum depth of 18 m and is 28 km in length. The outer harbor ►



5.3.9

is connected by a narrow channel, the *Narrows* with a huge inner harbor area, the *Bedford Basin*. The absence of ice leaves the harbor accessible year round. The Port of Halifax is the first inbound port and the last outbound port on the North American continent enabling the shortest ocean voyage for ships operating on the North Atlantic.

The multibeam relief image shows the direct harbor access from the sea and the adjacent inner *Scotian Shelf* with depths from 10 m to 200 m. The simulated sun illumination comes from north-west at an elevation of 45 degrees. The most conspicuous sea floor structure consists of outcropping bedrock. Apart from the fact that exposed bedrock is rare elsewhere on the continental shelf, this particular, very old bedrock of the Paleozoic *Cambrian-Devonian* period is found only as the seaward “front garden” of Nova Scotia, the inner Scotian Shelf, and nowhere else on the entire *continental margin of Eastern Canada*. In *geologic time scales*, a nearly recent, prominent low sea level stand near the end of the last glacial period about 10 000 years ago occurred at a depth of approximately 70 m on this inner shelf.

Above this depth the seabed was transgressed and eroded during the post glacial period, the Holocene, about 11 000 years ago to the present. Glacial imprints cover the whole inner shelf area, even the bottom of the harbor. On the left side of the image are a series of prominent ridges interpreted as ice retreat small moraines. The missing or widely interrupted sediment cover of the bedrock is evidence of a lack of glacial deposition, high energy transgression conditions, and strong currents and waves on this inner Scotian Shelf area. The formations and erosional features down to the small scale of meters shown could only be documented by means of multibeam imaging technology.

In contrast to the fundamental reshaping of natural origin during a long period of time a major man-made impact shall be mentioned: The ill-famed Halifax Explosion of 1917 occurred in the Narrows when two wartime vessels laded with explosives collided. One of the vessels, the *Mont Blanc* had a TNT equivalent of nearly 3 000 tons on board. The ensuing disaster was the largest man-made explosion prior to the atomic bomb. 2 000 people died. Despite the huge charge released there is no crater in the high resolution image visible though the *Mont Blanc* was grounded at the time on thin till over bedrock.

Project: Geological Survey of Canada and Canadian Hydrographic Service mapping programs; years of survey: 1991 to 1996

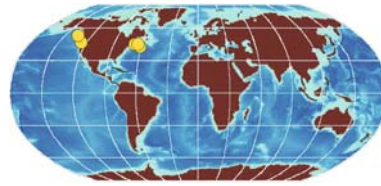
Survey vessel: *C.C.G.S. Matthew, F.G. Creed* (SWATH vessel; small water area twin hull)

Multibeam system: Simrad, type: EM1000, EM 100; frequency: 95 kHz, beamwidth: 2.3°, fan width: 120°

Resolution: 10-m grid

The image is a cut out of a large format poster with the frame latitudes 44°16'–41' N and longitudes 63°17'–39' W
Image ©: Gordon Fader, Geological Survey of Canada (Atlantic), Bedford Institute of Oceanography, Canada ■

5.3.9 Canadian Formations



This section is part of the series which combine various formations of the same continental or regional relationship.

To apply the uniting bracket of formations similar in kind but various geographical relationship instead does not appear appropriate here. Canada with its huge north-eastern shelf and complex coastal areas on both the *Atlantic* and *Pacific* side (Sect. 5.1.1.5) represents also a marine world of its own. The few examples presented can be only a tiny cut out of the vast variety of formations and specific features of the waters of Canada, a country much larger in size and non less manifold in its sea floors than the European continent.

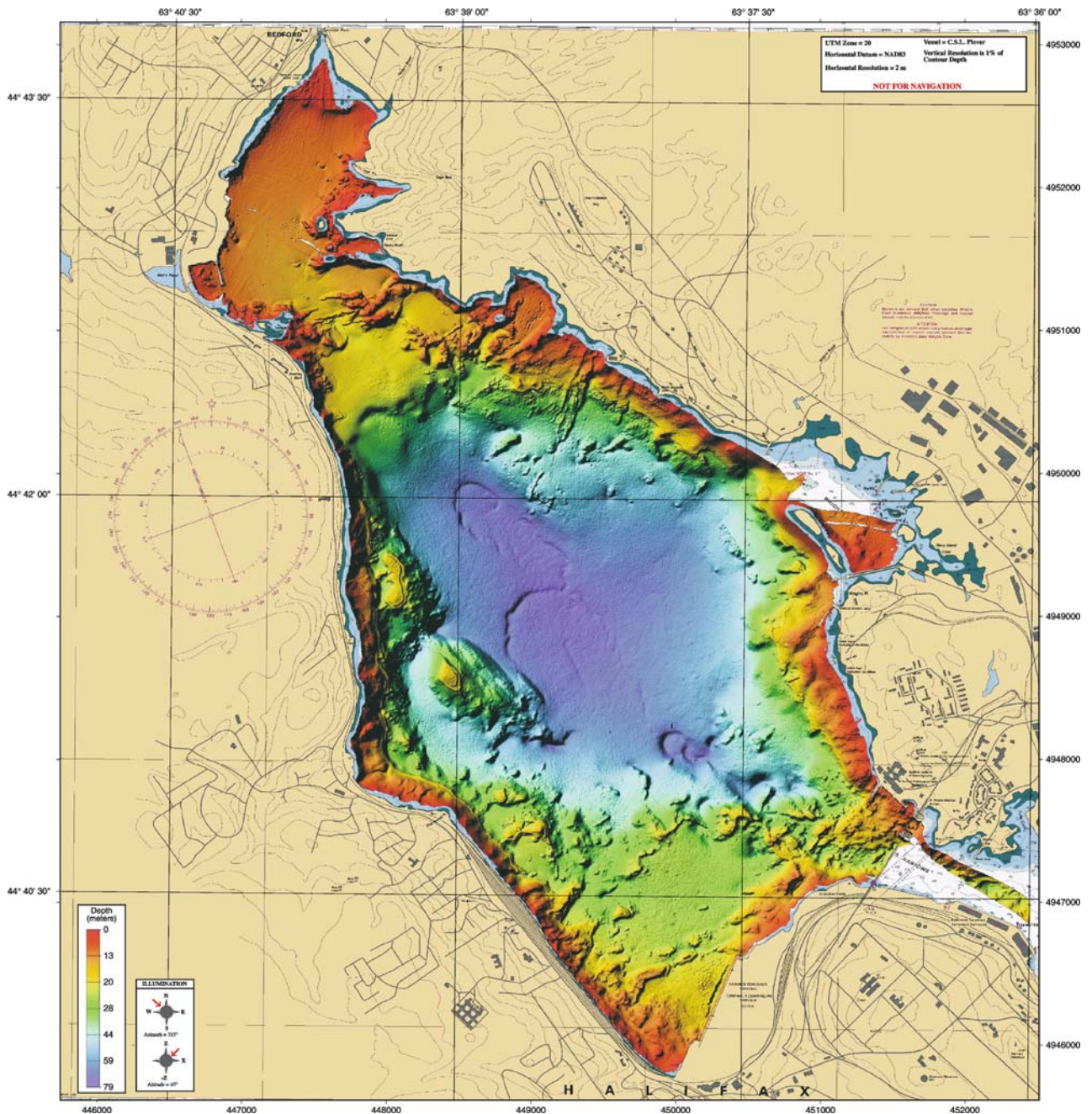
The selection concentrates mainly on the *Scotian Shelf* which has been subject of extensive research and geologic inventory during the last years. This is mentioned in the context of the separate section on a rare bedrock formation of the inner shelf off *Halifax* (Sect. 5.3.8). Several formations located on the Pacific side of Canada are also shown but these don't deal with tectonic margin features but with coastal peculiarities.

5.3.9.1 Scotian Shelf, Canada

Image 5.3.9.1-1. ►

Bedford Basin. Multibeam sound image. Bedford Basin at the head of *Halifax Harbor* is a heritage from glacial times. The “big hole” is an over-deepened glacial depression that was occupied by a lake until the marine transgression approximately 6 000 years ago. The bowl-shaped Bedford Basin, with a maximum depth of 71 m, is largely mud-covered in areas deeper than 20 m. Much of this clayey silt sediment is charged with biogenic methane gas from an abundance of organic material. Three large horseshoe-shaped, 1–3 m depressions are interpreted as subsidence features from methane release. Shallow areas of the basin consist of gravel with boulders and a few sites of outcropping bedrock. Two boulder berms ring the Basin at a depth of 23 m. They were formed when the basin was a lake. The berms define a suite of former islands on the west side of the Basin.

The anthropogenic imprint of Bedford Basin is pervasive. In parts, the basin floor is covered with much debris. There are about 10 shipwrecks, 22 automobiles, dredge spoils, airplanes,



and anchor marks on the seabed of Bedford Basin. The various kinds of misuse and contamination of sediments here and elsewhere brought to light – as it were – also by sound imaging, has sharpened the awareness of their impact on ecosystems and has led for Canada to the *Oceans Act* of 1997.

Project: Geological Survey of Canada and Canadian Hydrographic Service mapping programs; years of survey:

1996, 1997 and 1998

Survey vessel: *hydrographic survey launch*

Multibeam System: Simrad, type: EM 3000; frequency: 95 kHz, beamwidth: 2.3°; fan width: 120°

Resolution: 1-m grid

Image ©: Gordon Fader, Geological Survey of Canada (Atlantic), Bedford Institute of Oceanography, Canada ■

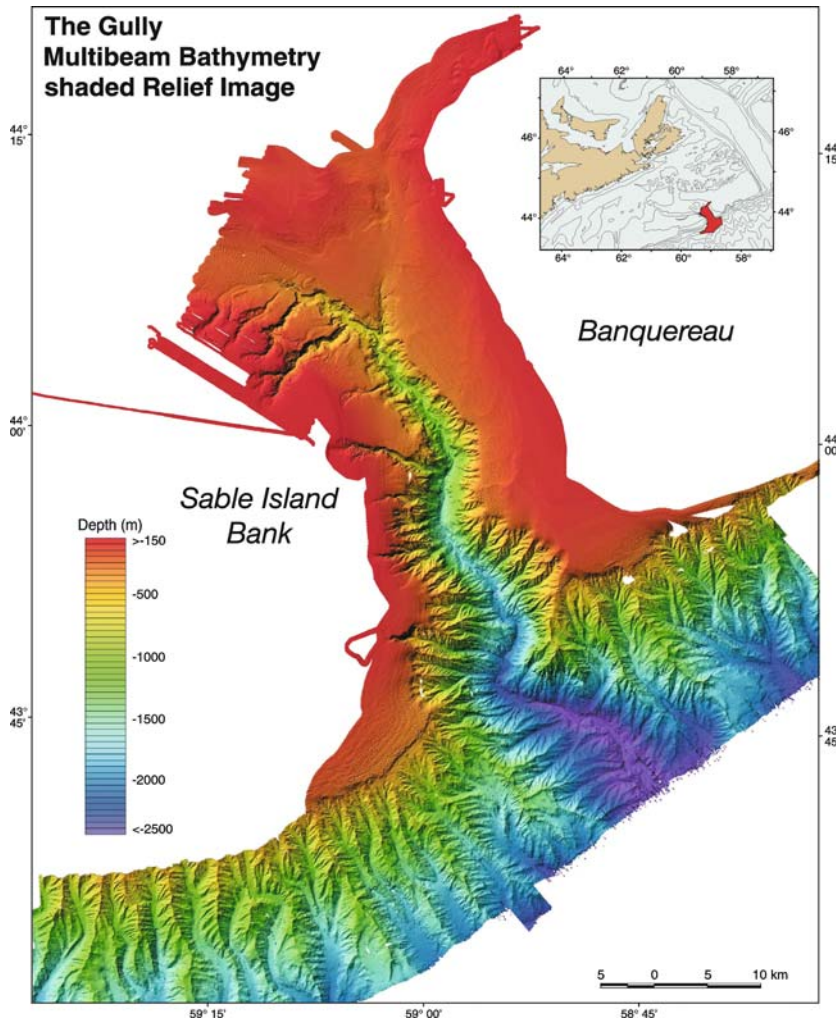


Image 5.3.9.1-2. The Gully. Multibeam sound image. A conspicuous, fascinating formation with the prosaic name *The Gully* is the largest submarine canyon along the eastern margin of Canada. Deeply incised into the edge of the Scotian Shelf off Nova Scotia, the Gully ranges to over 3 000 m in depth. This canyon system will be the first Canadian east coast offshore *Marine Protected Area (MPA)* in the framework of the *Ocean Act* of 1997. A pilot project for the eastern Scotian Shelf is a first step toward a comprehensive process for the integrated management of activities affecting estuarine, coastal and marine waters.

The Gully is interpreted to have started as a Tertiary age fluvial system that extended across the Scotian Shelf when the sea level was lower. It has later been modified by glaciation many times during the Pleistocene and there is evidence in the Gully of grounded glaciers at depths between 800 and 1 000 m. The Gully contains rare species of cold deep water corals and is the home of endangered bottlenose whales. Internally, it contains areas of slumping, gas escape pockmarks, moraines, sand wave fields, Tertiary bedrock outcrop and iceberg pits and furrows. The image which is artificially shaded from the northwest shows the entire canyon system. Unlike canyons of other shelf breaks, the Gully has a series of smaller feeder canyons reminiscent of a fir branch. The image resolution has been processed at a standard 10-m grid. The actual resolution of the deepest part of the Gully corresponds to other deep water imagery of several 10 m pixel size.

Project: Geological Survey of Canada, Canadian Hydrographic Service, petroleum industry east coast Canada: 1995–2000
Survey vessel: *F.G. Creed*, industry survey vessel

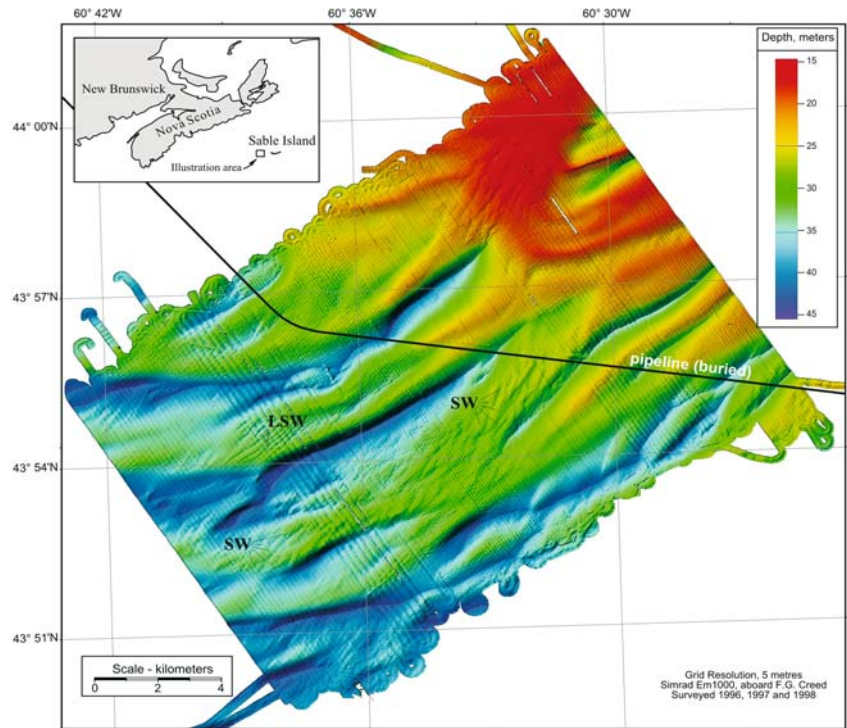
Multibeam System: Simrad, type: EM 1000, EM1002; frequency: 95 kHz, beamwidth: 2.3°, fan width: 120°

Image ©: Gordon Fader, Geological Survey of Canada (Atlantic), Bedford Institute of Oceanography, Canada ■

Image 5.3.9.1-3.

Sand ridges off Sable Island. The island, inhabited mainly by breeding seals and wild ponies is an isolated formation on the Canadian continental shelf close to its edge, 170 km off the coast of Nova Scotia and nearly 300 km east of Halifax. Sable Island, 40 km long and only 1.6 km wide is the exposed part of a sand shoal that stretches northeast-southwest for more than 100 km, infamous in past centuries as a hazard to navigation and known as the “graveyard of the Atlantic” having been the scene of many ship wrecks.

Today the area is of major interest because of its unique ecosystem and rich deposits of oil and natural gas, the origins of which reach back to the Jurassic at the opening of the Atlantic Ocean. Sediment accumulation abundant in organic matter created suitable conditions for the generation and preservation of hydrocarbon deposits. In the Sable area buried woody material is considered the principal source of organic matter. The pipeline route inserted into the 3D-map of the multibeam



bathymetry survey has been realized since and is part of the *Sable Offshore Energy Project (SOEP)*. The main deposits consist of six gas fields which are estimated to contain about 85 billion m³ of recoverable gas reserves. The SOEP is projected to last until the year 2025. The *Geological Survey of Canada Atlantic (GSCA)* conducts and supports exploration- and mapping programs for offshore geology of the Canadian continental margin. These long term scientific activities serve economic purposes as well. Multibeam high resolution bathymetry effectively quantifies the shelf morphology of various scales and enables guided geophysical surveys and in situ measurements of sediment dynamics with seabed instrumentations.

The conspicuous sand ridges of the relief section shown stem from an earlier phase of geological development and thus may be relic forms of the time when the sea level was about 15 or 20 m lower than present with presumably very dynamic reshaping of the sea floor. Since then the dominating ridge forms have undergone only minor modification such as the superimposed ripple- and dune bedforms indicated as sand waves SW and the more regular linear sand waves LSW, respectively. Repetitive surveys demonstrated little net migration of the sand ridges over 4–5 year time span. As transgression progressed, the forms extended along with Sable Island coast migration, more or less *parallel* to the existing crest axis. Much of sediment transport appears to propagate along the troughs. Thus at least some of the ridges appear to be erosional remnants. However, there is also some transport across the ridges, evident from a coarse to finer grain sand transition from the stoss (NW) to the lee (SE) side.

Altogether, the relief with its maximum slopes of less than 2% is not simply the rail system of sediment migration. Heavy storm induced sea waves and currents govern the transport and its direction temporarily though without much impact on the gross ridge pattern. This is advantageous for pipeline burial: a few meters of jetting plough depth provides sufficient protection against erosion which would otherwise cause the feared free span (Sect. 7.2.2). Moreover, the rather benign relief permits pipe routing which generally follows the ridge profile. These Canadian offshore conditions of gas and oil exploitation do not present the extreme engineering challenges of, for example the deep water gas fields in the Norwegian Storegga-Slide area with its highly irregular sea floor (Sect. 7.4.2). These conditions required deep diving AUV operations to achieve a similar mapping resolution as of this shallow water example. Similar hurdles will soon be met on the canyonized Canadian continental slope to exploit the hydrocarbon finds of these areas.

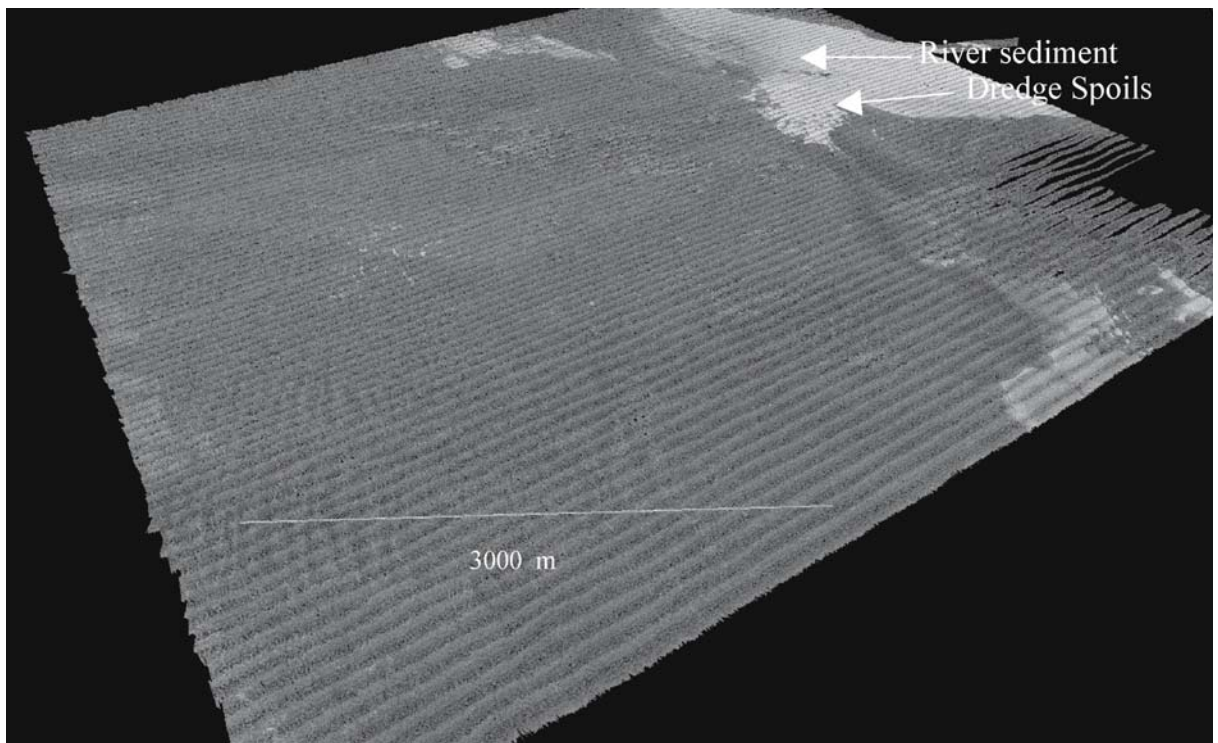
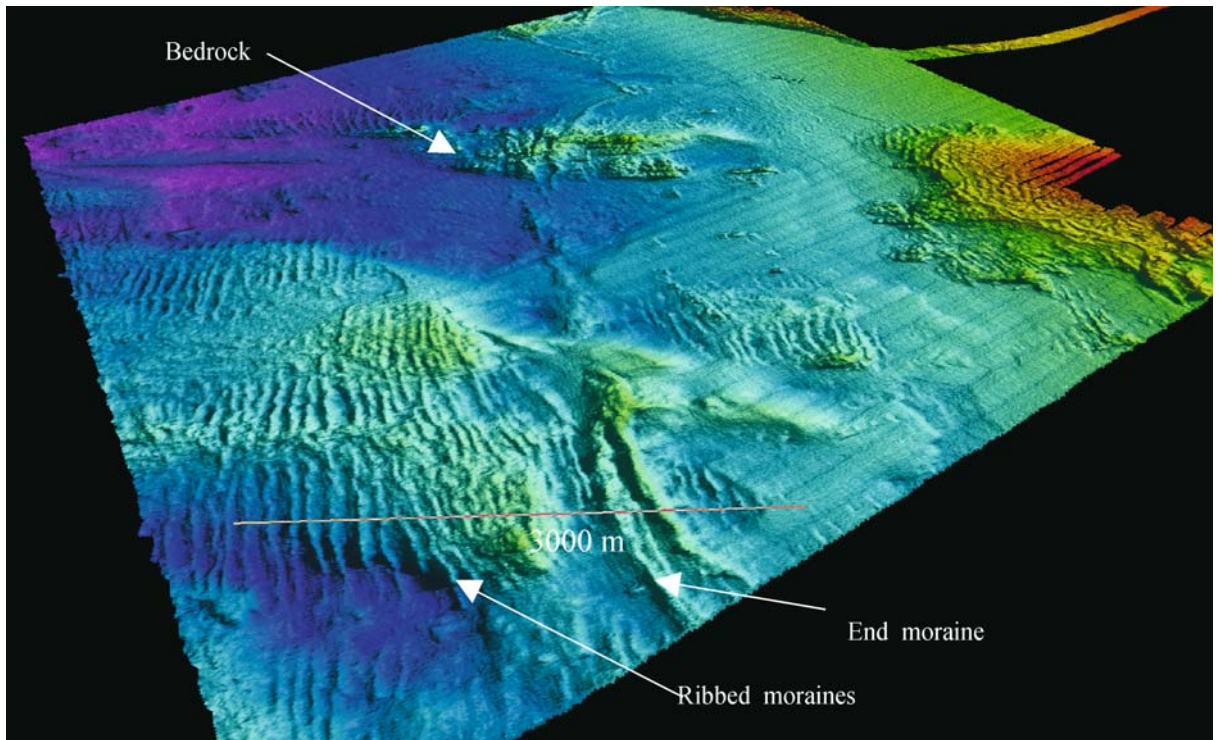
Project: Sand Ridge Morphodynamics on Sable Island Bank, Scotian Shelf; years of survey: 1996, 1997 and 1998

Survey vessel: *F.G. Creed* (SWATH vessel; small water area twin hull)

Multibeam System: Simrad, type: EM 1000; frequency: 95 kHz, beamwidth: 3.3°; number of beams: 60; resolution: 5-m grid.

(Note the exact ship meandering with interlocked hairpin bends. Each stripe represents 60 sounding lines in parallel.)

Image ©: Michael Z. Li and Edward L. King, Geological Survey of Canada (Atlantic), Bedford Institute of Oceanography, Canada ■



◀ Image 5.3.9.1-4.

Moraines on the inner Scotian Shelf of Canada. Multibeam relief image. The large, double ridged feature of up to 8–10 m crest height in the center of the image trending parallel to the shoreline is interpreted as an end moraine, a Holocene relic. A series of smaller rib moraines, about 2 m in height, occur parallel to this major feature and cover a field of which more than 10 km² are imaged. These rib moraines may represent ice recession features on the inner Scotian Shelf, deposited during the recession of the last glaciers across the area about 12 000–14 000 years ago. During the Holocene 11 600 years ago, the area was transgressed by a low stand of sea level, approximately 65 m below the present-day level, indicated by the area colored purple in the image.

The ridge distribution across this inner shelf area, in depths as shallow as 15 m in the near shore right side of the image, suggests that the relief survived the transgression largely intact. Rib moraines, which were previously considered to be absent from transgressed zones, are seen to dominate the study area, and similar features have subsequently been found to be widespread on the inner Scotian Shelf. Bottom photographs, sidescan sonar data and sub-bottom profiler data not shown here confirm that the moraines are erosional remnants, armored by boulder and cobbles. Bedrock outcrops such as depicted in the background are found in many areas forming isolated peaks but also larger interconnected fields such as near Halifax Harbor (Sect. 5.3.8).

Project: Survey Ma98074

Survey area: Liverpool, Nova Scotia, Canada. Water Depth: 15–65 m

Research vessel: Canadian Hydrographic Service survey launch *CSL Plover*

Multibeam echosounder: Simrad, EM 3000; frequency: 300 kHz, beamwidth: 1.5°, number of beams: 127, positioning: differential GPS; attitude sensing

Image depiction: color coded and shaded, relief enhancement factor: 5; grid width 2.5 m, viewing angle: westwards

Image ©: Russell Parrott, Geological Survey of Canada, Natural Resources Canada, Dartmouth, Nova Scotia, Canada ■

◀ Image 5.3.9.1-4a.

Backscatter intensity image of the preceding moraine field. Same data set; gray tone coded echo intensity. The dark areas represent high backscattering strength, typical of the gravel and boulder found in the area. It may appear surprising that the contours of the ridged relief are barely visible without the artificial shading and color coding used in the bathymetry image. This indicates the presence of a nearly uniform, strong backscatter, independent of the incidence angle of acoustic irradiation by the fan-echosounder and is caused by the rough gravel cover (Sect. 3.4.5). The pronounced stripe texture is an artifact from insufficient beam level adjustment. Intensity errors come out more strongly than travel time errors in the relief depiction of the preceding image.

The bright areas with low backscatter are typical of the sands and clays in the upper right corner of the image. The extent of the sandy silt sediments being deposited by the nearby Mersey River is unmistakably depicted by the scattering strength. Sub-bottom profiler data have revealed that the relatively young river sediment overlays the gravel of the moraines, sufficiently to screen them from the lower penetration achieved with the higher frequencies of the multibeam echosounder. An even more recent area of fine-grained dredge spoils is visible adjacent to the river sediments.

Image documentation: Same as of preceding image except evaluation and depiction of the simultaneously recorded echo-intensity of every image pixel corresponding to the respective sound beam of the multibeam fan instead of signal travel time evaluation needed to construct the 3D-relief

Image ©: Russell Parrott, Geological Survey of Canada, Natural Resources Canada, Dartmouth, Nova Scotia, Canada ■

5.3.9.2

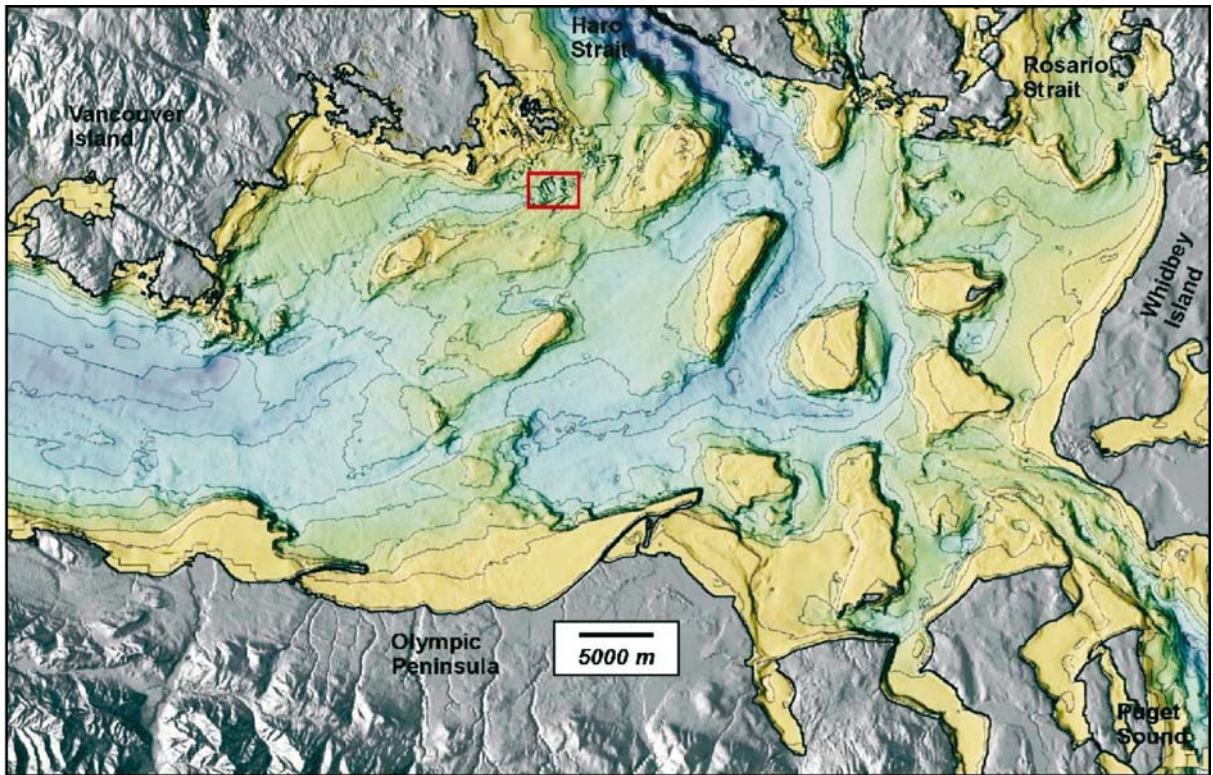
West Coast of Canada, Giant Underwater Dunes

Image 5.3.9.2-1. The place of giant underwater dunes. Bathymetric overview of the area, Eastern Juan de Fuca Strait, British Columbia, Canada. Submarine dunes of crest heights up to 25 m were formed in the eastern Juan de Fuca Strait south of Vancouver Island. These formations are considered the highest underwater dunes ever found. The place is bordered by Washington State and British Columbia at Canada's west coast. The insert box indicates the area depicted by the subsequent images taken by three mutually supplementing acoustic techniques, none of which can reveal all essential features of the dunes independently.

The current flow in this region is strongly estuarine, because of the dominance of the Fraser River outflow east of this location. Fresh water outflow on top forces the incoming denser saline oceanic water deep on the flood tide. Large volumes of water flush in and out of the Juan de Fuca Strait and up the Strait of Georgia at tidal periodicities. The combination of flood tides, strong estuarine conditions and restricted passages can cause bottom currents to reach in excess of 1 m s^{-1} during summer months in the Juan de Fuca Strait.

Dune bedforms of such an extraordinary height at this place appear nevertheless enigmatic under present conditions. Neither is the funnel-shaped bedrock trough unique as a focal point of tidal flow nor does the Juan de Fuca Strait provide an unusually large supply of mobile sediment. Moreover, the repetition of the survey after one year did not reveal any significant change or migration of the main structures. Presumably these dunes are relics of former times similar to the Sable Island dunes off Nova Scotia (Sect. 5.3.9.1). The source material to supply the Juan de Fuca Strait-dunes was probably tidal erosion of the coastline along Victoria as there are no present-day fluvial sources of sediment in the region. The city of Victoria has implemented significant shoreline protection, thus cutting off the supply of material.

Project: Neotectonics of the eastern Juan de Fuca Strait

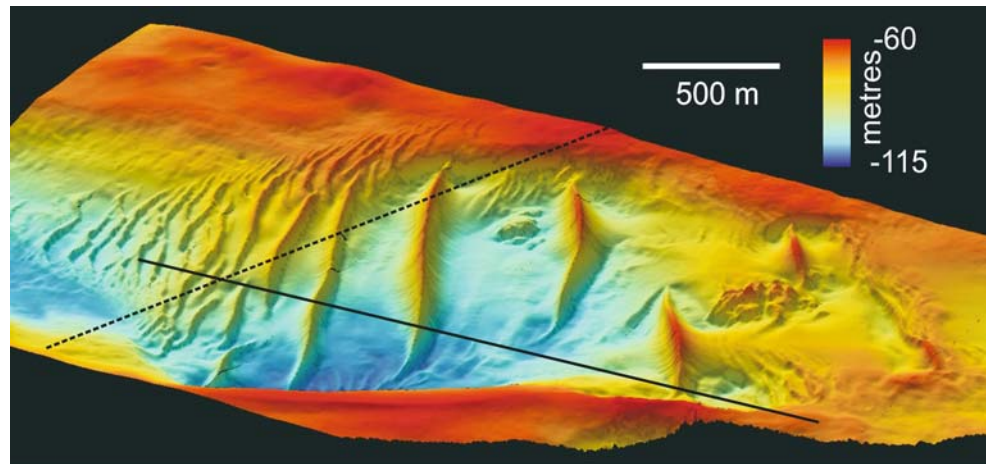
Land topography (gray): Canadian RadarSat-1, satellite radar imagery

Sea floor bathymetry of overview (color): Canadian Hydrographic Services and NOAA single beam bathymetric field sheet; depth lines: 50 m. Horizontal resolution: 100 m

Image ©: David C. Mosher, Natural Resources Canada, Geological Survey of Canada ■

Image 5.3.9.2-2.

The Giant sand dunes; perspective view of the bedrock trough. Multi-beam image. The relief image shows a series of large sediment dunes and sand waves that cross a funnel-shaped trough. (The insert lines indicate the tracks of the subsequent soundings.) The bedrock trough is up to 95 m deep, which is the level of maximum flood tide current. The maximum height of these dunes is 25 m. The three largest show wavelengths of 300 and 515 m, making these features arguably the largest shallow water sediment waves in the world. The bedforms are nearly symmetrical which indicates alternating flow as the probable construction mechanism. The slope angles on their flanks range up to 25°. The entire volume of sand and fine gravel of the dune field corresponds to a cube of 300 m on each side.



The bedforms are nearly symmetrical which indicates alternating flow as the probable construction mechanism. The slope angles on their flanks range up to 25°. The entire volume of sand and fine gravel of the dune field corresponds to a cube of 300 m on each side.

Area: Eastern Juan de Fuca Strait, southwestern British Columbia, Canada

Survey vessel: *MV Revisor*; 1998

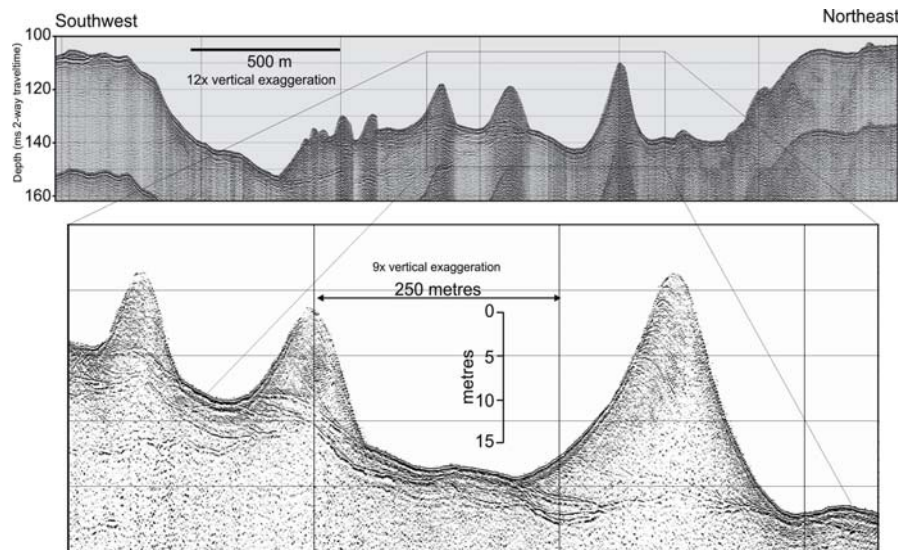
Multibeam system: *Simrad EM3000*, hull mounted; frequency: 300 kHz, beamwidth: ca 1°, number of beams: 120, spanning 120° of swath. *Strong line*: Sidescan track; *broken line*: subbottom profile

Resolution, vertical: 0.1 m; horizontal: 0.5 m, perspective view, looking north, grid width of mapping: 2 m

Image ©: David C. Mosher, Natural Resources Canada, Geological Survey of Canada ■

Image 5.3.9.2-3.

The giant sand dunes as sub-bottom profiles. The images of the large profile and the cut out close up below are seismic profiles through the trough. The track of the profiler relative to the dunes is shown in Image 5.3.9.2-2. The top profile shows the morphologic context of the dunes, crossing the floor of the bedrock trough. The second echo contour is produced by the sea surface acting as a mirror of the primary echo. The cut out in the lower panel shows cliniform structures within the dunes, suggesting cross-bedding and dune migration to the east. The profile reveals the pronounced symmetry of the dune flanks and also the substrate structure at the foot of the dunes.



Area: Eastern Juan de Fuca Strait, southwestern British Columbia, Canada

Survey Vessel: *CCGS John P. Tully*; 1996

Seismic reflection system: Huntec Deep Tow System boomer with separately towed hydrophone array; frequency band 800–8 000 Hz. Resolution: 0.25 m vertical and about 1.5 m horizontal along track

Image ©: David C. Mosher, Natural Resources Canada, Geological Survey of Canada ■

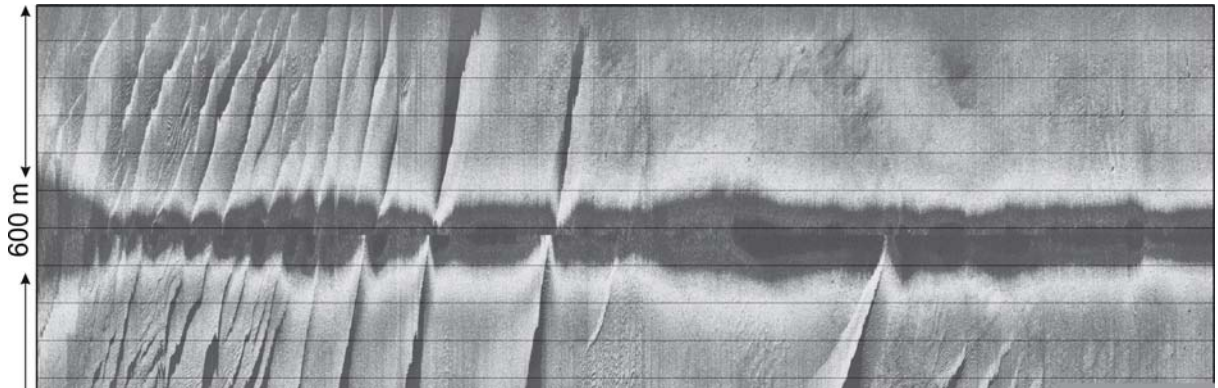


Image 5.3.9.2-4. ▲

The giant sand dunes and their small scale morphology. Sidescan sonar image. This two-dimensional sidescan image (Sect. 4.3) which covers a portion of the sand dune field (the track is shown in Image 5.3.9.2-2) highlights its morphology in kind down to small scales in the centimeter regime but cannot, of course, provide the height information. The indirect calculation of the height scale by quantified shadow length (Sect. 4.3.2) does not apply here because the sound incidence was nearly parallel to the dune crests. Only the constriction of the dark “blind stripe” below the towed sidescan sonar when crossing the high crests give a coarse estimate of their height because the signal travel time of the echo onset is correspondingly shorter. However, the high resolution reveals the ripples and sand waves of smaller scales – which are not recognized by the 3D-multibeam technique – as they are riding on the large dunes. It is remarkable in the context of the presumably stationary giant dunes that the superimposed small scale bedforms show a slant, nearly orthogonal crest angle relative to the giant dunes, visible in particular at the western side. This image also indicates that the dune troughs contain at least a veneer of sand on the bedrock, causing a smooth appearance of the echoreturn character.

Area: Eastern Juan de Fuca Strait, southwestern British Columbia, Canada

Survey Vessel: *CCGS John P. Tully*

Sidescan sonar: *Simrad 992*; 330 kHz, beamwidth athwart: 0.3°; range resolution: 5 cm

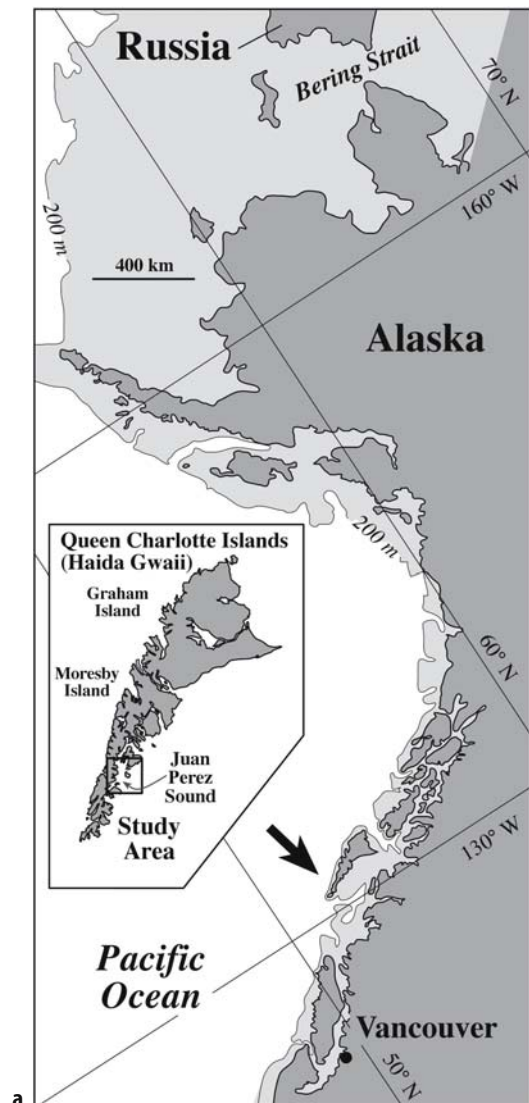
Image ©: David C. Mosher, Natural Resources Canada, Geological Survey of Canada ■

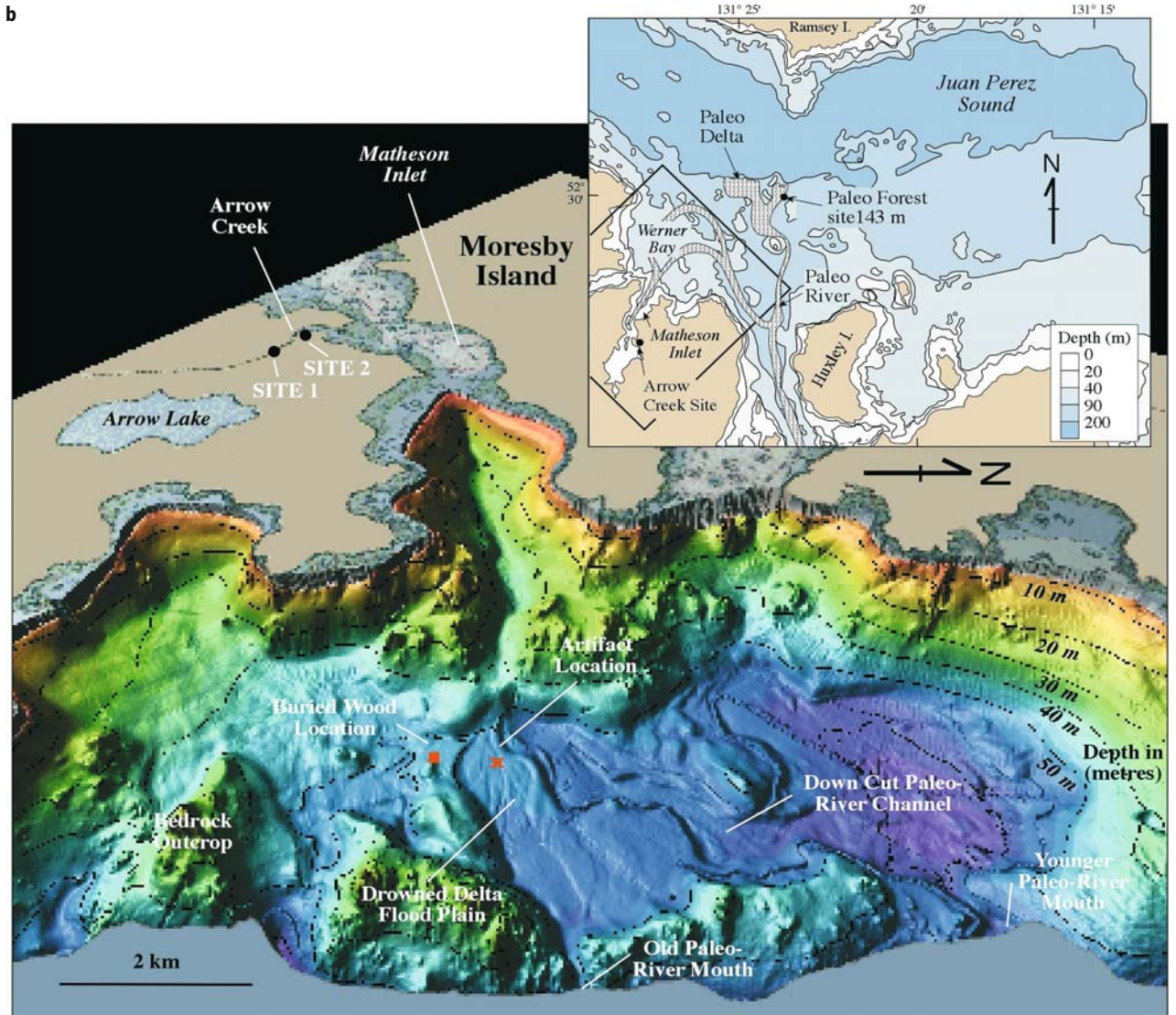
5.3.9.3

Queen Charlotte Islands off British Columbia, Canada

Image 5.3.9.3-1a, 1b. ►

Werner Bay, map of area (a) and multibeam image (b). The Bay, at present part of a drowned delta and paleo drainage system is located in the south of *Moresby Island* (see map), the southernmost of the two *Queen Charlotte Islands*. About 12 300 years





ago sea levels in this area were 150 m lower than today, according to dated forest floor and pine tree stump found. *Werner Bay* inside the *Juan Perez Sound* was probably a place of human settlement about 9 500 years ago when the sea level in this area was below the delta surface. A stone tool and a drowned forest were sampled from the drowned delta plain at 53 m depth, suggesting that early people, perhaps of a stone age period, inhabited this floodplain. The site investigation is part of a larger study of a possible early migration corridor into North America. At that time much of the continental shelf was exposed by the low sea level, which would have made travel down the coast much easier.

About 9 000 years ago sea levels were rising rapidly beyond the present coastline to flood *Arrow Lake* with sea water, thus

leaving only a few hundred years for people to live in the area. Sea levels gradually returned to the present shoreline by about 2 000 years ago. The morphology of the deeper floor at and below 50 m reveals paleo river beds and -mouths as indicated in the text inserts.

Project: Geological Survey of Canada and Canadian Hydrographic Service mapping programs; year of survey: 1997
 Survey vessel: hydrographic launch of 10 m
 Multibeam System: Simrad, type: EM 3000; frequency: 300 kHz, beamwidth: 1.5°, fan width: 120°
 EM 3000 digital terrain image gridded at 1 m
 Image ©: Heiner Josenhans, Geological Survey of Canada (Atlantic), Bedford Institute of Oceanography, Canada ■

5.4 Arctic Ocean

The subchapter presents the *International Bathymetric Chart of the Arctic Ocean (IBCAO)*, the detailed and coherent description of the morphology of the Arctic Ocean sea floor north of 64° N, resolved by a grid of 2.5 × 2.5 km. This most recent digital relief map includes legacy and modern data sets unavailable before the end of the east-west block confrontation and provides a significant improvement over previous bathymetric portrayals. The immense amount of work necessary to deal with all available data and maps, to investigate, compare, select, digitize and integrate the inhomogeneous data sources into comprehensive and treatable data files was conducted and supervised by an international team of experts. The concept of a weighted blend of inhomogeneous data followed the philosophy of the ETOPO mapping project (Sect. 5.1) where satellite altimetry and shipborne bathymetry data have been merged to achieve complete area coverage. In the Arctic beyond reach of radar satellites the relief maps have been exclusively based on soundings. Martin Jakobsson, the key authority in this matchless project and image author of the ETOPO2-Globes and the Fledermaus version in GEBCO5 shown in this book and attached CD, also contributed the article on the subject presented hereafter.

The other three sections of Sect. 5.4 deal with a 100-m grid multibeam relief close-up of the *Fram Strait*, the only deep water connection to the Arctic Ocean, showing the deepest depression north of 60° latitude; they present sidescan images under polar ice taken with an autonomous mini-submarine, and show high resolution sediment penetrating image examples of the *Arctic Shelf*, the largest in the world.

5.4.1

5.4.1 *Arctic Ocean and Its Constituent Seas;* **Bathymetry and Physiography**

Martin Jakobsson · Center for Coastal and Ocean Mapping, Joint Hydrographic Center, University of New Hampshire

The smallest of the world's oceans, the Arctic Ocean, is considered to play a critical role in the global climate system and tectonic history. It is a source for deep-water for-

mation that drives the global thermohaline circulation and, thus, the heat transfer from lower to higher latitudes. The perennial sea ice cover through its high sunlight reflectivity, the *albedo* affects the Earth's heat budget. On longer time scales the tectonic evolution controls the physiography of the Arctic Ocean basin, which in turn largely influences where and how the currents flow.

This said it is not difficult to comprehend that an accurate description of the sea floor morphology of this high-latitude region is critical for many scientists. However, it is just the climatically important perennial sea ice cover that severely has hampered a systematic collection of bathymetric information from surface vessels. This has resulted in that less is known about the Arctic Ocean bathymetry and physiography than for the other oceans.

For nearly 60 years after *Nansen's* collection of deep bathymetric soundings during his epic expedition with the vessel *Fram* drifting in the Arctic pack ice from the *New Siberian Islands* to the *Fram Strait* (Nansen 1902), it was a common belief that the entire central Arctic Ocean consisted of one deep basin. A major breakthrough in Arctic Ocean mapping followed the World War II when the former *Soviet Union* started to systematically collect bathymetric soundings in the central Arctic from ice stations established using airplanes to land scientists on the pack ice in order to carry out soundings through the ice. The collected data revealed an ocean underlain by a morphologically complex sea floor consisting of abyssal plains interspersed between large submarine ridges (see e.g. Weber 1983).

The most recent international contribution to Arctic Ocean bathymetric portrayals is the *International Bathymetric Chart of the Arctic Ocean (IBCAO)*. This digital 2.5 × 2.5-km grid-model on a polar stereographic projection hat provides a detailed and coherent description of the morphology of the Arctic Ocean sea floor north of 64° N (Jakobsson et al. 2000). IBCAO provides a significant improvement over previous bathymetric portrayals (e.g. Canadian Hydrographic Service 1979; Perry et al. 1985) because the compilers were able to use legacy and modern data sets that were previously unavailable. These data included echo soundings from United States and British navy nuclear submarine cruises between 1958–1988, echo soundings from nuclear submarine cruises from the SCICEX program 1993–1999, and echo soundings from icebreaker and research vessel cruises carried out by Canada, Germany, Norway, Russia, Sweden, and the United States. In addition, we

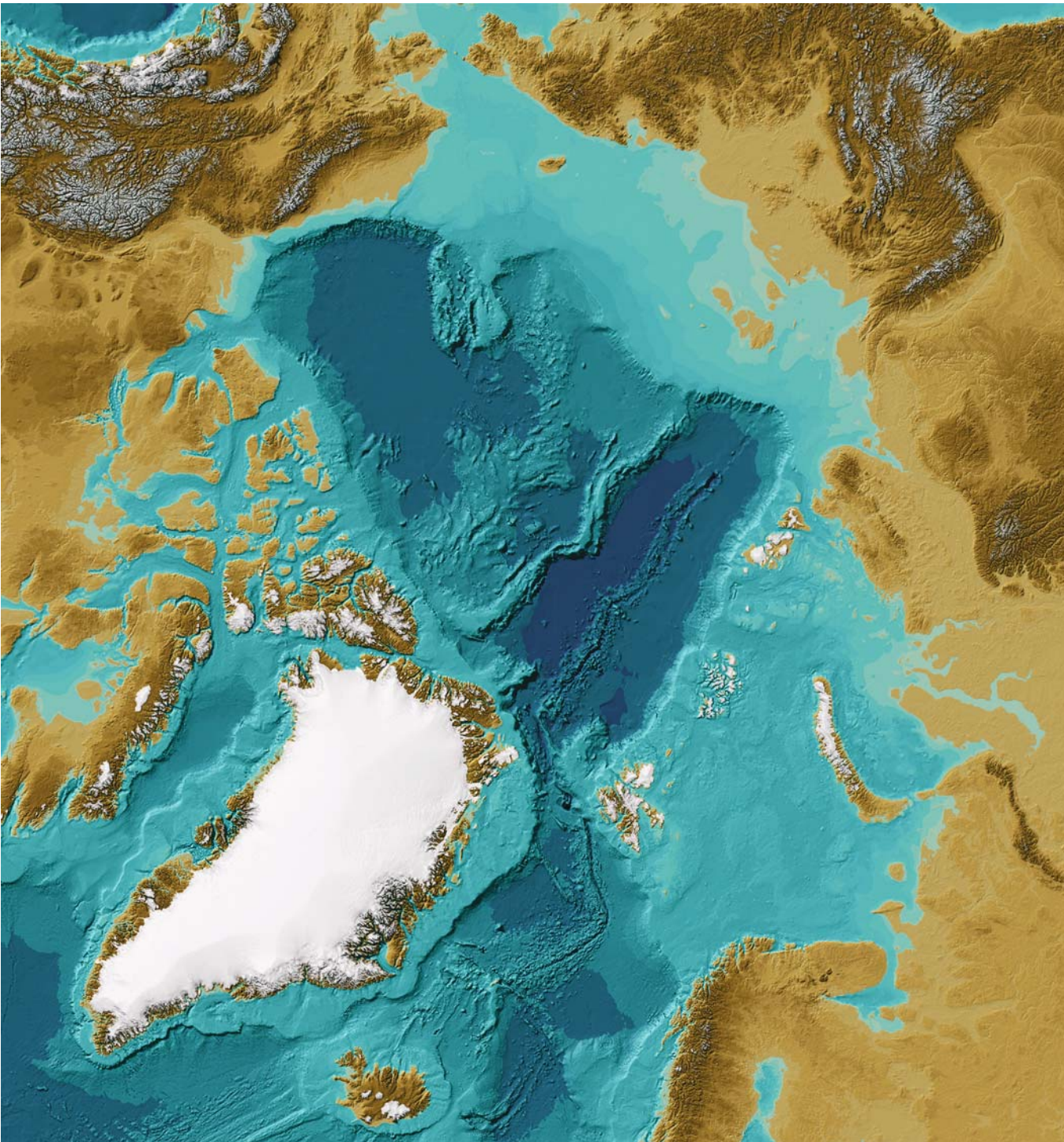


Image 5.4.1-1. Bird's eye view over the shaded, color coded relief of the *Arctic Ocean* area as a plain

Image ©: Martin Jakobssen, CCOM ■

Image 5.4.1-1a.
 Slant view of a cut-out of
 Image 5.4.1-1 with the axis
 cross through the *North Pole*

Image ©:
 Jörn Hatzky, AWI ■

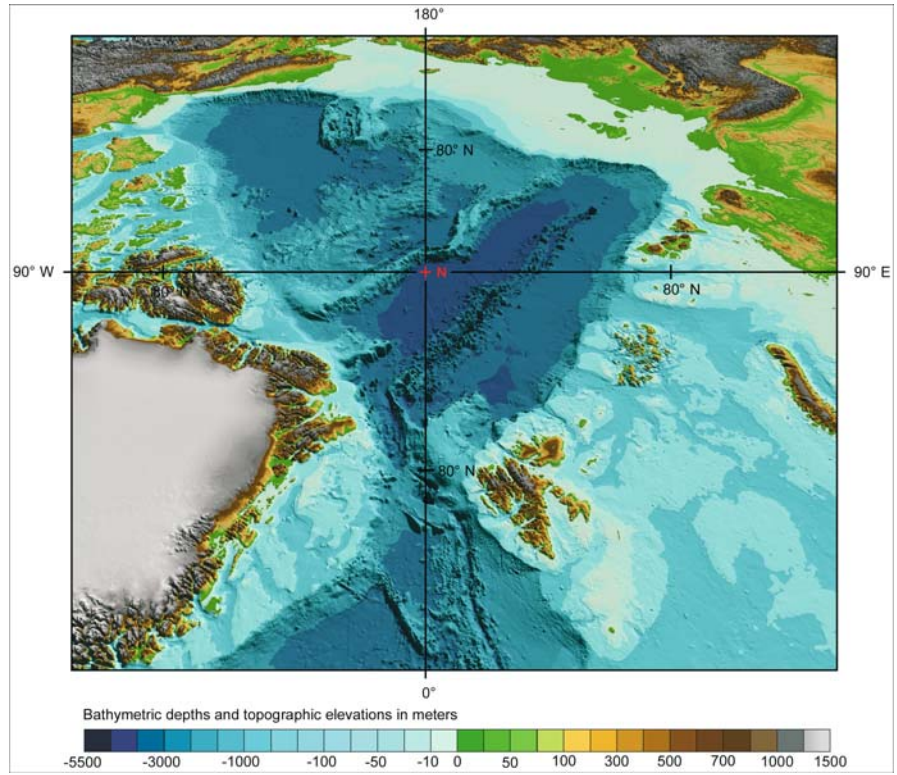
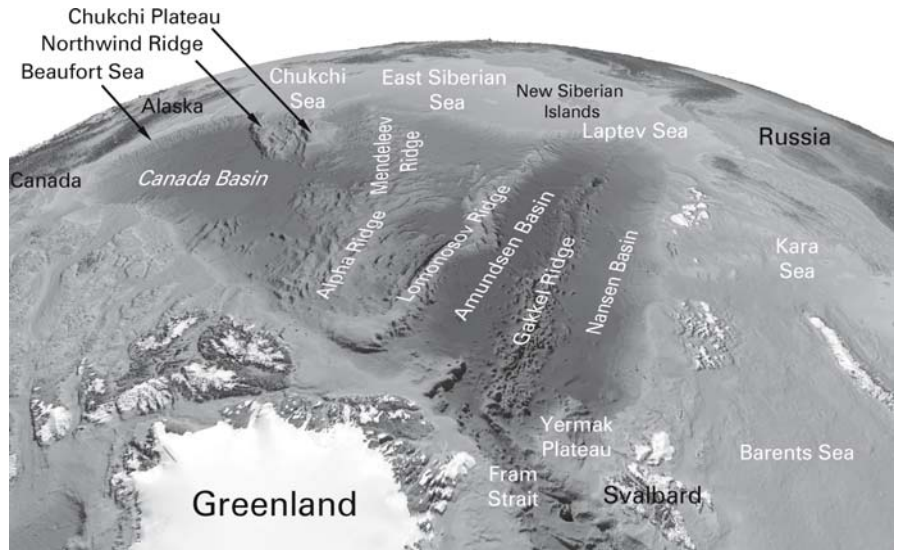


Image 5.4.1-2.
 The names of the major
 formations, attached to the
 spherical depiction

Image ©: Martin
 Jakobssen, CCOM ■



used for the IBCAO compilation published bathymetric contour maps in areas where original depth measurements were sparse or not available. These include the recently published Russian 1 : 5 000 000 scale bathy-

metric contour map “Bottom Relief of the Arctic Ocean” (VNIIOkeangeologia 1999).

In summary, IBCAO has been constructed from all available data of the Arctic Ocean to the compilers, i.e.

single beam echo sounding data, multibeam data, already gridded compilations and digitized contour maps. The primary philosophy while combining all the various data sources has been to use the best available data in all areas. In practice this means for example that if a multibeam survey covers a portion of a contour map, the digitized contours from the map would not be used in the IBCAO gridding algorithm where the multibeam data extends.

The IBCAO combined with predicted topography below 64° N from Smith and Sandwell (1997) has been used to construct the shaded relief of the Earth sea floor and land topography in Image 5.4.1-1. In order to get the glaciers rendered white irrespective of their elevation a database was used with information of today's glacier cover assembled from Digital Chart of the World and the Danish Cadaster and Mapping Agency.

From the illustration in Image 5.4.1-1 it is clearly seen that the deep central basin of the Arctic Ocean is nearly surrounded by continental massifs and the shallow continental shelves of *Russia, Alaska, Canada, and Greenland.*

The *Fram Strait* between northeastern Greenland and northwestern *Svalbard* is the only deep opening in this ring of continental shelves. It is through this deep-water passage that the majority of water exchange takes place between the Arctic Ocean and the North Atlantic.

The projection of *Image 5.4.1-1* provides a bird's eye view over the shaded, color coded relief of the Arctic Ocean area as a plain. The corresponding slant view of a cut-out of *Image 5.4.1-1* with the axis cross through the North Pole is shown in *Image 5.4.1-1a*, also derived from the IBCAO data base. The names of the major formations are attached to the spherical depiction in gray of *Image 5.4.1-2*, showing about the same view and projection as the shaded, color coded *Image 5.4.1-3.*

The *Eurasian Basin* and the *Amerasian Basin* are two sub-basins that are commonly applied as a sub-division of the Arctic Ocean basin. The *Lomonosov Ridge* and the shallow shelves of *Barents, Kara, and Laptev Seas* bound the former and the *Lomonosov Ridge* and the shelves of *East*

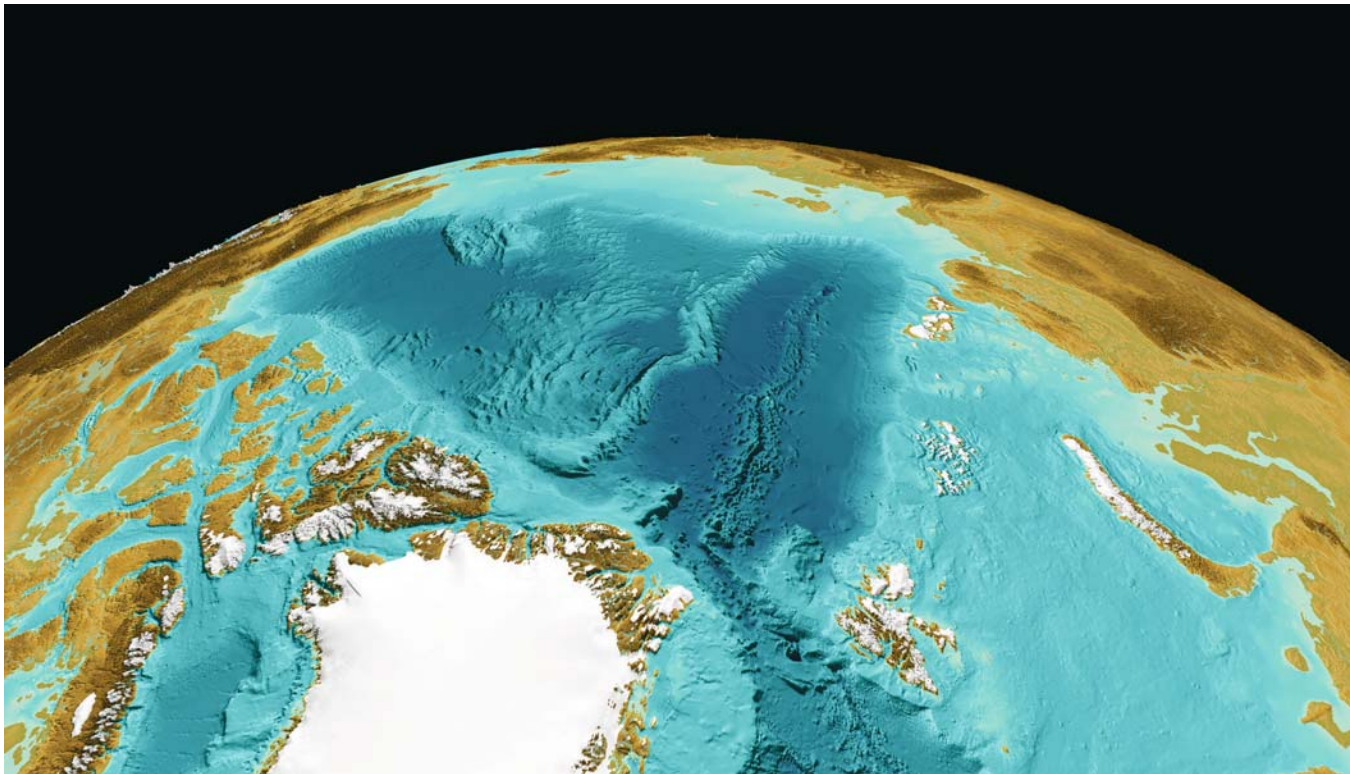


Image 5.4.1-3. Spherical depiction of the shaded, color coded relief of the *Arctic Ocean* area

Image ©: Martin Jakobssen, CCOM ■

5.4.2

Siberian, Chukchi, and Beaufort Seas and the Canadian Arctic Archipelago and Northern Greenland bound the latter.

The prominent submarine ridge named Lomonosov Ridge, after a Russian natural scientist, is considered to be a sliver of continental crust that broke of the Barents and Kara Sea continental margin during the initiation of the continuation of the mid-ocean spreading ridge system into the Arctic (e.g. Karasik 1968, 1974; Wilson 1963; Vogt et al. 1979; Vink et al. 1984). This occurred at about 50 million years ago (e.g. Jokat et al. 1995). The existence of a spreading ridge in the Arctic Ocean was first proposed on the basis of a small number of soundings and the pattern of earthquake epicenters (Heezen and Ewing 1961; Gakkel 1962). This spreading ridge is called the *Gakkel Ridge* and, in turn, it subdivides the Eurasian Basin into *Amundsen* and *Nansen Basins*. The deepest area of the Arctic Ocean is found in the actual axial valley of the *Gakkel Ridge* near 81°20' N 120°45' W close to the *Laptev Sea* margin where the IBCAO grid indicates 5 243 m (Jakobsson 2002). The Amerasian Basin is also commonly sub-divided into the two sub-basins *Canada* and *Makarov Basins* by the enormous submarine mountain ridge complex the *Alpha-Mendeljev Ridge*. This ridge complex extends an area of the size of the Alps and takes up much as much as 7.8% of the entire Arctic Ocean area (Jakobsson et al. in press). It was discovered by scientists on the drifting ice station ALPHA during the International Geophysical Year in 1957–1958 (Hunkins 1961). The physiography of the Alpha-Mendeljev Ridge complex is very different from the Lomonosov Ridge, with generally less steep slopes and numerous valleys and local elevations. Of the smaller submarine ridge systems in the Arctic should be mentioned in the Amerasian Basin the *Northwind Ridge* and the *Chukchi Spur-Chukchi Plateau* composite ridge of the *Chukchi Borderland* and in the Eurasian Basin the *Yermak Plateau* and *Morris Jessup Rise*.

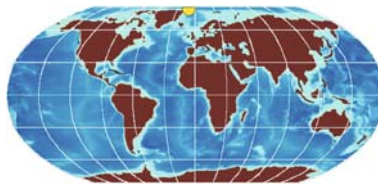
A striking characteristic of the Arctic Ocean compared to the rest of the world oceans is that the shallow continental shelves, defined as the area from the coastline out to the shelf break, make up as much as 52.7% of the total area (Jakobsson 2002). The combined area of continental shelves and slopes have been estimated to range from only 9.1% and 17.7% in all the other world oceans (Menard and Smith 1966).

References

See Sect. L.5.4.1.

5.4.2

The Fram Strait with the Deepest Depression in the Arctic



The only deep water connection between the *Arctic Ocean Basin* and the *North Atlantic* is called *Fram*

Strait. It is a comparatively narrow passage, about 500 km wide, between the north-east of *Greenland* and the *Spitsbergen* archipelago at the continental margin of the shallow shelf waters in the east. Only through this seaway is the *Arctic Ocean* involved in the exchange of deep water masses between the three interconnected world oceans *Atlantic, Pacific, and Indian*, thus sharing the global thermohaline circulation, also called *conveyor belt*.

The high resolution fan echosounder image is a color-coded shaded relief, visualizing that part of the Fram Strait which contains typical and extreme features of this passage. The direction of view is southbound. This area of investigation is a kind of close-up of the arctic polar region shown in Sect. 5.4.1. Among other features it reveals fracture zones, the result of changing shift directions of adjacent tectonic plates. The entire bathymetry is a complex sequence of transform faults and spreading centers. The deep water passage is thus disturbed by ridges with seamounts reaching heights of 1 600 m over the surrounding sea floor and plateaus which are sills between the Basins of the Arctic Ocean and the northern *North Atlantic*, also called *Nordic Seas*.

The main trough in the foreground, called “*Spitsbergen Deep*” is part of the “*Spitsbergen Fracture Zone*”, reaching depths of over 4 500 m. The Spitsbergen Deep follows a northwest-southeast direction typical of most morphological and geological features in the Fram Strait region. The most remarkable morphologic feature in the Fram Strait is located south of the chain of seamounts: the so called *Molloy Deep*. This is a nodal deep with a diameter of about 30 km reaching down to 5 670 m! It is the deepest known depression of the Arctic Ocean, the Norwegian-Greenland sea and the Atlantic Ocean north of 60° latitude. At the steepest slopes in the south the sea-floor plunges down from 2 500 m to 5 400 m over a horizontal distance of only 10 km. Local slopes reach values of nearly 100% or 42 degrees.

The topography of the Fram Strait controls the exchange of water masses between the *Arctic Basin* and

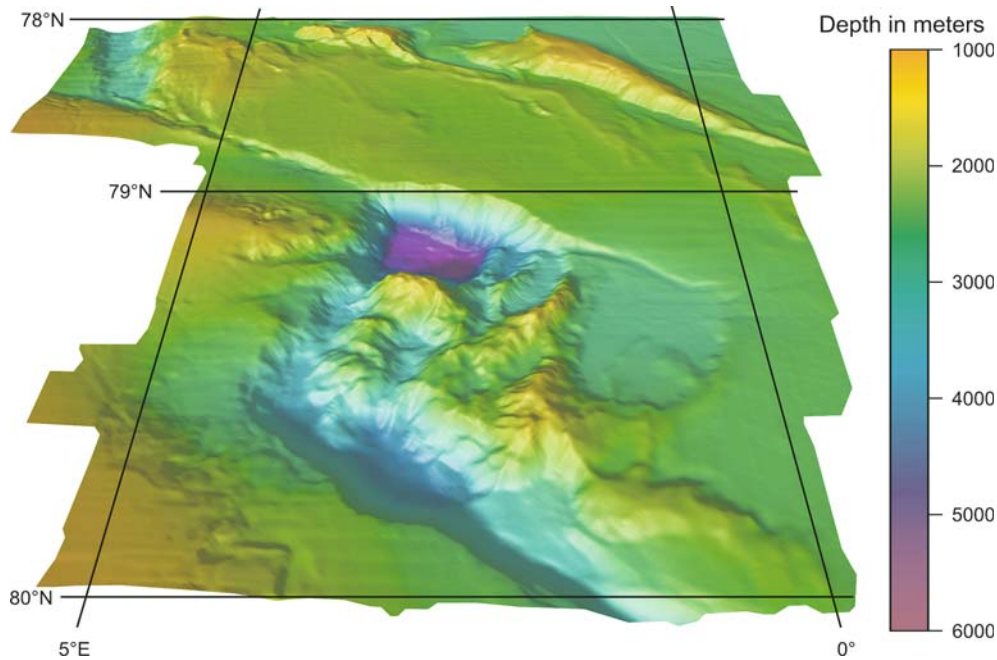


Image 5.4.2-1. View upon the deepest part of the Fram Strait. Multibeam 3D-image. The slant view as seen from the North Pole in southward direction visualizes the famous *Molloy Hole* in the middle of the image. Within a few tens of kilometers the sea floor descends from 1500 m depth of the nearest mountain summit in the north down to the deepest known depression 5700 m in the Arctic and the Atlantic north of 60° latitude. Molloy Hole is a nodal deep and part of a compact fault area with mountain formations on one side of a displaced trench, obviously the result of disruptive shear forces. The fault complex reveals a tectonic deformation process entirely different from subduction zones at the Pacific margins (Sect. 5.2.1, 5.2.2). The 3D-image has been derived from a Digital Terrain Model with 100 m cell size.

Project: AWI Bathymetric Charts of the Fram Strait and several other projects; sea trials between 1984 and 1997 (1984–1987: SeaBeam, 1990–1997: Hydrosweep)

Research Vessel: *RV Polarstern*, Germany

Multibeam echosounders:

- L3/SeaBeam 12 kHz; frequency: 12.3 kHz, number of beams: 16, beamwidth: 2.7°, fan width: 43°
- ATLAS Hydrographics/Hydrosweep DS-1; frequency: 15.5 kHz, number of beams: 59, beamwidth: 2.3°, fan width: 90°

Image ©: Martin Klenke, AWI, Bremerhaven, Germany ■

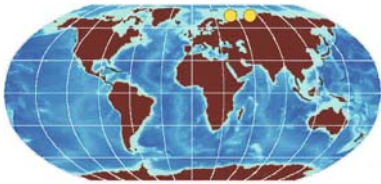
the *North Atlantic* through two main currents: The *East Greenland Current* conveys arctic surface water southwards along the western border of the Fram Strait. The *West Spitsbergen Current* is the northward conveyor of Atlantic Waters along the eastern margin of the Fram Strait. These major currents are separated by a transition zone of water density with some recirculation which adds cooled Atlantic water to the East Greenland Current.

The *East Greenland Current* of the Fram Strait is a major contributor to the cold, deep water backflow of the global thermohaline circulation. Part of its northbound, near surface, warm water counterpart which

governs the North European climate is well known as the *Gulf Stream*, and its extension, called the *North Atlantic Current*. In fact, the cold waters from the Greenland Sea and the Fram Strait mix with Atlantic waters after overflowing the Greenland-Scotland Ridge and then combine with further cold water from the Labrador Sea thus resulting in the southward flowing *North Atlantic Deep Water*, right at the bottom.

Another important process of relevance for the regional and global climate is the sea ice transport through the Fram Strait. The sea ice stream through this passage is the largest and most concentrated meridional ice flow worldwide (Sect. 5.4.4).

5.4.3 Arctic Sediments



Nowhere else are such extended shelf areas to be found than on the Russian side of the Arctic Ocean. Until recently the date of origin and the processes of formation were speculative, in particular the role of the last glaciation. The echo sounding survey performed during the multidisciplinary Russian-German *Boris Petrov* Expedition of 2001, the third of a series of three, permitted the mapping of part of the still unknown extent of the Ice Sheet during the eastern Last Glacial Maximum (LGM) of the

Barents- and Kara-Sea area. According to the echosounder profiles and sediment cores, the deposit sites of sediment material transported by the Siberian rivers *Ob* and *Yenisei* varied strongly throughout the postglacial period, the Holocene. During early Holocene periods of lowered sea level, major amounts were transported far offshore and accumulated on the shelf. In the late Holocene however, most of the sediment growth occurred in the river estuaries already. During the post-glacial sea-level rise, the center of sediment deposition migrated southward, reaching its actual site only about 5 200 years before the present day. Future studies of ^{14}C -dated sediment cores will allow a detailed reconstruction of the variability of fluvial sediment discharge and the glaciation history in the Kara Sea during late Quaternary times. The image series presents examples of the Kara Sea and the Barents Sea.

Image 5.4.3-1.

Siberian river run-off in the Kara Sea, Arctic Ocean: Map of the study area. The map of the Boris Petrov Expedition of 2001 into the inner Kara Sea and the Ob and Yenisei estuaries depicts the locations of the sediment echosounder profiles (A, C, D) shown in the Images 5.4.3-2 to 5.4.3-4, as well as the bottom sampling positions. Based on the profiling results, the extent of the south-eastern margin of the Last Glacial Maximum (LGM) ice sheet and the track of a paleo-river channel are indicated. The reconstruction of the proposed extent of the late Quaternary Eurasian ice sheet is shown on the small map.

Map ©: Rüdiger Stein, AWI, Bremerhaven, Germany ■

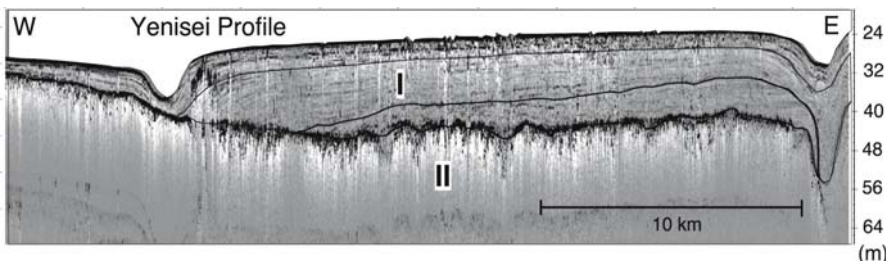
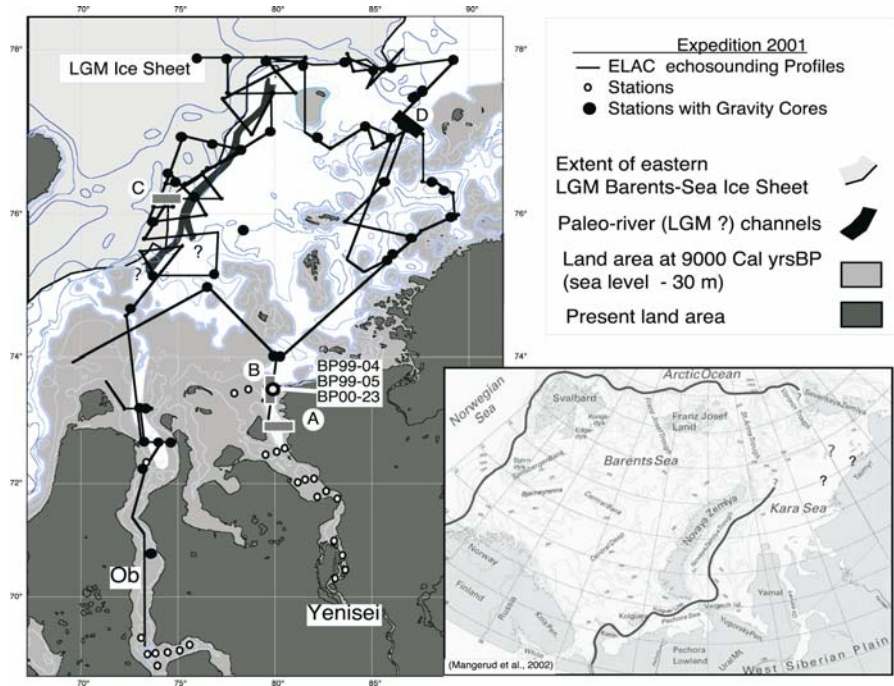


Image 5.4.3-2.

The Yenisei Estuary. High resolution seismic imaging. The interpretation of this clearly structured sediment echosounder profile at section A is a typical example of interdisciplinary cooperation in this field. The thick sequences of soft, post-glacial sediments, also found in the Ob Estuary

and indicated by the high penetration depth of the sediment profiler, are a guide for further, non acoustic analysis. The top layers of 20 m depth, labeled I, of the Yenisei-section overlay the less smooth pre-Holocene bottom topography II. According to core analysis, the deposits of I are mainly fine-grained sediments of river discharge, the predominant sediment origin of the entire study area. The stratification of the upper part of I is strongly disturbed by biologic activities. The distinct echo horizon below marks the upper boundary of undisturbed laminated sediments which were found to be of different provenance. According to mineralogical investigations including magnetic- and ^{14}C -analysis, these sediments are weathering products of basaltic material of 9000 years of age from the last deglaciation of a basaltic massif.

The high sedimentation rates of 2 m per millennium, more than 100 times the sediment growth of most deep-sea areas, are probably associated with the mixing zone of marine and riverine water, where large amounts of dissolved and particulate matter sink to the bottom due to flocculation and coagulation. It can be inferred from these observations that during late Holocene times, most of the sediment material was already deposited in the estuaries and only minor amounts were transported further offshore. Towards the north as well as towards the flanks of the estuaries, the penetration depth of the sediment profiler decreases sharply, indicating a more consolidated sediment of low accumulation rates.

The pre-Holocene sediments II of an even higher content of basalt were formed during times of lowered sea level when the shallow part of the Kara Sea shelf was exposed. The irregular bright zone below the pronounced reflector between I and II is due to less sound penetration.

Project: Siberian River run-off in the Kara Sea, 2001

Research vessel: *RV Akademik Boris Petrov*, Russian Federation

Acoustic device: GeoAcoustics, type: GeoChirp; wide band, high resolution towed sediment echosounder; frequency: 2–8 kHz, beamwidth: 55–30° respectively

Image ©: Rüdiger Stein, AWI, Wilhelmshaven, Germany ■

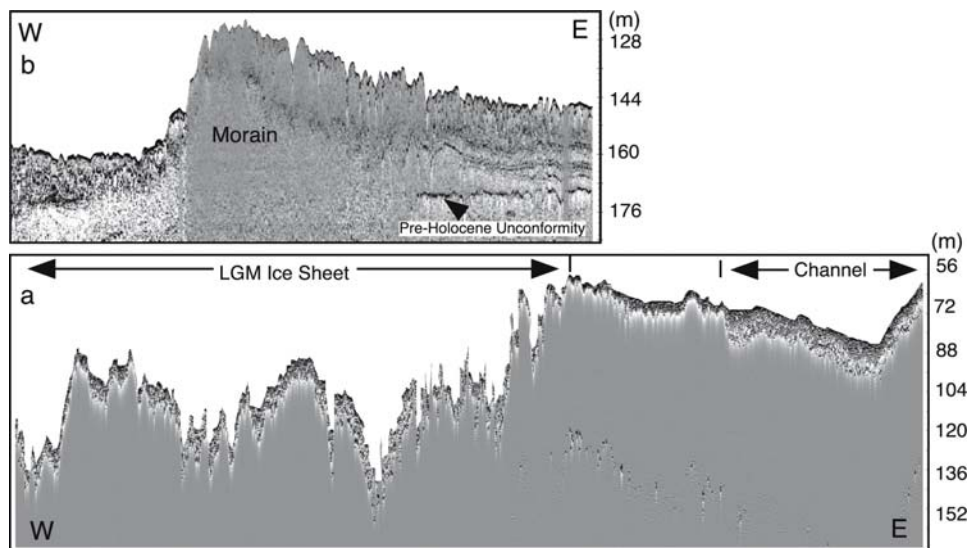


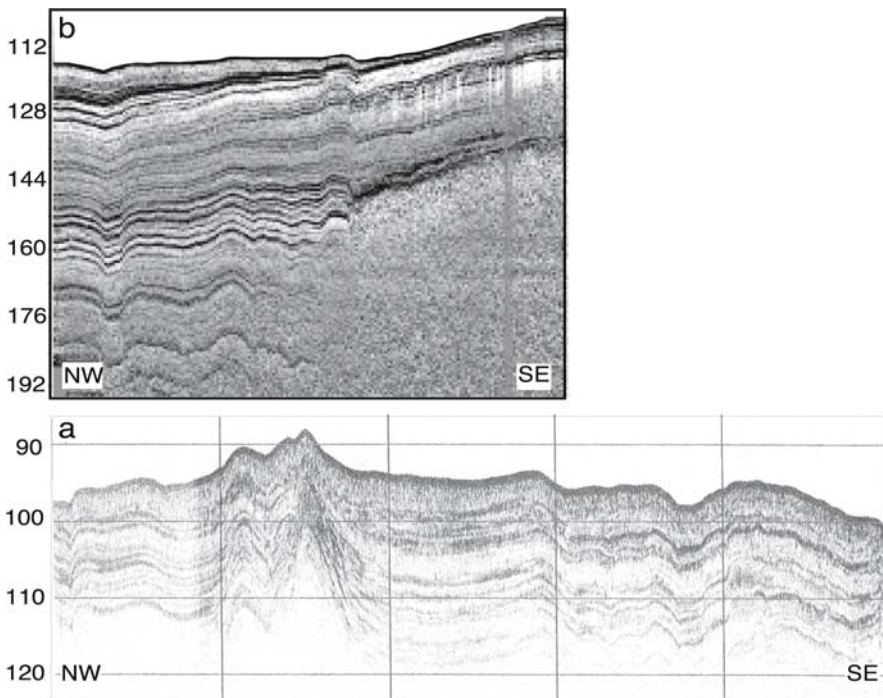
Image 5.4.3-3. Crossing the eastern Barents-Kara Sea margin. High resolution seismic image. This echo sounding profile along section C (lower image) crosses the presumed eastern margin of the Barents-Kara Ice Sheet during the last glacial maximum LGM. The sea floor is strongly furrowed here, which is interpreted as being a relatively fresh sub glacial moraine morphology. The chirp echosounder profile (top image) penetrating deeper, reveals that the young, strongly furrowed moraine overlays the pre-Holocene horizon in the east.

Project: Siberian River run-off in the Kara Sea, 2001

Research vessel: *RV Akademik Boris Petrov*, Russian Federation

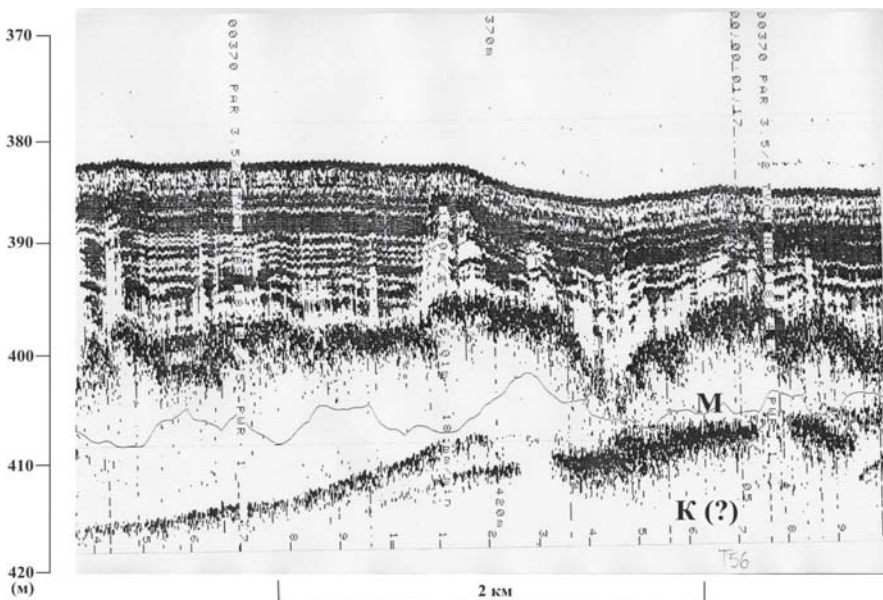
Acoustic devices: (top) GeoAcoustics, type: GeoChirp; wide band, high resolution towed sediment echosounder; frequency 2–8 kHz, beamwidth: 55–30° respectively; (bottom) ELAC sediment echograph, type: LAZ 72; frequency 12 kHz

Image ©: Rüdiger Stein, AWI, Germany ■

**Image 5.4.3-4.**

Thick well stratified mud, *Kara Sea*. High resolution seismic image. The echosounder profiles along section D of the map are considered to support the hypothesis that the rim of the ice sheet very probably did not reach this site because the typical clue structures like end-moraines and furrows are missing. Instead, this area is characterized by thick well-stratified mud, in places more than 80 m thick.

Image documentation: same as for Image 5.4.3-3 ■

**Image 5.4.3-5.**

South Barents Basin, Arctic Shelf; cross section of Quaternary sediments, part one. High resolution parametric sediment echosounding. The image reveals the stratification of a typical cross-section of Quaternary sediments in the South Barents Basin. Three vertical regimes of different internal structure are discriminated by the high resolution parametric echosounding. The topmost layers of Holocene marine clayey mud of 2–3 m thickness overlay stratified Quaternary glaciomarine clays of 6–10 m thickness. These layers accumulated under the floating shelf glacier and perennial pack ice. The thick, acoustically transparent layer below of up to 20 m thickness (*M*) is most likely a glacial moraine, which consists of clays and

loams with coarse debris. Finally, the lowest reflector (*K*) is the eroded surface of Cretaceous sediment bedrock. Despite sea state 4–5, causing the slightly wavy horizons, about twenty layers are resolved between 380 m and 400 m depth.

Project: Russian Academy of Sciences; high-resolution seismo-acoustic research in the Arctic Seas, Project 1.1 (2000–2003)

Survey Vessel: *RV Akademik Sergey Vavilov*, Kaliningrad, Russian Federation

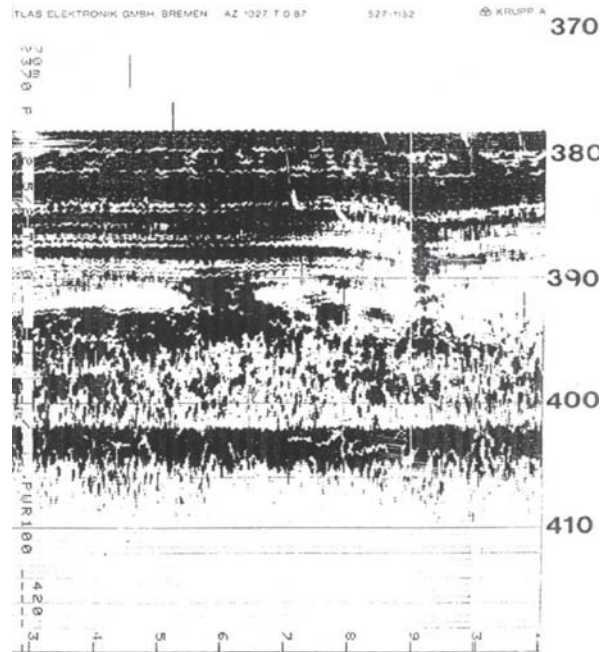
Echosounder: PARASOUND DS-2; 3.5 kHz, beamwidth 4°

Image ©: Lev R. Merklin, Shirshov Institute of Oceanology, Russian Academy of Sciences, Moscow, Russian Federation ■

Image 5.4.3-6.

South Barents Basin, Arctic Shelf; cross section of Quaternary sediments, part two. High resolution parametric sediment echosounding. The image is another part of the same track as shown in the preceding image. The narrow beamwidth and the short sound signal of the parametric system can resolve objects of small lateral and vertical size embedded in the sediment layers. Within the depth interval of 393–402 m the glacial moraine layer appears irregular like random sound scatterers. They are attributed to coarse debris and boulders in the size regime of meters and less. (Reproduction from paper record. The superimposed slight undulation is due to sea waves causing ship motion.)

Project: Basement Acoustical investigations in the Arctic, Russian Academy of Sciences (1990–1992)
 Survey Vessel: *RV Akademik Ioffe*, Kaliningrad, Russian Federation
 Echosounder: ATLAS Elektronik, PARASOUND DS-2; 3.5 kHz, beamwidth 4°
 Image ©: Lev R. Merklin, Shirshov Institute of Oceanology, Russian Academy of Sciences, Moscow, Russian Federation ■

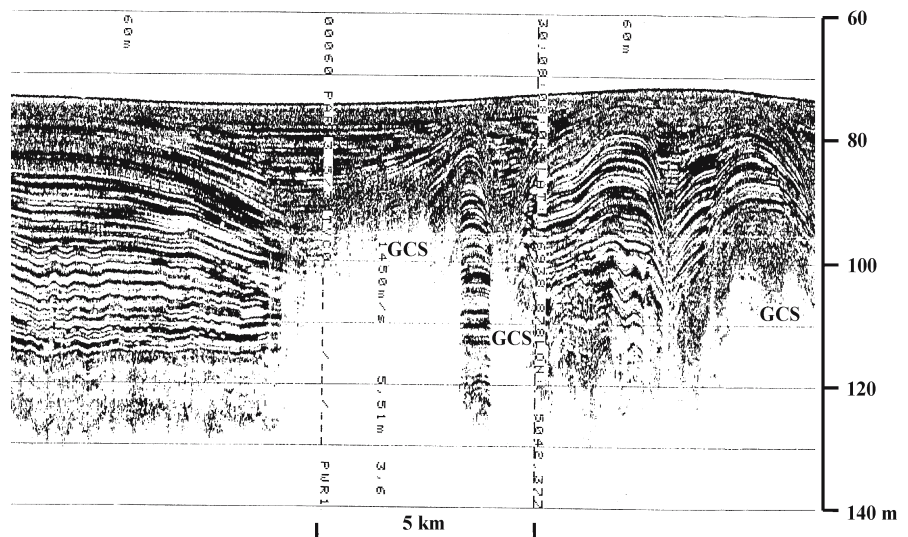
**Image 5.4.3-7.**

Gas-Charged Sediments (GCS) in the Arctic; South Barents Basin, Barents Sea. High resolution parametric sediment echosounding. Sediments containing undissolved gas – which is mostly methane – reveal this feature both by their more or less diffuse sound reflection at the bottom of the tight sediment “lid” and by extreme sound absorption inside. Thus there are no or nearly no echoes from inside the deposit. The sharp, sometimes abrupt lateral boundaries of the deposits are as conspicuous as the acoustic opaqueness of the volume. The narrow beam of the parametric system visualizes this boundary feature without broadening. In particular the gas-free sediment wall

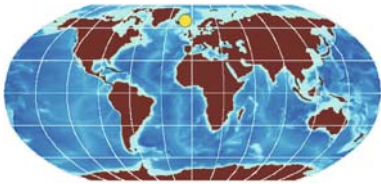
of less than a kilometer thickness subdividing the main gas-charged sediment appears like a sharply incised border. The sediment strata of twenty meters thickness on top of the deposit appear strongly disturbed. This is evident mainly around the gas-free wall which could be the remains of the last periodic deformations on the right side. It should be mentioned that the top of the main gas-charged sediment is at 90 m depth, which was the low sea level during the Last Glaciation Maximum (LGM).

Gas-charged sediments are found on many other continental shelf areas of different climate zones (Sect. 6.2). However, in this arctic region biogenic methane and hydrogen sulfide which have charged the sediments may be generated by deglaciated permafrost.

Project: High-resolution seismo-acoustic investigations in the Barents Sea; Russian Academy of Sciences (1997–1999)
 Survey Vessel: *RV Akademik Sergey Vavilov*, Kaliningrad, Russian Federation
 Echosounder: ATLAS Elektronik, PARASOUND DS-2; 3.5 kHz, beamwidth 4°
 Image ©: Oleg V. Levchenko, Shirshov Institute of Oceanology, Russian Academy of Sciences, Moscow, Russian Federation ■



5.4.4 5.4.4 Under Ice Sound Imaging in the Fram Strait



The ice caps of the polar regions, their growth and melting, and the amount of ice flow from its polar origin towards

lower latitudes are part of the global conveyor belt of the distribution of thermal energy and thus the state

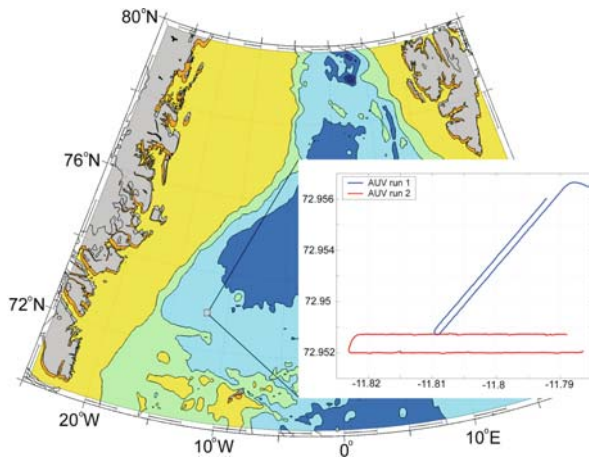


Image 5.4.4-1.

AUV-tracks Under Ice. The map of the AUV mission shows the two hair pin tracks of 1 700 m and 2 900 m length as insert. The tracks went through the marginal ice south of the Fram Strait with Greenland to the west and Spitsbergen to the north-east. The tracks are records of the AUV-inertial navigation data, with the AUV-path derived from the acoustic Doppler current profiler data by integration of the speed vector and supporting compass data.

Project: CONVECTION program supported by the European Union under contract EVK2-2000-00058
 Host vessel: *RV Lance*, Norsk Polarinstitutt, Norway
 AUV: *Maridan Martin 150*; length 4.5 m, height 0.6 m, dry weight 0.9 t, survey speed: 1.2 m s^{-1} , max. depth of operation: 150 m; operating depth during trial: 20 m and 10 m, matched to the maximum ice draught. Data transfer from emerged AUV and remote mission programming via radio link
 Inertial navigation system: MARPOS®. Ring laser gyro coupled with Doppler velocity log and DGPS between the missions. Accuracy of navigation: 0.1% of the track distance
 Sidescan sonar: Tritech, type: SeaKing; 675 kHz; further sensors: CTD (conductivity, temperature and depth unit)
 Image ©: Peter Wadhams, Dpt. Appl. Mathem. and. Theor. Physics, Cambridge University ■

and development of climate. Monitoring techniques which permit the determination of the instantaneous total ice volume related to the regional coverage of ice, both of inland-ice and sea ice are needed to improve realistic climate modeling. Moreover, the balance of ice flows depends on particular features of the ice, its age, its thermal history of melting and freezing, and its quality of consistence. To record such features including the ice thickness, other than by selected samples, was nearly impossible in the past.

The series of sound images from the *underside of Arctic sea ice* during an Arctic winter presented hereafter are the first made by an *autonomous underwater vehicle (AUV)*. These exemplary, pioneering investigations made in 2002 were instigated by alarming evidence of recent changes in the Arctic. They indicate that the sea ice cover is undergoing significant thinning and retreat.

The authors argue the two different mechanisms causing the shrinkage of polar ice: General circulation models using greenhouse gas forcing predict that the



Image 5.4.4-2.

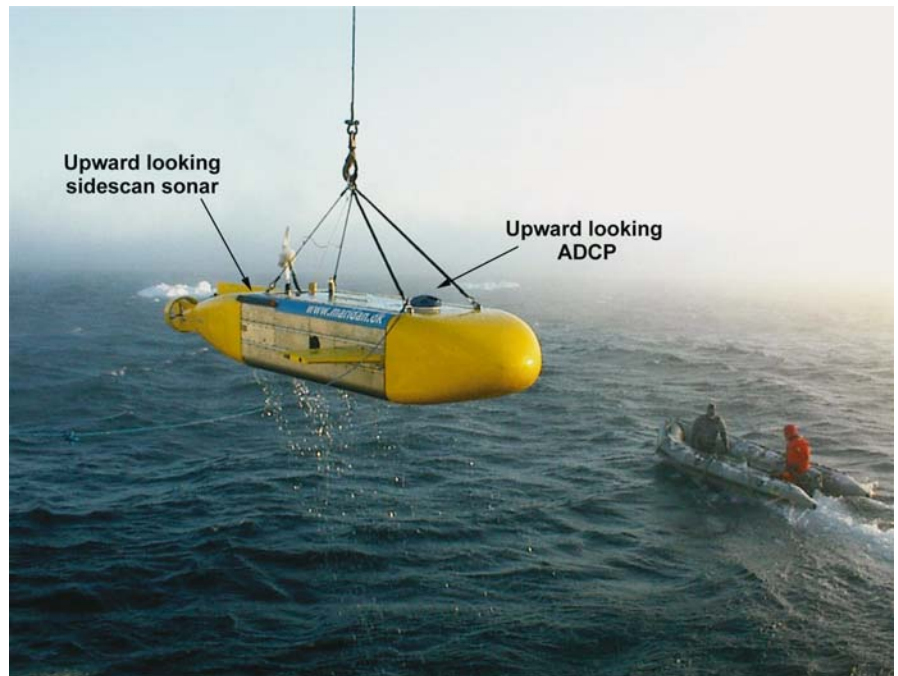
The Autonomous Underwater Vehicle (AUV). Nearly emerged before pick up in the marginal ice zone of the East Greenland Current. The short wings near the bow are for depth steering. The scientific payload is incorporated in the dark middle section. All ice types were present from newly formed ice to multiyear floes.

Image ©: Peter Wadhams ■

Image 5.4.4-3.

Recovery of the AUV by the starboard side crane. The photo shows the side-scan transducers, mounted at the two upper corners of the AUV and the upward looking ADCP for autonomous navigation.

Image ©: Peter Wadhams ■



Arctic ice cover will continue to diminish due to global warming and may become seasonal already by the 2080s. At the same time, it is possible that the current ice shrinkage is a response to oceanic and atmospheric changes associated with the so called Arctic Oscillation (AO) and that they will reverse when the AO itself changes phase. To resolve this question, it is considered essential to monitor the Arctic ice cover on a seasonal and interannual basis.

Though the instantaneous *ice coverage* is easily accessible by satellite imaging, it is difficult to map the *ice thickness* from above. Satellite laser-altimetry could perhaps measure the *freeboard*, the thickness of the ice floes cropping up but a full experimental validation is still pending. Since all local methods such as drilling or surface sounding cannot provide data for economic mapping, the authors consequently state that under-ice imaging by upward-looking sonar from submarines was the method of choice. Moreover, particular features such as melting surfaces can only be visualized from below. Two pioneering submarine experiments by the authors took place in the Arctic already in 1976 and 1987.

The adequate alternative to submarines, which are being operated more sporadic since the end of the Cold War, is doubtless the AUV for under ice surveying. This

unmanned platform conducts scientifically controlled missions on demand at any time, its operation is essentially cheaper and the scientific payload can readily be tailored to the respective mission.

One of the key capabilities of an AUV is its navigational accuracy, which has to rely on inertial navigation since a submerged vehicle has no access to GPS. The core of the inertial navigation system is a ring laser gyro coupled with a Doppler Velocity Log (Sect. 4.5.2) and fed by further data from pressure, salinity, and temperature sensors. The expected error from this system is 0.1% of the track distance, which depends on the battery capacity. This limitation could be overcome to a large extent by installing a fuel cell power plant in the future.

The first scientific trial under Polar ice with an upward looking sidescan sonar (Sect. 4.3) installed on an AUV took place in February 2002. The AUV was deployed by a research vessel in the East Greenland pack ice at 73°00' N, 11°47' W, as part of a research program of the European Union on convection in the Greenland Sea. The sound images presented are selected from this mission.

The sidescan under ice images reveal characteristic clues of first-year, multi-year, brash and frazil ice. Remarkable as well is the different appearance of the

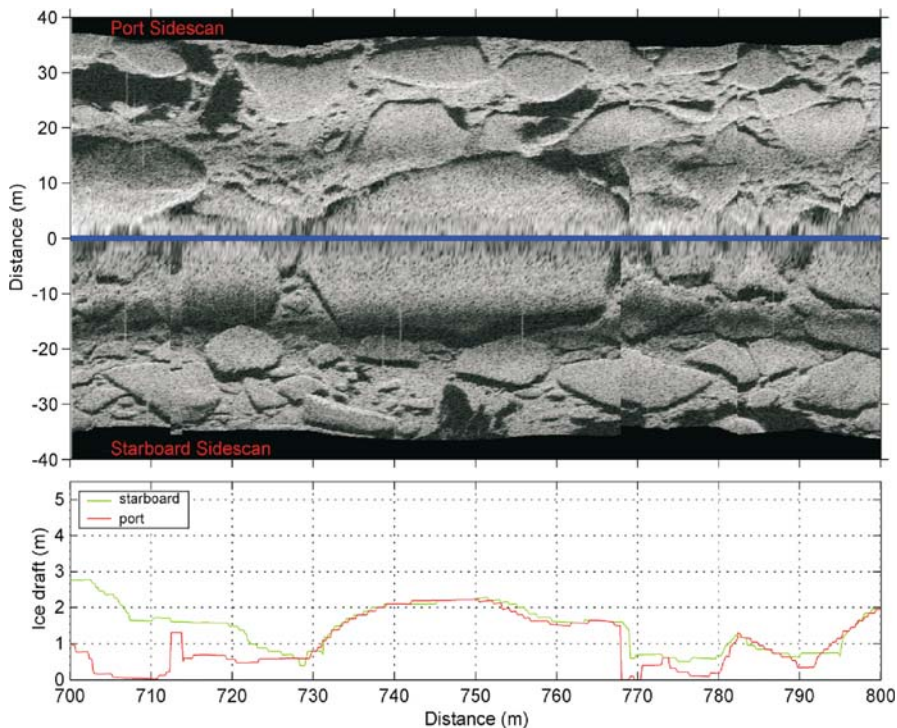
Image 5.4.4-4.

Sidescan image of ice floes from below. The section of 100 m shows the rear side of size and shape of typical ice floes of the area and time of the year. The pair of draught profiles below confirms the visual impression from the sidescan image that the sea surface is completely covered with floes and brash fragments. The large multi-year floe in the middle of 40 m length and 2 m draught has a shallow “keel” whereas others have wedge shaped undersides.

Image documentation:

see Image 5.4.4-1

Image ©: Peter Wadhams ■

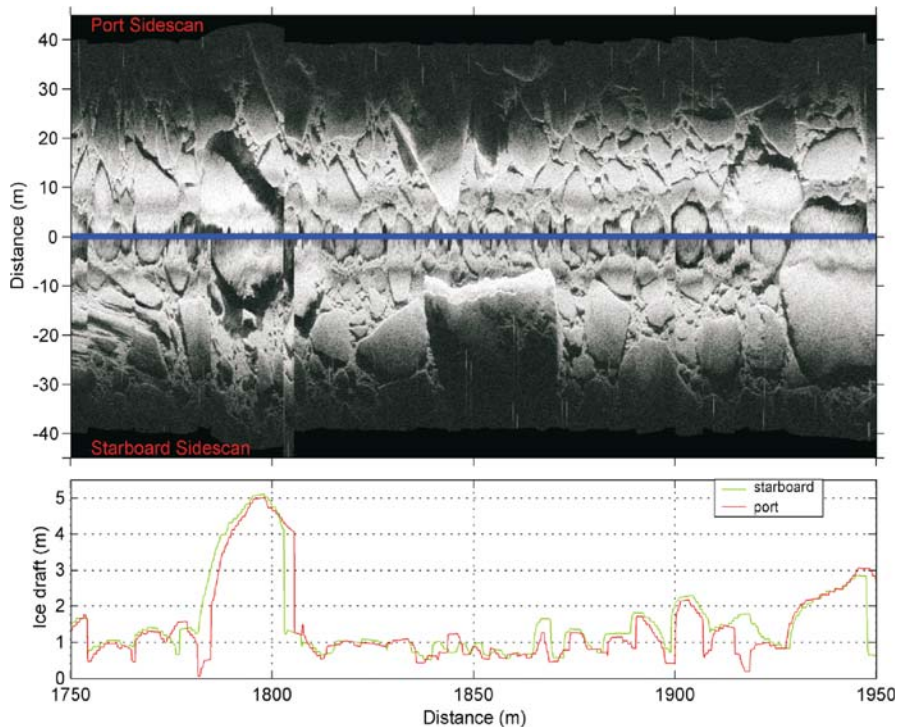
**Image 5.4.4-5.**

Example of a thick floe. The 200 m section underlines the irregular distribution of kind, size, and shape of the floes. The very thick 40 m floe with a keel depth of 5 m is surrounded by small rounded floes of a few meters as well as by sharp edged, broken examples.

Image documentation:

see Image 5.4.4-1

Image ©: Peter Wadhams ■



smooth underside of multi-year East Greenland pack ice, implying downstream bottom melt, as compared to the rough underside in the cold Arctic Basin, detected by the earlier submarine measurements.

The finding of direct climatic relevance was the essentially unchanged ice thickness statistics since the submarine measurements of 1987 in the same area. The

thickness of the individual floes was derived from their draught profile. The draught contour reminds of the depth profile of the sea floor as provided by a conventional downward looking echosounder. Here, this profile was obtained from the first echo arrival, which corresponds to the vertical part of the upward looking sidescan beam.

Image 5.4.4-6.

Examples of floe shapes. These 30 m flows occasionally parading along the track line exhibit a symmetrical keel, 2.5 m deep, similar to a ships hull. The gaps between the larger single floes are completely closed by all types of ice: frazil, brash and pancake floes with smaller ice debris in between. Nearly all the images of the missions show only floes side by side not one upon the other.

Image documentation:
see Image 5.4.4-1
Image ©: Peter Wadhams ■

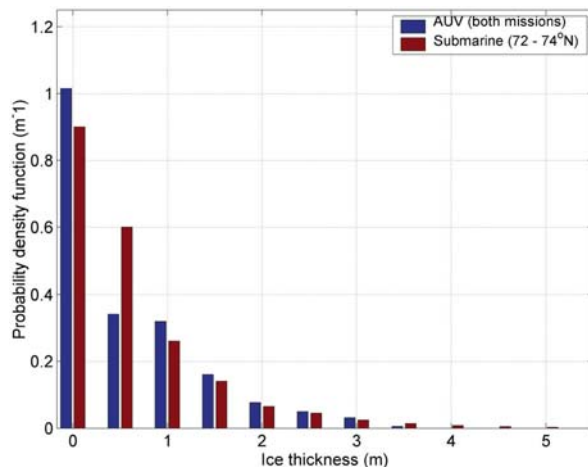
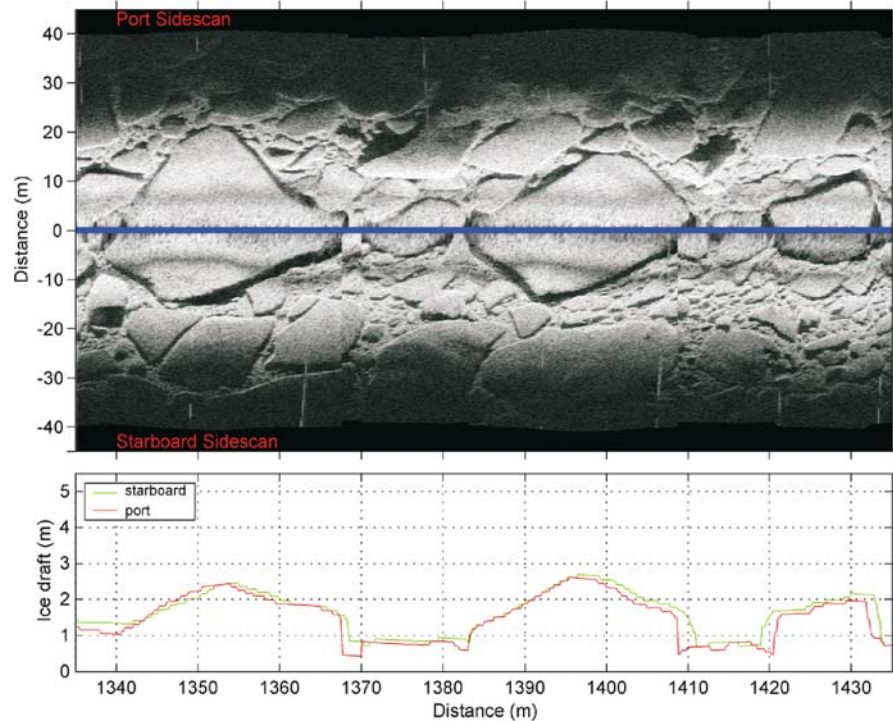


Image 5.4.4-7.

Statistics of ice floe draught. The blue bars depict the probabilities of the ice floe draught which means the plunged thickness, as measured along the centerline of mission 2 by the upward looking sidescan sonar mode. The data from the starboard and port side channels are combined. The red bars refer to the respective data obtained in May 1987 by the submarine *HMS Superb* from latitude ranges 72–74° N. The most frequent ice draught recorded was within 1–1.5 m. The maximum of the distribution close to zero draught is due to the open water sites covered. Within the 15 years between the two measurements the probabilities don't exhibit an alarming shrinkage of the less frequent thick floes of the East Greenland Current.

Image ©: Peter Wadhams ■

5.5

5.5
Antarctic Features

The Antarctic waters are even more adverse for research sea trials dealing with sea floor imagery than the *Arctic Ocean* areas because of the adjacent center of the largest permanent ice volume of the globe, covering the Antarctic continent several kilo-

meters thick. Even icebreaker research vessels are restricted to areas free of the huge tabular icebergs and most of the shelf ice is an invincible barrier at any time of the year. Bathymetric research at sea has concentrated more on the Weddell Sea than on the Ross Sea because of the key processes of tectonic break-up, the initial phase of the formation of the southern continents.

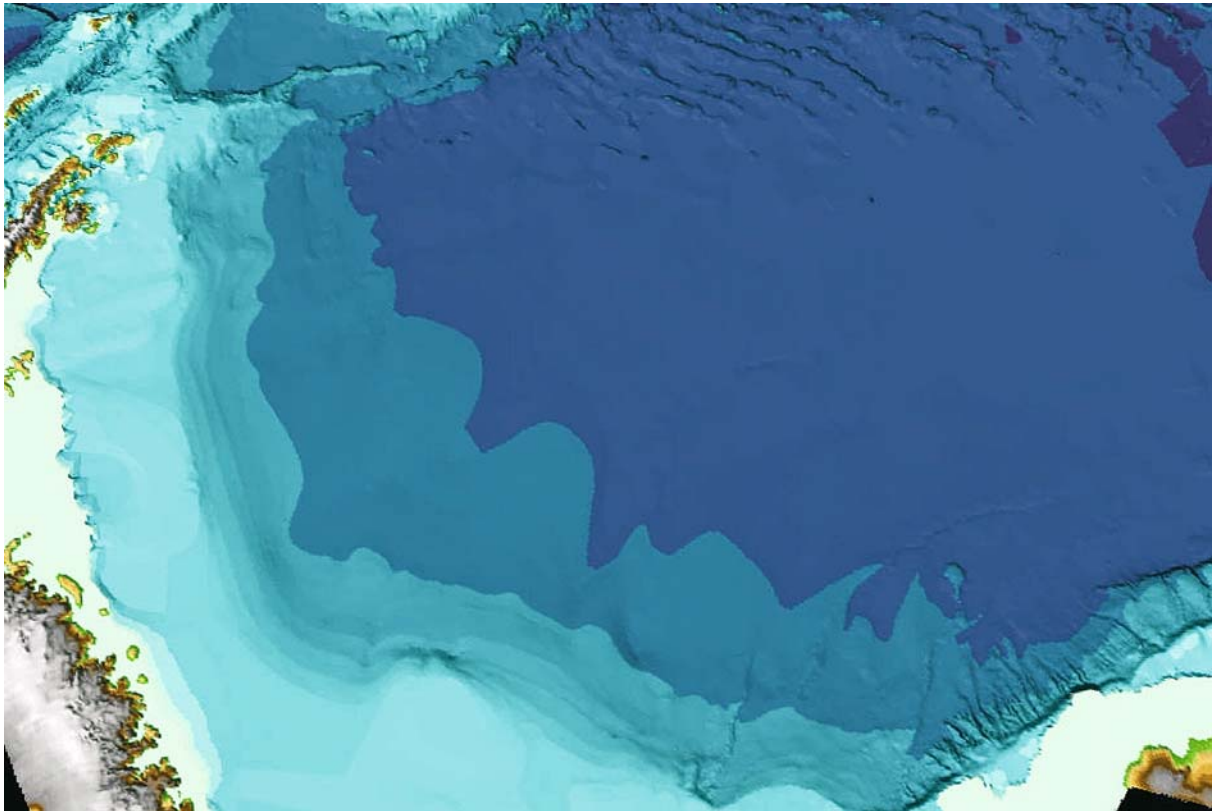


Image 5.5.1-1. Overview of the Weddell Sea. Composite and multibeam image. This overview of the central Weddell Sea with part of the Antarctic Peninsula on the left side shows the broad shelf areas in the west and south with their smooth relief, and also a short section of the *Explora Escarpment*, the narrow, fissured, double shelf break off Coats Land on the lower right edge of the image. Looking closer, a step break – though less pronounced – is also present on the peninsula side. The *Herringbone* relief, obvious on the upper right part of the image, is depicted completely in the Image pair 5.5.1-4a,b. The southern, large and gentle shelf break shows several hardly recognizable bight-like incisions, which carry canyon names in some maps, and appear to mark the northward propagation of the shelf ice. Iceberg plough scars in the Weddell Sea are shown in detail in the close-up images of Sect. 5.5.3. *The bathymetric Weddell Sea relief can be turned and zoomed with the Fledermaus-file on the CD attached to the book.*

Project: AWI, Antarctica, ANT series; years of survey: since 1984

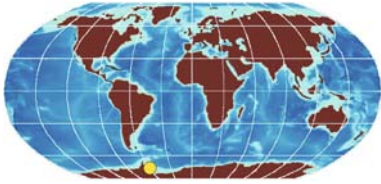
Polar research vessel: *RV Polarstern*, Germany

Multibeam system: 1984–1989: General Instruments, SeaBeam; frequency 12 kHz; thereafter: ATLAS Elektronik, type: Hydro-sweep; frequency 15.5 kHz; beamwidth 2°, 59 beams covering a fan of 90°

Bathymetric Chart of the Weddell Sea, AWI-BCWS

Image ©: Hans Werner Schenke, Alfred-Wegener-Institute for Polar and Marine Research, AWI, Bremerhaven, Germany ■

5.5.1 Features of the *Weddell Sea, Antarctica*



There is particular interest in the Weddell Sea regarding the origin of the present face of the Earth: The Weddell

Sea is considered to be the cradle of formation of the southern hemisphere's continents due to the break up of the southern super-continent *Gondwana* that is believed to have started here during the Jurassic, about 160 million years ago.

The *Weddell Sea* of the *Antarctica* with its nearly 3 million km² – about five times the area of France – is the larger of the two broad incisions into the Antarctic continent. The land boundaries of this large bay are defined by the coasts of the *Antarctic Peninsula* – separated from the southernmost tip of Argentina and

Chile by the *Drake Passage* – and *Coats Land* on the other side. The southern Weddell Sea shelf is covered by huge, permanent ice shelves: the *Ronne Ice Shelf* in the east of *Ellsworth Land* and the *Filchner-, Brunt-, and Fimbul Ice Shelves* off *Coats Land*. The frontal ice

5.5.1

Box 5.5.1-1. The *Explora Escarpment*

The cliff-like *Explora Escarpment*, that trends N 60° E and descends steeply up to 30° from the middle slope off *Queen Maud Land* at about 3 000 m to the abyssal plain of the *Weddell Sea* at about 4 500 m water depth, was discovered in 1978 during the BGR-78 *Antarctic Cruise* with *MS Explora*.

This distinct escarpment represents the initial break-up edge of *East Antarctica* from *Africa* at about 190 to 180 million years ago when Africa and East Antarctica began to move away from each other.

Karl Hinz · BGR, Hannover

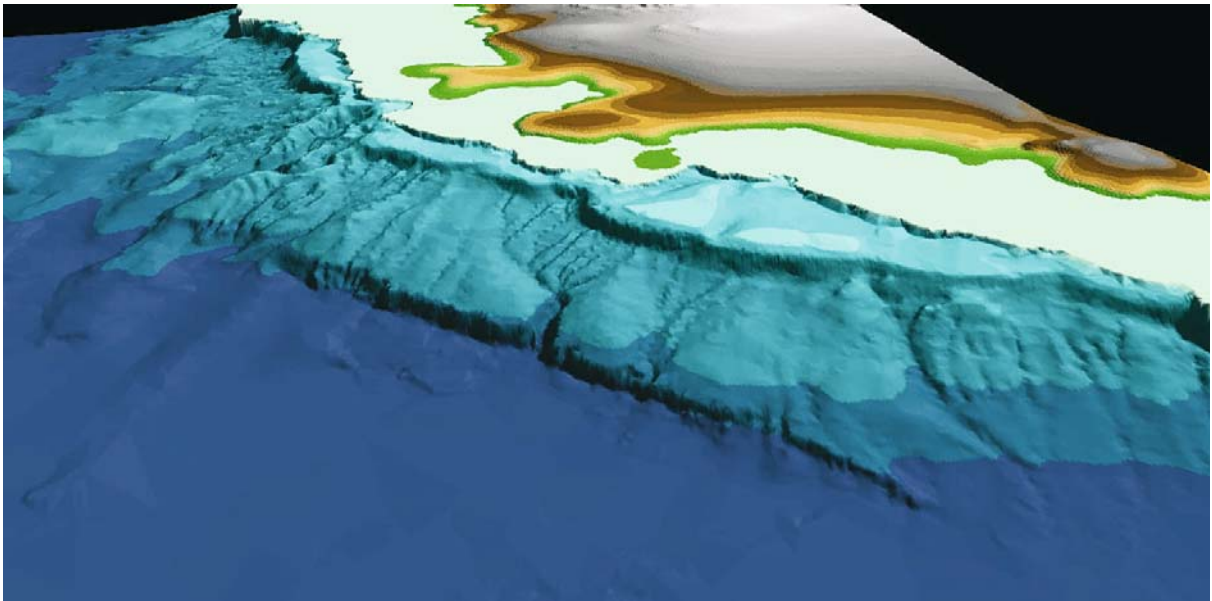


Image 5.5.1-2. The *Weddell Sea*; continental margin in the south-east. Multibeam image. The Shelf break along the *Explora Escarpment* of more than 200 km length with the center coordinates 70° S, 15° W running through the middle of the image shows the fissured step between the two breaks. A small third break above is presumably caused by ice induced erosion. Here, in the south-east, the submarine canyons deserve this name since they incise the lowest break with their tributaries starting directly below the second break, indicating suspension flow from melting ice. The deeply incising *Wegener Canyon* in the center of the image is a textbook-like example with its fan of eight tributaries. The large, irregular group of troughs visible on the left side is shown as a close-up in Image 5.5.1-3.

Image documentation: same as Image 5.5.1-1 ■

break of more than 200 m thickness is the source of tabular icebergs, even thicker than those of the *Ross Sea* (Sect. 5.5.4) on the opposite side of the continent. The Weddell Sea is considered to be the main source of the oceanic near-bottom cold water distributed worldwide through the *Southern Ocean* by its circum-polar current.

The sea is named after the British sailor *James Weddell* who entered the area in 1823 going as far as 74° S. Although the Antarctic Treaty effectively holds in abeyance all claims to sovereignty in Antarctica, the States of Argentina, Chile, Norway and the United Kingdom have made claims to the maritime space of most of the Weddell sea, which partly overlap. The Weddell Sea was first explored by the Scot *William Bruce* between 1902–1904 but systematic exploration including permanent research stations along the

southern coasts started only in 1956/1958 as part of the *International Year of Geophysics*. The first high resolution bathymetric mapping by multibeam echosounding was conducted by Germany in 1986 with the research icebreaker *Polarstern*. This research work, continued since and supplemented by many bathymetric measurements of further countries, has provided the *AWI Bathymetric Chart Weddell Sea (AWI BCWS)*, the first complete, quantitative relief map of this Antarctic area (Image 5.5.1-1). The unified grid width of the map is 1 000 m; selected regions have been acquired by multibeam imaging with 100 m resolution. The 1-km grid bathymetric image of one of the most remote and adverse areas of the world yields access to very early traces of the shift of continents.

The bathymetric relief of the Weddell Sea based on sound imaging is compared here with the sea

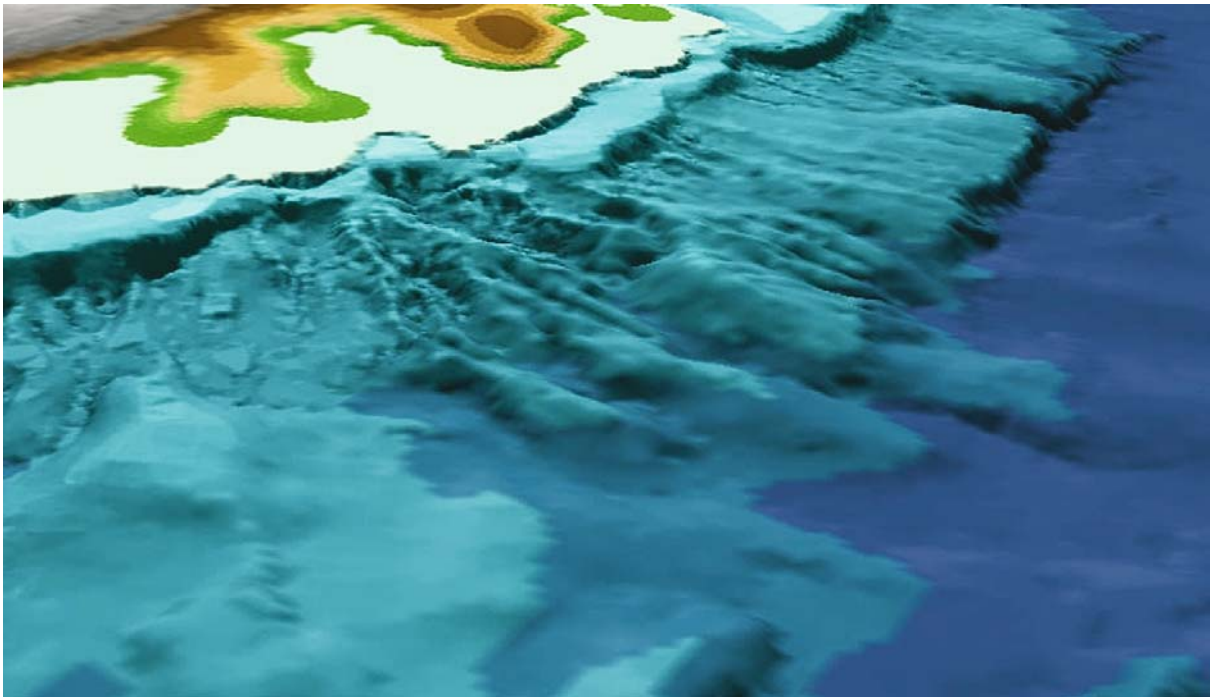


Image 5.5.1-3. The Weddell Sea; close-up of the preceding image, left part. Multibeam image. The conspicuous group of seemingly irregular troughs and ridges visualized in the middle of the image covers several thousand km² and marks the end of the double shelf break. It demonstrates that the second plateau is incised into the first. Though apparently different in shape from the neighboring *Wegener Canyon* this formation is considered to be also a consequence of sediment transport with the troughs acting as channels. The ridge-like sidewalls of these channels are part of a so-called *channel-levee-system*, indicating overflow and re-sedimentation of suspension load beyond the channel flanks, similar to the Bengal Fan (Sect. 5.3.2), caused by turbidite flow of high transport rates. Here, the transport comprehends both suspension caused by melting and debris flow of coarser material.

Image documentation: same as Image 5.5.1-1 ■

floor relief derived from the satellite radar altimetry data set of *Smith and Sandwell* (Sect. 5.1.1). The non-acoustic method which is essentially based on the recognition of gravity anomalies reveals also sea floor structures buried by thick sediment because its lower density does not compensate the unequal mass distribution below. This comparison (Image pair 5.5.1-4a,b) of the two independent methods reaches to 72° S – the maximum orbit latitude – and shows the most pronounced differences in the north of the Weddell Sea near the Antarctic Plate margin. This zone is infamous for its earthquakes since it is part of the tectonic strike slip fault (Sect. 5.2.5) conterminal to the subduction zone of the small Scotia Plate (Sect. 5.2, 5.1.1.6).

The Antarctic shelf with its average depth of 500 m is much deeper than other continental shelves which are typically 200 m deep. The Weddell Sea shelf is the broadest by far of the continent with nearly 240 km along the southern Antarctic Peninsula and twice that in the south of the sea (Image 5.5.1-1). However, there is an obvious deviation from the typical shelf profile with a single break, slope, and rise (Sect. 5.3). In the south-east off Coats Land, the Images 5.5.1-2 and 5.5.1-3 show a relatively narrow inner shelf and a wider outer shelf. The latter is characterized by an irregular seabed topography with canyons, sediment fans and drift sediments formed predominantly by water currents. A prominent escarpment with offsets in the range of 1000 m and more, named the *Explora Escarpment*, marks the steep transition from the outer shelf to the deep Weddell Sea off Coats Land. Such step profiles exist also on other continental margins but are mostly hidden by thick sediment coverage. Here the step was caused by an interruption in sedimentation of 80 million years, revealed by drilling information, obtained in 1986/1987 by expeditions of the *Ocean Drilling Program*. The step in basement topography remained mostly uncovered by sediment after the subsequent continental break up.

A particularly remarkable sea floor formation is found east of the northern Antarctic Peninsula island chain and is seemingly a rare feature: the so called *Herringbone Relief*, which is part of a fundamental process of plate tectonics described in the context of the Image pair 5.5.1-4a,b.

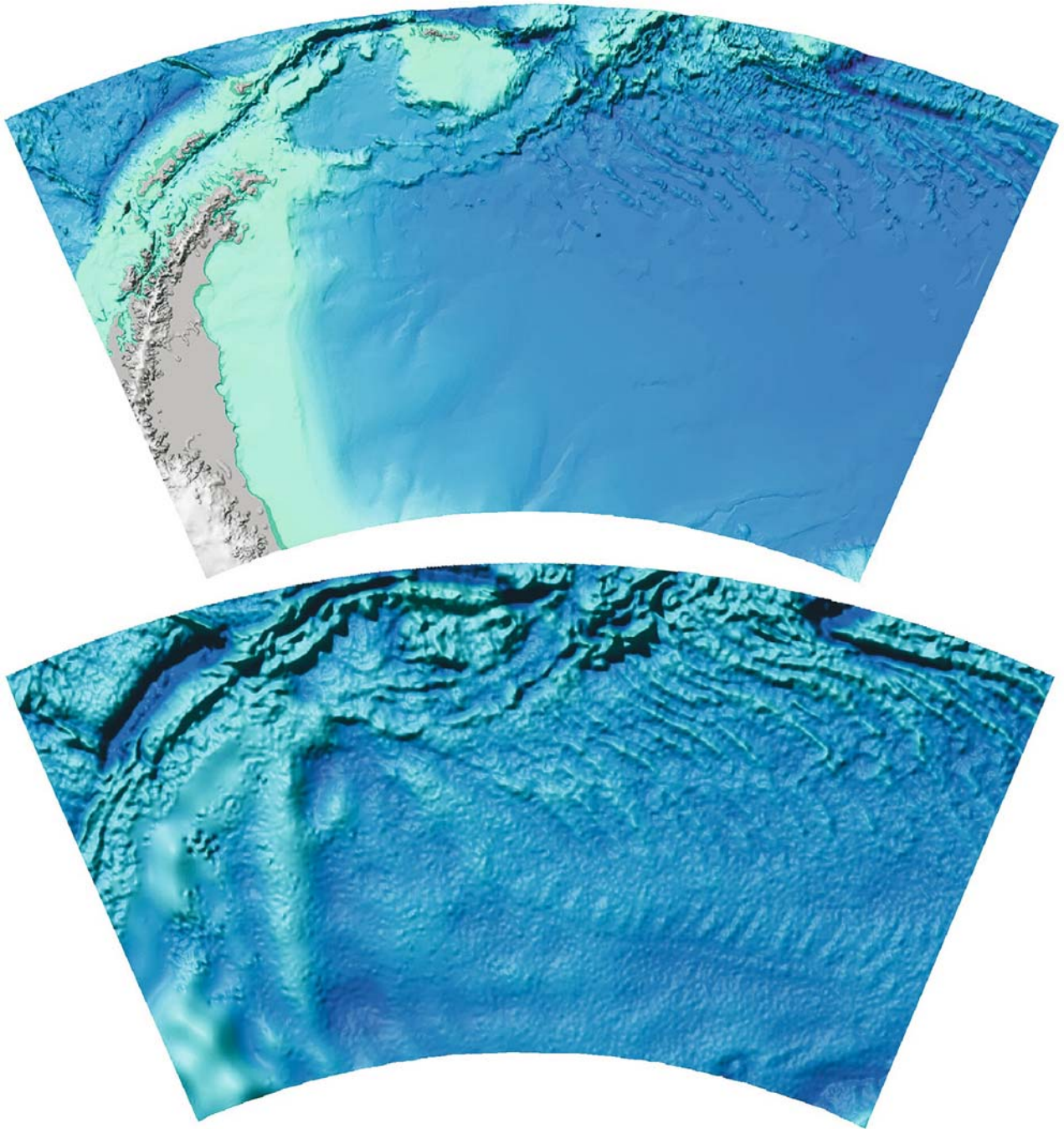
Images 5.5.1-4a,b. (see page 220)

The Weddell Sea. Herringbone Relief. Comparison of high resolution multibeam bathymetry and satellite altimetry. The so-called *Herringbone Relief* of self-evident shape dominates the north-eastern part of the Weddell Sea floor. It is one of the most fascinating relief structures of the ocean floor because it reaches back to the break up of the supercontinent Gondwana. The seemingly enigmatic, large-scale, curvilinear, periodic feature has been elucidated in its essence by comparative imaging of satellite radar altimetry and acoustic and seismic bathymetry.

The dating of feature elements has been based on measurements of the paleo-magnetic anomalies of the spreading sea floor. This method is of fundamental importance since it confirmed and quantified the continental drift as suggested by Alfred Wegener and the rise, shift, and set of new sea floor. The key discovery of Vine and Matthews in 1963 revealed the remanent magnetism of cooled down upwelling magma at spreading centers, documenting the contemporary orientation of the changing polarization of the magnetic axis of the Earth with periods of hundreds of thousand years, producing the famous magnetic *zebra stripes* of the ocean floor. The method is applied to determine both the spreading rates and the corresponding age of the ocean floor worldwide as repetitively mentioned in this book. The decisive facts and circumstantial evidence related to the early tectonic processes of the Weddell Sea area at the time of the continental break were achieved only in the late nineties of the last century by air- and shipborne surveys, mainly because of the adverse conditions for ship-borne measurements due to perennial ice coverage.

The following – simplified – comment on the character of the *Herringbone Relief* requires some effort of the reader to follow because four images are used in parallel. We inspect at first the globe image *Antarctica*, centered on the south pole (Sect. 5.1.1.6). This overview is essentially based on the Smith & Sandwell satellite data set and thus reflects mainly the gravity anomaly. There we see the most conspicuous sea floor feature at the prolongation of the Antarctic Peninsula: the dark arc of the deep subduction trench at the eastern end of the small *Scotia Plate* which is literally squeezed in between two large tectonic plates: the *South American Plate* and the *Antarctic Plate*. The location and margins of the Scotia Plate as well as of the other tectonic plates are depicted in the *schematic global map of plate tectonics* (Sect. 5.2), the second of the four figures. The short, arched subduction trench of the Scotia Plate is the southern one of only two in the entire Atlantic Ocean.

Returning to the globe image *Antarctica*: Behind the subduction trench arc, i.e. west of it, we see the *Sandwich Island-* and seamount-chain. This so-called *back-arc* ▶



◀ chain indicates the *Marianas* type of subduction (Sect. 5.2.2) where the subducted piece of sea floor is tearing the opposite side. Here it is a piece of the western Atlantic, belonging to the South American Plate, which is subducted.

The *schematic map* shows further that the Weddell Sea floor borders on *three* tectonic margins: in the west it is the strike slip fault along which the Scotia Plate moves westwards. Looking at *Image 5.5.1-4a*, the third of the four images, this strike slip fault area nearly coincides with the up-

per rim of the image. Going eastwards in the *schematic map*, the western strike slip fault transits to the southern end of the subduction trench arc, which is also visible near the upper rim of *Image 5.5.1-4a*. Further eastwards in the *map*, directly adjacent to the trench arc, we see the next strike slip fault where the South American Plate is also shifted westwards, or more correctly drawn along the common margin of the Antarctic Plate (Sect. 5.2). This part of the map summarizes and simplifies the *ongoing* tectonic processes of plate motion in the area. Their circumstantial evidence can be derived from the sea floor relief as we will see now. Thereafter we will comment on features dealing with the early beginning.

The globe image *Antarctica* demonstrates above all the character of the Herringbone relief. *First*: the image reveals that the herringbone series of the Weddell Sea is essentially the western continuation of the curvilinear pattern of fracture zones which reach to the southern end of the Mid-Atlantic Ridge (MAR) in the east, and altogether indicate the track of the strike slip fault. The fracture zone character is underlined by the strongest of these faults, visible as a strong dark line. In *Image 5.5.1-4a* it runs near the upper rim, forming an edge with the end of the trench arc. *Second*: the westward motion of the South American Plate, which contains the western Atlantic sea floor, and of the small Scotia Plate, appear directly evident from the curved fracture pattern, including the Herringbone relief of the Weddell Sea. The curvature indicates the deformation of the adjacent Antarctic Plate through shear stress. It could be reminiscent of hot, plastic glass with internal stripes, when *drawn sideways* by the glass-blower. A kind of quasi viscous deformation, instead of an abrupt break, typical of the Mid-Atlantic Ridge (Sect. 5.2.3) is visualized in the image of the *Wilkes Fracture Zone* of the *South Pacific Rise* (Sect. 5.2.4).

When looking closer by zooming the globe image *Antarctica* on the CD, we can see that some of the curvilinear faults on their northern side appear to have been stopped by the southernmost of the transform faults athwart of the MAR which are known to run nearly exactly along constant latitude (Sect. 5.2.3). This however constitutes circumstantial evidence that the field of faults which accompany the strike-slip plate margin on both sides has younger activities than the adjacent part of the MAR.

Hints as to the early beginning of the continental break up require the comparison of the two *Images 5.5.1-4a* and *5.5.1-4b*, again regarding the Herringbone structure. *Image 5.5.1-4b*, the fourth of the image quartet used in this context, is the relief derived from gravity anomaly measured by satellite radar altimetry as mentioned. Obviously the real bathymetry 4a and the relief based on gravity anomaly 4b show essentially the same Herringbone structure in the north. But whereas the bones disappear towards the south

in the bathymetry, they still show up in the gravity relief and, most interestingly: *they turn their orientation clockwise but disappear in between*. Since the satellite altimetry radar “sees” the mass-defects and -concentrations there must still be a relief but it is hidden from the “sight” of echosounding by thick sediment. Seismic measurements between 66° S and 72° S in the western Weddell Sea (not shown) have revealed a sediment fill of the basin of up to 7 km thickness! This underlines that the gravity anomaly method is a highly sensitive differential measurement; the main contribution from the body of the Earth is by orders of magnitude larger than that of a single ridge, which is nevertheless not masked by an even enormously thick sand layer, if this is sufficiently homogeneous in the horizontal. The main clue for this interpretation is the modeled variation of crustal thickness which shows a decrease to values of around 4 km to 2 km along the gravity minima.

Returning to the southern Herringbone fracture zones of *Image 5.5.1-4b*: The deeply buried southern Herringbone row – visible in the image below the interruption, its direction pointing towards the present strike-slip fault at more than a right angle – does not correspond to the same shear induced disruption caused by the westward motion of the adjacent plates. Instead, it indicates the contemporary predecessor to the present strike slip fault: It was a *spreading zone* dividing the present South American- and African Plates from each other and from the present Antarctic Plate diverging at very low speed. The final separation of the Antarctic from South America/Africa happened some 135 million years ago. Correspondingly, the gap between the northern and southern Herringbone relief sectors is already younger than the continental break up, as revealed by magnetic age determination. The conspicuous equidistance of about 100 km of these fracture zones is still under debate, reminiscent of the near equidistance of the large fracture zones crossing the Pacific, (Sect. 5.1.1) which are also a relic accompanying a former spreading zone.

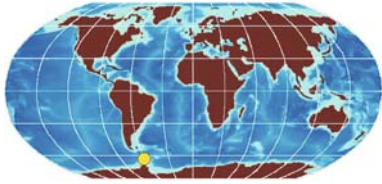
Finally it should be mentioned that the other relief deviations between the smooth bathymetry of *Image 5.5.1-4a* and the rugged gravimetry of *Image 5.5.1-4b* in the west and north-west are also due to thick sediment coverage, hiding sea-floor deformations generated during dramatic eras of the past.

Bathymetric image documentation: same as of *Image 5.5.1-1*, but plane-sector Lambert-projection, 59.5–72° S, vertical view depiction. Shaded bathymetric relief between +300 m and –5000 m. Land: gray/ white. Gravimetric image derived from ETOPO2-data set, Smith & Sandwell. 3-km grid. Emphasis is on morphologic structures; color scale not quantitatively corresponding to bathymetry.

Image pair ©: Ralf Krockner, Alfred-Wegener-Institute for Polar and Marine Research, AWI, Bremerhaven, Germany ■

5.5.2

5.5.2

The Orca Seamount Region, Antarctica

The *Orca Seamount* was discovered in the central basin of the *Bransfield Strait* around the position $62^{\circ}26' S$ and $58^{\circ}24' W$ on the west side of the *Antarctic Peninsula*, the most western area of the south polar continent. Though the discovery was made known in 1987, it was

only during three bathymetric surveys with high resolution fan echosounders between 1993 and 1995 that the character and complete shape of a remarkable volcano-seamount became evident. The data acquisition and processing revealed a spectacular crater of 350 m depth. The relative height of this 3 km wide “caldera” rim is 550 m with a basal diameter of the seamount cone of 11 km. Its flanks are about 15° steep but in some places the slope reaches up to 36° . The nearly circular shape of the Orca edifice spreads out with several pronounced spurs, trending parallel to the basin axis in a northeast-southwest direction.

Image 5.5.2-1.

Orca Seamount, Antarctica. Close up multibeam echosounder image. The color coded 3D-image reveals details of the inner crater and the partially irregular rim of the Orca volcano, being one of the largest known in the Antarctica region.

Project: Scientific Expeditions to Antarctica; cruise: ANT XI/3, 1994
 Research vessel:
RV Polarstern, Germany
 Multibeam echosounder:
 HYDROSWEEP DS-2; 15.5 kHz,
 beamwidth: $2.3 \times 2.3^{\circ}$, fan width:
 $90^{\circ}/8$ km at 4 km depth
 Height exaggeration factor: 3,
 simulated steep angle sunlight
 from north-west
 Image ©: Jörn Hatzky, AWI,
 Germany ■

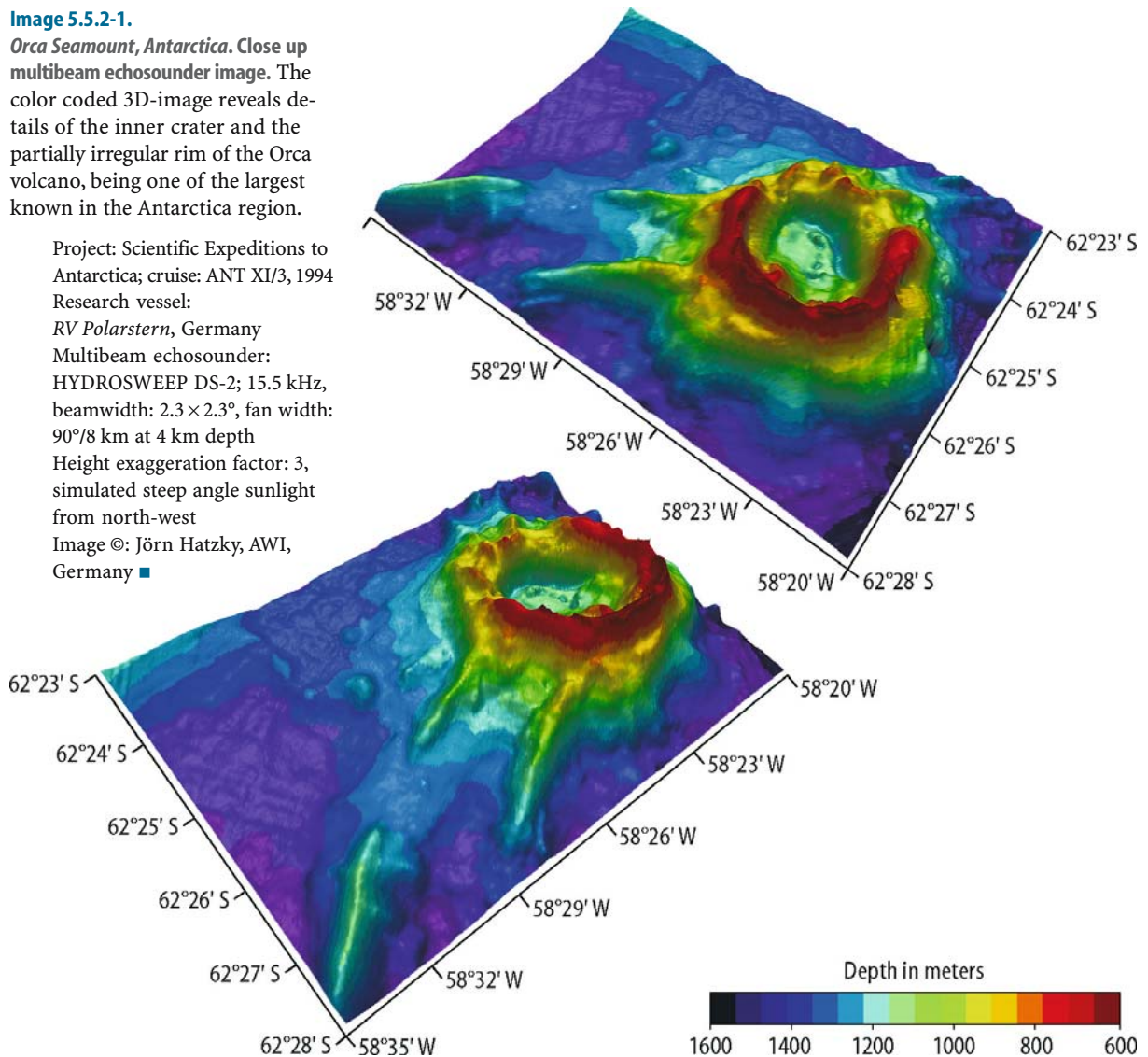
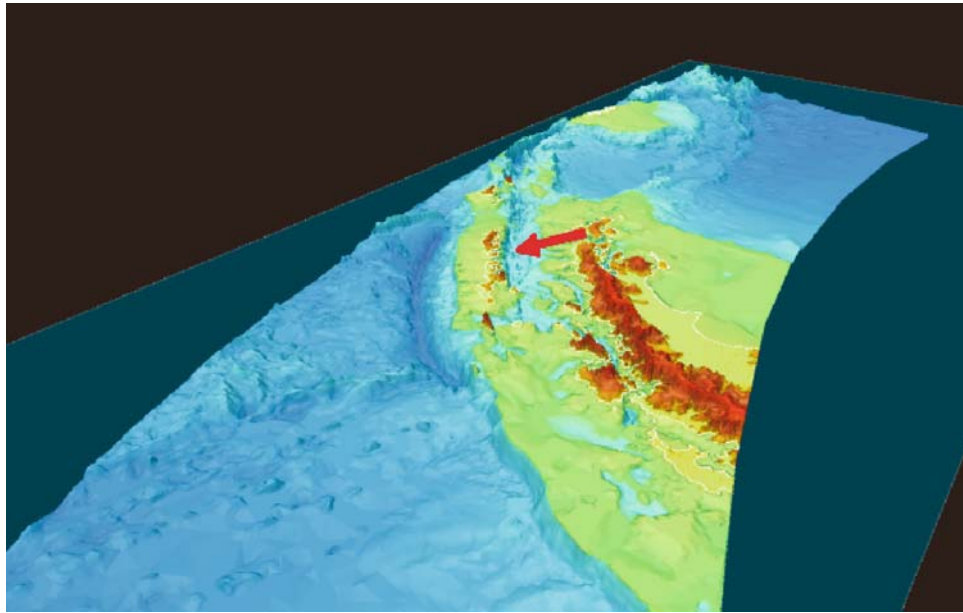


Image 5.5.2-2.

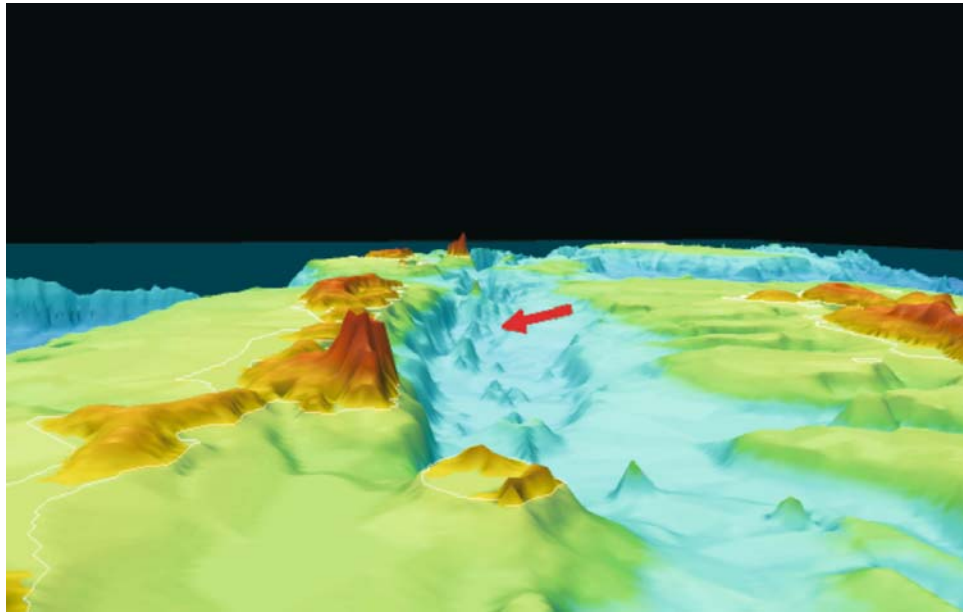
Environment of the Orca Seamount. Multibeam echosounder Image (overview). The arrow indicates the Orca position inside the *Bransfield Strait* along the Antarctic Peninsula. Despite the coarser resolution by the standard grid of 1 km the trench on the western side of 5000 m depth is clearly visible.

Image documentation: same as for Image 5.5.2-1, except: image width at Orca: ca. 670 km; height exaggeration factor: 6 ■

**Image 5.5.2-3.**

Environment of the Orca Seamount. Multibeam echosounder Image (semi close up). The arrow indicates the Orca as one of a chain of seamounts inside the *Bransfield Strait*. The standard grid of the depiction of 1 km, which cannot resolve the crater of the Orca volcano, demonstrates the peerless diagnostic capability of the best high resolution multibeam imaging shown in the close-up of Image 5.5.2-1.

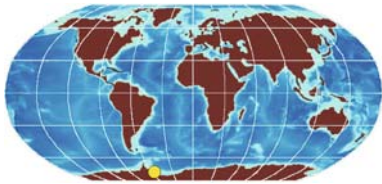
Image documentation: same as for Image 5.5.2-1, except: image width at Orca: ca. 180 km; height exaggeration factor: 6 ■



The globe Image 5.1.1.6, Antarctica, shows the large scale overview of the topography of the Bransfield Strait area: The Strait is the trough-shaped basin of 400 km length and 2 km depth between the *South Shetland Island Arc* and the Antarctic Peninsula, formed by rifting behind the islands. The separation of the South Shetland island chain from the peninsula began possibly several million years ago. The active rifting is still going on however, and

has caused recent earthquakes and volcanism along the Bransfield Strait. The Strait hosts a chain of submerged seamounts of volcanic origin (Images 5.5.2-2 and 5.5.2-3) with the presently inactive Orca Seamount as the most spectacular one. The South Shetland Islands owe their existence to a subduction related volcanism which is perhaps 5–10 times older than the age of Orca and the other seamounts along the central basin of the Bransfield Strait.

5.5.3

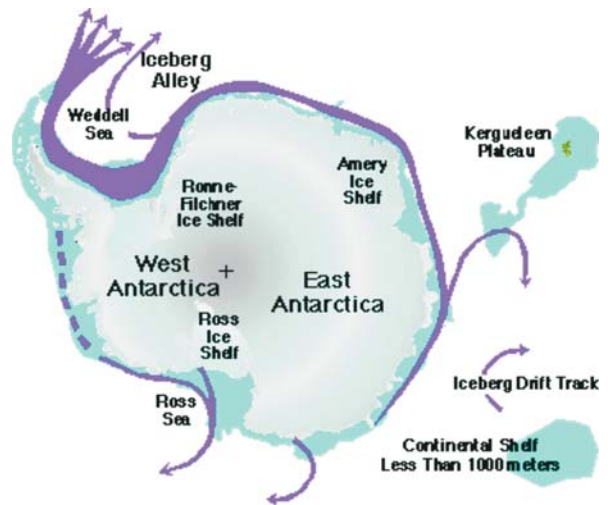
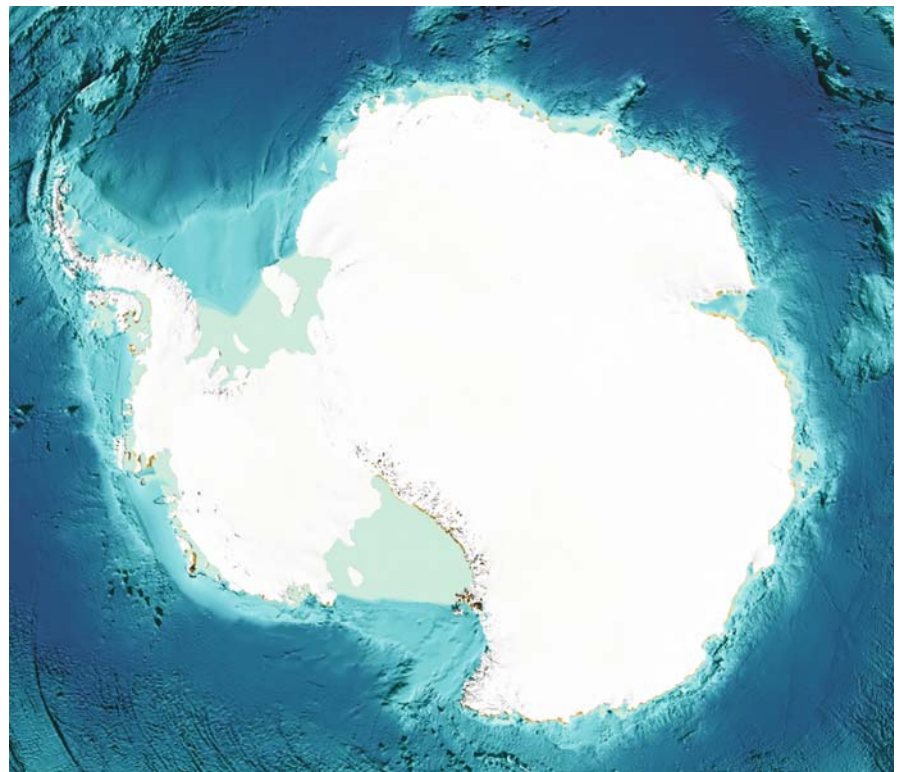
5.5.3
Antarctic Iceberg Plough Scars

Stranding icebergs of the Antarctica produce plough scars in the sediment which are several meters deep, hundreds of meters wide and up to kilometers long. By removing about a million cubic meters of sediment through a single plough scar the local sea floor fauna is completely destroyed. Since many species living in the Antarctica grow extremely slowly, the stranding of icebergs is considered one of the most enduring disturbances an ecosystem can undergo on Earth. Thus the knowledge of the regeneration of the sea floor fauna is as important as of the phase of destruction. New Icebergs, many of which are slabs of several hundred meters thickness are given birth by breaking off the marine based shelf ice margin. The birth rate is accelerated or retarded, depending on the temperature and thus on the development of climate. ▶p.226

Image 5.5.3-1.

Overview of the Antarctic Continent, cut out of Image 5.1.1.6-1. The cut out is part of the series of globe images (Sect. 5.1.1) with a resolution of 2 arc minutes or about 3 km grid width. The subsequent multibeam echosounder images of the submarine iceberg plough scars were made in the shelf area of the *Weddell Sea*, visible at the upper left corner between the *Antarctic Peninsula* and the continent. This shelf zone is also termed *Iceberg Alley*.

Image ©: Martin Jakobsson, Center for Coastal and Ocean Mapping, Joint Hydrographic Center, University of New Hampshire ■

**Image 5.5.3-2.**

The migration paths of the main iceberg drift. These paths are named the *Iceberg Alley* in the Antarctica. The alley is concentrated along the *Weddell Sea* shelf. The cross indicates the *South Pole*.

Graph ©: Constanze Hohmann, AWI, Bremerhaven, Germany ■

ROV 41

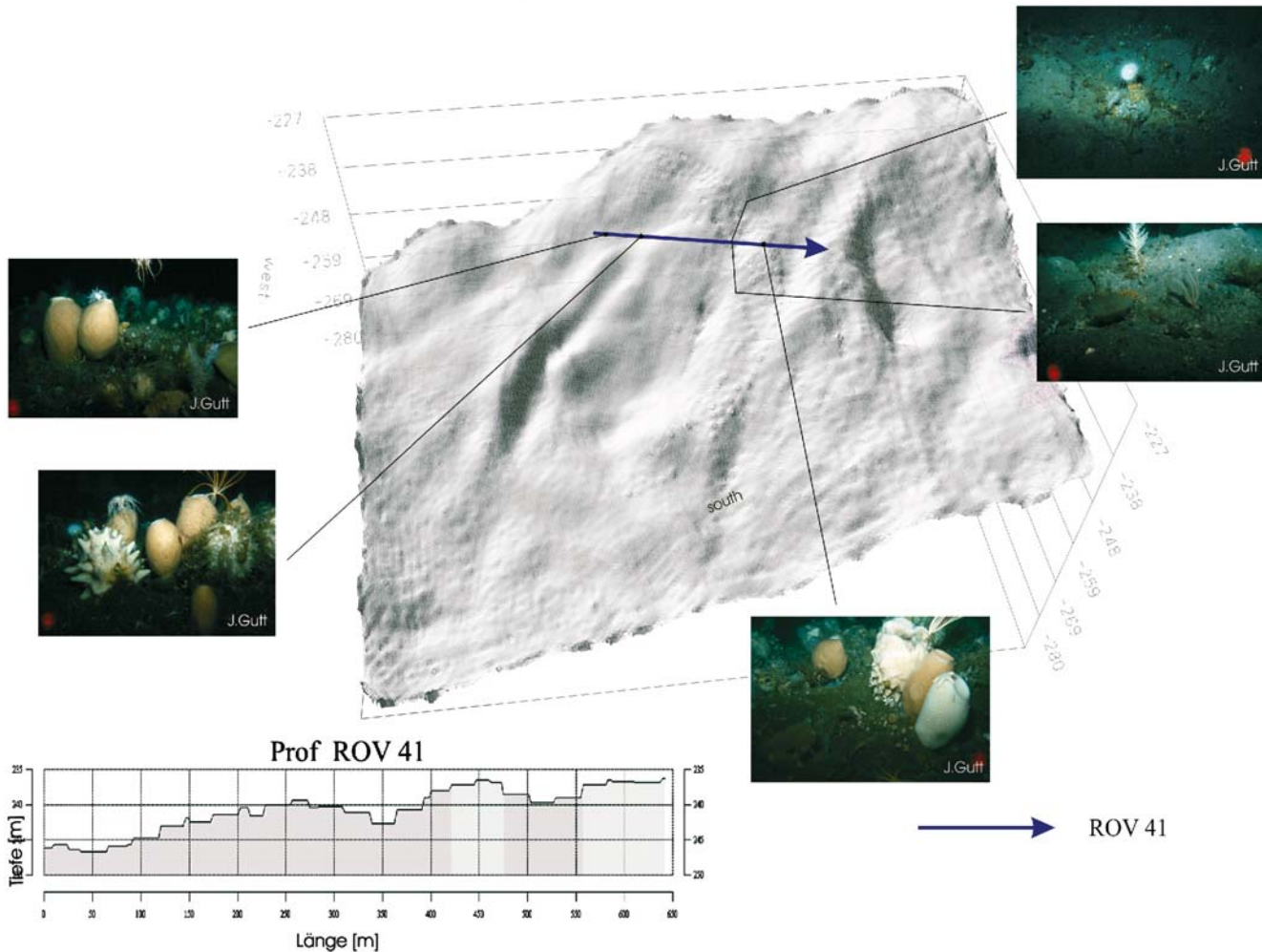


Image 5.5.3-3. Iceberg plough scars, Weddell Sea, Antarctica. Multibeam echosounder image. These shallow iceberg scars of 400–500 m length are 3–7 m deep and about 70 m wide. The close up photographs of the resident fauna were made by a remotely operated submarine vehicle (ROV) outside the iceberg scars, along the path indicated by the arrow. Three of the photographs show unimpaird rich populations of at least eight species (*Ophiuridea*, *Crinoidea*, *Bryozoas*, *Gogonarian*, *Anthozoa*, *Hydrozoa*, and *Asteroidean*); the two others on the right show the first signs of resettlement with three species, after an extinction which presumably occurred many decades of years ago.

The combination of close up photography which cannot recognize the larger scale iceberg plough scars and multibeam echosounding which cannot resolve the small animals is a necessary supplementary documentation concept of this research on natural hazards in the Antarctica.

Project: Iceberg plough scars, 2000, ROV station 41

Research vessel: *RV Polarstern*, AWI, Germany

Multibeam system: STN-ATLAS, type: Hydrosweep DS2; frequency: 15 kHz, beamwidth: 2, 3°, operated at 90° fan width with 59 beams

Standard terrain grid depiction; grid width: 5 m

Image ©: Constanze Hohmann, AWI, Bremerhaven, Germany

Photographs ©: J. Gutt, AWI, Bremerhaven, Germany ■

The investigation from which sound images of iceberg plough scars are presented was conducted near the ice-shelf area of the largest bay of the Antarctic continent, the Weddell Sea, between the Antarctic Peninsula and East Antarctica. The German research icebreaker *Polarstern* by which the shallow *Austaasen Bank* was discovered on the position 70°48' S, 10°30' W in 1997, conducted also the plough scar investigation of this bank several years

later, covering 320 km² with nearly 130 plough scars found. All icebergs of more than 225 m draught forced by the predominant south – south-east current to a collision course with the shallower bank inevitably plough scars of the corresponding depth, mostly along isobaths. Young, slab icebergs plough scars with a broad shallow ground; older, partly melted and tilted ones incise more sharply with maximum scar depths of 15–20 m. An iceberg, like a huge snow

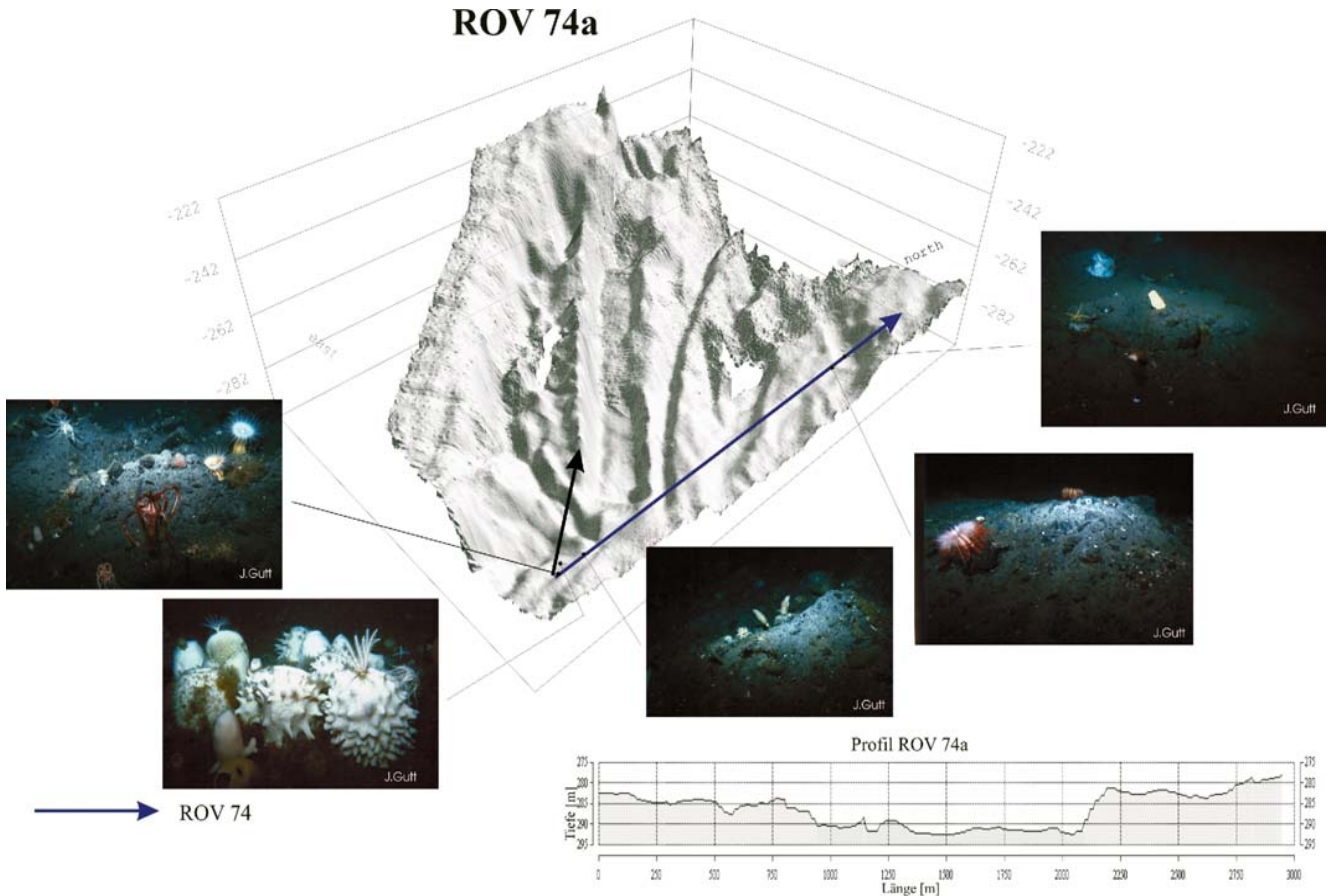


Image 5.5.3-4. Longest iceberg plough scars measured, *Weddell Sea, Antarctica*. Multibeam echosounder image. The ROV transect of about 3 km length indicated by the long arrow shows a scar on the left with a plane bottom profile, presumably ploughed by a tabular iceberg. Another one with an edge profile diverges from the first.

The first photograph shows a recreating population after extinction with seven species, though with small biomass. The dense resident fauna on the next photo is an example of an intact population undisturbed for a long time. The following pictures with very little fauna settlement reveal the empirical indicator of an area of destructive disturbance: a stony, irregular sea floor topography.

Image documentation: same as for Image 5.5.3-3 ■

plough thrusts a kind of sediment end moraine and fills in troughs of the bank relief; a gigantic ploughing equalizer.

The investigation of the state of fauna coverage or absence was possible by means of a remotely operated vehicle (ROV), a small unmanned, cable controlled submarine, as it were, with a video camera. Quantified estimates of the biomass enabled to conclude the age of the scars. The complete recovery appears to

last more than 200 years. The biomass destroyed by an average plough scar amounts to about thousand kilograms. The bathymetry of most of the Antarctic area where icebergs exist, a belt of thousands of kilometers width, is not yet sufficiently known. An estimation of the total amount of self-destruction of sea floor fauna by iceberg ploughing is not possible as yet. Doubtless it is life, dependent sensitively on changes of climate.

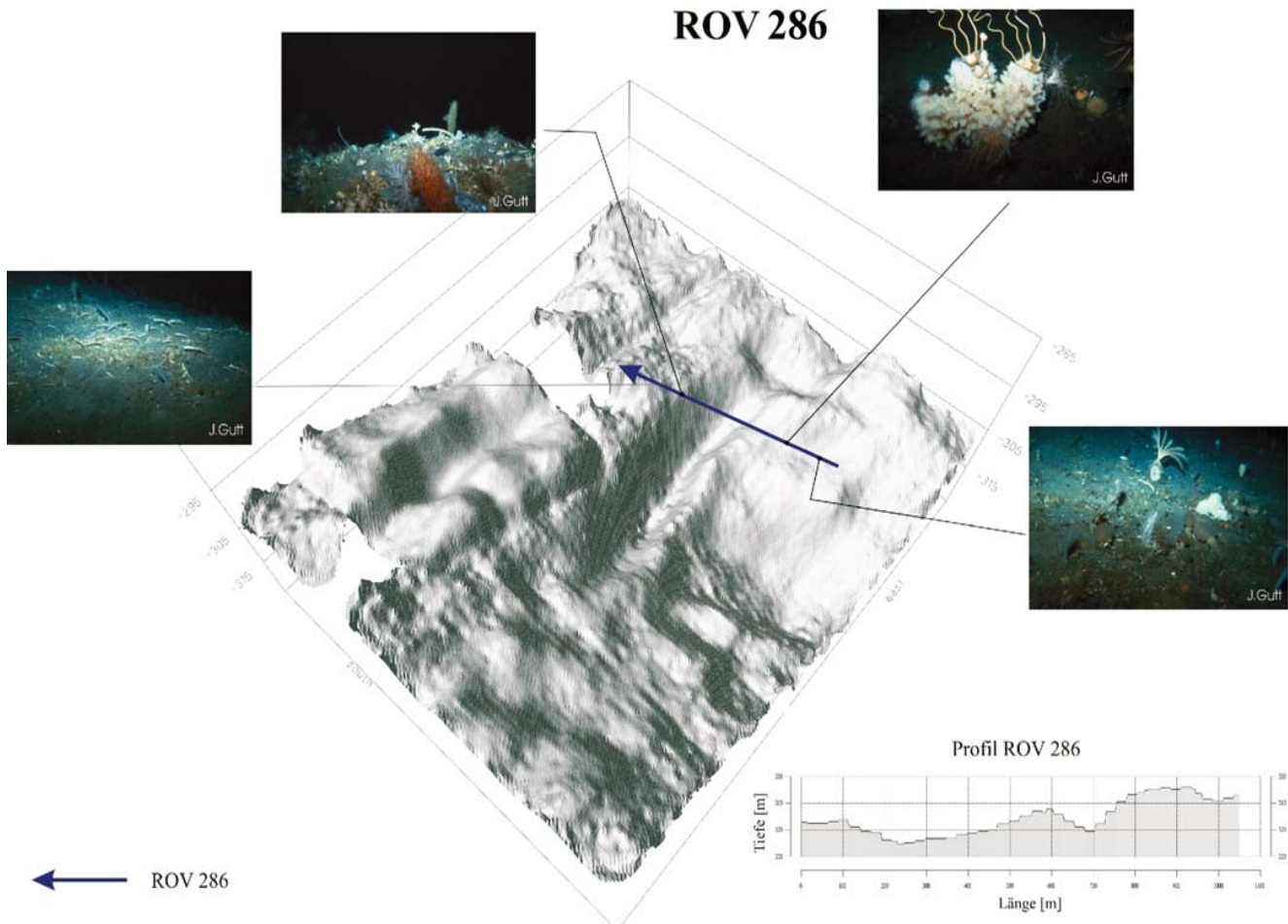
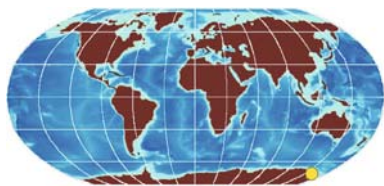


Image 5.5.3-5. Deep and old iceberg plough scars. Multibeam echosounder image. The pronounced plough scar in the middle is 9 m deep and about 130 m wide. The deepening at the end is attributed to an up and down tidal pumping effect of the ploughing iceberg. The photo-ROV took the 4 pictures along the arrow. The first photo confirms the bathymetric impression of an older scar: the fauna has begun to recreate. The other photos outside the scar profiles were taken as reference examples of an intact fauna of the Weddell Sea shelf.

Image documentation: same as for Image 5.5.3-3 ■

5.5.4 5.5.4 Features of the Ross Sea, Antarctica



The Ross Sea was first reached by James Ross in 1841, who took possession in the name of Queen Victoria of

the *Possession Islands* located about 72° S and 171° E. Although the Ross Sea is the least ice-covered of the marginal seas of the *Southern Ocean* surrounding the *Antarctica* (Sect. 5.1.1.6) it is still much less completely mapped by high resolution bathymetry than the *Weddell Sea* on the opposite side of the Antarctic. The *Ross Ice Shelf*, also named the *Great Ice Barrier* is the largest compact ice slab afloat worldwide. With its dimensions of 800 km by 1 000 km, nearly as large as France, it emerges 50 m from the sea surface with more than 300 m of ice below. The loss of substance by tabular icebergs breaking off the frontal rim is replaced by glaciers from the mountains up to a width of a kilometer per year. Neither the sea floor relief below the giant ice slab nor its rear side have been surveyed yet. It would be accessible in principle by *Unmanned Underwater Vehicle (AUV)* imaging, though the distances to be covered are still a problem of energy supply range.

Precise high resolution bathymetric inventories of the Ross Sea such as shown here have concentrated on areas

of interest for safe shipping and were limited by temporal ice coverage. The selected bathymetric inventory of the Ross Sea produced during this Antarctic survey program in 2001 by New Zealand has provided 7 500 km² multibeam images along 15 000 km track, which corresponds to just 1% of the surface of the Great Ice Barrier. The aim of the bathymetric survey was to verify a safe shipping route and anchorages from Cape Adare to Cape Hallett for the various commercial cruise ventures that are visiting the region in ever-increasing numbers, in particular the historic and wildlife sites dotted along the coast. Scientific research was also undertaken for fisheries, aquatic biodiversity, and oceanographic studies.

The first image presented was taken north of *Victoria Land* around the *Balleney Islands* in the west of the Ross Sea between 66°10' and 67°20' S, 162° and 165° E. The second image around *Cape Hallett* was taken between 72° and 72°30' S, 170–170°45' E, directly south of the *Possession Island*. The sea floor morphology of this area is conspicuously structured in contrast to the smooth floor on the opposite side of the Ross Sea. The floor shown appears partially covered by iceberg scars and troughs pointing towards the nearest *Transantarctic Mountains* in the south. The structure of the sea floor on the flanks of the Balleney Islands, presumably caused by erosion is unusual. It is a further example of the capability of multibeam imaging with relief depiction to reveal specific types of sea floor morphology as a guide for further on-site research.

Image 5.5.4-1. ►

Balleney Islands flank area, Antarctica. Multibeam image. The *Balleney Islands* at 67° S, 163° E are an isolated group consisting of five main islands of volcanic origin extending over a distance of 200 km, touching the *Southern Tropic* north of *Victoria Land*. Situated some 300 miles to the NW of *Cape Adare*, the island chain is in the path of meteorological depressions that continually sweep around the Pole with storms in excess of 140 km h⁻¹.

The Balleney Islands multibeam survey covered all coastal areas within 9 km of the coast and the data will be used for the first accurate hydrographic chart of the islands. The color-coded relief image of the southern island flanks, illuminated by simulated sunshine reveals details of an eroded volcanic submarine landscape. Note the unusual fabric-like texture on the flanks with intertwined “cords”, quite different from normal flank erosion. The valley structure between the two southernmost islands encoded blue shows structure elements with conspicuously sharp contours rather than smoothed by erosion. The investigation of these morphological features and their potential origin is pending as yet.

Project: *Western Ross Sea, Cape Adare, Cape Hallett* and *Possession Islands* Hydrographic Survey, 2001. Responsible funding Institution: Land Information New Zealand (LINZ). Management and survey performance: National Institute of Water and Atmospheric Research Ltd. (NIWA)

Research Vessel: *RV Tangaroa*, ice rated 1C, National Inst. of Water and Atmospheric Research Ltd. (NIWA), Wellington, New Zealand
Multibeam echosounder: *SIMRAD EM300*; 30 kHz, beamwidth: 1 × 2°, fan width 120°; data and image processing: *CARIS* Hydrographic Information Processing System (HIPS)

Area: 66°10'–67°20' S, 162–165° E; max. depths in the Balleney Islands image: approx. 2 000 m

Image ©: Land Information New Zealand (LINZ) ■

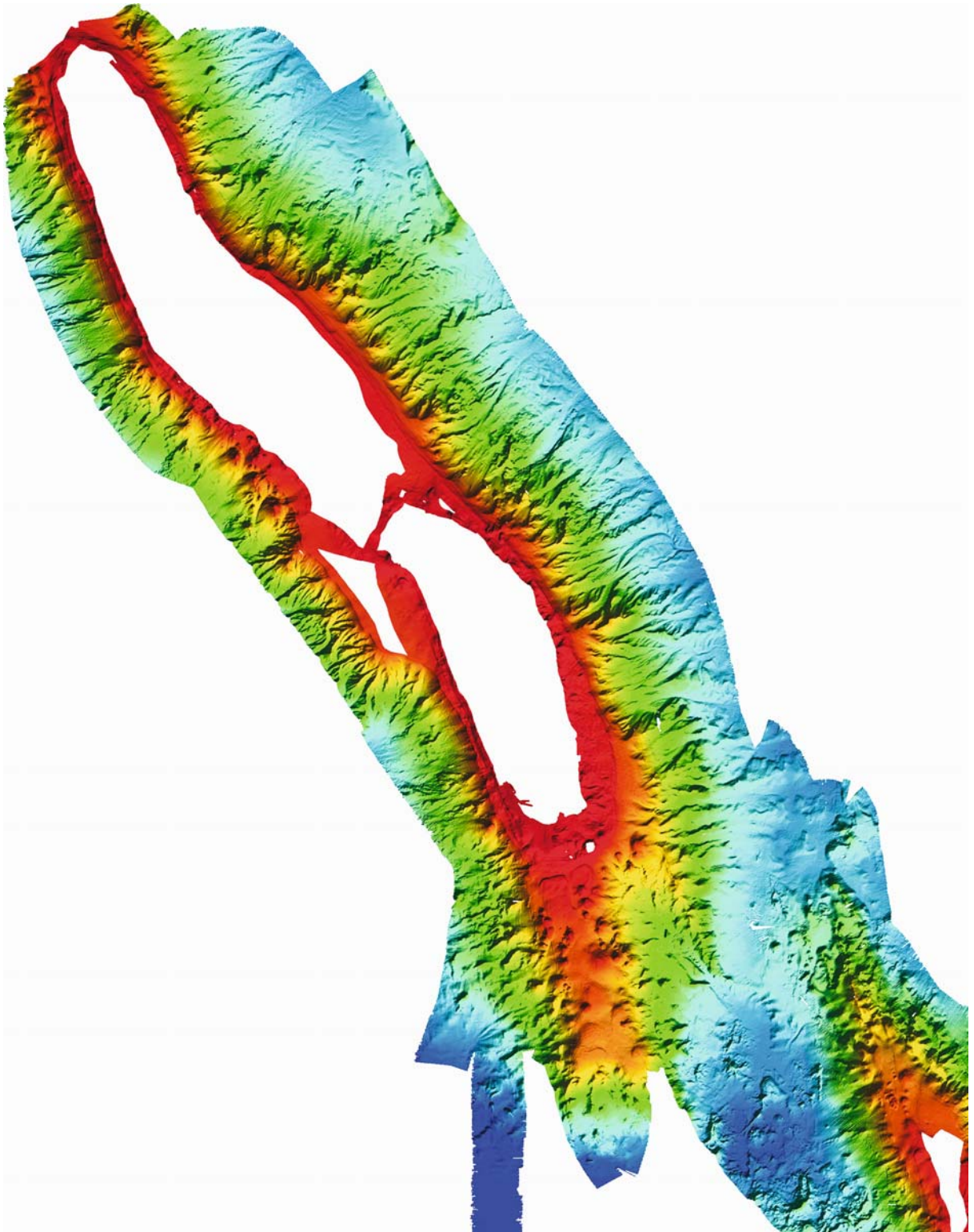
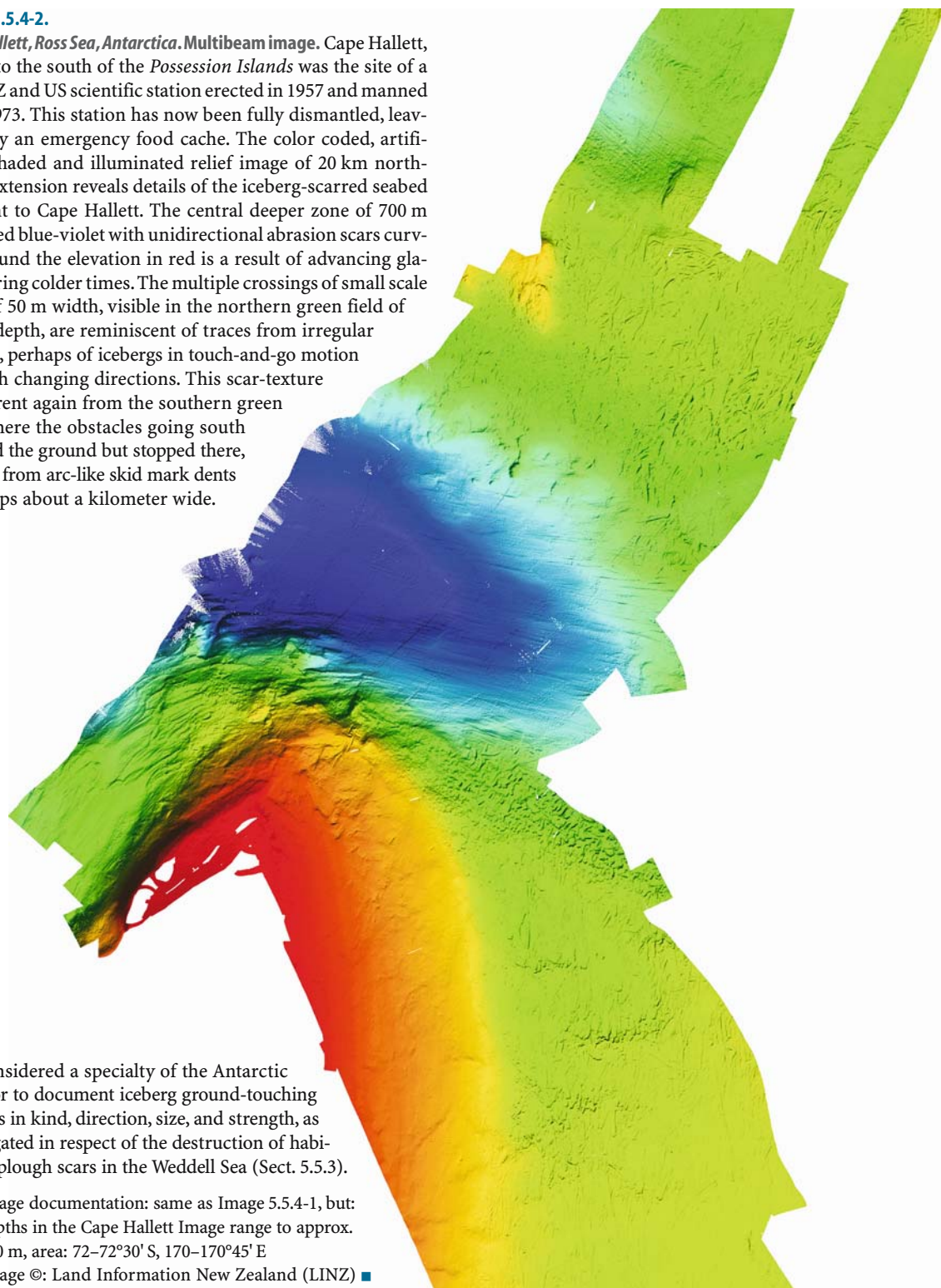


Image 5.5.4-2.

Cape Hallett, Ross Sea, Antarctica. Multibeam image. Cape Hallett, 50 km to the south of the *Possession Islands* was the site of a joint NZ and US scientific station erected in 1957 and manned until 1973. This station has now been fully dismantled, leaving only an emergency food cache. The color coded, artificially shaded and illuminated relief image of 20 km north-south extension reveals details of the iceberg-scarred seabed adjacent to Cape Hallett. The central deeper zone of 700 m indicated blue-violet with unidirectional abrasion scars curving around the elevation in red is a result of advancing glacier during colder times. The multiple crossings of small scale scars of 50 m width, visible in the northern green field of 300 m depth, are reminiscent of traces from irregular friction, perhaps of icebergs in touch-and-go motion but with changing directions. This scar-texture is different again from the southern green area where the obstacles going south touched the ground but stopped there, evident from arc-like skid mark dents in groups about a kilometer wide.



It is considered a specialty of the Antarctic sea floor to document iceberg ground-touching motions in kind, direction, size, and strength, as investigated in respect of the destruction of habitats by plough scars in the Weddell Sea (Sect. 5.5.3).

Image documentation: same as Image 5.5.4-1, but: depths in the Cape Hallett Image range to approx.

700 m, area: 72–72°30' S, 170–170°45' E

Image ©: Land Information New Zealand (LINZ) ■

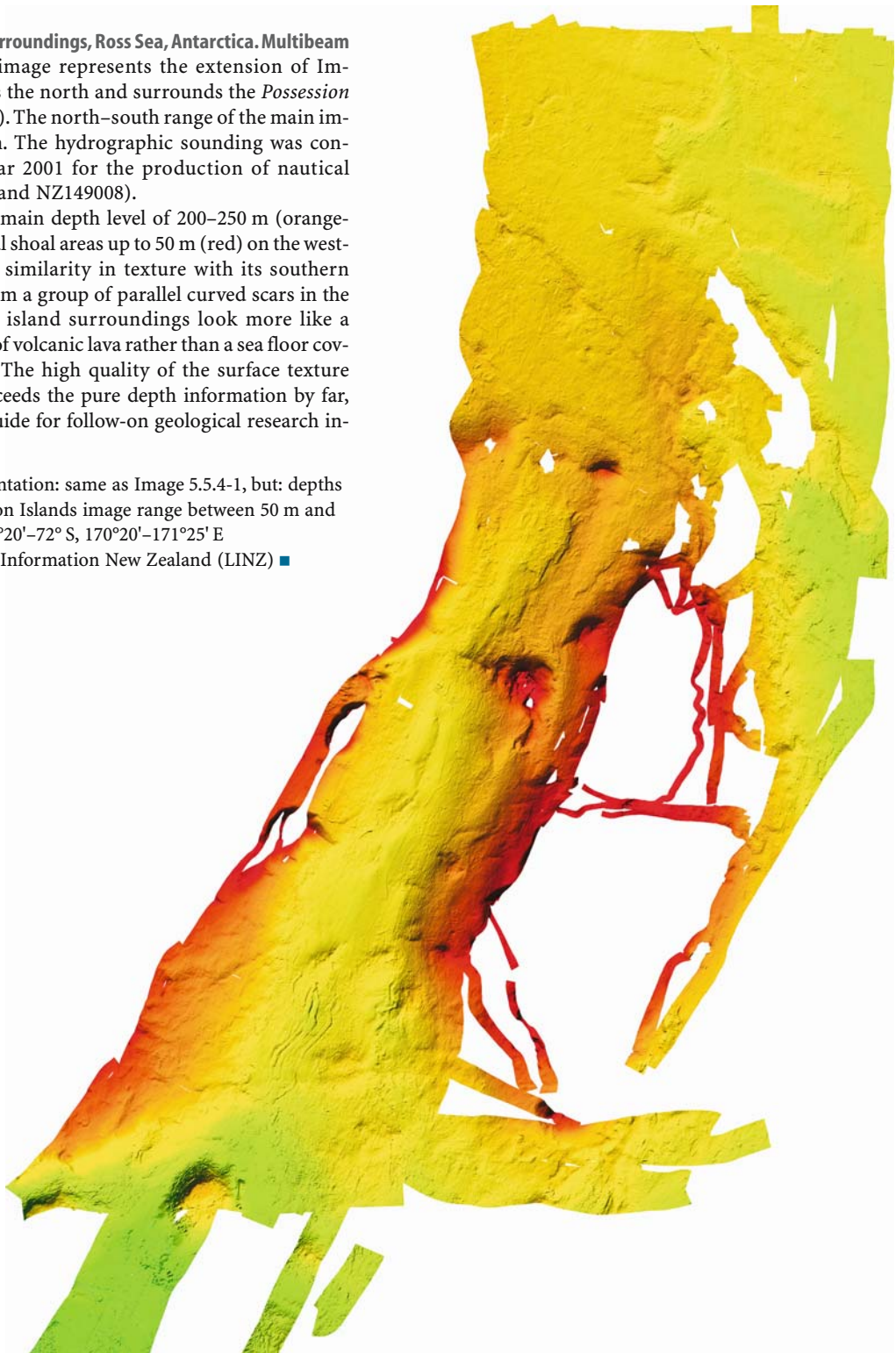
Image 5.5.4-3.

Possession Islands surroundings, Ross Sea, Antarctica. Multibeam image. The relief image represents the extension of Image 5.5.4-2 towards the north and surrounds the *Possession Islands* (blank area). The north–south range of the main image block is 25 km. The hydrographic sounding was conducted in Feb.–Mar 2001 for the production of nautical charts (NZ149007 and NZ149008).

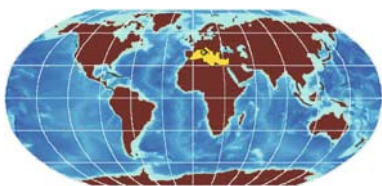
The area at the main depth level of 200–250 m (orange-yellow), with several shoal areas up to 50 m (red) on the western side, has little similarity in texture with its southern neighbor. Apart from a group of parallel curved scars in the south the western island surroundings look more like a weathered surface of volcanic lava rather than a sea floor covered by sediment. The high quality of the surface texture imaging, which exceeds the pure depth information by far, can be used as a guide for follow-on geological research investigations.

Image documentation: same as Image 5.5.4-1, but: depths in the Possession Islands image range between 50 m and 300 m, area: 71°20'–72° S, 170°20'–171°25' E

Image ©: Land Information New Zealand (LINZ) ■

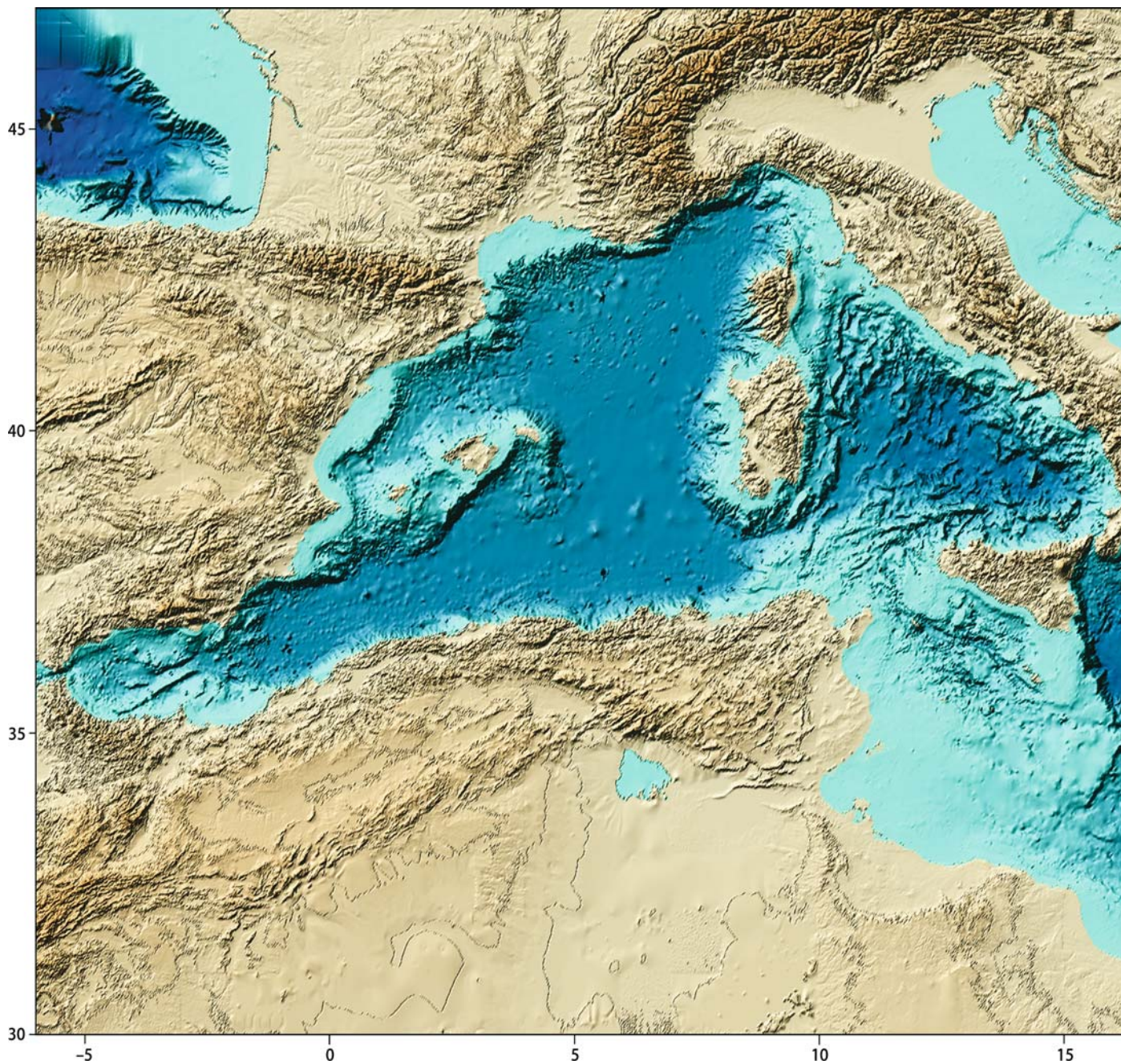


5.6



5.6 *Mediterranean Sea Formations, the Overview*

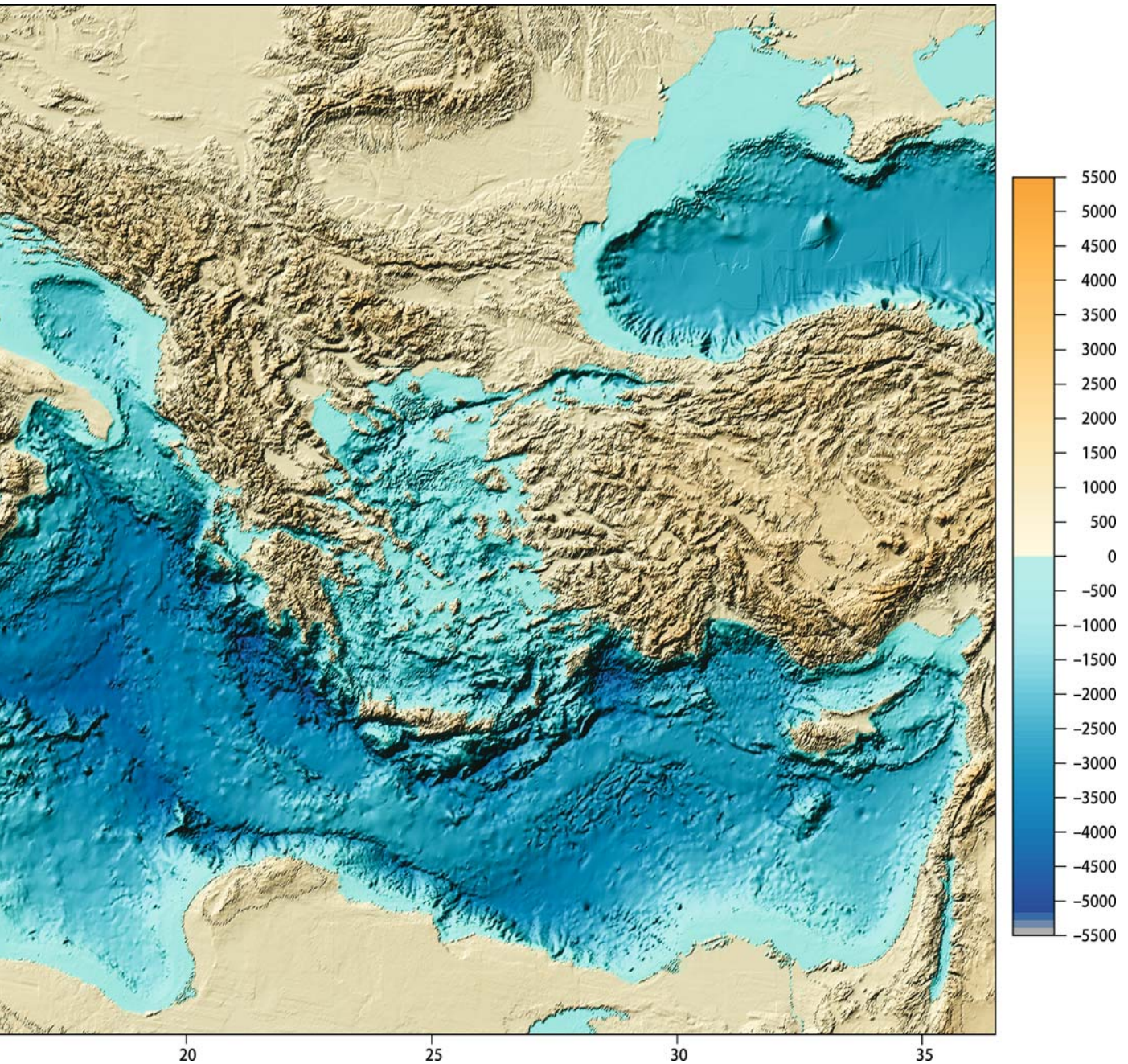
Revealing the sea floor topography of the Mediterranean by sound imaging may be emotionally considered differently from most other sites shown. It is like looking into the abyss, the subject of awe of those to whom we owe the



cradle of the occidental culture and the earliest encounter between Orient and Occident. These inhabitants of the Mediterranean area were privileged by the mild climate but they had also to live with weird, enigmatic hazards which they attributed to eruptions of divine rage: seemingly peaceful mountains were suddenly spouting fire and glowing flow and seemingly tranquil landscapes were suddenly shaken by unimaginable forces of destruction.

Image 5.6-1.

The Mediterranean sea floor. The relief image of the Mediterranean sea floor with its four large, deep basins indicates our present understanding of the origin of those phenomena, feared by our forefathers – as well as ►



by the present-day population, though for other reasons: The Mediterranean is crossed from west to east by a margin where two large tectonic plates of the Earth's crust and lithosphere collide: the *Eurasian Plate* and the *African Plate*. This zone of menace is the only one of its kind in Europe. *Collision* is not the correct description however. The African Plate is being *subducted* under the uplifted Eurasian Plate. This process which reaches deep into the Earth's mantle causes earthquakes and volcanism, mostly on the side of the upper plate.

The plate margin through the Mediterranean is less conspicuous than the four-basin topography and more complex than the uninterrupted *Central American Trench* for instance (Sect. 5.2.1). The effect of the underthrusting of the Eurasian Plate by the African Plate is visible however north of *Cyrenaica*, with an isolated trench arc and with further trench arcs south of *Cyprus* and the *Aegean Sea*. A number of tectonic lines are apparent, especially in the *Alboran* and *Tyrrhenian Seas*, and between the *Sicily-Malta Escarpment* and the *Hellenic Trenches*. It is more a conglomerate of subduction zone elements rather than a single, continuous margin line. This fact is interpreted by a non continuous and not completely unidirectional motion of the two large plates during the past 44 million years when the Mediterranean and the adjacent mountain chains were formed. The Mediterranean subduction zone continues beyond the eastern coast where its large southern tectonic plate neighbor is exchanged by the small *Arabian Plate* (Sect. 5.2) which is also subducted below the *Eurasian Plate*, causing similarly hazardous tectonic activities.

Five million years ago, when the *Strait of Gibraltar* opened, the Mediterranean Sea floor was already subdivided into several basins which were extremely salty seas due to rich salt deposits below the sea floor discovered only in the seventies of the twentieth century. Today, the higher salinity of the Mediterranean of 4% as against 3.5% of the open ocean is mainly attributed to evaporation dominating the river inflow, as opposed to the *Baltic Sea* (Sect. 5.7). The outflow of saline water through the Strait of Gibraltar – quantified by acoustic tomography (Sect. 6.1.3) – propagates across the entire Atlantic Ocean with a surprising acoustic effect: the *Sofar-Channel* of ocean-wide low frequency sound propagation descends 300 m to more than 600 m within the Atlantic tongue of Mediterranean water (Sect. 3.2.2).

The shallow northern Adriatic Sea, cooling down to near freezing point during wintertime, is one of the main origins of the cold sea floor water of the Mediterranean. The other origin is the shallow Aegean Sea: the water with higher salinity, due to strong evaporation during summer, sinks to the floor during winter due to its higher density. The distribution of currents and thus the mixing of waters is decisively determined by the bottom topography and the islands

of the Mediterranean. The famous bottleneck of flow, notorious since antiquity as *Scylla* and *Charybdis* is the *Strait of Messina* between Italy and Sicily, a demonstrator of huge internal gravity waves (Sect. 2.9) hazardous to shipping in the past.

The southern *Tyrrhenian Sea* with the *Aeolian Islands* chain is a center of volcanism with *Stromboli* as the most prominent active volcano (Sect. 5.2.6) The largest European volcano however is under water: *Marsili*, 2 million years of age, on top of a 30 km long ridge, ascending 2 300 m above the eastern Tyrrhenian floor north of the Aeolian chain.

The islands of the Aegean Sea between Greece and Turkey were the summits of mountains of the inundated Aegaeis, which was a landmass 18 thousand years ago when the sea level was lower. The Aegean Sea is separated from the eastern Mediterranean basin by the ridge-like island chain containing Crete and Rhodes. Two peculiarities of the eastern basin are mentioned: The *Nile*, with 6 650 km, the longest river on Earth with a famous broad and fertile delta has produced a submarine sediment fan which is comparatively modest in size compared to the huge *Bengal Fan*, the largest and fastest growing of all (Sect. 5.3.2). The other peculiarity is the generation of a saltwater layer of just the appropriate density to pass above the shallow areas between the other basins of the Mediterranean and form the high saline outflow through the Strait of Gibraltar. This saltwater tongue, spreading far into the Atlantic Ocean (Sect. 3.2.2) causes a specific density profile which is of biological importance (Sect. 5.3.4).

Concluding the Mediterranean features from west to east revealed by the complete relief, the seemingly long lake parallel to the coast of Israel deserves mentioning. In reality it is one of the largest and deepest depressions on Land: the area between the *Dead Sea* and the *Lake of Tiberias* lies about 200 m below sea level with the deepest point on land worldwide of –412 m.

Image ©: John Hall, Geological Survey of Israel, Tel Aviv ■

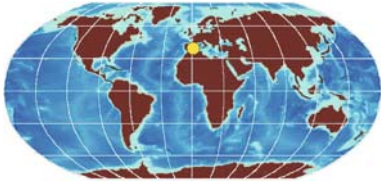
Box 5.6-1. Mapping the Mediterranean sea floor

The image of the complete relief of the Mediterranean sea floor presented here is a composite of several data sources: the digitized 200 m depth contour map (IBCM-II) supplemented by some million soundings taken from about 500 digitized charts provided by the Russian Federation. The new 0.1 arc minute IBCM-II compilation with 150 m resolution will be based upon French EM12D and EM300 multibeam surveys in the deep areas, with other multibeam data from Spanish, Italian, and German surveys.

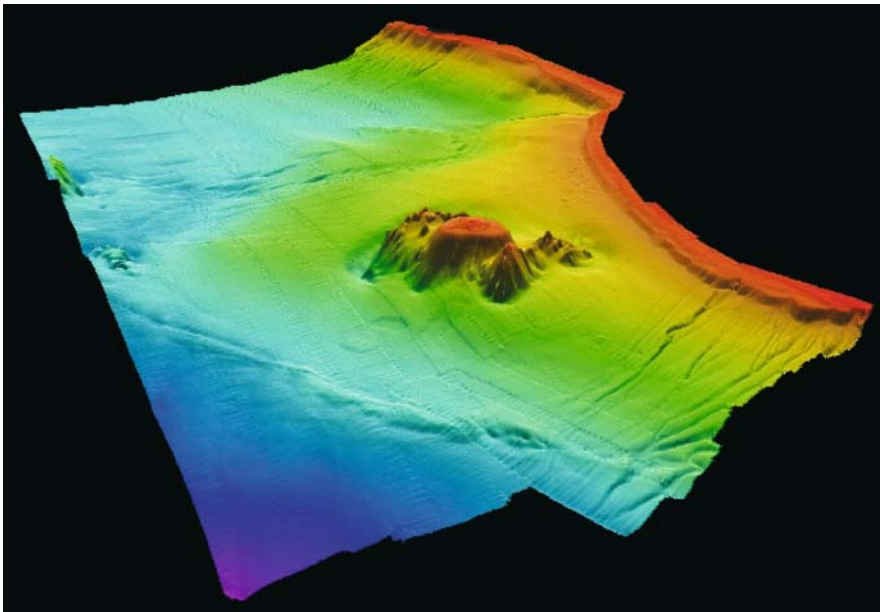
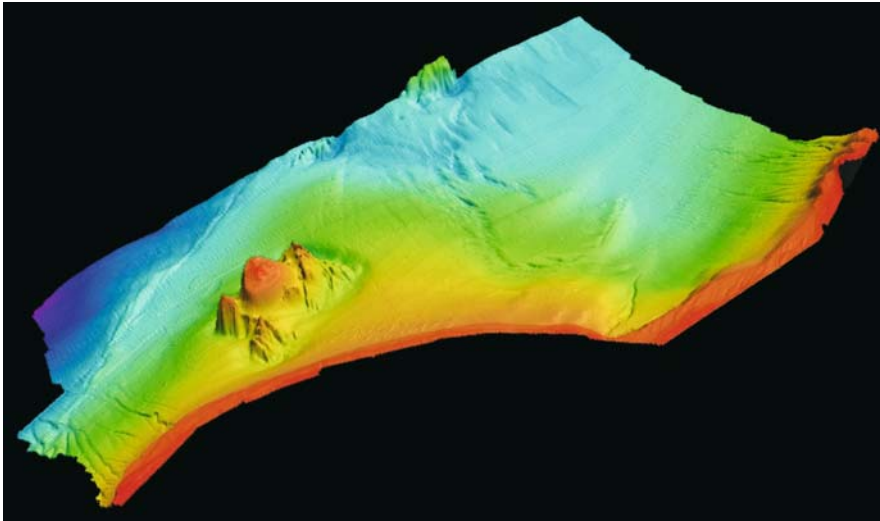
5.6.1

Chella Bank, Western Mediterranean Sea

5.6.1

**Image 5.6.1-1.**

A flat-top former volcano in the *Alboran Sea*. Multibeam image. This most pronounced formation of the Chella Bank in the Alboran Sea, the westernmost part of the Mediterranean is a seamount of volcanic origin which was an island during the last glacial periods when the sea level was lower by about 130 m in this area. The nearly complete erosion and abrasion of the emerged parts of the island by glacial forces formed the flat top. Such a formation is named *guyot*, which is thus a kind of prehistoric sea level indicator. The peak in the middle of about 30 m height is possibly due to a later eruption or corals.



The entire Chella Bank is a late tertiary volcanic rock massif, about 8 million years of age.

The area is part of the tectonic convergence zone of the *African Plate* and the *Eurasian Plate* that passes the *Strait of Gibraltar*. This subduction zone is accompanied by an agglomerate of faults, a result of the obliquely subducting African Plate which are not indicated in the general map of tectonic plates (Sect. 5.2). South-east of Chella a ridge-like feature runs NE-SW corresponding to the offshore prolongation of the *Serrata-Carboneras fault*. This strike-slip fault (Sect. 5.2.5) has a length of more than 21 nautical miles. The tectonic feature as well as sedimentary formations like canyons are visualized in detail in the animated flight around Chella Bank on the attached CD.

Project: Chella Bank; year of survey: 2002

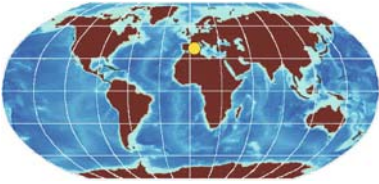
Site: South of Spain, 36°31' N, 2°51' W, offshore Almeria
Research vessel: *RV Vizconde de Eza* (SGPM)

Multibeam echosounder:

Simrad EM 300; frequency: 30 kHz, beamwidth: 1°; 135 beams, positioning: DGPS aid with IMU Sea-path 200

Image ©: Juan Acosta, Araceli Muñoz, Isabel Montoya, Instituto Español de Oceanografía, Madrid, Spain ■

5.6.2 Balearic Islands



The origin of the Balearic Island group in the western *Mediterranean* goes back 300 million years to the *Carboniferous* period and is considered to be a fraction of the mountain chain north of the Mediterranean of which the *Cordilleras* and the *Alps* are a part.

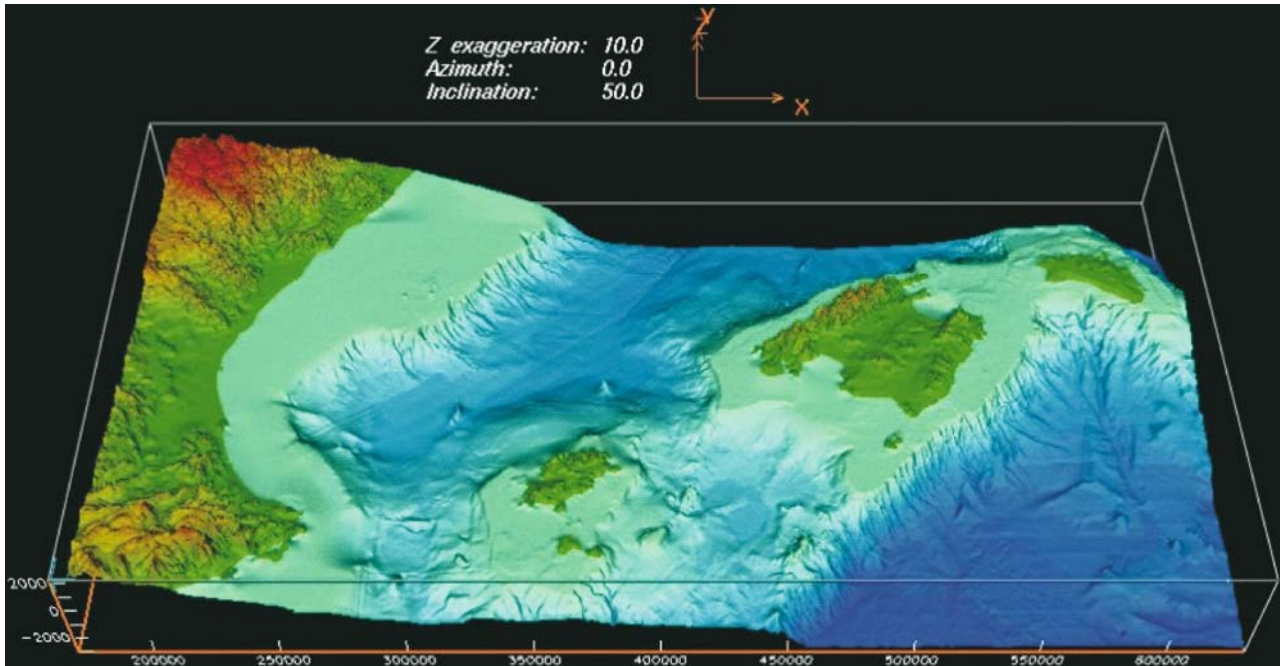


Image 5.6.2-1. The sea floor around the Balearic Islands. Multibeam image. The mountain massifs are results of the tectonic underthrusting of the *African Plate* under the *Eurasian Plate* (Sect. 5.2), which caused uplifting and multiple folding on the margin of the overriding plate. The oblique plate shift produced an agglomerate of faults, some of which are visible in the *Valencia Basin and Trough* between the island group and the mainland of *Spain*. Another related fault is shown in the preceding image. The various sedimentary contributions of the *Cretaceous* and earlier periods of the *Mesozoic*, as well as of the *Tertiary* and later are not discussed here, since the sound image reveals structures, not the composition of material. The predominant morphology – at least the most conspicuous – at the shelf break of the mainland as well as of the islands is the system of canyons and channels, the result of voluminous erosion and subsequent sediment transport. However, when looking closer, the non-erosive features are clearly discernible. The irregular furrows, ridges and dislocations in the basins on both sides of the island group, obviously not related to the canyons, are faults of tectonic origin, although smoothed and partially covered by sediments, but still manifest as witnesses of major Mediterranean formations.

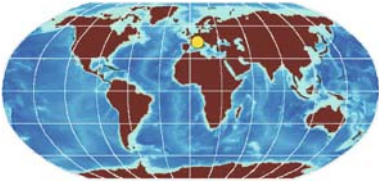
Project: Spanish Exclusive Economic Zone; 1995, 1996, 1997, and 2000

Research vessel: *RV Hesperides* and *RV Cornide de Saavedra*

Multibeam echosounder: Simrad EM 12 S; frequency: 13 kHz, beamwidth 1.8°, 81 beams, fan width: 120°, active electronic pitch and roll compensation, positioning: Differential GPS

Image ©: Juan Acosta Yepes, Araceli Muñoz, Geology and Geophysics Dept., Instituto Español de Oceanografía, Madrid, Spain; Miquel Canals, GRC Geociències Marines, Departament d'Estratigrafia, Paleontologia i Geociències Marines, Facultat de Geologia, Universitat de Barcelona ■

5.6.3 Tyrrhenian Sea Floor Features

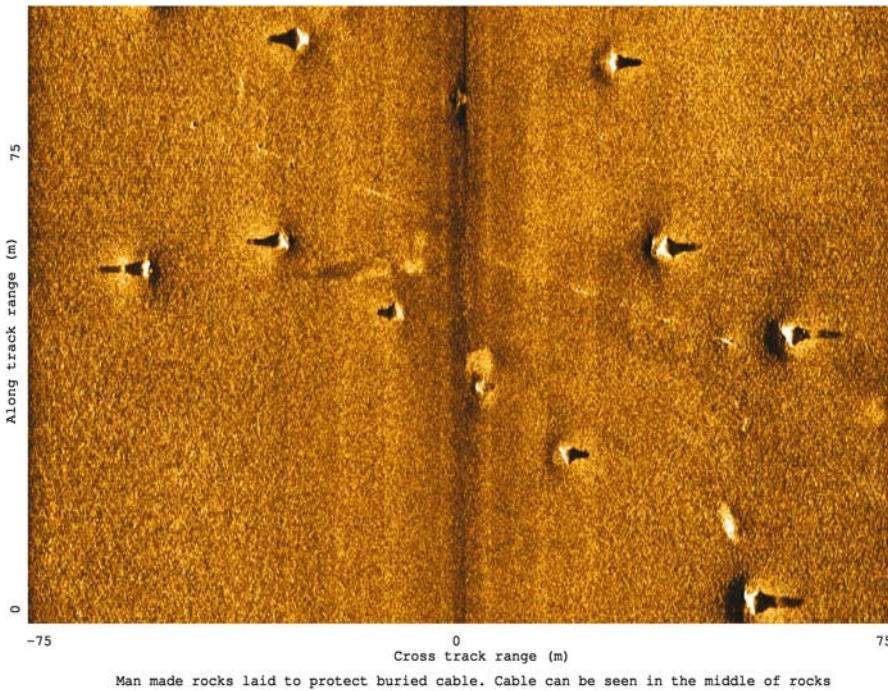


The features shown demonstrate the strength of the sidescan technique for imaging such small-scale and shallow objects, natural as well as technical.



Image 5.6.3-1. Calcareous bedrock near marble deposit areas on the north-west coast of Italy. Sidescan image. The coast of the northern Tyrrhenian Sea on the western side of Italy is famous for its marble deposits near Carrara. Some of the nearby islands also consist of limestone, in part also in crystallized form of various marble sorts, quality, and color. Accordingly, the coastal seabed of the Cinque Terre coast shows outcropping calcareous bedrock with sand coverage in between. An 80 m by 150 m cut-out is shown here to demonstrate that sidescan sonar can provide nearly photographic image quality showing the texture of the washed out limestone surface reminiscent of toadskin. The bedrock with its rounded forms is obviously subject to current induced erosion; the sand ripples, also current induced, indicate the direction of flow and its focusing by the bottlenecks between narrow rocks. The image is composed of both sides of the sidescan swath (Sect. 4.3) with the blind stripe in the middle cut-out.

Program: BP02 cruise, cooperation of NATO Saclant Undersea Research Centre, La Spezia, Italy, and GESMA, France, 2002;
 survey area: off Cinque Terre, Italy
 Survey vessel: *RV Thetis*, France
 Sidescan sonar: Klein, type: 5400; frequency: 465 kHz; swath width: 150 m; Athwart resolution: 20 cm at 75 m; water depth: 20 m
 Image ©: Edoardo Bovio, Saclantcentre, La Spezia, Italy ■

**Image 5.6.3-2.**

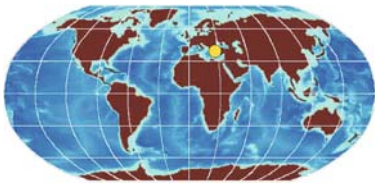
Tripod field on plane sand bottom off Cinque Terre, Italy. Sidescan image.

Though the form of the tripods which protect the area against trawlers is not resolved by the sidescan image, the shape of the long shadows and the highlights on the irradiated side of the concrete tripods are clear indicators. The conspicuously bright highlights are originated by the slanted “legs” of the tripods, which produce specular reflection of the incoming sound signal rather than scattering. The sand bottom of the area appears like an ideal plane with only few scars and minor erosion around the foot of each tripod. This image is also depicted without the blind stripe in the middle, typical of normal sidescan imagery.

Image documentation: same as Image 5.6.3-1; water depth 30 m
Image ©: Edoardo Bovio, Saclant-centre, La Spezia, Italy ■

5.6.4

5.6.4 Features of the Aegean Sea

**Image 5.6.4-1. ▶**

The North Aegean Trough system. Multi-beam image. The most pronounced submarine feature of the mostly shallow *Aegean Sea* is a deep trough system crossing the entire northern Aegean south-east of the three peninsula fingers of *Chalkidiki* up to the Turkish coast, where it forms the bight of *Saros Körfezi* near the *Dardanelles*. According to recent studies, this formation is considered part of the complex system of tectonic margins which cut through the *Mediterranean*. Following the schematic map of Image 5.6.4-2, the North Aegean Basin is interpreted as the westward prolongation of the *North Anatolian Fault (NAF)*, a *strike slip fault* (Sect. 5.6.5) where two adjacent tectonic plates move at different rates or in opposite directions along each other causing infamous earthquake hazards. The route of this strike slip fault which passes the *Marmara Sea* is assumed to coincide with the southern border of the North Aegean Basin where the

continental platform shows a pronounced break into the trough area. Fault elements are indicated red in the small inset map.

The relief image which depicts the broad western part of the North Aegean Basin is turned upside down to better visualize the south-western corner of the basin, adjacent to *Alonnisos Island*, where the maximum water depth of 1 610 m was found. The North Aegean Basin has a complex topography with approximately 20 sub-basins of different shape and water depths of more than 900 m. The sub-basins are separated by submarine sills and ridges ranging from a few tens up to several hundreds of meters above the basin floors. Sediments of the basin lying on the alpine rock basement are several kilometers thick, according to seismic profiling (not shown here).

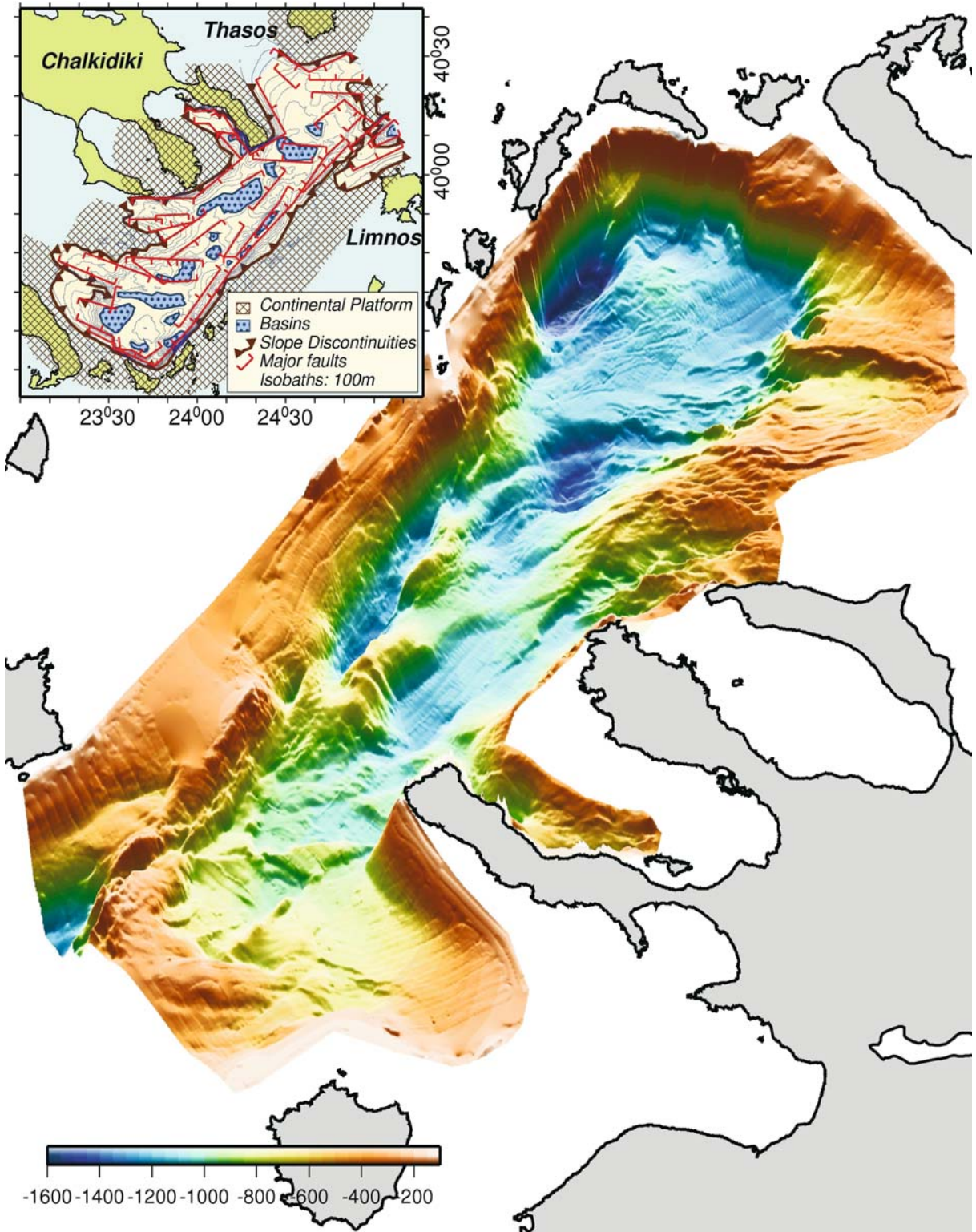
Project: Morphotectonic structure of the western part of the *North Aegean Basin*, based on swath bathymetry; year of survey: 2000

Research vessel: *RV Aegaeo* (HCMR)

Multibeam system: *SeaBeam* 2120; frequency: 20 kHz, beamwidth 1.5°, number of beams: 120

Height exaggeration factor: 15. The brown relief flank in the foreground reveals the multibeam meander and hair-pin bends which disappear towards greater depths where the fan widens and overlaps

Image ©: Matina Alexandri, Dept. of Marine Geology and Geophysics, Institute of Oceanography, National Centre for Marine Research, Anavyssos Attiki, Greece ■



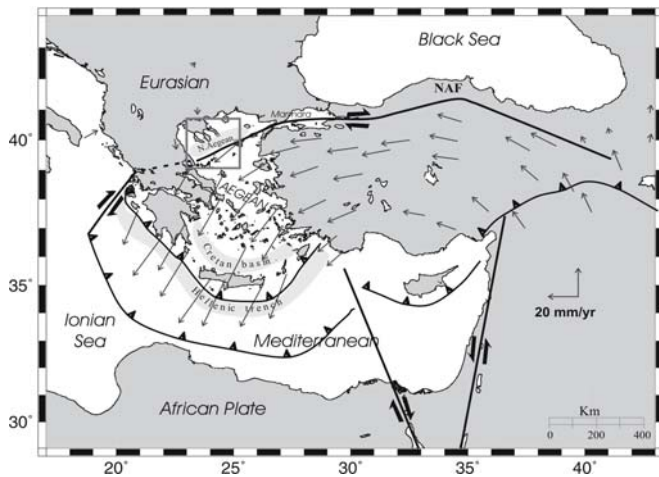


Image 5.6.4-2.

Schematic map of tectonic plate motion including the Aegean Sea.

The arrows indicate the recently published annual rate of motion measured on Aegean Islands by high precision satellite navigation GPS. The North Anatolian Strike Slip Fault (NAF) is obviously the border between the very slow motion of the Eurasian Plate (Sect. 5.2) and the comparably fast motion of the Anatolian-Aegean area. The North Aegean Basin is thus part of

the transition zone between slow and fast plate motion, similar to the Anatolian Block versus the Eurasian Plate. This annual rate of motion would imply an opening of approximately 40 km for a time period of 13 million years, which is generally accepted as the time span of the opening of the North Aegean Basin. There are still pending questions however regarding the route connection of the North Anatolian Fault between the Marmara Sea and the missing relief data of the eastern side of the North Aegean Basin as well as a potential continuation or disappearance of the fault in the west.

The data presented underline the scientific necessity to confirm such fundamental findings by mutually supplementing diagnostic methods. The detailed knowledge of the morphologic features of the North Aegean Basin and the evidence of its tectonic strike slip origin are the result of recent high resolution multibeam echosounding and GPS measurements respectively. The other types of plate boundaries, in particular the zones of plate subduction, with the Hellenic Trench among them are mostly identifiable in kind already by acoustic methods alone. On the map they are indicated by the lines with triangles and commented in the context of the general relief image of the Mediterranean (Sect. 5.6).

Image ©: D. Papanikolaou, Department of Marine Geology, University of Athens, Greece ■

Image 5.6.4-3. ▶

A slump in the North Aegean Basin – the largest single failure event ever observed in the Aegean. Multibeam and seismic image. The relief image is a tiny blown-up cut out of the North Aegean Basin shown in the previous image on the north east side. Only by this zoom is the dramatic feature visualized: a large submarine slide probably released by one of the frequent earthquakes of the tectonic strike slip area. The inset map depicts the epicenters and magnitudes of earthquakes greater than 4.0 *R* that occurred during only one month in 1983. Surprisingly the slide was discovered by continuous seismic sub-bottom profiling along lines, and has been imaged in detail as an area covering 3D-relief by multibeam sounding only thereafter.

This relief shows the entire slide area with the 4 km wide headwall at 300 m depth and the end of slide 550 m deeper. About 4 km³ of sediment slid along slopes up to 2.9° more than 6 km wide, covering 85 km² of the sea floor. In comparison to the largest submarine slide ever found, the Storegga Slide off Norway of about 3 000 km³ (Sect. 5.3.1), this slide is of modest size however, but the largest found in the Aegean. The uppermost part of the failure zone is about 6° steep which is also a significant difference compared to the extremely shallow slope of Storegga. Though both slides were most probably released by earthquakes, the slide mechanism will have hardly been similar in kind. The overpressure conditions of Storegga have presumably provided a kind of liquefaction of a critical sediment layer with drastically reduced friction, inducing a slide like a ship on soft soap after the Christening ceremony. In the Aegean the inclusion of weaker muddy layers with higher water content and lower shear strength will have caused the instability, though only at much steeper angles and along a slide range of 6 km, as against 800 km.

The track of the seismic profile showing the details of the slide strata is indicated inside the yellow framed slide contour of the overview map: The slide scarp debris (SLD) at the foot of the scarp (SC) or headwall, the glide plane (GP) and the slab slide (SLB). The age of the event, according to stratigraphic and sedimentological data is estimated to be about 5 000–8 000 years, in other words, it happened in Holocene times.

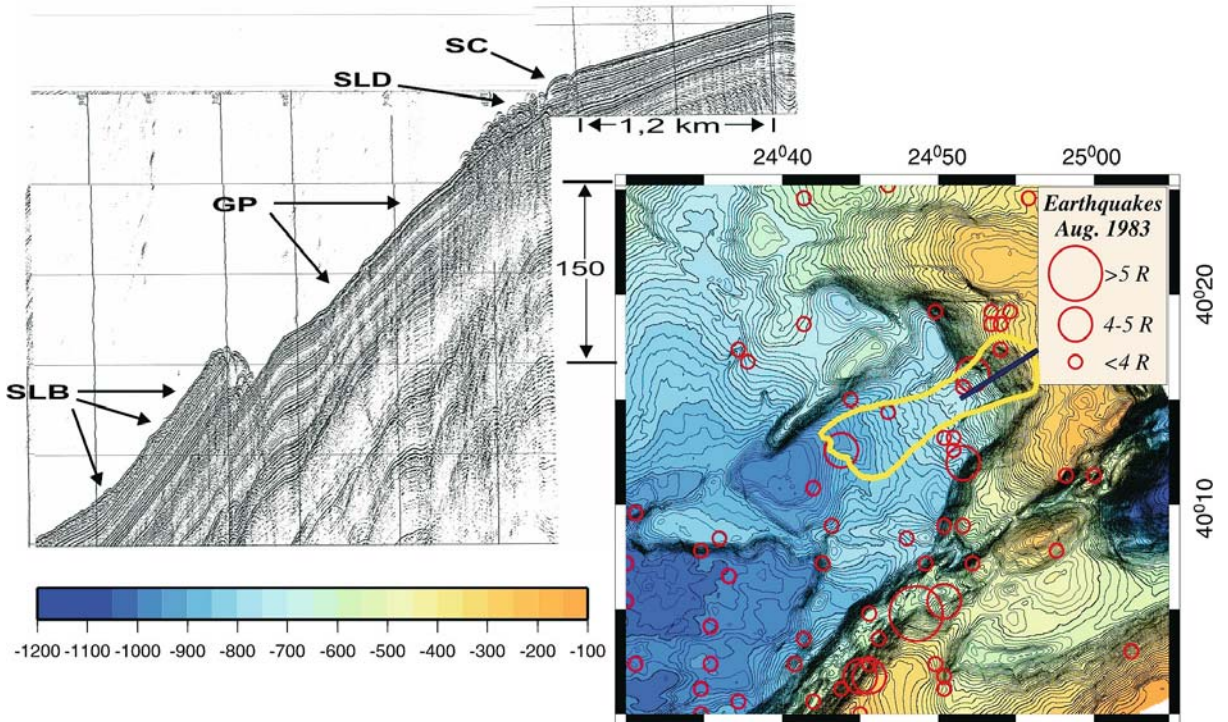
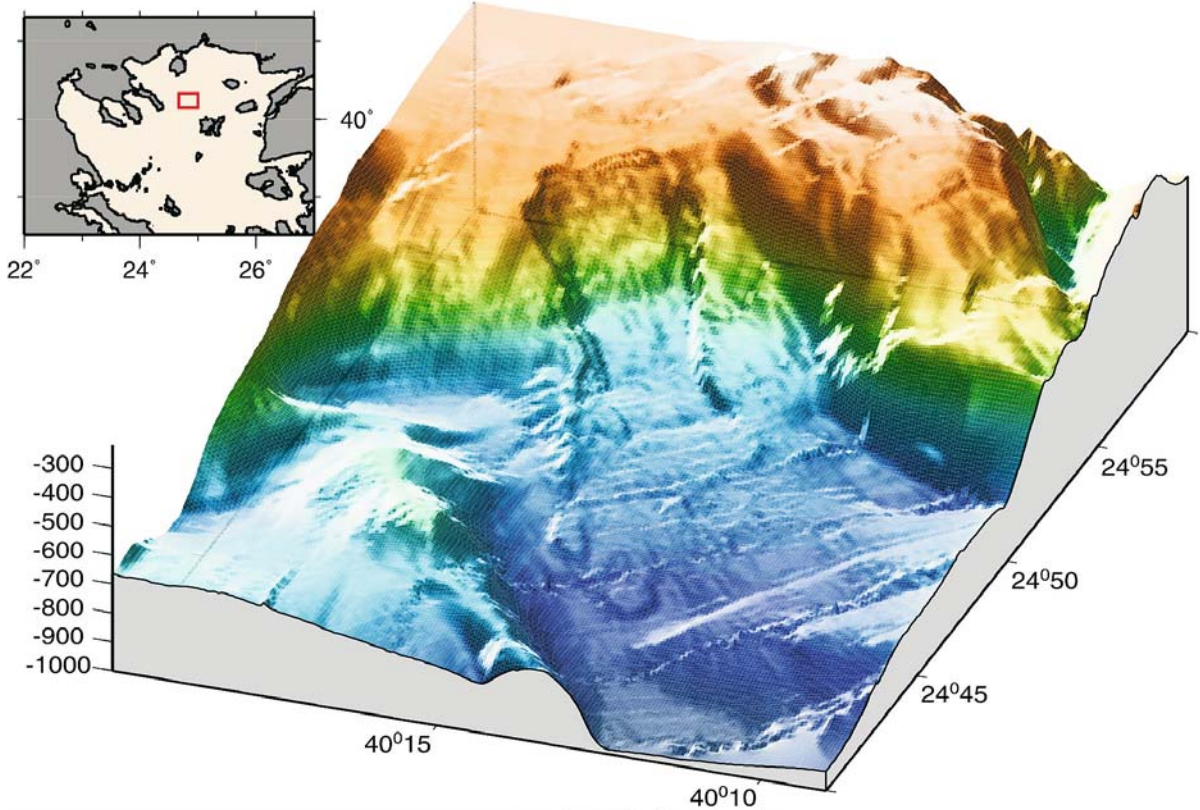
Project: The Active faults of the western part of North Aegean Trough; year of survey: 2000

Research vessel: *RV Aegaeo* (HCMR)

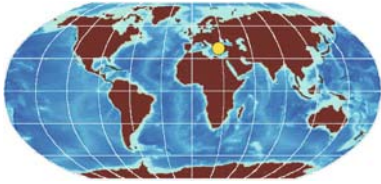
Multibeam system: *Reson SeaBeam* 2120; frequency: 20 kHz, beamwidth 1.5°, number of beams: 149; Height exaggeration factor: 15

Seismic profiler: Airgun, chamber volume: 80–160 cm³; frequency band: 200–1 100 Hz

Image ©: Matina Alexandri, Dept. of Marine Geology and Geophysics, Institute of Oceanography, Hellenic Centre for Marine Research, Anavyssos Attikis, Greece ■



5.6.5 5.6.5 The Marmara Sea Trough



The *North Anatolian Fault (NAF)*, one of the best-known prototypes of strike-slip faults (Sect. 5.2.5) is presumably the most infamous for its devastating earthquakes along the northern *Turkey* during history up to the end

of the twentieth century. The NAF splays into three branches in western Anatolia, the northernmost of which enters and traverses the *Marmara Sea*, the “forecourt” to Istanbul and is supposed to resume along the *North Aegean Trough* (Sect. 5.6.4). The *Marmara Sea*, connecting the *Mediterranean Sea* with the *Black Sea* through its narrow strait system with complex morphology has always attracted major interest. The *Marmara Sea Trough*, deeply incised into the shelf of the Marmara Sea is the primary structure of the tectonic fault system of the NAF. The main part of this

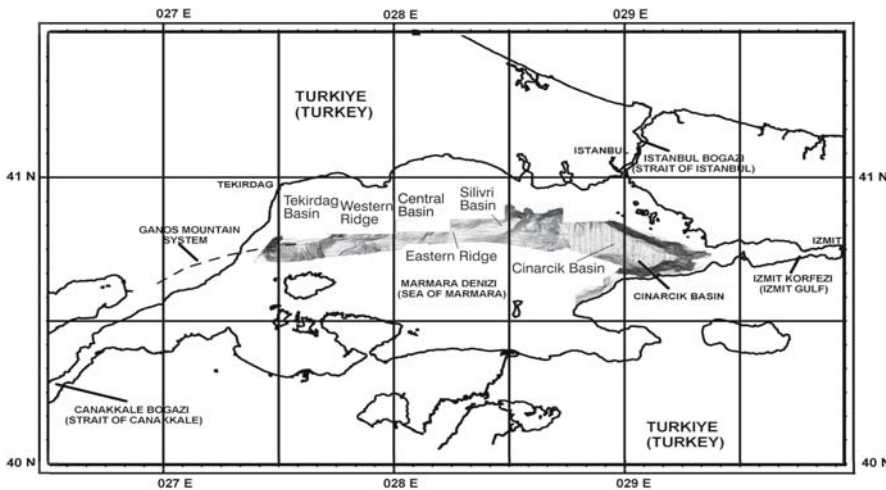


Image 5.6.5-1. Marmara Sea. Overview map with the imaged stripe area of the Marmara Sea trough in gray scale. The multibeam image covers the trough zone with the tectonic faults as described in the subsequent, color coded close-up cut-outs from east (Image 5.6.5-2) to west (Image 5.6.5-5).

Image ©: Halim Birkan ■



Image 5.6.5-2. Entrance (a) of the North Anatolian Fault into the Marmara Sea (Çınarcık Basin) (b) from Izmit Bay (c). The letter a indicates a section of the strike slip fault. The canyon “curtain” doesn’t intersect the fault line, indicating this fault section to be older than the former feature. All of the close ups of this series are multibeam images.

Project: Tectonic morphology of the Marmara Sea Trough; survey period: 1999–2000

Survey Vessel: *TCG Cubuclu*, TN-DNHO, Turkey

Multibeam echosounder: ELAC BCC MK I, hull mounted; frequency 50 kHz, beamwidth: 2°, 56 beams, fan width 120°

The data base is supplemented by bathymetry of various sources

Image ©: Halim Birkan, Turkish Navy Department of Navigation, Hydrography and Oceanography, Istanbul ■

trough has been imaged by high resolution multibeam echosounding, seismic profiles and sidescan to understand the mechanisms of its tectonic processes hazardous to the coastal areas of the Marmara Sea.

The Marmara Sea Trough occupies about half of the Marmara Sea area breaking the shelf at about 100 m depth. The trough consists of three main deep basins, the *Çınarcık Basin*, *Central*, and *Tekirdağ Basin* of 1 150 to 1 275 m depth with the smaller *Silivri Basin* between *Çınarcık* and *Central*. The basins are separated by complex ridges and are framed on both ends by steep

slopes which continue in parts beyond the sound image in the north. Submarine canyons and landslides constitute the secondary morphological units of the Marmara Sea. The conspicuous trough formations are shown as four sequential cut-out close-ups of the color coded bathymetric relief of Image 5.6.5-1 which extends along the approximately 280 km length of the Marmara Sea. The names of formations and adjacent cities are annotated in the shaded gray-tone version of Image 5.6.5-1 which shows the contours of the complete Marmara Sea. ▶

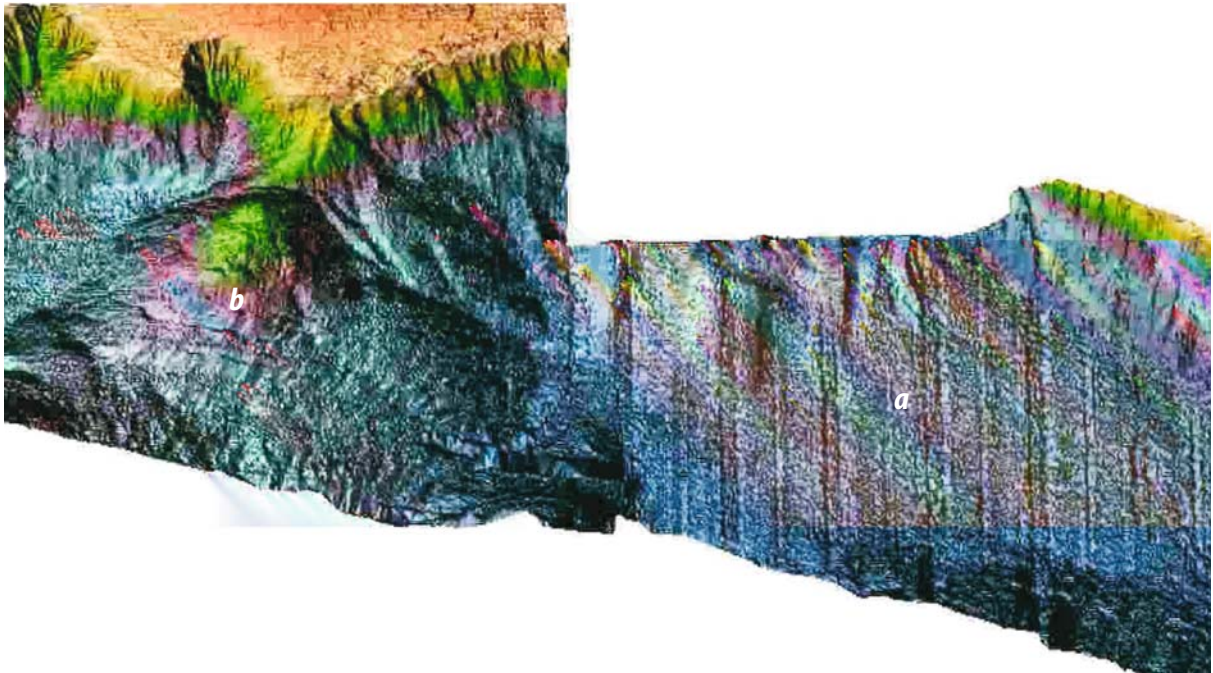


Image 5.6.5-3. *Çınarcık Basin and Eastern Ridge.* Landforms related to strike slip faults tend to be much less conspicuous, commonly discontinuous along the strike of the fault and usually shorter lived than those forming along convergent or divergent plate boundaries. An evolving strike slip shear zone generally creates a band of deformation. Generations of structures succeed and superimpose on one another, being the expressions of contrasting local and transient strain regimes. Segments of pure strike slip often appear as straight faults of modest topographic expression.

Çınarcık Basin (a). The principal displacement zone (PDZ) of the North Anatolian Fault Zone (NAFZ) enters the Marmara Sea as a single main dextral fault strand. It seems to continue along the northern escarpment of the *Çınarcık Basin*, but the precise manner of the junction is conjectural, due to a major landslide burying the fault trace.

Their strikes and trends fan northward into near N-S orientations visible in the bathymetry. Three prominent N-S trending spurs in the relief of the NW corner of the *Çınarcık Basin* are interpreted as complex box-folds bounded in part by step thrust faults.

Eastern Ridge (b). The *Çınarcık Basin* is delimited in the west by a broad high with complex bathymetry and structure. The PDZ seems to continue as a single strand to an E-NE trending elongate basin, called the *Silivri Basin* by Gazioğlu et al, 2001. The NE half of this basin is delimited by sinuous thrust faults that converge eastwards to the PDZ. South of the thrust front along the southern margin of the basin is a family of NW striking gently SW concave normal fault traces (Pichon et al. 2001).

Between the *Silivri Basin* and the *Central Basin*, the PDZ appears essentially as a single strand with E-NE striking short splays. (The conspicuous stripe pattern is an artifact from incomplete beam calibration.) ■

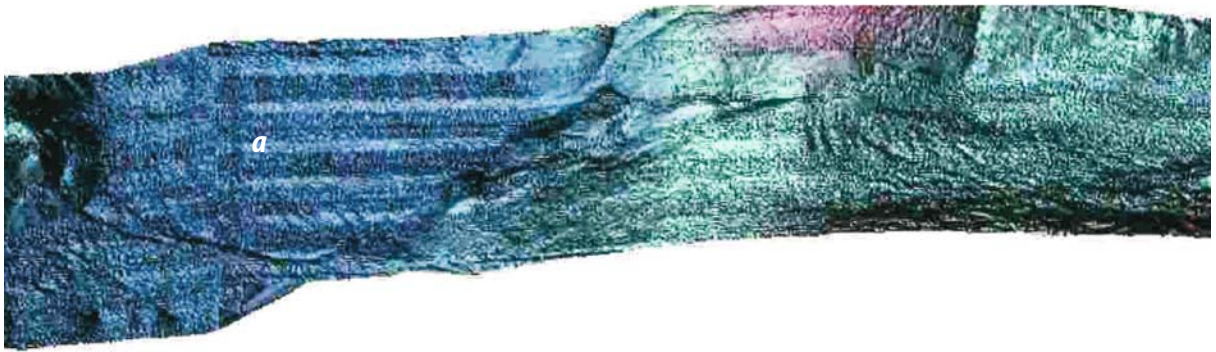


Image 5.6.5-4. Central Basin (a). The margins of the central Basin are morphologically sharp, the northern margin more so than the southern. A band of steeply dipping thrust and oblique compressional faults connect the PDZ of the western portion of the southern part of the Central Basin with a spindle shaped fault zone in the middle part of the Central Basin. The PDZ at the western end of the spindle shaped structure changes again into a single strand fault zone along which the western margin of the Central Basin appears dextrally offset for approximately 4 km. ■

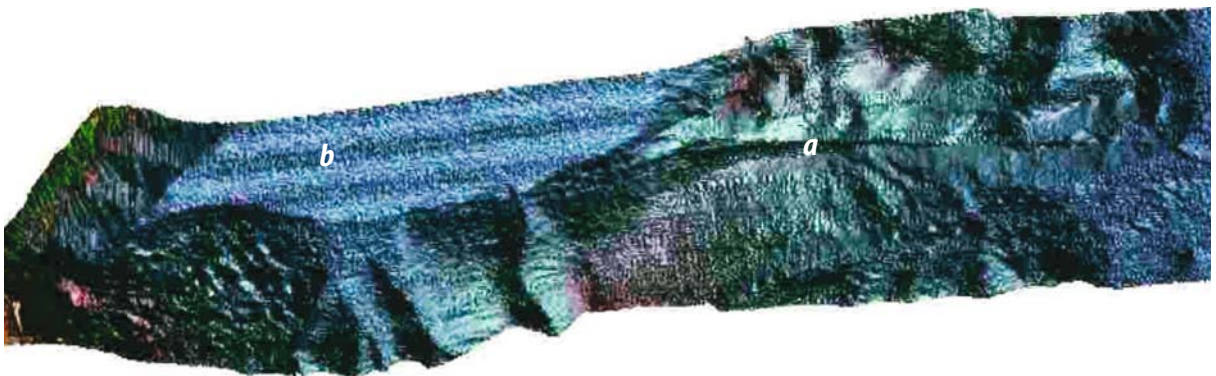


Image 5.6.5-5. Western Ridge and Tekirdağ Basin

Western Ridge (a). The Western Ridge is much narrower and smaller than the Eastern one, has a similar general NE trend and is deeply dissected by one E-W trending straight furrow that now contains the PDZ. No active scarps are associated with any of the fault systems and it is assumed they are inactive.

Tekirdağ Basin (b). The spindle shaped Tekirdağ Basin is the westernmost of the three major deeps of the Marmara Sea. It immediately adjoins the approximately 1 000 m high Mt. Ganos to the west, the most prominent and isolated topographic high of eastern Thrace south of the Istanca Mountain. PDZ defines the southern margin of the Tekirdağ Basin in the form of a near continuous string of low and fresh scarp segments, as seen on the relief.

The basin floor which is at present more than 1 100 m deep and appears nearly plane has a thick fill of about 2 500 m of late Tertiary to Quaternary sediments, discovered by separate seismic sounding. The original fault basin was correspondingly deeper. The near neighborhood of different features along the basin coast indicates dramatic processes of violent deformation of the fault trough in the past. ■

According to recent interpretations, the NAF-strand passing the Marmara Sea splays again into several strands which are considered the features bounding the trough basins. Both strike-slip and normal faulting occurs in this region and both are responsible for earthquakes. The characteristic, linear-shaped steep slopes

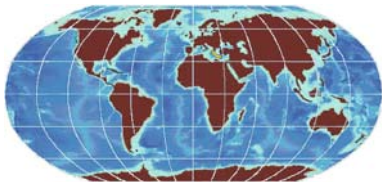
bounding the *Çınarcık Basin* at the east of the Marmara Sea and off the *Ganos Mountain System*, *Kapıdağ Peninsula* and *Armutlu Peninsula* – an uplift product of the NAF of the Marmara Sea – are attributed to strike-slip faulting. The curve-shaped slopes with low angles are considered to be associated with normal faulting.

The E-W-oriented lineaments along the trough are morphological expressions of strike-slip faults. They can be traced from the Ganos Mountain System to the *Çınarcık Basin*, cutting through the basins and ridges in the western Marmara Trough, and bounding the *Çınarcık Basin* at the slope-basin transitions. These lineaments indicate a late rupture of the North Anatolian Fault Zone which must have occurred after the formation of the Marmara Through.

Résumé

A single strike slip fault system nearly bisects the Marmara Trough and connects the Earthquake 1999 (İzmit) fault with the Earthquake 1912 (Şarköy) fault. In the eastern quarter of the Marmara Trough, the principal displacement zone PDZ follows closely the northern margin of the basin, whereas in the Tekirdağ Basin it hugs its southern margin. In the eastern quarter of the PDZ a minor component of its displacement is distributed across the *Çınarcık Basin* and adjacent central high, that are connected to the two successive sharp bends of the dextral PDZ.

5.6.6 The Deep Eastern Mediterranean Sea and Its Tectonic Convergence



The first Mediterranean large area multibeam relief map represents also one of the largest areas covered

by high resolution multibeam technique in general so far. It visualizes details of the eastern tectonic plate convergence zone and other morphologic features which the composite non-multibeam image of the complete Mediterranean Sea (Sect. 5.6) does not resolve. The main features are graphically summarized in the schematic Map 5.6.6-1b and commented hereafter.

Image 5.6.6-1a,b. (see page 246)

The Deep Eastern Mediterranean Sea formations. Multibeam bathymetric relief.

- The *Mediterranean Ridge (MR)* appears as an inconspicuous, broad, elongated elevation in previous, bathymetric maps of low resolution: about 1 500 km long and 200 km wide on average, running from west to east, from the

Ionian Basin, passing south-west and south of *Crete* to west of *Cyprus*. Its depth varies between 3 000 m in the *Ionian Basin* and less than 1 300 m north of *Libya*. However, as revealed by advanced high resolution sound imaging, the ridge region is the eastern part of the active tectonic margin system governing the Mediterranean sea floor topography where the tectonic *African Plate* is subducted under the *Eurasian Plate*.

This is unlike the subduction zones around the *Pacific* (Sect. 5.2.1) particularly along South America where an *oceanic plate* is subducted under a *continental plate*, causing partial sediment fill of the subduction trench and accretionary wedges of stripped off sediments. It is also unlike *western Pacific* (Sect. 5.2.2), where *converging plates are often oceanic* with only thin sediment coverage. Due to the subduction of most the oceanic domain the Mediterranean subduction is almost *continental versus continental*. Here, the processes are thus more complex, in parts with subduction towards north occurring below the MR and with shear forces and corresponding faults due to slant motion of the incoming African Plate. The accretionary wedge of stripped off sediments with its typical multi-folded profile is found all along the Ridge. A textbook-like trench-wedge deformation pattern is apparent on the southern side of the ridge off *Libya*, named *Herodotus Trough*. On the northern side of the Ridge, in particular south of *Crete* the accretionary wedges with the *Ptolemy-* and *Pliny Trench* are much more deformed by faults and thrusts. Due to the convergence massive quantities of muds, fluids and brine flows are released on the sea floor of the Ridge complex as has been seen in separate studies, including in situ dives.

- The *Anaximander Mountains* east of *Rhodes Island* and *Rhodes Basin* are the pronounced easternmost features of the northern margin of the Mediterranean Ridge. In tectonic terms they are a series of faulted blocks and in geological time scales recently – less than 4 My ago – detached from southern Turkey. More eastwards the much less expressed southern margin of the Mediterranean Ridge after having passed the *Herodotus Abyssal Plain* progressively connects (s. broken line in the Map 1b) between the *Anaximander Mountains* and *Cyprus* with the main, northern plate margin along the smaller and arcuate reliefs, named *Florence Rise*. This rise, partly inherited from previous subduction processes, constitutes now an active structural transitional relay with the ongoing convergence of the African margin and the island of *Cyprus*. Mud volcanoes, indicating also massive fluid emanation, characterize the whole area between southern Turkey and western *Cyprus*.
- The *Erathostene Seamount* south of *Cyprus* with its large flat top is a *guyot type* of a former continental block which emerged above the sea surface in the past about 5 My ago and lost parts of its former sedimentary cover by erosion. ▶

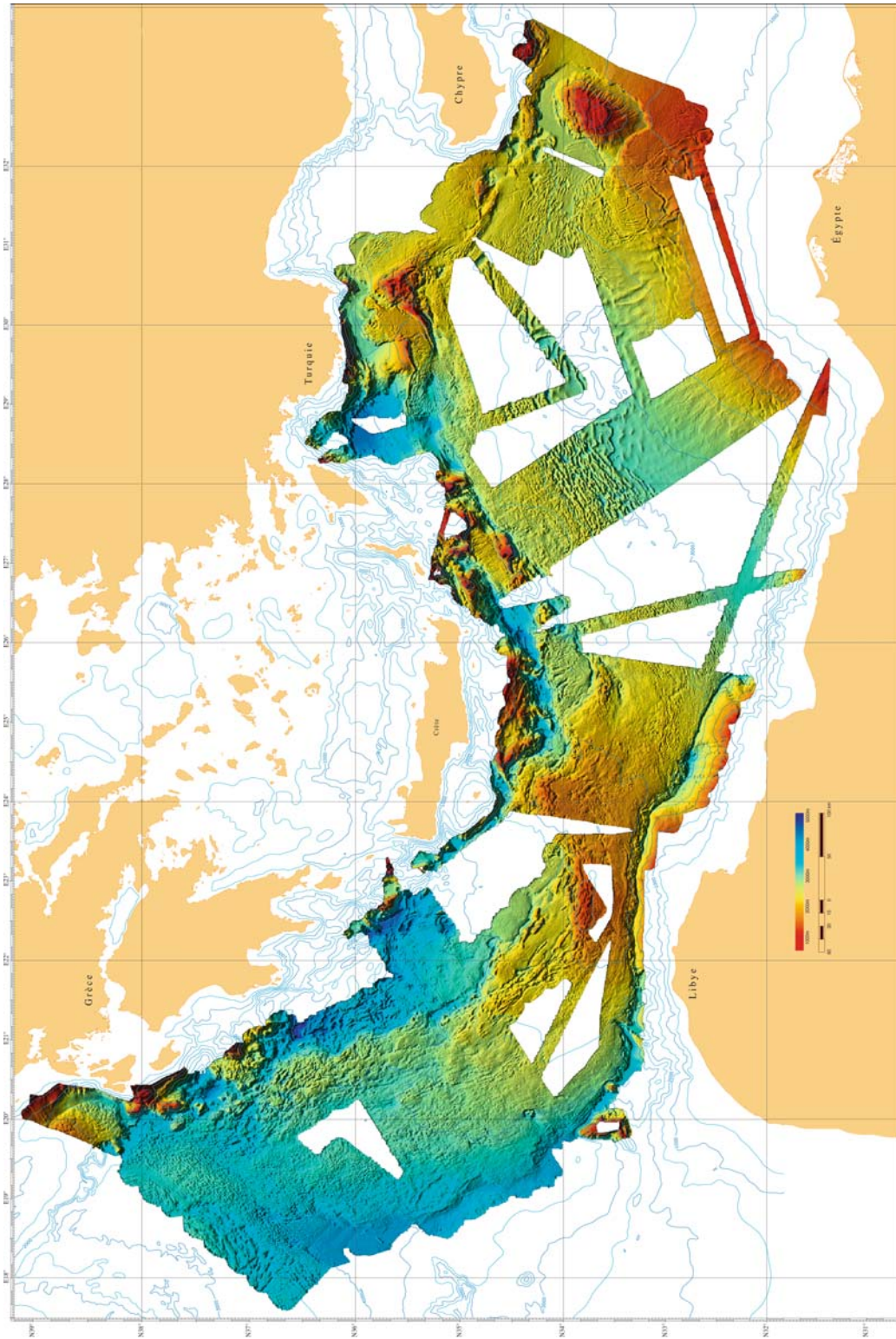


Image 5.6-1a. ■

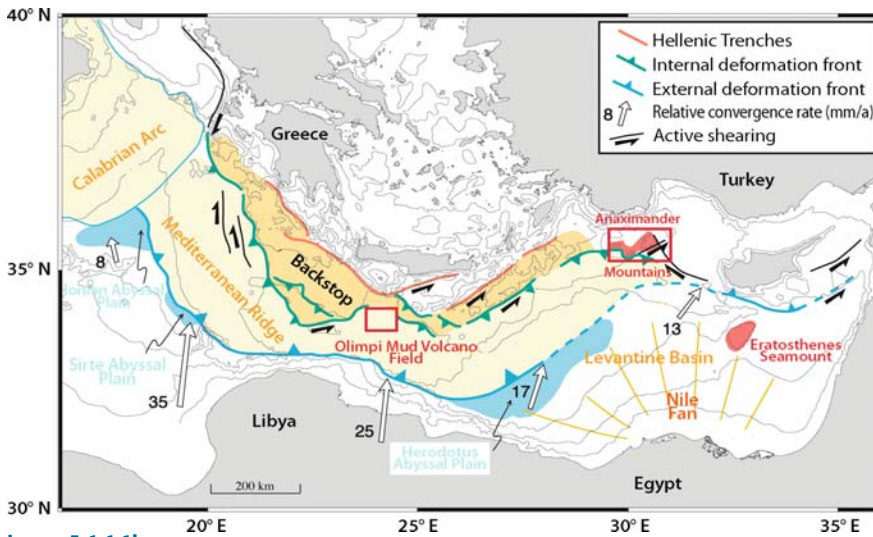


Image 5.6.6-1b. ■

Due to later subsidence of the area the plateau is now about 1 000 m below sea level. Its flank slope is only 8% and less, down to 2 000 m forming a large foot diameter of more than 50 km. This continental seamount was once part of the African mainland and bounds the northeastern domain of the Egyptian continental margin. The Eratosthenes Seamount is thus the exposed frontier moving now towards collision with Cyprus.

- The *Nile Deep-Sea Sediment Fan* constitutes the most prominent recent sediment accumulation of the entire Mediterranean Sea along the African continental margin. The Nile being the longest river worldwide is one of the most productive builders of inshore as well as offshore sediment fans, famous for the fertility of the *Nile Delta* during the history of one of the earliest civilizations of mankind. The complex morphology of the *Nile Deep-Sea Fan* results from the interaction of rapid, fast growing sedimentation mainly in the west with giant sedimentary collapses expressed by large gravity induced failures mainly present in the central domain, further of progressive gliding due to underlying salt-rich layers mostly in the eastern sector and, finally from abundant fluid releases also expressed by mud volcanoes.
- Off *Libya*, the continental slope appears quite narrow with only 30 km on average; this can be considered as a geological artifact since most of the former continental margin is now tectonically covered by the southward growing Mediterranean Ridge pile of sediments.
- Off *Peloponnesus and Crete* the *continental margin* is made of a series of massive faulted blocks and deep tectonic troughs which reflect its intense cutting by active faults related to the extensional tectonic activity of the *Aegean Sea* (Sect. 5.6.4).

The shaded bathymetric relief map as it is shown here, is now being revised by implementing recent multibeam datasets collected since 1998, particularly along the Egyptian Margin, the Levantine Margin and in several areas of the *Aegean Sea*. A new upgraded version will soon be published by *IFREMER* and *CIESM* in the series *Maps and Atlases*.

Project: Multibeam bathymetric map of the Deep Eastern Mediterranean Sea basin. Based on a compilation of swath data collected between 1992 and

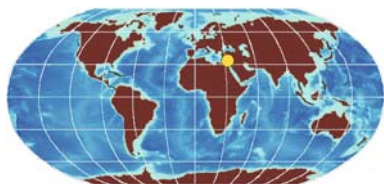
1998 in the Eastern Mediterranean Sea, this compilation has been promoted by J. Mascle, chairman of the CIESM Marine Geosciences committee, and jointly published by CIESM and IFREMER in 2001

Cooperating institutions and data provision:

- Geosciences Dept., Ifremer-Brest: Heralis survey across part of the Ionian Sea, 1992; chief scientist: J.-P. Foucher
 - Laboratoire de Géologie, Ecole Normale Supérieure de Paris: Médée survey, 1995; chief scientists: X. LePichon, N. Chamot-Rooke
 - Center for Marine Earth Science, Free University, Amsterdam: Anaxiprobe survey, 1995; chief scientist: J. Woodside
 - Géosciences-Azur, Observatoire Océanologique, Villefranche sur Mer: Prismed 2 survey, 1998; chief scientist: J. Mascle
Research vessel: *RV L'Atalante*, France
Multibeam system: Simrad EM12, Dual system; frequencies: 11/12 kHz
Data processing: Caraiibes software, IFREMER
Global Digital Terrain Model DTM, grid spacing: 500 m; Mercator projection at 35°N
Merger of contributed date sets: Ifremer Geosciences Cartographic office. Responsible: B. Loubrieu, Ifremer
- Image © and feature outline:
- B. Loubrieu and J.-P. Foucher, DRO Ifremer, Brest, France
 - J. Mascle Geosciences-Azur, Villefranche/Mer, France
 - N. Chamot-Rooke, Laboratoire de Géologie, ENS, Paris, France
 - John Woodside, Center for Marine Earth Sciences, Free University, Amsterdam, The Netherlands ■

5.6.7

5.6.7

Shelf Formations off *Israel*

The three subsequent multibeam images dealing with shelf- and shelf break formations off Israel reveal structure details which could not be resolved from surface vessels in the deep sea.

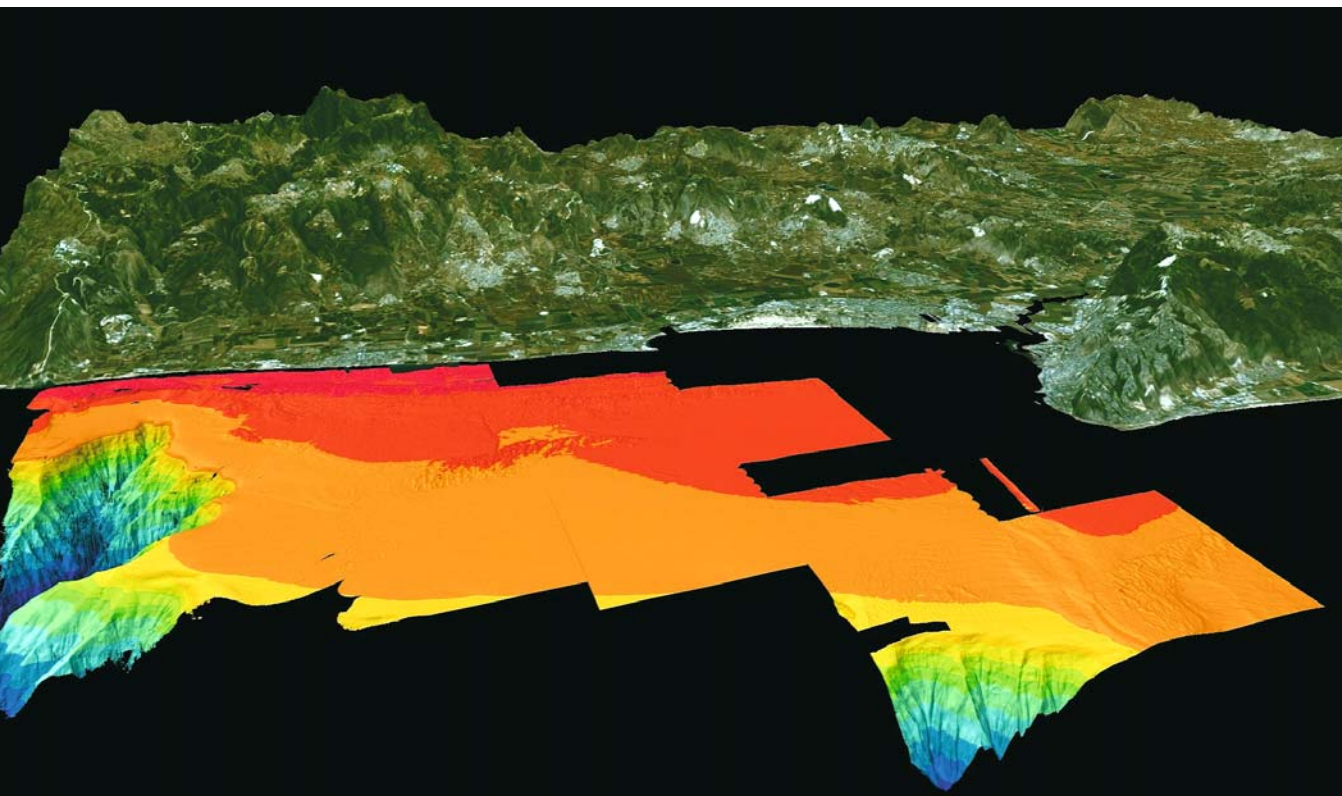


Image 5.6.7-1. Shelf break off Northern Israel. Multibeam image. The oblique eastward view towards *Haifa Bay* over the northernmost 30 km of the coast and shelf of Israel shows two major features: At the southern right side with the bight of *Haifa*, the mouth of the river *Qishon*, and *Mount Carmel*, a short section of an abrupt shelf break is apparent in the foreground, less than 10 km off the coast. A closer inspection reveals the folded morphology of this shelf break cut-out which does not appear very different in kind from the other large feature, the *Achziv Canyon*. This steep break incises the shelf on the left near the shore just south of the border with *Lebanon* where a series of further canyon formations exist along the coast. There is no direct connection of the *Achziv Canyon* to the coast by tributary canyon branches or channels (Sect. 5.3.6) however, but a sharp contour like a shelf break; it appears at present like a canyon without an obvious feeder system and without a major sediment fan below.

The slightly sloping, only at first sight seemingly plane shelf, is in reality structured by various bed forms. The grooved relief, reminiscent of the bark of a tree, off *Mount Carmel* and also off central *Galilee* in the middle of the image consists of carbonate cemented siliceous sands also named *kurkar*. This calcareous material is typical of the west coast of Israel onshore as well as offshore; for instance: *Mount Carmel*, known from the biblical story of *Elijah*, is considered part of an ancient carbonate barrier reef. The shallowest sediment stripe adjacent to the coastline coded red shows the most pro-

nounced kurkar structure like ploughed furrows. These structures are crossed by several faults extending offshore. They are clearly visible in the central part of the Galilee coast north of *Acre*.

Project: Israel National Bathymetric Survey (NBS); year of survey: 2001 to present – ongoing
 Cooperating institutions: Geological Survey of Israel (GSI), Jerusalem; Israel Oceanographic & Limnological Research Ltd. (IOLR), Haifa; Survey of Israel (SOI), Tel Aviv
 Survey vessel: *RV Etziona* of IOLR
 Multibeam system: Kongsberg Simrad EM1002; frequency: 95 kHz, beamwidth: 2°, 111 beams;
 Color code: red 0–50 m; dark blue: 1 000 m. 12 steps;
 Grid spacing of sea floor: 5 m, vertical exaggeration factor of the sea floor relief: 4; grid spacing of land relief from Landsat 7 satellite data: 30 m (Digital Terrain Model – DTM, Hall, 1997), vertical exaggeration factor land: ~3
 Image ©: Aharon (Ronnie) Sade, John K. Hall, Geological Survey of Israel, Jerusalem ■

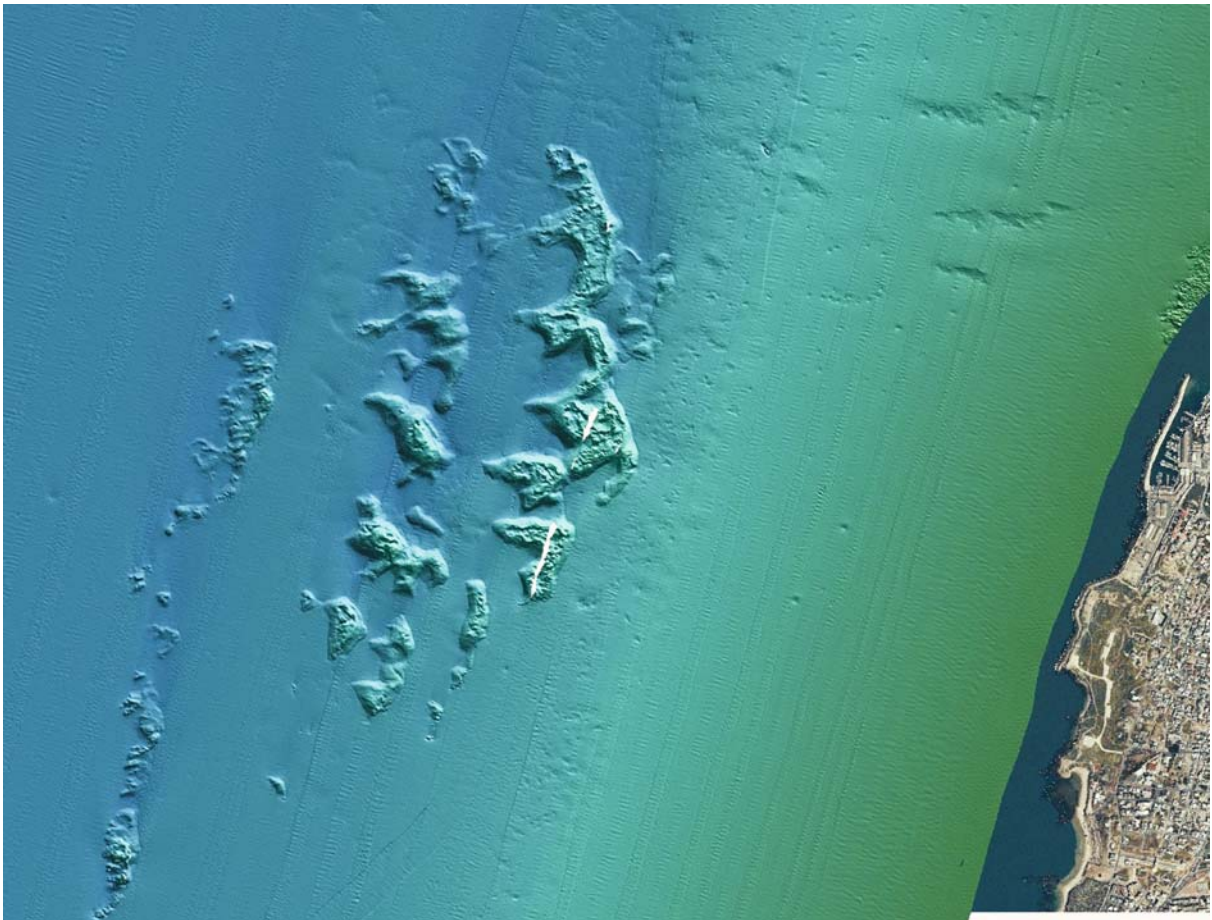
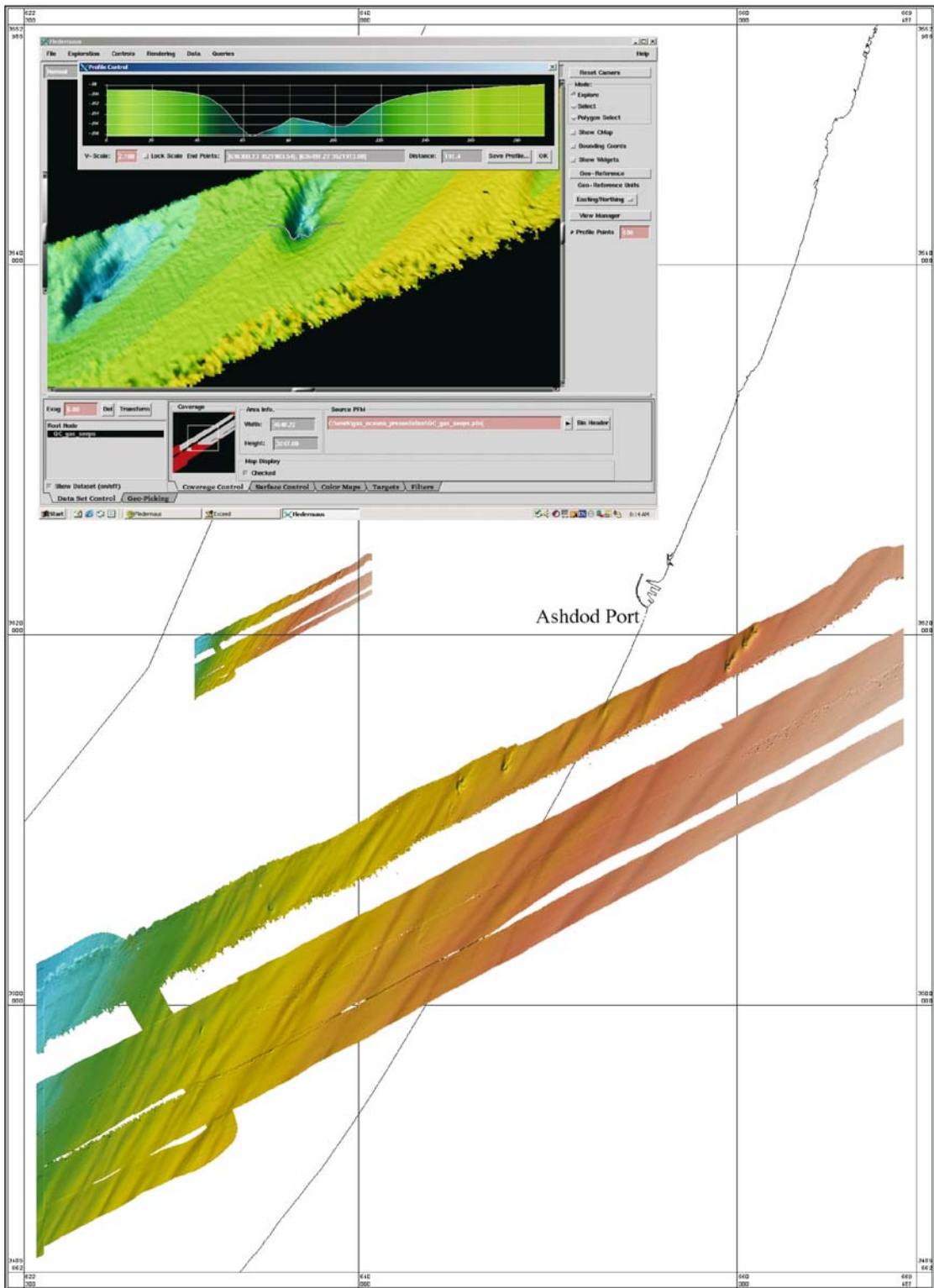


Image 5.6.7-2. Kurkar bedforms off Jaffa Port. Multibeam image. This cut-out of a larger sonar image south of *Tel Aviv* in Central Israel changes the perception that the kurkar only forms continuous ridges paralleling the coast as shown in the north of the previous image. Also evident is the existence of scour to the north of these bed forms, indicating a persistent south to north transport of sediment within the Nile littoral cell. The horizontal size of these 7–12 m high kurkar outcrops at a water depth of 30–40 m is evident by comparison with the town of Jaffa, visible at the right corner of the image.

Image documentation: same as for Image 5.6.7-1

Image ©: Aharon (Ronnie) Sade, John K. Hall, Geological Survey of Israel, Jerusalem ■



5.7 Baltic Sea Formations

The *Baltic Sea* is the arena of a major international trade route of a long tradition, rooted in the historic *North European Hanseatic League*. In geological time scales the Baltic is a young formation. Originating from the last glacial period of northern Europe the Baltic has been a shallow marginal sea (Sect. 5.7.1) of the *Atlantic Ocean* for about 7 000 years. In the last phase of a complex formation process the former freshwater sea of melted ice and river inflow was finally inundated during the postglacial sea-level rise which eventually exceeded the rise of *Scandinavia* when freed of the glacial ice burden. This inundation left a shallow sill connection to the *North Sea* of hardly more than 20 m depth which is part of the traditional sea route. The famous direct traffic connection which saves transfer time is the *Kiel Canal*. This artificial fairway built at the turn of the nineteenth century exceeds even the Panama Canal in number of ships passing.

The sill area of the *Danish Sounds* and the *Kattegat* (Sect. 5.7.2) limits the water inflow from the open sea to rare storm-induced spillover. Most of the time the Baltic river inflow generates a surplus of freshwater that dilutes the saltwater of North Sea origin from the 3.5% salinity of ocean water down to less than 1% at the northern end of the Baltic; this region is ice-covered half of the year. This large shallow water body in the center of northern Europe with an average width of about 200 km extends nearly 1 300 km between the *Gulf of Gdańsk* in the south and the border between *Sweden* and *Finland* in the north. It is, in fact, the largest area of brackish water in the world.

The southern part of the Baltic, where the salinity is least diluted has the most pronounced stratification of dense salt water below a more or less mixed layer of low salinity water near the surface. The stable near bottom layer is poor in dissolved oxygen, the prerequisite for marine fauna to exist, since it is ventilated only during the strong but rare inflow events of saline water from the North Sea. Microbiologic production of methane gas does not require oxygen but an abundance of organic material. The young, muddy sediments of the western Baltic offer these conditions, which were investigated in the framework of an international research project (Sect. 6.2.2).

◀ Image 5.6.7-3.

Pockmarks indicating gas deposits off Ashdod, southern Israel. Multibeam image (collage). This image shows the initial profiles run on the outer shelf off Ashdod, southern Israel. Of note is a series of elongated, asymmetric pockmarks (Sect. 6.2.2) in water depths between 80 and 110 m which are most likely gas seeps. These pits are around 30 m deep and 300 m across as shown in the upper depiction. The swaths are enlarged below. Note the rippling of the sediments parallel to the coast. The general SW-NE-trend of the features indicates sediment transport from the Nile Delta towards the north. The gas seeps may lie along shore-parallel faults. The offshore is the site of numerous gas field discoveries during the past decade.

Image documentation: same as for Image 5.6.7-1
Image ©: Aharon (Ronnie) Sade, John K. Hall, Geological Survey of Israel, Jerusalem ■

5.7.1

The unique oceanography of the Baltic exhibits a remarkable sound propagation feature which otherwise exists only in the deep ocean: the basins of the southern Baltic act as genuine Sofar-ducts (Sect. 3.2.2) during summer. In deep oceans Sofar-ducts are formed because the sound speed increases toward the ocean floor due to the static pressure. In the shallow Baltic the saline bottom layer with its higher sound speed has the same effect. Thus the sound propagating in a horizontal direction undulates up and down without touching surface and bottom. It is refracted downwards by warmer surface water and correspondingly higher sound speed in the same way as in the deep ocean. And it is subsequently refracted upwards by saline water below.

The Baltic with an average depth of only 50 m is subdivided into a sequence of basins of 100 m depth and more, with the deepest depression of 460 m near the Swedish coast north of the large isle of *Gotland*. The sills separating the basins are as shallow as the *Kattegat* and constrain the rare North Sea water inflow to propagate into the deeper Baltic basins. The sea floor of the Baltic follows the ongoing rise of the *Scandinavian Shield* with a maximum of 1 cm per year at the sill of the *Gulf of Bothnia*, the eastward branch of the Baltic.

The Baltic coast south of *Finland* and the east coast of *Sweden* is strewn with innumerable cliffs; most of them are submerged but many protrude the surface as islands. Presumably these cliffs of old granite were mechanically released during glacial times from less hard enclosures and weathered material. The furrows between the cliffs have become more or less filled with sediments (Sect. 5.7.5).

There are efforts under way to reduce pollution from contaminated river inflows and to remove dumped World-War ammunition. Permanent governmental surveillance ensures that shipping lanes are freed of sunken ships and other obstacles when the safe shipping clearance is at risk (Sect. 7.1.1, 5.7.3). Besides the surveillance of the shipping lanes regional research institutes explore the outer topography, morphology, bottom type (Sect. 5.7.2) and the internal sediment structure (Sect. 5.7.6, 5.7.7) using a variety of acoustic imaging techniques together with bottom sampling and coring.

Beyond all other remarkable features, the Baltic Sea is renowned worldwide for its amber. The largest deposit of amber is embedded in the beach of the *Sambian Peninsula* east of the Gulf of Gdansk. This amber, a former pinewood resin, is 5 to 10 thousand times older than the Baltic Sea.

5.7.1 Relief Image of the Baltic Sea; Overview

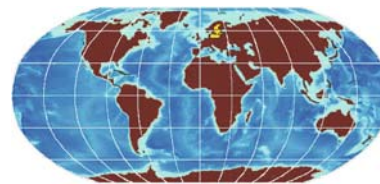


Image 5.7.1-1. ►

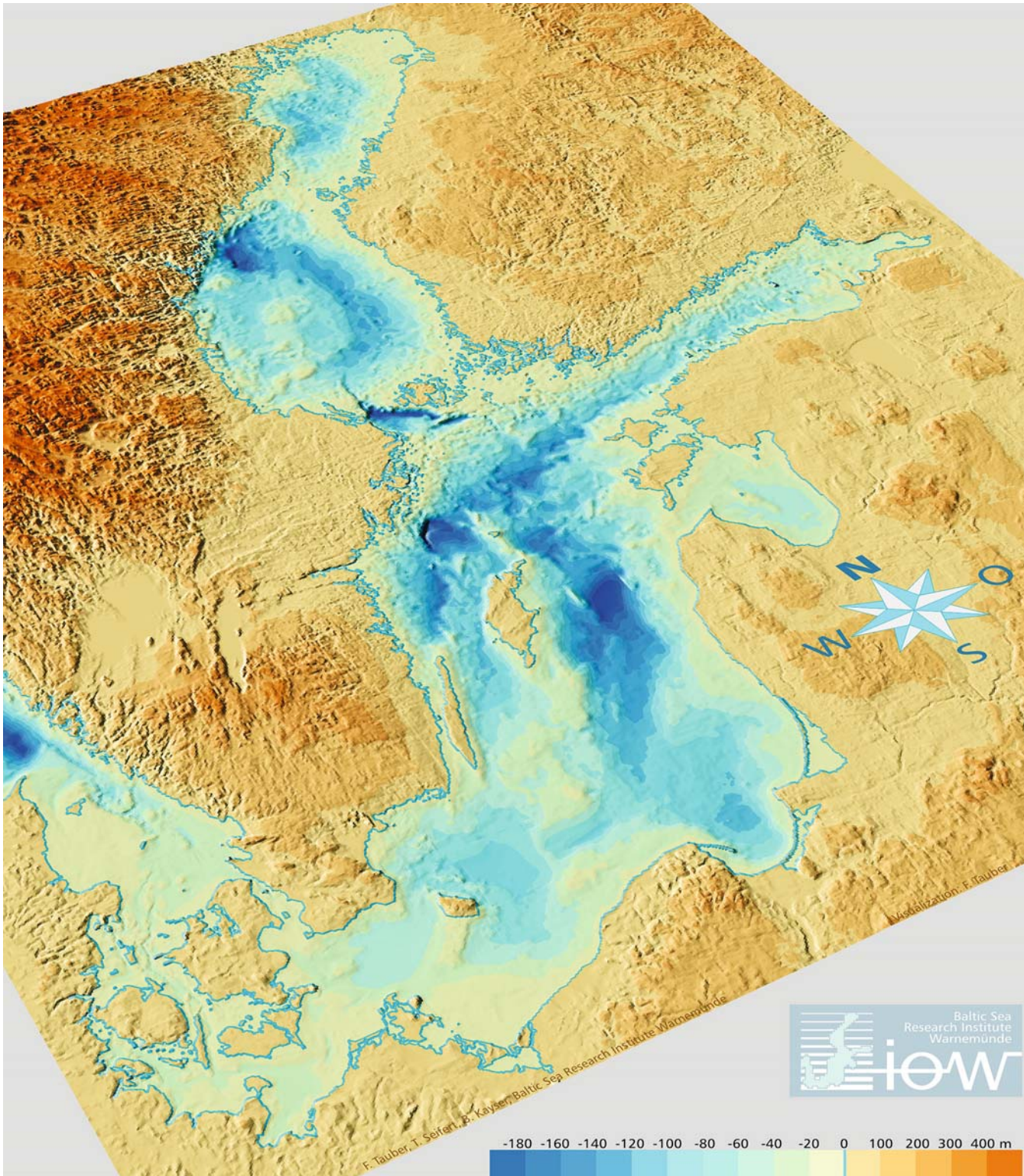
Relief image of the Baltic Sea. The numerical data set of the *Baltic Sea* relief presented here has been composed from several sources: The first numerical approach by digitizing existing sea charts was published in 1995. In 2001 the resolution and accuracy was improved by integrating new sea floor data sets, supplemented by land topography. These data sources are itemized in the image documentation below. The overall horizontal resolution of the entire Baltic relief is about 2 km; the *Belt Sea* in the west is resolved twice as well, by 1 km. Multibeam high resolution close-ups of Baltic sea floor sections resolving the morphology in the decimeter and meter range have been rare up to now.

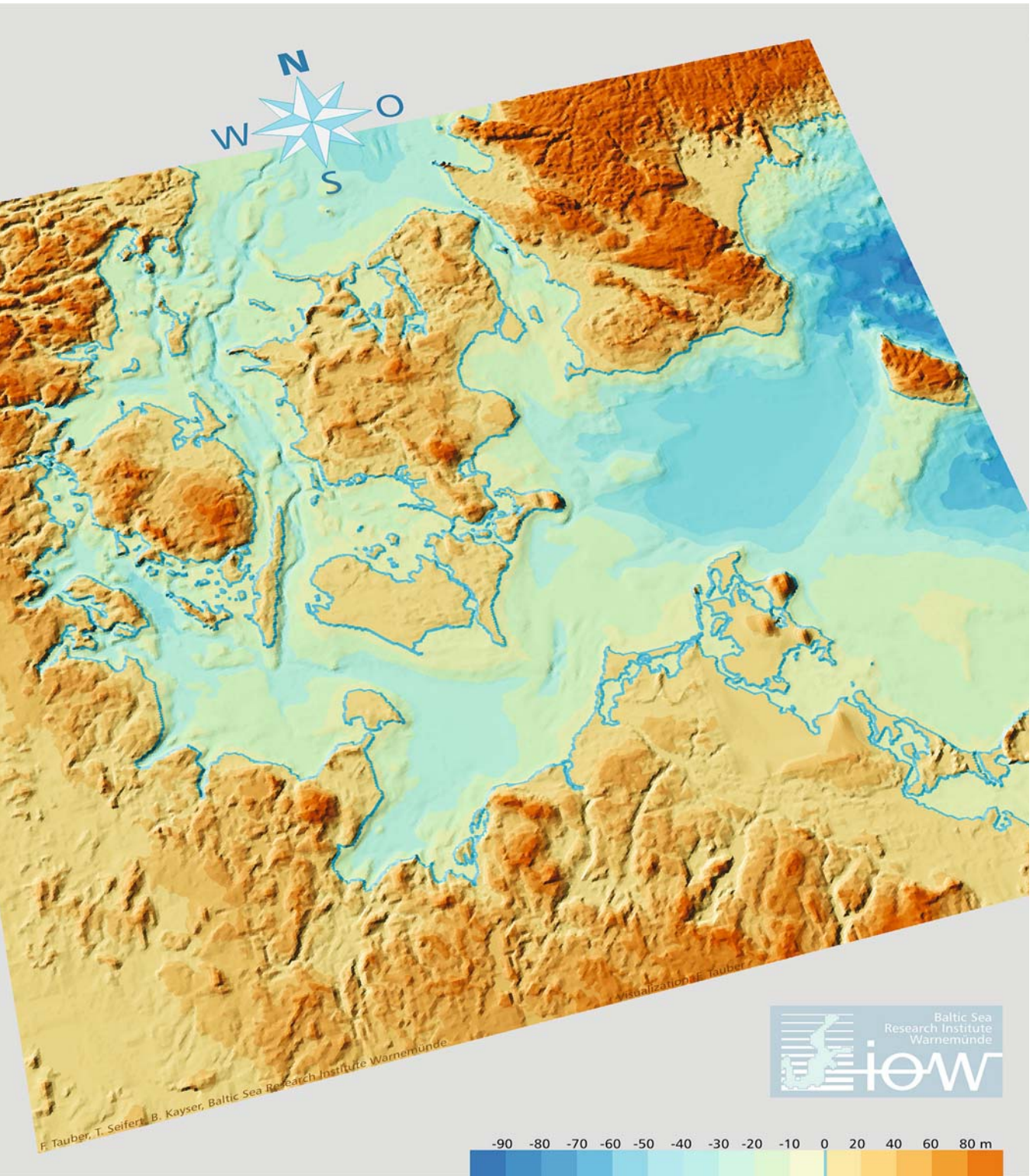
At first sight the impression of the Baltic Sea relief is its mostly non-dramatic shallow topography with a few basins deeper than 100 m. The basins are separated by sill areas of 20 to 30 m depth, sufficient for large freighters and ferries but too shallow for a frequent exchange of basin water. The nearly continuous transition of land and sea in the south requires visualization of the coast by a line.

Three morphologic features are most conspicuous: *first*, the broad but shallow connection to the North Sea in the west with the deep *Skagerrak* as the entrance. Its eastern contour is indicated dark blue at the left edge of the map. This shipping route is severely narrowed by an archipelago of a few larger and many smaller islands between the coasts of Sweden in the east and of *Denmark* and *Germany* in the west. *Second*, the lagoons in the south east with smooth coasts, and *third*, the entirely different coastline of eastern *Sweden* and southern and western *Finland*. These irregularly corrugated coasts with rocky promontories are surrounded by an immense number of subaqueous and subaerial cliffs and small to tiny islands. The deepest depression of 460 m is obvious by its dark-blue arc north of the *Isle of Gotland*. The fascinating variety of coastlines and islands, together with the wind conditions ideal for sailing, have made the Baltic Sea a center for sports and tourism.

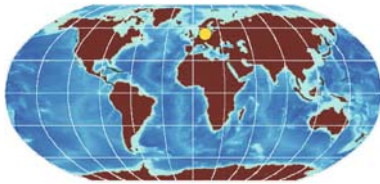
Project: Digitized map of the Baltic sea floor.

Data sources: Digitized sea Charts (IOW), GEOBALT-map of the Central Baltic, the German continental base (BSH), bathymographic acquisition of several deeper basins (IOW) and the high resolution bathymography of the Belt Sea (Danish Hydraulic Institute). The land relief is based on the satellite altimetric map GTOPO30 with 30 arc seconds or about 600 m grid. Sea floor grid: 2 km. Relief exaggeration factor: 5
Image ©: Franz Tauber, Torsten Seifert, IOW, Warnemünde, Germany ■





5.7.2 The Western Baltic Sea



Since the year 2000, the Western Baltic Sea is crossed completely by a bridge and tunnel system which connects

Germany, Denmark and Sweden. This outstanding technical and political achievement enables uninterrupted land traffic throughout Europe and beyond, an important supplement to the traditional sea traffic. The last and technically most demanding construction is the Øresund-Bridge of nearly 8 km length, closing the remaining gap between the Danish capital Copenhagen and the Swedish coast. The suspension bridge towers of 500 m height leave a gateway of more than 1 km with 50 m net height for passing ships. This construction has been based on one of the most comprehensive investigations regarding the potential impact on the environment. The Øresund, together with the two other connections between North Sea and Baltic, the Lille Belt and the Store Belt is considered a decisive element of the ecosystem and water exchange of the Baltic Sea.

◀ Image 5.7.2-1.

Relief image. The relief of the shallow western side of the Baltic has been more strongly enhanced by a factor of 10 to visualize the narrow shipping passage between the main Danish islands *Fyn* and *Sjælland* with the Danish capital *København*. This western part of the Baltic Sea with its shallow relief demonstrates why much of the Baltic is often called *inundated meadow*. The *Kiel Canal* and rivers are not resolved. The *Kiel Fjord*, the eastern terminal of the *Kiel Canal* as it were, and the *Bay of Eckernförde* (Sect. 6.2.2) are the pair of incisions next to the *Isle of Fehmarn* in the west. The more northern *Schlei Fjord*, the place of the earliest center of trade in the Baltic area (Sect. 7.3.4) is too shallow to be recognizable in the relief.

Project: Digitized map of the Western Baltic sea floor.
Data sources: Digitized sea Charts (IOW), GEOBALT-map of the Central Baltic, the German continental base (BSH), bathymographic acquisition of several deeper basins (IOW) and the high resolution bathymography of the Belt Sea (Danish Hydraulic Institute). The land relief is based on the satellite altimetric map GTOPO30 with 30 arc seconds or about 600 m grid. Sea floor grid: 1 km. Relief exaggeration factor: 10
Image ©: Franz Tauber, Torsten Seifert, IOW, Warnemünde, Germany ■

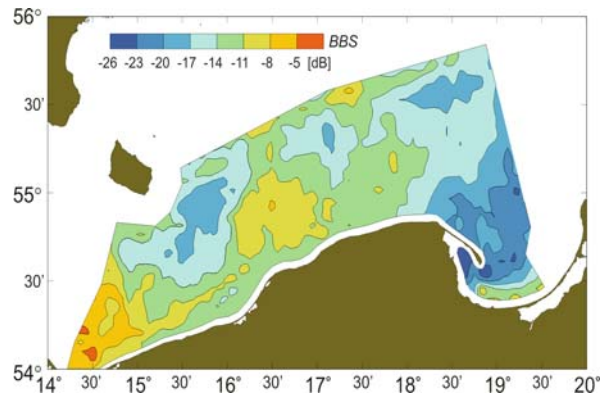
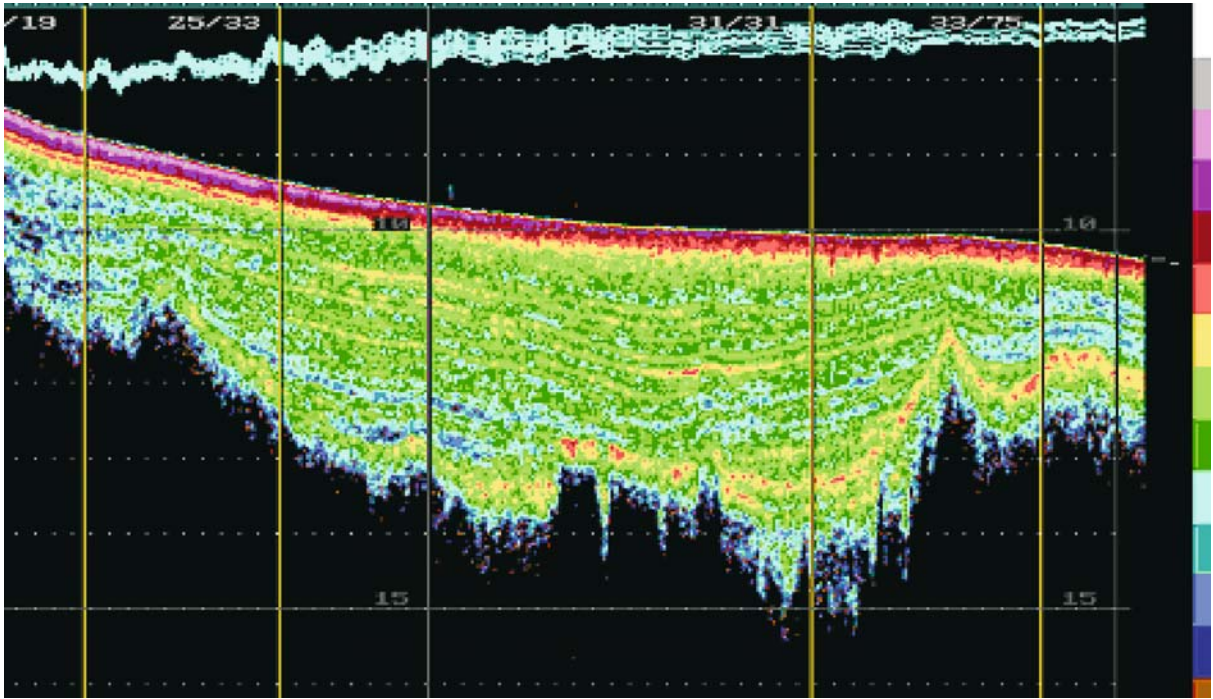


Image 5.7.2-2.

Sea floor backscattering. One of the possibilities to acoustically characterize the sea floor for mapping the bottom type is its vertical reflectivity mapped for instance by the *Acoustic Sea Floor Classification System (ASCS)* (Sect. 6.2.2). Another one is the backscattering strength, comparable to the optical *albedo* in astronomy. Examples are shown for the *Mid-Atlantic Ridge* (Sect. 5.2.3), the *North European Margin* (Sect. 5.3.6) and here for the southern part of the western Baltic from the *Island of Bornholm* to the *Gulf of Gdańsk*. The backscattering strength is mapped in steps of 3 dB corresponding to twice or half the value respectively. The bathymetric highs of the Baltic sea floor are normally but not always covered by less soft sediments than in the valleys. If this goes together with a rough surface, and thus stronger backscattering, then the highs appear acoustically bright compared to even and less dense sediment. The acoustically “dark” areas in the lagoon floor of the western Gulf of Gdańsk are not unexpected since it is partially muddy with fine grain sediment from river suspension load.

It should be stated however that the task of classifying bottom types by their acoustic fingerprint is problematic. Both the acoustic and – even more so – the sediment parameters are not just simple numbers but comprehend complicated relations, in particular when the sediment is inhomogeneous. Thus, the map shown will only demonstrate that even within limited areas the variability of this single quantity is strong. The level of –6 dB means that the echo intensity is one quarter relative to an ideal mirror reflecting backwards. The very low level of –26 dB means a quarter of one hundredth. There are deep-sea sediments however, which are extremely black as it were, 10 dB or ten times darker than in the Gulf of Gdańsk.

Project: Acoustical Mapping of Sea Bottom Properties in the South Baltic Sea. Grant of the Polish Committee for Scientific Research, 1992–1994
Survey vessel: *RV Oceania*, Poland
Echosounding device: ELAC, type: LAZ 4700, frequency: 30 kHz, beamwidth: 16°
Image ©: Jaroslaw Tegowski, Institute of Oceanology, Polish Academy of Sciences, Sopot, Poland ■



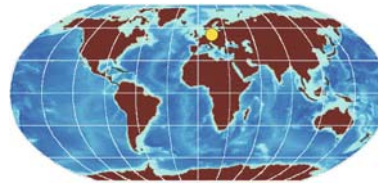
5.7.3

Image 5.7.2-3.

Trans-sediment section through the Bight of Kiel, western Baltic Sea, imaged by the Acoustic Sea Floor Classification System ASCS (Sect. 6.2.2). This sediment image represents a section of 2.5 km length through the Bight of Kiel with a continuous transition of surface sediments, identified by the ASCS-system. The surface sediments range from sand, with the highest reflectivity at the left side, to the less reflective mud at the right with muddy sand in between. This transition is indicated by the change in color at the sediment-water interface and by the echo strength lines at the top of the record. Beneath of these superficial sediments layered mud of a variable depths up to three meters are found. The strong contour denoted yellow below these deposits is a highly reflective glacial till throughout the area. The glacial till is recognized by its highly irregular surface marked red to yellow at the lower limit of the acoustic return. The identification of this contour dates the mud overlay to be post-glacial.

Project: Coastal Benthic Boundary Layer (CBBL) 1993–1998
 Survey vessel: *WFS Planet*, Kiel, Germany
 Echosounder: Acoustic Seafloor Classification System (ASCS), hull mounted; frequency: 15 kHz, beamwidth: 12°; depth resolution: 15 cm
 Depth scale: 5 m between white lines; yellow vertical lines: positions of core samples; compression of the range scale: 100
 Color key: the echo intensity increases 4 times (6 dB) per color step towards warm colors
 Image ©: Douglas N. Lambert, Naval Research Lab., Stennis Space Centre, USA; Thomas Wever, FWG, Kiel, Germany ■

5.7.3 Kadetrinne, Baltic Sea



Essentially all the sea traffic along the Baltic Sea passes along a shallow furrow named *Kadetrinne*, 6 km wide and 30 km long.

Box 5.7.3-1. Single hull tankers

The majority of tankers worldwide as of January 2004 is still single hull:

- *Global tanker fleet* for oil, oil products, oil-chemicals and pure chemicals: 8733 ships with 6317 (72%) single hull tankers.
- *Global oil-carrying fleet* for oil, oil products, oil-chemicals: 7671 ships with 5506 (72%) single hull tankers.

42% of the present tanker fleet is older than 20 years with a single hull percentage of 97% and 98% respectively. Source: Lindenau Shipyard, Kiel

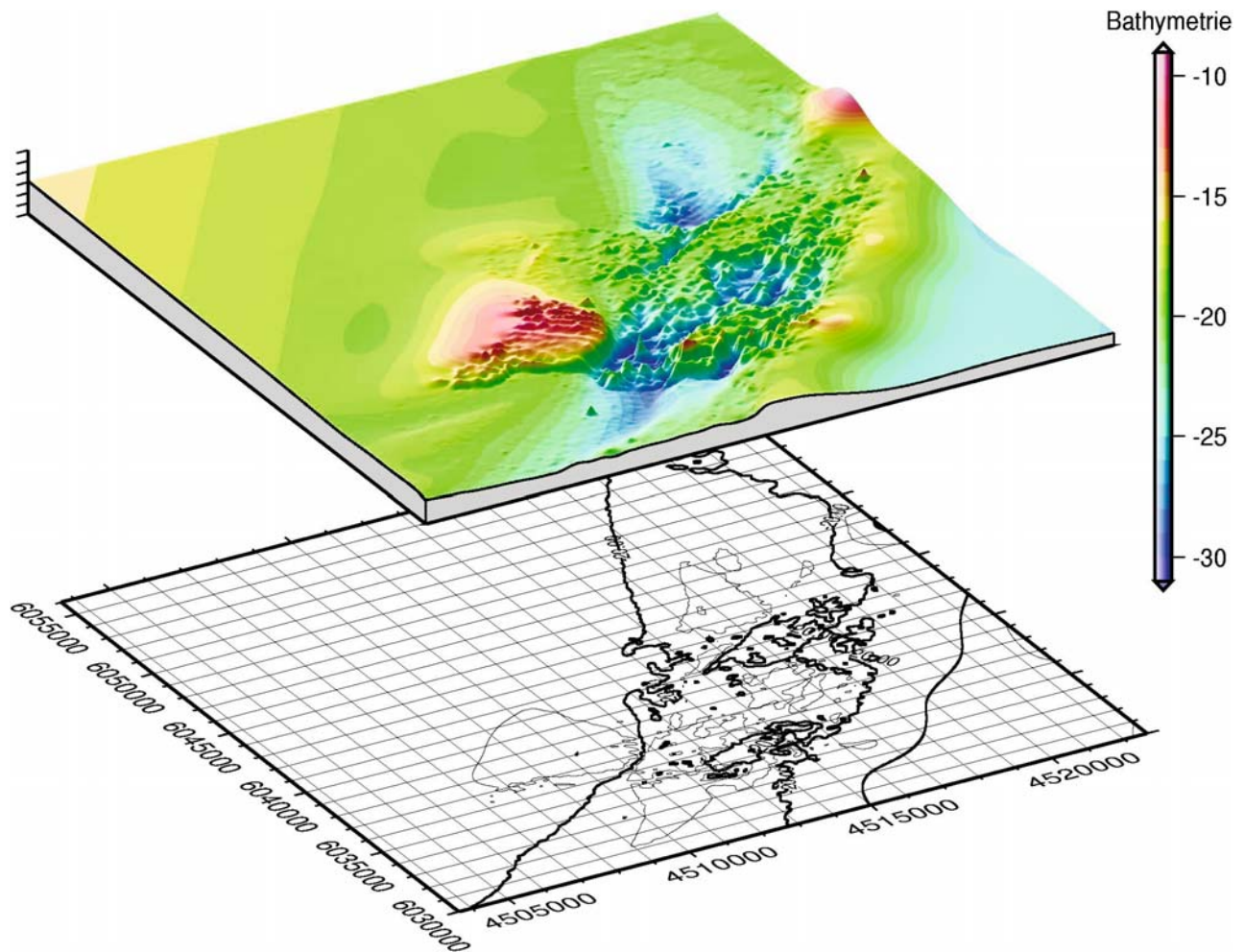


Image 5.7.3-1. A bottle neck passage of the Baltic Sea. Multibeam image. The furrow of 30 km length is the gross contour of the 20 m depth line but there are hazardous bottlenecks, which create a problem for safe shipping clearance. This passage between the Danish Island *Falster* and the German peninsula *Darss* in the western Baltic is one of the most frequented shipping lanes of the world with more than 150 passages per day. The floor relief of the Kadetrinne is subdivided by a kind of rugged sill shown in the perspective image. Due to the fissured boulder clay floor forming many narrow, irregular grooves, the remaining fairway width for large, deep draught tankers shrinks to about 500 m. The complex of shoals inside the Kadetrinne and the relatively narrow fairway are the reason for ongoing safety discussions, mainly because of the still large number of single-hull tankers (s. Box 5.7.3-1).

The geological origin of the groove structure subdividing the Kadetrinne is at present considered the result of late glacial erosion by melting ice. The image, reminiscent of an alpine scenario, shows this relief amplified by a factor of about a hundred. Such contrasting enhancements are used to emphasize the critical shoals.

Project: hydrographic surveying; year of survey: 1997

Survey vessel: *MS Deneb*, BSH

The depicted WGS-coordinates correspond to 54°24' N, 12°3.6' E of the lower left and 54°38' N, 12°21.3' E of the upper right corner of the image frame; depth range: 9–31 m

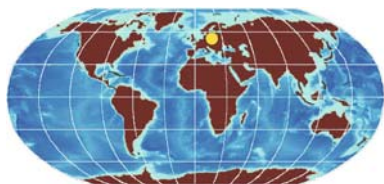
Multibeam system: ATLAS Hydrographic, Hydrosweep MD; frequency: 54 kHz, beamwidth: 1.9°, fan width:

max. 152° = 8 times/water depth

Data, Image ©: BSH Hamburg/Rostock, Germany ■

5.7.4

5.7.4

Gulf of Gdańsk, Baltic Sea

The *Gulf of Gdańsk* is part of the famous lagoon coast of the Baltic Sea. The narrow, tongue shaped western peninsula *Helska*, the former *Hela* protects the harbours of the western cities *Gdynia* and *Sopot* (Sect. 7.1.4.4) like a kind of half lagoon.

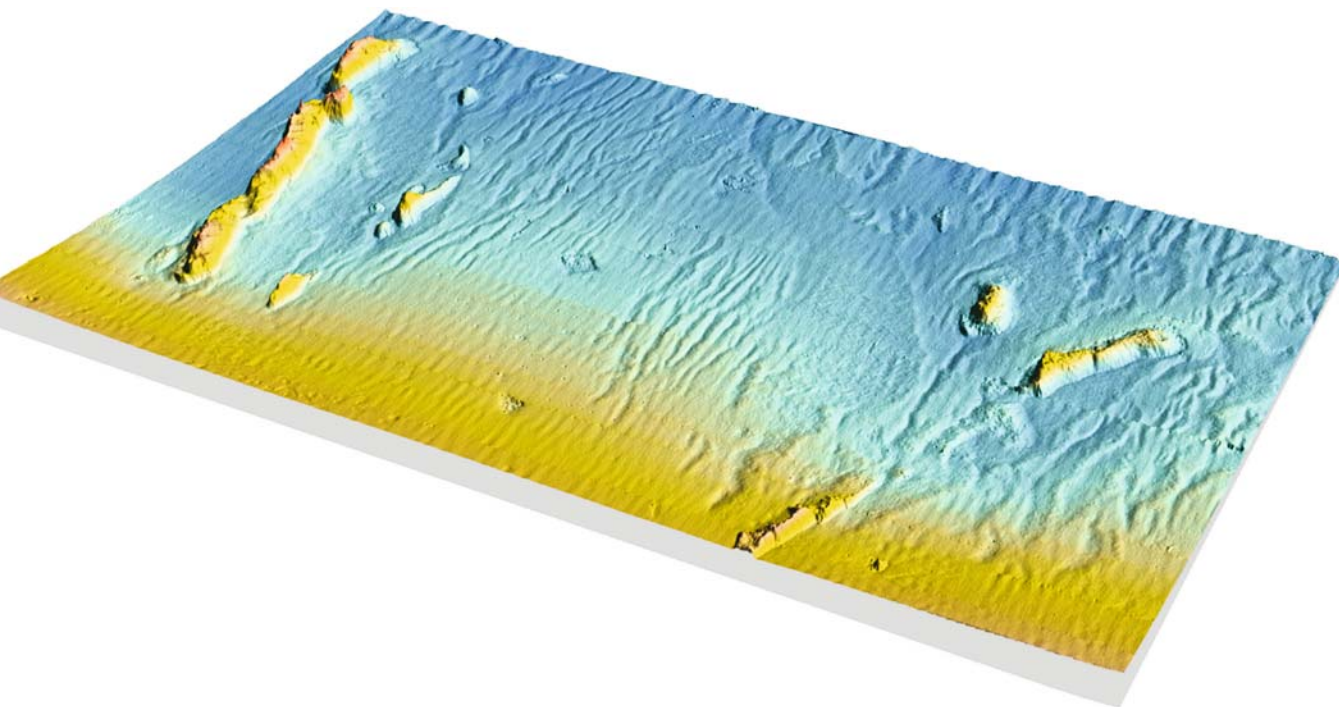


Image 5.7.4-1. Morphology of the sea floor near *Sopot*, *Gulf of Gdańsk*. 3D-multibeam image. The area of 500×800 m is part of the south-western Gulf of Gdańsk. The site is situated in 500 m distance from the shoreline, south of a narrow tongue of land forming an incomplete lagoon behind. This lagoon formation is typical only of the southern Baltic coast and famous with the two lagoons: *Vistula Lagoon* behind the Gulf of Gdańsk and *Curonian Lagoon* north-east of it.

The slightly inclined surface of fine to medium sand is covered by sand dunes of about 10 m crest distance and 0.5–1.0 m height. The most conspicuous features are the ridge fragments perpendicular to the shore. These enigmatic structures emerge by about 2 m above the sand cover. The first working hypothesis was: antropogenic origin such as remainders of hydrotechnical constructions. Thorough geological analysis however revealed the real character without doubt: fluvioglacial structures! They consist of consolidated sand and gravel with stones on the surface according to box corer samples.

Project: Bathymetric inventory south-east of Sopot, 2003

Location: Gulf of Gdańsk, nearshore, water depth: 4–12 m

Research vessel: *Doktor Lubecki*

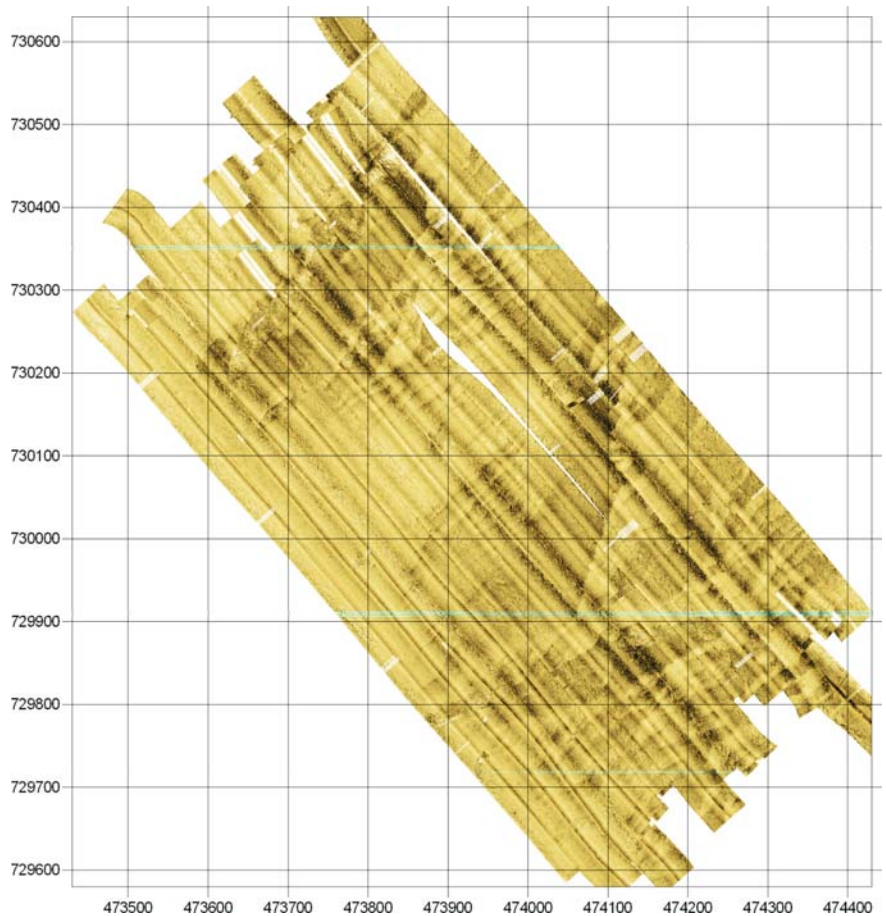
Multibeam: RESON 8101; frequency: 240 kHz, beamwidth: 1.5°, 101 beams

Image ©: Maritime Institute of Gdańsk ■

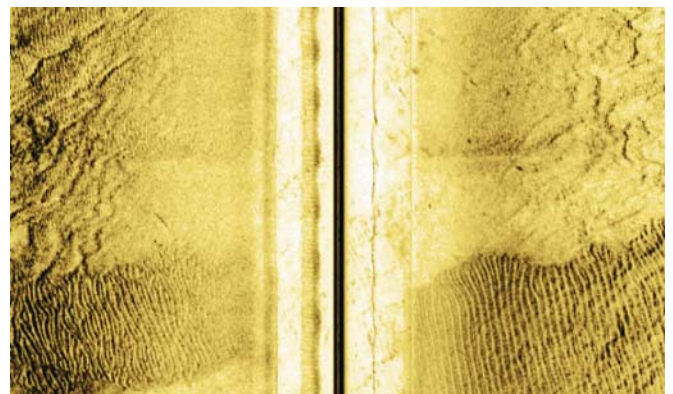
Image 5.7.4-2.

Sand dunes and ridges on the sea floor near Sopot. Sidescan sonar mosaic image. The area imaged by 2D-sidescan is the same as of the preceding 3D-multibeam image. The dunes and the ridge fragments are insonified along their crests which is evident from the sidescan stripes parallel to the shore. Accordingly the gray tone structure does not show the usually dominating dune and ridge shadows but indicates primarily the different backscattering from the respective fine structure. This may be either smaller or larger sediment grain size and/or small scale ripple structures. The close up shown in the succeeding image reveals the cause. To discriminate features of sediment material and small scale structures is the strength of sidescan imaging, thus supplementing the 3D-multibeam technique.

Project: Bathymetric inventory south-east of Sopot, 2003
 Location: Gulf of Gdańsk, near-shore, water depth: 4–12 m
 Research vessel: *Doktor Lubecki*
 Sidescan sonar: Edge Tech DF 1000; frequency: 400 kHz
 Image ©: Maritime Institute of Gdańsk ■

**Image 5.7.4-3.**

Close up of the preceding sidescan sonar image of dunes and ripples on the sea floor near Sopot. The preceding mosaic image of the entire area cannot resolve the small scale morphology which is shown in this 30×50-m close up of a single stripe taken from the same data set. On both sides of the blind central stripe typical of sidescan imaging (Sect. 4.3) the two governing features are clearly evident: the pattern of the long-crested symmetrical ripples spaced 4–8 dm with 1–2 dm height and the large dune crest parallel to the margin of the ripple field. Obviously the ripples generated by sea waves and swell cover only the dune troughs and they are oriented parallel to the shore in cross direction to the dune crests. A third feature complicates the clear bipolar system of dunes and inserted ripple fields: the flanks and even the crests of the dunes are superimposed in part by irregular mid scale ripples of slant direction. These bedform struc-

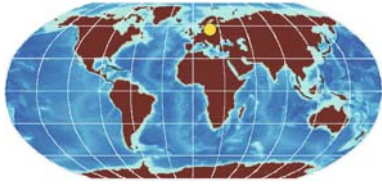


tures are document of a complex interaction of sea waves and currents.

Image documentation: same as for Image 5.7.4-2, but water depth: approx. 8 m ■

5.7.5

5.7.5 Stockholm Archipelago, Bedrock Area



The bedrock of the *Stockholm Archipelago* and its surroundings consists mainly of very old crystalline granites and gneisses formed about 1 800 million years ago. Though the nearest margin of a present tectonic plate is

far away, the Stockholm area is intersected by tectonic deformations and deep fracture zones such as the *Land-sort Trench* south east of the Stockholm archipelago which contribute to the large extension of the archipelago area. These structures were at least partly initiated in connection with the old bedrock formation and have been reactivated several times since then. Some of these geological structures are still active as evidenced by frequent small earthquakes and by outflow of thermogenically altered gas.

Most of the bedrock is covered by unconsolidated sediments. The lowest coverage is a thin layer of till,

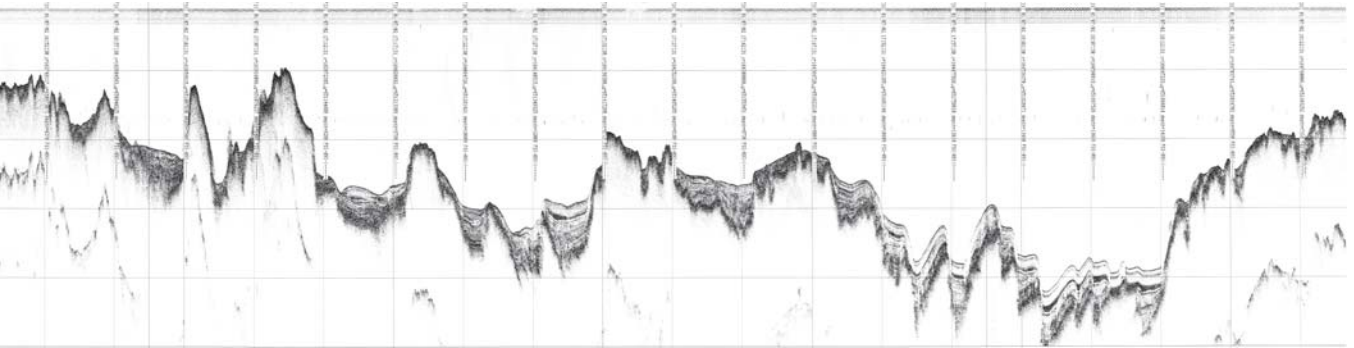


Image 5.7.5-1. Bedrock area off Stockholm, Baltic Sea. Seismic profile. The seismic profile represents part of the old crystalline bedrock area SE of the Stockholm Archipelago in the northern Baltic Sea. In between the steep rock peaks which are free or nearly free of sediment there are deposits of glacial and postglacial Holocene sediment, mostly clays. In the right part of the profile the sediment cover is almost absent. The full length of the profile is about 16 km with a maximum water depth of approximately 137 m (modified after Pihl et al. 2003).

Project: Geological Survey of the Swedish coastal areas; year of survey: 2001

Survey vessel: *Ocean Surveyor* operated by the Geological Survey of Sweden

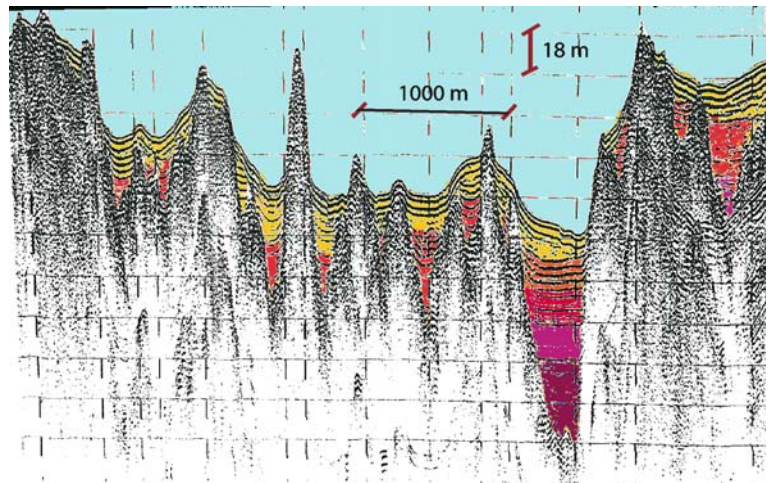
Seismic system: Towed airgun and line array receiver, called “streamer”; frequency band of the airgun sound source: 200–1 500 Hz

Text, image ©: Per Söderberg, FOI, Stockholm, Sweden ■

Image 5.7.5-2.

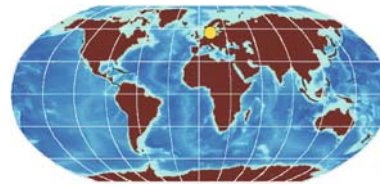
Cut out of the cliff profile. The section shows details of the sediment fills in between the steep rock peaks and the also the trough-like shape of the sediment surface, indicating interaction with flow. The color steps demonstrate that the deepest and broadest furrows are filled with the thickest and oldest sediment. The profile is enlarged by 17 times.

Image documentation: same as for Image 5.7.5-1 ■



typically some meters thick. On top of the till are deposits of glacial and post glacial clays. The glacial clay is quite uniform in thickness, frequently of a few meters. The glacial deposits are succeeded by post glacial clays and recent mud. The thickness of these sediments is highly variable due to local variations in condition of accumulation and erosion. Locally the post glacial sediment amounts to several tens of meters in thickness. Due to the ongoing land upheaval together with other acting agents the upper sediment layers may locally be missing and older sediments are exposed at the sea floor.

5.7.6 Sedimentation in the Baltic Sea; Examples of the *Bight of Mecklenburg*



The Project Dynas (Dynamics of natural and anthropogenic sedimentation) was conducted to investigate the development of the Baltic Sea floor during the entire post-glacial period. The main tool to study the fine-struc-

ture

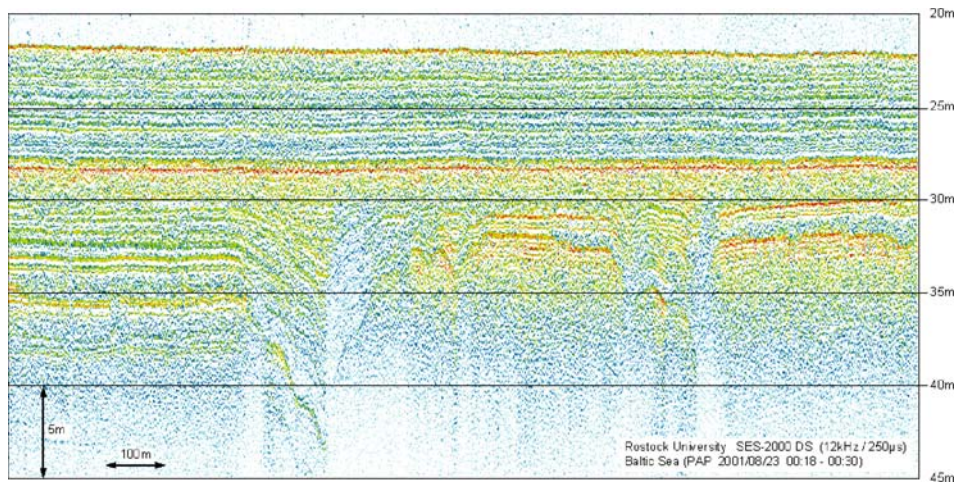


Image 5.7.6-1. Post glacial sediments. Parametric sediment echosounder image. The image shows several meters of undisturbed horizontal mud layers upon a strongly reflecting horizon which covers underlying older structures completely. The top layers are attributed to the postglacial period of the last 10 000 years, termed *Holocene*. The cause of the conspicuous and consistent lamination is still the subject of investigation. It appears enigmatic that the number of discernible layers, which usually label outstanding events of sediment import, differs strongly within the same seabight.

The pronounced reflector below is a surprisingly thin layer of a few centimeters of sand. This sand deposit is considered part of the fall-out of the melting glacial ice inside the Baltic ice reservoir at that time, thus indicating the beginning of the Holocene period like the page of a calendar. The sand layer stands out acoustically for two reasons: the sound speed and the density of sand strongly exceeds those of the muddy layers on top and the change is abrupt in comparison to the wavelength of 20 cm and less (Sect. 3.4.2). The two fault areas of the lower glacial clay-like sediment layers which may be several tens of meters thick are visualized clearly by the compression of the range scale by a factor of 33 against the depth scale.

The parametric echosounder resolves layers of two to three decimeters, or less than a thousand years of sedimentation in this area. The system was developed as a lightweight transportable modification of heavier ship-borne types for deeper penetration.

Project: DYNAS (Dynamics of natural and anthropogenic sedimentation)

Survey vessel: *Prof. Albrecht Penck*

Parametric echosounder, type: SES-2000DS, University of Rostock; 12 kHz center frequency, 0.25 ms pulse length or 19 cm depth resolution, beamwidth: 1.8°

Image ©: Gert Wendt, Institute of Telecommunications and Information Electronics; Rudolf Endler, BSRI, both: University of Rostock, Germany ■

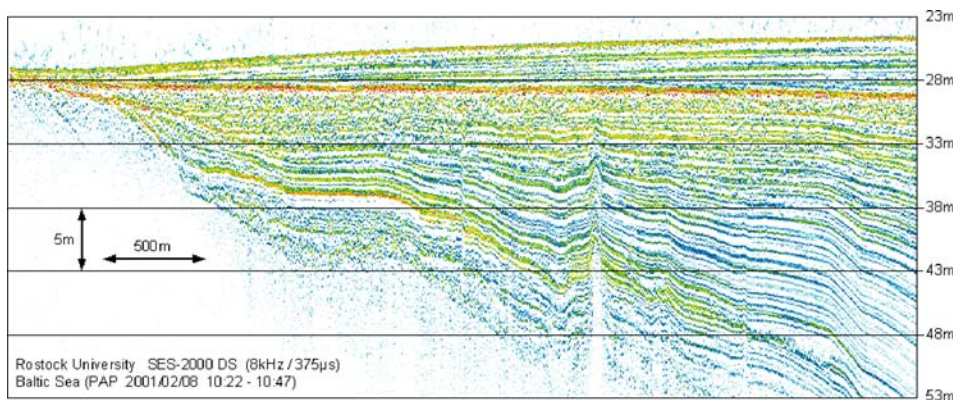


Image 5.7.6-2. Contour-following post glacial sediment. Parametric sediment echosounder image. The postglacial top layers of muddy sediment which are far more transparent acoustically than the older glacial substrate sediments follow these contours instead of smoothing and equalizing them. Such deformed structures are found in the vicinity of the bight margin. Apart from the obvious lateral contour deformation – enhanced by the scale compression – there is a pronounced lateral change of the top layer structure on both sides of the furrow from a few coarse to many fine layers. This inhomogeneity which comes out clearly in the sound image could not be revealed by core sampling. Such structures contain information of the processes of sedimentation, deformation, and motion within the last thousands of years in the *Baltic Sea* which are not yet investigated.

Project: DYNAS (Dynamics of natural and anthropogenic sedimentation)

Survey vessel: *Prof. Albrecht Penck*

Parametric echosounder: type: SES-2000DS; 8 kHz center frequency, 0.375 ms pulse length or 28 cm depth resolution, beam-width: 1.9°

Image ©: Gert Wendt, Institute of Telecommunications and Information Electronics; Rudolf Endler, BSRL, both: University of Rostock, Germany ■

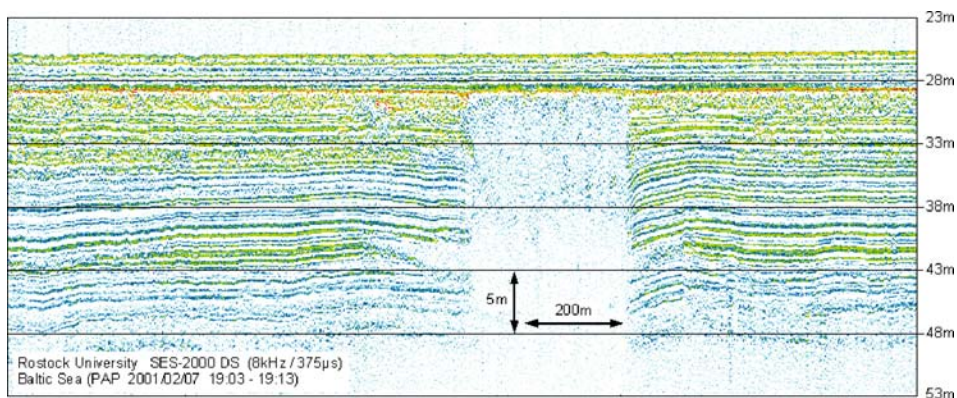
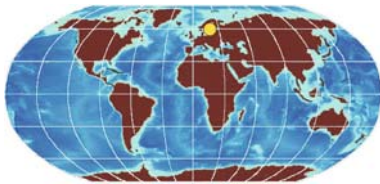


Image 5.7.6-3. Post glacial sediment with gas enclosure. Parametric sediment echosounder image. The non transparent enclosure of 300 m cross section is doubtless caused by unsolved gas of more than marginal concentration under a gas-tight sediment lid. Presumably it is methane produced by microbiologic decomposition of organic debris, which is unusually inactive inside the covering lid. On both sides of the acoustically opaque column the layers appear deepened in their horizon. This effect is known from other related phenomena such as mud volcanoes (Sect. 5.3.5) and indicates weak lateral gas diffusion, insufficient to screen the acoustic signal although sufficient to reduce the speed of sound, thus simulating deeper horizons. Such chimney-like gas containing structures are also found inside young, shallow water mud, with anaerobic bacteria converting organic debris into gaseous methane (Sect. 6.2.2). Sharp lateral boundaries in such cases can be found with fresh water exits, in this combination then called *pockmarks*.

Image documentation: same as for Image 5.7.6-2 ■

ture of the sedimentation and its variability within a large area was a high resolution sediment echosounder based on the parametric principle (Sect. 4.4.2). The parametric transmitter generates low frequency sound signals by superposition of two high frequency signals of high amplitude. The broad frequency band and the narrow beam achieved by this non-linear mixing permits an unusually high vertical and lateral resolution despite the low frequencies necessary for sufficient bottom penetration.

5.7.7 Gulf of Finland, Gaseous Sediment and Gas Plume



The pair of images visualizes a type of gas filled shallow sediments that is also found at much higher latitudes in the Barents Sea (Sect. 5.4.3): Series of column-like, acoustically opaque depicted dark, of

different width which screen the sediment strata inside. The inclusions have sharp vertical borders that reach up to a certain level through gas-free sediment layers acting like gas-tight lids on top of the columns (Image 5.7.7-1). The depicted section is 8 km long.

Here, in the Gulf of Finland we see moreover the result of a single leakage inside of a crater formation: a narrow gas plume escaping at a dent through the sediment cover at the track time instant 12 h 14 min. The stretched close up of the cut out of 750 m shows the details of the inhomogeneous plume up to 8 m above the sediment very

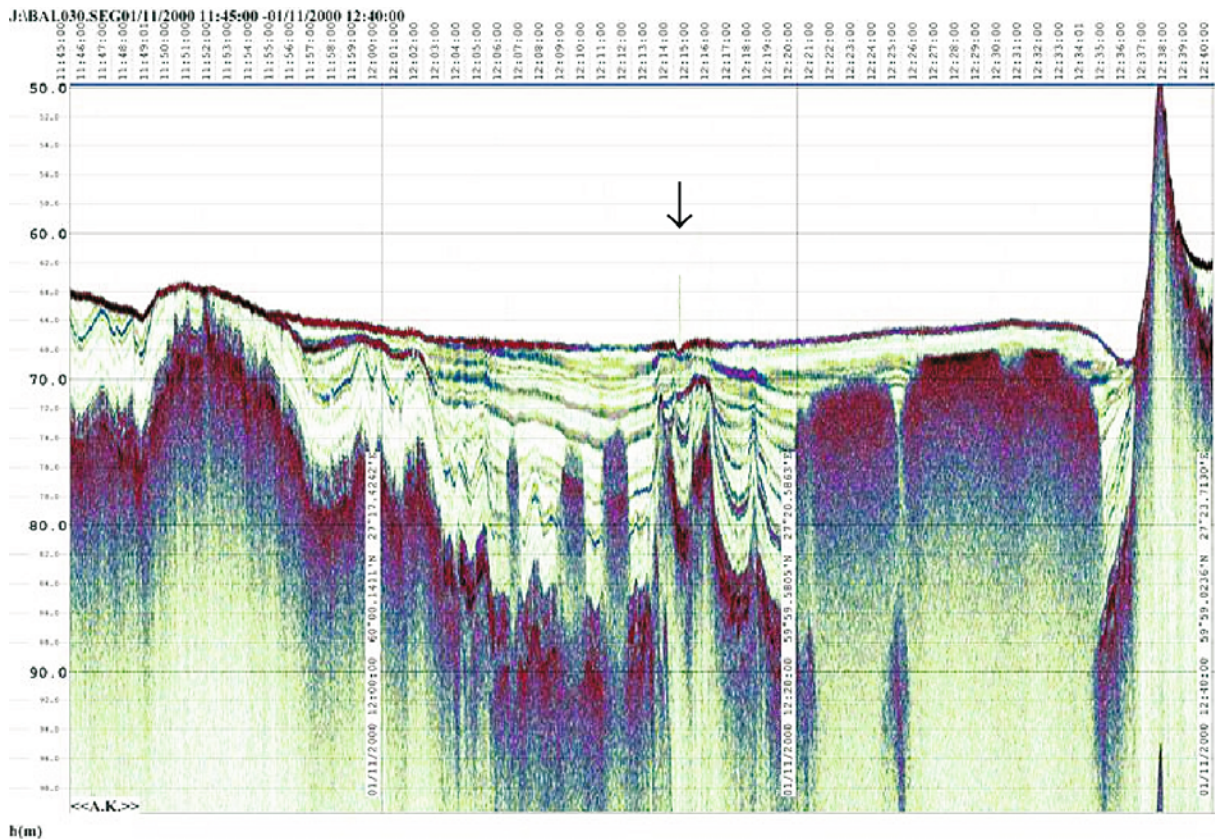
5.7.7

Image 5.7.7-1.
Gaseous sediment and gas plume. High resolution seismic image.
Interpretation and comment: previous text.

Project: 49th cruise of *RV Professor Shtokman*; year of survey: 2000

Seismic device: Datasonics Inc., Chirp-II, towed system, frequency 2–7 kHz, beamwidth: about 30°

Image ©: Lev R. Merklin, Shirshov Institute of Oceanology, Academy of Sciences, Moscow, Russian Federation ■



clearly with dark spots indicating conspicuously high bubble density bursts (Image 5.7.7-2). Since the plume diameter is only about 30 m, the probability was low to hit it with the sound beam – or there are possibly more of them in the area. Another conspicuous feature might support this: the deep crater-like deformation of the sediment strata below the later horizontal sediment lid on top at the gas seep is even more pronounced on the right hand side of the image. The huge two columns of gaseous sediment are framed by steeply inclined strata. This may be partially simulated by lowered sound speed inside a slightly gaseous sediment (Sect. 5.3.5) and –

perhaps or – large volumes of escaping gas in the past have caused genuine depressions, filled up by sediment to a flush surface later. (The undulation, as usual, is due to the ship motion in the sea waves which was not compensated here.)

It is supposed that the gas, mainly biogenic methane from organic material, originated from the top of fractured Baltic basement of sediment kurkar rock which was land surface prior to the last glaciation (Sect. 5.7). The gas might have migrated through laminated sediments of marine lake origin which were deformed during crust rising after deglaciation.

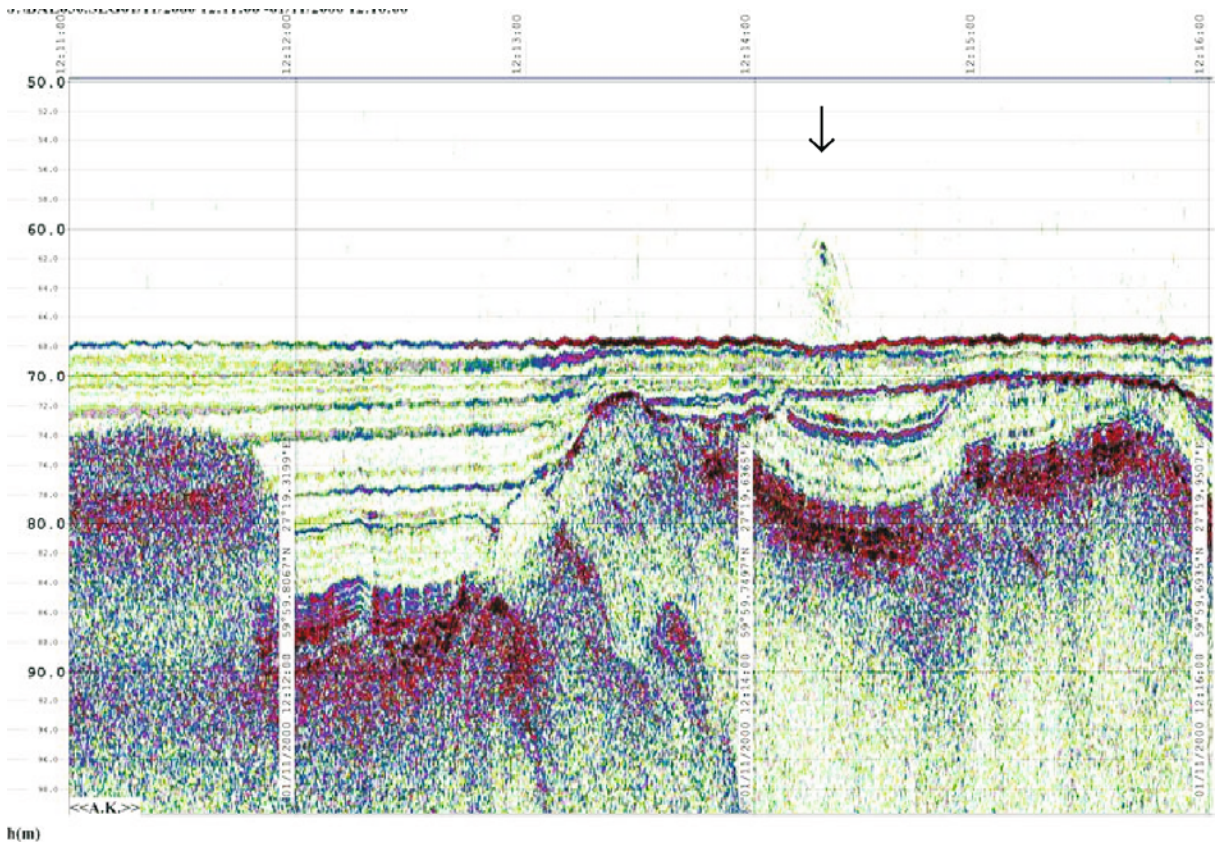


Image 5.7.7-2.

High resolution seismic image. Cut out of Image 5.7.7-1, visualizing the structure of the gas plume

Image documentation: same as for Image 5.7.7-1 ■

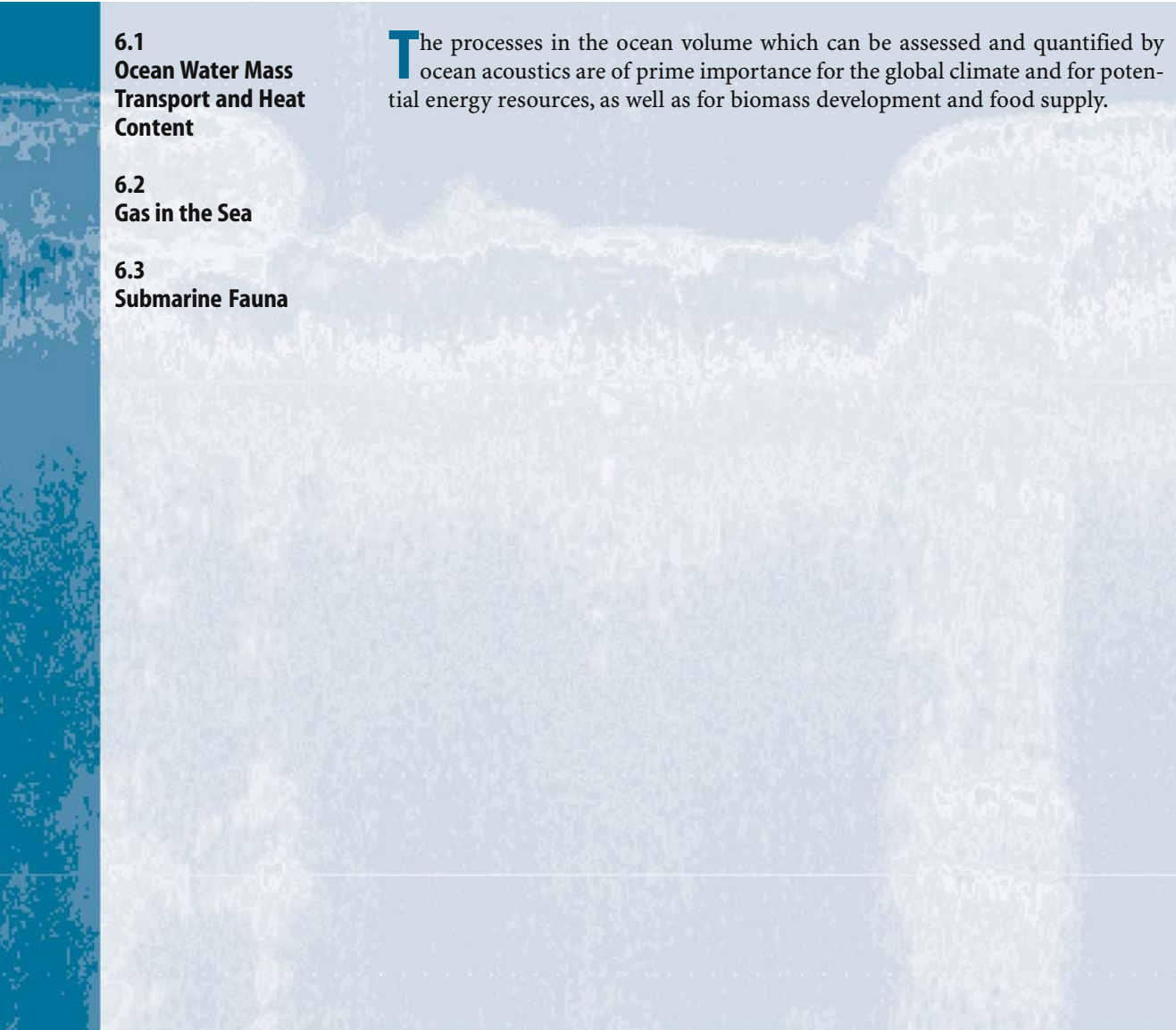
The Ocean Volume

6.1 Ocean Water Mass Transport and Heat Content

6.2 Gas in the Sea

6.3 Submarine Fauna

The processes in the ocean volume which can be assessed and quantified by ocean acoustics are of prime importance for the global climate and for potential energy resources, as well as for biomass development and food supply.



6.1

6.1 Ocean Water Mass Transport and Heat Content

The ocean currents embody the largest and also most complex transport system by far of the heat energy of the globe. Since the ocean water masses represent more than a thousand times the heat capacity of the atmosphere, the interaction between both is decisive for weather and climate. The features of ocean currents and associated mass, heat and freshwater transport variability are thus a key element of climate research and model development. The key to progress and success in this respect is the ability to acquire the flow data of entire ocean areas. This is necessary also for other reasons.

The ocean waters shelter the largest variety of species and moreover the bulk of all the biomass on Earth. An essential part of the oceanic food chain drifts passively with the currents as well as the content of oxygen, carbon dioxide, solutions and suspensions of various minerals and chemicals, of nutrients and of contamination.

Ocean currents, in particular tides, reinforced by storms, reshape the relief of the continental shelves, often in the short term by causing erosion and re-sedimentation. Ocean currents of the deep sea permanently distribute the suspension load from river inflows and from other origins, including outstanding, climate induced events. The slowly varying currents of the deeper water masses determine the regional features of the coverage and structure of the deep-sea sediments, representing documentation of the processes of their generation and redistribution over long periods of time.

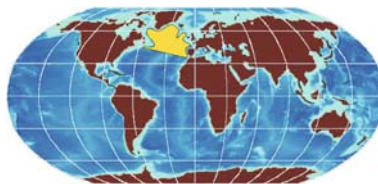
The various scales of the current variability patterns in space and time exclude single, general tool solutions (Sect. 4.5.9). Summarized briefly, there are essentially three fundamental methods of measuring ocean currents based on acoustics which supplement each other where necessary and possible:

- First, the measurement of the *local current*, by downward looking echosounders as the *Doppler shift* of echoes from drifting particles in the volume. At least 3 slant beams are required to provide the speed and direction of the current as a local vertical profile, in other words: the profile of the current vector. This is conducted continuously from the research ship underway or on station (Sect. 6.1.2) and neglects temporal changes during the transects. Physicists call the acquisition of the current field by measurement of the local particle speed the *Eulerian method*.

- Second, the tracking of *volume elements of the current field in space and time* by submerged drifters. At least two exactly positioned sound sources for the timer signals are required for tracking the instantaneous drifter positions and thus their path and speed by passive signal arrival triangulation. The drifter method with a large number of distributed buoys, adjusted to the depths of interest by neutral buoyancy (Sect. 6.1.1), enables ideal simultaneous three-dimensional sampling of large current fields in principle but is usually restricted to only a few selected depth horizons for cost reasons. The current acquisition by tracking the trajectories is named the *Lagrangian method*.
- Third, the *tomographic acquisition* which provides the total flow record through large cross sections between fixed positions by integration of sound travel time along ray paths, (Sect. 6.1.3) but with very limited information on the distribution of the flow passing the cross section. The peerless advantage of the tomographic method is its capability to measure the *integrated heat content* over long time periods. All three methods are demonstrated by results acquired in key areas.

6.1.1

6.1.1 Mid-Depth Circulation in the North Atlantic. Large Scale Drifter Field Experiment



The drifter field concept of *three-dimensional, simultaneous large scale current field acquisition* has been realized

by two different tracking techniques. The first one which has been applied in the long term experiment presented in this context relies on *acoustic tracking*. Two or more sound transmitter stations are fixed at positions selected and confirmed with satellite navigation GPS-accuracy to achieve an optimized geometry for subaqueous triangulation (Sect. 4.5.10), similar to the subaerial radio-navigation of ships by Decca or Loran before the era of GPS. The low frequency sound signal pulses are triggered for transmission by clocks of standard reference accuracy. The receiver on board the drifter float stores the time instant of signal arrival from each transmitter and for every call of the long term series. The reconstruction of the series of instantaneous drifter positions and velocities is con-

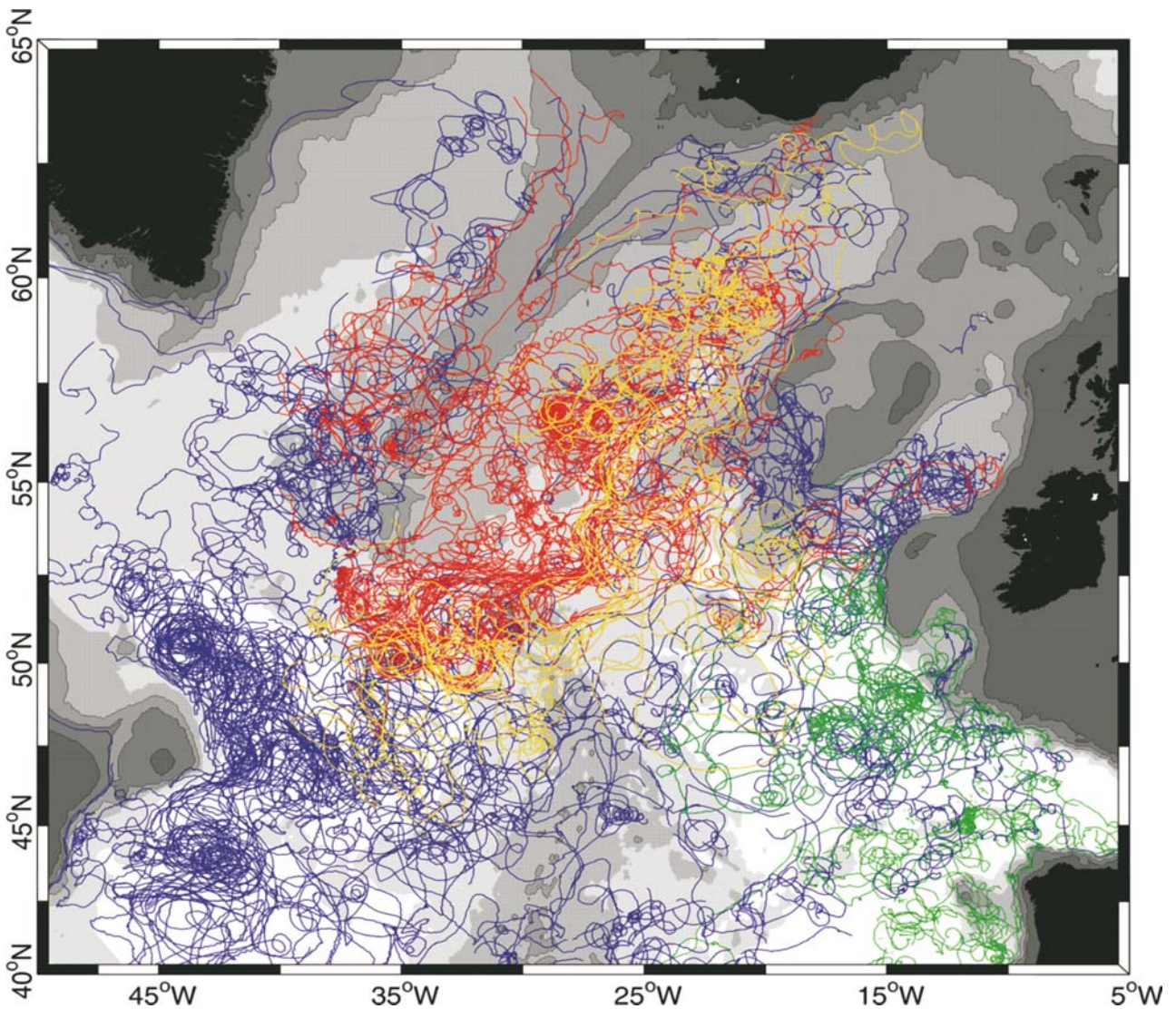
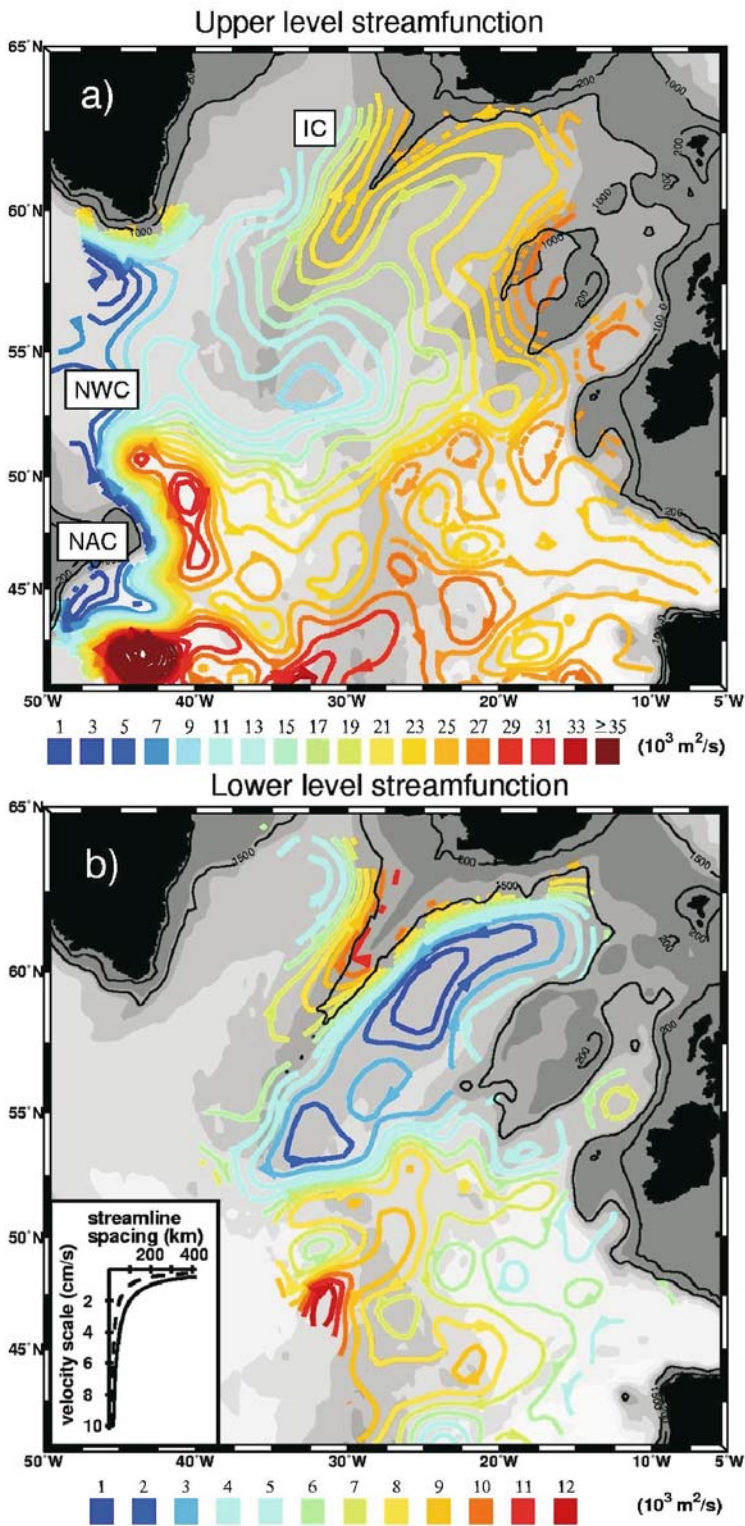


Image 6.1.1-1. Mid-ocean current in the northeastern North Atlantic; field of float trajectories. The image, looking like an inextricable agglomeration of spaghetti threads represents the superimposed trajectories of altogether 223 mid depth drifting floats during 1993–1995 and 1996–2001. Even prior to the evaluation of absolute current velocities from the acoustically tracked floats the image demonstrates several conspicuous and unexpected features: *First*, there is no predominant unidirectional flow. Instead, the main motion follows complicated eddies which are not equally distributed but are concentrated in clusters. *Second*: obviously the mean current shown in the subsequent pair images is only a fraction of the local and instantaneous motion.

Third: there are areas free or nearly free of trajectories, in other words: the current at the depth of the floats neither crosses the *Iceland-Faeroe Rise* nor the *Reykjanes Ridge* southwest of Iceland nor the *Greenland-Iceland Rise*. The entire current system at the two horizons of the floats is confined on the northern and northeastern side by sea floor rises, though these do not reach up to the float horizons. This is one of the surprising results of the mid-ocean current project and it is already evident from the trajectories: the dominating role of the sea floor relief in the current distribution. *The steering role of the sea floor profile goes far beyond its crest height.*

Blue, green, and yellow tracks: upper horizon, different float deployment series. Red tracks: lower horizon.

Image ©: Walter Zenk, IfM, Kiel University, Germany ■

**Image 6.1.1-2.**

a Mid-ocean mean current drifter field; upper level. The color lines represent the so called stream function, the resulting flow along the internal horizon at the depths where the floats were drifting. It is therefore a two-dimensional, nearly horizontal cut through the three-dimensional ocean current field. Accordingly, the unit of the stream function is m^2 per second. The red and purple values reach up to more than 30 000. *This means: a slice of only 1 m width at that level transports the same amount in tons of water per second along only one of the color lines.* Such high values are achieved both at low speeds, indicated by streamlines several hundred km apart, as well as at speeds ten times greater, corresponding to narrow streamlines.

The map of the stream function reveals several unexpected features some of which are qualitatively visible already in the spaghetti-Image 6.1.1-1:

1. There is no evidence of a continuous, broad-scale, eastern boundary current transporting Mediterranean water northward into the subpolar region. The streamlines remain mostly local and eddy like.
2. The *North Atlantic Current (NAC)* remains essentially undivided when crossing the *Mid-Atlantic Ridge* at the deepest northern gap and turning around the pronounced, peninsula-like *Reykjanes Ridge* southwest of Iceland. The NAC then turns northward again, into the Iceland basin, forming the so-called *Irminger Current*.
3. None of the streamlines crosses the *Iceland-Faroes Ridge*. This indicates that most of the warm inflow into the Norwegian Sea occurs above the level of the float horizon.
4. The flows cross the *Mid-Atlantic Ridge* preferably over ridge gaps, called fracture zones, surprisingly even at depths up to 1 500 m above the ridge crest. Such topographic steering may limit the ocean's response to climate variations, confining cross-ridge transports of heat and fresh water to certain latitudinal bands.

b Mid-ocean current drifter field, lower level. The main unexpected feature at the lower level is the huge gyro system in the western *Iceland Basin* which does not exist at the upper level. Similar to the upper level feature in this region, there is clockwise flow around the peninsula-like *Reykjanes Ridge* southwest of Iceland, but the closed recirculation is dissimilar. Moreover the lower, southwestward flow is significantly faster than the upper one, in contrast to the other side of the ridge. *Apparently the ridge structure, which steers the flow system up to far above the ridge crests is literally blocking the deeper flow levels.*

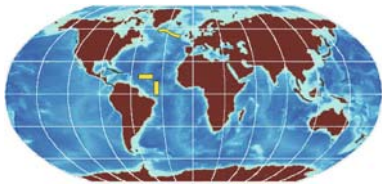
Image ©: Walter Zenk, IfM, Kiel University, Germany ■

ducted in the lab after the floats emerge automatically and are localized and recovered by means of radio-signals.

The other tracking concept works with GPS positioning of the drifters and thus requires the floats to rise to the surface many times. The frequent localization as with acoustic triangulation is not possible. Due to the slant upward and subsequent downward motion in the current field there is an unknown offset.

The most important message of the long term experiment based on acoustic float tracking is of major climate relevance: the ridge relief of the sea floor guides the current system up to far above the ridge crests. Only ridge gaps such as caused by tectonic fracture zones permit current transit. *This sea floor enforced current stability limits the ocean's response to climate variations.*

6.1.2 Acoustic Measurements of Ocean Currents by Doppler Profiling



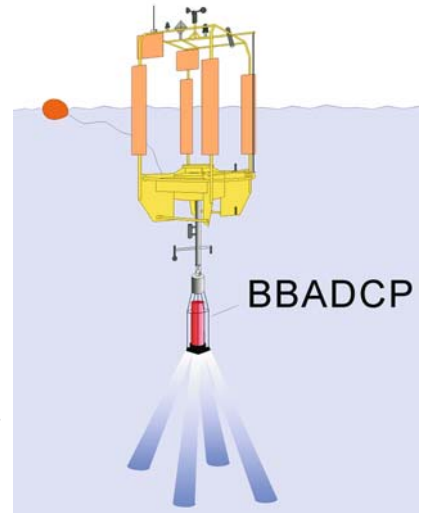
The *acoustic Doppler current profiler (ADCP, Sect. 4.5.2)* is the most capable system for acquiring the vertical stratification of the speed and direction of the instantaneous flow in the sea down to several hundred meters.

Recently the shipboard underway operation of the ADCP has been supplemented by on-station lowering of the instrument to achieve high vertical resolution of the current structure, even thousands of meters down to the deep-sea floor. This method of lowering an ADCP on station is briefly called *LADCP*.

An LADCP, combined with a usual hull mounted ADCP, which is operated continuously between the LADCP-stations, provides complete current transects between surface and bottom. The joint spatial resolution is tailored to the general features of deep-sea currents. The higher resolution of the upper hundreds of meters by the continuously sampling ADCP and the wider spaced on-station sampling by LADCP of the deep water column corresponds to the decrease of the horizontal variability of the current with depth.

This combined approach, when necessary in support of autonomous buoys distributed over the sea area of in-

Image 6.1.2-1.
Scheme of an autonomous acoustic Doppler current profiler system (ADCP, Sect. 4.5.2), mounted on a semi-submerged buoy. The scheme is shown to illustrate the principle of the measurement. The acoustic unit with the four diverging sound beams is part of the concept of combined ADCP versions to meet the requirements of both large scale and sufficiently high resolution ocean current measurements.



The Ocean Surveyor (OS) is a new generation of *shipboard acoustic current profilers* used for continuous underway measurements of upper ocean currents. The instrument is permanently mounted in the ship's hull. The depth range of the velocity profiles depends on the frequency of the Doppler profiler (ADCP) and the vertical resolution chosen (Sect. 4.5.6). While a 75 kHz ADCP with a resolution of 8 m surveys the upper 600 m of the water column, an 38 kHz OS-ADCP can cover the water column to depths below 1 000 m. A single velocity profile is obtained at a rate of 2–4 seconds.

Depending on the horizontal variability of the current under investigation, the profiles are subsequently averaged into ensembles of up to one hour duration, which means deriving one representative profile every 20 to 50 km. This is a necessary compromise between an adequate resolution both in the vertical and the horizontal and a sufficient accuracy despite the usually poor signal to noise ratio of the echoes. Averaging over the 1 000 profiles of one hour will reduce the noise induced random data scatter as if the echo intensity had been increased accordingly. It is as important to minimize the disturbance of the real current structure by single erroneous profiles which are unavoidable in practice but would feign a non-existent variability.

Since the speed of the ship may be higher by a factor of ten to a hundred than the current velocity, precise subtraction with exact navigation data is therefore indispensable. The high quality of present day ocean current measurements is essentially based on satellite navigation in connection with precise gyro data, quite similar to the acoustic imaging of the sea floor.

Image ©: Juergen Fischer, P. Brandt, M. Dengler and F. Schott, IfM, Kiel, Germany ■

terest (Sect. 6.1.1) drifting with the flow at adjusted depths, is considered the best approximation for sampling the three-dimensional current fields of entire ocean areas simultaneously. Such advanced multi-tool measurement programs have greatly enhanced our understanding of the global ocean circulation and its role in our climate system.

the upper hundreds of meters with the ship under way. At the price of lower vertical resolution the depth range is extendible to about a kilometer. This covers already most of the complex current structures in the sea but it is still only one quarter of the average depth of the deep ocean. Unfortunately the echosounder frequency regime which is sufficient to image the sea floor relief is too low for measuring the small Doppler shift induced by the deep-sea currents (Sect. 4.5.6).

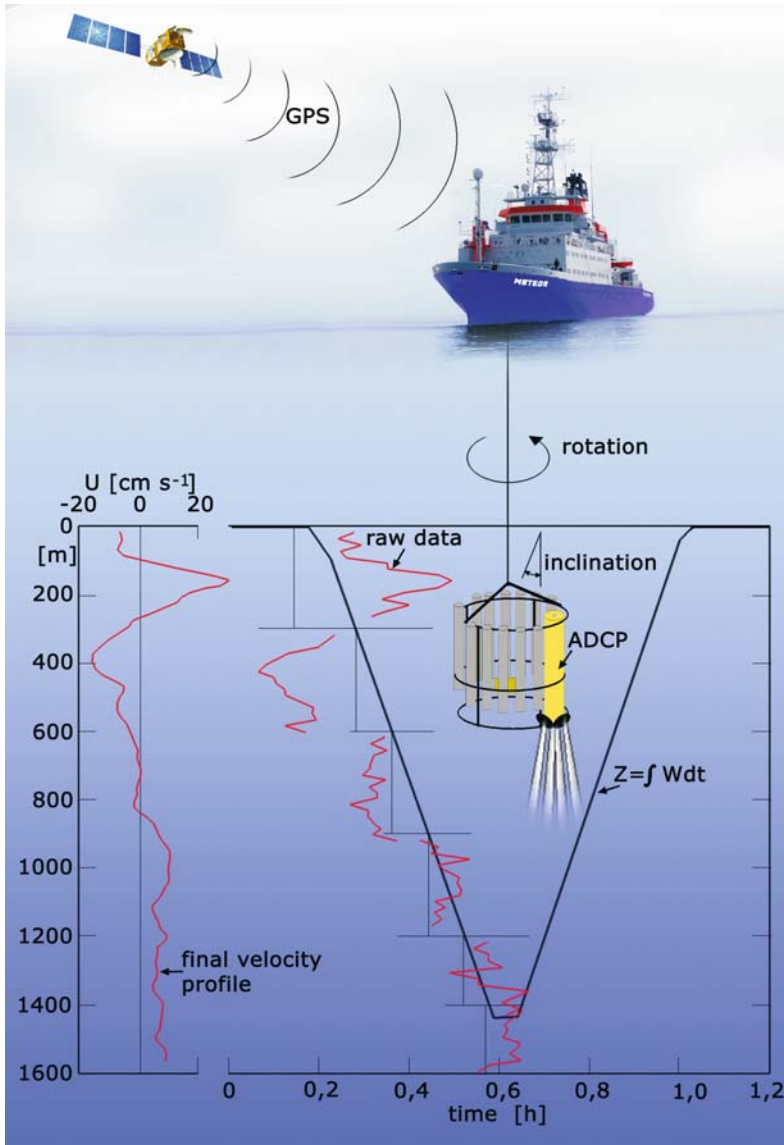


Image 6.1.2-2.

Lowered acoustic Doppler current profiler (LADCP). The acoustic Doppler current profiler (ADCP, Sect. 4.5.2) mounted on a ship's hull is unparallelled for measuring the ocean current profile of

It is therefore inevitable to lower a current meter down to the ocean floor from the ship drifting on station. It was found out that a usual, high frequency ADCP of 150–300 kHz attached to a standard cable connected sensor package for sea water properties works more rapidly and accurately than a lowered non acoustic current meter. This method of lowering an ADCP on station is briefly called LADCP and has been successfully realized as a self-contained LADCP-unit. At any instantaneous depth the LADCP covers the next 300 m by an overlapping mode of operation. The profile sections are combined afterwards and corrected for the motion of the sensor package by built in compass and gyro and of the drifting ship by Satellite navigation. A research trial of one month duration typically yields 100–150 full depth LADCP profiles.

An LADCP, combined with a usual hull mounted ADCP, which is operated continuously between the LADCP-stations, provides complete current transects between surface and bottom. The joint spatial resolution is tailored to the general features of deep-sea currents. The higher resolution of the upper hundreds of meters by the continuously sampling ADCP and the wider spaced on-station sampling by LADCP of the deep water column corresponds to the decrease of the horizontal variability of the current with depth.

This combined approach, when necessary in support of autonomous buoys distributed over the sea area of interest drifting with the flow at adjusted depths (Sect. 6.1.1), is considered the best approximation for sampling the three-dimensional current fields of entire ocean areas simultaneously. It provides so called *ground truth* datasets for the development and verification of ocean circulation models. Such advanced multi-tool measurement programs have greatly enhanced our understanding of the global ocean circulation and its role in our climate system.

Image ©: Juergen Fischer, P. Brandt, M. Dengler and F. Schott, IfM, Kiel, Germany ■

Image 6.1.2-3.
75 kHz Ocean Surveyor:
zonal velocity along 35° W
(see next page)

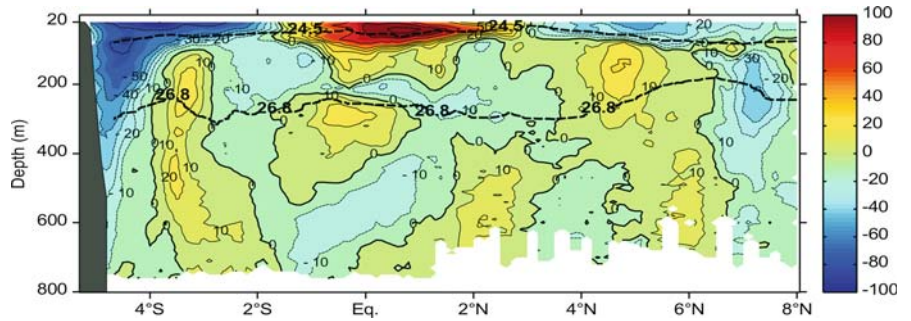


Image 6.1.2-4.
38 kHz Ocean Surveyor:
zonal velocity along 35° W
(see next page)

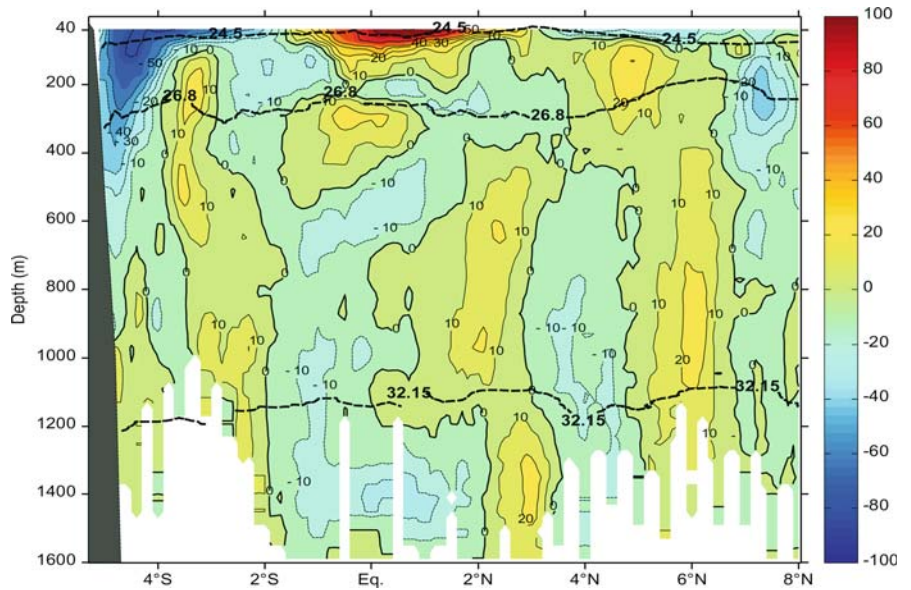
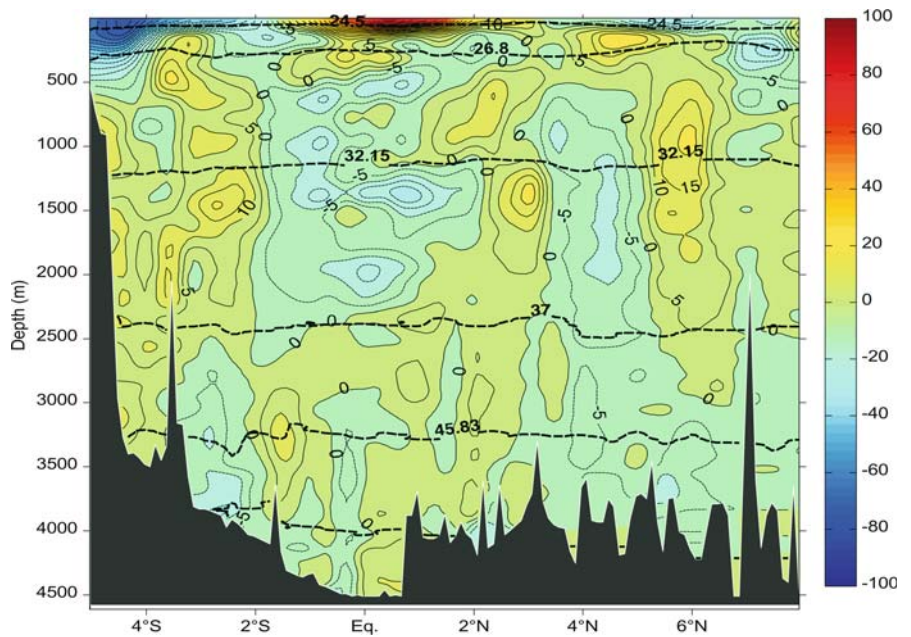


Image 6.1.2-5.
Lowered ADCP:
zonal velocity along 35° W
(see next page)



◀ Images 6.1.2-3-5.

Comparison of three echosounder current profiler systems. The three Images 6.1.2-3 to 6.1.2-5 correspond to the data from three independent ADCP-systems which were operated in parallel along the same long transect crossing the equator at 35° W during an expedition in 2002. Two of the three, the 75 kHz and the 38 kHz systems are mounted near the keel of the ships hull; the third of 150 kHz (LADCP) is lowered on station.

The hull mounted 75 kHz-system (Image 6.1.2-3) covers the top 700 m with the ship under way and provides the *vertical profile of the horizontal current velocity*, averaged over depth intervals of 8 m, which is the *vertical resolution*. The corresponding data of the 38-kHz system (Image 6.1.2-4) are 1 200 m and 32 m. The ADCP with 150 kHz (Image 6.1.2-5) and 300 m depth range is lowered on-station at a speed of 1 m s⁻¹. It covers the full ocean depth by patching together the profile-sections of 300 m. This system provides velocity averages of 8 to 16 m depth intervals. The two hull mounted systems resolve about 2 cm s⁻¹ current velocity which is less than 1% of the ship's speed during the expedition. The LADCP velocity resolution on station is about the same.

The three depictions with their respective depth regimes reveal strong regional differences of the currents along the meridional transect of 1 500 km taken at the narrowest section of the *Atlantic Ocean*. The red side of the current velocity scale in cm s⁻¹ stands for the westward component. The white bars indi-

cate insufficient data coverage. In the Tropics we observe strong gradients of the currents both in the vertical and the horizontal. Layers of alternating west/east currents were found around the equator at vertical scales of a few 100 meters with the strongest westward current near the surface. Near the coast of Brazil at the left side of the image the *North Brazil Current* is transporting water from the southern hemisphere to the equator; at the equator the *Equatorial Undercurrent* is the most intense eastward flow.

Further noticeable is the nearly unidirectional flow within several thousand meters depths intervals with alternating direction north and south of the equator: westward preference appears around 3° N as well as 6° N and 3° S whereas eastward preference occurs around 4.5° N. Alternating currents of this kind are observed in all three of the world oceans, the *Atlantic*, the *Pacific* and the *Indian Ocean*. These bands are highly variable in time, with the annual cycle being the dominant period in the Atlantic. An ongoing discussion is whether these current bands produce a long-term mean flow with a long-range effect or if they represent only periodic fluctuations.

Project: Meteor Cruise M53/2, Tropical Atlantic

Research vessel: *RV Meteor*, Germany

Acoustic devices: ADCPs of 38 kHz and 75 kHz; LADCP of 150 kHz

Image ©: Juergen Fischer, P. Brandt, M. Dengler and F. Schott, IfM, Kiel, Germany ■

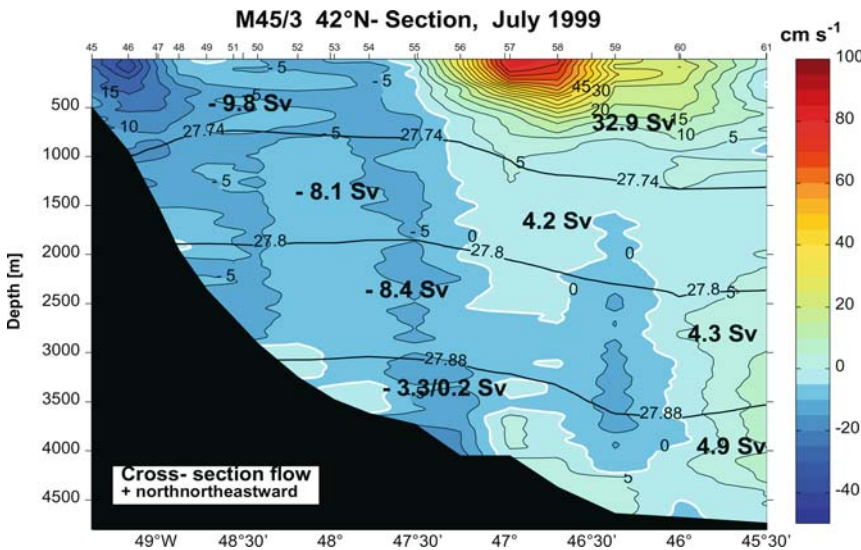


Image 6.1.2-6.

Subpolar current section. The current transect with the Lowered ADCP at 17 stations along 42°N latitude was crossing part of the continental slope south of the *Grand Banks of New Foundland* in 1999. The white line divides the southward currents (dark blue regime) from the northward currents (light blue to red regime). Three features of the current structure are noticeable:

- The currents are of much larger vertical extent than found at the examples of the equatorial region.
- The western boundary of the *New Foundland Basin* at about 47°W is also a kind of boundary between two types of currents: At the upslope side there is a *unidirectional cold southward current*

reaching from the surface to the bottom down to 4000 m. At the basin side there is a *bi-directional current system* with a *northward warm water flow* as part of the *North Atlantic Current* and a *southward cold water flow* at greater depths.

- The outstanding maxima of the current in both directions are concentrated at the sea surface, not different from low latitudes.

Project: SFB-460

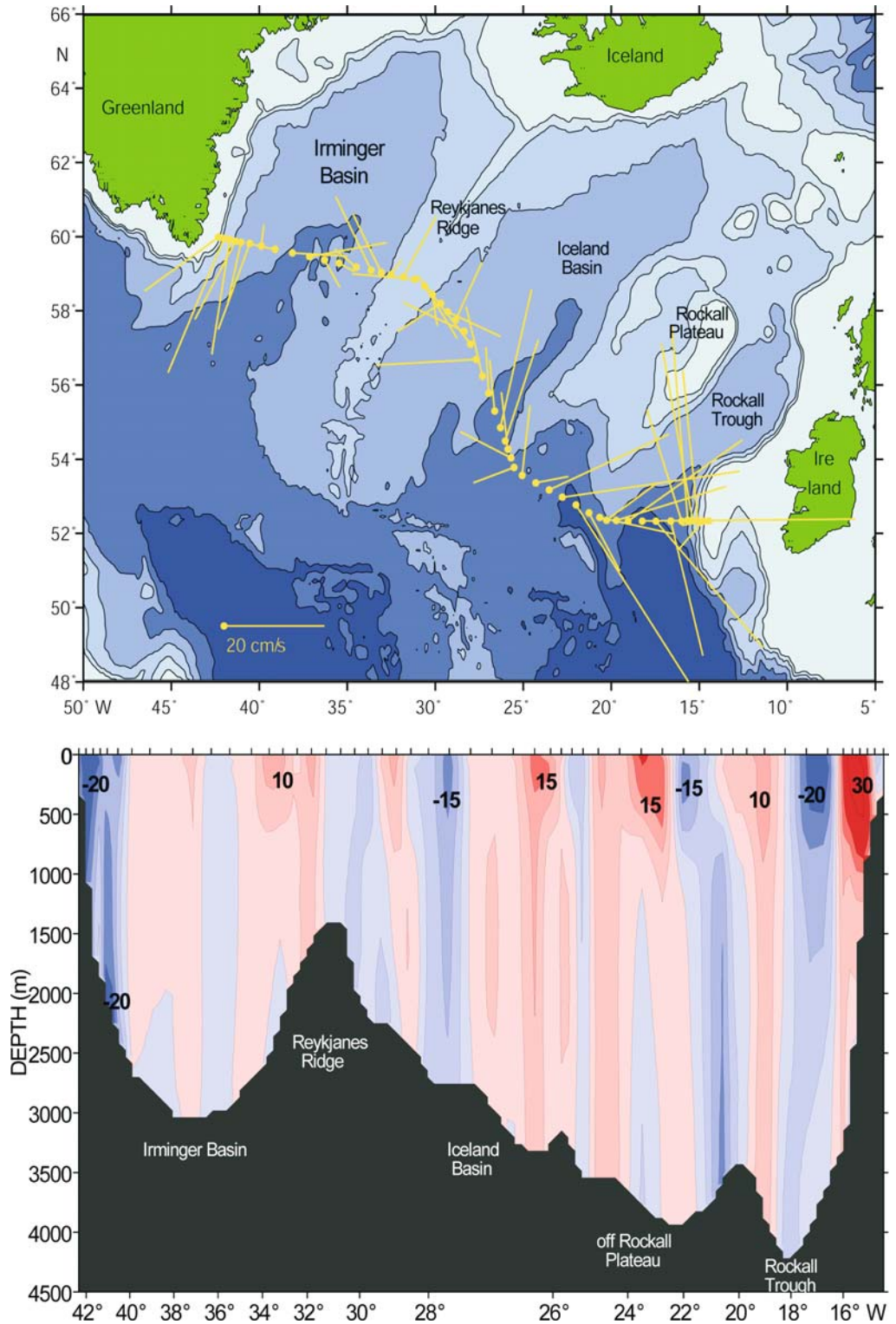
Research Vessel: *RV Meteor*; acoustic device: LADCP; 150 kHz. 1 Sv (Sverdrup) means 1 million m³ s⁻¹

Image ©: Juergen Fischer, P. Brandt, M. Dengler and F. Schott, IfM, Kiel, Germany ■

Image 6.1.2-7.

Deep water cross-section of the northern *North Atlantic current field*. Acoustic Doppler current profiler (ADCP) measurements combined with current computations from measured water density profiles. This vertical cross-section through the current field of the northern North Atlantic with the *Gulf Stream* was acquired during September 1991. It reveals part of the complicated reality instead of a simple conveyor belt of thermal energy. Details of the highly random current structure of the same area have been verified by the complementary method of current tracking with submerged drifter buoys (Sect. 6.1.1).

The current vectors attached to the yellow dots along the cross-section depict the mean direction and speed of flow between 70 and 350 m depth within the respective track intervals. The data are derived from continuous ADCP-measurements covering the upper 500 m depth and are corrected for tidal currents. The structure of the flow field down to the sea floor along the cross-section is shown in the image below. It is a merger of the acoustic data with results from model computations derived from water density profiles. These



were measured by sensor packages of temperature, pressure, and salinity, lowered from the research vessel on stations along the track. The concept of current modeling from density profiles is based on a fundamental equilibrium of forces: the horizontal forces resulting from water masses of different density at the same depth horizons are balanced by the so-called Coriolis-force acting on each volume element of water moving on the rotating Earth.

The most conspicuous phenomenon of the lower image is the column structure from top to bottom, with alternating directions of flow instead of a predominating unidirectional flow. Southward flow is indicated blue; red corresponds to northward directions. However, the relatively regular appearance of this current structure is mainly the result of spatial and temporal averaging along the subsections of 20–55 km and 1–3 h travel time between the ship stations. Similar column structures have been measured also at meridional sections with an ADCP lowered to the sea floor (Image 6.1.2-5).

The scale of spatial averaging determines the scale of the current eddies filtered out from the broad spectrum of eddy sizes and current meanders. These eddy currents of typically 30 cm s^{-1} are superimposed upon the mean flow of the same order of velocity, in particular the *North Atlantic Current* (Sect. 6.1.1) and the *East Greenland Current*, which are also structured in broad filaments. The net water mass transport by the mean northbound flow of warmer water of the upper layers is estimated at about 15 million m^3 per second or 15 Sverdrup (Sv), which corresponds to about half a million Giga-Watt thermal power. *This is roughly 1 000 times the total capacity installed in all power plants in Europe.* The northbound water-mass transport by the upper layers is essentially compensated by the southbound backflow near the sea floor.

Such large scale ship-borne current measurements have to cope with the fact that the eddy- and meander structures vary during the time of measurement and that the data can provide at most a two-dimensional cross-section of a three-dimensional current field. Therefore a combination of ADCP-sections with drifter fields, submerged at depths of interest, which yield genuine simultaneous samples along the selected internal horizons but cannot provide vertical current profiles, is expected to be the method of choice in the future (Sect. 6.1).

Project: Northern North Atlantic current field

Research vessel: *RV Meteor*, Hamburg, Germany

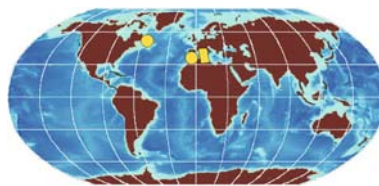
ADCP: RD Instruments, Frequency: 150 kHz; depth range: 500 m; depth resolution: 16 m; accuracy of section averages: 3.6 cm s^{-1} current velocity

The sea floor profile is enhanced by a factor of 500

Oceanographic sensor package for conductivity, temperature and static pressure, providing also the salinity and thus the local density

Image ©: Manfred Bersch, Institut für Meereskunde, Hamburg, Germany ■

6.1.3 Acoustic Tomography



Tomography is well known from medical X-ray imaging. The method provides three-dimensional images of the

interior of the body by computer-combined series of two dimensional images made from various directions of view.

The classical concept of *Ocean Acoustic Tomography* as suggested by *Walter Munk* represents three dimensional imaging of an ocean volume by *remote sensing* through multiple one way propagation in horizontal direction. It was first realized in the seventies with nine sound sources and -receivers, enclosing an ocean area of 300 times 300 km^2 and 3 km depth in the West Atlantic. The transducer configuration was designed to provide altogether 20 transmission paths with as many crossings as possible. The measurements of the various signal travel times yielded a coarse reconstruction of the three-dimensional temperature field inside the area, utilizing the fact of identical, though unknown sound speed profiles at the crossing points to derive a set of numerical equations. This demonstration of feasibility of ocean tomography in view of the effort and costs has led to more simple but very effective single range solutions realized by several institutions of oceanography. The nearly ideal acoustic transparency of the deep ocean at low frequencies (Sect. 3.3.1) enables large scale up to global scale measurements of average ocean temperatures needed to reveal and verify long-term trends of the global climate.

Ocean Acoustic Tomography of today has been deliberately restricted to quantify features of *heat contents* and *transport of water masses*, relevant to climate modeling. Its strength is the *simultaneous* and *continuous* large scale data acquisition; its weakness is the poor spatial resolution. Instead of real imagery it usually provides time series of numbers. *Ocean Tomography* works with one way transmission of radiation – typical of any kind of tomography – instead with returning echoes as applied by all methods of sound imaging based on the classical echosounder. Ocean Tomography requires separate sound sources and receivers, far apart from each other and with positions precisely known, in other words: fixed acoustic ranges instead of mobile vessels. What is the reason to make allowance for immobility and spatial separation?

The answer is the impossibility of *remote sensing* by *echo sounding* of one of the most important properties of the ocean: the *variation of its heat content* (Sect. 4.5.8, 4.5.9). Temperature stratification of ocean waters does not cause echoes because of smoothing transitions between the layers instead of abrupt steps required for echo formation. One way transmission in the *horizontal* however makes a particular virtue of necessity as we will see.

To start with a trivial statement: The travel time of a sound signal between two fixed points of course depends on the sound speed along the propagation path. We recall: a signal will speed up when passing a water mass of higher temperature, higher salinity or higher static pressure which latter means greater depth (Sect. 3.1). Since the dependence on depth is known and the salinity usually varies much less than the temperature in the open ocean in respect of sound speed, the signal travel time is a kind of thermometer of the water in between. It is like “listening to the ocean temperature”. This statement is a crude simplification however. The reality is more complex but it offers a decisive advantage which X-ray tomography does not have and which is in fact the prerequisite of genuine *acoustic ocean thermometry by tomography*, though this remains restricted to the deep ocean.

Whereas X-ray tomography as any X-ray imagery can only rely on the different *absorption* by tissues and bone, ocean acoustic tomography can utilize multiple *refraction* by the stratified ocean. Moreover, the requirement of fixed points of sound source and -receiver yields another decisive capability of the tomographic concept: In contrast to mobile but expensive research vessels, a fixed, unmanned acoustic range can monitor the genuine *spatial average of temperature and thus the heat content of large scale sections of an entire ocean remotely, simultaneously, and continuously*. It thus enables to investigate the development of the heat content within seasons, years, and even decades, to discriminate trends of climate from short term, random variability.

The key to sample an entire large scale ocean cross section without any source and receiver arrays, only by a single point source and a point receiver with no directionality is the existence of a unique natural sound speed profile (SSP) between the sea surface and the sea floor of the deep ocean. The decisive feature of this deep water SSP is the effect of ocean-wide sound channel formation (Sect. 3.2.2), also called *Sofar-Channel*. The increase of sound speed with temperature towards the surface and

with static pressure towards the bottom leaves a minimum in between. The horizon of this minimum of sound speed, which means a maximum of the acoustic refraction index connects the world oceans and is called *Sofar-axis* (Sect. 3.2.2). Sound rays leaving the source at modest angles of elevation or depression don't touch the ocean boundaries where they would lose most of their energy but are repetitively refracted towards the Sofar-Axis, forming ray garlands which oscillate around this horizon. Steeper rays will nearly reach the boundaries, thus oscillating essentially through the entire water column; shallow rays remain close to the axis and encounter only the corresponding water layer of lowest sound speed. The sound rays indicate the various paths of possible sound propagation and thus represent the way and the speed of a kind of synthetic integrator:

The travel time along each sound path is the integrating memory of the local sound speeds encountered.

It might be surprising that the fractions of the signal belonging to the steep rays oscillating nearly from surface to bottom with the longest paths arrive first: they travel most of the time through water of high sound speed. Correspondingly the least inclined paths are the slowest because they remain close to the horizon of minimum sound speed within the water column. Usual ray depictions are somewhat misleading in this respect because of the compressed range scale. In reality, even the steepest rays are inclined by a few degrees at most and their way is only a few per mille longer than the shortest.

The geometry of the ray garlands suggests the relatively simple principle of the method to derive the instantaneous heat content of the cross section between the source and receiver from the arrival pattern of a single signal. Normally 6 to 10 arrivals can be separated before the bulk of the latecomers merges into the maximum of sound energy (Sect. 3.2.2). To start the evaluation, one first needs to know how the ray pattern will look like. This is called initialization and is conducted using at least one “initial” sound speed profile to compute a first ray tracing with the sound source as the origin. This profile will usually be measured by a sensor-package lowered from a ship which of course will take further profiles on this occasion along the range for comparison and to get an example of the horizontal variability for testing the ray tracing. The sensor package samples also temperature and electric conductivity, providing salinity data to

enable the estimation of accuracy when deriving heat contents from signal travel time only. In principle, historical sound speed profiles from so called *climatological sources* will also suffice to initialize the ray computation.

The main ray tracing simplification, inevitable for this kind of single tomographic ranges is that the sound speed profile does not change along the range and thus the temperature stratification is assumed constant as well. This is inevitable because a single range cannot provide any horizontal resolution along the sound propagation, only averaging by integration. For further consideration only those rays are selected which “hit” the receiver. These rays are called the *eigen-rays* of the range. Only these rays produce the arrival peaks. The depiction of the ray pattern reveals how deep the individual rays “dive” into the water column. If one is interested only in the development of the total heat content without any information of its vertical structure then only one eigen-ray which oscillates through nearly the full water column will suffice in principle. Usually it will belong to the first arrival.

Though this kind of tomography is equalizing temperature in the horizontal as it were, it can, within limits, resolve a thermal layering in the vertical: The number of resolvable layers is the same as the number of resolvable arrivals indicating the corresponding eigen-rays which scan different, though overlapping depth intervals during their oscillating up and down propagation. The separation requires the repetitive treatment of a set of equations but is no fundamental problem. This numerical operation with the arrival times as the only input can be conducted for every signal transmitted.

How sensitive is this acoustic integrator? Warming by 1° centigrade will make the arrival earlier by 0.3 s of the 133 s total travel time at a range of 200 km. Since the bandwidth of the 400 Hz signal was 100 Hz as applied at the tomographic ranges of the examples presented hereafter, the tomographic resolution will be 10 ms (Sect. 3.6.6, 4.4.1) Thus the 200 km range can resolve a temperature difference of about 0.04 degree centigrade and even less at high signal to noise ratio. The longer the range, the better the resolution. The tomographic temperature resolution is comparable with sea going thermistors. But these can only acquire the *local* temperature of the water in contact with the sensor whereas the tomographic integration acquired *remotely*, holds for the total large scale average.

However, resolution is not accuracy. There are several causes of potential error and also fundamental problems. Since the sound signal cannot discriminate between the

three contributions to the sound speed, a variation of salinity as well as of static pressure by varying water level will inevitably cause inaccuracies of the real temperature data. Separate investigations and numerical simulations have quantified the amount of this type of potential inaccuracy. According to experience it is small enough to identify even small trends of the heat content to be significant.

A more fundamental problem is the assumption of a quasi stationary ray pattern. This simplification means: the individual ray does not primarily modify its path by a varying temperature, only its travel time. Also the sequence of the arrivals is assumed invariant which means that the slightly changing depth of the Sofar-Axis by temperature does not impair the set of eigen-rays. One approximation to deal with ray paths of limited stationarity is called the *matched peak method*. It compares the measured travel time pattern with those derived from a set of suitable sound speed – or temperature – profiles respectively looking for the best fit which is then used to determine the vertical structure of the heat content. This method was used for the tomographic ranges of the *Labrador Sea* and the *Western Mediterranean*.

Benign rays don't normally exist in shallow waters of the continental shelves where the static pressure is insufficient to make up the lower part of the Sofar-Channel and the rays therefore touch the boundaries. Then their behavior becomes chaotic: a tiny change of a single parameter will cause a fundamental change of the entire ray pattern. The attribution of a particular ray to a stable and reliable sound path is then impossible.

The tomographic examples presented hereafter come from two deep water sites: the western Mediterranean and the Labrador Sea. The nearly one year of operation of the Mediterranean 600 km range with careful investigation of the tomographic accuracy in comparison with ship borne sensors has proven the reliability and superiority of the tomographic concept to provide heat contents. The following five years of operating the Labrador Range of 200 km was an outstanding demonstration and confirmation that Ocean Tomography is the unequalled tool to monitor the variability of the heat content of large ocean areas reliably over time periods of climate relevance.

The other unrivaled potential of single range tomography is the remote and continuous monitoring of *water mass transport* through a cross section defined by the range. The basic concept of integration along the

sound ray paths is the same as of monitoring the heat content.

The range then needs to have a slant angle to the direction of flow because the actual sound speed is enhanced or reduced respectively by the flow component in the same direction. (Sect. 4.5). Accordingly, the travel time difference between upstream and downstream signal propagation has to be measured. This requires alternating sound propagation in both directions. The “deep diving” eigen-ray of the range will also suffice to yield the net total flow data for the same reason as for monitoring the total heat content. An example of tomographic monitoring the water mass transport through the Strait of Gibraltar will be shown.

It should be mentioned, that the signal energy of the tomographic sound sources is transmitted as a signal of many seconds duration to keep the instantaneous sound level low. This contributes to avoid potential hazards to marine mammals (Sect. 3.6.9). This long signal has a particular frequency modulation which covers the same

bandwidth as the corresponding short pulse, necessary for the required travel time resolution. A so called *matched filter computer* at the receiver side reconstructs the corresponding short pulse by frequency dependent time delays: all the frequency components of the long signal arrive at the same time at the filter exit.

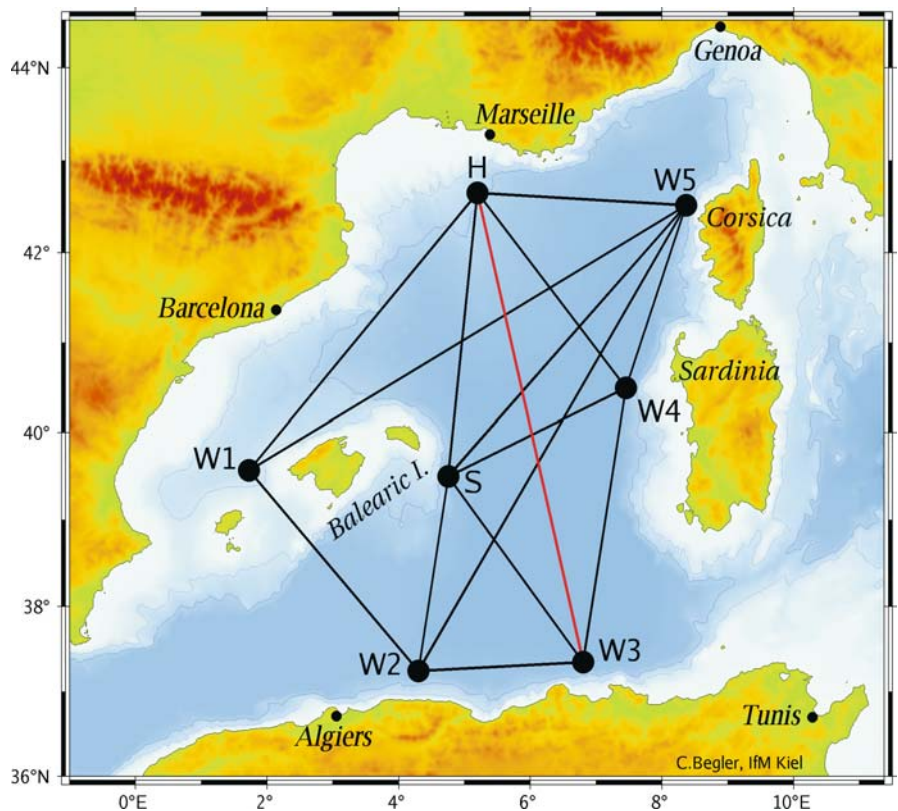
The evidence of superiority of the tomographic concept to provide the large scale integration of fundamental oceanographic quantities simultaneously and continuously is a major step forward to realistic climate modeling. The data quality is so convincing and their permanent availability so important as a reliable and precise reference that further tomographic ranges at key positions of meteorological and climate importance will hopefully become reality. Their incorporation into real-time data transmission by satellites would be to the benefit of weather- and climate forecasting.

6.1.3.1 Acoustic Measurements of Heat Content across the Mediterranean Sea

Image 6.1.3.1-1.

Tomographic network, project *Thetis II*. The map of the western Mediterranean shows the network of combined sound transmitters and -receivers, so called *transceivers*, which was operated during nine months of 1994. The transmission ranges were designed for horizontal and vertical sampling of entire cross sections of the deep basin between France, Spain and Algeria. The battery powered self-contained transceivers were held at 150 m depth between anchor weight and buoyant elements. Each of the transmission paths between the various pairs of transceivers provided about 10 well resolved and stable signal arrivals, corresponding to the travel times of the sound ray connections between the stations.

Image ©: Uwe Send, Christian Begler, IfM, University of Kiel ■



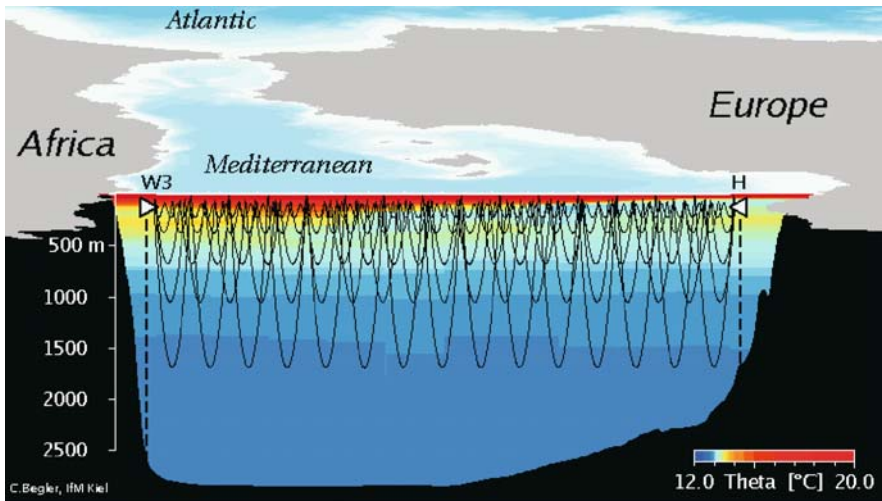


Image 6.1.3.1-2.

Sound rays along the main acoustic connection. The ray pattern example of the main range H-W3 depicts a few of the ray garlands, covering different depth intervals. The ray diving deepest without bottom and surface contact is sufficient to derive the heat content of the entire cross section covered: Warming will reduce the signal travel time correspondingly. The 15 diving loops of this ray recognize and integrate local changes of the temperature both in range and depth. The other ray paths passing through different depth intervals enable to sample the vertical dependence of the heat content and pro-

vide its average profile along the cross section. The network of transmission ranges permits to extend the heat content information from cross sections to the volume enclosed. The main acoustic connection H-W3 across the Mediterranean Sea was also sampled by temperature profiles every fortnight from a ship for comparison.

Project: Thetis II, 1994; funded by the European Commission and the Federal Ministry of Education and Science

Institutions: Institut für Meereskunde, Kiel, Germany; Ifremer Brest; FORTH/IACM Heraklion; LIS Univ. Grenoble; Woods Hole Oceanographic Institution

Survey vessel: *RV Poseidon*, Germany; *RV Le Suroit*, France

Acoustic transceivers: 250 Hz, 400 Hz; signal traveltime/temperature resolution of the range: 0.01 °C (standard deviation)

Image ©: Uwe Send, Christian Begler, IfM, University of Kiel ■

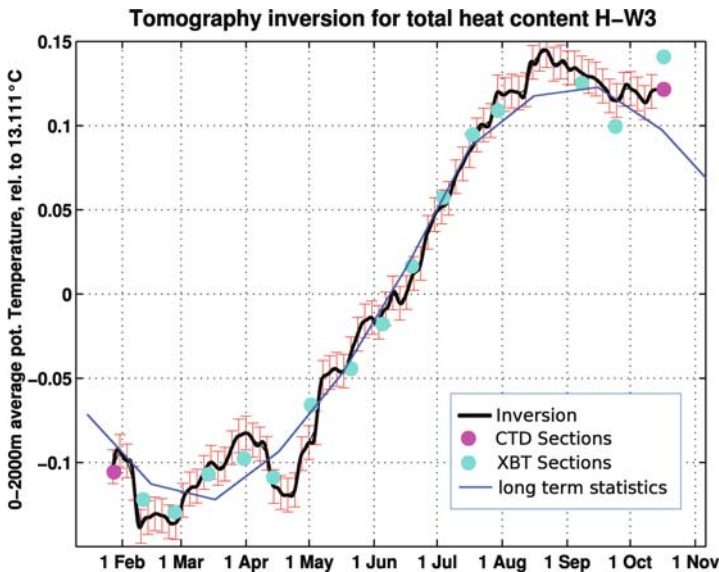


Image 6.1.3.1-3.

Seasonal cycle of heat content across the *Mediterranean Sea*. Tomographic data compared to local samples and long term statistics. The acoustic results of the seasonal cycle of the heat content expressed as temperature deviation from 13 °C are depicted as the heavy black line. The data cover the main cross section of 600 km length and 2 km depth (H-W3, depicted in Image 6.1.3.1-1). The error bars include the acoustic data scatter and estimates of other contributions such as salinity variability. The dots stand for the contemporary *shipborne temperature profiles*, averaged along the range. The thin line represents the long term statistics of 85 000 local profiles. The seasonal features of the year 1994 coincide when determined ship-based and acoustically but they deviate significantly from the long term statistics.

The systematic comparison confirms the capability of ocean acoustic tomography to yield valid heat content data of large scale deep-sea sections even when the salinity is less constant than in the open ocean. This experiment is considered a generic proof of applicability of acoustic tomography for other ocean areas.

Image documentation: same as for Image 6.1.3.1-2 ■

6.1.3.2 Acoustic Measurements of Heat Content of the Central Labrador Sea

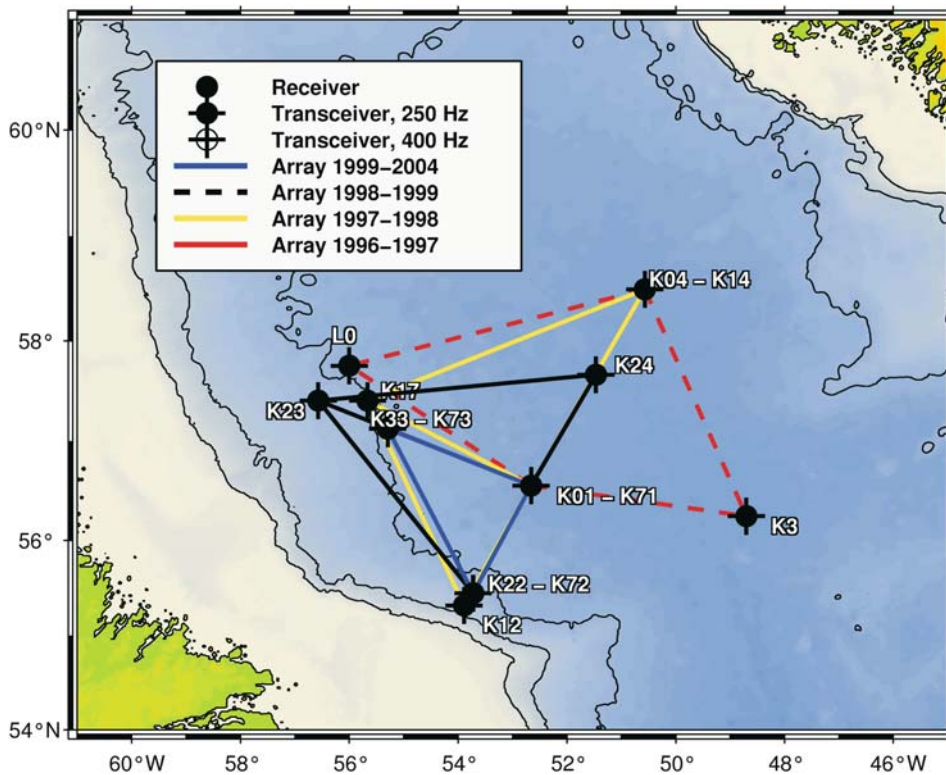


Image 6.1.3.2-1. The tomographic network. The now five year long time series of heat content observations in the *Central Labrador Sea* are based on the experience with the same tomographic concept which was realized over a nine months period across the western Mediterranean Sea. This preceding experiment confirmed the capability of tomography to monitor the *spatial average of temperature and thus the heat content of large scale sections of an entire ocean basin remotely, simultaneously, and continuously*. The Labrador experiment was conceived to discriminate climate trends from short term, random variability, an accomplishment which local measurements cannot provide.

The *Central Labrador Sea* is considered the key area of formation of the upper part of the *North Atlantic Deep Water (NADW)*. The storm periods of winter and spring time are cooling the surface water down, thus increasing its density. Having lost its buoyancy, the former surface water sinks and flows southward as a deep boundary current. This NADW current is part of the so called *conveyor belt*, a global distributor of heat and a decisive steering element of the system of climate.

The tomographic range system was configured to cover a representative section of the area. The main part of the range with five years of operation is the triangle of autonomous sound-transceivers combined with temperature sensors at the positions K1, K2 and K3. The second digit of the mooring designators indicates the position, the first stands for the current year of operation. The distances between K1 and K2, K2 and K3 and K3 and K1 are 140 km, 210 km and 172 km respectively.

Project: Labrador Sea Experiment, SFB460 (DFG)
 Research vessels: *RV Meteor*, *RV Poseidon*, *RV Hudson*
 Acoustic transceivers: Webb Research, 400 Hz, at times: HLF5, 250 Hz
 Temperature/ salinity sensors at K1, K2
 Image ©: Uwe Send, IfM, University of Kiel, Germany ■

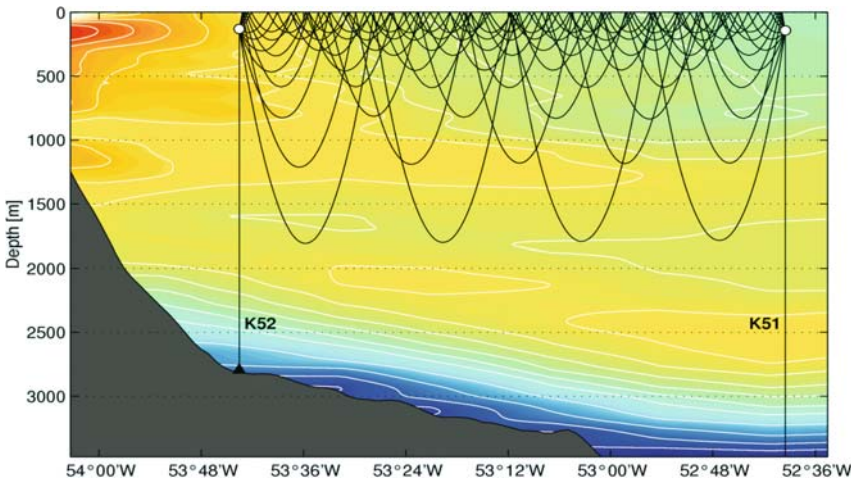


Image 6.1.3.2-2.

The sound ray paths between the stations K1 and K2. The figure depicts only so called *eigen-rays*, which connect source and receiver of the K1-K2-range. The first nine rays shown are separable by sufficiently different arrival times of the respective signal portions. They enable monitoring the vertical distribution of the heat content. The eigen-ray diving deepest covers the depth range between the sea surface and 1 800 m. This is the water column covered by tomography to acquire the heat content between K1 and K2. Unlike the Sofar-Channel at lower latitudes where the upper loops of the rays return without touching the sea surface, the surface water of the Labrador Sea

is not warm enough throughout the year for the backward sound *refraction* (Sect. 3.2.2) which is replaced by surface *reflection*. This fact is causing some inevitable spread of arrival time and loss of signal energy.

Image documentation: same as Image 6.1.3.2-1

Image ©: Uwe Send, Thomas Avsic, IfM, University of Kiel, Germany ■

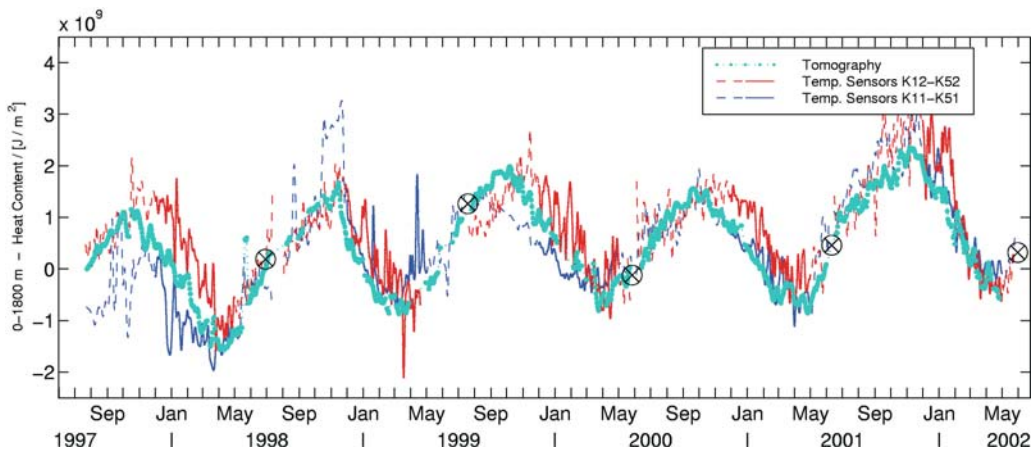


Image 6.1.3.2-3.

The results of the five years experiment. The figure depicts the five year history of the heat content of the K1-K2 cross section of the upper 1 800 m. The light blue data curve represents the tomographic results; blue indicates the local temperature records at K1; red corresponds to the temperatures at K2. The few crossed circles

are ship-borne measurements of temperature and salinity which were also used for calibration of the tomographic range. Since the upper tens of meters could not be covered by the local thermistors due to destruction risk, their temperature curves are depicted as solid lines only during the colder months where the water of the upper column is sufficiently mixed.

The comparison reveals some agreement and also strong and systematic deviations between the integrating tomography and the local sampling. The three curves come closest during the annual periods of lowest temperature which appears significant despite the strong variability of the local data. The reason is the effective mixing of the water also in the horizontal. However, the maxima of the curves are different in height and in time in some years and the flanks in between are found below or above the more consistent curve which is the product of tomography. Its superiority is clearly evident without much explanation. Conclusions regarding trends of the heat content can be drawn much more clearly and convincingly from the spatially integrating tomography. Five years may be a too short time span to judge on trends but the significant increase of the heat content over this period is evident. The years to follow will continue to provide a unique contribution to long term monitoring of a key element of the development of the global climate.

Image documentation: same as for Image 6.1.3.2-1

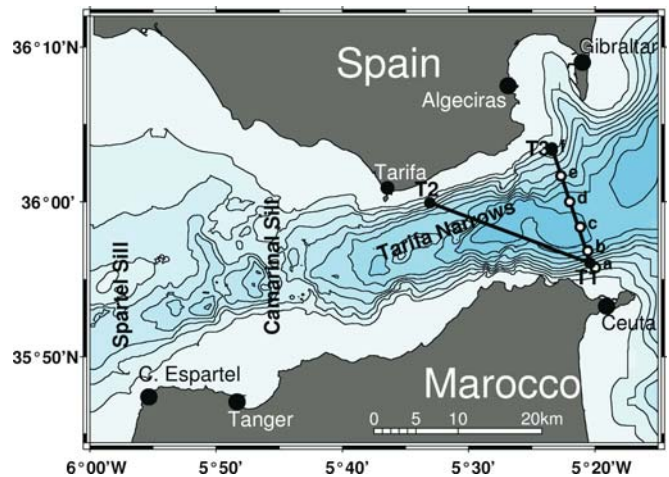
Image ©: Uwe Send, IfM, University of Kiel, Germany ■

6.1.3.3 Monitoring the Outflow through the Strait of Gibraltar by Acoustic Tomography

Image 6.1.3.3-1.

The transceiver range. The outflow of the Strait of Gibraltar is the most spectacular single feature of the global map of the *Sofar-Channel* which governs the ocean-wide sound propagation at low frequencies. (Sect. 3.2.2) The channel axis is 300 m deeper than that outside the broad tongue injected by *Mediterranean* water with its higher salinity, extending across the *Atlantic Ocean* to the *Gulf of Mexico*. The sound speed at channel depth is an even more sensitive indicator. The outflow tongue of this feature covers an area of the size of the African continent.

This far extended though diluted indicator of the Med-specific salinity of 4‰ instead of the 3.5‰ of the world's oceans (Sect. 3.1) represents a natural tracer for tracking water-masses, transported by ocean currents. To quantify this tracer outflow and its variability through the Strait exit requires a large number of current meters distributed over the cross section of the Strait. This may be necessary for a short term campaign of method comparison but would be prohibitive for long term monitoring. The seemingly ideal solution to this problem with the capacity of integration instead of sporadic sampling and acquiring continuous, real time data without vulnerable local sensors is *acoustic tomography*. The figure depicts the transceiver range T1–T2 implemented in slant direction across the Strait to monitor the different upstream and downstream travel times of the alternating sound signals. The transceivers were positioned near shore on short moorings, 100 m below the depth of the interface between outflow and inflow for optimum sound ray paths. (The additional cross range T1–T3 was used to monitor the heat content, similar to the tomographic range in the western Mediterranean, Sect. 6.1.3.1.)



Project: EU project CANIGO in collaboration with Scripps Institution of Oceanography (ONR funded)

Transceiver: wideband, center frequency 2300 Hz, bandwidth: 2300 Hz

Travel-time resolution: 0.7 m s^{-1} or 8 cm s^{-1} speed resolution

Image ©: Tom Avsic, IfM, University of Kiel, Germany ■

Image 6.1.3.3-2. Ray tracing through the Strait of Gibraltar.

The investigation was restricted to the outflow through the Strait. At the section chosen the water depth is 900 m. The width of only 20 km provides three relevant sound propagation paths along the corresponding eigen-rays shown in the figure. The lowest is the only existing deep diving sound ray loop without bottom contact through the outgoing cool, saline flow, indicated blue beneath the incoming warmer flow of Atlantic water, indicated in warm colors. The flow derived from the difference between upstream and downstream signal travel time along this deep diving ray path is indeed representative of the integrated transport of the saline flow through the Strait.

This was verified by comparison with ship mounted acoustic Doppler current profilers (ADCP), moored rotor current meters and an empirical tidal model.

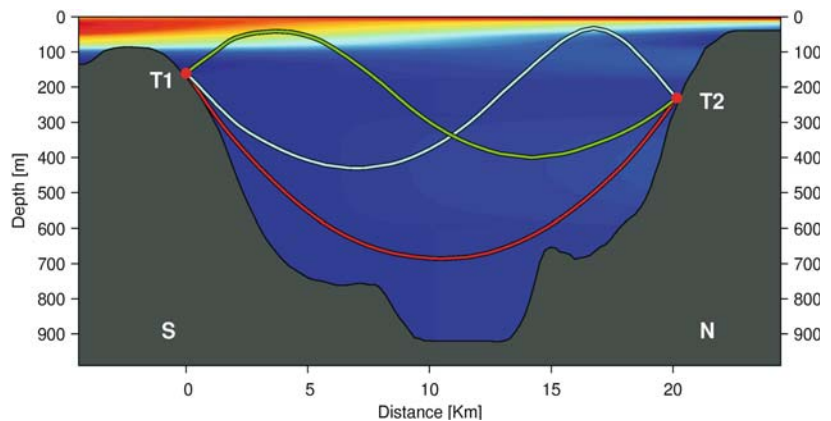


Image documentation: same as for Image 6.1.3.3-1

Image ©: Tom Avsic, IfM, University of Kiel, Germany ■

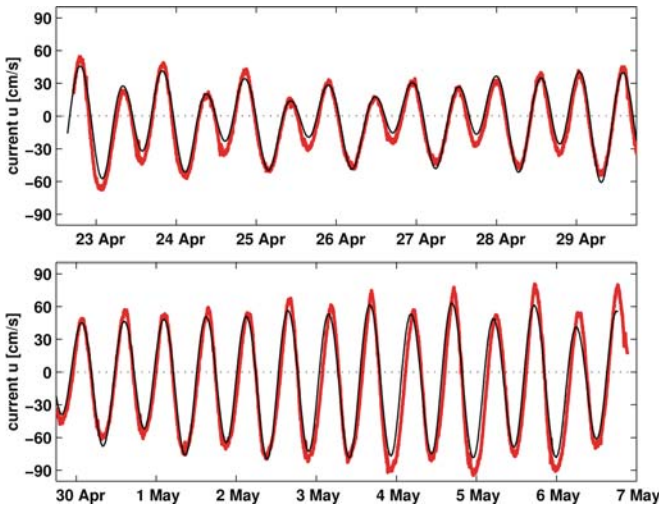


Image 6.1.3.3-3.

Tidal periodicity of the Gibraltar outflow. Tomographic monitoring. The conspicuous feature of the outflow history of a month's demonstration deployment is the *tidal flow*. It dominates the small low-frequency fluctuations of the through flow, which would be of interest in longer-term deployments.

The seemingly small net outflow of about 10 cm s^{-1} of Mediterranean water corresponds nevertheless to a volume transport of nearly $1\,000\,000 \text{ m}^3$ per second (this is just the unit of 1 Sverdrup, Sv.). It is this mean flow, not the much stronger tides, which is responsible for the distribution of the Mediterranean Water into the open ocean. The outgoing current averaged along the acoustic ray-path across the Strait is shown. The comparison between the tomographic data (red) and the directly measured current meter data (black) demonstrates a high degree of agreement. The remaining differences are more likely to be due to limitations in the discrete sampling with a few current meter moorings than to errors in the tomographic technique. This shows that tomography with its advantages of continuous long term and real time monitoring is not inferior to the accuracy of a more endangered field of local current meters. The time period of the test measurements is too short to judge whether the accuracy will permit discrimination of long term trends of climate relevance as it is evident with heat content monitoring.

Image documentation: same as for Image 6.1.3.3-1

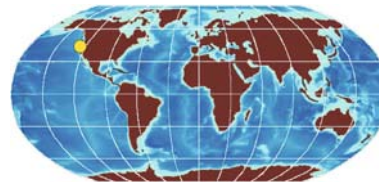
Image ©: Tom Avsic, Christian Begler, IfM, University of Kiel, Germany ■

6.2

6.2 Gas in the Sea

Echosounding is the most sensitive method to detect gas in the sea from a distance because of the maximum mismatch of the decisive property to generate echoes: the acoustic impedance, the product of sound speed and density (Sect. 3.4.1). Since both quantities are smaller than those of water, the reflected sound wave changes its sign, the unmistakable indicator of the presence of undissolved gas. This effect has enabled the detection and volume estimation of the largest hydrocarbon deposits on Earth (Sect. 6.2.1). Gas ascending from the sea floor to the atmosphere and gas intruding from the atmosphere into the sea volume are both high ranking players in the global climate game. Since gas bubbles are the only resonators in the sea vibrating in the frequency regime accessible by remote sensing echosounders, they are the only substance where ocean acoustic spectroscopy is applicable (Sect. 6.2.3), a tiny role compared to the role of light in this arena: Spectroscopy of electromagnetic waves, in particular of visible light, is the fundamental tool of remote sensing in astronomy to analyze the chemistry of the atmosphere of stars by their spectrum fingerprint.

6.2.1 Methane Hydrate Deposits



The assumption of the existence of almost unimaginably abundant deposits of a *solid form of methane* along the continental margins on a global scale became gradually evident during the last decades. This substance, termed *methane hydrate*, had already been known since the early twentieth century but was considered a chemical curiosity for a long time. In the seventies of the twentieth century, Russian scientists postulated its natural occurrence and verified this assumption by samples found on the floor of the Black Sea. A breakthrough in proving the existence of natural methane hydrates was achieved by the Deep-Sea Drilling Project with the famous RV *Glomar Challenger*, conducted in the seventies and its successor the RV *Joides Resolution* which still today is actively engaged in deep-sea drilling. These vessels retrieved methane hydrate from a depth of several hundred meters below the sea

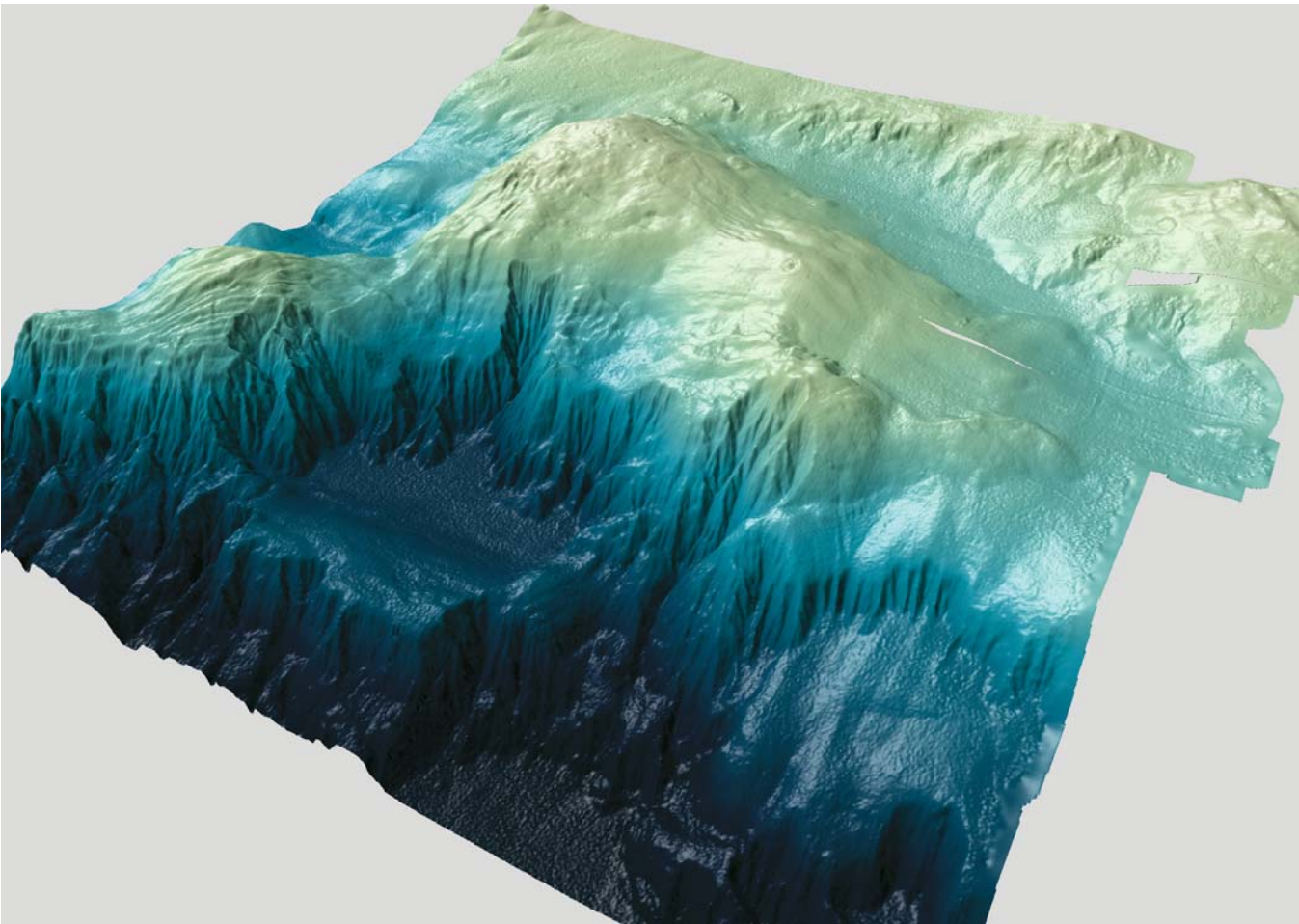


Image 6.2.1-1. The Hydrate Ridge, overview seen from southwest. 3D-multibeam image. The *Hydrate Ridge*, an inconspicuous, N-S elongated submarine mountain of 30 km length, 500 m below the sea surface at the North American Pacific slope offshore Oregon (USA) has become famous as a kind of demonstrator of rich methane hydrate deposits in various and rare forms. This Ridge at 44.6° N latitude has been subject of major international research projects on the physical, geological and biogeochemical conditions of methane hydrate formation and cold fluid venting.

The Hydrate Ridge is part of the parallel ridges created by tectonic subduction of the oceanic *Juan-de-Fuca Plate* under the North American continent and is known for its layers of nearly pure methane hydrate directly at or immediately below the sediment surface. These massive layers are up to 20 cm thick and appear to exist mainly at the southern summit of the double hilled ridge. More disperse occurring methane hydrate, which fills the internal porosity between sediment grains is found at both summits. Echo sounding has also revealed plumes of methane gas bubbles also called flares, presumably escaping from internal faults.

The Hydrate Ridge relief is also part of the “Fledermaus”-files of the CD-Rom, attached to the book. These files allow an interactive flight through the bathymetry at Hydrate Ridge, changing the direction of view and zooming the image on demand.

Project: SO109, SO 110, TECFLUX, LOTUS, OMEGA; data from SO165

Research vessel: *RV Sonne*, Germany

Multibeam system: EM120; frequency: 12 kHz, beamwidth: $2 \times 2^\circ$, fan width: 50° , 191 beams; grid size 20×20 m

Height exaggeration factor: 4. Wet surface effects by combined highlights and shadows

Image ©: Jens Greinert, GEOMAR, Kiel, Germany ■

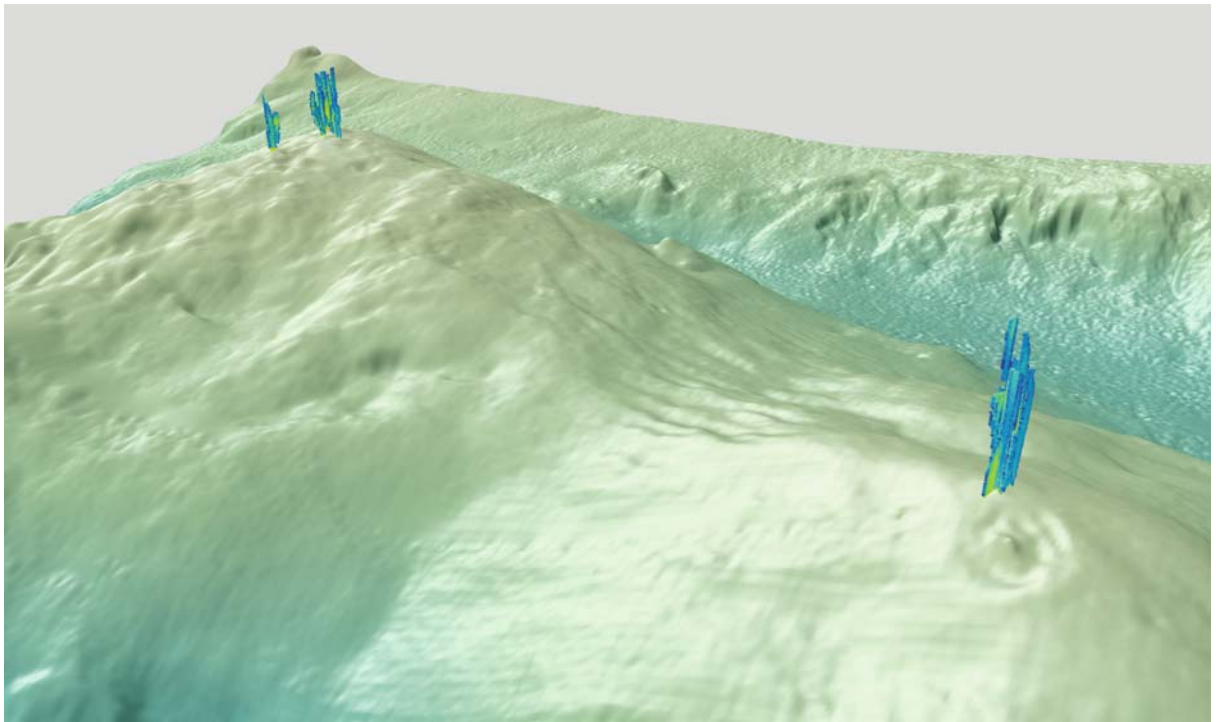


Image 6.2.1-2. The Hydrate Ridge with methane flares; close up seen from southwest. 3D-multibeam image with gas bubble flares. Plumes of methane gas bubble flares ascending from several spots of the Hydrate Ridge were detected with a single narrow beam parametric echosounder (Sect. 4.4.2). The flares are inserted onto the multibeam sea floor image at the gas exit positions called cold vents. Cold vents are mainly found at local summits such as the northern and southern summit at the Hydrate Ridge and are indicators of internal faults. These faults are pathways of ascending free gas released from decomposing methane hydrate or from gaseous methane below the *Bottom Simulating Reflector* (BSR, Image 6.2.1-3). Each of the flare lines corresponds to a sounding beam. The color code indicates fluctuating bubble concentrations in the flare. The real height of the flares may be larger than shown but the free gas is being dissolved in the water before it can reach the sea surface since the abundance of the sources is only small. The bulged surface of the Hydrate Ridge with numerous small mounds visible in the foreground is assumed to be caused in part by the methane hydrate formation process, which requires more volume than the pore water of the sediment. The 3D-depiction with its aerial photograph impression demonstrates the peerless resolution potential of the multibeam technology.

Project: LOTUS, data from SO165

Technical image documentation: same as for Image 6.2.1-1. Parametric sediment profiler: Atlas Elektronik, Parasound; bandwidth 1–10 kHz, beamwidth 4°

Image ©: Jens Greinert, GEOMAR, Kiel, Germany ■

floor off Central America and subsequently off other passive continental margins around the world.

The progress achieved since then does not permit an easy access to these deep deposits – this problem is still unsolved. More successful was the research to understand the environmental conditions for the formation and stable existence of methane hydrate as a solid state substance. However, only the discovery of specific and irrefutable clues revealed by acoustic surveying at low frequencies in the seismic regime which penetrate the sea floor down

to nearly a kilometer, has enabled an economic method of mapping the distribution and size of the methane hydrate deposits. Based on these methods, the global volume of methane hydrate was estimated to range between *5 and 12 thousand billion tons of carbon, about twice the combined amounts of presently known fossil fuel carbon, including coal, natural gas and oil.*

The chemical and physical properties of *methane hydrate* are as unusual as its condition of formation which is not yet understood completely. However, acoustic map-

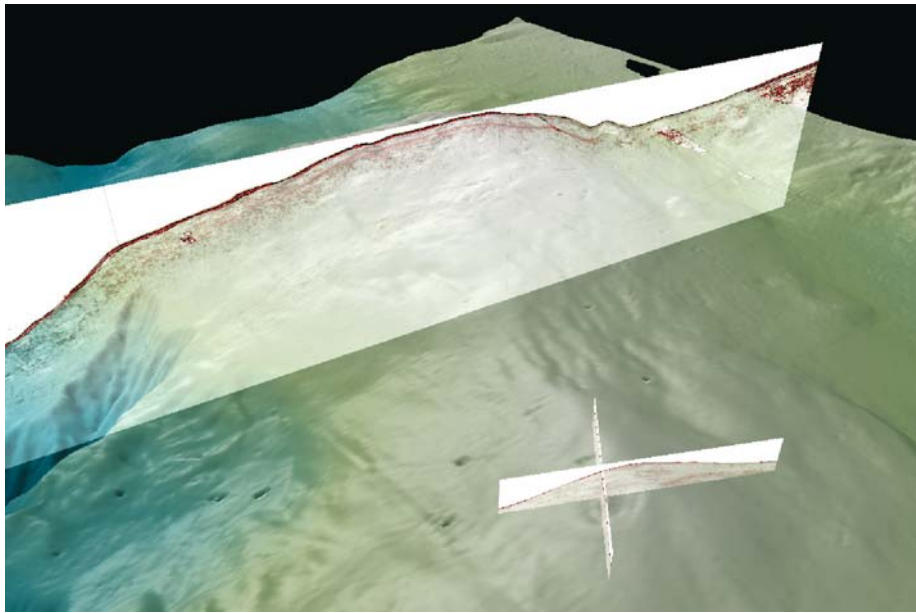


Image 6.2.1-3. The *Hydrate Ridge* with inserted seismic cross section; close up seen from southwest. 3D-multibeam image with seismic data. Profile inset from Image 6.2.1-5. The seismic cross section crossing *Hydrate Ridge* at its two summits is visualized as a superposition of the bathymetric relief by a semi-transparent depiction. Within the seismic sections the second strong reflector approximately 80 m below the sea-floor surface is the boundary between methane hydrate above and gaseous methane below, termed *Bottom Simulating Reflector (BSR)*. The high-resolution seismic cross section is separately shown. Obviously the BSR is most clearly pronounced at the summit area. The smaller seismic sections in the foreground indicate the position of one of the corresponding enlarged sections, which cross a pinnacle-like carbonate structure.

Project: LOTUS, OMEGA

Technical image documentation: same as for Image 6.2.1-1

Data of the seismic device: see Image 6.2.1-5

Image ©: Jens Greinert, Dirk Kläschen, GEOMAR, Kiel, Germany ■

ping of these sub sea deposits relies on specific acoustic features in contrast to gaseous methane in sediments. To understand the criteria of the acoustic discrimination between both substances it may help to deal with the surprising features of methane hydrate first.

What kind of compound is this substance? Methane itself is known as a light gas at room temperature and atmospheric pressure, the most simple chemical compound of carbon and hydrogen. The methane molecule is the smallest of all its chemical relatives known as hydrocarbons and of perfectly tetrahedral configuration: A single carbon atom at the center is connected to four hydrogen atoms which occupy its four valencies by single bonds. It is a completely saturated and thus stable molecule within a wide range of temperature and pressure. The major use of methane as an energy source is its com-

bustion under surplus of oxygen. This replaces the four hydrogen atoms by two oxygen atoms. The result is one of the most well known chemical compounds: *carbon dioxide*, notorious because of its role as a greenhouse gas, although methane itself is an even more potent greenhouse gas than carbon dioxide.

Methane will freeze only at $-183\text{ }^{\circ}\text{C}$, which requires low temperature laboratory facilities. What else can happen to convert this gas into solid state without changing its chemical identity?

The solution of the enigma is more of a physical rather than a chemical process and the compound partner to methane is water. More precisely, we are dealing with a seemingly insignificant peculiarity of the water molecule which turns out to be decisive even for the existence of life in general. According to a simplified

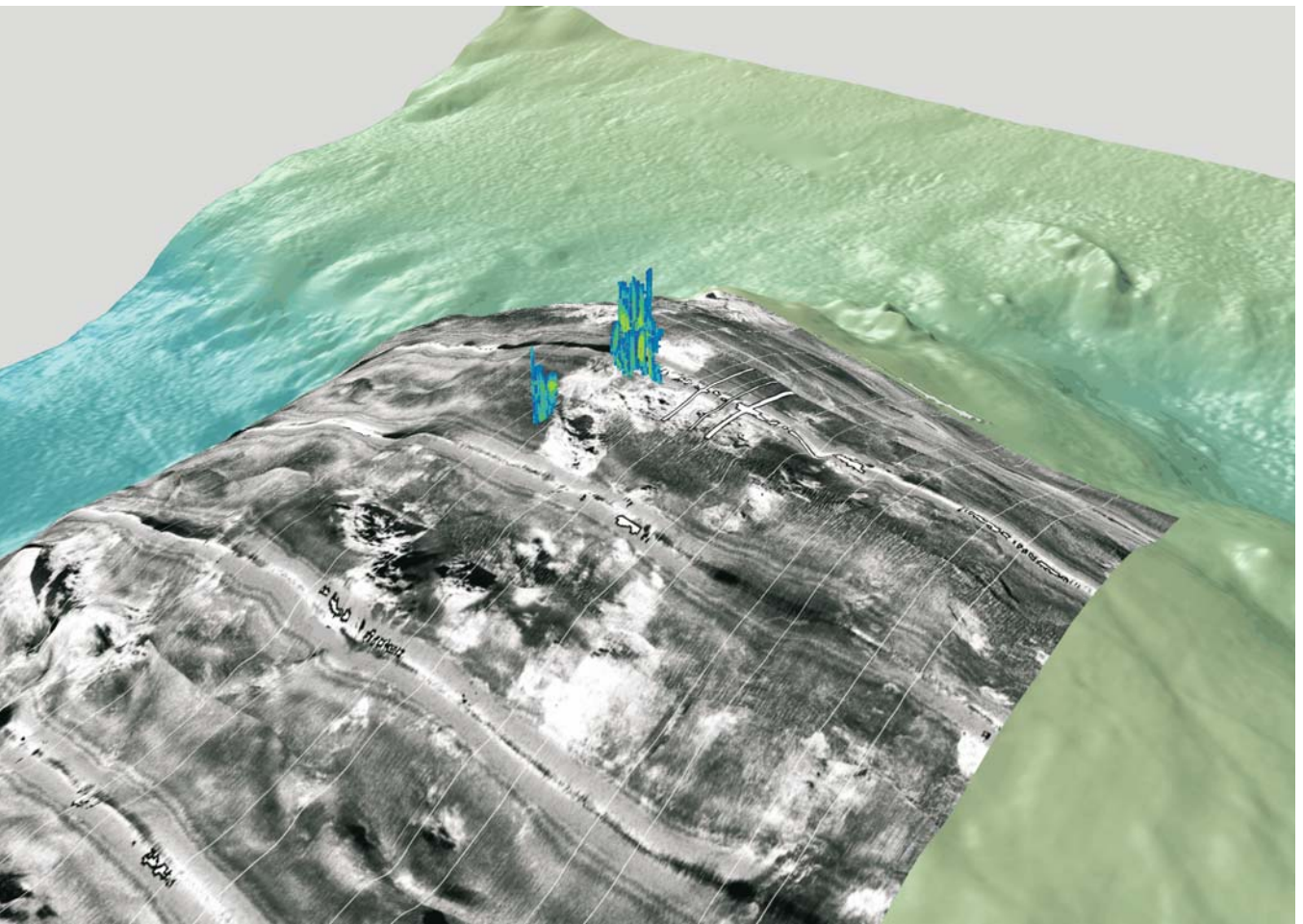


Image 6.2.1-4. The *Hydrate Ridge*, northern summit seen from southwest. 3D-multibeam image with sidescan image overlay and inserted methane flares. The two mutually supplementing concepts of acoustic surface imaging are combined in this image: the high resolution 3D-multibeam technique and the 2D-sidescan technique with the highest possible resolution of small scale morphologic features. The originally 2D-sidescan image is draped upon the bathymetric relief at the northern summit of Hydrate Ridge. No simulated sunlight and shade is added to this draped surface because here the gray tone is a measure of the backscattering intensity increasing with brightness. The sidescan overlay shows four overruns discernible by the four white and gray bands. They indicate also the poorly resolved part at nearly vertical sound incidence below the “keel” of the towed sidescan system (Sect. 4.3.3). The two inner adjacent stripes show strongly contrasting black and white structures which primarily reveal two different types of the sea floor in close neighborhood. The light parts represent the harder carbonate surface, a microbial product derived from methane as one of the reactants. Typically, gas bubbles ascend from these carbonate cemented areas. The darker parts indicate fine grained sand sediment with correspondingly weaker sound scattering when irradiated at the low grazing angles. The structure is superimposed by black acoustic shadow patches caused by a rough morphology.

Project: LOTUS, OMEGA; data from SO165

Research vessel: *RV Sonne*, Germany

Multibeam system: SIMRAD EM120; frequency: 12 kHz, beamwidth: $2 \times 2^\circ$, fan width: 50° , 191 beams, grid size 20×20 m

Sidescan system: EdgeTech DTS-1; 300 kHz, towed between 50 and 120 m above the sea floor

Height exaggeration factor: 4

Image ©: Jens Greinert, Ingo Klaucke, GEOMAR, Kiel, Germany ■

model, its two hydrogen atoms are not placed just opposite each other on both sides of the oxygen atom. Instead, the three atoms of the water molecule include a triangle where the electric charges of the polarized atoms do not compensate each other completely, but leave a resulting external electric dipole field. The electric forces which these molecular dipoles exert upon each other by the attraction of positive and negative charges are called *hydrogen bonds*. Though they are by far weaker than a genuine – covalent – chemical bond, they suffice in their function as structure elements of clusters, building three-dimensional networks of molecular cages.

The behavior of the cluster formation of the water molecules has already been mentioned as the anomaly which maintains part of the cluster structure of ice far beyond its melting point, resulting in the unusual increase of sound speed by temperature (s. Sect. 3.1.3). Higher temperature, which means stronger thermal molecular motion, finally disrupts the loose intermolecular structure.

However, it is only through these dipole forces or hydrogen bonds that water, which is part of any living tissue, is a liquid at temperatures where free methane with its similar molecular weight is a gas. Moreover, the three-dimensional structure of DNA and proteins is also based on hydrogen bonds, in fact the force that enables life. ▶ p.289

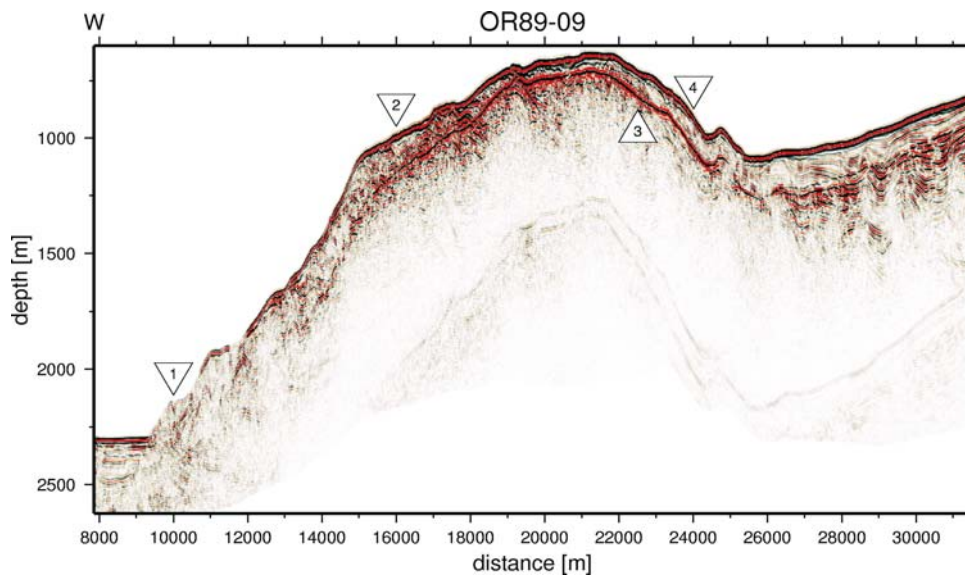


Image 6.2.1-5. Acoustic evidence of a methane hydrate deposit: Seismic profile crossing the northern Hydrate Ridge off Oregon. The seismic profile OR89-09 of 23 km length crosses the summit area of the *Hydrate Ridge* (label 1), famous for its exemplary methane hydrate deposits. This west to east profile represents the seismic close up of the combined overview semitransparent depiction of the 3D-sea-floor relief incised by this sediment penetrating profile (Image 6.2.1-3). The nearly uninterrupted internal boundary following the sea-floor contour about 60 m beneath is the horizon that indicates the lower boundary of the methane hydrate deposit (label 3) and is called *Bottom Simulating Reflector (BSR)*. The BSR in this area is apparently restricted to the ridge summit region from label 2 to 4.

The image processing visualizes the *onset phase* of the reflected acoustic signal: The sea-floor contour is marked by a *black onset line* which means the reflector is harder than the volume above. Expressed in acoustic terms: the *acoustic impedance*, the product of density and speed of sound of the sea floor is higher (Sect. 3.4.1) than the impedance of water. In contrast, the onset line of the deposit contour is labeled red, indicating the gaseous phase of methane below with a lower impedance of the gas filled sediment. (The very weak second pair of contours below with all the slopes doubled is the secondary echo called *multiple* that passed the water column again after reflection at the sea surface.)

Project: ODP-Pre Site Survey OR89-09, 1989, University Santa Cruz, California

Research vessel: DIGICON's *Geotide*

Seismic device: frequency regime: 5–80 Hz, streamer length: 3000 m, depth resolution: 5 m, penetration depth: 3000 m

Image ©: Dirk Klaeschen, Geomar, Kiel, Germany ■

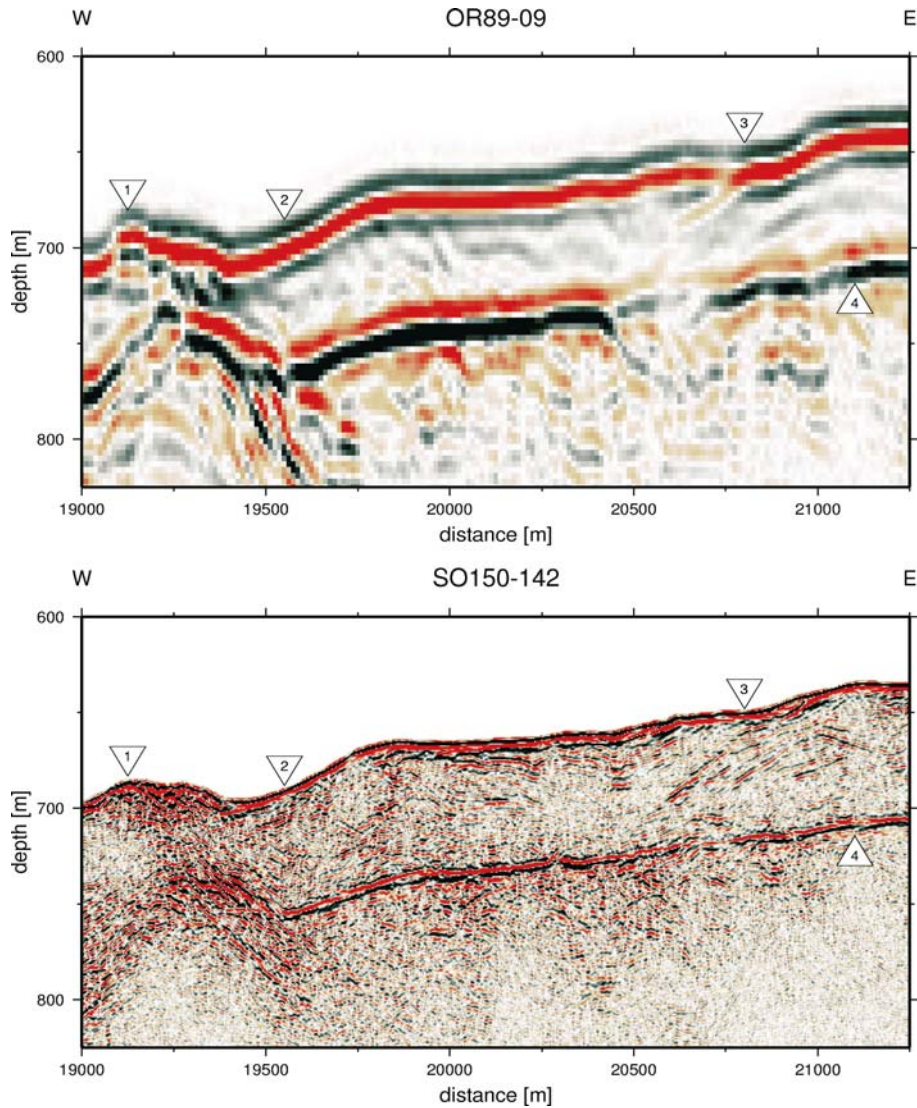


Image 6.2.1-5a. Zoomed cut outs of different resolution of the preceding seismic profile. The two enlarged seismic close-ups of 2 km length of the summit section of the *Hydrate Ridge* shows the acoustic indication of the *Bottom Simulating Reflector (BSR)* very clearly: The echo onset phase appears *black* at the sea floor and *red* at the BSR horizon. The lower resolution of the upper cut-out shows this contrast even more drastically than the seismic profile of higher resolution below which discriminates details of the varying structure. Label 1 indicates a typical biotherm structure with random echo zones connected with a thrust fault which was drilled by ODP at the location of label 2. Another fault system causing methane venting is visible at label 3. This corresponds to a reduced echo strength at the BSR-horizon (label 4). The two images are from separate sea trials.

Upper cut-out, lower frequency:

Project: ODP-Pre Site Survey OR89-09, 1989, University Santa Cruz, California
 Research vessel: *DIGICON's Geotide*
 Seismic device: frequency regime: 5–80 Hz, streamer length: 3000 m, depth resolution: 5 m, penetration depth: 3000 m
 Image ©: Dirk Klaeschen, Geomar, Kiel, Germany

Lower cut-out, higher frequency:

Project: Hydrate Ridge Survey SO150-142, 2001, Geomar, Germany
 Research vessel: *RV Sonne*, Germany
 Seismic device: frequency regime: 30–250 Hz, depth resolution: 1.5 m, penetration depth: 500 m
 Image ©: Dirk Klaeschen, Geomar, Kiel, Germany ■

One of the possible networks of cage units formed by the water molecules consists of elementary cells of 12 regular pentagons combined with slight modifications of this cell. The volumes enclosed by the pentagon-cells are just large enough to lodge one methane molecule each. The encaged molecule is not fixed by chemical bonds but can move and rotate freely inside. The combined, crystal-like structure of methane and water held together only by the weak electric forces is in fact a solid state substance and is called *methane hydrate*. This name, which suggests a genuine chemical compound is somewhat misleading. Chemists call such encaged connections, which can lodge even noble gas atoms, by the technical term *clathrates*.

At room temperature and atmospheric pressure, methane hydrate which has a whitish translucent appearance similar to compressed snow is unstable and disintegrates into gaseous methane and water. There is a relatively well defined regime of static pressure and environmental temperatures ranging between 50 bar/5 degrees centigrade and 90 bar/12 degrees, where methane exists as a hydrate. These conditions are found worldwide in the ocean below depths of about 500 m both in the free water column and inside ocean sediments. As a third condition, there must be an abundance of organic residue in the sediment which is converted into methane through microbiological activities. Only then will the supply of methane suffice to “fuel” the cell structure of the water molecules during the forming phase of methane hydrate. This end product is rather seldom found as compact, homogeneous material. At most, there are marbled, white enclosures of methane hydrate of a few millimeters, sometimes centimeters, in thickness close to the sediment surface. It is assumed that the bulk of the deposits consists of sediments where methane hydrate fills the gaps between the grains, replacing, i.e. converting the pore water similar to the cement between the gravel grains of concrete.

This is a most important feature because it provides the unmistakable acoustic indicator for the presence of methane hydrate. What does that mean? First, this methane hydrate “concrete” is impermeable, in contrast to pore water filled sediment. Second: the geothermic warming towards deeper sediment layers does not permit methane hydrate to exist below a certain depth, only gaseous methane. Since this gas cannot escape through the “concrete” lid, there is a strong boundary which makes a significant difference to the acoustic impedance – the product of sound speed and density – above and below (Sect. 3.4.1).

This boundary between hydrate filled and gas filled sediment is a kind of *pressure-release boundary* in acoustical terms (Sect. 3.4.1). It behaves similar acoustically to the boundary between the water column and the atmosphere above. This interface is the best possible acoustic reflector in the sea, due to the maximum mismatch of the acoustic properties of both media. The internal sediment boundary which separates the two types of methane occurrence, solid phase hydrate above and gas phase methane below is in fact a pronounced reflector, comparatively as strong as the seabottom itself and is called *Bottom Simulating Reflector (BSR)*.

This so-called pressure release boundary condition forces the sound pressure to be zero at that border, similar to an open beer bottle which will release the static pressure inside. That means: the sound wave sent out by a source from the ship will be reflected at the pressure release boundary with the opposite sign of the sound pressure. For instance: when the sound signal starts with an *increase* of pressure, it will return, starting with a *decrease*. Only then is the sum of the incident and the reflected wave zero at the boundary. When the echo returns with the opposite sign, which means the opposite phase of the wave train, it clearly indicates a boundary with gas content below. In contrast to this, a harder boundary, such as rock or coarser grained material beneath a soft sediment layer enforces a pressure maximum there: the returning wave train will have the same sign or phase as the outgoing one.

Of course, the reality is a bit more complicated. Neither the rock nor the gas-containing sediment are ideal reflectors; thus part of the sound signal will always enter the volume beneath.

Otherwise the acoustic imaging of that part of the sediment layers would be impossible. High concentrations of gas will indeed screen the sediment against penetration by sound, mainly because of the strongly enhanced absorption (Sect. 6.2.3).

However, this only partial reflection does not influence the sign of the reflected signal, which is therefore a *very robust indicator* of the presence of gas below a tight lid boundary. It is in fact the surface of the *gaseous state* that is acoustically identified; the presence of hydrate above is identified only indirectly.

The tight sediment lid requires import of more pore-water in addition to methane to fill the pore volume completely with methane hydrate “cement”. Nevertheless, the tight lid may have leakages of various origin

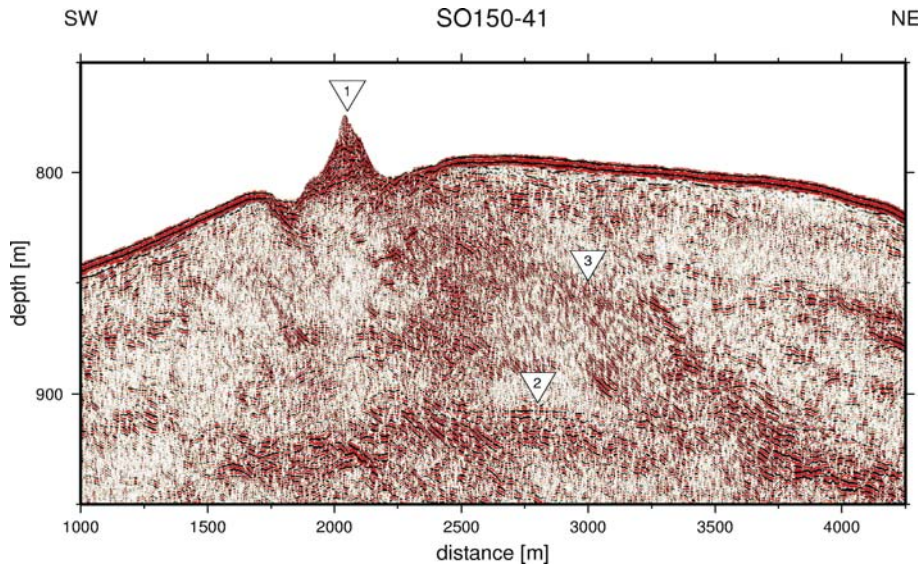


Image 6.2.1-6. Southern summit of the Hydrate Ridge. Seismic profile of a Pinnacle Area. The Pinnacle of profile SO150-41 is a carbonate edifice approximately 30 to 40 m high surrounded by a moat, possibly caused by differential subsidence (Label 1). The many irregular reflective layers inside up to the top appear typical of carbonate mounds situated on hydrocarbon deposits (Sect. 5.3.4.1). These, together with the constituents of the water current, feed chemical and biochemical processes, building such mounds which consist partly of cold water corals. The profile reveals a weakly indicated methane hydrate BSR-horizon (label 2) visualized by the red lined echo onset. Typical of BSRs, this nearly horizontal contour runs parallel to the sea floor and does not follow the sloping trend of the pronounced irregular internal reflectors north-east of the pinnacle (label 3).

Project: Hydrate Ridge Survey SO150-41, 2001, Geomar, Germany

Research vessel: *RV Sonne*, Germany

Seismic device: frequency regime: 30–600 Hz, depth resolution: 0.6 m, penetration depth: 300 m

Image ©: Dirk Klaeschen, Geomar, Kiel, Germany ■

whose causes are not totally clear. Methane gas does not simply escape like vapor from a defective pipe. When gaseous methane is passing through fractures of a sediment volume with stable conditions for methane hydrate, one would expect a kind of self healing of the defects by new hydrate. Thus it may be possible that gas escape indicates recent disrupting motions of the sea floor. Ascending gas plumes can be detected easily by normal, high frequency echosounders which are highly sensitive to any gas bubble clouds (Sect. 6.2.3).

Unfortunately the upper boundary of a methane hydrate deposit is not evident in the seismograms of the reflected signals though the acoustic impedance of the “cemented” layer is presumably higher than the normal sediment. This is not surprising, because a sharp, step-like boundary is considered improbable. A continuous transition however does not generate echoes (Sect. 3.4.2). The content of methane hydrate in a vol-

ume of sediment could nevertheless be revealed by *refraction seismics* instead of the *reflection seismics*, which is less expensive to acquire and from which the seismograms presented hereafter are derived. Whereas the simple seismic version needs only a single ship, the reception of sound signals at slant incidence to quantify the refraction indicating the distribution of methane hydrate would require a greater and more expensive effort, prohibitive for regional mapping. Thus the estimation of the methane hydrate content of a deposits has to rely on the regime of its stable existence.

Returning to the pressure release boundary, it is often evident already at a first glance at the seismogram because it does not necessarily follow the contours of the usual sediment layering. On the contrary: old sediment layers which typically contain interlayers of turbidites from exceptional sediment flow events (Sect. 5.3.2) have usually undergone geodynamic deformations; e.g.

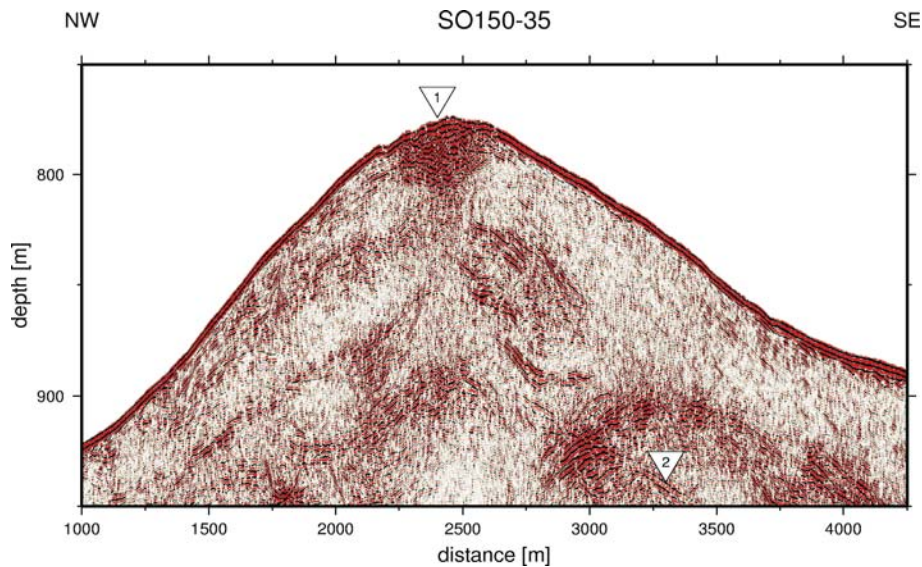


Image 6.2.1-7. Southern summit of the Hydrate Ridge. Seismic profile, crossing the preceding one. This BSR-feature is correspondingly evident at the seismic profile SO150-35 crossing the preceding profile SO150-41. Here the BSR, marked by label 2, follows the bottom contour again, different from the other layers around. The irregular internal structure at the top of the mountain (label 1) is similar to the carbonate pinnacle. Unlike the BSR horizon of the northern seismic profile which indicates a gas-tight lid, the agglomerate of disconnected reflectors of these southern profiles suggests fluid venting and thus ongoing generation of carbonate structures.

Project: Hydrate Ridge Survey SO150-35, 2001, Geomar, Germany

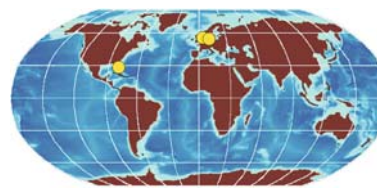
Research vessel: *RV Sonne*, Germany

Seismic device: frequency regime: 30–600 Hz, depth resolution: 0.6 m, penetration depth: 300 m

Image ©: Dirk Klaeschen, Geomar, Kiel, Germany ■

tilting, compaction, disruption, whereas the BSR-contour follows only the temperature-pressure limit of methane hydrate stability. In fact, any deformations of the sediment subsequent to the established equilibrium of a methane hydrate deposit will destabilize this sensitive pseudo-compound and release gaseous methane. The subsequent fate of the methane is not fully understood. A portion of it is either converted into limestone or carbon dioxide as a result of microbial consumption, respectively. Another portion is incorporated into biomass tissue and a third portion may escape into the atmosphere, where it enforces the greenhouse effect. Methane release from hydrate destabilization may also happen through an increase of water temperature or a reduction of static pressure due to a lowering of the water level. This means: the huge methane hydrate deposits play a major and doubtless global role in the complex network of climate factors and their interrelationships.

6.2.2 Methane in Shallow Sediments; Acoustic Sea-Floor Classification



Areas of rapidly accumulating fine grained muddy sediment rich in organic matter are ideal marine environments for the formation of *biogenic methane*. This elementary hydrocarbon gas, a by-product of metabolism of methanogenic bacteria, is often found as gaseous accumulations within near surface shallow water sediments of the continental shelf. These sites are detected and surveyed by sediment penetrating echosounders. Shallow methane deposits are easily identified in the sound images by a conspicuously strong sound scattering from bubble layers.

Biogenic, along with thermogenic, methane formation is also the origin of huge submarine deposits of *methane hydrate* (Sect. 6.2.1). However, this solid form of methane is stable only under limited conditions of temperature and static pressure which don't exist in shallow waters except in colder Arctic waters.

The complex conditions of biogenic methane formation can be studied best when the access is easy and by an interdisciplinary research approach in a protected natural laboratory. The shallow *Bay of Eckernförde* in the western *Baltic Sea*, with water depths of less than 30 m, is well-known for its interesting free methane gas related acoustic features. This site was selected for detailed studies based on previous studies and easy access from surrounding laboratories. The international research project named *Coastal Benthic Boundary Layer (CBBL)* on the physical, mineralogical and biochemical conditions of methane formation was conducted in the years 1993–2001. The project provided the opportunity for detailed studies of physical properties and processes related to the formation of gas-rich sediments which go beyond the conditions of gas-rich methane formation. They include various properties of coastal sediments, such as physical, acoustic and geo-technical characteristics related to acoustic scattering and detection of bottom mines, which are important for military mine countermeasures.

In the context of these comprehensive investigations an *Acoustic Sea-floor Classification System (ASCS)* for real-time mapping of sediment types was developed and applied to sea-floor sediments of two predominating mineralogical ingredients: silicate and carbonate. The western Baltic was chosen as the provider of sediments of the former category, whereas the latter were investigated off the Atlantic west coast near Key West.

The acoustic sediment classifier ASCS is based on the *acoustic reflectivity of the sediment surface at vertical incidence* which depends essentially on the acoustic impedance and at higher frequencies on the sea-floor roughness (Sect. 3.4.5). Acoustic impedance is the product of sediment sound speed and density and by using empirical relationships can be used to estimate other sediment properties such as mean grain size and water content. The acoustically derived sediment properties are ground-truthed from sediment core samples. This principle of classification is different from measuring the scattering strength of the sea floor at low grazing angles (Sect. 3.4.5, 4.3) by sidescan sound irradiation. Sidescan backscatter maps of raw data are inevitably ambiguous: the grain size, bottom roughness and slope, as well as the material impedance determine the backscattering strength. However, additional infor-

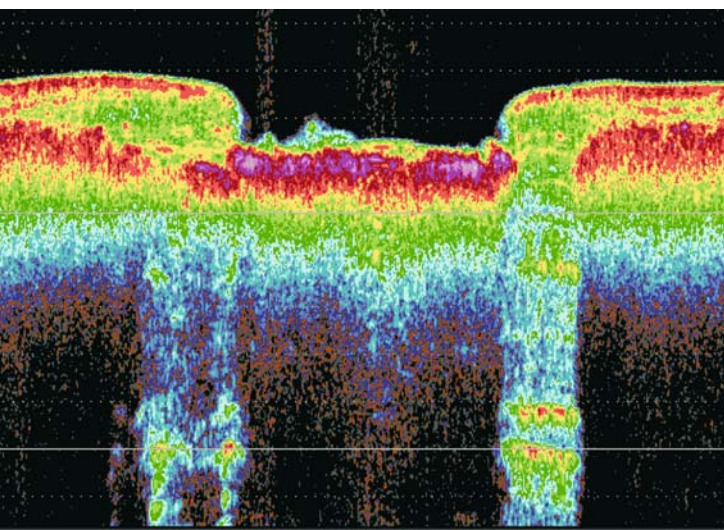


Image 6.2.1-1.

Sediment cross section of a pockmark, Eckernförde Bay, Baltic Sea. Sediment echosounder image. The sediment cross-section shows a particular methane gas enrichment feature in soft shallow water sediments called a *pockmark*. The example shown is a nearly plane depression of the sea floor by little more than a meter. Particularly conspicuous is the gas layer just beneath the sediment-water interface indicated by the strong scattering marked in red and purple colors on the image. The steep lateral boundary of the feature was found to be nearly circular in shape (Image 6.2.1-2). It is surrounded by a ring nearly free of gas, sometimes called “acoustic window”. It permits deeper sound penetration: layers are detected down to 5 m beneath the sea floor. Also present is a fluff of low acoustic impedance (Sect. 3.4.1, 2) at the left central portion of the pockmark basin, indicated in light blue and green. Gas bubbles can also be seen rising from the pockmark into the water column.

Project: Coastal Benthic Boundary Layer (CBBL) 1993–2001
Survey vessel: *WFS Planet*, Kiel, Germany

Echosounder: Naval Research Laboratory Acoustic Seafloor Classification System (ASCS); frequency: 15 kHz, beamwidth 12°
Image ©: Douglas N. Lambert and Donald J. Walter, Naval Research Laboratory, Stennis Space Center, MS, USA ■

mation, in particular from local bottom samples, is necessary whenever the kind of sediment material is determined by any remote acoustic methods. The vertical incidence method which yields the data along narrow track lines instead of along broad stripes has advantages as a supplementary diagnostic tool, it “opens” the third dimension, the depth below the sediment-water interface. The capability of the ASCS-system to penetrate sediments and to quantify the vertical profile of the acoustic impedance is used in particular to study the variability of methane occurrence.

6.2.2.1

Examples of Acoustic Features of Methane in Shallow Sediments

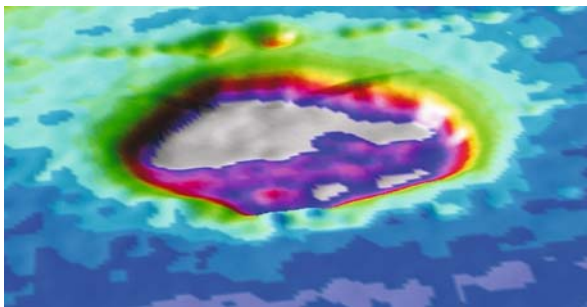


Image 6.2.2.1-2.

Pockmark of methane generating mud, Bight of Eckernförde. 3D-multibeam image from an autonomous underwater vehicle (AUV). The outer shape of this pockmarks is a more or less circular shallow basin of 20–30 m diameter with 2–2.5 m depth and steep flanks up to 20°. Similar to another pockmark shown as a vertical trans-sediment cross section (Image 6.2.2.1-1), this shallow basin feature is also an exit for submarine fresh water discharge, releasing up to several hundred liters of fresh water per m² and day.

Project: AWI pilot study with AUV, 2002
 Position: 54.50° N, 10.03° E, water depth 22 m;
 Supervising vessel: *RV Alkor*, Kiel, Germany
 AUV: *Maridan*, type: 600, 1 500 kg, length: 4.5 m, width: 2 m, height: 0.6 m, 1.5 m s⁻¹
 Multibeam echosounder: Simrad SVS; 240 kHz, janus-transducer for AUV-application, fan angle 70.4° (2.5 times height of flight; 12 m during survey)
 AUV-Navigation: MARPOS system developed by Maridan A/S and Kearfott Guidance and Navigation, New Jersey, USA
 Color code: aquamarine: 24.5 m; yellow: 25.5 m (half depth of pockmark; diameter 20 m); gray: 26.5 m
 Image ©: Eberhard Sauter, AWI, Bremerhaven, Germany ■

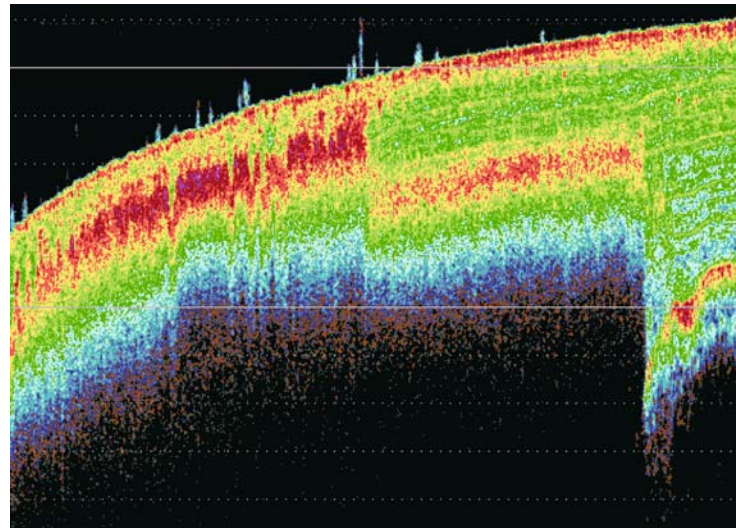
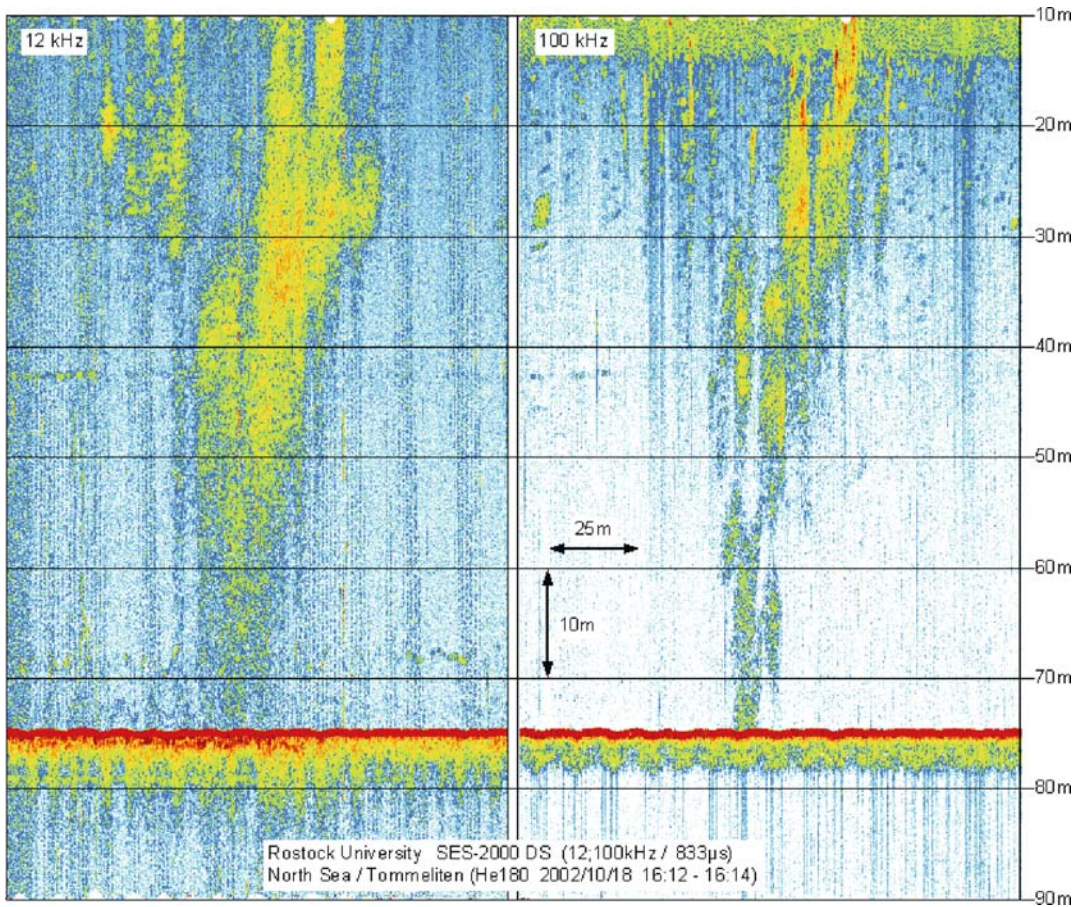
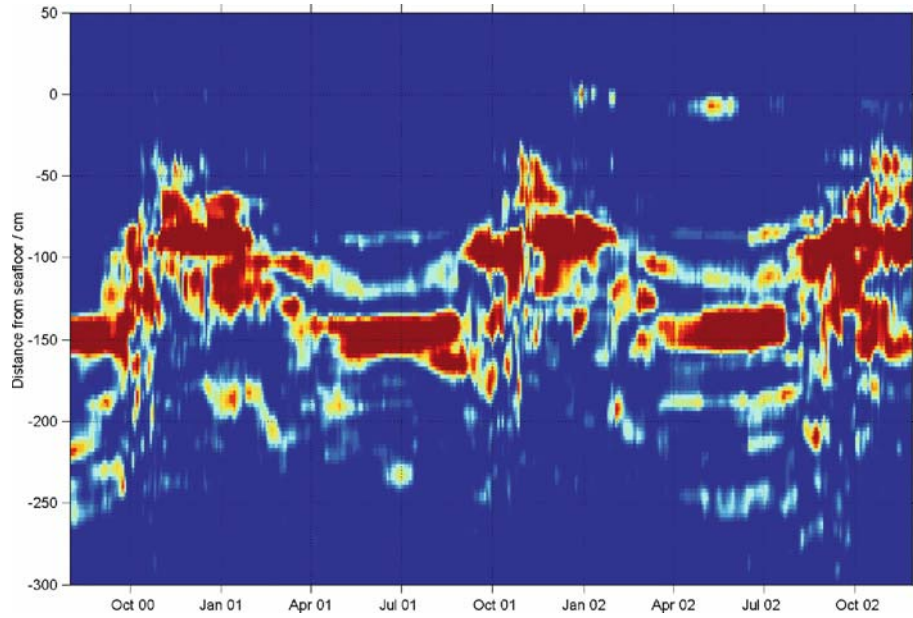


Image 6.2.2.1-3.

Gas layers in soft sediments of the western Baltic Sea. Trans-sediment section by the Acoustic Sea Floor Classification System ASCS. This image shows a 2.5 km long section through the Bay of Eckernförde with layers of methane gas in a silty clay sediment containing organic material. On the left side of the image the gas can be seen as red to purple colors representing very high reflectivity. The white lines of the depth scale are 5 m apart, indicating the thickness of the gas layer that appears deeply corrugated at the upper surface. The blue peaks at the sediment surface could indicate small methane flares. At the center of the image, the gas layer is now found 2 m deep below the sediment surface, an abrupt depression within a few meters distance. At the right edge of the image, methane gas is no longer present in the sediment. The surface of the glacial till, buried under more than 5 m of the soft sediments becomes visible. Such abrupt changes of the presence and depth of occurrence of methane gas is typical of these types of soft sediment structures.

Project: Coastal Benthic Boundary Layer (CBBL), 1993–1998
 Survey vessel: *WFS Planet*, Kiel, Germany
 Echosounder: Acoustic Seafloor Classification System (ASCS) with ELAC transducer; frequency: 30 kHz, beam-width: 6°
 Depth resolution: 7.5 cm, compression of the range scale: 200
 Color key: the echo intensity increases 4 times, at 6 dB per color step, towards warm colors. Depth scale: 5 m between white lines
 Image ©: Douglas N. Lambert and Donald J. Walter, Naval Research Laboratory, Stennis Space Center, MS, USA ■



◀ **Image 6.2.2.1-4. Seasonal variability of the methane gas horizon of the Bight of Eckernförde. Time series of a local depth profile of a methane layer.** This record of the horizon of gaseous methane over more than two years was made from a sensor tower, carrying the downward looking automatic echosounder 6 m above the sediment surface. The gas horizon appears conspicuously periodic with a constant low level during summertime followed by an irregular rise during the fall and winter. At first sight the seasonal dependence demonstrates the sensitivity of the methane solubility to temperature in the sediment pore water. But the periodicity also demonstrates the *phase shift* of the sea floor temperature with regard to the seasons. The stable temperature stratification of the water column during summer with its cold water on the sea floor keeps the sediments cool for nearly half a year. It is only through total mixing of the water by storms during the fall that the sea floor is affected by the warmer water from the summer. This “off season” increase in the sea floor temperature raises the gas horizon. But this storm induced increase happens obviously at random until the water and thus the sea floor cools down again. The superimposed variability of the static pressure by varying water level in the bight caused by inward and outward going storms contributes to the irregular horizon of the methane, which is more soluble under higher pressure.

Project: Part of the Coastal Benthic Boundary Layer (CBBL) project

Site: Bight of Eckernförde, Germany

Echosounder: mono-beam, Elac; 33 kHz, beamwidth 15°. One sample per hour from August 2000 to December 2002

Image ©: Thomas Wever, FWG, Kiel, Germany ■

◀ **Image 6.2.2.1-5. Methane plumes in the North Sea. Parametric echosounder image.** The goal of the parametric echosounder operation was to precisely localize sites of gas emission on the sea floor and to guide the different winch-operated geological sampling devices of several corer techniques to the identified spot. Furthermore, the beam steering function of the echosounder was applied for continuous tracking of the water sampler to capture the water from the gas plume above the emission sites. By this acoustically controlled approach, visualization of sediment structures related to free gas as well as gas emission into the water column together with targeted sampling, was feasible at the same instant. Though the gas plumes were detected in shallow water, they ascend from deeper and much older gas deposits of North Sea gas fields, different from the young, muddy, near surface gas sources of the western Baltic, characterized in the preceding images.

The parametric principle of echosounding (Sect. 4.4.2), originally developed for high resolution imaging of sediment structures, is particularly appropriate to investigate the shape and dynamics of gas bubble plumes (Sect. 6.2.3) and the magnitude of the gas source. Even the content of bubbles of a particular size in the plume can be remotely determined through irradiating the gas plume with sound signals at the frequency where these bubbles resonate and produce their strongest echo. The total echo intensity of the irradiated plume at that frequency is then a measure of the bubble population of that size. Tuning the sounding frequency over a wide range – which is easy for the parametric transmitter – achieves the sequential filtering out of the respective bubble size fractions. Integration over all fractions provides the instantaneous gas content of the plume. In the North Sea experiments it was found that the dissolved methane concentrations in the water column match the acoustic plume image which is restricted to non dissolved gas. The reason for this close relationship between acoustic gas imaging and dissolved methane concentrations is not yet understood.

The two examples visualize the plume at the bubble resonance frequencies of 12 kHz and 100 kHz. The corresponding bubble diameters are 0.5 mm and 0.06 mm. Obviously the larger bubbles prevail in this plume. Since the bubbles grow in size when ascending they migrate through their level of resonance. The 12 kHz filter views most of the bubbles at about 35 m depth or 40 m above the sea floor, indicated by the strongest echo. The tiny 100 kHz bubbles appear to ascend in the form of confined clouds with population maxima more towards the surface, where a kind of permanent layer of small bubbles is present. The gas plume drifts and broadens like chimney smoke during the ascension with an obviously small cross section at the bottom exit. It should be mentioned that Methane sources often release much larger bubbles than demonstrated here and larger still than the bubbles produced by air intrusion due to breaking sea waves (Sect. 6.2.3).

Project: Research trial HE180; location: 56°30' N, 3° E

Survey vessel: *RV Heinke*, Germany

Parametric echosounder: SES-2000DS, development of Rostock University; primary frequency: 95–106 kHz, tunable parametric frequency interval: 4–15 kHz

Image ©: Gert Wendt, BSRI, Rostock University; Antje Boetius, AWI, Bremerhaven, Germany ■

6.2.2.2 Application of the Acoustic Sea Floor Classification System (ASCS) for Shallow Sediments

The application of the system ASCS to classify sediment types and bedforms is treated in the context of Sect. 6.2.2 to demonstrate the versatility of the concept.

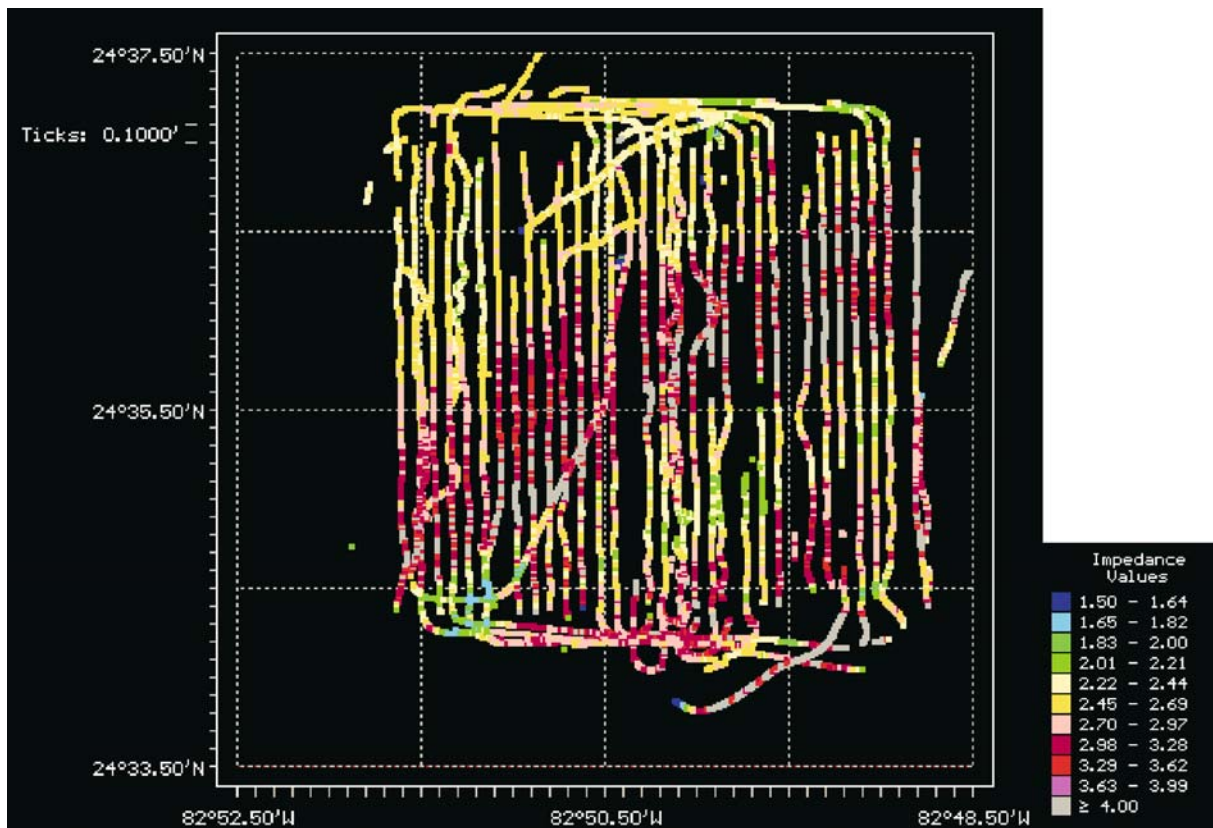


Image 6.2.2.2-1. Acoustic mapping of carbonate sediments. Track plot of echo strength. The meander lines are tracks of echo sounding an area of about 6×6 km² in respect of its reflectivity to classify the varying bottom type. The color code indicates the *acoustic impedance* of the sediment, the product of its sound speed and density which determines the reflection factor (Sect. 3.4.1). This area of the western Atlantic near *Key West, Florida* was selected as reference for its predominantly carbonate sediments to be compared with the silicate sediments of the Baltic Sea study site. Both sediment types are often found on continental margins, in layers or even in major structures composed of organic and inorganic matter such as carbonate mounds (Sect. 5.3.4).

Project: Coastal Benthic Boundary Layer (CBBL), 1993–1998

Survey vessel: *WFS Planet*, Kiel, Germany

Echosounder: Acoustic Seafloor Classification System (ASCS) with ELAC transducer; frequency: 15 kHz, beamwidth: 12°

Color code:

- blue: low echo return (signal loss on steep slopes)
- green: mud, silt size; sand:mud ratio < 1:9
- yellow: sandy mud; sand:mud ratio < 1:1, may include shell
- pink: muddy sand; sand:mud ratio > 1:1, may include shell
- red: sand; sand:mud ratio > 9:1
- gray: Limestone rock or coral reef

Image ©: Donald J. Walter, Naval Research Laboratory, Stennis Space Center, MS, USA ■

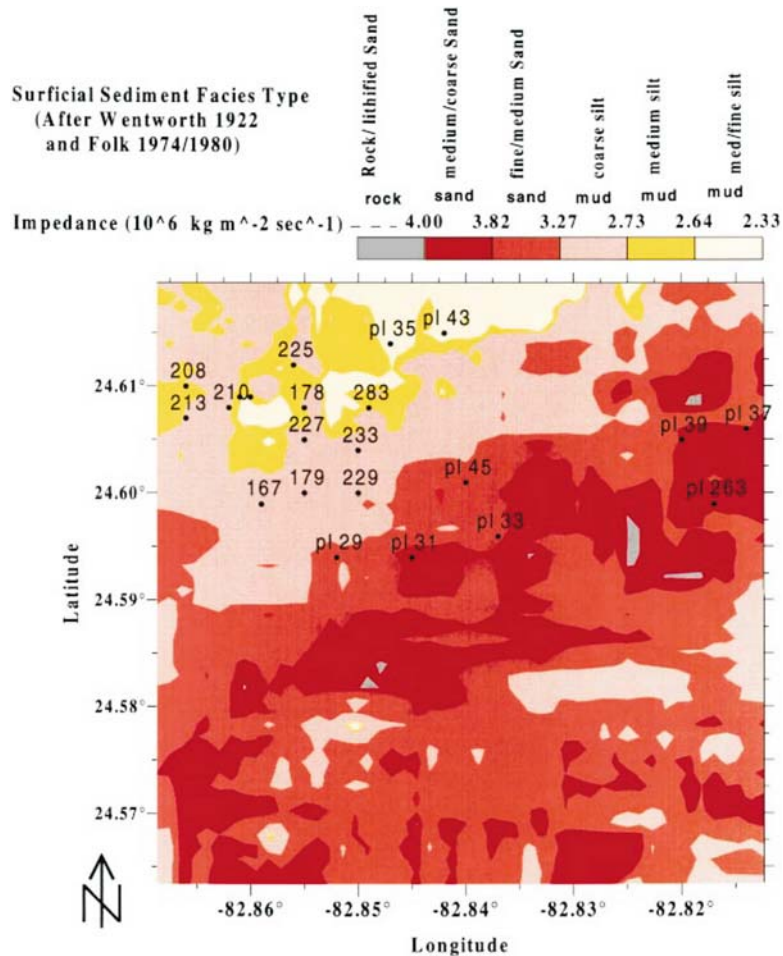


Image 6.2.2.2-2. Contour Map of carbonate sediment types, based on echosounder data. The map with two sand- and three mud sediment classes in addition to consolidated sand, indicated by the color key is derived from the meander track data of the preceding image. The sediment classes are defined by their *acoustic impedance*, the product of density and sound speed (Sect. 3.4.1). This quantity determines the signal reflection factor for vertical echo sounding of sufficiently smooth and horizontal surfaces. The impedance regime between 4.0 and 2.3 units is subdivided into the five sediment classes according to an empirical relationship between acoustic impedance and the mean grain size and sand-to-mud ratio. The map represents the sediment type in the upper 40 cm of the bottom and is derived by interpolating the data of the preceding meander line pattern into the reference plane.

It may appear surprising that *acoustic* and *non acoustic* sediment characteristics are interrelated by a simple one-dimensional scale. This is neither fully understood yet nor is it really a universal scale. In fact, the relations hold at most approximately and they appear to differ significantly between carbonate and silicate sediments and also between shelf and deep-sea sediments to mention only the most frequent domains of approximate relationships.

The core sample (#167) indicated in this map was used to “locally calibrate” the ASCS data. After setting the ASCS normalization at that site, the remaining data was replayed for the entire data set. Such non trivial relationships enable to map key features of matter by economic remote sensing. They are essential supplements to the acoustic acquisition of shape and structure of the sea floor as tools of differential diagnosis of complex processes.

Project: Coastal Benthic Boundary Layer (CBBL), 1993–1998

Image ©: Donald J. Walter, Naval Research Laboratory, Stennis Space Center, MS, USA ■

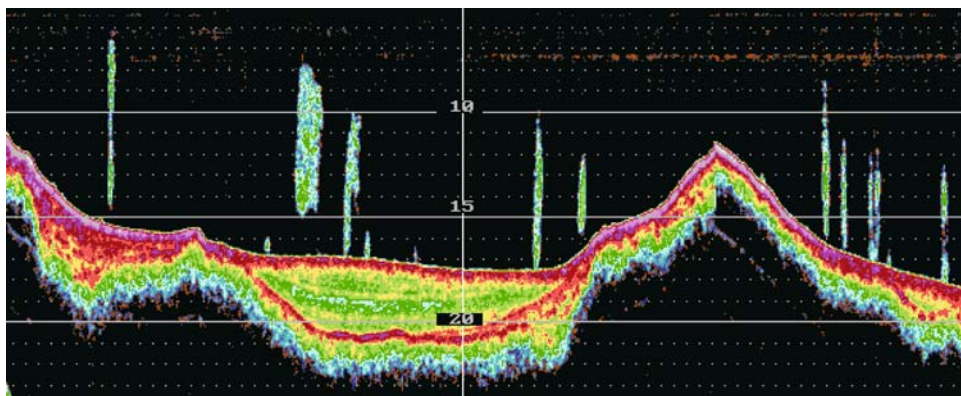


Image 6.2.2.2-3. Sediment pond in the western *Baltic Sea*. Trans-sediment section by the Acoustic Sea Floor Classification System (ASCS). The acoustic transect of 2.5 km at the mouth of the *Bay of Eckernförde* shows a modest ridge of 6 m height at the right side named *Mittelgrund* and the surface of a glacial till with a slight slope at the left side of the image. A *sediment pond* of very soft organic material with weak layers and a nearly plane surface is enclosed between both topographic highs. The glacial till is indicated by the highly irregular contour marked red to yellow at the lower limit of the acoustic return. The oldest layers of the postglacial fill of the sediment pond are presumably up to ten thousand years of age. The vertical “blue” streaks in the water column are believed to be large schools of herring (Sect. 6.3.1).

Project: Coastal Benthic Boundary Layer (CBBL), 1993–1998

Survey vessel: *WFS Planet*, Kiel, Germany

Echosounder: Acoustic Seafloor Classification System (ASCS) with ELAC transducer; frequency: 30 kHz, beamwidth: 6°;

Depth resolution: 7.5 cm; compression of the range scale: 200

Color key: the echo intensity increases 4 times, at 6 dB per color step, towards warm colors. Depth scale: 5 m between white lines

Image ©: Douglas N. Lambert and Donald J. Walter, Naval Research Laboratory, Stennis Space Center, MS, USA ■

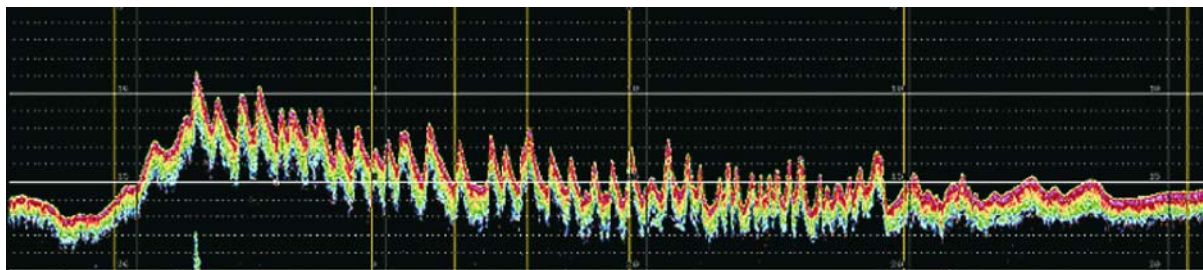


Image 6.2.2.2-4. Trans-sediment section through the carbonate sand wave *Rebecca Shoal* west of *Key West, Florida*. Imaged by the Acoustic Sea Floor Classification System (ASCS). Large sand waves can look and behave quite different from well known periodic dune fields (Sect. 5.3.3). The height of the crests and the length of the valleys of this 300 m long cross section from the west coast off *Florida* vary strongly like a mountain chain profile rather than a field of submarine sand waves. However, this sediment is not the normal silicate sand known from the beach but a so called carbonate sand, with a high content of small shell fragments. Underwater dunes of carbonate sediments often have steeper flanks than those of silicate sediments which are mostly less cohesive. The sharp edged grains are responsible for the steep flanks of more than 30% and the irregular profile. The symmetric flanks differ also from the saw tooth profile of migrating dunes.

Project: Coastal Benthic Boundary Layer (CBBL), 1993–1998

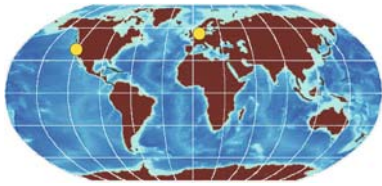
Survey vessel: *RV Seward Johnson*, Harbor Branch Oceanographic Institute, FL, USA

Echosounder: Acoustic Seafloor Classification System (ASCS); frequency: 15 kHz, beamwidth: 12°

Penetration depth of the hard sediment reduced to 3 m; depth resolution: 15 cm; depth scale: 1 m between dotted lines; compression of the range scale: 18; color key: the echo intensity increases 4 times, at 6 dB per color step, towards warm colors

Image ©: Douglas N. Lambert and Donald J. Walter, Naval Research Laboratory, Stennis Space Center, MS, USA ■

6.2.3 Air Intrusion by Breaking Sea Waves



During a heavy storm the raging sea surface, almost invisible due to the dense spray may appear like a kind

of continuous transition between air and sea. This intrusion of sea water aerosol into the atmosphere is the counterpart to the less well known intrusion of air into the water. Storm driven clouds of droplets above correspond to air bubble clouds below, driven and carried down many meters by storm induced turbulent advection (Box 6.2.3-1). In fact, the fragmentation of an air volume inside a

breaking wave crest into billions of tiny bubbles a short moment after is a highly non-linear chaotic process, which is still far from being fully understood.

This dramatic hydrodynamic process of air intrusion is of fundamental importance to climate and marine biology. It is of climatic relevance because it extracts *carbon dioxide*, a notorious greenhouse gas from the atmosphere by dissolution and in parts by later conversion into carbonates. Further, in many areas, the intruded air contains more *oxygen* needed by the marine fauna than the flora can provide.

Regarding the role of bubbles in gas dissolution it needs to be mentioned that the situation with respect to *carbon dioxide* is essentially different compared with *nitrogen* and *oxygen* because these two main constituents of air are only weakly soluble. Hence the volume

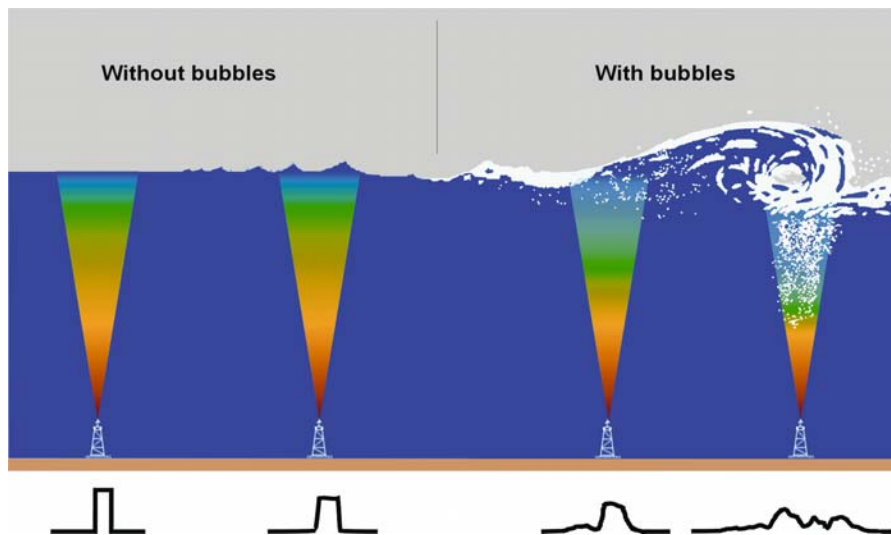


Image 6.2.3-1. Upward looking echosounder for monitoring air intrusion by breaking waves in shallow water of 30 m depth. Schematic depiction. The acoustic measurements of air intrusion into the sea from below the surface and of their indirect acquisition by radar from above were conducted at the research platform *Nordsee*. The permanently manned platform erected at a fixed position 75 km west of the *Island of Sylt* was operational for 15 years before being dismantled in 1992 (Sect. 7.2.4).

The series of four graphic figures demonstrates what happens to an echo from the sea surface when increasing wind generates sea waves and finally wave breaking. The echo contours are shown below the four schematic echosounders. *First figure:* The echo is an identical replica of the transmitted ultrasonic signal pulse because the dead calm sea surface acts as an ideal mirror (Sect. 3.4.1). *Second figure:* The contour of the echo is already modified due to commencing sea waves. Crests and troughs widen the time interval of signal return and thus the echo contour on both flanks. Part of the signal is scattered in other directions causing a decrease of the received signal. *Third figure:* The onset of wave breaking adds a forerunner echo caused by sound scattering from the bubble cloud which appears beneath the wave troughs. The echo amplitude is further reduced by strong absorption in the bubble cloud. *Fourth figure:* Fully developed breaking waves cause extreme echo spread in travel time and strong absorption. The sea surface is screened by the clouds and does not contribute to the echo anymore. The bubble clouds intrude the air to a depth of many meters. The variability of the bubble cloud dynamics is a random process.

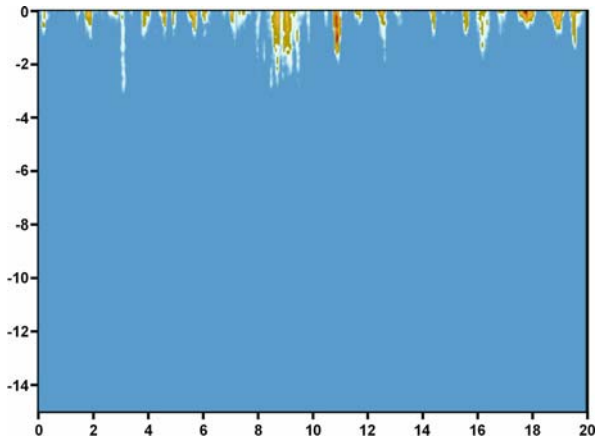


Image 6.2.3-2.

Air intrusion by bubble clouds, the sound image of a cloud. The series of 7 subsequent images represents time intervals of 20 min of downward echoes caused by bubble clouds at different wind speeds. The intrusion depth of bubbles of different size and therefore different resonance frequencies is demonstrated by image pairs. They correspond either to different wind speeds or different echosounder frequencies. The depth axis is in meters, the time axis in minutes. The echo level is color coded in 11 steps adjusted to the respective echo level variability.

This first, single image demonstrates the result in kind. It shows the bubble clouds reaching a maximum depth of 3 m at a wind speed of 10 m s^{-1} or Beaufort 5 but the average depth is hardly more than one meter in that moderate wind condition. The life time of these baby clouds is of the order of only 10 seconds. The intensity of the maximum echo measured was 20 times (13 dB) the minimum intensity.

The echosounder frequency of 50 kHz corresponds to a real bubble diameter at resonance of about 0.13 mm close to the sea surface, where the bubbles are not yet compressed. These bubbles are acoustically enlarged at a sharp resonance to a virtual diameter of about 2.6 mm. They produce the strongest echoes by far and are thus filtered out from the bubble cloud. Tuning the echo filter frequency to cover all the bubble sizes of the cloud is then named *acoustic spectrometry*.

Project: Air intrusion by breaking sea waves, 1986–1990

Research platform: *Nordsee*, Germany

Fixed position: about 75 km west of the *Island of Sylt* at 30 m water depth

Echosounder: Tunable parametric device (Sect. 4.4.2); frequencies applied for the examples presented: 10 kHz, 25 kHz, and 50 kHz, beamwidth is 10° , 4° , and 2° respectively

Height of wind speed measurements: 47 m above sea level
Image © (all 12 images of this section, except 6.2.3-2a):

Heinz Herwig, Bernd Nützel, FWG, Kiel, Germany ■

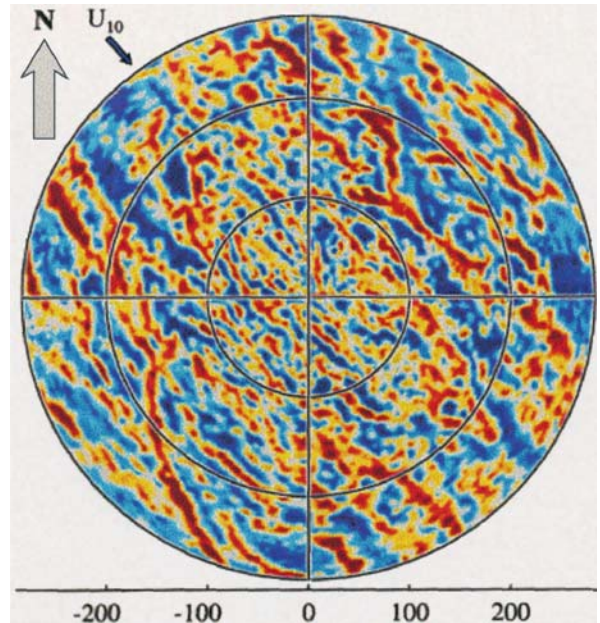


Image 6.2.3-2a.

Panorama of bubble clouds scanned by a submerged buoy. The time series of the intrusion of air bubble clouds imaged by upward looking echosounders reveal the vertical dynamics and quantify the bubble size distribution but neither the horizontal cloud formation nor the mechanism of downward bubble transport. Image 6.2.3-2a is an acoustic backscatter panorama taken from a submerged buoy by Farmer (s. Box 6.2.3-1). It shows the bubble clouds forming streaks preferably aligned with the wind direction, *athwart* the wave crests. This qualitative image indicates a type of convection commonly known as *Langmuir circulation*: vortex structures counter-rotate similar to horizontal cylinders in touch. The conclusions drawn from the buoy measurements dealing with the bubble size distribution and cloud dynamics concur with the long term measurements at the research platform *Nordsee*.

Image documentation: s. Box 6.2.3-1

Image ©: David M. Farmer, Graduate School of Oceanography, University of Rhode Island, USA ■

of gas in the small persistent bubbles seen in sonar images can be significant. The effect of increased pressure at depth leads to dissolution of these bubbles. It is quite possible in certain cases that the dissolution by deeply penetrating bubbles results in supersaturation, since bubbles at depth can still go into solution, even though the water is saturated or supersaturated at the surface. This cannot readily happen with carbon

Box 6.2.3-1. The shape of discrete bubble cloud patterns

Image 6.2.3-2a is like a radar panorama scan, but with measurements acquired from beneath the surface with a mechanically rotated sonar system. *The goal of the panorama measurements was to map the shape of discrete bubble cloud patterns as they evolve in time, rather than seek a direct and quantitative interpretation of signal intensity in terms of bubble concentration.*

The signal is obtained by transmitting with a fan beam – essentially a sidescan sonar transducer but with the narrow beam angle in azimuth and the wide beam angle in elevation. There are four of such sonar heads mounted on motors which step around the corresponding quadrants every 30 s. They acquire intensity and Doppler information of the backscattered signals. The sonar system is suspended at a depth of 25–30 m from a surface buoy using a rubber cord, so as to isolate it from active wave motion. The color code spans a *relative* intensity range of 30 dB, with red being maximum and blue being minimum. Because of the wide transducer beam angle in elevation, the depth distribution of the bubbles at any range from the sonar cannot be derived from the panorama acquisition. The intensity thus represent an effective vertical integration within the range bin. These considerations motivate an approach to signal processing that is quite different from the more traditional one used in vertical sonar measurements: A smooth range dependent empirical intensity function is generated from time averaged sonar measurements. This function changes slowly with time, depending on conditions. The actual sonar intensity measurements at any instant are then differenced with respect to this smooth time averaged signal in order to form the image. This has the effect of highlighting the local intensity variations and greatly aids discrimination of the time evolving bubble cloud shapes. *The quantitative scientific information is thus contained in the shapes and ranges alone whereas the color coded intensities should be seen as qualitative.*

The subsequent interpretation of the measurements deals with the curriculum vitae of the bubbles after their birth at the surface and the mechanism of downward transport where the panorama results play a key role.

Breaking waves inject air bubbles to some fraction of the wave height beneath the surface. The combination of air entrainment and turbulence then creates a distribution of bubble sizes over a few decades of radius with very approximately a -3 power law. This initial injection is then subject to various factors which sort the bubble size distribution and organize it in space. The sorting process begins within seconds of the bubble injection.

Large bubbles have a greater buoyancy than small bubbles and they therefore rise faster. Small bubbles tend to decrease in size due to gas dissolution. The rate of gas dissolution depends on the gas saturation level; supersaturation of gas will actually cause the bubble radius to grow close to the surface, but below some modest depth, depending on the saturation level, bubbles will always tend to dissolve. The combination of these two factors, buoyancy sorting and dissolution, reduce the bubble concentration at either end of the size distribution leading to bubbles predominantly of radius 100 microns, give or take a factor of 2.

These residual bubbles are further acted upon by the background circulation in the actively mixing layer beneath the surface. The depth of this layer varies from a few to many tens of meters, but a distinctive feature is the formation of counter-rotating vortex structures aligned with the wind direction, commonly known as *Langmuir circulation* after Irving Langmuir who first described them. Since counter-rotating vortices give rise to alternately convergent and divergent zones along the surface, near surface properties such as temperature anomalies, surface contaminants and bubbles, tend to collect in the convergences. In shallow stratification typical of some lakes and coastal waters with salinity stratification, the resulting lines are often visually observed and can be remarkably straight as well as being coherent over many times their local spacing. They tend to be less obvious in the open ocean, but nevertheless become apparent in sonar observations of the bubble clouds. Image 6.2.3-2a shows the general alignment of the bubble clouds with the wind direction. However, we note that in contrast to some visual observations in shallow stratification, there is great variability in the structure. One explanation for this is the interaction of neighboring vortices which can even lead to amalgamation of the structures and the formation of “Y-junctions” in the bubble clouds, described in the literature. It is a characteristic of these Y-junctions that they typically point downwind.

The convergent flow leads to a downward movement of the bubble clouds. While bubbles descend to depths of 10 m or more, the increase in pressure increases the rate of gas dissolution. At some depth the bubbles disappear from sonar record and can be assumed to have gone into solution.

David M. Farmer · Graduate School of Oceanography,
University of Rhode Island, USA

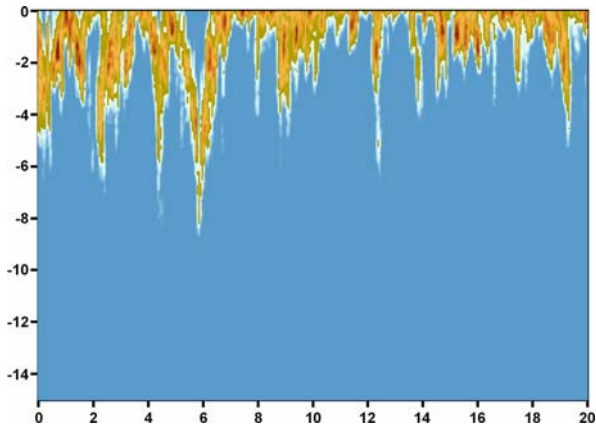


Image 6.2.3-3.

Air intrusion by bubble clouds; wind speed effect. The pair of Images 6.2.3-3 and 6.2.3-4 shows the dramatic effect of increasing wind speed on the intrusion depth and persistence of the bubble clouds or more correctly: of the partial clouds of bubbles of the same resonance size filtered out and visualized at 50 kHz. At 18 m s^{-1} wind speed which is Beaufort 8 or *Gale*, the clouds penetrate the water column down to 8 m with about 5 m depth average. The lifetime varies between a fraction of a minute up to 2 minutes with occasional overlap. Now the maximum echo intensity is 100 times (20 dB) the minimum. Note that the deepest cloud at minute 6 seems to have a core with a very weak echo. In fact, the strongly increased bubble density causes strong sound absorption. To derive the real bubble concentration from the instantaneous echo intensity this effect has to be corrected. At a depth of 8 m the bubbles are less compressible due to the static water pressure and their real resonance size at 50 kHz is now 0.17 mm diameter. That means: the resonance size of the bubbles has to be corrected according to their instantaneous depth as well. The virtual enlargement at resonance achieves a diameter of 7.3 mm. ■

dioxide. Its concentration in a bubble is small and the dissolution rate high. Carbon dioxide would not persist in a bubble beyond a few seconds even for the largest bubbles. The only significant transfer is likely due to the large bubbles right at the surface during wave breaking, since these are the ones that contain enough volume to matter. The transport downwards of the dissolved gas is at least as effective however as of the bubbles which tend to rise due to their buoyancy.

Echo sounding is the most sensitive method to remotely determine even very small amounts of undissolved gas of any kind in the sea (Sect. 3.4). Moreover

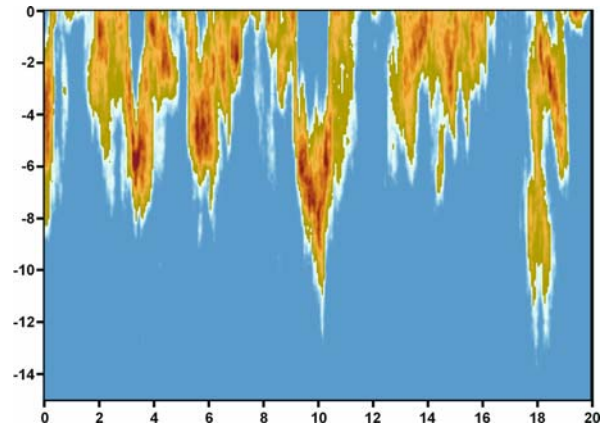


Image 6.2.3-4.

Effect of strong gale. These air bubble clouds were measured at a wind speed of 23 m s^{-1} or Beaufort 9 which is *Strong Gale*. Now the largest clouds reach a depth of 12 m and more than 3 minutes lifetime. The maximum echo intensity is already 700 times (28 dB) the minimum. All the deep clouds show the pronounced core with a very weak echo due to very high sound absorption. At 12 m depth the real resonance diameter of the even more compressed bubbles is 0.19 mm and the virtual blow-up extends to about 9.5 mm. ■

it is the only method to investigate the dynamics of bubble clouds intruded by atmospheric forces into the ocean interior. However, it is a local method. The question is: what can be done to provide climate research with a monitoring method on a global scale?

The key experiment to find the relationship between sea surface properties accessible by radar from above and the resulting air intrusion measured by upward looking echosounders from below was conducted at a fixed research platform in the open sea. These long-term simultaneous measurements under essentially all sea states have indeed quantified that indirect monitoring of air intrusion by radar is possible. This means nothing less than the chance to reach the final goal of satellite remote sensing global distributions of air intrusion into the sea, instantaneous as well as long term. The realization would provide a further substantial input to climate models. Acousticians have found out that the effect of air entrainment will already occur at wind conditions far below that of a storm. Air bubbles, forced to oscillate at the instant of their genesis, thus radiating part of their kinetic energy as sound for a brief moment, (Sect. 3.6.2, 3.6.3) are the dominating source of surface noise in the sea, not the splash as originally

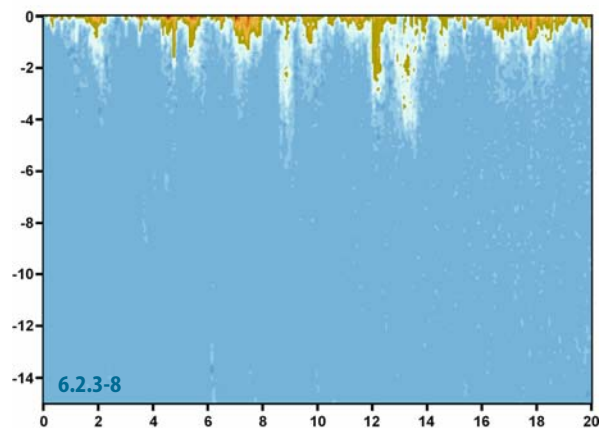
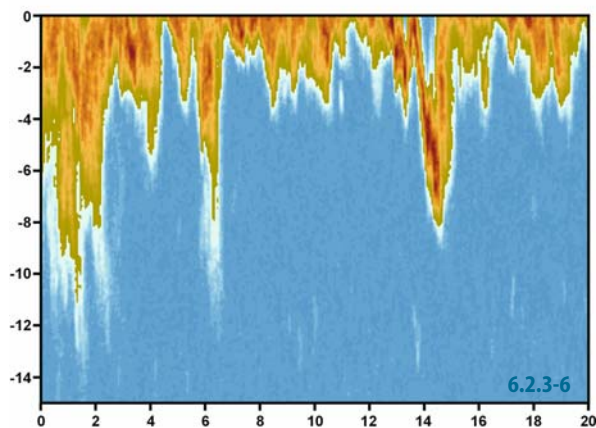
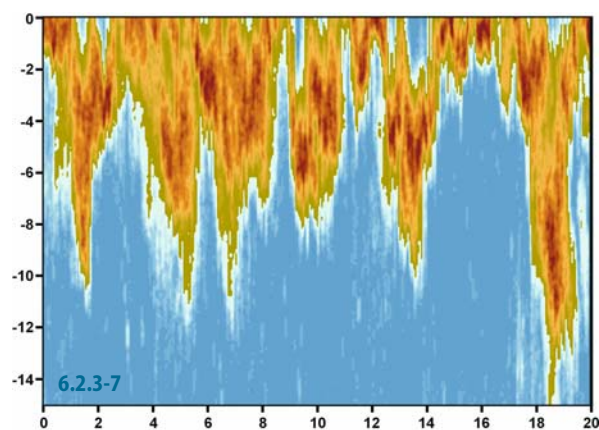
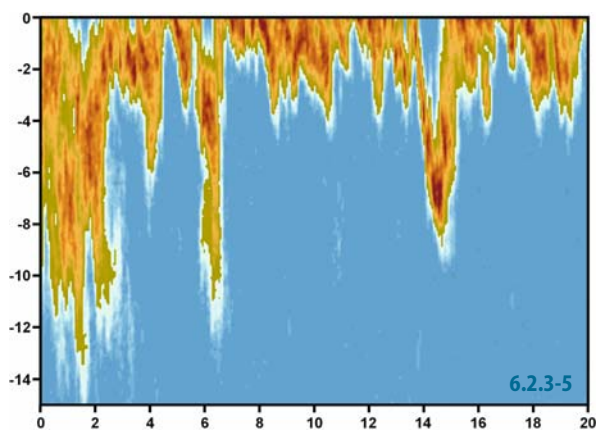


Image 6.2.3-5.

Frequency effect. The Images 6.2.3-5 and 6.2.3-6 are taken at the same time and wind speed of 22 m s^{-1} . The comparison demonstrates the effect of the bubble size filter of the echosounder when the frequency of 50 kHz of this image is bisected to 25 kHz of the next image. ■

Image 6.2.3-6.

Half the frequency. Since the bubble size at resonance is the reverse of the frequency, we are dealing with twice the bubble diameter now. However the depth reached by the larger bubbles which contain 8 times the air volume is not dramatically reduced: only about ten percent. Further, the shape of the partial clouds remains similar. These images also demonstrate that the cloud depths are in fact denoting a random process: though the average wind speed is less than the value of Image 6.2.3-4, the instantaneous penetration can be deeper. ■

Image 6.2.3-7.

Effect of strongly different frequencies. This image and the next are taken at a wind speed of 23 m s^{-1} . The image pair compares the depths of intrusion of partial bubble clouds when the bubbles selected differ by 5 times the diameter. The acous-

tic filter frequencies applied are 50 kHz and 10 kHz respectively. In this image the bubbles resonating at 50 kHz reach down to 15 m with a real diameter of 0.21 mm and a virtual resonance blow-up to 10.6 mm. Here the ratio of maximum and minimum echo intensity is extreme: 2 800 times! ■

Image 6.2.3-8.

10 kHz instead of 50 kHz. When applying 10 kHz the resonance bubbles are about 1.1 mm in real diameter. This is more than 100 times the volume of the 50 kHz-bubbles. Their virtual blow-up achieves the proud diameter of 60 mm. Bubbles beyond 1 mm real diameter occur only rarely however, except immediately beneath the sea surface. The bulk of intruded air bubbles have real diameters between 0.2 and 0.1 mm according to long term empirical results at the research platform. The large bubbles of Image 6.2.3-8 obviously have a much shorter lifetime than those of Image 6.2.3-7 although both were measured at the same time. The maximum-minimum echo intensity ratio produced by the large 10 kHz bubbles is comparatively modest: only 20 times. It is further noticeable that the partial clouds of 50- and 10 kHz have no similarity of shape anymore, quite different to the 50- and 25 kHz clouds of the Images 6.2.3-5 and 6.2.3-6. ■

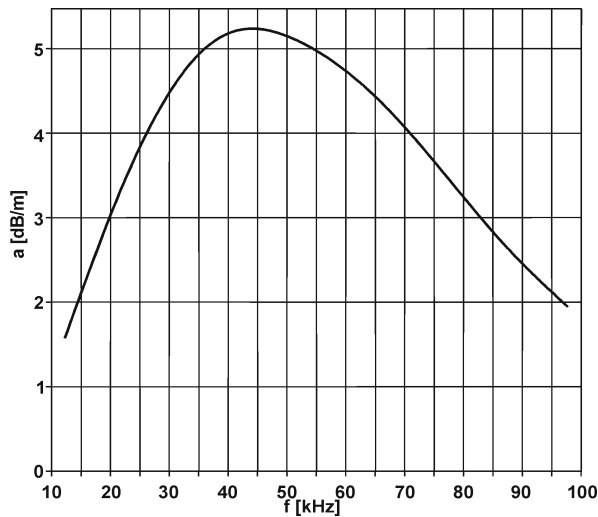


Image 6.2.3-9.

Sound absorption inside the bubble clouds. The acoustic spectrometry of the bubble size distribution by irradiating a bubble cloud from a distance is classical remote sensing. However, to provide data of the internal losses by sound absorption necessitates measuring inside the clouds. This was realized by a ladder of light frames hanging down from the research platform crane cantilever and kept vertical and fixed by weights. Each of the frames carried a sound source-receiver pair vis à vis with 2 m transmission path in between and the received signal amplitude indicating the absorption. The sea waves varied the instantaneous distance to the sea surface recorded by a pressure gauge. This set-up enabled measurements of the dependence of sound absorption on depth continuously. Actually, this type of measurement is not really an in-situ concept but a kind of miniature version of a one-way transmission path array of an ocean size tomography range (Sect. 6.1.3) where the signal travel time is the quantity to be measured. Here it is the signal amplitude. These one way transmissions don't provide sound images, but numbers. Thus the subsequent figures are only diagrams, though with fascinating information.

Image 6.2.3-9 represents an example of the long term average of sound absorption inside a bubble cloud at 2.5 m depth and 18 m wind speed or Beaufort 8 to explain the standard diagram of figure 10. The frequency axis covers the interval between about 10 kHz and 100 kHz. Obviously the absorption is strongest around 45 kHz. Thus the cloud must preferably be populated by bubbles of 0.15 mm diameter. The absorption of 5 dB per meter means a sound *penetration depth* reference of only 2 m (Sect. 2.1). We recall the definition of this reference distance: Only 10% or -10 dB of the initial sound intensity is left over at the end of the *penetration depth*. This abstract number becomes interesting by comparison. In sea water free of bubbles this reference range of 10% remaining is 1 km at 50 kHz instead of 2 m in the bubble cloud. Even the range superiority

of sound in sea water over light is replaced by a pronounced inferiority under these conditions: Very clear tropical waters achieve a light *penetration depth* of about 100 m (Sect. 2.1). ■

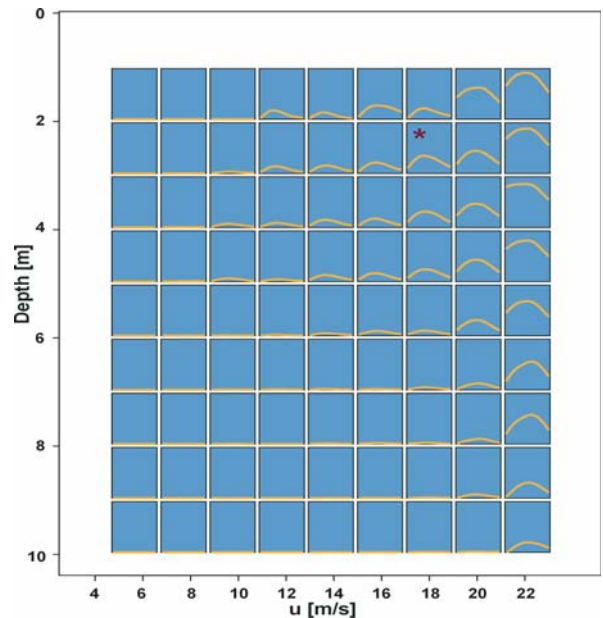


Image 6.2.3-10.

General results of sound absorption inside of air bubble clouds. Each of the mini diagrams shows the frequency dependence of the sound absorption for other wind speeds and depths in the same way as depicted in the previous Image 6.2.3-9, which is indicated by an asterisk in Image 6.2.3-10. We see the expected strong increase of absorption by increasing wind speed confirmed. Surprising however is that the frequency of maximum absorption is nearly independent of depth and wind speed: *the bubble size of about 0.1 mm remains the most frequent under all environmental circumstances*, as long as the hydrodynamic water properties remain.

Finally we can state that significant absorption at a depth of more than 10 m is only to be expected beyond 20 m s^{-1} or more than Beaufort 8. At and beyond such *Strong Gales* the noise from the sea surface around 50 kHz which is generated by the breaking wave process (Sect. 3.6.2) is nearly totally absorbed. This frequency regime is used by smaller marine mammals for their echo sounding clicks which they then can hear in “selective silence” when they are swimming deep enough, despite even a hurricane blowing. We should mention that already much less dramatic wind conditions may cause strong reductions of the surveillance range of *horizontal sonars* in shallow water because their paths of sound propagation touch the sea surface often and under low grazing angles. In other words: the paths through the bubble layers are long, quite different from vertical or slant angle echo sounding for sea floor imaging. ■

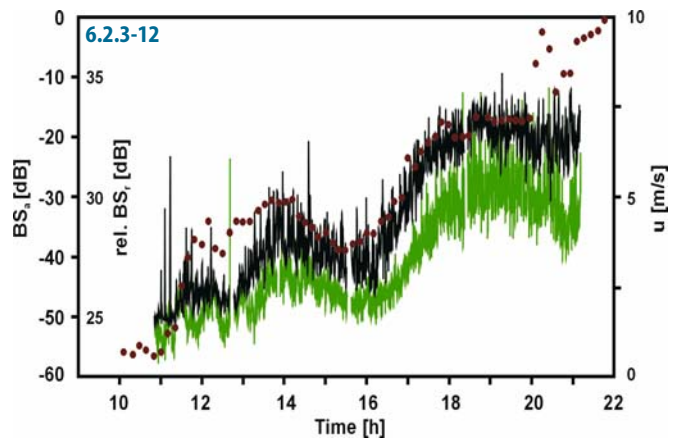
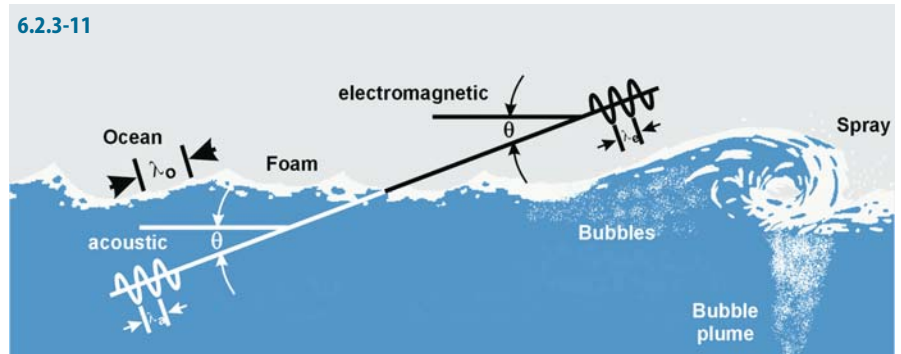
Images 6.2.3-11, 12.

Radar and sonar backscatter from the sea surface. Air intrusion by breaking sea waves is an important element of air-sea interaction in general and thus of weather and climate through the transport of oxygen and carbon dioxide into the sea. Satellite radar can provide global mapping of sea surface features within a few days but cannot look beneath the surface where the intrusion by bubble clouds is manifest only by local sonar imaging. How far can both methods be combined to achieve short term global mapping of air-sea intrusion? In other words: can the radar echo formation be scaled to quantify the air intrusion? The answer is yes, though with potential caveats.

The key experiment were simultaneous measurements of radar and sonar backscatter from both sides of the sea surface which requires a fixed platform in the open sea, resistant to violent storm conditions. The research platform *Nordsee* was equipped for this campaign with a 5-GHz radar adjusted to irradiate the same sea surface spot as the 26-kHz sonar did from below under the same shallow grazing angle. Thus both “echosounders” received their backscatter signal at the same wavelength and were thus sensitive to the same roughness scale of the sea surface. The slant angle configuration provides scattering only, no specular reflection and corresponds to the geometry of sea surface sampling by radar satellites.

Image 6.2.3-11 shows the scheme of the sea surface where acoustics and electromagnetics met near the research platform *Nordsee*. Note that the grazing angle of the irradiation of both as well as the wavelength were the same.

Image 6.2.3-12 presents the results of a short time interval of simultaneous measurements where the wind raised from nearly dead calm to 10 m s^{-1} within only 10 minutes. This is Beaufort 5, a *Fresh Breeze*. Obviously, the continuous records of the sonar backscatter (black) and the radar backscatter (green) are essentially identical in shape (the scale offset is applied to avoid the complete overlap). The wind (red dots) causing the sea roughness goes the same way ahead except at the beginning and at the end, indicating delay between wind increase and sea-wave response. Since the wind was measured at



a height of 47 m above the sea surface, the near surface wind profile will not follow immediately under such non stationary wind conditions. Further measurements, not shown here provide evidence that the radar backscatter increases continuously with increasing wind though with less steep slope when spray weakens the radar signal. This behavior is different from the sonar backscatter. As shown in the previous images, the increasing sound absorption caused by the growing, denser bubble clouds reduces the backscatter more and more. Nevertheless, since the radar signal increase remains, the determination of the bubble features from the radar echo remains unambiguously. The verification by real satellite radar records vis à vis local acoustic measurements is pending however. The research platform *Nordsee* was dismantled. ■

assumed. This noise mechanism works down to very modest wind speeds. Accordingly, the onset of wave breaking, which happens at about 6 m s^{-1} average wind-speed, is already accompanied by air entrainment during local wind squalls where the entrainment depths depend on how far turbulent mixing has developed.

The reason for the high sensitivity of echosounders to detect even small gas bubbles in the sea is twofold: Any gas filled object will produce a stronger echo than any other material due to the maximum mismatch possible of the acoustic impedance (Sect. 3.4.1). In this context the second reason is even more important: gas filled bubbles, either as swim bladders of fish (Sect. 6.3.1) or as entrained

and dispersed air or as hydrocarbon gas bubbles ascending from the sea floor (Sect. 6.2.1, 6.2.2), are the only natural resonators in the sea at frequencies within reach of acoustic devices (Sect. 3.4.3). Bubbles enlarge their acoustic size by a factor of several hundred when artificially excited at resonance by a tunable sound source. It is therefore possible to filter out the fraction of bubbles of the respective diameter by measuring the collective echo at that frequency. The relation of bubble radius and resonance frequency is simply inverse: 0.03 mm radius corresponds to 100 kHz; 0.3 mm therefore to 10 kHz at sea surface pressure. In fact, the bulk of the bubbles of an intruded cloud appears to occur within that bubble size regime, in other words, within the frequency range of most echosounders, whereas ascending methane bubbles can be much larger, and swim bladders reach an order of centimeters in size.

Unlike the acoustic determination of the population of fish shoals, which works beyond the resonance of the swim bladders the measurement of bubble contents of an intrusion cloud may be considered a kind of genuine spectrometry, comparable to optics, where the spectrum of a radiating or absorbing substance enables determination of the chemical constituents.

At its resonance frequency, the real geometric radius of any bubble is of a factor of about 500 smaller than the wavelength. In other words: without its resonance blow up, any bubble would be deep in the regime of echo reducing diffraction at this frequency (Sect. 3.4.4). Thus the resonance effect provides both: sufficiently strong echoes despite the very small size and the remote determination of size.

Scattering theory states that an ideal impedance-zero-sphere remains nearly at its geometrical size and does not shrink acoustically when insonified by low frequency sound. This impedance presumption however is more or less violated in reality.

On the other hand, the advantage of echo enhancing resonance blow up is counterbalanced greatly, so to speak, by mutual shadowing of the acoustically enlarged bubbles. In any event bubble densities in a cloud are orders of magnitude larger than fish populations within dense shoals (Sect. 6.3.1). Further: the amount of echo blow up by bubble resonance depends on actual loss conditions in the bubble cloud. All these facts have to be considered to estimate realistic quantities of entrained air from the data of acoustic spectrometry.

6.3

Submarine Fauna

There is no genuine imaging of the ocean fauna by sound. The *acoustic wavelength handicap* (Sect. 3.3.4) set by physics excludes an image resolution that can compete with imaging by light, in other words: The price of the peerless submarine range of sound is the resolution handicap; the price of the peerless resolution of light in the sea is the range handicap. Moreover, sound imaging is colorless (Sect. 3.4.3). All the colors of the sound images shown in this book have been added by computer and signify other quantities, such as the depth scale of shaded reliefs or the scattering intensity of echoes. What is then the justification for dealing with the ocean fauna in this context? There are three reasons and there is no substitute for sound in any of them.

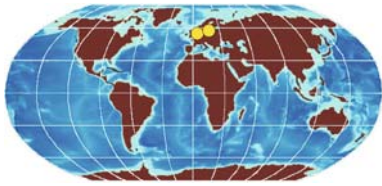
- *First:* fishery, as one of the most important food economies, relies on echosounding though sound cannot discriminate species directly but it is indispensable for the location of fish and biomass acquisition (Sect. 6.3.1).
- *Second:* the habitat of species and their survival is often decisively dependent on features of currents (Sect. 5.3.4) and of the sea floor morphology (Sect. 5.5.3) and mineralogy. This applies to fauna as well as to flora. Acoustic imaging covers the two former features directly and the latter at least indirectly.
- *Third:* the identification of the voices of marine mammals and fish and the noise of crustacea is a specialty of underwater acoustics. The inventory of the living natural acoustic environment made by passive listening includes tracking of motion of mammals; the discrimination of the nature of their radiated sound (Sect. 6.3.3) relates their social communication to us as well as their hunting for prey by echosounding.

It should be mentioned that marine flora can also be visualized by sound when their chlorophyll product oxygen is temporarily attached to the leaves before the gas bubbles ascend or are dissolved. Without gaseous attachment or enclosures the leaves are acoustically transparent and thus withdrawn from

a sound image. The only example shown is taken near the Greek Isle of Korfu and is remarkable because the species *Posidonia* is assumed to grow only in the Mediterranean Sea and considered important for the ecosystem.

6.3.1

Estimation of Fish Stocks by Echosounding



The development of the population of fish species within their regional habitats, their variability and migration,

growth or decrease is of major interest both for reasons of economy and ecology. The monitoring of territorial waters in this respect is taking place under the supervision of the ministries concerned and is coordinated with the States sharing fishery interests regarding the waters involved. The regular surveys are conducted and evaluated by institutes of fishery research in order to derive recommendations, particularly regarding fishing quotas and to observe and investigate extraordinary or alarming phenomena. The quota shall maintain economic fishing; the balance of costs and profit. Extermination of fish species by extensive but still economic fishing is considered impossible by experts.

To achieve instantaneous estimates of the fish population inventories, which vary by migration within the large areas of occurrence, the European Union regulations require surveys by an international fleet during defined periods of time. Up to six vessels from several nations are involved at sea during these regular synoptic surveys, coordinated by the *International Council for the Exploration of the Sea (ICES)*, Copenhagen.

The research and survey vessels of these institutions are usually equipped with echosounders similar in kind to those which are used by fishing vessels. The scientific sounders are calibrated however to conclude fish population densities from their standardized survey courses, called *transects*. According to this unified survey strategy, the institutions provide quantified data sets for national and international comparison. Research is taking place to im-

prove the degree of automation in the discrimination of fish species and further features of interest for protection.

What are the acoustic characteristics of a single fish and of entire fish shoals and what do their sound images look like? Are there specific features for species discrimination?

In fact, every fish reveals its presence by a remarkably strong echo, which is essentially generated only by its swim bladder. The fish tissue, as well as its bones, contribute only little to the echoformation because their acoustic impedance, the product of density and sound speed (Sect. 3.4.1) is close to the water value. Recalling the fundamental acoustic relations of echoformation, an object of any kind is invisible for echosounders if its impedance does not differ from the environment. The air-filled swim bladder however represents one of the strongest acoustic contrasts possible in water. An undisturbed air-water interface is the best existing reflector, because of the outstanding impedance mismatch of about 5 000. This means a degree of reflection of 99.98%, much better than any optical mirror. Due to some damping by the fish tissue the reflectivity of the bladder is slightly less than the value under ideal conditions.

The size of the swim bladder is also decisive for the echo strength, representing the *target strength* in the sonar equation (s. Appendix). When excited at resonance, its “acoustic size” appears blown up by orders of magnitude (Sect. 6.2.3). This well known effect would – in principle – provide the possibility of acoustic spectrometry of the bladder size and thus of the entire fish: to achieve equilibrium buoyancy there is a nearly fixed ratio of both volumes. However, since the resonance frequency of a typical swim bladder is in the range of only some hundred Hertz, the echosounder transducers would need to be extremely voluminous and expensive, and even more so if they had to be tuned over a frequency decade and more by combining echosounders of adjacent frequency bands.

In reality, echosounders for monitoring the actual populations of fish species are operated in the region of some tens of kilohertz for two reasons. First, these frequencies are beyond resonance of even the smallest swim bladders. Otherwise their acoustic blow-up would simulate very large individuals. Second, these frequencies correspond to sound wavelengths which are no larger than the swim bladders. If not, the echoes would

be drastically reduced by sound diffraction (Sect. 3.4.4). Under both these conditions the target strength is a direct measure of the actual cross-section of the bladder and therefore approximately of the fish-biomass.

Fortunately another problem of echoreduction does not occur: i.e. the mutual acoustic shadowing of fish within a shoal. If we consider tropical waters, where fish shoals may look like dense clouds, it might be surprising to note that there are only 2–3 individuals per cubic meter within a fish shoal typical of European shelf waters. Thus all the fish will contribute their individual and unimpaired echo when their joint biomass is determined by echo integration. This is independent of the capability of the echosounder to resolve the individual fish of a swarm.

However, there could be a fundamental cause for a systematic measuring error: fish are normally shy of ship noise, the effect of the propulsion noise being much stronger than that of the echosounder. Part of the images shown here have therefore been made by mounting the echosounder in a streamlined body towed 40 m away from the vessel outside its wake.

Regarding recognition of the fish species, this is impossible by acoustic identification of body shape, simply because the resolution of the echosounder is far below such a requirement, due to reasons of physics. Already the *depth resolution* which is usually better than the *angular or cross resolution* (Sect. 4.3.4) is insufficient to discriminate any specific characteristics.

We recall: Both dimensions of resolution together form the so-called *resolution cell* within which all structure clues are averaged out. Thus the counting of individual fish is only possible when a resolution cell does not contain more than a single fish. This is a rare case, even in European shelf waters. The resolution cell of a mono-beam echosounder is simply a circular section of a spherical shell, like an orange peel, cut out by the beam cone. The *thickness* of the peel represents the length of the signal pulse and corresponds to the range or *depth resolution* respectively. The *diameter* of the peel section, which grows of course along the diverging beam cone with increasing depth, represents the *cross resolution*. At a great distance, which means a large radius of the spherical sound wave with the echosounder as the center, the shell becomes nearly flat. Its diameter is also called *pixel size*, when the resolution of the sea floor relief is described.

A thin resolution cell, in other words a greater depth resolution, requires a short signal. This means a correspondingly large bandwidth which is more easily achieved at high frequencies. (Sect. 4.1.5). This choice is limited however by the increasing sound absorption. In practice, the resolvable depth interval is limited to some decimeters when continental shelf waters typically of 200 m are to be covered. Already at 100 m depth and a beam cone of 7° the resolution cell amounts to about 30 m³.

The echosounder is calibrated by a standard target, which is a small sphere showing the same well-known target strength from all sides and doesn't need mechanical adjustment. To verify the acoustic data they are compared with the trawl catches conducted during the echosounding trials. This evaluation is complicated and requires special experience to attribute the fish of a particular species to their echoes, considering size and weight according to their maturity.

This attribution for "calibration" works best when only one species predominates in the catch or a second or third species is present, which can be identified on the sound image when they occupy a characteristic depth regime or form typical swarms. Up to now, it is human expertise that is indispensable when doing this demanding work of division into species because the clues to the behavior of a fish species vary from place to place and from time to time resulting in a multi-parameter dependence. On the other hand detailed knowledge of this variability enables the optimization of sites and time to select essentially mono-species conditions for the most reliable results.

In general, carefully conducted acoustic transects by experienced scientists are considered more reliable for the achievement of quantitative data than trawl catches, which are thus subject to correction by the simultaneous acoustic reference data.

The sound image examples presented hereafter stem from the Baltic, North Sea and North Atlantic and deal nearly exclusively with herring, sprat and redfish, the prevailing species of the areas and time of the year chosen. Their specific peculiarities are described in the image captions. The surveys were conducted by the Federal Research Centre for Fisheries, Hamburg.

6.3.1.1 Monitoring of Fish Stocks, South Eastern North Sea. Vertical Echosounder Images

The sound images shown were acquired in June/July of 2002 during the regular annual survey of the North Sea herring conducted by 5 European countries. The south east of the North Sea surveyed by the *German Federal Research Board for Fisheries* is considered a kind of nursery of the North Sea herring, the prevailing fish species of the area. Coastal waters lodge also large populations

of sprat. The acoustic trials were mainly conducted during daylight because both species then use to gather in dense swarms and can be easily distinguished from plankton clouds because of their stronger echoes. Other fish species practically don't exist in the surveyed area. Thus the identification and segmentation of herring and sprat is relatively reliable, though not by their echo signature only. Herrings often form remarkably large and concentrated swarms up to 20 m height and several tens of meters length. A single swarm may contain about a million herrings with more than 10 tons of biomass.

Image 6.3.1.1-1. The depiction of herring swarms is – as usual – strongly compressed in the horizontal for quick inspection of long runs: The distance of the vertical lines is half a nautical mile (925 m) whereas the water depth, the distance between both broad stripes is 45 m in this case. The wavy contour of the bottom stripe indicates the pitch motion of the vessel.

Coordination: Planning Group for Herring Surveys (ICES)
Time of survey: 21.06.–02.07. 2002; area:
south of 57° N, east of 3° E – coastline
Research vessel: *FFS Walther Herwig III*, BLE
Echosounder: *Simrad*, EK 500; 38 kHz,
beamwidth 7.5° (split-beam), pulse: 1 ms
Image © and information: Eberhard Goetze,
IFF, Hamburg, Germany ■

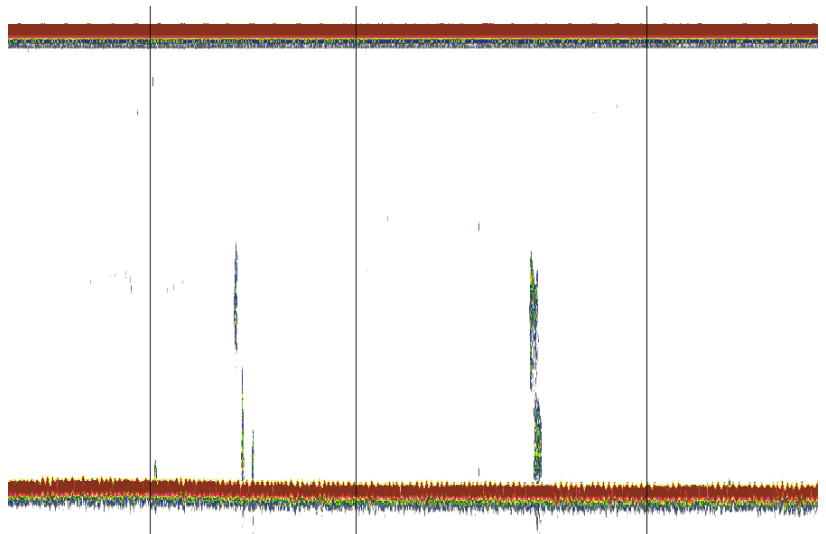
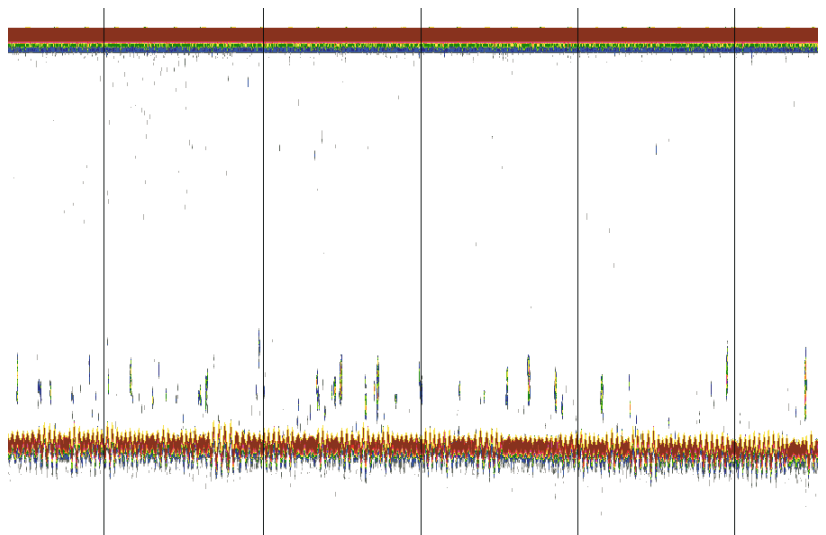


Image 6.3.1.1-2. Though the size of sprat swarms is much smaller, typically a few meters only, there are also herring swarms of similar size. According to the necessary comparison with fishery results, herring and sprat contribute nearly equal shares of this record. The echograms represent areas of high fish population densities. No fish was found in many other sites of the region surveyed.

Image documentation; same as for Image 6.3.1.1-1 ■



6.3.1.2 Monitoring of Fish Stocks, Baltic Sea. Vertical Echosounder Images

The annual survey of the prevailing fish species in the major basins of the *Baltic Sea* by German and Russian research vessels is part of the *Global Ocean Ecosystem Dynamics* program. Sprat as a natural

enemy of cod by eating their spawn and larvae may critically diminish cod stocks, depending on the regional and temporal coincidence of both species. To survey the unadulterated regional stocks of sprat, springtime is advantageous because only this species is then concentrated in the deep basins of the Baltic whereas Herring prefers the shallow coastal areas at that time of the year.

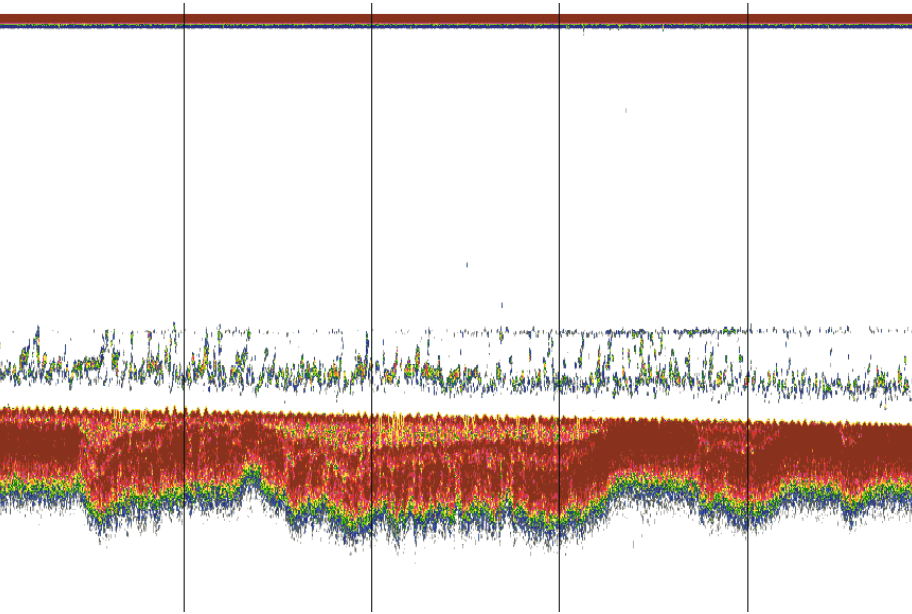


Image 6.3.1.2-1.

Sprat likes to stay in layers at 60 to 80 m depth, just below the varying horizon where the salinity and thus the water density is increasing steeply, a rare phenomenon elsewhere but typical of the central Baltic. This so called *halocline* is marked as a thin line in the echograms by plankton, resting on this density step.

Project: Global Ocean Ecosystem Dynamics (GLOBEC)

Time of survey: 05.–21.05. 2002; area: Baltic Sea 54–57° N, 12–19° E

Research vessel:

FFS Walther Herwig III, BLE

Echosounder: Simrad, EK 500; 38 kHz, beamwidth 7.5° (split-beam), pulse: 1 ms

Image © and information:

Eberhard Goetze, IFF ■

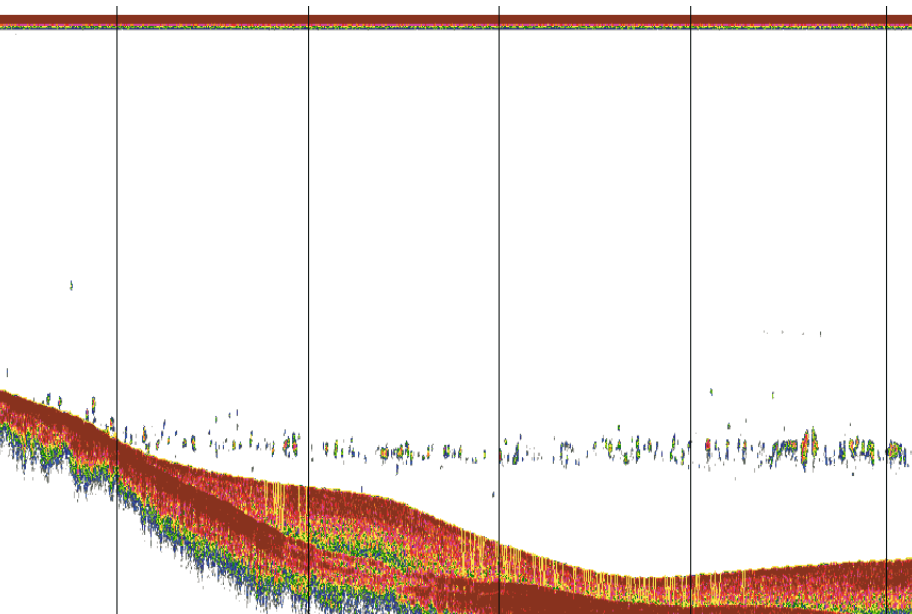


Image 6.3.1.2-2.

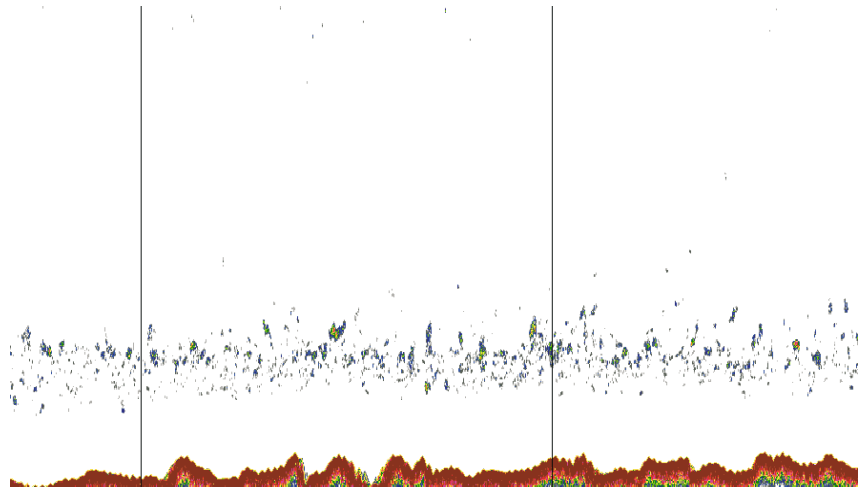
Due to the notorious deficiency of oxygen near the bottom the fish stay away from it. Where the sea floor ascends beyond the halocline the fish disappear.

Image documentation; same as for Image 6.3.1.2-1 ■

Image 6.3.1.2-3.

Since the salinity of the Baltic Sea decreases with the distance from the western entrance to the North Sea, the sprat behaves different in the *Gotland Basin*. The halocline is less sharp and the water density transition more gradual. Thus the sprat is found within a less defined depth range. Though the average fish population density is small in the examples shown, the estimated number of sprats within the entire survey area amounts to about 70 billion individuals.

Image documentation; same as for Image 6.3.1.2-1 ■



6.3.1.3 Monitoring of Fish Stocks in Shallow Waters, Western Baltic Sea. Mono-Beam Echosounder Images

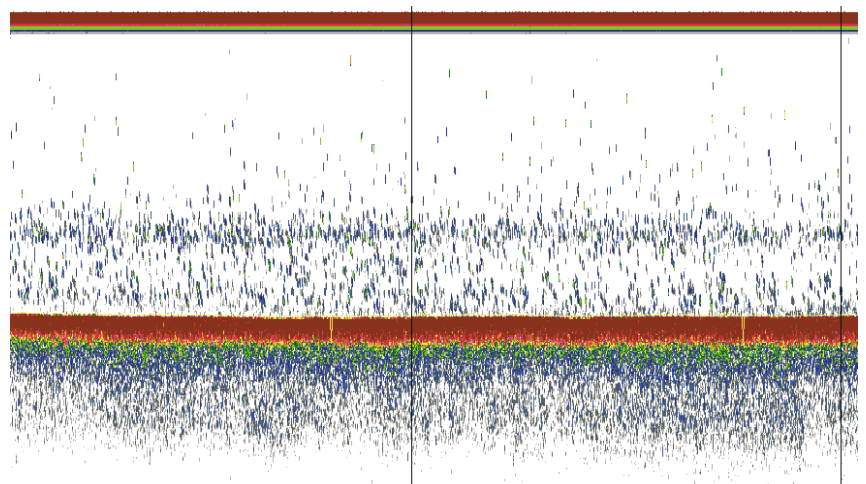
The international echo survey of the entire *Baltic Sea* which commenced in 1978 is being conducted under the coordination of ICES during October every year since. Surveying the shallow western Baltic up to 15° E, which is performed by Germany requires a vessel with particularly small draught. The cutter *FFK Solea*, BLE, drawing only 3.5 m is equipped with an echosounder system towed 100 m behind the vessel with lateral displacement of 30 m to prevent the fish from being scared away by the noise of the ship. This precaution is required due to the small clearance between ship and fish.

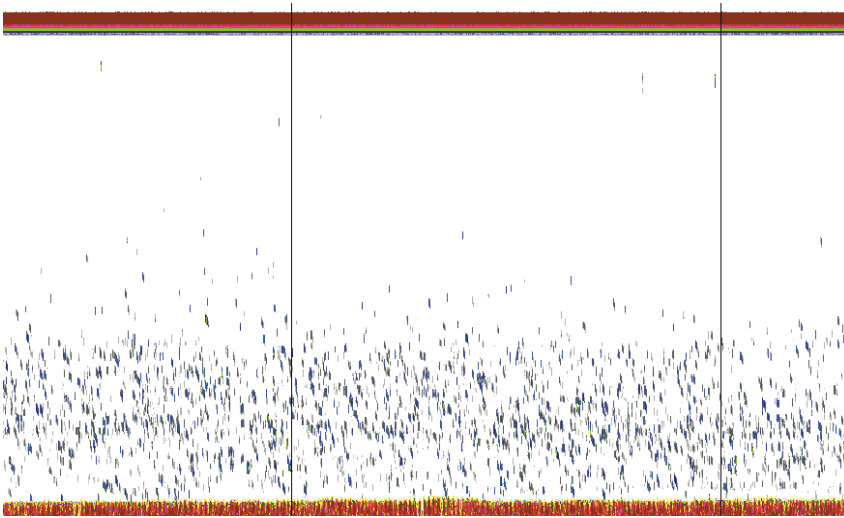
Further, since the fish are gathering in swarms too close to the bottom for echo sounding them during the day, the survey has to be conducted at night-time. This strategy considers the light dependent behavior of herring and sprat, the prevailing fish species of that area. Their swarm formation requires contact of sight. During dawn, the swarms thus ascent towards more light and eventually dissolve into individual fish with sufficient distance from the floor to be clearly resolved and “counted” by the echosounder according to the integrated echo strength. Since the classification into species by swarm features is then not possible anymore, the relevant information is derived from fishery results which are necessary anyway to yield the distribution of size and other biological parameters such as weight, age, sex, and maturity.

Image 6.3.1.3-1.

Part of the fish stays at a preferred depth of 8 m above the sea floor.

Coordination of survey: ICES, Copenhagen
Time of survey: 28.09.–18.10. 2001;
area: Baltic Sea, west of 15° E
Survey vessel: *FFK Solea*, BLE
Echosounder: Simrad, 38–26M;
38 kHz, beamwidth: $8.5 \times 14^\circ$, pulse length: 1 ms
Image © and information: Eberhard Goetze, IFF, Hamburg, Germany ■



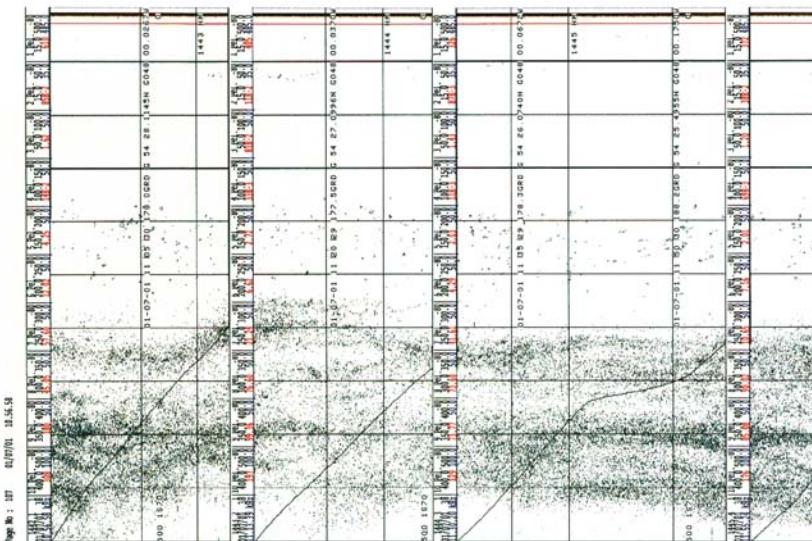
**Image 6.3.1.3-2.**

The record reveals no other preference of spatial distribution than the vicinity to the floor. The fish density in both cases is between 0.4 and 0.7 individuals per m^2 water column.

Image documentation; same as for Image 6.3.1.3-1 ■

6.3.1.4 Monitoring of Fish Stocks, North Atlantic, Irminger Basin. Vertical Echosounder Images

The standard records of this section with accompanying time- and depth scales, supplemented by biomass integration during the time intervals provide overviews for easy comparison during the trials.

**Image 6.3.1.4-1.**

The most suspicious echo formations, looking like dense clouds between 300 and 500 m depth, are *not* the targets of interest of the fish stock monitoring program, dealing with *redfish* in this case. The predominating cloud echoes are produced by the so-called *Deep Scattering Layer (DSL)*, which consists mainly of plankton. The fish echoes are visible only above the DSL, mainly within depth intervals of about 150–300 m. The upper boundary of the DSL is also the limit for detecting the fish: The strongly scattering DSL masks potential fish occurrence inside and below.

The survey was conducted in June/July when the *redfish* don't form schools in the *Irminger Basin*. Instead, the record shows the rare case of single, acoustically dis-

cernible fish echoes, typical of *redfish* in this area. The information on the total biomass of fish of different sizes is provided as usual by echo integration. However, since the echoes don't yield direct clues to the fish species, additional information is thus indispensable. This is obtained from accompanying fishery results. Trawling is also necessary to retrieve fish from inside the DSL where the *redfish* is masked, to correct the data.

Nevertheless the most accurate and representative reference data regarding fishing quota decisions are derived from acoustic measurements, not from fishery. The fish population density determined by this survey section in comparison to the results of the entire survey did not indicate the *redfish* to be endangered at this time and in this area.

Image documentation; same as for Image 6.3.1.4-2 ■

Image 6.3.1.4-2.

The echo record shows compact schools of *herring* and *sprat*. These schools are typical formations during daytime in the *North Sea*. Schools of herring normally resolve during night-time when the fish are catching their prey to eat, and are then distributed more at random. However, they don't do so during summer at that latitude, when the nights are not really dark. Schools of herring reveal their presence by so called *pole formations*: relatively short schools with conspicuous vertical extension and strong echoes, coming from a high population density. Sprat behave differently: they form stripes of smaller schools within a less wide depth interval.

The classification of the fish species derived from sound images of school features works best in bright daylight. Nevertheless, the discrimination is often difficult and requires additional information from trawls, which are needed anyway to acquire reference data of the distribution of fish size and further characteristics.

Survey coordination: ICES, Copenhagen; survey: WH229; time of survey: June/July 2001

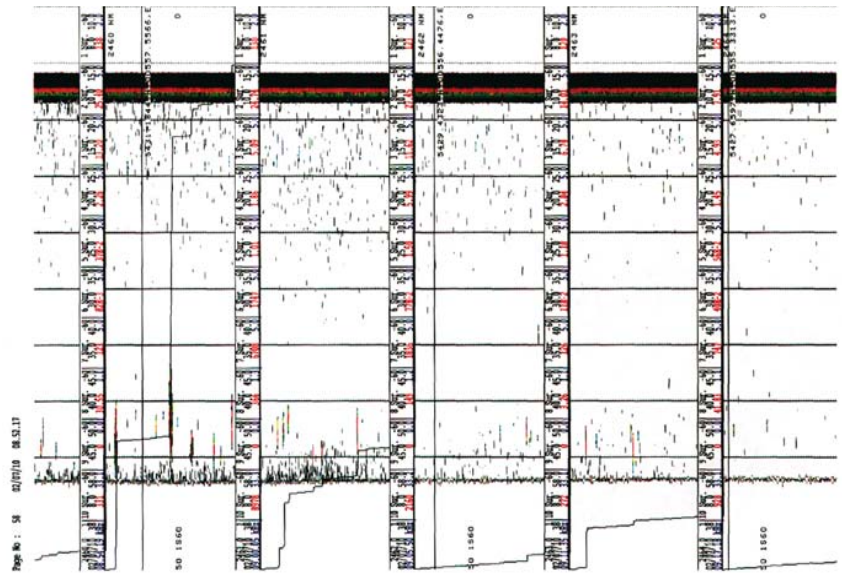
Area: Irminger Sea ,North Atlantic

Survey vessel: *FRV Walther Herwig III*, BLE

Echosounder: Simrad, EK 500; 38 kHz, beamwidth 7° (split-beam), pulse: 1 ms

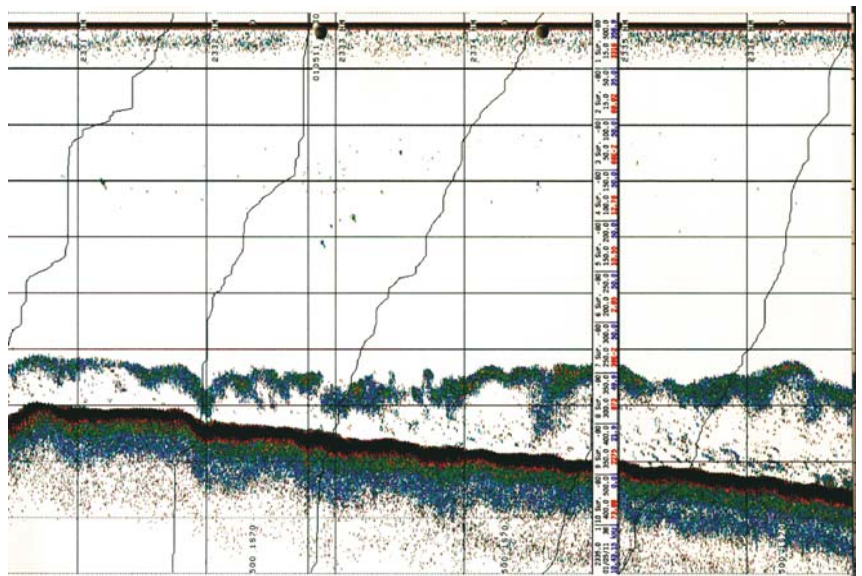
Depth scale: 50 m per division; width of the records: Image 6.3.1.4-1: 7.5 km; Images 6.3.1.4-2 and 6.3.1.4-3: 11 km; sloping curves: echo integration within the respective section showing the horizontal variability

Image © and information: Eckhard Bethke, IFF ■

**Image 6.3.1.4-3.**

This record taken near Bodø is typical of echograms of the *Blue Whiting* off the coast of northern Norway. These fish form huge stripe-like schools at a depth of 300–500 m. This species is more concentrated during daytime but the *Blue Whiting* maintain the characteristic stripe formation similarly at night.

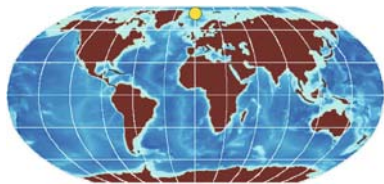
Image documentation; same as for Image 6.3.1.4-2 ■



6.3.2

6.3.2

Finding Food in the Deep Sea



The only strategies of deep-sea animals living in total darkness to find food from a distance are to rely

either on their acoustic sensor or on chemoreceptors, in other words: the taste or scent of the water which has been in contact with the prey. Crustaceans like the scavenging carcass eating amphipods can apply nothing other than their chemosensors, except of course the mechanical contact of nutriment sinking down. The success of these scavengers in finding their prey with purpose in due time is a decisive mechanism of the deep-sea food chain and thus of the global carbon cycle. Up to recently, scientific investigations of their behavior were conducted by photographic or video graphic observations of the scavengers approaching baits laid out close to the deep-sea camera and spotlight. From experience only very few square meters of the sea floor can be covered optically thus not providing relevant data of the distance of reaction and time of approach.

For the first time a high resolution scanning sonar system was applied to acquire the complete history of the reaction of the amphipods and their approach from a distance up to 50 m in a horizontal plane. These first quantitative observations were conducted at a Polar region inside the Fram Strait at 2500 m depth on the sea floor. For this purpose a so called *autonomous lander* was let down from the research vessel into the water column, sinking freely to the ground. The lander is a tripod equipped with a baited time-lapse camera with flash-light and a scanning sonar system adapted to autonomous operation. An acoustic Doppler current profiler (Sect. 4.5.2), glass spheres and ballast to adjust the buoyancy were also part of the equipment as well as the power supply and the computer system controlling the experiment and storing the data.

The lander exposed the bait which was dead fish fixed to the support at the bottom. The scanning sonar of 675 kHz and 2.7° beamwidth to reduce the bottom backscattering was set to rotate once per 5 min-

utes with 400 pulses transmitted. The lander stood on the bottom slightly inclined by about 4° evident from partial sea floor backscattering with-in the panorama. The echosounder had a range resolution of 0.2 m and could detect individual scavengers larger than 2 cm. After preliminary tests with few resolvable individuals approaching, the full panorama was subdivided into 8 sectors and 10 rings of 5 m width for data record and evaluation, providing the time history of the integrated backscattering strength of 60 segments together with time-lapse camera-observations of the bait neighborhood. The region contaminated by backscattering from the sea floor was excluded from the evaluation. The camera verified that essentially a single species was present. At the end of each experiment the lander was acoustically called back to the surface, leaving ballast behind.

This principle of evaluation by eechointegration has similarities with the quantitative determination of fish biomass (Sect. 6.3.1). Due to similar conditions of acoustic resolution, it was no longer possible to count individuals as soon as the first groups of numerous amphipods appeared inside the scanned circle. The amphipods apparently swam in compact groups upstream in narrow sectors following the scent trace until arrival at the bait, and left it after saturation, drifting passively back with the bottom current. Since the net average speed of approaching organisms was only seven centimeters per second the 50 m distance was crossed during 4 hours by a maximum of over 600 individuals only an hour later. This was followed by a stationary population along the upstream “runway” because of the balance of arrival and departure. Since part of the smell of the bait was resistant even after the complete consumption, the slowly decaying approach remained for a while. The comparison of the instantaneous numbers of amphipods counted on the photographs with the biomass measured in the two “runway” sectors confirmed the measuring concept as a quantitative acoustic method.

The measurement, although it has also been a first test of the feasibility of this combined acoustic and optic acquisition, has also brought a better understanding of the determined response, the group behavior and effectiveness of these scavengers, specialists in the removal of organic debris descending into the deep arctic waters.

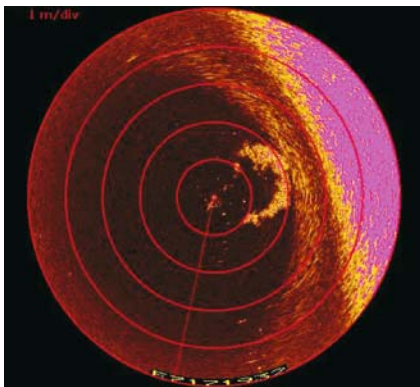


Image 6.3.2-1

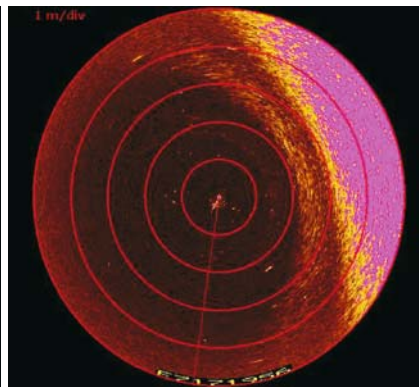


Image 6.3.2-2

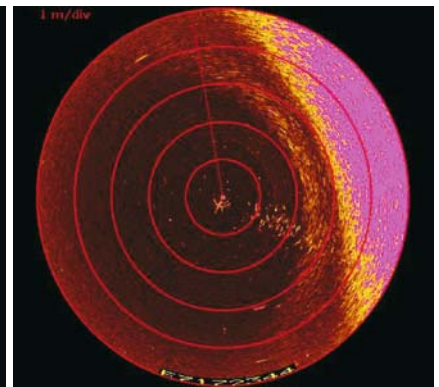


Image 6.3.2-3

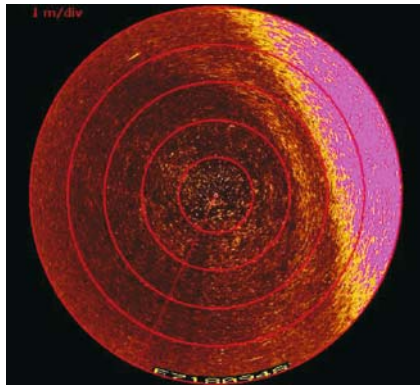


Image 6.3.2-4

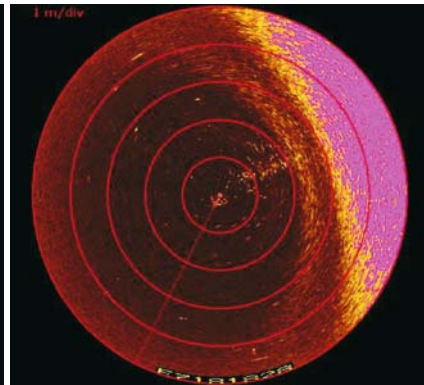


Image 6.3.2-5

Image 6.3.2-1 to 6.3.2-5. Time series of 5 images: Groups of carcass eating scavengers approach a bait in the Arctic. Panorama scanning echosounder images. The five panorama-sonar depictions of 50 m radius scaled by the five rings show the same, nearly horizontal circular slice of the sea volume near the bottom of the *Arctic Fram Strait* at 2500 m depth. The self-contained tripod *Lander*, carrying the instrumentation was incidentally inclined by 4° when landing on an irregular sea floor location, thus irradiating part of the bottom within the corresponding sectors of the panorama. The dark brown area is the free measurement field, which is acoustically uncontaminated by sea floor backscattering indicated in violet. The diffuse light brown arc between the center and the violet area of contamination is attributed to a so-called side lobe of the echosounder.

Image 6.3.2-1, taken directly after the arrival of the lander shows a suspension cloud released through the bottom contact, drifting away with the flow. In *Image 6.3.2-2*, taken a quarter of an hour later, the field of vision of the panorama sonar was free of scattering particles, representing the “zero condition with no targets present”. Four hours after landing, the *Image 6.3.2-3* documents the maximum concentration of the animals in sector 6, approaching upstream, following the scent trace from the bait at the center. Ten hours afterwards, the screen of *Image 6.3.2-4* is temporarily covered by a random distribution of particles, presumably plankton. 23 h after landing, *Image 6.3.2-5* shows that the “animal runway” with maximum traffic density has turned into sector 7, upstream of the actual direction of flow, now offset by about 50°.

Project: Evidence for long-range chemoreceptive tracking of food odor in deep-sea scavengers by scanning sonar data, Deep Sea Project Group, AWI Bremerhaven; time of experiment: summer 2001

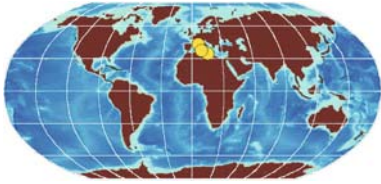
Position of measurement: Fram Strait, 78°50' N, 02°42' E

Research vessel: *RV Polarstern*, Germany

Echosounder: Simrad MS1000; frequency: 675 kHz, beamwidth: 2.7°

Image ©: Sergey Mu yakshin, IAP, RAS, Nizhny Novgorod, Russian Federation; Katrin Premke, AWI, Bremerhaven, Germany ■

6.3.3 6.3.3 Voice Sonograms of Marine Mammals



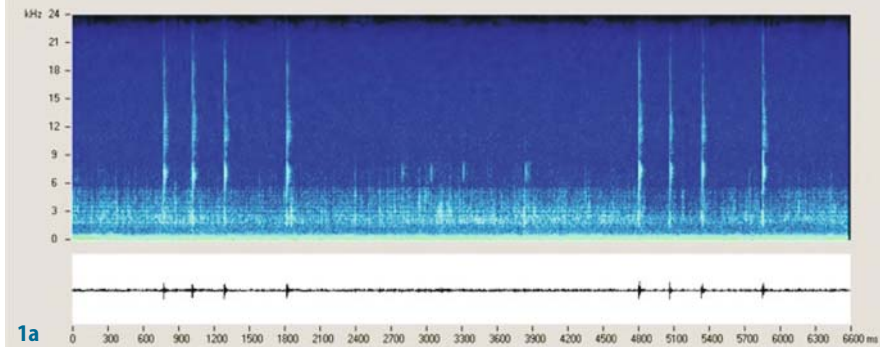
Toothed whales or *Odontocetes* are the unequaled and admired artists of echosounding in the sea, the central

subject of this book. Four species which inhabit the Mediterranean, the area of a major research project on bioacoustics (s. below) have been selected for presentation with examples of both types of their sound signals: short clicks for echolocation and various whistles and melodies for social communication. Both types are made visible as *sonogram* images and audible as sound tracks on the CD, attached to the book. All of the four species chosen, the *Sperm Whale*, the *Striped Dolphin*, the *Pilot Whale* and the *Bottlenose Dolphin* reside in large numbers in the Mediterranean Sea and in many other areas of warm and temperate waters of the oceans.

Sonograms depict the characteristics of a voice or other sounds which vary with time. They represent the time series of the instantaneous sound spectrum, in other words: the varying frequency components with their respective intensity which are present in a complex sound. Such sonograms are used in particular for forensic purposes to identify human voices but they are applied in many other sound analysis tasks such as investigation of musical instruments and monitoring of mechanical wear or faults in machinery and even undersea earthquakes and volcano eruptions (Sect. 3.2.2). Biologists use sonograms of the voices of animals, in this context of marine mammals, to study their behavior under various environmental and social conditions. In marine bioacoustics sonograms are also used to identify vocalizing species even if they are out of sight. Thus passive acoustic techniques can be applied for environmental studies which require the monitoring of the presence of certain species and their census. Acoustic identification of species is a key tool for the implementation of acoustic risk mitigation policies aimed at reducing the impact of high power sound



1



1a

Images 6.3.3-1, 1a, 1b, 2, 2a, 2b.

The Sperm Whale, famous as *Moby Dick* in Melville's novel, is the largest toothed whale (*Odontocetes*). Sperm whales are among the deepest diving marine mammals (*cetaceans*), reaching more than 1 000 m depth and are found in all oceans of the world. The large blunt head makes up to 1/3 of the total body length and more than 1/3 of its mass. It contains a very special organ named spermaceti whose functions are not completely understood, though related to sound production. A single blowhole is located forward on the left side of the head, projecting the blow forward (Image 6.3.3-1) rather than straight up as in other whales. This is because the right respiratory channel has evolved as a pneumatic system for producing sound. The broad flukes measure up to 5 m from tip to tip (Image 6.3.3-2). Males reach lengths of up to 18 m and weigh up to 40 tons. Females are much smaller with 11 m and 14 tons maximum. A Sperm

Whale consumes about one ton of food each day, mainly medium-sized deep water squid. The lower jaw contains 18–25 teeth of 3–8 inches in length on each side.

Sperm Whales radiate impulsive sounds, named clicks, used for echolocation and communication. The clicks, composed of a main pulse followed by a few pulses reflected in the spermaceti (sonogram Image 6.3.3-1a), are of 5–20 milliseconds in duration. While diving, the clicks are produced at nearly constant rates of 0.5–2 clicks per second (Image 6.3.3-1b, including echoes from the ships hull) or at increasing rates (Image 6.3.3-2a) for echolocating objects at short range. The sound of the slower sequences coined the popular name: *carpenter fish*. While at the surface and in complex social contexts, clicks are produced at highly variable rates. The signal sequence of Image 6.3.3-2b is called a trumpet signal. Though similar in periodicity these signals are not clicks for prey location but for communication. The attached CD contains the corresponding sound tracks.

Site: Aeolian Sea north of Sicily, Mediterranean;

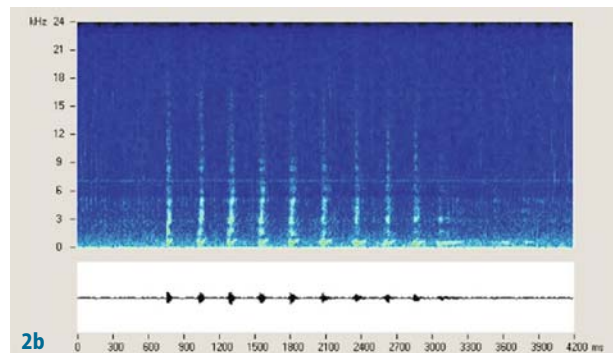
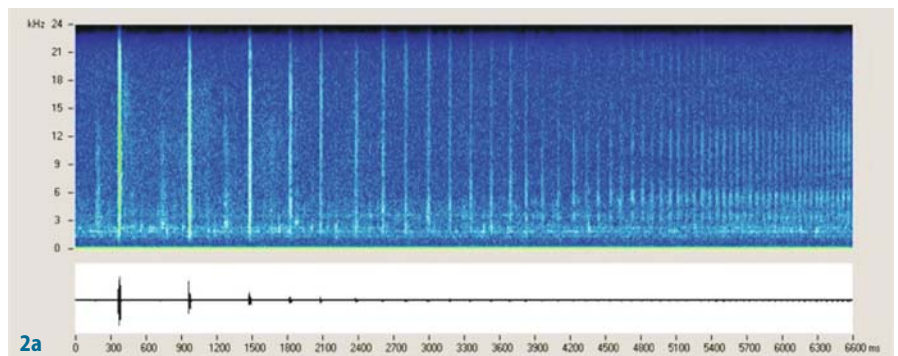
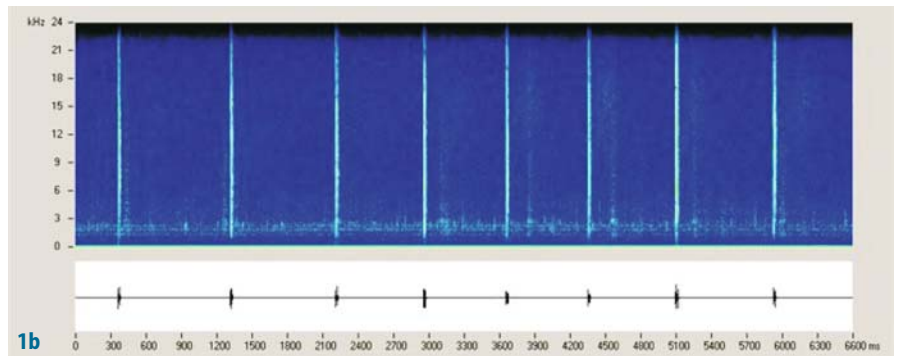
Year of survey: 2003

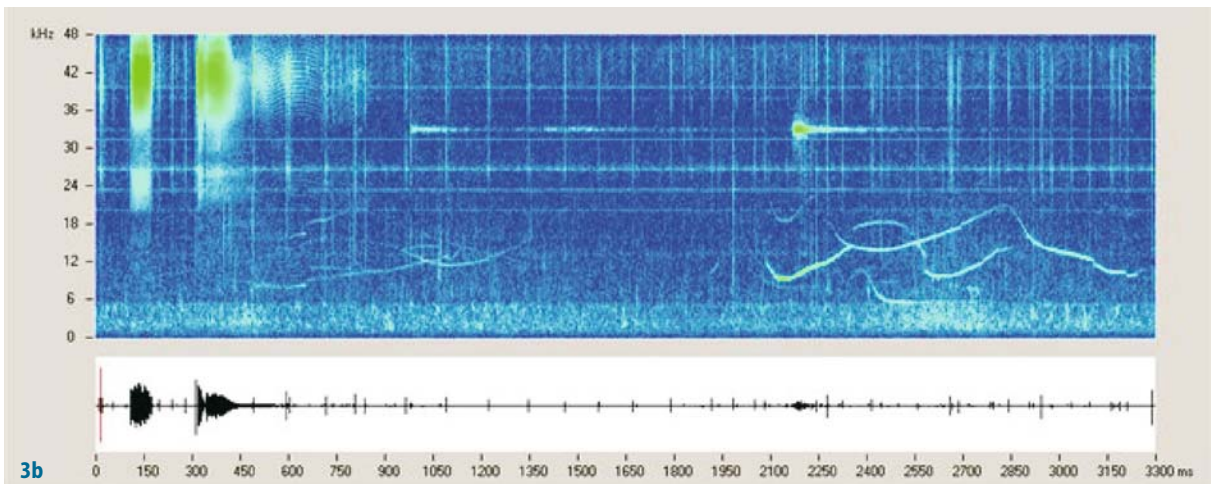
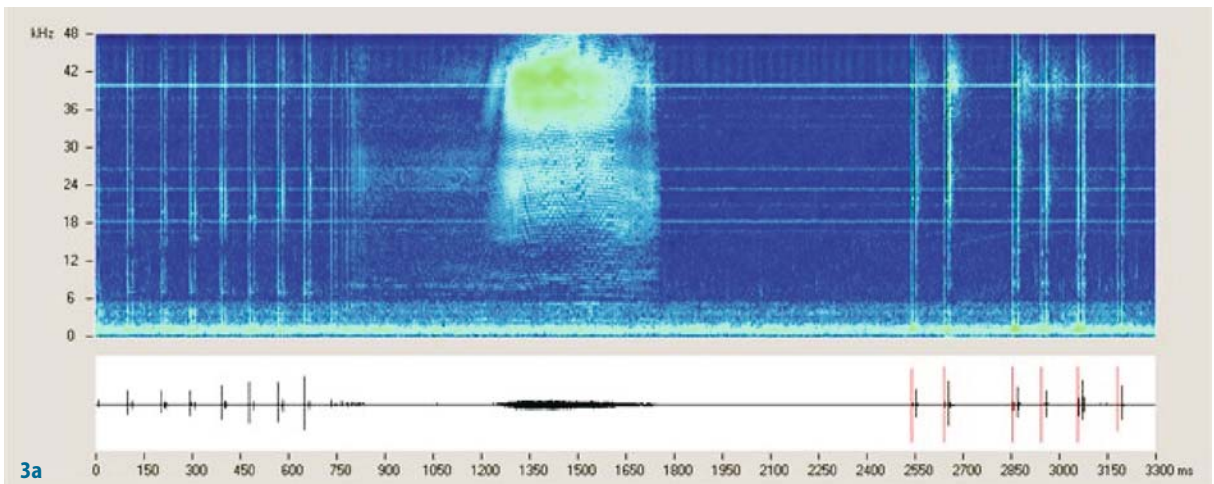
Recording device: custom made wideband towed array of hydrophones, 45 kHz and 50/300 kHz bandwidth respectively, low self noise, omnidirectional. The sonograms are derived from individual hydrophones in the array

Alternative device: Sonobuoy with single hydrophone at ca. 100 m depth, 5.5 kHz bandwidth

Sonograms: higher spectral intensities are coded brighter and further indicated by the separate figure of the total intensity record below the sonogram

Photographs and sonograms ©: Gianni Pavan, Centro Interdisciplinare di Bioacustica e Ricerche Ambientali, University of Pavia, Italy ■





◀ Images 6.3.3-3, 3a, 3b.

The Striped Dolphin. This cetacean species of marine mammals look like a prototype of streamlined elegance with their slender body, narrow head and long, dark beak (Image 6.3.3-3). The striped dolphins are famous for their acrobatics, including somersaults and tail spins, reaching to heights of 7 m above the surface. A lateral stripe and spinal blaze distinguish the striped dolphin from other white-bellied oceanic dolphins, but these markings vary between individuals and probably geographically. Mature striped dolphins range in length from 180 cm to 250 cm and from 110 to 160 kg in weight.

The striped dolphin inhabits warm temperate and tropical pelagic waters around the world and is also the most common species in the western and central Mediterranean. It is usually found close to the shore only in places where the water is deep. Striped dolphins tend to favor waters with large seasonal changes in surface temperature and thermocline depth, and with seasonal upwelling. When foraging, striped dolphins may dive 5–10 minutes to depths of 200 m. The animals feed mainly on small, mid-water fish and squid, about 3 kg per day; their mouth is well equipped with 80 to more than 100 small teeth. Striped dolphins are fast swimmers; when traveling at speed, up to a third of the members of a school of typically more than a hundred will be above the surface at any one time. In the Mediterranean, they have been estimated to swim at an average speed of about 8 to 14 km per hour alongside a boat. The main hazards threatening striped dolphins are pollution and incidental capture in pelagic drift gill nets. Contaminants have been extensively studied in this species, more than in any other cetacean.

Like all cetacean species of marine mammals, striped dolphins apply sound signals to locate prey and to communicate. Typical signals are depicted as their instantaneous spectrum as it varies with time, which is named *sonogram* (Images 6.3.3-3a, 6.3.3-3b). The short impulse signals or clicks for echo location cover a spectrum up to far into the ultrasonic regime with the main sound energy between 30–100 kHz. Pulse bursts reach 900 clicks per second. In comparison to the much larger sperm whale, the acoustics of the striped dolphin is shifted to essentially higher signal frequencies and pulse repetition rates. The example shown in the middle of the sonogram 3a is conspicuous because it is not tonal with distinct and varying pitch but a kind of broadband hiss though with spectral line structure. This block is in fact a burst of pulses or a so called *buzz*, consisting of a very fast series of very narrow broadband pulses. The purpose of these bursts is not clear as yet. The maximum source level is about 170 dB related to 1 μ Pa at 1 m distance, which corresponds to 0.7 Watt of acoustic power. Whistles for communication range between 6 to about 20 kHz in the Image 6.3.3-3b, which shows also clicks and buzzes. The whistles stem obvi-

ously from several animals: the spectral lines show cross over. These whistles are not only tonal, they are a pure tone with a single frequency and a melody-like pitch variation without a repetitive pattern, a kind of musical improvisation, as it were.

Site: Ligurian Sea, north of Corsica, Mediterranean; year of survey: 2003

Recording device: custom made wideband towed array of hydrophones, 45 kHz and 50/300 kHz bandwidth respectively, low self noise, omnidirectional. The sonograms are derived from individual hydrophones in the array

Sonograms: higher spectral intensities are coded brighter and indicated further by the separate figure of the total intensity record below the sonograms

Photographs and sonograms ©: Gianni Pavan, Centro Interdisciplinare di Bioacustica e Ricerche Ambientali, University of Pavia, Italy ■

sources such as military and civilian sonars and air-guns for geophysical exploration.

The signal generation of toothed whales is not yet fully understood. Recent studies have shown that whistles and clicks are produced by the same organ that is located in the upper respiratory channel, namely by the *phonic lips*, that are located in the nasal sac region just behind the rounded region of a dolphin's forehead named *melon*. For the same species it is evident that clicks and whistles can be produced independently at the same time in the two branches of the respiratory channels, before they converge in the unique blow hole that is typical of *Odontocetes*.

Dolphins produce clicks in trains. Each click lasts a fraction of a millisecond with a peak acoustic pressure level that can reach more than 170 dB rel. 1 μ Pa at 1 m source distance; the repetition rate can be slow for long-range detection up to a few hundreds of meters or can accelerate up to hundreds of clicks per second when locating targets at close range. The click trains pass through the rounded region of a dolphin's forehead named *melon* which consists of fat tissue and has a lower sound speed than water. The melon thus acts as an acoustical lens which focuses the signals forward into the water in front of the animal like an acoustic searchlight. This beam-forming does not physically achieve the pencil beams of technical facilities but considering the capability of the brain to correct the distortions of the eye lens it appears probable that the factual directionality of the

Images 6.3.3-4, 4a.

The Pilot Whale. This toothed whale or cetacean species is a member of the dolphin family and is second only to the killer whale in size. Pilot whales are found in both the northern and southern hemispheres, in tropical and temperate waters throughout the world. The long finned variety tends to prefer colder waters than the short finned whales. There is some regional overlap between the two varieties, but they remain segregated. There are likely to be almost a million long-finned pilot whales and at least 200 000 short-finned pilot whales worldwide. The species is easily trained and renowned for its intelligence, which equals that of the bottlenose dolphin (Image 6.3.3-5). The all black pilot whale has a rounded head with a very slight beak. Its prominent and strongly curved dorsal fin is located on the forward part of its back (Image 6.3.3-4). Males grow up to 6 m and weigh up to 3 tons; the smaller females reach nearly 5 m and 1.5 tons.

The animals feed primarily on squid, up to 15 kg per day, but also on octopus, cuttlefish, herring and other small fish when squid is not available. This dolphin species has only 40 to 48 teeth, used for grasping, compared to more than 100 teeth in many other dolphin species. The pilot whale is extremely social, living in groups up to several hundred individuals and their calves. Humans have taken advantage of the social nature of pilot whales. *Drive fisheries*, where groups of this whale species are herded to the beach for slaughter, have taken place on several northern sites. The whales have been used in great numbers for meat, bone, fertilizer, and oil. Pilot whales are displayed in many aquariums and zoos.

The sonogram of Image 6.3.3-4a shows examples of communication signals, reminiscent of a melody with increasing and subsequent decreasing tonal pitch. Particularly conspicuous are the tonal harmonics which are pronounced mainly in the phase of decreasing pitch. The bulk of the sound energy appears within the regime of 1–6 kHz in this example. The sonogram should be compared with the audio signal presented

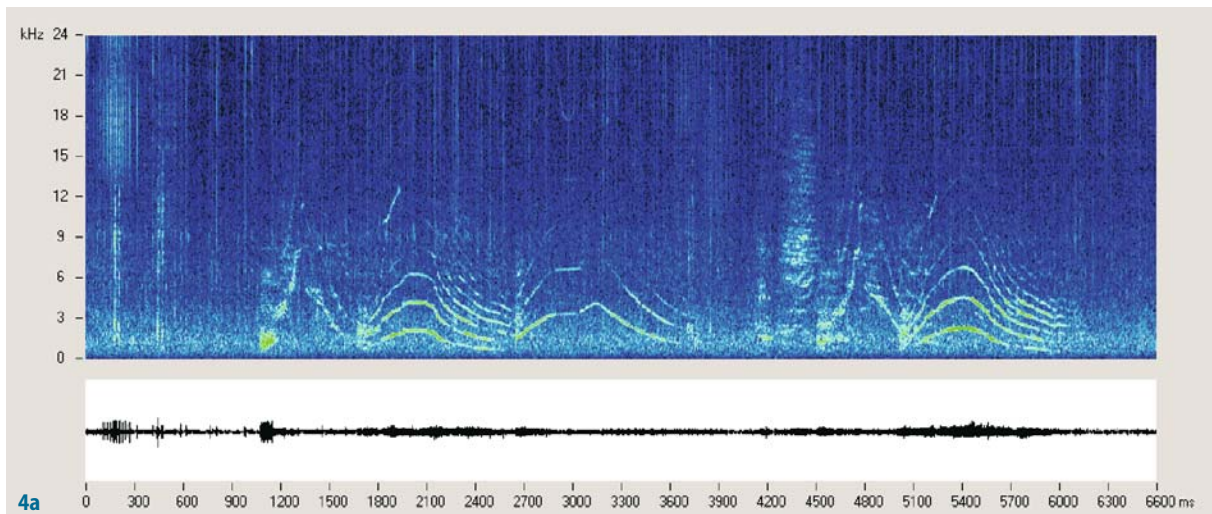


on the attached CD. Closer inspection reveals also broadband sections with less pronounced pitch prior to the melody. Note that the background is full of dense clicks of lower level which come mostly from other whales at a distance. Since many animals swim together in herds, their communication melodies as well as their echo location clicks and bursts are often hardly separable, in particular by non directional hydrophones.

Site: Ligurian Sea, north of Corsica, Mediterranean; year of survey: 2003

Recording device: custom made wideband towed array of hydrophones, 45 kHz and 50/300 kHz bandwidth respectively, low self noise, omnidirectional. The sonograms are derived from individual hydrophones in the array
Sonograms: higher spectral intensities are coded brighter and indicated further by the separate figure of the total intensity record below the sonograms. The estimated distance of the singing pilot whale in the sonogram was within one nautical mile

Photograph and sonogram ©: Gianni Pavan, Centro Interdisciplinare di Bioacustica e Ricerche Ambientali, University of Pavia, Italy ■

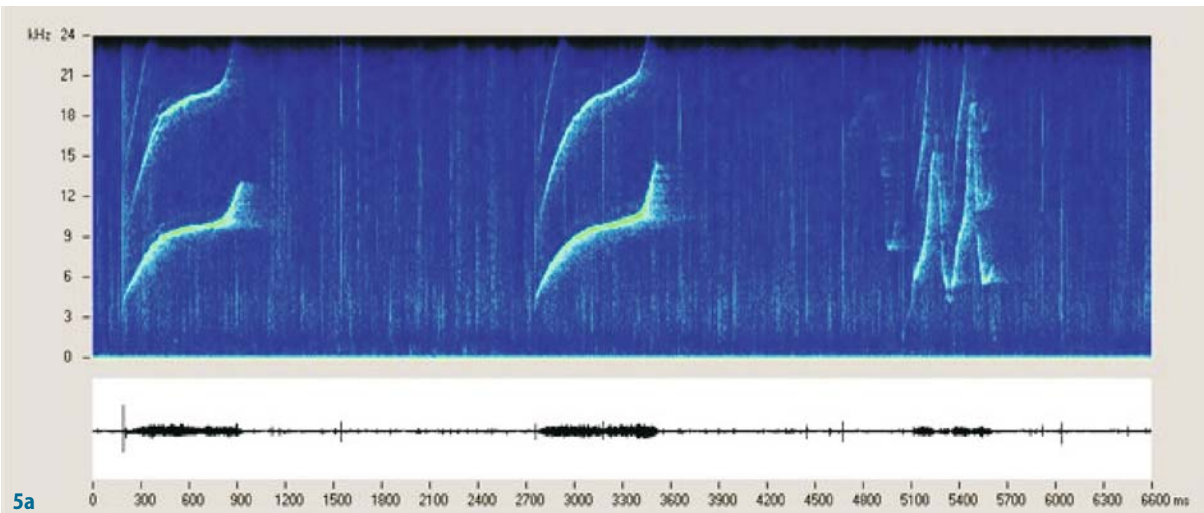




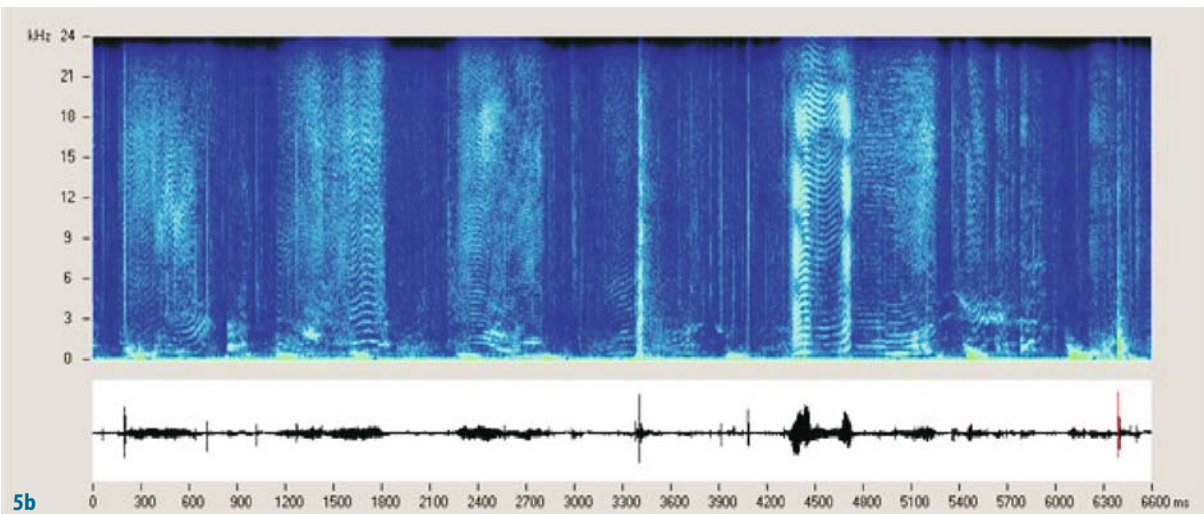
5

Images 6.3.3-5, 5a, 5b.

The Bottlenose Dolphin. The Bottlenose Dolphins are small toothed whales, at most 3½ m long, then weighing about 600 kg. The animals inhabiting the Mediterranean are smaller: 2.5 to 3 m. Bottlenose Dolphins have stream-lined bodies, a rounded head with a long, beaklike snout, a tall, sickle-shaped dorsal fin and broad, slightly pointed flippers (Image 6.3.3-5). This dolphin species live in small groups called pods of up to 12 individuals. Often, many pods group together to form congregations of hundreds of dolphins. Like all toothed whales, Bottlenose Dolphins live in warm to temperate waters near the coast though in different areas during breeding and giving birth. They hunt for fish and squid mostly at the surface of the water, thereby using their many pairs of sharp, pointed teeth for grasping, not for chewing. Dolphins can dive down to more than 300 m and can jump up to 6 m ▶



5a



5b

◀ out of the water. They need to breathe about every 2 minutes, but can hold their breath for several minutes. Their blow is a single, explosive cloud through the blowhole near the top of the head. Dolphins are very fast swimmers; they like to surf using the bow wave in front of a ship. Their natural predators are sharks; the main hazard is unintentional fishing; at present, Bottlenose Dolphins which belong to the most intelligent mammals are not yet considered as endangered species.

Image 6.3.3-5a shows the sonogram of characteristic whistles with two distinct frequencies at the distance of an octave, a non-linear increase of pitch within 2/3 of a second and a sudden break-off. Only the keynote remains completely within the human audible range. The third whistle with two increasing and decreasing phases of pitch is also a double tone. The selected example is only one of a variety of different melodies used by this species. The acoustic background is full of echolocation clicks of other individuals of the pod.

Image 6.3.3-5b looks entirely different from 6.3.3-5a and appears similar to the burst of pulses or a so called *buzz* of a Striped Dolphin (Image 6.3.3-3a). Though Image 6.3.3-5b consists also of very fast series of very narrow broadband pulses, the Bottlenose signal has still a tonal structure but with a large number of spectral lines, instead of only two of the preceding image. These lines are in parts conspicuously equidistant in frequency as the sonograms clearly reveals, in particular during the time interval 4.4–4.7 s. At the end of the series depicted, the buzz blocks appear to dissolve into separate narrow lines, now recognisable as bursts of broadband clicks. The extremely high repetition rate together with the extremely broadband signal which reaches down far below 1 kHz and at the same time far up into the ultrasonic regime is perhaps unique in the acoustic capability of animals in general.

6.3.4

Site: Ligurian Sea, north of Corsica, Mediterranean; year of survey: 2003

Recording device: custom made wideband towed array of hydrophones, 45 kHz and 50/300 kHz bandwidth respectively, low self noise, omnidirectional. The sonograms are derived from individual hydrophones in the array

Sonograms: higher spectral intensities are coded brighter and indicated further by the separate figure of the total intensity record below the sonograms. The estimated distance of the singing pilot whale in the sonogram was within one nautical mile

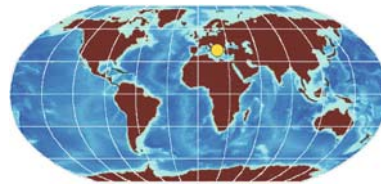
Photograph and sonograms ©: Gianni Pavan, Centro Interdisciplinare di Bioacustica e Ricerche Ambientali, University of Pavia, Italy ■

echolocation of a dolphin resolves small objects of prey at a close lateral distance. Due to the short click pulses the range resolution is correspondingly high anyway and the dolphins capability to discriminate different materials is peerless. How far dolphins compose the click train echoes to a moving 3D-image by signal processing in their brain is a pending question.

The other signal type, often called *whistle*, appears to serve in particular for self-identification vis a vis other individuals. A mother dolphin may whistle to her calf almost continuously for several days after giving birth. This acoustic imprinting helps the calf learn to identify its mother. Though repetitively suspected, researchers found no evidence of a dolphin language. The changes in the communication signal characteristics as indicators of potential hazards of varying environmental conditions including the acoustic environment are the subject of ongoing research.

Project: Bioacoustic Characterization of the Mediterranean Sea. Supported by the Office of Naval Research ONR, USA, in respect of the impact of underwater sounds on the marine environment, for conservation strategies and the definition and application of Acoustic Risk Mitigation Policies Project development in coordination with the NATO Undersea Research Centre (SOLMAR Project) under cooperation of the Italian Navy, the Centro Studi Cetacei (CSC), and the Centro Interdisciplinare di Bioacustica e Ricerche Ambientali (CIBRA), Università di Pavia, Italy ■

6.3.4 Example of Marine Flora Sound Imaging



The only example of a flora and exception in the fauna section shown as a sound image is a colony of *Posidonia oceanica* off the Greek Island of Korfu. *Posidonia* is a marine plant which forms meadows with flowers and is only found in the Mediterranean Sea. *Posidonia* plays an important role for the local ecosystems since other species find nutrients and housing in these meadows.

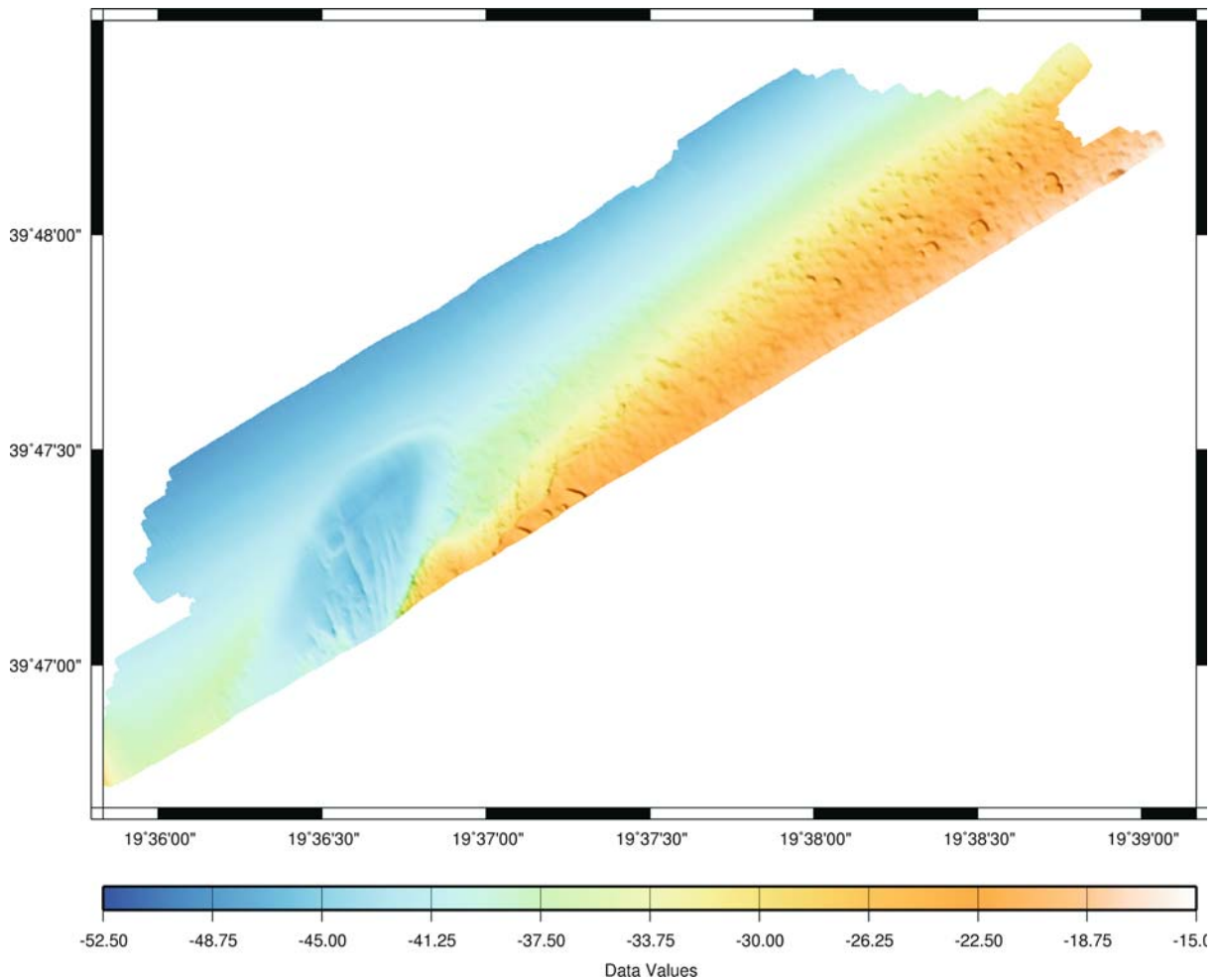


Image 6.3.4-1. Posidonia meadow. Multibeam image. The characteristic *Posidonia* formation reminiscent of a Swiss cheese with nearly circular holes is found on the upper slope of the sandy sea floor indicated in brown. Obviously the meadow ceases to exist below about 30 m water depth, where there is no longer sufficient sunlight. The “cheese holes” within the colony of several square kilometers imaged are natural interrupts of the roof of leaves, which reveals itself on the sound image because of the air-chambers inside the leaves. The “spaghetti-shaped” long thin air chambers are acoustically bright scatterers over a wide range of frequencies according to records between 5 kHz to 1 MHz. The findings have been verified by dives but the typical meadow texture is easily identifiable from sound images alone. Note that the deeper formation indicated in blue, southwest of the posidonia field, is an erosional fan. The meadow appears to protect the covered area from erosion similar to dune protection on land.

Survey vessel: *NRV Alliance*, Nato Undersea Research Centre; year of survey: 1999

Multibeam system: Simrad EM3000; frequency: 300 kHz, beamwidth: 1.5°, beam spacing: 0.9°

Image ©: Alex Trangeled, Nato Undersea Research Centre, La Spezia, Italy ■

Man-made Matter

7.1 Surveillance and Maintenance of Coastal Sea Lanes

7.2 Submarine Constructions

7.3 Underwater Archaeology

7.4 Close-Up Deep Water Imagery by Autonomous and Remotely Operated Underwater Vehicles (AUV and ROV)

Ocean acoustics dealing with man-made matter enables the various kinds of mapping and inventory taking, of surveillance and maintenance. The effort is indispensable for keeping the sea traffic fairways operational and safe. It is the prerequisite for planning and conducting of offshore constructions and it is the main tool for the exploration and exploitation of hydrocarbon resources. Since recently, archaeological research of historic relics in the sea, such as shipwrecks and sunken settlements and cities, utilizing high resolution sound imaging, has become of growing importance. Up to now, these activities have been mostly restricted to the shallow water areas of the continental shelves. But the development of deep diving autonomous or remotely controlled vehicles which provide close-up images of previously unknown quality has already demonstrated their peerless potential. Examples of their capability are also shown in this chapter.

7.1

7.1

Surveillance and Maintenance of Coastal Sea Lanes

Coastal sea lanes are endangered mainly by three kinds of hazards apart from risks of ship collision and emergent polluting cargo: *sediment shoals*, *wrecks* and *sea mines*. Safe shipping clearance can be at risk by the former two and wrecks can be hazardous also by polluting, poisonous or explosive cargo. Regular surveillance is a must and acoustic bathymetry is the tool of choice.

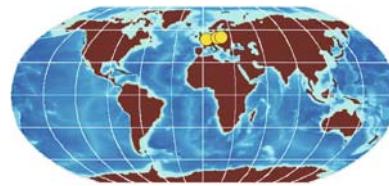
7.1.1

Regarding *safety clearance*, the highest protruding element of a wreck is the main factor in salvage decisions (Sect. 7.1.1, 7.1.4). Similarly dangerous by deteriorating safety clearance is sediment dune formation and -migration when generating shoals (Sect. 7.1.2, 7.1.3). *Hazardous material* such as mineral oil and chemicals as the load of sunken tankers and freighters but also dumped, lost, or misfired ammunition from times of war (Sect. 7.1.1) are subject of surveillance. Sound images sometimes provide only indirect clues to the type of hazard. In case of doubt, diver operations are inevitable. Sunken tankers,

non less hazardous in deep water, are a major challenge of reconnaissance and even more for salvage operations. Unmanned deep water reconnaissance strategy and performance is demonstrated in Sect. 7.4.1.

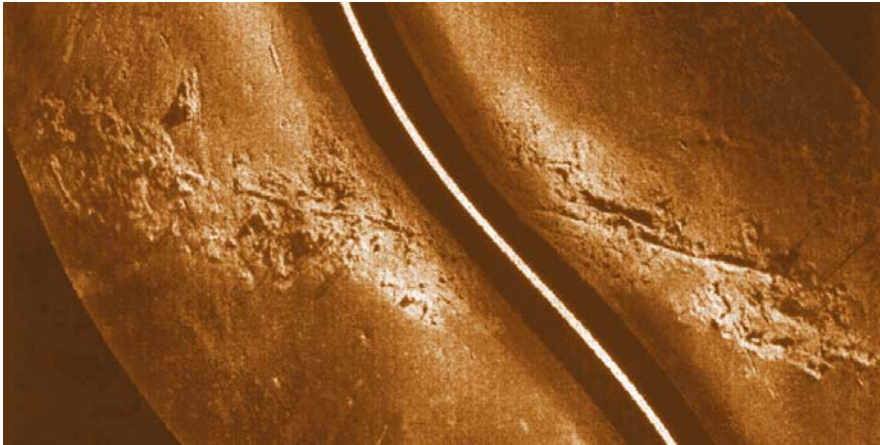
The most dangerous hazard are sea mines (Sect. 7.1.5), in particular in times of no war but of terrorism. These are the greatest technical challenge for reliable acoustic surveillance because they enable sabotage with a maximum of devastation by a minimum of effort, risk and costs.

7.1.1

Surveillance of Sea Lanes and Fairways

Surveillance of coastal shipping routes to maintain safe fairways is conducted by the Hydrographic and Naval Authorities. The surveillance program includes three main subjects:

Surveillance of coastal shipping routes to maintain safe fairways is conducted by the Hydrographic and Naval Authorities. The surveillance program includes three main subjects:

**Image 7.1.1-1.**

Wreck residues of the German passenger ship *Gneisenau* in the Baltic Sea. Sidescan image. The image reveals the traces of a wreck of about 200 m length imprinted in the sediment of the Baltic Sea. For only seven years this place in the Kadetrinne (Sect. 5.7.3) was the tomb of the German passenger ship *Gneisenau* of 18 000 tons. The ship was built in 1935 and sank due to a mine in 1943. Five years after the war the wreck at 30 m depth was scrapped by underwater breakdown. One year prior to the mine-disaster the *Gneisenau* was

the subject of conversion plans to be rebuilt as an aircraft carrier. The plan was canceled however as well as another one to use the *Gneisenau* as a troop-ship.

The path of the sidescan echosounder is indicated by the white line. The flanking black bands are the so-called blind stripes which correspond to the time needed by the signal to reach the bottom (Sect. 4.3). Due to this geometry the two sides of the image are correspondingly offset. The sea floor around the middle line of the wreck imprint is littered by scrap metal debris. Though the debris doesn't affect the safe fairway, much of it could hardly be discriminated from a mine when intentionally placed inside the field of wreck residues.

Project: Naval Surveillance of the Baltic Sea; year of survey: 2003

Sidescan sonar: Klein, type: 2000; frequency 500 kHz, beamwidth 0.5°, swath range 75 m on each side

Image ©: Walter Offenborn, Naval Office Rostock, Germany ■

- *safety clearance,*
- *hazardous material* and
- *inventories of features with camouflage potential to hide sea mines.*

To investigate or if necessary to eventually remove a wreck requires its detection, location and detailed knowledge of its state to guide divers for the preparation of the always expensive lifting procedure. This is the field of work of high resolution echosounding. Before applying fan echosounders to provide the most informative three-dimensional sound images, side-scan sounding with wider swath range is often used to survey a site of suspicion in order to save ship time.

Since *Safe Shipping Clearance* over wrecks is a matter of legal responsibility there is no room for any doubt.

The necessary resolution of multibeam echosounders, in other words the *pixel size* of the three dimensional sound image has often been debated controversially.

Box 7.1.1-1. Ferries sunk in the Baltic

In the space of a few years three ferries sank in the Baltic. In 1990 the ferry *Scandinavian Star*, going from Norway to Denmark, caught fire and around 150 people were killed. In 1993 the Polish ferry *Jan Hevelius* sank en route to Sweden, and 54 people died. The disaster was attributed to strong, adverse winds. In 1994 the Tallinn-Stockholm ferry *Estonia* capsized during a heavy storm. About 850 people lost their lives. Presumably a shift in the cargo could have caused the accident. None of the three accidents could be attributed to unquestionable causes.

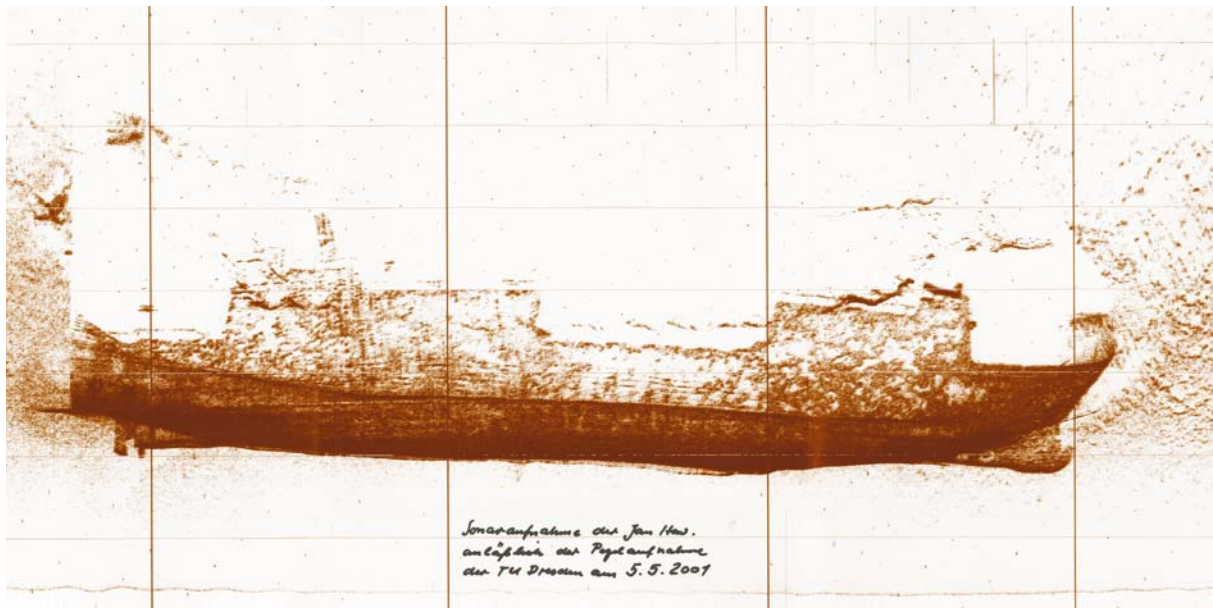


Image 7.1.1-1a. The wreck of the ferry *Jan Hevelius*. Sidescan sonar image. The ferry, 125 m long, built in 1977 sank in 1993 in the southern Baltic off the Island of Rügen. The sidescan image taken in 2001, viewing the wreck from the keel side, shows an essentially intact hull and superstructure lying on the portside at about 20 m depth. The bow – as well as the stern construction – can be identified in detail. The pair of funnels near the stern are still in place (the port side one lies under the starboard funnel here). Conspicuous is the acoustic difference between the strongly reflecting hull coded dark and the less reflecting superstructure of considerable height. The broken upper contour in the middle is an open deck; the railings are only weakly recognizable. The mast constructions are not resolved. The white shadow contours are most evident on the stern side; near the bow the sea floor surface appears rough; part of the bow near the keel is buried by sediment.

Image documentation: same as Image 7.1.1-1
Image ©: BSH, Rostock, Germany ■

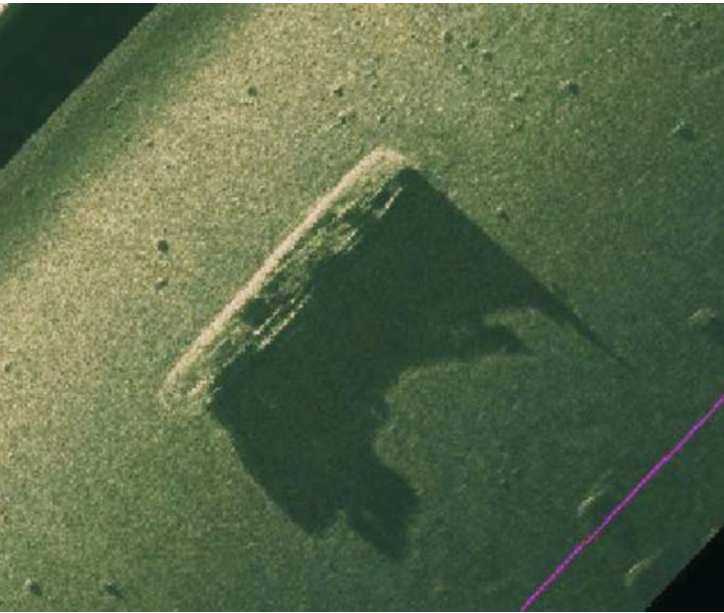


Image 7.1.1-2.

Wreck of a tjalk-type ship in the Baltic Sea. Sidescan image. The wreck of a tjalk, a traditional Dutch ship with a plane keel is lying upright at 19 m depth in the Western Baltic on a smooth sediment field with few stones. Neither the date nor the reason for the accident are known. The acoustic irradiation by the sidescan sonar from the upper left – the black band indicates the ship's path – generates a long shadow revealing and enhancing the intact contour of the superstructure. Such an intact wreck is an exception. Wooden constructions in particular, but steel wrecks hardly less so, suffer severely from decay over the years and remain often only as debris. Particularly remarkable is the fact that there is no visible erosion of the sediment around the wreck, quite different from the state of the wreck of the *Richard Montgomery* for instance (Sect. 7.3.2). The reason is the absence of tidal activity in the Baltic and very little near-bottom current. Due to the depth of the water at the site, salvage of the wreck is not necessary.

Image documentation: same as Image 7.1.1-1

Image ©: Walter Offenborn, Naval Office, Germany ■

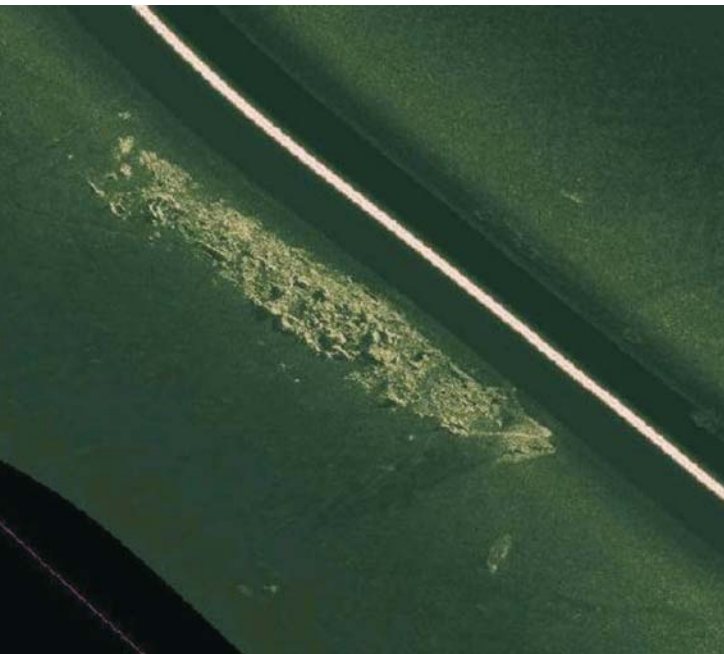


Image 7.1.1-3.

Wreck of the Condul in the Baltic Sea. Sidescan image. Similar to the wreck of the *Gneisenau*, the *Condul* exists only as a contoured aggregate of debris on a plane sediment area but with no traces of salvage. Neither the reason nor the time of the accident in the Central Baltic is known. These remnants are typical of the hundreds of anonymous wrecks discovered by German Hydrographic and Naval Authorities during the last decades, providing systematic inventories by sound imaging in the Baltic as well as in the North Sea.

The sidescan sonar did not generate long shadows from this totally destroyed wreck as in Image 7.1.1-2. Moreover the white line with the two blind stripes indicating the ship's path is directly adjacent to the wreck, thus causing a steep downward irradiation like sunlight at noon. Whereas the bow on the lower side of the image appears to show a defined contour, the stern is only debris as if the ship sank with the stern ahead. The only long shadow is behind the bow, the only protruding element of the wreck relics. Since the water is 23 m deep at the wreck site, there is no need for expensive salvage.

Image documentation: same as Image 7.1.1-1

Image ©: Walter Offenborn, Naval Office Rostock, Germany ■

The sharp edges of the wreck and all the more pointed ends like mast tops must not be averaged out by an insufficient resolution under on-site conditions. Unavoidable and incompletely compensated movements of the survey vessel for instance might slightly and thus dangerously blur an otherwise sufficiently fine mesh of

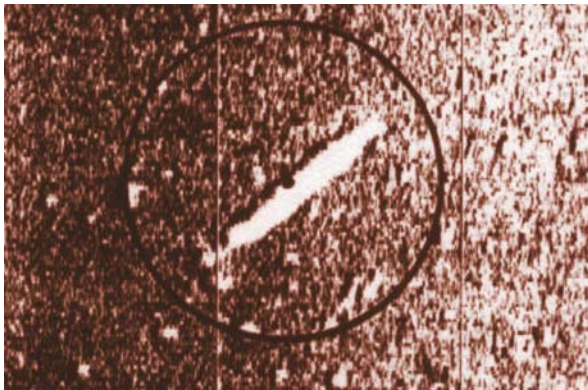
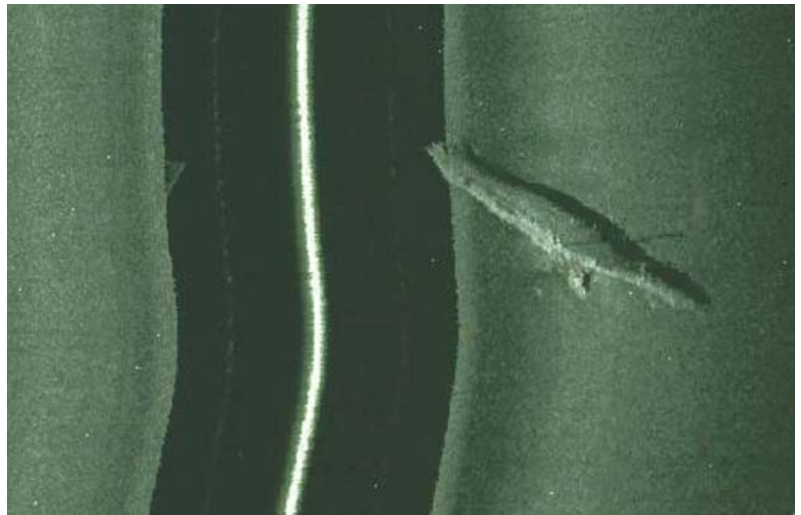
image pixels. Therefore in cases of doubt the responsible Hydrographic Institutions authorize divers to conduct final manual measurements of the clearance or they rely on the classical mechanical but very laborious, expensive and weather dependent method of wire-sweeping, as happens in the United Kingdom, for final

Image 7.1.1-4.

Wreck of a submarine in the North Sea. Sidescan image. The English submarine sank in 1915 west of *Heligoland*. The boat of 55 m length, lying on its starboard side appears nearly unimpaired, similar to other submarines found, presumably due to the strong pressure hull wall. As with the tjalk wreck of Image 7.1.1-2 there is no significant sediment erosion, although this area of the North Sea is tidal. This is due to fine grain sediment sticking together by adhesion. Salvage is not necessary because safe shipping clearance is not affected.

Image documentation: same as for
Image 7.1.1-1

Image ©: Walter Offenborn, Naval Office
Rostock, Germany ■

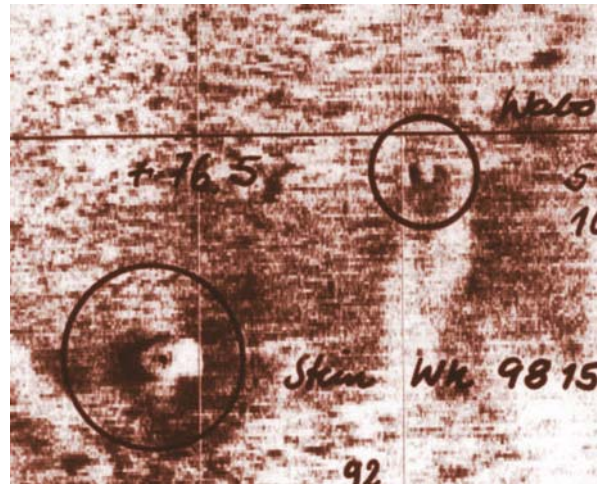
**Image 7.1.1-5.**

Misfired sunken torpedo found in the Baltic Sea. Sidescan image. The image is scanned from an earlier paper record and shown as an enlarged cut-out. The length of 4 m and the diameter of 0.5 m indicate a German WW II torpedo which must have been misfired and sank after the buoyancy was lost. Divers disposed of the torpedo, which was found in the western Baltic, *Bight of Lübeck*, in 2001 at 20 m depth.

Image documentation: same as for Image 7.1.1-1

Image ©: Thomas Dehling, BSH, Hamburg, Germany ■

confirmation. This method works with a tight, horizontal wire, stretched below the vessel at the depth in question. With more experience and systematic comparison of the methods of preference, advanced high resolution multibeam echosounders will probably remove in the course of time such doubts of reliability which were justified in the past. ▶p.335

**Image 7.1.1-6.**

Misfired water-bomb found in the Baltic Sea. Sidescan image. The paper record cut-out shows two objects indicated Wabo (Water-bomb) and Stein (stone) respectively. The fantasy of a non expert would hardly suffice to recognize these objects. In fact, the limited resolution of the sidescan image with a pixel size of about 30 cm times 5 cm at the distance of detection neither reveals the typical features of the stone which was 1½ m of size verified by divers nor the characteristic clues of the bomb shape. However, the specific light-shadow pattern of the upper object could be attributed to a water-bomb by experienced ammunition hunters. The WW II bomb of 0.6 times 0.4 m size was discovered in the southern Baltic, *Bight of Lübeck*, in 2001; its disposal was conducted by divers.

Image documentation: same as for Image 7.1.1-1

Image ©: Thomas Dehling, BSH, Hamburg, Germany ■

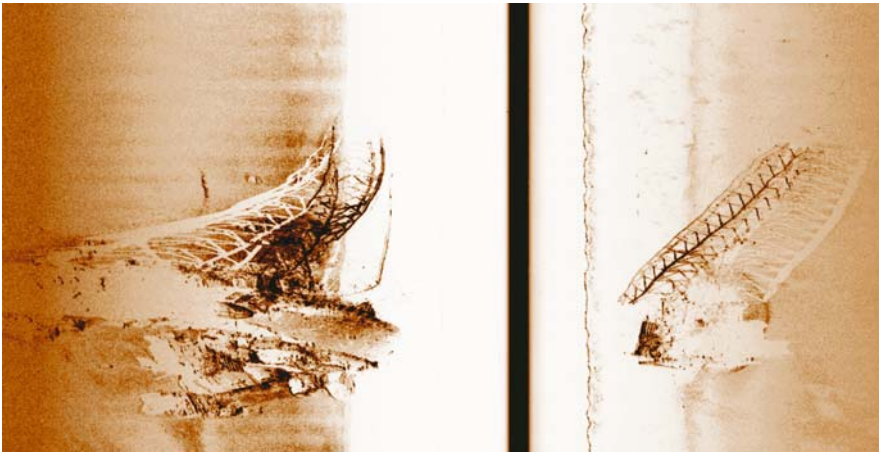


Image 7.1.1-7.

Wreck of an offshore tower, German Bight, North Sea; sidescan image. The offshore shelter *West Gamma* was lost during transport in 1994 and is still lying at 40 m depth because it does not affect the safe shipping clearance. Biologic investigations have confirmed that the often observed function of wrecks as biologic habitats applies also for the *West Gamma*.

The construction with clearly recognizable struts appears distorted at the port side of the image, which is caused by the ship track directly on top of the tower.

as the nearly vertical view is the worst case for the sidescan method applied here and best under grazing angles this is just the opposite of the multibeam echosounder (Sect. 4.2.3). The image covers 110 m on the port side and 235 m along track.

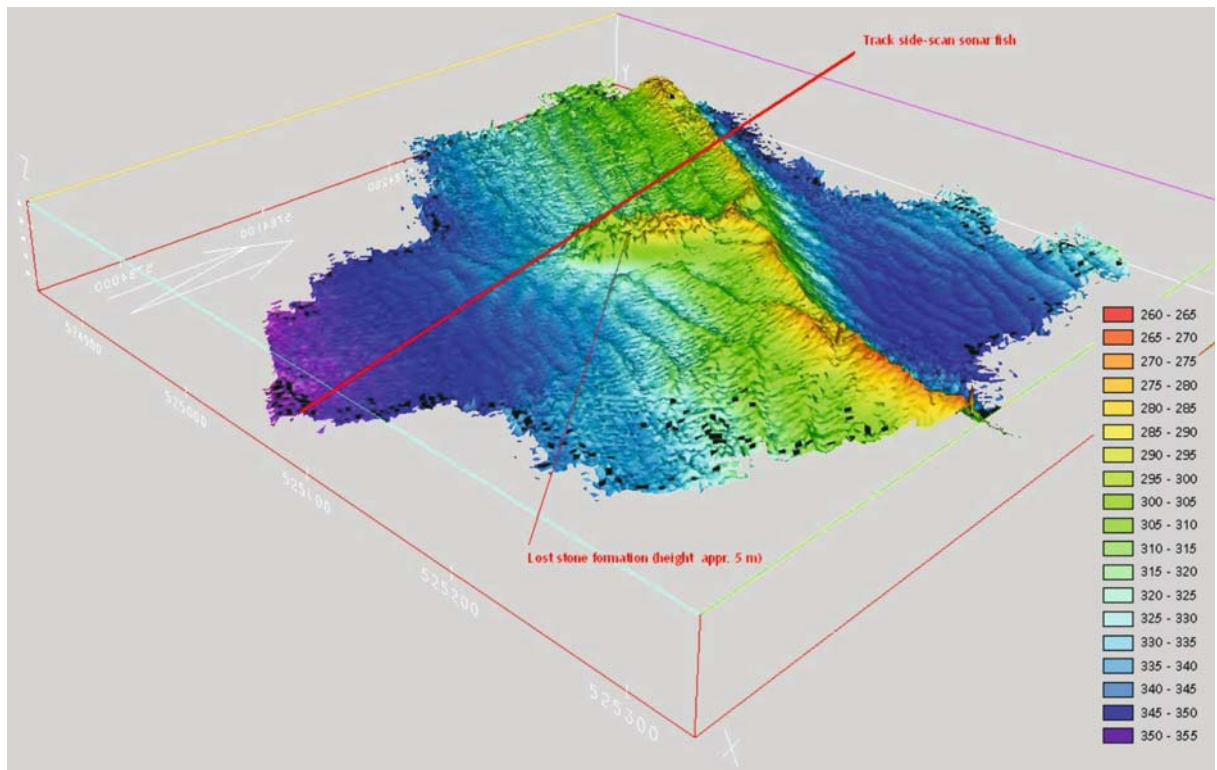
Project: Wreck monitoring of shipping lanes by BSH, 1996

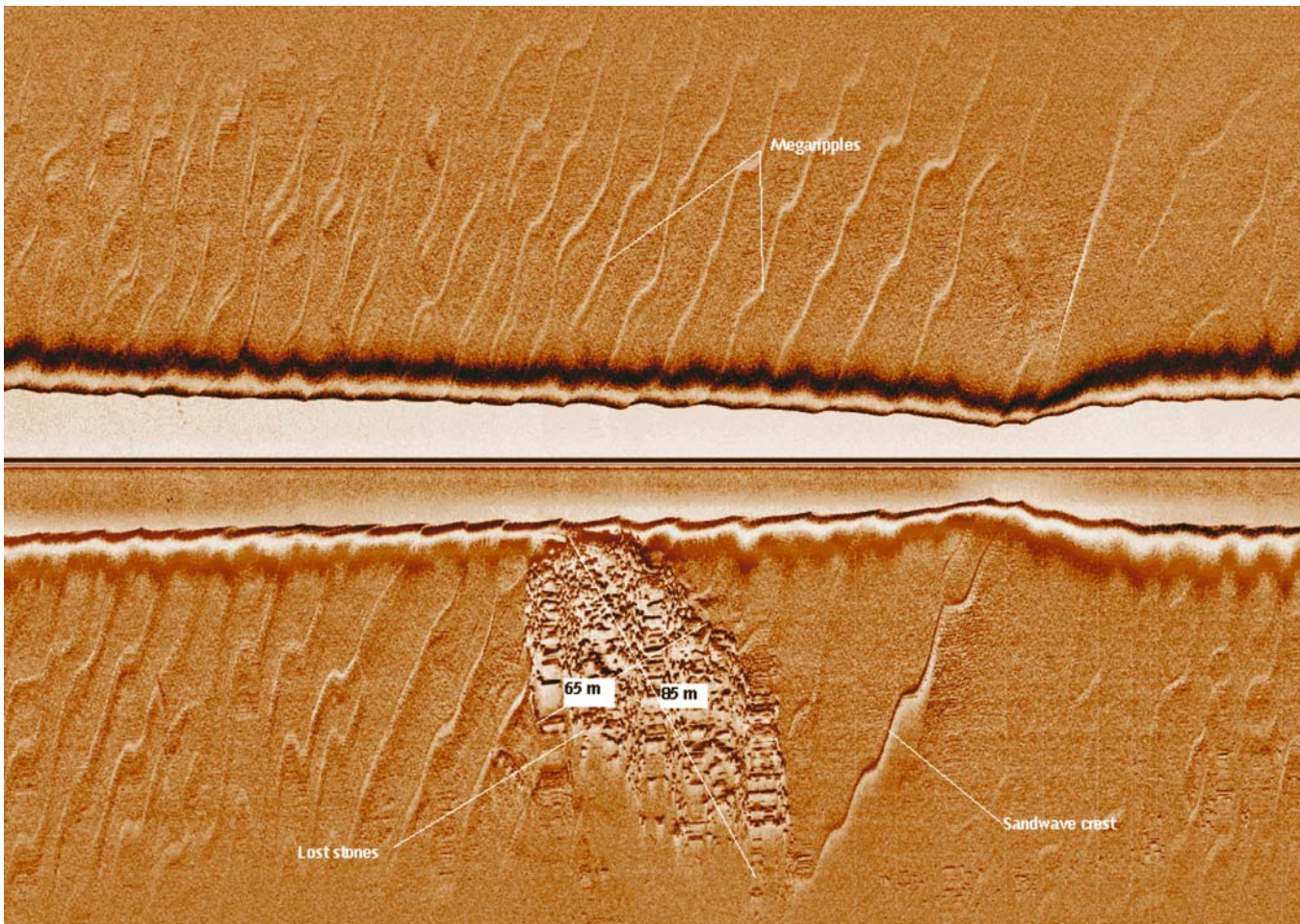
Survey vessel: *RV Gauss*, BSH, Hamburg

Sidescan sonar: Klein, Model 595; frequency: 385 kHz, horizontal beamwidth: 0.5°, unfocussed, towed 5–8 m above the sea floor

Towing device: EdgeTech, DF 1000

Image ©: Manfred Zeiler, BSH, Hamburg, Germany ■





◀ Image 7.1.1-8.

Lost load of stones, Dutch Continental Shelf. Multibeam 3-D-relief image. A towed barge load of 10 000 t dumping stones was lost outside of shipping lanes in 2001 on the Dutch Continental Shelf. The accident, leaving a stone hill of about 5 m height with stones between decimeters and meters of size fortunately did not cause a hazardous shoal. The crest of a large sand dune nearby is about the same height. The image which covers a depth range of 80 m shows the periodicity of sand ripples “riding” on the dune (Sect. 5.3.3), oriented east-west. It is one of the seabed-forms typical of coastal areas of the North Sea. The red line indicates the sidescan track of the subsequent image.

Institution: Rijkswaterstaat, North Sea Directorate
 Area: North Sea, Dutch Continental Shelf
 Survey vessel: *Zirfaea*
 Multibeam echosounder system: Simrad EM3000; frequency 300 kHz, beamwidth 1.5°, fan angle 157°, depicted box size: 0.5 × 0.5 km
 Image ©: RWS DNZ ■

Image 7.1.1-9.

The same lost load of stones. Sidescan image of the sea floor structure. The image depicts the size of the dumping stone hill to be 85 × 65 m. The survey vessel passed the hill nearly on top, just outside the two echo-onset lines, typical of all sidescan images. The lines appear squeezed due to the reduced water depth at the ridge of the dune. The motion caused by the towed sonar fish instability feigns wavy crests of the ripple field superimposed on the dune flanks.

Institution: Rijkswaterstaat, North Sea Directorate
 Area: North Sea, Dutch Continental Shelf
 Survey vessel: *Zirfaea*
 Sidescan sonar system: Ultra, frequency 325 kHz, beamwidth 0.5°
 Image ©: RWS DNZ ■

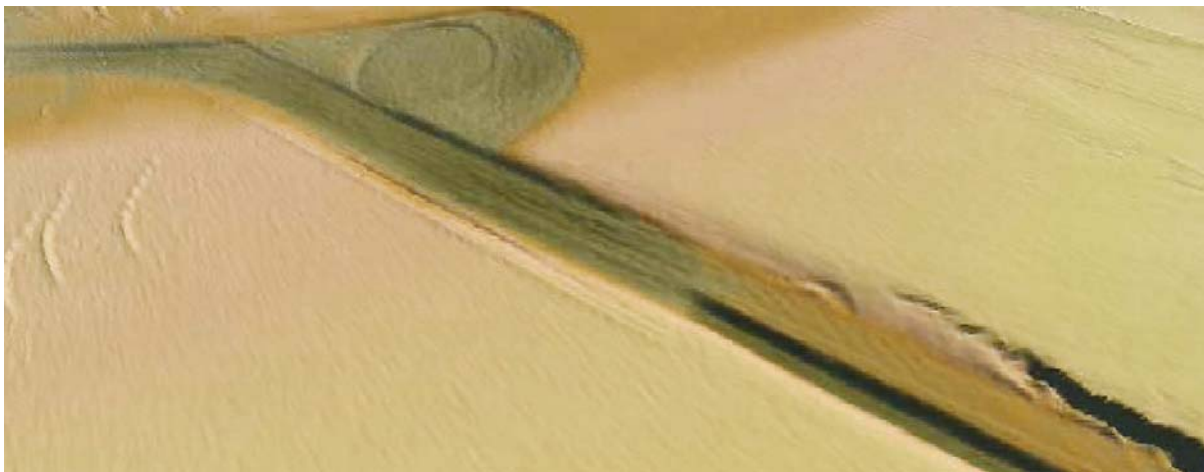


Image 7.1.1-10. Maas-Channel. Multibeam image. The three-dimensional multibeam image displays the *Maas-Channel*, the fairway of 600 m width for ships approaching *Rotterdam Harbor*. The adjacent circular field is the turning circle and emergency anchoring area at the end of the Channel. The natural trench of 1.5 km length in the foreground is about 50 m wide and 6 m deeper than the Channel. The channel section shown is free of hazardous wrecks.

Institution: Rijkswaterstaat, North Sea Directorate

Area: North Sea, Dutch Continental Shelf

Survey vessel: *Zirfaea*

Multibeam echosounder system: Simrad EM3000; frequency 300 kHz, beamwidth 1.5°, fan angle 157°

Image ©: RWS DNZ ■

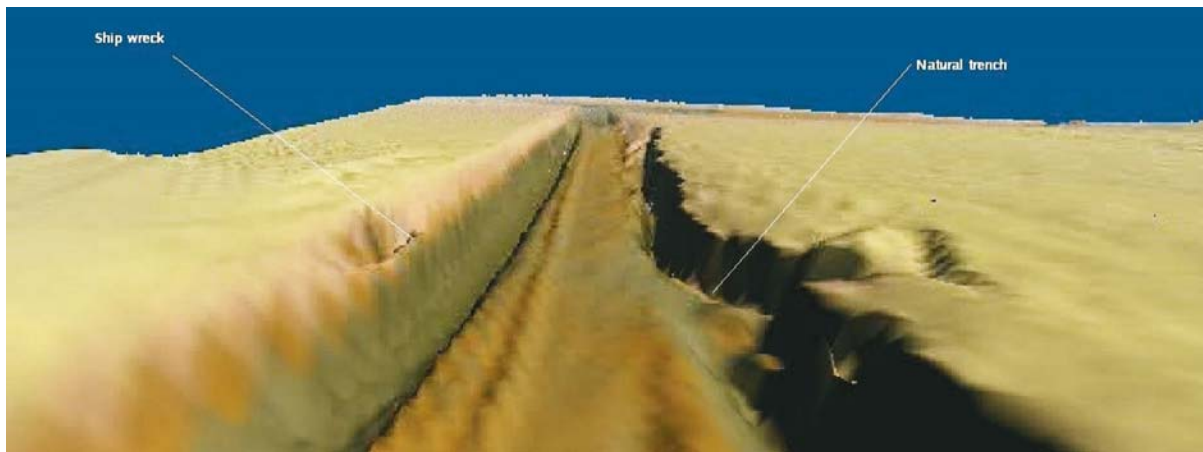


Image 7.1.1-11. Maas-Channel. Multibeam 3-D image, depicted as low angle view. The three-dimensional multibeam image simulates an impression of the *Maas Channel*, while looking offshore from *Hook of Holland*. On the right hand side of the fairway more and stronger erosion effects are found than at the steep and smooth other side. The natural trench in the foreground on the right is a drastic example. Presumably this asymmetry is caused by the stronger flood current of more than 1 m s^{-1} , coming in from the left side of the image. It erodes the opposite channel flank more severely than the benign ebb current does with the left flank. The fairway has a safe shipping clearance of 20 m, while the channel flanks depths changes with distance. A small wreck (coaster) is visible on the left flank.

Documentation: same as preceding image

Image ©: RWS DNZ ■

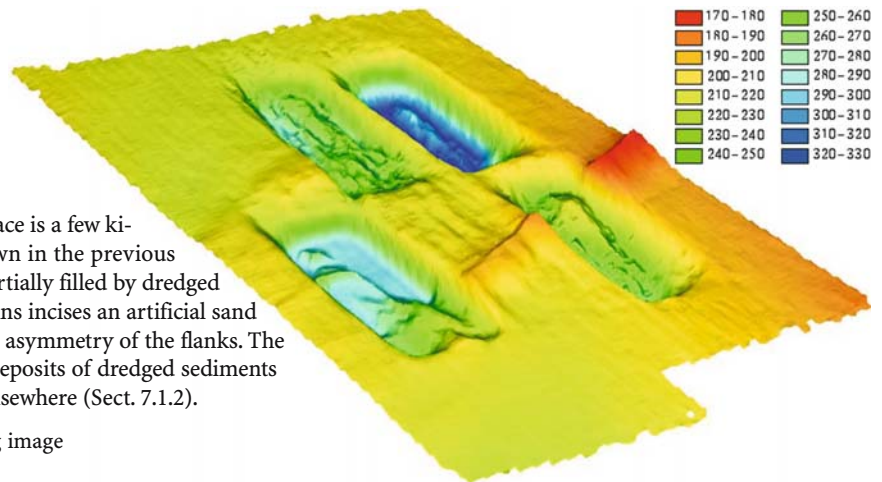


Image 7.1.1-12.

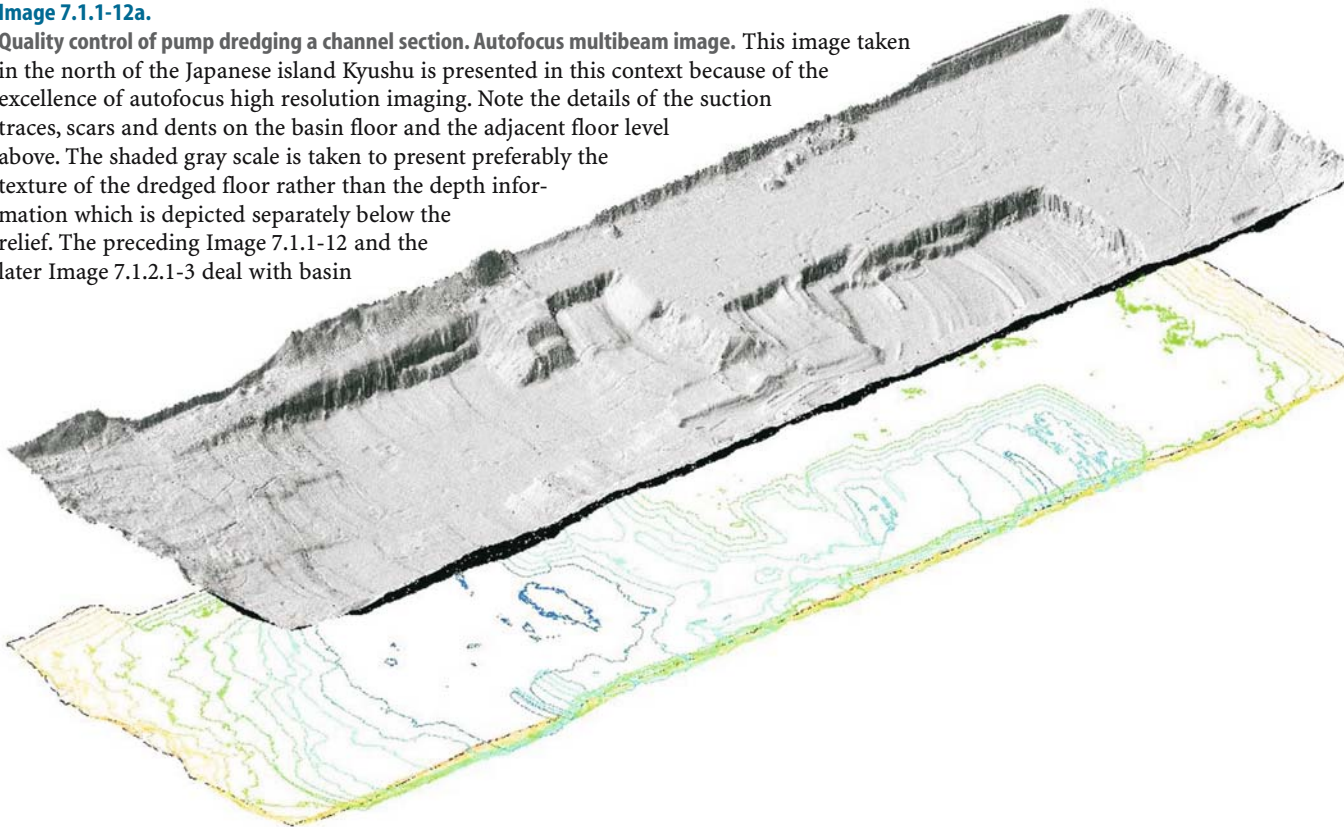
Dumping location. Multibeam image. This place is a few kilometers north of the *Maas Channel* shown in the previous images. The basins of $450 \times 1\,250$ m are partially filled by dredged sediment from the fairway. One of the basins incises an artificial sand dam to reduce sedimentation with evident asymmetry of the flanks. The depth scale is in decimeters. Underwater deposits of dredged sediments from shoal removal work are usual also elsewhere (Sect. 7.1.2).

Documentation: same as for preceding image

Image ©: RWS DNZ ■

Image 7.1.1-12a.

Quality control of pump dredging a channel section. Autofocus multibeam image. This image taken in the north of the Japanese island Kyushu is presented in this context because of the excellence of autofocus high resolution imaging. Note the details of the suction traces, scars and dents on the basin floor and the adjacent floor level above. The shaded gray scale is taken to present preferably the texture of the dredged floor rather than the depth information which is depicted separately below the relief. The preceding Image 7.1.1-12 and the later Image 7.1.2.1-3 deal with basin



dredging as well but are taken without beam focusing. Instead, the bathymetric information is superimposed by color coding. Depending on the purpose of surveillance, both versions of multibeam imaging are adequate, though the nearly photographic quality achieved by focusing is self-explanatory. Of course, color coding the depth levels is applicable, independent of focusing.

Project: Quality control of pump dredging

Multibeam system: RESON, type: SeaBat 8125; frequency: 455 kHz, beamwidth: $0.5 \times 1^\circ$, 240 beams, fan width: 120° , zoom auto-focus

Image ©: Nihon Zitan/Toyo Corporation ■

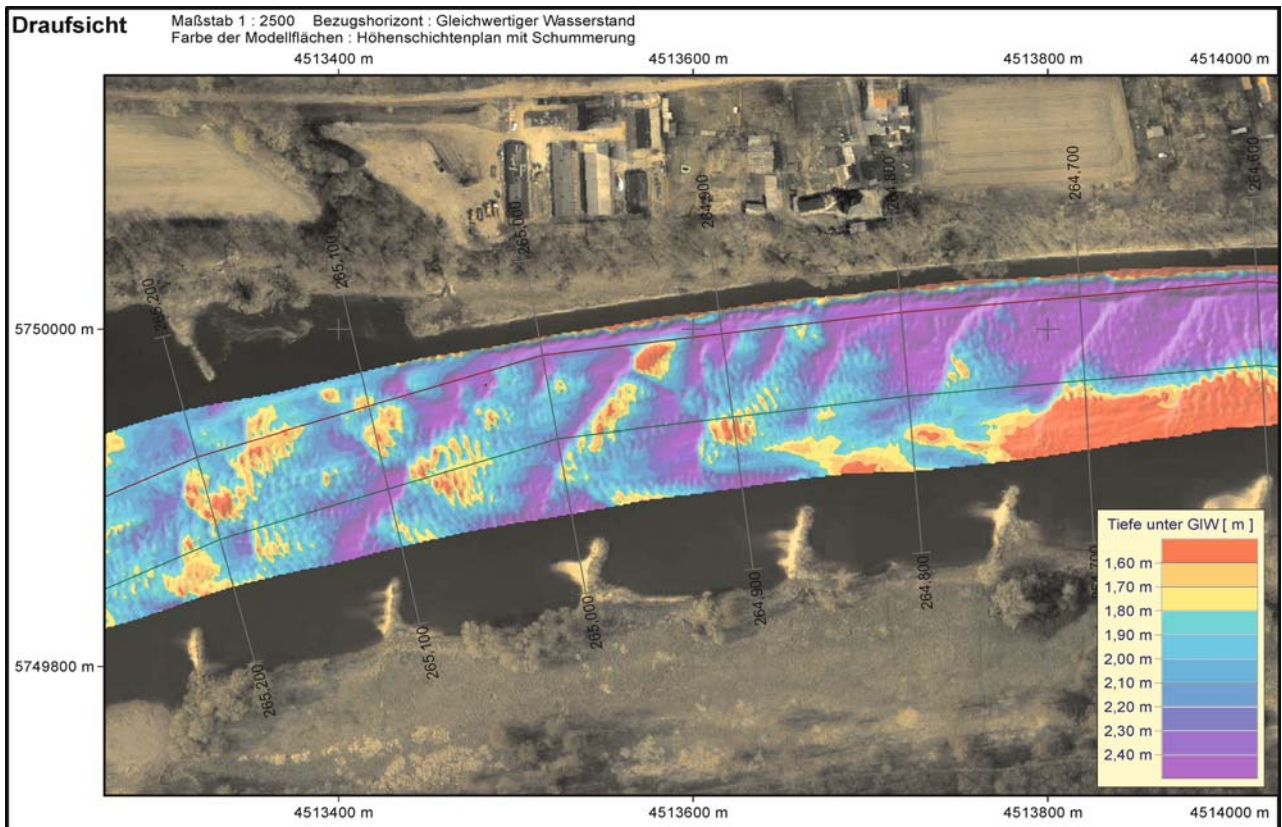


Image 7.1.1-13.

Elbe River near Dessau, Sachsen-Anhalt, Germany. Multichannel sound image inset. Upstream of Hamburg Harbor (Sect. 7.1.3), the Elbe River remains an important shipping lane though restricted to inland vessels of shallow draught. The multi-channel image presents the river floor relief of a 600 m long reference section and is shown here together with an aerial laser scanning image of the river banks with buildings and vehicles for comparison with the size of the sediment morphology. The image was taken in March 2004 in the framework of regular sediment transport surveillance of a complete cross section of the fairway, situated 357 km upstream in the Elbe River. The depths refer to the officially defined equivalent water level.

The very shallow water of partially less than 2 m depth is particularly hazardous to heavy cargo- and passenger-shiping because shoal formation by migration of sediment and possibly detritus is highly probable. The geometry of the relatively wide but shallow shipping lane excludes the bathymetric area coverage by a multibeam fan-echosounder. Such special surveillance tasks are conducted best by the technical predecessor to present day multibeam systems. Modernized by digital technology this multichannel echosounder is indispensable for rapid, high accuracy 3D-mapping of very shallow, in-

land waters. The principle of measurement (Sect. 4.2.7) is based on a row of submerged echosounder heads mounted below a pair of cantilevers above the water, athwart like wings of the shallow draught surveillance vessel. Typically a dozen downward looking sounders one meter apart from each other are operated separately by a joint digital control unit for synchronous signal generation and echo recording.

The accuracy requirements exceed those of the open sea by far. The differential satellite navigation DGPS is additionally supported by beacons ashore to achieve a horizontal positioning accuracy of 3–5 cm throughout the entire area of surveillance. Corresponding accuracies are required for the depth acquisition and realized by high precision control of the motion components of the vessel (Sect. 4.2.9), in particular the roll motion during the meandering tracks. The horizontal resolution refers to the distance of the echosounders on the cantilevers of normally 1 m but can be enhanced by three times the echosounder units to meet high level safety requirements depending on the river floor characteristics.

The river bed in this section is dominated by a double structure as is often found also offshore: a dune-like periodicity of nearly the distance of the breakwater units on the west-bank superimposed by a short-wave ripple field of less than a 20th of the long period in this case. It is remarkable

that even within this section of a few hundred meters the character of the relief features undergoes a transition from nearly random on the left, downstream side to very regular on the upstream side where the river bed has two plateaus separated by only 80 cm: the higher one indicated in red with no apparent morphology and the lower one indicated in violet showing the regular double structure. This deeper cross section presumably carries the main flow and at higher speed, sufficient to cause erosion and sediment transport.

The actual shipping clearance related to the respective Elbe River sections is distributed daily; selected shallow cross-sections are surveyed weekly. The fairway margins are indicated by the two lines; red: portside, green: starboard. Complete area coverage like the image shown is conducted on demand. The state of this section as imaged does not yet require dredging.

Project: Area surveillance of the Elbe River sediment migration and bedform for fairway maintenance at the reference section Elbe-km 265 (counted from the Czech border), March, 2004

Survey vessel: *MB Rosslau*, WSA Dresden

Multichannel echosounder system: *Fahrentholz*, type:

Fz-Hydrosearch; frequency: 200 kHz, 13 channels, 12 m swath width

Image ©, multibeam relief: Thomas Brüggemann, Bundesanstalt für Gewässerkunde, Koblenz

Image ©, aerial photograph: Bundesanstalt für Gewässerkunde, Koblenz ■

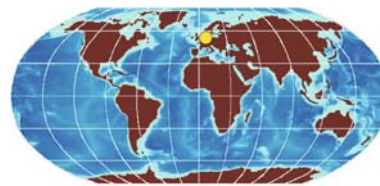
A continuous problem, hazardous to shipping lanes is the fall-out of suspension in river mouths and estuaries, as well as sediment transport by migrating dunes in coastal areas. Both produce shoals which can cause blocking of ships by sea-floor contacts. Here the regular surveillance by fan-echosounders is mandatory to guide the dredging service in time. Contrary to sedimentation, erosion such as caused by storm enhanced tidal currents, can be dangerous to offshore constructions, another field of acoustic surveillance (Sect. 7.2). In the context of hazardous sediment shoals, the critical question of *Safe Shipping Clearance* involves a decisive detail in echosounding the clearance rather than the decision between remote measurement by acoustics or final proof by mechanical means as in cases of hazardous wrecks. Fresh sediments such as the fallout of suspension are often close to the acoustic properties of water or they may even act as a kind of continuous transition between both media. Then mid-frequency echosounders may penetrate the sediment somewhat before they touch the horizon of a harder substrate, thus only seeming to have measured safe shipping depths. Depending on the local sediment

conditions the choice of 100 kHz instead of 50 kHz for instance usually solves the problem.

The few examples of hazardous material shown are WW II ammunition. Though they were found unburied, the comparatively small dimensions demonstrate the difficulty of discrimination from benign objects.

The third subject of route surveillance is still one of the most difficult tasks of sound imaging in the sea. “Mine-like objects” means acoustic similarity. Wreck debris as well as stones and stone fields can hide sea mines. Improved self-masking of mines by development of shape and material increases the hazard and requires continuously increasing sophistication of surveillance and reconnaissance techniques to maintain the sea lane protection. The most demanding problem in this context is the detection and even more the reconnaissance of buried mines, which maintain their destruction potential nearly completely. This problem is treated separately (Sect. 7.1.5). Advanced acoustic concepts to cope with the challenge of buried mines are still under development.

7.1.2 Estuary Surveillance



Sea harbors need and offer protection against adverse weather. The favorite sites for them are therefore

natural bights, preferably framed by steep, rocky coastlines. Seacoasts of alluvial land however can offer protection mainly upstream of a major river. In tidal areas like the *North Sea*, where a river estuary is a typical ocean side entrance to a sea harbor, there is the permanent problem of keeping the fairway operational. An estuary is an area of interaction of the tide coming in and the river flow going out. Both bring in suspension load, reshape the river bed and cause shoals inside the fairway. Accidents where ships may lose cargo or containers cause more hazards for shipping than in deep water harbors. Regular surveys are thus mandatory to maintain safe shipping clearance.

The image series presented hereafter deal primarily with the estuary of the *Elbe*, the largest continental river flowing into the North Sea. It is the entrance to the harbor of the *City of Hamburg* which is also called the *gateway to the world*. The fairway is about 120 km long with an average width of 400 m and a “bottleneck”

of 250 m, which is also the width of the *Kiel Canal* for instance. The two Shipping Authorities of WSA Hamburg share responsibility for 60 km each of the fairway.

The regular clearance survey is conducted every month to provide sufficient lead time for the dredging work on demand. The safe clearance is adequate for ships up to 12.7 m draught, related to fresh water displacement. These dimensions permit the passage of freighters, passenger ships, and other vessels up to a length of 350 m and a beam of 60 m.

The 100-t survey-vessel, operating the high resolution multibeam echosounder (MBES), is equipped with special propulsion allowing correction of the course at very short notice. The necessary high precision bathymetry is achieved by precise differential GPS navigation of the vessel and inertial gyro reference for computerized motion compensation to stabilize the MBES-basis. The accuracy achieved is about 1 decimeter horizontal and vertical, with reference to the actual tide level. According to the nearby GPS-reference stations and tide gauges inshore, the accuracy is much better than possible in the open ocean. Only within the estuary mixture zone, the strong changes of the sound velocity structure due to fresh- and salt water-masses, with drifting ice in winter and flow of heated

water from very shallow sites in summer, are causing varying sound refraction, thus reducing the depth accuracy to about 2 decimeters, despite various measures of correction and caution.

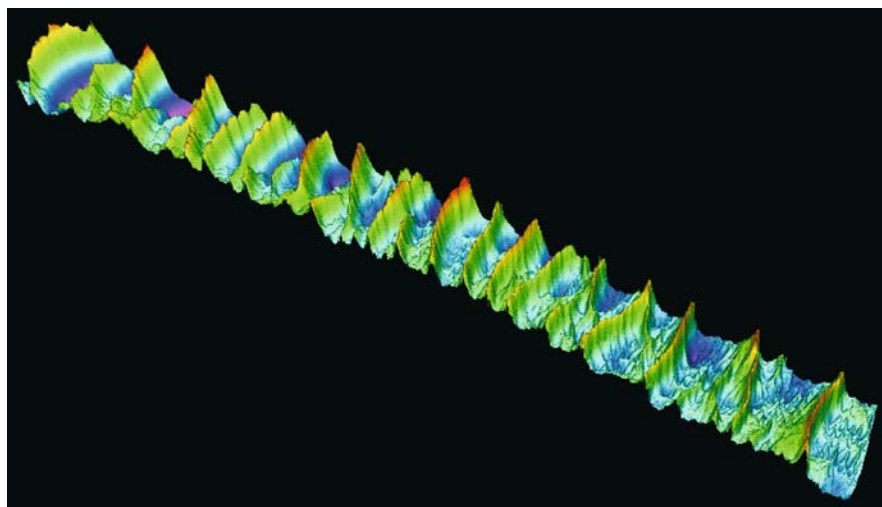
The wide-angle multibeam echosounder spreads a fan of 140°, covering a stripe width of about six times the water depth when 158 of the total of 256 beams are being operated. With some overlapping of the data carpet, the vessel has to pass the 60 km section of the fairway 10 times every month. In addition there are further surveys beyond the fairway, necessary to observe hazardous changes in time. In fact, the complete coverage of the fairway with no gaps in data and only a few crossings is a remarkable achievement in the progress of ship safety and an economic advantage as well. The MBES technology which enabled this state of the art in fairway surveying was implemented by the WSA Hamburg in 1998/1999.

The other example presented in this context is a tidal area adjacent to the Elbe Estuary in the north, the *Bight of Meldorf*, which is of interest because of long term variability of the sea floor relief revealed by sound imaging.

7.1.2.1 Floor Features of the *Elbe Estuary*

Image 7.1.2.1-1.

Dune field in the *Elbe-Estuary*, sea lane of *Hamburg Harbour*. Multi-beam image. A plain sand bottom is not a stable state. When the flow speed exceeds a critical value, it generates ripples and dune structures (Sect. 5.3.3). Dunes in estuaries are up to several meters high, comparable in size with off-shore dunes in tidal areas. However, estuary dunes generated by a varying superposition of the river outflow and the alternating tidal current are more or less asymmetrical in shape, with the steeper flanks on the lee side of the dominant local flow. The section shown is 1 km long and 120 m wide with the profile enhanced 10 times for easy indication of potential excess of the safe shipping clearance.



Project: Surveillance of the Elbe-Estuary, 2001; Center of area: 55°35' N, 9°38' E

Survey vessel: launch of 100 tons

Multibeam system: Simrad EM 3000; 300 kHz, 1.5°/140°

Color scale from red 12 m to violet 15 m depth, black: no measurements

Image ©: C. Roedle, WSA Hamburg-Wedel, Germany ■

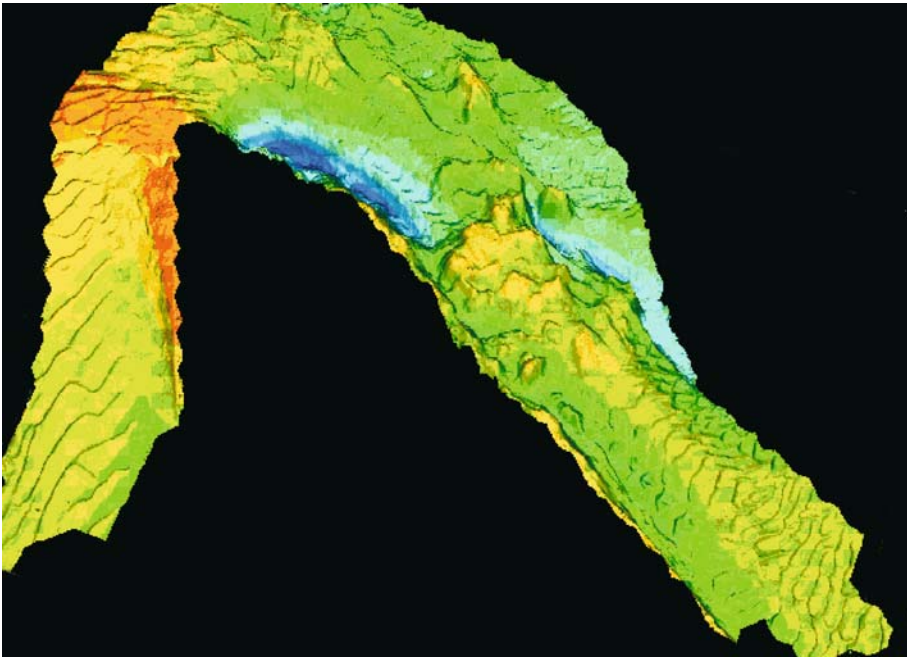


Image 7.1.2.1-2. Flow induced deep erosion of the river *Elbe Estuary*. Multibeam image. The black “nose” in the middle is the northern rim of the isle of Luehesand, dividing the Elbe with the sea lane arm on the right. The flow has caused a deep erosion hole of 50 m length and 6 m depth in the sandy river bed in front of the island on the side of the main river arm, indicating major sediment transport.

Image documentation same as for Image 7.1.2.1-1, but in 2000; Color scale from orange 10 m to dark blue 18 m depth
Image ©: C. Roedle, WSA Hamburg-Wedel, Germany ■

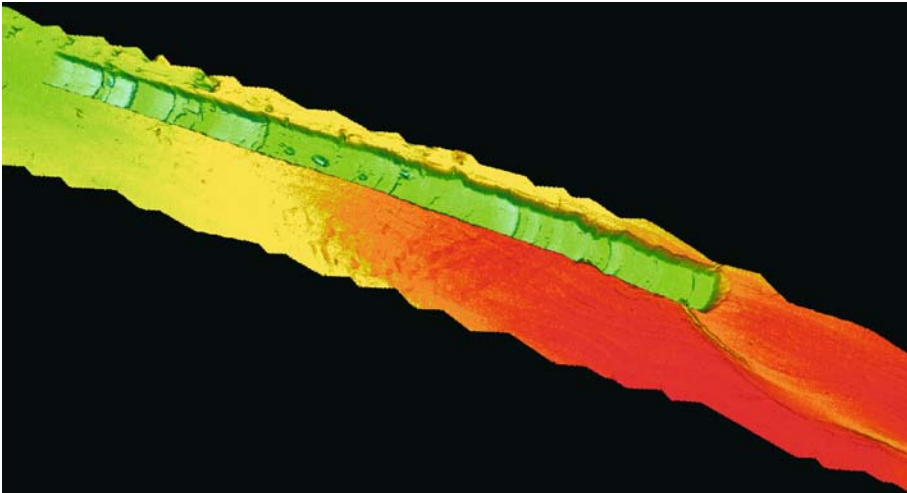
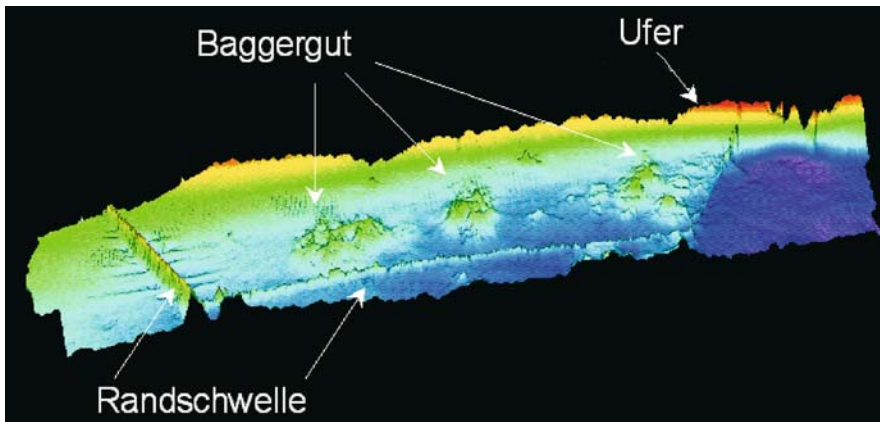


Image 7.1.2.1-3. Traces of dredging work for sand mining off the fairway; *Elbe Estuary*. Multibeam image. The dredging operations for the removal of sand are evident from the shallow thresholds along the sharp edged trace of 500 m length, 8 m width, and 2 m depth in the river bed of the side arm Hahnover.

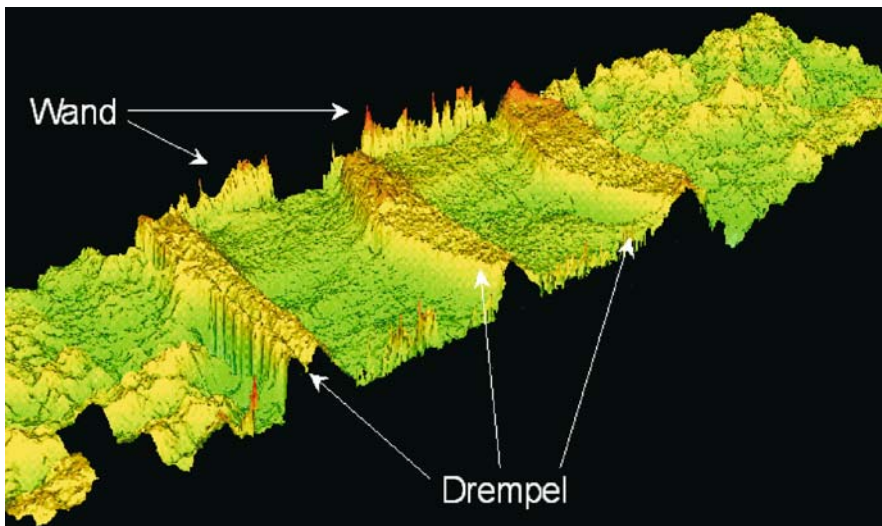
Image documentation same as for Image 7.1.2.1-1, but in 2000; Color scale from red 10 m to blue 15 m depth
Image ©: C. Roedle, WSA Hamburg-Wedel, Germany ■

**Image 7.1.2.1-4.**

Deposit of dredged material. Multibeam image. The sill construction fixed by special textile is an underwater dike 3 m high, enclosing a deposit area of 1 600 m by 400 m at *Krautsand North*. The irregular hills inside are of dredged sand.

Image documentation same as for Image 7.1.2.1-1, but in 2002
Color scale from red 10 m to violet 15 m depth

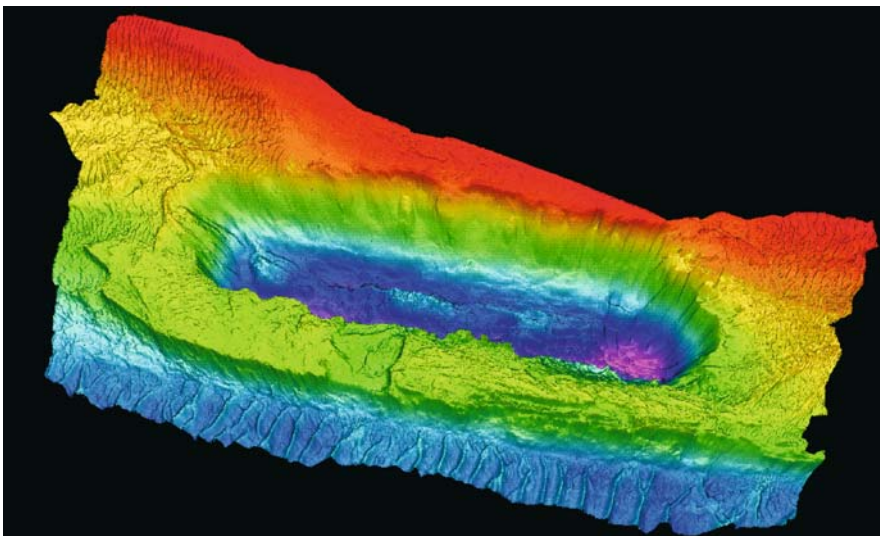
Image ©: C. Roedle, WSA Hamburg-Wedel, Germany ■

**Image 7.1.2.1-5.**

Sperrwerk Este (locking device), river Elbe. Multibeam image. The pointed sill profiles are part of the underwater construction of the Sperrwerk Este. The two door wings are open and not visible. The high resolution bathymetry reveals irregular sedimentation before, behind and slightly between the group of concrete sills broadening their base and covering their roof. The river flow is from left to right.

Image documentation same as for Image 7.1.2.1-1, but in 2000
Color scale from red 10 m to blue-green 15 m depth

Image ©: C. Roedle, WSA Hamburg-Wedel, Germany ■

**Image 7.1.2.1-6.**

Deposit basin of dredged material. Multibeam image. The artificial basin of 500 m length and 150 m width, reminiscent of a huge bath tub was dredged out of the river bed near *Giesensand* for the economic exchange of sand for other dredged soil, to avoid its downstream migration. The deep ripple field in the foreground is the rim of the fairway, the opposite, shallow side is the river bank.

Image documentation same as for Image 7.1.2.1-1, but in 2000
Color scale from red 6 m to violet 20 m depth

Image ©: C. Roedle, WSA Hamburg-Wedel, Germany ■

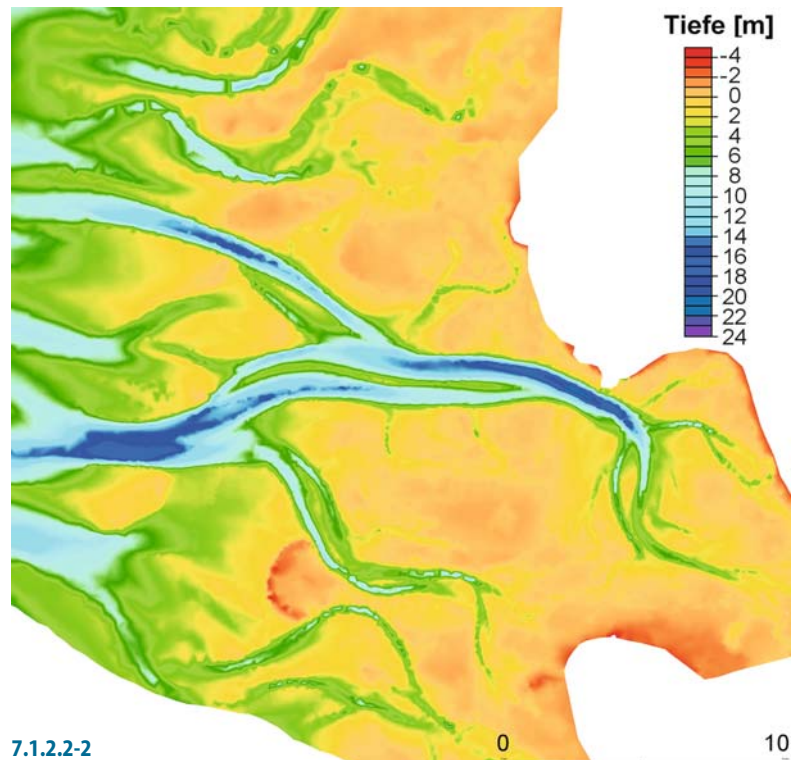
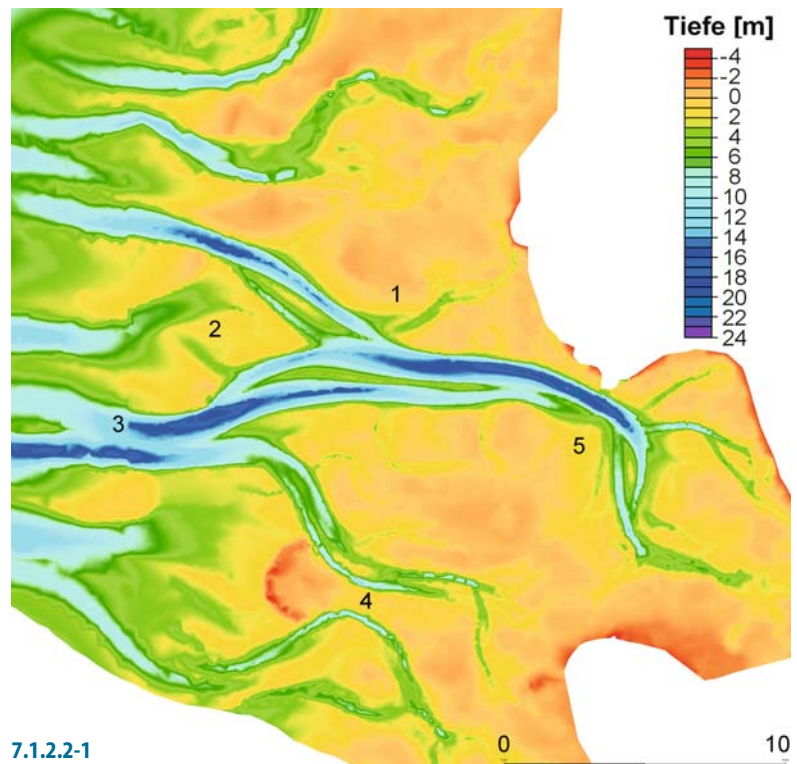
7.1.2.2 Relief Changes of the Sea Floor in the Bight of Meldorf

The west coast of *Schleswig-Holstein*, the most northern state of the Federal Republic of Germany is famous for its North Sea islands and the tidal shoals and mud flats which can be seen at low tide. These areas are protected because of the rare fauna and flora. Changes of the bathymetry due to storm induced erosion and sediment motion are carefully observed and acoustically monitored, in particular the development of the channels of the water backflow after high tide and the shape of the shoals in between.

Image 7.1.2.2-1, 2.

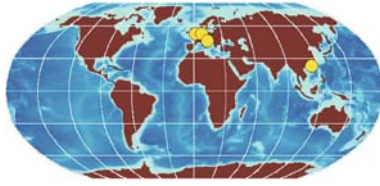
Reliefs of the Bight of Meldorf. Composite images. The Bight of Meldorf north of the estuary of the river *Elbe* visualize several significant bathymetric changes between 1990 and 1999. The state of 1990 is documented by the image indicating sub-areas of later significant changes by numbers. Quite obvious is the backformation of the channel above No. 2 whereas the channel immediately below has been widened and deepened. The sediment of the shoal in between shifted eastwards. The other numbers indicate further morphologic changes, in particular the deepening indicated by No. 5. Model computations simulating the next ten years, validated by the measured changes have shown that this relief development will go on, though not dramatically reducing the size of the biotopes.

Project: Prediction of Medium Term Coastal Morphodynamics (PROMORPH) of 2000–2002. Funded by German Federal Ministry of Education and Research
Bathymetry: The data are based on measurements of 1977–1999 of the Federal Maritime and Hydrographic Agency in Hamburg (BSH) and the Office for Rural Development in Husum (ALR)
Image ©: Ingo Junge, ISERB, University of Hannover ■



7.1.3

7.1.3 Harbor Surveillance and Maintenance



The examples are taken from projects conducted in Hamburg, Venice, London, and Hong Kong.

7.1.3.1 Hydroacoustic Spotlights of the *Port of Hamburg*

The Port of Hamburg, the main center of international and intercontinental transshipment of *Germany* is a tidal harbor, deeply incised into the alluvial lowland of this

country. The distance from the estuary entrance along the fairway of the river Elbe (Sect. 7.1.2.1) to the port area, embedded between the two river arms *Norderelbe* and *Suederelbe/Koehlbrand* is more than 120 km.

The Port of Hamburg is both a major seaport, open to all kinds of large seagoing vessels as well as a hub and interface of cargo transport in general. This includes inland waterway-, rail-, road-, and air- traffic. Though the city-state of Hamburg is a center of industry and trade of its own, the transshipment of goods between other states and countries with Hamburg Harbor as a focal point covers the majority of the port activities.

A few numbers may illustrate the economic importance and technical size of this port with 140 000 employees and a utility area of 65 km². The yearly turn-

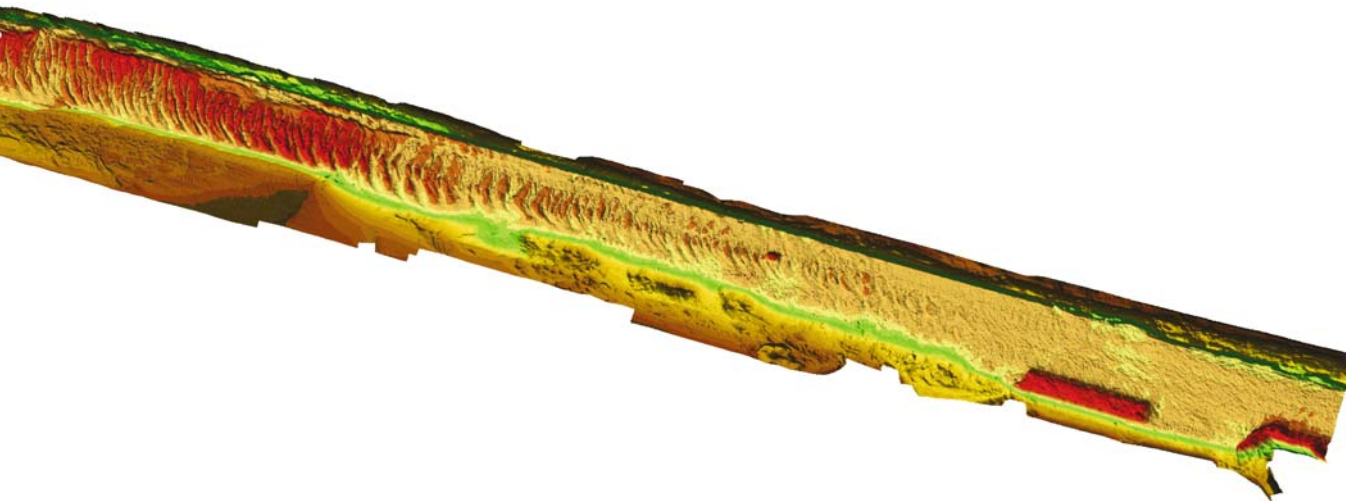


Image 7.1.3.1-1. Overview of the fairway near the *Port of Hamburg*, 2002. 3D-standard grid image derived from multibeam echosounder data. Large dunes cover the full width of about 350 m of the fairway floor along many kilometers of the 5.8 km long section shown. The migrating dunes of 30–40 m feet width with 4 m and more crest height require regular acoustic surveys, supervised by the port authorities. The speed of dune migration apparently increases towards the middle of the fairway according to the crest curvature. The dredged out rectangle indicated in red on the right hand side is a mooring and waiting place for deep draught ships. The arched deep region in red further right is a current induced erosion furrow.

The relief data indicate the sections where and when dredging of the dune crests is necessary to maintain the safe shipping depth (SSD). Red, orange, and beige indicate the sections of the fairway floor where the SSD of 15.3 m below zero sea level is reached or surpassed respectively.

Surveys conducted by Peil- und Vermessungsdienst, Strom und Hafengebäude, Hamburg
 Survey vessel: *Deepenschriewer II*, MCES, 94.5 tons; *Deepenschriewer III*, MBES, 50 tons
 Multichannel echosounder: BOMASWEEP, 38; 210 kHz, ATLAS Hydrographic
 Multibeam echosounder: ATLAS Hydrographic, Fansweep 20; 200 kHz, fan width used: up to 6 times the water depth, standard grid of all images: 2.5 × 2.5 m

The combination of both echosounders was used for Images 7.1.3.1-1 and 7.1.3.1-2. Images 7.1.3.1-4 and 7.1.3.1-5 are based on multibeam data alone

Image ©: Dieter Seefeldt, Strom- und Hafengebäude, Hamburg, Germany ■

over of goods, 94% of which are containerized, amounts to nearly 100 million tons. 12 000 vessels per year are accommodated by 40 km length of quays in connection with 150 km railway- and road bridges. The harbor and the City of Hamburg are protected against extreme tidal waves by dykes of 124 km length, whereby the mean range of the tide is already 3.60 m.

The unimpaired and safe functioning of the port at any time, above and below the water level, varying sev-

eral meters by tide is a vital necessity and the permanent, reliable maintenance is indispensable. The fundament of underwater maintenance is the comprehensive surveying by a suite of various tools of acoustic imagery operated by special survey-vessels. This surveillance work covers the entire port area of the fairways, harbor basins with quayside walls, fundamentals of port edifices, bridges and other underwater constructions.

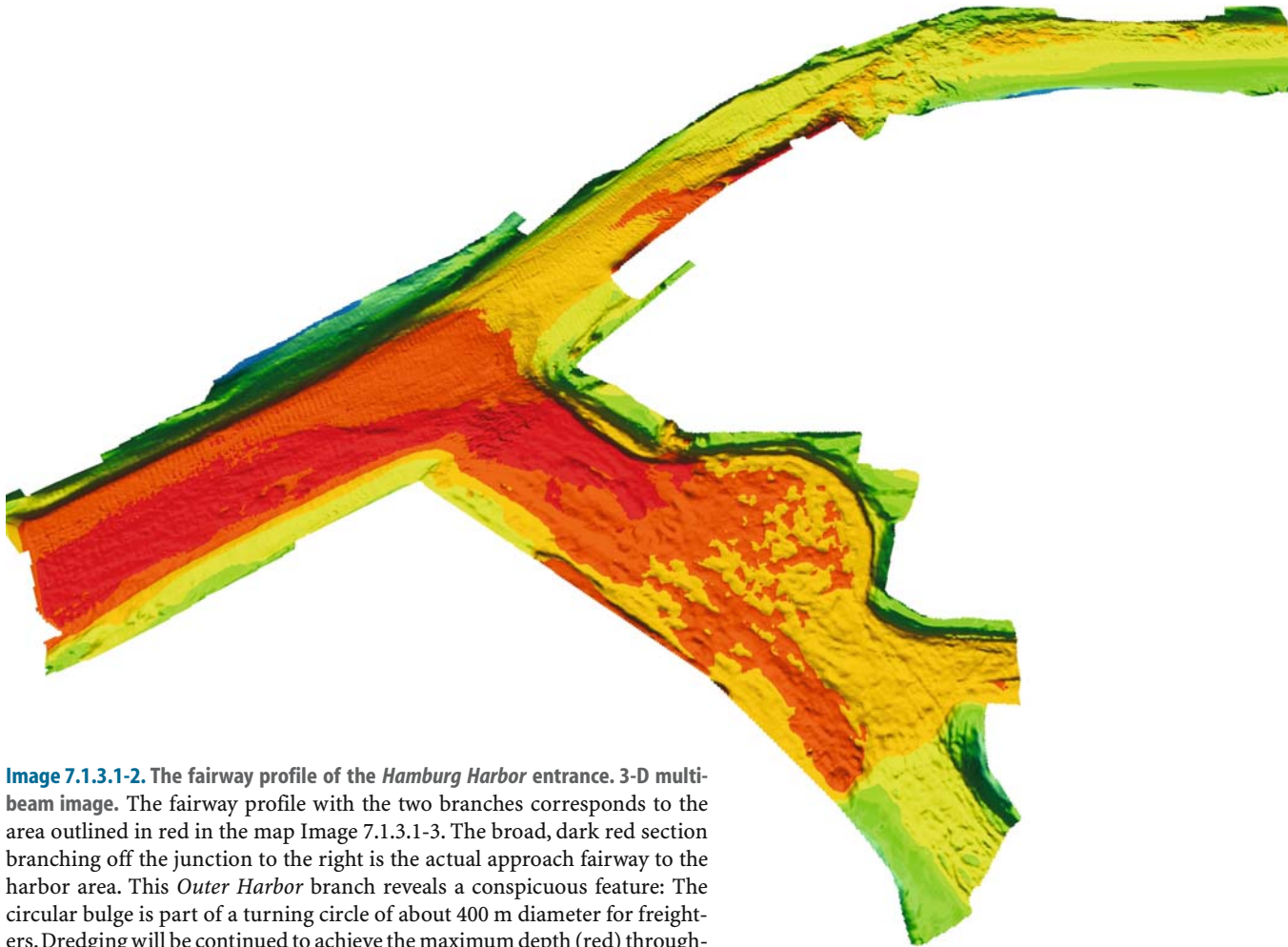


Image 7.1.3.1-2. The fairway profile of the Hamburg Harbor entrance. 3-D multi-beam image. The fairway profile with the two branches corresponds to the area outlined in red in the map Image 7.1.3.1-3. The broad, dark red section branching off the junction to the right is the actual approach fairway to the harbor area. This *Outer Harbor* branch reveals a conspicuous feature: The circular bulge is part of a turning circle of about 400 m diameter for freighters. Dredging will be continued to achieve the maximum depth (red) throughout the circle area and the adjacent main branches, the connections to *Kuhwerder Hafen* and *Rosshafen*. The other comparatively narrow but shallower branch to the east leads directly to a famous part of Hamburg city. The width and depth of this lane are sufficient for smaller international cargo ships like car-transporters, fruit-freighters and also for the largest cruiseliners.

Image documentation: same as for Image 7.1.3.1-1

Image ©: Dieter Seefeldt, Strom- und Hafengebäude, Hamburg, Germany ■

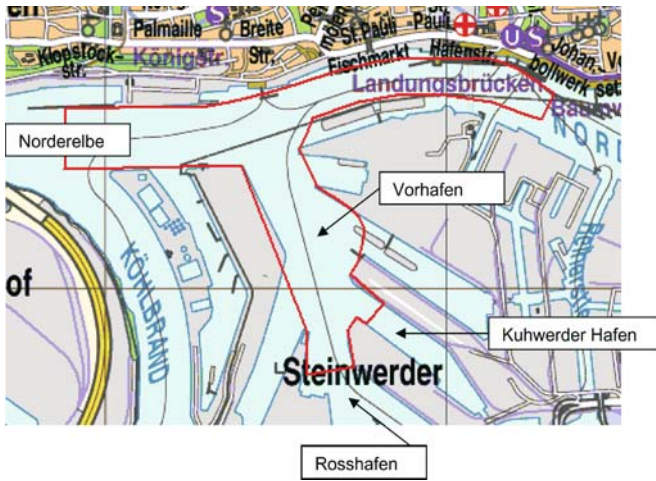


Image 7.1.3.1-3.

Map of the city side of the harbor entrance. The zone outlined in red corresponds to the fairway profile relief of the acoustic multibeam Image 7.1.3.1-2. The eastern branch enters downtown Hamburg with St. Pauli Landungsbrücken. The entire southern area in the map is already part of the *Centre Harbor* area which includes the *Outer Harbor* with the turning circle.

Image ©: Landesbetrieb für Geoinformation und Vermessung, Hamburg, Germany ■

The sounding surveys are carried out regularly once up to ten times a year in defined areas to maintain the safe shipping clearance (Sect. 7.1.1, 7.1.2). This comprehends decisions on dredging activities and on the removal of hazardous obstacles such as lost containers and even wrecks having been acoustically detected and localized. Further surveys are carried out on demand of the responsible authorities and companies in case of necessary repair, rebuild or extension of any kind of underwater and embankment construction. In addition, special hydrological survey vessels acquire non acoustic data of water quality for hydrological surveillance and studies. Of course, the supplementary work of divers is indispensable to inspect the state of corrosion or erosion of constructions in detail. But, the high turbidity of the port sea water usually doesn't permit underwater photography at more than a meter distance.

The Port Authorities of Hamburg operate four different hydrographic survey vessels. Two of them are equipped with single-beam echosounders (SBES), the third one with a multichannel-echosounder (MCES), a

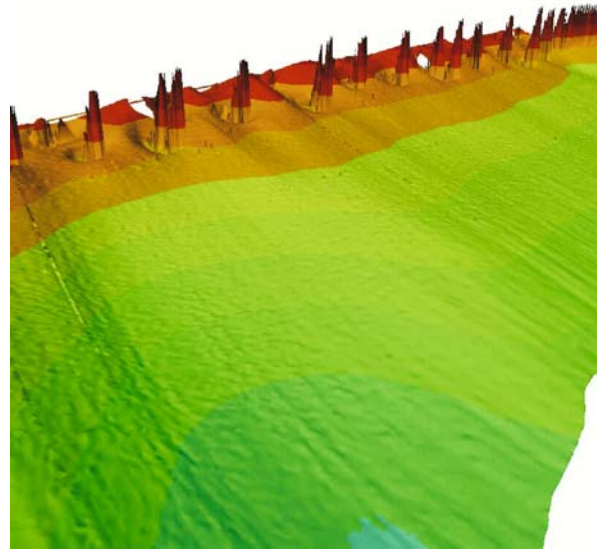


Image 7.1.3.1-4.

Row of steel poles of a quay construction. The image is an example of an underwater inspection of quay constructions, by means of high resolution multibeam imaging. The row of quay-poles is visible with depressions around the poles which are typical of current induced erosion. The quay-plate on top is outside the receiving multibeam fan. The color scale is selected for easy recognition. (White spots: no data.)

Survey conducted by Peil- und Vermessungsdienst, Strom und Hafenaufbau

Survey vessel: *Deepenschriewer II*, 95 tons

Multibeam sounder: RESON, type: SeaBat 8125; 455 kHz, 120°-fan with 240 beams, covering 3.5 times the water depth, center beamwidth: 0.5°, along-track beamwidth 1°

Image ©: Dieter Seefeldt, Strom- und Hafenaufbau, Hamburg, Germany ■

system with 38 echosounder transducers mounted on 2 cantilever booms (Image 7.1.1-13). The last vessel surveys with a multibeam echosounder (MBES), which provides high resolution three-dimensional relief images. The Port of Hamburg was the first governmental user of MBES-technology in Germany. Now also the other authorities apply MBES for the surveillance of the long fairway from Hamburg downstream the river Elbe (Sect. 7.1.2). For special tasks like the identification of hazardous obstacles a high resolution sidescan echosounder (Sect. 4.3) is also in use.

As usual and necessary with all kinds of remote sensing, the hydroacoustic survey data are debugged,

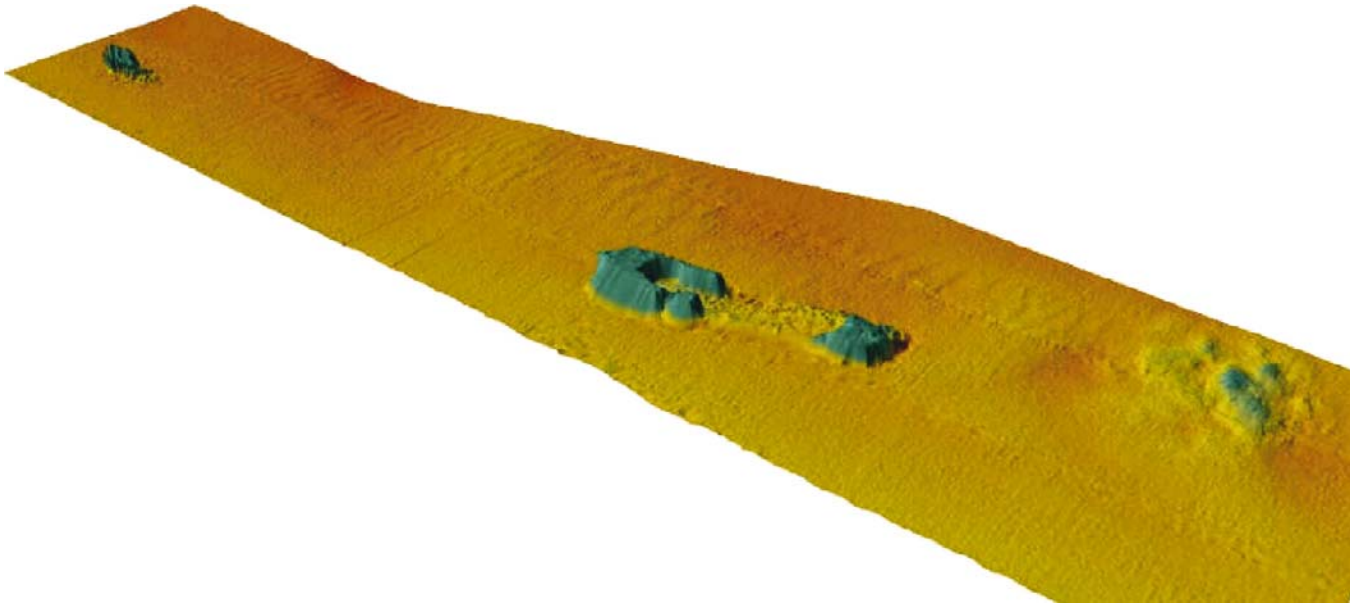


Image 7.1.3.1-5. Ship accident inside the *Port of Hamburg*, mid fairway. 3D-standard grid image computed from *Multibeam echosounder data*. The tugboat and the barge sank near St. Pauli- Landungsbrücken Pier in 2001. The accident area was immediately safeguarded and cordoned off by buoys. Within hours both wrecks were removed and the cordon canceled. The seemingly conical ship hull and the less recognisable shape is the result of the standard grid data treatment.

Accident survey conducted by Peil- und Vermessungsdienst, Strom und Hafengebäude

Survey vessel: *Deepenschriewer III*

Multibeam sounder: ATLAS Hydrographic, type: Fansweep 20; 200 kHz, fan width used: up to 6 times the water depth

Image ©: Dieter Seefeldt, Strom- und Hafengebäude, Hamburg, Germany ■

validated, and processed for the various applications and depictions. The governmental institution of the Port of Hamburg, which is responsible to provide official and standardized data relies on the *Geographic and Hydrographic Information System HydroCAD (GIS/HIS)*. The results are available as survey maps, dredging maps, cross sections, dredging volumes and further depictions when necessary. The service includes hydrographic reference information for other users like the harbor planning board and the river- and embankment engineering and construction board. The continuously extended and improved data base also provides the permanently up-to-date relief chart of 2.5 × 2.5 m grid standard covering the entire port area. The original map can be itemized and zoomed on request and is electronically accessible. A few selected survey examples are presented as relief images, together with sound images from other ports.

7.1.3.2

Inspection of *Canale Grande, Venice*

The profound inspection of the main transport route of *Venice*, the famous *Canale Grande* became necessary because the strict prohibition of dumping was unceasingly violated and safe shipping clearance became at risk. Sound imaging was without alternative for surveying the *Canale Grande* since divers can hardly see their own arm stretched out in the highly turbid waters of Venice. Their work is indispensable however, once the obstacles are detected and their removal is considered necessary. Surprisingly, among the scrap material even car wrecks were found. The main problem to image the cross section of the channel floor completely was the dense boat traffic which forced involuntary interrupts of the survey even at night time. Only the wide angle multibeam system enabled to conduct a successful survey at all and to cover the floor by only one central track from edge to edge.

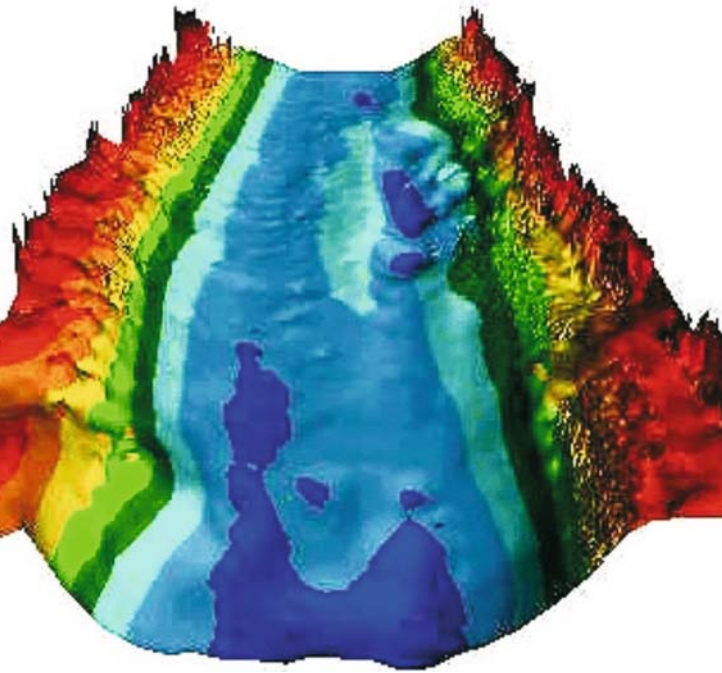


Image 7.1.3.2-1.

A floor section of Canale Grande. 3D-multibeam image. The color coded relief image in central perspective reveals a relatively plane channel floor along this section of 200 m length. There is a kind of shoal indicated light blue near channel axis framing a depression near the shore. This depression is caused by the daily boat thruster activity along the channel. The shoreline is smooth on the left side but conspicuously irregular at the right. Shipping clearance for low draught boats is provided at 1.0 m depth, indicated green. This section of the Canale Grande is 70 m wide and not adjacent to palace fundaments in touch with the water.

Project: Environmental Acoustic inspection of Canale Grande
Survey vessel: small motor launch

Multibeam system: RESON SeaBat 8125; frequency: 455 kHz,
beamwidth: $0.5 \times 1^\circ$, 240 beams, fan width: 120° , dynamic
autofocus beamforming

Positioning and motion control: RTK GPS, PDS2000 RESON
navigation Software, TSS motion sensor, SG Brown Gyro
compass

Water depths: color code: red 1 m; dark blue 9 m in steps
of 1 m

Image ©: Pietro Basciano, RESON MEDITERRANEAN ■

7.1.3.3

The Dock of London: A Dumping Area of Scrap Iron

The scrapped cars shown as sound images were found in the Docks of London within only a small area of a few hundred meters square. The site is about 10 m deep. The 3D-sound images were made occasionally and are only random samples of presumably innumerable scrap parts lost

or dumped in the riverbed to let them disappear from view. This intentional or negligent pollution by anonymous perpetrators is of different dimensions to ship sinking by accidents and disasters, though many of these latter could possibly have been avoided by available safety measures. According to such image documents the sea floor, at least near shipping lanes, is apparently both: a ship cemetery during human history (Sect. 7.1.4, 7.3.2) and a huge dumping place.

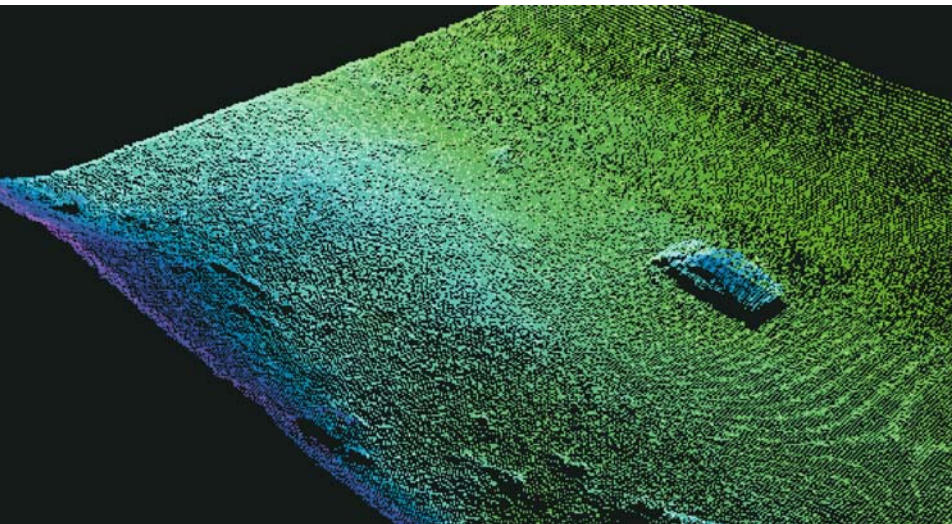


Image 7.1.3.3-1.

Passenger car wreck. High resolution multibeam image. The car was dumped upright by chance upon the riverbed with further scrap parts around. The depiction of the 3D-image is tailored to such objects with steep or vertical elements. For this purpose the image pixels along the sounding lines are not connected by a closed surface but displaced and additionally color coded according to the local depth of the pixel. Further, the scene is illuminated by simulated sunlight to enhance the 3D-impression. This depiction avoids pseudo surfaces closing data gaps in shadow zones ▶

of sound irradiation under slant angles. The moiré pattern is the typical artifact when sampling a grating of narrow lines under grazing angles.

Project: London OI; year of survey: 2002

Survey vessel: *Coastal Explorer*

Multibeam system: RESON, type: SeaBat 8125 with PDS2000 Hydrographic software; frequency: 455 kHz, beamwidth: $0.5 \times 1^\circ$, 240 focused beams; fan width: 120° ; swath width: 37 m at the sea floor of 10 m depth; zoom auto-focus with pixel size 7–15 cm at the water depth of 10 m

Image ©: NCI van Woerkom, RESON B.V., The Netherlands ■

Image 7.1.3.3-2.

Capsized car wreck. High resolution multibeam image. This passenger car wreck has fallen upside down upon the sea floor with a tyre lying behind.

Image documentation: same as for Image 7.1.3.3-1 ■

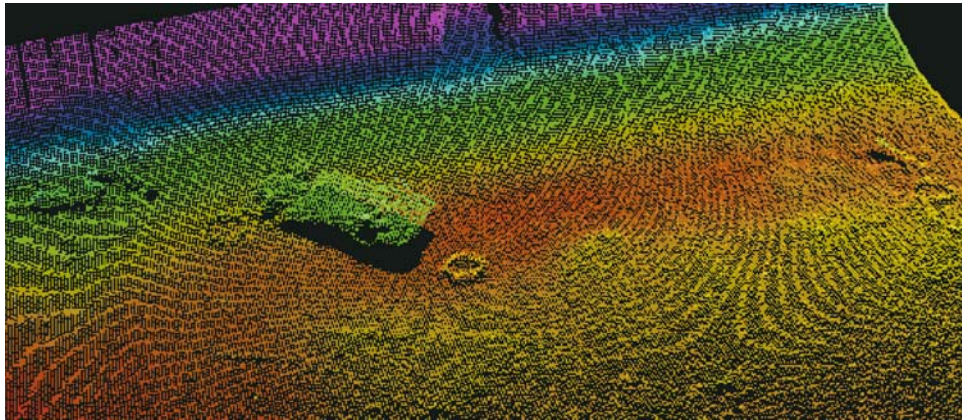
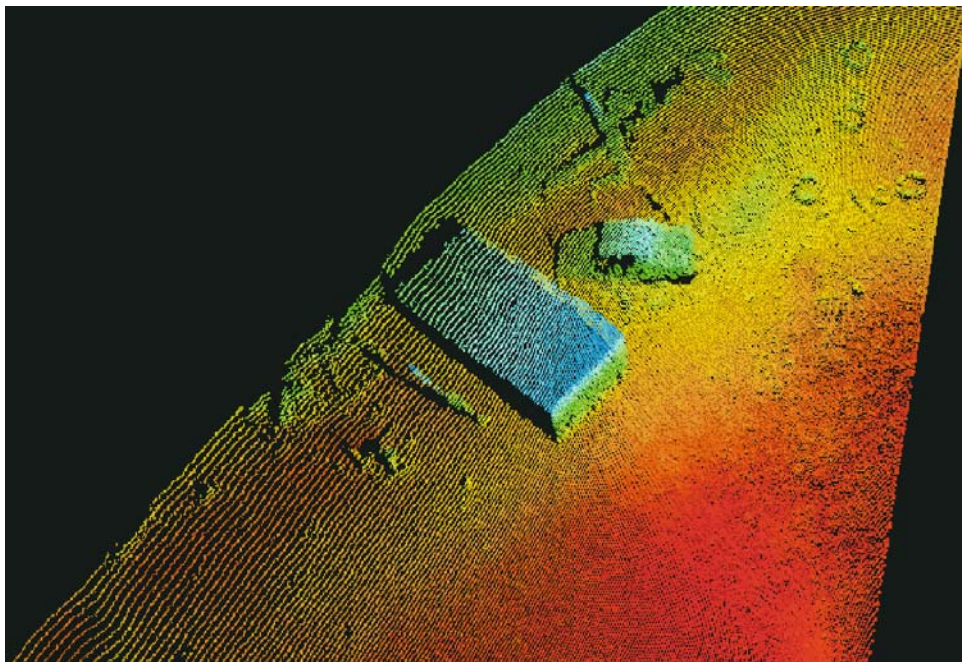


Image 7.1.3.3-3.

Car and container of a truck trailer; imaged by a forward scanning multibeam system. This passenger car is lying upright with the rear window intact and the side window open or broken. The four tyres spread around in the upper right corner of the image appear too large for the car wreck. Possibly they belong to the large box lying to the left of the passenger car, which might be the container of a truck trailer, partially subsided into the sediment. There are several pieces of scrap material distributed around; some look like construction beams. One of them, on the left side of the large box stands slanting in the sediment, visualized by its diverging long shadow.

The multibeam system was tilted for scanning the sea floor in forward direction with the survey vessel sailing 4 knots. The scanning fan of 120 degrees illuminates the objects with an update rate of 20 tomes per second resulting in 4800 depth soundings per second. The distance between the profile lines decreases when the sailing speed decreases, which increases the along-track resolution.

Image documentation: same as for Image 7.1.3.3-1, apart from the horizontal scanning pattern ■



7.1.3.4 Seabed Surveys in the *Hong Kong Area*

This image series is one of the rare cases with depth line delineation presented in the book instead of land-scape depiction. The classical isobath mapping can be

advantageous when measures of sea floor reshaping have to be quantified for planning and comparative confirmation.

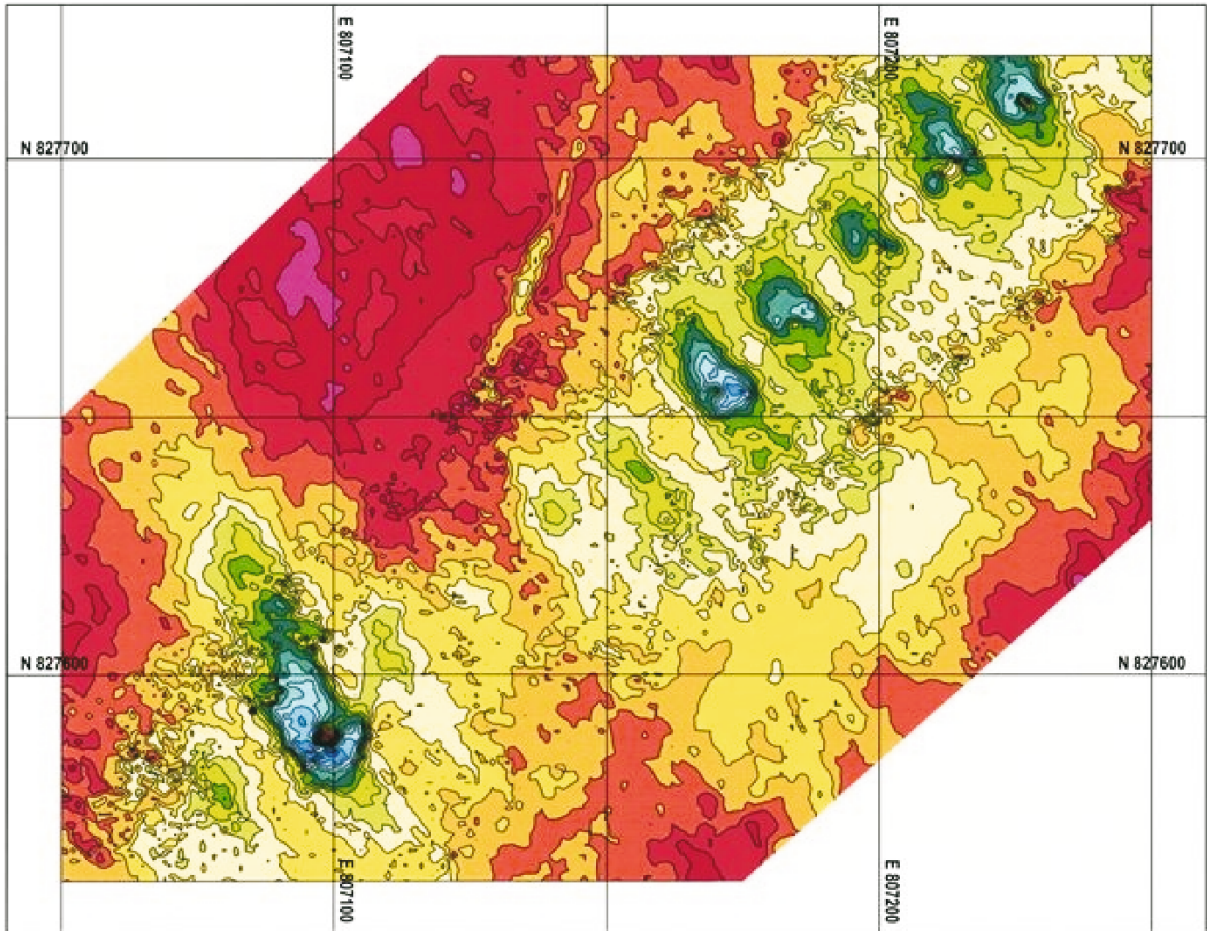


Image 7.1.3.4-1. Sewage outfall diffusers in Hong Kong. Bathymetric map derived from high resolution multibeam surveying. The routine inspection of an underwater sewage diffuser series by multibeam bathymetry in turbid coastal water reveals which of the pipe outlets are operational. This state is indicated by depressions of the muddy seabed, which are kept clear of sediment by the exhaust of sewage from riser pipes. The sewage outfall is an approximately horizontal pipeline, in this case laid in a dredged trench, which was backfilled afterwards. At the end of the outfall a number of vertical pipes rise to the level of the seabed from which the sewage is expelled. The bathymetric map shows these depressions as a regularly spaced set of holes in the seabed. Two of them even reveal the mouth of the diffuser in the middle of the depression. In contrast, the depressions of the blocked diffusers is filled almost to the level of the original seabed.

Project: North West New Territory Sewage Outfall, Hong Kong; year of survey: 1996
Survey vessel: Local Hong Kong Survey Vessel *Luen Hop IV*
Multibeam system: L3 SeaBeam 1180; frequency: 180 kHz,

beamwidth: 1.5° fan width: 153°
Length of the diffuser series: 150 m
Water depth: 25 m. Color code: violet: 20 m; dark blue: 25 m
Image ©: Gijs Nieuwenhuijs, EGS Asia Ltd. ■

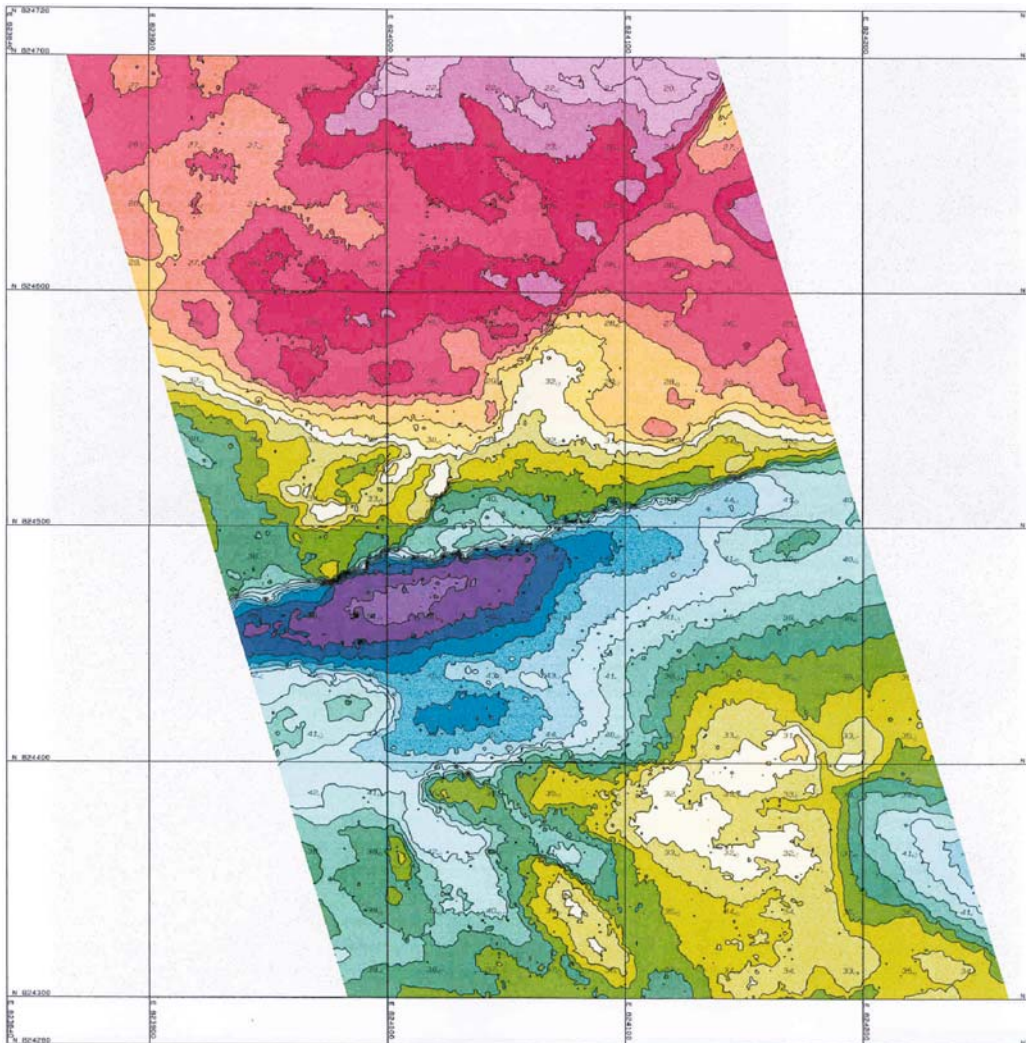


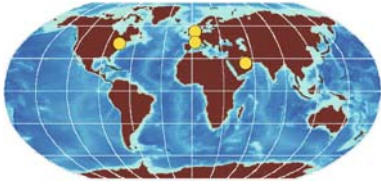
Image 7.1.3.4-2. Seabed exploration off Hong Kong for tunnel drilling. Bathymetric map derived from high resolution multibeam surveying. Submarine tunnels require careful investigations of the sea floor, one of many offshore engineering applications of multibeam bathymetry. Uneven geological conditions along a tunnel alignment will slow the drilling machine and add significantly to the construction costs, also by necessary reinforcement of the tunnel walls.

The bathymetric map shows a seabed channel between the mainland of Hong Kong and the island of *Ma Wan*. The channel formation was already known to be a zone of geological faulting, including a major trench feature along the channel axis. The decisive first task of sea floor engineering was to provide a complete inventory of the geological features of the site to avoid – if possible – the area of heavy faulting. The complex environment and the risks involved required application of the full range of diagnostic tools, including bottom samples from vertical test boreholes. Multibeam imaging of the sea floor relief within a short period of time was the most economic and comprehensive method for guiding the expensive test borehole work to the positions of suspected faults. In addition a sediment penetrating echosounder completes and confirms the findings of the exploration. The bathymetric map indicates local fault alignments and their extent by nearly linear and partially abrupt depth changes.

Project: Ma Wan Water Pipe Installation; year of survey: 1996
 Survey vessel: Local Hong Kong Survey Vessel *Luen Hop IV*
 Multibeam system: L3 SeaBeam 1180, frequency: 180 kHz,

beamwidth: 1.5° fan width: 153°
 Water depth: 50 m. Color code: violet: 25 m; dark blue: 50 m
 Image ©: Gijs Nieuwenhuijs, EGS Asia Ltd. ■

7.1.4 7.1.4 Survey of Wrecks in Coastal Waters



The sea floor in many parts of the world is also a kind of ship cemetery. Maritime battlefields, piracy, and accidents have left countless relics through the centuries and most of these shipwrecks are still in their place, often partially or even totally buried in sandy or muddy sediments. Aside from the fascination glorified ship disasters exert on the public and also on adventurous treasure-seekers, there are several rational reasons for dealing with ship relics: there is the requirement to investigate the causes of actual casualties including sabotage. In shallow waters wrecks can be hazardous to shipping (Sect. 7.1.1). Historic wrecks are technical, cultural and in many cases military records of their time and of human tragedies. In this context such historic relics are the subject of marine archaeology (Sect. 7.3.2–7.3.5, 7.4.1). This research substantiates the governmental establishment of *Marine Protected Areas*. Since recent years there has been particular governmental concern regarding environmental pollution and hazards caused by poisonous or explosive cargoes.

The sound images of this section are mainly selected to demonstrate imaging peculiarities. Partial overlap with the sections dealing with historic wrecks and other relics is intentional. The images provide examples of the highest absolute resolution of advanced multibeam echosounders so far, tailored to shallow water requirements and already attaining with this capacity the limits set by physics. High resolution sidescan imaging demonstrates the supplementary capacity for wreck identification when relief features of smaller scale yield decisive clues. In this context, the wrecks of three large German refugee ships sunk at the end of WW II in the *Baltic Sea* are shown as detail discriminating and -identifying sidescan images: *General von Steuben*, *Wilhelm Gustloff*, and *Goya*.

7.1.4.1 Freighter Sunk in the Persian Gulf

The *Al Mansoura* was a *Saudi-Arabian* freighter carrying iron bars in the Middle East when she hit an oil platform at night. She sank shortly afterwards in a water depth of around 50 m. Both images are derived from the same single run with a high resolution multibeam system by the data acquisition computer. The auto-focused image pixels are intentionally not connected to form a closed surface in order to avoid the irritating curtain effect bridging non insonified shadow zones.

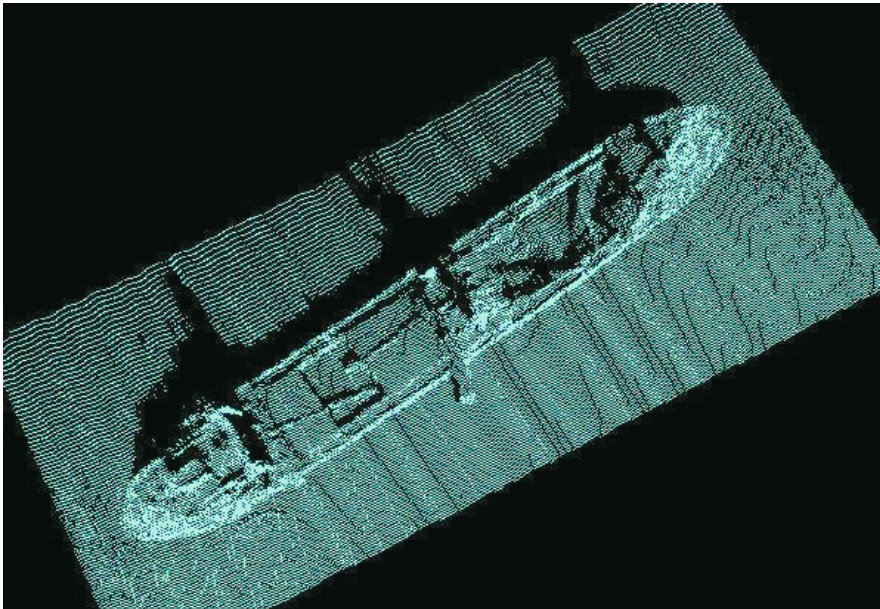


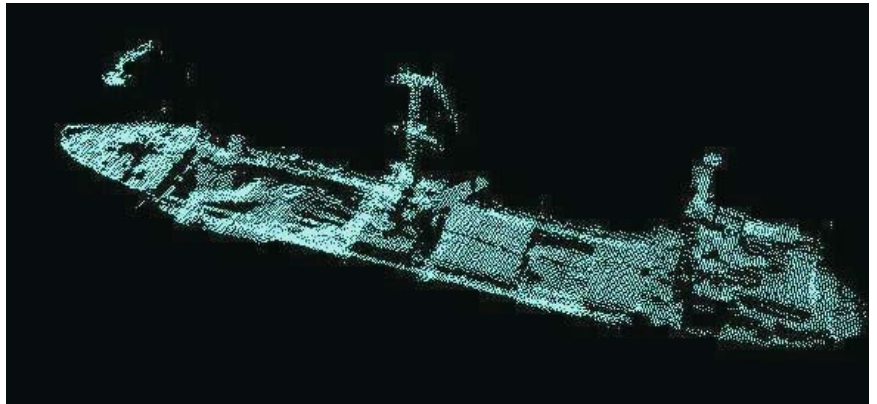
Image 7.1.4.1-1.

Bird's eye view of the wreck. Multi-beam image. The shadow marking the side view silhouette of the wreck reveals that the imaging vessel made its run along the star board of *Al Mansoura*. The computed direction of view is from above: the bird's eye view. The *Al Mansoura* lies upright. Mainly conspicuous is the open bow hatchway with the hatch cover removed or presumably demolished. Otherwise the hull and superstructure with the cranes appear essentially unimpaired.

Image documentation: same as for Image 7.1.4.1-2 ■

Image 7.1.4.1-2.**Side view of the wreck. Multibeam image.**

The superstructure and also the demolished hatchway are visualized more clearly in the side view, looking towards the port side. The two masts, not evident in the previous view are revealed here with construction details. Because of the water depth the wreck is not considered hazardous to traffic lanes and recovery is not required. The invisible portside hull below the superstructure was not irradiated by the multibeam run on the starboard side.



Multibeam system: RESON, type: SeaBat 8125; frequency: 455 kHz, beamwidth: $0.5 \times 1^\circ$, 240 beams, fan width: 120° , zoom auto-focus
The position of the wreck and further details are not available for publication
Image ©: Richard Lear. RESON, UK ■

7.1.4.2**Two Shipwrecks on Plain Sandy Bottom off Cinque Terre, Northern Italy**

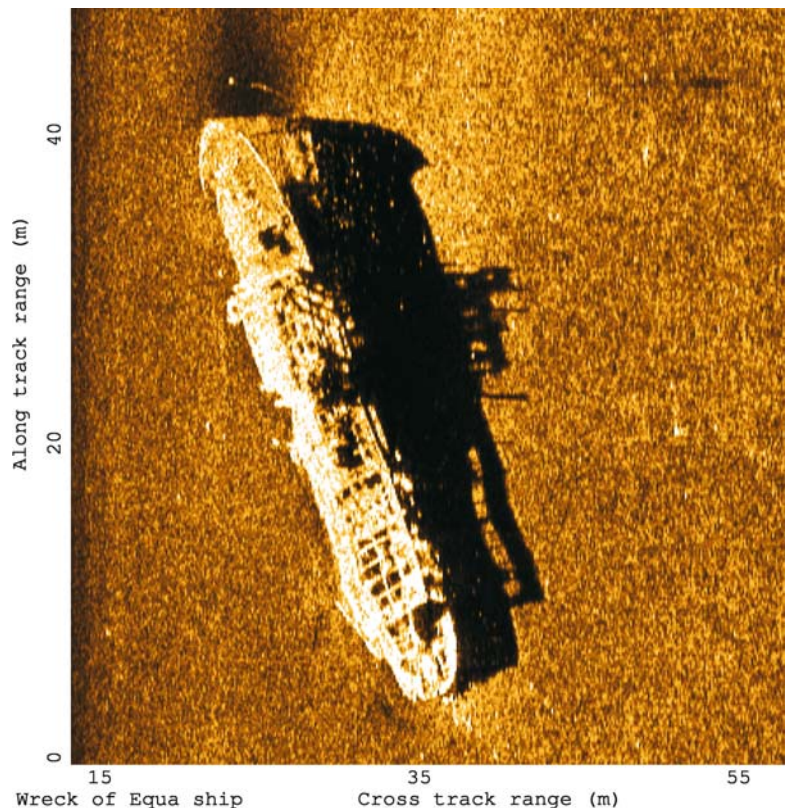
The side scan images of this series demonstrate two peculiarities of acoustic feature recognition: structure

information provided by the object shadow and high-light echo-formation provided by technical structures.

Image 7.1.4.2-1.**Sunken torpedo-boat destroyer. Side-scan image.**

The vessel of about 40 m length appears nearly intact, even with its superstructure indicating the fragile sun-blind construction on the stern side. Advantageous for reconnaissance and salvage work planning is the sidescan image composition of the bird's eye view and the sound shadow with its clear contours, which provide height information. In June 1944 the vessel was rammed by a German ship, sunk and remained upright like many other wrecks found. Safe shipping clearance is not affected here.

Program: BP02 cruise, cooperation of NATO Saclant Undersea Research Centre, La Spezia, Italy, and GESMA, France, 2002; survey area: off Cinque Terre, Italy
Survey vessel: *RV Thetis*, France
Sidescan sonar: Klein, type: 5400; frequency: 465 kHz, swath width: 150 m, athwart resolution: 20 cm at 75 m; water depth: 40 m
Image ©: Edoardo Bovio, Nato Undersea Research Centre, La Spezia, Italy ■



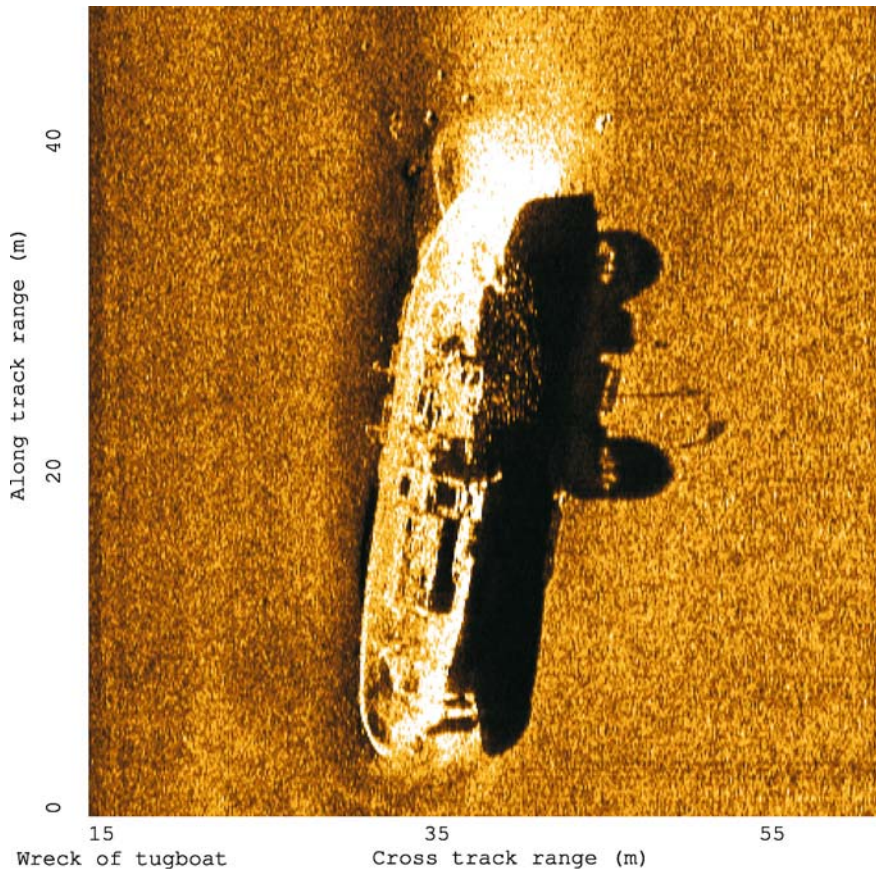


Image 7.1.4.2-2. Wreck of the tug boat *Vittoria*. Sidescan image. This wreck image is interesting as an example of highlight echo formation by technical objects in contrast to natural formations of the sea floor. The extremely bright acoustic highlights coming from the stern are probably generated by so called corner reflectors, known from passive radar beacons and also from rear reflectors of cars. A rectangular re-entering corner reflects incoming slant rays threefold, resulting in exactly backward reflection to the source. The acoustic corner reflectors on the inner side of the steel bulwarks of the ship are an involuntary by-product of the necessary stability achieved by stiffening ribs. Of course pronounced highlight generation by single reflection happens as well with technical objects in the sea when the angle of signal incidence is occasionally perpendicular to a nearly-plane surface. This effect is visible in this image on some parts of the inner side of the bow. We recall that a surface acts as a mirror when its roughness is slight compared to the wavelength of the signal (Sect. 3.4.4).

The shadow with its two “crescent moon” contours indicates – without complicated physics – the round towers carrying fire extinguisher devices. This vessel as well as the ship wreck of Image 7.1.4.2-1 shows very little sea floor erosion, as if the ship had just reached the bottom. Cause and time of the accident are unknown.

Image documentation: same as for Image 7.1.4.2-1; water depth 30 m

Image ©: Edoardo Bovio, Nato Undersea Research Centre, La Spezia, Italy ■

7.1.4.3 Intact Wreck of a Sailing Ship

The reason to show the wreck image of the *Cleona* is not an interesting history. Little more is known than that the ship was built in 1918 and shipwrecked off *Asker* in *Nor-*

way, lying in 18 m water depth. However, *Cleona* is the only intact wreck of a sailing ship in the image collection of shipwrecks presented in this book. Most remarkable: the wreck is still rigged with the slim mast and the two ropes which carried the front sail and support the mast at the bow. Both the superstructure and its plane, strongly

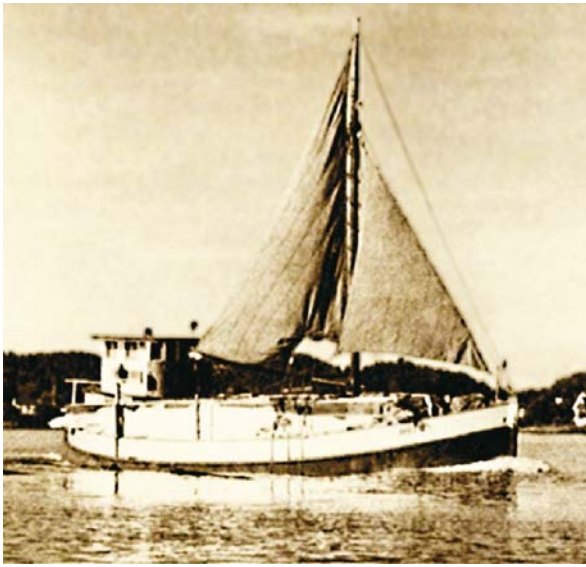


Image 7.1.4.3-1.
Photograph of the *Cleona* under sail. The slightly blurred amateur photo does not reveal details, neither of the superstructure nor of the hatches, only the fact that the rigged vessel has two ropes connected to the mast.

Photograph ©: RESON Denmark, Archive ■

reflecting roof throw sound shadows. Accordingly, the image pixels generated by the auto-focusing fan echosounder of highest resolution are intentionally not interconnected as usual to form a closed surface which would bridge the shadow zones here with irritating pseudo curtains. The slight irregularities of the pixel rows to starboard indicate a rougher sea floor than behind the vessel and at a greater distance. The hatch between mast and superstructure is revealed better than by the photo. It is a small boat however with no further characteristic clues, quite different from the huge ocean liners shown in the subsequent sidescan images.

7.1.4.4 **The Wrecks of the German Refugee Ships *Wilhelm Gustloff*, *Goya*, and *General von Steuben*, Sunk in the Baltic Sea at the End of WW II**

The end of the Second World War caused enormous numbers of German refugees to leave the *East Prussia* of that time towards the west, and finally across the *Baltic Sea* as the only remaining possibility. About

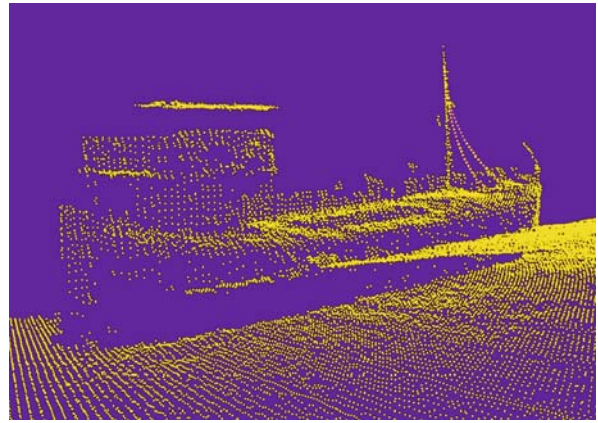


Image 7.1.4.3-2.
Wreck of the *Cleona*. Multibeam image. The sound image shows the starboard side whereas the single-run multibeam track was nearly on top along the portside. Note that the mast is resolved by several rows of pixels.

Project: Demonstration of the SeaBat 8125 on occasion of the users conference in Norway, 2002

Multibeam system: RESON, type: SeaBat 8125; frequency: 455 kHz, beamwidth: $0.5 \times 1^\circ$, 240 beams, fan width: 120° , zoom auto-focus

Image ©: RESON Denmark ■

600 merchant ships of more than 100 tons and nearly 800 warships were involved in the refugee operation. According to documents and estimations between 1.2 and 2 million people were evacuated. The refugee ships facing Russian naval forces were overcrowded and about 250 merchant vessels sunk from torpedoes and bombs. The sinking of the three largest of these ships, the *Wilhelm Gustloff*, the *Goya*, and the *General von Steuben* shortly after departure were the greatest ship disasters of all time. The three wrecks are the tombs of nearly 20 000 refugees, wounded soldiers and crew. Altogether about 40 000 refugees and soldiers lost their lives, according to recent estimations. As stated later by Admiral Nimitz, US Navy, the evacuation by sea was the largest of its kind in history.

The wreck sites of *Wilhelm Gustloff*, *Goya*, and *General von Steuben* are classified war graves and off limits. The positions have been promulgated in the Notices to Mariners, and inserted in nautical charts compiled by the Hydrographic Office of the Polish Navy.

The high-resolution sidescan sound images of these three ship wrecks taken recently by the Polish Navy con-

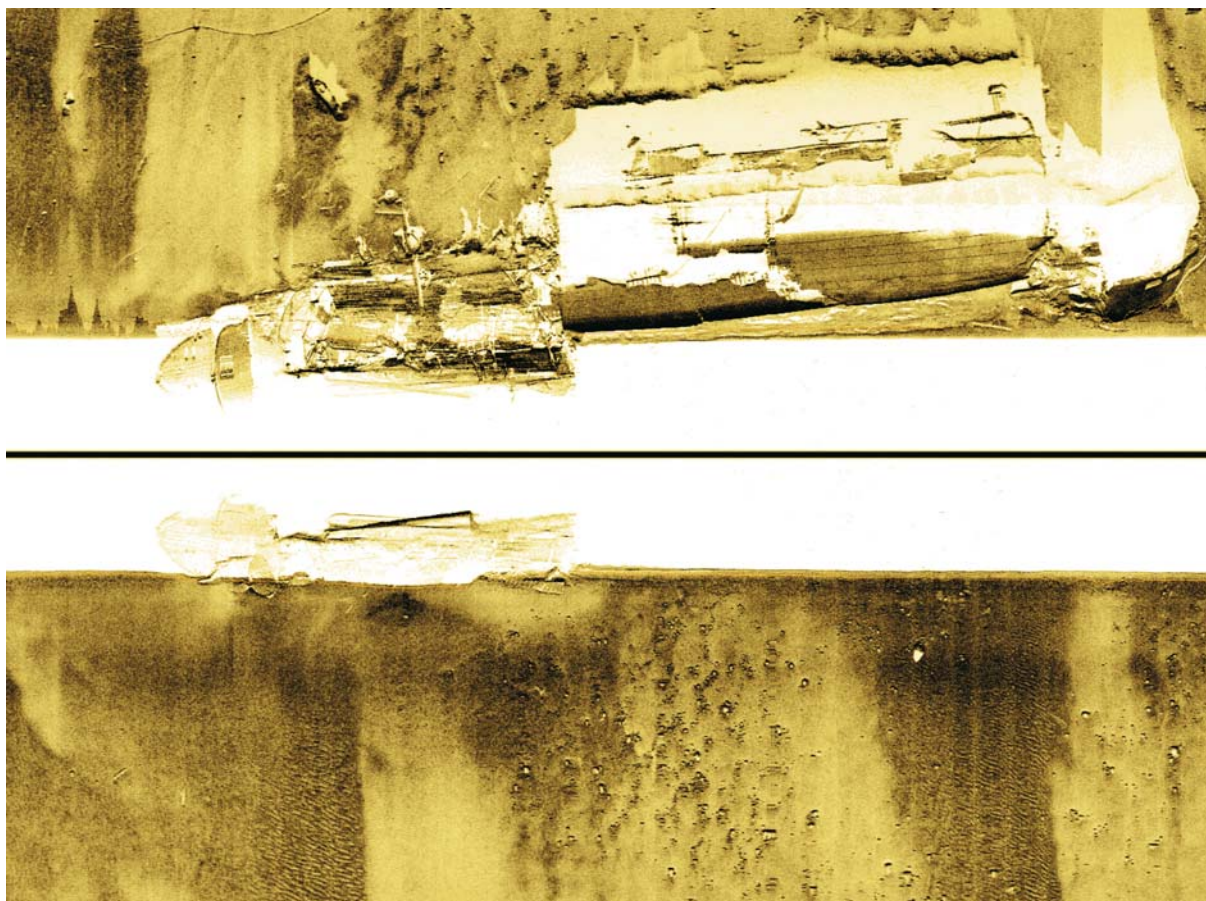


Image 7.1.4.4-1. Wilhelm Gustloff. Sidescan image. The ship of 25 000 tons was commissioned in 1937 by Hitler as the first new liner of the *Kraft durch Freude* (Power by pleasure) fleet. The ship was the largest, most modern and comfortable cruise liner of her time. When the war began she was converted into a hospital ship, served later as a submariner school and finally became the last hope of more than 10 000 refugees and wounded soldiers on board when she was hit by three Russian submarine torpedoes on January 30, 1945 after departure from Gotenhafen/Gdynia. Only about 1 200 people survived. The commander of the *submarine S13* assumed that the *Gustloff*, painted gray at that time, was a regular military troop carrier. In fact, the transport of soldiers was part of the operation.

The sidescan image was taken by a single run slanting along the wreck directly on top of the bow. Thus the image has the inevitable blind stripe in the middle (Sect. 4.3.2) and the ship image appears cut through the bow. Obviously *Gustloff* is broken into three sections: the longer bow section and the shorter stern are lying upright; the longest midship section lies on the starboard side. This section reveals an enormous crevice – presumably from one of the torpedo hits – having torn half of this section open, leaving a deep shadow as the entire mid section and the stern. Part of the superstructure of the midship fragment is still visible, whereas the deck units of the bow section are completely devastated. *Gustloff* is altogether the most completely destroyed of the three ships, the main reason being that Russians divers, who were intensively exploring the wreck in the late 40s and early 50s, used explosives to get inside the ship. They might have looked for the famous Amber Chamber and other missing artifacts. Much of the explosion debris covers the sea floor with a kind of sediment headwall beyond the midship section.

Project: SSS Testing; year of survey: 2003

Survey vessel: *ORP Arctowski*

Water depth: 44 m. The shadows are set bright

Sidescan system: Digital Towed SSS Edge Tech DF-1000; frequency: 100 kHz and 500 kHz; standard Range Settings 100–300 m

Image ©: Czesław Dyrz, Chief, Hydrographic Office of the Polish Navy ■



Image 7.1.4.4-2. Goya. Sidescan image. The ship was a modern twin propeller freighter of the *Hamburg-Amerika-Linie*. Built in Oslo, she was chartered by the German Navy and finally used as a refugee ship and to evacuate people from the easternmost part of Germany of that time. After four successful crossings of the Baltic since 1944 with a total of about 20 000 refugees rescued, the *Goya* departed from the Baltic *Hela Peninsula* near *Danzig/Gdańsk* on April 16, 1945 with about 7 000 refugees, expellees, wounded soldiers and members of a German Tank Regiment. Hit by two torpedoes fired by the Russian *L3 submarine-minelayer* she sank bow first within only seven minutes. About 300 passengers survived. The wreck was discovered by the Polish Navy in April 2004 by means of sound imaging.

The sidescan image of *Goya* is shown with the bow on the right hand side and the sound shadows coded dark, unlike the *Gustloff* image where the negative depiction of bright-dark exchange appears clearer in contrast. Here, the conspicuously bright contours of hatch frames and other elements come from specular reflection at right angle incidence rather than from sound scattering by oblique surfaces. The other side of the sidescan swath containing no objects is cut off here.

The wreck is lying upright and is seemingly intact at first sight. Closer inspection reveals the fracture caused by the torpedo impact behind the bow section with the mast in the middle. This broken off bow section is offset against the rest of the ship's hull, presumably from the bow-first bottom impact during sinking. The section in front of the large superstructure shadow is strongly deformed and cuts through the hatch area with a broad gap in the portside contour. There is further obvious destruction at the stern and amidships. Only the bow and the two aft hatches appear more or less unimpaired.

Project: Shipping Route Survey; year of survey: 2004

Survey vessel: *ORP Arctowski*

Water depth: 70 m. The shadows are set dark

Sidescansystem: Digital Towed SSS Edge Tech DF-1000; frequency: 100 kHz and 500 kHz; standard range settings 100–300 m

Image ©: Czesław Dyrz, Chief, Hydrographic Office of the Polish Navy ■

tribute to the ship identification and enable the documentation of their state. Inspections by divers found only moderate coverage by growth and little corrosion in the water low in oxygen near the sea floor but many

trawler nets torn by the wrecks. The dense coverage by the nets hides part of the ships from the view of photography by divers, but does not screen sound imaging because of its acoustic transparency.

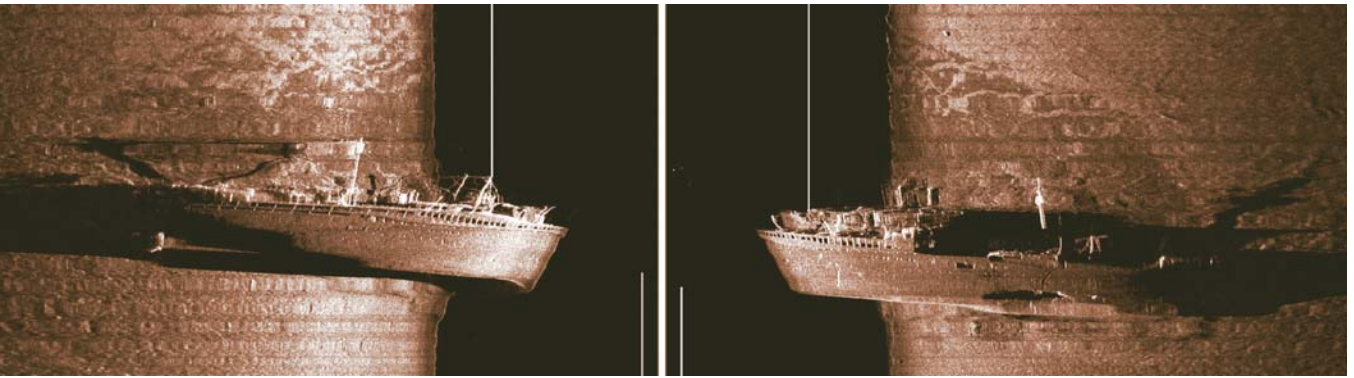


Image 7.1.4.4-3. General von Steuben. Composite sidescan image. The elegant passenger ship of 168 m length, commissioned in 1922, was originally christened with the name *München*. In 1931 she received the name of the famous *General von Steuben* who fought in the *American War of Independence* in 1778 on the American side. During WW II the ship was used as a troopship and hospital ship. In the last year of the war, the Steuben became part of the fleet for evacuating civilians and wounded soldiers from the surrounded *East Prussia* of that time.

On February 10, 1945, the ship with about 4 000 refugees and soldiers was sunk by two Russian torpedoes fired by the same *submarine S13* that had sunk *Gustloff* shortly before and in the same area. About 400 passengers survived.

The double image is the composite of two sidescan runs: the bow on the right; the stern on the left. The shadow is again set dark. The ship lying on her starboard side shows unmistakably the long and broad rupture along the portside flank from one of the torpedoes and an additional vertical fissure branching off the main cleft. Demonstrating details of windows and bull's-eyes rows, the quality of the pair of high-resolution images enables identification with the certainty of a fingerprint in comparison with a photo.

Two remarks on image peculiarities: first, the dark band incised by the ship is the well-known blind stripe of the sidescan echosounder before the sound signal reaches the sea floor. Since the hull is reached earlier, the echo contour is shifted correspondingly towards the line of vertical sound incidence. Secondly, the slightly wavy contours come from the motion of the survey ship, caused by sea waves

Image documentation: same as for Image 7.1.4.4-2 ■

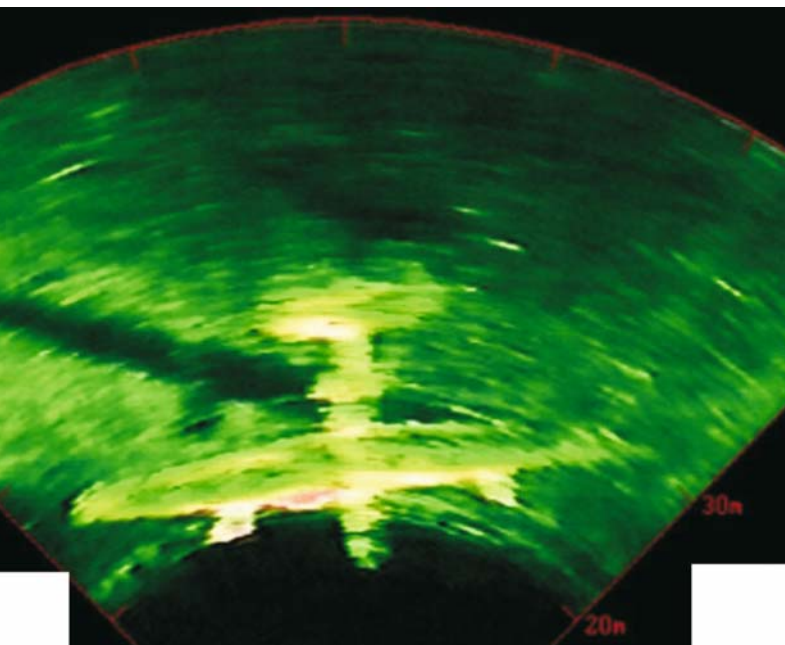


Image 7.1.4.5-1.

A PB4Y-2 Privateer Aircraft wreck on the bottom of Lake Washington, Seattle region, USA. Forward looking 2D-sonar image. The two-engine aircraft of 35 m wingspread has been imaged by a sector panorama system with the typical astigmatism of resolution (Sect. 4.3.4); good in range; less good athwart with 1.5° beamwidth. The resolution cells are nominal 5 cm times 5 m at the specified maximum range of 200 m. Such compact forward looking systems which cover a wide and permanently updated sector panorama and can be operated by small vessels are particularly appropriate in the search phase. For the purpose of subsequent identification and damage inventory, the high resolution downward looking 3D-multi-beam versions are superior, in particular when equipped with autofocus (Sect. 7.1.4.1 and 7.1.4.3, 7.3.2) though the area is covered only line by line when proceeding.

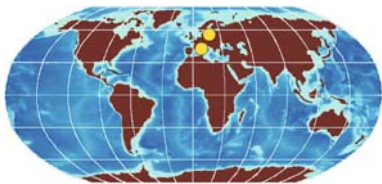
Forward looking sonar: RESON SeaBat 6012, frequency 455 kHz, beamwidth horizontal: 1.5°, vertical: 15°, 60 beams, sector width: 90°

Image ©: Cris A. Sabo, RESON Inc., Goleta, United States of America ■

7.1.4.5 Wreck of an Aircraft Sunk in a Lake at 50 m Depth

The image shown is a rare example of an intact aircraft wreck; the cause of the accident is unknown. Many of the remnants of other aircraft disasters are small fragments strewn over a wide area and cannot be found by means of a hull mounted echosounder of a surface vessel when the casualty happened over the deep ocean. Due to the typical image pixel size of about hundred meters at 4 000 m depth which is the average of the deep-sea floor, not even the wreck of a large tanker can be detected under such circumstances, let alone the identification of it. As it is pointed out and demonstrated in Sect. 7.4.1, the only option to achieve close up sound images of the required resolution in the deep ocean is to apply deep diving facilities such as remotely operated or autonomous underwater vehicles, i.e. ROV and AUV respectively.

7.1.5 Acoustic Search for Buried Objects and Sea Mines



Hunting for sea mines is one of the most demanding challenges and in many cases the most difficult task

of sound imaging. Safety of sea lanes by reliable surveillance (Sect. 7.1.1) is of vital interest, more and more also in times and areas of no declared war. A frequent problem is the natural camouflage of mines by other objects like boulder or scrap metal which may appear acoustically similar to a mine of the typical size and shape of an oil barrel. High resolution sound imaging which reveals complex formations of the sea floor for instance (Sect. 5.2, 5.3) or identifies ship wrecks in type and state of destruction (Sect. 7.1.1, 7.1.4) resolves small objects like mines by only too few pixels when imaged from a safe distance. Thus the acoustic reconnaissance of sea mines requires the judgment of experienced operators and the assistance of divers in the frequent cases of doubt.

Mines lying occasionally on plane, hard, and non erosive ground as so called *proud mines* are the optimum for acoustic hunting despite the resolution limit which can be overcome in principle by closely ap-

proaching, autonomous underwater vehicles (AUV; Sect. 5.4.4). The most severe problem however, is hunting for *buried mines*. Sandy, mobile sediments in shallow coastal areas can bury a mine completely, leaving a flush, inconspicuous floor surface after just one storm. Once a mine is buried flush, the sea wave induced erosive burial process ceases completely. The sediment coverage of just a few decimeters, sufficient to hide the mine from sight of high resolution side-scan echosounders does neither screen the mine sensors nor the explosive charge, which defines the worst case. It happens that a mine buried by a dune is excavated by dune migration but this cannot be part of a search concept. Thus the challenge and chance is high resolution, sediment penetrating, and scanning echosounding which are contradicting requirements and elegant concepts of solution are more welcome than only compromises.

A small buried object like a mine is normally either hidden by backscattered sound from the environment of the mine when the searching beam is broad or it is missed by a narrow beam. Even when the detection is successful, the safe discrimination from mine-like objects, such as equally buried boulder of comparable size requires image pixels of the order of a decimeter or so inside the sediment to achieve at least the imaging situation known from proud mines.

That means: a mine hunting sediment echosounder needs at first a bandwidth of about 5 kHz at a comparatively low center frequency (Sect. 4.4.1). About 10 kHz suffices already because the mine burial is only shallow. And second: the usual requirement of a narrow beamwidth of a few degrees at the center frequency is not sufficient: A conventional low frequency echosounder with a diameter of several meters irradiates the necessary narrow spots only when the beam is focused (Sect. 4.3.5) Moreover, the focus needs automatic zooming when passing the sea floor of varying depth by a surface vessel. And – finally – the focused, zoomed beam needs additional scanning to produce a search stripe instead of a line which would otherwise miss the mine at high probability. Beamforming for the search of buried mines is being realized at present by one conventional and two non-conventional approaches, all of which are still in the state of experimental versions or prototypes at most. It may still need a long and arduous effort before achieving operational systems which provide all essentials: detection *and*

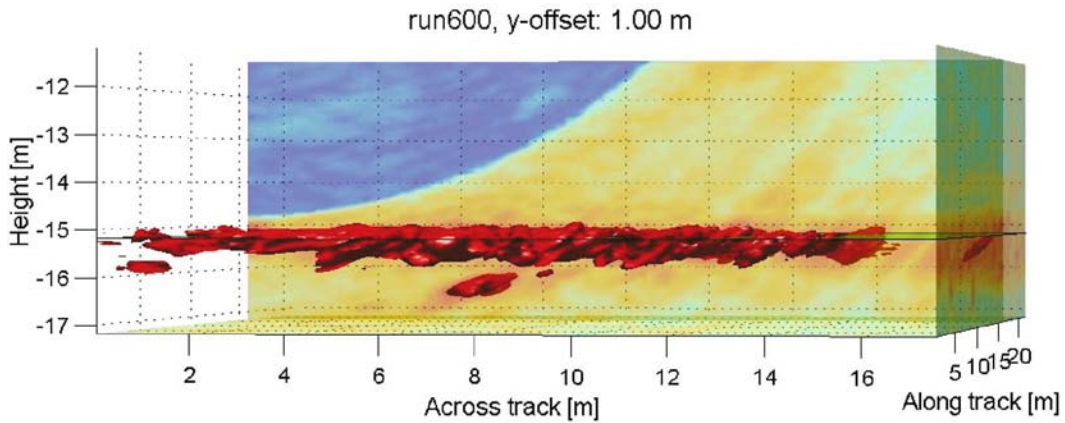


Image 7.1.5-1. Finding of buried objects and sea mines; the conventional approach. Multibeam sediment-penetrating image, enhanced contours. The contour-enhanced acoustic image of a sea floor section reveals a conspicuous, clearly separated “potato-shaped” echo, indicated red, at 8 m across-track. The echo is localized more than a meter below the sea floor surface which is visualized by its sound scattering and depicted as the upper red band. The processed echo comes from a cylindrical sea-mine substitute, artificially buried deeper than normal in sand sediment. The “stunt mine” is a cylindrical concrete-filled steel cylinder of 160 cm length and a diameter of 65 cm, approximately the size of the mine echo.

The single echo and the reverberation are depicted here like three-dimensional bodies with simulated sunlight and shadows similar to most of the sea floor relief images shown in the book. To achieve such a well defined acoustic surface instead of a more random echo scatter (Image 7.1.5-2) the points where the echo level reaches a selected threshold value are interconnected and interpolated to form a closed surface of constant “acoustic brightness”. A volume element which scatters occasionally weaker than its neighbors thus causes a “dent” in the surface. However, this method of surface formation differs from the sea floor depiction, where normally only the signal travel time, not the echo level, is used to define the surface. Of course, the acoustic brightness distribution could also be wrapped on a surface defined only by the travel time, as applied to depict sea floors of varying scattering strength, indicating varying kinds of sediment (Sect. 5.3.6, 5.2.3).

It should be mentioned that such an ideal separation between mine echo and sea floor scattering is not the rule, to say the least. The most difficult but frequent case is the flush buried mine covered by sand. Then the travel time difference is significantly smaller than shown here. Moreover, a single snapshot image as shown cannot yet solve the problem of shape recognition and thus the discrimination from non-mine objects of similar size. (A smaller one is visible at the left hand side and a tiny one was found near the mine echo.) The straight contours of a mine are deformed due to the random scintillation of echo centers of the mine. Superposition of several images taken at adjacent instants of time when passing by, which means slightly different angles of view, would average out part of the “dents” by filling in the occasionally darker spots.

Focusing of the acoustic array (Sect. 4.3.5) was realized for each volume element below, at, and also above the sea floor to include the marker buoy indicating the location of the buried mine. For the purpose of focusing on each volume element the echo signals received by all individual array units were added according to the correct geometry of their respective travel-time to and from the respective volume element. Despite focusing the resolution remains strongly anisotropic: The diameter of the slightly convex “resolution cell” is estimated to be about half a meter here and its “thickness” is 15 cm, the shape of a contact lens as it were. This single vertical cut through the data volume shows also the onset of bottom reverberation at a particular instant of time, as the outer contour of the circular segment indicated blue prior to the first response from the sea floor. The originally divergent sampling of the sea floor by the matrix array of the echosounder is rearranged to the depicted rectangular grid.

Project: Search of buried mines; year of survey: 2001

Survey area: Baltic Sea near Warnemünde; water depth: 20 m; transducer draught: 5 m

Research vessel. *RV Planet*, FWG

Experimental matrix array (EXSESO): 6 horizontal by 18 vertical transducer elements; frequency: 10/20 kHz, beamwidth 3°, inclination of the transducer axis: 30°

Image ©: Harald Peine, FWG, Kiel, Germany ■

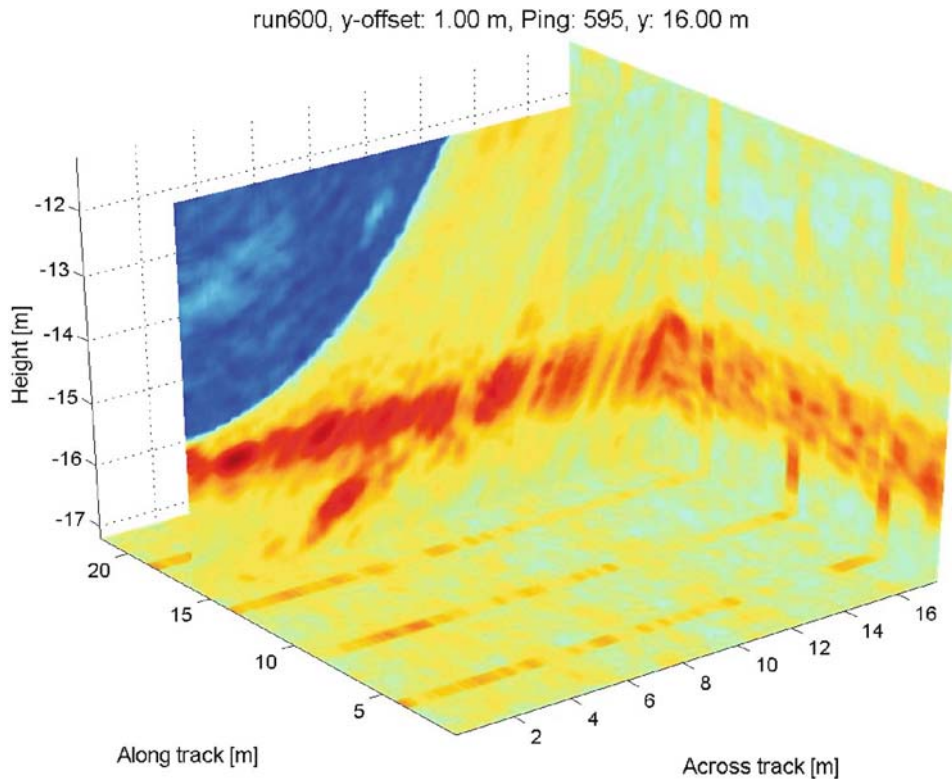


Image 7.1.5-2. Finding of buried objects and sea mines. Conventional multibeam image, depiction of the original data. The data box is identical with that of Image 7.1.5-1. The angle of view is turned here to visualize also the bottom and the rear side of the data box acquired by the echosounder while the survey vessel proceeded along track. Every 20 cm (0.1 s) a new signal was sent out across track. The focused echo response was scanned vertically for every signal ping, thus producing a sequence of vertical slices. The slice shown here at 16 m is the same as shown in Image 7.1.5-1. Again, it contains the stunt mine. Here, the unequal lateral- and radial resolution is even more obvious than in Image 7.1.5-1: the slice shows the series of red arcs of about one meter length but of a minimum thickness of only one to two decimeters. These arcs are the cuts through the resolution cells of “contact-lens” shape. Unlike Image 7.1.5-1, the echoes don’t have the artificially sharpened contours but show the real diffraction transients.

The stripes across track indicate short transponder signals of the experimental set-up.

Image documentation: same as Image 7.1.5-1

Image ©: Harald Peine, FWG, Kiel, Germany ■

reconnaissance of buried sea mines with adequate reliability and area coverage.

The *first, conventional approach* demonstrated by the first two images consists of a matrix of transmitters/receivers which are steered electronically in azimuth and elevation, similar to a fixed radar with phase array technique (Sect. 4.2.4) to scan the scenario of interest in lines and rows. The acoustic version however needs the additional zoom autofocus throughout the entire beamsteering. This is an ambitious technique and con-

ventional only in the sense that the transmitter generates the broad band sound in a linear mode of operation: the frequency of the electric input signal is the same as the radiated acoustic signal, well known from airborne loudspeakers.

The *second approach*, demonstrated by Image 7.1.5-3, is the non-linear method, also named the *parametric echosounder* (Sect. 4.4.2). Up to now it has been mainly used for high resolution echosounding of strongly varying sediment strata. Instead of radiating

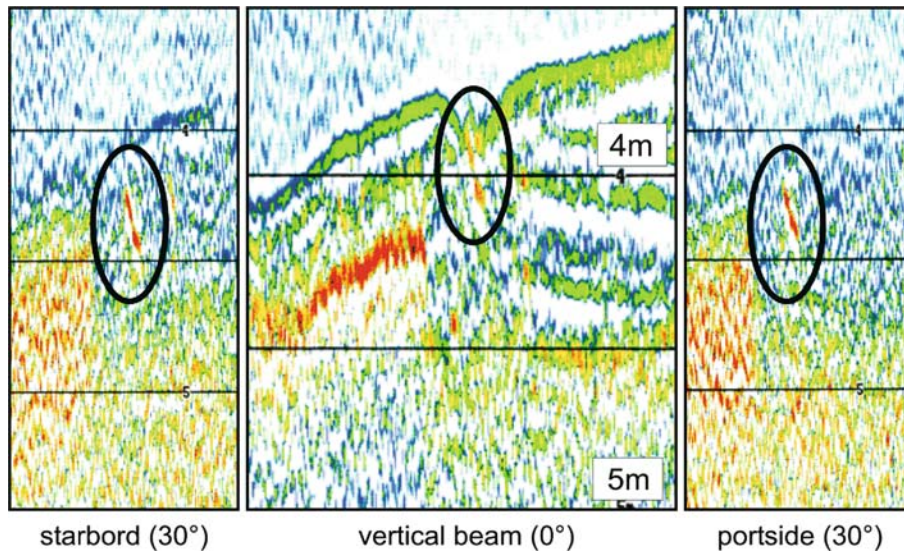


Image 7.1.5-3. Detection of a buried relic of Viking times; the parametric alternative. Imaged by a tilted, narrow beam sediment echosounder. The small oakwood object discovered by sound imaging in the *Schlei Fjord*, western *Baltic* near the former Viking settlement of *Haitabu* is possibly a construction element of Viking times of the 9th century, according to ¹⁴C analysis.

The innovative technique of detecting small objects buried in the sediment is the *multibeam parametric echosounder*. Tilting the very narrow beam accentuates the object of interest and suppresses the otherwise dominating sediment strata. The enlarged image in the middle is taken by the usual view in vertical direction downwards. The only conspicuous feature of the object of interest is a small depression. The buried object below is hardly visible and is dominated by a horizon of pronounced echo formation indicated in orange. The slant views shown from both sides under 30° blur the entire sediment strata to inconspicuous cloudlike areas of the profile and the object comes out clearly.

This image triplet demonstrates an important type of the multibeam application of “pencil beam” sediment echosounders. The seeming weakness of blurring the layers under slant angles is a strength in reality: it converts the parametric high resolution echosounder (Sect. 4.4.2) into a sensitive detector of buried objects within a *search stripe* instead of a *search line*, which would miss all objects between the meander lines. Thus the multibeam parametric echosounder offers both: the peerless advantage of high horizontal *and* vertical resolution in the conventional downward direction of view and at the same time the object finder function within a search stripe.

Project: Acoustic survey of archaeological relics in the Schlei Fjord; guided by: Archäologisches Landesamt Schleswig-Holstein
 Water depth: 3 m
 Parametric echosounder: SES-2000DS, development of Rostock University; tunable parametric frequency interval: 4–15 kHz, primary frequency: 95–106 kHz
 Image ©: Gert Wendt, Institut für Nachrichtentechnik und Informationselektronik, Rostock University, Germany ■

a low frequency signal directly, two high frequency sound signals are transmitted at high intensity by the same high directivity transducer. The water volume in front of the radiating surface reacts slightly non-linearly and thus generates both the sum frequency of the two primary frequencies as well as the difference frequency, though at very low efficiency. The sum frequency is of no interest here because its sound is even more rapidly absorbed in the sediment than the signals of the two primary frequencies. It is the *sound of*

the difference frequency, also named *secondary frequency* which is used to enter the sediment.

This secondary frequency signal has two substantial and surprising advantages: *First*, it maintains the identical bandwidth of the primary high frequency signal. Such a bandwidth of several kHz is difficult to generate directly at low frequencies. The broad frequency band inherited by the secondary signal enables a *short pulse* (Sect. 3.6.6) and thus provides the correspondingly high range resolution when penetrating

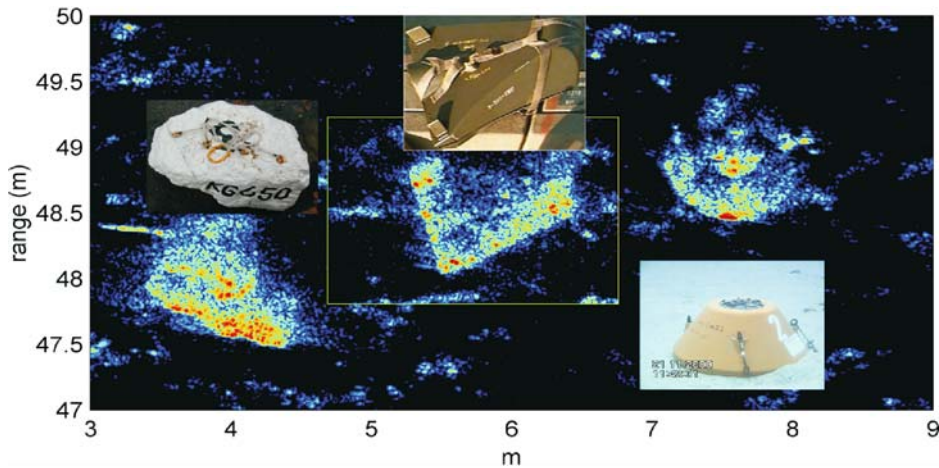


Image 7.1.5-4. Proud rock and mines; the synthetic aperture sonar alternative. Synthetic sidescan sonar image. The *synthetic aperture sonar* image shows, from left to right, a rock, a *Rockan mine* and a *Manta mine*. The *Rockan mine* image in the yellow square inlet was actually in a different position, but at the same range of about 48 m. Photographic images of the targets are shown for comparison. The synthetic aperture processing gives an azimuthal, focussed resolution of 3 cm, 60 times better than the resolution of the physical aperture. Even though the data were obtained by controlled displacement of the sonar along a rail on the sea floor, random deviation from the nominal straight trajectory were large compared to the wavelength. Data driven techniques, together with yaw and pitch sensing by means of gyroscopes, were used to estimate the true sonar trajectory. Note that, in addition to the strong specular echo, a large portion of the lower circular contour of the *Manta* is visible, albeit at a lower dynamic level. Similarly, the front contours of the other two targets display clearly distinct and characteristic features that fit very well with their photographic counterparts.

Project of: NATO Undersea Research Centre, La Spezia, Italy; year of experiment: 2000

Area: Marciana Marina, Elba Island, Italy

Sidescan sonar system mounted on a rail: QinetiQ Bincleaves, UK; frequency 120–180 kHz, beamwidth of the real array: 28° (transmission), 2° (reception), length of the synthetic aperture: 8 m

Image ©: NATO Undersea Research Centre, La Spezia Italy ■

the sediment at the low center frequency. The *second* advantage is as unusual and even more important: the secondary frequency is being radiated as a *narrow beam* – despite the small cross-section sufficient for the high frequency transducer. This narrow beam is formed by the water column itself by radiating the secondary frequency signal. The beam-forming by radiation along the axis of an array is known from television antennas and is named *end-fire array* (Sect. 4.4.6). The longer this kind of array, the narrower the beam. One could say: the non-linear echosounder works as a kind of *synthetic end-fire array*. The effective length and thus the beamwidth depend on the intensity of the primary frequencies, which govern the non-linear sound production along the transducer axis. A beamwidth of very few degrees of the parametric echosounder is typical.

Of particular importance for imaging a buried sea mine is an additional feature: The effective cross section of the radiating low frequency beam is small, much smaller than that of a conventional, unfocused beam. The non-linear approach thus provides the required spot irradiation without autofocus effort. The electronic beam-steering however is necessary – and possible – to provide the search stripe for hunting of mines and other small objects. This second solution appears particularly elegant. The price for the striking acoustic advantages is the poor net conversion of electric- into low frequency acoustic energy.

The *third approach* demonstrated by the Images 7.1.5-4 to 7.1.5-6 is perhaps the most ambitious regarding precision of motion compensation. It is the acoustic version of that kind of synthetic aperture (SA)-principle which is most successfully used by satellite

Image 7.1.5-5.

Buried mines in very shallow water. Synthetic aperture sonar image with an 8–15 kHz sidescan sonar. The *synthetic aperture sonar* image shows a big proud rock (1) at 20 m distance and three buried objects. First: a flush buried water-filled cylinder (2), 2 m long and 0.5 m thick, seen from the broadside direction, second a buried Manta mine (3) and third a buried Rockan mine (4). Both the Manta and the Rockan were buried with their upper rim 5–10 cm below the sand-water interface. The synthetic aperture processing gives an azimuthal resolution of 20 cm, 15 times better than the resolution of the physical aperture or array size. Even though the data were obtained by controlled displacement of the sonar on a 5.3 m high tower moving along a rail on the sea floor, random deviation from the nominal straight trajectory were significant compared to the wavelength. Data driven techniques have been used to estimate the sonar trajectory along the rail. The resolution gain clearly allows the detection of the Manta mine and the classification of the broadside cylinder, but the image shows also that small mines like the Rockan, when buried, may still present a difficult detection problem, let alone the classification of the target in kind. The dynamic sound level range of the image was 17 dB; the maximum echo of the rock and the cylinder saturates the dynamic range.

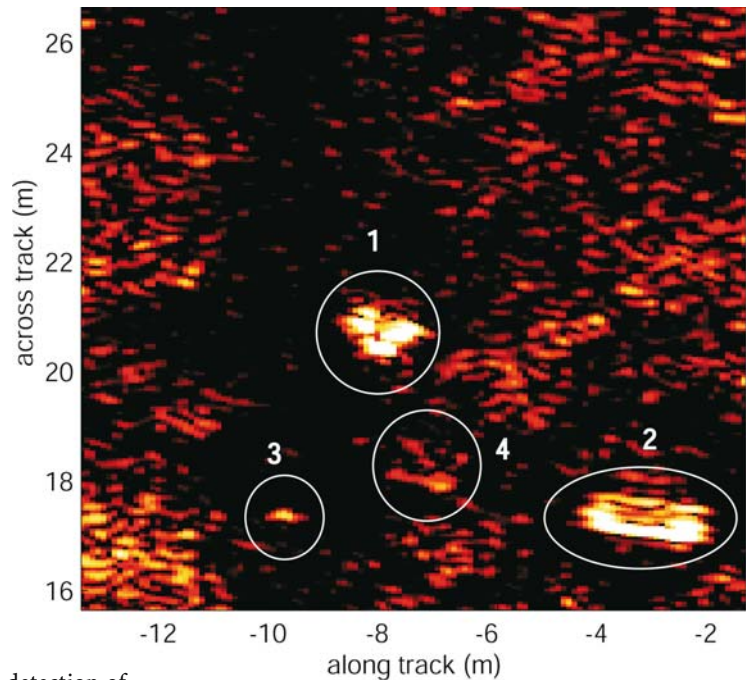
Project of: NATO Undersea Research Centre, La Spezia, Italy; year of experiment: 2003

Area: Marciana Marina, Elba Island, Italy

Sidescan sonar system mounted on a rail: NATO Undersea Research Centre Low Frequency sonar; frequency 8–16 kHz, beamwidth of the real array: 137° (transmission), 8° (reception), length of the synthetic aperture: 6.3 m

Image ©: NATO Undersea Research Centre, La Spezia Italy ■

radar where it is incomparably easier to realize than in the sea. This virtual antenna prolongation provides an extremely sharp beam and excellent image resolution of the Earth's surface taken from the orbit. Translated into acoustics, the idea is simply to take a section of the track of a single echosounder along the ship's course and combine the stored incoming echoes by placing them along a virtual array by the computer as if the array would be real. While the ship proceeds, the virtual array moves the same way by adding new virtual elements at the front end and canceling those at the aft. This works similar to



a sidescan sonar which is also a linear array though at much higher frequencies and thus without the need of artificial array prolongation. However, whereas the sidescan echosounder works simultaneously with all its elements, the synthetic or virtual array has to replace spatial sampling by along-track time sampling and thus relies on imaging a still scenario as it were, in other words: the scenario at the sea floor is assumed quasi frozen during the time of imaging.

This is no serious restriction of course, when dealing with the seabed but the geometry of the synthetic array is all the more a major problem. It requires the precise reconstruction of the real positions of the echosounder at the time instants of the echo arrivals. Precise means: exact within a small fraction of a wavelength. That requirement is easy to fulfill with a satellite and nearly impossible at sea with the inevitably large and irregular motions of a proceeding ship exposed to sea waves, currents, and wind. Synthetic acoustic arrays at sea can thus be realized only when the instantaneous location of the echosounder is known from precise inertial sensors like gyros and accelerometers and by taking the sea floor structure for the final autofocus adjustment similar to an autofocus camera. For demonstration the echosounder can be operated

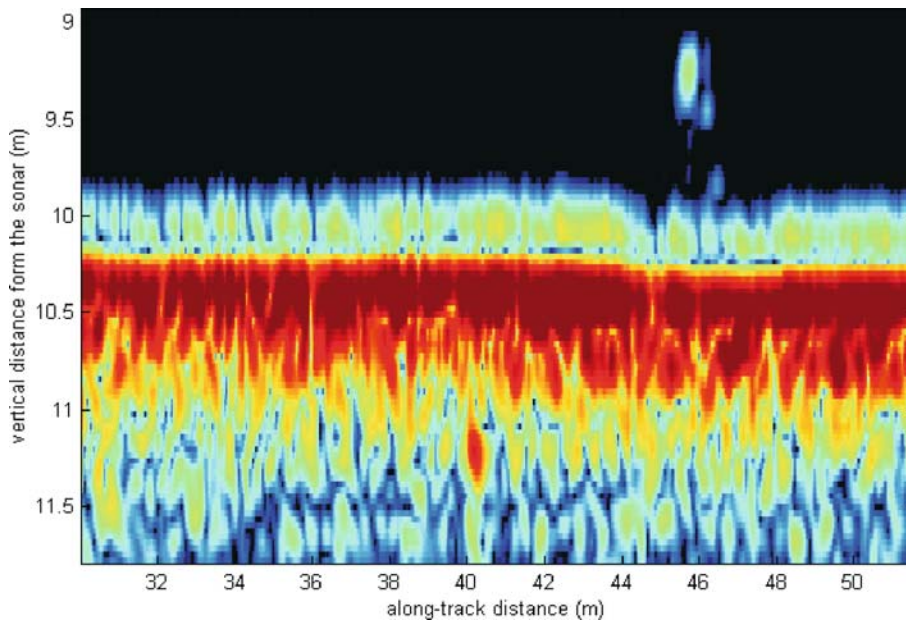


Image 7.1.5-6. Deeply buried mine detection in shallow water. Synthetic aperture sonar image with a low frequency sonar looking vertically down from an autonomous underwater vehicle AUV. This *synthetic aperture sonar image* shows the detection of a 2.30 m long, 57 cm diameter, concrete-filled cylinder, buried in such a way that the top is 1 m below the sand-water interface. The same sonar as in the previous figure was mounted on an Autonomous Underwater Vehicle (AUV) looking vertically down. The AUV performed a linear trajectory at an altitude of 10.5 m above the seabottom, in order to avoid the danger of collision with two towers standing nearby. Both towers (one of which visible in the image) were detected through the sidelobes of the across-track beampattern, allowing the precise geo-referencing of the AUV trajectory. The AUV was flying over the buried cylinder perpendicular to its length. The synthetic aperture processing gives an along-track resolution of 15 cm, 10 times better than the resolution of the physical aperture. The synthetic aperture gain is essential for the detection performance. The displaced phase center antenna (DPCA) technique, together with attitude sensing by means of gyroscopes, was used to estimate the relevant deviations from the nominal linear trajectory. The dynamic range of the image is 40 dB.

Institution: NATO Undersea Research Centre, La Spezia Italy, in collaboration with FWG, Kiel, Germany
 Area: Tromper Wiek, Rügen Island, Baltic Sea, Germany (2004)
 Survey vessel: *Ocean Explorer C* AUV. The experiment was conducted using *RV Alliance* as support ship
 Sonar system: NATO Undersea Research Centre Low Frequency Sonar; frequency 8–16 kHz
 Image ©: NATO Undersea Research Centre, La Spezia Italy ■

on a rail forcing the exactly strait motion. Of course, the autofocus beamforming is necessary anyway for the same reason as with the first approach described above applying the real large array. The advantage of the synthetic array concept would be that the lateral resolution corresponds to an array size that can be made longer than the ship and avoids a towed array.

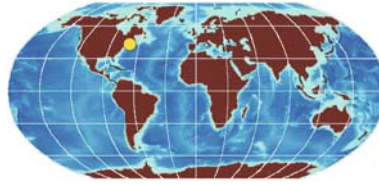
The technology of choice to realize a rail-like motion that is considered to become operational is a non towed, autonomous underwater vehicle (AUV) which carries the *synthetic aperture* low frequency equipment and the motion control- and inertial navigation sensor

package, delivering the data files to the command ship after the pre-programmed search mission. Such AUVs are already in use with real aperture, high frequency systems; and are the peerless solution for under arctic ice research (Sect. 5.4.4) and deep-sea floor reconnaissance (Sect. 7.4), in particular of ship and aircraft accidents. Image 7.1.5-6 presents an image example of a deeply buried stunt mine taken by a SA-AUV prototype-combination. The additional combination with real aperture high frequency acoustic and close-up video systems to include the search for proud mines and other objects appears realistic.

7.2 Submarine Constructions

The examples presented deal mainly with the most extended undersea constructions, which are moreover particularly endangered by various hazards: submarine cables for telecommunication and pipelines for oil and gas transport. The images will illustrate the role of sound imaging in this context rather than inform of technical details and geographic positions of the imaged objects. This had to be respected also regarding breakwater constructions and in particular offshore platforms. Correspondingly, the only subsurface sound image of a platform shown was taken from the research platform *Nordsee*, which was dismantled in 1990.

7.2.1 Submarine Cables



Submarine cables are the longest and most numerous underwater constructions worldwide.

The first fiber optic cable crossed the Atlantic in 1988, 130 years after the first transatlantic cable became operational. At the turn of the 21st century more than 1 million km submarine cables of this revolutionary technology covered the oceans, continental shelves, and coastal waters, with 90% of international communications using them.

The first fiber optic

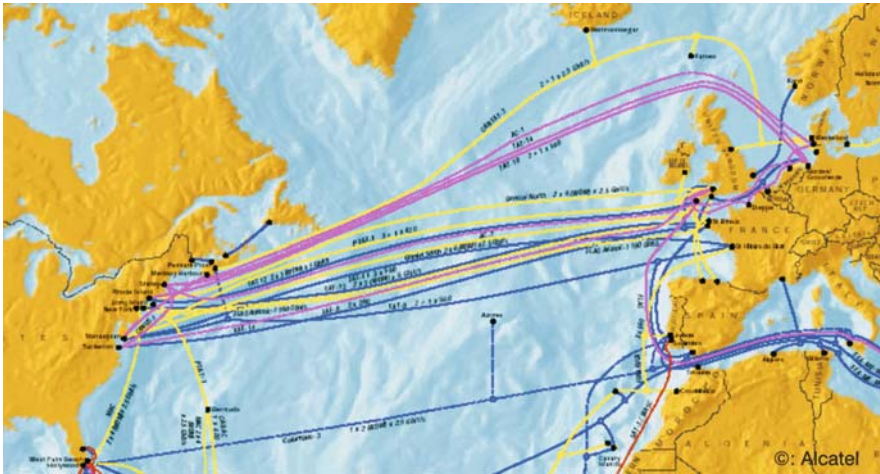


Image 7.2.1-1.

Map of North Atlantic fiber-optic submarine cables. Nearly all of the depicted fiber-optic cables crossing the North Atlantic as of 2003 connect Europe with the main economic and political centers along the upper east coast of the United States. The hub-like concentrations on both sides are evidence of the strong *Trans-Atlantic* ties as well as an illustration of the technical achievement and the need of its protection.

Image ©: Mark Lawrence, Alcatel, Paris ■

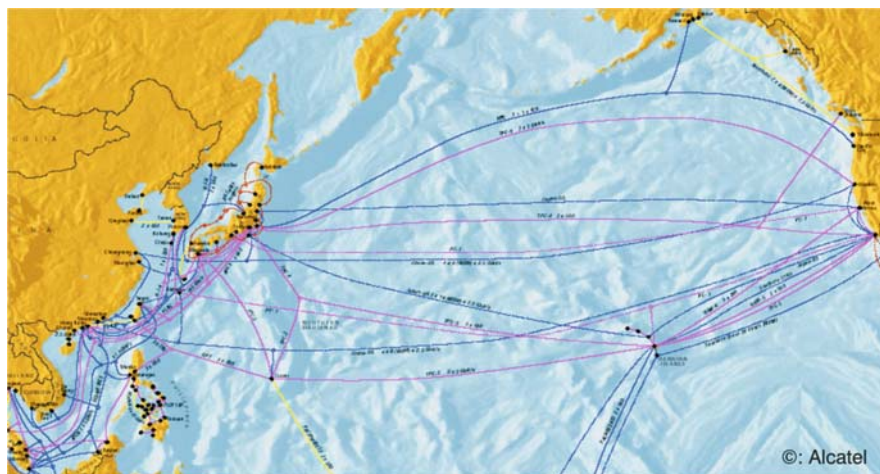


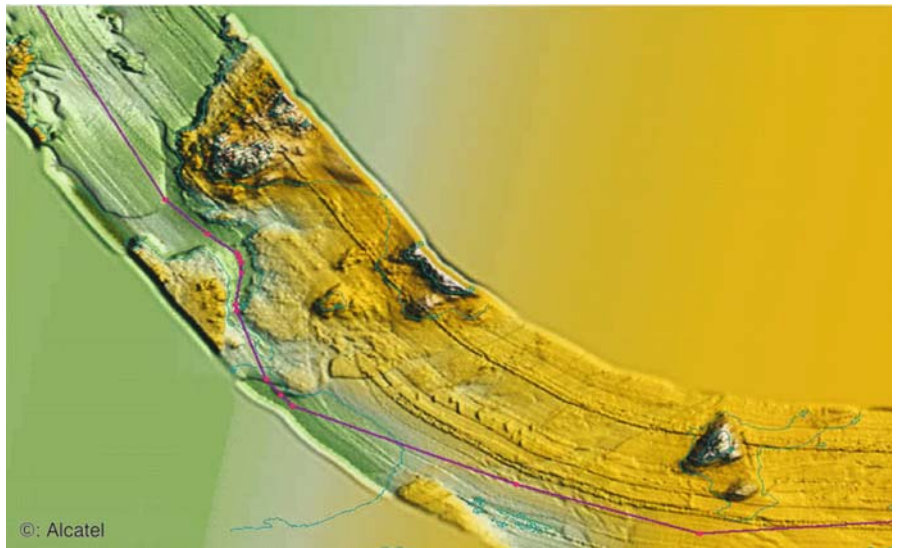
Image 7.2.1-2.

Map of North Pacific fibre-optic submarine cables. The main concentrations of cable connections in the *Pacific* have developed along the coastal areas of *East Asia*. This is where shallow waters require particular effort of cable protection. More than half of the wide spread northern *Trans-Pacific* cables are connections with Japan, in parts via the hub of the *Hawaiian Archipelago*.

Image ©: Mark Lawrence, Alcatel, Paris ■

Image 7.2.1-3.

Section of a projected transatlantic cable route. 3D-multibeam strip mosaic image. This sea floor section of approximately five kilometers in length at a depth of between 40 and 50 m is located in the north-west Atlantic inside the cable route area of the first map. The 3D-image in bird's eye view depiction is a strip mosaic approximately one km wide, composed of 7 parallel multibeam echosounder stripes. The site was surveyed by a dedicated cable survey vessel along the proposed route in a series of parallel runs. The proposed cable route shown in red was designed to follow shallow valleys and smooth slope transitions of the sea floor. The red alter course points of reference connect a polygonal track with as many straight sections as possible.



Project: Route Survey Alcatel, 2000/1
 Company: Alcatel
 Multibeam system: Simrad, Type: 1000
 Image ©: Mark Lawrence, Alcatel, Paris ■

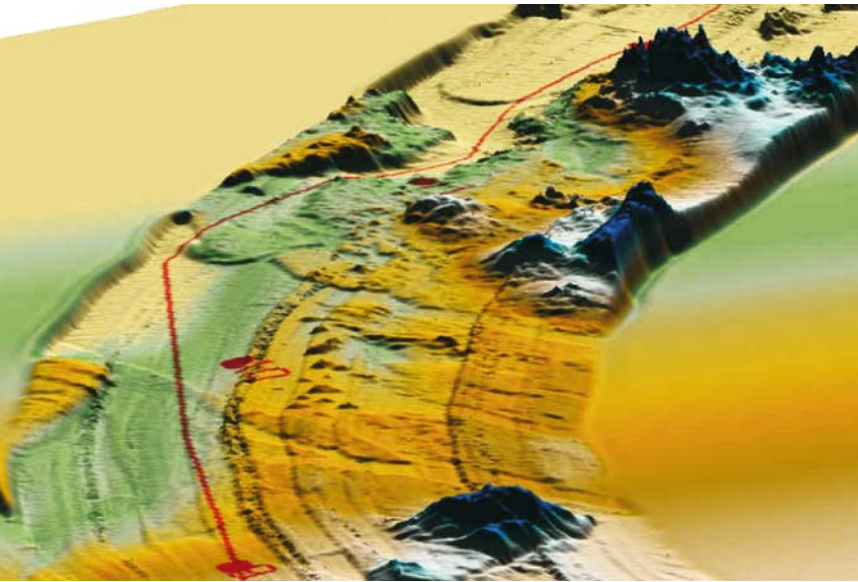
Submarine cables can be very vulnerable. They have to cross hazardous coastal waters where ship's anchors or trawling equipment may break or cause damage to the steel armored cables, which is the reason for more than two thirds of all cable faults. From experience, the only reliable protection over long time periods is to bury the cables deep into the sea floor in areas where they are at risk from external hazards. Submarine cable protection has always been a major concern, from the days of the first undersea connections. It was the original reason for the surveying of the sea floor by the newly invented ocean echosounder in the second and third decade of the twentieth century (Sect. 2.11), mainly however, to avoid the suspension of the cable between outcropping rocks.

At the beginning of the satellite era and the first successful intercontinental radio transmission, many people thought they could hear the funeral bells of the submarine cables, as they were expensive, endangered and limited in transmission quality. At that time however, one could hardly imagine that an explosive expansion of intercontinental communication was about to come, the prerequisite of a functioning and continu-

ously expanding global market. The rapid development of the demand for reliable information and data transfer capacity both in numbers of channels as well as in speed and quality of data transmission could not be met by satellite technology. This urgent requirement was the thrust needed to push forward a second era of submarine-cables. This new era is based on the broadband fiber-optic technology, most recently with a capacity for 100 million simultaneous messages passing along a single cable.

The requirement for cable protection became even more urgent and more difficult when trying to avoid buried crossings with in-service cables, pipelines and other conduits which often occupy the more benign routes. The technical effort required is in fact considerable, in particular in the Far East which is crowded with an immense number of islands of all sizes, many of which are or have to be cable-connected with this modern technology.

Reliable sea floor surveys to identify safe routes for new cables and to avoid damaging already installed cables requires acoustic multi-tool instrumentation. High resolution multibeam echosounders can provide small scale three dimensional bathymetric charts which assist in avoiding steep slopes and trough crossings. Sidescan sonar enables the classification of seabed features, and sub-bottom profilers can confirm a sufficient sediment depth, without hazardous rocks. Problematic sea floors may require a full marine survey. This includes geo-technical surveying by taking samples of the

**Image 7.2.1-4.**

Section of a projected transatlantic cable route. 3D-multibeam strip mosaic image, slant direction of view. The slant view demonstrates the necessity of route optimizing even more clearly than the view from above. There are surprisingly steep rock ridges, leaving only a narrow, benign route for the cable in between, requiring precise route definition. This cut out section shows also several artifacts which look like plough furrows following the surveyed lines. This kind of artifact occurs often at both edges of a multibeam swathe. The sounding beams then touch the sea floor under the most slant angles and the depth uncertainty is maximum. The effort of correcting was not necessary here because the artifacts did not hide the decisive sea floor features.

Project: Route Survey Alcatel, 2000/1

Company: Alcatel

Image ©: Mark Lawrence, Alcatel, Paris ■

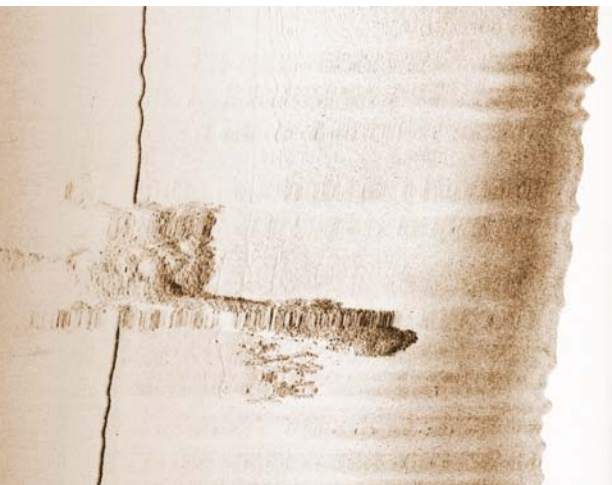


Image 7.2.1-4a. Protection of a cable and pipeline crossing by stone coverage, German Bight; side scan image. The regular surveillance, maintenance and protection of pipelines and other offshore constructions is mandatory for the companies operating the respective constructions. The approving and supervising German authority of the exclusive national economic zone is the BSH, Hamburg. The image example shows a protection measure: a cargo of stones was released to protect a submarine cable crossed by a gas pipeline against friction motions in the tidal area of 30 m depth. The cable was completely buried as is normal for protection from the onset by the cable layer plough. The undulating image of the pipe is caused by ship motion from the seaway. The image is 80 m wide and 400 m along track.

Project: Surveillance of gas pipelines, EUROPIPE 1, 1999

Survey vessel: *FS Gauss*, BSH, Hamburg

Side scan sonar: EG&G, DF 1000. Towed 5–8 m above the sea floor. Frequency: 385 kHz; horizontal beamwidth: 0.5°, unfocussed

Image ©: Manfred Zeiler, Rolf Kunze, BSH, Hamburg, Germany ■

seabed with grab samplers or gravity core devices to determine how hard the seabed is and to what depth the cable can be buried.

These survey systems are being operated by specialized vessels prior to cable laying and parallel to it, together with the towed burial devices. These do the ploughing work down to 1 000 m water depth or more and with ploughs up to 40 tonnes of weight. Supplementing the acoustic tools, magnetometers are used to detect existing cables and pipes. This is necessary because the as laid *Route Position Lists (RPLs)* are often inaccurate when provided prior to DGPS navigation.

The interpretation of the sonar images and geo-technical data requires professional geologists and engineers for off shore constructions – altogether the field of specialized companies with interdisciplinary technical expertise working in international environments. Submarine cable projects represent an indispensable part of the expanding global market. The hardware connection lanes at the sea floor to *transport information* are in fact the counterpart to the sea lanes at the sea surface to *transport hardware* by ship. Both together embody the comprehensive network of intercontinental and global supply.

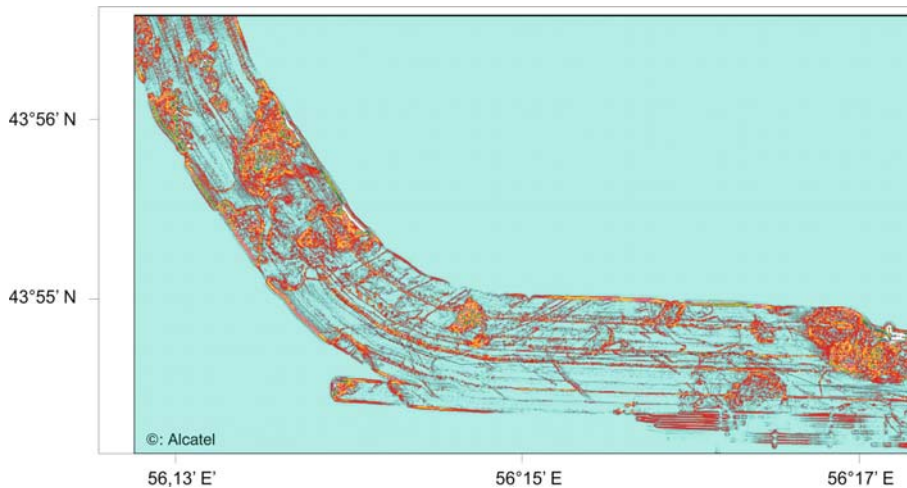


Image 7.2.1-5. Section of a projected transatlantic cable route; map of escarpment slopes. The slopes are derived from the 3D-multibeam strip mosaic map. The benign cable route depicted red in the preceding images differs decisively from the originally projected one indicated black in this image. The artifact furrows stand out more strongly than in the relief images but analysts recognize the real slope distribution by experience.

Project: Route Survey Alcatel, 2000

Company: Alcatel

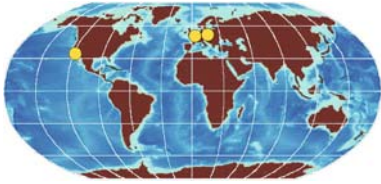
Image ©: Mark Lawrence, Alcatel, Paris ■



Image 7.2.1-6. Jetting tool – equipment for submarine cable burial. The jetting tool with its saw toothed edge jets to 5 m deep into sediments of varying consistency. The jetting blade is mounted on a sledge and towed along the sea floor by the cable lay vessel. The fiber optic cable is guided by a groove on the reverse side of the slant jetting blade. Jetting and cable laying is thus directly combined. Normally, the open furrow will be closed by sediment motion already during the next storm period.

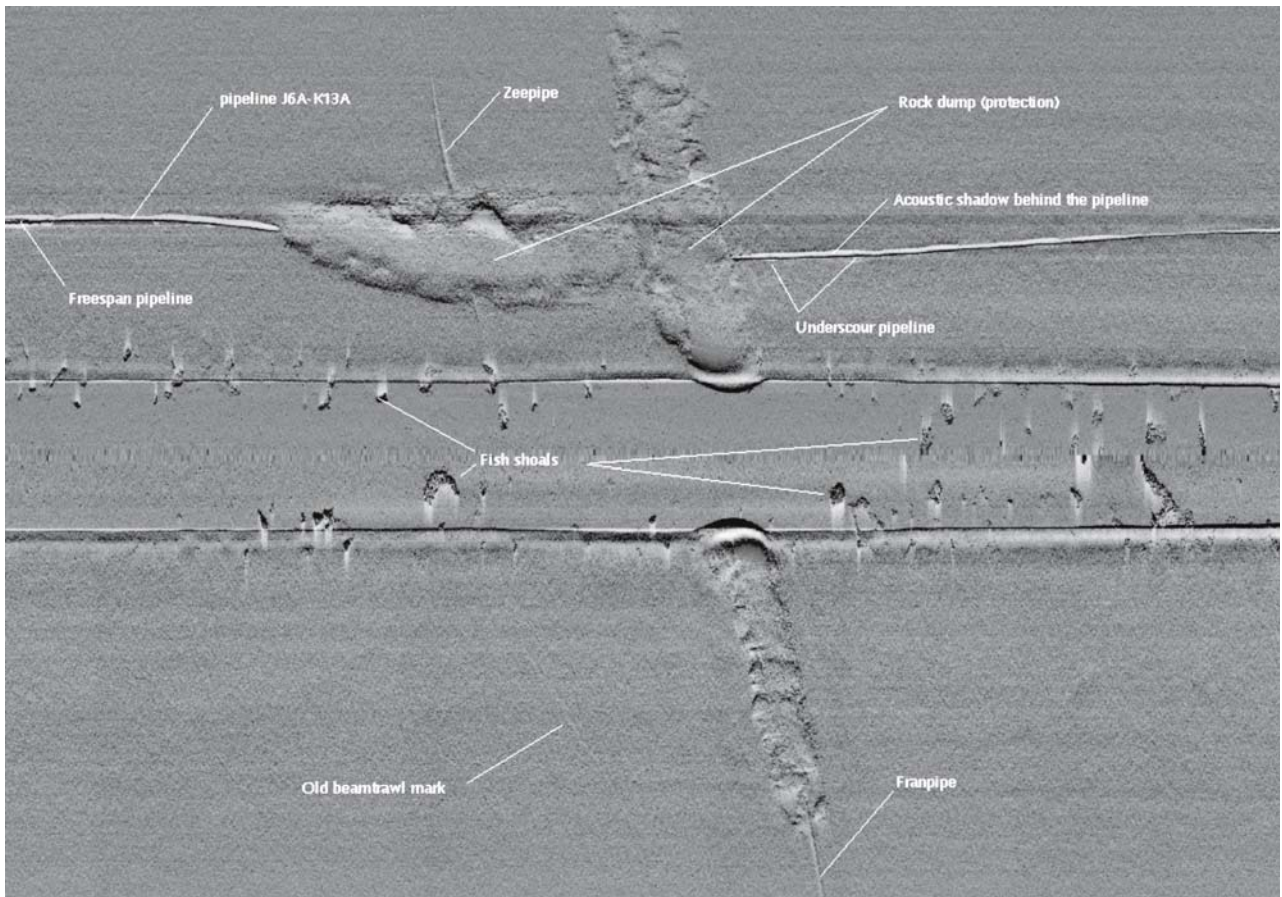
Image ©: Mark Lawrence, Alcatel, Paris ■

7.2.2 Submarine Pipelines



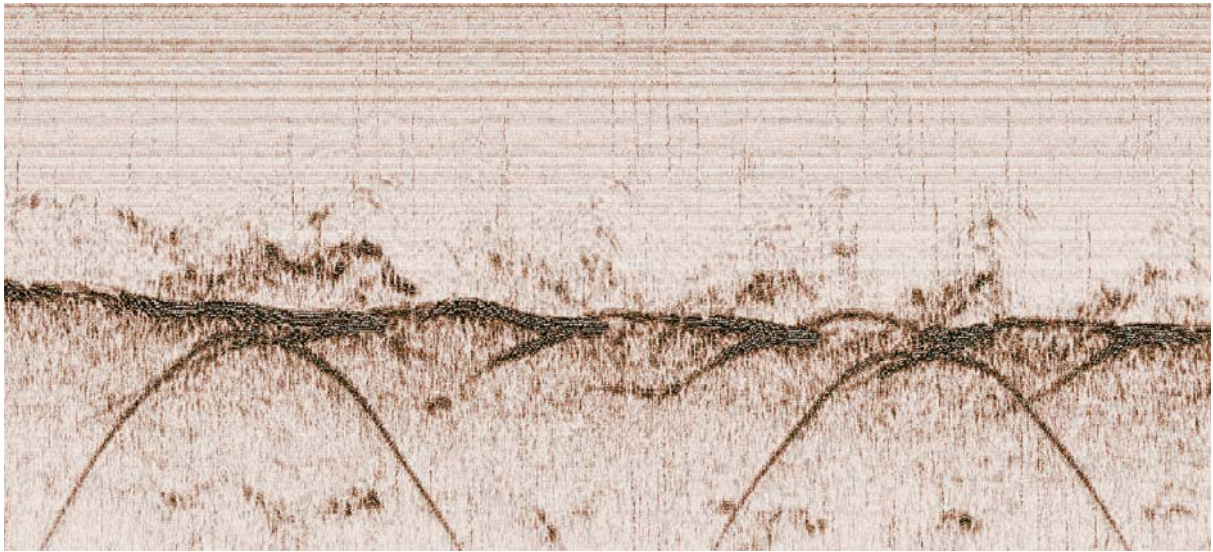
Whereas submarine cables for telecommunication connect land stations, submarine pipelines are usually the connections between pit-heads in the gas and oil fields and the refineries on land. The main tasks for sound imaging are the support of route planning, control of implementation and the surveillance of any potential damage afterwards. The planning phase includes identifying the optimum route to minimize costs and risk of damage. The risk of breakage by involuntary free span on rugged or mobile soil is

even greater than for submarine cables and more difficult to avoid in deep water where sound imaging of sufficient resolution requires substitution of surface vessels by deep diving units (Sect. 7.4.2). In shallow, coastal waters, the predominant hazard is often trawling, casting and weighing anchor but free span in tidal areas with migrating dunes and megaripples is also a frequent hazard. Burial is normally the most effective protection and the method of preference for protecting submarine cables is burial by jetting ploughs (Sect. 7.2.1). However, the much larger diameter of pipelines and their correspondingly larger bending radius make safe handling difficult. One of the protection methods applied for critical pipeline sections crossing shipping lanes or other pipes or cables is by fixing and burying them by casting shiploads of stones.



The permanent task subsequent to the implementation of the submarine construction is thus the surveillance of operational pipeline networks including underwater pipe connections and ramifications. Three methods of acoustic imaging are applied, alone or in combination. Two dimensional sidescan imaging is often preferred as the primary

survey technique. It is the cheapest technology for achieving sufficient resolution and a broad swath carpet. Expert interpretation of the images decides whether additional three dimensional multibeam high resolution imaging is necessary to confirm a suspicion of hazardous vertical displacement. This may require also sediment penetrating echosound-



◀ **Image 7.2.2-1. Pipeline crossings. Sidescan sonar image of the external structure.** The *sidescan sonar* image of 2002 shows two pipeline crossings: The gas pipeline of 24 inch diameter between the North Sea gas production platforms *J6 Alpha* and *K13 Alpha*, crosses the 40-inch gas pipeline *Zeepipe* to *Zeebrugge*, Belgium, which is nearly completely buried, and the 42-inch gas pipeline *Franpipe*. The crossing areas are protected by gravel dumping. The image visualizes that sections of the 24-inch pipeline are underscoured (on the right) and even dangerously in a state of free span (on the left) from the details of the shadows. (Echoes of fish shoals are visible near both onset lines of the sidescan sonar image on the sea floor, symmetrical to the image axis but they have been received earlier, due to their difference in distance from the sea floor).

Institution: Rijkswaterstaat, North Sea Directorate
 Area: North Sea, Dutch Continental Shelf
 Survey vessel: *Zirfaea*, RWS DNZ
 Sidescan sonar system: Ultra; frequency 325 kHz, beam-width 0.5°
 Image ©: RWS DNZ ■

Image 7.2.2-2. Pipeline crossings. Sub-bottom profiler image. The image visualizes the *Zee-pipe* (40 inch) and *Franpipe* (42 inch) as a vertical cross section, similar to a seismic cut. This image is less self explanatory than the preceding side-scan sonar image. Instead of the two expected dot-like echoes from the buried pipes several meters below the seabed when the sounding vessel passes them abeam immediately on top of them, the pipes produce echoes in the form of hyperbolas. The reason is the poor directionality of the low frequency sediment penetrating sounder applied. It receives the echo already at slant ranges before crossing the pipe and also after. The other “half hyperbolas” are presumably echoes from the smooth but asymmetric sand dunes which produce a noticeable echo mainly on their steeper side. (The fish shoals near the bottom appear like dark clouds in this image, also with a kind of hyperbolic shape.)

Institution: Rijkswaterstaat, North Sea Directorate; Area: North Sea, Dutch Continental Shelf
 Survey vessel: *Zirfaea*, RWS DNZ
 Sub bottom profiler system: ORE pipeliner; frequency 3.5 kHz, range resolution about 1 m
 Image ©: RWS DNZ ■

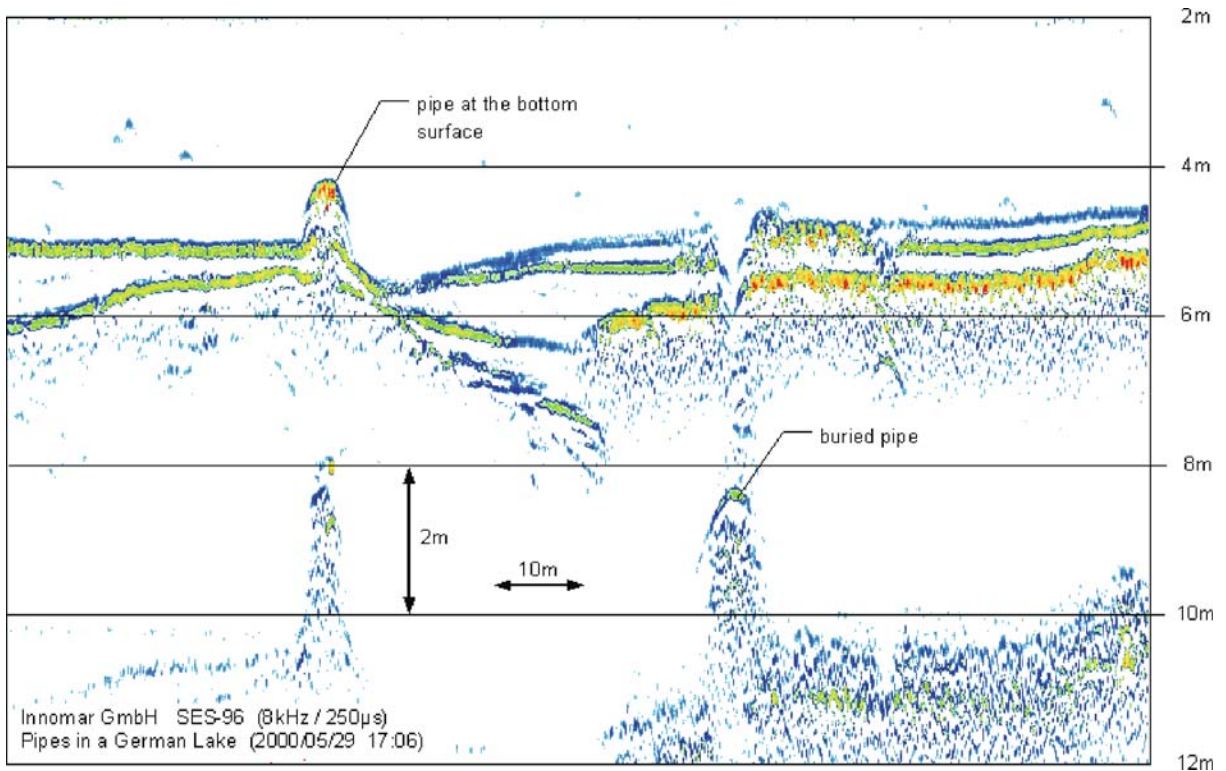


Image 7.2.2-3. Proud and buried pipe. Parametric sediment echosounder image. The parametric method of generating narrow beams with high depth resolution at sediment penetrating frequencies (Sect. 4.4.2) is also a candidate for the surveillance of pipelines on the sea floor. The narrow beam is of advantage when the actual state of hazardous scouring by currents has to be determined quantitatively. It can be of similar importance to ascertain the thickness of the protective sediment cover in sea areas of migrating dunes.

The sound image made in a shallow lake shows – like a model demonstration – a pipe on the left which appears in the state of *free span*, the most dangerous state in the open sea. The bottom on the right side of the pipe appears deeply eroded with sediment layers deformed. The direct echo of the pipe at 4 m depth appears a second time, though much weaker, at 8 m depth produced by the sea surface as a mirror of the primary echo. A kind of opposite extreme is visible on the right side of the image. The pipe is buried or more correctly: sunken 3 m deep, however with an open furrow on top which suggests a soft muddy sediment at this place. Both pipe echoes appear widened by mustache-like tails, the typical hyperbolae due to the finite width of the sounding beam. A sediment echosounder with a wider beam will have ‘seen’ the pipe under slant angles already earlier, and still later indicated by longer mustache tails (Image 7.2.2-2) instead in this nearly vertical view only. The short hyperbolae are also apparent at the steeply incised flanks of the furrow on the right.

Project: Test of pipeline detection in a lake

Survey vessel: small motor boat

Parametric echosounder: SES-2000DS, development of Rostock University; primary frequency: 95–106 kHz, tunable parametric center frequency 8 kHz, bandwidth 4 kHz, depth resolution 20 cm

Image ©: Gert Wendt, Institute of Telecommunications and Information Electronics, Rostock University, Germany ■

ing to clarify a potential and unintentionally deep burial. The former two imaging techniques document also whether contacts with trawling equipment or anchors have taken place, because their high reso-

lution visualizes the scars of the sediment sensitively and reliably. Images taken by all three methods are shown, though with incomplete documentation for obvious reasons.

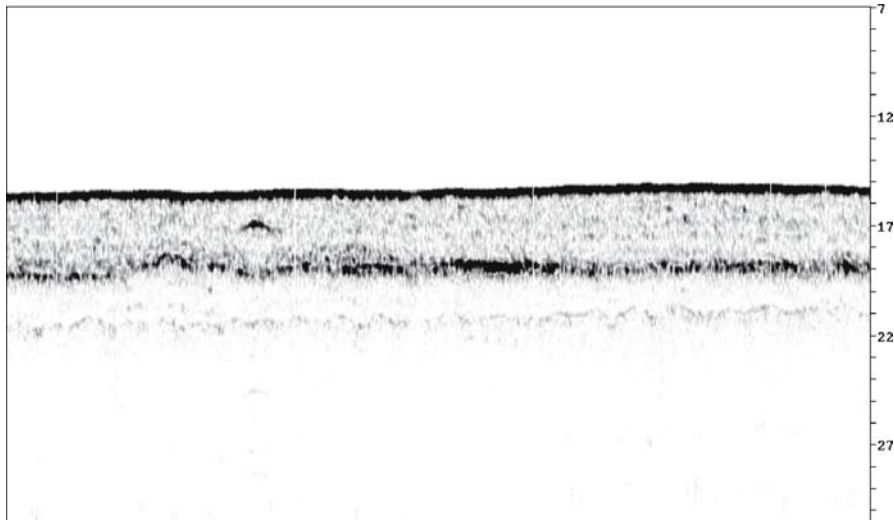


Image 7.2.2-4. Buried pipeline, German Bight; sediment profiler image. The sediment cross section reveals a pipeline, buried 1.5 m deep within a layer of fine sand of 3.5 m depth. The echo is stretched laterally by the usual moustache-like hyperbola arcs. According to governmental requirements, pipelines must be surveyed regularly by the operating companies which have to report annually to BSH. The pipes have to be laid *on* the sea floor; near the coast and in endangered areas they are buried. Cable-pipeline crossings have to be protected by sufficient gravel dumping. The supervising authorities differ regarding exclusive economic zones and 12 miles zones respectively.

Project: inspection of gas pipelines, Europipe1, 1999

Area: North Sea, German Bight

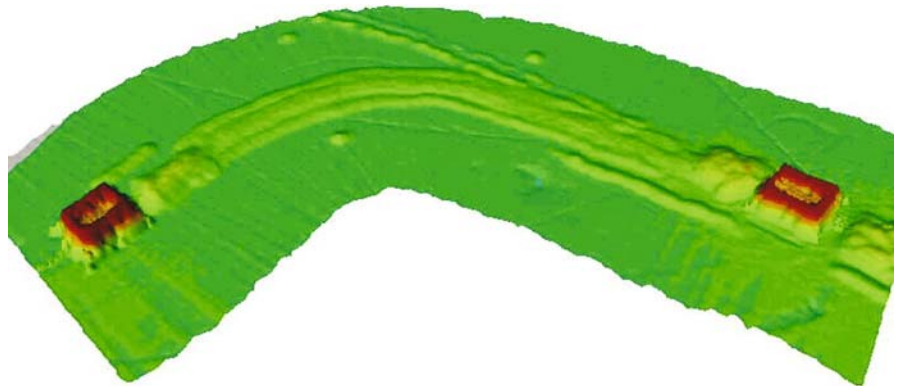
Survey vessel: *FS Gauss*, BSH Hamburg

Sub-bottom profiler: Towed chirp sonar, Edgerton EdgeTec, Xstar; frequency 2–10 kHz, beamwidth 24°. Towfish SB-512; towed 5–10 m above sea floor.

Image©: Manfred Zeiler, Rolf Kunze, BSH Hamburg, Germany

Image 7.2.2-5.

Pipeline diffusers, off Santa Barbara, California. Multibeam image. Submarine pipeline connections and ramifications need hub-like units for easy access and safe protection. These diffusers enable the creation of pipe networks reminiscent of railway cargo terminals and provide flexible management of oil and gas flow respectively. The access for maintenance of the remotely operated joints, valves, and switches is through the central opening of the block. The massive diffuser housing constructions don't require additional protection themselves but the incoming and outgoing tubes are buried either by ploughing or by dumping gravel upon sections exposed for connections. This image shows a pair of diffuser units connecting several curved pipes and a straight ramification. The two types of burial for pipe protection are clearly visualized for maintenance control.



Multibeam system: RESON, type: SeaBat 8125; frequency 440 kHz, 0.5° beamwidth, fan of 240 beams, autofocus

Image ©: Cris Sabo, RESON Inc., Goleta, California, USA ■

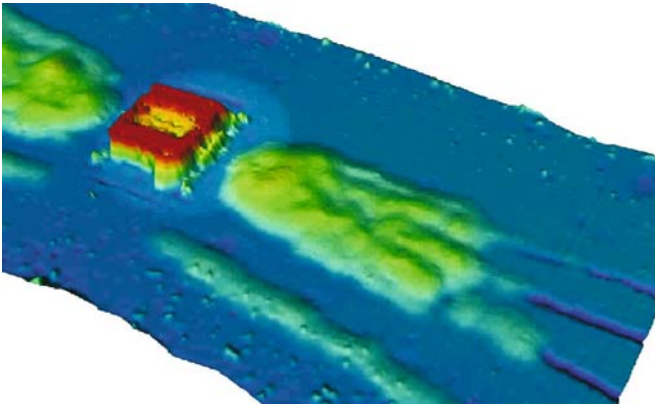


Image 7.2.2-6.

Close-up of a diffuser. Multibeam image. The slant view shows the ploughed furrows for pipe burial in front of the protecting gravel dumping. The multibeam image resolves the individual stones in the foreground.

Image documentation: same as for Image 7.2.2-5 ■

7.2.3 Protection of Shores and Harbors



Coastal areas exposed to the open sea often suffer severely from massive erosion and destruction by break-

ers, surf and tidal flow. Constructions and buildings facing the force of the sea directly, like pier heads of harbors and breakwater walls, need solid protection for their foundations. Wedges of concrete elements dumped along the endangered walls usually provide effective defense against erosion. The irregular, rugged outer and inner surface of the wedges of concrete cubes and tetrapods calms the aggressive flow and breaker impact both by friction and mass, but may undergo displacement and destruction under extreme condi-

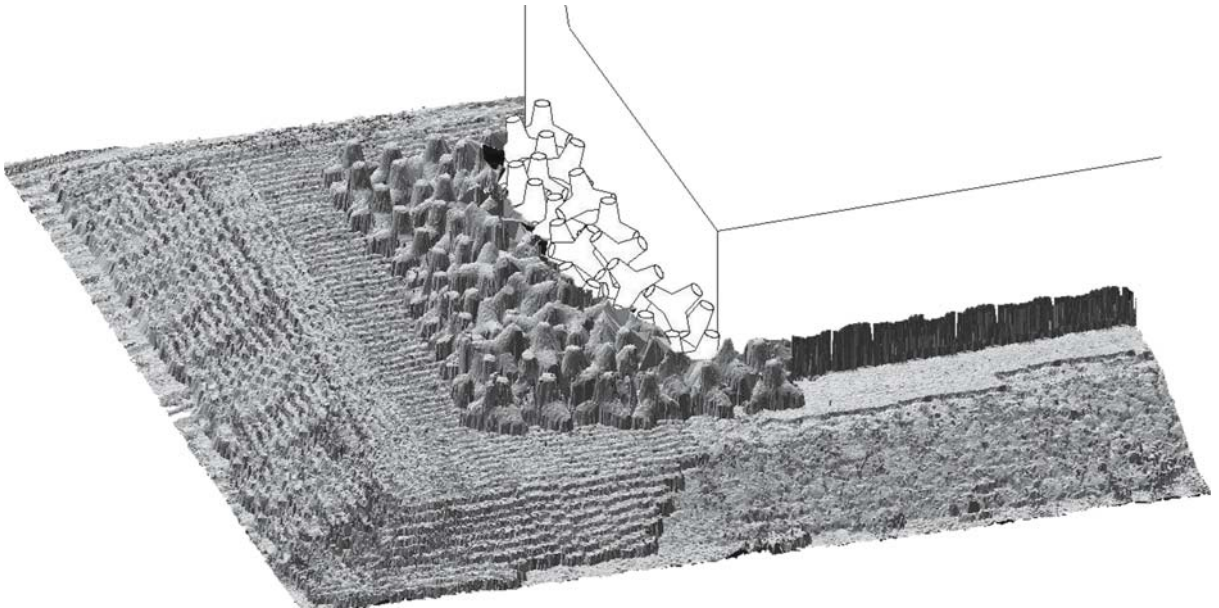


Image 7.2.3-1. Tetrapods protecting a breakwater, Bay of Hibikinada, Kyushu, Japan. Multibeam image. The densely packed wedge of tetrapods is mainly placed in front of the breakwater headwall-foot. The drawing continues the missing part of the sound image and indicates the emerged top of the wedge out of reach of the wide angle multibeam echosounder. Even details of the incomplete pavement of the slanted basement flanks are depicted in detail. Here, the dense image pixels are connected to form a closed surface. The “curtain effect” is much less conspicuous than that from large ship hull flanks (Sect. 7.3.3) lying in the sound shadow.

Project: RESON SeaBat on site performance test

Multibeam system: RESON, type: SeaBat 8125 with Terra Model software; frequency 455 kHz, beamwidth: $0.5 \times 1^\circ$, 240 beams, fan width: 120° , autofocus

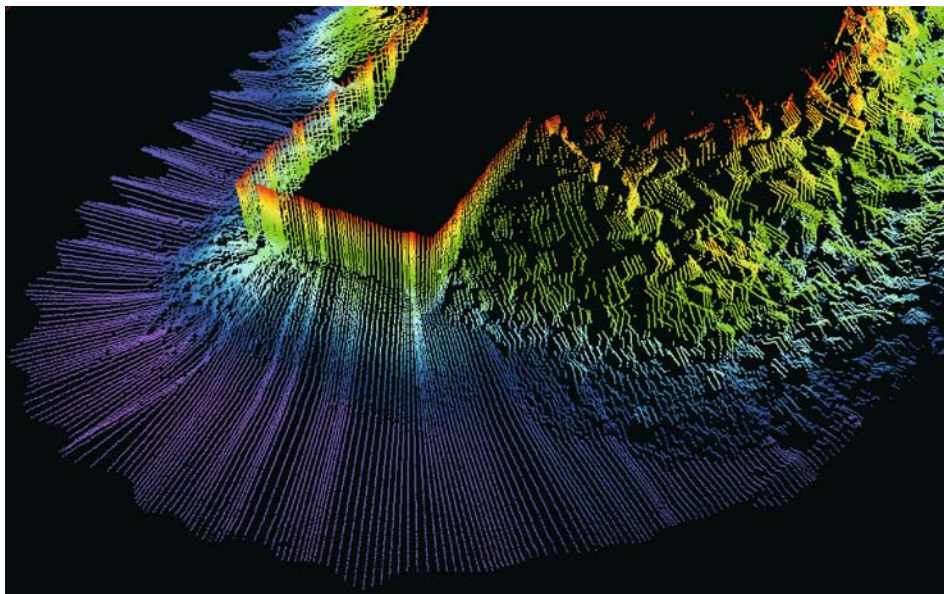
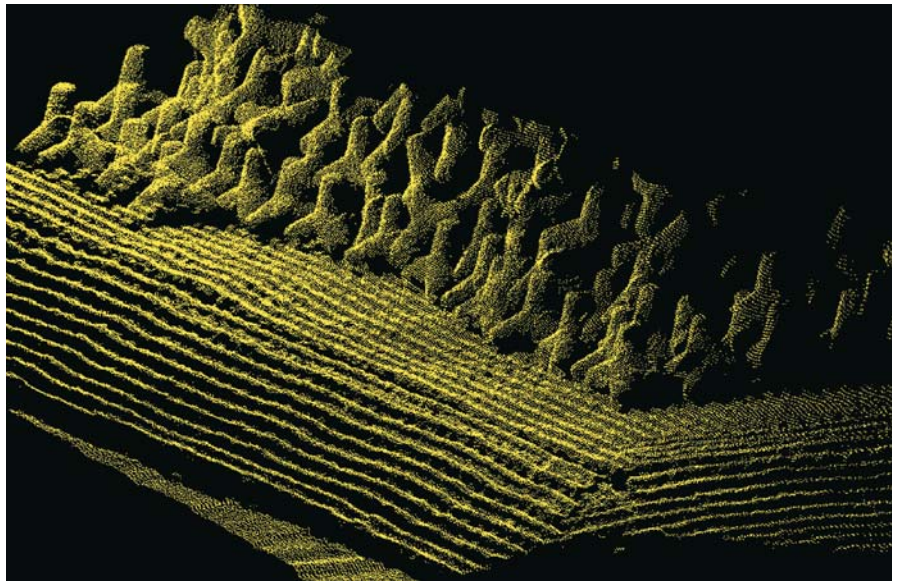
Image ©: Toshio Ohyagi, Toyo Corporation, for Nihon Zitan, Japan ■

Image 7.2.3-2.

Tetrapods protecting a breakwater, Bay of Hibikinada, Kyushu, Japan. Multibeam image, unconnected image pixels. This close-up image of another breakwater, also enforced by a tetrapod wedge in the same Bay as Image 7.2.3-1 visualizes the extremely dense rows of image pixels. The line spacing of centimeters is hardly resolvable by the print reproduction. The very narrow, focussed beams provide about the ultimate high resolution multibeam imaging under conditions at sea.

Image documentation: same as for Image 7.2.3-1

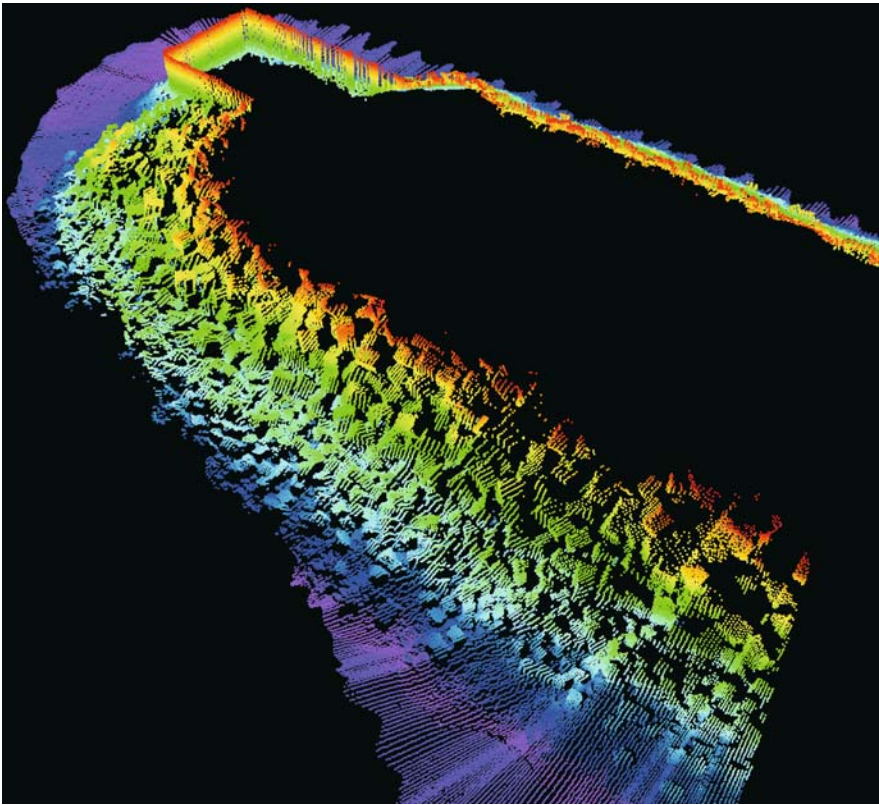
Image ©: Toshio Ohyagi, Toyo Corporation, for Nihon Zitan, Japan ■

**Image 7.2.3-3. Wedge of concrete cubes protecting a breakwater in Bilbao Harbor, Spain. Multibeam image, unconnected image pixels.**

The more distant, diverging scanning lines show the course of the sounding vessel sailing round the breakwater head. The superimposed wavy contours and the more, or less dense lines mainly on the left hand side indicate the motion of the boat exposed to seaway. Here, the unconnected image pixels are color coded to visualize the depths of potential wedge defects. Though the imaging geometry is below optimum here – compared to the preceding images – it provides the essential information of the state of completion of the protecting wedge and the fact that the rudimentary wedge on the left side consists of gravel. The right side reveals gravel below the package of cubes.

Multibeam system: RESON, type: SeaBat 8125; frequency 455 kHz, beamwidth: $0.5 \times 1^\circ$, 240 beams, fan width: 120° , autofocus
Visualized with HHToolkit software, Helical Systems, Canada

Image ©: Richard Hill, RESON Offshore Ltd. ■

**Image 7.2.3-4.**

The same wedge of concrete cubes as in the preceding image of a breakwater in Bilbao Harbor. The image consists of the same sound data set of a single run round the breakwater, this time turned to visualize the already complete side of the concrete cube wedge reaching up to the water surface, and beyond forming a broad escarpment of protection. Unlike the carefully piled up tetrapods of Images 7.2.3-1 and 7.2.3-2, the cubes are simply dumped against the wall and a lot of them obviously rolled away. The image thus demonstrates also the result of the work as a reference for comparison with later damage surveillance.

Image documentation: same as for Image 7.2.3-3

Image ©: Richard Hill, RESON Offshore Ltd. ■

tions. Thus underwater surveillance is mandatory. The dumping work itself needs control by sound imaging, which is less time consuming and more comprehensive than divers can provide, since the water can be highly turbid after dumping. Routine surveillance during the lifetime of these installations is necessary as it is with all underwater measures of protection.

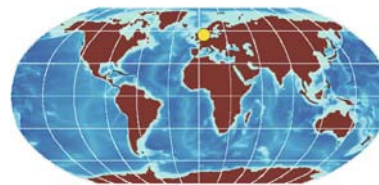
7.2.4

The images demonstrate that such three dimensional artificial wedge constructions are adequately visualized by three dimensional multibeam echosounding. Autofocus technique is particularly effective because of the relatively close distance between the scene and the imaging vessel (Sect. 4.3.5). However, the steep flanks and gaps of the concrete units produce sound shadows, which would falsify the image severely when the image pixels are connected by the image processing program to form closed surfaces, as is appropriate and usual with sea floor imagery. To avoid the irritating “curtain effect” bridging sound shadows of wreck images for instance, the original sounding pixels of the

scanning rows are shown unconnected in images 2–4. This depiction has been applied also for the sound images of other shadow producing man-made objects shown in this book (Sect. 7.3.3).

7.2.4

Basement of the Off-Shore Research Platform *Nordsee*; Sidescan Image



The research platform *Nordsee*, located 74 km west of the island of Sylt in the southern *North Sea* at a water depth of 30 m was the first and only permanently manned offshore platform for marine research. The fixed construction enabled long-term studies of sea surface dynamics and its acquisition by and impact on sound below and radar



Image 7.2.4-1. Polygonal concrete basement. Sidescan image. The construction of 70 m diameter was a flat, flooded, hollow basement without poles standing directly on the sediment consisting of sand and moraine fragments. The adjacent smaller basement on the left was the carrier of a directional sound source as part of a sound transmission range for long-term experiments. The sidescan image was taken at the time of platform operation.

Project: Basement erosion inspection, 1986

Research vessel: *WFS Planet*

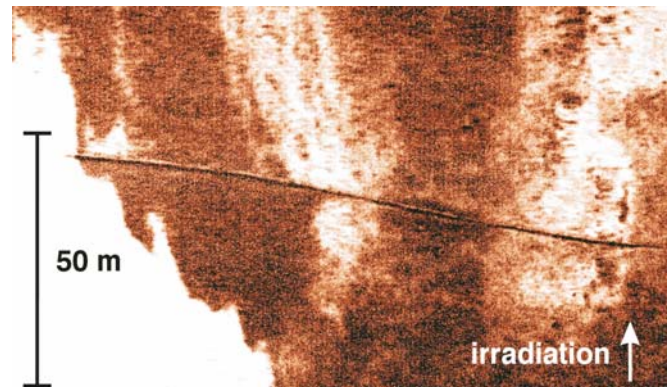
Sidescan system: Klein 595; frequency: 100 kHz, beamwidth: 1°, unfocussed; image section: 100 m

Image ©: Doris Milkert, FWG ■

Image 7.2.4-2.

Submarine cable, research platform *Nordsee*. Sidescan image. The cable lying on patchy sediment connected the research platform *Nordsee* with underwater acoustic devices at a distance. The local sediment types range from fine sand to coarse sand and cobble; the cable was partly buried in the finer grained sediment by tidal current action. The image shows the state of natural burial after about 10 years of operation. Hazardous free-span was not observed.

Image documentation: same as for Image 7.2.4-1 ■



above (Sect. 6.2.3) up to extreme weather conditions inaccessible by ships. Commissioned in 1972 the platform with its research ship-like equipment was dismantled in 1990 with the basement still at its origi-

nal place but without the steel tube superstructure depicted here. The net height of 5 m is not considered a hazardous shoal but a protective place of natural fish upbringing.

7.3

7.3 Underwater Archaeology

Subsidence of coastlines by geological processes doesn't happen only during so called geological time scales. They were the reason – rather than an increase in sea level – that for instance Roman settlements near Naples were submerged. Such slow but inexorable sinking and final doom of extended architectural ensembles and even entire cities covered by a water column up to tens of meters has often preserved much of the substance in its original state. The state of preservation of such submerged stone memorials of culture can be better than that of their contemporary remains inland.

7.3.1

The usual access to archaeological research by divers to sunken architectural treasures may be less difficult and more conservative than excavation. However, the reconstruction of the ground-plan of large ensembles, as well as the reconnaissance of weak, interrupted traces, connections and interrelationships of geometrical concepts, can be an extremely time consuming challenge for divers, very difficult and sometimes impossible in more or less turbid waters.

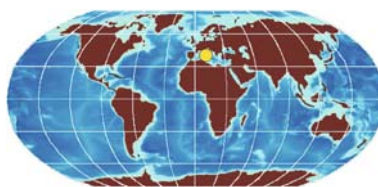
Recently a nearly ideal support of underwater archaeology has been tested and applied. It is a kind of underwater substitute to aerial photographs and radar imagery which has helped to reveal hidden traces of ancient settlements on land. The substitute is high resolution multibeam echosounder bathymetry (Sect. 4.2). Though sidescan echo sounding has been successfully applied before, this was restricted to two-dimensional images (Sect. 4.3). Now, wide-angle, auto focus (Sect. 4.3.5) sounding can provide genuine 3D-imagery which covers broad areas taking only a few stripes to and fro within a short time. Divers on their own usually cannot contribute much more to revealing entire municipal concepts other than the reconstruction of their ground plans.

Of course, where underwater visibility allows, archaeological underwater research will always require photographic close-ups and hands-on work but the rapid availability of complete reliefs of entire sunken cities may presumably develop to a complementary standard tool for archaeology. By combination with sediment penetrating high resolution sounders the discovery of buried parts of even pre-historical settlements will perhaps be decisively supported.

There is another major historical and archaeological research interest offshore. The subjects of research are found both in shallow and deep water: Sunken ships, wrecks and remnants of early epochs represent cultural and technical documents, and further information such as details of shipbuilding concepts and construction, relics of cargo and ancient sea lanes. Of particular and perhaps even public interest may be historic battlefields in the sea (Sect. 7.3.5, 7.4.1). Underwater archaeology has only recently begun to recognize that acoustic imaging undoubtedly provides important methodological and economic advantages.

7.3.1

Sunken Roman City Complex



Just a few kilometers from *Naples* lies a unique example of how geological change can affect a coastline.

Baia and the coast of the *Campi Flegrei* are today radically different to how they appeared in ancient times, after large scale subsidence caused all the old coastline to sink into the sea. In Roman times the small bay of *Baia* was a lake, connected to the sea via a canal on whose banks many luxurious villas had been constructed. Among the most illustrious owners were Scipio, Caesar, Nero, Augustus and Tiberius. *Baia* was also the stage of political intrigues and crimes, the most infamous being the assassination of Nero's mother Agrippina. Some of the doomed ancient splendour is still intact. Divers can admire the remains of thermal baths with colored mosaics and frescoed walls of streets and doorways.

7.3.1.1

City of *Baia*, Italy.

Multibeam 3-D Imaging of Urban Architecture

The intention of the survey was to establish a comprehensive *three-dimensional documentation* of the present state of the ancient urban architecture was realized by applying the latest high resolution underwater acoustic imaging and image processing systems. The sound image examples show two monumental complexes in total, supplemented by some structural details to demonstrate the resolution of the multibeam sounder system.

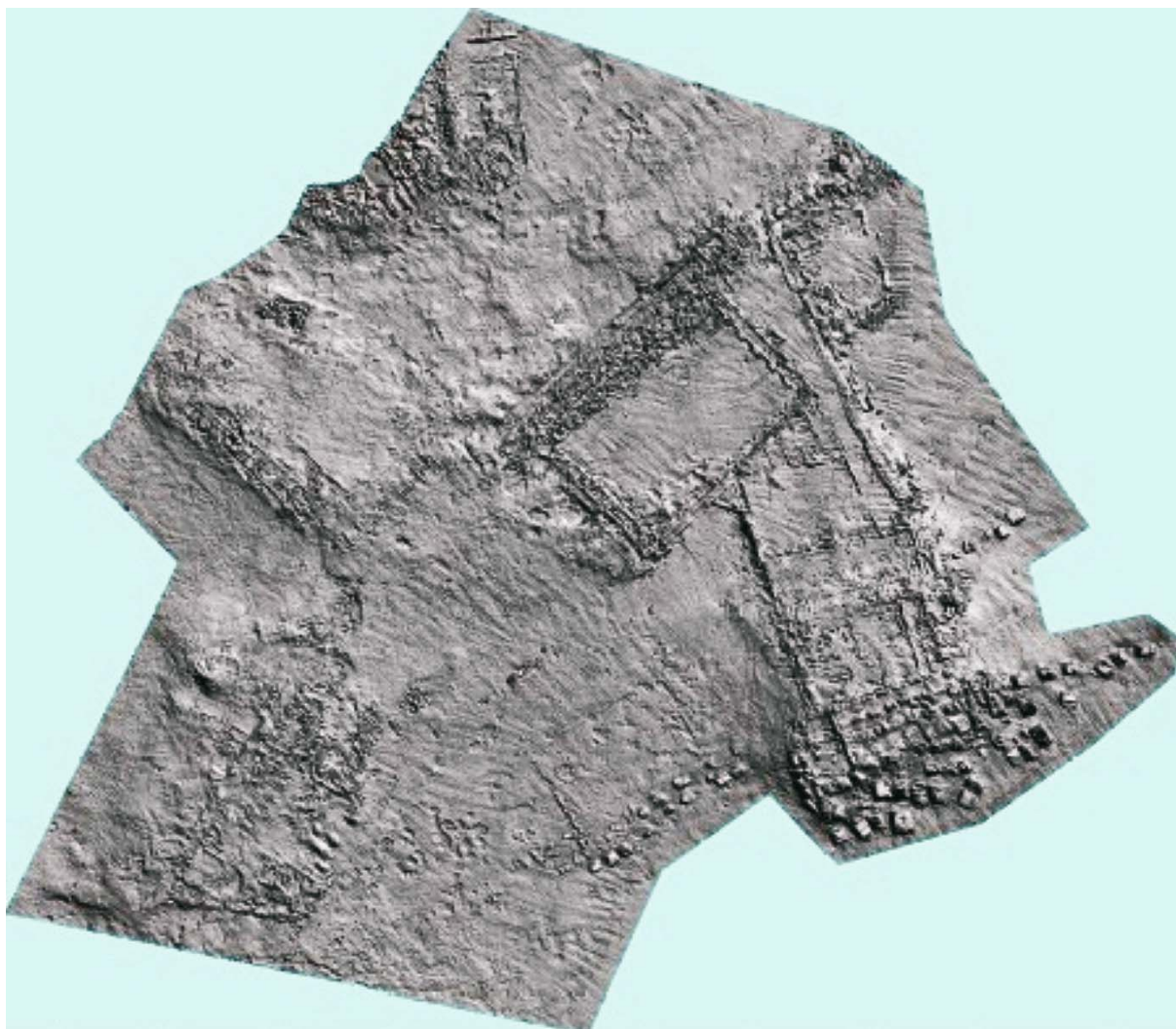


Image 7.3.1.1-1. Submerged environment of the sunken Baia with the city complex outline. The relief in bird's view depiction is visualized only by simulated sunlight from north.

Project: Application of recent advanced technology on underwater archaeology; year of survey: 2001

Survey vessel: *Red Fish*, Italy

Multibeam system: RESON, type: SeaBat 8125 with PDS2000 Hydrographic software; frequency 455 kHz, beamwidth: $0.5 \times 1^\circ$, 240 beams, fan width: 120° /stripe width: 37 m at sea floor of 10 m depth, zoom autofocus with pixel size of 8.5 cm at the sea floor sampled

Average water depth at the site: 7.5 m. Image frame: 2.8×2.8 km

Image ©: Pietro Basciano, NeSA Med. Srl. and RESON MEDITERRANEAN SRL, Italy ■

The first complex is a large garden surrounded by a portico and a thermal bath ensemble along one side of the garden. A series of service rooms on the opposite side lead down to the maritime part of the house, made up of

two small jetties and large tanks for fish farming. A series of 25 poles protected the house from high tides and rough seas. The second monumental complex on the southern side of the park demonstrates the urban fabric

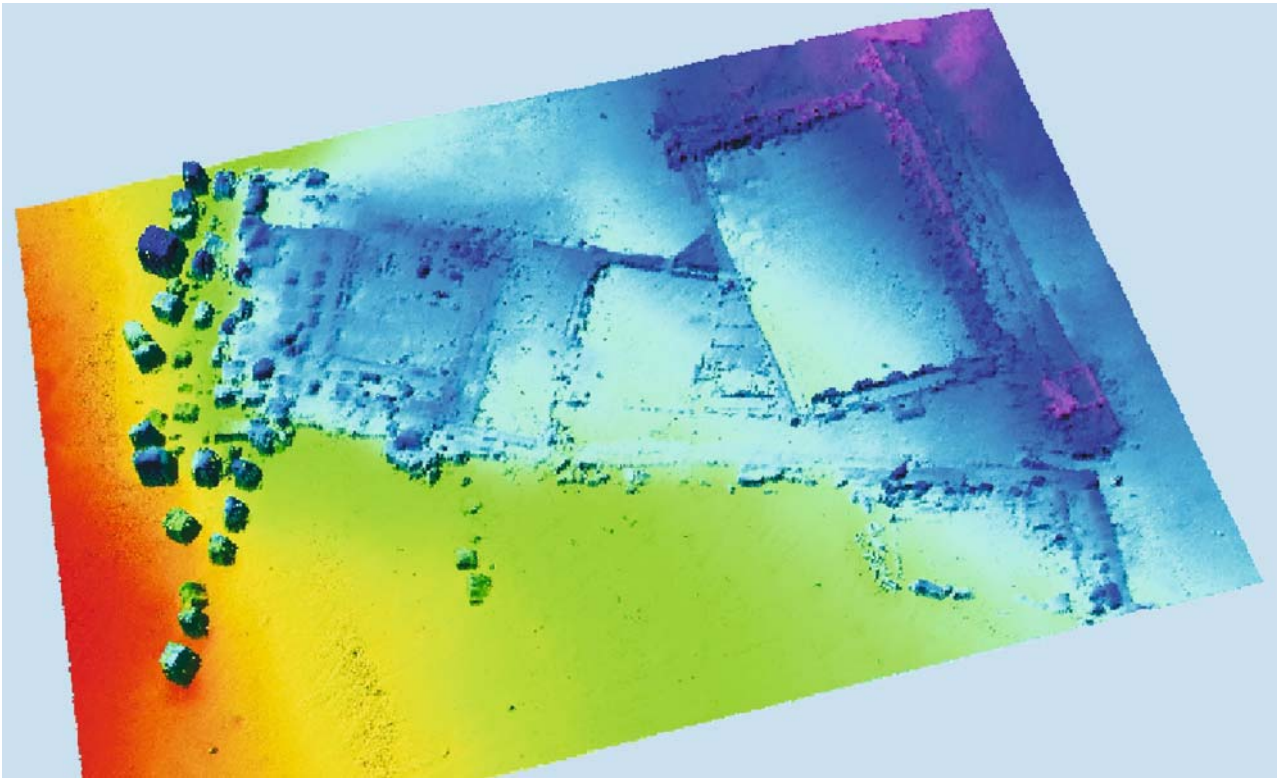


Image 7.3.1.1-2. Baia, overview of city complex, birds view. The color code indicates the slope of the area (–8 to –16 m). Simulated sunlight from north.

Image documentation: same as for Image 7.3.1.1-1 ■



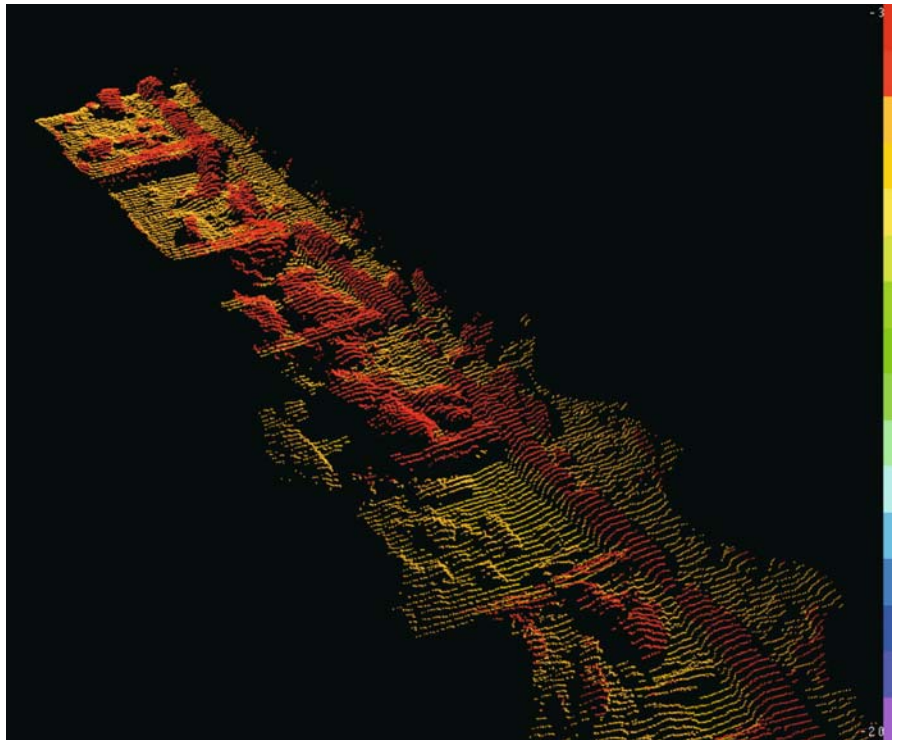
Image 7.3.1.1-3. Slant view upon Baia with the protecting poles in the foreground. Simulated sunlight from north; color code matched to the architectural relief.

Image documentation: same as for Image 7.3.1.1-1 ■

Image 7.3.1.1-4.

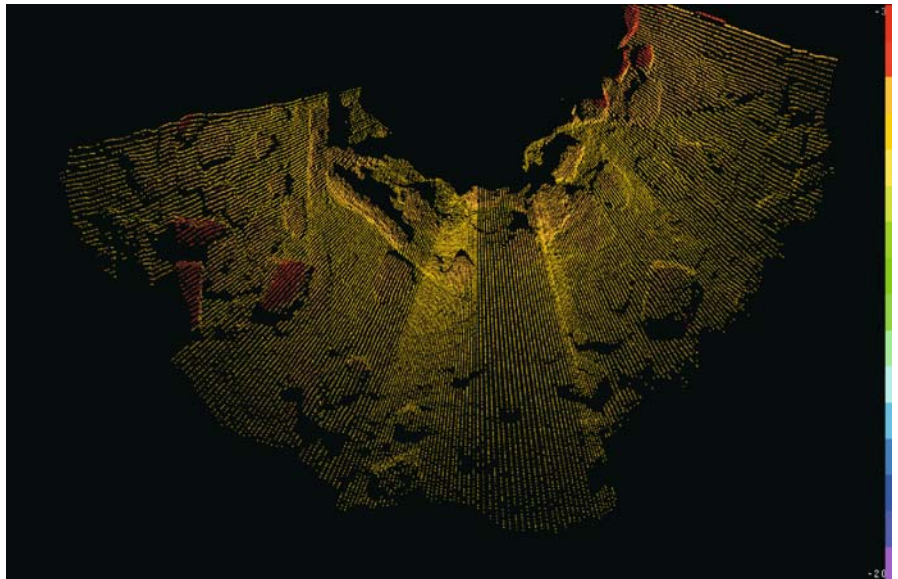
Details of the caldarium. The individual scanning lines of the multi-beam echosounder are depicted as separate height profiles visualizing the relief by denser and wider distance between the profiles, enforced by artificial sunlight. Length of the section: about 10 m.

Image documentation: same as for Image 7.3.1.1-1 ■

**Image 7.3.1.1-5.**

Another detailed section with the survey vessel scanning along circle course, showing only irregular fragments. Scanning lines as height profiles, enhanced by artificial sunlight. Length of the section: about 10 m.

Image documentation: same as for Image 7.3.1.1-1 ■



of the ancient Baia. A road with tabernae, caldarium and a private villa, typical of Roman houses: A series of rooms face onto a central atrium which provides the lighting.

The image series demonstrates different kinds of depiction, derived from the same data sets by signal processing to enhance the features of interest.

7.3.1.2 The Submerged *Porto Giulio*, Italy. Multibeam 3-D Imaging of Port Architecture

Porto Giulio, *Portus Julius Baiæ* in Latin, was the first naval defense built by the Romans. The historic harbor complex in the *Bay of Naples* vis à vis the sunken *City of Baia* was connected with this abode of celebrities by

a dyke protecting the port. *Portus Julius* was designed and constructed around 37 BC by Agrippa, the brilliant engineer and military leader; the facility was named after Julius Caesar. The originally military port became one of the most important commercial ports later. Due to geological changes caused by the presence of the nearby Volcano *Vesuvius*, the dyke submerged in the fifth century. During the following centuries the re-

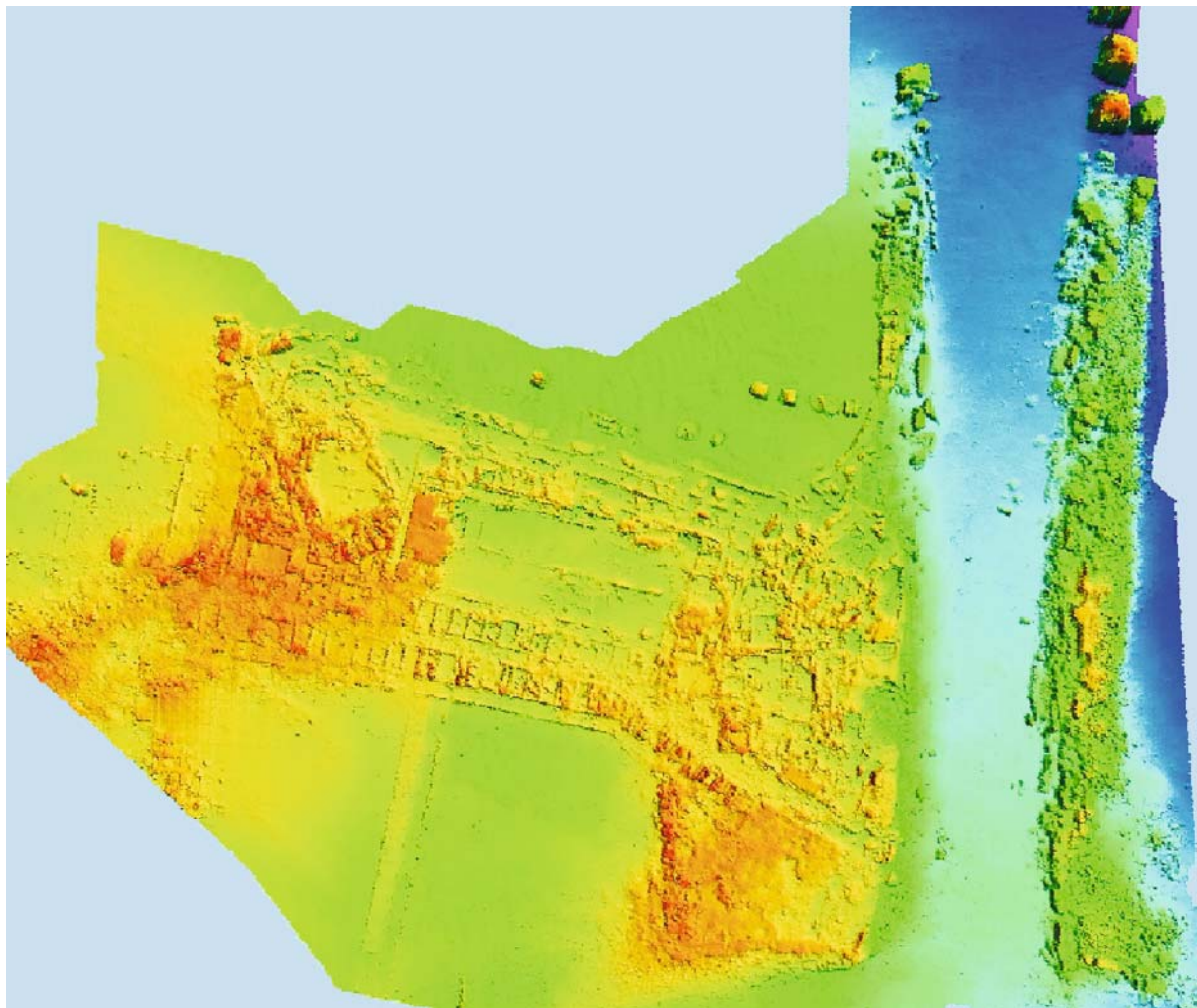


Image 7.3.1.2-1. Porto Giulio, relief of the port outline with the access canal in bird's view depiction. Color coded 3D-image

Project: Application of recent advanced technology on underwater archaeology; year of survey: 2001

Survey vessel: *Red Fish*, Italy

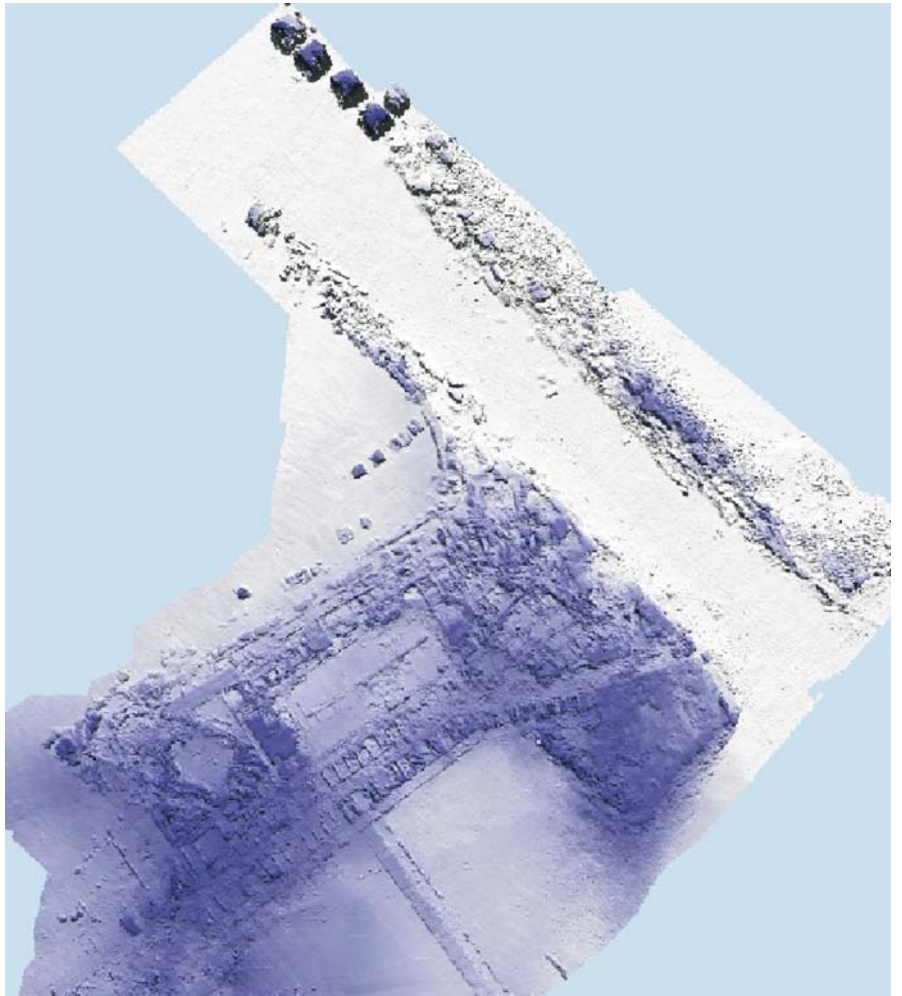
Multibeam system: RESON, type: SeaBat 8125 with PDS2000 Hydrographic software; frequency 455 kHz, beamwidth: $0.5 \times 1^\circ$, 240 beams, fan width: 120° /stripe width: 37 m at sea floor of 10 m depth, zoom autofocus with pixel size of 8.5 cm at the sea floor sampled; average water depth at the site: 7.5 m. Image frame: 2.7×2.7 km

Image ©: Pietro Basciano, NeSA Med. Srl. and RESON MEDITERRANEAN SRL, Italy ■

Image 7.3.1.2-2.

Same as Image 7.3.1.2-1, but coded by shaded gray scale to enhance contours

Image documentation: same as for Image 7.3.1.2-1 ■

**Image 7.3.1.2-3.**

Same, but slant view, underlining the optical relief impression

Image documentation: same as for Image 7.3.1.2-1 ■



mainder of the port was engulfed by the sea. *Lake Lucrino*, originally behind the dyke, became part of the *Mediterranean*.

At the end of the second World War Porto Giulio was “rediscovered” by scuba divers and aerial photography which revealed the outline of the port, the access canal and the ground plans of many warehouses.

Though the water cemetery of the buildings is very shallow and sufficiently transparent in benign weather, three-dimensional acoustic imaging has provided supplementary information to marine archaeologists, ironically despite the very shallow water, which is a challenge for wide angle multibeam technology, requiring zoom auto-focusing.

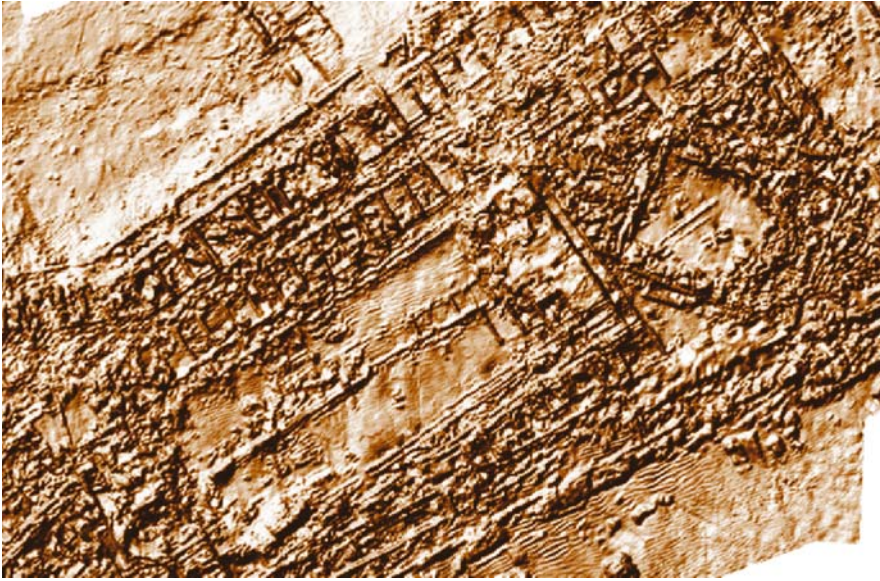


Image 7.3.1.2-4.

Close up with contour enhancement processing showing the geometrical structure of details

Image documentation: same as for Image 7.3.1.2-1 ■

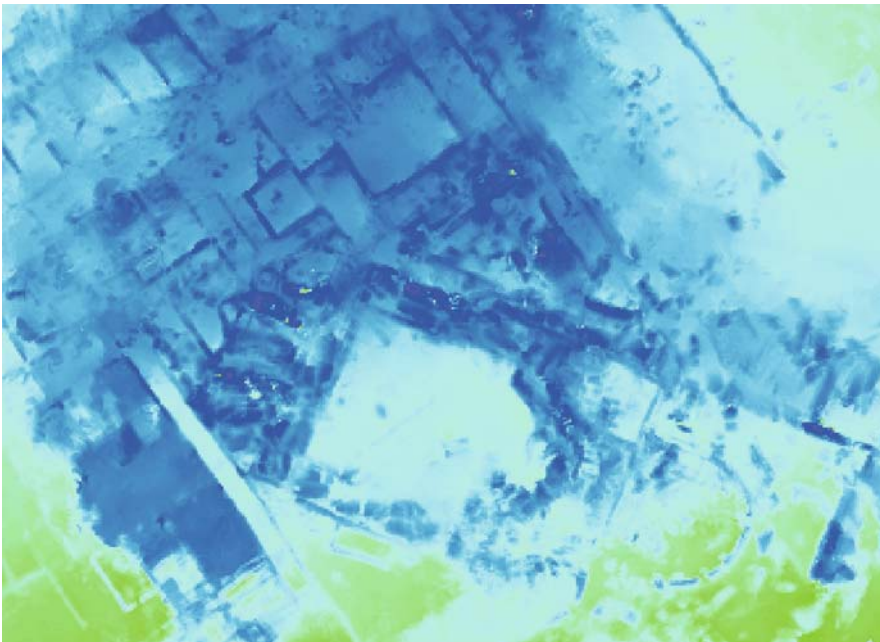
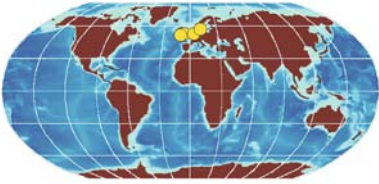


Image 7.3.1.2-5.

Aerial photograph of *Porto Giulio*, nearly vertical direction of view, visualizing ground plan structures ■

7.3.2

Historic Ship Wrecks and Wreck Sites



Wrecks of wooden ship constructions built in former centuries have left mainly their metal relics rather than recognisable parts of the ship's hull and superstructure. Some of the famous wrecks of history have been

salvaged and restored or, more correctly, reconstructed and are on display in museums. Original wreck sites of importance with the remains of relics still in place and traces of sinking impact, and of later salvage work are legally protected areas now. The separation of these objects of archaeological interest from more recent victims of accidents does not follow a defined age criterion but more the historic context. The sound images of this collection have in common that they are restricted to shallow water sites. However, nearly all of them have been taken with the most advanced

salvaged and restored or, more correctly, reconstructed and are on display in museums. Original wreck sites of importance with the remains of relics still in place and traces of sinking impact, and of later salvage work are legally protected areas now. The separation of these objects of archaeological interest from more recent victims of accidents does not follow a defined age criterion but more the historic context. The sound images of this collection have in common that they are restricted to shallow water sites. However, nearly all of them have been taken with the most advanced

7.3.2

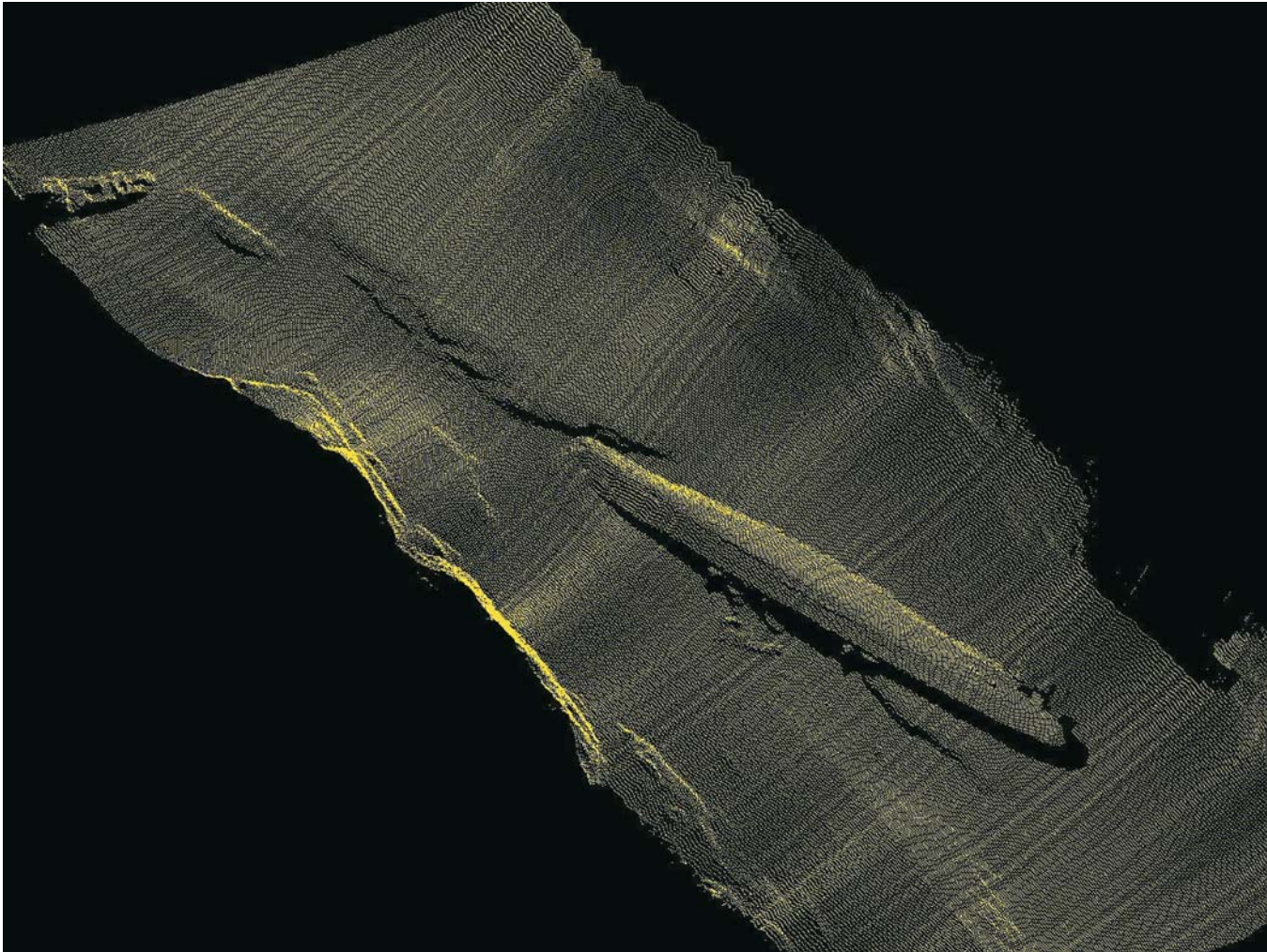


Image 7.3.2-1. Wreck of the WW II battle cruiser *Blücher*. Multibeam image. The German battle cruiser, commissioned three weeks after the outbreak of the second World War, was the third warship carrying the name of the popular Field Marshal who led the army against *Napoleon*. The first *Blücher* was a Korvette, commissioned in 1877 with *von Tirpitz* as first officer, who ►

◀ became famous as Admiral later. The ship however, was laid up after an explosion in peacetime, 1907. The second Blücher sank in the second year of the First World War during the *Battle of the Doggerbank* in the *North Sea*. The third Blücher, the wreck of which is shown here, sank in the second year of the second World War in the *Oslo Fjord*. The ship of about 14 000 tons and 206 m length, considered the most modern warship of its time, was involved in the occupation of Norway by German naval forces and embarked troops as ordered by Hitler. During this operation the Blücher was hit in April 1940 by 28-cm shells from the nineteenth century Krupp guns of the Norwegian fortress *Oskarsborg* and further by two torpedoes from Norwegian underground turrets of *North Kaholmen*.

The Blücher sank capsized with its damaged portside and the bow ahead and has since remained 90 m deep at the bottom of the *Oslo Fjord*. The sound image shows the bow on the left side partially buried and the stern uplifted, due to an exposed step of a geological fault causing the sloping position. This fault area continues beyond the bow of the Blücher. Further away in the left upper corner of the image there is another, smaller wreck and quite close to it the floor of the fjord shows the contour of a nearly completely buried small hull. The hull of Blücher appears remarkably unimpaired on the keel- and starboard side. Some parts of the superstructure lie amidships on the fjord floor, which was imaged by two survey runs – back and forth – by the sounding vessel. This superposition of the two sets of narrow sounding lines has caused the moiré pattern of the image, in addition to the pitch motion effect of the vessel producing more or less dense lines which are shifted to their real location according to accelerometer- and gyro-sensors.

The wreck of Blücher, which is the tomb of hundreds of soldiers, was not subject to salvage operations apart from explosive dismantling of the three propulsion propellers in 1951. The image is available on the CD attached to this book for turning and zooming by Fledermaus software.

Survey vessel: *MV Line*, Copenhagen; year of survey: 2001
 Multibeam system: RESON, type: SeaBat 8125; frequency: 455 kHz, beamwidth: $0.5 \times 1^\circ$, 240 beams, fan width: 120° , zoom autofocus
 Image ©: Kai Martin Dührkop, RESON GmbH, Kiel Germany ■

high resolution multibeam echosounders already, applying autofocus technique with resolution to the values of centimeters or low decimeters. This permits imaging of nearly photographic quality also of the surrounding sea floor features and texture. Violations of the prohibition to access or robbery can be easily

recognized with periodic acoustic surveillance from a distance. At present, this technology is still in a preparatory state before becoming available also for the deep ocean to be operated on submersibles.

The series of six wreck sites starts with two WW II ships, goes back to the turn of the century and two decades before, then continues with wreck sites of the late 17th and mid 16th century respectively and ends with a famous underwater arena of many ship disasters through the centuries with no identifiable single wreck but remarkable, rocky sea floor features which could hide many undiscovered objects.

Box 7.3.2-1. Operational submarines around 1900

Already at the turn of the nineteenth century seven states owned operational submarines: France: 26, Great Britain: 9, United States: 8; further: Germany, Japan, Russia, and Italy. The British *HMS A1* of 1903, shown as a sound image of the sunken boat (Image 7.3.2-3) late after its second casualty, was the first submarine with a formed out conning tower. An early predecessor was the *USS Humley* of the *Southern States*, fighting the *Northern States* 1864. The submarine is famous for having been sent to the bottom altogether three times with the last recovery only in 2000.

A few other renowned Submarines are mentioned:

Laubeuf's *Narval* achieved particular interest of the French Navy in 1896 and was built in several copies thereafter. The first operational German submarine, the *Forelle*, built in 1903 was sold to Russia with a follow on contract for three larger boats, again for Russia. The German Navy had their first submarine operational only in 1906.

The most advanced submarines of their time were conceived by the Irish-American inventor and former schoolteacher *John Philip Holland* and built by the *Holland Torpedo Boat Company*. Several of the Holland-submarines commissioned in 1903 were still operated in WW I. The basic configuration of the *Holland VI* remained the guideline for five decades to follow with a dual propulsion systems, a fixed longitudinal center of gravity, separate main and auxiliary ballast systems, a hydrodynamically advanced shape, a modern weapons system, and the ability to recharge its battery and compressed air reservoirs without returning to port.

Hannes Ewerth · ret. Chief, German Submarine Flotilla

Image Series 7.3.2-2 to 7.3.2-2c: S.S. *Richard Montgomery*

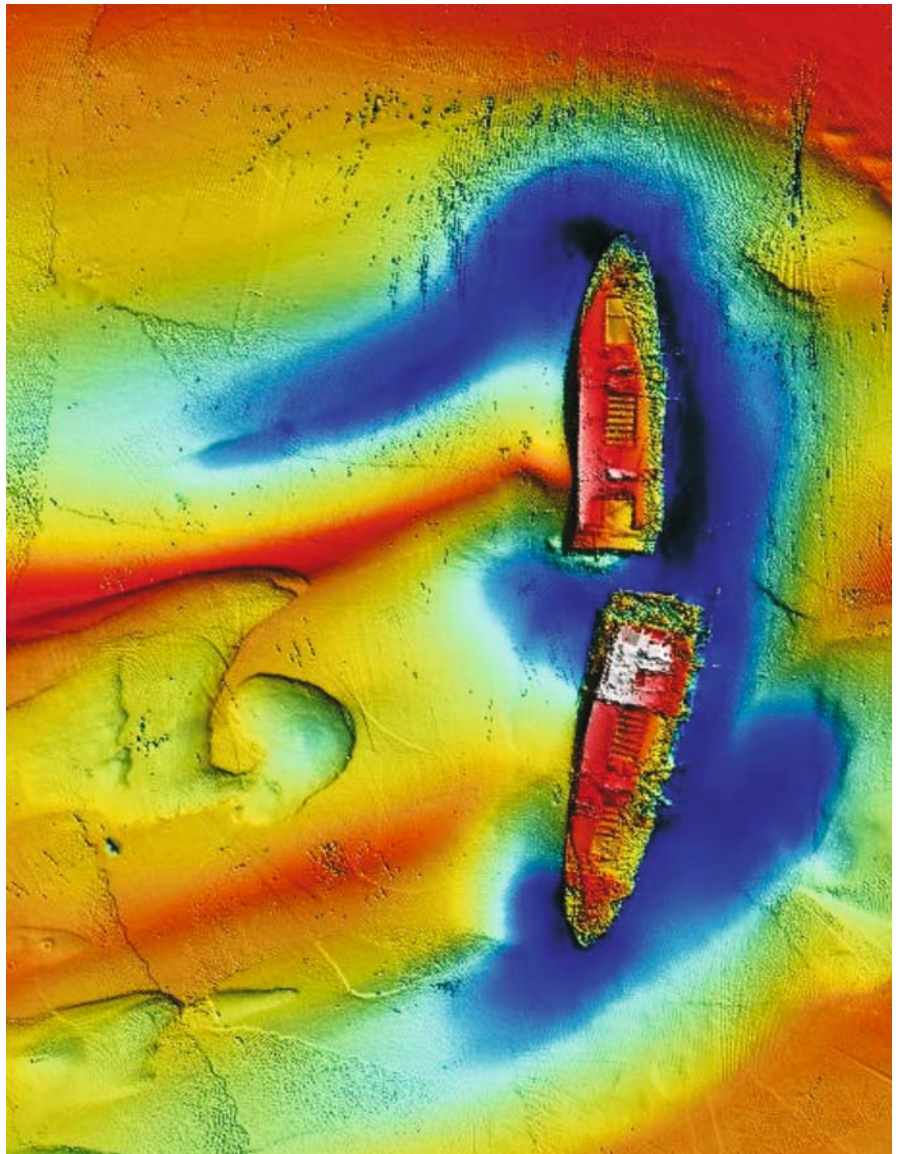
The ship was built in 1943 and named after a celebrated Irish-American soldier of the 18th Century was one of the American *Liberty* cargo ships. In August 1944, the ship left *Philadelphia*, carrying about 6 000 tons of explosives destined for the *Battle of Normandy*. While anchoring in the *Thames* Estuary the *Richard Montgomery* awaited the formation of a convoy to travel to *Cherbourg*, which had already fallen to the Allies. On August 20, 1944, the ship ran aground on sand banks at the northern coast of *Kent*

off *Sheerness* and broke her back. Within a month, about half of the explosives could be removed from the wreck but to complete the discharge was considered too dangerous and the ship was abandoned. As with much of World War II ammunition, 60 years of sea water will have made the wreck's explosive cargo hardly less dangerous. The state of the *Richard Montgomery* is therefore monitored by the *Maritime and Coastguard Agency*. The multi-beam sound images show the wreck broken into two upright halves with the sand banks deeply eroded by tidal flow around the large obstructions.

Image 7.3.2-2.

Overview of the wreck and its environment. Multibeam image. The broken wreck of *Richard Montgomery* appears particularly well preserved despite the six decades since the accident, perhaps because of the dangerous cargo prohibiting partial recovery or dismantling of units of value. Documentation of the accident area by repeated imagery, quantified by color code of the kind shown, can monitor wreck motions and progress of sediment erosion around the *Richard Montgomery* by tidal flow. The upper decks of the two halves of the wreck indicated red are meanwhile sunken to about the same depth level as the non-eroded sediment at a distance. The furrows indicated blue are about 12 m deeper and show the bizarre morphology caused by scouring of the sediments. Both parts of the wreck together are about 100 m long. Although the port side appears damaged the close ups of the next images show however, that the damage is an artifact of the echosounder data processing.

Project: ADU CRM Survey; year of survey: 2001
 Support vessel: *SV Scimitar*
 Multibeam system: RESON, type: SeaBat 8125; frequency: 455 kHz, beamwidth: $0.5 \times 1^\circ$, 240 beams, fan width: 120° , swath: 128 m, zoom autofocus
 Average water depth: 16 m
 Image ©: ADU/RESON ■



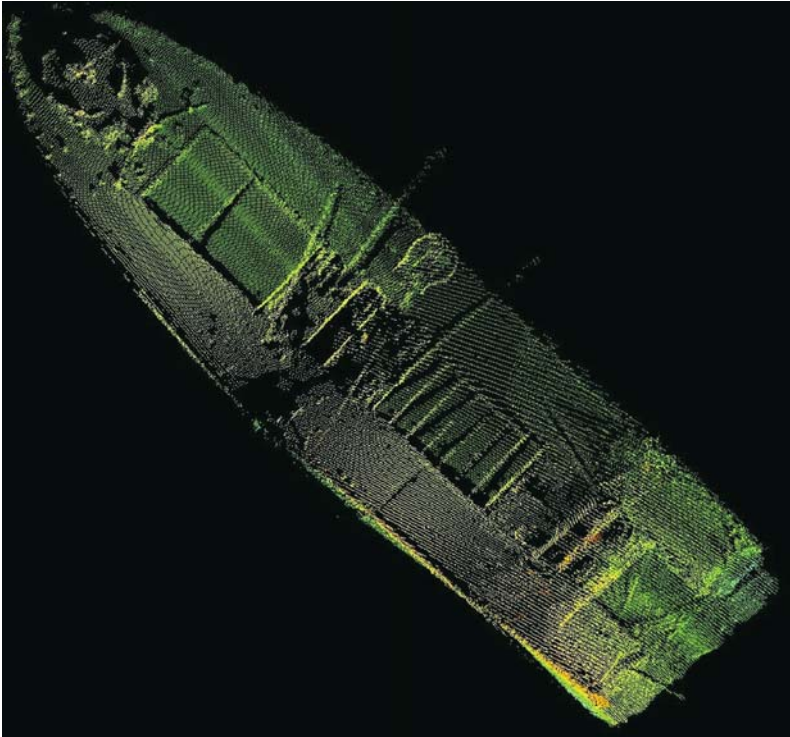


Image 7.3.2-2a.

Close up of the bow part of SS Richard Montgomery. The depiction of the bow section is different in kind from the preceding overview. The image pixels of the lines and rows produced by the scanning multibeam system (Sect. 4.2.3) are not interconnected to form closed surfaces as with the overview. This representation composed of individual pixels is preferable when imaging objects with complex, shadow forming structures. Then the shadow zones such as those below the hatch grating remain shadows instead of forming non existing, pseudo-interconnecting, curtain-like surfaces (Sect. 7.3.3). The image pixels are color coded however, to maintain the third dimension. The circular mounting of the bow gun is clearly visible as well as major damage to the hull. Particularly remarkable is the sharp cut off like rupture at the lower end.

Image documentation: same as for
Image 7.3.2-1 ■

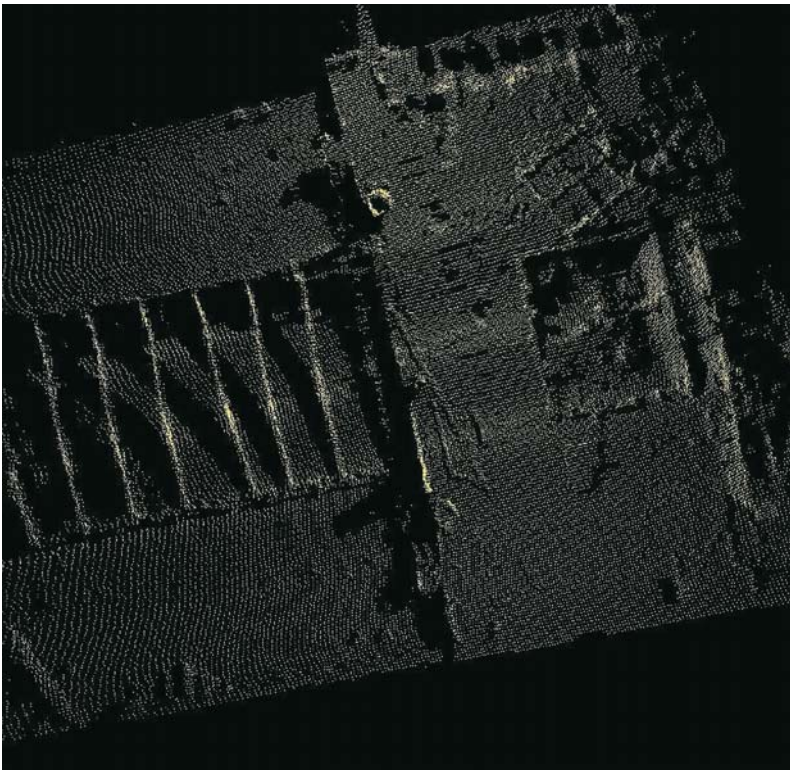


Image 7.3.2-2b.

Further close up of a mid-ship section. The multi-beam sound image is impressive by its high resolution, reminiscent of a photograph. Though the depiction has no color code, structure details come out clearly by the shadows caused by oblique irradiation. Steep elements of the superstructure like the square hatch wall are recognizable by denser scanning lines. Even slight dents in the deck are obvious because of the scanning line curvature near the hatch grating.

Image documentation: same as for
Image 7.3.2-1 ■

Image 7.3.2-2c.

Further close up of the bow section. The front end of the bow with the front hatch and the circular base of the gun appears nearly unimpaired. The edge of the mid ship damage is visible at the upper left with two beams crossing the deck. These close up images may serve as a documentation of state of the wreck.

Image documentation: same as for Image 7.3.2-1 ■

**Image 7.3.2-3.**

Wreck of the historic submarine HMS A1. Multibeam image. *HMS A1*, commissioned in 1903, was the first British-designed and built submarine used by the Royal Navy. Only one year later it became the Royal Navy's first submarine casualty, being rammed and sunk by the mail steamer *Berwick Castle* whilst on exercises off the *Isle of Wight*. She sank in 11 m of water with the loss of all hands. After being recovered and repaired, the submarine was employed in trials and experiments for the Anti Submarine Committee. During one such trial in 1911, when running unmanned and under automatic pilot as a submerged target, she sank again, this time off *Selsey Bill* at a depth of 12 m. The submarine, just 12 m long, was accidentally discovered in 1989; the wreck site has formally been depicted on Admiralty Charts.

The multibeam sound image of 2002 which required less than half a minute pass time shows the wreck upright inside a depression of sediment erosion with an essentially unimpaired hull and conning tower. It is not unusual for sunken submarines to be well preserved due to the strength of their pressure hulls. The rapid and detailed acoustic imagery enabled informed protection management decisions without the time and expense of waiting for favorable diving conditions. The *HMS A1* is now designated under the Protection of Wrecks Act 1973 which protects important wrecks from unauthorized interference because of their historical, archaeological or artistic importance. Divers can visit the site under license and with the cooperation of the wreck's owner. The protected area of *HMS A1* extends 100 m around 50°45' north and 00°55' west.

Support vessel: *SV Scimitar*; year of survey: 2002

Multibeam system: RESON, type: SeaBat 8125; frequency: 455 kHz, beam-width: $0.5 \times 1^\circ$, 240 beams, fan width: 120° , swath: 128 m, zoom autofocus
Image ©: ADU/RESON ■



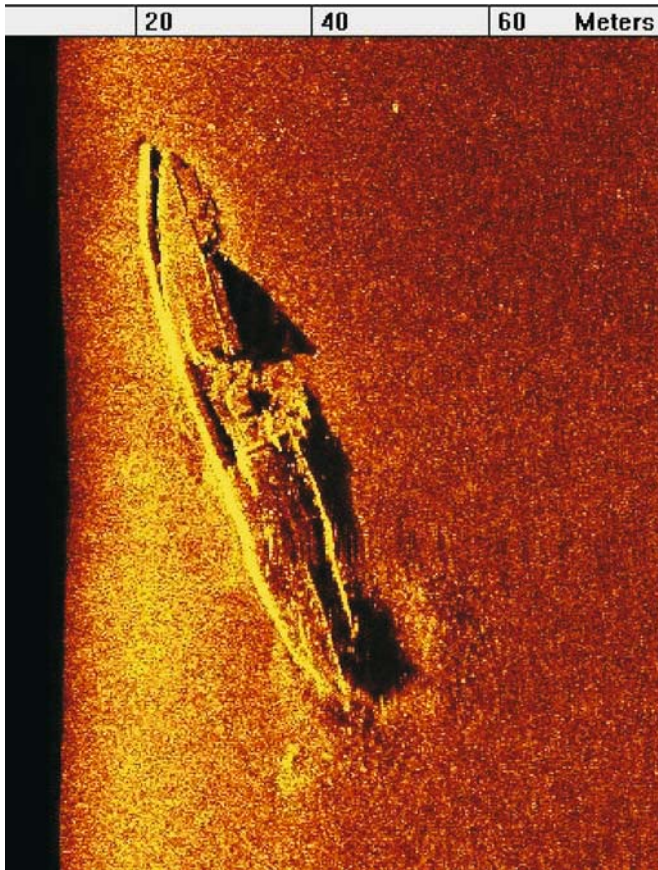


Image 7.3.2-3a.

Wreck of a historic warship. Sidescan sonar image. The high speed sidescan sonar image made in 2002 shows the wreck of the Dutch warship *Hr. Ms. Adder*. This ram monitor ship sunk on July 5 1882, in the coastal waters near the harbor of Scheveningen at a water depth of 15 m. Apart from slight scouring, evident at the port side, the ship's hull of 90 m length and 12 m width appears unimpaired. The *Adder* was a heavy armored, steel plated warship with powerful steam engines and a reinforced protruding underwater bow, to act as a ramming vessel for penetrating the vulnerable flanks of enemy vessels. This ship type was conceived as a modern version of an ancient Roman galley. However, the ship was a fiasco: it sank at fair weather due to its inherent instability. All hands were lost. Moreover the concept had already been superseded by contemporary constructions of battleships.

Area: North Sea, Dutch Continental Shelf

Survey vessel: *Zirfaea*, RWS DNZ

Sidescan sonar system: EdgeTech MPX; frequency 270 kHz, beamwidth 0.75°

Image ©: Rijkswaterstaat, North Sea Directorate ■

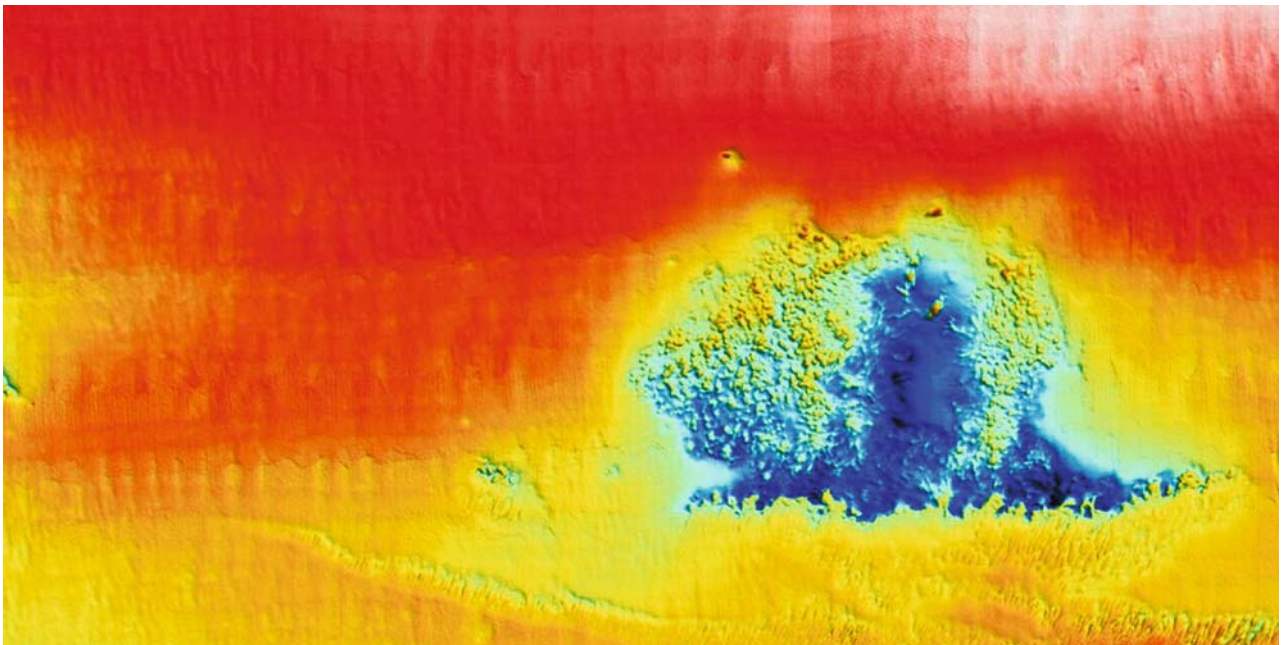


Image Series 7.3.2-4, 7.3.2-4a: Wreck Site of *HMS Hazardous*

The *HMS Hazardous*, built in 1698 was originally called *Le Hazardeux* and was a French 3rd rate warship. In 1703 she was captured by the Royal Navy and taken as a prize to Portsmouth. There she was refitted as the 4th rate ship *HMS Hazardous* in 1704, but in November 1706 the ship was lost in a storm to the north east of the Isle of Wight.

In 1977 the wreck was discovered by Sub-Aqua Association divers. Designated as a protected historic wreck site, the former ship has been surveyed and excavated by the finders. The site has also been documented by high resolution multibeam imagery in 2001. The result is presented here as an overview of the surrounding and nearly featureless area with the conspicuously structured wreck site. A close up visualizes the major features of this site. 10 iron cannons were found, a concreted mass of iron canon balls, and elements of the ship's structure which protrude from the seabed and from under the concretions. The investigation of this place by diver surveys took many years to complete whereas the multibeam survey of the wreck site together with the surrounding area was a matter of just a few hours. Geo-referenced multibeam image of a site and its environment, such as this, can be used by boats help them drop their anchors in non-sensitive areas. When superimposed with acoustic tracking the multibeam image also allows divers or remotely operated vehicles (ROVs) to be navigated efficiently to specific parts of the site.

◀ Image 7.3.2-4.

The wreck site. Multibeam image. The smooth, slightly sloping sandy sediment is interrupted by a strongly eroded field of about 50 m diameter containing the wreck site of the *HMS Hazardous*. The upper part of the surrounding slope, indicated red, is about 5 m deep and the deepest area, indicated dark blue inside the wreck is at about 9 m. The central (blue) wreck site is surrounded by what seems to be a lot of debris at a plateau of 7 m depth (light green) but most of it is blocks of soft sandstone and clay displaced when the ship first settled on the seabed.

Support vessel: *SV Scimitar*; year of survey: 2001
Multibeam system: RESON, type: SeaBat 8125; frequency: 455 kHz, beamwidth: $0.5 \times 1^\circ$, 240 beams, fan width: 120° , swath: 128 m, zoom autofocus
Image ©: ADU/RESON ■

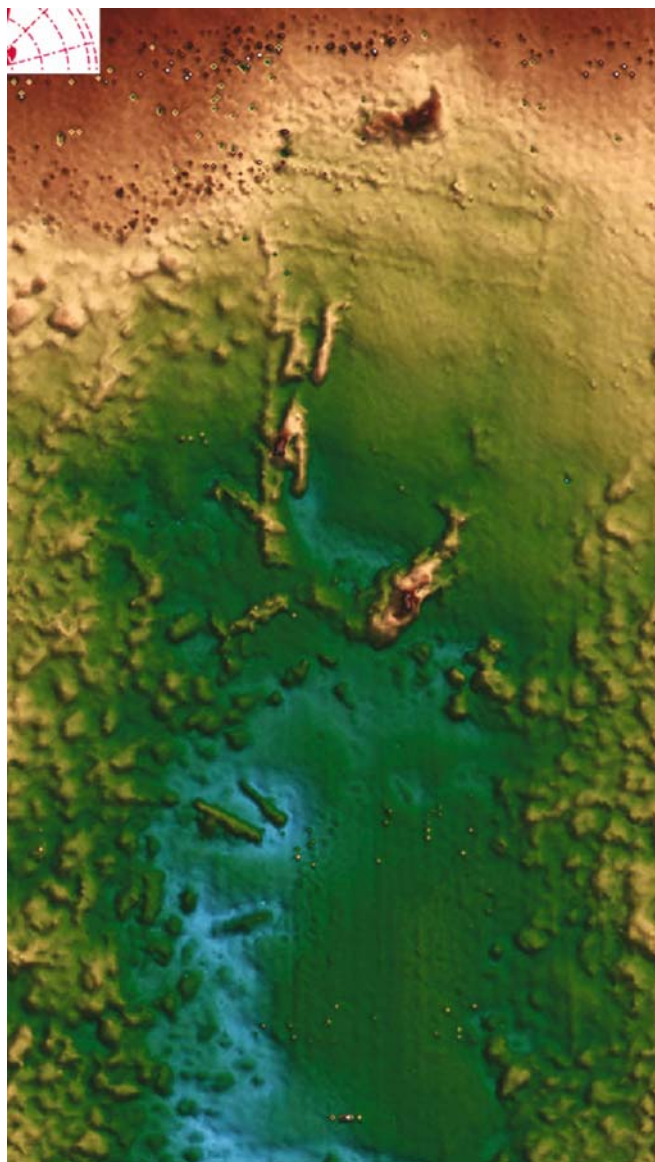
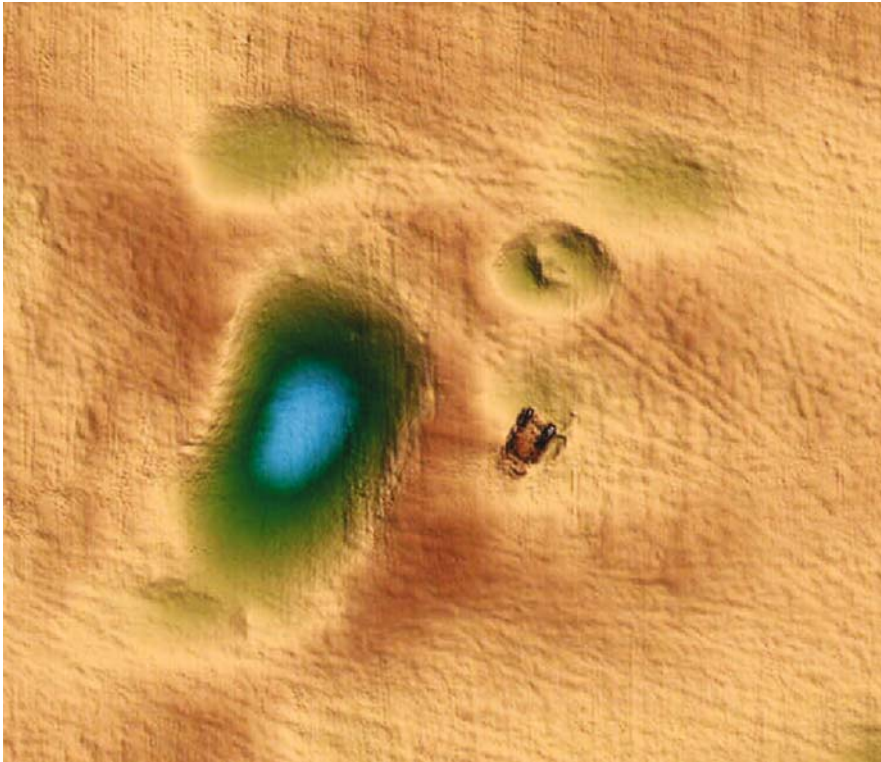


Image 7.3.2-4a.

The central area. Multibeam image. The close up of the central area, approximately 40 m long by 11 m in width (depicted with a reduced color code), allows discrimination between man-made objects and eroded sea floor morphology. The southern, lower part of the image reveals three cannons lying in a depression. In the northern section more cannons and elements of the ship structure are visible. The rectangular feature just south of the upstanding stem post is the outline of an archaeological trench, now backfilled, outlined by steel scaffold tubing which is now buried under a thin layer of sediment.

Image documentation: same as for Image 7.3.2-4 ■

**Image 7.3.2-5.**

Place of excavation of the historic ship wreck HMS Mary Rose. Multibeam image. The *HMS Mary Rose* was the favorite warship of Henry VIII. Commissioned in 1511 she sank in the Solent in 1545 with over 700 men on board as the King watched his warships engage the French fleet. The wreck of the *Mary Rose* was first discovered in 1836 but then forgotten and systematic search only began again in 1965. The main wreck site was located in 1970 and in 1971 as excavation began to reveal the extent of the wreck, plans were formulated to recover the ship. The ship was surveyed and recorded by a team of 600 volunteer divers, scientists and archaeologists as part of the world's largest underwater excavation. The hull was recovered in 1982 and are now on display in the *Mary Rose* Museum together with finds from the site. Fragments of the wreck still remain on the seabed. The excavation site near Ports-

mouth at 50°46' N, 01°06' W is a designated *Historic Wreck Site* under the *Protection of Wrecks Act* of 1973 and is monitored by the *Mary Rose Trust*.

The recent multibeam survey of the excavation site shows the 30 m long depression where the ship rested for over 450 years. The smaller and shallower depressions are the result of scouring of the sediment from around the heavy sinkers of navigation buoys, one of which is still in situ. Also visible are the remains of a small catamaran diving platform used by the investigating team in the 1970s. Interestingly, the whole seabed in the area is criss-crossed by straight lines probably caused by fishermen dragging oyster 'dredges' in the area. These devices incorporate a frame with steel teeth used to dislodge the shellfish which live partially buried in sediment. These grooves were just not obvious to any of the divers on the site and the intensity of this activity in this protected area was unknown before the multibeam survey.

Project: ADU Cultural Resource Management (CRM) Survey; year of survey: 2002

Support vessel: *SV Scimitar*

Multibeam system: RESON, type: SeaBat 8125; frequency: 455 kHz, beamwidth: $0.5 \times 1^\circ$, 240 beams, fan width: 120° or about 80 m swath at the sea floor of 16 m depth, zoom autofocus

Image ©: ADU/RESON ■

Image Series 7.3.2-6, 7.3.2-6a: Salcombe Wreck Site

The area is situated about 30 km southeast of Plymouth in South England is famous as a site of many ancient ship wrecks and even more as the place of the discovery of a huge gold treasure. The British Museum considered this find the "finest assemblage" of gold coins

ever found in Europe. The historic heritage of ship wrecks is an important component of underwater archaeological research, and has benefited from the recent advances in high resolution sound imaging. The example shown is also of particular interest because the extremely corrugated sea floor is a like a natural camouflage which hides smaller relics.

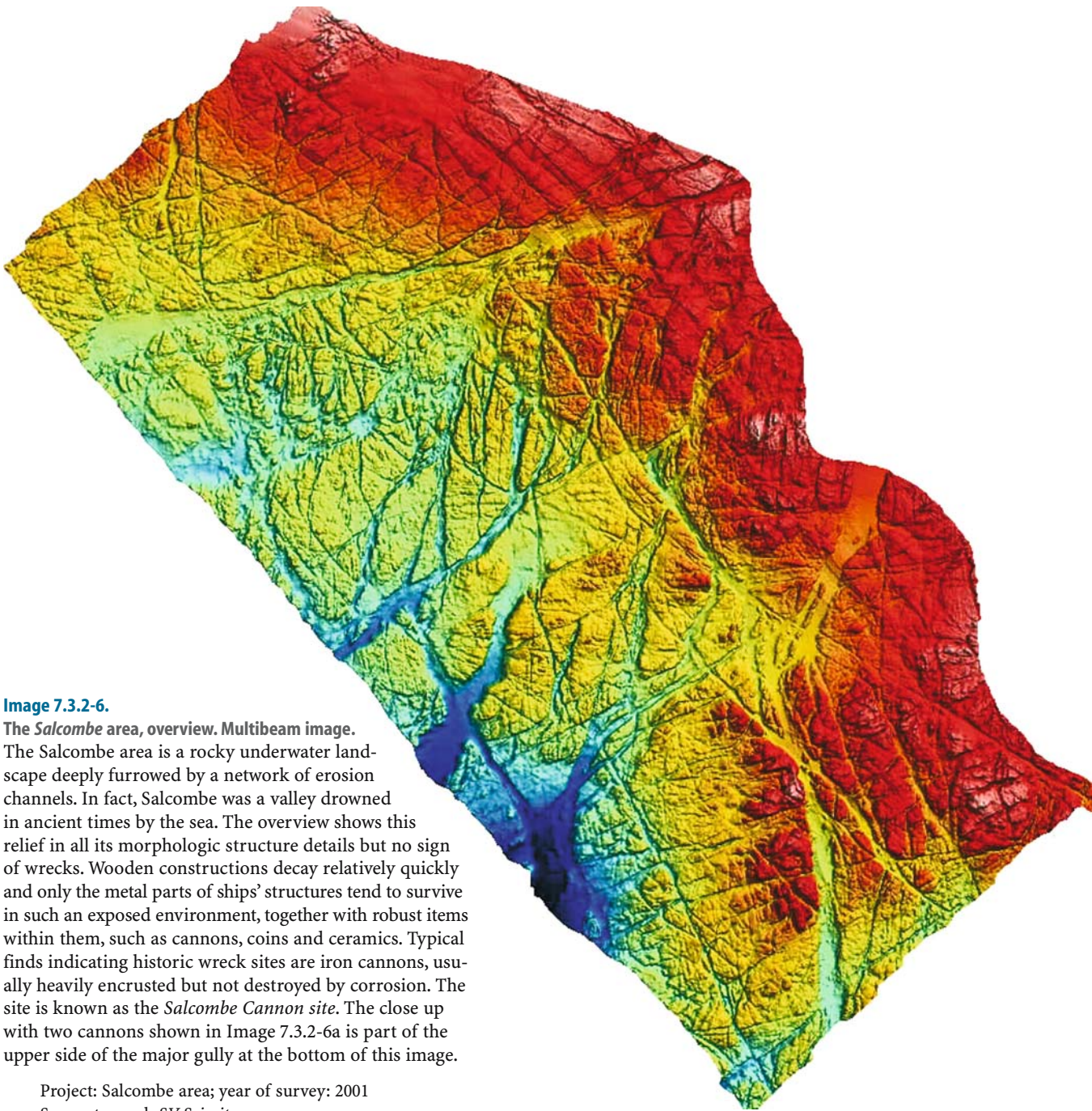


Image 7.3.2-6.

The Salcombe area, overview. Multibeam image.

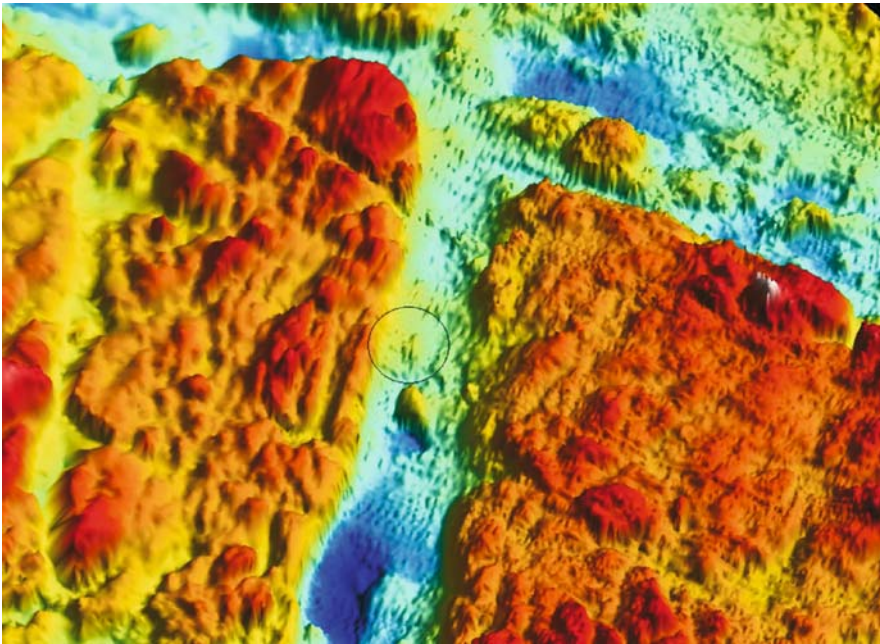
The Salcombe area is a rocky underwater landscape deeply furrowed by a network of erosion channels. In fact, Salcombe was a valley drowned in ancient times by the sea. The overview shows this relief in all its morphologic structure details but no sign of wrecks. Wooden constructions decay relatively quickly and only the metal parts of ships' structures tend to survive in such an exposed environment, together with robust items within them, such as cannons, coins and ceramics. Typical finds indicating historic wreck sites are iron cannons, usually heavily encrusted but not destroyed by corrosion. The site is known as the *Salcombe Cannon site*. The close up with two cannons shown in Image 7.3.2-6a is part of the upper side of the major gully at the bottom of this image.

Project: Salcombe area; year of survey: 2001

Support vessel: *SV Scimitar*

Multibeam system: RESON, type: SeaBat 8125; frequency: 455 kHz, beamwidth: $0.5 \times 1^\circ$, 240 beams, fan width: 120° , swath: 128 m, zoom autofocus; color scale: red and dark blue 15 m and 25 m depth respectively

Image ©: ADU/RESON ■

**Image 7.3.2-6a.**

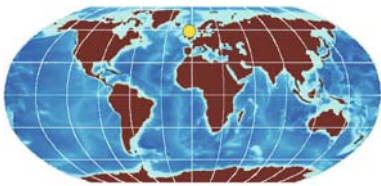
Close up of the Salcombe wreck site. The encircled objects are two “seven-footer” cannons, relics of a vessel of unknown origin of the 17th century. The cannons are revealed because they are visible lying on flat sand within a broad gully. The pleated structure of the sea floor in the upper part is an imaging artifact, only visualized by this enlargement.

Image documentation: same as for Image 7.3.2-1

Image ©: ADU/RESON ■

7.3.3

7.3.3 Battleship Archaeology at Scapa Flow. German War-Ship Wrecks of WW I



One year after the First World War, the remainder of the proud Imperial German Fleet disappeared from the sea surface within a few hours, deliberately scuttled by order of a German Admiral. The place of this huge warship cemetery is the Bight of Scapa Flow, framed by the southern *Orkney Islands*, where two dozen battleships and cruisers, associated with fifty torpedo-boats were drawn together at the end of the war.

Between the twenties and the seventies most of the vessels were recovered. Only seven, all of them battleships and cruisers, are still lying on the sea floor. In 2001, a joint initiative of three Universities: the British Heriot-Watt and St. Andrews and the American New Hampshire conducted a systematic inventory of these wrecks called ScapaMAP. The intention of this Maritime Archaeology Project was dedicated to the documentation, preservation and protection of this promi-

nent historic heritage. The project included gathering of undersea data of the local environment and the regular observation of the condition of the wrecks as part of the management of the site. The documentation and complete mapping was supported and effected respectively by the technical expertise and advanced survey facilities of several companies, in particular one of the leading specialists in high resolution acoustic imaging, RESON.

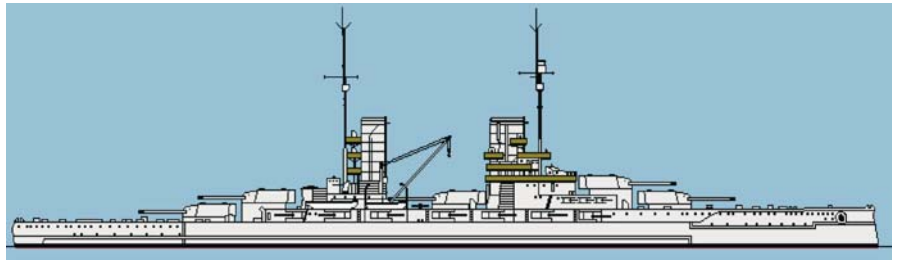
For the first time it was possible to image the individual wrecks of such a size each with only one run. The technique applied was a wide-angle multibeam echosounder with auto-adaptive zoom-focusing (Sect. 4.3.5). Before this project only short range underwater photography of small sections of such scenarios was usual. In fact, there is a decisive prerequisite for this success: the relatively shallow water of the Scapa-Flow, mostly of less than 50 m depth. Though the beamwidth of the individual fan echosounder beams was less than a degree, wrecks in much deeper water could not have been resolved in detail from a surface vessel.

It is known that the spectacular wreck discoveries of the famous *Titanic* in 1985 and of the pride of the German World-War-II Fleet, the battle-ship *Bismarck*

Image 7.3.3-1.

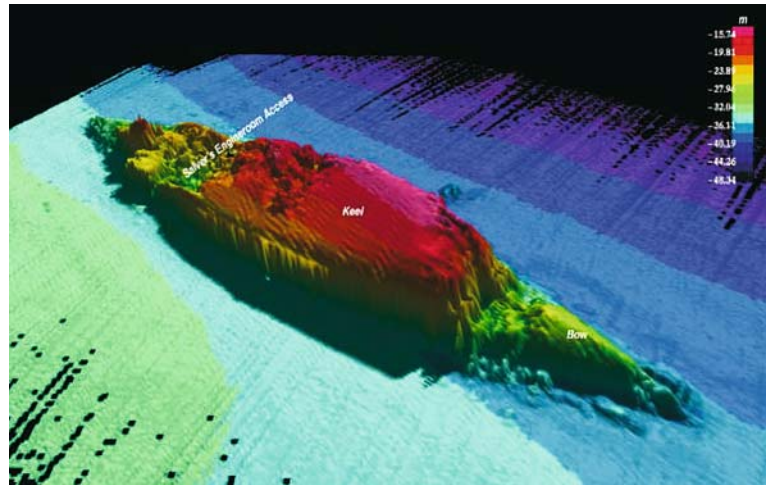
Battle cruiser *SMS König*. Schematic drawing. Same as for *SMS Kronprinz Wilhelm*, and *SMS Markgraf*.

Image ©: Michael Emmerich ■

**Image 7.3.3-1a.**

The *SMS König*, built in Wilhelmshaven and launched in March 1913 was name-ship for the class of battleships of the *Imperial Fleet* which included the *SMS Markgraf* and the *SMS Kronprinz Wilhelm*. The *König* class battleships were an answer to the British *dreadnoughts* of the time. They were 177 m long, carried 14" steel plate armor, displaced 25 390 tons and were armed with ten 12" guns in five towers to serve as mobile artillery platforms. Even so, they could still make 21–23 knots.

Flat bottomed and top-heavy with superstructure, the three remaining battleships have all turtled as they sank, mostly resting on the remaining superstructure, slowly crushing it with their own weight. The wreck of *König* lying in 40 m of water is in poor condition similar to *Markgraf*.



Project: *ScapaMap*; year of survey: 2001

Support vessel: *SV Scimitar*

Multibeam system: RESON, type: SeaBat 8125; frequency: 455 kHz, beamwidth: $0.5 \times 1^\circ$, 240 beams, fan width: 120° or 128 m swath in 35 m of water, zoom autofocus

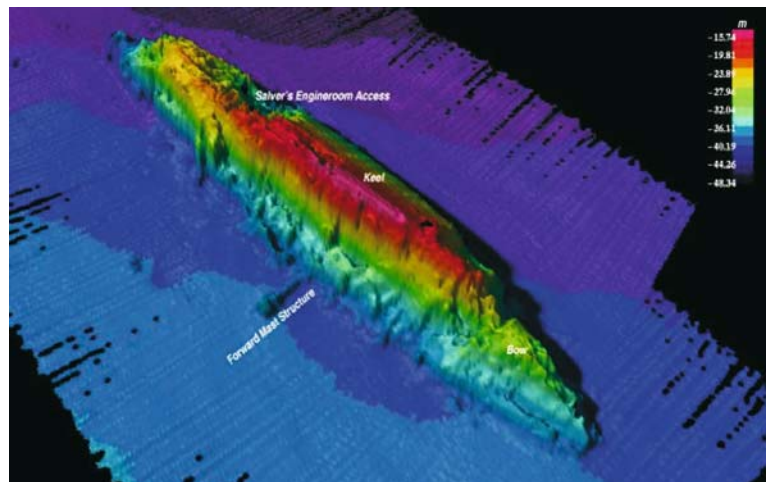
Image ©: Dean Martin, ADU/RESON/Heriot Watt/UNH ■

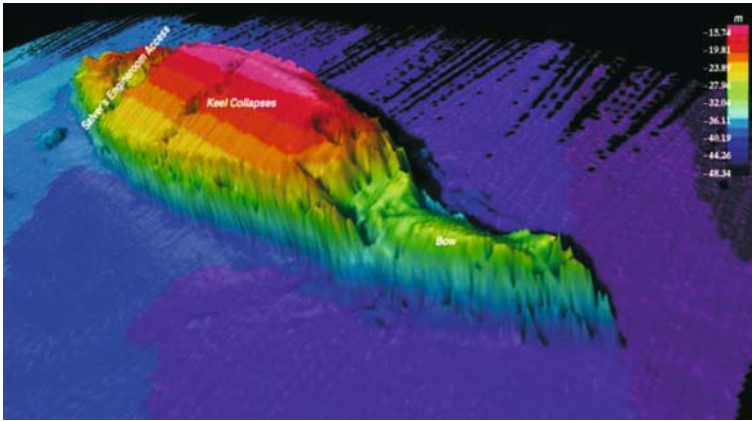
Image 7.3.3-2.

The *SMS Kronprinz Wilhelm*, built in Kiel and launched in February 1914 was a *König* class battleship with the same dimensions, armor, and armament.

The wreck rests almost upside down on her port side superstructure in about 40 m of water. The *Kronprinz Wilhelm* is mostly complete, except for the bow and engine-room sections,

Sound image documentation and schematic drawing: see *SMS König* ■

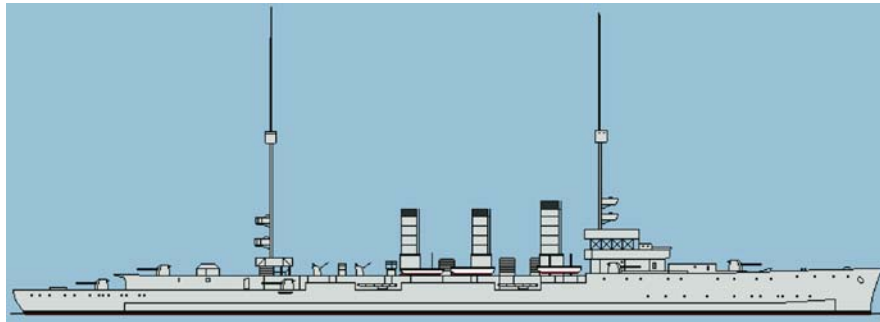


**Image 7.3.3-3.**

The *SMS Markgraf*, built in Bremen and launched in June 1913 was a *König* class battleship with the same dimensions, armor, and armament.

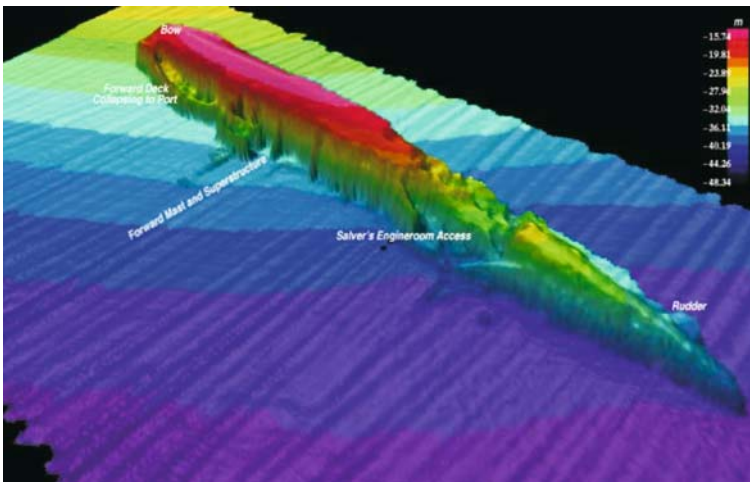
The wreck now lies on the starboard side superstructure in about 45 m of water. Most of the bow section of the ship is missing, and there is significant damage to the stern through salvage attempts.

Sound image documentation and schematic drawing: see *SMS König* ■

**Image 7.3.3-4.**

Light cruiser *SMS Dresden II*. Schematic drawing. Same as for *SMS Cöln II*.

Image ©: Michael Emmerich ■

**Image 7.3.3-4a.**

The *SMS Dresden II*, built in Kiel and launched in April 1917 was name-ship for the *Dresden II* class of light cruisers to which the *SMS Cöln II* belongs. 156 m long and displacing 5 600 tons she was the heaviest of the light cruisers in the fleet, carrying 2.5" armor, and armed with eight 5.9" guns.

The wrecks of the four light cruisers still remaining in the *Bight of Scapa Flow* show various states of decay. The *Dresden II* is lying on her port side on a sloping sea floor ranging from 25–45 m depth. The wreck has suffered significant upper hull damage. The weather deck has fallen out to port, exposing the underside and burying the forward armaments in the mud of the area.

Sound image documentation: see *SMS König* ■

in 1989 at water-depths of 3 800 m and 4 700 m respectively were not suitable for imaging by surface-mounted sonar. At that time, the search expedition didn't have an unmanned submarine available, neither autonomous (AUV) nor remotely cable-controlled (ROV).

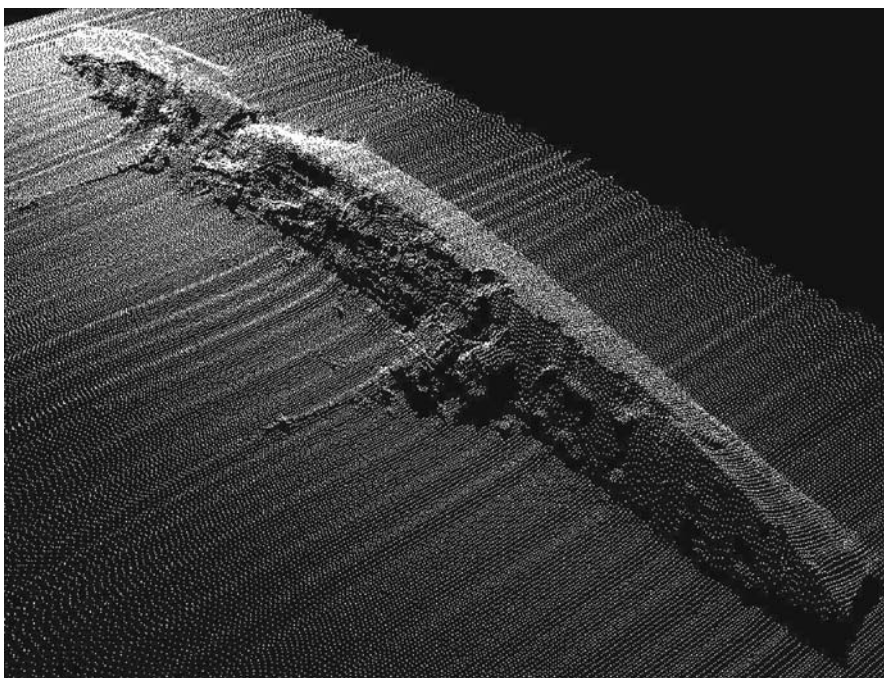
Thus, the image documentation was made of many section photos taken by the cable TV-camera lowered down to a few meters on top of the wrecks, and the complete image had to be an artist's view based on an incomplete photo-puzzle. Today, thanks to advanced

Image 7.3.3-5.

The *SMS Cöln II*, built in Hamburg and launched in October 1916 was a *Dresden II* class cruiser. The *Cöln II* was 156 m long, displaced 5 600 tons and was armed with eight 5.9" guns.

The *Cöln II* is probably the best preserved of the four cruisers, lying on its starboard side in about 35 m of water. Careful inspection of the data shows the remaining portholes, superstructure, rear guns and even lifeboat davits to be in place. Extensive damage has been done to the rear hull to salvage and exploit the engine-room non-ferrous materials, as with all of the remaining wrecks.

The first multibeam sound image of *SMS Cöln II* shows the view from the bow along the upper deck. The depiction of the two sound images of *SMS Cöln II* is different from the preceding ones. The image pixels of the lines and rows produced by the scanning multibeam system (Sect. 4.2.3) are not interconnected here to form closed surfaces. This point-wise depiction is preferable when imaging objects with complex, shadow forming structures. Then the shadow zones remain shadows instead of forming non existing, curtain-like surfaces which are visible on other images of this series.



Sound image documentation: see *SMS König*. Schematic drawing: see *SMS Dresden II* ■

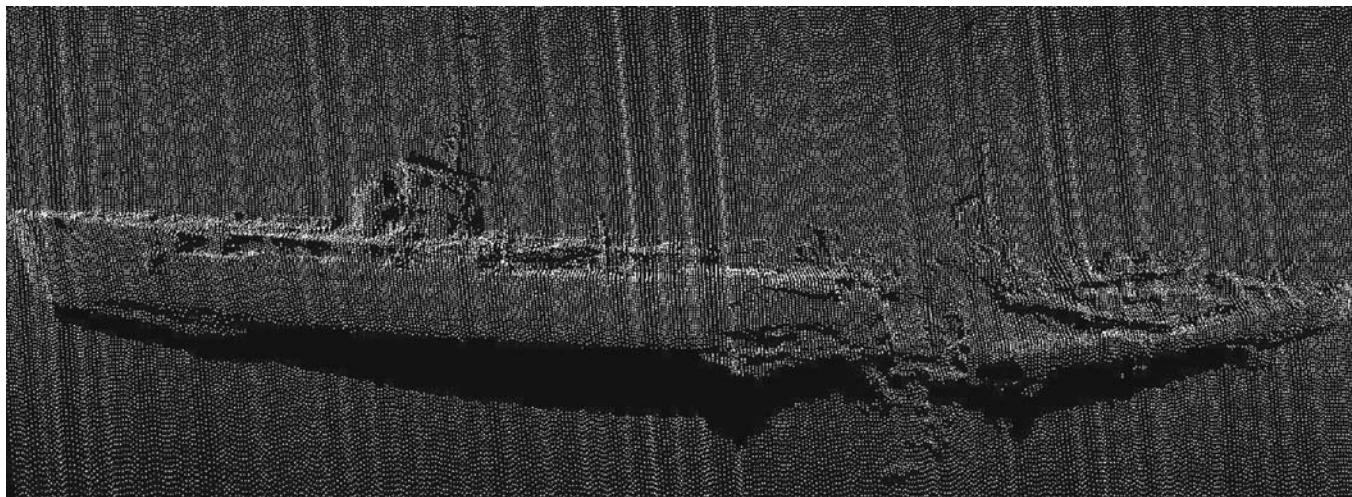


Image 7.3.3-5a. The *SMS Cöln II*. View from the stern along the hull. The large hole in the stern was blown in to make the salvage of engine-room units possible, but the rear guns and gun platform are still intact and clearly visible on the rear deck and super-deck, aft of the rear superstructure. (Same data set as of the preceding image.)

Sound image documentation: see *SMS König*. Schematic drawing: see *SMS Dresden II* ■

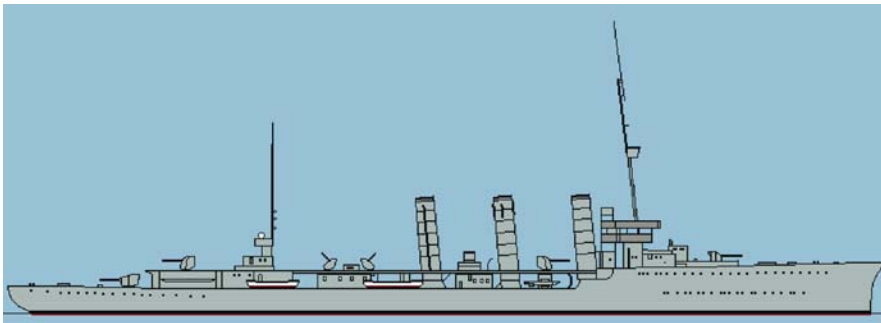


Image 7.3.3-6.
Light cruiser *SMS Brummer*. Schematic drawing

Image ©: Michael Emmerich ■

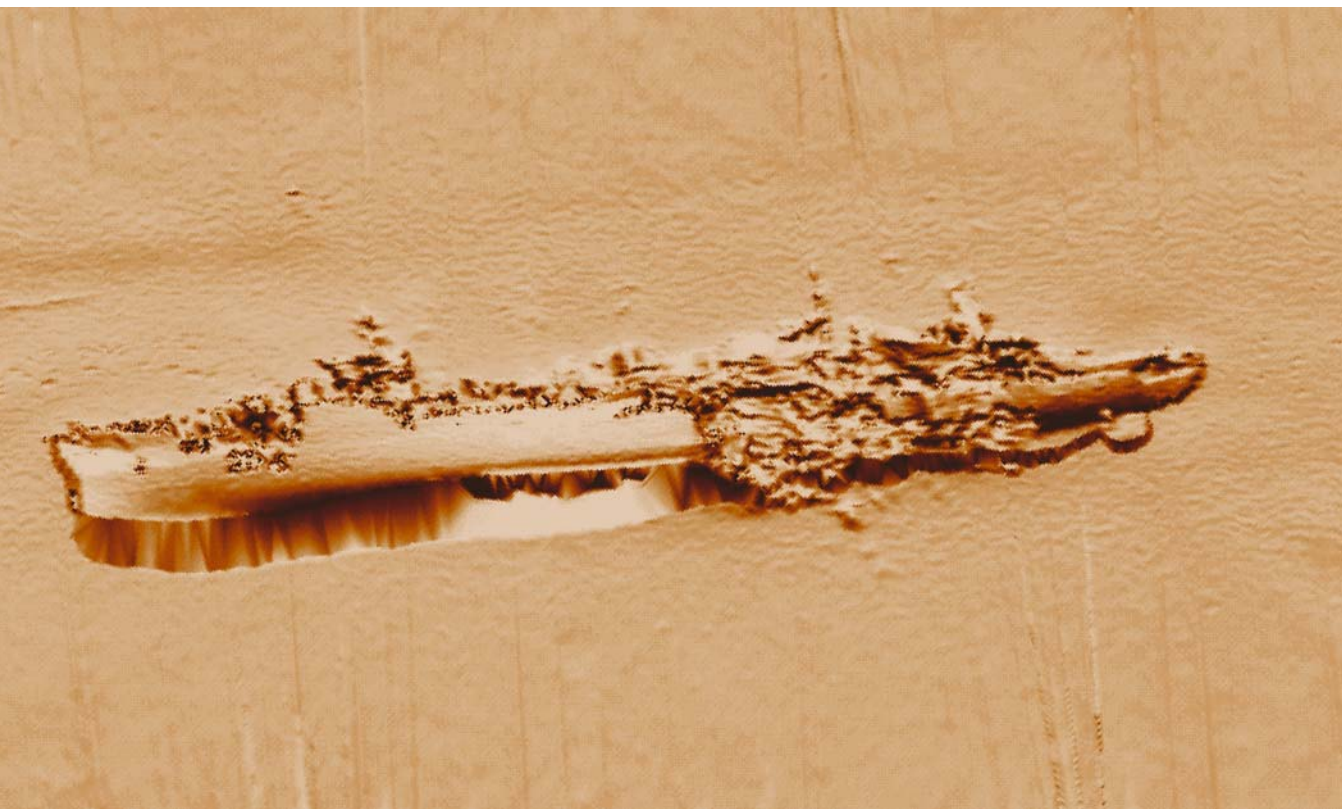


Image 7.3.3-6a. The *SMS Brummer*, built in Stettin and launched in March 1916 was a *Bremse* class light cruiser to serve as a mine layer. Displacing 4 400 tons and armed with four 5.9" guns, the *Brummer* was 140 m long and capable of 28 kts.

Her wreck, viewed from the bow along the upper deck is on her starboard side in about 30 m of water. The hull has had recent fore-plate collapses forward of the superstructure.

Sound image documentation: see *SMS König* ■

deep water AUVs, it would be possible to achieve high quality sound images of entire ships aground on the deep ocean floor as from the Scapa-wrecks as soon as

the autofocus technique will be matched to deep water conditions. This will doubtless be the prevailing technique of the future (Sect. 7.4.1) to investigate and re-

Image 7.3.3-7.
Light cruiser *SMS Karlsruhe*. Schematic drawing

Image ©: Michael Emmerich ■

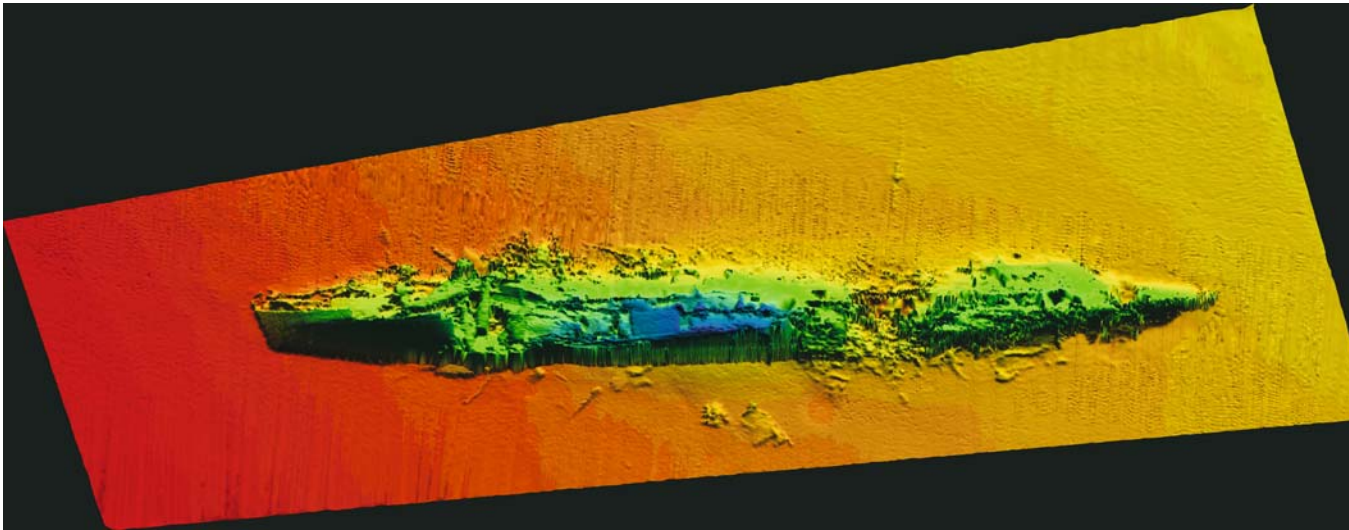
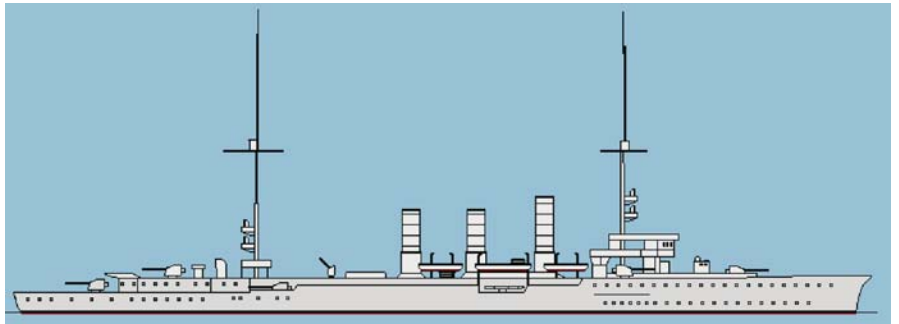


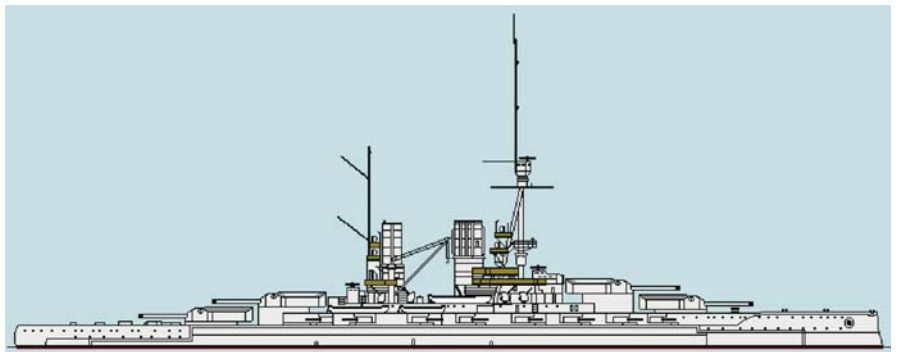
Image 7.3.3-7a. The *SMS Karlsruhe* built in Wilhelmshaven and launched in January 1916 was a *Königsberg II class* cruiser. 151 m long with 2.5" armor and armed with eight 5.9" guns, the *Karlsruhe* could make 27–28 kts at a sprint.

The *Karlsruhe* wreck is in poorest condition of all of the cruisers and resting at the shallowest site in only 25 m of water. Her present state is primarily due to extensive salvage work in the 1970s. The damage is most severe towards the stern of the ship where the wreck is almost broken into two parts.

Image documentation: see SMS König ■

Image 7.3.3-8.
Battle cruiser *SMS Bayern*. Schematic drawing

Image ©: Michael Emmerich ■



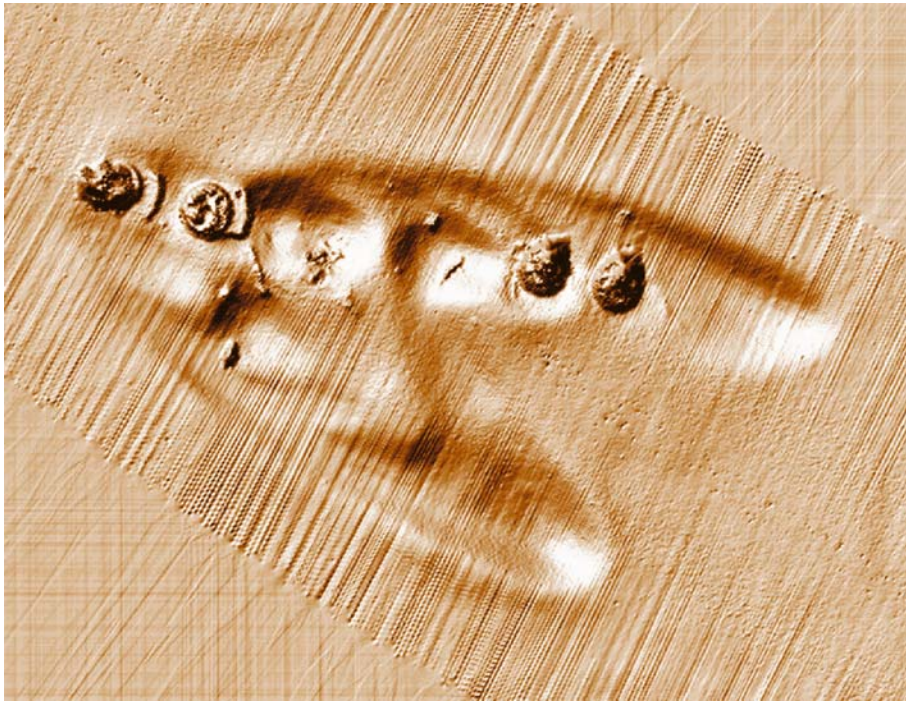


Image 7.3.3-8a. The *SMS Bayern*, built in Kiel, launched in February 1914 and self-scuttled in June 1919 together with the other ships of the *Imperial Fleet* in the *Bight of Scapa Flow* was the heaviest battle ship of the *Imperial Fleet*, together with her sister ship, the *SMS Baden*. Her wreck does not exist anymore. After preceding unsuccessful trials of salvage the *SMS Bayern* was finally raised in September 1933. Only the four heavy gun towers which fell down when the ship was sinking capsized are still there, half buried in the mud. The sound image of the original site of the removed wreck shall demonstrate that this survey technique can reveal and help to identify remaining wreck units.

With 28 075 tons, *SMS Bayern* and *SMS Baden* were the first to be armed with eight guns of the enormous caliber of 15". They were built as an answer to the *HMS Queen Elizabeth*, Britain's first super-dreadnought.

Image documentation: see *SMS König* ■

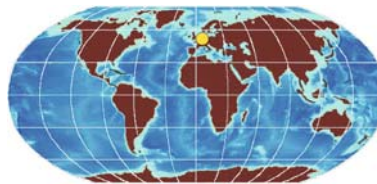
7.3.4

construct the cause of major accidents both of ships and aircraft.

The sound images of Scapa Flow shown here comprehend essentially all of the remaining wrecks of the Imperial German Fleet. The images are remarkable also as they reveal details of interest for inspection of the various types of destruction and damage. The practical experience of the Scapa Flow project has demonstrated that multibeam surveys can provide important advantages for archaeological investigations underwater including the collection of metric data at a rate tens of thousands of times faster than by conventional diving survey methods. Moreover, the data collected by the multibeam sonar can be manipulated by suitable software so that detailed three-dimensional images of each wreck can be viewed from various angles.

7.3.4

Submerged Viking Dike Built around AD 740



The sidescan image of the Viking period dike relics near the later *Haitabu* is shown in the context of submarine archaeology because the site was used for shipping already before *Haitabu* was first mentioned in historic documents and became the center of trade of the western *Baltic Sea* area and far beyond in the 9th century. The *Schlei*, a shallow glacial fjord deeply incised into the coastline (Sect. 5.7.2) provided natu-

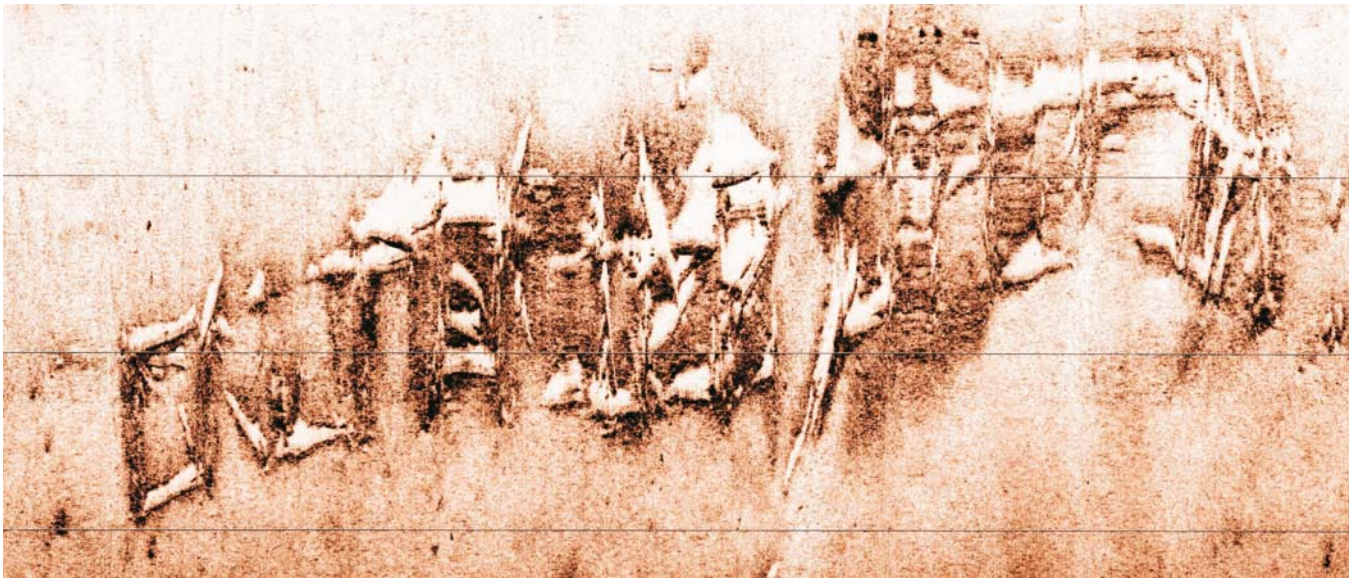


Image 7.3.4-1. The place of the semi-buried ancient wooden pole- and stone construction on the bottom of the fjord Schlei is located on the *German Baltic* coast near the former Haitabu. The construction was of a total length of around 1 300 m. The presumed main duty was to protect the bay and to enable navigation by boats. Wooden relics of that age are rare and difficult to find in the sea when completely buried by sediment. The problem is similar to detecting buried sea mines, which also relies on sediment penetrating sound imaging. A successful approach, demonstrated by a detected Viking relic is shown in the Sect. 7.1.5.

Project: Marine Archeology; 2000

Location: Schlei Fjord, Kiel Bay, Baltic Sea; water depth: 4 m

Vessel: support boat

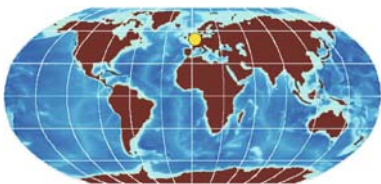
Sidescan System: Klein 595; frequency: 500 kHz, beamwidth: 0.2°; image range: 50 m; unfocused; bright shadows

Image ©: Doris Milkert, FWG, Kiel, Germany ■

ral harbor protection for the shallow draught boats of the Viking era. The prosperous early trade center was the peaceful counterpart of the militant and ill famed predatory *Scandinavian Vikings* who destroyed Haitabu in 1050.

7.3.5

D-Day: Documentation of the Relics



Canadian Royal Navies provided the naval support for *Operation Overlord*, the Allied landings on the *Coast of Normandy*. The invasion was the decisive turning

Operation Neptune was the largest Naval Armada ever assembled. On D-Day, 6 June 1944, the US, British and

point of the Second World War. *Operation Neptune* launched nearly 5 000 vessels, including 672 warships and more than 4 000 other major and minor landing and support vessels. By the end of June more than one million men, 177 000 vehicles and 586 000 tons of supplies landed on the Normandy coast.

In order to outflank the strongly defended harbors of *Cherbourg* and *Le Havre*, two fully functional ports, codenamed *Mulberry*, were built off the *Omaha Beach* and the *Gold Beach*. In less than two weeks these artificial harbors provided the capacity of the Port of Dover that had taken seven years to construct. The *Mulberry* port construction units were concrete floatable caissons of different sizes up to 60 m long, 17 m wide, and 18 m high, displacing 6 000 tons, towed by ocean tugs across the English Channel to Normandy. The caissons with their cellular, hollow structure were scuttled 1½ km off the coastline in

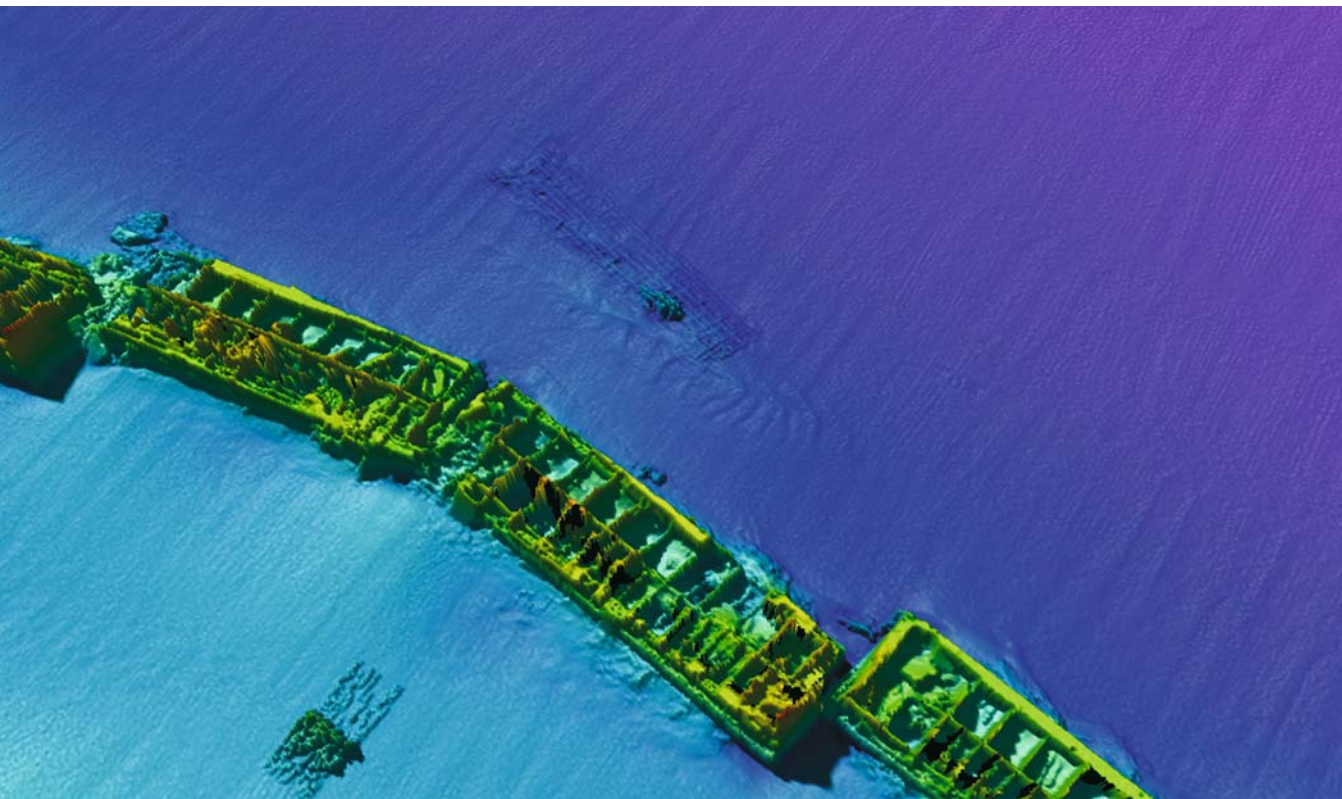


Image 7.3.5-1. The multibeam image reveals a well-preserved example of caisson units in the middle of the Omaha Beach harbor area. The cellular concrete structure is shown with the clearness of a photograph. The ultra-wide-angle imagery was a necessary prerequisite because of the distance of only a few meters from above to the upper contour of the caissons.

Project: D-Day; year of survey: 2002; conducted by: NHC, CCOM, RESON, Inc.

Survey catamaran: *MV Genesis*, 11.3 m length; survey speed: 3–6 knots

Multibeam system: RESON, type: SeaBat 8125; frequency 440 kHz, 0.5° beamwidth, fan of 240 beams, autofocus; positioning: Differential GPS Trimble AG 132 (FUGRO OmniStar); monitoring of vessel pitch, roll, yaw, and heave: multi-component accelerometer and gyro TSS

Image © and information: Larry Mayer, CCOM, Steve Schmidt, NHC, USA ■

about 9 m of water. Inside the line of caissons, the floating loading docks, pier heads and metal roadways created a sheltered anchorage leading to the beach. For added protection the Allies sunk a string of obsolete warships and merchant ships, known as block-ships along with the caissons.

In the third week of June, a storm struck Normandy, washing more than 800 vessels onto the beaches. Strong winds devastated the American Omaha Beach harbor, destroying 20 of the 30 caissons and forced the Allies to abandon it, while the British Gold Beach harbor, which was less exposed, survived the storm.

Nearly six decades later, two US scientific institutions and one of the leading manufacturers of advanced multibeam-echosounders conducted a joint research project in 2002 to investigate and document in detail the state of the underwater remnants of the battlefield. The participants were the US-Naval Historical Center (NHC), the Center for Coastal and Ocean Mapping (CCOM)/Joint Hydrographic Center at the University of New Hampshire and the company RESON Inc. The strategy of the investigation was based on the earlier documentation work by the NHC, prior to the availability of high-resolution 3D-sound-imag-

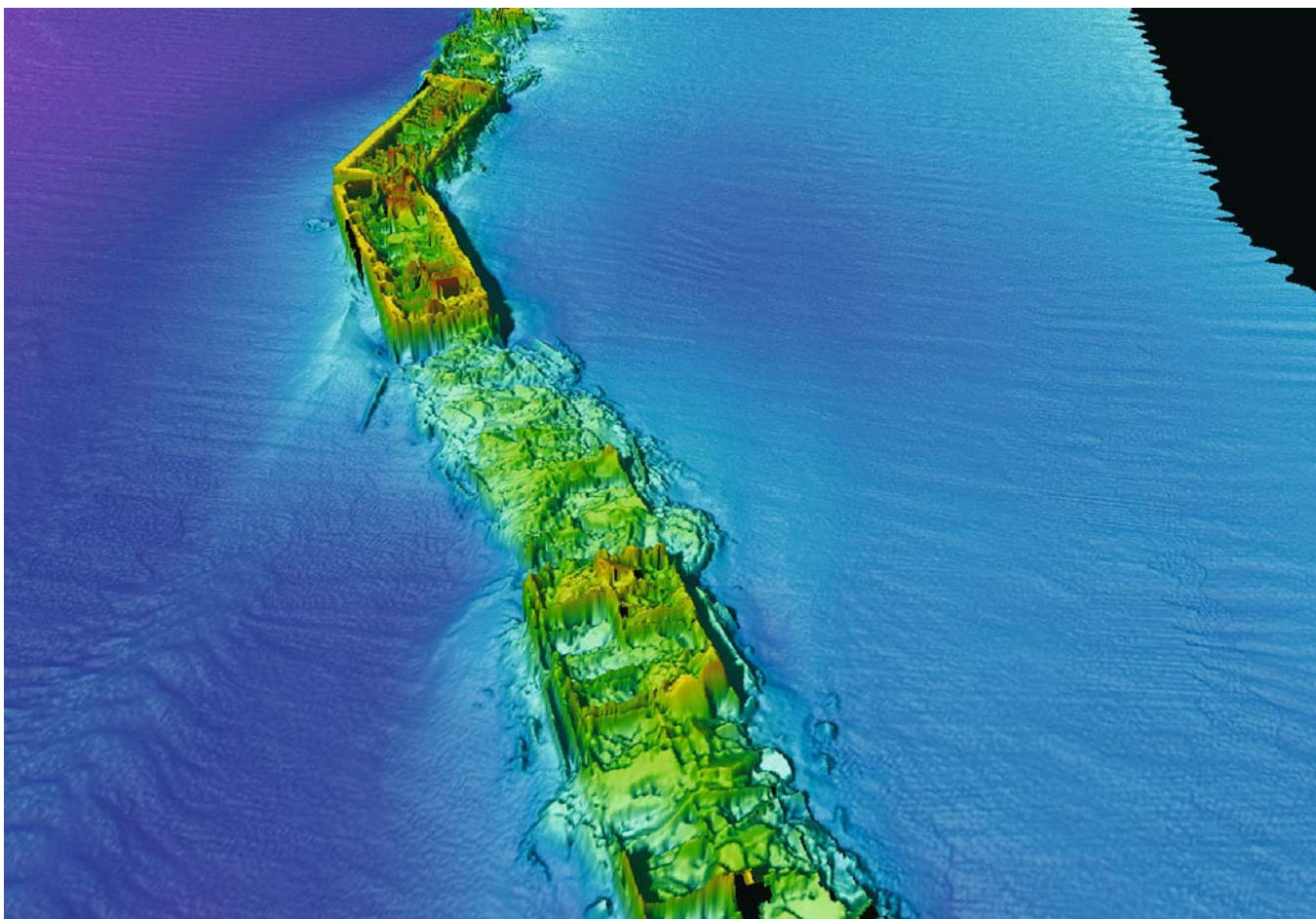


Image 7.3.5-2. These strongly damaged caissons of the former Omaha Beach harbor belong to the western edge of the caisson-line parallel to the shore. The image shows the extent of the damage. On 19 June, a heavy storm destroyed a significant part of the breakwater.

Image documentation: same as for Image 7.3.5-1 ■

ing. The new possibility to achieve metric 3D-mapping in the regime of decimeters and centimeters by zoom autofocus imagery was considered an innovative approach. The main part of the 2002-documentation was conducted by this multibeam technique because it offered a complete and quantitative inventory of essentially all significant wreckage of the historic battlefield in a short time.

Similar to the post war history of the WW I shipwrecks from Scapa Flow (Sect. 7.3.3), the original state of the D-Day undersea remnants has been significantly altered and reduced. During the invasion, U.S. Navy

salvage units commenced operations to sink and/or tow sinking and non-operational craft out of the approach channels. In addition to wartime salvage, commercial operations removed many of the wrecks deemed hazardous to safe navigation and activities of the local fishing communities. But unlike the Scapa Flow ship cemetery, where seven large wrecks of battleships and cruisers still lie on the sea floor, there are no larger ship wrecks in the D-Day field left except for a Tank Landing Ship (USS LST-523) and the almost completely destroyed troop ferry *USS Susan B. Anthony* (AP-72). This extensive removal is surprising since



Image 7.3.5-3. This image appears to document a major ship disaster. However, it is a block ship that was deliberately sunk by the Allies to protect their artificial harbor. The outer breakwater of sunken ships was in place by 11 June 1944. By late 1946, in inspection by a local salvage company revealed that many of the ships' fittings and electrical installations had already been pillaged.

Image documentation: same as for Image 7.3.5-1 ■

several hundred Allied vessels were lost off the Normandy coastline. The *USS Corry* (DD-463), *USS Glennon* (DD-620), *USS Meredith* (DD-726), *USS Rich* (DE-695), *USS Tide* (AM-125), and, the *USS Partridge* (ATO-138) sunk due to battle damage were the subject of post-war salvage as were many smaller units, leaving only large debris fields and few readily identifiable objects. Thus most of the sound images are much less self-explanatory for non experts than those collected during the ScapaMap project. Best preserved and most informative as sound images are those units, which were of no interest for scrap metal exploitation: the large concrete caissons of the provisional harbors. The images selected for demonstration thus concentrate on these objects.

The high-resolution images are based on multiple, overlapping passes of the objects by an 11-m catamaran carrying the high-resolution multibeam system to achieve insonification free of shadows. The data from these multiple passes have been gridded by 25 cm meshes, the horizontal resolution of the 3D-reliefs. Since each grid node represents input from several passes, any positional uncertainty would have defocused the image accordingly. In reality, the horizontal positioning by differential GPS (Sect. 4.2.1) was highly accurate, providing remarkably sharp images. Only single-pass images surpassed them in resolution, though with inevitable sound shadows. The caisson images are from the Omaha Beach harbor, which was devastated by storm during the invasion. They show different states of destruction.



Image 7.3.5-4. These remnants were the former concrete pontoons or Beetles, which supported a section of bridge running from the Mulberry Artificial Harbor complex to the shore. The remains are in very shallow water depths of 2–4 m. The image depicts the texture details and defined edges of the flat top barge structure as well as the depositional and scour features.

Image documentation: same as for Image 7.3.5-1 ■

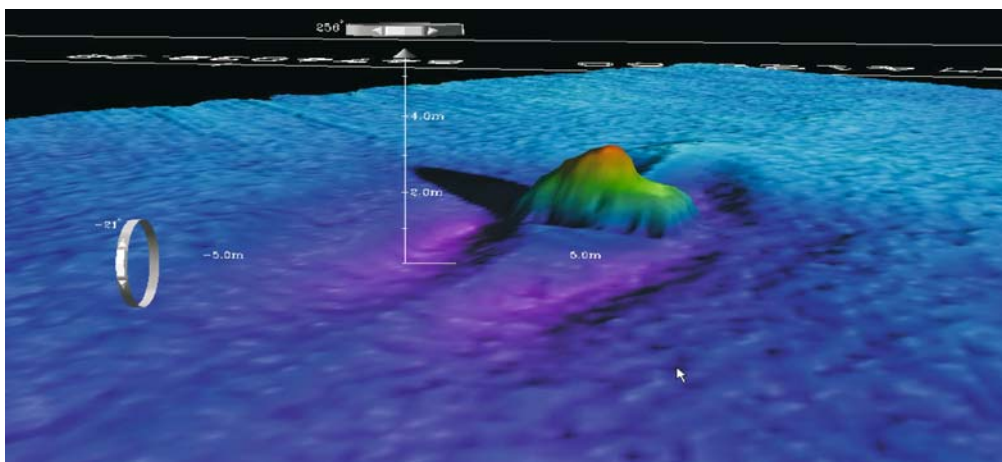


Image 7.3.5-5. The object in the center is one of three wrecks of a special Sherman duplex drive (DD) tank found 4 km off Omaha Beach. These tanks were modified into amphibious vehicles with the addition of twin propellers and a canvas skirt around the hull to provide flotation. They were designed to be part of the first wave of the invasion, maintaining a low profile while swimming to shore to provide covering fire for the first waves of infantry. The fragile construction failed however to cope with the rough sea and, after nearly all but three tanks sank during the first wave (Assault Group O-1). The other tanks were launched closer to the beach by amphibious Landing Craft, Tank (LCT). The contour of the tank-wreck image shows unquestionably a Sherman tank. It is located in 19 m of water and points towards the beach. The typical sediment scour around the tank is quite evident. The 25-cm image grid does not suffice however to resolve the 9-cm gun barrel. It was revealed only by looking into the original sounding data.

Image documentation: same as for Image 7.3.5-1 ■

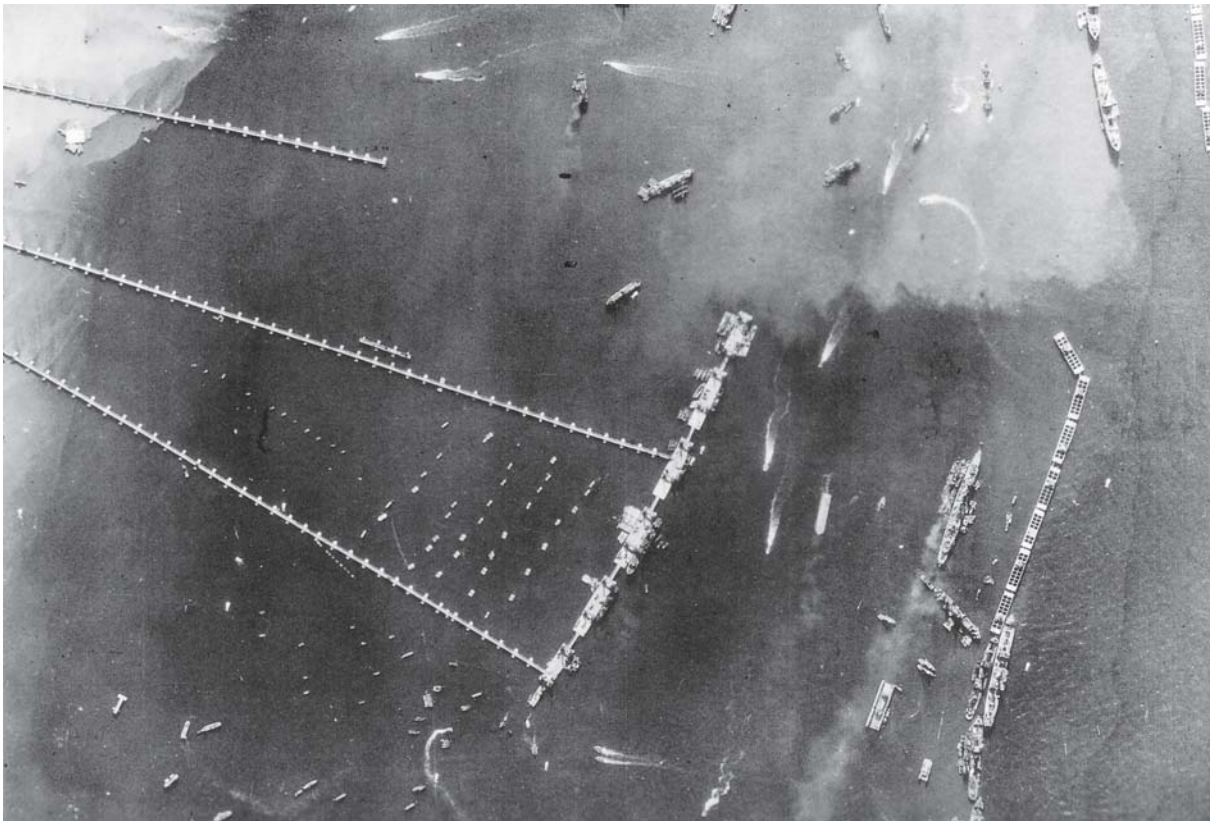


Image 7.3.5-6. Aerial photograph of *Mulberry Harbor*. The Photograph was taken by the Allies during the Operation Neptune, Normandy. The floating caissons are visible at the right side. ■

7.4

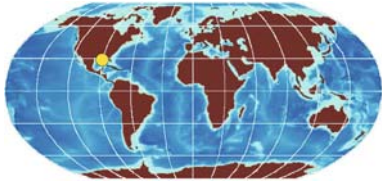
7.4 Close-Up Deep Water Imagery by Autonomous and Remotely Operated Underwater Vehicles (AUV and ROV)

This chapter is intentionally placed at the end of the sound image chapters of the book because it is considered as giving a prospective insight into an essential part of the future of underwater sound imaging. This future has already begun and the AUV technology, which is a kind of oceanic version of unmanned space vehicles based on the same concept of risk avoidance and economy, has proven to offer unique options. Considering the inevitable *wavelength handicap* of imaging the ocean by sound which means: shallow water images are resolved by orders of magnitude better than deep water images when taken by surface vessels, the simple message can only be: *Go shallow!* In other words: the AUV can travel automatically as a terrain

follower close to the sea floor, it can be programmed to react on findings and, particularly important: it can scan large areas by meandering courses more densely than a ship can and at incomparably lower costs, once the challenge of large capacity onboard power-plants like fuel cells has been tailored to the scale of these autonomous deep diving vehicles. The strategy includes remotely operated deep diving vehicles (ROV), usually operated subsequent to AUV surveying to provide selected close-ups and even mechanical manipulations.

The image examples shown hereafter and others made below arctic ice (Sect. 5.4.4) already demonstrate most important applications in the field of research and offshore economy. But they may also inspire the imagination of a finally complete close-up mapping of the still widely unknown side of our own planet.

7.4.1 Deep-Water Sound Imaging of Shipwrecks – Wrecks of Two US-Cargo Freighters and a German Submarine Sunk in the Gulf of Mexico during WW II



Before the era of satellite navigation it was a matter of pure luck if archaeologists could find or even identify

historical shipwrecks in deep water. Even nowadays high resolution multibeam echosounders looking down from the survey ship's hull cannot discriminate a shipwreck from a sea floor feature in the deep ocean, let alone to recognize the type of the sunken ship. One to two degrees beamwidth of the deep-sea echosounder will not resolve more than about 30 m at 2 000 m depth. Such mesh widths are by far too coarse to provide a ship's image of any value. Thus, lowering a searchlight camera close to subjects of suspicion within the reported area of the historic casualty was the only possibility for reconnaissance at that time.

The deep-sea sound imaging evolution to reveal structures in the scale regime of decimeters and less came in three steps. The fascinating story of the discovery of WW II shipwrecks in the Gulf of Mexico, some of which will be shown as sound images, is also a demonstration of this progress of strategy. The basic idea is simple: to overcome the deep water handicap which restricts echo sounding to frequencies around 15 kHz, the sounding device itself should go deeper, and closer to the scenario to enable acoustic close-ups of details. In other words, the demand was: *apply high frequency shallow water imaging technology of several hundred kHz to deep water!* The technical problems to be solved were twofold: resistance to high water pressure, and precise track navigation.

Consequently, the first step of the evolution was to protect the well proven *towed* sidescan sonar for shallow water application against pressure, and extend the tow cable length, leaving the problem of navigation and depth of operation to the tow ship. This is still a useful technique, depending on the task. The next logical step was to use a slack cable connection only for the transfer of data and operational commands and implement the propulsion and power supply into the carrier body of the acoustic devices and other payload. The semi-autonomous body

guided by the supply ship was shaped similar to a small, unmanned submarine and named Remotely Operated Underwater Vehicle, ROV. The vehicle supports the track commands of the supply ship by reporting its actual depth and also its relative position, independently measured by acoustic Doppler navigation.

The third step was to finally achieve a fully autonomous operation, the Autonomous Underwater Vehicle, AUV. It operates with a pre-programmed mission and relies on the most advanced inertial navigation combined with Doppler tracking, to replace the inaccessible satellite navigation GPS. The supply ship is no longer detained during the AUV-mission and can use its expensive ship time for other tasks until retrieval of the AUV. Further, the AUV can operate even under a close polar ice coverage (Sect. 5.4.4) where the supply ship does not or cannot follow. The payload may comprehend a set of mutually supplementing acoustic tools, in particular side-scan-, multibeam-, and sediment-penetrating echosounders, together with video cameras and oceanographic sensors. The strategy of search tracks, mostly meandering lines, is programmed in advance as well as the return track and the schedule in case of emergency. The manufacturers of the AUVs used for the wreck images presented are mentioned in the image captions.

The series of sound images were made in the *Gulf of Mexico* during several campaigns, operating all three technical concepts: *deep towed*, *ROV* and *AUV*. Three wrecks are shown which shared a WW II fate in 1942: *U166*, the only German submarine sunk in the gulf and two of seventy civilian US-freighters sunk or damaged by the torpedoes from 11 of the 24 German submarines that entered the Gulf of Mexico: the cargo freighter *Alcoa Puritan* sunk by *U507* and the passenger freighter *Robert E. Lee*, torpedoed by *U166*. The search area was approximately known from reported positions but only *Robert E. Lee* could be found during the first, deep tow campaign of 1986. The reliable identification was the combination of several circumstantial clues of evidence.

A second, much less conspicuous wreck, also detected in the area during this first campaign was preliminary attributed to *Alcoa Puritan*. It took 15 years and required the technical progress achieved in between to reveal that the second wreck was in reality the *U166*. Finally, the real wreck of *Alcoa Puritan* was found during a separate trial of several months. The invested endeavour and its final success has contributed to the reconnaissance and historical documentation of the

unconditional submarine war during the second half of WW II.

The technical and scientific achievements of the *Three Wreck Site* investigations are primarily due to Robert Church and Daniel Warren of C & C Technologies, who also provided the complete AUV-imagery. Both marine archaeologists were responsible for the initial identification of the *U-166*. Part of the texts of Sect. 7.4.1, which have been revised and supplemented by R. Church are quotations of their publications.

7.4.1.1

The Sinking of the Passenger Freighter *Robert E. Lee*

The passenger freighter *Robert E. Lee* was built in 1924. In July of 1942 the vessel was en route from Trinidad to their final destination of New Orleans with cargo and 268 passengers, many of whom were American construction workers or survivors of U-boat attacks in the Caribbean.

The German submarine *U166*, prowling the shipping lanes of the Gulf of Mexico, attacked the *Robert E. Lee* on 30 July 1942. The torpedo slammed into the starboard side of the vessel exploding just aft of the engine room. “Within minutes the *Robert E. Lee* slipped beneath the waves.” All but 25 passengers and crew were rescued. The wreck was revealed and imaged by deep tow technique in 1986.

The discovery of the wreck of *U166* 15 years later at a short distance from its victim, instead of a place 140 miles away as had been suspected since 1986 was made possible by a deep diving AUV. The primary premise that the *U166* was sunk with all 52 crewmembers was based only on the fact that the *U166* never returned from its war patrol and was never heard from again. The present state of research based on historical evidence and the discovery of the wreck indicates that shortly after its torpedo attack, *U166* was sunk by the *Patrol Craft 566* escorting the *Robert E. Lee*.



Image 7.4.1.1-1. The passenger freighter *Robert E. Lee*. Photograph

Image ©: The Mariners' Museum, Newport News, VA, USA ■



Image 7.4.1.1-2. Wreck of the *Robert E. Lee*. Sidescan sonar image of a deep tow array. The wreck of the passenger freighter lies upright on the sea floor, which is evident from the visible deck structure. The ship is surrounded by debris and impact traces at the bottom. The reported position of the wreck and its size and superstructure in comparison to photographs enabled indubitable identification already in 1986.

The image looks unusual however because of the bright stripe preceding the hull contour and the deep shadow behind. This conspicuously strong echo formation was caused accidentally by specular sound *reflection* at the ship's hull instead of the much weaker sound scattering. The main reason was that the sidescan sonar saw the ship with its side view exposed. The irradiation under a shallow angle indicated by the long shadow, together with a presumably slight list of the wreck would suffice for nearly perpendicular sound incidence and backward reflection. The later sidescan image of *Robert E. Lee* made by an AUV on the occasion of the U166 discovery (Image 7.4.1.3-2) shows a similarly strong side contour, though less pronounced due to the slant angle of sound incidence.

Project: Kepler; time of survey: September 1986

Acoustic device: EDO 4075 sidescan sonar deep tow system; 120 kHz

Water depth: 1 500 m; data collected by Shell International Exploration and Production Inc.

Image ©: National D-Day Museum, New Orleans, Louisiana ■

7.4.1.2

Wreck Images of the Cargo Freighter *SS Alcoa Puritan* Sunk in the Gulf of Mexico during WW II. Deep-Sea Sidescan, Multibeam and Subbottom Profiler Images

The *Alcoa Puritan* was a one-year-old US-freighter of 6 760 tons, 120 m long and 18 m wide. It was sunk on 6 May 1942 by the German submarine *U507* while

transporting a load of bauxite from *Trinidad* to *Mobile Bay*. As *America* geared up for World War II, aluminum was in great demand and production by ALCOA, the Aluminum Company of America, increased correspondingly. ALCOA deployed steamships such as the *Alcoa Puritan* to transport bauxite from mines in *South America* to their plants in the USA. The *Alcoa Puritan*, damaged by the deck-gun fire of *U507* was torpedoed

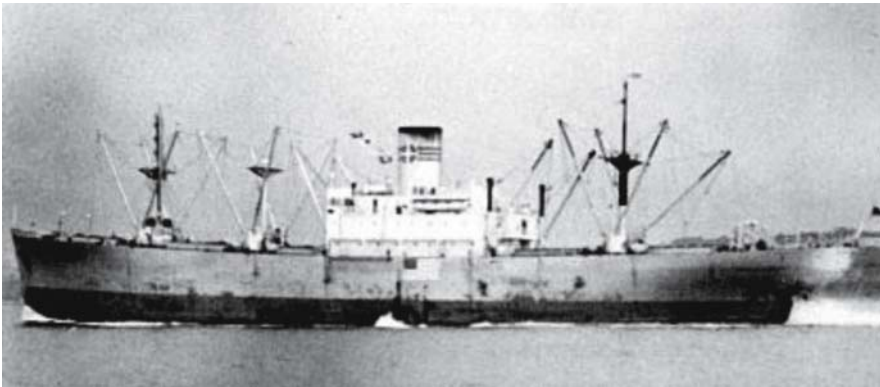


Image 7.4.1.2-1.
The *SS Alcoa Puritan*. Photograph

Image: Steamship Historical Society of America Collection, University of Baltimore ■

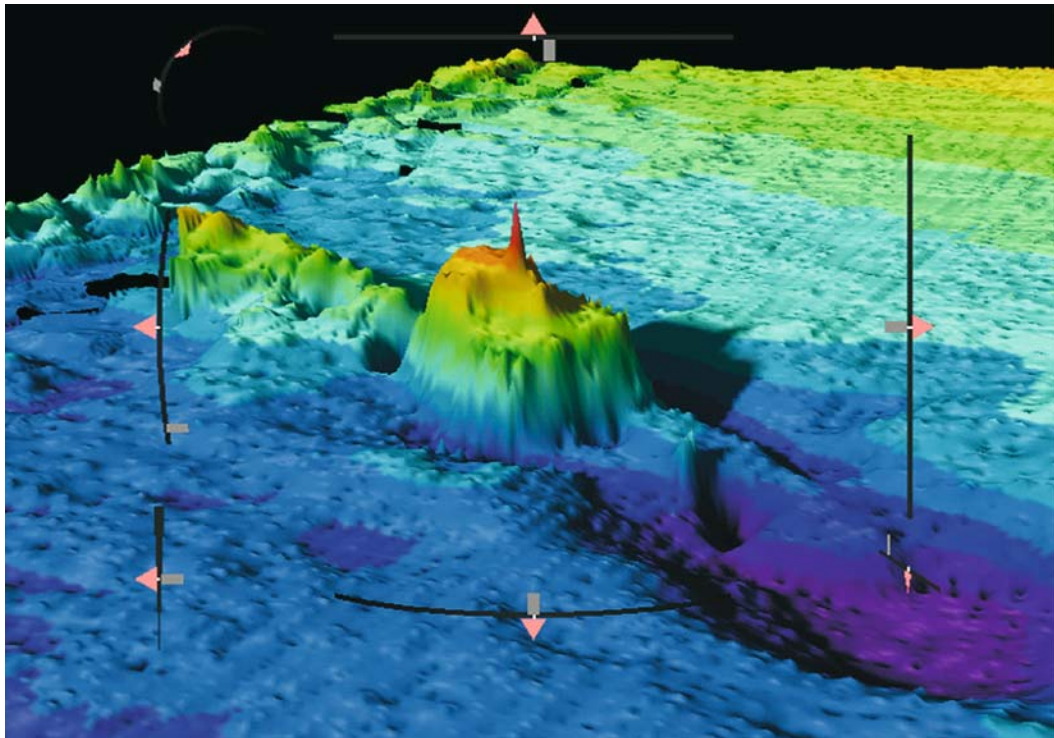


Image 7.4.1.2-2. The wreck of *SS Alcoa Puritan*. Multibeam 3D-image generated from multibeam bathymetry data acquired by a deep tow system. The wreck lies upright on the sea floor oriented parallel to the bathymetric contour. The impact crater is more prominent at the stern of the vessel, which corresponds to the historical account of the vessel sinking stern first. Though the cargo hatches and holds are visualized, those and other structures are less resolved than by the sidescan images, the 3D-image provides the silhouette contour with the pronounced mid section. The weak stripes on the sea floor are sampling pattern artifacts.

Project: Nakika Pipeline; time of survey: March 5 to June 8, 2001

Survey vessel: *MV Geodetic Surveyor* with FGS DeepTow II system

Acoustic equipment: Chirp Deep-Tow sidescan sonar; 120 kHz; subbottom profiler, and Simrad EA 500 bathymetric multi-beam system; acquisition Processing Software: Triton/Elrics Delph Seismic and ISIS Acquisition Processing Suite. Positioning was accomplished by a Sonardyne Ultra-Short Baseline (USBL) acoustic array

Image ©: Shell International Exploration and Production Inc. ■

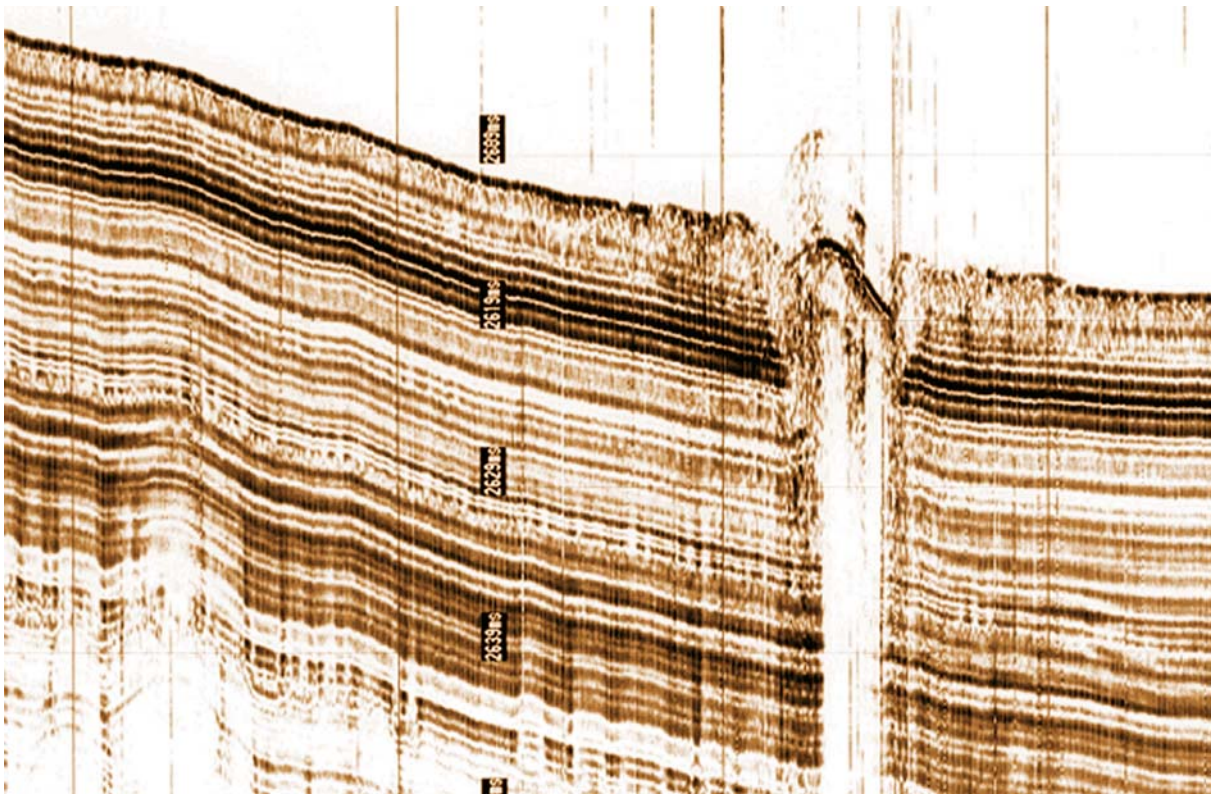


Image 7.4.1.2-3. Seismic cross section of the wreck of *SS Alcoa Puritan*. Subbottom profiler image made by a deep tow system. The cross section shows a contour of the ship, possibly part of the stern, incised into the otherwise undisturbed, strongly layered, soft sediment. These layers are highly transparent to the sounder signals whereas the wreck is nearly opaque, leaving a sharp sound shadow beneath. The mid ship superstructure appears only weakly on top of the bent contour because it was not covered by the center of the sounding beam.

Image documentation: same as for Image 7.4.1.2-2. Sound shadow set bright.

Image ©: Shell International Exploration and Production Inc. ■

after all the passengers and crew had abandoned ship. All were rescued after about 4 hours at sea.

Nearly 60 years later in 2001, Shell International Exploration contracted Fugro GeoServices FGSI to conduct a deep tow survey for a pipeline project in the *Gulf of Mexico*. Several miles southeast of the site where the wrecks of *Robert E Lee* and *U166* were found before, a large shipwreck was discovered at a depth of about 2 000 m. This wreck was identified as the real *Alcoa Puritan*, having been confused with the wreck of *U166* for 15 years. In 2002, following the initial identification of the vessel, Shell asked C & C Technologies to conduct further investigation of the wreck site with

their revolutionary autonomous underwater vehicle, henceforth named AUV. The indubitable recognition of *Alcoa Puritan* was based on the quality of the high resolution acoustic imagery, which allowed the quantification of the geometry of the shipwreck and the characteristic structural clues.

The AUV HUGIN 3000 (Renamed C-Surveyor ITM) developed for deep-sea survey projects was the world's first commercially operated AUV capable of surveying to 3 000 m water depth. Unlike deep towed devices, the C-Surveyor ITM AUV can operate even in rough seas. It achieves higher speeds, greater mobility and an accuracy of navigation within 3 m in 1 500 m of water.

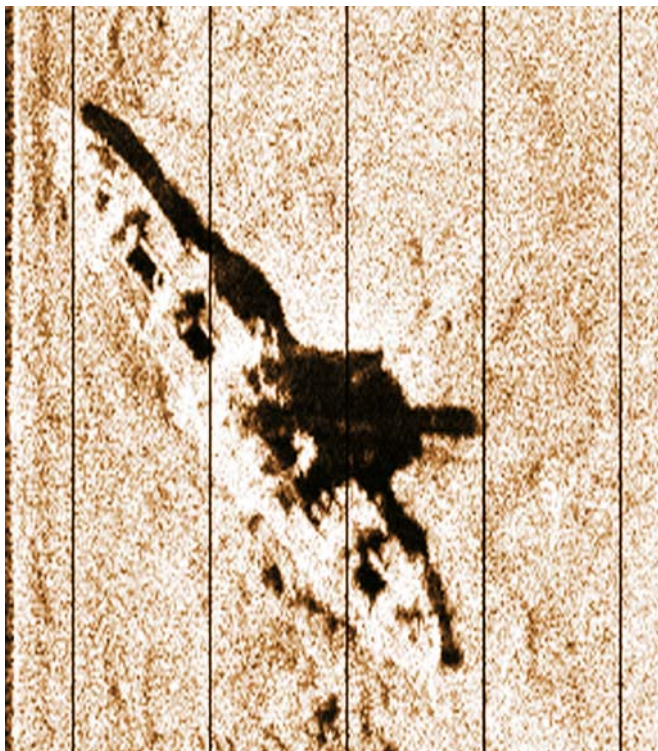


Image 7.4.1.2-4.

The wreck of *SS Alcoa Puritan*. Low frequency (120 kHz) version of a sidescan image made by a deep diving autonomous underwater vehicle (AUV). The image shows the wreck with approximate outlines of the cargo holds and the mid-ship superstructure, with its contour visualized by the characteristic sound shadow. Rather limited debris is observed on the sea floor surrounding the wreck, but the traces of sediment whirled up on the impact of the ship are still visible. The survey strategy was to run line triplets around the wreck site creating a grid like a star pattern. The 0.16 km² coverage required only 90 minutes to complete.

Project: Alcoa Puritan; time of survey: February 2002
 Support vessel: *RV Rig Supporter*; AUV: C-Surveyor™ I
 Sidescan sonar applied for the sound image: 120 kHz.
 Further acoustic equipment of the AUV: multibeam bathymetry and imagery system, dual frequency chirp sidescan sonar, chirp sub-bottom profiler, and inertial navigation system
 Image ©: C&C Technologies Inc. ■



Image 7.4.1.2-5.

The wreck of *SS Alcoa Puritan*. High frequency (410 kHz) sidescan-image made by a deep diving autonomous underwater vehicle (AUV). The increase of resolution by 410 kHz compared to the 120 kHz is striking. Now, the mid ship superstructure, the central stack, the bases of the cranes and all five cargo hatches are clearly visible. The image is a mosaic from two survey lines and therefore the typical acoustic shadow is absent. The sound image taken at about 2000 m depth appears similar to a high quality aerial reconnaissance photo. To take such

deep-sea images from the sea surface is no doubt impossible due to the limits of physics.

The image example of high resolution clearly demonstrates more than the superiority of the AUV technology for high quality sound imaging close-ups in the deep sea. In fact: there is no substitute for the autonomous concept of systematic search patterns. The cable connection of an ROV, which is the indispensable solution for nearest distance photo close-ups (not shown) would be a severe and vulnerable hindrance to the extended meandering courses. The problem may seem similar to a cable connected lawn mover but is of incomparable dimensions.

Project: Alcoa Puritan; time of survey: February 2002
 Support vessel: *RV Rig Supporter*; AUV: C-Surveyor™ I
 Sidescan sonar: 410 kHz
 Image ©: C&C Technologies Inc. ■

7.4.1.3 Wreck of the Only German Submarine Sunk in the Gulf of Mexico in WW II

The surprising discovery of the long-sought undersea wreckage of the German WW II submarine, *U166* in

Image 7.4.1.3-1.

Mid scale survey of the two wreck area with the passenger freighter *Robert E. Lee* and the German submarine *U166*. Overlay of search track pattern with sidescan image made by a deep-sea AUV. The smooth and even search area appears optimum for the detection of objects by AUVs on low level flight. Three targets stand out clearly already at the coarse overview survey of the 2.4-by-3.2-km search area. The right hand circle contains two small objects. The survey time of less than 9 hours was only about one tenth of the time it would have taken to conduct the same survey with deep tow system. The track pattern of the following (Image 7.4.1.3-5) site specific close up strategy loaded into the AUV computer was based on these findings.

Project: Okeanos; time of survey: March 2001
Support vessel: *RV Rig Supporter*; AUV: C-Surveyor I™
Sidescan sonar applied for the sound image: 120 kHz; line spacing: 150 m
Further acoustic equipment of the AUV: multibeam bathymetry and imagery system, chirp sub-bottom profiler
Water depth 1500 m; height of operation above sea floor: 15 m; grid width: 0.5 m; data collected by C & C Technologies under contract to BP and Shell
Image ©: National D-Day Museum, New Orleans Louisiana ■

the *Gulf of Mexico* by BP and Shell in 2001 was in fact a re-identification made by marine archaeologists at C & C Technologies. In reality the position of the submarine wreck was discovered already in 1986 together with the nearby wreck of its victim, the passenger freighter *Robert E. Lee*. But the second, weakly imaged wreck at

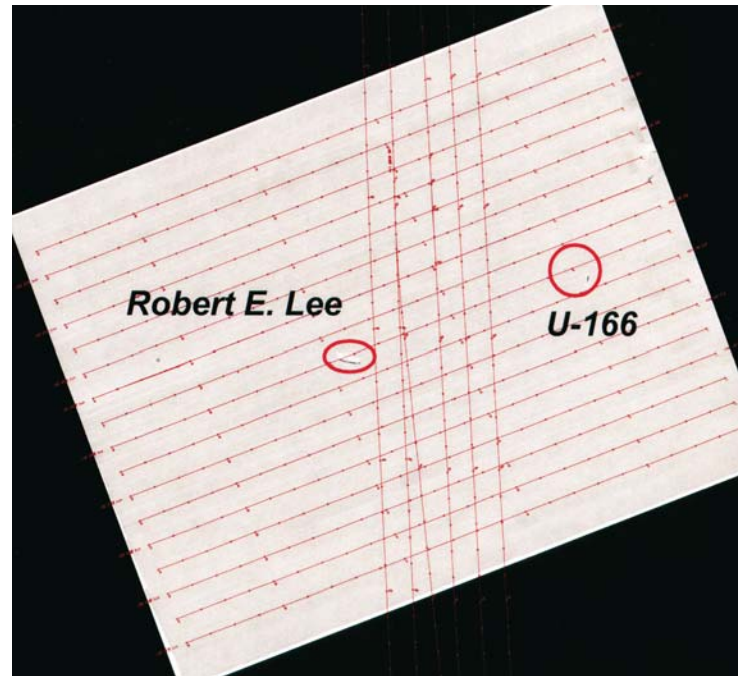


Image 7.4.1.3-2.

Close up of the wreck of the passenger freighter *Robert E. Lee*. Sidescan image made by a deep-sea AUV. The close up of the left hand contact confirms the discovery of the passenger freighter *Robert E. Lee* of 1986. Its position was a reference for the investigation of the other wreck nearby, which was thought to be the remains of the *Alcoa Puritan* since 1986. The sidescan image reveals the wreck sitting upright on the sea floor with a lot of debris surrounding the main structure. The image is depicted with dark shadows.

Image documentation: same as for Image 7.4.1.3-1
Image ©: National D-Day Museum, New Orleans Louisiana ■

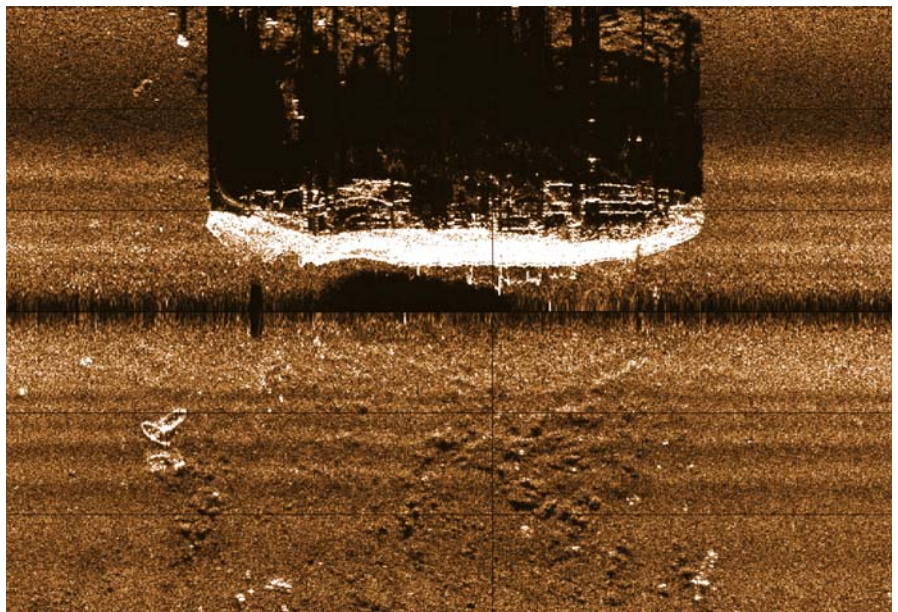




Image 7.4.1.3-3.

Close up of two units of the wreck of the *U166*. Sidescan image made by a deep-sea AUV. The combined length of the two sections are just over half the length of the *Robert E. Lee*. The size of the trough shaped craters is too small to be the impact trace of a freighter the size of the *Alcoa Puritan*. The light stripe structure of the image is an artifact of the sidescan mosaic imagery.

Image documentation: same as for Image 7.4.1.3-1

Image ©: National D-Day Museum, New Orleans Louisiana ■

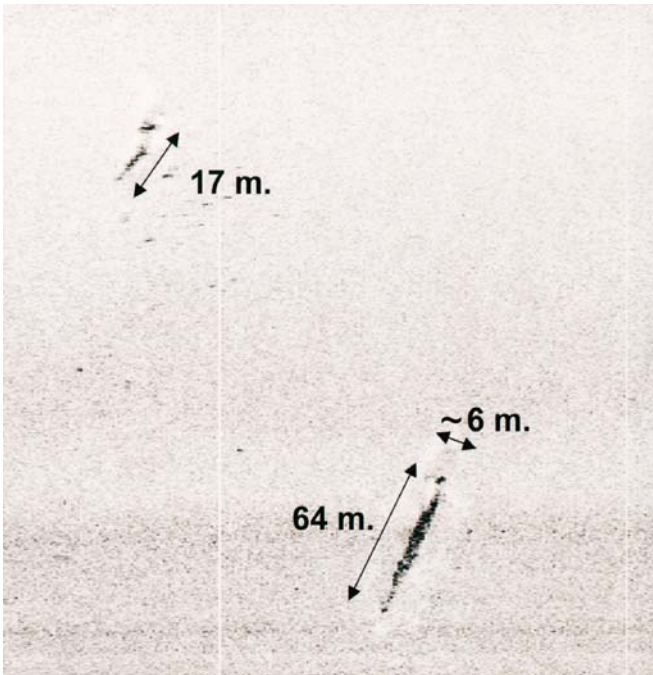


Image 7.4.1.3-4.

Analyzed close up of the main units of the wreck of the *U166*. Sidescan image made by a deep-sea AUV. The measures of the enlarged wreck units supported the suspicion of a broken submarine. In fact, the added lengths of the units appeared to fit a German WW II Type IXC submarine. The reconnaissance of identifiable boat structures however required a narrow search pattern and a further AUV mission with high frequency sidescan imaging.

Image documentation: same as for Image 7.4.1.3-1

Image ©: National D-Day Museum, New Orleans Louisiana ■

this site was erroneously regarded as the wreck of the passenger freighter *Alcoa Puritan*. Indubitable recognition was not successful with the technology of that time. “The area in which the *U166* was thought to have been sunk, is probably one of the most surveyed regions in the world. Oil and gas development in the area has led to numerous intensive surveys using various

echosounding methods. For decades individuals, companies, and governments have extensively searched the area for the *U166*. In 1997 a team from the German Navy even searched for the U-boat, but no trace of the *U166* was identified during over fifty years of examination”.

The discovery of the wreck of *U-166*, the only German submarine sunk in the Gulf of Mexico during the

Image 7.4.1.3-5.**Site Specific close up pattern of U166.**

The center area enclosing the wreck units of the supposed submarine was covered at three different angles of approach and a low level flight of the AUV. This reconnaissance strategy secured optimum directions of view and a maximum exploitation of the resolution capability of structures. The narrow line spacing required hairpin bends of the meandering course. The pattern enclosing the wreck units of the *U166* (arrows) was conducted at an average AUV-speed of 6.5 km h^{-1} .

Image documentation: same as for Image 7.4.1.3-1

Image ©: National D-Day Museum, New Orleans Louisiana ■

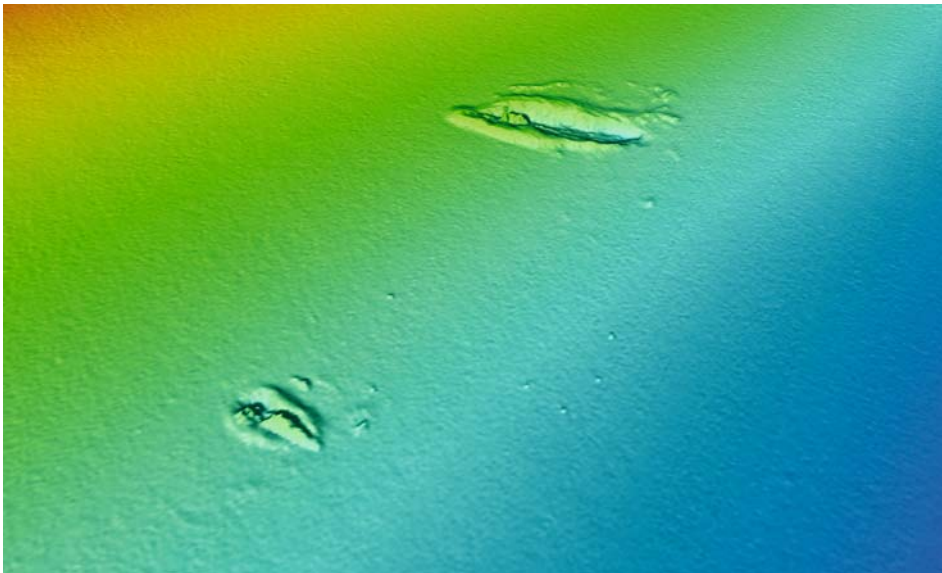
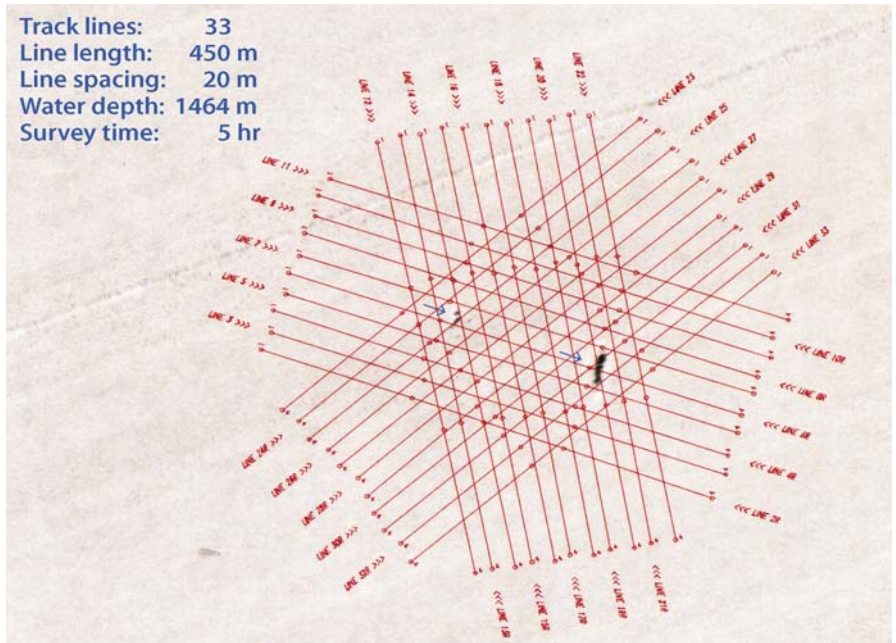


Image 7.4.1.3-6. Two parts of the wreck of the German submarine *U166* inside of impact craters. 3D-multibeam image made by a deep-sea AUV. The 3D-image shows the displaced sediment volume around the larger and the smaller lengthy crater. The color steps in meters depth indicate the slight slope of the conspicuously uniform sea floor. The resolution of the 3D-image cannot compete with the subsequent sidescan image at this distance but quantifies the dimensions of the crater relief. As the transducer array is unfocused, the resolution cell of 0.5 m is nearly the same as the length of the transducer at this short range of some ten meters.

Project: U-166 Archaeology and Microbiology Investigation; time of survey: October 2003

Support vessel: *RV Rig Supporter*; AUV: C-Surveyor™, flight height: 10 m

Multibeam system: Simrad EM2000; frequency: 200 kHz; 111 beams; coverage: $5 \times$ the altitude

Image ©: C&C Technologies Inc. ■



Image 7.4.1.3-7. Main part of the wreck of the German submarine *U166*. Sidescan image made by a deep-sea AUV. The main section of the submarine wreck at a depth of 1 500 m appears surprisingly intact, even though the bow is separated from it. Though *U166* was not air-bombed after having sunk the *Robert E. Lee* as initially assumed, the depth charges by the escort vessel of the sunken freighter either weakened or broke the hull of *U166* and the submarine subsequently broke in two scattering debris across the sea floor. The bow of the submarine is missing at this site and was found at a distance of 152 m away. Further noticeable is the sediment trough with the wreck inside and the traces of displaced muddy sediment, presumably due to the wreck impact, though the destruction occurred nearly 60 years before this sound image was made.

Image documentation: same as for Image 7.4.1.3-1

Sidescan sonar: 410 kHz

Depiction: dark shadows

Image ©: C&C Technologies Inc. ■

war, was made when BP and Shell contracted C & C Technologies to survey the planned underwater pipeline route *Okeanos*. This deep-water pipeline was for transport of natural gas to shore from ultra-deepwater fields. As a result of the find, BP and Shell elected to re-route the *Okeanos* pipeline farther away from the site where the wrecks of the *Robert E. Lee* and the *U166* lie in approximately 1 500 m of water about 72 km from the mouth of the Mississippi River.

The discovery was made using a one-of-a-kind, unmanned autonomous underwater vehicle (AUV), owned and operated by C & C Technologies. The vehicle was developed through the cooperative efforts of C & C and Kongsberg Simrad and was on contract to BP and Shell at the time of the discovery. The AUV utilizes sonar and other equipment to provide detailed images of the seabottom needed for determining optimum pipeline routes.



Image 7.4.1.3-8. Two parts of the wreck of the German submarine *U166*; images combined. Sidescan images made by a deep-sea AUV. The framed sound image of the missing bow of *U166* is digitally attached to the main wreck, a bit offset to indicate the fragments more clearly. The conning tower and the forward and aft gun as well as the main deck structure elements of the submarine can be recognized. The adjusted collage fits to the shape and dimensions of *U166* as shown by the class plan drawing.

Image documentation: same as for Image 7.4.1.3-1

Sidescan sonar: 410 kHz

Depiction: light shadows

Image ©: C&C Technologies Inc. ■

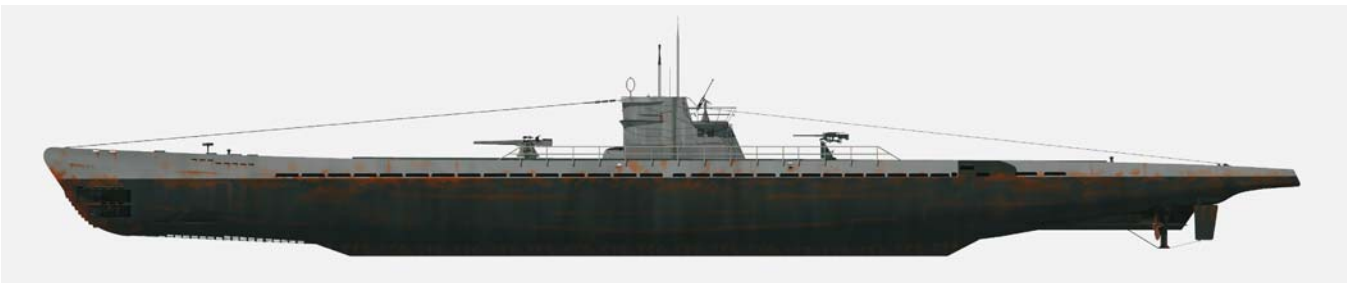
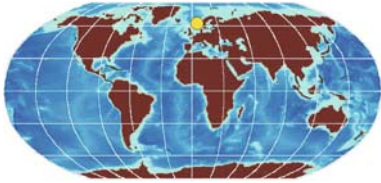


Image 7.4.1.3-9, 9a. Schematic plan and side view of the class drawing with superstructure. The comparison of the combined wreck images with the plan of the class drawing demonstrates the approximate coincidence of the dimensions, the contours and the main elements of the deck structure.

Illustration ©: Andrew W. Hall, courtesy: The PAST Foundation, Ohio, USA ■

7.4.2

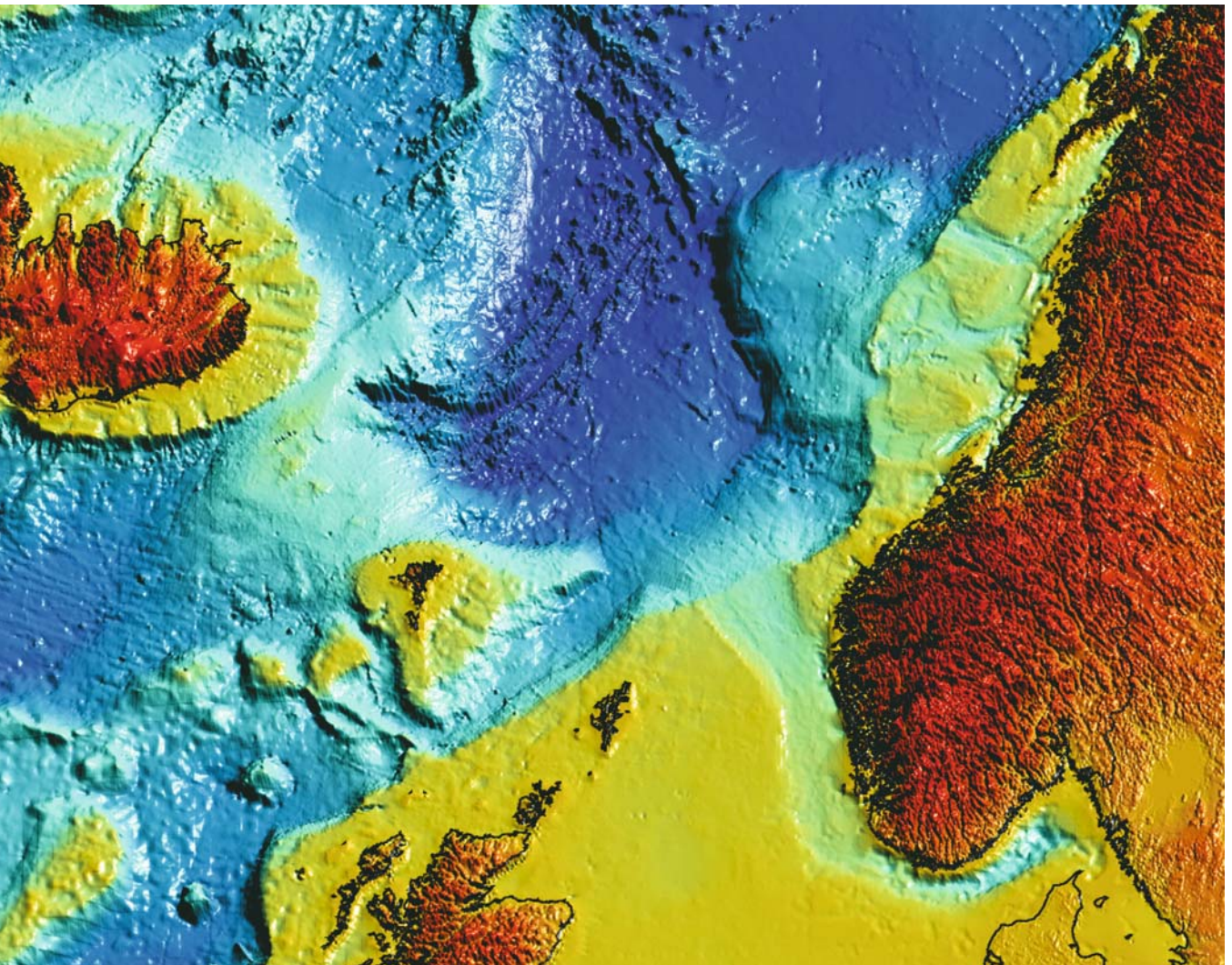
7.4.2
The Ormen Lange Gas Field inside the Storegga Slide Area.
A Sea-Floor Relief Exploration for Pipeline Route Planning.
Multibeam Sound Imaging by Surface Vessels
and Deep Diving AUV

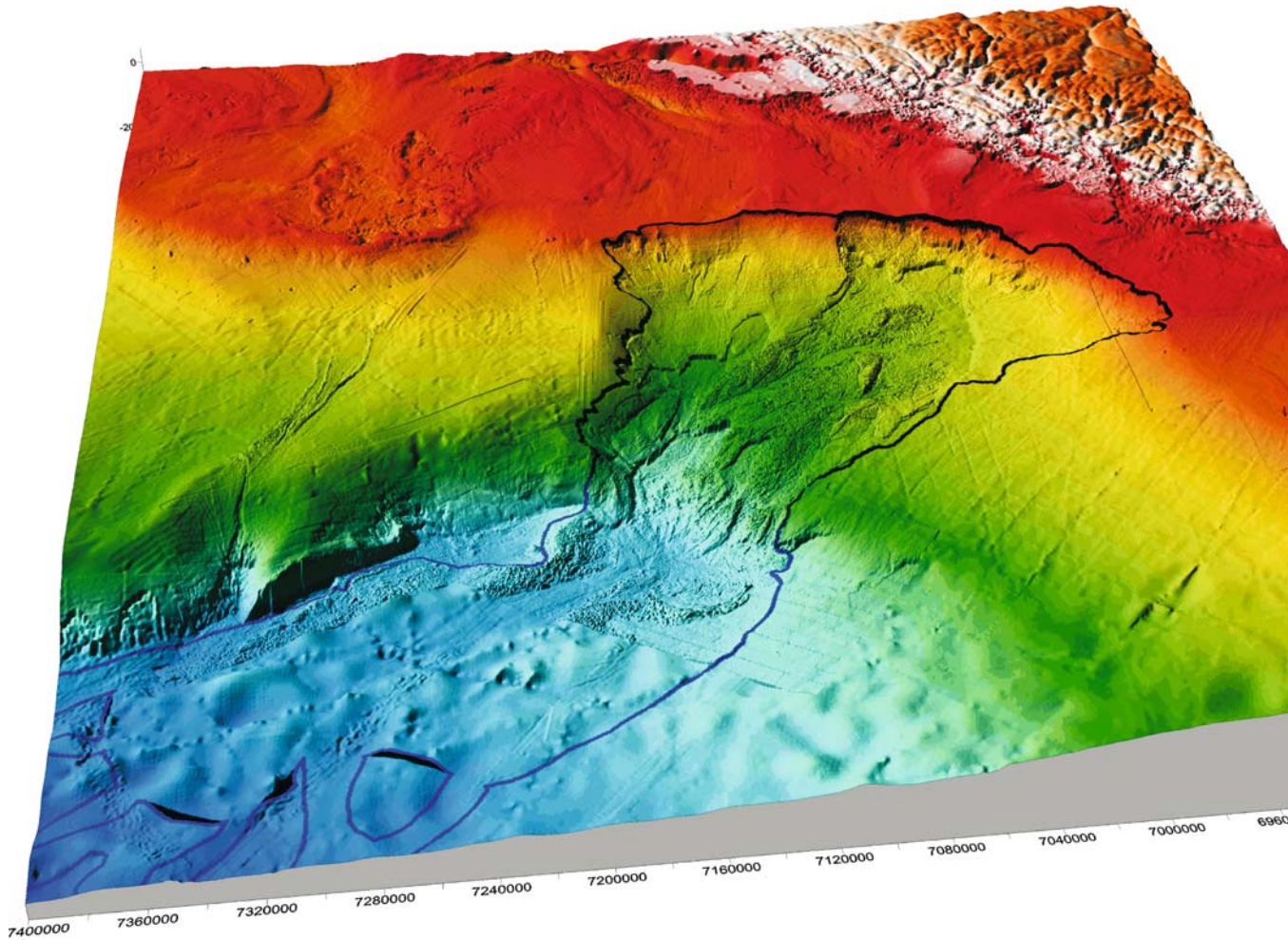


major mineral gas deposit: the *Ormen Lange* gas field, 120 km west-north-west of Kristiansund. The access to this

The *Storegga Slide* (Sect.5.3.1.1), probably the largest exposed landslide of the planet, is also the location of a

site off the Norwegian coast can only be achieved by crossing the prehistoric slide area with a pipeline down to 850 m depth. This is already the depth regime of the continental slope and a technical challenge of another dimension to the gas and oil fields on the continental shelf, where the water depth is often less than 100 m. Moreover, the surface of the Storegga Slide is similar in kind to the bed of a large avalanche on land but much larger in the scale of the debris and with a thicker coverage of sediment grown over thousands of years. Huge blocks up to 60 m in size and innumerable seamount-like block features stand out, from a few meters up to tens of meters above the sediment coverage. According to bottom samples, the soil varies from very stiff clay with boulders to soft clay sediments.





◀ Image 7.4.2-1.

Large area overview of the Storegga Slide. Composite image. The relief depiction shows the escarpment as part of the southern shelf break off Norway. It is adjacent to the channel of the Norwegian Deep and both terminate in the major deep basin of the Norwegian Sea, indicated dark blue, halfway between Iceland and Norway. The impressive relief depiction combines the usual simulated shadowing with simulated highlights which together provide a “wet surface” effect.

The relief map is based on several data sets, in particular the IBCAO-map covering the Polar Basin (Sect. 5.4.1), the ETOPO2-satellite altimetry map, supplemented and improved in resolution by available echometric bathymetry (Sect. 5.1.1.5), and finally the TERRAINBASE map which incorporates recent regional bathymetry. Altogether the resolution is better than 3 km grid width.

Image ©: Stein Wendel, Egil Ingebretsen, Norsk Hydro ASA ■

Image 7.4.2-2.

Cut out map containing the upper part of the Storegga Slide area.

The slide area is indicated by a black line. The headwall representing the sharp shelf break is nearly 200 km wide. The pipeline transition across the shelf break must be placed in the center of the middle section of the slide. This sub-area is evident by a broad field of conspicuously coarse debris cluttered in aggregates of several hundred kilometers square. The water depth at the top of the headwall is 250 m; the dark blue area is 3 200 m deep. Since the critical part of the slide escarpment to be crossed by the pipeline route is near the headwall, the respective sound image close ups of highest resolution by AUV surveys have been selected to be shown hereafter (Images 7.4.2-4, 7.4.2-6).

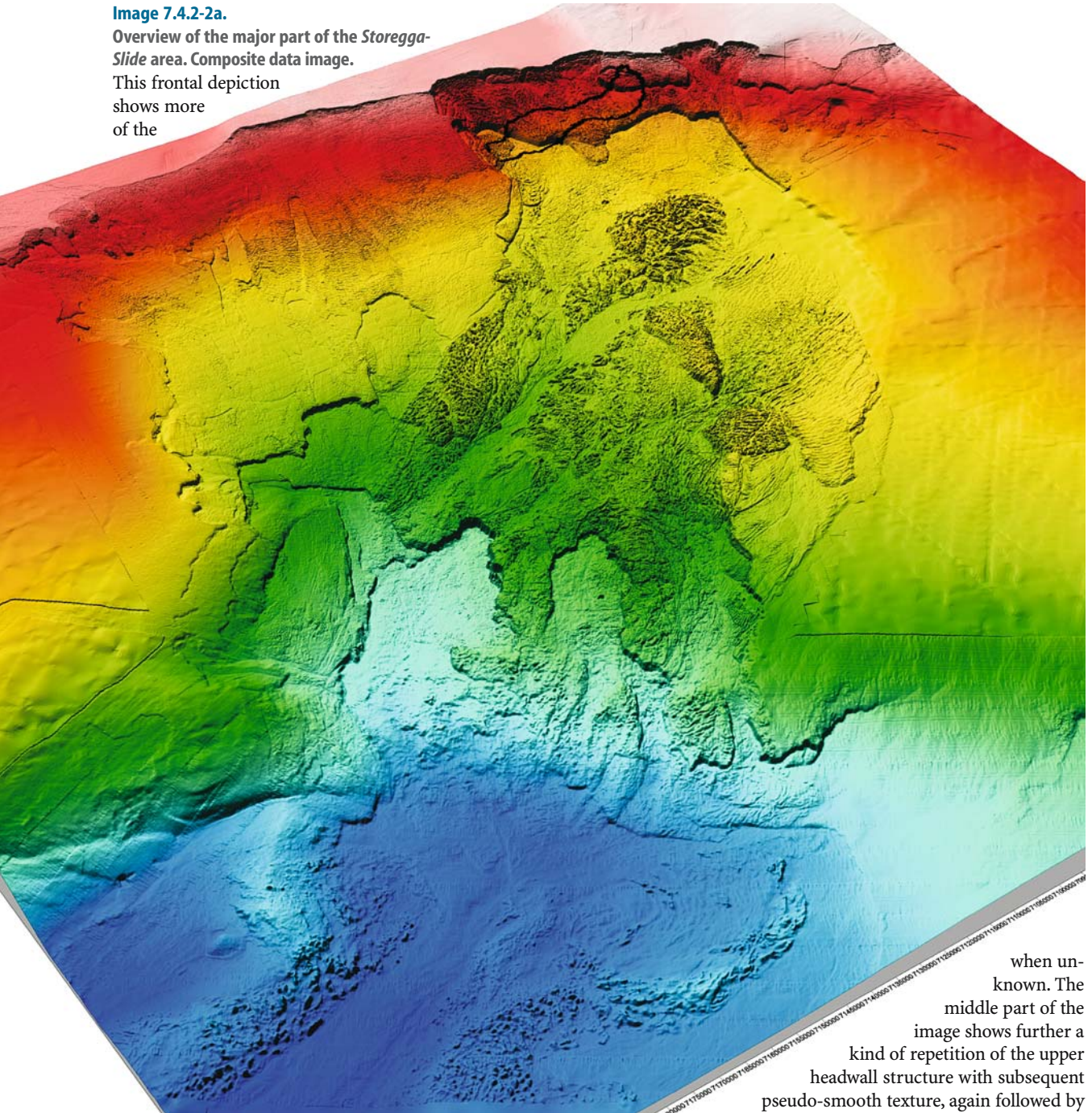
The relief map is based on a merger of all available bathymetry, including high resolution multibeam data. The average grid is 10 m, corresponding to surface vessel multibeam resolution down to about 800 m at most.

Image ©: Stein Wendel, Egil Ingebretsen, Norsk Hydro ASA ■

Image 7.4.2-2a.

Overview of the major part of the *Storegga-Slide* area. Composite data image.

This frontal depiction shows more of the



highly irregular, corrugated sea floor morphology in the middle with seemingly benign fields of smooth bottom adjacent to the upper slide headwall. Only the low altitude AUV-multibeam images of the subsequent series reveal their real nature with dense, outcropping mounds, highly hazardous to pipelines

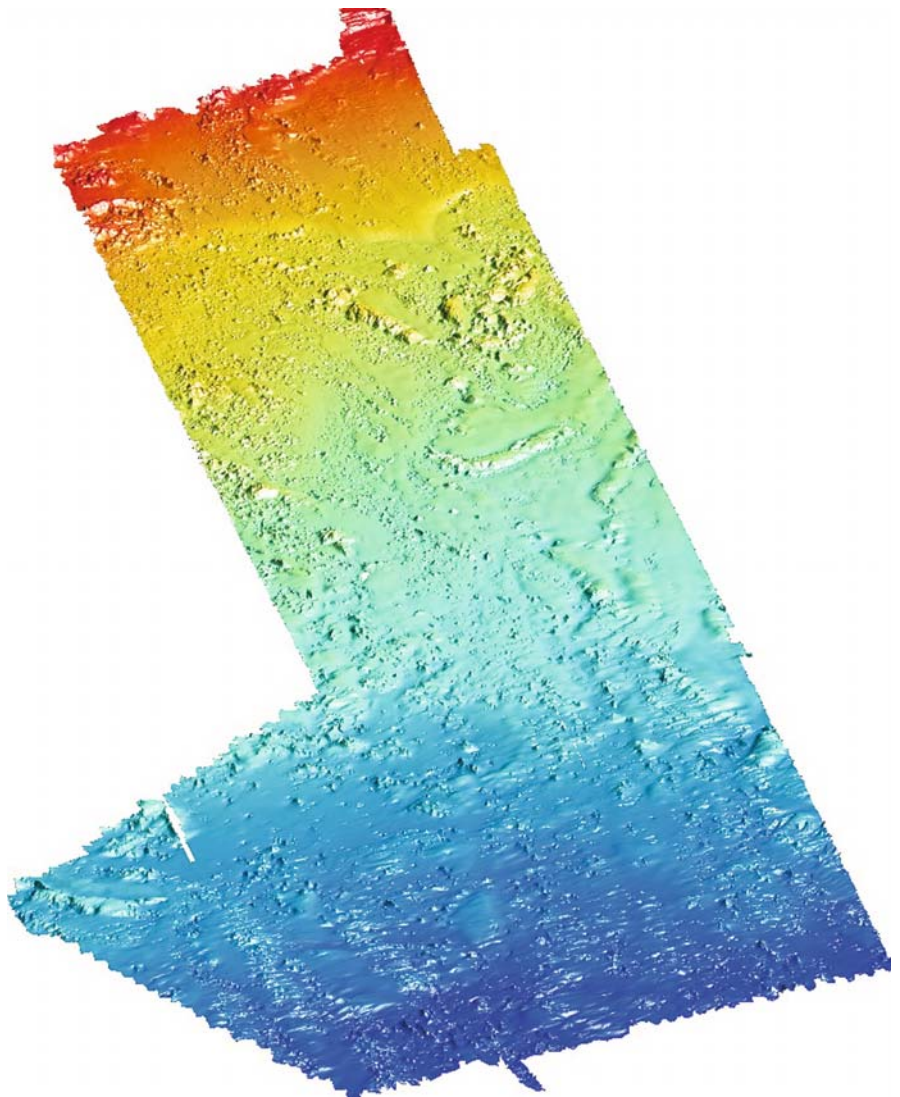
when unknown. The middle part of the image shows further a kind of repetition of the upper headwall structure with subsequent pseudo-smooth texture, again followed by fields of suspicious roughness. A less pronounced repetition is visible one floor deeper. The relief overview thus reveals different phases of the huge Storegga slide process more comprehensively and detailed than depth charts can provide.

Image ©: Stein Wendel, Egil Ingebretsen, Norsk Hydro ASA ■

Image 7.4.2-3.

First composite close up image of a *Storegga Slide* area taken by the prototype AUV. The autonomous unmanned submarine carrying the multibeam echosounder was pre-programmed to operate 50 m above the sea floor. The upper part of the image in upslope direction of view is 4 km wide and contains a pronounced ridge-like bottom feature in the yellow-green part. A further cut out from the same data set including this formation is shown in Image 7.4.2-4 as an example of the highest resolution of a deep water escarpment slide structure so far.

Project Ormen Lange; survey: AS
Geoconsult; year of survey: 2000
Multibeam system: Simrad,
EM3000; frequency: 300 kHz,
beamwidth: 1.5°, number of
beams: 127
AUV: Kongsberg Simrad, HUGIN,
type: NUI Explorer
Image ©: Stein Wendel, Egil Inge-
bretsen, Norsk Hydro ASA ■



This very irregular, sloping surface would damage or break pipelines if these were to be laid straight across with a long free span over troughs or between mounds. The tolerable width of the free span depends on several parameters, one of them being the maximum speed of the water current. At 1 m s^{-1} , a safe span width of the 30" steel-pipeline is of the order of 40 m. This means simply: the pipe connection through the Storegga Slide area cannot be realized if the profile of the sea floor relief along the optional routes is not known with sufficient precision. Unfortunately the question is not to identify a benign, adequately smooth

path between the peaks and troughs for the pipe route in order to avoid free span, as is the usual method in other areas. According to recent high resolution sea floor mapping of the *Ormen Lange* site by deep diving autonomous vehicles (AUV, Sect. 5.4.4, 7.4.1), such a completely benign route does not exist. Pipelines of the required diameter cannot follow a route with narrow curves between obstructions. In fact, it requires considerable technical effort and costs either to dredge a channel through an outcropping ridge or to dump material to provide a support element for the pipe to bridge a trough where this

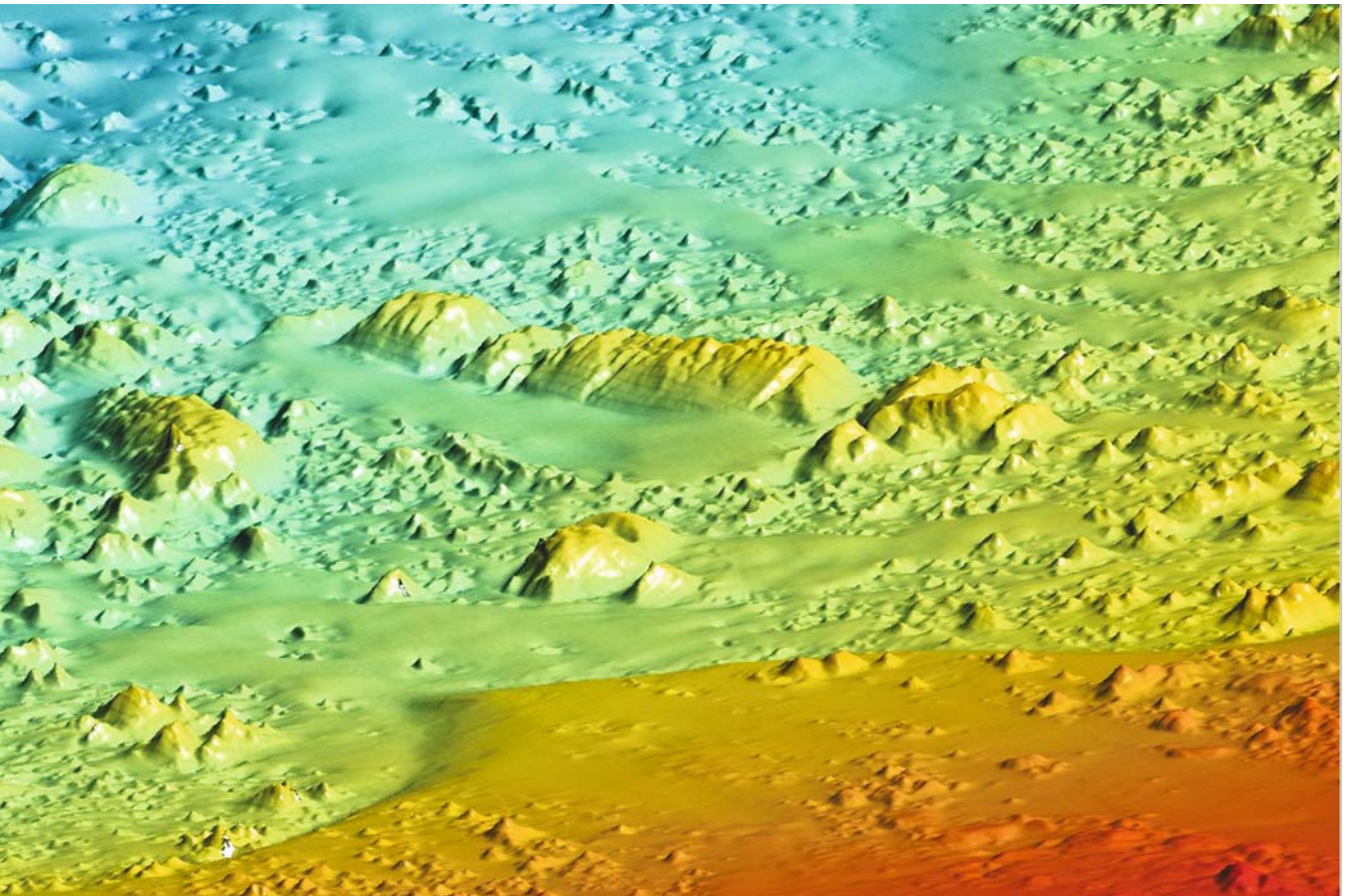


Image 7.4.2-4. Cut out of the preceding area. The ridge in the middle of the image in downslope direction of view is 900 m long and stands out 46 m above the sediment at 675 m depth. The innumerable smaller mounds of patchy debris are from several up to tens of meters high. Between the mound fields there are smooth areas of sediment which form a kind of sloping plane, interrupted by the mound fields. There are no data gaps in the image; the smooth segments are genuine and there are no interpolations. The resolution in the horizontal is about one meter; in the vertical it is of the order of a decimeter. The height exaggeration is only a factor of 2, much less than usual.

Image documentation: same as for Image 7.4.2-3

Image ©: Stein Wendel, Egil Ingebretsen, Norsk Hydro ASA ■

is inevitable – whichever is less expensive. In other words: the Ormen Lange exploitation could not have been conceived and planned before a deep diving vehicle equipped with a high resolution multi-beam echosounder (MBES) for close-ups had been developed.

The identical landslide area, explored by a surface vessel with the same MBES yields a 3D-relief which appears less rough. (Image 7.4.2-2) The real peak and trough profile is averaged to a pseudo-benign shape

by a grid width of about 10 m at a depth of 850 m. In contrast, the deep diving vehicle, following the sea floor at a flight height of only 50 m, achieves a resolution grid of no more than 1 m (Images 7.4.2-3 to 7.4.2-6). Averaging the data of the fine grid of 1 m of the real section of a potential pipe routing, to simulate grids of 2 m and 5 m respectively, has made evident that even a grid of 2 m resolution would not suffice.

These extreme requirements of high resolution sound imaging for technical reasons demonstrates

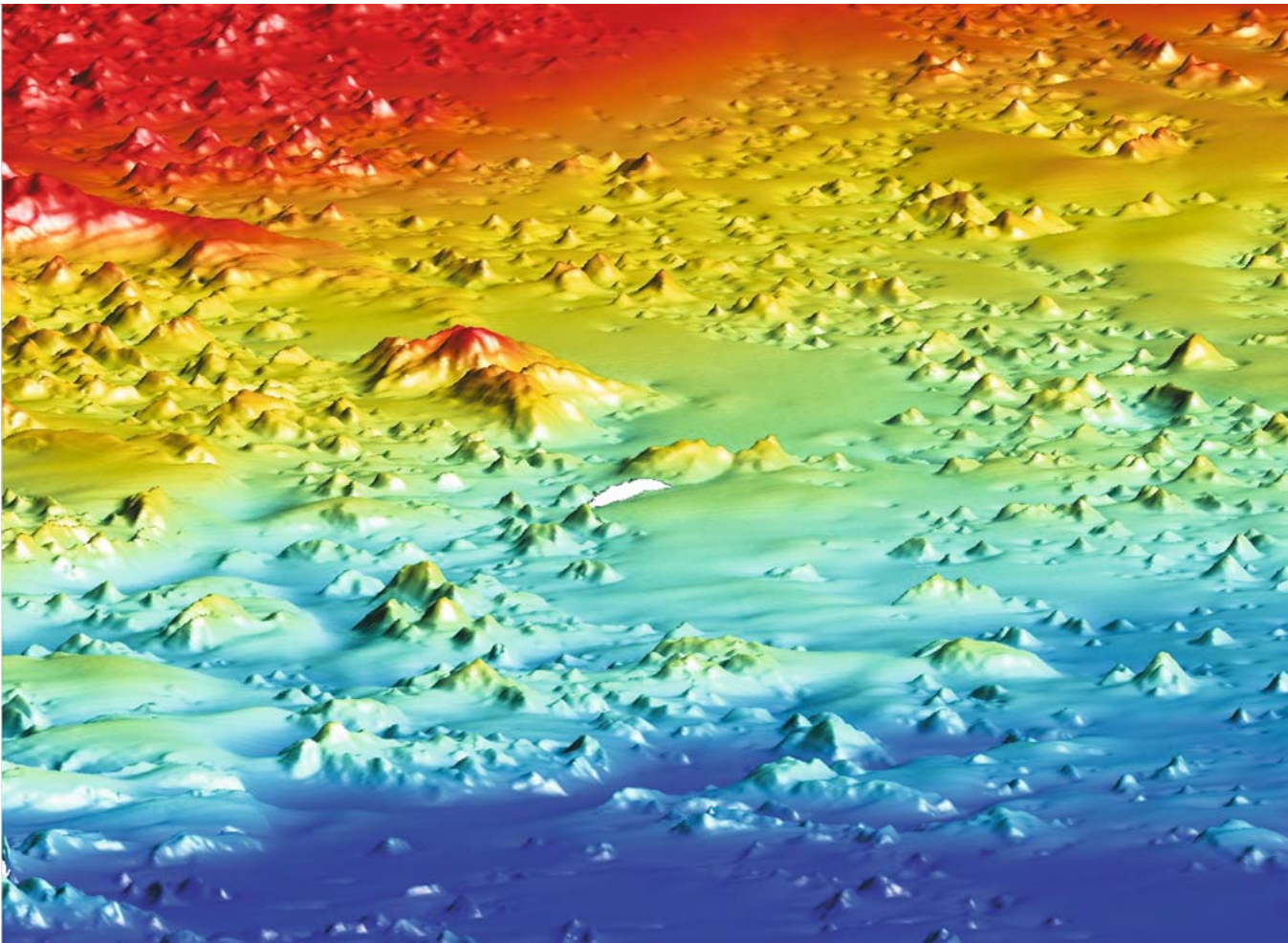


Image 7.4.2-5. Close up image taken by an essentially improved AUV. This relief image and the following one were achieved during the second survey phase in 2002. This time the system was operated as a commercial survey tool. The AUV followed the difficult terrain at an altitude of 50 m from the top of the back wall at 250 m water depth down to the field development area at 850 m depth. A total of 1 000 km swath length was surveyed in 10 days and the results were impressive. Not only the bathymetry data, but also the data of the sub-bottom profiler (not shown) also carried by the AUV were of very good quality.

Both image examples shown were taken near the Storegga Slide headwall as described in Image 7.4.2-2. The slant view in upslope direction is inclined 35°. The “massif” in the center is 360 m long and 56 m above the surrounding sediment at 745 m depth. The deeper foreground seems to show traces of current erosion transverse to the slope which are not visible more uphill. The only data gap is the white spot in the middle.

The morphology of this irregular sea floor relief is resolved by a hundred times more image pixels than a surface vessel can provide. A drastic comparison with a normal TV-screen demonstrates the difference: the image taken by the surface vessel would correspond to only 60 lines and rows instead of the 625 TV-standard. The decisive difference however does not mean only the loss of all the details. The pseudo-smoothing of the relief, inevitable with surface vessel imaging suggests nearly ideal routings for pipelines in contrast to reality.

Project Ormen Lange; survey: Stolt Offshore AS; year of survey: 2002

Multibeam system: Simrad, EM3000; frequency: 300 kHz, beamwidth: 1.5°, number of beams: 127

AUV: Kongsberg Simrad, HUGIN, improved NUI Explorer, operated by Nui AS

Image ©: Stein Wendel, Egil Ingebretsen, Norsk Hydro ASA ■

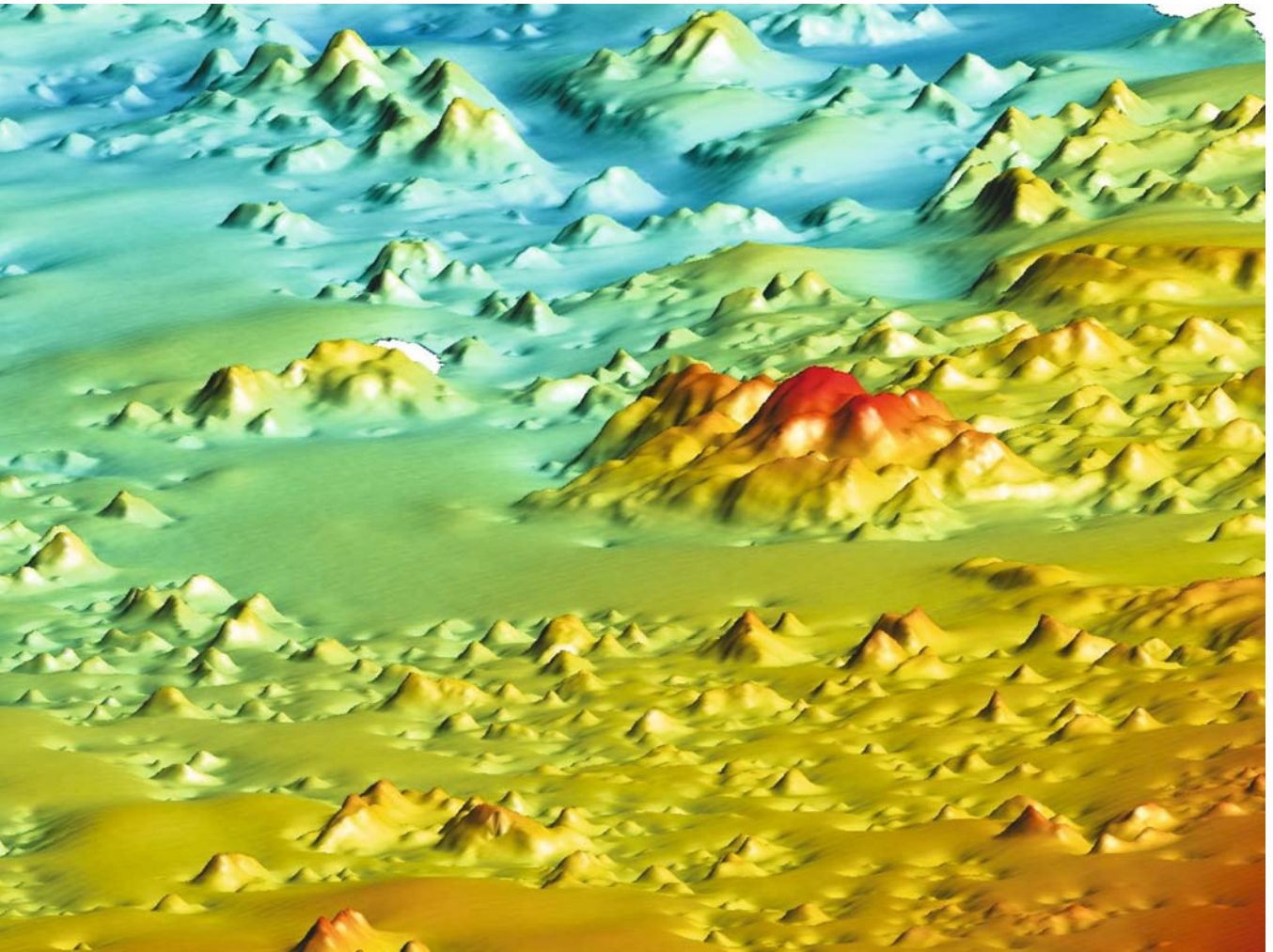


Image 7.4.2-6. Close up near the site of Image 7.4.2-5, seen in downward direction; improved AUV. Again, the mounds of different size stand out from the smooth sediment surface but the mounds in the foreground appear surrounded by a circular mould, like a dent. Such features are also observed at carbonate mounds in the Porcupine area (Sect. 5.3.4) and are attributed to erosion by tidal flow. This image is also free of data gaps except the small white dot near the middle.

Image documentation: same as for Image 7.4.2-5

Image ©: Stein Wendel, Egil Ingebretsen, Norsk Hydro ASA ■

again that industry is often the driving force of technical innovations, as it was in the early days of echosounding the North-Atlantic for safe submarine cable laying (Sect. 2.11).

At the time of the first survey trials of the Ormen Lange area in 2000, the available AUV was more a prototype than a commercial system but the stunning close-up images of sea floor features never seen before encouraged

professionalization of the method. Altogether, the final high resolution route mapping was only achieved in several steps from 2000 to 2002. The regional overview survey by a surface vessel with hull mounted multibeam echosounder was followed by two close-up surveys at two years distance from each other. The final, confirming route survey was conducted by a remotely controlled deep diving vehicle (ROV, Sect. 7.4.1).

Final Remarks

In hindsight, recalling the present state of the art of acoustic ocean imaging in general, one may say: yes, all that is needed technically to meet the various needs of research, industry and governmental surveillance appears available in principle. This may even include the greatest challenge of ocean imaging: to complete the inventory of our own planet's hidden side. Since it deals with the living conditions of man and nature of today and the future, one could even argue that this knowledge has a higher priority by far for mankind than an expedition to another planet. However, it requires more than money and priority setting. Above all, there are the more than 200 ship years (Sect. 5.1) that it would take to complete the coverage by multibeam imaging standard in view of the small fraction of work done as yet. Even if the ships of the necessary size and equipment were available with professional crews, the costs would amount to 1–3 billion dollars minimum, depending on the costs per day at sea. One could think of a coordinated share between perhaps ten nations for 5 years but even then it would cause national research budgets to go out of balance. Moreover, ocean research requires much more, and costs more than mere high quality imaging. Further, a kind of crash program dealing exclusively with the detailed sea floor relief inventory would neglect other options which would bring in more than coping with this challenge.

One option which has shown its future potential already should be recalled. The *autonomous, unmanned underwater vehicle (AUV)* is by orders of magnitude less expensive in production and operation than a full size, conventional ocean going ship, and in principle ideally suited to conduct routine, pre-programmed area coverage work but also special tasks where deep diving robotic capability is decisive. Of course, large area mapping by AUV requires a power supply technology other than batteries, forcing the host ship to stay nearby. Advanced non-nuclear submarine power-plant technology with fuel cells has shown that continuous, uninterrupted underwater operations are possible for weeks. There is certainly further development needed to downsize this technology, to standardize refueling, and further requirements to enable a wide reaching application, but there is apparently a wider international market than that of ocean research. This research application, setting the tone in long term missions would derive its priorities for area coverage from the already existing global relief maps of large scale features (Sect. 5.1).

Just a few hints on further applications may suffice: automatic underwater surveillance of harbors and fairways is a cost reduction and safety requirement, as well as for military reconnaissance of combat or other hazardous areas, in particular for search and destruction of sea mines. A growing market of underwater

robotics is that for the offshore industry which needs cost effective optimizing of safe pipeline and cable routing and routine surveillance after installation. And, not to forget: AUVs are essentially the only solution for searching for casualty relics in the deep sea. The technological challenge to develop genuine long duty cycle AUVs, including automatic updating of the on-board inertial- and sonar-Doppler navigation by brief emersions for GPS access and mission control may be

comparable to unmanned space vehicle technology. But the market is undoubtedly wider and the secondary effects like further applications of robotics are certainly rewarding. There is another welcome advantage in addition: AUVs don't emit combustion gases and are essentially free of propulsion noise emission: a modern and real underwater version of the *Flying Dutchman*, the famous, unmanned ghost ship of the fairy tale.

Literature Index

L.1–4

- Beranek LL (1993) Acoustics. American Institute of Physics, Inc., ISBN 0-88318-494-X
- Blondel P, Murton BJ (1997) Handbook of seafloor sonar imagery. John Wiley & Sons, Inc., ISBN 0-471-96217-1
- Brekhovskikh L, Lysanov Y (1982) Fundamentals of ocean acoustics. Springer-Verlag, ISBN 3-540-11305-3
- Camp L (1970) Underwater acoustics. Wiley-Interscience, ISBN 0-471-13150-4
- Coates RFW (1989) Underwater acoustic systems. John Wiley & Sons, Inc., ISBN 0-470-21544-5
- Crocker MJ (ed) (1998) Handbook of acoustics. John Wiley & Sons, Inc., ISBN 0-471-25293-X
- Edgerton HE (1986) Sonar images. Prentice Hall, ISBN 0-13-822651-2
- Enflo BO, Hedberg CM (2002) Theory of nonlinear acoustics in fluids. Kluwer Academic publishers, ISBN 1-4020-0572-5
- Etter PC (1991) Underwater acoustic modeling: principles, techniques and applications. Elsevier Applied Science, ISBN 1-85166-528-5
- Frisk GV (1994) Ocean and seabed acoustics: a theory of wave propagation. Prentice Hall, ISBN 0-13-630112-6
- Hubbell JH (1982) Photon mass attenuation and energy-absorption coefficients from 1 keV to 20 MeV. *Int J Appl Radiat Isot* 33:1269–1290
- Jensen FB, Kuperman WA, Porter MB, Schmidt H (1994) Computational ocean acoustics. AIP Press, ISBN 1-56396-209-8
- Kinsler LE (2000) Fundamentals of acoustics, 4th ed. John Wiley & Sons, Inc., ISBN 0-471-84789-5
- Landolt-Börnstein (1986) Numerical data and functional relationships in science and technology; New Series, Group V: Geophysics and space research, Vol. 3: Oceanography; Subvolume a (Gierloff-Emden HG, Høgerslev NK, Krause G, Peters H, Siedler G, Weichart G, Wille P, Ed.: Sündermann J, Springer-Verlag, Berlin Heidelberg New York, ISBN 3-540-15092-7 and 0-387-15092-7
- Leighton TG (1994) The acoustic bubble. Academic Press, ISBN 0-12-441920-8
- Lurton X (2003) An introduction to underwater acoustics: principles and applications. Springer-Verlag, Praxis Publ., ISBN 3-540-42967-0
- Maurer H, Stocks T (1933) Die Echolotungen der "Meteor". Deutsche Atlantische Exped. Meteor, 1925–1927. *Wiss. Ergeb.* 2:1–309
- Maury MF (1855) The physical geography of the sea. Harper, New York
- Mechel FP (ed) (2002) Formulas of acoustics. Springer-Verlag, ISBN 3-540-42548-9
- Medwin H, Clay CS (1998) Fundamentals of acoustical oceanography. Academic Press, ISBN 0-12-487570-X
- Mienert J, Weaver P (eds) (2003) European margin sediment dynamics: side-scan sonar and seismic images. Springer-Verlag, ISBN 3-540-42393-1
- Ross D (1976) Mechanics of underwater noise. Pergamon Press, ISBN 0-08-021182-8
- Schmincke H-U (2004) Volcanism. Springer-Verlag, ISBN 3-540-43650-2

- Stocks T, Wüst G (1935) Die Tiefenverhältnisse des offenen Atlantischen Ozeans. Deutsche Atlantische Exped. Meteor, 1925–1927. *Wiss. Ergeb.* 3:1–31
- Tolstoy I, Clay CS (1987) Ocean acoustics: theory and experiment in underwater sound. American Inst. of Physics, ISBN 0-88318-527-X
- Urban HG (2002) Handbook of underwater acoustic engineering. STN-ATLAS-Elektronik, ISBN 3-936799-04-0
- Urick RJ (1982) Sound propagation in the sea. Peninsula Publishing, ISBN 0-932146-08-2
- Urick RJ (1983) Principles of underwater sound. McGraw-Hill, ISBN 0-07-066087-5
- Urick RJ (1986) Ambient noise in the sea. Peninsula Publishing, ISBN 0-932146-13-9
- Ziehm GH (1999) The city of Kiel – an early center of underwater acoustics. FWG, ISBN 3-980-62814-0
- L.5.1**
- Sandwell DT, Smith WHF (1995) Marine gravity from satellite altimetry (poster). The Geological Data Center, Scripps Inst. of Oceanography, La Jolla, CA 92093, (digital file, Version 7.2), anonymous ftp to baltica.ucsd.edu
- Sandwell DT, Smith WHF (1997) Marine gravity anomaly from Geosat and ERS-1 altimetry. *J Geophys Res* 102: 10039–10054
- Smith WHF, Sandwell DT (1994) Bathymetric prediction from dense altimetry and sparse shipboard bathymetry. *J Geophys Res* 99:21803–21824
- Smith WHF, Sandwell DT (1997) Global seafloor topography from satellite altimetry and ship depth soundings. *Science* 277:1957–1962
- L.5.1.2**
- Bacon CR, Gardner JV, Mayer LA, Buktenica M (2002) Morphology, volcanism, and mass wasting in Crater Lake, Oregon. *Geol Soc Am Bull* 114:675–692
- Gardner JV, Mayer LA, Hughes-Clarke JE (1998) North Maui and Pailolo, Auau, and Kealaikahiku Channels (Maui, Molokai, Lanai, and Kohoolawe, Hawaii): a high-resolution multibeam survey. Abs. American Geophysical Union Fall Mtg, p F827
- Gardner JV, Mayer LA, Hughes-Clarke JE, Kleiner A (1999) High-resolution multibeam bathymetry of East and West Flower Gardens and Stetson Banks, Gulf of Mexico. *Gulf of Mexico Science* 16:131–143
- Gardner JV, Mayer LA, Hughes-Clarke JE (2000) Morphology and processes in Lake Tahoe (California-Nevada). *Geol Soc Amer Bull* 112:736–746
- Gardner JV, Dartnell P, Sulak KJ, Calder B, Hellequin L (2001a) Physiography and Late Quaternary-Holocene processes of northeastern Gulf of Mexico outer continental shelf off Mississippi and Alabama. *Gulf Of Mexico Science* 19:132–157
- Gardner JV, van den Ameele EJ, Gelfenbaum G, Barnhardt W, Lee H, Palmer S (2001b) Mapping southern Puget Sound delta fronts after the 2001 Nisqually earthquake. *EOS* 82(42):485–489
- Marlow MS, Gardner JV, Normark WR (2000) Using high-resolution multibeam bathymetry to identify seafloor surface rupture along the Palos Verdes fault complex in offshore southern California. *Geology* 28:587–590
- L.5.2.1**
- Caress DW, Chase DN (1996) Improved processing of Hydro-sweep DS multibeam data on the RV Maurice Ewing. *Mar Geophys Res* 18:631–650
- Flueh ER, Vidal N, Ranero CR, Hojka A, von Huene R, Bialas J, Hinz K, Cordoba D, Dañobeitia JJ, Zelt C (1998) Seismic investigation of the continental margin off and onshore Valparaiso, Chile. *Tectonophysics* 288:251–263
- Fruehn J, von Huene R, Fisher M (1999) Accretion in the wake of terrane collision: the Neogene accretionary wedge off Kenai Peninsula, Alaska. *Tectonics* 18:263–277
- Gung Y, Panning M, Romanowicz B (2003) Global anisotropy and the thickness of continents. *Nature* 422:707–711
- Howell DG (1989) Tectonics of suspect terranes, mountain building and continental growth. Chapman and Hall, London, 232 pp
- Le Pichon X, Henry P, Lallemand S (1993) Accretion and erosion in subduction zones: the role of fluids. *Annu Rev Earth Pl Sc* 21:307–331
- Moore JC, Vrolijk (1992) Fluids in accretionary prisms. *Rev Geophys* 30:113–135
- Parsons B (1981) The rates of plates creations and consumption. *Geophys J R Astron Soc* 67:437–448
- Ranero CR, Von Huene R (2000) Subduction erosion along the Middle America convergent margin. *Nature* 404: 748–752
- Reymer A, Schubert G (1984) Phanerozoic addition rates to the continental crust and crustal growth. *Tectonics* 3: 63–77
- von Huene R, Ranero CR (2003) Subduction erosion and basal friction along the sediment starved convergent margin off Antofagasta Chile. *J Geophys Res* 108:2079, doi10.1029/2001JB001569
- von Huene R, Scholl D (1991) Observations at convergent margins concerning sediment subduction, subduction erosion, and the growth of continental crust. *Rev Geophys* 29:279–316
- von Huene R, Corvalan J, Flueh ER, Hinz K, Korstgard J, Ranero CR, Weinrebe W, CONDOR Scientists (1997) Tectonic control of the subducting Juan Fernández Ridge on the Andean margin near Valparaiso, Chile. *Tectonics* 16:474–488

- von Huene R, Klaeschen D, Gutscher M, Fruehn J (1998) Mass and fluid flux during accretion at the Alaskan margin. *Geol Soc Am Bull* 110:468–482
- Werner R, Hoernle K, van den Bogaard P, Ranero CR, von Huene R, Korich D (1999) Drowned 14 m.y. old Galapagos archipelago off the coast of Costa Rica: implications for tectonic and evolutionary models. *Geology* 27:499–502
- Wessel P, Smith WHF (1998) New improved version of generic mapping tools released. *EOS Trans Am Geophys Union* U 79(47):579
- Yáñez GA, Ranero CR, von Huene R, Díaz J (2001) A tectonic interpretation of magnetic anomalies across a segment of the convergent margin of the Southern Central Andes (32°–34° S). *J Geophys Res* 106:6325–6345

L.5.2.2

- Baker N, Fryer P, Martinez F, Yamazaki T (1996) Rifting history of the northern Mariana Trough: SeaMARC II and seismic reflection surveys. *J Geophys Res-Solid* 101(5): 11427–11455
- Coffin MF, Karner GD, Falvey DA (1994) Research cruise yields new details of Macquarie Ridge Complex. *EOS Trans Am Geophys Union* 75:561–564
- Delteil J, Collot J-Y, Wood R, Herzer R, Calmant S, Christoffel D, Coffin M, Ferriere J, Lamarche G, Lebrun J-F, Mauffret A, Pontoise B, Popoff M, Ruellan E, Sosson M, Sutherland R (1996) From strike-slip faulting to oblique subduction: a survey of the Alpine Fault-Puysegur Trench Transition, New Zealand. Results of Cruise Geodyn-sud Leg 2, *Mar Geophys Res* 18:383–399
- Garcia MO, Liu NWK, Muenow DW (1979) Volatiles in submarine volcanic rocks from the Mariana Island arc and trough. *Geochim Cosmochim Acta* 43:305–312
- Horibe Y, et al. (1987) PAPTUA Expedition III; Hydrothermal vents in the Mariana Trough and Kagoshima Bay (Sakurajima Volcano). *EOS Trans Am Geophys Union* 68(7):100
- Howard AH, Stolper E (1981) Experimental crystallization of boninites from the Mariana Trench. Abstract AGU Fall Meeting. *EOS Trans Am Geophys Union* 62(45):1091
- Kato C, Li L, Tamaoka J, Horikoshi K (1997) Molecular analyses of the sediment of the 11 000-m deep Mariana Trench. *Extremophiles* 1:117–123
- Massell C, Coffin MF, Mann P, Mosher S, Frohlich C, Schuur CL, Karner G, Ramsay D, Lebrun J-F (2000) Neotectonics of the Macquarie Ridge complex, Pacific-Australia Plate boundary. *J Geophys Res* 105(B6):13457–13480
- Schuur CL, Coffin MF, Frohlich C, Massell CG, Karner GD, Ramsay D, Caress DW (1998) Sedimentary regimes at the Macquarie Ridge complex: interaction of Southern Ocean circulation and plate boundary bathymetry. *Paleoceanography* 13:646–670
- L.5.2.3**
- Bideau D, Hekinian R, Sichler B, Gracia E, Bollinger C, Constantin M, Guivel C (1998) Contrasting volcanic-tectonic processes during the past 2 Ma on the Mid-Atlantic Ridge: submersible mapping, petrological and magnetic results at lat. 34 degrees 52' N and 33 degrees 55' N. *Mar Geophys Res* 20(5):425–458
- Bonatti B, Harrison CGA (1988) Eruption styles of basalts in oceanic spreading ridges and seamounts: effect of magma temperature and viscosity. *J Geophys Res* 93: 2967–2980
- Detrick RS, Needham HD, Renard V (1995) Gravity anomalies and crustal thickness variations along the Mid-Atlantic Ridge between 33° N and 40° N. *J Geophys Res* 100: 3767–3787
- Gràcia E, Parson LM, Bideau D (1998) Volcano-tectonic variability along segments of the Mid-Atlantic Ridge between Azores platform and Hayes fracture zone: evidence from submersible and high-resolution sidescan sonar data. In: Mills RA, Harrison K (eds) *Modern ocean floor processes and the geological record*. *Geol Soc London Spec Publ* 148:1–15
- Gràcia E, Bideau D, Hékinian R, Lagabrielle Y (1999) Detailed geological mapping of two contrasting second-order segments of the Mid-Atlantic Ridge between Oceanographer and Hayes fracture zones (33 degrees 30' N–35 degrees N). *J Geophys Res Solid Earth* 104(B10): 22903–22921
- Lin J, Purdy GM, Schouten H, Sempere J-C, Zervas C (1990) Evidence for focused magmatic accretion along the Mid-Atlantic Ridge. *Nature* 344:627–632
- Macdonald KC (1986) The crest of the Mid-Atlantic Ridge: models for crustal generation processes and tectonics. In: Vogt QR, Tucholke BE (eds) *The geology of North America; The western North Atlantic region*. *DNAG Ser M*, *Geol Soc Amer*, Boulder, CO, pp 51–58
- Magde LS, Sparks DW, Detrick RS (1998) The relationship between mantle flow, melt migration, and gravity bull's eyes at the Mid-Atlantic Ridge between 33° N and 35° N. *Earth Planet Sc Lett* 148:59–67
- Needham HD, SIGMA Scientific Team (1991) The crest of the Mid-Atlantic Ridge between 40° and 15° N: very broad swath mapping with the EM 12 Echo Sounding System. *AGU Fall Meeting* 470
- Sempere J-C, Purdy GM, Schouten H (1990) The segmentation of the Mid-Atlantic Ridge. *Nature* 344:427–431
- Smith DK, Cann JR (1992) The role of seamount volcanism in crustal construction of the Mid-Atlantic Ridge (24°–30° N). *J Geophys Res* 97:1645–1658
- Smith DK, Humphris SE, Tivey MA, Cann JR (1997) Viewing the morphology of the Mid-Atlantic Ridge from a new perspective. *EOS Trans Am Geophys Union* 78:26

- Tolstoy MA, Harding AJ, Orcutt JA (1993) Crustal thickness on the Mid-Atlantic Ridge: bull's eye gravity anomalies and focused accretion. *Science* 262:726–729
- Udintsev GB (ed) (1994) International geological-geophysical atlas of the Atlantic Ocean. Intergovernmental Oceanographic Commission of UNESCO, Ministry of Geology of the USSR, Academy of Sciences of the USSR
- L.5.2.4.1**
- Alexander RT, Macdonald KC (1996a) Sea Beam, SeaMARC II and ALVIN-based studies of faulting on the East Pacific Rise 9 degrees 20' N–9 degrees 50' N. *Mar Geophys Res* 18:557–587
- Alexander RT, Macdonald KC (1996b) Small off-axis volcanoes on the East Pacific Rise. *Earth Planet Sc Lett* 139: 387–394
- Carbotte SM, Macdonald KC (1994) Comparison of seafloor tectonic fabric at intermediate, fast and super fast spreading ridges: influence of spreading rate, plate motions, and ridge segmentation on fault patterns. *J Geophys Res* 99:13609–13632
- Cochran JR, Goff JA, Malinverno A, Fornari DJ, Keeley C, Wang X (1993) Morphology of a “superfast” mid-ocean ridge crest and flanks: the East Pacific Rise, 7–9° S. *Mar Geophys Res* 15:65–75
- Edwards MH, Smith M, Fornari DJ (1992) CCD digital camera maps the East Pacific Rise. *EOS Trans Am Geophys Union* 73
- Edwards MH, Fornari DJ, Scheirer DS, Haymon RM, Shanks WC III (1994) High-resolution bathymetric maps and photomosaics of vent fields on the East Pacific Rise, 9°–10° N. *EOS Trans Am Geophys Union* 75:601
- Fornari DJ, Perfit MR, Batiza R, Edwards MH (1992) Submersible transects across the East Pacific Rise crest and upper flanks, 9°31'–32' N: 1. Observations of seafloor morphology and evidence for young volcanism off-axis. *EOS Trans Am Geophys Union* 73:525
- Gallo DG, Fox PJ, Macdonald KC (1986) A Sea Beam investigation of the Clipperton transform fault: the morphotectonic expression of a fast slipping transform boundary. *J Geophys Res* 91:3455–3467
- Haymon RM, Fornari DJ, Von Damm KL, Lilley MD, Perfit MR, Edmond JM, et al. (1993) Volcanic eruption of the mid-ocean ridge along the East Pacific Rise crest at 9 degree 45–52' N: direct submersible observations of seafloor phenomena associated with an eruption event in April, 1991. *Earth Planet Sc Lett* 119: 85–101
- Kurras GJ, Edwards MH, Fornari DJ (1997) High-resolution bathymetry and imagery of the East Pacific Rise axial summit trough [9°49'–51' N]: fine-scale volcanic and hydrothermal morphology and processes in a submarine rift zone. *EOS Trans Am Geophys Union* 78:F647
- Macdonald KC (1991) Mid-ocean ridges: the quest for order. *Oceanus* 34:9–10
- Macdonald KC (1992) Mid-oceanic ridge. In: Parker SP (ed) McGraw-Hill Yearbook of Science & Technology. McGraw-Hill Inc., New York, pp 259–262
- Macdonald KC (1997) Sea Beam/SeaMARC II Studies of the East Pacific Rise and its flanks in preparation for a geologic/acoustic natural laboratory
- Macdonald KC, Fox PJ (1990) The mid-ocean ridge. *Sci Am* 262:72–79
- Macdonald KC, Fox PJ, Perram LJ, Eisen MF, Haymon RM, Miller SP, Carbotte SM, Cormier M-H, Shor AN (1988) A new view of the mid-ocean ridge from the behaviour of ridge axis discontinuities. *Nature* 335:217–225
- Macdonald KC, Scheirer DS, Carbotte S, Fox PJ (1992) Recent advances in the understanding of mid-ocean ridge tectonics and volcanism using swath-mapping tools. *Acta Geol Hispanica* 27:13–32
- Macdonald KC, Fox PJ, Alexander RT, Pockalny R, Gente P (1996) Volcanic growth faults and the origin of Pacific abyssal hills. *Nature* 380:125–129
- Shen Y, Scheirer DS, Forsyth DW, Macdonald KC (1995) Trade-off in production between adjacent seamount chains near the East Pacific Rise. *Nature* 373:140–143
- Toomey DR, Solomon SC, Purdy GM (1994) Tomographic imaging of the shallow crustal structure of the East Pacific Rise at 9°30' N. *J Geophys Res* 99:24135–24157
- Tucholke BE, Macdonald KC, Fox PJ (1991) ONR seafloor natural laboratories on slow- and fast-spreading mid-ocean ridges. *EOS Trans Am Geophys Union* 72:268–270
- van Avendonk HJA, Harding AJ, Orcutt JA, McClain J (1998) A two-dimensional tomographic study of the Clipperton transform fault. *J Geophys Res* 103:17885–17899
- Von Damm KL, Buttermore LG, Oosting SE, Bray AM, Fornari DJ, Lilley MD, et al. (1997) Direct observation of the evolution of a seafloor ‘black smoker’ from vapor to brine. *Earth Planet Sci Lett* 149: 101–111
- Von Damm KL, Oosting SE, Koslowski R, Buttermore LG, Colodner DC, Edmonds HN, Edmond JM, Grebmeier JM (1995) Evolution of East Pacific Rise hydrothermal vent fluids following a volcanic eruption. *Nature* 375:47–50
- Wright DJ (1998) Formation and development of fissures at the East Pacific Rise: implications for faulting and magmatism at mid-ocean ridges. In: Buck WR, Delaney PT, Karson JA, Lagabriele Y (eds) *Faulting and magmatism at mid-ocean ridges*. American Geophysical Union, Washington, D.C., *Geophysical Monograph* 106, pp 137–152
- L.5.2.4.3**
- Jordahl K, Caress D, McNutt M, Bonneville A (2003) Seafloor topography and morphology of the Superswell region. In: Hékinian R, Stoffers P, Cheminée J-L (eds) *Oceanic hotspots: intraplate submarine magmatism and tectonism*. Springer-Verlag, pp 9–28

- Norton IO (1995) Plate motions in the North Pacific; the 43 Ma nonevent. *Tectonics* 14(5):1080–1094
- Sandwell DT (1986) Thermal stress and the spacings of transform faults. *J Geophys Res* B 91(6):6405–6417
- Smith WHF, Sandwell DT (1997) Global sea floor topography from satellite altimetry and ship depth soundings. *Science* 277:1956–1962

L.5.2.5

- Gardner JV, van den Ameele EJ, Gelfenbaum G, Barnhardt W, Lee H, Palmer S (2001) Mapping southern Puget Sound delta fronts after the 2001 Nisqually earthquake. *EOS Trans Am Geophys Union* 82(42):485–489
- Marlow MS, Gardner JV, Normark WR (2000) Using high-resolution multibeam bathymetry to identify seafloor surface rupture along the Palos Verdes fault complex in offshore southern California. *Geology* 28:587–590

L.5.2.6

- Naveh Z (1990) Fire in the mediterranean – a landscape ecological perspective. In: Goldammer JG, Jenkins MJ (ed) *Fire in ecosystem dynamics – mediterranean and northern perspectives*. SPB Academic Publishing, The Hague, pp 1–20
- Simkin T, Siebert L, McClelland L, Bridge D, Newhall C, Latter JJ (1981) *Volcanoes of the world*. Smithsonian Inst. Hutchinson Ross Publ, Stroudsburg, pp 1–232

L.5.2.6.1

- Kuhn T, Halbach P, Maggiulli M (1995) Formation of ferromanganese microencrustations in relation to glacial/interglacial stages in Pleistocene sediments from Ampere Seamount (subtropical NE Atlantic). 85. Jahrestagung der Geologischen Vereinigung e. V.; summary: *Terra Nostra* (Bonn). *Glob Change Mar Geol* 1-95:28
- Litvin VM, Matveyenkov EL, Onishchenko EL, Rudenko MV, Sagalevich AM (1982) New data on the structure of Ampere Seamount. *Oceanology+* 22(1):62–64
- Marova NA, Yevsyukov YuD (1988) The geomorphology of the Ampere submarine seamount (in the Atlantic). *Oceanology+* 27(4):452–455
- Matveyenkov VV, Poyarkov SG, Dmitriyenko OV, Al'mukhamedov AI, Gamsakhurdia GR, Kuznetsov OL (1993) Geological particularities of the seamount structure in the Azoro-Gibraltar Zone. *Oceanology+* 33(5):664–673

L.5.2.6.2

- Chadwick WW Jr, Embley RW, Fox CG (1991) Evidence for volcanic eruption on the southern Juan de Fuca Ridge between 1981 and 1987. *Nature* 350:416–418

- Gunster U, Mottl MJ, Von Herzen RP (1994) Heat flux from black smokers on the Endeavour and Cleft segments, Juan de Fuca Ridge. *J Geophys Res* 99:4937–4950
- Johnson HP, Embley RW (1990) Axial Seamount: an active ridge axis volcano on the central Juan de Fuca Ridge. *J Geophys Res* 95:12689–12696
- Johnson HP, Holmes ML (1989) Evolution in plate tectonics: the Juan de Fuca Ridge. In: Winterer EL, Hussong DM, Decker RW (eds) *The geology of North America: the Eastern Pacific Ocean and Hawaii*. Geological Society of America, Boulder, Colorado, pp 73–91

L.5.2.7

- ANZECC (1999) Strategic plan of action for the national representative system of marine protected areas – a guide for action by Australian governments. Australian and New Zealand Environment and Conservation Council, Taskforce on Marine Protected Areas, Canberra
- Collie JS, Escanero GA, Valentine PC (1997) Effects of bottom fishing on the benthic megafauna of Georges Bank. *Mar Ecol-Prog Ser* 155:159–172
- Commonwealth of Australia (2000) Commonwealth policy on fisheries by-catch. Commonwealth of Australia, Canberra
- Koslow JA (1997) Seamounts and the ecology of deep-sea fisheries. *Am Sci* 85:168–176
- Koslow JA, Bulman CM, Lyle JM (1994) The mid-slope demersal fish community off southeastern Australia. *Deep-Sea Res* 41:113–141
- Richer de Forges B, Koslow JA, Poore G (2000) Diversity and endemism of the benthic seamount fauna in the southwest Pacific. *Nature* 405:944–947
- Rintoul SR, Bullister JL (1999) A late winter hydrographic section from Tasmania to Antarctica. *Deep-Sea Res Pt I* (46)8:1417–1454
- Rintoul SR, Donguy JR, Roemmich DH (1997) Seasonal evolution of upper ocean thermal structure between Antarctica and Tasmania. *Deep-Sea Res* 44:1185–1202

L.5.2.8

- Gardner JV, Mayer LA, Hughes-Clarke JE (1998) North Maui and Pailolo, Auau, and Kealaikahiku Channels (Maui, Molokai, Lanai and Kohoolawe, Hawaii): a high-resolution multibeam survey. *American Geophysical Union Fall Mtg*, p F827

L.5.2.9

- Lallemand S, Liu CS, ACT cruise scientific team (1997) Swath bathymetry reveals active arc-continent collision near Taiwan. *EOS Trans Am Geophys Union* 78(17):173–175

- Lallemand S, Liu C-S, Dominguez S, Schnurle P, Malavieille J, ACT scientific crew (1999) Trench-parallel stretching and folding of forearc basins and lateral migration of the accretionary wedge in the southern Ryukyus: a case of strain partition caused by oblique convergence. *Tectonics* 18:231–247
- Liu C-S, Liu SY, Lallemand SE, Lundberg N, Reed D (1998) Digital elevation model offshore Taiwan and its tectonic implications. *TAO* 9(4):705–738
- Liu C-S, Deffontaines B, Lu C-Y, Lallemand S (n.Y.) Deformation patterns of an accretionary wedge in the transition zone from subduction to collision offshore southwestern Taiwan. Submitted to *Marine Geophysical Research*
- Malavieille J, Lallemand SE, Dominguez S, Deschamps A, Lu C-Y, Liu C-S, Schnurle P, ACT scientific crew (2002) Arc-continent collision in Taiwan: new marine observations and geodynamic model. In: Byrne T, Liu C-S (eds) *Geology and geophysics of an arc-continent collision, Taiwan*. *Geol Soc Am Special Paper* 358, 344:103–134
- Schnurle P, Liu C-S, Lallemand S, Reed D (1998) Structural controls of the Taitung Canyon in the Huatung Basin east of Taiwan. *TAO* 9(3):453–472
- Smith WHF, Sandwell D (1997) Measured and estimated sea-floor topography. World Data Center-A for Marine Geology and Geophysics Research Publication RP-1, Annou
- L.5.3.1.1**
- Dokken TM, Jansen E (1999) Rapid changes in the mechanism of ocean convection during the last glacial period. *Nature* 401:458–461
- Evans D, King EL, Kenyon NH, Brett C, Wallis D (1996) Evidence for long-term instability in the Storegga slide region off western Norway. *Mar Geol* 130:281–292
- Haflidason H, Gravdal A, Sejrup HP (2003) Northern Storegga slide escarpment morphology and features. In: Mienert J, Weaver P (eds) *European margin sediment dynamics: side-scan sonar and seismic images*. Springer-Verlag
- L.5.3.1.2**
- Laberg JS, Vorren TO (2003) The Traenadjupet slide: sediment disintegration and flow. In: Mienert J, Weaver P (eds) *European margin sediment dynamics: side-scan sonar and seismic images*. Springer-Verlag, pp 67–70
- L.5.3.1.3**
- Gee MJR, Watts AB, Masson DG, Mitchell NC (2001) Landslides and the evolution of El Hierro in the Canary Islands. *Mar Geol* 177:271–293
- Masson DG (1996) Catastrophic collapse of the flank of El Hierro about 15 000 years ago, and the history of large flank collapses in the Canary Islands. *Geology* 24: 231–234
- Masson DG, Canals M, Alonso B, Urgeles R, Hühnerbach V (1998) The Canary debris flow: source area morphology and failure mechanisms. *Sedimentology* 45:411–432
- Urgeles R, Canals M, Baraza J, Alonso B, Masson DG (1997) The most recent megaslides on the Canary Islands: the El Golfo Debris Avalanche and the Canary debris flow, west El Hierro Island. *J Geophys Res* 102:20305–20323
- Urgeles R, Masson DG, Canals M, Watts AB, Le Bas T (1999) Recurrent large-scale landsliding on the west flank of La Palma, Canary Islands. *J Geophys Res* 104:25331–25348
- Watts AB, Masson DG (1995) A giant landslide on the north flank of Tenerife, Canary Islands. *J Geophys Res* 100: 24487–24498
- L.5.3.2.1**
- Auffret GA, Zaragosi S, Voisset M, Droz L, Loubrieu B, Pelleau P, Savoye B, Bourlillet JF, Baltzer A, Bourquin S, Dennielou B, Coutelle A, Weber N, Floch G (2000) Premières observations sur la morphologie et les processus sédimentaires récents de l'Eventail celtique. *Oceanol Acta* 23(1):109–116
- Droz L, Auffret GA, Savoye B, Bourlillet JF (1999) L'éventail profond de la marge Celtique: stratigraphie et évolution sédimentaire. *CR Acad Sci Paris* 328:173–180
- Sibuet JC, Monti S, Pautot G (1994) Carte bathymétrique du Golfe de Gascogne. *CR Acad Sci Paris* 318(2):615–625
- Zaragosi S, Auffret GA, Faugères JC, Garlan T, Pujol C, Cortijo E (2000) Physiography and recent sediment distribution of the Celtic Deep-sea Fan, Bay of Biscay. *Mar Geol* 169: 207–237
- L.5.3.2.2**
- Nygård A, Haflidason H, Sejrup HP (2003a) Morphology of a non-glacigenic debris flow lobe in the Helland Hansen area investigated with 3D-seismic data. In: Mienert J, Weaver P (eds) *European margin sediment dynamics: side-scan sonar and seismic images*. Springer-Verlag, pp 63–65
- Nygård A, Sejrup HP, Haflidason H (2003b) Morphology of glacigenic debris flows on the upper North Sea Fan. In: Mienert J, Weaver P (eds) *European margin sediment dynamics: side-scan sonar and seismic images*. Springer-Verlag
- L.5.3.2.3**
- Laberg JS, Vorren TO (1995) Late Weichselian submarine debris flow deposits on the Bear Island Trough Mouth Fan. *Mar Geol* 127:45–72

- Laberg JS, Vorren TO (2000) Flow behaviour of the submarine glaciogenic debris flows on the Bear Island Trough Mouth Fan, western Barents Sea. *Sedimentology* 47: 1105–1117
- Mohrig D, Elverhøi A, Parker G (1999) Experiments on the relative mobility of muddy subaqueous and subaerial debris flows, and their capacity to remobilize antecedent deposits. *Mar Geol* 154:117–129
- Vogt PR, Crane K, Sundvor E (1993) Glaciogenic mudflows on the Bear Island submarine fan. *EOS Trans Am Geophys Union* 74:449, 452–453

L.5.3.2.4

- Hübscher C, Spieß V, Breitzke M, Weber M (1997) The youngest channel-levee systems of the Bengal Fan: results from digital sediment echosounder data. *Mar Geol* 141: 125–145
- Hübscher C, Breitzke M, Michels K, Kudraß H, Spieß V, Wiedicke M (1998) Late Quaternary seismic stratigraphy of the eastern Bengal Shelf. *Mar Geophys Res* 20(1):57–71
- Michels K, Kudraß HR, Hübscher C, Suckow A, Wiedicke M (1998) The submarine delta of the Ganges-Brahmaputra: cyclone-dominated sedimentation patterns. *Mar Geol* 149:133–154
- Schwenk T, Spieß V, Hübscher C, Breitzke M (2003) Frequent channel avulsion within the active channel-levee system of the middle Bengal Fan – an exceptional channel-levee development derived from parasound and hydrosweep data. *Deep-Sea Res Pt II* 50:1023–1045
- Weber ME, Wiedicke M, Kudraß H-R, Hübscher C, Erlenkeuser H (1997) Active growth of the Bengal Fan during sea-level rise and highstand. *Geology* 25(4):315–318

L.5.3.2.5

- Reinhardt L, Kudraß HR, Lückge A, Wiedicke M, Wunderlich J, Wendt G (2003) High-resolution sediment echosounding off Peru. Late Quaternary depositional sequences and sedimentary structures of a current-dominated shelf. *Mar Geophys Res* 23:335–351
- Wendt G, Müller S (2003) High resolutions with parametric acoustical systems. *Prodelta Technology Forum DELTECH International Workshop, Venice, Italy, May 2003*
- Wunderlich J, Müller S (2003) High-resolution subbottom profiling using parametric acoustics. *Int Ocean Sys* 7(4):6–11
- Wunderlich J, Wendt G (2001) Advantages of parametric acoustics for the detection of the dredging level in areas with siltation. 7th Workshop on Dredging and Surveying, Scheveningen (Den Haag), 07.–08. Juni 2001. Tagungsband, Scheveningen 2001, pp 67–75

- Wunderlich J, Wendt G (2003) Detection of embedded archaeological objects with parametric sub-bottom profilers. *Prodelta Technology Forum DELTECH International Workshop, Venedig (Italien), Mai 2003*
- Wunderlich J, Wendt G (2004) High-resolution echo-sounding and estimation of sediment properties using nonlinear acoustics. *Near Surface 2004, Conference of the European Association of Geoscientists and Engineers (EAGE)*, 06.–09. September 2004, Utrecht (NL); In: *Near Surface 2004 Extended Abstracts Book*, ISBN 90-73781-37-X
- Wunderlich J, Wendt G, Müller S (2003) Non-linear Acoustics in Echosounding and Sediments. *Hydro International* 7(9):44–47

L.5.3.3

- Ashley GM (1990) Classification of large-scale subaqueous bedforms: a new look at an old problem. *J Sediment Petrol* 60:160–172
- Belderson RH, Johnson MA, Kenyon HH (1982) Bedforms. In: *Stride AH (ed) Offshore tidal sands*. Chapman and Hall, London, pp 27–57
- Dalrymple RW, Rhodes RN (1995) Estuarine dunes and Bars. In: *Perillo GME (ed) Geomorphology and sedimentology of estuaries*. Elsevier, Amsterdam, pp 359–422
- Langhorne DN (1982) Consideration of meteorological conditions when determining the navigational water depth over a sand wave field. In: *Stride AH (ed.): Offshore tidal sands*. 15th Annual Canadian Hydrographic Conference, Ottawa. Chapman and Hall, London
- McCave IN (1971) Sand waves in the North Sea off the coast of Holland. *Mar Geol* 10:199–225
- Salsman GG, Tolbert WH, Villars RG (1966) Sand-ridge migration in St. Andrew Bay, Florida. *Mar Geol* 4:11–19
- Terwindt JMJ (1971) Sand waves in the southern bight of the North Sea. *Mar Geol* 10:51–67
- Wever ThF, Stender IH (2000) Strategies for and results from the investigation of migrating bedforms in the German Bight. In: *Trentesaux A, Garlan TE (eds) Marine sandwave dynamics*. International Workshop, March 23.–24. 2000, University of Lille 1, Proceedings, pp 221–226
- Yalin MS (1964) Geometrical properties of sandwaves. *J Hydr Eng Div-Asce* 90(HY5):105–119

L.5.3.4.1

- Beyer A, Schenke HW, Klenke M, Niederjasper F (2003) High resolution bathymetry of the eastern slope of the Porcupine Seabight. *Mar Geol* 198:27–54
- De Mol B, Van Rensbergen P, Pillen S, Van Herreweghe K, Van Rooij D, McDonnell A, Huvenne V, Ivanov M, Swennen R, Henriët JP (2002) Large deep-water coral banks in the Porcupine Basin, southwest of Ireland. *Mar Geol* 188:193–231

- Henriet JP, De Mol B, Vanneste M, Huvenne V, Van Rooij D, Porcupine-Belgica 97, 98 and 99 shipboard parties (2001) Carbonate mounds and slope failures in the Porcupine Basin: a development model involving fluid venting. In: Shannon PM, Haughton PDW, Corcoran DV (eds) *The petroleum exploration of Ireland's offshore basins*
- Henriet JP, Guidard S, ODP Proposal 573 Team (2002) Carbonate mounds as a possible example for microbial activity in geological processes. In: Wefer G, Billett D, Hebbeln D, Joergensen BB, Schluetter M, van Weering TJ (eds) *Ocean margin systems*. pp 439–455
- Huvenne VAI, De Mol B, Henriet JP (2003) A 3D seismic study of the morphology and spatial distribution of buried coral banks in the Porcupine Basin, SW of Ireland. *Mar Geol* 198:5–25
- Van Rooij D, De Mol B, Huvenne V, Ivanov M, Henriet JP (2003) Seismic evidence of current-controlled sedimentation in the Belgica mound province, upper Porcupine slope, southwest of Ireland. *Mar Geol* 195:31–53
- Van Weering TJ, Dullo C, Henriet JP (2003) An introduction to geosphere-biosphere coupling; cold seep related carbonate and mound formation and ecology. *Mar Geol* 198:1–3
- L.5.3.4.2**
- Freiwald A, Fosså JH, Grehan A, Koslow T, Roberts JM (2004) Cold-water coral reefs. UNEP-WCMC-Report, Biodiversity Series 22:1–84
- L.5.3.5.1**
- Dowdeswell JA, Kenyon NH, Elverhøi A, Laberg JS, Hollender FJ, Mienert J, Siegert MJ (1996) Large-scale sedimentation on the glacier-influenced Polar North Atlantic margins: long-range side-scan sonar evidence. *Geophys Res Lett* 23:3535–3538
- Hjelstuen BO, Eldholm O, Faleide JJ, Vogt PR (1999) Regional setting of Håkon Mosby Mud Volcano, SW Barents Sea Margin. *Geo-Mar Lett* 19:22–28
- Mienert J, Posewang J, Lukas D (2001) Changes in the hydrate stability zone on the Norwegian Margin and their consequence for methane and carbon releases into the oceanosphere. In: Schäfer P, Ritzrau W, Schlüter M, Thiede J (eds) *The northern North Atlantic: a changing environment*. Springer-Verlag, New York, pp 281–290
- Van Rensbergen P, Depreiter D, Pannemans B, Henriet JP (2005) Sea floor expression of sediment extrusion and intrusion at the El Arraiche mud volcano field, Gulf of Cadiz. *J Geophys Res-Sol Ea*, *in press*
- Vogt PR, Crane K, Pfirman S, Sundvor E, Cherkis N, Fleming H, Nishimura C, Shor A (1991) SeaMARC II sidescan sonar imagery and swath bathymetry in the Nordic Basin. *EOS Trans Am Geophys Union* 72:486
- Vogt PR, Gardner J, Crane K (1999) The Norwegian-Barents-Svalbard (NBS) continental margin: introducing a natural laboratory of mass wasting, hydrates, and ascent of sediment, pore water, and methane. *Geo-Mar Lett* 19:2–21
- L.5.3.5.2**
- Acosta J, Palomo C, Uchupi E, Muñoz A, Escartin J, Herranz P, Sanz JL (1998) Morphology and seismic character north slope Tenerife, Canary Island. Evidence episod. Massive Landslides. In: *The European Laboratory Volcanoes, Volcanic Risk*. E S F (EVOP), pp 579–588
- Palomo C, Acosta J, Sanz JL, Herranz P, Muñoz A, Uchupi E, y Escartin J (1997) Morphometric interpretation of the northwest and southeast slopes of Tenerife, Canary Islands. *J Geophys Res* 102(B9):20325–20342
- L.5.3.6**
- Augustin M, Le Suave R, Lurton X, Voisset M, Dugelay S, Satra C (1996) Contribution of the multibeam acoustic imagery to the exploration of the sea-bottom. *Mar Geophys Res* 18:459–486
- Beyer A, Chakraborty B, Schenke HW (2005) Seafloor characterization of the mound and channel provinces of the Porcupine Seabight – an application of the multi-beam angular backscatter data. Springer-Verlag, *submitted*
- Hill PJ, De Deckker P (2004) AUSCAN seafloor mapping and geological sampling survey on the Australian southern margin by RV Marion Dufresne in 2003. *Geoscience Australia Record* 2004/04, 136 pp and CD-ROM
- Hill PJ, De Deckker P, Exon NF (2005) Geomorphology and evolution of the gigantic Murray Canyons on the Australian southern margin. *Aust J Earth Sci* (*submitted*)
- Hugh Clarke JE (1993) The potential for seabed classification using backscatter from shallow water multibeam sonars. *Proceedings of the Institute of Acoustics* 15(2)
- Sprigg RC (1947) Submarine canyons of the New Guinea and South Australian coasts. *T Roy Soc South Aust* 71(2):296–310
- Von der Borch CC (1968) Southern Australian submarine canyons: their distribution and ages. *Mar Geol* 6:267–279
- L.5.3.7**
- Davies TA, Bell T, Cooper AK, Josenhans H, Polyak L, Solheim A, Stoker MS, Stravers JA (1997) *Glaciated continental margins. An atlas of acoustic images*. Chapman and Hall, London

Plassen L, Vorren TO (2003) Fluid flow features in fjord-fill deposits, Ullsfjorden, North Norway. *Norwegian Journal Of Geology* 83:37–42

Plassen L, Vorren TO, Forwick M (2004) Integrated acoustic and coring investigation of glacial deposits in Spitsbergen fjords. *Polar Res* 23:89–110

Syvitski JPM, Shaw J (1995) Sedimentology and geomorphology of fjords. In: Perillo GME (ed) *Geomorphology and sedimentology of estuaries*. *Developments in Sedimentology*, pp 113–178

Syvitski JPM, Burell DC, Skei JM (1987) *Fjords – processes and products*. Springer-Verlag, New York, 379 pp

L.5.3.8

Loncarevic BD, Courtney RC, Fader GBJ, Giles PS, Piper DJW, Costello G, Hughes Clarke JE, Stea RR (1994) Sonography of a glaciated continental shelf. *Geology* 22:747–750

L.5.3.9.1

Fader GBJ, Miller RO, Craft A (2001) Bedford Basin, Nova Scotia: an interpretation of seabed materials, features and processes on multibeam bathymetry. *Geological Survey of Canada Open File No. 3941*

Hooker SK, Whitehead H, Gowans S (1999) Marine protected area design and the spatial and temporal distribution of cetaceans in a submarine canyon. *Conserv Biol* 13(3): 592–602

Li MZ, King E, Smyth C (2003a) Morphology and stability of sand ridges on Sable Island Bank, Scotian Shelf. *GSCA Open File 1836*, 52 pp

Li MZ, Parrott DR, Yang Z (2003b) Stability and dispersion of dredged material at the black point ocean disposal site, Saint John Harbour, New Brunswick. *Proceedings of 2003 Canadian Coastal Conference*, 15–17 October 2003, Kingston, Ontario

Preston JM, Parrott DR, Collins WT (2003) Sediment classification based on repetitive multibeam bathymetry surveys of an offshore disposal site., *Proceedings IEEE Oceans 2003 San Diego, California*, 22–26 Sept, MTS document 0–933957–31–9, pp 69–75

L.5.3.9.2

Dalrymple RW, Rhodes RN (1995) Estuarine dunes and bars. In: Perillo GME (ed) *Geomorphology and sedimentology of estuaries*. *Developments in sedimentology*. Vol., 53, Elsevier Science, pp 359–422

Miller MC, McCave IN, Komar PD (1977) Threshold of sediment motion under unidirectional currents. *Sedimentology* 24:507–527

Mosher DC, Moran K (2001) Post-glacial evolution of Saanich Inlet, British Columbia: results of physical property and seismic reflection stratigraphic analysis. *Mar Geol*

Rubin DM, McCulloch DS (1980) Single and superimposed bedforms: a synthesis of San Francisco Bay and flume observations. *Sediment Geol* 26:207–231

Southard JB, Boguchwal LA (1990) Bed configurations in steady uni-directional water flows, part 2. Synthesis of flume data. *J Sediment Petrol* 60:658–679

Yalin MS (1977) *Mechanics of sediment transport*, 2nd edition. Pergamon Press, Toronto, 298 pp

L.5.3.9.3

Fedje DW, Josenhans H (2000) Drowned forests and archaeology on the continental shelf of British Columbia, Canada. *Geology* 28:99–102

Josenhans H, Fedje DW, Pienitz R, Southon JR (1997) Early humans and rapidly changing Holocene sea levels in the Queen Charlotte Islands, Hecate Strait, British Columbia, Canada. *Science* 277:71–74

L.5.4.1

Canadian Ya Ya (1962) The exploration and development of polar lands. In: Harris CD (ed) *Soviet geography; accomplishments and tasks*. *American Geographical Society Occasional Publication 1*, New York, pp 265–274

Heezen BC, Ewing M (1961) The mid-oceanic ridge and its extension through the Arctic Basin. In: Raasch GO (ed) *Geology of the Arctic*. University of Toronto Press, pp 622–642

Hunkins K (1968) Geomorphic provinces of the Arctic Ocean. In: Sater JE (ed) *Arctic drifting stations*. *Arctic Institute of North America*, pp 365–376

Hydrographic Service (1979) General bathymetric chart of the oceans (GEBCO) sheet 5.17. *Canadian Hydrographic Service, Ottawa*, scale 1:6 000 000. 1 sheet

Jakobsson M (2002) Hypsometry of the Arctic Ocean and its constituent seas. *Geochem Geophys Geosyst* 3(5)

Jakobsson M, Cherkis N, Woodward J, Coakley B, Macnab R (2000) A new grid of Arctic bathymetry: a significant resource for scientists and mapmakers. *EOS Trans Am Geophys Union* 81(9):89, 93, 96

Jokat W, Weigelt E, Kristoffersen Y, Rasmussen TM (1995) New insights into the evolution of Lomonosov Ridge and the Eurasia Basin. *Geophys J Int* 122:378–392

Karasik AM (1968) Magnetic anomalies of Hakkell Ridge and origin of the Eurasia subbasin of the Arctic Ocean. *Geophysical Methods Of Prospecting In The Arctic* 5:8–19

- Karasik AM (1974) The Euro-Asian Basin of the North Polar Ocean from the standpoint of plate tectonics. In: NIDRA (ed) Problems of the geology of the polar regions of the Earth. Leningrad, pp 24–31 (in Russian)
- Menard HW, Smith SM (1966) Hypsometry of ocean basin provinces. *J Geophys Res* 71:4305–4325
- Nansen F (1902) The Norwegian North Polar Expedition 1893–1896: scientific results. London Longmans, Green, v. III
- Perry RK, Flemming HS, Weber HR, Kristoffersen Y, Hall JK, Grantz A, Johnson GL (1985) Bathymetry of the Arctic Ocean. Naval Research Laboratory, Washington, Scale 1:4704075, 1 Sheet
- Vink GE, Jason Morgan W, Zhao WL (1984) Preferential rifting of continents: a source of displaced terranes. *J Geophys Res* 89:10072–10076
- VNIIOkeangeologia (All Russia Research Institute for Geology and Mineral Resources of the World Ocean) (1999) Bottom relief of the Arctic Ocean. Department of Navigation and Oceanography, St. Petersburg, Russian Federation, scale 1:5 000 000, 1 Sheet
- Vogt PR, Taylor PT, Kovacs LC, Johnson GL (1979) Detailed aeromagnetic investigation of the Arctic Basin. *J Geophys Res* 84:1071–1089
- Weber JR (1983) Maps of the Arctic Basin sea floor: a history of bathymetry and its interpretation. *Arctic* 36(2): 121–142
- Wilson JT (1963) Hypothesis of Earth's behavior. *Nature* 198:925–929
- L.5.4.2**
- Klenke M, Schenke HW (2003) A new bathymetric model for the central Fram Strait. *Mar Geophys Res* 23(4) 367–378(12)
- L.5.4.3**
- Bauch HA, Mueller-Lupp T, Taldenkova E, Spielhagen RF, Kassens H, Grootes PM, Thiede J, Heinemeier J, Petryashov VV (2001) Chronology of the Holocene transgression at the North Siberian margin. *Global Planet Change* 31:125–141
- Dittmers K, Niessen F, Stein R (2003) Holocene sediment budget and sedimentary history for the Ob and Yenisei Estuaries. In: Stein R, Fahl K, Fütterer DK, Galimov EM, Stepanets OV (eds) Siberian river run-off in the Kara Sea: characterisation, quantification, variability, and environmental significance. *P Mar Sci* 6:457–484
- Fairbanks RG (1989) A 17 000-year glacio eustatic sea level record: influence of glacial melting rates on the Younger Dryas event and deep-ocean circulation. *Nature* 342:637–642
- Kleiber HP, Niessen F (1999) Late Pleistocene paleoriver channels on the Laptev Sea shelf – implications from sub-bottom profiling. In: Kassens H, Bauch HA, Dmitrenko I, Eicken H, Hubberten HW, Melles M, Thiede J, Timikhov L (eds) Land-ocean systems in the Siberian Arctic: dynamics and history. Springer-Verlag, Berlin, pp 657–665
- Merklin LR, Kuznetsov VP, Timoshenko VI, Tarasov SP (1991) Parametric sonars in ocean studies. Proceedings of OSATES-91 (Ocean Space Advanced Technology Show) International Congress, Brest, France (in English)
- Merklin LR, Dunaev NN, Levchenko OV, Pavlidis YuA (1994) The Quaternary deposits of the Barents Sea and Valdai Glaciation of the Eurasian Arctic Shelf. In: DK Thurston, K Fujita (eds) 1992 Proceedings of Int. Conf. on Arctic Margins. Anchorage, 1994, pp 327–332
- Polyak L, Gataullin V, Okuneva O, Stelle V (2000) New constraints on the limit of the Barents-Kara ice sheet during the Last Glacial Maximum based on borehole stratigraphy from the Pechora Sea. *Geology* 28:611–614
- Polyak L, Levitan M, Khusid T, Merklin L, Mukhina V (2002) Variations in the influence of riverine discharge on the Kara Sea during the last deglaciation and the Holocene. *Global Planet Change* 32:291–309
- Stein R, Fahl K (2000) Holocene accumulation of organic carbon at the Laptev Sea continental margin (Arctic Ocean): sources, pathways, and sinks. *Geo-Mar Lett* 20:27–36
- Stein R, Niessen F, Dittmers K, Levitan M, Schoster F, Simstich J, Steinke T, Stepanets OV (2002) Siberian river run-off and Late Quaternary glaciation in the southern Kara Sea: preliminary results. *Polar Res* 21:315–322
- Stein R, Fahl K, Dittmers K, Niessen F, Stepanets OV (2003) Holocene siliciclastic and organic carbon fluxes in the Ob and Yenisei Estuaries and the adjacent inner Kara Sea: quantification, variability, and paleoenvironmental implications. In: Stein R, Fahl K, Fütterer DK, Galimov EM, Stepanets OV (eds) Siberian river run-off in the Kara Sea: characterisation, quantification, variability, and environmental significance. *P Mar Sci* 6:401–434
- Stuiver M, Reimer PJ, Bard E, Beck JW, Burr GS, Hughen KA, Kromer B, McCormic G, van der Plicht J, Spurk M (1998) INTCAL 98 radiocarbon age calibration, 24 000–0 cal BP. *Radiocarbon* 40:1041–1083
- Svendsen JI, Astakhov VI, Bolshiyakov DY, Demidov I, Dowdeswell JA, Gataullin V, Hjort Ch, Hubberten HW, Larsen E, Mangerud J, Melles M, Möller P, Saarnisto M, Siegert MJ (1999) Maximum extent of the Eurasian ice sheets in the Barents and Kara Sea region during the Weichselian. *Boreas* 28:234–242
- L.5.4.4**
- Rothrock DA, Yu Y, Maykut GA (1999) Thinning of the Arctic sea-ice cover. *Geophys Res Lett* 26(23):3469–3472

- Schramm JL, Flato GM, Curry JC (2000) Toward the modeling of enhanced basal melting in ridge keels. *J Geophys Res* 105(C6):14081–14092
- Wadhams P (1988) The underside of Arctic sea ice imaged by sidescan sonar. *Nature* 333(6169):161–164
- Wadhams P (1992) Sea ice thickness distribution in the Greenland Sea and Eurasian Basin, May 1987. *J Geophys Res* 102(C4):5331–5348
- Wadhams P (1997) Variability of Arctic sea ice thickness – statistical significance and its relationship to heat flux. In: Stel JH, Behrens HWA, Borst JC, Droppert LJ, Van der Meulen JP (eds) *Operational oceanography. The challenge for European co-operation*. Elsevier Oceanogr Srs 62:368–384
- Wadhams P (2000) *Ice in the ocean*. Taylor and Francis, 351 pp
- Wadhams P, Davis NR (2000) Further evidence for ice thinning in the Arctic Ocean. *Geophys Res Lett* 27(24):3973–3975

L.5.5.1

- Hinz K (1981) A hypothesis on terrestrial catastrophes, wedges of very thick oceanward dipping layers beneath passive margins. *Geologisches Jahrbuch* E22:3–28
- Hinz K, Krause W (1982) The continental margin of Queen Maud Land/Antarctica: seismic sequences, structural elements and geological development. *Geologisches Jahrbuch* E23:17–41
- Hinz K, Kristoffersen Y (1987) Antarctica, recent advances in the understanding of the continental shelf. *Geologisches Jahrbuch* E37:3
- Jacobs SS, Weiss RF (1998) *Ocean, ice and atmosphere: interactions at the Antarctic continental margin*. Published under the aegis of the Board of Associate Editors, Antarctic Research Series 75, American Geophysical Union
- Jokat W, Hübscher C, Meyer U, Oszko L, Schöne T, Versteeg W, Miller H (1996) The continental margin off East Antarctica between 10° W and 30° W. In: Storey BC, King EC, Livermore RA (eds) *Weddell Sea tectonics and Gondwana break-up*. *Geol Soc Spec Publ* 108:129–141
- Jokat W, et al. (2003) Timing and geometry of early Gondwana break-up. *J Geophys Res* 108(B9) 2428, doi: 10.1029/2002JB001802
- Miller H, et al. (1990) A fine-scale stratigraphy of the eastern margin of the Weddell Sea. In: Bleil U, Thiede J (eds) *Geological history of the Polar Oceans: Arctic versus Antarctica*. 131

L.5.5.2

- Bohrmann G, Chin C, Petersen S, Sahling H, Schwarz-Schampera U, Greinert J, Lammers S, Rehder G, Daehlmann A, Wallmann K, Dijkstra S, Schenke HW (1999) Hydrothermal activity at Hook Ridge in the Central Bransfield Basin, Antarctica. *Geo-Mar Lett* 18: 277–284

- González-Ferrán O (1991) The Bransfield rift and its active volcanism. In: Thomson MRA, et al. (eds) *Geological evolution of Antarctica*. Cambridge University Press, Cambridge, UK, pp 505–509
- Lawver LA, Ghidella M, von Herzen RP, Keller RA, Klinkhammer GP, Chin CS (1996) Distributed, active extension in Bransfield Basin, Antarctic Peninsula: evidence from multibeam bathymetry. *GSA Today* 6(11):1–4

L.5.5.3

- Vogt PR, Crane K, Sundvor E (1994) Deep Pleistocene iceberg plowmarks on Yermak Plateau: sidescan and 3.5 kHz evidence for thick calving ice fronts and a possible marine ice sheet in the Arctic Ocean. *Geology* 22: 403–406
- Woodworth-Lynas CMT, Josenhans HW, Barrie JV, Lewis CFM, Parrott DR (1991) The physical process of seabed disturbance during iceberg grounding and scouring. *Cont Shelf Res* 11:939–961

L.5.5.4

- Land Information New Zealand (2003) Cape Adare and Cape Hallett, Possession Islands, Cape Adare to Cape Daniel. Available for downloading at <http://www.hydro.lin.govt.nz/charts/catalogue/index.asp>

L.5.6

- Krasheninnikov VA, Hall JK, Hirsch F, Benjamini C, Flexer A (2003) *Geological framework of the Levant, Vol. I: Cyprus and Syria*. Historical Productions-Hall Ltd., Jerusalem
- Krasheninnikov VA, Hall JK, Hirsch F, Benjamini C, Flexer A (2005) *Geological framework of the Levant, Vol. II: The Levantine Basin and Israel*. Historical Productions-Hall Ltd., Jerusalem, in press

L.5.6.1

- Rodríguez-Fernandez J, Martín-Penela AJ (1993) Neogene evolution of the Campo de Dalias and the surrounding offshore areas (northeastern Alboran Sea). *Geodin Acta* 6:255–270

L.5.6.2

- Acosta J, Muñoz A, Herranz P, Palomo P, Ballesteros CM, Vaquero M, Uchupi E (2001a) Geodynamics of the Emile Baudot Escarpment & the Balearic Promontory, Western Mediterranean. *Mar Petrol Geol* 18/3: 349–369

- Acosta J, Muñoz A, Herranz P, Palomo C, Ballesteros M, Vaquero M, Uchupi E (2001b) Pockmarks in the Ibiza Channel and western end of the of the Balearic promontory (western Mediterranean) revealed by multibeam mapping. *Geo-Mar Lett* 21:123–130
- Acosta J, Canals M, López-Martínez J, Muñoz A, Herranz P, Urgeles R, Palomo C, Casamor JL (2002) The Balearic promontory geomorphology (western Mediterranean): morphostructure and active processes. *Geomorphology* 49:177–204
- Acosta J, Ancochea E, Canals M, Huertas MJ, Uchupi E (2004) Early Pleistocene volcanism in the Emile Baudot Seamount, Balearic promontory (western Mediterranean Sea). *Mar Geol* 207(1–4):247–257
- Fornos JJ, Rodriguez-Perea A, Massuti C, Pomar L, Acosta J, Herranz P, y Sanz JL (1989) Recent carbonate sedimentation on the Balearic platform: model for temperate-climate shelves. *AAPG Bull* 73:315–429
- Maldonado A, Swift DJP, Young RA, Han G, Nittrouer CA, DeMaster DJ, Rey J, Palomo C, Acosta AJ, Ballester A, Castellvi J (1983) Sedimentation on the Valencia continental shelf: preliminary results. *Cont Shelf Res* 2(2–3): 195–211
- L.5.6.3**
- Bovio E (2003) The autonomous underwater vehicle programme at the NATO Undersea Research Centre. UUVS03, September 2003, Southampton
- Bovio E, Schmidt H, Tyce R (2000) Autonomous underwater vehicle and ocean modelling networks. GOATS 2000 conference proceedings, August 2000, SACLANT-CEN CP-46
- Bovio E, Baralli F, Cecchi D (2004) Autonomous underwater vehicles for scientific and naval operations. IFAC Conference on Control Applications in Marine Systems, July 7–9 2004, Ancona
- Tyce R, Coelho E, Bovio E, MREP (2003) Maritime reconnaissance for NATO recognized environmental picture. SACLANTCEN CD-70, December 2003
- L.5.6.4**
- Lykousis V, Rousakis G, Alexandri M, Pavlakis P, Papoulia I (2002) Sliding and regional slope stability in active margins: North Aegean Trough (Mediterranean). *Mar Geol* 186:281–298
- Papanikolaou D, Alexandri M, Nomikou P, Ballas D (2002) Morphotectonic structure of the western part of the North Aegean Basin, based on swath bathymetry. *Mar Geol* 190:465–492
- L.5.6.5**
- Gazioğlu C, Yücel ZY, Doğan E (2004) Morphological features of major submarine landslides of Marmara Sea using by multi beam data. *J Coastal Res* 20(4)
- Gazioğlu C, Gokasan E, Algan O, Yucel Z, Tok B, Doğan E (2002) Morphologic features of the Marmara Sea from multi-beam data. *Mar Geol* 190(1–2):397–420
- Gokasan E, Ustaömer T, Gazioğlu C, Yucel ZY, Öztürk K, Tur H, Ecevitoglu B, Tok B (2003) Morpho-tectonic evolution of the Marmara Sea inferred from multi-beam bathymetric and seismic data. *Geo-Mar Lett* 23(1):19–33
- L.5.6.6**
- Huguen C (2001) Tectonique active et volcanisme boueux associé au sein de la Ride Méditerranéenne. Thèse de Doctorat de l' Université P. M. Curie de Paris, 260 pp
- Loncke L (2002) Structure et évolution du delta profond du Nil. Thèse de Doctorat de l' Université P.M. Curie de Paris, 180 pp
- Loubrieu B, Satra C, Cagna R (2000) Cartographie par sondeur multifaisceaux de la Ride Méditerranéenne et des domaines voisins, éditions Ifremer/CIESM 2001, échelle 1 / 1 500 000^{ème}. Deux cartes (Morphobathymétrie et mosaïques d'images acoustiques)
- Nielsen C (2003) Etude de zones de subduction en convergence hyper-oblique: Ride Méditerranéenne et Marge Indo-Birmanne. Thèse Université Paris XI-Orsay, 172 pp
- Sardou O, Mascle J (2003) Cartographie par sondeur multifaisceaux du delta sous marin profond du Nil et des domaines voisins. Deux cartes (Morphobathymétrie et mosaïques d'images acoustiques), special publication CIESM/Géosciences-Azur
- Zitter T (2004) Mud volcanism and fluid emissions in Eastern Mediterranean neotectonic zones. Phd academic thesis, Vrije Universiteit Amsterdam, 99 pp
- L.5.6.7**
- Almagor G, Hall JK (1984) Morphology of the Mediterranean continental margin of Israel (a compilative summary and bathymetric chart). *Geol Surv Israel Bulletin* 77
- Ben-Avraham Z, Hall JK (1977) Geophysical survey of Mount Carmel structure and its extension into the eastern Mediterranean. *J Geophys Res* 82(5):793–801
- Hall JK (1996) Historical bathymetric surveys of the inner continental shelf of the southeastern Levant. In Bogoch R, Weissbrod T (eds) Geological survey of Israel. *Curr Res* 10:40–46
- Neev D, Almagor G, Arad A, Ginzburg A, Hall JK (1976) The geology of southeastern Mediterranean Sea. *GSI Bull* 68
- L.5.7.1**
- Gelumbaускаite L-Z, Grigelis A, Cato I, Repecka M, Kjellin B (1999) Bottom topography and sediment maps of the Central Baltic Sea. LGT series of marine geological maps No. 1, SGU series of geological maps Ba No. 54, Scale 1 : 500 000, Vilnius, Uppsala, Lithuanian-Swedish project GEOBALT

Seifert T, Tauber F, Kayser B (2001) A high resolution spherical grid topography of the Baltic Sea – revised edition. Proceedings of the Baltic Sea Science Congress, Stockholm 25–29, November 2001

L.5.7.2

Lambert DN, Carnaggio FS, Young DC (1994) Sediment classification system, patent application and award. Navy Case No. 75520. Patent Issued September 24, 1996, Patent Number 5559754

Slowey NC, Bryant WR, Lambert DN (1996) Comparison of high-resolution seismic profiles and the geoaoustic properties of Eckernförder Bay sediments. *Geo-Mar Lett* 16:240–248

Tęgowski J (2003) Acoustical classification of the bottom sediments in the southern Baltic Sea. *Quatern Int* (after positive revisions)

Tęgowski J, Klusek Z (1999) Acoustic properties of the Pomeranian Bay bottom sediments. *Oceanologia* 41(3): 475–487

Tęgowski J, Łubniewski Z (2002) Seabed characterisation using spectral moments of the echo signal. *Acta Acustica* 88(6):623–626

Tęgowski J, Gorska N, Klusek Z (2003) Statistical analysis of acoustic echoes from underwater meadows in the eutrophic Puck Bay (southern Baltic Sea). *Aquat Living Resour* 16:215–221

Walter DJ, Lambert DN, Young DC, Stephens KP (1997) Mapping sediment acoustic impedance using remote sensing acoustic techniques in a shallow-water carbonate environment. *Geo-Mar Lett* 17(4):260–267

L.5.7.3

Erbguth W, Jenish U, Streufert U (2003) Maritime safety in the Baltic Sea area. Final Report of the Baltic Sea Institute for Maritime and Environmental Law, Faculty of Law, Rostock University

L.5.7.4

Gajewski L, Gajewski L, Rudowski S, Stachowiak A (2004) The relief of the offshore sea bottom at Karwia-Chałupy, Polish Baltic coast. *Proc. Conf. “Rapid transgressions into semi-enclosed basins”*, Polish Geological Institute Special Papers vol. 11, pp 91–94

Klusek Z, Gorska N, Tęgowski J, Groza K, Faghani D, Gajewski L, Nowak J, Kruk-Dowgiało L, Opiola R (2003) Acoustical techniques of underwater meadow monitoring in the Puck Bay (southern Baltic Sea). *Hydroacoustics* 6:79–80

Rudowski S, Gajewski L (1998) Classification of sea floor geology by complex acoustic methods, at Chłapowo, Poland. *Baltica* 11:41–44

L.5.7.5

Flodén T; Söderberg P (1994) Shallow gas structures and gas migration models in crystalline bedrock areas offshore Sweden. *Baltica* 8:50–56

Kulhanek O, Wahlström R (1981) Macro seismic observations in Sweden 1977–1979. Geological Survey Of Sweden C776:1–26

Pihl J, Ivansson I, Karlsson P, Lennartsson R, Levonen M, More'n P, Nilsson B, Olsson M, Staaf Ö, Sundin G, Söderberg P (2003) Low frequency active sonar – reverberation and performance in the Baltic. Report FOI-0887-SE, pp 1–29, ISSN 1650–1942

Söderberg P; Flodén T (1992) Gas seepages, gas eruptions and degassing structures in the seafloor along the Strömme tectonic lineament in the crystalline Stockholm Archipelago, east Sweden. *Cont Shelf Res* 12:1157–1171

L.5.7.6

Leinke W (1998) Sedimentation und paläogeographische Entwicklung im westlichen Ostseeraum (Mecklenburger Bucht bis Arkonabecken) vom Ende der Weichselvereisung bis zur Litorinatransgression. *Meereswissenschaftliche Berichte, Institut für Ostseeforschung Warnemünde*, 31, 156 S

Wunderlich J, Müller S (2003) High-resolution subbottom profiling using parametric acoustics. *Int Ocean Sys* 7(4):6–11

Wunderlich J, Müller S (2003) Nonlinear echosounders for high-res sub-bottom profiling. *Sea Technol* 44(9):23–26

Wunderlich J, Wendt G, Müller S (2003) Non-linear acoustics in echosounding and sediments. *Hydro International* 7(9):44–47

L.5.7.7

Merklin LR, Levchenko OV (2002) Seismoacoustic investigations of IO RAS by parametric profilers (1988–2001). In: Kuznetsov VP, Mordvinov BG, Timoshenko VI (eds) *Acoustical oceanological investigations and expeditions. Rostov-Don, Rostizdat*, pp 396–413

L.6.1.1

Bower AS, et al. (2000) Warm-water pathways in the Subpolar North Atlantic: an overview of the ACCE RAFOS float programme. *WOCE International Newsletter* 38:14–16

Bower A, Zenk W, et al. (2002) Directly measured mid-depth circulation in the northeastern North Atlantic Ocean. *Nature* 419:604

Heywood KJ, McDonagh EL, White MA (1994) Eddy kinetic energy of the North Atlantic subpolar gyre from satellite altimetry. *J Geophys Res* 99:22525–22539

- Lavender KL, Davis RE, Owens WB (2000) Direct velocity measurements describe a new circulation regime in the Labrador and Irminger Seas. *Nature* 407:66–69
- McCartney MS, Mauritzen C (2001) On the origin of the warm inflow to the Nordic Seas. *Prog Oceanogr* 51:125–214
- McCartney MS, Talley LD (1984) Warm-to-cold conversion in the northern North Atlantic Ocean. *J Phys Oceanogr* 14:922–935
- Paillet J, Arhan M, McCartney MS (1998) Spreading of Labrador Sea water in the eastern North Atlantic. *J Geophys Res* 103:10223–10239
- Speer K, Gould J, LaCasce J (1999) Year-long float trajectories in the Labrador Sea water of the eastern North Atlantic Ocean. *Deep-Sea Res Pt II* 46:165–179
- Sy A, Schauer U, Meincke J (1992) The North Atlantic Current and its associated hydrographic structure above and eastwards of the Mid-Atlantic Ridge. *Deep-Sea Res* 39:825–853
- Zenk W (2000) Labrador Sea water in the Iceland Basin: an overview of the present Kiel RAFOS float program. *WOCE International Newsletter* 39:3–6
- Zenk W, Pinck A, Becker S, Tillier P (2000) The float park: a new tool for a cost-effective collection of Lagrangian time series with dual release RAFOS floats. *J Atmos Ocean Tech* 17:1439–1443

L.6.1.2

- Bersch M (1995) On the circulation of the northeastern North Atlantic. *Deep-Sea Res I* 42:1583–1607
- Bersch M (2002) North Atlantic Oscillation-induced changes of the upper layer circulation in the northern North Atlantic Ocean. *J Geophys Res* 107(C10):3156, doi:10.1029/2001JC000901
- Bersch M, Meincke J, Sy A (1999) Interannual thermocline changes in the northern North Atlantic. *Deep-Sea Res Pt II* 46:55–75
- Fischer J, Visbeck M (1993) Deep velocity profiling with self-contained ADCPs. *J Atmos Ocean Tech* 10:764–773
- Fischer J, Brandt P, Dengler M, Mueller M, Symonds D (2003) Surveying the upper ocean with the ocean surveyor: a new phased array doppler current profiler. *J Atmos Ocean Tech* 20:742–751

L.6.1.3

- Dushaw B, Bold G, Chiu C-S, Colosi J, Cornuelle B, Desaubies Y, Dzieciuch M, Forbes A, Gaillard F, Gavrillov A, Gould J, Howe B, Lawrence M, Lynch J, Menemenlis D, Mercer J, Mikhalevsky P, Munk W, Nakano I, Schott F, Send U, Spindel R, Terre T, Worcester P, Wunsch C (2001) Observing the ocean in the 2000s: a strategy for the role of acoustic tomography in ocean climate observation. In: Koblinsky CJ, Smith NR (eds) *Observing the oceans in the 21st Century*. Godae Project Office, Bureau of Meteorology, Melbourne, Australia, pp 391–418, ISBN0642-70618-2
- Gaillard F, Desaubies Y, Send U, Schott F (1997) A 4-D analysis of the thermal structure in the Gulf of Lions. *J Geophys Res* 102(C6):12515–12537
- Kindler D, Send U, Skarsoulis E (2001) Relative-time inversions in the Labrador Sea acoustic tomography experiment. *Acta Acust Acustica* 87:738–747
- Menemenlis D, Webb T, Wunsch C, Send U, Hill C (1997) Basin-scale ocean circulation from combined altimetric, tomographic and model data. *Nature* 385:618–621
- Send U, Krahnmann G, Mauuary D, Desaubies Y, Gaillard F, Terre T, Papadakis J, Taroudakis M, Skarsoulis E, Millot C (1997) Acoustic observations of heat content across the Mediterranean Sea. *Nature* 385:615–617
- Send U, Worcester PF, Cornuelle BD, Tiemann CO, Baschek B (2002) Integral measurements of mass transport and heat content in straits from acoustic transmissions. *Deep-Sea Res* 49(19):4069–4096

L.6.2.1

- Gerdom M, Tréhu AM, Flueh ER, Klaeschen D (2000) The continental margin off Oregon from seismic Investigations. *Tectonophysics* 329:79–97
- Heeschen KU, Tréhu AM, Collier RW, Suess E, Rehder G (2003) Distribution and height of methane bubble plumes on the Cascadia Margin characterized by acoustic imaging. *Geophys Res Lett* 30(12):1643, doi:10.1029/2003GL016974
- Johnson JE, Goldfinger C, Suess E (2003) Geophysical constraints on the surface distribution of authigenic carbonates across the Hydrate Ridge region, Cascadia margin. *Mar Geol* 202:79–120
- Paull CK, Dillon WP (eds) (2002) *Natural gas hydrates: occurrence, distribution, and dynamics*. American Geophysical Union, Washington, Special Publication 124, 315 pp
- Suess E, Torres ME, Bohrmann G, Collier RW, Greinert J, Linke P, Rehder G, Tréhu A, Wallmann K, Winckler G, Zuleger E (1999) Gas hydrate destabilization: enhanced dewatering, benthic material turnover and large methane plumes at the Cascadia convergent margin. *Earth Planet Sc Lett* 170:1–15
- Tréhu AM, Bangs NL, Arsenault MA, Bohrmann G, Goldfinger C, Johnson JE, Nakamura Y, Torres ME (2002) Complex subsurface plumbing beneath southern Hydrate Ridge, Oregon continental margin, from high-resolution 3-D seismic reflection and OBS Data. *Fourth Int. Conf. Gas Hydrates, Yokohama, Japan, 19023*, pp 90–96
- Tréhu AM, Long PE, Torres ME, Bohrmann G, Rack RR, Collett TS, et al. (2004) Three-dimensional distribution of gas hydrate beneath southern Hydrate Ridge. Constraints from ODP Leg 204./*Earth Planet Sc Lett* 222:845–862

L.6.2.2

- Anderson AL, Abegg F, Hawkins JA, Duncan ME, Lyons AP (1998) Bubble populations and acoustic interaction with the gassy seafloor of Eckernfoerder Bay. *Cont Shelf Res* 18:1807–1838
- Davis KS, Bryant WR, Slowey NC, Lambert DN (1995) Reflections on the geoacoustic and geotechnical characteristics of Eckernfoerder Bay sediments. In: Wever TF (ed) *Proceedings of modeling methane-rich sediments of Eckernfoerder Bay*. Eckernfoerder, Germany, 26–30 June, 1995, FWG Report 22, pp 39–43
- Lyons AP, Duncan ME, Anderson AL, Hawkins JA (1996) Predictions of the acoustic scattering response of free-methane bubbles in muddy sediments. *J Acoust Soc Am* 95:163–172

L.6.2.3

- Crawford GB, Farmer DM (1987) On the spatial distribution of ocean bubbles. *J Geophys Res* 92:8231–8243
- Dahl P, Plant W, Nützel B, Schmidt A, Herwig H, Terray E (1997) Simultaneous acoustic and microwave backscattering from the sea surface. *J Acoust Soc Am* 101
- Detsch RM (1991) Small air bubbles in reagent grade water and sea water 1. rise velocities of 20- to 1000- μm -diameter bubbles. *J Geophys Res* 96
- Farmer DM, Lemon DD (1984) The influence of bubbles on ambient noise in the ocean at high wind speeds. *J Phys Oceanogr* 14:1762–1778
- Farmer DM, Vagle S (1989) Waveguide propagation of ambient sound in the ocean-surface bubble layer. *J Acoust Soc Am* 86(5):1897–1908
- Farmer DM, Vagle S, Ding L (1991) Acoustical studies of breaking waves and bubble clouds. *Air/Sea Acoustics Conference*, Sidney, B.C., Canada
- Farmer DM, McNeill CL, Johnson BD (1993) Evidence for the importance of bubbles in increasing air-sea gas flux. *Nature* 361:620–623
- Farmer DM, Deane GB, Vagle S (2001) The influence of bubble clouds on acoustic propagation in the surf zone. *IEEE J Oceanic Eng* 26(1):113–124
- Garrett CC, Li M, Farmer D (2000) The connection between bubble size spectra and energy dissipation rates in the upper ocean. *J Phys Oceanogr* 30:2163–2171
- Herwig H, Nützel B (1994) Attenuation and scattering by bubbles and their influence on surface backscattering strength. In: Bjørnø L (ed) *Proceedings of the 2nd European Conference on Underwater Acoustics*, Luxembourg
- Hühnerfuss H, Garrett WD (1981) Experimental sea slicks: their practical applications and utilization for basic studies of air-sea interactions. *J Geophys Res* 86:439–447

- Nützel B, Herwig H (1991) Measurements of acoustic backscattering of the near-surface layer during SAXON-FPN 1990, IGARSS 1991 *Remote Sensing: Global Monitoring for Earth Management*, Vol. IV, Helsinki
- Nützel B, Herwig H (1994) A two-frequency scatterometer for bubble scattering investigations. *IEEE J Oceanic Eng* 19(1)
- Nützel B, Herwig H (1995) Wind speed dependence of acoustic backscattering. *J Geophys Res* 100
- Vagle S, Farmer DM (1992) The measurement of bubble-size distributions by acoustical backscatter. *J Atmos Ocean Tech* 9(5):630–644
- Vagle S, Farmer DM (1998) A comparison of four methods for bubble size and void fraction measurements. *IEEE J Oceanic Eng* 23(3):211–221
- Zedel L, Farmer DM (1991) Organised structures in subsurface bubble clouds: Langmuir circulation in the open ocean. *J Geophys Res* 96:8889–8900

L.6.3.1

- Böttcher U, Götze E, Gröhsler T (2003) Survey report for RV “Walther Herwig III” 03.05.–21.05.2002. ICES Baltic International Fish Survey Working Group 2003, ICES CM 2003/G:05 (Annex 2), pp 140–152
- Gröhsler T, Götze E (2002) Survey report for RV “SOLEA” 28.09.–18.10.2001. ICES Planning Group for Herring Surveys 2002, ICES CM 2002/G:02 (Appendix III), pp 134–150
- MacLennan DN, Fernandes PG, Dalen J (2002) A consistent approach to definitions and symbols in fisheries acoustics. *ICES J Mar Sci* 59:365–369
- Ona E (1987) The equivalent beam angle and its effective value when applying an integrator threshold. *ICES C.M.* 1987/B35, 13 pp
- Reynisson P (1992) Target strength measurements of oceanic redfish in the Irminger Sea. *ICES C.M.* 1992/B:8, 13 pp
- Reynisson P (1996) Evaluation of threshold-induced bias in the integration of single-fish echoes. *ICES J Mar Sci* 53: 345–350
- Sigurdsson T, Pedchenko A, Stransky C, Mamylov V, Bethke E, Reynisson P, Bakay Y, Malmberg SA, Nedreaas K, Dalen J (2001) Draft report on the joint German/Icelandic/Norwegian/Russian trawl-acoustic survey on pelagic redfish in the Irminger Sea and adjacent waters in June/July 2001. *NAFO SCR Doc.* 01/161, Ser. No. N4555, 43 pp
- Zimmermann C, Jansen S, Bethke E, Götze E (2003) Survey report for FRV “Walther Herwig III” cruise 240. International Herring Acoustic Survey in the North Sea, ICES Planning Group for Herring Surveys 2003, ICES CM 2003/G:03 (Appendix IIF), pp 129–143

L.6.3.2

- Busdosh M, Robilliard GA, Tarbox K, Beehler CL (1982) Chemoreception in an Arctic amphipod crustacean: a field study. *J Exp Mar Biol Ecol* 62:261–269
- Klages M, Vopel K, Bluhm H, Brey T, Soltwedel T, Arntz WE (2001) Deep-sea food falls: first observation of a natural event in the Arctic Ocean. *Polar Biol* 24:292–295
- Klages M, Muyakshin S, Soltwedel T, Arntz WE (2002) Mechanoreception, a possible mechanism for food fall detection in deep-sea scavengers. *Deep-Sea Res* 49:143–155
- Premke K, Muyakshin S, Klages M, Wegner J (2003) Evidence for long-range chemoreceptive tracking of food odour in deep-sea scavengers by scanning sonar data. *J Exp Mar Biol Ecol* 285/286:283–294
- Sainte-Marie B (1992) Foraging of scavenging deep-sea lysianassid amphipods. In: Rowe GT, Pariente V (eds) *Deep-sea food chains and the global carbon cycle*. Kluwer Academic Publishers, pp 105–124
- Smith KL, Baldwin RJ (1982) Scavenging deep-sea amphipods: effects of food odor on oxygen consumption and a proposed metabolic strategy. *Mar Biol* 68:287–298
- Weissburg MJ (1997) Chemo- and mechanosensory orientation by crustaceans in laminar and turbulent flows: from odor trails to vortex streets. In: Lehrer M (ed) *Orientation and communication in arthropods*. Birkhäuser Verlag, Basel, pp 215–246

L.6.3.3

- American Cetacean Society Fact Sheet (n.y.) Pilot whale, <http://www.acsonline.org/factpack/PilotWhale.htm>
- Cetacean Research & Rescue Unit (2004) Striped dolphin, Scottish Charity No. SC 035473, Scotland, UK, <http://www.crru.org.uk/homemain.htm>
- Col J (1996) Bottlenose dolphin. <http://www.enchantedlearning.com/subjects/whales/activities/whaletemplates/Bottledolphintemplate.shtml>
- Cornish J (2000) Sperm whale. Gander Academy, Newfoundland, Canada
- Folkens P, Reeves RR, Stewart BS, Clapham PJ, Powell JA (2002) *National Audubon Society guide to the marine mammals of the world*. Alfred A. Knopf, New York
- Leatherwood SL, Reeves RR (1983) *The Sierra Club handbook of whales and dolphins*. Sierra Club Books, San Francisco
- Maptia A (1990) *Whales and dolphins*. Salamander Books, London
- Perrin WF, Wursig B, Thewissen JGM (2002) *Encyclopedia of marine mammals*. Academic Press, New York
- Richardson WJ, Greene Jr. CR, Malme CI, Thomson DH (1995) *Marine mammals and noise*. Academic Press, San Diego
- Ridgeway SH, Harrison R (1981) *Handbook of marine mammals*. Vol. 6, Academic Press, London, pp 245–279

Whitehead H (2003) *Sperm whales: social evolution in the ocean*. University of Chicago Press, Chicago

L.6.3.4

- Acunto S, Lyons AP, Pouliquen E (2000) Characteristics of the Mediterranean seagrass *Posidonia oceanica* contributing to high frequency acoustic scattering. Nato Undersea Research Centre, Saclantcen Memorandum SM-372

L.7.1.1

- Ellmer W (1997) The integrated survey system of the German survey and wreck search vessel DENEK. In: XVth International Hydrographic Conference. Hydrographic Symposium 21–22 April 1997, S. VII.2.1–VII.2.11, Monaco, International Hydrographic Organization
- Ellmer W, Vahrenkamp B (2002) Surveying the Jadebusen as an example of hydrographic surveys for multiple uses. *Hydro 2002, Papers of the 17th Hydrographic Days 2002*, The Hydrographic Society Special Publication No. 46
- Zeiler M, Schulz-Ohlberg J, Figue K (2000) Mobile sand deposits and shoreface sediment dynamics in the inner German Bight, North Sea. *Marine Geology* 170:363–380

L.7.1.2

- Zielke W, Gross G, Hoyme H, Mayerle R, Ricklefs K, Winter C (2003) Promorph – Prognosis of medium-term coastal morphology. Final Report, Institut für Strömungsmechanik und ERiB, Universität Hannover

L.7.1.5

- Brecht D, Peine H, Fedders B (2002) Detection and imaging of buried objects with a sediment sonar. *Acta Acustica Acustica* 88:763–766
- Müller S, Wunderlich J (2003) Detection of embedded objects using parametric sub-bottom profilers. In: *Int Hydrogr Rev* 4(3):76–82
- Pinto MA, Belletini A, Hollet R, Tesei A (2002) Real- and synthetic-array processing of buried targets. *IEEE J Oceanic Eng* 27(3):484–494
- Schock SG, Tellier A, Wulf J, Jason S, Ericksen M (2001) Buried object scanning sonar. *IEEE J Oceanic Eng* 26(4):677–689
- Wunderlich J, Wendt G, Müller S (2004) Detection of embedded archaeological objects using nonlinear sub-bottom profilers. In: Simons G (ed) *Proceedings of the seventh European Conference on Underwater Acoustics. 7th European Conference on Underwater Acoustics (ECUA)*, 05–08 Juli, Delft (NL)

L.7.2.1

- Evans GS (1999) Route planning for security – the essential ingredients. Proceedings Submarine Communications Asia Pacific, Tokyo & Proceedings 3rd Annual Submarine Communications Conference, Cannes
- Evans GS (2001) Identification & accurate mapping of small scale obstructions & hazards to cable burial in deep water. Proceedings ICPC Plenary, Tokyo 2001, Proceedings KMI 7th Annual Fibre Optics Symposium, Dublin 2001 & Proceedings 5th Annual Submarine Communications Conference, Rome
- Evans GS, Byous JP (1999) Route planning for security – the shore end dilemma 2. Proceedings 5th Annual KMI Submarine Systems Symposium, Baltimore

L.7.2.2

- Wendt G (2002) Detection of embedded objects with parametric sub-bottom profilers. 8th Workshop on Dredging and Surveying, Southampton (UK)

L.7.3

- Akal T, Stoll RD (2004) Determination of physical/mechanical characteristics of the seabed for archeological applications. In: Akal T, Ballard RD, Bass G (eds) The application of recent advances in underwater detection and survey techniques to underwater archeology. Conference Bodrum, Turkey, May 2004, Institute of Nautical Archaeology, Texas A&M University, p 263
- Akal T, Ballard RD, Bass G (2004) The application of recent advances in underwater detection and survey techniques to underwater archeology. Conference Bodrum, Turkey, May 2004, Institute of Nautical Archaeology, Texas A&M University
- Basciano P (2004) Survey to establish comprehensive high-resolution data of the state of ancient urban architecture realised by application of a high-resolution multibeam sonar system. In: Akal T, Ballard RD, Bass G (eds) The application of recent advances in underwater detection and survey techniques to underwater archeology. Conference Bodrum, Turkey, May 2004, Institute of Nautical Archaeology, Texas A&M University, p 67
- Bass GF (2004) A brief history of underwater detection and survey techniques used in underwater archeology. In: Akal T, Ballard RD, Bass G (eds) The application of recent advances in underwater detection and survey techniques to underwater archeology. Conference Bodrum, Turkey, May 2004, Institute of Nautical Archaeology, Texas A&M University, p 9
- Bikonis K, Moszynski M, Stepnowki A (2004) Submerged object imaging using virtual reality modeling language. In: Akal T, Ballard RD, Bass G (eds) The application of recent advances in underwater detection and survey techniques to underwater archeology. Conference Bodrum, Turkey, May 2004, Institute of Nautical Archaeology, Texas A&M University, p 215
- Blondel PH, Pouliquen E (2004) Acoustic textures and detection of shipwreck cargo – Example of a roman ship near Elba, Italy. In: Akal T, Ballard RD, Bass G (eds) The application of recent advances in underwater detection and survey techniques to underwater archeology. Conference Bodrum, Turkey, May 2004, Institute of Nautical Archaeology, Texas A&M University, p 135
- Blondel Ph, Cosci M, Dobbins PF, Jayasundere N (2004) Bistatic sonars – theory, applications and potential for underwater archaeology. In: Akal T, Ballard RD, Bass G (eds) The application of recent advances in underwater detection and survey techniques to underwater archeology. Conference Bodrum, Turkey, May 2004, Institute of Nautical Archaeology, Texas A&M University, p 161
- Coleman DF, Ballard RD (2004) Archeological oceanography of the Black Sea. In: Akal T, Ballard RD, Bass G (eds) The application of recent advances in underwater detection and survey techniques to underwater archeology. Conference Bodrum, Turkey, May 2004, Institute of Nautical Archaeology, Texas A&M University, p 49
- Dean M, Frazer J (2004) The application of high resolution multibeam sonar to the investigation of archaeological sites. In: Akal T, Ballard RD, Bass G (eds) The application of recent advances in underwater detection and survey techniques to underwater archeology. Conference Bodrum, Turkey, May 2004, Institute of Nautical Archaeology, Texas A&M University, p 59
- Gunsenin N (2004) Underwater archeological research in the Sea of Marmara. In: Akal T, Ballard RD, Bass G (eds) The application of recent advances in underwater detection and survey techniques to underwater archeology. Conference Bodrum, Turkey, May 2004, Institute of Nautical Archaeology, Texas A&M University, p 31
- Javidan R, Jones ISF (2004) High resolution acoustic imaging of archaeological artifacts in fluid mud. In: Akal T, Ballard RD, Bass G (eds) The application of recent advances in underwater detection and survey techniques to underwater archeology. Conference Bodrum, Turkey, May 2004, Institute of Nautical Archaeology, Texas A&M University, p 177
- Karovic G, Nenadovic M (2004) Multibeam sonar on the remains of Trajan's bridge. In: Akal T, Ballard RD, Bass G (eds) The application of recent advances in underwater detection and survey techniques to underwater archeology. Conference Bodrum, Turkey, May 2004, Institute of Nautical Archaeology, Texas A&M University, p 91

- Mayer L, Calder B, Schmidt JS, Malzone C (2004) Exploring the third dimension: high-resolution multibeam sonar as a tool for archaeological investigations – an example from the D-Day beaches of normandy. In: Akal T, Ballard RD, Bass G (eds) *The application of recent advances in underwater detection and survey techniques to underwater archeology*. Conference Bodrum, Turkey, May 2004, Institute of Nautical Archaeology, Texas A&M University, p 71
- Naoui J, Saito H, and Tsuchiya T (2004) Search for objects on the deep-sea floor using sidescan sonar with a tilted transducer array arrangement. In: Akal T, Ballard RD, Bass G (eds) *The application of recent advances in underwater detection and survey techniques to underwater archeology*. Conference Bodrum, Turkey, May 2004, Institute of Nautical Archaeology, Texas A&M University, p 143
- Prior MK (2004) The long-range detection of wrecks in shallow water, using low-frequency active sonar. In: Akal T, Ballard RD, Bass G (eds) *The application of recent advances in underwater detection and survey techniques to underwater archeology*. Conference Bodrum, Turkey, May 2004, Institute of Nautical Archaeology, Texas A&M University, p 151
- Sabra KG, Roux P, Kuperman WA (2004) Detection of buried targets with passive iterative time reversal processing. In: Akal T, Ballard RD, Bass G (eds) *The application of recent advances in underwater detection and survey techniques to underwater archeology*. Conference Bodrum, Turkey, May 2004, Institute of Nautical Archaeology, Texas A&M University, p 199
- Schmidt H, Leonard J, Edwards JR, Liu T-C (2004) Seabed mapping using AUV-based multi-static acoustic sensing and adaptive control. In: Akal T, Ballard RD, Bass G (eds) *The application of recent advances in underwater detection and survey techniques to underwater archeology*. Conference Bodrum, Turkey, May 2004, Institute of Nautical Archaeology, Texas A&M University, p 111
- Tripati S (2004) Exploration of Portuguese shipwreck in Goa waters of India: with special reference to Sunchi Reef. In: Akal T, Ballard RD, Bass G (eds) *The application of recent advances in underwater detection and survey techniques to underwater archeology*. Conference Bodrum, Turkey, May 2004, Institute of Nautical Archaeology, Texas A&M University, p 19
- Tsuchiya T, Naoui J, Kikuchi T (2004) Acoustic instruments in deep water search for sunken ship “Tsushima Maru” During WW II. In: Akal T, Ballard RD, Bass G (eds) *The application of recent advances in underwater detection and survey techniques to underwater archeology*. Conference Bodrum, Turkey, May 2004, Institute of Nautical Archaeology, Texas A&M University, p. 81
- Vestgard K, Espen Hagen P, Storkersen N (2004) Use of autonomous underwater vehicles – AUVs in underwater archeology investigation and surveying. In: Akal T, Ballard RD, Bass G (eds) *The application of recent advances in underwater detection and survey techniques to underwater archeology*. Conference Bodrum, Turkey, May 2004, Institute of Nautical Archaeology, Texas A&M University, p 119
- Vettori G, Gambogi P, Rizzerio A, Casalino G, Caiti A (2004) Recent experiences in underwater archaeological surveys with remotely operated vehicles in the North Tyrrhenian Sea. In: Akal T, Ballard RD, Bass G (eds) *The application of recent advances in underwater detection and survey techniques to underwater archeology*. Conference Bodrum, Turkey, May 2004, Institute of Nautical Archaeology, Texas A&M University, pp 127
- Woodworth-Lynas C, Guigne JY, Charron R, McDermott I (2004) DRUMS®: a shallow water sonar for detection and classification of buried objects. In: Akal T, Ballard RD, Bass G (eds) *The application of recent advances in underwater detection and survey techniques to underwater archeology*. Conference Bodrum, Turkey, May 2004, Institute of Nautical Archaeology, Texas A&M University, p 169

L.7.3.2

- Bingeman JM, Mack AT (1997) The dating of military buttons: second interim report based on artifacts recovered from the 18th-century wreck *Invincible*, between 1979 and 1990. *Int J Naut Archaeol* 26:39–50
- Englert A (1997) Conference report: the maritime archaeology of the eastern Baltic Sea, Vyborg, 10 and 11 June 1997. *Int J Naut Archaeol* 26:260–262
- Frazer J (2002) RESON multibeam echosounders – explanation, clarification and truth. In: *Multibeam echosounding – the total inshore solution? The Hydrographic Society of the United Kingdom – Southern Region*
- Hall RA, Hall AW, Arnold JB III (1997) Presenting archaeology on the web: the La Salle shipwreck project. *Int J Naut Archaeol* 26:247–251
- Keith DH, Carlin W, de Bry J (1997) A bronze cannon from La Belle, 1686: its construction, conservation and display. *Int J Naut Archaeol* 26:144–158
- Marsden P (2003) *Sealed by time, the loss and recovery of the Mary Rose*. Mary Rose Trust, Portsmouth
- Okorokov AV (1997) Complex underwater and ground investigations of 16th–18th century settlements in the Baltic. *Int J Naut Archaeol* 26:293–299
- Owen N (1988) HMS *hazardous* wrecked 1706. Pre-dis-turbance Survey report 1987. *Int J Naut Archaeol* 17(4):285–293
- Quinn R, Bull JM, Dix JK, Adams JR (1997) The Mary Rose site – geophysical evidence for palaeo-scour marks. *Int J Naut Archaeol* 26:3–16
- Rule M (1982) *The Mary Rose, the excavation and raising of Henry VIII's flagship*. Leicester. ISBN 0–7112–0323–7

L.7.3.3

- George SC (2003) *Jutland to Junkyard*. Birlinn, Edinburgh
- Hewson WS (2000) *This Great Harbour Scapa Flow*. Kirkwall
- Van Der Vat D (2000) *The Grand Scuttle*. Birlinn General Edinburgh
- Web information: [ScapaMap Historic Scotland.gov.uk/Orkney-research agenda](http://ScapaMap.HistoricScotland.gov.uk/Orkney-research-agenda)
- Wood L (2000) *The bull and the barrier: the wrecks of Scapa Flow*. Trafalgar Square, Letchworth

L.7.4.1

- Browning RM Jr. (1996) *U.S. merchant vessel war casualties of World War II*. Naval Institute Press, Annapolis
- Church RA, Warren DJ (2001) New technology rewrites history: unraveling the mystery of the U-166. *Gogulf Magazine* July/August 2001:27–29
- Church RA, Warren DJ (2002) Unraveling the mystery: the discovery of the U-166. *Proceedings of the Minerals Management Services Twenty-first Annual Gulf of Mexico Information Transfer Meeting*, pp 105–114

- Church RA, Landry L, Warren DJ, Smith JS (2003a) The SS Alcoa Puritan: deepwater discovery and investigation. *Underwater Intervention Conference Proceedings*
- Church RA, Warren DJ, Hill AW, Smith JS (2003b) The discovery of U-166: rewriting history with new technology. No. OTC 14136, *Offshore Technology Conference Proceedings*
- Garrison EG, Giammona CP, Kelly FJ, Tripp AR, Wolff GA (1989) *Historic shipwrecks and magnetic anomalies of the northern Gulf of Mexico: reevaluation of archeological resource management zone 1, Vol. II: Technical narrative*. OCS Study 89–0024. U.S. Department of the Interior, Minerals Management Service, Gulf of Mexico OCS Regional Office. New Orleans, Louisiana
- McNamara D (2000) *Thunder in the Gulf: Nazi subs torpedoed ships off the Louisiana coast, and at least one paid the price*. Louisiana Life, Summer 2000
- Miller D (2000) *U-boats: history, development and equipment, 1914–1945*. Conway Maritime Press, London
- National Archives and Records Administration (1985) *Records of the German Navy, 1850–1954: records relating to the U-boat warfare, 1939–1945*. Compiled by Timothy Mulligan. Washington, D.C., United States National Archives

Appendix

The section numbers correspond to the sections of the Chap. 1–4 of the basic facts.

A.3.1 The Speed of Sound, Determining Quantities

Simple nine-term equation for the sound speed (m s^{-1}) in the ocean (Del Grosso/Mackenzie, see Landolt-Börnstein, Acoustical properties of the ocean, L.1–4)

- V : sound speed (m s^{-1})
- T : temperature ($^{\circ}\text{C}$) in ($-2 \dots 30$)
- S : salinity (‰) in ($25 \dots 40$)
- D : depth (m) in ($0 \dots 8000$)

$$V(T,S,D) = 1448.96 + 4.591T - 0.05304T^2 + 0.0002374T^3 \\ + 1.34(S - 35) + 0.0163D + 1.675 \cdot 10^{-7}D^2 \\ - 0.01025T(S - 35) - 7.139 \cdot 10^{-13}TD^3$$

Expressed by pressure instead of by depth with $D = P(0.97845 + 0.00008T)$ we receive with the pressure P (dbar):

$$V(T,S,P) = 1448.96 + 4.591T - 0.05304T^2 \\ + 0.0002374T^3 + 1.34(S - 35) \\ + 0.03195P(0.49918 + 0.000041T) \\ - 0.01025T(S - 35) \\ + 6.435433 \cdot 10^{-7}P^2(0.49918 + 0.000041T)^2 \\ - 5.37628 \cdot 10^{-12}TP^3(0.49918 + 0.000041T)^3$$

A.3.2 Sound Refraction in the Sea

A.3.2.1 Snell's Law

$$\frac{c_1}{\sin\Theta_1} = \frac{c_2}{\sin\Theta_2}$$

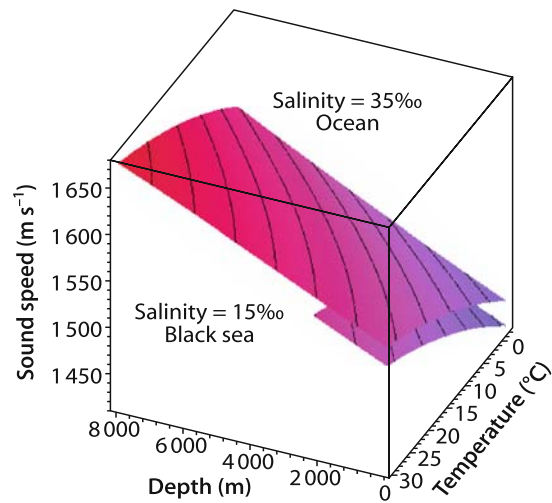


Image A.1.
Sound speed in the ocean ■

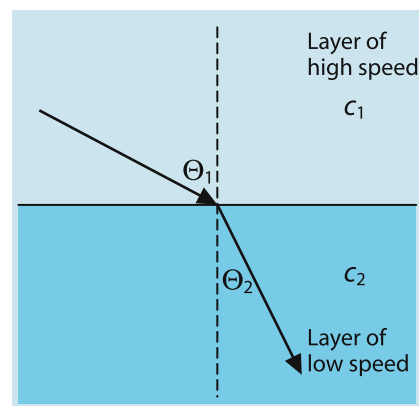


Image A.2.
Sound refraction in the sea. The scheme shows a sound ray penetrating the boundary between high and low sound speed. The ray becomes steeper due to refraction. ■

A.3.2.2 Sound Refraction and Ducted Propagation

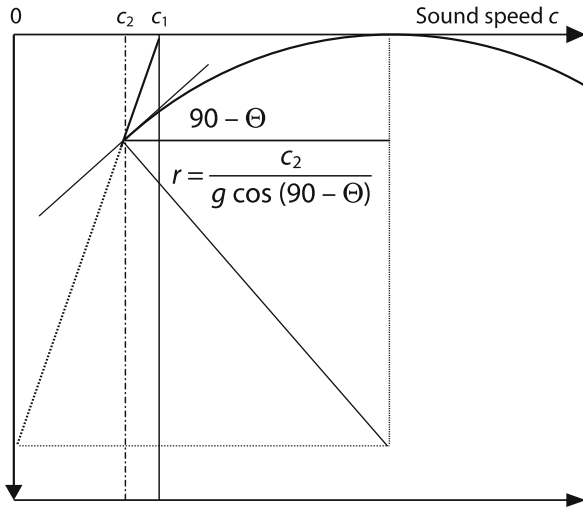


Image A.3.

Sound refraction and ducted propagation. Snell's law applied to a layer of constant rate of change of sound speed $c(z) = c_0 + gz$ (s^{-1}). The ray follows an arc of a circle with radius r . ■

A.3.3 Sound Attenuation

A.3.3.1 Absorption

The Decibel Definition

The Decibel-scale in underwater acoustics, abbreviated dB-scale, is used similarly to audio acoustics. It is defined as *10 times the decimal logarithm of the ratio of two sound intensities*. The denominator of the ratio in underwater acoustics is the reference intensity generated by the sound pressure P_0 of $1 \mu\text{Pa}$. (In audio acoustics the reference intensity is derived from the human hearing threshold in air and is standardized as $20 \mu\text{Pa}$). The numerator of the ratio is the actual sound intensity generated by the sound pressure P_1 . Sound intensities are proportional to P^2 , the square of the sound pressure, similar to electric power which is

proportional to the square of the voltage. Expressed in sound pressure, which is the quantity measured by a technical sound receiver, the *10 log sound intensity ratio* becomes the corresponding *20 log sound pressure ratio*. This dimensionless quantity is named *sound level*.

$$20 \log_{10} \frac{P_1}{P_0} = 10 \log_{10} \frac{P_1^2}{P_0^2} \quad (\text{dB})$$

Historically the dB definition is derived from the human hearing capability which senses an increase of sound intensity fortunately only by its logarithm rather than by the enormous span of intensities between hearing threshold and pain threshold. This is a factor with 13 digits, but ten times its logarithm is just 130 dB, a number with merely 3 digits. The seemingly arbitrary factor of 10 (deci-Bel!) of the logarithm is again chosen by human hearing experience. A sound level increase of 1 dB is about the minimum step, recognisable by man.

1 dB level increase corresponds to an increase of the sound intensity by roughly 10%. 10 dB increase in level is exactly factor 10 in intensity; 20 dB amounts to a factor of a hundred and so forth. Factors which *reduce* a sound intensity such as propagation loss or spatial filtering by the receiver beam lead to negative numbers. For instance: 1/10 means -10 dB. The advantage of the dimensionless sonar equation dealing with levels is the very practical compression of huge ratios between the radiated sound signal and the tiny echo and the correspondingly simple treatment of sums and differences of the terms in the equation instead of multiplication and division.

Image A.4 compares the absorption of sound waves and electromagnetic waves in the sea. The blue curve of sound absorption in sea water is valid without reflection loss at the sea floor and the sea surface which requires Sofar propagation in the low loss frequency region. The variability below 100 Hz is due to leakages of the Sofar-Channel. The two broad deviations from the straight slope around 1–10 kHz and 100 kHz–1 MHz are caused by re-configuration of molecules and ions following varying pressure in the sound field with time delay. This mechanism

of absorption is named relaxation (Medwin and Clay, L.1–4).

Sound absorption in bubble layers near the sea surface is of the order the highest loss in shallow waters. Note that the slope of the loss in sediments is only proportional with frequency. Around 1 MHz, the sound absorption equals the absorption of visible light in clear water.

Ultralong radio waves can finally compete with light in penetration but only at 1 kHz with 1000 km wavelengths. The two extreme maxima of absorption at infra-red and ultraviolet/X-ray, framing the sharp minimum at the light window, mean nearly total screening within microns and less of penetration. The X-ray regime of about 10 cm penetration at 9/10 loss as applied in medical diagnosis is already beyond the interval depicted.

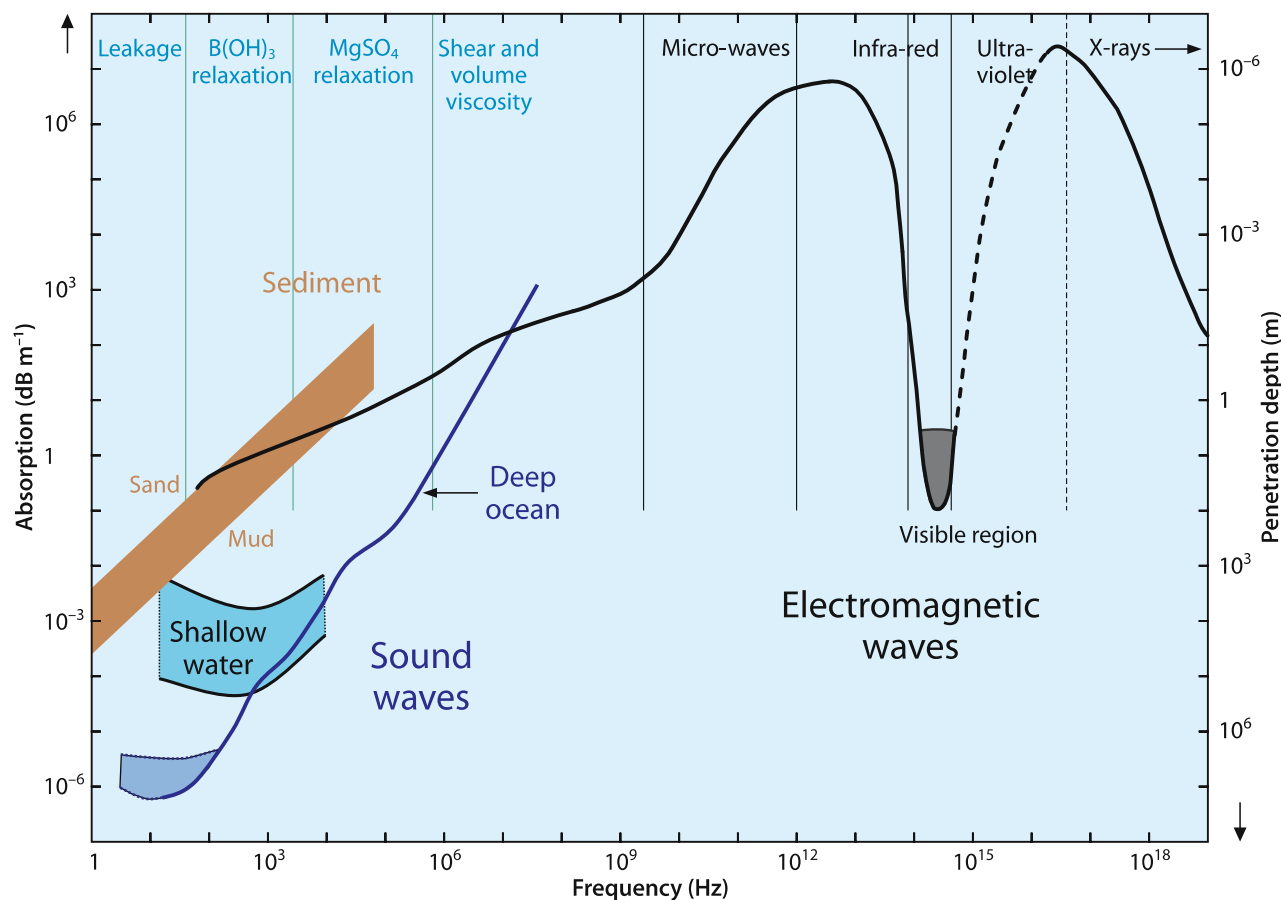


Image A.4. Absorption of sound waves and electromagnetic waves in the sea. The broad area of varying sound absorption in shallow water, shaded light blue, is due to two types of horizontal sound propagation. The upper margin refers to steep downward refraction with multiple reflections of high loss at bottom and surface, typical for the *North Sea* during summer. The lower margin refers only to the *Baltic Sea* during summer with ducted Sofar-type propagation of lowest loss. The warm, saline bottom water increases the sound speed towards the sea floor similarly to the static pressure effect in the deep ocean (Sect. 5.7), necessary for upward refraction. The unique shallow water Sofar-Channel of the Baltic is at most a few tens of meters thick with much stronger leakage at lower frequencies than its oceanic relative but, due the low salinity of the brackish water of the Baltic, the loss can be even lower than in the open ocean. (Sources: Acoustics: Landolt-Börnstein, Acoustical properties of the ocean; Optics: Landolt-Börnstein, Optical properties of water, L.1–4; X-ray: Hubbell, L.1–4.) ■

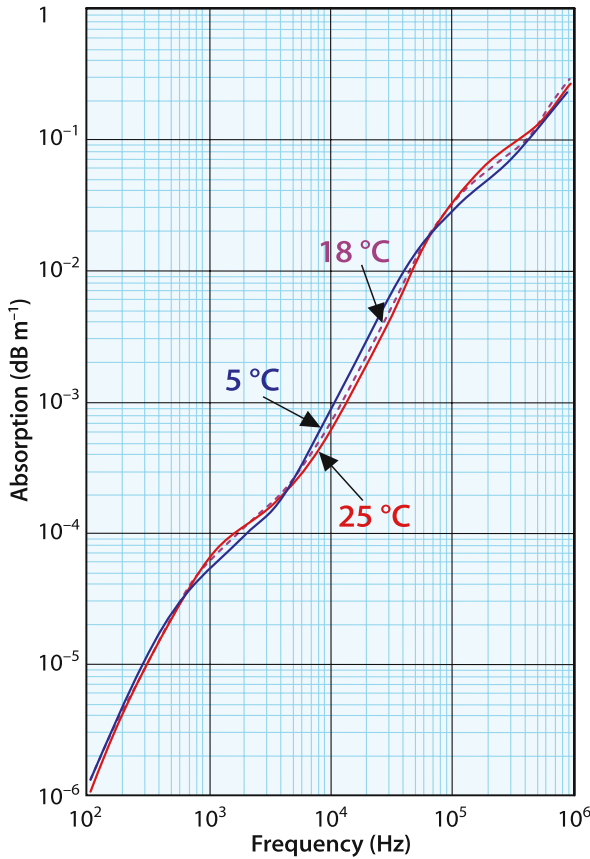


Image A.5. Temperature effect in the absorption; cut out of Image A.4 (Urick, L.1–4). There are several cross overs. Note that cold water absorbs less than warmer water beyond the cross-over at 80 kHz. ■

**A.3.4.1
Acoustic Impedance**

The acoustic impedance $Z = \rho c$ provides the reflection factor R as follows:

$$R = \frac{P_R}{P_I} = \frac{m \sin(90 - \Theta) - \sqrt{n^2 - \cos^2(90 - \Theta)}}{m \sin(90 - \Theta) + \sqrt{n^2 + \cos^2(90 - \Theta)}}$$

$$= \frac{m \cos \Theta - \sqrt{n^2 - \sin^2 \Theta}}{m \cos \Theta + \sqrt{n^2 + \sin^2 \Theta}}$$

with

- P_I as the pressure of the incident wave
- P_R of the reflected wave
- n the refraction index (c_1/c_2) and $m=(\rho_2/\rho_1)$ as density ratio

At vertical incidence $\Theta = 0$ the formula simplifies to

$$R = \frac{m - n}{m + n}$$

**A.3.5
Reverberation/Scattering Strength of the Sea Floor and Sea Volume**

**A.3.5.1
Sea Floor**

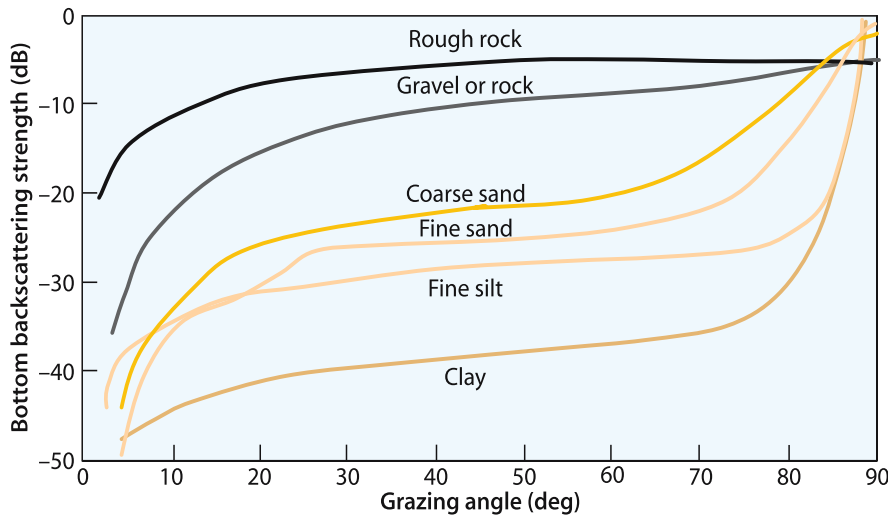


Image A.6. Bottom backscattering strength. The bottom backscattering strength refers to 1 m² sea floor. There is a wide regime of incident angles with little change of backscattering. At vertical incidence a (plain) fine grain sediment surface acts as a mirror whereas rough, rocky surfaces scatter under vertical incidence about as strongly as under slant incidence (Landolt-Börnstein, Acoustical properties of the ocean, L.1–4). ■

A.3.5.2 Sea Volume

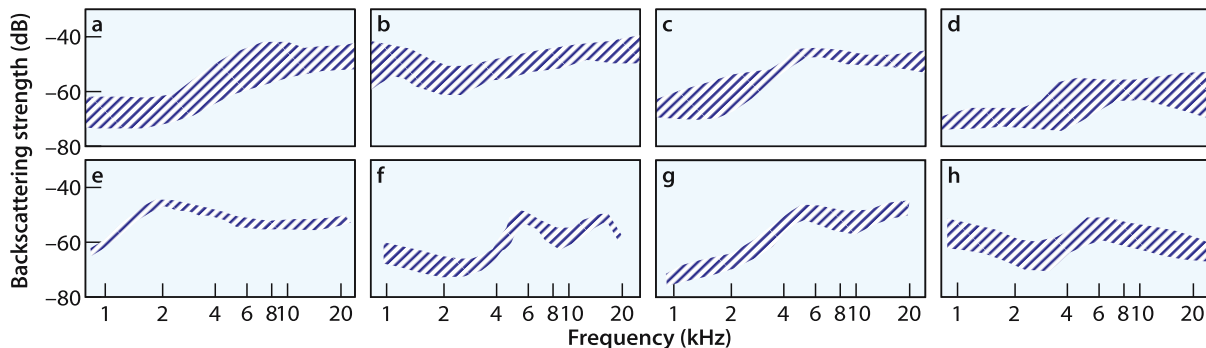
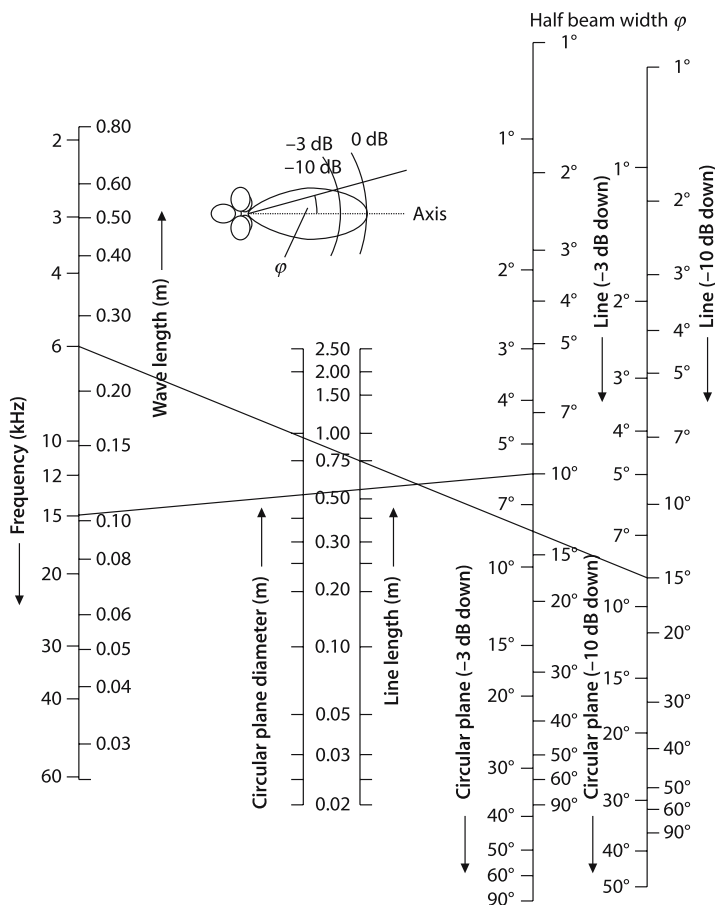


Image A.7. Volume backscattering strength. The *volume backscattering strength* refers to 1 m^3 of sea water with distributed scatterers such as plankton (Landolt-Börnstein, Acoustical properties of the ocean, L.1–4). The eight figures show the measured variability of volume backscattering in different deep ocean areas over a wide frequency regime. Such data are relevant for measuring the ocean current by acoustic Doppler current profilers (ADCP) which are usually operated at higher frequencies. The variability is typical but unpredictable. ■

A.3.6 Noise

A.3.6.5 The Spatial Filter

Image A.8. The graphic scheme provides the beamwidth of a transducer of the indicated size and the frequency by connecting the quantities by a straight line as indicated (Urlick, L.1–4). ■



A.3.6.6 The Frequency Filter

The bandwidth B (Hz) of a signal with a duration T (s) is connected by the so called *uncertainty relation* of classical physics

$$B \approx \frac{1}{T} \text{ (Hz)}$$

A.3.7 Sonar Equation

For an active remote sensing device or echosounder the sonar equation is

$$DT = SL - 2TL + TS - (NL - DI)$$

with the parameters shown in Table A.1.

Parameter	Symbol	Definition	Reference
Source level	SL	$10\log \left[\frac{\text{intensity of source}}{\text{reference intensity}^a} \right]$	1 m from source on its acoustic axis
Transmission loss	TL	$10\log \left[\frac{\text{signal intensity at 1 m}}{\text{signal intensity at object}} \right]$	1 m from source and at target or receiver
Target strength	TS	$10\log \left[\frac{\text{echo intensity at 1 m from object}}{\text{incident intensity}} \right]$	1 m from acoustic center of target
Noise level	NL	$10\log \left[\frac{\text{noise intensity}}{\text{reference intensity}^a} \right]$	At hydrophone location
Receiving directivity index	DI	$10\log \left[\frac{\text{noise power generated by an equivalent non-directional hydrophone}}{\text{noise power generated by actual hydrophone}} \right]$	At hydrophone terminals
Detection threshold	DT	$10\log \left[\frac{\text{signal power to just perform a certain function}}{\text{noise power at hydrophone}} \right]$	At hydrophone terminals

Table A.1.

Parameters of the sonar equation. The *target strength* TS in the sonar equation is mainly used for single objects. In this context TS is used for backscattering strengths of the sea floor or of the sea volume of distributed objects in the water column, for instance fish and plankton. ■

^a The reference intensity is that of a plane wave of rms pressure 1 μPa .

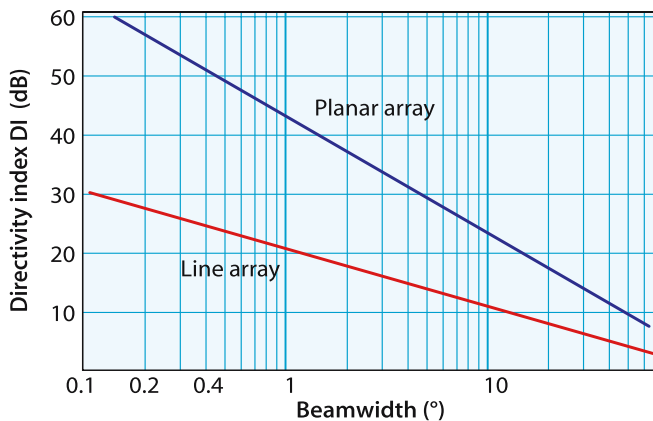


Image A.9.

Directivity index DI and beamwidth. The logarithmic depiction reveals the simple relation between directivity index and beamwidth: narrowing the beamwidth to 1/10 gains 10 dB of the directivity index of a linear array, and 20 dB of a planar array. Note, that the DI becomes zero at 180° beamwidth, which means: the so called “half space” in front of the ships hull is covered without directional preference. This is the case of a so called “point source” or point receiver mounted in a sound tight wall. ■

Image A.10.

Source level and acoustic power. Typical source level values (SL) of echosounders are 210–220 dB relative to $1 \mu\text{Pa}$. ■

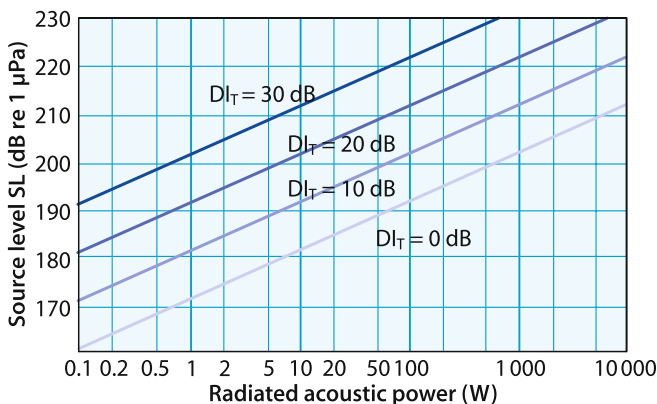


Image A.11.

Transmission loss with absorption and geometrical spreading combined. The dashed lower boundary of the transmission loss curves assumes spherical spreading loss with 20 dB per every 10 times the range. This is realistic only up to a range of transition between about 1 and 10 km beyond which the spread is merely cylindrical due to ducted Sofar-Channel propagation. The real deep water transmission loss at the individual frequencies is lower according to the red curve below as the cylindrical spreading reference. The difference amounts to about 30 dB at 1000 km. The range interval of transition may vary somewhat however, depending on the regional and seasonal sound speed profile and the depth of the sound source (figure derived from Sect. A.3.3.1, Image A.4). ■

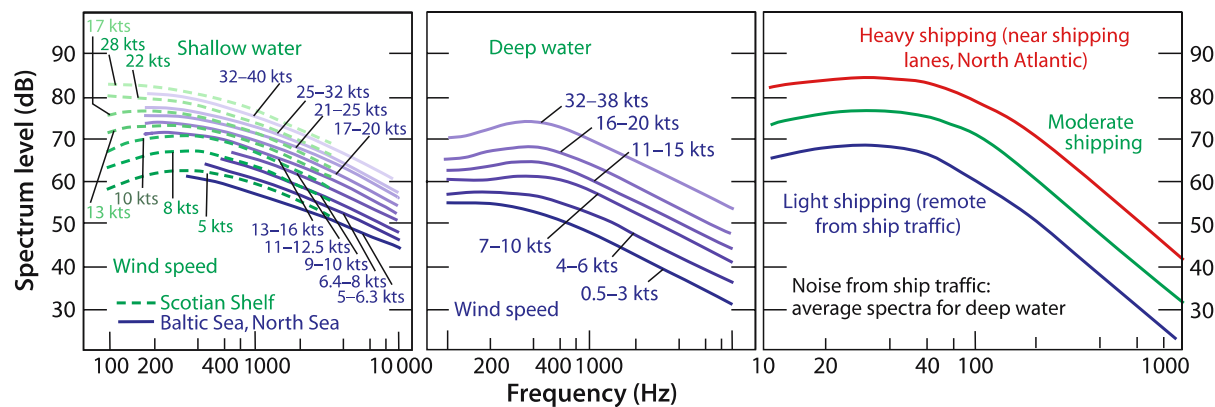
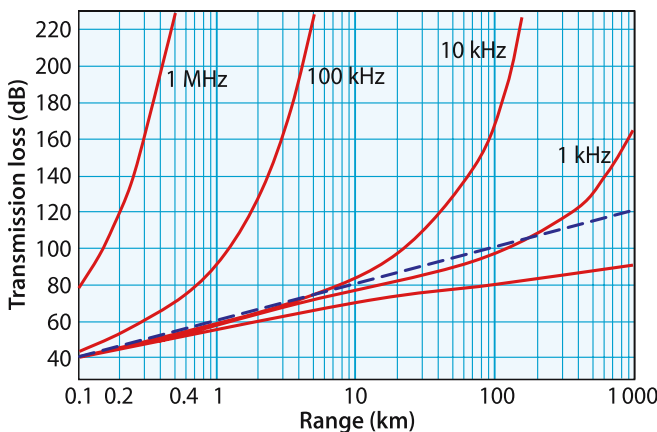


Image A.12. Noise spectrum level of wind- and sea traffic noise (Landold-Börnstein, *Acoustical properties of the ocean*, L.1–4). The depicted noise spectrum level refers to a frequency bandwidth of 1 Hz. A bandwidth of 100 Hz for instance adds 20 dB and a bandwidth of 1 kHz adds 30 dB to the spectrum level received by an omnidirectional receiver which then represents the noise level (NL) in the sonar equation. Most of the echosounders are directional by beamforming however which acts as a spatial filter of noise. This reduction of the received noise appears in the sonar equation as directivity index DI . If the beamwidth achieves a noise reduction of 20 dB for instance, the DI is 20 dB. ■

A.4.5 The Fourth Type of Sound Imaging: The Acoustic Doppler Current Profiler (ADCP)

A.4.5.3 Speed Components and Doppler Shift

Echo reception – Source and receiver at same place

- Frequency at the receiver

$$f_{\text{receiver}} = f_{\text{source}} \frac{(c - v_{\text{object}})(c + v_{\text{source}})}{(c - v_{\text{source}})(c + v_{\text{object}})}$$

v_{source} relative speed source/receiver

v_{object} relative speed object

- With

$$\frac{v_{\text{source}}}{c}, \frac{v_{\text{object}}}{c} \ll 1$$

the approximate Frequency at the receiver is

$$f'_{\text{receiver}} = f_{\text{source}} \left(1 + \frac{2(v_{\text{source}} - v_{\text{object}})}{c} \right)$$

- The Doppler shift of the received echo is

$$\frac{2(v_{\text{source}} - v_{\text{object}})}{c}$$

- The Doppler shift of the one way signal is

$$\frac{(v_{\text{source}} - v_{\text{receiver}})}{c}$$

CD Attachment Index

Large Images, Fledermaus Files, Sound Tracks, and Animations

- 1 The first approach to sea floor imaging: North Atlantic, Maury, 1853
- 2.11 Atlantic sea floor imaging, 1940 with Meteor data 1925–1927; *large image*
- 3.2.2 Acoustic “superconductivity”; *sound tracks* of earthquake, volcano eruptions, and nuclear explosion test
- 5.1.1 GEBCO5 Globe of the sea floor relief; *Fledermaus*
- 5.1.1.1 ETOPO2 Atlantic Ocean, *large image*
- 5.1.1.2 ETOPO2 Pacific Central, *large image*
- 5.1.1.3 ETOPO2 Pacific Australian, *large image*
- 5.1.1.4 ETOPO2 Indian Ocean, *large image*
- 5.1.1.5 ETOPO2 Arctic Ocean, *large image*
- 5.1.1.6 ETOPO2 Antarctica, *large image*
- 5.1.2 High resolution bathymetry versus Satellite altimetry, Eltanin; *Fledermaus*
- 5.2.1 Subduction of tectonic plates; Alaska, *large image*
- 5.2.1 Subduction of tectonic plates, Chile Type; Central America 1a, *large image*
- 5.2.1 Subduction of tectonic plates, Chile Type; Central America 1b, *large image*
- 5.2.1 Subduction of tectonic plates, Chile Type; Central America 4a *large image*
- 5.2.9 East Asian formations, Taiwan, *large image*
- 5.3.1 Submarine Escarpment Slides; Storegga Slide, *large image*
- 5.3.3 Sediment bedforms, migrating dunes, *animation*
- 5.3.5 Salt diapirs, *animation*
- 5.3.6 Canyons, channels, Porcupine Bight; *animation*
- 5.3.8 Canadian formations; Inner Scotian Shelf, *large image*
- 5.4.1 Arctic Ocean and its constituent seas, IBCAO, *large image*
- 5.5.1 Features of the Weddell Sea, *Fledermaus*
- 5.5.4 Features of the Ross Sea, 2 *large images*
- 5.6.1 Chella Bank, Mediterranean, *animation*
- 6.2.1 Methane hydrate deposits, Hydrate Ridge, *Fledermaus*
- 6.3.3 Marine mammal voices; *sound tracks*
- 7.3.2 Historic ship wrecks and wreck sites; Blücher, *Fledermaus*

Subject Index

A

- AABW (*see Antarctic bottom water*)
- absorption 7, 275, 449
- abyssal plain 145
- accretionary prism 87, 105
- Achziv Canyon 248
- acoustic
 - , array axis 46
 - , bathymetry 64
 - , current measurement 56
 - , Doppler current profiler (ADCP) 19, 56, 57, 269
 - , concept 56
 - , impedance 296, 297, 446
 - , Risk Mitigation Policies 322
 - , Sea-floor Classification System (ASCS) 255, 282, 292
 - , spectrometry 287, 300
 - , tomography 275, 281
 - , tracking 60
- ADCP (*see acoustic Doppler current profiler*)
- Adelaide 187
- Aegean Sea 234, 238, 240, 247
 - , features 238
- Aeolian Islands 234
- Africa 69, 183, 217
- African Plate 75, 131, 145, 234–236, 245
- air
 - , bubble sound absorption 304
 - , intrusion 299
- aircraft wreck 355
- airgun 55
- AKF (*see Avalon Knoll Fault*)
- Al Idrissi mud volcano 178
- Al Mansoura (wreck) 348
- Alaska 87, 139, 205
 - , continental slope 103
 - , Peninsula 77
 - , subduction zone 102
- albedo 202, 255
- Alboran 234
- Alcoa Puritan 403, 405, 407, 409, 410
- Aleutian
 - , Islands 77
 - , Trench 71, 77
- Aleutians 127
- Alonnisos Island 238
- Alpha-Mendeljev Ridge 206
- Alps 236
- altimetry satellite 64, 65
- Amber Chamber 352
- Amerasian Basin 205
- America 69, 71, 405
- Ampère
 - , Massif 131
 - , Seamount 131, 132
- Amundsen Basin 77, 206
- Anaximander Mountains 245
- Andaman 114
- Andes 94
- angular (or cross) resolution 308
- anomaly
 - , gravity 10
 - , magnetic 11
- Antarctic
 - , Bottom Water (AABW) 132
 - , Circumpolar Current 116
 - , Continent 67, 79
 - , Cruise 217
 - , Peninsula 79, 216, 217, 222, 224
 - , Plate (tectonic) 75, 79, 83, 116, 125, 219
- Antarctica 83, 187, 217, 219, 221, 222, 228, 230
 - , globe 79
- aperture, synthetic 361
- Arabian Plate 75, 234
- archaeology 374
 - , battleship a. 390
- architecture, ancient urban 374
- Arctic
 - , Basin 206
 - , Fram Strait 315

- , Ocean 67, 77, 202, 206
 - , bathymetry 202
 - , depression 206
 - , globe 77
 - , physiography 202
 - , sediments 208
 - , sea ice 212
 - , Shelf 202
 - Armutlu Peninsula 244
 - array
 - , axis 46
 - , beam, phased forming 46
 - , end-fire 54
 - , length 54
 - , phased 50
 - , two line 47
 - Arrow Lake 201
 - Ascension Fracture Zone 121
 - ASCS (*see acoustic sea-floor classification system*)
 - Asker (wreck) 350
 - asteroid impact 83
 - astigmatism acoustic 50
 - astronomical navigation 45
 - Atlantic 75, 77, 86, 192
 - , Islands 147
 - , landslide 153
 - , Margin 178
 - , Ocean 69, 77, 186, 206, 251, 272, 281
 - , globe 69
 - ATLAS Werke AG, Bremen 16
 - Austaasen Bank 226
 - Australia 25, 79, 115
 - Australian
 - , Plate 111
 - , Shelf 187
 - autonomous
 - , lander 314
 - , underwater vehicle (AUV) 212, 355, 402, 421
 - AUV (*see autonomous underwater vehicle*)
 - Avalon Knoll Fault (AKF) 130
 - AWI Bathymetric Chart Weddell Sea (AWI BCWS) 218
 - axial ridge 122
 - Azores-Gibraltar 131
-
- B**
- back-arc
 - , basin 73, 106
 - , chain 220
 - Bahamas 38
 - Baia 374, 375
 - Balearic Islands 236
 - Balleny Islands 228
 - Balsfjord 188
 - Baltic Sea 8, 15, 190, 234, 251, 252, 262, 310, 311, 328, 348, 351, 358, 396, 445
 - , fish stocks 310, 311
 - , formations 251
 - , Gulf of Gdansk 258
 - , Kadetrinne 256
 - , relief 252
 - , salinity 22
 - , sedimentation 261
 - , western 255
 - , wrecks 351
 - bandwidth 43
 - Bangladesh 114, 161, 162
 - barchan 170
 - Barents Sea 159, 178, 205
 - bathymetry
 - , acoustic 12, 64
 - , high resolution 80
 - Battle
 - , of Normandy 383
 - , of the Doggerbank 382
 - battleship archaeology 390
 - Bay of
 - , Bengal 161, 162
 - , Biscay 146
 - , Eckernförde 255, 292, 293, 298
 - , Kiel 256
 - , Naples 378
 - beam, narrow 54
 - beamwidth 54
 - Bear Island
 - , Fan 159
 - , Trough Mouth Fan (TMF) 159, 161
 - Beaufort Sea 206
 - Bedford Basin 192
 - bedrock structures 190
 - Behm, Alexander 14, 16
 - Belt Sea 252
 - Bengal Fan 161–166, 234
 - Bergen 189
 - Berwick Castle 385
 - Bight of
 - , Lübeck 329
 - , Mecklenburg 261
 - , Meldorf 336
 - , sea floor 339
 - , Scapa Flow 392, 396
 - Bismarck 390
 - Bjørnsundet 188
 - Black Sea 242

- Blücher (wreck) 381
blue
 -, whale 24
 -, whiting 313
BODC (*see British Oceanographic Data Center*)
Boknafjorden 190
Boris Petrov Expedition 208
Boston
 -, Centre 15
 -, USA 14
Bottlenose dolphin 316
Bottom Simulating Reflector (BSR) 284–289
boundary, pressure-release 289
Brahmaputra River 161
Bransfield Strait 222, 223
Bremse class 394
Britain 175
British
 -, Columbia 198, 200
 -, Oceanographic Data Center (BODC) 66
Bruce, William 218
Brummer 394
Brunt Ice Shelve 217
Bryozoas 225
BSR (*see bottom simulating reflector*)
bubble oscillations 34
Burma Trench 162
buzz 298, 299, 319, 322
-
- C**
- C.C.G.S. Matthew 192
cable
 -, submarine 362
 -, Trans-Atlantic 362
 -, Trans-Pacific 362
California margin 130
Callao/Peru 166
Campi Flegrei 374
Canada 190, 200, 205
 -, west coast 198
 -, Basin 206
Canadian
 -, Arctic Archipelago 206
 -, Gully 186
Canale Grande 343
Canary
 -, Channel 183
 -, Islands 147, 153
canyon, submarine 184
Cape
 -, Adare 228
 -, Hallett 228, 230
 -, Horn 79
carbon dioxide 299
carbonate mounds 171
Carboniferous 236
Caribbean 69
carpenter fish 317
Carrara 237
cavitation 43
 -, bubble 43
 -, limit 43
CBBL (*see coastal benthic boundary layer*)
CCGS John P. Tully 199, 200
Celebes Basin (Sulawesi Basin) 111
Celtic
 -, Deep-sea Fan 156
 -, Fan 155
 -, Margin 155
 -, Shelf 146, 172, 186
Central
 -, America 71, 87
 -, subduction zone 87
 -, American Trench 90, 234
 -, Basin 243, 244
 -, Chile 87, 97
 -, subduction zone 94
 -, Costa Rica 91
 -, Fracture Zone 108
 -, Labrador Sea 279
 -, Pacific 127
Chagos-Laccadive Ridge 75
Challenger Deep 107, 109
 -, Trench 106
channel 184
 -, axis 25
 -, submarine 167
 -, levee
 -, process 185
 -, complex 164
 -, effect 187
 -, system 218
Charybdis 13, 234
Chella Bank 235
Cherbourg 383
Chi-Mei Canyon 143
Chile 126
 -, continental slope 101
 -, Trench 71
 -, -type margin 85
Chilean Margin 100
Chinese Continental Margin 145
Christelle Volcano 118

- Chukchi Borderland 206
 Chukchi
 –, Sea 206
 –, Spur-Chukchi Plateau 206
 Çınarcık Basin 243–245, 456
 Cinque Terre 237
 –, wrecks 349
 circulation, Langmuir 300
 City of Baia 374, 378
 Claire Volcano 118
 clathrates 289
 Cleona (wreck) 350
 climate history 4
 close-up deep water imagery 402
 Coastal Benthic Boundary Layer (CBBL) 292, 293, 295, 298
 Coats Land 217
 Cocos
 –, Plate 70
 –, Ridge 87
 cold water corals 176
 Colladon, J. Daniel 15
 Cöln II 393
 Comprehensive Test-Ban Treaty (CTBT) 27
 compressibility 22
 –, non-linear 53
 –, of water 53
 compressional wave 55
 computer capability and data storage 14
 concept
 –, combined 59
 –, drifter 56
 –, tomographic 56
 Condul (wreck) 328
 construction, submarine 362
 continental
 –, margin 106
 –, rise 145
 –, shelf 8, 145
 –, slope 8, 145
 convergence
 –, tectonic 245
 –, vector 93
 conveyor belt 206, 279
 coral reef 139
 Cordilleras 236
 Coriolis force 189
 Corsica 298, 299, 320, 322
 Costa Rica 87, 90
 Crete 245, 247
 Crinoidea 225
 CTBT (*see United Nations Comprehensive Test Ban Treaty*)
 Curonian Lagoon 258
 current
 –, bi-directional system 272
 –, circumpolar 26
 –, Doppler profiling 269
 –, measurement 56
 –, profile, vertical 56
 –, resolution, vertical 272
 –, sampling problem 59
 –, slow 58
 –, tracking 19
 –, turbidity c. 155
 –, unidirectional cold southward 269
 –, variability
 –, spatial 58
 –, temporal 58
 –, vector
 –, determination 57
 –, profile 56
 –, velocity, horizontal 272
 –, volume 266
 Cyprus 234, 245
 Cyrenaica 234
-
- D**
 D-Day relics 341
 Daikakuji Seamount 80, 81
 Daito Ridge 108
 Danish Sounds 251
 Danzig 353
 Dardanelles 238
 Darss Peninsula 257
 data, climatological 25
 Dead Sea 234
 debris flow 156, 157, 159
 –, non-glacigenic 158
 Decibel, definition 444
 deep
 –, sea food 314
 –, Scattering Layer (DSL) 312
 –, towed 403
 Denmark 252
 density 22
 depiction
 –, bathymetric 44
 –, landscape 44
 depression 206
 depth 35
 –, chart 44
 –, profile 49
 –, resolution 54, 308
 description
 –, Eulerian 60
 –, Lagrangian 60

Dessau 334
 detection range limited 31
 DGPS navigation 364
 diapir 178, 183
 –, evaporitic 183
 diffraction 30
 digital terrain model (DTM) 189
 dipole domain 42
 direction of radiation 46
 Dock of London 344
 dolphin, stranding 38
 Doppler
 –, effect 56
 –, frequency-speed relation 58
 –, shift 56, 57, 450
 Drake Passage 217
 dreadnoughts 391
 Dresden II 392, 393
 –, class 392
 drifter concept 56
 drive fisheries 320
 DSL (*see deep scattering layer*)
 DTM (*see digital terrain model*)
 dune 170
 –, underwater 198

E

Earth
 –, crust 4
 –, surface, deepest place 109
 earthquake
 –, magnitude 112
 –, submarine, sonogram 36
 –, tsunami generating 113
 East Antarctica 217
 East Asia 71, 362
 East Greenland Current 207, 215, 274
 East Mariana Basin 108
 East Mariana Ridge 107
 East Pacific Rise (EPR) 70, 71, 75, 79, 117, 123, 125, 130
 East Prussia 351, 354
 East Siberian Sea 206
 Eastern Ridge 243
 echo
 –, formation 29
 –, imaging
 –, radar 19
 –, sound 19
 –, intensity 48
 –, strength 307
 –, sounding 275
 –, intensity 49
 echosounder
 –, characteristics 41
 –, evolution 18
 –, fan (*see multibeam*)
 –, hardware 14
 –, high resolution 41
 –, information 35
 –, monobeam 308
 –, multibeam (or fan) 19, 31, 44, 46
 –, angle 54
 –, parametric 358
 –, transducer 48
 –, object discrimination 35
 –, optimization 44
 –, resolution 44
 –, sediment e. 162
 –, conventional 55
 –, parametric 53, 54
 –, sediment penetrating 19, 52
 –, sidescan 19, 28, 48, 49
 –, transducers 50
 –, steering signal 46
 echosounding 14
 –, direct, quantitative imagery 19
 –, high resolution 19
 –, sediment 52
 –, slant angles 31
 effect
 –, Doppler 56
 –, hydrodynamic 12, 13
 –, piezoelectric 42
 eigen-frequency 43
 eigen-rays 280
 El Golfo 153
 –, -landslide 154
 El Hierro 153, 154
 El Niño 166
 Elba Island 359, 360
 Elbe
 –, Estuary, floor features 336
 –, River 334, 335, 339
 electromagnetic wave, penetration depth 9
 electrostrictive 42
 Ellsworth Land 217
 Eltanin
 –, Impact Area 83
 –, Massif 10, 80, 82
 –, relief 11
 Emperor Seamount Chain 71, 77, 80, 139
 –, map 80
 encounter speed 57
 end-fire array 54, 359
 –, synthetic 359

- energy
 –, acoustical 42
 –, conversion 42
 –, electrical 42
 –, irradiation 7
 –, remaining 7
- England 190
- English Channel 15, 155
- Eolian
 –, Islands 134
 –, Volcanic Arc 134
- EPR (*see East Pacific Rise*)
- Epsom Salts 22
- Equatorial Undercurrent 272
- equipotential surface 65
- Erathostene Seamount 245
- erosion 142
 –, tectonic 87, 93, 94, 102
- eruption volcanic, sonogram 36
- escarpment slide 146
- Estonia 326
- estuary, surveillance 335
- Etna 133
- ETOPO2 64, 84
 –, data 110, 112
- Eulalla Volcano 118
- Eulerian
 –, description of flow 60
 –, method 266
- Eurasian
 –, Basin 205
 –, Plate 73–77, 110, 112, 131, 140, 145, 161, 234–236, 240, 245
- Europe 69
- European Continental Margin 145, 153
- Explora Escarpment 216, 217, 219
- explosion nuclear, sonogram 37
- exponential law 8
-
- F**
- F. G. Creed 192, 194, 195
- facies 163
- Faeroe Islands 159
- fairway surveillance 326
- Falster Island 257
- fan echosounder (*see multibeam echosounder*)
- Fara Volcano 118
- Farallon Plate 70
- fauna, submarine 306
- ferry, sunken 326
- Fessenden
 –, Oscillator 15, 16
 –, Reginald A. 14
- FFK (*see vessel/ship*)
- FFS (*see vessel/ship*)
- field
 –, Fraunhofer far 51
 –, Fresnel near 51
 –, magnetic 11
- Fiji Islands 73
- Filchner Ice Shelve 217
- filter
 –, frequency 35, 448
 –, spatial 34, 447
 –, tailoring 35
- Fimbul Ice Shelve 217
- Finland 251, 252
- fish
 –, stock, estimation 307
 –, towed 49
- fishery, drive 320
- fjord 188
- Fledermaus visualization 110, 114, 206, 210, 220
- flora, marine
 –, sound imaging 322
- Florence Rise 245
- Flores 75, 112
- Florida 296, 298
- flow
 –, debris 157
 –, eddy 158
 –, Eulerian description 60
 –, Lagrangian description 60
 –, nearly horizontal 57
 –, tidal 168, 282
 –, turbidite 161
 –, type 167
 –, unidirectional 158
- focus, gliding 50
- focusing 50
 –, effect 51
 –, limits 51
 –, scheme of 50
- formation
 –, Canadian 192
 –, natural 63
 –, volcanic 131
- Fracture Zone 118
- Fram (vessel) 202
- Fram Strait 77, 202, 205, 206, 212
- Franpipe 367
- Fraser River 198
- Fraunhofer far field 51
- freeboard 213
- Freedden
 –, Seamount 82, 83

–, Wilhelm von 82
 frequency
 –, difference 53
 –, filter 35
 –, low, generation 53
 –, resolution 58
 –, shift 57
 Fresnel near field 51
 FRV (*see vessel/ship*)
 Fuerteventura 183
 Fyn 255

G

Gagua Ridge 140
 Gakkel Ridge 77, 206
 Galapagos 87
 Gale 302
 –, Strong 302
 Galilee 248
 gamma radiation 10
 Ganges
 –, Delta 75
 –, River 161
 Ganos Mountain System 244
 gas 282
 –, indicator 289
 –, plume 263
 GDA (*see GEBCO digital atlas*)
 Gdańsk 353
 GDF (*see glaciogenic debris flows*)
 GEBCO (*see general bathymetric chart of the oceans*)
 GEBCO Digital Atlas (GDA) 66
 General Bathymetric Chart of the Oceans (GEBCO) 66
 General von Steuben (wreck) 348, 351, 354
 geodynamics 85
 Geographic and Hydrographic Information System
 HydroCAD (GIS/HIS) 343
 Geological Survey of Canada Atlantic (GSCA) 195
 Geosat 65
 German Federal Research Board for Fisheries 309
 Germany 252, 340
 giant
 –, shelf canyon 161
 –, tsunami 114
 –, underwater dune 198
 Gibraltar 119, 131
 Giesensand 338
 GIS/HIS (*see geographic and hydrographic information system HydroCAD*)
 glaciogenic debris flows (GDF) 159
 gliding focus 50
 Global Ocean Ecosystem Dynamics program (GLOBEC) 310
 global positioning satellite navigation (GPS) 14, 45, 46
 GLOBEC (*see Global Ocean Ecosystem Dynamics Program*)
 Gloria (sidescan echosounder) 52
 Gneisenau (wreck) 328
 Gogonarian 225
 Gondwana 187, 217
 Gorleben salt diapir 183
 Gorringe Bank 131
 Gotland 252
 –, Basin 311
 Goya (wreck) 348, 351
 GPS (*see global positioning satellite navigation*)
 Grand Banks 272
 gravity
 –, anomalies 10
 –, field 65
 –, unipolar 11
 –, relief 10
 –, wave, internal 14
 Great Ice Barrier 228
 Greece 145
 Greenland 205, 206
 Grosse Atlantische Expedition 16
 ground truth 270
 GSCA (*see Geological Survey of Canada Atlantic*)
 Gulf of
 –, Aden 75
 –, Bengal 75
 –, Biscay 155
 –, Bothnia 252
 –, California 71, 128, 130
 –, Finland 263
 –, Gdansk 251, 255, 258
 –, Mexico 281, 403, 407, 409
 Gulf Stream 5, 207
 Gustloff (wreck) 354
 guyot 81, 87, 135, 235, 249
 gyro 46

H

Haifa 248
 Haitabu 358, 396
 Håkon Mosby Mud Volcano (HMMV) 178, 181
 Halifax 190, 192
 –, explosion 192
 –, Harbor 192
 halocline 310
 Hamburg 335
 –, Harbor 340, 341
 Hanseatic League 251
 harbor
 –, protection 370

- , surveillance 340
 - Hardangerfjord 188
 - hardware transport 364
 - Hawaii 84, 138
 - Hawaiian
 - , Archipelago 138, 362
 - , Chain 75, 77, 80
 - , map 80
 - , Emperor Chain 80
 - , Islands 87, 138, 139
 - Hayes
 - , Fracture Zone 119
 - , Ridge Transform Intersection 120
 - heat
 - , content 278
 - , large scale measurement 279
 - , measurements 277
 - , energy, transport and distribution 59
 - , transport 266
 - Hecht, Heinrich 15
 - Hela Peninsula 353
 - Hellenic Trench 234, 240
 - Hengchun Ridge 140, 142
 - Herodotus
 - , Abyssal Plain 245
 - , Trough 245
 - herring 313
 - , pole formation 313
 - Herringbone Relief 216, 219
 - Himalayan 161, 162
 - Himalayas 75, 138, 161
 - Historic Wreck Site 388
 - Hjort
 - , Ridge 116
 - , Trench 115, 116
 - HMMV (*see Håkon Mosby mud volcano*)
 - HMS
 - , A1 (wreck) 385
 - , Hazardous (wreck) 387
 - , Mary Rose (wreck) 388
 - , Superb (submarine) 215
 - Hobart 137
 - Holocene 261
 - holography 44
 - Hong Kong, seabed survey 346
 - Hook of Holland 332
 - Horlaland 188
 - Horseshoe Seamounts 131
 - hot spot
 - , hypothesis 138
 - , islands 138
 - , temperature anomaly 23
 - house, Roman 377
 - Hr. Ms. Adder 386
 - Hsiukuluan-chi River 143
 - Hualien Canyon 143
 - Huatung Basin 140, 145
 - Hydrate Ridge 283–285, 287, 288
 - Hydrodynamic effects 13
 - hydrogen bond 287
 - hydroplaning 161
 - Hydrozoa 225
 - Hylsfjorden 190
-
- IBCAO (*see international bathymetric chart of the Arctic Ocean*)
 - ice
 - , coverage 213
 - , thickness 213
 - Iceberg Alley 224
 - iceberg plough scars 224
 - Iceland 77
 - , Basin 268
 - , -Faroes Ridge 268
 - ICES (*see International Council for the Exploration of the Sea*)
 - IHO (*see International Hydrographic Organization*)
 - illumination 7
 - image
 - , processing 287
 - , radar 12
 - , visual 6
 - imaging
 - , acoustic 19
 - , application 61
 - , by sound 6, 32
 - , limiting background 32
 - impedance
 - , acoustic 29, 287, 296, 297, 446
 - , definition 29
 - , steps 30
 - Imperial Fleet 396
 - India 162
 - Indian Ocean 25, 75, 79, 86, 112, 162, 206
 - , globe 75
 - , sound speed at Sofar-axis depth 26
 - Indo-Australian Plate 73, 75, 112, 116, 161
 - Indonesia 110
 - Indonesian
 - , Island Arc 112
 - , passage 25
 - information, transport 364
 - infrared 9
 - inhomogeneity, backscattering 31
 - intensity 8

- International
 →, Bathymetric Chart of the Arctic Ocean (IBCAO) 202
 →, Council for the Exploration of the Sea (ICES) 307
 →, Hydrographic Organization (IHO) 66
 →, Oceanographic Commission (IOC) 66
 IOC (*see International Oceanographic Commission*)
 Ionian Basin 245
 Ireland 146, 172, 175
 Irish Sea 155
 Irminger
 →, Basin 312
 →, fish stocks 312
 →, Current 268
 irradiation 7
 →, energy 7
 island arc 138
 Island of
 →, Bornholm 255
 →, Sylt 299
 Isle of
 →, Fehmarn 255
 →, Gotland 252
 →, Guam 107
 →, Wight 385
 isobath 44, 67
 Israel shelf, formations 248
 Italy 145, 349, 374, 378
 Izu Ogasawara Trench 107
-
- J**
- J6 Alpha platform 367
 Jan Hevelius (wreck) 326
 Japan 107, 113
 Japanese Sea 36
 Java 75, 112
 →, Ridge 112
 →, Trench 75, 111, 112
 →, -Sunda Trench 112
 Juan de Fuca
 →, Plate 70, 128, 133, 283
 →, Ridge 133
 →, Strait 198
 Juan Fernández Ridge 94, 97
 Juan Perez Sound 201
-
- K**
- K13 Alpha platform 367
 Kadetrinne 256, 257
 Kahoolawe 138, 139
 Kaiko (submersible) 107
 Kamchatka Trench 77
 Kapıdağ Peninsula 244
 Kara Sea 205
 Kattegat 251
 Kauai 139
 →, Island 80, 84
 Kent 383
 Kerguelen Plateau 79
 Kermadec Trench 71
 Key West 296
 Kiel 14
 →, Canal 251, 255, 336
 →, Fjord 15, 255
 København 255
 König (wreck) 391
 König class battleships 391, 392
 Königsberg II class 395
 Korfu 322
 Krautsand 338
 Kristiansund 188
 Kronprinz Wilhelm (wreck) 391
 kurkar 248
 Kyusyu 107
 →, -Palau Ridge 107, 108
-
- L**
- L3 submarine-minelayer 353
 Labrador Sea, heat content 279
 LADCP 270
 →, method 274
 Lagrangian
 →, description of flow 60
 →, method 266
 Lake Lucrino 380
 Lake of
 →, Geneva 15
 →, Tiberias 234
 Lanai 138, 139
 landslide 159
 Landsort Trench 260
 Langmuir circulation 300
 Lanzarote 183
 Laptev Sea 205, 206
 Large Scale Drifter Field Experiment 266
 law, exponential 8
 Le Hazeux (wreck) 387
 Lead-Zirconate-Titanate (LZT) 42, 43
 →, as sound source 42
 →, polarization 42
 →, -transducer 43
 lee wave 12
 length, apparent 54
 Levitus 25

–, Atlas of Oceanography 25
 Libya 245, 247
 Lichte, Hugo 15
 light
 –, blue-green 9
 –, intensity 8
 –, visible 8
 –, penetration depth 8
 Ligurian Sea 320, 322
 lithosphere 4
 Lomonosov Ridge 205
 Longitudinal Valley 143
Lophelia pertusa 176, 177
 Loran 45
 Los Angeles
 –, Area 130
 –, Basin 128
 loudspeaker, electrodynamic 15
 Luzon
 –, Island Arc 140
 –, Volcanic Arc 145
 LZT (*see lead-zirconate-titanate*)

M

Ma Wan Island 347
 Maas Channel 332, 333
 Macquarie
 –, Island 115
 –, Ridge 115
 –, Complex (MRC) 115, 116
 Madagascar 75
Madrepora oculata 177
 magnetic anomalies 11
 magnetostrictive 42
 magnitude 112
 Makarov Basin 206
 mammal, marine
 –, noise 38
 –, voice sonogram 316
 Manila Trench 140
 Manta mine 359
 map, global 67
 MAR (*see Mid-Atlantic Ridge*)
 Marciana Marina 359, 360
 margin
 –, Chile type 85, 106
 –, continental 128, 247
 –, active 178
 –, Marianas type 106
 –, passive 145, 178
 –, convergent 106, 145
 –, Chile type 106, 107
 –, Marianas type 106, 107
 –, passive 145, 178
 Mariana
 –, Trench 107, 110, 112
 –, Trough 107
 Marine Protected Area (MPA) 194
 marine reserve 137
 Maritime and Coastguard Agency 383
 Markgraf (wreck) 391
 Marmara Sea 238, 242
 –, Trough 242
 Marquesas Fracture Zone 127
 Marsili 234
 Mary Rose Trust 388
 mass distribution 10
 matched
 –, filter computer 277
 –, peak method 276
 material
 –, electrostrictive 42
 –, hazardous 326
 –, magnetostrictive 42
 –, piezo-ceramic 42
 Maui 138, 139
 Maury Map 117
 MB (*see vessel/ship*)
 meadow, inundated 255
 Mediterranean 145, 236, 238, 320, 322, 380
 –, outflow 25
 –, water (MOW) 132
 –, Ridge (MR) 245
 –, Sea 235, 242, 316, 322
 –, formations 232
 –, heat content 277, 278
 –, salinity 22
 –, tectonic 245
 –, sound speed at Sofar-axis depth 26
 Meghna River 161
 Melanesia 73
 melon 319
 Mentawai Ridge 112
 Merz, A. 16
 Meteor 17, 18
 methane
 –, acoustic features 293
 –, biogenic 291
 –, hydrate 289, 292
 –, deposits 282
 –, properties 284
 –, resources 284
 –, in shallow sediments 291
 method
 –, Lagrangian 266

- , matched peak 276
 - MFZ (*see Mocha Fracture Zone*)
 - microwaves 9
 - Mid-Atlantic Ridge (MAR) 6, 17, 69, 75, 77, 79, 117–122, 127, 131, 145, 255
 - mid-ocean ridge 75, 117, 119, 126, 127, 129, 138
 - , fast spreading 123, 125, 127
 - , slow spreading 117, 119, 121, 122
 - Middle Marianas Ridge 107
 - Mittelgrund 298
 - mixing, non-linear 53
 - Mobile Bay 405
 - Moby Dick 316
 - Mocha
 - , Fracture Zone (MFZ) 100
 - , Island 100
 - Molde 188
 - Molloy
 - , Deep 206
 - , Hole 207
 - Molokai 138
 - Mont Blanc
 - , Massif 132
 - , vessel 192
 - Moresby Island 200
 - Morocco 178
 - morphology, small scale 48
 - Morris Jessup Rise 206
 - motion
 - , compensation 46, 48
 - , of ship 46
 - Mount Carmel 248
 - MOW (*see Mediterranean outflow water*)
 - MPA (*see marine protected area*)
 - MR (*see Mediterranean Ridge*)
 - MRC (*see Macquarie Ridge complex*)
 - MS (*see vessel/ship*)
 - mud volcano 178
 - multi-aspect sounding 52
 - multibeam echosounder 19, 44, 46
 - , transducer 48
 - München (*see General von Steuben*)
 - Munk, Walter 274
 - Murray-Darling River 187
 - MV (*see vessel/ship*)
-
- N**
- NAC (*see North Atlantic Current*)
 - NADW (*see North Atlantic deep water*)
 - NAF (*see North Anatolian Fault*)
 - Nanga Parbat 75
 - Nansei Syoto Trench 107
 - Nansen Basin 77, 206
 - Naples 133, 374
 - Narrows 192
 - navigation
 - , astronomical 45
 - , DGPS 364
 - , GPS 45
 - , radio 45
 - Nazca Plate 70, 94, 97
 - , Margin 99
 - Neptunian water 22
 - New Foundland 272
 - , Basin 272
 - New Guinea 73
 - New Siberian Islands 202
 - New Zealand 71, 79, 115
 - Nicaragua 87, 90, 93
 - , Trench 71
 - Nicobar 114
 - Nicoya Peninsula 93
 - Nile 234
 - , Deep-Sea Fan 247
 - , Delta 247
 - Ninety East Rise 75
 - nitrogen 299
 - noise
 - , by bubble oscillations 34
 - , by rain 33, 34
 - , fighting 38
 - , fighting, technical 34, 35
 - , in the sea 32
 - , limited 31
 - , self n. 38
 - , signal to noise ratio 32
 - , sources 32, 36
 - , spectrum level 449
 - , wind-driven 33
 - , intensity 33
 - non-linearity parameter 54
 - Norderelbe 340
 - Nordic Seas 206
 - Nordsee (research platform) 299, 300, 362, 373
 - North Aegean
 - , Basin 238, 240
 - , Trough 240, 242
 - North American
 - , continent 190
 - , Plate 77, 128, 145
 - North Anatolian Fault (NAF) 238, 240, 242
 - North Atlantic 5, 146, 206, 207
 - , bathygraphic map 5
 - , Circulation 266
 - , Current (NAC) 272, 274

- , Deep Water (NADW) 132, 207, 279
- , fish stocks 312
- , submarine cables 362
- North Brazil Current 272
- North European Margin 255
- North Kaholmen 382
- North Luzon Trough 140
- North Pole 67, 77
- North San-Hsian Canyon 143
- North Sea 15, 168, 251, 313, 328, 372, 382, 445
 - , Fan 158
 - , fish stocks 309
 - , TMF 159
- Northern Greenland 206
- Northern Hemisphere 119, 122
- Northwind Ridge 206
- Norway 188, 350
- Norwegian
 - , Channel 156
 - , Fjords 188
- Nova Scotia 190
 - , Shelf 186
- NRV (*see vessel/ship*)

O

- Ob 208
- object
 - , acoustic size 30
 - , buried 355
 - , minimum size 30
- ocean
 - , acoustic
 - , physics 15
 - , tomography 59, 274
 - , Drilling Program (ODP) 139, 219
 - , floor, subduction 106
 - , remote sensing by sound 27
 - , salinity 22
 - , surface topography 64
 - , surveillance 19
 - , temperature 23
 - , volume 265
- oceanic plate 106
- Oceanographer
 - , Fracture Zone 119
 - , Transform Fault 118
- Oceans Act 190, 193
- Odontocetes* 38, 316, 319
- ODP (*see Ocean Drilling Program*)
- OFZ (*see Owen fracture zone*)
- Okeanos (vessel) 412
- Oki-Daito Ridge 108

- Omega (navigation) 45
- Operation
 - , Neptune 397
 - , Overlord 397
- Ophiuridea 225
- optimization, sounding 35
- optimum compromise between range and resolution 29
- orange peel texture 111
- Orange Roughy 137
- Orca Seamount 222
- Ormen Lange 417
 - , gas field 414
- ORP Arctowski 352, 353
- Oscillator 16
 - , Fessenden 15, 16
- Oskarsborg 382
- Oslo Fjord 188, 382
- Owen Fracture Zone (OFZ) 75
- oxygen 299

P

- Pacific 71, 75, 80, 86, 106, 112, 192, 245, 362
 - , Australia, globe 73
 - , Central, globe 71
 - , -Cocos Plate 126
 - , Fracture Zone 123
 - , -Nazca Plate 126
 - , Ocean 138, 206
 - , sound speed at Sofar-axis depth 26
 - , Plate 70, 73, 83, 108, 116, 125, 128
 - , Ring of Fire 71, 73, 77, 106, 111
 - , submarine cables 362
- Palau Trench 107
- Paleozoic Cambrian-Devonian period 190, 192
- Palos Verdes
 - , Fault (PVF) 130
 - , Peninsula 130
- Panarea Island 134–135
- parameter, non-linearity 54
- parametric echosounder 54
- Parasound 166
- Parece Vela Basin 108
- Patrol Craft 566 404
- Patton Escarpment 128
- Pelagia (survey vessel) 175
- Peloponnesus 247
- penetration depth 7, 304
 - , visible light 8
- Penghu Canyon 142
- Persian Gulf, wreck 348
- Peru 166
- phase 46

- , delay 46
 - , front 46, 50
 - , axis 46
 - , propagation 23
 - , shift 47, 295
 - phased array beam-forming 46
 - Philadelphia 383
 - Philippine 110
 - , Basin 108, 111
 - , Plate 73, 107, 110–112, 140
 - , tectonic activities 140
 - , Trench 73, 107, 110, 111
 - Philippines 106
 - phonic lips 319
 - photography, underwater 19
 - piezoceramic material 42
 - piezoelectric effect 42
 - piezoelectricity 42
 - pilot whale 316
 - pipe 368
 - , state of free span 368
 - pipeline
 - , route planning 414
 - , submarine 366
 - pixel size 308, 327
 - plain, abyssal 145
 - plate
 - , collision 234
 - , continental 106
 - , margin 145
 - , converging 245
 - , margin 129
 - , convergent 106
 - , motion 221
 - , oceanic 106
 - , subduction 111–113
 - , subduction 106
 - , tectonic 86
 - , convergent 85
 - , map 86
 - , tectonics 85
 - , map 220
 - Pleistocene 156
 - Pliny Trench 245
 - pockmark 262, 292
 - Polarstern (vessel) 172
 - pole formation 313
 - Porcupine Bight 171, 172
 - Porto Giulio 378
 - Portus Julius Baae 378
 - Posidonia* 307
 - , *oceanica* 322
 - Possession Islands 228, 230, 231
 - pressure
 - , sound 53
 - , static 22, 53
 - prism, accretionary 87
 - Prof. Albrecht Penck (ship) 261, 262
 - project, EU C-Star 12
 - Protection of Wrecks Act 388
 - PVF (*see Palos Verdes Fault*)
-
- ## Q
-
- Qishon 248
 - quartz 42
 - Queen Charlotte Islands 200
 - Queen Maud Land 217
 - Quepos Plateau 87
-
- ## R
-
- radar
 - , image 12
 - , satellite 9
 - radiation
 - , absorption 7
 - , axis 46
 - , direction 46
 - , gamma 10
 - , ultraviolet 10
 - radiator, coherent 44
 - radio
 - , navigation 45
 - , waves 9
 - rain noise 33
 - raindrop impact 34
 - receiving mode 55
 - Red Sea 75
 - , sound speed at Sofar-axis depth 26
 - redfish 312
 - reflection 280
 - , seismics 290
 - , specular 29, 30
 - refraction 280
 - , index 23, 24
 - , seismics 290
 - relief, gravity 10
 - remote sensing 6, 274
 - , of motion 59
 - remotely operated vehicles (ROV) 192, 229–231, 359, 391, 396, 406
 - research platform Nordsee 372
 - resolution
 - , angular (or cross) 50, 291, 292, 308
 - , cell 308
 - , depth 54, 308

- , dilemma 53
- , frequency 58
- , lateral 44, 50
- , necessary 44
- , possible 44
- , radial 44, 50
- , speed 58
- , time r. 45
- resonance 43
- reverberation 31, 446
 - , limited 31
- Reykjanes Ridge 77, 268
- rheology 87
- Rhodes
 - , Basin 245
 - , Island 245
- Richard Montgomery
 - , vessel 328
 - , wreck 383
- ridge
 - , erosional 142
 - , subduction-induced 142
- ripples 168
- rise, continental 145
- Robert E. Lee (vessel) 404, 405, 409, 410, 412
- Rockall Trough 175
 - , margin 171
- Rockan mine 359
- Rogaland 188
- Roman City, sunken 374
- Ronne Ice Shelf 217
- Ross
 - , Ice Shelf 228
 - , James 228
 - , Sea 67, 79, 218, 228, 230
- Rotterdam Harbor 332
- Route Position Lists (RPLs) 364
- ROV (*see remotely operated vehicles*)
- RPLs (*see route position lists*)
- Russia 205
- RV (*see vessel/ship*)
- Ryukyu
 - , Island Arc 140
 - , Trench 140, 142
- , wreck site 388
- salinity 22
 - , sensor 59
- Salomon Islands 73
- Sambian Peninsula 252
- sampling 47
 - , line by line 49
 - , problem 59
 - , simultaneous 47
 - , time parallel 47
- San Andreas Fault 70, 128, 130
- San Antonio Canyon 97, 102
- San Francisco 130
- San-Hsian Canyon 143
- sand
 - , ribbons 170
 - , dune 168, 169
- Sandsfjord 188
- Sandwich Island Chain 219
- Saros Körfezi Bight 238
- satellite
 - , altimetry 64, 65, 80
 - , navigation 45
 - , radar 9, 19
- Scandinavia 251
- Scandinavian
 - , Shield 252
 - , Star 326
 - , Vikings 397
- scatterer 57
- scattering 29, 48, 446
- Schlei 396
 - , Fjord 255, 358
- Schleswig-Holstein 339
- Sciara del Fuoco 135
- Scotia 69
 - , Plate 116, 219
- Scotian Shelf 190, 192
- Scotland 188
- SCUFN (*see Sub-Committee on Undersea Feature Names*)
- Scylla 13, 234
- sea
 - , features, acoustic 19, 21
 - , floor 63
 - , acoustic classification 291, 296
 - , image 6
 - , maps 64
 - , random backscatter 32
 - , relief 48, 66
 - , sounding 15
 - , spreading 115
 - , surface 29, 174
 - , type 172

S

- S/N (*see signal to noise ratio*)
- Sable Island 198
- Sable Offshore Energy Project (SOEP) 195
- Safe Shipping Clearance 327
- Salcombe 190
 - , cannon site 389

- , volume 174
- , ice, Arctic 212
- , lane, surveillance 326
- , mine 326, 355
- , noise 32
- , surface 32
 - , image 4
 - , gravity deformed 64
- , traffic, noise spectrum 449
- , water 22
 - , density 22
- , waves, air intrusion 287, 300
- search
 - , acoustic 355
 - , line 358
 - , stripe 358
- sediment
 - , bedform 167
 - , characteristics 297
 - , echosounder
 - , conventional 55
 - , parametric 162
 - , echosounding 52
 - , resolution 53
 - , fan 155, 161
 - , gaseous 263
 - , identification 48
 - , layer, liquefied 161
 - , penetrating echosounder 19
 - , penetration 53
 - , pond 298
 - , shoal 326
 - , strata, bifurcation 166
 - , structure 53
 - , surface reflectivity 292
- seismic
 - , sounding
 - , receiver 55
 - , source 55
 - , tomography 139
- seismics
 - , reflection 290
 - , refraction 290
- seismology 31
- self noise 38
- Selsey, Bill 385
- Serrata-Carboneras Fault 235
- shadow 49
- Shamrock Channel 155
- shear wave 31
- sheerness 383
- shelf 145
 - , canyon 161
 - , continental 8, 145
 - , formations 248
- ship
 - , motion compensation 46
 - , traffic 32
 - , noise 32
 - , vertical axis 46
- shore protection 370
- Sicily-Malta Escarpment 234
- sidescan
 - , echosounder 19, 48, 49
 - , long-range version 52
 - , sound irradiation 49
 - , transducers 50
 - , sonar 367
- signal
 - , bio-acoustic 38
 - , hydroacoustic 27
 - , length 43
 - , onset phase 287
 - , phase 46
 - , seismic 27
 - , to noise ratio (S/N) 32, 35, 39
 - , transmission 19
 - , one way 19
- Signal-Gesellschaft, Kiel 16
- Simeulue Island 114
- size, acoustic 307
- Sjælland 255
- Skagerrak 252
- slide 159
- slip face 170
- slope, continental 8, 145
- SMS (*see vessel/ship*)
- Snell's law 23, 443
- SOEP (*see Sable Offshore Energy Project*)
- Sofar
 - , -axis 275
 - , depth 25
 - , -channel 24, 26, 27, 234, 275, 281
 - , -location 24
 - , map 25
- sonar
 - , sidescan, towed 403
 - , equation 35, 39, 448
 - , target strength 307
 - , horizontal 304
 - , synthetic aperture 359
- sonogram 316, 319
 - , voice s. 316
- sound
 - , absorption 25, 27, 304
 - , frequency dependence 30

- , attenuation 27, 444
- , beam 28
- , carpet 26
- , channel 24
- , ducted propagation 444
- , fixing and ranging (Sofar) 24
- , frequency 29
- , generation by rain 34
- , image 3
 - , colorless 30
 - , minimum size of an object 30
- , imaging 6, 48
 - , optimization 35
 - , type 44, 56
 - , under ice 212
- , intensity 444
- , negative pressure 44
- , non-directional source 28
- , one-way transmission 28
- , pressure 31, 53
- , propagation
 - , computation 24
 - , ducted 23
 - , horizontal 23
 - , in air 33
 - , in sea 32
 - , saw-tooth-like 53
- , range limitation 26
- , refraction 23, 26, 443, 444
 - , in air 33
- , resolution limit 29
- , scatterer 31
- , signal 289
 - , length 35
 - , spectrum 35
- , speed 22, 443
 - , at Sofar-axis depth 26
 - , change 24
 - , dependence on pressure 22
 - , dependence on salinity 22
 - , dependence on temperature 23
 - , horizontal components 23
 - , in sea water 22
 - , profile 24
 - , regional variability 23
- , ultrasonic 43
- , wave 31, 55
 - , penetration depth 9
- sounding
 - , multi aspect 52
 - , sea floor 15
 - , seismic 55
 - , receiver 55
 - , source 55
- sources, climatological 276
- South America 71, 405
- South American Plate 145, 219
- South Atlantic 25
- South China Sea 140, 142
- South Greenland 77
- South Kauai Debris Avalanche 84
- South Pacific 10, 80
 - , Rise 71, 119, 120, 216
- South Pole 67, 79
- South San-Hsian Canyon 143
- South Sandwich Trench 79, 116
- Southern Chilean Margin 99
- Southern Hemisphere 121
- Southern Ocean 79, 116, 218, 228
- Southern Okinawa Trough 140
- Southern Tropic 228
- Soviet Union 202
- Spain 236
- spectrometry, acoustic 300
- speed
 - , components 450
 - , measuring sensitivity 58
 - , sound 15
 - , resolution 58
 - , slow 58
- sperm whale 316
- Spitsbergen 202
 - , Deep 206
 - , Fracture Zone 206
- sprat 313
- spreading
 - , center 117
 - , geometrical 449
 - , loss 28
 - , ridge 86
 - , zone 221
- Sri Lanka 114
- SS (*see vessel/ship*)
- state, gaseous 293
- Stavanger 190
- Stockholm Archipelago 260
- Storegga Slide 146-151, 159, 240, 414
 - , secondary effects 150
- Strait of
 - , Georgia 198
 - , Gibraltar 134, 145, 234, 235, 281
 - , outflow monitoring 281
 - , Messina 13, 234
- streamer 55
- strike slip fault 86, 114, 129, 238
- striped dolphin 316

- Stromboli 133, 134, 234
 Sturm, J.K.F. 15
 sub-bottom profiling 52
 Sub-Committee on Undersea Feature Names (SCUFN) 66
 subduction 142
 -, Marianas-type 106
 -, zone 86, 129
 -, tectonic processes 85
 submarine 399
 -, HMS A1 (wreck) 385
 -, S13 352, 354
 -, U166 (wreck) 403, 404
 -, U507 403, 405
 Suederelbe/Koehlbrand 340
 Sula Reef Complex 176
 Sulawesi Basin (*see Celebes Basin*)
 Sulu Basin 111
 Sumatra 75, 112, 114
 Sunda Trench 75, 114
 superconductivity, acoustic 23, 25
 surface, equipotential 65
 surveillance 326, 335, 340
 -, program 326
 SV (*see vessel/ship*)
 Svalbard 205
 swatch of no ground 162
 swath width 49
 Sweden 190, 251, 252
 Sylt 372
 synthetic aperture 361
 -, sonar 359, 360, 361
-
- T**
- Taitung
 -, Canyon 143
 -, Trough 143
 Taiwan 140
 Talamanca Cordillera 90
 target strength (TS) 448
 Tasmanian Seamounts 137
 TCG Cubuclu 242
 technology, multibeam 18
 tectonic
 -, erosion 87, 92, 93, 97
 -, plate, geodynamics 85
 -, theory 4
 Tekirdağ Basin 243, 244
 Tel Aviv 249
 temperature 22
 -, anomaly 23
 -, large scale measurement 279
 -, local 276
 -, profile, remote sensing 59
 Tenerife 153, 154
 Thames Estuary 383
 The Gully 194
 theory of tectonic plate 4
 thermistor 59
 thermometry, acoustic 23
 Tibetan Plateau 161, 162
 tidal flow 168, 282
 time delay 46
 Timor 75, 112
 Titanic 15, 390
 TMF (*see trough mouth fan*)
 Tobi (sidescan echosounder) 52
 tomography
 -, acoustic 19, 59, 274, 281
 -, seismic 139
 Tonga 73
 -, Trench 73
 towed fish 49
 tracking, acoustic 60
 trade winds 26
 Trænadjupet 152
 -, Slide 147, 151
 traffic noise 32
 Transantarctic Mountains 228
 transceiver 277
 transducer 42
 -, cavitation 44
 -, electromagnetic 15
 -, LZT- 43
 -, resonance 43
 transect 307
 transform fault 86, 129
 transmitter, acoustic 42
 transport, mass 266
 trench
 -, Chile-type 106, 109
 -, Marianas-type 109, 110
 -, roll-back 102
 Trevelyan Escarpment 155
 Trinidad 405
 trough 236
 -, Mouth Fan (TMF) 159, 161
 TS (*see target strength*)
 tsunami 113, 147
 -, giant 114
 turbidite flow 161
 turbidity current 155
 Turkey 134, 242
 two line array 47
 Tyrrhenian Sea 134, 135, 234, 237
 -, features 237

U

U166 (wreck) 403, 404, 407, 409–413
 U507 403, 405
 ultraviolet radiation 10, 448
 uncertainty relation 448
 underwater archaeology 374
 United Kingdom 146
 United Nations Comprehensive Test Ban Treaty (CTBT) 24
 unmanned underwater vehicle (AUV) 228
 Upper North Sea Fan 156
 USS (*see vessel/ship*)

V

Valencia Basin 236
 Vancouver Island 198
 Venice 343
 vessel/ship
 –, Atalante (survey vessel) 156
 –, CP 875 (survey vessel) 134
 –, FFK Solea 311
 –, FFS
 –, Victor Hensen 176
 –, Walther Herwig III 309, 313
 –, MB Rosslau (vessel) 335
 –, MS
 –, Deneb (vessel) 257
 –, Explora (vessel) 217
 –, MV
 –, Genesis 398
 –, Geo Scanner 189, 190
 –, Geodetic Surveyor 406
 –, Line 382
 –, Revisor 199
 –, NRV Alliance (vessel) 323
 –, RRS
 –, Charles Darwin 123, 148, 150, 153, 157
 –, James Clark Ross 181
 –, RV
 –, Aegaeo 238, 240
 –, Akademik Boris Petrov 209
 –, Akademik Sergey Vavilov 210, 211
 –, Alkor 293
 –, Alliance 361
 –, Atalante 118
 –, Belgica 173, 178, 179, 180
 –, Cornide de Saavedra 236
 –, Deepenschriewer II 340
 –, Deepenschriewer III 340, 343
 –, DIGICON's Geotide 287, 288
 –, Doktor Lubecki 258, 259
 –, Eltanin 82
 –, Gauss 330
 –, Glomar Challenger 282
 –, Heinke 295
 –, Hesperides 236
 –, Hudson 279
 –, Jan Mayen 182
 –, Joides Resolution 282
 –, Kairei 107, 109, 110
 –, L'Atalante 115, 116, 137, 247
 –, Lance 212
 –, Le Suroit 278
 –, Meteor 272, 274, 279
 –, Nadir 118
 –, Ocean Alert 84, 130, 138
 –, Ocean Surveyor 260
 –, Oceania 255
 –, Planet 356
 –, Polarstern 83, 131, 172, 184, 185, 207, 216, 222, 225, 226
 –, Poseidon 278, 279
 –, Professor Shtokman 263
 –, Rig Supporter 408, 409, 411
 –, Seward Johnson 298
 –, Sonne 81, 90, 99, 121, 125, 133, 162, 163, 164, 165, 166, 283, 286, 288, 290, 291
 –, Tangaroa 228
 –, Thetis 237, 349
 –, Vizconde de Eza 183, 235
 –, Witjas 107
 –, Zirfaea 331, 332
 –, SMS
 –, Baden (wreck) 396
 –, Bayern (wreck) 396
 –, Brummer (wreck) 394
 –, Cöln II (wreck) 392, 393
 –, Dresden II (wreck) 392, 393
 –, Karlsruhe (wreck) 395
 –, König (wreck) 391
 –, Kronprinz Wilhelm (wreck) 391
 –, Markgraf (wreck) 391, 392
 –, SS
 –, Alcoa Puritan (wreck) 405
 –, Richard Montgomery (wreck) 383
 –, SV
 –, Coastal Explorer 345
 –, Luen Hop IV 346, 347
 –, Red Fish 375, 378
 –, Scimitar 383, 385, 387, 388, 391
 –, Zirfaea 367, 386
 –, USS
 –, Glennon 400
 –, Meredith 400
 –, Partridge 400
 –, Rich 400

–, Susan B. Anthony 399
 –, Tide 400
 –, VWFS Atair 169
 –, WFS Planet 168, 256, 292, 293, 296, 298, 373
 Vesuvius 378
 Victoria Land 228
 Vienna 15
 Viking
 –, Dike 396
 –, settlement 358
 visible light 8
 Vistula Lagoon 258
 voice, sonogram 316
 volcano 133
 –, mud 178
 –, strombolian 133
 volume, ocean 265
 Vøring Plateau 148, 150, 151
 VWFS (*see vessel/ship*)

W

Washington State 198
 water
 –, anomaly 23
 –, coastal 145
 –, wrecks 348
 –, compressibility 42
 –, depth 22
 –, heat content 266
 –, mass transport 59, 266, 276, 274
 –, neptunian 22
 –, non-linear compressibility 53
 –, sound absorption 25
 wave
 –, breaking 299
 –, compressional 31, 55
 –, electromagnetic, penetration depth 9
 –, internal 12
 –, lee 12
 –, radio 9
 –, secondary 29
 –, shear w. 31
 –, sound 31
 –, penetration depth 9
 wavelength
 –, acoustic, handicap 306, 402

Weddell
 –, James 218
 –, Sea 67, 79, 83, 216, 217, 224, 228
 Wegener Canyon 217, 218
 Werner Bay 201
 Weser River 169
 West Africa 171
 West European Continental Margin 184
 West European Margin 171, 176
 West Gamma (offshore shelter) 330
 West Mariana Ridge 107
 West Spitsbergen Current 207
 western Pacific 245
 Western Ridge 244
 WFS Planet (*see vessel/ship*)
 whistle 322
 Whittard
 –, Channel 155
 –, Ridge 155
 Wilhelm Gustloff (wreck) 348, 351
 Wilkes
 –, Fracture Zone 124, 221
 –, Transform Fault 123
 wind noise, spectrum 449
 wreck 326, 330, 351
 –, aircraft 355
 –, deep-water sound imaging 403
 –, safety clearance 326
 –, sailing ship 350
 –, survey 348
 WSA Dresden 335

X

X-rays 10

Y

Yaeyama Ridge 140, 142
 Yap Trench 107
 Yenisei 208
 Yermak Plateau 206

Z

zebra stripes, magnetic 11, 219
 Zeepipe 367